

**THE
JOURNAL OF
PHYSICS
AND
CHEMISTRY
OF SOLIDS**

**AN
INTERNATIONAL
JOURNAL**

VOLUME 30

NUMBER

SEPTEMBER 1969

Editor-in-Chief

HARVEY BROOKS

Cambridge, Mass.

Associate Editors

H. B. G. CASIMIR

Eindhoven

B. CHALMERS FRAZER

Brookhaven

JACQUES FRIEDEL

Paris

I. M. LIFSHITZ

Khar'kov

PERGAMON PRESS

NEW YORK · OXFORD · LONDON · PARIS

THE JOURNAL OF PHYSICS AND CHEMISTRY OF SOLIDS

Editors

- PROF. HARVEY BROOKS (*Editor-in-Chief*), 217 Pierce Hall, Harvard University, Cambridge 38, Mass., U.S.A.
 PROF. DR. H. B. G. CASIMIR, *N.V. Philips' Gloeilampenfabrieken, Eindhoven, The Netherlands*
 DR. B. CHALMERS FRAZER, *Brookhaven National Laboratory, Upton, Long Island, New York, U.S.A.*
 PROF. JACQUES FRIEDEL, *Laboratoire de Physique des Solides, Bâtiment 210, Faculté des Sciences, 91-Orsay, France*
 PROF. I. M. LIESHITZ, *Physico-Technical Institute, Academy of Science, Yumorskii tupik, Khar'kov, U.S.S.R.*

Editorial Advisory Board

U.S.A.

- E. N. ADAMS, White Plains, N.Y.
 D. ALPERT, Urbana, Ill.
 L. APKER, Schenectady, N.Y.
 J. BAIRDEN, Urbana, Ill.
 D. S. BILLINGTON, Oak Ridge, Tenn.
 R. G. BRICKENRIDGE, Canoga Pk., Calif.
 LEO BREWER, Berkeley, Calif.
 E. BURSTEIN, Philadelphia, Penn.
 J. A. BURLON, Murray Hill, N.J.
 N. CABRERA, Charlottesville, Va.
 G. C. DANIELSON, Ames, Iowa
 G. J. DIENES, Long Island, N.Y.
 J. C. FISHER, Schenectady, N.Y.
 F. G. FUMI, Chicago, Ill.
 H. K. HENISCH, University Park, Penn.
 F. HERMAN, Palo Alto, Calif.
 C. HERRING, Murray Hill, N.J.
 A. R. VON HIPPEL, Cambridge, Mass.
 J. H. HOLLOMON, Washington, D.C.
 W. V. HOUSTON, Houston, Texas
 H. B. HUNTINGTON, Troy, N.Y.
 H. M. JAMES, Lafayette, Ind.
 C. KITTEL, Berkeley, Calif.
 W. KOHN, La Jolla, Calif.
 J. A. KRUMHANS, Ithaca, N.Y.
 A. W. LAWSON, Riverside, Calif.
 H. W. LEVERENZ, Princeton, N.J.
 O. T. MARZKE, Pittsburgh, Penn.
 B. T. MATTHIAS, La Jolla, Calif.
 L. R. MAXWELL, Silver Spring, Md.
 J. E. MAYER, La Jolla, Calif.
 J. W. MITCHELL, Charlottesville, Va.
 E. W. MONTEOLI, Rochester, N.Y.
 D. PINES, Urbana, Ill.

- M. H. L. PRYCE, Los Angeles, Calif.
 G. T. RADO, Washington, D.C.
 H. REISS, Thousand Oaks, Calif.
 J. R. RITZ, Dearborn, Mich.
 A. ROSE, Princeton, N.J.
 R. A. SMITH, Cambridge, Mass.
 R. SMOLUCHOWSKI, Princeton, N.J.
 F. H. SPEDDING, Ames, Iowa
 D. TERNBULL, Cambridge, Mass.
 J. H. VAN VLIET, Cambridge, Mass.
 B. E. WARREN, Cambridge, Mass.
 E. P. WIGNER, Princeton, N.J.
 B. H. ZIMM, La Jolla, Calif.

Canada

- R. E. BURGESS, Vancouver
 W. B. PEARSON, Ottawa

United Kingdom

- M. BORN, Bad Pyrmont
 A. CHARLESBY, Slivenham, Berks.
 W. J. DENNING, Bristol
 F. C. FRANK, Bristol
 H. JONES, London
 A. B. PIPPARD, Cambridge
 O. C. SIMPSON, Baldock, Herts.
 K. W. H. STEVENS, Nottingham
 F. C. TOMPKINS, London

Czechoslovakia

- J. TACE, Praha

France

- E. F. BERTAUT, Grenoble
 J. BOR, Paris

- B. DREYFUS, Grenoble
 A. GUENIER, Orsay
 A. HERPIN, Saclay
 B. JACROT, Grenoble
 LOUIS NIEL, Grenoble

Germany

- ULRICH DEHLINGER, Stuttgart
 R. HILSCH, Göttingen
 G. LEIBERFED, Aachen
 E. MOLIWO, Erlangen
 H. PICK, Stuttgart
 W. WELKER, Erlangen

Israel

- I. ESTERMANN, Haifa

Italy

- F. G. FUMI, Palermo

Japan

- TOSHIOSEKI MITO, Tokyo

The Netherlands

- A. MICHELS, Amsterdam
 G. W. RAUHENAU, Eindhoven

Sweden

- J. O. LINDL, Stockholm
 PER-OLOF LOWDIN, Uppsala

Switzerland

- G. BUSCH, Zurich
 P. SCHERRER, Zurich

U.S.S.R.

- G. S. ZHDANOV, Moscow

Publishing Offices

American Continent: Pergamon Press Inc., Maxwell House, Fairview Park, Elmsford, N.Y. 10523

Rest of the World: Pergamon Press Ltd., 84-86 Malahide Road, Cobdock, Dublin 5

Published monthly. Annual subscription for libraries, research establishments and all other multiple-reader institutions, £60 (\$150.00), private individuals, whose departmental libraries subscribe, may obtain this Journal for their personal use at a reduced price of £6 (\$15.00) per annum, including postage. All subscription enquiries are to be addressed to The Manager, Subscriptions Department, Pergamon Press, Headington Hill Hall, Oxford OX3 0BW, England. Back issues are available, write for Back Issues Price Lists.

Copyright © 1969 Pergamon Press Ltd.

PERGAMON PRESS INC.

MAXWELL HOUSE, FAIRVIEW PARK, ELMSFORD, N.Y. 10523
 HEADINGTON HILL HALL, OXFORD OX3 0BW

FERROELECTRIC ELECTROREFLECTANCE OF GOLD FILMS

Y. ISHIBASHI and H. L. STADLER

Scientific Laboratory, Ford Motor Company, Dearborn, Michigan, U.S.A.

(Received 7 February 1969, in revised form 3 April 1969)

Abstract—The modulation of the reflectivity of gold film deposited on BaTiO₃ was studied as the ferroelectric polarization of the substrate was reversed repeatedly. The fractional modulation of the reflectance, $\Delta R/R$, was measured as a function of the frequency, ν , of the incident light. The positions of anomalies in $(\Delta R/R)(\nu)$ agree with the positions of similar anomalies found previously in the modulated reflectance of an electrolyte-gold interface. This similarity suggests strongly that the $\Delta R/R$ is due to excessive charges induced on the gold.

INTRODUCTION

REFLECTIVITY modulation has been accomplished by several different techniques over the last three years. Since the brief report of the ferroelectric method [1] there has been the electrolyte electric field method [2,3], the piezo-reflectance method [4], and the temperature variation method [5]. The modulated reflection spectra have shown structure not seen in the unmodulated reflectivity. However, their interpretation is not very clear because the details of the band structure of metals (especially the poorly defined metal films commonly used) are not necessarily well understood, compared with those of semiconductors. Although the *electric field* modulation effect is expected to be more direct and simpler to explain than the other two, there is the added complication that this method measures the reflection from a thin film of metal in intimate contact with another material (electrolyte or ferroelectric) which might be changed by the same process that changes the metal film reflectance. This was, in fact, the interpretation of [3] and [6]. Thus, it is interesting to measure the field modulation effect using a ferroelectric and compare the result with that found by the electrolyte method. The common features of the observed spectra derived from these two methods are

most likely due to the inherent modulation of the metal films. The present paper reports the wavelength dependence of the reflectance of thin gold films modulated by the ferroelectric method and compares it to the measurements by Feinleib of the reflectance of gold films modulated by the electrolyte electric field method [3].

EXPERIMENTAL METHOD AND RESULTS

Gold films were evaporated at 10^{-8} Torr. onto BaTiO₃ c plates. The crystals were flux grown and had been etched in boiling H₃PO₄, poled, and carefully washed before the evaporation. Gold was chosen for its chemical stability. Films of 200, 400 and 1000 Å thickness were studied. Monochromatic light, selected by a monochromator from a tungsten or deuterium source, was shown continuously at near normal incidence onto the air side of the gold film to be measured, which reflected the light into a 1P28 phototube. A diagram of the experimental arrangement is shown at the bottom of Fig. 1. A 350 c/s square-wave voltage, applied between the measured gold film and another metal film on the opposite face of the BaTiO₃ crystal, reversed the crystal's ferroelectric polarization, altering the charge induced on the film by $\pm 52 \mu\text{C}/\text{cm}^2$ at each half cycle. In order to make the rever-

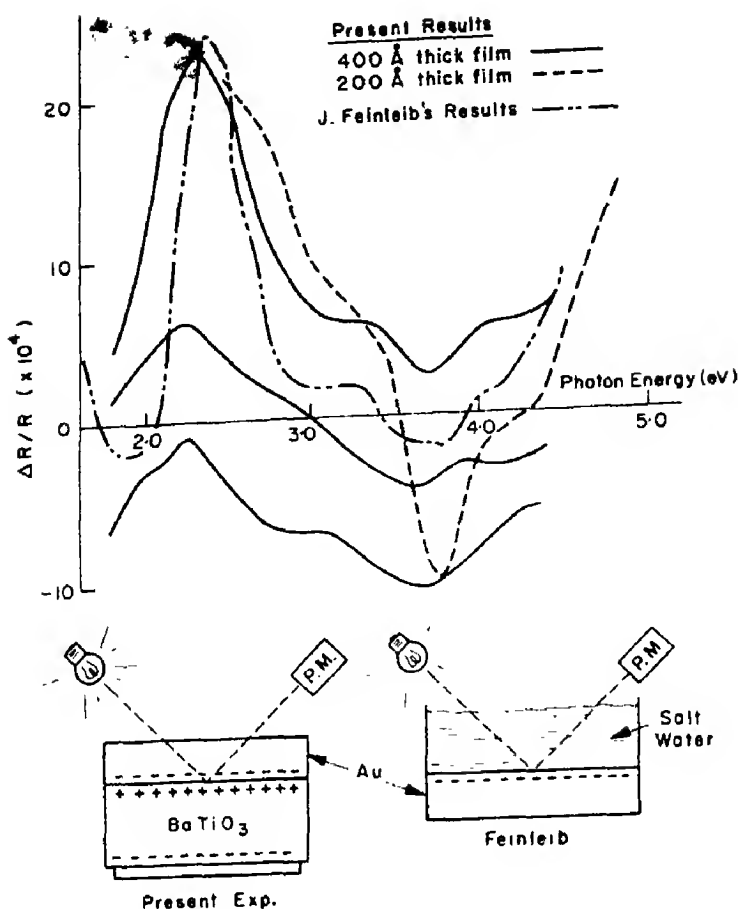


Fig. 1. Relative reflectivity modulation, $\Delta R/R$, of thin gold films due to the polarization reversal of their ferroelectric BaTiO_3 substrates, as a function of photon energy. $\Delta R = R_+ - R_-$, where R_+ is the reflectivity of the film with a positive induced charge and R_- is that of the film with a negative induced charge. The diagrams below the graph compare the experimental arrangements of the present experiment with that of Feinleib[3].

sal time much less than a half-period, about 60 V was applied to the ~ 0.02 cm thick crystals. A phase-sensitive amplifier, using the 350 c/s square wave as a reference, detected the changes in the phototube output which were synchronous with the changes in induced charge on the gold film. This signal, ΔR , divided by R , the unmodulated reflectivity at that wavelength, is plotted as a function of wavelength in Fig. 1, for several 400 Å thick films and one 200 Å thick film. Since the ΔR signal for the 1000 Å thick films was considerably smaller than these, its wave-

length dependence could not be discerned reproducibly through the noise.

The electric field and the induced charge in the gold film are expected to be localized very close to the gold- BaTiO_3 interface, so the light can only be affected if it penetrates the metal film both before and after reflection. Since the attenuation length is about 400 Å, it is plausible that the 1000 Å thick films gave much smaller effects than the 400 Å films. On the other hand, the 200 Å thick films are hard to reproduce. Results were not reported below 2.5 eV for the 200 Å thick films because

they were not sufficiently reproducible from one film to another at those low energies.

In Fig. 1 the modulated reflectivity, $\Delta R/R$, for three different 400 Å films, is shown to have very similar structure, but to differ in absolute value. This type of signal variation was also found by merely moving the spot at which the light was reflected from place to place on the same film. It looks very similar to the difference Feinleib reported between his two apparently similar silver films[3], but is presumably of different origin.

DISCUSSION AND CONCLUSIONS

The results of Feinleib for electroreflectance of a gold film measured by the electrolyte method are also shown in Fig. 1 for comparison. They agree with the present results in the peak at 2.3 eV, the dip at 3.7 eV, and the plateau at 3.0–3.3 eV. These similarities, in spite of the use of an electrolyte (KCl in water) by Feinleib and the use of BaTiO₃ in the present experiment, suggest strongly that the two methods are measuring the same effect, *the reflectivity changes of the gold film*, not, primarily, the electrolyte or BaTiO₃. This indicates that, contrary to previous interpretations[3,6] the excess charges in the ~ 1 Å thick surface[7] of the gold film (next to the BaTiO₃ or the electrolyte) are able to change the reflectivity by the same order of magnitude as the far thicker charged layers in semiconductors[8]. This may mean that the reflectivity depends mainly on the number of electrons/cm² the photon sees, not how deep they are.

One possible spurious effect is the change of reflectivity of the film by stretching caused by the piezoelectric strain of the crystal due to the applied voltage. Since the piezoelectric strain is proportional to the dot product of the field and polarization, it is approximately the same during successive half periods. However, if some of the domains are not reversed or if the reversal time is very different in the two directions, there could be a piezoreflective signal. To estimate an upper limit on

this effect, a d.c. voltage larger than the peak a.c. switching voltage was added to the a.c. to keep the total voltage applied to the crystal always of one sign. This voltage sequence, since it could not reverse the polarization but changed the applied voltage as much from one-half cycle to the next as the usual sequence, created a piezoelectric strain clearly greater (and probably very much greater) than that created by the usual voltage sequence. However, in agreement with an estimate based on the results of Garfinkel *et al.* [9,10] the reflectivity change, ΔR , even in this case was not large enough to observe, thus proving that piezoreflective effects are not contributing observably to the results shown.

There are two principal advantages of the ferroelectric method over the electrolyte method. One is that the electroreflectance can be measured for light which is absorbed by saltwater, such as infrared. A second is that with a suitable ferroelectric substrate, say triglycine sulfate, measurements can be made at low temperatures. Taken together these allow the electroreflectance to be measured over the same wavelength and temperature ranges as the thermal and piezoreflectance, thereby promoting cross comparisons. In fact, a very close comparison of the four modulation methods could be made on a single film on a ferroelectric substrate. The ferroelectric field effect would be measured as described here; the piezoreflectance would be measured by use of simultaneous dc and ac (of amplitude 20–50 times that used presently); the thermal modulation reflectance and electrolyte electroreflectance could be measured as previously reported[3,5]. Such an experiment would have the great advantage of avoiding questions about the reproducibility of thin metal films.

SUMMARY

The modulation of reflectivity of gold films deposited on BaTiO₃ single crystals due to their polarization reversal has been measured

for photons from 2 to 5 eV. The positions of several anomalies in this spectrum agree with those found previously in the modulated reflectance of an electrolyte-gold interface. This similarity suggests strongly that the modulation is due to excess charges on the gold.

Acknowledgements—It is a pleasure to thank Professor M. Cardona, of Brown University, and Dr. J. Feinleib of Lincoln Laboratories, for stimulating suggestions, Dr. J. J. Lambe for suggesting the experiment and for helpful criticisms, W. Vassell and P. J. Zacmanidis for their suggestions and unpublished results, and Dr. T. Kushida and Dr. G. Alers for comments about the manuscript.

REFERENCES

1. STADLER H. L., *Phys. Rev. Lett.* **14**, 979 (1965).

2. SHAKLEE K. L., POLLAK F. H. and CARDONA M., *Phys. Rev. Lett.* **15**, 883 (1965).
3. FEINLEIB J., *Phys. Rev. Lett.* **16**, 1200 (1966).
4. ENGELER W. E., FRITZCHE H., GARFINKEL M. and TIEMANN J. J., *Phys. Rev. Lett.* **14**, 1069 (1965).
5. SCOULER W. J., *Phys. Rev. Lett.* **20**, 445 (1967).
6. CARDONA M., SHAKLEE K. L. and POLLAK F. H., *Phys. Rev.* **154**, 696 (1967).
7. McIRVINE E. C., *Phys. Rev.* **148**, 528 (1966).
8. See also PROSTAK A. and HANSEN W. N., *Phys. Rev.* **160**, 600 (1967); ASPNES D. E., HANDLER P. and BLOSSEY D. F., *Phys. Rev.* **166**, 921 (1968); PROSTAK A., MARK H. B., Jr. and HANSEN W. N., *J. phys. Chem.* **72**, 2576 (1968).
9. GARFINKEL M., TIEMANN J. J. and ENGELER W. E., *Phys. Rev.* **148**, 695 (1966).
10. BERLINCOURT D. and JAFFE H., *Phys. Rev.* **111**, 143 (1958).

THE INFLUENCE OF THE ELECTROLYTE ON THE COMPOSITION OF 'ANODIC OXIDE FILMS' ON TANTALUM*

G. AMSEL, C. CHERKI, G. FEUILLADE† and J. P. NADAI

Groupe de Physique des Solides de l'Ecole Normale Supérieure, Tour 23, 9 Quai Saint-Bernard, Paris 5ème

(Received 26 December 1968; in revised form 24 February 1969)

Abstract—We have studied the influence of the electrolyte on the composition of dielectric films formed by anodic polarisation of tantalum. The electrolytes used were mainly aqueous solutions of salts and acids (H_2SO_4 , H_3PO_4 , HNO_3 , etc.) at various concentrations. A new method of microanalysis of the light elements (O^{16} , O^{18} , N^{14} and D) contained in the films has been coupled with the more classical methods of study (growth rate, capacity measurements, and the use of Redox systems in solution). The absence of large incorporation of elements other than oxygen and tantalum in films formed in aqueous salt solution and very dilute acids has been shown. In films formed in concentrated acids the incorporation of anions of the type Ax Oy^{n-} is so important — 30 per cent of the total number of anions in the case of films formed in 95% H_2SO_4 — that it is no longer possible to consider these films as oxides. The results obtained by deduction from the analysis of oxygen are in good agreement with those obtained from direct analysis for nitrogen. The film properties (rate of chemical attack, dielectric constant, formation field, molar volume etc.) depend on the nature of the electrolyte used for formation.

1. INTRODUCTION

WHILE it has long been known that tantalum can be anodically oxidized in nearly all electrolytes except fluorides [1], the role played by the electrolyte in determining the chemical composition, physical properties and mechanism of formation of the films developed at the surface of the tantalum has not been clarified. The purpose of this article is to point out the new aspects taken by the study of the influence of the electrolyte on film properties, when the classical methods of investigation in this domain (growth rate, capacity measurements, use of Redox systems in solution) are coupled with the techniques of non-destructive nuclear microanalysis of the isotopes of oxygen, nitrogen and other light elements [2–4]. These elements do not have isotopes with radioactive lifetimes long enough to permit the use of radioactive tracing measure-

ments. The nuclear methods used here have been developed in our laboratory and certain of their aspects applied as early as 1962 to the study of anodic oxidation of metals [5].

As the properties of anodic films as well as the oxidation kinetics, are bound to the chemical composition of the film formed, it is essential to solve the problem of the determination of film composition. In the light of the literature (see later) this problem is posed with acuteness, for the massive incorporation of elements other than oxygen contained in the bath has been observed in certain cases. Thus the notion of oxide itself must be submitted to a critical examination; in reality it is preferable to reserve the term oxide for the case where it has been proved that the film contains nothing but oxygen and metal, or where other elements are incorporated only in trace amounts. We will speak of 'anodic films' in the other cases.

The new experimental methods of which we dispose permit in particular the specification of the origin of the oxygen contained in

*Supported by the Centre National de la Recherche Scientifique RCP No. 69–157 and the D.R.M.E.

†Present address: Centre de Recherches C.G.E., 91-Marcoussis.

the films by tracing with O^{18} . Furthermore, the nature and ratios of incorporations when these are important, can be obtained by comparison of the quantities of oxygen determined by nuclear analysis of O^{18} with those equivalent to the ionic charge Q_{ox} passed during formation. Likewise, nuclear methods allow the presence in the films of elements, such as nitrogen, which are unobservable with classical methods of radioactive tracing, to be established directly. We propose in this article to study the connection existing between the growth rate, the nature and quantity of incorporations, and the properties of the films formed in different types of electrolyte. In particular, we have tried to establish whether the incorporation of elements other than oxygen occurs in the form of monoatomic ions or by the intermediary of polyatomic ions of the type $AxOy^{n-}$ originating in the solution. It should be emphasized that in this study only total incorporations are studied, possible non-homogeneities of the films not being taken into account. The electrolytes used were essentially aqueous solutions of salts, acids of various concentrations, and in some cases, anhydrous organic solvents containing different types of solute.

2. LITERATURE SURVEY

In most studies it is tacitly assumed that anodic films are little different in chemical composition from pure tantalum oxide Ta_2O_5 . Nevertheless, as early as 1954 Vermilyea[6] demonstrated a difference in chemical reactivity in HF between oxide films formed in concentrated and dilute acids. In the case of oxidation in 45% and 60% H_2SO_4 he deduces an inhomogeneity of undetermined nature in the thickness of the film. Then again he found a yield, defined as the ratio of the gain in weight of the electrode to the weight of oxygen equivalent to the current passed, greater than 100 per cent. With the aid of radioactive tracers P^{32} and S^{35} Randall *et al.*[7] have shown that the inhomogeneities discovered by Vermilyea are chemical in nature and due

to the presence of sulphur and phosphorus whose concentration in the film depends on the concentration of the sulphuric and phosphoric acids used for formation. Again, in the case of oxidation in H_3PO_4 , they observed a decrease in the dielectric constant of the oxide on increasing the concentration of the acid. Their results on the distribution of impurities in the oxide are, however, in contradiction with the earlier results of Draper[8-9], who proposed a logarithmic distribution of impurities with depth in the film. The results of Randall *et al.*[7], who show that the ratio of the number of moles of phosphorus to the number of moles of tantalum in films formed in 14.7 M H_2PO_4 is of the order of 20 per cent, indicate massive incorporation of elements foreign to the oxide. For his part, in a comparative study of anodic oxidation of various metals, Kover[10] supposes the massive incorporation of protons in the films and the existence of lower valencies of the metals, in order to explain anomalies in the apparent charge of the oxygen ion observed in oxidation in various electrolytes. However, no direct experimental proof has been presented to support these hypotheses.

The influence of the electrolyte and the presence of chemical impurities originating in the solutions are observed in the anodic oxidation of other metals such as zirconium[11, 12], aluminium[13, 14], and niobium[7], and of semiconductors such as silicon[15]. These experiments were performed mainly in dilute acids and only small amounts of incorporation were observed.

Among the numerous investigations on the kinetics of oxidation of tantalum the little information that is available on the influence of the electrolyte is due to Young[16] who showed that the potential necessary for the formation of a film of given optical thickness, at given current density, increases markedly with the concentration of sulphuric acid while the charge necessary for this formation decreases. On the other hand Vermilyea[6] and Young[16] have shown that the product CV

(C = capacity of the film measured in the electrolyte, V = limiting potential of formation of the film) remains almost constant whatever the nature and concentration of the electrolyte. Vermilyea[6] pointed out that the constancy of this product indicates that the superficial charge carried by the interfaces is constant. In consequence, the nature of the electrolyte has little influence on the value of the field ϵE inside the dielectric. Young[16] interprets the ensemble of the results on the kinetics in non-aqueous solutions by a change in oxide structure caused by a decrease in the thermodynamic activity of the water (source of oxygen for the film), and a change in kinetics at the oxide-solution interface. However, Calvert and Draper[18] observed no fundamental changes in the structure of the films which remain amorphous at the temperature of oxidation for all concentrations of the sulphuric acid of formation.

It can be seen that the problem of the origin of the oxygen in anodic films has not been studied in detail. With few exceptions[7, 9, 11] most authors make the tacit assumption that the only source of oxygen is water. In addition, it has until now been difficult to distinguish between the incorporation of substances in the oxide under the form of polyatomic ion of type $A_xO_y^{n-}$, of monoatomic ions, or even of incorporation of the electrolyte itself in the eventual pores or micro-fissures of the oxide [19, 20]. As will now be shown, these difficulties can be overcome by using nuclear methods for the precise analysis for oxygen.

3. PRINCIPLES OF THE EXPERIMENTAL METHODS

(A) *The use of Redox systems in solution for the evaluation of electronic losses in the course of anodic oxidation*

The starting point for any quantitative study of anodic oxidation is the determination of the ratio of the ionic current to the total oxidation current. Gravimetric methods of determining the current efficiency used by Vermilyea[21], assume a priori the chemical

purity of the oxide and a knowledge of its density. In this paper we have used the variation during oxidation of the potential of platinum electrode in a solution containing a Redox system to determine directly the electronic losses, without making any hypothesis on the nature of the oxide.

A known reversible Redox system (Fe^{2+}/Fe^{3+}), capable of absorbing a current of electrons at least equal to the real losses during oxidation, is substituted for the natural Redox (O^{2-}/OH^-) responsible for the electronic losses (Fig. 1). It has been experimentally

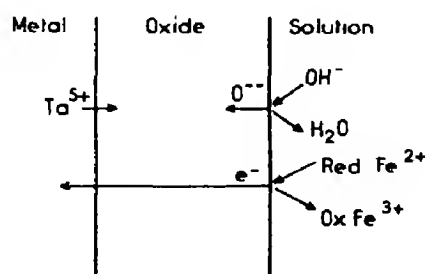


Fig. 1. Charge transfer during oxidation in an electrolyte containing a Redox system in solution.

verified that the introduction of Fe^{2+}/Fe^{3+} at the concentrations used does not perturb the growth rate of the films, which guard their properties.

We have established experimentally that the form of Red used (10^{-3} M/l. Fe^{2+}) presents a limiting current density of oxidation varying between $500 \mu A/cm^2$ on agitation by bubbling with nitrogen, and $50 \mu A/cm^2$ without agitation. These values appear sufficiently large to absorb all electronic losses for oxidation current densities comprised between $0.1 mA/cm^2$ and $10 mA/cm^2$. The variations of Redox potential of a platinum probe can be related, using Nernst's formula, to the quantities of electricity ΔQ due to the electronic losses by:

$$\Delta Q = nFW[Red]_1 \frac{A-1}{A+\mu} \quad (1)$$

$$\text{with } \mu = \frac{[Red]_1}{[Ox]_1} \text{ and } A = 10^{\Delta V/2,3kT/nF}$$

where n is the number of electrons exchanged during the oxidation-reduction reaction, $|\text{Ox}|_i$ and $|\text{Red}|_i$ are the initial concentrations of the oxidized and reduced forms, $\Delta\Psi$ is the variation of equilibrium potential $\Psi_{\text{eq.}}$, and W the volume. The chosen values of the parameters are at ambient temperature: $|\text{Red}|_i = 10^{-3} \text{ M/l}$, $W = 5 \text{ cm}^3$ and $\mu = 20$. Under these conditions a variation of $\Delta\Psi \sim 1 \text{ mV}$ corresponds to $\Delta Q \sim 10^{-3} \text{ C}$. It is known that 1000 \AA of Ta_2O_5 corresponds approximately to 0.2 C/cm^2 , which would correspond to a total oxidation charge of the order of a coulomb in the range of oxidized surfaces studied ($4\text{--}30 \text{ cm}^2$). It can be seen that if a sufficient charge has passed, the sensitivity of the method is excellent, and electronic losses inferior to 1 per cent of the total charge Q_{ox} passed during oxidation can be detected.

(B) Growth rate at constant current density

Let us consider a planar sample of tantalum, surface S , on which is grown a non-porous anodic oxide. Let V be the potential at the terminals of the cell, and I the current density of oxidation, held constant in these experiments. The potential drop in the oxide of geometric thickness x , is V_{ox} . V is the sum of V_{ox} , the potential drop in the electrolyte, and the interfacial overpotentials. At constant I it can be considered that the variations in V are equal to those in V_{ox} : $dV_{\text{ox}} = dV$. The film formation ionic current density is J_{ox} . If the current efficiency is constant, I is constant and hence J_{ox} is constant. This also leads to the field E across the film $E = V_{\text{ox}}/x$ being constant under the condition that the law connecting E and J_{ox} , $J_{\text{ox}} = f(E)$ remains unchanged throughout the whole duration of the process. One therefore obtains, noting that $dV_{\text{ox}} = dx$:

$$\frac{dx}{dt} = \frac{1}{E} \frac{dV}{dt} \quad (2)$$

It must be emphasized that (2) is verified for all the growth laws of the oxide, $J_{\text{ox}} = f(E)$,

(whatever the type of mobile ions, and therefore the form of the relation between J_{ox} and E) to the extent that these remain the same throughout the growth of the film.

Using (2) and Faraday's law, one obtains for a current efficiency of 100 per cent

$$\frac{dV}{dt} = \frac{\omega}{10F} EI \quad (3)$$

where $\omega = M/\rho$ is the molar volume.

If the film composition remains constant during oxidation the gradient of the curve $V = V(t)$ is constant. The other parameters being constant, this gradient is proportional to the molar volume and the field. On the other hand, any deviation from linearity necessarily indicates a change during the process, either of the molar volume or of the relation $J_{\text{ox}} = f(E)$ characterising the growth.

Capacity measurements may give:

$$\frac{d}{dV} \left(\frac{S}{C} \right) = \frac{1}{\epsilon E} \quad (4)$$

a quantity directly accessible to experimental measurement. It is known[22] that the variation of ϵ as a function of frequency between 10^2 and 10^4 Hz is of the order of 1 per cent only. It follows that any variation in ϵ implies necessarily a change in the nature of the film.

The study of $V(t)$ and (S/C) as function of V therefore permits by means of (3) and (4), the experimental determination of ωE and ϵE in various electrolytes whose influence on film properties can hence be illustrated.

The knowledge of the thickness x allows separate determination of ω , E and ϵ . Direct measurements of the geometric thickness (Tolansky, Nomarsky) necessitate mechanical polishing of the surfaces in order to obtain optically plane surfaces. These have not been employed here since mechanical polishing perturbs the oxidation kinetics. It will be shown later what conclusions may be drawn from the measurements described here in the absence of precise information on the thickness x .

(C) Nuclear microanalysis

The method of nuclear microanalysis employed to analyse the constituents of oxide layers consists of direct observation of the charged particles originating from nuclear reactions induced by the beam from a particle accelerator. A detailed account of this method is given in references [2-4].

The quantitative analysis therefore consists of comparing the counting rate, in a conveniently chosen energy range, of particles from the target under study, with those from a standard. The results obtained are completely independent of the nature and structure of the analyzed films or of the substratum. We can thus determine the surface density of the nuclei of O^{16} , O^{18} , N^{14} , etc. . . The essential characteristics of the nuclear reactions used are indicated in Table 1.

dently of the use of standard targets), we have determined the number of O^{16} atoms present in the target from the oxidation charge Q_{ox} , on assuming that the chemical formula of these films is Ta_2O_5 . Knowing that the charge on an oxygen atom in the layer was two electrons, Faraday's law gives 0.312×10^{19} atoms of oxygen 16 per cm^2 for an oxidation charge of 1 C/ cm^2 . To the amount of oxygen deduced from Q_{ox} must be added the number of oxygen atoms present on a metallic plate not oxidized anodically contained in the initial oxide (20 Å to 40 Å).

Nuclear methods give a number proportional to the true quantity of analyzed atoms per unit surface, whatever the roughness of the substratum. To obtain a standard it is sufficient to know the absolute value of this true quantity by weighing or any other method

Table 1. Experimental conditions for nuclear microanalysis

Nucleus	O^{16}	O^{18}	N^{14}	D	S
Nuclear reaction	$O^{16}(d,p)O^{17*}$	$O^{18}(p,\alpha)N^{15}$	$N^{14}(d,p)N^{15*}$ $N^{14}(d,\alpha)C^{12*}$	$D(d,p)T$	$S^{32}(d,p)S^{33}$
Bombarding energy (KeV)	900	730	1270	550	800
Mylar	19 μ	12 μ	19 μ	6 μ	19 μ
Energy of particle at detector (MeV)	1	1.1	3.56 4.62	2.3	6.61
Counting† rates	160	450	43		

†The counting rates are given for a target containing 10^{15} atoms/ cm^2 bombarded with a current beam of 1 μA for 1 mn.

Standard targets were chosen according to the following principles. For O^{16} , tantalum oxide formed in aqueous solutions of salts, more particularly of ammonium citrate, potassium nitrate and sodium chloride was used. As the current efficiency in these conditions is nearly 100 per cent, and the incorporation of impurities in oxides formed in aqueous solutions is negligible (both these results have been established during this work, indepen-

such as coulometric measurements (if the current efficiency and the nature of the film are known). Thus the roughness does not intervene if the absolute value is determined in this way. Nevertheless, it is useful to have standards as smooth as possible ($r \approx 1$) to increase the accuracy of the measurements, the uniformity of the samples being assured.

The standards for O^{18} are oxides of tantalum formed in solutions of water enriched in O^{18}

to a known isotopic concentration and containing very small quantities of a non-oxygenated salt. The isotopic concentration O^{18} in such a target is known with the same precision as that of the water[3].

The absolute precision of the oxygen standards, taking account of the various intervening factors (surface, charge current efficiency, initial oxide layer) is between 3 to 4 per cent. The microanalysis reproducibility was found to be better than 1 per cent.

In the case of nitrogen, the standard target is a thin layer of tantalum nitride obtained by reactive sputtering, whose nitrogen content is determined by destructive chemical analysis[4]. In the actual state of advancement of the work the nitrogen content of the target is known to within 10 per cent.

The detection of deuterium arising from treatments carried out in heavy water, has been used only to prove its absence in certain targets. The reaction serving as analysis, $D(d,p)T$ requires a beam of deuterons. This creates the peculiar situation where the beam itself introduces deuterium into the target. The sample under examination is therefore compared with a sample of the same nature containing a priori no deuterium: if the two samples give identical counting rates the absence of deuterium can be concluded with an upper limit of $3 \cdot 10^{15}$ atoms/cm² calculated from the data of (22).

For sulphur, we have not as yet any convenient standard targets for this nucleus, and no quantitative determination has been made. Radioactive tracing methods are very sensitive for sulphur, and we have been content to compare our results with those given in the literature[7-9].

(D) The use of nuclear microanalysis

After undergoing anodic treatment during which the growth rate was studied, the samples were submitted to nuclear microanalysis. Thus the true total number of O^{16} per cm², N_o16 , contained in the target was obtained. In order to make a comparison with coulometric

measurements the oxygen content of the spontaneous initial oxide layer, which is determined beforehand with precision, must be subtracted from N_o16 . Let N'_o16 be the corrected value thus obtained, due entirely to the anodic treatment. Since the coulometric measurements provide Q_{ox} , a theoretical number of oxygen atoms per cm², N_oq can be deduced on assuming that oxygen is incorporated in the film in the form of divalent ions O^{2-} . Thus a film formation oxygen yield R is defined by:

$$R = \frac{N'_o16}{N_oq}$$

An R greater than unity signifies an average charge per oxygen atom of less than two. This can only be explained if a fraction of the oxygen atoms is incorporated in the form of polyatomic anions, where the charge per oxygen atom is less than two. For example this charge is equal to $\frac{1}{2}$ in SO_4^{2-} , $\frac{1}{3}$ in NO_3^- , 1 in OH^- , etc. On making a hypothesis on the nature of the oxygenated anion in question for a given electrolyte, the fraction of oxygen atoms incorporated in the form of polyatomic anions (or the fraction of polyatomic anions) can be deduced from the value of R (if $R > 1$).

The values of R may be obtained with a good precision as the two main sources of error cancel out. In virtue of the remarks made earlier it can be seen that the roughness factor does not influence the values of R . On the other hand, the absolute error on the standard target drops out also, as the yield may be written:

$$R = \frac{N'_o16}{N'_o16 \text{ aqueous}} \frac{N_oq \text{ aqueous}}{N_oq}$$

Since by definition of the standard target $N_oq \text{ aqueous} = N'_o16 \text{ aqueous}$. Thus R depends in fact on relative measurements and the only errors to be taken into account are related to the non-reproducibility of the results.

With a view to determining the origin of oxygen in the films, tracing experiments have

been carried out using a salt enriched in O^{18} and dissolved in various concentrations in water*. To increase the precision of the method we have in certain cases used water depleted 30 times in O^{18} content, that is with an O^{18} concentration certainly less than 0.01 per cent. Nuclear analysis for O^{18} in oxide films formed in these solutions allows the proportion of oxygen coming from the salt to be determined. In order that the determination of the source of oxygen be unambiguous, there must be no isotopic exchange between the salt used and water at ambient temperature. The results obtained by Samuel[24] at the Weizmann Institute, showing that isotopic exchange between KNO_3^{18} and water in various oxidation baths is negligible even at $100^\circ C$, lead to the use of KNO_3 enriched 77 per cent in O^{18} .

Such methods cannot be extended to studying the origin of oxygen in acids such as boric acid, or in concentrated acids, where isotopic exchange may be very important at ambient temperature. But work with labelled ammonium citrate, whose isotopic exchange with water is equally reduced[26], is in progress on diverse metals.

4. EXPERIMENTAL

(A) Preparation of the films

The tantalum used was unannealed, of 99.95 per cent purity, and 0.2 mm thick. The samples are rectangles (2 cm² for each face), to which a tantalum wire, 0.5 mm dia. was electrically welded to ensure electrical contact. Traces of copper deposited by the weld electrodes were eliminated during chemical polishing. A special cutting tool was used to obtain geometrically identical samples. In addition, the thin tantalum wire had the advantage that it reduced the influence of the level of the electrolyte on the oxidized surface. The standard samples are usually cleaned with

acetone before being chemically polished for 15 sec in a mixture of 5 vol. of 95% H_2SO_4 , 2 vol. of 53% HNO_3 and 2 vol. of 40% HF. Electrochemical polishing, in a solution of 9 vol. of 95% H_2SO_4 and 1 vol. of 48% HF at 100 mA/cm² during 20 min did not demonstrate a notable influence of the state of the surface on the oxidation. In these two types of polishing it is supposed, after Young[25], that the ratio of the real to the apparent surface is near unity. This allows the use of nuclear analysis in all cases without corrections, since the effect of roughness can be ignored. All acids used during polishing were of high purity. After polishing, prolonged rinsing with deionised and twice-distilled water is necessary to eliminate traces of impurity. The organic solvents, anhydrous salts with natural isotopic concentration, and acids are analytically pure products whose maximum water content is known. Particular care is taken in their manipulation to avoid contact with the ambient atmosphere and absorption of water. Concentrations of the electrolytes are expressed in weight.

When water with an isotopic concentration different from natural (enriched or depleted) is used, particular care must be taken in its manipulation to avoid isotopic exchange with the constituents of the atmosphere (humidity, CO_2)[3]. The particular techniques for manipulating such water will be described in a future article mentioned below. A special 5 cm³ cell[26] was used for the high cost of labelled electrolytes with a sample support described in [27].

Oxidation is carried out at constant current, which can be regulated between 0.1 and 10 mA/cm² until a given limiting voltage is reached. The oxidation charge Q_{ox} is in this case determined by the time of oxidation. The current given by the programmed supply Harrison 6209 B is stable to 1.5 per cent for a variation in output voltage of 100 V. The current variation can be reduced to 0.5 per cent by manual control. The variation of the voltage at the terminals of the cell is continuously recorded.

*All products with non-natural isotopic concentrations of oxygen were provided by the Weizmann Institute (Israel).

A Keithley voltmeter, input impedance 10^{14} ohms, measures the voltage to within 1 per cent. To avoid the u.v. effects described in [28], oxidation is carried out in darkness. Typical conditions for oxidation are $T = 27.5^\circ\text{C}$ with $0.5 \text{ mA/cm}^2 < I < 2 \text{ mA/cm}^2$. After oxidation the samples are rinsed and conserved in high purity acetone. Capacity measurements are made at 1590 Hz in a 40 per cent solution H_2SO_4 by means of a Wayne Kerr measuring bridge. The chemical reactivity of the oxides is studied in a solution of 300 g $\text{NH}_4\text{F/l.}$ of HF , as used by Pringle [29]. The addition of ammonium fluoride to the hydrofluoric acid reduces the speed of dissolution of the oxides formed in aqueous solution to $62 \pm 3 \text{ \AA/min}$ at 27.5°C , while in pure hydrofluoric acid it is of the order of 1200 \AA/min [6]. The bath used for dissolving is regulated to within 0.25°C . To avoid inhomogeneities in chemical attack, the samples are agitated gently during the dissolution.

(B) *The use of the Redox systems*

The measurement of current efficiency by means of Redox systems necessitates the use of a cell with separated anode and cathode compartments, connected by a capillary tube whose resistance ($\sim 10^4 \Omega$) imposes a current flow of less than a few mA. A second cell encloses the reference calomel electrode and the potential of a platinum probe immersed in the anode compartment is measured with respect

to this electrode by means of a high impedance electronic millivoltmeter. For high intensities the separation of the compartments is given up; a cathode of small surface area ($< 1 \text{ mm}^2$) is chosen in order to easily reach the limiting current for reduction of the oxidised form Fe^{3+} which, in addition, is maintained at very low concentration ($\mu = \text{Fe}^{2+}/\text{Fe}^{3+} = 20$). Contamination of the bath by evolved H_2 is avoided by placing the cathode very near the surface of the liquid. To improve the sensitivity of the method we have used samples of standard dimensions and samples having large surfaces (30 cm^2) obtained by coiling a wire.

5. EXPERIMENTAL RESULTS

(A) *Determination of current efficiency*

Measurements have been carried out in three aqueous solutions (0.5 per cent ammonium citrate, 1 N H_2SO_4 and 0.01 N H_2SO_4) at different densities of oxidation current (from 0.1 mA/cm^2 to 7 mA/cm^2), and for chemically polished electrode surfaces varying between 4 and 30 cm^2 . In Table 2 we have indicated the electronic losses expressed as a percentage of the total current for different values of the density of oxidation current, and for different values of Q_{ox} . It can be seen that current efficiency is at least 99 per cent for oxidation in aqueous media. It should be noted that no gaseous oxygen appears at the anode during film formation, in accordance with the ob-

Table 2. Determination of electronic losses during anodic oxidation

Electrode area cm^2	Current density mA/cm^2	Electrolyte	Q_{ox} C/cm^2	Electronic losses (per cent)
30	1	0.01N H_2SO_4	0.16	0.1
30	1	0.01N H_2SO_4	0.34	0.4
30	0.1	0.01N H_2SO_4	0.1	0.25
30	0.1	0.01N H_2SO_4	0.3	0.3
4	7	0.01N H_2SO_4	0.3	0.05
30	0.1	1N H_2SO_4	0.3	0.45
30	1	0.5% ammonium citrate	0.1	0.1
30	1	0.5% ammonium citrate	0.3	0.15

servations of Young[17]. With tantalum polished mechanically but not chemically the electronic losses are not reproducible and are of the order of several per cent of the total oxidation current. In this case bubbles of oxygen appear at the anode.

For oxidation in non-aqueous media Redox systems cannot be used because they are irreversible. To determine the current efficiency we have attempted to estimate the electronic losses, which can cause evolution of oxygen at the anode on simulating such evolution with an anode which is not oxidisable (platinum). In all the media studied, film formation takes place without evolution of bubbles at the anode. To improve the sensitivity of the measurement, the oxidation charge Q_{ox} was increased by using sintered or rolled tantalum anodes with large surfaces (400 cm^2). Here again the absence of evolved gas indicated that the electronic losses are indeed less than a few per cent.

Although these results are less precise and more difficult to make quantitative than those obtained with Redox systems, they constitute nevertheless a rather convincing indication that the current efficiency can be assumed to be very near to unity in non-aqueous media. This assumption will be made in the present article.

(B) Influence of the nature of the electrolyte on growth rate and physical properties

(1) *Aqueous solutions of salts* (concentration between 0.5 per cent and saturation). In this type of electrolyte the increase of the potential is a linear function of time in accordance with equation (3), and for a given oxidation current density, the gradient dV/dt is independent of the nature and concentration of the solute. At 27.5°C $dV/dt = 20.3\text{ V/min}$ at 1 mA/cm^2 . The optical thickness, capacity and oxygen content of the oxide obtained for a given J_{ox} , and given limiting potential remain independent of the solute used and its concentration.

(2) *Acids* (H_3PO_4 , H_2SO_4 , HNO_3 ,

HCOOH). With this type of electrolyte the following effects are observed: The potential $V(t)$ is no longer a strictly linear function of time when the acids used are at high concentration (95% H_2SO_4 ; 98% HCOOH). In Fig. 2 the variation of $(V(t) - V_0)/t$ is plotted as a function of time for oxidation at $1\text{ mA/cm}^2 \cdot V_0$

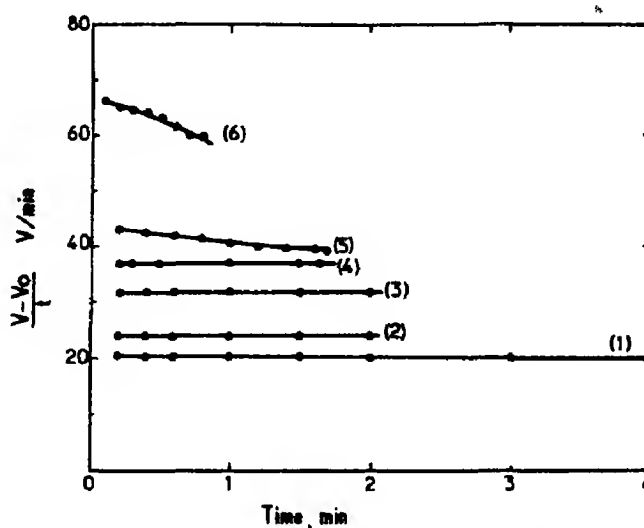


Fig. 2. Variation of $V - V_0/t$ as a function of time in different electrolytes. Current density for oxidation $J_{ox} = 1\text{ mA/cm}^2$. (1) Aqueous solutions of salts, 1% H_2SO_4 , 53% HNO_3 , 1% HNO_3 dimethyl sulfoxide + KNO_2 . (2) 93% HNO_3 . (3) 85% H_3PO_4 . (4) 80% H_2SO_4 . (5) 98% HCOOH . (6) 95% H_2SO_4 .

is the initial potential drop. The deviation of $V(t)$ from linearity is specially marked for 95% H_2SO_4 . However, even in this case, the variation of dV/dt from the beginning to the end of the oxidation is not greater than 10 per cent, and becomes negligible in 80% H_2SO_4 , 85% H_3PO_4 , and in more dilute acid solutions. The average slope (defined as the average of the slopes at the beginning and end of oxidation), increases with acid concentration. Figure 3 shows the variation of average slope with the concentration in weight of H_2SO_4 . The lower limit corresponds to the slope dV/dt obtained for aqueous solutions of salt. For oxidation in very dilute H_3PO_4 (1 per cent) the value of $dV/dt = 22.6\text{ V/min}$ at 1 mA/cm^2 is however slightly greater than dV/dt in aqueous solutions. As for the physical properties, it is

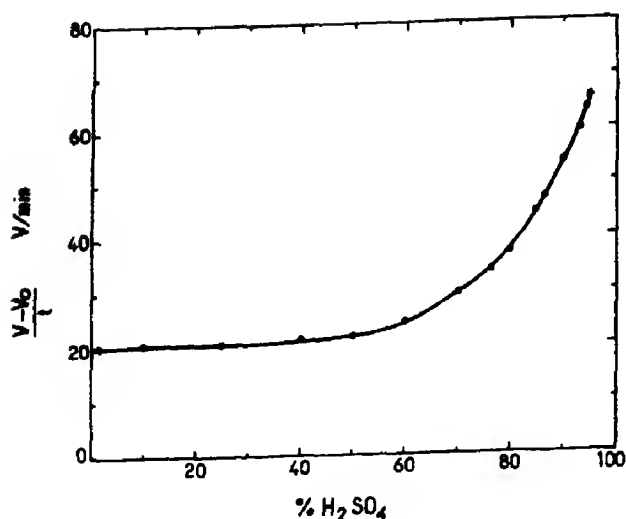


Fig. 3. Variation of the average $V - V_0/t$ as a function of concentration in weight of H_2SO_4 . Current density of oxidation $j_{ox} = 1 \text{ mA/cm}^2$.

established by observation of interference colours of the films, that the optical thickness (nx where n is the refractive index) of anodic films formed in concentrated acids, is less than that of film formed at the same current density and limiting potential in aqueous solutions. This effect becomes very clear for H_2SO_4 concentration greater than 50 per cent, that is about the concentration where the growth rate deviates markedly from the rate in aqueous solution. For example, an oxide formed at 50 V in 95% H_2SO_4 has the same optical thickness as an oxide formed in aqueous solution at 31 V and at the same current density.

The capacity measurements confirm the observations of Vermilyea[6] and Young[16] who found that the product CV remains approximately constant at constant current density whatever the electrolyte used for formation. In Fig. 4 S/C is plotted as a function of the limiting potential of oxidation, straight lines are obtained whatever the electrolyte used. According to equation (7) this implies that ϵE is constant during oxidation. The curves of S/C against V are almost the same for the different electrolytes except for

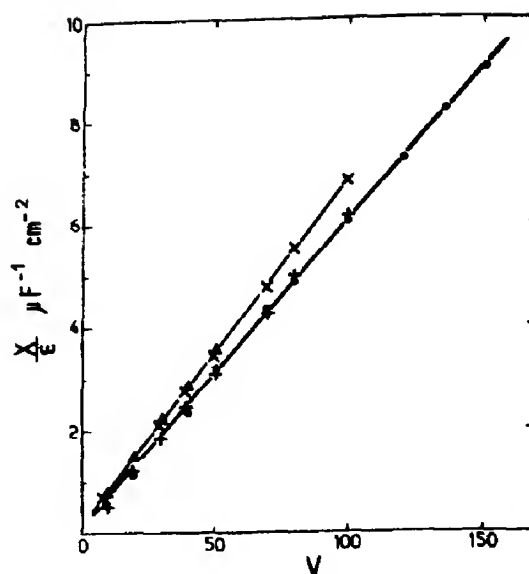


Fig. 4. Dielectric thickness (X/ϵ) of films formed in various electrolytes as a function of the limiting potential of oxidation. $J_{ox} = 1 \text{ mA/cm}^2$. ● Aqueous solutions of salts and dilute acids, + 93% HNO_3 , ▲ 95% H_2SO_4 , × 85% H_3PO_4 .

95% H_2SO_4 and 94% HNO_3 where the slope is slightly greater.

The speed of chemical attack in the mixture NH_4F-HF depends on the nature and concentration of the acid. At 27.5°C it varies from $62 \pm 3 \text{ \AA/min}$ for oxides formed in aqueous solution or very dilute acids, to about 500 \AA/min and 120 \AA/min for films formed in 95% H_2SO_4 and 80% H_2SO_4 respectively. In the latter cases the velocity of attack is no longer strictly constant.

(3) *Organic anhydrous solutions containing various types of solute.* The organic solvents used, dimethyl sulfoxide ($\epsilon = 48.9$), dimethyl formamide ($\epsilon = 36.7$), aceto-nitrile ($\epsilon = 36.2$), were chosen for their large dissolving power and their low water content: 0.1 per cent. The anhydrous salts used were dissolved to saturation point.

The following observations were made: tantalum is oxidized in the absence of water only when salts with oxidizing anions (nitrite, bichromate, permanganate) are used; in the presence of stable anions (SO_4^{2-} , NO_3^- , PO_4^{3-} , Cl^-) oxidation occurs only when water

is added. The breakdown potential increases with the quantity of water added to the solvent; for oxidation in organic solutions containing oxidizing anions or water at a concentration > 3 per cent, the increase of V as a function of t is linear. The slope dV/dt is the same as that for oxidation in aqueous solution (20.3 V/min at 1 mA/cm²), and the films obtained have the same physical characteristics; when the solute is a concentrated acid (95% H₂SO₄) the average value of the slope dV/dt depends on the absolute concentration of the acid in the solvent and on the nature of the solvent. At low total concentration (2% SO₄H₂ at 95% in volume in dimethyl sulfoxide), the value of the slope, 23.3 V/min at 1 mA/cm² is close to that obtained in aqueous solution. The slope increases with absolute concentration of acid in the solvent. In parallel the optical thickness decreases for the same oxidation current and limiting potential, and the rate of chemical attack increases.

(C) *Origin of oxygen in films formed in aqueous solutions of salts*

The origin of the oxygen was sought in aqueous solutions of KNO₃ at concentrations varying between 0.5 and 5 per cent. The salt was enriched to 77 per cent in O¹⁸ and the water depleted 30 times. The ratio of the O¹⁸ content of the salt and the solvent was thus about 1.1×10^4 . Measurements showed that at all concentrations the quantity of oxygen originating in the salt is negligible; it is therefore the same for the incorporation of NO₃⁻. In fact the O¹⁸ content in the layers was evaluated at 0.8×10^{-4} , the water depleted 30 times corresponding to 0.7×10^{-4} . Given the lack of precision of the determination of the depletion (measured by mass spectrometry), a conservative estimation shows that less than 2×10^{-5} of the oxygen atoms in the film come from the salt.

It is observed that the counting rate due to the reaction O¹⁸(p, α)N¹⁵ in a layer formed at 1 mA/cm² up to 100 V in an enriched KNO₃ solution (5 per cent) is only about three times

greater than the counting rate of a non-oxidized tantalum plate. This corresponds to the O¹⁸ content of the natural oxide film, ($\approx 30 \text{ \AA}$) whose isotopic composition is normal (0.204% O¹⁸). The correction due to this initial film was therefore very important. It can be made by subtraction since experiments have shown that the oxygen present in the thermal layer before oxidation remains there afterwards. These results illustrate the extreme sensitivity of nuclear methods combined with the use of greatly depleted water.

(D) *Influence of the nature of the electrolyte on the oxygen yield*

In this study films were formed at a current density of 1 mA/cm² and up to a predetermined limiting potential of oxidation V . In Figs. 5 and 6 we have plotted the variation of Q_{ox} and N'_016 with V for different types of electrolyte. The following remarks can be made: the variation of S/C , Q_{ox} and N'_016 with V is linear

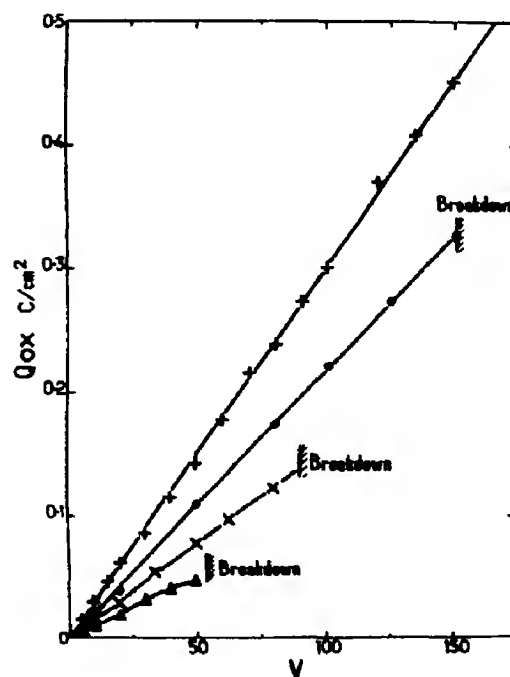


Fig. 5. Charge Q_{ox} required for formation of films in various electrolytes as a function of the limiting potential of oxidation $J_{ox} = 1 \text{ mA/cm}^2$. + Aqueous solutions of salts and dilute acids, ● 93% HNO₃, × 85% H₃PO₄, ▲ 95% H₂SO₄.

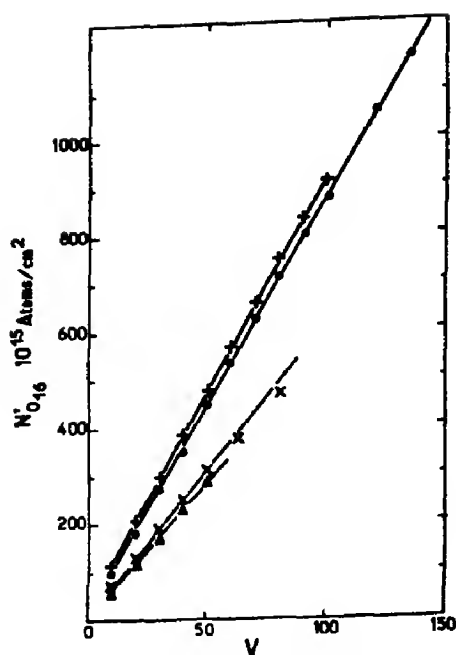


Fig. 6. Number of oxygen atoms contained in the films formed in various electrolytes, as a function of the limiting potential of oxidation. $J_{ox} = 1 \text{ mA/cm}^2$. \bullet Aqueous solutions of salts and dilute acids, $+ \text{HNO}_3$ 93%, $\Delta \text{H}_2\text{SO}_4$ 95%, $\times \text{H}_3\text{PO}_4$ 85%.

in all the electrolytes studied except 95% H_2SO_4 . In the last case the relation between Q and V is no longer strictly linear, this being a direct consequence of the variation of dV/dt during film formation at constant current. For films formed in aqueous solutions of salts the slopes of $Q_{ox}(V)$, $N'_{O_{16}}(V)$ are independent of the nature and concentration of the salts. When the electrolyte is a concentrated acid, on the contrary, the slopes do depend on the nature and concentration of the acid. For very dilute acids the slopes are the same as in aqueous salt solutions.

In Table 3 the oxygen yields for films formed at 1 mA/cm^2 and 50 V are shown for a great variety of electrolytes (concentrated and dilute acids, aqueous solutions of salts, dimethyl sulfoxide + KNO_2). It is clear from this table that the yield R increases with acid concentration, and on the other hand that aqueous solutions of salts, very dilute acids and organic solutions containing an oxidizing

Table 3. Determination of oxygen yield†

Electrolyte	$N'_{O_{16}}$	$N'_{O_{16}}/q_{\text{aqueous}}$	R (per cent)
	$N'_{O_{16}}/q_{\text{aqueous}}$	$N'_{O_{16}}$	
95% H_2SO_4	0.657	2.855	187
N/10 H_2SO_4	1	1	100
85% H_3PO_4	0.694	1.855	129
70% H_3PO_4	0.897	1.324	119
N/10 H_3PO_4	0.998	0.994	99
93% HNO_3	1.04	1.26	131
50% HNO_3	1.13	0.978	104
N/10 HNO_3	1.01	0.985	99.5
Dimethylsulfoxide + KNO_2	1.02	1.01	103
Aqueous solution KNO_3 5%	1.01	1.01	102
Aqueous solution ammonium citrate 0.5%	1	1	100

† Conditions of formation of the films $J_{ox} = 1 \text{ mA/cm}^2$; $V = 50 \text{ V}$.

salt, have equivalent yields R . Taking into account the errors in

$$\frac{N'_{O_{16}}}{N'_{O_{16}}/q_{\text{aqueous}}} \quad \text{and} \quad \frac{N_{O_{16}}/q_{\text{aqueous}}}{N_{O_{16}}/q}$$

the absolute accuracy of the measurement of yield can be estimated as 2 to 3 per cent. The influence of the oxidation current density on the values of R is under study.

(E) Direct analysis of incorporated elements other than oxygen

Analysis of nitrogen by the study of particles energy spectra obtained from nuclear reactions in anodic films has been carried out for films formed in 93% HNO_3 , 50% HNO_3 , 10% HNO_3 , in aqueous solutions of KNO_3 at a concentration of 5 per cent, and in organic solutions saturated in KNO_2 . The presence of nitrogen has been established in the case of 93% HNO_3 only. The number of nitrogen atoms in the film increases linearly with the quantity of oxygen, (see Fig. 7, p. 2133) whatever the current density for oxidation (between 1 mA/cm^2 and 10 mA/cm^2). On comparing with the standard target of tantalum

nitride known to within 10 per cent an incorporation ratio of 8.75 ± 0.90 atoms of nitrogen per 100 atoms of oxygen is found. This corresponds to an incorporation of $7.7 \pm 0.8 \times 10^{14}$ atoms $\text{cm}^2 \text{V}^{-1}$ for oxidation at 1 mA/cm^2 . For oxidation in 50% HNO_3 , 10% HNO_3 and in the aqueous and organic solutions studied, no nitrogen was observed in the films. The total quantities measured in this case were of the order of 2×10^{15} atoms/ cm^2 corresponding to the traces caused by chemical polishing, detected in a non-oxidized sample of metal. This shows that for these films there is less than one atom of nitrogen per 1500 atoms of oxygen in oxides formed at 100 V.

For oxides formed in 95% H_2SO_4 and 80% H_2SO_4 we have observed nuclear reactions characteristic of sulphur. However, the instability of the standard targets to bombardment makes quantitative analysis imprecise at present.

Analysis by nuclear reaction of deuterium in films formed at up to 100 V in aqueous solutions of D_2O^{18} or in solutions of H_3PO_4 in D_2O^{18} (7 vol. of H_3PO_4 for 3 vol. of D_2O^{18}) have given negative results. Taking account of the limited sensitivity of the detection of deuterium is less than one deuterium atom per 100 oxygen atoms.

6. INTERPRETATION

(A) Growth rates

For oxidation in aqueous solution at constant temperature the ionic current density is related to the electric field by:

$$J_{\text{ox}} = \alpha \exp \beta E \quad (5)$$

where α and β are constants and $\beta E \gg 1$. This law is obtained from the classical theory of ionic conduction in high field for the case of only one type of carrier. The value of dV/dt for given J_{ox} is obtained on combining (3) and (5), which leads to:

$$\frac{dV}{dt} = \frac{\omega}{10F} J_{\text{ox}} \frac{1}{\beta} \text{Log} \frac{J_{\text{ox}}}{\alpha} \quad (6)$$

The constants α and β characteristic of the oxidation of tantalum in aqueous media have been determined by Vermilyea[30] from a study of the Tafel slope. He gives $\alpha (\text{mAcm}^{-2}) = \exp(-32.5)$ and $\beta (\text{\AA V}^{-1}) = 505$ at 27.5°C . Assuming that the film formed is pure Ta_2O_5 , density $\rho = 8.74 \text{ g cm}^{-3}$ then one obtains for $J_{\text{ox}} = 1 \text{ mA/cm}^2$; $dV/dt = 19.8 \text{ V/min}$ and for the differential thickness (which often quantitatively characterises the growth) $dx/dV = 15.6 \text{ \AA/V}$. The experimental values of the growth constants obtained in aqueous electrolytes for $J_{\text{ox}} = 1 \text{ mA/cm}^2$: $dV/dt = 20.3 \text{ V/min}$ and $dx/dV = 15.3 \text{ \AA/V}$, deduced from dV/dt with the same assumptions on the purity and density of the films, are therefore in good agreement with the values deduced from the constants given by Vermilyea.

With two types of electrolyte: aqueous salt solutions and organic solutions containing water, or unstable oxygenated anions, the growth rate, oxygen content, dielectric thickness, optical thickness and chemical reactivity in $\text{HN}_4\text{F-HF}$ are almost identical. The absence of any influence of the solute on the nature and properties of the films tends to prove that the incorporation of anions is small. Thus the oxide developed at the metal surface should be very close to chemical purity. The oxygen entering the film in the form O^{2-} comes either from the hydroxyl ion, or from the unstable oxygenated anions. The absence of O^{18} and nitrogen in films formed in aqueous solutions of KNO_3 enriched in O^{18} , confirms that the incorporation of anions originating in the salt is very small in that case.

For acids the growth rates are strongly dependent on the concentration when this is greater than 40% per cent, in the case of H_2SO_4 , H_3PO_4 , HCOOH , and 80 per cent in the case of HNO_3 , where the acid-water bonds are weaker. Below these concentrations the growth rate and the characteristics of the films formed are almost the same as those for oxidation in aqueous solutions, leading to the supposition that in this case too, the incorporation of anions is small. The analogy

between these two types of film is confirmed by the absence of nitrogen in films formed in HNO_3 at concentrations less than 50 per cent, and is in fact in agreement with the results of Randall *et al.*[7] who, using radioactive tracers, showed that in films formed in 0.1 M H_2SO_4 and 0.01 M H_3PO_4 the incorporation of sulphur and phosphorus amounted to only 5/1000 and 1/100 respectively of the total weight of the film. Such proportions have negligible influence on film properties. The fact that for the same current of formation the average slope dV/dt increases with the acid concentration is, according to (3), due to an increase, with increasing acid concentration, either in the total molar volume of the oxide formed, or in the field of oxidation E . The first hypothesis can be explained by the large incorporation of polyatomic anions (SO_4^{2-} , NO_3^- , PO_4^{3-} , etc...) characteristic of the acid. The possible increase of the field E will be discussed later. It can be pointed out in addition that the variation with time of dV/dt , observed in concentrated acids (95% H_2SO_4), may be caused by the variation with time of the molar volume of the film formed, corresponding to a chemical inhomogeneity in the thickness of the film which agrees with the observation in [6-8]. That the chemical reactivity, i.e. the rate of dissolution of the anodic film, is strongly influenced by the nature and concentration of the acid used confirms the fact that the electrolyte plays an active role in the growth

rate, by changing the physico-chemical nature of the film developed on the tantalum.

(B) *Oxygen yield and the incorporation of anions*

The anomaly in the oxygen yield R for oxides formed in concentrated acids (see Table 3) confirms the hypothesis, deduced from the variation of dV/dt , that there is incorporation of polyatomic ions. The incorporation of protons by way of OH^- ions assumed by Kover[10] seems unlikely. Indeed, the anomaly in the yield R increases, the greater the hydration energy of the acid. This should lead to a reduction in the concentration of free water (i.e. not bound by the solvation of the acid anions and in the coordination spheres of acid molecules). On the other hand, the search for deuterium by nuclear reaction in films formed in deuterated solutions gave negative results. The limit of sensitivity of the method indicates in all cases a concentration of less than one proton per hundred oxygen atoms. Elsewhere, Nannoni[31] confirms the absence of tritium in niobium oxides (which have a behaviour analogous to tantalum oxides) formed in solutions of tritiated water. Thus the anomaly in the yield R would seem to be better explained by the incorporation of anions AxOy^{n-} characteristic of the acid of formation, than by the incorporation of hydroxyl ions. Table 4 gives the number of oxygen atoms $N'_0/16$ determined

Table 4. *Percentage of polyatomic anions with respect to the total number of anions in films formed at 50 V and 1 mA/cm²*

Electrolyte	Total number of oxygen atoms (10^{15} atoms/cm ²)	Number of divalent oxygen atoms to Q_{ox} (10^{15} atoms/cm ²)	Number of oxygen atoms in the anions SO_4^{2-} , NO_3^- , PO_4^{3-} , (10^{15} atoms/cm ²)	Number of atoms of S, N, P (10^{15} atoms/cm ²)	Polyatomic anions (per cent)
95% SO_4H_2	292	156	184	46	30
93% HNO_3	410	313	115	37	10.3
85% H_3PO_4	309	240	104.5	27.5	12.2
70% H_3PO_4	400	336	100	25	7.7

by nuclear reaction, the number of O^{2-} ions equivalent to the oxidation charge Q_{ox} , and the total number of $AxOy^{n-}$ anions deduced from Q_{ox} and $N_0/16$, for various concentrated acids in which the yield is markedly greater than 100 per cent. In H_2SO_4 , H_3PO_4 and HNO_3 , it has been assumed that the only complex anions present are SO_4^{2-} , PO_4^{3-} and NO_3^- respectively. It can be seen that in the case of 95% H_2SO_4 there is more oxygen in the form of polyatomic anions $AxOy^{n-}$ than in the form of monoatomic anions O^{2-} . The quantitative results obtained on oxidation in 93% HNO_3 are important, since they confirm that the hypothesis of incorporation in the form of polyatomic anions is valid in this case. Indeed the total number of nitrogen atoms (7.4×10^{14} atoms $cm^{-2}V^{-1}$) present in the layer determined from Q_{ox} and $N_0/16$, on assuming incorporation in the form of NO_3^- , is close to the number determined directly ($7.7 \pm 0.8 \times 10^{14}$ atoms $cm^{-2}V^{-1}$).

Given the high proportion of polyatomic anions which they contain, the films developed on the surface of tantalum in concentrated acids, may be considered as oxysalts, whose global chemical composition is given by $Ta_2O_{5(1-\gamma)}(AxOy)_{10\gamma/n}$ where γ depends on the acid concentration.

(C) Water dependence of the amount of incorporation

It is clear that the incorporations increase with decreasing water content of the solutions. Nevertheless, it seems that the governing factor for this process is not the simple ratio of the number of anions to that of water molecules in the bath. Rather the hydration energy of the electrolyte seems to be the fundamental parameter determining the amounts of incorporation. In fact, incorporations from acids are observable only at rather low water concentrations, and are more important in H_2SO_4 and H_3PO_4 where the hydration energy is higher than in HNO_3 for an equivalent water concentration. (The energy released in forming an equimolar

mixture of acid and water is twice as high for H_2SO_4 than for HNO_3 [32].) The fact that the hydration energy of the electrolyte is an important parameter is also found in the study of the growth rate in 95% H_2SO_4 diluted in dimethyl sulfoxide or acetonitrile. We have observed that for a given concentration of acid, the growth depends on the absolute concentration of acid in the bath. This dependence seems to be due to the fact that sulphation of the organic solvent changes the bond energy between the acid and water, and this favours the creation in the bath of free water.

(D) Variation of physical values

The variation in chemical composition of films formed in concentrated acids with respect to the pure oxide developed in 'aqueous' or 'oxidizing' media, would seem to be the essential reason for variations in the values characterising these films (molar volume, field of formation, dielectric constant, refractive index). Although the geometric thickness is unknown the quantitative variation of the characteristic values of films formed in 95% H_2SO_4 can be determined, knowing the proportion of sulphur in the film. Assuming that the molar volumes of oxide and sulphate are additive, the molar volume of the sulphate is determined on supposing that the difference in steric hindrance between the SO_4^{2-} and O^{2-} ions is the same for tantalum as for other metals (Cu, Ni, In, Bi). For these metals it is empirically verified that :

$$\frac{V_{sulf.} - V_{oxide}}{\text{Valency of metal}} \approx 30$$

where $V_{sulf.}$ = molar volume of sulphate, V_{oxide} = molar volume of oxide.

If 30 per cent of the anions are SO_4^{2-} (electrolyte 95% H_2SO_4) the density of the layer becomes 5.92 g/cm³ instead of the 8.74 g/cm³ generally quoted for pure Ta_2O_5 . The increase of 95% in the molar volume of the films formed in 95% H_2SO_4 with respect to the molar

volume of films formed in aqueous solution, is not sufficient to explain the observed increase in dV/dt , which is more than 250 per cent. To explain such a variation the increase in E in expression (3) must be considered. Taking into account the variations of dV/dt and the molar volume, the field E for oxidation in 95% H_2SO_4 can be determined as a function of the field E for oxidation in aqueous solution at the same current density. It is found that $E_{H_2SO_4} = 1.77E_{aq. sol.}$

ϵ and E being determined separately, it is found that the product ϵE is constant whatever the concentration of H_2SO_4 used for formation. For oxidation at 1 mA/cm^2 $\epsilon E = 1.75 \pm 0.2 \cdot 10^{18} \text{ V/cm}$. The value of ϵE determined from the product CV given by capacity measurements is $\epsilon E = 2 \pm 0.2 \cdot 10^{18} \text{ V/cm}$. The reasonable agreement between these two values of ϵE justifies the hypothesis used to determine the density and the differential thickness dx/dV at 1 mA/cm^2 for films formed in 95% H_2SO_4 , that is that the molar volumes of the oxide and sulphate of tantalum are additive. It should be noted that this result confirms [6, 16] that the effective field acting on mobile carriers during oxidation (that is the Lorentz field which is proportional to ϵE when ϵ is large), is independent of the dielectric constant of the film developed on the tantalum.

7. DISCUSSION AND CONCLUSION

One of the most important points of our experimental observations is that anodic films formed on tantalum in concentrated acids are not pure tantalum oxide Ta_2O_5 , but have different chemical compositions. In fact for acids of very high concentration the film formation oxygen yield differs greatly from unity, which indicates clearly that foreign elements are incorporated under the form of polyatomic anions. Taking into account that this occurs in large quantities, these incorporations can no longer be considered as traces of impurity, as in the case of films formed in very dilute acids. Apparently above a certain

range of acid concentration the films formed on tantalum are oxysalts, whose exact chemical composition depends on the nature and concentration of the acid. Assuming that the composition of films formed in H_2SO_4 , HNO_3 and H_3PO_4 is $Ta_2O_{5(1-\gamma)}(SO_4)_{5\gamma}$, $Ta_2O_{5(1-\gamma)}(NO_3)_{10\gamma}$ and $Ta_2O_{5(1-\gamma)}(PO_4)_{10\gamma/3}$ respectively, the proportion of polyatomic ions in the films with respect to the total number of ions bound to the tantalum have been calculated from Q_{ox} and $N_0/6$ (Table 4). The hypothesis has been verified quantitatively for the oxynitrate. It can be confirmed from the results of Randall *et al.* [7] on the presence of P^{32} in films formed in 85 per cent (14.7 M) $H_3P^{32}O_4$. We had 5.5×10^{14} atoms of phosphorous per cm^2 per V for films formed at 1 mA/cm^2 in the electrolyte, while from the curves of Randall *et al.* [7], giving the weight of phosphorous in films formed under analogous conditions, the presence of phosphorous can be estimated as between 3 and 4×10^{14} atoms per cm^2 per V. Given the uncertainty in the determination of the absolute value by radioactive tracing, and the fact that the comparison is not made on the same samples, the agreement between the results is satisfactory.

It therefore seems that although decomposition of the PO_4^{3-} ion into PO_3^- and O^{2-} , and consequent oxidation by oxygen arising from this decomposition is possible, these are not the dominant processes. In fact, on assuming incorporation under the form PO_3^- , the quantity of phosphorous in the film calculated from oxygen yields is an order of ten greater than the quantity determined by Randall *et al.* [7]. Nevertheless, in certain cases oxidation by oxygen arising from the decomposition of anions must be considered. Thus Draper [8] explains film formation in a totally anhydrous medium such as 100% H_2SO_4 by the existence of the oxygen liberating action:



It should be noted that decomposition of a fraction of the SO_4^{2-} ions at the anode does not change the oxygen yield and chem-

ical formula of films formed in 95% H_2SO_4 , as only tracer experiments could distinguish between O^{2-} ions coming from water or from SO_4^{2-} . Amsel *et al.* [33] proved, using O^{18} tracing that a similar effect occurs in films formed in solutions of KNO_3 in glycol or N-methylacetamide containing a small percentage of water (≈ 1 per cent). The absence of nitrogen in these films indicated the probable decomposition of the NO_3^- ions. This phenomenon, which could also explain the oxidation of tantalum in organic media containing unstable anions (permanganate, bichromate, etc. . .) is under study.

Earlier work [6–8] showed that films formed in concentrated acids were chemically inhomogeneous. An additional proof of the inhomogeneity of the films formed in 95% H_2SO_4 is given by our observation of a non-linear growth rate at constant current. According to (6) this implies a variation either of the total molar volume, or the relation between the current and the oxidation field. However, the fact that the growth rate is almost constant in the other cases (85% H_3PO_4 , 93% HNO_3 , etc. . .) or that the number of polyatomic ions increases linearly with thickness (Fig. 7) does not necessarily imply

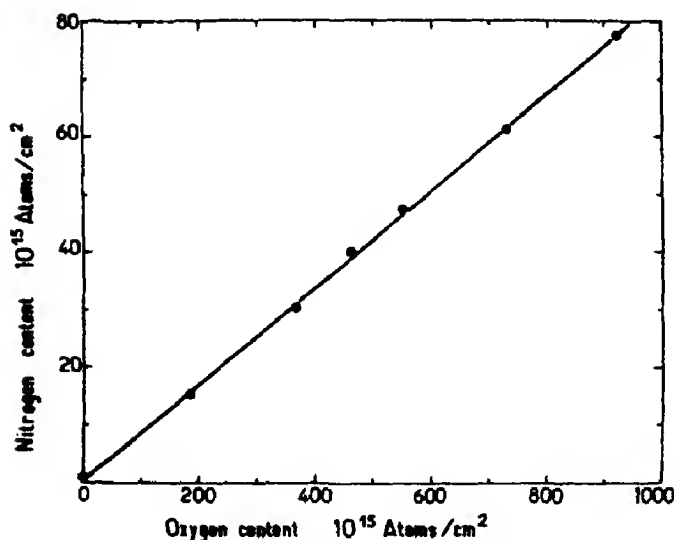


Fig. 7. Nitrogen content as a function of oxygen content for films formed in 93% HNO_3 at various current densities $0.1 \text{ mA/cm}^2 < j_{\text{ox}} < 10 \text{ mA/cm}^2$.

that the films are homogeneous; it means that the mechanism of formation and total molar volume of the film, (i.e. the composition profile) do not change as the thickness increases. This possibility has been discussed by Randall *et al.* [7] who explained the inhomogeneous structure of films formed in concentrated acids by the migration of anions and cations with equivalent transport number. In the next paper of this series the atomic transport phenomena in the film, as related to its composition, will be studied using O^{18} tracer techniques.

Acknowledgements—The authors wish to thank Professor D. Samuel for illuminating discussions on problems related to the use of labelled compounds. They are indebted to J. Rivière for his constant help during the experiments.

REFERENCES

1. GUNTHERSCHULZE A. and BETZ H., *Elektrolyte Kondensatoren*. Krayn. Berlin (1937).
2. AMSEL G. and SAMUEL D., *Anal. Chem.* **39**, 1689 (1967).
3. NADAI J. P., Thesis, Orsay (1967).
4. AMSEL G., BÉRANGER G., BOISOT P. and DAVID F., *Rev. Phys. Appl.* **3**, 373 (1968).
5. AMSEL G. and SAMUEL D., *J. Phys. Chem. Solids* **23**, 1707 (1962).
6. VERMILYEA D. A., *Acta Metall.* **2**, 482 (1954).
7. RANDALL J. J. Jr., BERNARD W. J. and WILKINSON R. R., *Electrochem. Acta* **10**, 183 (1964).
8. DRAPER P. H., *Electrochem. Acta* **8**, 847 (1963).
9. DRAPER P. H., *Acta Metall.* **11**, 1061 (1963).
10. KOVER F., Thesis, Paris (1967); KOVER F. and MUSSELIN M. J., *Thin Solid Films* **2**, 211 (1968).
11. BANTER J. C., *J. electrochem. Soc.* **114**, 508 (1967).
12. ROGERS G. T., DRAPER P. H. and WOODS S. S., *Electrochem. Acta* **13**, 251 (1968).
13. PLUMB R. C., *J. electrochem. Soc.* **105**, 497 (1958).
14. BERNARD W. J. and RANDALL J. J. Jr., *J. electrochem. Soc.* **108**, 822 (1961).
15. SCHMIDT P. F. and OWEN A. E., *J. electrochem. Soc.* **111**, 682 (1964).
16. YOUNG L., *Proc. R. Soc. A* **258**, 496 (1960).
17. YOUNG L., *Anodic Oxide Films*. Academic Press, New York (1961).
18. CALVERT L. D. and DRAPER P. H., *Can. J. Chem.* **40**, 1943 (1962).
19. VERMILYEA D. A., *J. electrochem. Soc.* **110**, 250 (1963).
20. VERMILYEA D. A., *J. electrochem. Soc.* **110**, 345 (1963).

21. VERMILYEA D. A., *Acta Metall.* **1**, 282 (1953).
22. WENZEL W. A. and WHALING W., *Phys. Rev.* **88**, 1149 (1952).
23. CHERKI C., COELHO R. and MARIANI J. L., *Solid State Commun.* **4**, 411 (1966).
24. SAMUEL D., Private Communication.
25. YOUNG L., *Proc. R. Soc. A* **244**, 41 (1958).
26. AMSEL G., *Ann. Phys.* **9**, 297 (1964).
27. FEUILLADE G. and JACOUD R., To be published in *Electrochem. Acta*.
28. BRAY A. R., JACOBS P. W. M. and YOUNG L., *J. nucl. Mater.* **4**, 356 (1959).
29. PRINGLE J. P. S., Private Communication.
30. VERMILYEA D. A., *Acta Metall.* **1**, 282 (1953).
31. NANNONI R. and MUSSELIN M. J., Private Communication.
32. PASCAL P., *Chimie Minérale*. Mason, Paris (1956–1968).
33. AMSEL G., CROSET M. and SAMUEL D., To be published.

ZEEMAN EFFECT OF FREE AND BOUND EXCITONS IN CuCl

M. CERTIER, C. WECKER and S. NIKITINE

Laboratoire de Spectroscopie et d'Optique du Corps Solide, associé au C.N.R.S., Institut de Physique, Université de Strasbourg, France

(Received 29 November 1968; in revised form 20 February 1969)

Abstract—The exciton spectra of CuCl have been investigated in the presence of high transient magnetic fields up to 180 kG.

The Zeeman splitting of the broad orthoexciton line ν_{1f} (25,865 cm^{-1} at 4.2°K) is unresolved because of a too small effective g factor ($g = 0.9$). The paraexciton line ν_1 (25,814 cm^{-1} at 4.2°K) is detected in magnetic field. The mixing of the ortho and paraexciton states Γ_{1s} and Γ'_2 in magnetic fields is discussed.

The bound exciton line ν_2 (25,654 cm^{-1} at 4.2°K) splits in four components in magnetic field, both in absorption and in emission. The sharp line ν_2' (25,665 cm^{-1} at 4.2°K) behaves similarly. The g factors of both the ground and excited states are obtained from the temperature variation between 1.9° and 20°K of the intensities of the absorption lines. This allows us to ascribe the above lines to exciton-neutral acceptor complexes.

1. INTRODUCTION

THE OPTICAL properties of CuCl at low temperatures have been extensively studied[1–4]. Nikitine and Reiss[1] have shown that the spectrum of thin layers of CuCl is composed of two strong lines, one sharp ν_{1f} (25,865 cm^{-1}) and one diffuse ν_{1d} (26,420 cm^{-1}) and a number of weak lines (see Fig. 1). ν_{1f} and ν_{1d} are suggested to be first lines of two different series of exciton lines the sharp and diffuse series. The separation is due to spin orbit splitting. The sharp series is obviously composed of further lines ν_{2f} and ν_{3f} . ν_{2s} and ν_{3s} are suggested by Ringeissen and Nikitine[5] to be vibrational satellite lines. Numerous satellite lines are furthermore observed on the continuum. Some of them have been previously suggested to be lines of higher order of the diffuse series but another interpretation has been suggested recently[5].

Some very weak lines are observed on the low energy side of ν_{1f} . These lines have been named sensitive lines[6] because their observation depends on external factors. Some of these lines are observed in absorp-

tion. Many are observed in emission[7]. One of these lines ν_1 (25,814 cm^{-1}) appears under the action of the magnetic field and has been suggested[7–8] to be a forbidden exciton line. Another line ν_2 (25,654 cm^{-1}) as observed in absorption is probably connected with the formation of excitons bound to defects. In emission, it has been shown[9–10] that the line is probably a superposition of an exciton complex line as stated above and of an emission line combined with an emission of a longitudinal optical phonon.

The aim of the present work is to describe the Zeeman effect of the 1s exciton ν_{1f} and to identify the sensitive lines of the ν_2 group.

We will not be concerned with the other lines of the spectrum of CuCl.

2. THEORETICAL

(A) *Zeeman effect of the 1s exciton ν_{1f}* (25,865 cm^{-1})

The symmetry of exciton states of CuCl, according to the theoretical band structure of Song[11], agrees well with the earlier investigations of Nikitine and Sennett[10]. The extrema of both the lowest Γ_1 conduction

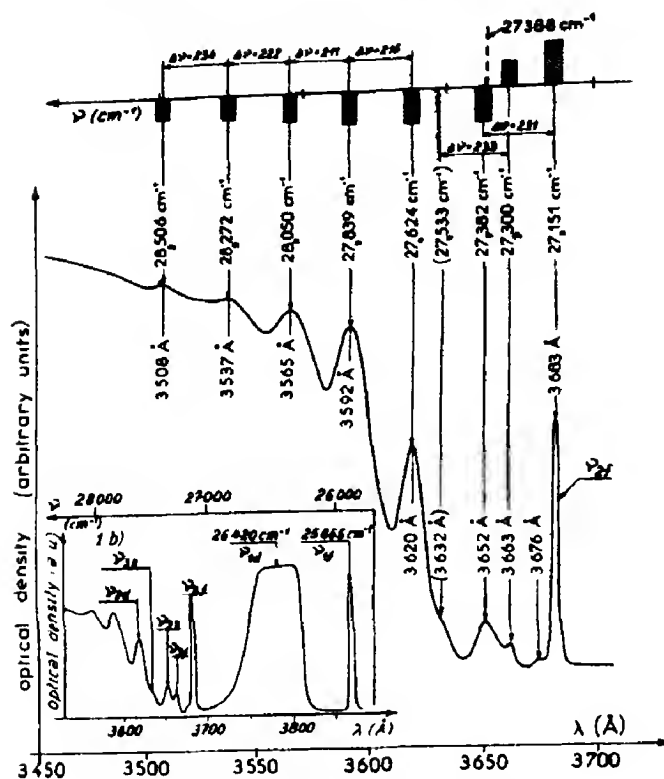


Fig. 1. Absorption spectrum of CuCl at 4.2°K.

band and the highest Γ_{15} valence band occur at $k=0$. Near the fundamental absorption edge, there are two $1s$ exciton lines arising from a spin orbit splitting of the Γ_{15} band giving an upper twofold degenerate Γ_7 and a lower fourfold degenerate Γ_8 band.

The $1s$ exciton built from a Γ_7 hole and a Γ_6 electron is fourfold degenerate giving, in the electric dipole approximation, one allowed transition Γ_{15} and one forbidden transition Γ_2^* .

The splitting between the two Γ_{15} and Γ_2 states shows the magnitude of the exchange interaction between the spins of the electron and of the hole, or in other words, the splitting between the ortho Γ_{15} and para Γ_2 excitons.

In a first approximation, neglecting the paraexciton Γ_2 , the orthoexciton Γ_{15} must split into three levels under the action of a magnetic field as follows:

$$\Delta E = \Delta m g \mu_B H; \Delta m = 0 \pm 1 \quad (1)$$

where g is the sum of the spectroscopic splitting factors of the electrons in the conduction and valence bands and μ_B the Bohr magneton:

$$g = g_e(\Gamma_1) + g_h(\Gamma_{15}).$$

The g factor of an electron in the top Γ_1 conduction band is slightly different from two, because the energy gap $E_g(\Gamma_1 - \Gamma_{15}) \approx 26,000 \text{ cm}^{-1}$, is large as compared to the spin orbit separation $E(\Gamma_7 - \Gamma_8) \approx 600 \text{ cm}^{-1}$. The effective masses for the electron and the hole are respectively $m_e(\Gamma_1) = 0.415 m_0$, $m_h(\Gamma_{15}) = 20 m_0$ after Song. Using these values, Kahn* has calculated an isotropic $g_e(\Gamma_1)$ value of 2.02 by the method of Roth[12] in which the spin orbit coupling is taken into account. Furthermore, the experimental

*By analogy with atomic spectra, we previously called the Γ_{15} and Γ_2 exciton states, $J=1$ and $J=0$.

*Personal communication of A. KAHN.

value for the hole g_h is known to be about -1.1 (see below). Therefore we have the set:

$$g_e(\Gamma_1) = 2.05 \pm 0.05$$

$$g_h(\Gamma_{15}) = -1.1 \pm 0.1$$

so that the effective g value for the exciton is small 0.9 .

Furthermore, in magnetic field the Γ_{15} and Γ_2 exciton states mix producing the appearance of a fourth line ν_1 and shifting in opposite directions both the new line and the $m=0$ component of (1).

At low magnetic field the shift of these lines is:

$$\Delta E_\nu = \frac{1}{4} \frac{(g_e - g_h)^2 \mu_B^2 H^2}{\Delta E_0} \quad (2)$$

where $\Delta E_0 = E(\Gamma_{15}) - E(\Gamma_2) = \nu_{1f} - \nu_1$.

Elliott[13] has evaluated the ortho-para splitting in the case of a $1s$ Wannier exciton. Assuming that the Γ_1 and Γ_{15} bands are mainly due to $4s$ and $3d$ functions of copper, the effective exchange interaction is:

$$J_{\text{eff}} = V_0 (\phi(0))^2 J_{sd} \quad (3)$$

where J_{sd} is an atomic exchange interaction, $|\phi(0)|^2 = 1/\Omega a_0^3$ the probability of finding an electron and hole on the same atom, V_0 the volume of unit cell, and a_0 the exciton radius. Taking a ${}^3D-{}^1D$ splitting of the $3d^9 4s$ Cu^+ configuration of 3000 cm^{-1} a value of $V_0 = 160 \text{ \AA}^3$ and of $a_0 = 7 \text{ \AA}$ the calculation gives for the ortho-para splitting a value of about 70 cm^{-1} . The accuracy of this evaluation is not very good, due to a possible breakdown of the effective mass approximation for small orbits.

(B) *Bound exciton* ($\nu_2 = 25,654 \text{ cm}^{-1}$; $\nu_2^1 = 25,665 \text{ cm}^{-1}$)

Lines due to bound excitons have been found in a great variety of semi-conductors. The Zeeman effect enables us to determine what kind of defects trap the exciton following a method of investigation suggested by Hopfield and Thomas[14].

In the formation of exciton complexes, the ground state can be a neutral acceptor in an unperturbed crystal. In the excited state an exciton is formed in a state bound to the neutral acceptor. The ionised acceptor having no moment the g factor of the ground state of the neutral acceptor must be that of the hole. In the excited state the holes form orbitals with compensated spins, and the angular momentum of the complex must be that of the remaining electron. In a magnetic field, the bound exciton exhibits four lines due to the twofold degeneracy of both the ground and excited states (Fig. 2). The magnetic splitting of these components will be a linear function of the field. Generally, it will be possible, by means of thermalisation effects in absorption, to distinguish between the g factors of the ground and the excited state, which permits the identification of the type of center.

3. EXPERIMENTAL

The magnetic fields[15] up to 180 kG are produced by discharging a 9 kJ capacitor bank, through a split coil of copper wire. A flash light is synchronised with the maximum of the pulsed field. The duration of the field and light are respectively 10^{-3} and 10^{-5} sec . The luminescence is excited with the same light source through a UG11 Schott filter. The observation is made at right angles to the magnetic field so as to observe the Π and σ components of the Zeeman patterns. The various spectra are recorded photographically with a Bauch and Lomb grating spectrograph having a dispersion of 4 \AA-mm^{-1} . The samples studied are either thin film (1μ) obtained by evaporation or thick polycrystals (100μ) purified by zone melting (10 ppm). They are directly immersed in the refrigerating liquid.

4. RESULTS

(A) *The ortho and paraexciton lines ν_{1f} and ν_1*

The Zeeman splitting of the $1s$ (Γ_{15}) absorption line ν_{1f} ($25,865 \text{ cm}^{-1}$) is unobservable largely because a low effective

g value of 0.9 (see above) and a too large width of this line, about 30 cm^{-1} . But both in the absorption and emission spectra of thin layers we see the appearance of the forbidden line called $\nu_1(\Gamma_2)$. An analysis of the magnetic behaviour of the ν_1 ($25,814 \text{ cm}^{-1}$) line has been reported previously [7, 8]. The intensity of this line increases with the field both in emission and in absorption. The line behaves in the same way in high field. At 120 kG the line becomes so strong that in the reflection spectrum a residual ray [16] is formed at this frequency. Unobservable in the absence of field, the line ν_1 becomes of about the same order of magnitude as the sharp $n = 1$ exciton line at high fields. On the other hand, the line shifts to lower energies in increasing magnetic fields (Fig. 3).

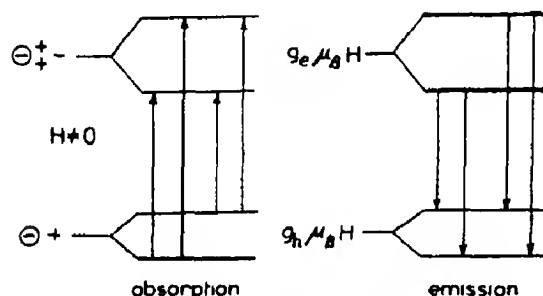


Fig. 2. Zeeman effect of the complex exciton-neutral acceptor.

The quadratic Zeeman effect arises both from the diamagnetic of the exciton and from the second order term of the paramagnetic perturbation. Each of these effects shifts to higher energy the central component of (1). However both effects are of a different order of magnitude for CuCl.

The diamagnetic shift for an $1s$ exciton is:

$$\Delta E_d = a_0^2 \frac{e^2 H^2}{4\mu c^2}$$

while the paramagnetic shift is given by (2).

Assuming $\mu = 0.4 m_0$, $a_0 = 7 \text{ \AA}$ and the values of g_e and g_h found experimentally with an ortho paraexciton splitting of 50 cm^{-1} .

$$\frac{\Delta E_d}{\Delta E_p} = 0.04.$$

The experimental shift of ν_1 in a magnetic field of 150 kG is of about 1.5 cm^{-1} , so the diamagnetic perturbation is entirely negligible. The magnetic behaviour of ν_1 , triplet and ν_1 singlet agree well with the hypothesis of mixing of the Γ_{15} and Γ_2 exciton states as shown on Fig. 3.

(B) The group of lines ν_2

The line ν_2 ($25,654 \text{ cm}^{-1}$) is situated on the low energy side of the $n = 1$ exciton line ($25,865 \text{ cm}^{-1}$) of the sharp series; This line is observed both in absorption (with thick crystals) and in emission. It has been shown [4, 9] that this line is due to the creation or annihilation of an exciton bound to a defect, the nature of which is still to be determined. There is however in emission [7, 10] a possible participation of a mechanism involving the emission of a LO phonon (215 cm^{-1}) and a photon.

(a) *Zeeman effect of the emission line ν_2 .* The splitting [17] of the line ν_2 is shown on Fig. 4 in a field of 120 kG at 1.9° and 4.2°K . Four components are observed 1 ($25,646 \text{ cm}^{-1}$), 2 ($25,652 \text{ cm}^{-1}$), 3 ($25,656 \text{ cm}^{-1}$) and 4 ($25,663 \text{ cm}^{-1}$).

1 and 4 are Π components. 2 and 3 are σ components. The intensity of the components decreases strongly from 1 to 4. The ratio of intensities between 1 and 4 is larger at 1.9°K than at 4.2°K .

(b) *Zeeman effect of the absorption lines.* In the absorption spectrum of CuCl a group of lines ν_2 is observed. The strong line ν_2 is accompanied by a number of satellite lines ν_2^i ($i = 1-4$). The intensity of these lines depend on the quality of the samples. All these lines disappear when the temperature is slightly raised. The splitting of the lines ν_2 , ν_2^1 and the behaviour of ν_2^3 as a function of the magnetic field, is shown on Figs. 5 and 6.

The line [18] ν_2 ($25,654 \text{ cm}^{-1}$ at 4.2°K). At 30 kG the line is broadened but the

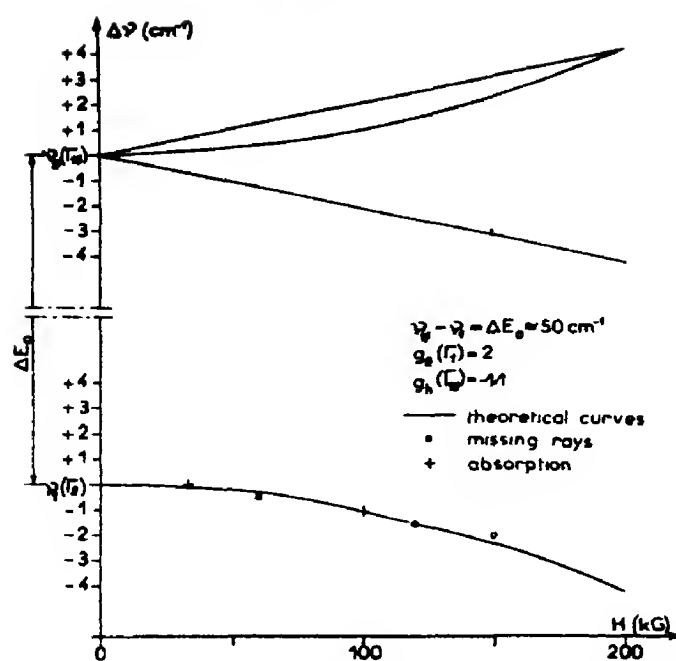


Fig. 3 The ortho and paraexciton lines ν_{1f} and ν_1 in high magnetic field.

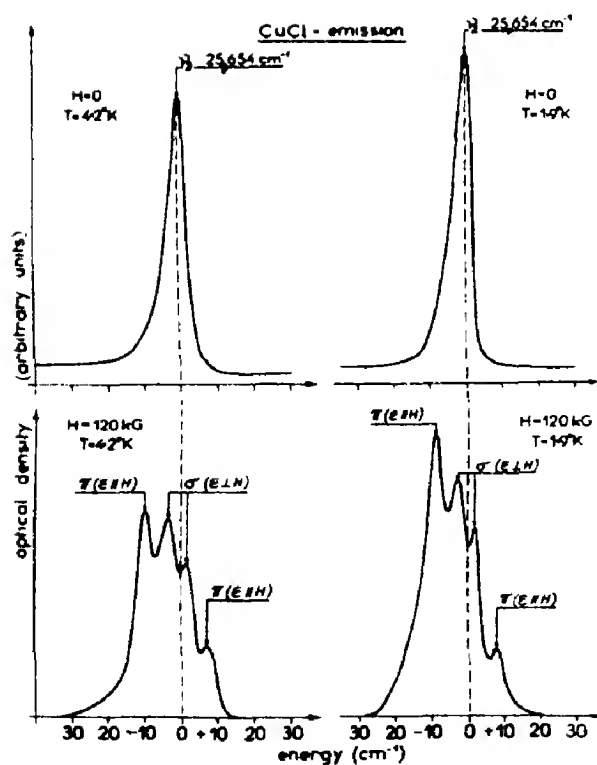


Fig. 4. Zeeman effect of the emission line ν_2 of a thin recrystallised layer, 1 μ thick.

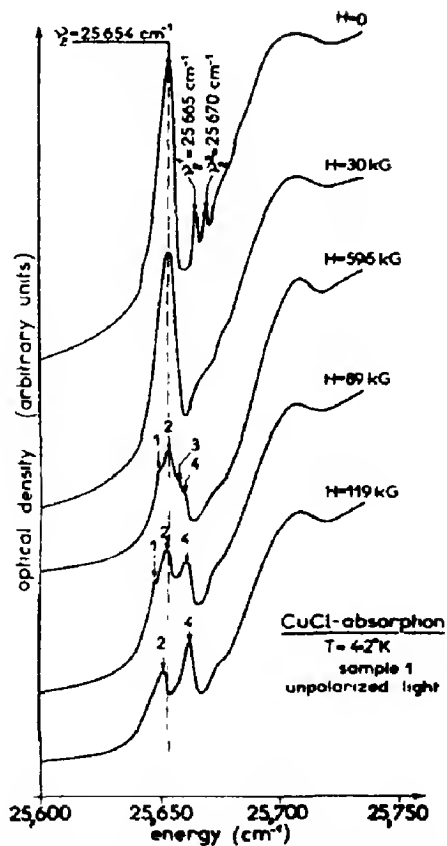


Fig. 5. Zeeman effect of the absorption spectrum of a polycrystalline sample, 120 μ thick (sample 1).

Zeeman pattern unresolved. Four components (though with a poor resolution) are observed at 59.5 kG. A triplet (1, 2 and 4) is observed at 89 kG. Finally a doublet (components 2 and 4) is observed with 119 kG. Note that 2 is a σ component and 4 is a Π component. The components 1 and 3 are not observed for higher fields at 4.2°K. However, in high fields the components 1 and 3 reappear at higher temperatures. This is shown on the diagram of Fig. 7. With the field used (120 kG) kT at 4.2°K is smaller than the magnetic splitting of the ground state. Therefore, 2 and 4 must be transitions arising from the lowest Zeeman level, which is alone populated, and two excited levels. This enables us to obtain the g factor for both the ground state and the excited state. It is found that $g_0 = 1.1$ for the ground state and $g_{\text{exc.}} = 2.05$ for the excited state.

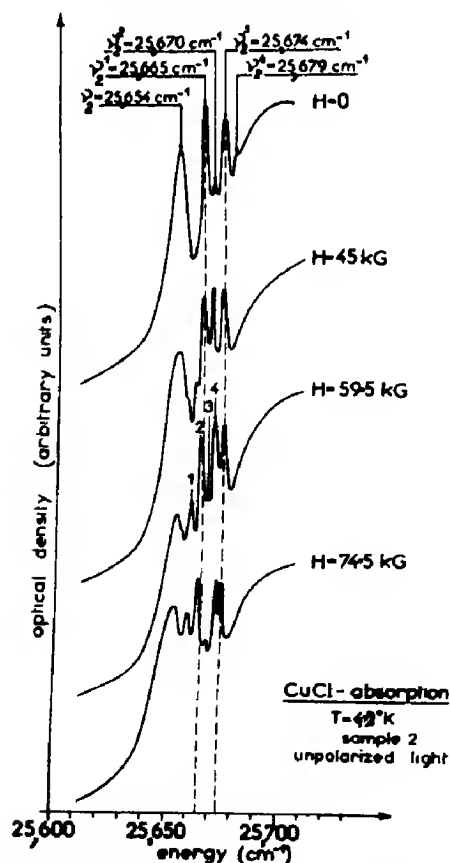


Fig. 6. Zeeman effect of the absorption spectrum of a polycrystalline sample, 200 μ thick (sample 2).

The splitting of the four components is a linear function of the magnetic field. This is shown on Fig. 8. The coincidence of the Zeeman patterns as observed in emission with that observed in absorption has been used in drawing this diagram at 120 kG.

The line ν_2^1 (25,665 cm^{-1} at 4.2°K). The Zeeman effect of ν_2^1 is similar to that of line ν_2 described above. A field of 59.5 kG splits the line in four components at 4.2°K 1 (25,661 cm^{-1}), 2 (25,664.5 cm^{-1}), 3 (25,666.5 cm^{-1}) and 4 (25,671 cm^{-1}). At this field the Zeeman effect of this line is not perturbed by the neighbouring lines. The components 2 (σ) and 4 (Π) have roughly the same intensity, but the components 1 and 3 are much weaker. They disappear at 1.6°K (Fig. 5). The g factors are $g_0 = 1.2$ and $g_{\text{exc.}} = 2.3$. The variation of the splitting of this line with the magnetic field is represented on Fig. 8. It can be seen that the Zeeman patterns of ν_2 and ν_2^1 overlap for high values of the field. However, the emission pattern is observed for ν_2 only. This helps to analyse the rather complicated situation.

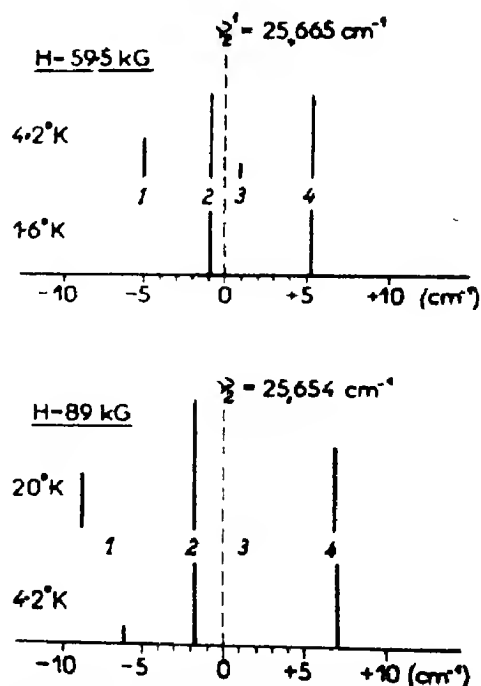


Fig. 7. Diagram of the ν_2 and ν_2^1 Zeeman absorption patterns as function of the temperature. The length of the lines represents the apparent intensity of the components.

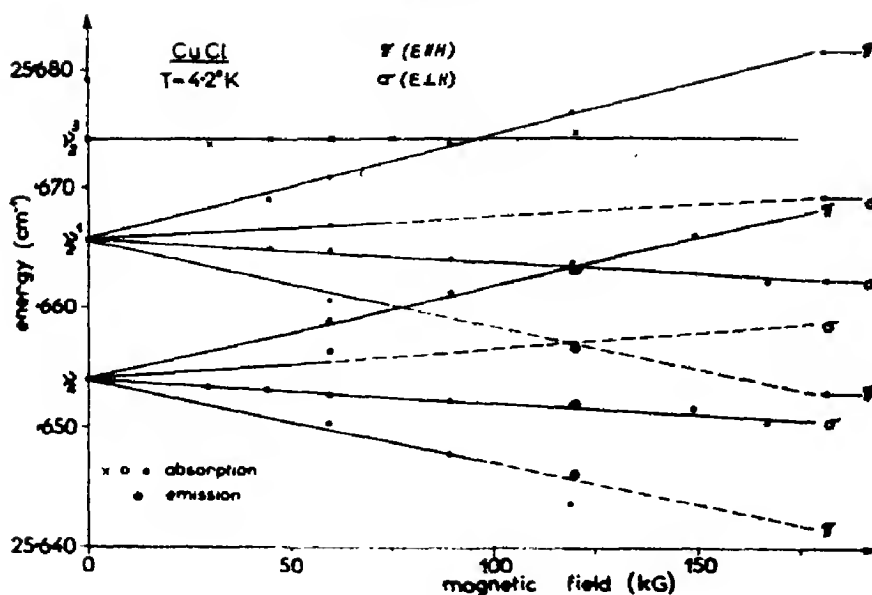


Fig. 8. Zeeman effect of ν_2 , ν_2^1 and ν_2^3 lines as a function of the field intensity at 4.2°K.

The line ν_2^3 ($25,674\text{ cm}^{-1}$ at 4.2°K). This line is not affected by the magnetic field; see Fig. 6.

The lines ν_2^2 ($25,670\text{ cm}^{-1}$) and ν_2^4 ($25,679\text{ cm}^{-1}$ at 4.2°K). These lines are very weak. On account of that no reliable observations have been made.

5. DISCUSSION

The fine structure of 1s exciton is now well understood in spite of the fact that the Zeeman splitting is unresolved. The paraexciton Γ_2 appears and is shifted towards lower energies quadratically with the field according to (2). The ortho-para splitting between ν_{1f} and ν_1 agrees surprisingly well with Elliott's theory. The influence of Cl^- must be negligible.

The Zeeman splitting of ν_2 and ν_2^1 line is practically the same. The g factors of excited states are in excellent agreement with the electronic g value so that the two lines correspond to excitons bound to neutral acceptor. The other lines ν_2^2 , ν_2^3 and ν_2^4 must be assigned to some other kind of centers.

We have seen that Π and σ components are in a reversed order as compared to the usual Zeeman patterns. This fact is also due to the

circumstance that the hole is responsible for the splitting of the ground state and the electron for that of the excited state. Therefore this consideration is in agreement with the above assignment. As the crystals are very pure it is likely that the acceptor involved has a stoichiometric character. It can be tentatively suggested that Cu^+ vacancies can form the acceptor. However, the very high mass of the hole may bring along some difficulties in understanding the structure of such an acceptor.

Though not all magnetic properties of the sensitive lines of CuCl are yet understood, it is believed that considerable progress has been made in their assignment.

Acknowledgements—The authors are thankful to Professor Daniel for stimulating discussions, and to Dr Kahn for permission to use the g values he has calculated prior to their publication.

REFERENCES

1. REISS R. and NIKITINE S., *C.r. hebd. Séanc. Acad. Sci., Paris* **250**, 2862 (1960).
2. NIKITINE S., RINGEISSEN J. and DEISS J. L., *J. Phys.* **23**, 890 (1962); NIKITINE S., *Prog. Semiconductors* **6**, 233 (1962).
3. CARDONA M., *Phys. Rev.* **129**, 69 (1963).

4. UETA M. and GOTO T., *J. phys. Soc. Japan* **20**, 401 (1965); *ibid.* **20**, 1024 (1965).
5. RINGEISSEN J., CORET A. and NIKITINE S., In *Localized excitations in Solids*, p. 297. Plenum Press, New York (1968).
6. NIKITINE S., *Phil. Mag.* **4**, 1 (1959).
7. NIKITINE S., RINGEISSEN J. and CERTIER M., *Acta Phys. Pol.* **26**, 745 (1964).
8. NIKITINE S., CERTIER M., RINGEISSEN J. and MERLE J. C., *J. Phys.* **27**, 104 (1966).
9. RAGA F., KLEIM R., MYSYROWICZ A., GRUN J. B. and NIKITINE S., *J. Phys.* **28**, C3-116 (1967).
10. NIKITINE S., RINGEISSEN J. and SENNETT C., 7ème Cong. Intl Physique des Semiconducteurs, Paris, p. 279 (1964).
11. SONG K. S., *J. Phys.* **28**, 195 (1967); *J. Phys. Chem. Solids* **28**, 2003 (1967).
12. ROTH LAURA M., *Phys. Rev.* **118**, 1534 (1960).
13. ELLIOTT R. J., *Phys. Rev.* **124**, 340 (1961).
14. THOMAS D. G. and HOPFIELD J. J., *Phys. Rev.* **128**, 2135 (1962).
15. CERTIER M., MERLE J. C., NIKITINE S., and WECKER C., *J. Phys.* **28**, C3-88 (1967).
16. CERTIER M., WECKER C., and NIKITINE S., *Phys. Lett.* **28**, 307 (1968).
17. CERTIER M., WECKER C. and NIKITINE S., *J. Phys. Chem. Solids* **30**, 1281 (1969).
18. CERTIER M., WECKER C. and NIKITINE S., *C.r. hebd. Séanc. Acad. Sci., Paris* **226**, 1215 (1968).

OPTICAL STUDIES OF THE THERMAL DISSOCIATION OF OH⁻ ION AGGREGATES IN MgO

T. M. SEARLE

Department of Physics, Sheffield University, Sheffield, England

(Received 16 December 1968; in revised form 27 January 1969)

Abstract—The thermal dissociation of two OH⁻ ion aggregate centres has been studied through the decay of the associated optical absorption bands. The first of the centres studied, with an absorption band at 3296 cm⁻¹, has been shown to consist of an OH⁻ ion in association with a magnesium vacancy (I), the (OHV) centre. The second (absorption band at 3310 cm⁻¹) is an (OHV) centre in association with a trivalent impurity (I)[2]. We term this the (OHVI) centre. Over the temperature range 470°–620°C the decays take a simple form, predicted by rate theory. From these measurements, and new data on the equilibrium concentration of the centres as a function of temperature, the dissociation activation energy (1.43 eV), the binding energy (≥ 0.23 eV) and the association activation energy (≤ 1.20 eV) of the (OHV) centre are found, together with the binding energy of the trivalent impurity I to the (OHVI) centre (84 meV).

RECENTLY, several studies have been made of OH⁻ ion containing centres in magnesium oxide[1–3]. The centres in general consist of an OH⁻ ion at an oxygen substitutional site, in association with one or more magnesium vacancies; some in addition contain a trivalent impurity, which substitutes at a magnesium site.

These centres give rise to a series of narrow absorption bands, lying in the region 3200–3700 cm⁻¹; the spectral position of the bands is determined by the stretch frequency of the OH⁻ ion, as modified by the environment at a particular centre. The most prominent of these bands are at 3310 and 3296 cm⁻¹. Kirklin *et al.*[1] have shown that the latter band is due to a centre consisting of an OH⁻ ion at an anion site, in association with one magnesium vacancy in a nearest neighbour cation position. The centre has axial symmetry, the proton lying along the $\langle 100 \rangle$ direction. We write this centre as (OHV). It bears a net negative charge.

Optical studies [2] suggest that the centre giving the 3310 cm⁻¹ absorption band is the (OHV) centre in association with an unknown trivalent impurity (I, say). This centre is charge neutral. The position of this band is

unchanged in MgO samples doped with different trivalent transition metal ions; it also appears in nominally undoped crystals, which contain quite high concentrations of iron (100–200 ppm), and also 1–5 ppm of Cr³⁺ ions. The band shifts to a slightly higher energy in MgO:Mn crystals after quenching from temperatures below about 800°C. This probably corresponds to the observed conversion of Mn³⁺ to Mn⁴⁺ below this temperature in these heavily manganese doped crystals[3]. The absorption studies give no information on the position of the trivalent impurity. Simple calculations of the expected frequency for the centre are in accord with this model. Shortly we hope to present more detailed calculations on the OH⁻ ion impurity system in MgO, and to be able to suggest a geometry for this centre, which we write as (OHVI).

In the previous work[2], particular attention was paid to the concentrations of the centres in thermal equilibrium, as a function of temperature T , as found from absorption measurements after a rapid quench from T . This procedure has been found to freeze in the equilibrium concentration of several types of aggregate defects, including those studied here[2, 5]. The temperature dependence of

the equilibrium concentrations of the (OHV) and (OHVI) centres could be accounted for with a model involving only three types of defects: OH^- ions, magnesium ion vacancies, and an unknown defect, X , say. At low temperatures the vacancies associate preferentially with this unknown defect. It was not possible to obtain the activation energies for association or dissociation, or the binding energies of the centres from this work; however, by following the decays of the absorption bands at 3296 and 3310 cm^{-1} , it has been possible to measure the activation energy of dissociation of the (OHV) centre, and the binding energy of the (OHV) defect to the (I) defect in the (OHVI) centre. The rate theory used to determine the latter has been confirmed by a new analysis of the equilibrium data. The more accurate equilibrium data of this work have also enabled an estimate to be made of the (OHV) centre binding energy, and thus of the activation energy for association of this centre from the (OH) and (V) defects.

In Section 1 we present the experimental results. Sections 2(a) and 2(b) are concerned with the analysis of the decays of the (OHV) and (OHVI) centres respectively, and Sections 3(a) and 3(b) with the analysis of the equilibrium measurements on these centres. The results are summarised and discussed in Section 4.

1. EXPERIMENTAL AND RESULTS

As in the previous work, the absorption spectra were measured with a Unicam SP700 spectrophotometer. Details of the method of analysis, the crystals and of the quenching methods used to freeze in high temperature defect populations are given in [2].

Figure 1 shows the dependence of the absorption coefficient at 3296 cm^{-1} and 3310 cm^{-1} , A_∞ and A'_∞ respectively, on the quench temperature. The subscripts emphasise the fact that the crystal had reached thermal equilibrium before the quench. It shows a rise in absorption (and thus in the defect concentra-

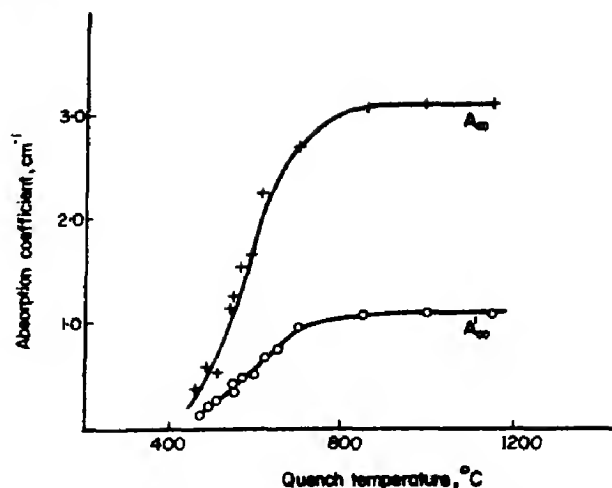


Fig. 1. The equilibrium values of the absorption coefficients at 3296 and 3310 cm^{-1} , A_∞ and A'_∞ respectively as a function of quench temperature.

tions) with increasing temperature, as the vacancies move from association with the unknown defect X to association with the OH^- ions. The figure also shows that at quench temperatures above about 700°C , the concentration of both centres becomes approximately constant. This is more typical behaviour than that of the crystal discussed in [2], where there was a continuing slow increase of A_∞ and A'_∞ with temperature above 700°C . This, and the data presented in [2] on the equilibrium concentration of the V' centre (a magnesium ion vacancy that has trapped a hole), indicate that the limit of concentration of the (OHV) centre is the amount of OH^- ion impurity in the sample, not the cation vacancy concentration, nor the failure of the quenching process to 'freeze in' the high temperature equilibrium concentrations. For the (OHVI) centre, the high temperature concentration depends also on the concentration of trivalent impurity available to (OHV) centres.

Before the decay measurements, the samples were brought to thermal equilibrium at 900°C . The decays of the two absorption bands were then followed, the sample being held at a fixed, lower temperature, T say, until the absorption coefficients reached the equilibrium values for that temperature. The

absorption measurements during the decay were made at room temperature, the sample being removed from the furnace and rapidly quenched, between each measurement. The decays were recorded at seven temperatures between 620° and 470°C. Above 620°C, the difference between the initial and final absorption coefficients becomes small, and the decay rapid; below 470°C, the time required to reach equilibrium is impractically long (>1 week).

In attempts to analyse the resulting decay curves, it was found that neither plots of $\exp A$ nor $\exp(A - A_\infty)$, where A is the absorption coefficient at 3296 cm⁻¹ at time t , vs. t were linear; that is, the decay is not monomolecular. However, though A^{-1} vs. t was non-linear also, $(A - A_\infty)^{-1}$ vs. t gave consistently good linear plots over the whole temperature range. Examples are shown on Figs. 2 and 3. Clearly a form of bimolecular decay operates over this range of T and t .

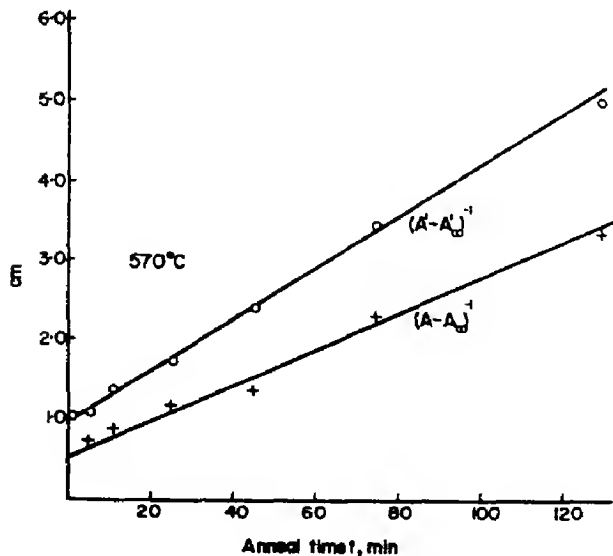


Fig. 2. The decays of the (OHV) and (OHVI) centres at 570°C. $(A - A_\infty)^{-1}$ and $(A' - A_\infty)^{-1}$ vs. anneal time t .

The decay of the (OHVI) centre is more complex, as we might expect, since it is a three, rather than two, defect aggregate. For $T \geq 530^\circ\text{C}$, we find that $(A' - A_\infty)^{-1}$ vs. t is linear, as before, (Fig. 2), but that at lower

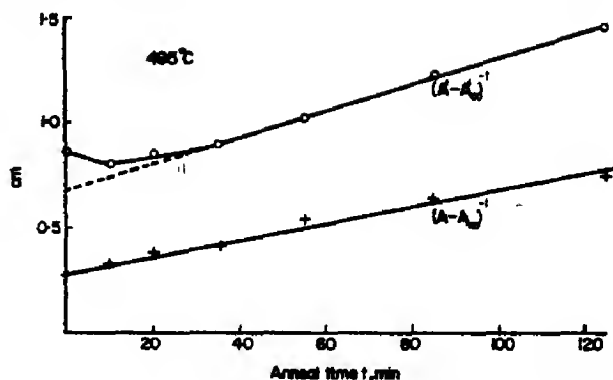


Fig. 3. As for Fig. 2, but at 495°C; the plot of $(A' - A_\infty)^{-1}$ vs. t shows the deviation from linearity discussed below.

temperatures the plots are only linear for long times (Fig. 3). During the initial stage of the 'decay' there is, for $T \leq 530^\circ\text{C}$ a slight increase in A' , before the essentially bimolecular decay takes over.

Despite the comparatively simple form of the decay, we cannot gain useful information from them without a closer examination of the decay mechanism. For, writing the results in the form $(A - A_\infty)^{-1} = Rt$, where R is a rate constant, we find that R is not a simple function of temperature. A plot of $\ln 10R$ vs. $1/T$ is shown dashed on Fig. 4. Clearly we must examine the decay in more detail.

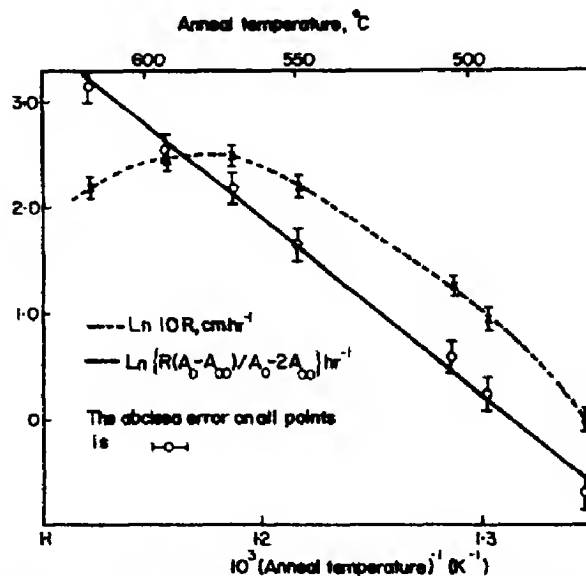


Fig. 4. The quantities $\ln 10R$ (dashed) and $\ln \{R(A_0 - A_\infty)^2 / (A_0 - 2A_\infty)\}$ (full) plotted against the anneal temperature.

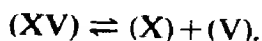
2. ANALYSIS OF THE DECAYS

It is familiar that the decay of any constituent of a reversible reaction is a complex function of time, and that it is difficult to obtain information, such as activation energies, except by curve fitting procedures (see, e.g. Hoogenstraaten[4], on the emptying of electron traps in solids). Often the complete equation contains both terms which decrease exponentially with t , and terms which depend on t^{-n} (n positive). Fortunately, these processes often operate at very different rates, so that within an experimentally realisable time scale one of the terms dominates the others (see e.g.[4, 11]. With these considerations in mind we shall examine the kinetics of the (OHV) centre decay.

(a) The decay of the (OHV) centre

Our approach to the non-equilibrium situation which exists during the decay is the following. We first decide which of the possible reactions occurring between OH^- ions, vacancies, the unknown defect X , and other defects will be most important, using the earlier treatment of the equilibrium situation as a guide. We can then write down the rate equations for these reactions. It will be shown that, because the concentration of (OHV) centres is small compared with the total vacancy concentration, as shown in the equilibrium studies of OH^- ion centres and of V' centres (vacancy + hole)[2], an analytical solution can be found. This solution is examined for long and for short decay times, when the decay is found to take monomolecular and bimolecular form respectively. Comparing the bimolecular form with the experimental results, we are able to find the value of the (OHV) centre dissociation energy.

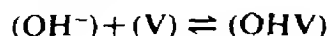
It was shown in [2] that the data of Fig. 1 could only be explained if these were in the crystal a vacancy producing reaction, which was written



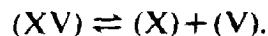
If no additional vacancies were produced

as the temperature was raised, then A_∞ , A'_∞ would be decreasing functions of temperature. The nature of the (X) was not specified though Glass, from his studies of $\text{MgO}:\text{Cr}$ [5] where a similar reaction is found necessary estimated a lower limit to the association energy of the (XV) associate of about 1.0 eV. The implications of this high value for the nature of X are discussed in [5].

We must clearly take the above reaction into account when formulating a model for the decay of the (OHV) centre. First we consider only the two reactions



and (i)



Since most of the OH^- ion content of the crystal exists either as isolated OH^- ions ((OH^-)) or in (OHV) centres, these will be the dominant reactions. The same pair of reactions give a good description of the equilibrium situation (2).

The equations governing the decay are then

$$\frac{d}{dt}[\text{OHV}] = -\gamma_1[\text{OHV}] + [\text{V}][\text{OH}^-]\alpha$$

and

$$\frac{d}{dt}[\text{XV}] = -\gamma_2[\text{XV}] + [\text{V}][\text{X}]\beta$$

where the square brackets indicate concentrations.

The first term on the right in these equations represents the thermal dissociation of the associate; the second, the recombination of the isolated defects. γ_1 and γ_2 are Boltzmann terms of the form $\gamma'_i \exp(-E_i/kT)$. E_1 , defined as E_1 and E_2 , are the activation energies for dissociation of the (OHV) and (XV) aggregates respectively, and the corresponding pre-exponentials γ'_1 and γ'_2 contain the dissociation entropies. Before recombination can occur one of the isolated defects must

diffuse thermally; if we assume the vacancy is the more mobile species, i.e. the activation Gibbs free energy for vacancy diffusion is less than that for (OH⁻) or (X) diffusion, then $\alpha = \beta = \gamma' \exp(-E/kT)$. E and γ' are the activation energy and entropy for vacancy diffusion, respectively. It is known that in MgO impurities diffuse via a vacancy mechanism[12].

There is no experimental evidence for intrinsic vacancy production at these temperatures; this is supported by an estimate of 4.0 eV for the energy required for vacancy production made by Lidiard[12].

Thus we can write $[V]_T = [XV] + [OHV] + [V]$, where $[V]_T$ is the total vacancy concentration. Similarly, $[OH]_T = [OHV] + [OH^-]$ and $[X]_T = [XV] + [X]$.

Using these relations, and the notation $[XV] \equiv x$, $[OHV] \equiv y$, $[OH^-]_T \equiv a$, $[X]_T \equiv b$, and $[V]_T \equiv c$, the rate equations become

$$(dy/dt) = -\gamma_1 y + (c - x - y)(a - y)\beta$$

and (ii)

$$(dx/dt) = -\gamma_2 x + (c - x - y)(b - x)\beta.$$

As they stand, these equations are difficult to solve analytically. However, they may be simplified by noting that the concentration of OH⁻ ion-vacancy associates is much less than the total vacancy concentration[2] i.e. $y \ll c$. The equations then simplify to

$$(dy/dt) = -\gamma_1 y + (c - x)(a - y)\beta \quad (\text{iii})$$

and

$$(dx/dt) = -\gamma_2 x + (c - x)(b - x)\beta. \quad (\text{iv})$$

It should be noted that these simplified equations give, on setting $(dx/dt) = (dy/dt) = 0$, the same equilibrium conditions as given by mass action theory from equation (i). Equation (iv) has as its solution

$$x = B - D \coth(A\beta t + K)$$

with $2B = ((\gamma_2/\beta) + b + c)$, $D^2 = B^2 - bc$, and $K = \coth^{-1}(B - x_0/D)$, where x_0 is the value of x at time $t = 0$. By inserting this expression for x into (iii), $y(t)$ can be found. The resulting expression for y is

$$y - y_\infty = E(e^{-K - D\beta t} + G e^{-Ft}) \cosh(K + \beta D t) \quad (\text{v})$$

where $E = (\beta\gamma_1 a D / F^2 - D^2 \beta^2)$, $F = \gamma_1 + (c - B)\beta$, and G is a constant of integration determined by $y = y_0$ at $t = 0$.

Equation (v) is too complicated and contains too many parameters to be useful. As noted above, however, the analysis of decay curves is often simplified by the dominance, over a restricted range of t , of a few terms in the exact equation. For example, at sufficiently long times, such that $D\beta t$ and $Ft \gg 1$, and $D\beta t \gg K$, then equation (v) gives

$$y - y_\infty = 2E e^{-D\beta t} (e^{-D\beta t} + G e^{-Ft}).$$

Thus the decay has a simple exponential form at long times. Experimentally, we may not be able to measure the difference $y - y_\infty$ at times sufficiently long for the above inequalities to be obeyed, and thus will not observe this monomolecular decay.

To understand the experimental results presented here, we examine equation (v) for small t , such that $D\beta t$ and $Ft \ll 1$. From equation (v) and with these restrictions only, we have, after a little algebra,

$$(y - y_\infty)^{-1} = \{\gamma_1(y_0 - 2y_\infty) - \beta(c - x_0) \times (a - y_0)\} \{y_0 - y_\infty\}^{-2} t + O(Ft)^2. \quad (\text{vi})$$

It was noted above that the high temperature limit to the (OHV) centre concentration is set by the total OH⁻ ion concentration; so, if we neglect other reactions the starting condition is $y_0 = a$. Neglecting the small higher order terms equation (vi) then becomes

$$(y - y_\infty)^{-1} = \gamma_1(y_0 - 2y_\infty)(y_0 - y_\infty)^{-2} t. \quad (\text{vii})$$

The experimental results can be written as $(A - A_\infty)^{-1} = Rt$, where R depends only on the anneal temperature. Since the peak absorption is directly proportional to the defect concentration, comparison of the last two equations gives

$$(R(A_0 - A_\infty)^2)/(A_0 - 2A_\infty) = \gamma_1 \\ = \gamma'_1 \exp - (E_1/kT) \quad (\text{viii})$$

In Fig. 4, the logarithm of the left-hand side of equation (viii) has been plotted against reciprocal temperature: it is linear, and from its slope E_1 , the dissociation activation energy of the (OHV) centre, is found to be 1.43 ± 0.03 eV and $\gamma'_1 = 3 \times 1.5 \times 10^8 \text{ sec}^{-1}$. (I am indebted to Dr. J. E. Bishop of this university for the suggestion of the sign \times to indicate errors determined from a logarithmic plot).

Before proceeding, it is worth summarising the assumptions made above. The reactions (i), involving only vacancies and the (OH⁻) and (X) defects, together with the aggregates of these, the (OHV) and (XV) defects, are believed to be dominant in the (OHV) centre decay, since the same equations give a good description of the equilibrium behaviour[2]. That there is not intrinsic vacancy production is reinforced by the high estimated energy for Schottky defects[12]. The equilibrium behaviour also suggests that the vacancy concentration is much higher than the (OHV) concentration. This is not surprising, since, in the absence of intrinsic production, most vacancies in MgO are produced via charge compensation of charged defects, and the concentrations of these (indeed, of Fe³⁺ alone) are much greater than the (OHV) concentration. This assumption allowed us to simplify the rate equations (equations (ii-iv)). The same arguments allow us to simplify the expression for the time dependence of the (OHV) concentration, obtained for short times, (equation (vi)) by taking the initial (OHV) concentration as equal to the total (OH⁻) concentration. The rate equations were further simplified by the assumption that vacancies diffuse more readily

than the impurities (OH⁻) and (X), as suggested by diffusion experiments[12].

With these simplifying assumptions, the model used here gives a satisfactory description of the (OHV) centre decay, and enables us to find the dissociation energy. We now turn to the more complex (OHVI) centre decay.

(b) The decay of the OHVI centre

The model presented above describes the decay of the (OHV) centre in terms of the two equations (i) only. Since the (OHV) centre is also present in the crystal, a rigorous treatment would solve the two rate equations (ii) for reactions (i), together with the rate equations for reactions of the kind



and



simultaneously. This leads to considerable mathematical difficulties.

We tackled the decay of the (OHVI) centre in the following approximate way. We assume that one only of the reactions (ix) and (ixa) is significant. If it is argued, as above, that an isolated (I) or (OH⁻) defect is comparatively immobile, then the relative importance of reactions (ix) and (ixa) is determined by the relative mobilities of the (OHV) and (VI) defects. We shall treat both cases, considering the chosen reaction ((ix) or (ixa)) as a small perturbation on reactions (i). The rate equation is solved, and the solution combined with that found above for the (OHV) centre decay. First we examine the situation when reaction (ix) is dominant.

(i) $(\text{OHV}) + (\text{I}) \rightleftharpoons (\text{OHVI})$ dominant. Writing $y' \equiv [\text{OHVI}]$, the rate equation for reaction (ix) is

$$\frac{dy'}{dt} = -\gamma_3 y' + (d - y') y \delta \quad (\text{x})$$

where $\gamma_3 = \gamma'_3 \exp - (E_3/kT)$, E_3 is the activa-

tion energy for dissociation of the (OHVI) centre required to form an (OHV) centre, $d = [I]_T$, the total concentration of the isolated impurity I , and δ the probability that an (OHV) centre will associate with an impurity I . δ has Boltzmann form, $\delta' \exp(-E_4/kT)$, E_4 being the activation energy for diffusion of the more mobile of the defects (OHV) and (I), and δ' is the corresponding entropy.

Combining this with the previous result that $(y - y_\infty)^{-1} = fRt$ (f is a constant of proportionality between absorption coefficient and concentration) we have on solution

$$y' = d\delta(y_\infty/g) + He^{-\omega t}t^{-h} + (d/g)e^{-\omega t}t^{-h}\gamma_3 \int_0^t e^{\omega t'}t'^{h-1} dt'$$

with $g = \gamma_3 + y_\infty\delta$, $h = \delta/Rf$, and H is a constant of integration. The integral is simplified if we approximate h by the nearest integer, p say, which we may do so long as $h \gg 1$, i.e. $Rf \gg \delta$, or $(y - y_\infty)^{-1} \ll \delta t$. For the concentrations of (OHV) in our crystals, this means $\delta t \gg 10^6$, and since we would expect $\delta > 10^6$, the inequality is easily satisfied for long times. Then

$$y' = d\delta((y_\infty/g) + He^{-\omega t}t^{-h}) + \frac{d\gamma_3 h}{g^2 t} + \frac{dh\gamma_3}{g} e^{-\omega t} \sum_{k=1}^{p-1} \frac{(-1)^k (p-2) \dots (p-k)}{(gt)^{k+1}} \quad (\text{xi})$$

Putting $y' = y'_\infty$ at $t = \infty$, we have $y'_\infty = (\delta dy_\infty/g)$, in agreement with the mass-action expression. If $gt \gg 1$, then $y' - y'_\infty = (\gamma_3 h d/g^2 t)$. This is the experimentally observed form for the (OHVI) centre decay over the whole observation time at temperatures above about 530°C, and also over the latter part of the decay at lower temperatures. Equation (xi) shows the reasons for the deviation from bimolecular kinetics at low temperatures and short times: γ_3 and $y_\infty\delta$ both decrease with decreasing temperature and thus at low temperatures gt

becomes insufficiently large to justify our inequality, at least until t is large. The second and fourth terms in (xi) can then no longer be ignored.

Qualitatively, the maximum of $A'(t)$, the (OHVI) concentration results from the competition of two processes, the pairing of (I) and (OHV), occurring more rapidly as the temperature is lowered, and the decrease of (OHV) with decreasing temperature. For t small, that is with high (OHV) and (I) concentrations, the first process dominates: when t is large, the (OHV) concentration has decreased sufficiently for the second process to dominate, and the (OHVI) concentration falls.

Writing the experimental results for the bimolecular region as $(A' - A'_\infty)^{-1} = R't$, we have the relation between the decay rates of the (OHV) and (OHVI) centres,

$$\frac{\gamma_3}{d\delta} = \frac{\gamma'_3}{d\delta'} \exp(-(E_3 - E_4/kT)) = (R/R') \left(\frac{y_\infty}{y'_\infty} \right)^2$$

The logarithm of the right-hand side of the above equation is plotted in Fig. 5 vs. reciprocal temperature. $E_3 - E_4$, the binding energy of the impurity I to the (OHV) centre is evidently small and positive (i.e. the

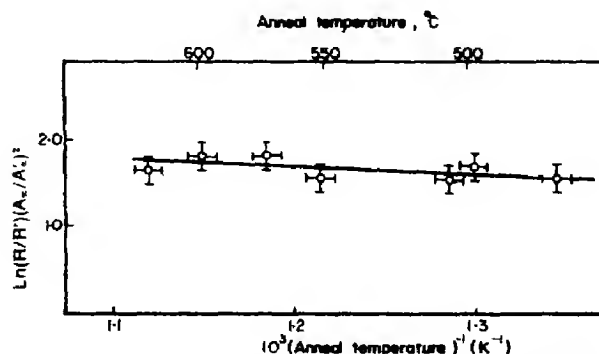


Fig. 5. The quantity $\ln(R/R') (A_\infty/A'_\infty)^2$ vs. the reciprocal of the anneal temperature.

(OHVI) centre is slightly more stable than the (OHV) centre, as we would expect after considering the total charges carried by the

centres).^{*} The experimental errors are, however, rather large: $E_3 - E_4 = 47 \pm 57$ meV, and $(\gamma'_3/d\delta') = 10 \pm 1.7$. We shall discuss in Section 3 a method of measuring these quantities more accurately.

(ii) $(OH^-) + (VI) \rightleftharpoons (OHVI)$ dominant. The approach and the solution of the rate equation is very similar in this case to that given above; for long times, and with the same approximations, we find (constant) $\exp(-(E'_3 - E'_4/kT)) = (R/R')(y_0 - y_\infty/y'_\infty)^2$, where $E'_3 - E'_4$ is the binding energy of the (OH^-) impurity to the (VI) defect.

Although a plot of the logarithm of the right hand side of this equation vs. $1/T$ appears roughly linear, it leads to a large negative estimate of the binding energy. This is physically unrealistic, and we therefore conclude that reaction (ix) is dominant, i.e. the (OHV) defect is more mobile than the (VI) defect.

3. ANALYSIS OF THE EQUILIBRIUM MEASUREMENTS

(a) The $(OHVI)$ centre

The equilibrium data provide another way in which we can measure the binding energy; besides a more accurate value, this also gives a check to the decay analysis. Consider the equilibrium concentrations of (OHV) and $(OHVI)$, y_∞ and y'_∞ . Then from equation (x), setting $dy'/dt = 0$ or from the law of mass action, using reaction (ix),

$$\frac{y_\infty}{y'_\infty} = \frac{\gamma_3}{\delta(d - y'_\infty)}.$$

At low temperatures, y'_∞ is small, and thus $d \gg y'_\infty$, since d is greater or equal to the high temperature concentration of $(OHVI)$ centres. At low temperatures, then,

$$\frac{A_\infty}{A'_\infty} = \frac{\gamma_3}{\delta d} = \frac{\gamma'_3}{\delta' d} \exp - \left(\frac{E_3 - E_4}{kT} \right). \quad (\text{xii})$$

^{*}Throughout this work, the sign of binding energies is taken such that they are positive when the associate is stable at low temperatures.

Figure 6 shows a plot of $\log(A_\infty/A'_\infty)$ vs. $(1/T)$, over the range $475^\circ - 620^\circ\text{C}$: the data points (a) are taken from the crystal used in the decay experiments (Fig. 1), and points (b) from a crystal containing a lower concentration of the impurity I , as judged from the high temperature equilibrium concentrations of the $(OHVI)$ centre in the two crystals. The highest temperature points show deviation

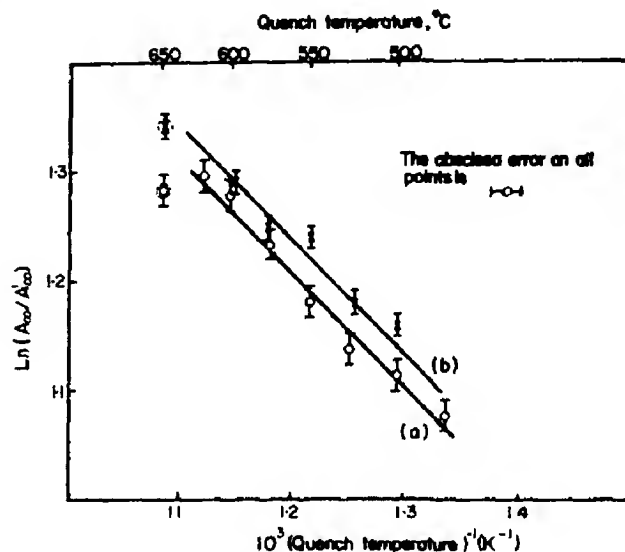


Fig. 6 The quantity $\ln(A_\infty/A'_\infty)$ vs. the reciprocal of the quench temperature. Points on (a) are from the crystal used in this work (the data from Fig. 1), those on (b) are from a crystal with a lower concentration of the impurity I . The two dashed-circled points show the expected deviation from linearity at high temperature.

from linearity, as the approximation $d \gg y'_\infty$ begins to break down. The gradients are equal within the experimental errors, and give $E_3 - E_4 = 84 \pm 8$ meV. $(\gamma'_3/\delta'd)$ for the plot (a) is 11 ± 1.2 . These values are well within the ranges of the same parameters evaluated via the decay data. For the points (b) $(\gamma'/d\delta') = 12 \pm 1.4$. The ratio of the intercepts of the two plots is equal, within the experimental errors, to the inverse ratio of the concentrations of I in the two crystals, d , assuming d is directly proportional to the high temperature equilibrium value of A'_∞ ; this is expected from equation (xii).

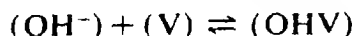
Given these values of $(\gamma'_3/\delta'd)$, we can

estimate a lower limit on the value of (γ'_3/δ') . The concentration of the (OHVI) centre can be estimated with a relationship given originally by Kats[6], and used in [2], between the absorption coefficient and number of centres. For the sample used in the decay measurements, this gives $[\text{OHVI}] = 3 \text{ ppm}$ at high temperatures. Since this is $\leq d$, $(\gamma'_3/\delta') \leq 3.3 \times 0.36 \times 10^5$.

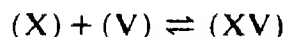
Use of reaction (ixa) in the place of reaction (ix) again leads to an apparent high negative binding energy.

(b) The (OHV) centre

Finally, the more accurate measurements of A_∞ as a function of temperature (Fig. 1) permit measurement of the (OHV) binding energy. For, writing the two reactions,



and



mass action theory gives

$$[\text{OH}^-][\text{V}] = [\text{OHV}]K_6$$

and

$$[\text{X}][\text{V}] = [\text{XV}]K_5$$

where K_5 and K_6 have the form $K'_i \exp(-E_i/kT)$. E_6 is the binding energy of the (OHV) associate, and E_5 the binding energy of (XV). At low temperatures, very little (OH^-) is associated so $[\text{OH}^-]_T \gg [\text{OHV}]$. Assuming with Glass[5] that $[\text{X}]_T \approx [\text{X}]$, then combining the above two equations and the conservation equations,

$$[\text{OHV}] \approx [\text{OH}^-]_T [\text{V}]_T K_6^{-1} \{1 + K_6^{-1} \times ([\text{OH}^-]_T + [\text{V}]_T) + K_5^{-1} [\text{X}]_T\}^{-1}.$$

For this to be an increasing function of temperature, $E_5 > E_6$, and so at sufficiently low temperatures

$$[\text{OHV}] \approx ([\text{OH}^-]_T [\text{V}]_T / [\text{X}]_T) (K_5/K_6).$$

A plot of $\ln A_\infty$ vs. $1/T$ gives the energy $E_6 - E_5$ (Fig. 7). We find $E_5 - E_6 = 0.75 \pm 0.04 \text{ eV}$. The high temperature points show deviation from linearity, since $[\text{OH}^-]_T$ is no longer $\gg [\text{OHV}]$.

From his measurements on MgO:Cr , Glass[5] found a value for the (XV) centre binding energy, $E_5 \geq 0.98 \text{ eV}$. Thus we have the binding energy for the (OHV) centre, $E_6 \geq 0.23 \text{ eV}$.

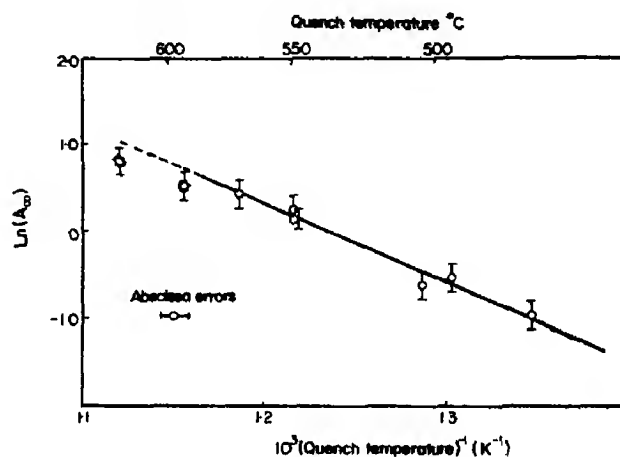


Fig. 7. Plot of $\ln A_\infty$ vs. reciprocal quench temperature. Data from Fig. 1. The high temperature points (circled) show the expected deviation from linearity.

4. DISCUSSION AND CONCLUSIONS

The analysis presented above of the thermal decays of the (OHV) and (OHVI) centres has shown that, through a careful treatment of the decay kinetics, useful information can be obtained without recourse to many parameter curve fitting procedures. This is in part because, as mentioned above, the different time dependent parts of the expression for the defect concentration have very different rates: it has been shown that by careful choice of temperature and starting conditions, the analysis may be further simplified. An important point is that in this study not all the components in the reaction were directly observable, as they were in a recent study of the dissociation of chromium-vacancy associates in MgO [7]. The model developed here should

be applicable to many thermal decay mechanisms in solids, with little modification.

We find that the activation energy for dissociation of the (OHV) centre is 1.43 ± 0.03 eV, and the corresponding pre-exponential $(\gamma'_1) = 3 \times 1.5 \times 10^6 \text{ sec}^{-1}$. The binding energy of the (OHV) centre is ≥ 0.23 eV; that of the impurity (I) in the (OHVI) centre was found to be 84 ± 3 meV, and the pre-exponential $(\gamma'_3/\delta') \leq 3.3 \times 0.36 \times 10^5$. Thus the binding energy of the (OHVI) centre is ≥ 0.31 eV. From the values of the association activation energy and the binding energy of the (OHV) centre, the activation energy for dissociation (the difference between the two former energies) is ≤ 1.20 eV.

Both the pre-exponentials contain an entropy term, which is the product of two contributions, one from the change of configurational entropy on dissociation, and the other from the change in vibrational entropy [8]. Thus to calculate the pre-exponentials, a knowledge is required of the defect vibrational modes. This is at present unavailable.

It is interesting to compare the dissociation of the (OHV) centre with that of the monoclinic $(\text{Cr V Cr})_2$ centre (two trivalent chromium ions in association with a magnesium ion vacancy)[7]. The dissociation energy of the latter is 2.05 ± 0.1 eV, and the pre-exponential is of the order 10^9 sec^{-1} . It is believed to dissociate via the reaction $(\text{Cr V Cr})_2 \rightleftharpoons (\text{Cr}) + (\text{CrV})$, (an isolated chromium and a chromium-vacancy associate), with the isolated chromium remaining essentially immobile. The pre-exponential is much larger for the latter reaction than that for the (OHV) dissociation; this is a result of the much larger change in entropy associated with the motion of the large (CrV) associate.

If during the formation of the (OHV) centre, the vacancy is the mobile species, then the association activation energy is the energy of migration for magnesium vacancies (≤ 1.20 eV). This is in reasonable agreement with the conductivity measurements of Davies, who found a value of 0.92 eV [13], and also with an estimate made from diffusion measurements by Lidiard of 1.4 eV [12].

Studies of the kinetics of association, and the determination of the energies and entropies involved are important not only for their intrinsic interest, but also in reaching an understanding of conduction and diffusion measurements in MgO. In particular, at the temperatures at which conventional measurements have been made, the diffusion mechanism may be either extrinsic or intrinsic [9, 10].

Acknowledgements—The experimental part of this work was done at King's College, London, under a contract from the A.E.R.E., Harwell. It is a pleasure to thank Dr. A. M. Glass for his interest in this work, and his advice during the preparation of this report.

REFERENCES

1. KIRKILIN P. W., AUZINS P. and WERTZ J. E., *J. Phys. Chem. Solids* **26**, 1069 (1965).
2. GLASS A. M. and SEARLE T. M., *J. chem. Phys.* **46**, 2092 (1967).
3. SEARLE T. M., To be published.
4. HOOGENSTRAATEN N., *Philips Res. Rep.* **13**, 575 (1958).
5. GLASS A. M., *J. chem. Phys.* **46**, 2080 (1967).
6. KATS A., *Philips Res. Rep.* **1**, 133 (1962).
7. GLASS A. M. and SEARLE T. M., *J. chem. Phys.* **48**, 1420 (1968).
8. KRÖGER F., In *The Chemistry of Imperfect Crystals*, p. 262. New-Holland, Amsterdam (1964).
9. WUENSCH B. J. and VASILOS T. J., *Chem. Phys.* **36**, 2917 (1962).
10. RUNGIS T. and MORTLOCK A. J., *Phil. Mag.* **14**, 821 (1966).
11. SEARLE T. M. and GLASS A. M., *J. Phys. Chem. Solids* **29**, 609 (1968).
12. LIDIARD A. B., *Second Conf. Point Defects in Non-Metallic Solids*, British Ceramic Soc. (1966).
13. DAVIES M. O., *J. chem. Phys.* **38**, 2047 (1963).

EFFECT OF PRESSURE ON THE KNIGHT SHIFT IN V^{51} AND β - Mn^{55} METALS

B. OKAI, Y. ONODA, S. MINOMURA and S. NAKAMURA*
Institute for Solid State Physics, University of Tokyo, Tokyo, Japan

(Received 27 May 1968; in revised form 14 October 1968)

Abstract—The pressure dependence of the Knight shift in vanadium and β -manganese has been measured up to 10 kbar. In vanadium $(\Delta K/K)/(\Delta V/V)$ is approximately -0.8 , while in β -manganese the shift increases with pressure and $(\Delta K/K)/(\Delta V/V)$ amounts to -7.5 for zero pressure shifts of 0.58 and 0.4 per cent respectively. In β -manganese the pressure dependence of the quadrupole coupling constant has also been measured, which increases by 20 per cent at 10 kbar. Contributions from thermal expansion were separated. For the Knight shift, the experimental explicit temperature dependence is negligible in the range 200°–300°K, while for the quadrupole coupling constant, the explicit thermal contribution is orders of magnitude larger than the thermal expansion contribution.

1. INTRODUCTION

THE SHIFT of nuclear magnetic resonance in transition or rare earth metals shows somewhat anomalous behavior compared with that in alkali and noble metals. For example platinum, palladium, and some intermetallic compounds containing transition metals or rare earth metals exhibit negative shifts, while vanadium and niobium show large positive shifts. Scandium and lanthanum exhibit a large temperature dependence of the Knight shift which increases with decreasing temperature. These anomalous behaviors are due to a competition between a positive contribution from the s conduction electron hyperfine interaction and orbital paramagnetism and a negative one from the d electrons via the core-polarization effect.

The pressure dependence of the Knight shift has been measured in several metals, mostly non-transition metals with the exception of platinum[1, 2]. This lack of measurements for transition metals may be due to the fact that the interpretation of the shift is more difficult even at the atmospheric pressure than in the case of simple metals having closed inner shells. In fact, whether the Knight

shift increases or decreases under pressure can not easily be predicted beforehand. In this paper we present the results of a study of the pressure dependence of the Knight shift in vanadium and β -manganese metals at room temperature.

The space group of the β -manganese structure is $P4_132$ (or $P4_332$)[3]. Of the twenty atoms per unit cell eight atoms, denoted as type I, occupy sites with a threefold $\langle 111 \rangle$ rotation axis of symmetry and it has been shown that the resonance signal comes from atoms of type I alone[4]. The twelve atoms of type II occupy sites having a twofold $\langle 110 \rangle$ rotation axis. The Knight shift of V^{51} in vanadium metal is 0.58 per cent at the atmospheric pressure[5]. As for β -manganese, -0.125 per cent was obtained first as the Knight shift at 1 bar[6]. Recently, however, the magnetic moment of Mn^{55} was redetermined by ENDOR experiments[7] and a new value of $\mu^{55} = 3.4438 \pm 0.0020 \mu_n$ was assigned instead of $\mu^{55} = 3.4610 \mu_n$. Thus the Knight shift of β - Mn^{55} is believed to be 0.4 per cent, which we use in this paper.

2. EXPERIMENTAL PROCEDURE

The metal samples were obtained from the Johnson and Matthey Company. In the case of vanadium (better than 99 per cent purity),

*Faculty of Science, University of Kagoshima, Kagoshima, Japan.

after arc melted, the resulting ingot was ground on a bonded alumina wheel, which was lubricated by paraffin oil, to produce powders, which were washed in acetone and sieved through a no. 400 mesh. Then the vanadium powders were dispersed in epoxy resin to prevent them from contacting one another electrically under high pressure. The β -manganese sample was obtained by annealing the electrically deposited manganese of 99.99 per cent purity in an evacuated sealed-off quartz tube for 6 hr at 1200°K. After the crystallographic phase was confirmed by X-ray diffraction patterns, the metal was crushed in a quartz mortar and sifted through a no. 400 mesh. The particle size was less than 37 μ m. Since the values of resistivity for vanadium and β -manganese are 59 and 90 $\mu\Omega$ cm respectively, a substantially complete penetration of the radio-frequency field was ensured at all of the frequencies used.

The pressure bomb was constructed of beryllium-copper and utilized the usual unsupported-area seals. The hydrostatic pressure was generated by an intensifier with piston ratio of 18:1 and transmitted into the bomb through a flexible stainless steel tubing. White gasoline was used as the pressure-transmitting medium. The pressure in the Be-Cu bomb was measured with a manganese gauge of Harwood Engineering company.

The magnetic field from a JEOL 16 cm magnet was monitored by a proton NMR signal using a Pound-type spectrometer. The frequency of this spectrometer was stabilized against a crystal oscillator of an accuracy of the order of a few parts in 10^7 through a feedback loop, consisting of a mixer between the crystal and the spectrometer frequency, a frequency to voltage converter, an integrator, and a voltage-sensitive diode in the tank circuit of the spectrometer. The monitor proton signal was phase-detected and fed back to the power supply of the magnet subcoil. The NMR signals of V^{51} and β -Mn 55 were observed with another Pound-type spectrometer, whose frequency was swept over the reson-

ance line, while the magnetic field was kept constant with the control system described above. The frequencies of characteristic points of the resonance line were measured with a digital frequency counter. All the measurements were done at 8–9 Mcps.

3. EXPERIMENTAL RESULTS

(1) V^{51}

No noticeable change was observed in the line shape up to the highest pressure of 9 kbar. The pressure shift of the resonance frequency is, therefore, well represented by the shift of the middle point between peaks of the derivative of the resonance curve. The result is shown in Fig. 1. By using the compressibility

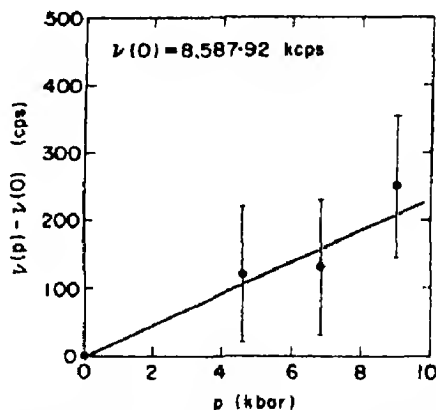


Fig. 1. The pressure dependence of V^{51} NMR frequency as a function of hydrostatic pressure. The sample temperature was 23°C.

of V metal[8], the volume dependence of the Knight shift is given as

$$\frac{d \ln K}{d \ln V} = -0.8 \pm 0.2,$$

which is in agreement with a more reliable value -0.89 ± 0.05 , recently obtained by Kushida and Murphy[9] using an accumulator.

(2) β -Mn 55

A remarkable change was observed with increasing pressure both in the line shape and the Knight shift (Fig. 2). As for the line shape, at atmospheric pressure it is already unsym-

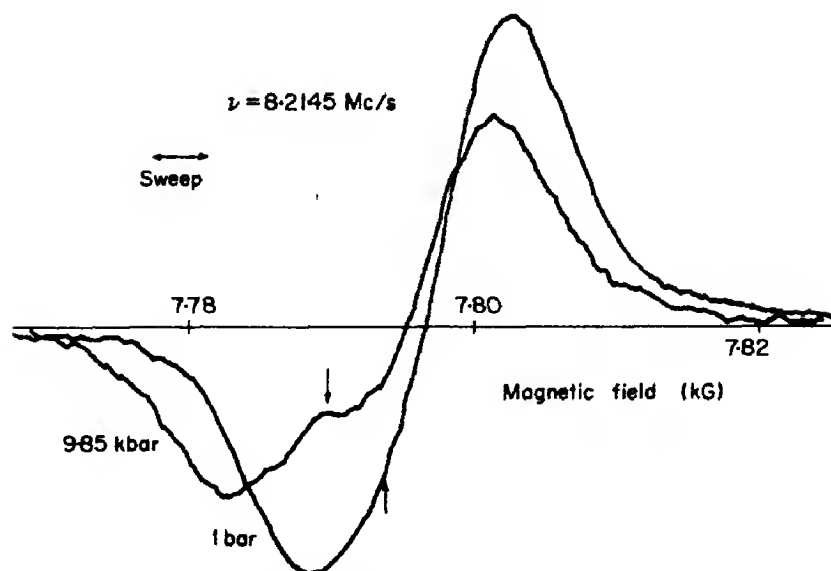


Fig. 2. The line shape of $\beta\text{-Mn}^{55}$ at 1 bar and 9.85 kbar. Field sweep is shown instead of frequency sweep which covers only a part of the shape. The arrows indicate the resonance field.

metrical indicating second-order quadrupole interaction[4] which increases with increasing pressure. Thus it becomes necessary to reduce the center-of-gravity resonance frequency, ν_0 , from the observed line shape $f(\nu)$, the derivative of the absorption line. One procedure for extracting ν_0 is to relate it to some quantities characterizing the line shape and for such, ν_1 is given which suffices the following relation:

$$f(\nu_1) = \{f(\nu_{\max}) + f(\nu_{\min})\}/2,$$

where $f(\nu_{\max})$ and $f(\nu_{\min})$ correspond to the two peaks and $\nu_{\max} > \nu_{\min}$. For this purpose, a relation

$$(\nu_0 - \nu_{\min})/(\nu_{\max} - \nu_{\min}) \text{ vs. } (\nu_1 - \nu_{\min})/(\nu_{\max} - \nu_{\min})$$

was calculated beforehand on the assumption that resonance line shape for any given crystal orientation is a Gaussian function, the derivative of which has a peak-to-peak width of 2δ . Thus $f(\nu)$ is given by the equation[10]

$$f(\nu) = \int_{-\infty}^{\infty} (\nu' - \nu)g(\nu') \exp[-(\nu - \nu')^2/2\sigma^2] d\nu',$$

where

$$g(\nu) = [(5+3x)^{-1/2} + (5-3x)^{-1/2}]/4x,$$

$$\nu_0 - 16A/9 \leq \nu \leq \nu_0,$$

$$g(\nu) = (5-3x)^{-1/2}/4x; \quad \nu_0 \leq \nu \leq \nu_0 + A$$

$$g(\nu) = 0; \quad \text{everywhere else,}$$

$$x = [16/9 - (\nu - \nu_0)A]^{1/2}.$$

In Fig. 3, $(\nu_0 - \nu_{\min})/(\nu_{\max} - \nu_{\min})$ and $(\nu_1 - \nu_{\min})/(\nu_{\max} - \nu_{\min})$ are plotted as func-

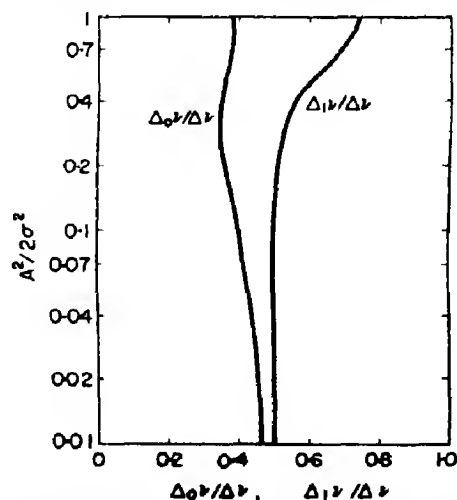


Fig. 3. The relation between $\Delta_0\nu/\Delta\nu$ and $\Delta_1\nu/\Delta\nu$ where $\Delta_0\nu/\Delta\nu = (\nu_0 - \nu_{\min})/(\nu_{\max} - \nu_{\min})$ and $\Delta_1\nu/\Delta\nu = (\nu_1 - \nu_{\min})/(\nu_{\max} - \nu_{\min})$. For further explanation the body of the paper is referred.

tions of $A^2/2\sigma^2$, where

$$A = \frac{I(I+1) - 3/4}{16\nu_0} \times \frac{3e^2Qq}{2I(2I-1)h}.$$

I is the nuclear spin, e^2qQ is the quadrupole coupling constant, and h is Planck's constant. In Fig. 4 the Knight shift is plotted

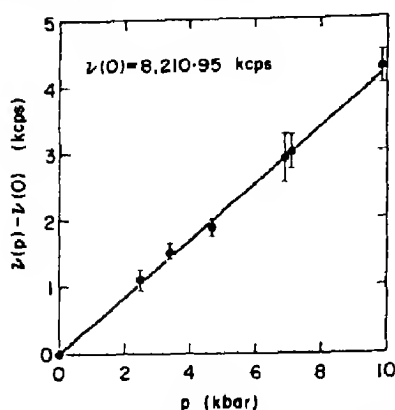


Fig. 4 The pressure dependence of β -Mn⁵⁵ NMR frequency as a function of hydrostatic pressure. The sample temperature was 23°C.

as a function of pressure up to 10 kbar. The resonance frequency increases with pressure and a relative change $\Delta K/K$ is 0.13 at 10 kbar, while the volume change of only 1.7×10^{-2} has been measured by X-ray diffraction at high pressures[11]. Thus

$$\frac{d \ln K}{d \ln V} = -7.5.$$

The change of quadrupole coupling constant is obtained from the separation of satellite pairs, as shown in Fig. 5. It increases by 20 per cent at 10 kbar.

4. DISCUSSION

According to Butterworth[12], of the nuclear shift of 0.58 per cent in pure V, 0.045 per cent is from the $4s$ -band, between 0.54 and 0.82 per cent from the orbital paramagnetism of the $3d$ -band and the remainder (0 ~ -0.28 per cent) is made up by a diamagnetic contribution from core polarization. The orbital contribution to the shift, K_1 , is predominant in

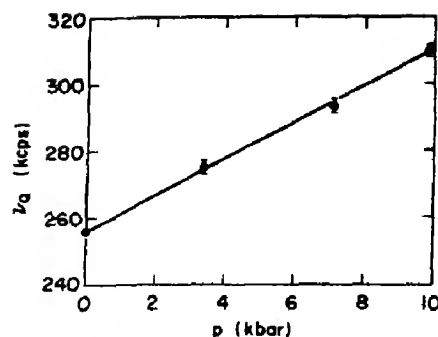


Fig. 5. The quadrupole coupling constant ν_q of β -Mn⁵⁵ as a function of hydrostatic pressure, where $\nu_q = 3e^2qQ/2I(2I-1)h$. The sample temperature was 23°C.

this case, which may be written as

$$K_1 = 2\langle r^{-3} \rangle_d \chi_1 / N,$$

where χ_1 is the orbital contribution to the molar susceptibility, N is Avogadro's number and $\langle r^{-3} \rangle_d$ is averaged over the contributing states. Our result exhibits that the pressure dependence of K_1 is approximately the same of magnitude as the volume change.

In β manganese the temperature change in the quadrupole coupling constant and the Knight shift has been given[4]

$$\begin{aligned} (\partial \ln q / \partial T)_p &= -3.1 \times 10^{-3} / \text{deg}, \\ (\partial \ln K / \partial T)_p &= 1.8 \times 10^{-4} / \text{deg}. \end{aligned}$$

Since these quantities are obtained at constant pressure, the thermal expansion contribution is to be separated in order to get an explicit temperature dependence at constant volume. By using the thermal expansion coefficient[13], the Knight shift proved to be temperature independent approximately at least in the range 200°–300°K, while the quadrupole coupling constant is shown to be explicitly dependent on temperature at constant volume with the contribution in this case being orders of magnitude larger than the thermal expansion contribution,

$$(\partial \ln q / \partial T)_v = -3.4 \times 10^{-3} / \text{deg}.$$

Internal parameters may influence on the

Knight shift and the electric field gradient differently.

From the volume dependence of β -Mn Knight shift,

$$\frac{d \ln k}{d \ln V} = -7.5,$$

various contributions to K are estimated on some crude assumptions. Generally the volume dependence of the Knight shift can be written as

$$\frac{d \ln K}{d \ln V} = \frac{K_s}{K} \frac{d \ln K_s}{d \ln V} + \frac{K_1}{K} \frac{d \ln K_1}{d \ln V} + \frac{K_d}{K} \frac{d \ln K_d}{d \ln V}, \quad (1)$$

where K_s is the contribution from the s conduction electron hyperfine interaction and K_d is the indirect Knight shift from d electron via the core polarization effect. The volume dependence of K_s , estimated from the experimental data of alkali metal, is

$$\frac{d \ln K_s}{d \ln V} = -0.1,$$

which is the average value for Na and Rb[14]. Since for the first-row transition metals[15] $0 < K_s < 0.2$ per cent, the first term of equation (1) is negligible. The derivative in the second term, $d \ln K_1/d \ln V$ is estimated as -0.8 from the volume dependence of the V metal Knight shift in which the orbital contribution is the most important. As for the last term of equation (1), K_d is expressed as

$$K_d = \frac{8\pi}{3} \rho_d \Omega \chi_d, \quad (2)$$

where ρ_d is the effect of core polarization due to the exchange interaction between core and d electrons, Ω is the atomic volume and χ_d is the volume susceptibility of the d band. From equation (2)

$$\frac{d \ln K_d}{d \ln V} = \frac{d \ln \rho_d}{d \ln V} + \frac{d \ln (\Omega \chi_d)}{d \ln V}. \quad (3)$$

The second term of equation (3), the volume dependence of the susceptibility, is estimated from the observed value of α -Mn[16] as

$$\frac{d \ln (\chi \Omega)}{d \ln V} \sim 7. \quad (4)$$

The first term, the volume dependence of the core polarization, may be substituted by the volume dependence of the coupling constant A in a ferromagnet, since A , the ratio of the NMR frequency ν to saturation magnetization σ , has the same meaning as ρ_d . An obtained value of $d \ln A/d \ln V$ for Fe, however, is -0.19 [17] which is negligible as compared with (4). Putting these into (1), one can estimate K_d/K as

$$-1.3 > \frac{K_d}{K} > -1.4,$$

which leads to $K_s < 0.2$, $0.7 < K_1 < 0.9$, $K_d \sim -0.5$ per cent.

Acknowledgements—The authors express their gratitude to Dr. Kushida for communicating his results prior to publication and to Professor V. Jaccarino for information concerning the new measurement of μ^{55} . Thanks are also due to Miss N. Sakai for compressibility measurements of β manganese. Y. Onoda wishes to thank Professor H. Inokuchi of the University of Tokyo for much encouragement during these experiments.

REFERENCES

1. KUSHIDA T. and RIMAI L., *Phys. Rev.* **148**, 593 (1966).
2. MATZKANIN G. A. and SCOTT T. A., *Phys. Rev.* **151**, 361 (1966).
3. KRIPYAKEVICH P. I., *Soviet Phys. Crystallogr.* **5**, 253 (1960).
4. DRAIN L. E., *Proc. phys. Soc.* **88**, 111 (1966).
5. BUTTERWORTH J., *Phys. Rev. Lett.* **5**, 305 (1960).
6. JACCARINO V., PETER M. and WERNICK J. H., *Phys. Rev. Lett.* **5**, 53 (1960).
7. MIMS W. B., DEVLIN G. E., GESCHWIND S. and JACCARINO V., *Phys. Lett.* **24A**, 481 (1967).
8. GSCHNEIDER A., Jr., In *Solid State Physics* (Edited by F. Seitz and D. Turnbull), Vol. 16, p. 276. Academic Press, New York (1966).
9. KUSHIDA T. and MURPHY J. C., Private communication.
10. CASABELLA P. A., *J. chem. Phys.* **40**, 149 (1964).

11. SAKAI N., Private communication.
12. BUTTERWORTH J., *Proc. phys. Soc.* **83**, 71 (1964).
13. FINKEL, *Zh. eksp. teor. Fiz.* **54**, 1697 (1968).
14. BENEDEK G. B. and KUSHIDA T., *J. Phys. Chem. Solids* **5**, 241 (1958).
15. JACCARINO V., In *Proc. Intl Sch. Physics (Enrico Fermi) Course XXXVII* (Edited by W. Marshall), p. 335. Academic Press, New York (1967).
16. SVECHKAREV I. V. and PANFILOV A. S., *Zh. eksp. teor. Fiz. Pis'ma* **2**, 501 (1965).
17. BENEDEK G. B., In *Magnetic Resonance at High Pressure*. Interscience, New York (1963).

¹⁶¹Dy ISOMER SHIFTS IN DYSPROSIUM COMPOUNDS*

TOM P. ABELES† and WILLIAM G. BOS

Department of Chemistry

and

P. J. OUSEPH

Engineering Physics Department, University of Louisville, Louisville, Ky 40208, U.S.A.

(Received 6 January 1969; in revised form 17 April 1969)

Abstract—Mössbauer absorption spectra were obtained for the 25.7 keV transitions of ¹⁶¹Dy in dysprosium metal and several compounds at room temperature. Isomer shifts relative to DyF₃ are: Dy (metal), 3.05 mm sec⁻¹; DyN, 0.85 mm sec⁻¹; Dy₂O₃, 0.56 mm sec⁻¹; DyH₂, 0.55 mm sec⁻¹; DyH₂, 0.50 mm sec⁻¹; DyF₃ · ½H₂O, -0.04; and Dy₂(SO₄)₃ · 8H₂O, -0.46 mm sec⁻¹. The relative isomer shifts of these compounds are attributed to varying degrees of covalency. The isomer shifts for the hydrides are compared to the predictions of the protonic and hydridic models for these compounds and appear to favor the hydridic model.

INTRODUCTION

MEASUREMENTS of the isomer shifts of Mössbauer absorption lines afford a means for the study of the electronic structure of solids. The spacing of nuclear energy levels is sensitive to the chemical environment of the nucleus because of hyperfine interactions between the nucleus and the electrons surrounding it. Thus the energy of the γ-radiation emitted or absorbed in a transition between the nuclear ground state and an excited state will in general differ from one compound to another. The γ-radiation emitted by the nuclei in a source will not be of the energy required for absorption by nuclei in a sample of different chemical composition. If, however, the source is moved at an appropriate velocity relative to the absorber, the emission and absorption lines can be brought back into coincidence and absorption can occur. The isomer shift measures changes in the spacing of nuclear energy levels in terms of the velocity required to bring about absorption. For a source and

absorber of different chemical composition, the isomer shift, δ , is given by [1]

$$\delta = \frac{4\pi}{5} Ze^2 R^2 \frac{\Delta R}{R} S'(Z) [|\psi(0)|_a^2 - |\psi(0)|_s^2]$$

where Z is the atomic number of the nucleus, e is the charge of the electron, R is the radius of the nucleus in the ground state $\Delta R = R_{ex} - R_{gd}$ is the difference in the radii of the excited and ground states, $S'(Z)$ is a relativistic correction factor and $|\psi(0)|_a^2$ and $|\psi(0)|_s^2$ are the electron densities at the nucleus in the absorber and source, respectively. For a given isomeric transition the isomer shift is directly proportional to the difference in electron density at the nucleus in the absorber and in the source with a proportionality constant determined by the characteristics of the nucleus. If $\Delta R/R$ is positive, a positive δ indicates a greater electron density at the nucleus in the absorber than in the source. Since the isomer shift is a linear function of $|\psi(0)|_a^2$ comparisons of electron densities in different absorbers can be made without explicit reference to the source.

The dominant direct contribution to $|\psi(0)|^2$ is from s electrons, though relativistic

*Based in part, on a Ph.D. dissertation submitted by T. P. Abeles to the Graduate School, University of Louisville (1968).

†Present address: Department of Chemistry; Virginia Polytechnic Institute; Blacksburg, Va 24061, U.S.A.

calculations show that there can be small direct contributions from p electrons. It should be emphasized that the s electrons from all occupied levels contribute to $|\psi(0)|^2$. Only s electrons from the valence level are gained or lost upon chemical reaction, but changes in $|\psi(0)|^2$ due to indirect effects occur and are of importance. In particular the density distribution of s electrons in the atom core is affected by the gain or loss of valence electrons because of changes in shielding. The removal of valence electrons leads to slight increases in the contribution of inner s electrons to $|\psi(0)|^2$. The degree to which valence electrons shield inner s electrons depends on the kind of orbital they occupy— s , p , d or f —as well as their principle quantum number. Further, the degree of ionicity of a chemical bond affects the isomer shift since $|\psi(0)|^2$ will be sensitive to the extent to which electrons are gained or lost.

In binary compounds of the rare earths with elements of relatively high electronegativity, the bonding is predominantly ionic. An estimate of the extent of covalent contributions can be made on the basis of electronegativity differences between the rare earth ion and the anion or on the basis of the polarizability of the anion. The measurement of isomer shifts provides an experimental approach to this question. Differences in rare earth isomer shifts for nominally ionic compounds are due to varying degrees of covalency which place electron density in the rare earth valence shell.

The Mössbauer effect has been observed for ten of the rare earth elements and is predicted for three others[2, 3]. Apart from studies of metals and alloys, isomer shift studies of rare earth compounds have been limited in number[4, 5]. Only in the case of europium have a large number of compounds been studied[6–9]. Because of the stability associated with $4f^7$ configuration of europium (II), the $4f$ level plays a prominent role in determining the isomer shifts of europium compounds. In compounds of other rare earth

elements, $4f$ electrons play a less important role in determining the isomer shift. Alloys of dysprosium with several other metals have been studied using Mössbauer spectroscopy [9–13]. The isomer shift of Dy metal relative to Dy_2O_3 has been reported as 2.5 mm/sec by Ofer[10].

The rare earth hydrides present an especially interesting problem with regard to bonding. A general review of the properties of rare earth hydrides is given in reference [14]. The hydrogen species in transition metal hydrides has been variously described as protonic, hydridic or atomic in nature. The arguments for and against each model have been reviewed by Gibb[15], by Libowitz [16] and by Ebisuzaki and O'Keefe[17]. The magnetic properties of yttrium and lanthanum hydrides favor either a protonic model [18, 19] or a hydridic model[20], rather than an atomic model. For the other members of the rare earth series which have been studied, the magnetic properties of the metals and their hydrides are dominated by unpaired $4f$ electrons and their interpretation is less straightforward. Kopp and Schreiber [21, 22] have interpreted hydrogen Knight shifts for the hydrides of cerium, praseodymium, neodymium and gadolinium in terms of a protonic model. The magnetic susceptibilities of several rare earth hydrides were interpreted in terms of a hydridic model by Wallace *et al.*[23] though more recently Wallace and Mader[24] pointed out that the magnetic susceptibilities of praseodymium hydrides can be interpreted in terms of either a protonic or hydridic model. The reason for this ambiguity can be traced to the fact that the conduction band parameters involved are $N(E_F)$ and the product $n(n'-n)$. $N(E_F)$ is the density of states at the Fermi energy, n is the number of electrons in the band per atom and n' is the number of electrons which the band can hold per atom. Both of $N(E_F)$ and $n(n'-n)$ approach zero as a band is either filled or emptied[20].

Heckman[25] has recently reported that the

Hall coefficients for cerium hydrides are positive, increasing with increasing hydrogen content. These results favor the protonic model, but further study is needed to account for the lack of a linear relationship between the number of holes per metal atom and the hydrogen/cerium ratio and to account for the negative sign of the Seebeck coefficient measured by Heckman earlier[26]. The results of a preliminary study of positron annihilation in cerium hydrides favor a hydridic model[27].

EXPERIMENTAL

(A) Mössbauer system

The Mössbauer system was a twin 'speaker drive' system, driven at constant acceleration by a triangular pulse. The trigger pulse for the start of each cycle was fed to a RIDL 54-6 time base generator, coupled with a RIDL 34-12B 400 channel analyzer. The mechanical drive system and the concomitant electronics are described by Bowers[28].

The detection system was assembled from commercially available components. A gas proportional tube powered by a Hamner N4305 high voltage power supply was utilized. The output was amplified and gated through Austin Scientific Associates equipment and then sent to the RIDL multichannel analyzer which was operated in the time-base mode. The coupling of the drive system with the detector was that described by Wertheim [29]. The triangular pulse drives the source at constant acceleration. At one point in the cycle a trigger pulse trips the 400 channel analyzer. By adjusting the time base generator and the triangular pulse properly, the scale from channel 1 to 400 is linear in velocity. As the time base generator advances from one channel to the next, the analyzer stores the pulses sent by the detector in the appropriate location. To obtain the velocities necessary for dysprosium, it was necessary to remove the speaker cones and enlarge the gap in the speaker magnet surrounding the drive coils.

The velocity was adjusted to a maximum of approximately ± 3 cm/sec and the instrument was calibrated utilizing an Fe-Pd source and an iron foil adsorber. The values for the magnetic splittings of the iron absorber were taken from the data of Wertheim and Herber [30] and Preston *et al.*[31] and the IS for the iron foil absorber relative to the Fe-Pd source was taken from Herber's data[32]. No drift was detectable in the systems during the course of the runs.

The sample holders utilized were machined from lucite and allowed a circular sample of 3 cm rad. to be sandwiched between two pieces of $\frac{1}{2}$ in. thick lucite. These were sealed with a solution of lucite dissolved in dichloromethane. A sample density of approximately 30 mg/cm² was found to be adequate.

The 15 mCi source used in this study was prepared as ^{161}Tb in $\text{GdF}_3 \cdot \frac{1}{2}\text{H}_2\text{O}$ by Nuclear Science (A division of International Chemical and Nuclear Corporation). ^{161}Tb decays to ^{161m}Dy which in turn yields the 25.7 keV Mössbauer gamma ray whose absorption was measured.

The spectra reported here were all obtained at room temperature.

(B) Sample preparation

Dy metal was used in the form of filings obtained from an ingot (United Mineral and Chemical Corp., 99.9 per cent). Filing was carried out under mineral oil which was subsequently removed by washing with tetrahydrofuran and ether.

Dysprosium hydrides were obtained as powders from the reaction of the metal with hydrogen from an Elhygen electrolytic generator. Freshly polished samples of the metal, approximately 0.5 g in weight, were placed in molybdenum pans suspended from a Cahn Gram electrobalance mounted in a vacuum chamber with a quartz hangdown tube. The initial reaction was carried out by heating each sample to 500°C and then introducing hydrogen to a pressure of 50 cm Hg. Compositions near DyH_2 resulted. Upon

cooling, additional hydrogen was taken up to a maximum composition of approximately $\text{DyH}_{2.9}$. Each sample was thermally cycled between room temperature and 500°C several times to insure reaction by all portions of the metal. If a sample of the higher composition was desired, the sample was cooled to room temperature under hydrogen and the system was evacuated. No change in composition was observed for samples under vacuum at room temperature for periods up to 4 hr. To obtain samples of the dihydride, the trihydride was heated under vacuum until the desired composition was achieved, then cooled to room temperature. Samples were dumped from the pan and passed through a Whitey 43S4 ball valve into a glass sample tube. The valve was closed and the protected sample transferred to a dry box for grinding and mounting.

DyN was prepared from the hydride at 900°C under a nitrogen atmosphere using the procedure described by Schumacher and Wallace[33]. The composition of the sample was monitored by measuring pressure changes in the reaction system whose volume was precalibrated. It is likely that the nitride thus obtained was slightly nitrogen deficient [34].

Dy_2O_3 was obtained from the American Potash and Chemical Corp. and was of 99.9 per cent purity designation. This material was used as a Mössbauer absorber and as the starting material for the preparations described below.

Anhydrous DyF_3 was prepared by the reaction of Dy_2O_3 with prepurified ammonium bifluoride (MC & B) at 325°C in an Inconel reaction vessel using the procedure described by Spedding and Daane[35].

$\text{DyF}_3 \cdot \frac{1}{2}\text{H}_2\text{O}$ was obtained using the method of Spedding and Daane[36]. The dried product was ground in a mortar and stored in a stoppered vial.

$\text{Dy}_2(\text{SO}_4)_3 \cdot 8\text{H}_2\text{O}$ was crystallized from a dilute sulfuric acid solution by cooling and evaporation as described by Wendlandt[37].

RESULTS AND DISCUSSION

Mössbauer absorption spectra were obtained for ^{161}Dy in Dy metal, $\text{DyH}_{2.90}$, $\text{DyH}_{2.08}$, DyN , Dy_2O_3 , DyF_3 , $\text{DyF}_3 \cdot \frac{1}{2}\text{H}_2\text{O}$ and $\text{Dy}_2(\text{SO}_4)_3 \cdot 8\text{H}_2\text{O}$. The isomer shifts for each spectrum were found by applying the method of centroids to the normalized curves. The values thus obtained are reported relative to DyF_3 in Table 1. The error limits given are maxima based on the estimated stability of the electronics system. Somewhat greater accuracy was probably realized; separate measurements of the isomer shift for the trihydride yielded values of -2.49 and $-2.51 \text{ mm sec}^{-1}$. The short half-life of the ^{161}Tb source prevented additional tests of reproducibility. The difference in isomer shifts between Dy metal and the Dy_2O_3 , 2.51 mm sec^{-1} , is in good agreement with the value reported by Ofer[10].

Table 1. Isomer shifts of dysprosium compounds

Compound	Isomer shift* (mm sec^{-1})
Dy	3.05 ± 0.08
DyN	0.85 ± 0.08
Dy_2O_3	0.56 ± 0.08
$\text{DyH}_{2.90}$	0.55 ± 0.08
$\text{DyH}_{2.08}$	0.50 ± 0.08
DyF_3	0.00 ± 0.08
$\text{DyF}_3 \cdot \frac{1}{2}\text{H}_2\text{O}$	-0.04 ± 0.08
$\text{Dy}_2(\text{SO}_4)_3 \cdot 8\text{H}_2\text{O}$	-0.46 ± 0.08

*Isomer shift values were measured relative to a source containing ^{161}Dy in a $\text{GdF}_3 \cdot \frac{1}{2}\text{H}_2\text{O}$ matrix but are reported here relative to the measured DyF_3 spectrum

Small uncertainties existed in the composition of the hydride and nitride samples. These compounds exhibited a tendency to desorb gas while under γ -irradiation. For the hydrides, the change in composition due to desorption is estimated to have been less than $\text{H/Dy} = 0.05$. X-ray powder patterns of the hydride and nitride samples

were taken before and after their use in the Mössbauer spectrometer. No phase changes were detected. The dihydride is single phase, face-centered cubic, from $\text{DyH}_{1.9}$ to $\text{DyH}_{2.1}$, and the trihydride single phase, hexagonal close packed, from $\text{DyH}_{2.7}$ to compositions approaching DyH_3 [38]. Samples of compositions below $\text{DyH}_{1.9}$ and between $\text{DyH}_{2.1}$ and $\text{DyH}_{2.7}$ contain two phases.

Of the compounds whose isomer shifts are reported here, DyF_3 is the most ionic. We take it to be completely ionic on the basis of an electronegativity difference of 2.9 and the Dailey and Townes[39] method of estimating ionic character. The isomer shifts of the other Dy compounds and of Dy metal provide a measure of the extent to which the Dy electron configurations in these materials differ from the $\text{Xe } 4f^9$ configuration of Dy^{+3} .

The isomer shift of Dy metal relative to

DyF_3 can be attributed to the conduction electrons of the metal. On the basis of specific heat and Hall effect results, Gschneider [40] has proposed a simple model for the conduction band of Dy and several other rare earth metals. As shown in Fig. 1(a), the $6s$ and $5d$ bands overlap to the extent that the Fermi level lies near the top of the $6s$ band. The $6s$ band is nearly filled by two electrons per metal atom and the d band is occupied to the extent of just over one electron per metal atom. While there may be some question as to whether distinct s or d character can be attributed to the electrons in the conduction band, Gschneider's treatment, which depends explicitly on the number of holes in the $6s$ band and the number of electrons in the $5d$ band, gives a good explanation of conductivity in the metals to which it has been applied. In any case, this band picture provides a convenient method for recognizing

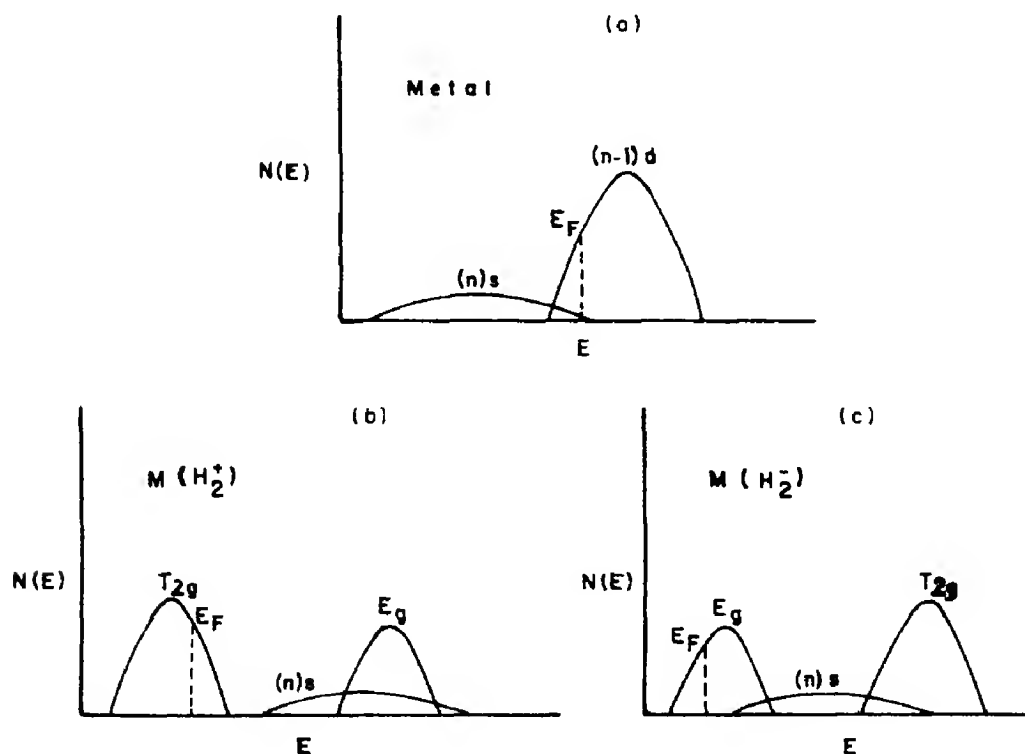


Fig. 1. Schematic band diagrams showing the location of the Fermi energy, E_F , in yttrium and the rare earth metals and in their dihydrides; (a) metal; (b) dihydride according to the protonic model; (c) dihydride according to the hydridic model.

the relative contributions of the atomic orbitals to the character of the conduction band.

For the 25.7 keV transition of ^{161}Dy , $\Delta R/R$ is positive. Therefore, positive isomer shifts correspond to increased electron density at the Dy nucleus. The positive isomer shift for Dy metal can be attributed to the presence of two 6s electrons per Dy atom in the conduction band of the metal. There is, in addition, one 5d electron per Dy atom present in the metal. This latter should give rise to a negative contribution to the isomer shift for the metal since it shields the nucleus from the s electrons. Since a large positive shift is observed, the presence of s electrons must be the dominant effect on the isomer shift. To the extent that the d electron affects the isomer shift, the shift due to the s electrons must be larger than the measured shift. We will assume that the effect of the d electron is small and take the measured shift to be a good approximation of the shift due to the s electrons. This approximation is reasonable since only one d electron is present per Dy atom; the shielding of s electrons in the core by 5d electrons is expected to be small because most of the 5d electron density lies farther from the nucleus than that of the inner s electrons; and the d electron in the metal is delocalized and is therefore less effective in shielding core electrons than otherwise.

Following Brix *et al.*[9], we estimate the 6s electron density at the nucleus in the metal to be reduced to 0.5 of the free atom value due to delocalization. Then in our approximation, the isomer shift between Dy metal and DyF_3 is due to the presence of the equivalent of one localized 6s electron. On this basis we establish an approximate scale of 1.0 6s electrons per 3.0 mm sec⁻¹ for measuring the gain or loss of 6s electrons in terms of the isomer shift.

The isomer shifts of DyF_3 , Dy_2O_3 and DyN increase linearly with decreasing anion electronegativity. In these compounds the

direction of electron transfer via covalency effects must be from the anion to Dy. Since the isomer shift of these compounds are positive relative to DyF_3 , the dominant effect on the isomer shift must be the transfer of electron density to the Dy 6s orbitals. Since the isomer shift is less sensitive to the indirect effect of 5d, 5p or 4f orbital occupancy, some transfer of electron density to these orbitals is also possible. For these predominantly ionic compounds, the degree of covalency will be determined largely by the spatial extent of the unoccupied cation orbitals. For the free atom, the radius of the principal maximum of the 6s wave function is significantly larger than that of the 5d[41]. If the same were true in the +3 ion, the 6s orbital would be more readily available to participate in covalency than the 5d. Assuming no d orbital participation, we calculate from the isomer shifts that 0.20 and 0.27 electrons are transferred to the 6s orbitals of Dy in Dy_2O_3 and DyN , respectively. To the extent that the 5d orbitals are occupied, greater occupancy of the 6s orbitals is required to account for the measured shift. The 6s occupancy derived here represents, therefore, an estimate of the minimum degree of covalency.

Both hydrated salts reported here exhibit negative isomer shifts relative to DyF_3 , though that of $\text{DyF}_3 \cdot \frac{1}{2}\text{H}_2\text{O}$ is small and within experimental error of zero. The isomer shift of $\text{Dy}_2(\text{SO}_4)_3 \cdot 8\text{H}_2\text{O}$ is relatively large and must be taken as real. In aqueous solution, Dy^{+3} is hydrated to the extent of eight or more water molecules[42]. In $\text{Dy}_2(\text{SO}_4)_3 \cdot 8\text{H}_2\text{O}$ there is some possibility of coordination with sulfate ion as well as water. The rare earth ions frequently achieve coordination numbers of eight or more[43]. Covalent bond formation in these species involves some combination of 6s, 5d, 6p and, possibly, 4f orbitals[44]. In $\text{Dy}_2(\text{SO}_4)_3 \cdot 8\text{H}_2\text{O}$ coordination to Dy^{+3} occurs through covalent bond formation in such a way as to decrease the electron density at the Dy nucleus and a negative isomer shift results.

Even if the Dy $6s$ orbital is one of those so used, the occupancy of the other orbitals which shield the nucleus and decrease the electron density there must be the dominant effect.

The isomer shifts for dysprosium hydrides are of particular interest because they provide information concerning the electron distribution around Dy in these compounds. The isomer shifts of DyH_2 and DyH_3 are approximately equal to that of Dy_2O_3 . The amount by which the shift for DyH_2 is less positive than that of DyH_3 is small and within the maximum experimental uncertainty.

Based on an analysis of the magnetic properties of yttrium metal and yttrium hydrides, Parks and Bos[45] have formulated the simple band schemes for the protonic and hydridic models of rare earth hydrides shown in Fig. 1(b) and Fig. 1(c). Because yttrium has no unpaired electrons, the magnetic properties are due primarily to conduction band electrons. The great similarity of yttrium hydrides [46] to the rare earth hydrides [14] in properties which are less sensitive to the rare earth $4f$ electrons indicates that the general features of these band schemes should apply to the rare earth hydrides as well as to yttrium hydrides. The similarity is especially striking for yttrium and dysprosium. Both yttrium[47] and dysprosium[48] are hexagonal close packed (Y: $a_0 = 3.654 \text{ \AA}$, $c_0 = 5.750 \text{ \AA}$; Dy: $a_0 = 3.590$, $c_0 = 5.647 \text{ \AA}$) and have very similar Fermi surfaces[47]. Both dihydrides are f.c.c. (YH_2 : $a_0 = 5.205 \text{ \AA}$; DyH_2 : $a_0 = 5.201 \text{ \AA}$) and both trihydrides are hexagonal close packed[38] (YH_3 : $a_0 = 3.674 \text{ \AA}$, $c_0 = 6.595 \text{ \AA}$; DyH_3 : $a_0 = 3.671 \text{ \AA}$, $c_0 = 6.615 \text{ \AA}$). The heats of formation of the hydrogen deficient dihydrides are -44.4 and -45.4 kcal per mole of hydrogen for yttrium[46] and dysprosium[49], respectively.

The protonic model requires that the conduction band in the hydrides be split in such a way as to accommodate a maximum of six electrons per metal atom in the lower portion of the band[18]. The limiting composition of

the hydrides, MH_3 , results when three hydrogens per metal atom have donated their electrons to the conduction band. At this point the band is full and the metallic character of the dihydrides has disappeared. The dihydrides have the fluorite structure with hydrogen occupying the tetrahedral interstices around the metal atoms. In the crystal field of eight positive charges representing the ionized hydrogen in a cubic configuration surrounding the metal, the T_{2g} orbitals of the central atom would be lowered relative to the E_g orbitals. In Fig. 1, the $6s$ band is placed above the T_{2g} band to preserve the role of the latter in determining the limiting composition. In addition, the long nuclear spin-lattice relaxation time for Y in YH_2 indicates that there is little s character at the Fermi energy.

In the hydridic model the limiting composition is attributed to depopulation of the conduction band with the three electrons per metal being transferred to three hydrogens. Taking the eight cubic hydrogens of the dihydrides as being negatively charged, the d orbitals of the metal split such that the E_g band lies below the T_{2g} band. The $6s$ band is placed above the Fermi energy of the dihydride to account for the long Y relaxation time in YH_2 .

Predictions of the isomer shifts of Dy in Dy hydrides based on each of the two band schemes can be compared to the experimental results and used as one criterion of the validity of the schemes. According to the protonic model, the electron configurations of Dy in DyH_2 and DyH_3 are $(\text{Xe}) 4f^9 5d^5$ and $(\text{Xe}) 4f^9 5d^6$, respectively, with the $5d$ electrons being somewhat delocalized in DyH_2 . Isomer shifts at least slightly more negative than that of DyF_3 are predicted for both hydrides, with that of DyH_3 slightly more negative than that of DyH_2 . The observed isomer shifts are, of course, positive relative to DyF_3 . No covalency effects in the usual sense can be postulated here since the proton of this model has little or no electron density to contribute. Incomplete transfer of the hydro-

gen electrons to the conduction band, so long as the band is of d character, also fails to account for a more positive shift than that of DyF_3 .

The hydridic model leads to $(\text{Xe})4f^95d^1$ and $(\text{Xe})4f^95d^0$ configurations for Dy in DyH_2 and DyH_3 , respectively. If the bonding were purely ionic, DyH_3 would have a shift of zero and DyH_2 would have a slightly negative shift relative to DyF_3 . In the case of hydride ions, however, partial covalent bonding effects of some significance would be expected on the basis of hydrogen electronegativity and hydride ion polarizability. That these effects should result in a positive shift nearly equal to that of Dy_2O_3 or even greater is not surprising. Further, a slightly less positive shift is predicted for DyH_2 than for DyH_3 due to the presence of a single, delocalized electron per metal atom in DyH_2 . The third hydrogen of DyH_3 occupies the octahedral interstices of the fluorite structure. The metal-hydrogen distance for the octahedral hydrogen is 2.58 Å compared to 2.25 Å for the tetrahedral hydrogens. Libowitz[50] has shown that the observed Dy-H distance in DyH_2 is near that to be expected from the ionic radii of Dy^{+3} and H^- . Both the loss of a d electron and covalency contributions from the octahedral hydrogen would contribute to a positive shift from DyH_2 to DyH_3 . Since the observed shift is small, partial covalent bonding by the octahedral hydrogens must not occur to any significant extent. Hydrogen is less electronegative than either oxygen or nitrogen. The fact that a larger positive shift is not observed for DyH_3 may be attributed to the fact that only two-thirds of the hydrogen contribute to partial covalent bonding.

Acknowledgements—This work was supported, in part, by a National Science Foundation Grant and, in part, by a Sustaining University Program Grant to the University of Louisville from the National Aeronautics and Space Administration. T.P.A. held a National Defense Education Act Title IV Fellowship from 1966 to 1968.

REFERENCES

1. SHIRLEY D. A., *Rev. mod. Phys.* **36**, 339 (1964).
2. GREENWOOD N. N., *Chem. Brit.* **3**, 56 (1967).
3. KAINDL G. and MÖSSBAUER R. L., *Phys. Lett.* **26B**, 386 (1968).
4. CLIFFORD A. F., In *The Mössbauer Effect and its Application in chemistry* (Edited by R. F. Gould), p. 113. American Chemical Society, Washington D.C. (1967).
5. HENNING W., HÜFNER S., KIENTLE P., QUITMANN D. and STEICHELE E., In *Applications of the Mössbauer Effect in Chemistry and Solid-State Physics*, p. 173. IAEA, Vienna (1966).
6. DEENEY F. A., DELANEY J. A. and RUDDY V. P., *J. inorg. nucl. Chem.* **30**, 1175 (1968).
7. DEENEY F. A., DELANEY J. A. and RUDDY V. P., *Phys. Lett.* **25A**, 370 (1967).
8. WICKMAN H. H., NOWIK I. and WERNICK J. H., *J. appl. Phys.* **37** 1246 (1966).
9. BRIX P., HÜFNER S., KIENTLE P. and QUITMANN D., *Phys. Lett.* **13**, 140 (1964).
10. OFER S. and SEGAL E., *Phys. Rev.* **141**, 448 (1966).
11. OFER S., RAKAVY M., SEGAL E. and KHURGIN B., *Phys. Rev.* **138**, A241 (1965).
12. STONE J. A., NICOL M., JURA G. and RASUSSEN J. O., Rep. No. UCRL-1063, Rev. (1963).
13. KHURGIN B., OFER S. and RAKAVY M., *Nucl. Phys.* **A110**, 577 (1968).
14. BOS W. G. and GAYER K. H., *J. nucl. Mater.* **18**, 1 (1966).
15. GIBB T. R. P., In *Progress in Inorganic Chemistry* (Edited by F. A. Cotton), Vol. 3, p. 315. Interscience, New York (1962).
16. LIBOWITZ G. G., *The Solid State Chemistry of Binary Metal Hydrides*. Benjamin, New York (1965).
17. EBISUZAKI Y. and O'KEEFFE M., In *Progress in Solid State Chemistry* (Edited by H. Reiss), Vol. 4, p. 187. Pergamon Press, Oxford (1967).
18. SCHREIBER D. S., *Phys. Rev.* **137**, A860 (1965).
19. SCHREIBER D. S. and COTTS R. M., *Phys. Rev.* **131**, 1118 (1963).
20. BOS W. G. and GUTOWSKY H. S., *Inorg. Chem.* **6**, 552 (1967).
21. KOPP J. P. and SCHREIBER D. S., *J. appl. Phys.* **38**, 1373 (1967).
22. KOPP J. P. and SCHREIBER D. S., *Phys. Lett.* **24A**, 323 (1967).
23. WALLACE W. E., KUBOTA Y. and ZANOWICK R. L., In *Nonstoichiometric Compounds* (Edited by R. Ward), p. 122. American Chemical Society, Washington, D.C. (1963).
24. WALLACE W. E. and MADER K. H., *J. chem. Phys.* **48**, 84 (1968).
25. HECKMAN R. C., *J. chem. Phys.* **46**, 2158 (1967).
26. HECKMAN R. C., *J. chem. Phys.* **40**, 2958 (1964).
27. GUSTAFSON D. R., Rep. No. SC-CR-67-2572, to Sandia Corporation (1966).
28. BOWERS K. R., Msc. University of Louisville (1968).
29. WERTHEIM G. K., *The Mössbauer Effect*. Academic Press, New York (1964).

30. WERTHEIM G. K. and HERBER R. H., *J. chem. Phys.* **38**, 2106 (1963).
31. PRESTON R. S., HANNA S. S. and HEBERLE J., *Phys. Rev.* **128**, 2207 (1962).
32. HERBER R. H., In *Applications of the Mössbauer Effect in Chemistry and Solid-State Physics*, p. 121. IAEA, Vienna (1966).
33. SCHUMACHER D. P. and WALLACE W. E., *Inorg. Chem.* **5**, 1563 (1966).
34. SCLAR N., *J. appl. Phys.* **35**, 1534 (1964).
35. SPEDDING F. H. and DAANE A. H., *Prog. nucl. Energy* **1**, 413 (1956).
36. DAANE A. H. and SPEDDING F. K., *J. electrochem. Soc.* **100**, 442 (1953).
37. WENDLANDT W. W., *J. inorg. nucl. Chem.* **7**, 51 (1958).
38. PEBLER A., and WALLACE W. E., *J. phys. Chem.* **66**, 148 (1962).
39. DAILEY B. P., and TOWNES C. H., *J. chem. Phys.* **23**, 118 (1955).
40. GSCHNEIDER K. A., In *Rare Earth Research III* (Edited by L. Eyring), p. 153. Gordon and Breach, New York (1965).
41. WABER J. T. and GROMER D. T., *J. chem. Phys.* **42**, 4116 (1966).
42. HOARD J. L., LEE B. and LIND M. D., *J. Am. Chem. Soc.* **87**, 1612 (1965).
43. MUETTERTIES E. L. and WRIGHT C. M., *Q. Rev. chem. Soc.* **21**, 109 (1967).
44. LIPPARD S. J., In *Progress in Inorganic Chemistry* (Edited by F. A. Cotton), Vol. 8, p. 109. Interscience, New York (1962).
45. PARKS C. D. and BOS W. G., To be published.
46. LUNDIN C. E. and BLACKLEDGE J. P., *J. electrochem. Soc.* **109**, 838 (1962).
47. SPEDDING F. H., DAANE A. H. and HERRMANN K. W., *Acta crystallogr.* **9**, 559 (1956).
48. KEETON S. C. and LOUCKS T., *Phys. Rev.* **168**, 672 (1968).
49. BECK R. L., Rep. No. LAR-10 (1962).
50. LIBOWITZ G. G., In *The Solid State Chemistry of Binary Metal Hydrides*, pp. 7-9. Benjamin, New York (1965).

EXPERIMENTAL PROOF FOR A TWO-BAND CONDUCTION IN NICKEL ALLOYS

P. LEONARD, M. C. CADEVILLE, J. DURAND and F. GAUTIER

Service de Physique des Solides*, Institut de Physique-3, rue de l'Université, Strasbourg, France

(Received 18 September 1968; in revised form 7 April 1969)

Abstract—Evidence for a two-band conduction in nickel alloys is given through a study of $Ni(CoCr)$ ternary alloys. Spin sub-band resistivities for $NiCo$ and $NiCr$ alloys are determined and found to be in agreement with theoretical analysis.

INTRODUCTION

THE RESIDUAL resistivity of dilute alloys of transition metals arises mainly from the scattering of 's' electrons by the $s-d$ part of the impurity perturbing potential[1]. Because of this $s-d$ coupling, the conductivities for the spin \uparrow and spin \downarrow bands are quite different in ferromagnetic alloys: this accounts for strong deviations from the Matthiessen rule (M.R.)[2]. The sub-band resistivities can be deduced from the temperature variation of the resistivity of binary alloys or from a study of ternary alloys[2, 3].

We report here the first results of a study of these deviations in alloys with a nickel matrix. The present work on the low temperature resistivities of ternary alloys $Ni(CoCr)$ gives a direct and unambiguous proof for a two-band conduction in ferromagnetic alloys: it allows the experimental determination of the resistivities associated with each spin sub-band (\uparrow , \downarrow) for binary alloys $NiCo$, $NiCr$.

I. EXPERIMENTAL RESULTS

The alloys were prepared in argon atmosphere by melting the pure components with an induction furnace: the purity of the elements was 99.997 per cent for nickel and cobalt and 99.998 per cent chromium. The weight losses during the melting were negligible.

A standard potentiometric method was used for the resistivity measurements at 4.2°K and room temperature. The sample was shaped to cylinders (2.5 mm dia. and about 70 mm in length). The resistance could be measured with an accuracy of 0.1 per cent.

For binary alloys with low values of the atomic impurity concentration C ($C < 4$ per cent), the alloys are homogeneous and the interactions between impurities are negligible as shown by the linear variations of the residual resistivity and saturation magnetization with impurity concentration. The residual resistivities for cobalt and chromium impurities are in good agreement with previous data[4, 5]: $\rho_1 = 0.20 \mu\Omega \cdot \text{cm/at.}\%$ for cobalt, and $\rho_2 = 5.0 \mu\Omega \cdot \text{cm/at.}\%$ for chromium.

For ternary alloys, the total impurity concentration is less than 4 per cent. The interactions between impurities are shown to be negligible by magnetization measurements. The saturation magnetization of a ternary alloy; $\mu(C_1, C_2)$, is given by a simple superposition law (see Table 1):

$$\mu(C_1, C_2) = \mu_{Ni} + C_1 \left(\frac{d\bar{\mu}_1}{dC_1} \right)_{C_1=0} + C_2 \left(\frac{d\bar{\mu}_2}{dC_2} \right)_{C_2=0}; \quad (1-1)$$

in (1-1), C_1 and C_2 are the cobalt and chromium concentrations, μ_{Ni} is the pure nickel magnetization, $(d\bar{\mu}_1/dC_1)_{C_1=0}$ and $(d\bar{\mu}_2/dC_2)_{C_2=0}$ are the variations of magnetization

*Equipe de Recherches sur la structure électronique des Solides, associée au CNRS (no. 100).

Table 1. Saturation magnetization and residual resistivity of ternary alloys Ni(CoCr)

	NiCo _{0.5} Cr ₂	NiCo ₁ Cr ₁	NiCo ₁ Cr ₂	NiCo ₂ Cr ₁
$\mu_{\text{calc.}} (\mu_B/\text{At.})$	0.514	0.568	0.515	0.571
$\mu_{\text{exp.}} (\mu_B/\text{At.})$	0.511	0.553	0.510	0.569
$\rho = C_1\rho_1 + C_2\rho_2 (\mu\Omega\cdot\text{cm})$	10.1	5.2	10.2	5.4
$\rho_{\text{exp.}} (\mu\Omega\cdot\text{cm})$	11.25	7.18	11.76	8.82

of binary alloys NiCo, NiCr (per at.% of impurity).

2. DEVIATIONS FROM THE MATTHIESSEN RULE AND DETERMINATION OF THE $s \uparrow$ AND $s \downarrow$ RESISTIVITIES

In the low concentration limit and when the interactions between impurities are negligible, the residual resistivity $\rho(C_1, C_2)$ should be written, according to the Matthiessen rule,

$$\rho(C_1, C_2) = C_1\rho_1 + C_2\rho_2; (\text{M.R.}) \quad (2-1)$$

in (2-1), C_1 (or C_2) is the atomic concentration of cobalt (or chromium); ρ_1 (or ρ_2) is the residual resistivity of cobalt (or chromium) in nickel.

The experimental results are not in agreement with this simple law (see Table 1 and Figs. 1, 2):

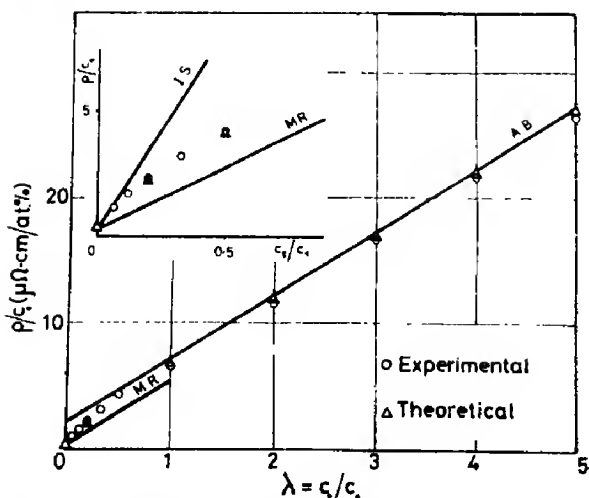


Fig. 1. ρ/C_1 as a function of $\lambda_1 = C_2/C_1$. M.R.: behaviour deduced from Matthiessen rule; I.S.: initial slope of $f(\lambda_1)$; A.B.: asymptotic behaviour deduced theoretically.

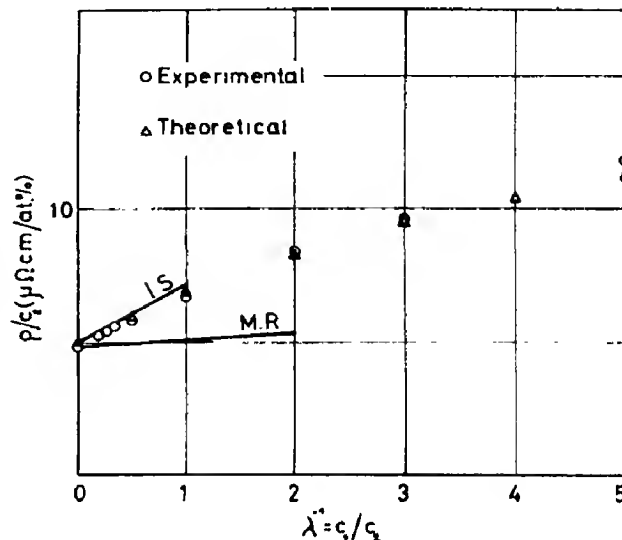


Fig. 2. ρ/C_2 as a function of $\lambda_2 = C_1/C_2$. M.R.: behaviour deduced from Matthiessen rule; I.S.: initial slope of $g(\lambda_2)$.

$\rho(C_1, C_2)$ is not a linear function vs. each impurity concentration.

However, the experimental results show that the resistivity is a linear function of either C_1 or C_2 for a given value of the concentration ratio: $\lambda = C_2/C_1$ (Fig. 3):

$$\rho(C_1, C_2) = C_1 f(\lambda) = C_2 g(\lambda^{-1}). \quad (2-2)$$

The functions $f(\lambda)$ and $g(\lambda^{-1})$ as shown by Figs. 1 and 2 are different; there is no simple relation between them.

Such a functional law is easily derived from a two-band model if we assume that: (1) the interactions between impurities are negligible, (2) the temperature T is such that the electron-magnon and electron-phonon mean free paths are much larger than the impurity mean free path ($T \rightarrow 0$).

Consequently, the measured conductivity is the sum of the conductivities associated with each band. We obtain [2]:

$$f(\lambda) = \frac{(\rho_{1\uparrow} + \lambda\rho_{2\uparrow})(\rho_{1\downarrow} + \lambda\rho_{2\downarrow})}{\rho_{1\uparrow} + \rho_{1\downarrow} + \lambda(\rho_{2\uparrow} + \rho_{2\downarrow})} \quad (2-3a)$$

$$g(\lambda) = \frac{(\rho_{2\uparrow} + \lambda\rho_{1\uparrow})(\rho_{2\downarrow} + \lambda\rho_{1\downarrow})}{\rho_{2\uparrow} + \rho_{2\downarrow} + \lambda(\rho_{1\uparrow} + \rho_{1\downarrow})} \quad (2-3b)$$

In (2-3) $\rho_{i\sigma}$ is the resistivity per at.% of the i th impurity (Co, Cr) in the band σ ($\sigma = \uparrow, \downarrow$). We can easily deduce these resistivities from the following experimental data:

(1) resistivities of the binary alloys:

$$\rho_1 = f(0) = \frac{\rho_{1\uparrow}\rho_{1\downarrow}}{\rho_{1\uparrow} + \rho_{1\downarrow}} \quad (2-4a)$$

$$\rho_2 = g(0) = \frac{\rho_{2\uparrow}\rho_{2\downarrow}}{\rho_{2\uparrow} + \rho_{2\downarrow}} \quad (2-4b)$$

(2) initial slopes α and β of the function $f(\lambda)$ and $g(\lambda^{-1})$:

$$\alpha = \left(\frac{df}{d\lambda}\right)_{\lambda=0} = \frac{\rho_{1\uparrow}^2\rho_{2\downarrow} + \rho_{2\uparrow}\rho_{1\downarrow}^2}{(\rho_{1\uparrow} + \rho_{1\downarrow})^2} \quad (2-5a)$$

$$\beta = \left(\frac{dg}{d\lambda}\right)_{\lambda=\infty} = \frac{\rho_{2\uparrow}^2\rho_{1\downarrow} + \rho_{1\uparrow}\rho_{2\downarrow}^2}{(\rho_{2\uparrow} + \rho_{2\downarrow})^2} \quad (2-5b)$$

From equations (2-4) and (2-5) we obtain easily:

$$\rho_{1\uparrow} = 2\rho_1 \left[1 \pm \sqrt{1 + \frac{4\rho_1(\rho_2 - \alpha)^2(\rho_1 - \beta)}{(\alpha\beta - 3\rho_1\rho_2)^2 + 4(\alpha\rho_1^2\rho_2 + \beta\rho_2^2\rho_1 - 3\rho_1^2\rho_2^2)}} \right]^{-1} \quad (2-6a)$$

$$\rho_{2\uparrow} = 2\rho_2 \left[1 \mp \sqrt{1 + \frac{4\rho_2(\rho_1 - \beta)^2(\rho_2 - \alpha)}{(\alpha\beta - 3\rho_1\rho_2)^2 + 4(\alpha\rho_1^2\rho_2 + \beta\rho_2^2\rho_1 - 3\rho_1^2\rho_2^2)}} \right]^{-1} \quad (2-6b)$$

In (2-6) we assume that $\rho_{1\uparrow} < \rho_{1\downarrow}$ (see Section 3).

In the present case, we obtain from the experimental values ($\rho_1 = 0.2\mu\Omega\cdot\text{cm}/\%$, $\rho_2 = 5\mu\Omega\cdot\text{cm}/\%$; $\alpha = 17$, $\beta = 2.2$) the following result:

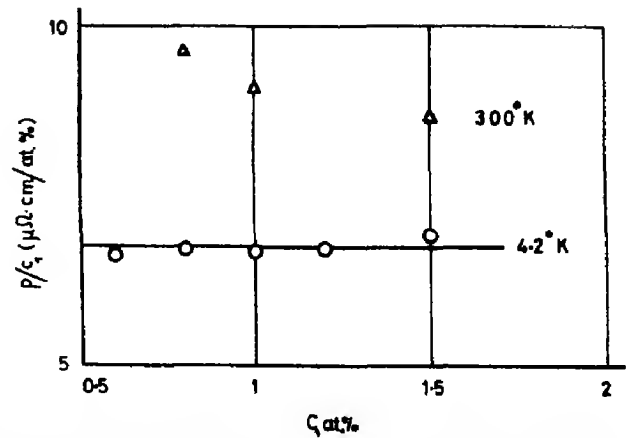


Fig. 3. ρ/C_1 as a function of C_1 for $\lambda = 1$: ρ/C_1 is independent of C_1 for a given value λ from formula (2-2).

for cobalt: $\rho_{1\uparrow} = 0.21\mu\Omega\cdot\text{cm}/\text{at.}\%$

$$\rho_{1\downarrow} = 4.3\mu\Omega\cdot\text{cm}/\text{at.}\% \quad (2-7)$$

for chromium: $\rho_{2\uparrow} = 17.6\mu\Omega\cdot\text{cm}/\text{at.}\%$

$$\rho_{2\downarrow} = 7\mu\Omega\cdot\text{cm}/\text{at.}\%.$$

The experimental values of f and g are then in agreement with (2-3) not only for $\lambda = 0$ or $\lambda = \infty$ but for all values of λ (see Figs. 1, 2).

In conclusion, the experimental results are in agreement with the functional forms (2-2), (2-3) deduced from a two-band conduction model (1) for all values of the impurity concentration ratio $\lambda = C_2/C_1$, (2) for one and only one set of values of $\rho_{i\sigma}$ ($i = 1, 2$; $\sigma = \uparrow, \downarrow$).

Let us mention that another derivation of $\rho_{i\sigma}$, assuming a two-band conduction, has been suggested by Campbell *et al.* [2, 7] who deduced $\rho_{i\sigma}$ from the temperature variation of the resistivity of binary alloys; their recent results obtained from the temperature depen-

dence of the resistivity in *Ni Co* and *Ni Cr* alloys between 10°K and 50°K are in good agreement with ours. However this derivation assumes a temperature dependence of the pure nickel resistivity.

Greig has also derived values of $\rho_{i\sigma}$ from room temperature measurements assuming that: (1) the electronic structure of impurities remains unchanged between 0 and 300°K, (2) the resistivity of pure nickel is much larger than the impurity resistivities $C_1\rho_{i\sigma}$, (3) the spin sub-bands resistivities of pure nickel $\rho_{Ni\uparrow}, \rho_{Ni\downarrow}$ are equal. These values are in qualitative agreement with our work: however, the concentration dependence of the room temperature resistivity shows that the assumptions (2) and (3) are not verified, so that this derivation is not quantitatively justified for nickel alloys. Detailed results of the temperature dependence of nickel binary and ternary alloys will be published elsewhere.

3. DISCUSSION

The present values (2-7) are in qualitative agreement with the theoretical predictions. It has been pointed out a long time ago [1] that the main origin of the large resistivities of transition metals is to be found in *s-d* transitions. Three processes are expected to contribute to the resistivity: (1) the direct *s-s* transitions as in normal metals, (2) the indirect *s-s* transitions via the '*d*' bands (3) the *s-d* transitions where the scattered state is a non-conducting '*d*' state. The last two processes arise from the *s-d* mixing on the impurity site: only the second is present in the case of an isolated *d* (virtual) bound state in a normal metal; the third one, which is essential in order to account for the resistivity of the pure transition metals [1], reflects the itinerant character of the '*d*' electrons of the matrix. The enhancement of the processes (2) and (3) by resonance (*d-d* or *s-d* virtual bound states) leads to the conclusion that the *s-s* term is negligible: this is easily seen on the expression of the contributions (2) and (3) to the resistivity [8] which can be written in

the following manner:

$$\rho_{i\sigma} = \frac{m}{n_{\sigma} e^2} |V_{sd}^{i\sigma}|^2 n_d^{i\sigma}(E_F); \quad (3-1)$$

in (3-1) n_{σ} is the number of s_{σ} electrons per atom, m^* is the effective mass of the s_{σ} band assumed to be parabolic, $n_d^{i\sigma}(E_F)$ is the density of occupation of d_{σ} states on the impurity atom per unit energy at the Fermi level E_F , $|V_{sd}^{i\sigma}|^2$ is the mean value at the Fermi level of all $s_{\sigma}-d_{\sigma}$ matrix elements of the impurity potential $V^{i\sigma}$. Formula (3-1) is valid (1) when the *s-d* mixing of the matrix is negligible at the Fermi level (2) when the impurity potential is well localized on the impurity site (3) when the *s-s* direct process is negligible; the present formula (3-1) is equivalent to the result used in reference [8] for a calculation of the resistivity of iron alloys.

Let us now discuss the results (2-7):

(1) *Ni Co alloys*: if the spin up '*d*' band is the filled nickel '*d*' band there is no available '*d*' state at the Fermi level so that only processes (1) and (2) contribute to the resistivity; this is the reason why one of the resistivities $\rho_{i\sigma}$ is very low (i.e. of the order of magnitude of the resistivity of a normal alloy with an impurity excess charge $Z \sim 1$): this resistivity has been associated in (2-7) with the spin up band.

The spin down $n_{d\downarrow}(E_F)$ density of occupation of $d\downarrow$ states is important for the resonant *d-d* state which appears near the Fermi level: thus, we obtain a large value for $\rho_{i\downarrow}$. This value is consistent with (3-1) and with the standard nickel band structure if we choose $V_{sd}^{i\sigma} \sim 1$ eV [9, 10].

(2) *Ni Cr alloys*: the impurity potential is sufficient to repel a '*d*↑' bound state above the Fermi level; this is a well-known result deduced from magnetic measurements [11]. The corresponding *s*↑-*d*↑ virtual bound state implies a large resistivity $\rho_{2\uparrow}$ (process (2)); the spin down resistivity is of the same order of magnitude as in *Ni Co* alloys.

In conclusion, the present analysis of the

deviations from Matthiessen rule in ferromagnetic alloys allows the derivation of the resistivities associated with each spin subband and gives a new kind of information on the electronic structure of binary alloys of transition metals.

Acknowledgements—It is a pleasure to thank Dr. Campbell for stimulating discussions and Professor Pauthenet's Laboratory for making magnetization measurements available.

REFERENCES

1. For a general discussion see MOTT N. F., *Adv. Phys.* **13** (1964).
2. CAMPBELL I. A. *et al.*, *Phil. Mag.* **15**, 977 (1967).
3. FERT A. and CAMPBELL I. A., *Phys. Rev. Lett.* **21**, 1190 (1968).
4. CHEN C. W., *Phys. Lett.* **7**, 16 (1963).
5. GREIG D., Private communication.
6. BOZORTH R. M., *Ferromagnetism*. Van Nostrand, C¹e Edition) (1959).
7. CAMPBELL I. A., Private communication.
8. GOMES A. A., *J. Phys. Chem. Solids* **27**, 451 (1966).
9. HAYAKAWA H., *Prog. theor. Phys.* **37**, 213 (1967).
10. DEMANGEAT C., Private communication.
11. FRIEDEL J., *Nuovo Cim. Suppl.* **7**, 287 (1958).

A NEUTRON DEPOLARIZATION STUDY ON DYSPROSIUM AND TERBIUM

E. LÖFFLER and H. RAUCH

Atominstitut der Österreichischen Hochschulen, Vienna, Austria

(Received 4 February 1969; in revised form 27 March 1969)

Abstract—The neutron depolarization of a polycrystalline 0.25 mm thick dysprosium foil has been measured in the temperature range from 4.2° to 300°K in external magnetic fields up to 2.2 kOe. From 85° to ~130°K, where Dy should behave as an antiferromagnet, domains with a net magnetic moment were found to exist in the antiferromagnetic material. Above 130°K the depolarization effect is very small, indicating that only a few domains are present. In the ferromagnetic region ($T < 85^\circ\text{K}$) the calculation of the domain size from the depolarization data is possible. The domains were found to be very small ($\sim 10^{-6}$ – 5×10^{-5} cm) and grew with the applied field, H , as expected. If the sample is cooled in zero field and then H is applied, a sort of internal coercive force for the Bloch-wall mobility is observed. The depolarization and, hence, the size of the domains were found to be very sensitive on the magnetic field acting on the sample during the cooling process. The depolarization measurements on terbium were combined with measurements of the small angle scattering, so that the induction, B , in the domains and the mean domain size were obtained separately. The values B found in this way are lower than those corresponding to the saturation magnetization.

1. INTRODUCTION

POLARIZED neutrons are most frequently used for magnetic form factor and magnetic moment determinations[1–3], but also measurements on the spin wave spectrum[4] and the critical scattering of magnetic substances[5] were performed. In all these investigations either the intensity or the polarization of the scattered neutrons was measured.

Another way to get information on magnetic substances consists of measuring the polarization of the transmitted beam. The depolarization caused by the magnetic material depends on the strength and the distribution of the magnetic induction in the sample. Such investigations were performed by Burgy, Hughes *et al.*[6], the theory was developed by Halpern and Holstein in 1941[7]. In 1965, the metals Fe, Ni and Co were investigated at room temperature, far below the Curie point, by means of a Stern–Gerlach apparatus[8, 9]. Recently we used the depolarization method to get information on the ferromagnetic domain structure in Dy[10] near its transition points. Furthermore, a short

communication concerning depolarization measurements on Ni was published[11], where the internal magnetic field strength near the Curie point was determined.

Another application of this method was given by Rauch and Weber who measured the depolarization caused by the internal magnetic flux lines in superconducting niobium[12].

We now report some new results, measured in a more systematic manner than in our previous paper[10]. Especially the strong dependence of the depolarization on the magnetic field acting on the sample during the cooling process ('cooling field') was investigated very carefully.

2. MAGNETIZATION PROCESS IN Dy

For a better understanding of our results some important experimental and theoretical work dealing with the magnetization process in Dy is reviewed briefly.

The magnetization of a Dy single crystal was measured by Behrendt *et al.*[13]. They found that in zero field Dy was ferromagnetic below 85°K, with the moments perpendicular

to the c -axis of the hexagonal crystal. The magnetic susceptibility in the c -direction is low, a strong axial anisotropy ($\sim 10^8$ erg/cm³) hinders the moments to deviate appreciably from the basal plane, even at higher temperatures. From 85° to 179°K the crystal behaves like an antiferromagnetic if the external field is weak and directed parallel to the basal plane. At a certain temperature dependent critical field, H_c , however, ferromagnetic alignment occurs. Above 179°K Dy is paramagnetic.

Wilkinson *et al.*[14] determined the magnetic structure of Dy by neutron diffraction measurements on a single crystal. From 87° to 179°K a helical spin arrangement was observed with an interlayer turn angle varying with temperature. At the Curie point the turn angle is 26°, at the Néel point 43°.

Much work was done to explain the AFM-FM transition in Dy[15–18]. Only a few aspects of the problem as discussed by Enz [19, 20] and Elliott[21] will be mentioned. Enz first pointed out that the giant magnetostriction in the basal plane ($\sim 10^{-3}$) was the driving force for the ferromagnetic alignment. Let us assume a positive exchange energy $2I_1$ (per unit volume) between adjacent spin layers, and a negative exchange energy $2I_2$ between second-nearest neighbors. The total exchange energy per unit volume can then be written as

$$E = -m^2(2I_1 \cos \alpha + 2I_2 \cos 2\alpha) \quad (1)$$

m , reduced magnetization; α , angle between two adjacent layers. If $|I_1| < |4I_2|$, a helical structure with an interlayer turn angle α_0 , given by

$$\cos \alpha_0 = -I_1/4I_2 \quad (2)$$

represents the state of minimum energy. According to (1) and (2) the energy of the antiferromagnetic state is given by

$$E_{AF} = -m^2 I_1 (2 \cos^2 \alpha_0 + 1)/2 \cos \alpha_0. \quad (3)$$

According to Elliott[21] α is equal 0 in the ferromagnetic state, so that the energy is given

by:

$$\begin{aligned} E_F &= -m^2 (2I_1 + 2I_2) - E_d - HM_s \\ &= -m^2 I_1 (4 \cos \alpha_0 - 1)/2 \cos \alpha_0 - E_d - HM_s \end{aligned} \quad (4)$$

(4) M_s is the saturation magnetization when a field H is applied in the easy direction of magnetization. E_d , the 'driving energy' of the transition, is the sum of the magnetostriction energy E_{MS} and the anisotropy energy E_A gained when the helix is destroyed and all spins are lined up in the easy direction. The transition occurs if $E_F = E_{AF}$, so that the critical field, H_c , is defined by the equation

$$H_c M_s = m^2 I_1 \{ (1 - \cos \alpha_0)^2 / \cos \alpha_0 \} - E_d. \quad (5)$$

E_d/M_s^2 vanishes as $m \rightarrow 0$ [22]. Therefore, assuming only a weak variation of I_1 with temperature H_c/M_s and $(m/M_s)^2 I_1 (1 - \cos \alpha_0)^2 / \cos \alpha_0$ may be plotted vs. the temperature in such a manner that they are equal at the Néel point. According to (5) the difference between the two curves yields E_d/M_s^2 . This was done, at an early stage, by Elliott[21]. His values agree well with the theoretical values of the magnetostriction, and anisotropy, energies calculated by Cooper[22]. This agreement proves the physical reality of Enz's model. In the last years E_A [23], the magnetostriction constants[24] and the elastic moduli [25] of Dy were measured and found in best agreement with theory[26, 27], hence E_d is known in every temperature range. At $T = 0$ the order of magnitude of E_A and E_{MS} is 10^7 erg/cm³ and $E_A \approx E_{MS}$. E_A drops much more rapidly with temperature than E_{MS} and vanishes practically at $\sim 120^\circ\text{K}$ [23].

In Tb, the magnetization process is qualitatively the same as in Dy. The Néel- and Curie-temperatures are 216°K and 226°K [28].

3. NEUTRON DEPOLARIZATION AND MAGNETIC DOMAIN SIZE

For the interpretation of depolarization measurements it is necessary to point out the connection between depolarization and internal field distribution in a magnetic

sample. Following in general Halpern's treatment[7] some principles of the theory of neutron depolarization are outlined below.

The motion of the expectation value, \mathbf{s} , of the neutron spin is expressed by the equation

$$d/dt \mathbf{s} = g\mathbf{s} \times \mathbf{B} \quad (6)$$

g , gyromagnetic ratio of the neutron; \mathbf{B} , magnetic induction. According to equation (6) the spin performs a precession movement around the direction of \mathbf{B} , with the Larmor frequency $(1/2\pi)g|\mathbf{B}|$.

Assuming no correlation between the directions of domain magnetization and between the δ_i throughout the magnetic material and assuming further that the domain walls are much thinner than the distance δ_0 which a neutron travels during a Larmor period, the general expression for the neutron depolarization is given by

$$P = P_0 \left\langle \prod_{i=1}^n (1 - 2 \sin^2 \vartheta_i \sin^2 gB_i \delta_i / 2v) \right\rangle_{av} \quad (7)$$

P , neutron polarization of the transmitted beam; P_0 , neutron polarization of the incident beam; δ_i , neutron path in the i -th domain; B_i , magnetic induction in the i -th domain; ϑ_i , angle between the magnetic induction in the i -th domain and a magnetically preferred direction (in general: the direction of the applied external field); v , neutron velocity; n , number of domains traversed by the neutron.

The symbol $\langle \rangle_{av}$ denotes averaging over all neutron paths. If the sample is not magnetized and if the magnetic induction in all domains is B we get the well known expression[7]

$$D_m = P/P_0 = \left\langle \prod_{i=1}^n (1 - \frac{4}{3} \sin^2 gB\delta_i / 2v) \right\rangle_{av} \quad (8)$$

The neutron depolarization is defined by the equation

$$(P_0 - P)/P_0 = 1 - D_m \quad (9)$$

Equation (8) was evaluated for a foil thickness $d = 2.5 \times 10^{-2}$ cm, on the IBM 7040 computer* at the Institut für Numerische Mathematik der Technischen Hochschule Wien. B was put equal to $4\pi M_s$ as measured in[13]. For n the value $d/\bar{\delta}$ was used, where $\bar{\delta}$ denotes the mean neutron path in a domain ('mean domain size'). The 'domain size', δ_i , was assumed to be normally distributed. It was shown earlier[10] that for small domains ($\delta_i \ll \delta_0$) the depolarization does not depend strongly on the distribution of the δ_i , so that $\bar{\delta}$ is obtained unambiguously from the depolarization results. The demagnetization was neglected, since it has no influence on the order of magnitude of the values $\bar{\delta}$ as obtained from the experiments.

The shape of the $D_m - \bar{\delta}$ curve for $B = 37.5$ kOe corresponding to the saturation magnetization at 4.2° K is shown in [10], Fig. 1.

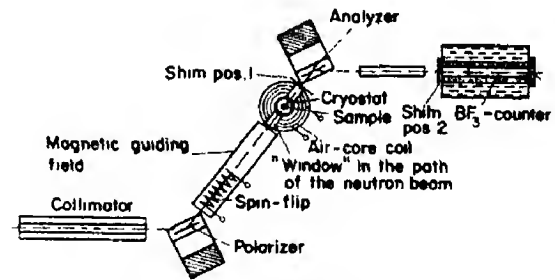


Fig. 1. Sketch of the experimental set-up.

Since in the case of small domains (as present in Dy) the depolarization is a measure of the product $B^2\bar{\delta}$, the values $\bar{\delta}$ for any other temperature T were evaluated by multiplying the values $\bar{\delta}$ obtained from the 4.2° K-curve by $B^2(4.2)/B^2(T)$.

If the domains are small D_m may be approximated, according to (7), by the expressions

$$D_m \approx \left\langle \prod_{i=1}^n [1 - \frac{1}{2}(gB_{\perp}\delta_i/v)^2] \right\rangle_{av} \quad (10a)$$

$$\approx [1 - \frac{1}{2}(g/v)^2 \bar{B}_{\perp}^2 \bar{\delta}^2]^{d/\bar{\delta}} \quad (10b)$$

*The authors thank Mr. E. Seymann who developed the program.

$$\approx \exp \left[-\frac{1}{2}(g/v)^2 \bar{B}_\perp^2 (\bar{\delta}^2/\bar{\delta}) d \right] \quad (10c)$$

$$\approx \exp \left[-\frac{1}{2}(g/v)^2 \bar{B}_\perp^2 \bar{\delta} d \right] \quad (10d)$$

$B_{\perp i}$ is the component of the magnetic induction in the plane perpendicular to the direction of the applied field, in the i -th domain; \bar{B}_\perp^2 is the mean value of $B_{\perp i}^2$.

In an antiferromagnet like Dy where the direction of the magnetization induced in a crystal grain by an external field H lies in the plane perpendicular to the c -axis, \bar{B}_\perp^2 is equal to $(2/15)(4\pi\chi_\perp)^2 H^2$ [29]. Hence the depolarization is given by

$$(1 - D_m) \approx 1 - \exp \left[-\frac{1}{15}(g/v)^2 (4\pi\chi_\perp)^2 H^2 \bar{\delta} d \right] \quad (11)$$

χ_\perp susceptibility in the basal plane.

In this case $\bar{\delta}$ is the mean neutron path in a crystal grain ('mean grain size'). Equation (11) remains unchanged under the additional assumption that the magnetization is restricted to a single direction in the basal plane [29]. Therefore, the validity of (11) is not affected by any magnetic anisotropy in the basal plane.

4. EXPERIMENT

All measurements were taken at the tangential beam tube of the TRIGA Mark II reactor, where a polarized-neutron apparatus is installed. The assembly was the same as in [10] and is schematically shown in Fig. 1. The wave-length of the polarized neutrons was 1.5 Å; they were produced and analyzed by magnetized Co-Fe-single crystals. The sample was mounted in an In-sealed Al-container and placed into a liquid helium cryostat between polarizer and analyzer. An air-core coil supplied magnetic fields up to 2.75 kOe in the vertical direction. To achieve very small cooling fields the stray field of the analyzer magnet (28 Oe) had to be compensated partly or totally by the application of small opposing fields in the coil. In the middle of the coil a 'window' permitted an undisturbed transmission of the neutron

beam. Fig. 2 shows schematically the assembly described above.

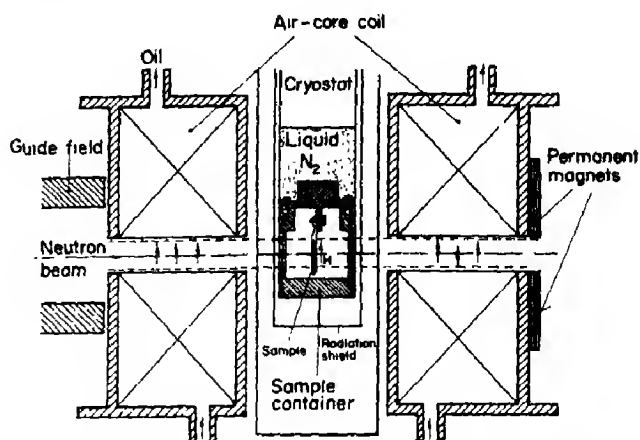


Fig. 2. Apparatus used for sample cooling and magnetic field supply.

The sample itself was a Dy-foil with linear dimensions $0.025 \times 2 \times 2$ cm. It was prepared by L. Light & Co. The impurities, gases included, were less than 1 per cent.

The 'combined shim-spinflip method' used for the depolarization measurements was described in [10] and [30]. This method, however, will be discussed in more detail below to point out its great advantages.

Before transmitting the sample the neutron beam passes through a spinflip device. The connection between the polarization P' of the neutron beam and the intensities I_s and I_f measured with the shim before and behind the analyzer, respectively, is

$$eP'P_2 = 1 - (I_f/I_s) \quad (12)$$

$$e = 2k - 1$$

k , flipping efficiency of the spinflip device; P_2 , polarizing efficiency of the analyzer. (The shim was placed in a small magnetic field (< 40 Oe) and has depolarized the beam completely, as shown in [10].)

If the measurement (12) is performed with ($P' = P$) and without the sample ($P' = P_0$) D_m is obtained in a very direct way:

$$\frac{e P P_2}{e P_0 P_2} = \frac{P}{P_0} = D_m. \quad (13)$$

If the magnetic guide field is well adjusted no additional depolarization occurs and P_0 is identical with P_1 , the polarizing efficiency of the polarizer.

The combined method ($k = 1$) is much more precise than the usual shim method ($k = 0$). If all intensities are measured for the same time t the general expression for the error of the polarization product $eP'P_2$ is given by

$$\Delta(eP'P_2) = (I_s t)^{-1/2} \left[(1 - eP'P_2) + (1 - eP'P_2)^2 + \frac{I_L}{I_s} \{1 + (eP'P_2) + (1 - eP'P_2)^2\} \right]^{1/2} \quad (14)$$

I_L , background intensity. If $(1 - eP'P_2) \ll 1$ and if I_L may be neglected we get the expression

$$\Delta(eP'P_2) \approx (I_s t)^{-1/2} (1 - eP'P_2)^{1/2}. \quad (15)$$

From (15) it may be deduced easily that the error has its minimum in the case of a total inversion of the polarization.

The polarization product of our apparatus is 91.0 ± 0.2 per cent, the flipping efficiency is 99 ± 1 per cent. If $\Delta(eP_0P_2)$ is calculated according to (14), using $I_L = 30$ neutrons/min, $I_s = 6000$ neutrons/min and $t = 1$ min the following values for the error of the polarization product are obtained:

0.42 per cent for the combined method ($e = +1$)

3.0 per cent for the usual shim method ($e = -1$).

For the intensities and the polarization product given above the error using the combined method is, therefore, seven times smaller than with the usual method. This combined method is also preferable to simply measuring the ratio of intensities with the spin-flipper turned on and off, because the spin-flipper can be operated continuously, whereby instabilities are avoided.

5. RESULTS

(a) Dysprosium

The depolarization at various temperatures and magnetic fields was measured. Figure 3 shows the dependence of D_m on magnetic field at 6 temperatures in the antiferromagnetic range, for zero cooling field.

It can be seen that in the temperature range 130–170°K the depolarization is very small, even at high fields (~ 4 per cent at 2.2 kOe). At lower temperatures, however, appreciable depolarization is observed, even at fields below H_c , which increases with field and decreases with temperature. Furthermore, no discontinuities can be observed at the critical fields as measured in [13]. The depolarization, however, was expected to be zero for $H < H_c$ and to increase when the field is increased beyond H_c , because of the formations of ferromagnetic domains.

To explain these surprising results first an attempt has to be made to estimate the order of magnitude of the 'antiferromagnetic depolarization' caused by the magnetization which is induced in the crystal grains by the external field. For this purpose the size of the crystal grains was determined, by means of a Debye-Scherrer photograph*, and was found to be smaller than 10^{-4} cm. Using the

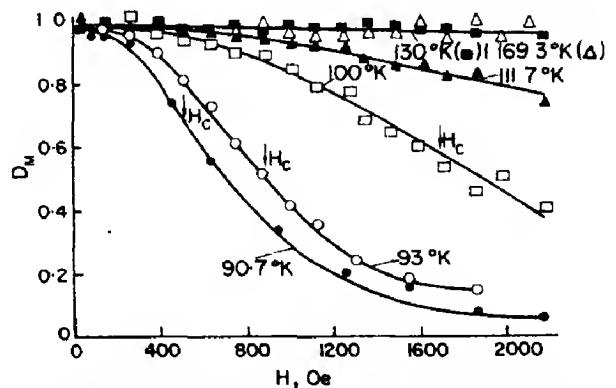


Fig. 3. D_m vs. applied field in Dy. at various temperatures in the antiferromagnetic range, for zero cooling field.

*We are greatly indebted to Dr. A. Wagendristel (Institut für Angewandte Physik der Technischen Hochschule Wien) for the determination of the grain size and to Professor Dr. F. Lihl for the permission to take this investigation at his institute.

values χ_i from [13] equation (11) may be evaluated and the depolarization is obtained for all temperatures and fields. It turns out that the calculated values are smaller than the observed values, the difference being at least two orders of magnitude. At $T = 111.7^\circ\text{K}$ and $H = 2 \text{ kOe}$, e.g. the calculated depolarization is 0.2 per cent, the observed value 20 per cent. At temperatures above 120°K the calculated depolarization is less than 0.1 per cent.

From this we have to conclude that the strong depolarization effect is caused by the formation of domains with a net moment, even below H_c .

Hence our results confirm the conclusions drawn by Nikitin[31] from his coercive force measurements. Nikitin concluded from his results that such domains were present in the antiferromagnetic material. He explained this fact by assuming the presence of internal stresses within the sample. The basic idea of the following discussion is taken from Nikitin's treatment.

If the stress τ_i acts on the i -th crystal grain, additional magnetoelastic energy $\lambda\tau_i$ in the basal plane is gained per unit volume when the transition takes place. Hence the driving energy is given by

$$E_{di} = E_d + \lambda\tau_i \quad (16)$$

E_{di} , driving energy in the i -th crystal grain. The order of magnitude of the magnetostriction λ is 10^{-3} [24]. According to equation (5) H_c is changed by

$$\Delta H_{ci} = -\lambda\tau_i/M_s \quad (17)$$

The sign of ΔH_{ci} depends on the sign and the direction of τ_i . Up to $\sim 160^\circ\text{K}$ the variation of H_c with temperature is approximately linear[13], and $h = dH_c/dT = 125 \text{ Oe}/^\circ\text{K}$ [13, 31]. Hence the change of the critical temperature at constant field is given by

$$\Delta T_{ci} = -\lambda\tau_i/hM_s \quad (18)$$

$2\Delta T_{ci}$ was estimated by Nikitin to be on the average $\sim 10^\circ\text{K}$, hence $\tau_i \approx 20 \text{ kg/mm}^2$.

The wide range of values H_c may be responsible for the fact that no discontinuities in the depolarization curves are observed at the values H_c taken from [13].

With increasing magnetic field an increasing number of grains fulfils the condition for an alignment involving a net magnetic moment

$$H_{\perp i} > H_c + \Delta H_{ci} \quad (19)$$

($H_{\perp i}$, component of the applied field in the basal plane of the i -th grain), so that the depolarization increases continuously with field.

The depolarization isotherms at $T = 100^\circ\text{K}$ and $T = 111.7^\circ\text{K}$ clearly show this behavior. The 90.7°K - and 93°K -isotherms have a somewhat different shape and will be discussed later.

At temperatures above 130°K only a few grains satisfy condition (19) at fields below 2.2 kOe, the depolarization effect is, therefore, very weak.

Figure 4 shows the temperature dependence of D_m at constant external field, $H = 1856 \text{ Oe}$, when the sample is cooled from $T = 169.3^\circ\text{K}$ to 110°K .

The temperature dependence of 'ferromagnetic' alignment is governed by the following condition:

$$T < T_{ci} + \Delta T_{ci} \quad (20)$$

T_{ci} , critical temperature at $H_{\perp i}$. The critical temperature at 1856 Oe is 102°K [13]. Since

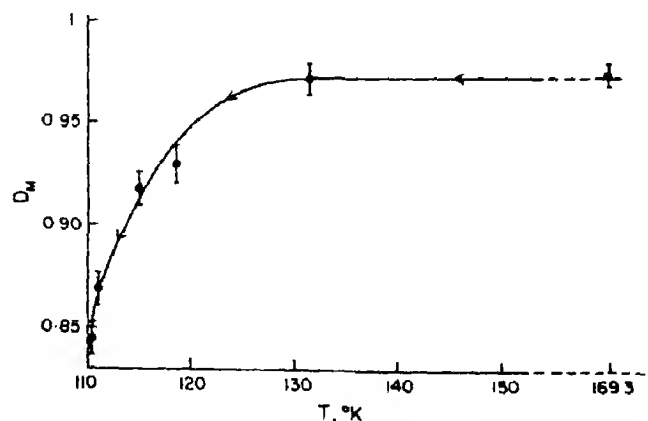


Fig. 4. D_m vs. temperature in Dy, at $H = 1856 \text{ Oe}$, when the sample is cooled from 169.3° to 110°K .

the onset of appreciable depolarization starts at $\sim 130^\circ\text{K}$ it may be concluded from Fig. 4 that the maximum value of ΔT_{cl} is

$$(\Delta T_{cl})_{\max.} \approx 28^\circ\text{K}. \quad (21)$$

In Figs. 5 and 6 (upper curves, full lines) the dependence of the depolarization on the applied field is shown for zero cooling field, measured at four temperatures in the ferromagnetic range.

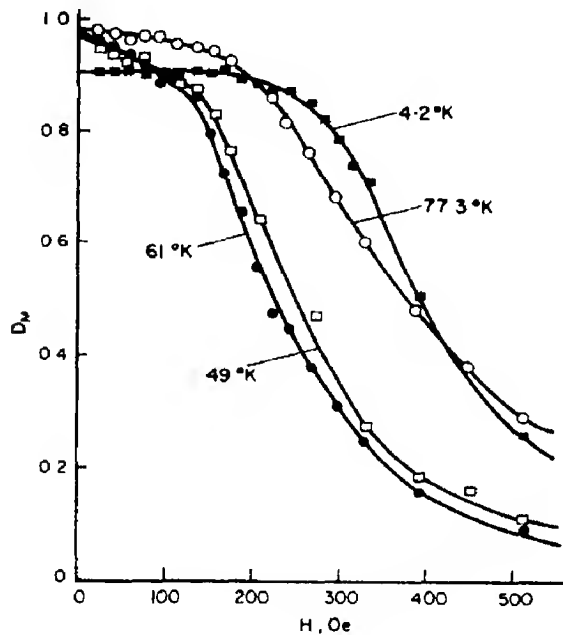


Fig. 5. D_m vs. applied field in Dy, at various temperatures in the ferromagnetic range, for zero cooling field.

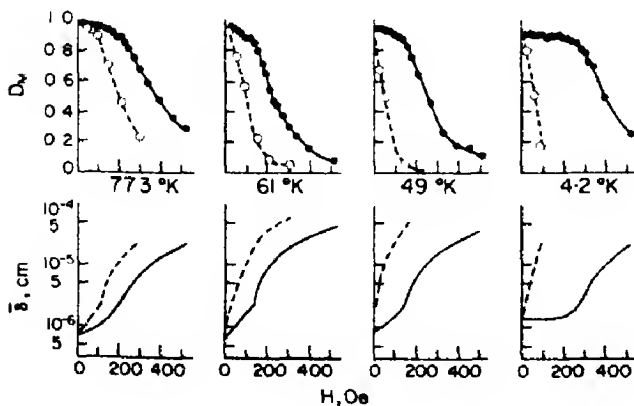


Fig. 6. Plot of D_m and mean domain size $\bar{\delta}$ in Dy vs. field. — sample cooled at zero field, then field applied; ----- field applied, then sample cooled.

At low fields the depolarization is small (2–10 per cent) and increases slightly with field. Above a certain critical field H_{cr} a much sharper decrease of D_m with field takes place. From the fact that the depolarization increases with field and, therefore, with domain size it is concluded that the domains are small (i.e. $\bar{\delta} \ll \delta_0$) [7]. Since $\delta_0 \approx 10^{-3}$ cm for $B = 30$ kOe, $\bar{\delta}$ must be $\ll 10^{-3}$ cm.

It is seen that the depolarization curves at 90.7°K and 93°K (Fig. 3) are very similar to the ferromagnetic curves in Fig. 5 and that they also show a critical field H_{cr} of ~ 250 Oe. If the temperature spread according to equation (21) is taken into account these results may be explained by the assumption that even at zero field large parts of the sample consist of domains with a net magnetic moment, which determine the shape of the depolarization curve, at least in the low field region. At temperatures $\geq 100^\circ\text{K}$ the 'ferromagnetic' critical field H_{cr} cannot be observed.

The dashed curves in Fig. 6 show the dependence of the depolarization on the magnetic field applied during the cooling process. When thermal equilibrium was reached the depolarization was then measured at constant field. Except for the 77.3°K curve, no knees are observed in the cooling field depolarization curves. Furthermore, the depolarization effect is much stronger than that obtained from the zero cooling field measurements (full lines).

From this it may be concluded that H_{cr} is a sort of internal coercive force for the Bloch-wall mobility which hinders the growth of the domains [10]. If the field, H , is applied when cooling the sample, the formation of the domains occurs in such a way that the domain structure at the equilibrium temperature, T , represents the state of minimum energy, $E_{\min.}(T, H)$. If the sample is cooled in zero field, however, the domain structure corresponding to the energy $E_{\min.}(T, 0)$ can only be changed by domain wall motion which is hindered by the coercive force H_{cr} .

Because of the heterogeneity of the material

in the antiferromagnetic temperature range no information on the domains with a net moment can be obtained from the depolarization measurements in this case. It may be assumed, however, that at temperatures below 85°K the sample is almost entirely ferromagnetic, hence the relation between the depolarization and the mean domain size holds.

The corresponding values $\bar{\delta}$ (Fig. 6, lower curves) were calculated according to equation (8). The bulk magnetization at 78.5°K in a field of 500 Oe is only 1.4 per cent of its saturation value [13, 31]. Hence the distribution of the magnetization directions of the domains is almost isotropic and equation (8) can be used. The size of the domains is $\sim 10^{-6}$ – 5×10^{-5} cm.

At fields above H_{cr} the decrease of D_m with field is nearly the same at 61°, 49° and 4.2°K (Fig. 5, Fig. 6). Only at 77.3°K it is less steep than at the lower temperatures. This may be due to the onset of antiferromagnetism, according to the spread of the transition temperatures. Antiferromagnetic reflections below the Curie-point were also observed in Tb by neutron diffraction [28].

The influence of the cooling field on the magnetization process is shown in Fig. 7. The dependence of the depolarization on field for various cooling fields was measured at 61°K. As shown above (Fig. 6, dashed curves), even a low cooling field strongly influences the magnetization process, so that the domains are larger than for zero cooling field. When the field is raised the domains cannot grow at first, because of the immobility of the domain walls, so that the depolarization remains constant. At higher fields, however, the internal coercive force is overcome and the growth of the domains sets in.

The cooling field depolarization values measured at 77.3°, 61° and 49°K (Fig. 6, dashed curves) were obtained in such a way that the sample was cooled step by step from one temperature to the other. From the lowest temperature it was warmed up again

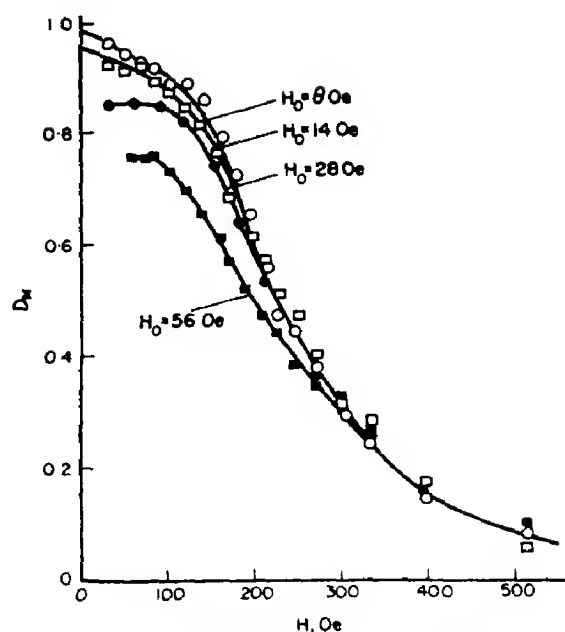


Fig. 7. D_m vs. applied field in Dy, at 61°K, for various cooling fields.

to 77.3°K. In Fig. 8, such temperature cycles are shown.

The depolarization and, therefore, the domain size remains almost unchanged when the sample is warmed up. The same result

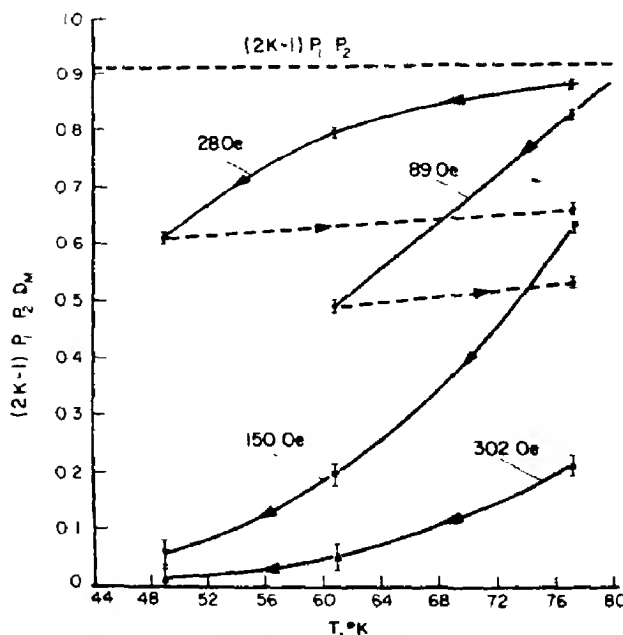


Fig. 8. $(2k-1)P_1P_2D_m$ vs. temperature at various fields, in Dy. The field was applied during the whole cooling process, even at room temperature. The arrows indicate the direction of temperature variation.

was obtained from depolarization measurements on Ni[11]. It was shown earlier[10] that in the antiferromagnetic state the depolarization decreases with temperature because of the destruction of the ferromagnetic-like order.

At 300°K only a weak depolarization (~ 1 per cent) was observed. This effect, which is independent of the applied field[10], seems unlikely to be caused by the slight field distortions which result from the macroscopic sample magnetization, this magnetization being proportional to the applied field. It may be due to impurities in the sample.

(b) Terbium

Figure 9 shows measurements on Tb (for the corresponding measurements on Dy see Fig. 6). The sample was 0.25 mm thick. Here again great differences in the depolarization are observed when either the foil is cooled in zero field and then the field is applied or

vice versa. Because of the small absorption cross section of Tb, small angle scattering measurements[32] (sample thickness: 3 mm) were taken in addition to the depolarization measurements. The small angle scattering depends on the magnetic induction within the domains and the domain size as well. It was, therefore, possible to determine the induction and the domain size by two independent methods i.e. without any assumptions. The results are shown in the lower part of Fig. 9. The experimental values of the average magnetic induction are lower than those obtained from the Brillouin curve. This may be due to the existence of a mixed ferromagnetic-antiferromagnetic state, the influence of the smaller magnetization within the Bloch-walls[33] and demagnetizing effects.

6. DISCUSSION

The neutron depolarization method was used to get information on the magnetization

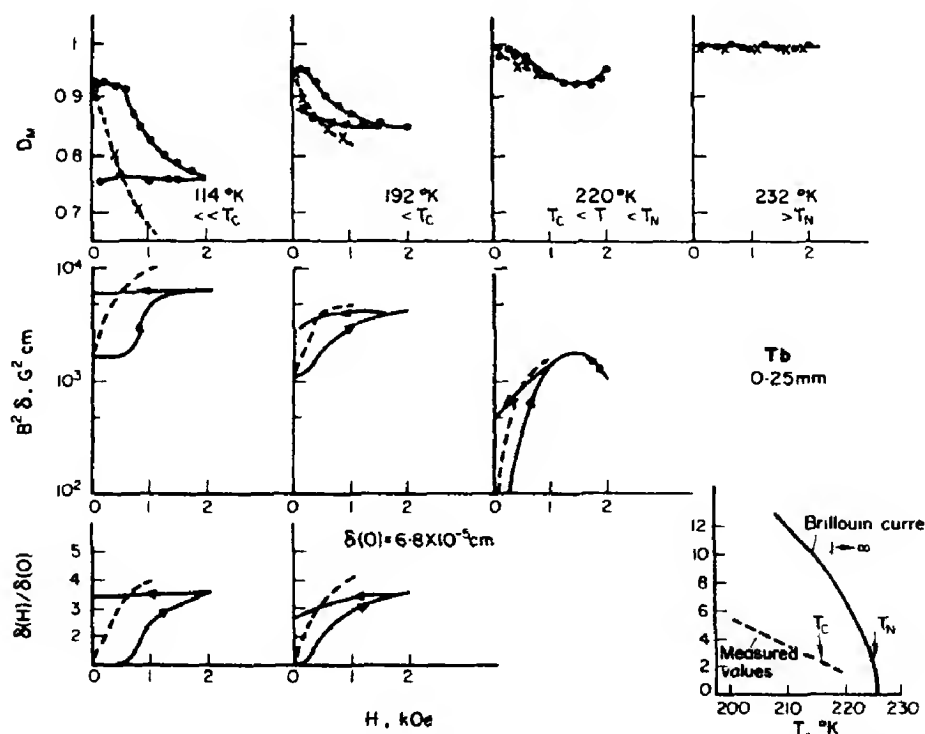


Fig. 9. Plot of D_m and mean domain size δ in Tb vs. field. — sample cooled at zero field, then field applied; ---- field applied, then sample cooled. Curve below, on the right side: — theoretical Brillouin curve; ---- magnetic induction B obtained by combining depolarization- with small angle scattering measurements.

process in Dy and Tb. The method was found to be very valuable to indicate ferromagnetism in any material, since the ferromagnetic domains are directly 'seen' by the polarization vector.

It was proved that domains with a net magnetic moment are present in Dy even in the antiferromagnetic temperature range, in agreement with the coercive force measurements of Nikitin[31].

It is characteristic of the neutron depolarization method that quantitative results can only be obtained if assumptions are made on the strength of the magnetic induction in the domains and the correlation between the directions of domain magnetization. It was assumed, as usual, that there was no correlation. Certainly this assumption is not in full agreement with the physical reality, because of the strong anisotropy energy in Dy which determines the possible directions of magnetization in a crystal grain. Hence the values $\bar{\delta}$ calculated from equation (8) merely indicate the order of magnitude of the domain size.

If a uniform shape of the domains is assumed, the mean domain size, $\bar{\delta}$, can be expressed by its characteristic geometrical dimensions. The value $\bar{\delta}$ as obtained from the experiment is a measure of the shortest linear dimension of the domain's shape[29]. For plated domains, e.g. $\bar{\delta}$ is twice the plate thickness, for a globe it is $2D/3$ (D = diameter).

In the ferromagnetic state of Dy the mean domain size was found to be very small (10^{-6} – 5×10^{-5} cm). A sort of internal coercive force for the Bloch-wall mobility was observed.

From the shape of the 77.3°K—depolarization curve it may be concluded that Dy is not homogeneously ferromagnetic at this temperature. Further neutron depolarization measurements on annealed samples should provide valuable information on the smeared AFM-FM transition in Dy and Tb, concerning the dependence of the spread of the transition temperature on the internal stress.

Acknowledgements—The authors thank Professor Dr. Gustav Ortner for his interest in this work and for many discussions. Furthermore, we thank Dr. Harald Weber for the maintenance of the air-core coil, Mr. H. Niedermaier and the reactor crew for their obligingness during the measurements.

REFERENCES

1. NATHANS R., SHULL C. G., SHIRANE G. and ANDRESEN A., *J. Phys. Chem. Solids* **10**, 138 (1959).
2. SHULL C. G. and YAMADA Y., *J. phys. Soc. Japan* **17**, Suppl. B-III, 1 (1962).
3. NATHANS R., PIGOTT M. and SHULL C. G., *J. Phys. Chem. Solids* **6**, 38 (1958).
4. DRABKIN G. M., ZABIDAROV E., KASMAN Ya. A., OKOROKOV A. I. and TRUNOV V. A., *Soviet Phys. JETP* **20**, 1548 (1965).
5. DRABKIN G. M., ZABIDAROV E. I., KASMAN Y. A. and OKOROKOV A. I., *JETP Lett.* **2**, 336 (1965).
6. BURG Y. R., HUGHES D. J., WALLACE J. R., HELLER R. B. and WOOLF W. E., *Phys. Rev.* **80**, 953 (1950).
7. HALPERN O. and HOLSTEIN T., *Phys. Rev.* **59**, 960 (1941).
8. BRAND K., NAGIB M. and WEBER G., *Atomkernenergie* **11**, 283 (1966) (In German); NAGIB M., *Atomkernenergie* **11**, 286 (1966).
9. WEBER G., *Atomkernenergie* **10**, 177 (1965) (In German).
10. RAUCH H. and LÖFFLER E., *Z. Phys.* **210**, 265 (1968) (In German).
11. BAKKER H. K., REKVELDT M. Th. and VAN LOEF J. J., *Phys. Lett.* **27A**, 69 (1968).
12. RAUCH H. and WEBER H. W., *Phys. Lett.* **26A**, 460 (1968).
13. BEHRENDT D. R., LEGVOLD S. and SPEDDING F. H., *Phys. Rev.* **109**, 1544 (1958).
14. WILKINSON M. K., KOEHLER W. C., WOLLAN E. O. and CABLE J. W., *J. appl. Phys.* **32**, 485 (1961).
15. YOSIDA K. and MIWA H., *J. appl. Phys.* **32**, 8S (1961).
16. YOSIDA K. and MIWA H., *J. phys. Soc. Japan* **17**, Suppl. B-I, 5 (1962).
17. NAGAMIYA T., NAGATA K. and KITANO Y., *J. phys. Soc. Japan* **17**, Suppl. B-I, 10 (1962).
18. KAPLAN T. A., *J. phys. Soc. Japan* **17**, Suppl. B-I, 3 (1962).
19. ENZ U., *Physica* **26**, 698 (1960).
20. ENZ U., *J. appl. Phys.* **32**, 22S (1961).
21. ELLIOTT R. J., *Phys. Rev.* **124**, 346 (1961).
22. COOPER B. R., *Phys. Rev. Lett.* **19**, 900 (1967).
23. RHYNE J. J. and CLARK A. E., *J. appl. Phys.* **38**, 1379 (1967).
24. CLARK A. E., DE SAVAGE B. F. and BOZORTH R., *Phys. Rev.* **138**, A216 (1965).
25. FISHER E. S. and DEVER D., *Trans. AIME* **239**, 48 (1967).
26. CALLEN H. B. and CALLEN E., *J. Phys. Chem. Solids* **27**, 1271 (1966).

27. CALLEN E. and CALLEN H. B., *Phys. Rev.* **139**, A455 (1965).
28. DIETRICH O. W. and ALS-NIELSEN J., *Phys. Rev.* **162**, 315 (1967).
29. LÖFFLER E., Thesis. Atominstitut der Österreichischen Hochschulen, Universität Wien (1969).
30. WEBER H. W. and RAUCH H., *Z. Phys.* **219**, 482 (1969).
31. NIKITIN S. A., *FMM* **15**, 2, 187 (1963); (Translated in *Phys. Metals Metallogr.* **15**).
32. RAUCH H., *Acta Phys. Aust.* In press (1969).
33. KLAMUT J. and KOZŁOWSKI G., *Acta Phys. Polon.* **33**, 743 (1968).

THE STATISTICAL MECHANICS OF IMPERFECT MOLECULAR CRYSTALS

A. R. ALLNATT and L. A. ROWLEY

Department of Chemistry, The University, Manchester 13, England

(Received 20 December 1968; in revised form 26 March 1969)

Abstract—Equations are developed for the calculation of thermodynamic functions of imperfect molecular crystals containing one species of point defect on a cubic lattice, following a method proposed by Mayer[7]. The treatment of vibrations requires essentially only the techniques applicable to a perfect crystal, requires no static relaxation calculation, and can allow for defect–defect interactions. The free energy of solution, and the activity coefficient in an approximation similar to that of Bragg and Williams, are calculated for argon in krypton in moderate agreement with experiment. Results for vacancy concentrations in krypton are less satisfactory. The limitations of the method are indicated.

1. INTRODUCTION

IF A MOLECULAR lattice contains point defects such as impurity atoms, vacant sites, or interstitial atoms then the calculation of the thermodynamic functions is much more difficult than for the corresponding perfect crystal. The three dimensional periodicity of atomic sites in the perfect lattice allows an analysis of the thermal vibrations based on independent normal co-ordinates and the interaction between them due to anharmonicity. In the imperfect crystal the point defects destroy the three dimensional periodicity and the calculation of thermodynamic functions generally proceeds as follows. The displacement of the atoms around a single point defect is first calculated either by an approximate analytic method, or by a relaxation calculation on a fast computer. The vibrational properties of the imperfect crystal are then calculated treating the difference in the Hamiltonian of imperfect and perfect crystal as a perturbation to the vibrations of the perfect crystal. The last step is not very simple because the lattice is not triply periodic. The details have varied from calculation to calculation [1–4] but the following general remarks can be made about the programme outlined. The relaxation calculation and the use of perturbation theory appear to be practicable

only for very dilute defect systems in which the point defects are independent or at most interacting in pairs rather than higher aggregates. A few attempts have been made to treat solid solutions at higher concentrations [5, 6] but an adequate treatment is not yet available, because it is difficult to treat both the configurational (order–disorder) problem and the vibrational problem and the interaction between them to an adequate approximation.

It was pointed out by Mayer[7] that in principle there is an alternative procedure for imperfect crystals in the classical region. The order of the averaging processes in the evaluation of the partition function can be inverted. One may first average over all possible occupations of each site in the crystal for a fixed displacement of the occupant of each particular site from the site centre, to obtain a potential of mean force which is triply periodic with respect to the site centres. This function can then be expanded in powers of the displacements and the integration over displacements be performed by the same methods as for a perfect crystal. The advantages of the Mayer method are that the tedious relaxation calculation is eliminated and the vibrational properties can be treated by exactly the methods developed for the perfect crystal even when defect interactions between

up to three or four defect sites are allowed. Further, one is forced to perform the calculation in a more self-consistent manner than is usual because calculation of the equation of state and chemical potentials must generally be performed simultaneously, thus providing a more complete check on the model used. Unlike most previous methods there is no question of adding together separate calculations of 'defect contributions' and the 'perfect crystal contributions' for the various thermodynamic functions.

A price must be paid for these advantages and we do not wish to imply that the Mayer method is any easier to use than the conventional methods. A mixing of the static and vibrational aspects of the problem occurs as compared with the conventional method, and the relaxation calculation is eliminated only at the cost of both increasing the importance of and increasing the algebraic complication in the vibrational part of the theory. Furthermore, a series of iterations is sometimes necessary to solve the equations for the thermodynamic functions.

The present paper describes an attempt to discover just how practicable the Mayer method is. Section 2 outlines the general equations of the method. Sections 3 and 4 give equations for the vibrational part of the calculation for a single defect type in a cubic lattice. Some illustrative calculations for rare gas solids are described in Sections 5 and 6.

2. GENERAL EQUATIONS

We consider a solid of several species of monatomic molecules in a volume V at temperature T . The activity of species s , z_s , is defined by

$$z_s = (2\pi m_s kT/h^2)^{3/2} \exp(\beta\mu_s) \quad (2.1)$$

where $\beta = (kT)^{-1}$, μ_s is the chemical potential per atom of species s , and m_s the mass of one atom of s . Let N denote a set of N atoms, N_1 of species 1, N_2 of species 2, We use the abbreviations

$$z^N = z_1^{N_1} z_2^{N_2} \dots z_s^{N_s} \dots \quad (2.2)$$

$$N! = N_1! N_2! \dots N_s! \dots \quad (2.3)$$

At temperatures at which the classical approximation is valid the grand partition function, Ξ , is given by [8]

$$\Xi(z, V, T) = \sum_N \frac{z^N}{N!} \int \exp(-\beta U_N\{N\}) d\{N\}. \quad (2.4)$$

$\{N\}$ denotes the $3N$ co-ordinates of the set N , and $d\{N\}$ the $3N$ dimensional volume unit $dx_1 \dots dz_N$. $U_N\{N\}$ is the potential energy.

Let the lattice sites of a unit cell be labelled by the integer λ , $1 \leq \lambda \leq r$, including any interstitial sites occupied only in the imperfect crystal, and let the integers l_1, l_2, l_3 specify the positions of the unit cells in terms of primitive translation vectors a_1, a_2, a_3 . The total volume V of M unit cells can be subdivided into $N = Mr$ non-overlapping cells, one cell being associated with each lattice site $l = l_1, l_2, l_3, \lambda$. We call these Mayer cells. Let n_{sl} be the number of atoms of species s in cell l and let n_{0l} be unity if cell l is vacant and zero otherwise. Denote by $(l) = u_1(l), u_2(l), u_3(l)$ the displacement of the atom in cell l from the cell centre. The occupation set n , comprising the n_{sl} for all s and l , and the co-ordinate set $\{L\}$, representing the set of all co-ordinates (l) , completely specify the state of the system. Provided the Mayer cells have been chosen so that we may restrict consideration to configurations with not more than one atom per cell then equation (2.4) can be written [7] in the equivalent form

$$\Xi = \sum_n z^n \int \exp(-\beta U_n\{L\}) d\{L\} \quad (2.5)$$

where

$$z^n = \prod_s \prod_l z_s^{n_{sl}} \quad (2.6)$$

$$z_{\lambda 0} = 1/v_{\lambda 0} \quad (2.7)$$

where $v_{\lambda 0}$ is the volume of an empty cell of

kind λ , and in the product $s = 1, 2, \dots, 10, 20, \dots, r0$. In equation (2.5) the artifice of writing an integration over fictitious co-ordinates (l) has been adopted for empty cells. The factors $z_{\lambda 0}$ correct for this integration.

An alternative method for treating vacancies has also been used. If the occupation set n has a vacancy at l then one adds $\delta(u_1^2(l) + u_2^2(l) + u_3^2(l))$ to the potential energy. In the integration over displacements the range is always extended over the range $-\infty$ to ∞ , and so this gives an additional factor $(\pi kT/\delta)^{3/2}$. We therefore define

$$z_{\lambda 0} = (\delta/\pi kT)^{3/2} \quad (2.8)$$

and proceed as before. The value of δ is arbitrary and the result of an exact calculation of Ξ would be independent of its value. For an approximate calculation the best choice of δ is that which satisfies

$$\left(\frac{\partial \log \Xi(z, V, T, \delta)}{\partial \delta} \right)_{z, V, T} = 0. \quad (2.9)$$

Let m denote the occupation set for the perfect crystal. The function θ defined by identifying the integrand of equation (2.5) with the integrand in

$$\Xi = z^m \int \exp(-\beta\theta(z, V, T, \{L\})) d\{L\} \quad (2.10)$$

can readily be shown to be a true potential of average force such that $-\partial\theta\{L\}/\partial u_\alpha(l)$ is the average force in direction α on the occupant of cell l for fixed $\{L\}$, the average being over all crystal occupation sets. However, this is not the case if the alternative method for vacancies is used.

A useful expression for θ can be derived. Let $s\lambda$, $s = 1, 2, \dots$, denote the species occupying a cell of kind λ in the perfect crystal and define y_s by

$$y_s = z_s/z_{s\lambda}. \quad (2.11)$$

A set of numbers ν_{sl} such that ν_{sl} is non-zero

only when site l is occupied by a point defect of species s is defined by the equation

$$\nu_{sl} = n_{sl} - \delta_{s,\lambda} n_{s\lambda l}. \quad (2.12)$$

Comparison of equations (2.5) and (2.10) yields

$$\exp(-\beta\theta\{L\}) = \exp(-\beta U_m\{L\}) \times \sum_\nu y^\nu \exp(-\beta U_\nu^*\{L\}) \quad (2.13)$$

where

$$U_\nu^*\{L\} = U_n\{L\} - U_m\{L\}. \quad (2.14)$$

Next, let $\{n_\alpha\}_N$ denote a particular subset, number α , of n cells out of the totality of N lattice cells and let $\Sigma\{n_\alpha\}_N$ represent summation over all the $N!/(N-n)!n!$ such subsets for $n = 0, 1, \dots, N$. Denote by ν_{n_α} an occupation set such that there are defects at every cell of $\{n_\alpha\}_N$ but no defect at any other cell and let $\Sigma_{\nu_{n_\alpha}}$ denote summation over all occupation sets of this kind. Define

$$S(\{n_\alpha\}_N, \{L\}) = 1 + \sum \{m_\beta\}_{n_\alpha} \times \left(\sum_{\nu_{m\beta}} y^\nu \exp(-\beta U_{\nu_{m\beta}}^*\{L\}) \right) \quad (2.15)$$

where $U_{\nu_{m\beta}}^*$ is U_ν^* for the set $\nu_{m\beta}$. Equation (2.13) can be rewritten

$$\theta\{L\} = U_m\{L\} - kT \log S(N, \{L\}). \quad (2.16)$$

Finally, define

$$\sigma(\{n_\alpha\}_N, \{L\}) = \sum \{m_\beta\}_{n_\alpha} (-)^{n-m+1} \times kT \log S(\{m_\beta\}_{n_\alpha}, \{L\}) \quad (2.17)$$

the inverse of which is

$$-kT \log S(\{n_\alpha\}, \{L\}) = \sum \{m_\beta\}_{n_\alpha} \sigma(\{m_\beta\}_{n_\alpha}, \{L\}). \quad (2.18)$$

From equations (2.16) and (2.18) we obtain

$$\theta\{L\} = U_m\{L\} + \sum \{n_\alpha\}_N \sigma(\{n_\alpha\}_N, \{L\}) \quad (2.19)$$

where the functions σ can be calculated from equations (2.17) and (2.15). If the important terms of σ are those whose occupation sets n differ little from m then it is reasonable to hope that the summation converges, the terms for n_α greater than 3 or 4 or corresponding to spatially distant sites being negligible. The preceding results summarize the essentials of the Mayer [7] scheme in condensed form. They may be used as follows.

The position of an atom in cell $l = l_1, l_2, l_3$, λ can be written as $\mathbf{x}\left(\frac{l}{\lambda}\right)$, where in this context $l = l_1, l_2, l_3$. We define

$$\mathbf{r}\left(\frac{l}{\lambda} \frac{l'}{\lambda'}\right) = \mathbf{x}\left(\frac{l}{\lambda}\right) - \mathbf{x}\left(\frac{l'}{\lambda'}\right) \quad (2.20)$$

and write

$$\mathbf{r}\left(\frac{l}{\lambda} \frac{l'}{\lambda'}\right) = \mathbf{r}_0\left(\frac{l}{\lambda} \frac{l'}{\lambda'}\right) + \mathbf{u}\left(\frac{l}{\lambda} \frac{l'}{\lambda'}\right) \quad (2.21)$$

$$\mathbf{u}\left(\frac{l}{\lambda} \frac{l'}{\lambda'}\right) = \mathbf{u}\left(\frac{l}{\lambda}\right) - \mathbf{u}\left(\frac{l'}{\lambda'}\right) \quad (2.22)$$

where \mathbf{r}_0 denotes vectors between cell centres and \mathbf{u} denotes displacement from cell centres. θ can be expanded as a Taylor series in the $\mathbf{u}\left(\frac{l}{\lambda}\right)$

$$\begin{aligned} \theta &= \sum_{i=0} \theta_i \\ &= \theta_0 + \sum_{i=1} \frac{1}{i!} \sum_{l_1, \dots, l_i} \sum_{\lambda_1, \dots, \lambda_i} \theta_{\alpha, \gamma} \left(\frac{l_1 \dots l_i}{\lambda_1 \dots \lambda_i} \right) u_\alpha \left(\frac{l_1}{\lambda_1} \right) \dots u_\gamma \left(\frac{l_i}{\lambda_i} \right) \end{aligned} \quad (2.23)$$

and the partition function, equation (2.10), evaluated by methods similar to those ordinarily used for the canonical partition function. Unfortunately the general formulae for the $\theta_{\alpha, \gamma}$ are excessively cumbersome. Explicit formulae for a common example are given in Section 3.

The details of evaluation of thermodynamic

functions are slightly different from the perfect crystal canonical ensemble case and these are now summarized. For a crystal of M unit cells one may define a quantity f depending only on intensive variables by

$$Mf(z, a, T) = \log \left(\int \exp(-\beta\theta\{L\}) d\{L\} \right) \quad (2.24)$$

where a denotes the set of lattice parameters. Equation (2.10) can then be written

$$\log \Xi(z, V, T, a) = (V/\Delta) \times \left(\sum_s \alpha_s \log z_s + f(z, a, T) \right) \quad (2.25)$$

where $\Delta = V/M$ is the unit cell volume, $\alpha_s = M_s/M$, and M_s is the number of sites occupied by species s in the perfect crystal.

For cubic lattices one has

$$\Delta = \nu a^3$$

where ν is a constant and a the lattice parameter (the extension to other lattices is straightforward). Maximization of $\log \Xi$ with respect to a at constant z, V, T to find the lattice parameter yields

$$\sum_s \alpha_s \log z_s = \frac{a}{3} \cdot \left(\frac{\partial f}{\partial a} \right)_{z, T} - f. \quad (2.26)$$

From the theory of the grand partition function

$$pV = kT \log \Xi, \quad N_s = \left(\frac{\partial \log \Xi}{\partial \log z_s} \right)_{V, T} \quad (2.27)$$

and from these equations one finds

$$p = \left(\frac{kT}{3\nu a^2} \right) \left(\frac{\partial f}{\partial a} \right)_{T, z} \quad (2.28)$$

$$c_s = (M_s - N_s)/M = - \left(\frac{\partial f}{\partial \log z_s} \right)_{a, T, z_s(r \neq s)} \quad (2.29)$$

3. θ FOR ONE KIND OF DEFECT IN A CUBIC LATTICE

When there is only one kind of defect equations (2.15) and (2.17) yield

$$\sigma(l, \{L\}) = -kT \log(1 + h_l) \quad (3.1)$$

$$\sigma(l, k\{L\}) = -kT \log(1 + h_{lk}) \quad (3.2) \quad \text{the results}$$

where

$$h_l = y_l \exp(-\beta u_l^*) \quad (3.3)$$

$$h_{lk} = h_l h_k f_{lk} / [(1 + h_l)(1 + h_k)] \quad (3.4)$$

$$f_{lk} = \exp(-\beta U_{lk}^*) - 1 \quad (3.5)$$

$$u_l^* = U_{vl}^*\{L\} \quad (3.6)$$

$$u_{lk}^* = U_{vkl}^*\{L\} - u_l^* - u_k^* \quad (3.7)$$

where by previous definition U_{vl}^* and U_{vkl}^* are the change in potential energy when defects are introduced at l and l, k respectively in perfect crystals.

In the remaining equations we assume that we have only one kind of substitutional defect in one of the cubic lattices. Mayer cells may then be chosen to be the same as crystallographic cells. We also assume that the potential energy is the sum of pairwise forces

$$U = \frac{1}{2} \sum_l \sum_k \phi(|\mathbf{r}(lk)|) \quad (3.8)$$

(a) Expressions for Θ_0 and Θ_1

Θ_0 follows straightforwardly by combining equations (2.19) and (3.1) to (3.8), the function Θ being evaluated with all $\mathbf{r} = \mathbf{r}_0$. Θ_1 is zero for the present model.

(b) Expression for Θ_2

By straightforward manipulations Θ_2 can be written in the form

$$\Theta_2 = \frac{1}{2} \sum_{l_1, l_2} \sum_{\alpha, \beta} \Theta_{\alpha\beta}(l_1 l_2) u_\alpha(l_1) u_\beta(l_2) \quad (3.9)$$

where

$$\Theta_{\alpha\beta}(l_1 l_2) = \sum_{i=0} \Theta_{\alpha\beta}^{(i)}(l_1 l_2). \quad (3.10)$$

The superscript $i = 0, 1, 2, \dots$ refers to the contribution from U_m , $\sigma(l)$ functions, $\sigma(l, k)$ functions, ... respectively. One finds, using the abbreviation

$$D = \frac{1}{r} \frac{\partial}{\partial r}$$

$$\Theta_{\alpha\beta}^{(0)}(l_1 l_2) =$$

$$- [r_\alpha(l_1 l_2) D(l_1 l_2) r_\beta(l_1 l_2) D(l_1 l_2) \phi(l_1 l_2)]_0, \quad (3.12)$$

$$\sum_{l_2} \Theta_{\alpha\beta}^{(0)}(l_1 l_2) = 0 \quad (3.13)$$

$$\Theta_{\alpha\beta}^{(1)}(l_1 l_2) = - \sum_l \sigma_{\alpha\beta}(ll_1, ll_2) \quad (3.14)$$

$$\sigma_{\alpha\beta}(ll_1, ll_2) =$$

$$- [r_\alpha(ll_1) D(ll_1) r_\beta(ll_2) D(ll_2) \sigma(l)]_0, \quad (3.15)$$

where the remaining $\sigma_{\alpha\beta}$ are defined by

$$\sum_{l_2} \sigma_{\alpha\beta}(ll_1, ll_2) = 0 \quad (3.16)$$

$$\sum_{l_1} \sigma_{\alpha\beta}(ll_1, ll_2) = 0. \quad (3.17)$$

The subscript zero on a bracket denotes that the functions are evaluated with all $\mathbf{r} = \mathbf{r}_0$.

The contribution from $\sigma(lk)$ functions was evaluated only in the approximation $h_{lk} \ll 1$ so that from equation (3.2)

$$\sigma(lk) = -kT h_{lk}. \quad (3.18)$$

The result is then

$$\begin{aligned} \Theta_{\alpha\beta}^{(2)}(l_1 l_2) = & - (h/1 + h) \left(\sum' f \right) \\ & \times \left(\frac{\partial \sigma_{\alpha\beta}}{\partial \xi} (\xi, l_1 l_2) \right)_{\xi=1} \\ & - kT (h/1 + h)^2 F_{\alpha\beta}(l_1 l_2) \end{aligned} \quad (3.19)$$

where

$$\begin{aligned} F_{\alpha\beta}(l_1 l_2) \\ = [r_\alpha(l_1 l_2) D(l_1 l_2) r_\beta(l_1 l_2) D(l_1 l_2) f_{l_1 l_2}]_0, \\ l_1 \neq l_2 \end{aligned} \quad (3.20)$$

$$\sum_{l_2} F_{\alpha\beta}(l_1 l_2) = 0. \quad (3.21)$$

h and f denote h_l and f_{lk} functions evaluated at $\mathbf{r} = \mathbf{r}_0$. For any function X we denote by $X(\xi)$ the function derived by replacing each h_l by ξh_l . Finally we used the abbreviation

$$\sum' f \equiv \sum_k' f_{ik}$$

where here and elsewhere the prime denotes that $k = l$ is omitted.

(c) *Harmonic approximations*

The harmonic approximation, indicated by subscript H , is

$$\Theta_H = \Theta_0 + \Theta_2. \quad (3.22)$$

The harmonic Einstein approximation, HE , is

$$\Theta_{HE} = \Theta_0 + \frac{1}{2} \sum_l \sum_\alpha \Theta_{\alpha\alpha}(ll) u_\alpha^2(l). \quad (3.23)$$

(d) *Anharmonic approximations*

The sensitivity of the calculations of defect concentrations to the anharmonic terms has been studied using the Henkel[9] approximation. An alternative would be to calculate the first order anharmonic perturbation to $\log \Xi$ following the methods for perfect crystals[10, 11]. However, a formidable amount of additional algebra would be required for the imperfect crystal and higher order terms may also be important in the classical region. A more promising alternative would be a variational method[12]. Until perfect crystal calculations are more highly developed we do not feel that these more elaborate methods can be justified in the present context. The anharmonic Einstein, AE , calculations therefore use the approximation [9]

$$\begin{aligned} \Theta_{AE} = \Theta_{HE} + \frac{1}{4!} \sum_l \sum_\alpha (\Theta_{\alpha\alpha\alpha\alpha}(llll) \\ + 2\Theta_{\alpha\alpha\beta\beta}(llll)) \times u_\alpha^4(l) \end{aligned} \quad (3.24)$$

where

$$\Theta_{\alpha\beta\gamma\delta}^{(0)}(llll) = - \sum_l' [E_{\alpha\beta\gamma\delta}(l; l_1 l_1 l_1 l_1) \phi(ll_1)]_0 \quad (3.25)$$

$$\Theta_{\alpha\beta\gamma\delta}^{(1)}(llll) = - \sum_l \sigma_{\alpha\beta\gamma\delta}(l_1; llll) \quad (3.26)$$

$$\begin{aligned} \sigma_{\alpha\beta\gamma\delta}(l; l_1 l_2 l_3 l_4) = - [E_{\alpha\beta\gamma\delta}(l; l_1 l_2 l_3 l_4) \sigma(l)]_0, \\ l_1, l_2, l_3, l_4 \neq l \end{aligned} \quad (3.27)$$

$$\sigma_{\alpha\beta\gamma\delta}(l; llll) = \sum_{l_1, l_2, l_3, l_4 \neq l} \sigma_{\alpha\beta\gamma\delta}(l; l_1 l_2 l_3 l_4) \quad (3.28)$$

$$\begin{aligned} E_{\alpha\beta\gamma\delta}(l; l_1 l_2 l_3 l_4) \\ = [r_\alpha(ll_1) D(ll_1) r_\beta(ll_2) D(ll_2) r_\gamma(ll_3) D(ll_3) \\ \times r_\delta(ll_4) D(ll_4)]. \end{aligned} \quad (3.29)$$

4. EVALUATION OF f

It is convenient to separate f , equation (2.24), into static and vibrational parts, $f^{(0)}$ and $f^{(v)}$, defined by

$$f^{(0)} = -\beta\Theta_0/M \quad (4.1)$$

$$f^{(v)} = f - f^{(0)}. \quad (4.2)$$

In addition to f one also requires its derivatives with respect to a and z for a self-consistent treatment of thermodynamic properties. These cumbersome expressions are easily derived from the results for f given below and will not be quoted.

(a) *Harmonic approximations*

Θ_2 may be transformed to a sum of squares by the normal co-ordinate transformation

$$u_\alpha(l) = M^{-1/2} \sum_{\mathbf{k}, j} e_\alpha(\mathbf{k})_j Q(\mathbf{k})_j \exp(2\pi i \mathbf{k} \cdot \mathbf{x}(l)). \quad (4.3)$$

The Jacobian for the transformation may be shown to be unity. By steps quite analogous to those used by Bradburn[13] it may then be shown that the harmonic approximation obtained by combining equations (2.24), (3.9), (3.22) gives

$$\begin{aligned} f_H(z, T, a) = f^{(0)} + \frac{3}{2} \log(2\pi kT) \\ - \sum_{\mathbf{k}} \log(|D_{\alpha\beta}(\mathbf{k})|) 2M \end{aligned} \quad (4.4)$$

provided that the matrix $D_{\alpha\beta}(\mathbf{k})$, defined by

$$D_{\alpha\beta}(\mathbf{k}) = \sum_l \Theta_{\alpha\beta}(ll_1) \exp(-2\pi i \mathbf{k} \cdot \mathbf{r}_0(ll_1)) \quad (4.5)$$

is positive definite at all points in \mathbf{k} space.

From equations (3.12)–(3.17) the contributions to $D_{\alpha\beta}$ from $\Theta_{\alpha\beta}^{(0)}$ and $\Theta_{\alpha\beta}^{(1)}$ are

$$D_{\alpha\beta}^{(0)}(\mathbf{k}) = \sum_l' [1 - \exp(-2\pi i \mathbf{k} \cdot \mathbf{r}_0(l_l))] \times [r_\alpha(l_l)r_\beta(l_l)\phi^{(2)}(l_l)/r(l_l)^2 - (r_\alpha(l_l)r_\beta(l_l)/r(l_l))^3 - \delta_{\alpha\beta}/r(l_l)]\phi^{(1)}(l_l)]_0 \quad (4.6)$$

and, after simplification

$$D_{\alpha\beta}^{(1)}(\mathbf{k}) = -2(h/1+h)D_{\alpha\beta}^{(0)}(\mathbf{k})^* - [h/(kT(1+h)^2)] \times \left[\sum_l' (r_\alpha(l_l)\phi^{(1)}(l_l)^*/r(l_l)) \times \exp(-2\pi i \mathbf{k} \cdot \mathbf{r}_0(l_l)) \right]_0^2 \quad (4.7)$$

where

$$\phi^{(n)}(l_l) = \left(\frac{\partial^n \phi(l_l)}{\partial r(l_l)^n} \right)_0 \quad (4.8)$$

and $\phi(l_l)^*$ denotes the potential function such that u_l^* from equations (3.6) and (3.7) can be written in the form

$$u_l^* = - \sum_l' \phi(l_l)^* \quad (4.9)$$

and $D_{\alpha\beta}^{(0)}(k)^*$ is $D_{\alpha\beta}^{(0)}(k)$ with ϕ replaced by ϕ^* .

The harmonic Einstein approximation yields

$$f_{HE} = f^{(0)} + \frac{3}{2} \log(2\pi kT) - \frac{3}{2} \log \Theta_{\alpha\alpha}(l) \quad (4.10)$$

for cubic lattices, and one finds

$$\Theta_{\alpha\beta}^{(0)}(l) = \sum_l' [r_\alpha(l_l)r_\beta(l_l)\phi^{(2)}(l_l)/r(l_l)^2 - (r_\alpha(l_l)r_\beta(l_l)/r(l_l))^3 - \delta_{\alpha\beta}/r(l_l)]\phi^{(1)}(l_l)]_0 \quad (4.11)$$

$$\Theta_{\alpha\beta}^{(1)}(l) = -2(h/1+h)\Theta_{\alpha\beta}^{(0)}(l)^* - [h/(kT(1+h)^2)] \times \left[\sum_l' r_\alpha(l_l)r_\beta(l_l) \times (\phi^{(2)}(l_l)^*)^2/r(l_l)^2 \right]_0 \quad (4.12)$$

where the asterisk again denotes replacement of ϕ by ϕ^* .

The explicit expressions for $\Theta_{\alpha\beta}^{(2)}$ and for the anharmonic contributions discussed below are very unwieldy but straightforward to derive and will not be stated.

(b) Anharmonic terms

Equations (2.24) and (3.24) yield

$$f_{AE}(z, T, a) = f^{(0)} + 3 \log I \quad (4.13)$$

where

$$I = \int_0^\infty \exp(-A\beta x^2 - B\beta x^4) dx \quad (4.14)$$

$$A = \Theta_{\alpha\alpha}(l)/2 \quad (4.15)$$

$$B = (\Theta_{\alpha\alpha\alpha\alpha}(llll) + 2\Theta_{\alpha\alpha\beta\beta}(llll))/4! \quad (4.16)$$

By expanding the exponential one obtains

$$I = I_0 \sum_{n=0}^\infty (-\beta B)^n I_n/n! \quad (4.17)$$

$$I_n = \int_0^\infty x^{4n} \exp(-\beta A x^2) dx / I_0 \quad (4.18)$$

$$I_0 = \int_0^\infty \exp(-\beta A x^2) dx \quad (4.19)$$

and this may be converted to a power series for $\log I$

$$\log I = \log I_0 + \sum_{n=1}^\infty (-\beta)^n w_n/n! \quad (4.20)$$

From the general relation between w_n and I functions[14] combined with reduction of the integral I_n by integration by parts one can obtain the following general expression for calculation of w_n as a function of A and B :

$$w_n = x^n \left[(4n)!/(2n)! - (n-1)! \sum_{m=1}^{n-1} ((4(n-m))! / ((n-m)!(m-1)!)) \times (w_m/x^m) \right] \quad (4.21)$$

where

$$x = B/(16A^2\beta^2). \quad (4.22)$$

Equations (4.13), (4.20), and (4.21) combine to give f_{AE} as a function of A , B and β . The successive partial sums of the series in (4.20)

oscillate with increasing amplitude in the regions of interest below. The series was summed by the method of Padé approximants [15], which form a convergent sequence generally constant to 0.1 per cent after the fourth approximant.

5. RESULTS FOR RARE GAS SOLID SOLUTIONS

The conventional form for the chemical potential of an impurity, s , dissolved in a host, t , is

$$\mu_s = \mu_s^{(0)} + kT \log c_s \gamma_s \quad (5.1)$$

where $\gamma_s \rightarrow 1$ as $c_s \rightarrow 0$. From equations (2.29), (3.1), (4.1) and (4.2) and using the fact that $z_s \rightarrow 0$ as $c_s \rightarrow 0$ one finds

$$\mu_s^{(0)} = (u_0^* + \mu_t + \frac{3}{2}kT \log (m_t/m_s)) - kT \log \left(1 - \frac{z_s}{h_s} \left(\frac{\partial f^{(v)}}{\partial z_s} \right)_{z_s=0} \right) \quad (5.2)$$

$$\gamma_s = \left(1 - \frac{z_s}{h_s} \left(\frac{\partial f^{(v)}}{\partial z_s} \right)_{z_s=0} \right) / \left(1 - \frac{z_s}{h_s} \left(\frac{\partial f^{(v)}}{\partial z_s} \right) \right) \quad (5.3)$$

where u_0^* is u^* , equation (3.6), evaluated with all $\mathbf{r} = \mathbf{r}_0$.

The first term in brackets in equation (5.2) is the static contribution but it is clearly different from the static approximation in conventional treatments since the energy u^* is calculated without lattice relaxation. The effect of the latter is therefore wholly in the vibrational term. In the limit $z_s \rightarrow 0$ only the σ functions for single sites contribute to $(\partial f^{(v)}/\partial z_s)$ as expected physically.

Figure 1 shows results for $\mu^{(0)}$ at zero pressure in the approximations H , HE , AE for argon in krypton at three temperatures, and also values calculated from the experimental results of Fender and Halsey [16]. The result from using experimental values of z_t [16] and a [17] for the AE approximation is also shown. Ar and Kr potential parameters for the 6-12 Lennard-Jones potential given by Horton and Leech [18] were used and the Ar-Kr parameters calculated from the com-

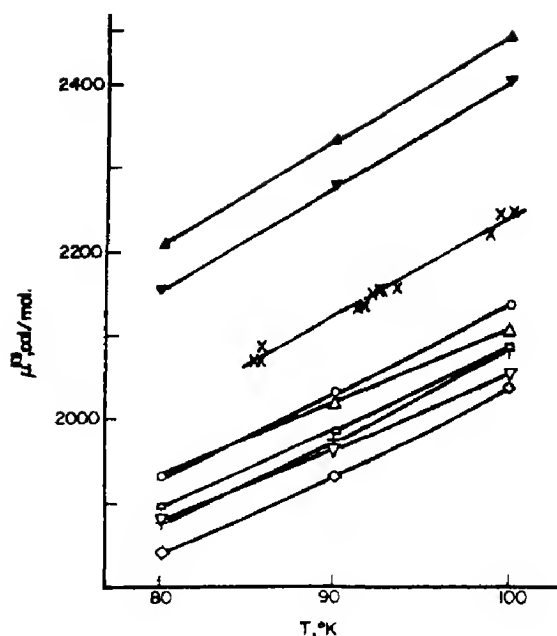


Fig. 1. Free energy of solution, $\mu^{(0)}$, as a function of temperature, T , for Ar in Kr at zero pressure \times , experiment [16], \circ , H , 5:5; \square , HE , 5:5; \triangle , AE , 5:5; $+$, H , 5:6; \diamond , HE , 5:6; ∇ , AE , 5:6; \blacktriangle , AE , 5:5, using experimental z_{Kr} and a ; \blacktriangledown , AE , 5:6, using experimental z_{Kr} and a . (Letters refer to approximation and numbers to the equation for the potential parameter combining rule).

binning rules

$$2r_{AB}^* = r_{AA}^* + r_{BB}^* \quad (5.4)$$

$$\epsilon_{AB} = (\epsilon_{AA}\epsilon_{BB})^{1/2} \quad (5.5)$$

and from the rule [19] which replaces (5.5) by

$$\epsilon_{AB} = 2\epsilon_{AA}\epsilon_{BB}/(\epsilon_{AA} + \epsilon_{BB}). \quad (5.6)$$

The procedure followed was to first calculate the equation of state of pure krypton to find the lattice spacing and chemical potential corresponding to zero pressure at a fixed T . The values were used to calculate $\mu^{(0)}$ from (5.2). Some lattice summations additional to those required for the perfect crystal [13] were calculated on a computer. The numerical integrations over \mathbf{k} used 30 points in the irreducible element of the Brillouin zone [13]. Increasing the density to 149 points has a negligible effect on the very similar calculations of Section 6.

From the straight line drawn through the points the corresponding enthalpies and entropies of solution were calculated:

$$\mu_s^{(0)} = h_s^{(0)} - TS_s^{(0)}. \quad (5.7)$$

Some results are summarized in Table 1 together with calculations for other mixtures. For solutions of Xe in Kr the *H* and *HE* approximations gave

$$\frac{z_s}{h_s} \left(\frac{\partial f^{(v)}}{\partial z_s} \right)_{z_s=0} > 1$$

so that (5.2) cannot be evaluated or, equivalently, (2.29) predicts $c_s < 0$. Also included in Table 1 are volumes of solution defined by

$$V_s^{(0)} = \left(\frac{\partial \mu_s^{(0)}}{\partial p} \right)_T = \left(\frac{\partial \mu_s^{(0)}}{\partial a} \right)_T / \left(\frac{\partial p}{\partial a} \right)_T \quad (5.8)$$

calculated at 90°K, the differentiations being performed analytically. The volume of solution is slightly temperature dependent as is shown in Fig. 2 for calculations using the simple combining rules (5.4) and (5.5).

The significance of these results is as follows. For moderate misfit in size, as for Ar in Kr, the predictions of the three approximations span a range of about 10 per cent in h_s and 14 per cent in s_s . This is quite com-

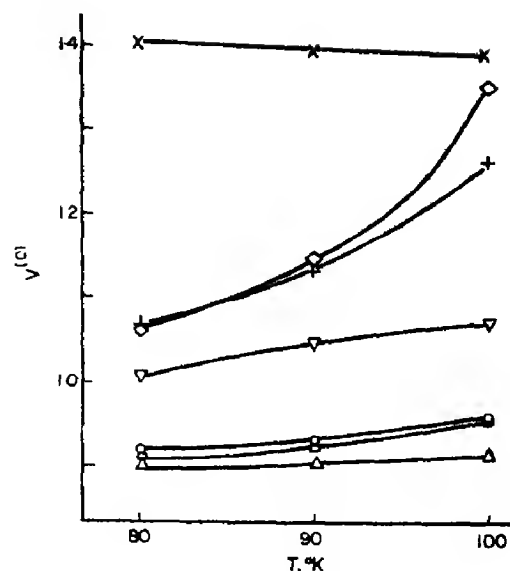


Fig. 2. Volume of solution, $V_s^{(0)}$ (at. vol.), as a function of temperature, T , for impurities in Krypton at zero pressure using the combining rule of equation (5.5) for the 3 approximations. +, Ne (*H*); \diamond , Ne (*HE*); ∇ , Ne (*AE*); \circ , Ar (*H*); \square , Ar (*HE*); \triangle , Ar (*AE*); \times , Xe (*AE*).

parable to the errors arising from uncertainty in potential parameters, as is illustrated by using the different combining rules for $\epsilon(\text{Ar-Kr})$. The values used were 193.04×10^{-6} ergs from equation (5.5) and 190.56×10^{-6} ergs from equation (5.6). The agreement with experiment is not unreasonable considering the expected accuracy of calculations and

Table 1. Mean enthalpy ($h_s^{(0)}$ cal. mol.⁻¹) and entropy ($s_s^{(0)}$ R units) of solution in the temperature range 80–100°K, and volume of solution ($V_s^{(0)}$ at. vol.) at 90°K for impurities in Krypton at zero pressure

Combining rule equation	Approximation	Neon			Argon			Xenon		
		$h_s^{(0)}$	$s_s^{(0)}$	$V_s^{(0)}$	$-h_s^{(0)}$	$s_s^{(0)}$	$V_s^{(0)}$	$-h_s^{(0)}$	$s_s^{(0)}$	$V_s^{(0)}$
(5.5)	<i>H</i>	1960	6.84	1.13	1110	5.13	0.93			
	<i>HE</i>	2010	6.62	1.14	1130	4.81	0.92			
	<i>AE</i>	1680	5.06	1.04	1250	4.33	0.90	2930	10.01	1.40
(5.6)	<i>H</i>	2420	7.14	1.19	1050	5.19	0.96			
	<i>HE</i>	2490	7.32	1.21	1060	4.88	0.93			
	<i>AE</i>	2120	5.43	1.08	1180	4.38	0.91	2840	9.94	1.39
Experimental [16]					1074	5.86				
					± 25	± 0.14				

experiment. As the misfit in size becomes greater the inadequacy of the H and HE approximations must increase since the bigger relaxation about each defect throws greater weight on the vibrational calculation (cf. remarks after (5.3)) and on the anharmonic terms—compare Ne and Ar results. Indeed for Xe only the AE method yields a prediction. For such large anharmonic effects the Henkel approximation may presumably be seriously wrong, whereas for Ar this error is probably no worse than the uncertainty arising from the potential parameters. Finally we note that Fig. 1 seems to suggest that taking account of the anharmonic terms without the Einstein approximation would lead to a better agreement with experiment.

In consequence of these conclusions calculations of activity coefficients have been limited to Ar in Kr at zero pressure for concentrations up to 4×10^{-2} . The HE approximation was used retaining σ functions up to two sites only. As the concentration is increased the lattice parameter at zero pressure becomes smaller. The method adopted was to calculate the value of ' a ' for which $p = 0$ for fixed $(z_s/z_t, T)$ from equations (2.28). γ_s was then calculated at these values $(a, z_s/z_t, T)$ from (5.3) at a known concentration found from equation (2.29). Results are summarized in Fig. 3. The calculations are for approximations retaining one, and for one and two sites, for the two combining rules using the HE approximation and a rigid static lattice approximation (equation (5.9) below). The experimental results shown are actually extrapolations from measurements at higher concentrations. The most striking feature is the sensitivity to change in the potential parameters; even the relative order of the approximations changes with change in combining rule for ϵ_{AB} .

It may be shown that for the static rigid lattice approximation retaining σ functions for single sites corresponds to an ideal solution. Retaining σ functions up to two sites yields, for $h \ll 1$,

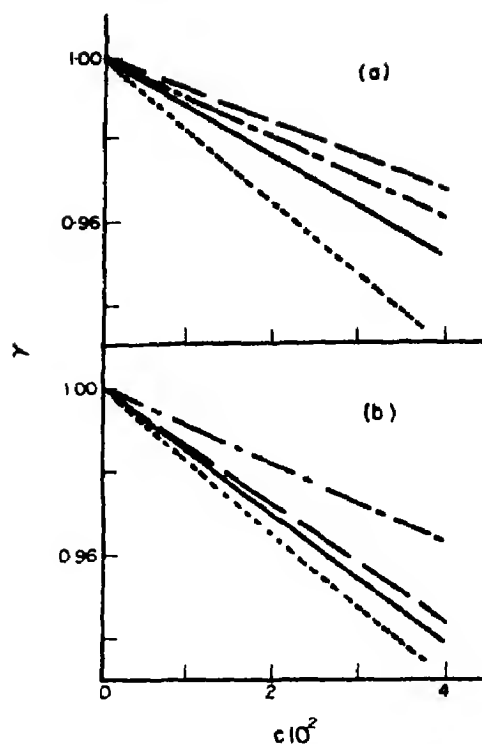


Fig. 3. Activity coefficient, γ , for Ar in Kr as a function of Ar concentrations, c , at 90°K and zero pressure: (a) using combining rule (5.5); (b) using combining rule (5.6). — σ for single sites; --- σ for up to pairs of sites; - · - static approximations; · · · experiment [16].

$$\gamma_s = \exp \left(\frac{1}{2} \sum' f c_s (c_s - 2) \right). \quad (5.9)$$

With the approximations (i) $f = 0$ except at nearest neighbour separations and (ii)

$$f = \exp(-u^*\beta) - 1 = -u^*\beta \quad (5.10)$$

this reduces to the Bragg-Williams approximation. Figure 4 shows that whereas (ii) is not too unreasonable (i) is not a good approximation.

Extension to higher concentrations would require using the complete expression for h_{ik} instead of the approximation of (3.18), and probably allowance for the three site σ function. Without a more certain potential and inclusion of anharmonicity this is scarcely worthwhile at present. We note that the summations over f_{ik} functions in calculations allowing for defect interactions cannot be

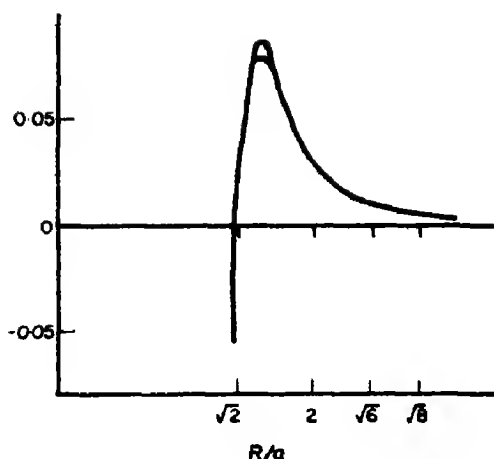


Fig. 4. Mayer f function and $-u\beta$ (the lower curve) [equation (5.10)] as functions of distance r for Ar in Kr at 90°K and zero pressure.

parametrized to a functions of ' a ' times a dimensionless lattice sum and so must be calculated for each ' a ' and T , leading to extra numerical work.

6. RESULTS FOR VACANCIES IN RARE GAS SOLIDS

To determine the pressure of the pure solid with vacancies from equation (2.28) it is necessary to determine z from equation (2.26) at the selected (a, T) . Equation (2.26) was solved by iteration taking the perfect crystal value of z , at given (a, T) , as the starting point. The function f is independent of z for the perfect crystal and (3.26) can be solved explicitly in this case.

In the alternative method for vacancies defined by equations (2.8) and (2.9) the partition function was maximised numerically at each stage of the iteration with respect to δ at constant (z, a, T) .

By these methods the lattice parameter corresponding to zero pressure for Kr was found retaining σ functions for single sites. The concentration of vacancies, c_v , was then calculated from equation (2.27) and the results are summarized in Fig. 5. From least squares lines the enthalpy and entropy of formation in the equation

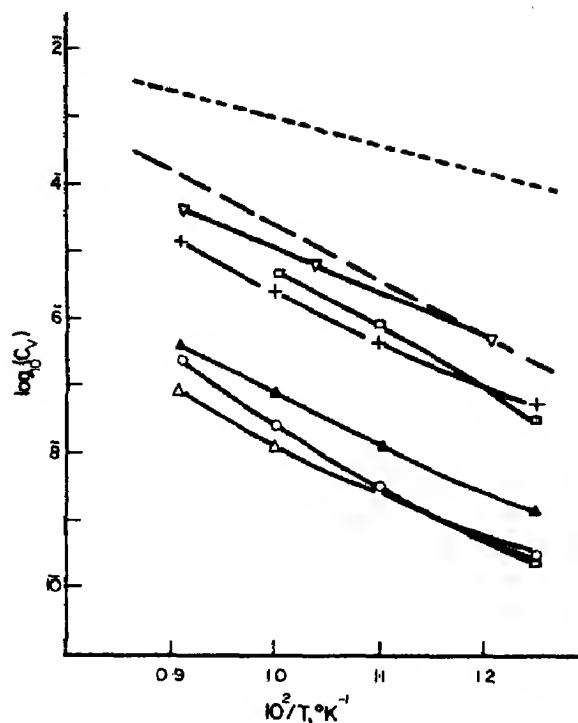


Fig. 5. Vacancy concentrations, c_v , as a function of temperature, T , for Krypton at zero pressure. A prime on the approximation means the alternative vacancy method was used, \circ , H ; \square , HE ; \triangle , AE ; $+$, H' ; \blacktriangle , AE , using experimental z and a ; ∇ , Glyde[4]; ——— Nardelli [3]; - - - - experiment[17]. To the scale of the graph the approximations H and AE coincide at 80° and 90°K and the approximations H and HE coincide at 90° and 100°K.

$$\log c_v = -\beta h_v + s_v/k \quad (6.1)$$

were found. The results are summarized in Table 2. They are mean values since the slope increases slightly as $1/T$ decreases. It may be shown by applying the method of corresponding states that c_v depends only on the reduced temperature

$$T = kT/\epsilon$$

at zero pressure. Calculations[3, 4] for Ar were converted in this way.

For the AE approximation using the alternative method for vacancies the iteration for z did not converge, whereas for the other approximations three iterations suffice for 0.01 per cent constancy. For the H approximation δ varied monotonically from 2408 to 1205 dyn cm⁻¹ in the range 80–110°K.

Table 2. Mean enthalpy (h_v , cal. mol.⁻¹) and entropy (s_v , R units) of formation of vacancies in krypton at zero pressure in the temperature range 80–110°K. A prime on the approximation means the alternative vacancy method was used (equations (2.8), (2.9))

Approximation	h_v	s_v
H	3870	2.23
HE	3720	1.21
AE	3290	-1.25
H'	3180	3.30
HE'	3130	3.56
AE'		
Glyde[4]	2900	3.21
Nardelli[3]	3620	8.1
Experimental[17]	1780 ± 200	2.1 ± 0.5

The effect of the σ functions for pairs of sites was negligible in the HE approximation.

Figure 6 shows the volume of formation

$$V_v = kT \left(\frac{\partial \log c_v}{\partial p} \right)_T \quad (6.2)$$

as a function of temperature and another calculated[3] value.

The results for c_v are in no better agree-

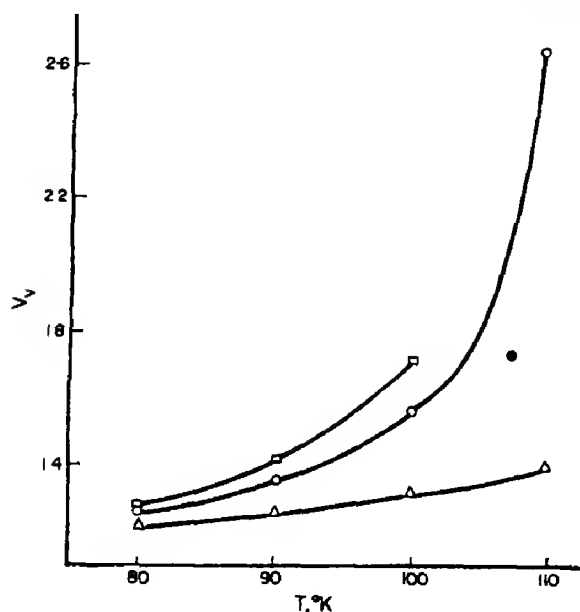


Fig. 6. Volume of vacancy formation, V_v (atomic volumes), as a function of temperature, T , at zero pressure for Krypton. \circ , H ; \square , HE ; \triangle , AE ; \bullet , Nardelli[3].

ment with experiment[20] than those of previous calculations[3, 4]. Since the approximate inclusion of anharmonicity does not have a very marked effect on the results one might be tempted to join previous workers in ascribing the failure of the calculation to neglect of three-body forces[21, 22] and other many body effects[23]. However, there remains a slight doubt as to the validity of the method whereby the sum of integrals is converted to an integral of a sum in the partition function using the method described after equation (2.7). As Mayer[7] has remarked, this method would break down for large c_v . This objection does not apply to the alternative method. The failure of the latter might possibly be ascribed to inadequate treatment of the lattice dynamics, but we remain uncertain. The status of the method for systems with vacancies is therefore much less clear than for solid solutions.

7. CONCLUSIONS

(1) The Mayer method appears promising for substitutional solid solutions provided the misfit in size and potential curves is not too great.

(2) The adequate treatment of the anharmonic terms becomes increasingly important as the misfit increases because the relaxation calculation of conventional methods has been replaced by a modified vibrational calculation. However, the methods for perfect crystal lattice dynamics can be applied, the only essential difference being a rise in algebraic complexity.

(3) These calculations are often very sensitive to errors in the potential functions assumed and this is one of the major inhibitions to undertaking the large amount of work required by more adequate treatment of vibrations e.g. by a self-consistent phonon method.

(4) For interstitial defects the method does not appear particularly promising because (a) the number of elements in the dynamical matrix increases, (b) the misfit will often be large, (c) the alternative method for vacancies

would have to be used for the vacant interstitial sites, and this method has not been very successful in the present work.

(5) Mayer[7] expressed the view that the method might prove adequate for calculating the solubility of sparingly soluble impurities and for phase transitions in general. Since these impurities tend to have large misfits the considerations of (2) and (3) above apply.

Acknowledgement—One of us (L.A.R.) acknowledges the receipt of the S.R.C. maintenance grant.

REFERENCES

1. KANZAKI H., *J. Phys. Chem. Solids* **2**, 24 (1957).
2. BURTON J. J. and JURA G., *J. Phys. Chem. Solid*, **27**, 961 (1966).
3. NARDELLI G. F. and TERZI N., *J. Phys. Chem. Solids* **25**, 815 (1964).
4. GLYDE H. R. and VENABLES J. A., *J. Phys. Chem. Solids* **29**, 1093 (1968).
5. WOJCIOWICZ P. J. and KIRKWOOD J. G., *J. chem. Phys.* **33**, 1299 (1960).
6. MARADUDIN A. A., MONTROLL E. W. and WEISS G. H., In *Solid State Physics* (Edited by F. Seitz and D. Turnbull), Suppl. 3. Academic Press, New York (1963).
7. MAYER J. E., In *Phase Transformations in Solids* (Edited by R. Smoluchowski, J. E. Mayer and H. Weyl), p. 38. Wiley, New York (1951).
8. HILL T. L., *Statistical Mechanics*. McGraw-Hill, (1956).
9. HENKEL J. H., *J. chem. Phys.* **23**, 681 (1955).
10. LEIBFRIED G. and LUDWIG W., In *Solid State Physics* (Edited by F. Seitz and D. Turnbull), Vol. 12, p. 276. Academic Press, New York (1961).
11. FELDMAN J. L. and HORTON G. K., *Proc. phys. Soc.* **92**, 227 (1967).
12. GILLIS N. S., WERTHAMER N. R. and KOEHLER T. R., *Phys. Rev.* **165**, 951 (1968); and references therein.
13. BRADBURN M., *Proc. Camb. Phil. Soc.* **40**, 113 (1943).
14. HILL T. L., In *Statistical Mechanics*, p. 135. McGraw-Hill, New York (1956).
15. WALL H. S., *Analytic Theory of Continued Fractions*. van Nostrand, Princeton, N.J. (1948).
16. FENDER B. E. F. and HALSEY G. D., *J. chem. Phys.* **42**, 127 (1965).
17. LOSEE D. L. and SIMMONS R. O., *Phys. Rev.* **172**, 944 (1968).
18. HORTON G. K. and LEECH J. W., *Proc. phys. Soc.* **82**, 816 (1963).
19. FENDER B. E. F. and HALSEY G. D., *J. chem. Phys.* **36**, 1881 (1962).
20. LOSEE D. L. and SIMMONS R. O., *Phys. Rev.* **172**, 934 (1968).
21. JANSEN L., *Phil. Mag.* **8**, 1305 (1963).
22. FOREMAN A. J. E., *Phil. Mag.* **8**, 1211 (1963).
23. DONIACH S. and HUGGINS R., *Phil. Mag.* **12**, 393 (1965).

ON THE FORMATION AND MIGRATION ENTROPIES OF VACANCIES IN METALS

P. WYNBLATT

Scientific Research Staff, Ford Motor Company, Dearborn, Michigan, U.S.A.

(Received 10 March 1969)

Abstract—An approach has been developed for calculating defect entropies from an entirely discrete vibrational point of view. Calculations have been performed within a discrete finite spherical array of atoms which includes all contributions to the defect entropy predicted by linear isotropic continuum elasticity. The method used, however, does not demand an explicit knowledge of the strength of the defect and thus avoids certain conceptual difficulties that arise in both the elastic and the combined discrete-elastic approaches.

The vibrational spectra for the various defect configurations have been obtained using a quasi-harmonic Einstein model in conjunction with a modified Morse function as force law. Values of the vacancy formation and migration entropies were computed for the cases of copper, nickel and aluminum. Where experimental values were available for comparison, fair agreement was found with the calculated entropies. In addition, Arrhenius D_0 's calculated on the assumption that diffusion is controlled by the migration of single vacancies were found to be lower than experimental D_0 's, thus lending support to previous suggestions in the literature that divacancies make a significant contribution to the diffusion flux in f.c.c. metals at high temperatures.

INTRODUCTION

IT IS NOW well established that in the case of self diffusion controlled by a single equilibrium defect species, the diffusion coefficient or diffusivity, D , can be written as:

$$D = f\lambda^2 \nu_e \exp\{(\Delta S_m + \Delta S_f)/k\} \times \exp\{-(\Delta E_m + \Delta E_f)/kT\} \quad (1)$$

where f represents a product of geometric factors and includes the correlation factor, λ is the defect jump distance, ν_e is an effective frequency, ΔE_m and ΔS_m are the migration energy and entropy of the defect, ΔE_f and ΔS_f are the formation energy and entropy of the defect and k and T are the Boltzmann constant and the absolute temperature respectively. Empirically, the diffusivity can be described by an Arrhenius equation:

$$D = D_0 \exp\{-Q/kT\} \quad (2)$$

where Q is the activation energy for self diffusion and D_0 is a constant. Comparison

of equations (1) and (2) leads to the well known interpretation of the Arrhenius constants in terms of defect properties:

$$Q = \Delta E_m + \Delta E_f \quad (3)$$

$$D_0 = f\lambda^2 \nu_e \exp\{(\Delta S_m + \Delta S_f)/k\}. \quad (4)$$

The bulk of experimental and theoretical work aimed at understanding the role played by point defects in diffusion has been concerned with the energetics of the basic processes. However, the recent realization that Arrhenius plots representing both the volume and surface self diffusion data of some f.c.c. metals show a measure of curvature has prompted a closer look at some of the terms which make up the Arrhenius D_0 , namely, the entropy and frequency terms.

A few attempts have been made in the past at calculating point defect formation entropies [1–5] as well as defect migration entropies [1–3]. Most of these have proceeded by treating a defect crystal in two parts, a central atomically discrete region around the

defect from which a vibrational contribution is obtained and elastic continuum in which the discrete region is embedded and which provides an elastic contribution to the entropy; such an approach, however, may lead to conceptual difficulties which will be discussed later. In the present study an attempt has been made at obviating these problems by calculating defect entropies from an entirely discrete model. Calculations were performed for three f.c.c. metals, namely copper, nickel and aluminum.

CONCEPTUAL CONSIDERATIONS

We shall first consider the problem of obtaining the formation entropy of a vacancy. The formation entropy of a vacancy may be defined as the difference between the entropy of a perfect crystal and that of the same crystal after a vacancy has been introduced into it. From the point of view of a simple vibrational solid, it is possible to write the high temperature limit of the vacancy formation entropy, for a crystal containing N atoms as:

$$\Delta S_f/k = \ln \left(\prod_{j=1}^{3N} \nu_j^0 / \prod_{j=1}^{3N} \nu_j \right) \quad (5)$$

where the ν_j^0 's and ν_j 's are the normal mode frequencies for the perfect and defect crystals respectively. Thus, if it is possible to calculate vibrational spectra for perfect and imperfect crystals, one may obtain the associated entropy change by means of equation (5).

The formation entropy of a vacancy can also be treated entirely from the point of view of linear isotropic continuum elasticity. Consider a vacancy to be represented by a cavity in an infinite elastic medium. Let us initially form the vacancy without allowing any collapse around the cavity, the net volume change of the medium on forming the vacancy is then one atomic volume. If we now allow some collapse to occur around the cavity so as to represent atomic relaxation around the vacancy, the volume of the cavity changes by ΔV^∞ . According to Eshelby [6], for a spherical

cavity, this volume change does not lead to any dilation in the medium but is associated with a displacement field given by:

$$\mathbf{U} = -\frac{\Delta V^\infty}{4\pi} \nabla \left(\frac{1}{r} \right) \quad (6)$$

and a strain energy in the medium, outside a radius r , given by

$$E^\infty = \frac{\mu (\Delta V^\infty)^2}{2\pi r^3} \quad (7)$$

where μ is the shear modulus and $\Delta V^\infty/4\pi$ is known as the strength of the defect. Thus the total strain energy in the medium outside the cavity is simply given by equation (7) with $r = r_c$, where r_c is the radius of the cavity. If it is assumed that this elastic energy is indeed an elastic free energy then it is possible to obtain a corresponding entropy

$$S^\infty = -\frac{\partial E^\infty}{\partial T} = -\frac{\partial E^\infty}{\partial \mu} \frac{\partial \mu}{\partial T} = -\frac{(\Delta V^\infty)^2}{2\pi r^3} \frac{\partial \mu}{\partial T} \quad (8)$$

Elasticity theory provides a second entropy contribution for a vacancy existing in a finite, surface-bounded, medium. The requirement of zero normal stresses at the surface gives rise to an image field associated with a uniform dilation and a corresponding volume change $\Delta V'$ which is related to ΔV^∞ by the expression [6]:

$$\Delta V' = \frac{2(1-2\sigma)}{1+\sigma} \Delta V^\infty$$

where σ is Poisson's ratio. Despite the fact that the uniform dilation, $\Delta V'$, does not give rise to an energy term for a solid under zero pressure, it does give rise to an entropy term through the volume dependence of the vibration frequencies. This can be seen by considering the entropy change in an Einstein solid resulting from a small uniform dilation:

$$S'/k = \ln \frac{\nu^{3N}}{(\nu + \delta\nu)^{3N}} \approx -3N \frac{\delta\nu}{\nu}.$$

Since the frequency ratio $\delta\nu/\nu$ is related to the fractional volume change $\Delta V'/V$ through the Grüneisen constant, γ , by

$$\frac{\delta\nu}{\nu} = -\gamma \frac{\Delta V'}{V}$$

it follows that

$$S'/k = 3\gamma\Delta V'/\Omega \quad (9)$$

where $\Omega = V/N$, is the atomic volume. This result can be obtained in various ways and is in fact equivalent to the result of McLellan[5]

$$S' = 3\beta B \Delta V'$$

where β is the coefficient of linear expansion and B is the bulk modulus.

Thus, it is possible to define the formation entropy of a vacancy from linear isotropic continuum elasticity as

$$\Delta S_f = S^\infty + S'$$

This simple theory has several shortcomings, it does not provide any information regarding the strength of the defect and furthermore, the strength of the defect is defined in the region of largest displacements where the theory is least adequate.

Probably the most detailed method that has thus far been used for calculating defect entropies is that of Huntington *et al.*[1] which combines the discrete vibrational and elastic approaches. Girifalco and Welch[3] and Schottky *et al.*[4] have essentially adopted the same technique in their calculations. In all these cases the vibrational entropy for the discrete region in the vicinity of the defect was obtained by using expressions similar to equation (5), and elastic corrections were made according to formalisms resembling equations (8) and (9). In order to use equations (8) and (9) it is still necessary to determine ΔV^∞ . This is generally obtained from the magnitude of the calculated atomic relaxation

in the discrete region around the defect, by means of equation (6). It is this aspect of the combined approach which produces the conceptual difficulties mentioned earlier.

Several discrete calculations have been performed to determine the atomic configuration around a relaxed vacancy[7-10]. These have shown that inward as well as outward displacements of atoms can occur in the surroundings of the vacancy, a result which is certainly inconsistent with the monotonic displacements predicted by equation (6). An additional complication arises from the fact that in general, displacements need not be radial, in effect it appears that non-radial displacements have been calculated whenever radial relaxation has not been assumed[7, 11]. Thus it is not straightforward to define the strength of a defect and the associated volumes on the basis of the simple theory. These considerations, coupled with the doubtful validity of deriving the image entropy, S' , from a linear elastic dilation, $\Delta V'$, by means of a nonlinear Grüneisen constant, have prompted the alternative approach developed in this study.

The basic idea proposed here is that the calculation be performed for a discrete, finite, spherical array, thus implicitly allowing for any image effects. The vacancy formation entropy can then be calculated entirely from a discrete, vibrational point of view. As will be shown below, the calculation does indeed include the image entropy contribution. In order for such a calculation not to be prohibitive in terms of computer time the size of the spherical array must be limited to several hundred atoms; however, this aspect does not present severe difficulties since the strain entropy, S^∞ , decreases as $1/r^3$ and the image entropy, S' , is independent of the volume of the sphere. The approach used is therefore qualitatively consistent with all the features of the elastic approach, without demanding explicit knowledge of the quantities which lead to complications in the formalism of linear continuum elasticity theory.

We can now consider the problem of calculating the vacancy migration entropy from the vibrational frequencies. The vacancy migration entropy may be defined as the difference between the entropy of a crystal containing an equilibrium vacancy and that of the same crystal containing the vacancy in a saddle point configuration. Vineyard[12] has derived a statistical mechanical expression for the frequency factor, $\nu_e \exp\{\Delta S_m/k\}$, of a diffusing defect. For a crystal containing N atoms:

$$\nu_e \exp\{\Delta S_m/k\} = \prod_{j=1}^{3N} \nu_j / \prod_{j=1}^{3N-1} \nu_j^* \quad (10a)$$

where the ν_j 's are the normal vibration frequencies for a crystal containing a single defect in equilibrium with its surroundings and are therefore identical with the ν_j 's of equation (5) and where the ν_j^* 's are the normal frequencies for the same crystal when the defect is present in a saddle point configuration. In Vineyard's formalism, if the configuration containing the equilibrium vacancy is constrained so as to vibrate in directions other than the jump direction, then

$$\Delta S_m/k = \ln \left[\prod_{j=1}^{3N-1} \nu_j' / \prod_{j=1}^{3N-1} \nu_j^* \right] \quad (10b)$$

where the ν_j' 's are the appropriate normal frequencies for this constrained state. The vacancy migration entropy can therefore also be calculated from a discrete vibrational analysis within the proposed spherical array of atoms.

Recently, in atomistic calculations concerned with diffusive jumps, the extent of atomic relaxation about the migrating atom has been limited by invoking a kinetic criterion [13, 14] which has proved useful in predicting acceptable values for the vacancy migration energies in a number of cubic metals[15]. This criterion suggests that the size of the region which can relax during a diffusive jump

may be estimated from the distance to which an elastic disturbance would propagate during the time required for the jump. Since the 'time of flight' of a diffusing atom is of the order of an atomic vibration, we can define the radius of such a 'relaxation sphere' as:

$$R_{rel.} = v_s/\nu \quad (11)$$

where ν is taken to be the Debye frequency and v_s is the velocity of sound estimated from $v_s = \sqrt{B/\rho}$ where B is the bulk modulus and ρ is the density of the material. This criterion will be used in the present calculations of the migration entropy to limit relaxation around the saddle point configuration. It is worth pointing out that in their calculation of defect entropies in copper, Huntington *et al.*[1] considered this issue, albeit couched in different terms, and suggested that because of the short time spent by the diffusing atom at the saddle point configuration, it might be quite unrealistic to consider any image entropy contribution to the defect migration entropy.

METHOD OF CALCULATION

1. Force law and normal mode analysis

We shall first describe the general method employed here for calculating the frequency distribution in any given atomic configuration. The procedure adopted was based on the quasi-harmonic Einstein approximation of a solid in which each atom was allowed to vibrate independently in the potential well formed by the surrounding atoms while the surroundings were held fixed and in which the atomic force constants were allowed to vary with the local atomic arrangement. The potential energy function due to Girifalco and Weizer[16] provides a suitable force law for this type of calculation, furthermore, it has proved useful in a number of previous calculations of defect properties[7, 8, 13-15]. This function expresses the energy of a hypothetical isolated pair of atoms, i and j ,

separated by a distance r_{ij} as:

$$\varphi(r_{ij}) = L[\exp\{-2\alpha(r_{ij} - r_0)\} - 2\exp\{-\alpha(r_{ij} - r_0)\}]$$

where L , α and r_0 are empirical constants. The energy of the i th atom in a crystal is then given by the pairwise sum of $\varphi(r_{ij})$ over all pairs made by the i th atom in the crystal

$$\Phi_i = L \sum_{j \neq i} [\exp\{-2\alpha(r_{ij} - r_0)\} - 2\exp\{-\alpha(r_{ij} - r_0)\}] \quad (12)$$

where r_{ij} may be written in terms of cartesian atom coordinates as

$$r_{ij} = |\mathbf{r}_j - \mathbf{r}_i| = \{(x_{1j} - x_{1i})^2 + (x_{2j} - x_{2i})^2 + (x_{3j} - x_{3i})^2\}^{1/2}.$$

The empirical constants L , α and r_0 are established by matching the sublimation energy, lattice parameter and compressibility to the experimental values as has been described in detail by Girifalco and Weizer [16]. The parameters used in the present calculation are given in Table 1.

Given such a force law, it is possible to determine the three independent vibration modes of an atom lying in an atomic array. Consider an atom with coordinates $(x_{1i}^0, x_{2i}^0, x_{3i}^0)$ corresponding to the equilibrium position for the atom in a specified array. These coordinates for the atom then correspond to a minimum value of Φ_i , Φ_i^0 , for the atom. Under these conditions, the net force acting on the atom is zero and we may expand

Φ_i as a Taylor series about the equilibrium position, for small displacements u_1 , u_2 and u_3 :

$$\Phi_i = \Phi_i^0 + \frac{1}{2} F_{kl} u_k u_l \quad (k, l = 1, 2, 3) \quad (13)$$

where the atomic force constants which vary from site to site are defined by:

$$F_{kl} = \left. \frac{\partial^2 \Phi_i}{\partial u_k \partial u_l} \right| (x_{1i}^0, x_{2i}^0, x_{3i}^0)$$

and where terms higher than second order have been neglected.

The equations of motion of an atom moving in such a potential are

$$m \ddot{u}_k = -F_{kl} u_l \quad (k, l = 1, 2, 3) \quad (14)$$

where m is the atomic mass and \ddot{u} is the second time derivative of the displacements. Assuming solutions to equations (14) of the form

$$u_k = A_k \sin(2\pi\nu t + \delta)$$

where A_k and δ are constants and t is time, we find

$$\ddot{u}_k = -(4\pi^2\nu^2) u_k \equiv -\lambda u_k. \quad (15)$$

Substituting equations (15) into equations (14), we have

$$\lambda m u_k = F_{kl} u_l \quad (k, l = 1, 2, 3). \quad (16)$$

Solutions to equations (16) exist only if the determinant

$$\begin{vmatrix} F_{11}/m - \lambda & F_{12}/m & F_{13}/m \\ F_{12}/m & F_{22}/m - \lambda & F_{23}/m \\ F_{13}/m & F_{23}/m & F_{33}/m - \lambda \end{vmatrix} = 0. \quad (17)$$

Equation (17) is the so-called secular equation and provides a cubic equation in λ . The three roots of this equation, λ_1 , λ_2 , and λ_3 , yield the three appropriate normal frequencies for the particle of interest through the definition of λ in equations (15). Mathematically, the three

Table 1. Morse function constants

Metal	α (\AA^{-1})	L (eV)	r_0 (\AA)
Cu	1.3588	0.3429	2.866
Ni	1.4199	0.4205	2.780
Al	1.1646	0.2903	3.253

roots λ represent the eigenvalues of the matrix of elements F_{kl} [17] and physically, the roots λ are proportional to the three principal curvatures of the 3-dimensional energy hypersurface described by equation (13). Since we expect the potential energy surface to display a relative minimum at the point corresponding to the equilibrium position of an atom, all three principal curvatures must be positive, leading to three real normal vibration frequencies as indicated above. The Taylor expansion of the potential energy given by equation (13) is also valid for an atom at a saddle point since at that kind of extremum too, the net force acting on the atom must be zero. Thus the normal mode treatment is equally applicable to an atom located at a potential energy saddle point. In this case however, one of the three principal curvatures of the potential energy hypersurface will be negative, as a result, one of the three frequencies obtained from equation (15) will be imaginary. This 'frequency' is the one corresponding to 'translation' of the saddle point atom and is just that frequency which is absent in the product $\prod_j^{3A-1} \nu_j^*$ of equations (10a) and (10b). In addition, since the λ 's are the eigenvalues of the matrix of coefficients F_{kl} it is possible to obtain the eigenvectors or directions corresponding to the three normal frequencies. These directions will also prove useful in some of the subsequent considerations.

2. Array size

Having established a procedure for calculating the normal frequencies of any atom in a given array, it is now possible to turn to another important issue, namely determination of the size of the spherical array of atoms to be used in the computations. There is no obvious or simple criterion that can be invoked to fix this size, however, previous calculations on vacancies [15] have shown that the vacancy relaxation energy for f.c.c. metals converges, for all practical purposes, by the 4th neighbor shell of the vacancy. Based on this knowledge,

we propose that the spherical array is of reasonable size if the energy of an atom in the 8th neighbor shell of the central atom is not changed by the presence of the surface by more than 1 per cent. The use of the 8th neighbor shell, rather than the 4th, as a discriminator may be viewed as an ignorance factor correction. This procedure gives an array that extends to the 24th neighbor shell of the central atom and which contains 767 atoms. The radius of this sphere is 3.54 lattice parameters.

3. Computation of the vacancy formation entropy

In order to compute the normal frequencies corresponding to each atom in the spherical array it is first necessary to determine the equilibrium positions of each atom. The numerical technique employed here to do this has been described in detail elsewhere [15]. Briefly, the technique consists of solving for all three coordinates of an atom which fulfill the condition that the resultant forces on the atom (due to its pairwise interactions with all other atoms in the crystal) must be zero. This procedure was applied first to a perfect spherical array, i.e. one in which the central site was occupied, so as to obtain the ν_j^0 's of equation (5). It was convenient to consider any given atom in the array as belonging to a certain neighbor shell of the central site. It was then possible to take advantage of the symmetry of such a configuration in that a representative atom out of each neighbor shell was relaxed and all other atoms in the same shell then relaxed in a symmetrical way. Some neighbor shells of the central atom in a perfect sphere (or for that matter, of a central vacancy in defect sphere) are degenerate in the sense that they are made up of more than one atom species, e.g. the 9th neighbor shell contains atoms having both $(2, \frac{1}{2}, \frac{1}{2})$ and $(\frac{2}{3}, \frac{2}{3}, 0)$ type coordinates; in those cases a representative atom from each atomic species was relaxed independently. Each shell was relaxed in turn

and the whole process iterated several times. Relaxation was terminated when displacements in each and every shell between successive iterations became smaller than 0.0005 lattice parameters. This was found to take about 20 iterations. At this point, the characteristic frequencies for the atoms in each shell were obtained by applying the normal mode analysis described earlier.

The calculation for the case of the defect sphere with a vacant central site was performed in an identical fashion and the set of ν_j 's of equations (5) and (10a) thus obtained. In principle then, the formation entropy for a vacancy is given by the ratio of the frequencies of the perfect and of the defect spheres according to equation (5). However, the sets of frequencies obtained for the two cases were not immediately comparable since the number of particles in the two calculations differed by one. Ideally, the atom removed from the center of the perfect sphere, in order to create the vacancy, should have been replaced at a kink site on the surface of the sphere. Such a solution would have been extremely undesirable as it would have unnecessarily complicated the calculation by destroying the spherical symmetry of the array. However, as will be shown, placing an atom at a surface kink site is equivalent to the introduction of 3 new frequencies characteristic of an atom in the bulk of the material. For simplicity, this fact will be illustrated using a nearest neighbor bond model.

Consider a large crystal having a terrace ledge-kink surface. A portion of a (111) surface of such a crystal is illustrated schematically in Fig. 1(a). Each atom is numbered according to the number of bonds that it makes with its nearest neighbors. In this approximation the three normal frequencies of a given atom will depend only on the number of bonds that it makes and the spatial distribution of its neighbors. Figure 1(b) shows the same region of the crystal surface after the addition of an atom at the kink

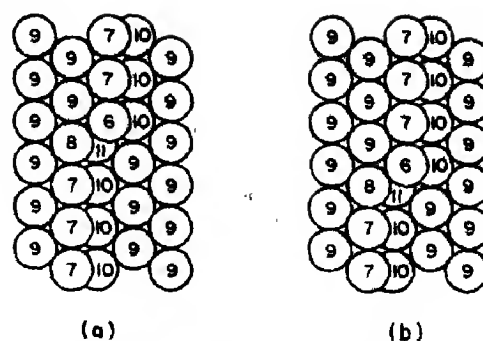


Fig. 1. Schematic representation of a kink on the surface of an f.c.c. crystal. The number of first neighbors of each atom is indicated. (a) Initial kink configuration. (b) Configuration after addition of an atom to kink site.

site. Comparison of Figs. 1(a) and 1(b) shows that the number of visible atoms of each kind have remained the same and that in fact we have acquired one atom with 12 neighbors, i.e. an atom with bonds and frequencies characteristic of the bulk of the material. Although this effect has only been illustrated for the simple nearest neighbor bond model it is intuitively clear that the effect must be true in any pairwise interaction model.

The significance of the above considerations in the present calculation is that when the central atom of the array is removed, a loss of three normal frequencies characteristic of a bulk atom is entailed; however, if it were possible to replace the atom at a surface kink site then the identical three frequencies would be regained, thus contributing no change in vibrational entropy. It is therefore possible to obtain the formation entropy of a vacancy by simply omitting the three frequencies of the central atom in the ratio of equation (5).

4. Computation of the vacancy migration entropy

The calculation of the normal mode frequencies for the case of sphere containing the vacancy in a saddle point configuration, i.e. the ν_j 's of equations (10a) and (10b), was performed in a manner that differed somewhat from the previous two cases. The starting

configuration for this computation was taken to be that obtained previously for an equilibrium vacancy with one of the neighbors of the vacancy initially positioned at a point halfway between its lattice site and the vacant site. Only those atoms whose centers fell within a distance R_{rel} from the site were then allowed to relax one at a time to minimum energy positions. As a result the number of atoms involved in the relaxation process was only 54 for copper and aluminum and 42 for nickel. The need to perform an atom by atom relaxation arose in this case because the saddle point configuration destroyed the spherical symmetry which had been present in the previous cases. Only the small number of atoms involved made an atom by atom relaxation possible in terms of computer time. The atom at the saddle point was also allowed to move to its zero force coordinates corresponding to its true saddle point position. All other atoms in the spherical array were held fixed. The relaxation procedure was again iterated until the displacements of every atom were less than 0.0005 lattice parameters. At the end of the relaxation process, the normal frequencies of each atom in the spherical array were calculated.

Having obtained the $3N-1$ ν_j^* 's and the $3N$ ν_j 's as outlined above it is possible to calculate the frequency factor for the jump process by means of equation (10a). However, if a value of ΔS_m is desired it is necessary to evaluate either the effective frequency, ν_e , or the set of ν_j 's defined in equation (10b). The physical significance associated with ν_e , as generally defined in equation (1), is that it represents the number of attempts per unit time made by the diffusing atom to cross the potential barrier separating it from the vacancy. In examining the three eigenvectors corresponding to the three (in general different) frequencies of the first neighbors of a vacancy, we find each atom to have its lowest normal frequency directed along the line joining the atom site and the vacant site. This frequency is then precisely that which corresponds to

the number of attempts per unit time at crossing the barrier, thus we may equate this frequency to ν_e and obtain the vacancy migration entropy by means of equation (10a). Alternatively we may try to determine the set of frequencies ν_j which is defined as that set corresponding to a constrained state where vibrations are allowed in directions other than the jump direction. Thus if we prescribe the jumping atom and the associated jump direction, the set of frequencies ν_j in the present case becomes identical with the set ν_j from which the eigenfrequency in the jump direction has been abstracted. Both approaches therefore lead to the same result and ΔS_m can be evaluated without difficulty.

RESULTS AND DISCUSSION

Before presenting the results obtained for the various entropy terms, it is worth examining some of the assumptions of the model. The approach used here to calculate the various frequency distributions has been based on an Einstein model where each particle has been considered as independent oscillator and in which coupling effects have been neglected. Such a model could be criticized on the basis that the local change in force constants which occurs when an atom is removed to form a vacancy might lead to localized coupled vibrations in the vicinity of the vacant site. Recent calculations on copper and other metals by Land and Goodman[18] have shown however, that localized modes will not generally accompany vacancy formation. Such local coupled modes were found to arise in the case of copper when the range of the potential extended only to first neighbors but tended to disappear when second neighbor interactions were included. Thus it may be safe to assume that the use of a long range potential as in the present calculations makes the neglect of these modes not serious and, in a certain sense, self-consistent with the approximations used. Furthermore, Litzmann[19] has found that significant local modes will appear only if the ratio of force constants in the defect and per-

fect crystals is greater than 2. The relevance of this simple criterion to the present type of calculation has been extensively discussed by Girifalco and Welch. [3]. It was found here that the maximum ratio of force constants for the case of an equilibrium vacancy was about 1.1 and about 1.6 for the case of a saddle point configuration.

It is also worth examining the assumption that the calculated vacancy formation entropy is practically independent of the size of the spherical array (for reasonable sized arrays), as predicted by the simple elastic theory. In order to check this issue, the vacancy formation entropy of copper was calculated for two additional arrays having volumes about 25 per cent larger and smaller than the array used in all other calculations. The results obtained are given in Table 2 and are seen to oscillate somewhat with the size of the array, thus evidence of discrete behavior is still apparent even at relatively large distances from the defect. In addition, these results indicate that we may expect uncertainties of the order of 5 per cent in the calculated entropies.

Table 2. Influence of array size on the vacancy formation entropy in copper

Number of atoms in perfect array	$\Delta S_f/k$
603	1.55
767	1.67
959	1.56

In order to evaluate the effect of the surface on the vacancy formation entropy in the present calculations, similar calculations were performed for the case of copper in which the vacancy and its associated relaxed region were embedded in an effectively infinite crystal. Relaxation in this effectively infinite crystal was limited to the first 10 neighbor shells (as compared with 24 shells for the case of the spherical array) because of computational restrictions. The cumulative entropy on a shell by shell basis is given for both calculations in Fig. 2 which shows that the presence of the surface decreases the vacancy formation entropy by about $0.4k$, in

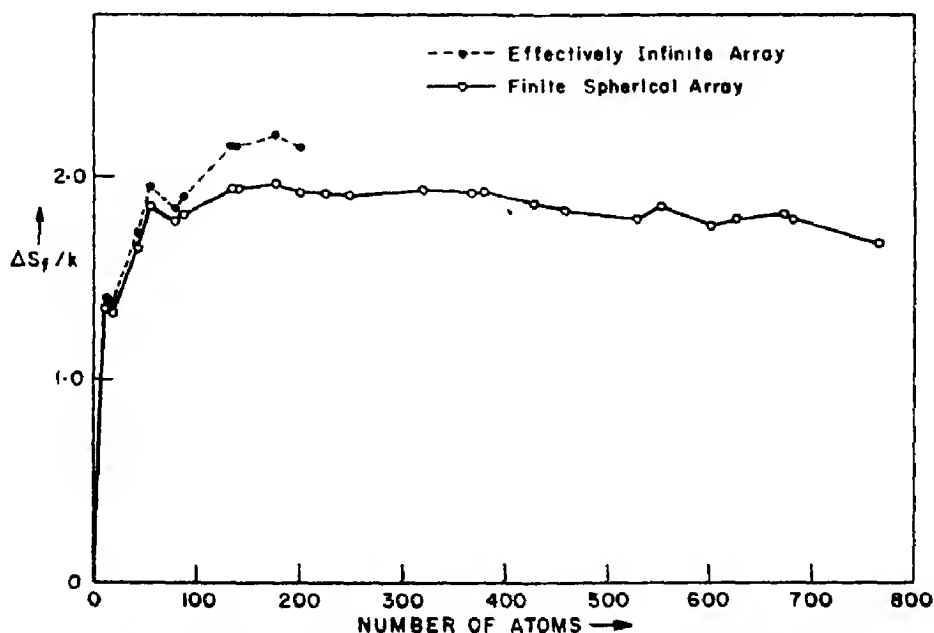


Fig. 2. Comparison of the vacancy formation entropy of copper as calculated for an effectively infinite array and for a finite spherical array. The figure shows the cumulative entropy on a shell by shell basis.

qualitative agreement with the simple elastic theory.

The values of the calculated vacancy formation and migration entropies are given in Table 3 together with some experimental values and the results of previous calculations.

terms is the Arrhenius D_0 . A theoretical value for this constant can be obtained from equation (4) by using the calculated values of the entropies and the effective frequency, ν_e . Calculated values of ν_e and D_0 are given in Table 4 together with the range of experimental D_0

Table 3. Calculated vacancy entropies together with experimental and other theoretical values

Metal	$\Delta S_f/k$			$\Delta S_m/k$	
	Present calculation	Experimental	Other calculations	Present calculations	Other calculations
Cu	1.67	1.5 [25]	1.47 [1], -0.2 to 0.2 [3], 2.7 [5], 0.5 [4]	-0.346	0.93 [1], -0.18 to -0.32 [3]
Ni	2.06			-0.351	
Al	1.72	2.4 [26]	2.1 [5]	-0.317	

Comparison with experiment is severely limited by the dearth of experimental values, in particular, no experimental values of the vacancy migration entropy could be found. Where comparable values are available, reasonable agreement between the calculated and experimental values is found. The negative values obtained for the vacancy migration entropies may be surprising in view of Wert and Zener's assertion that they should always be positive [20]. Wert and Zener's approach, however, included only a strain dependent entropy analogous to equation (8), which is always positive. Their approach therefore neglected the negative entropy contribution resulting from the increased frequencies in the vicinity of the saddle point atom. These increased frequencies come about because of the constrained state of the atoms in and about the saddle point which, as indicated earlier, can increase the local force constants by as much as a factor of 1.6. This is not to say that the migration entropy must always be negative, indeed, preliminary calculations for b.c.c. metals show that the vacancy migration entropy is positive in some cases.

Perhaps the most easily available experimental quantity that depends on the entropy

Table 4. Calculated values and experimental ranges of the Arrhenius D_0 for self diffusion

Metal	ν_e, sec^{-1} Calculated	$D_0, \text{cm}^2/\text{sec}$ Calculated	$D_0, \text{cm}^2/\text{sec}$ Experimental range [27]
Cu	5.93×10^{12}	2.90×10^{-2}	0.1-47
Ni	7.03×10^{12}	4.82×10^{-2}	0.4-5.1
Al	7.21×10^{12}	4.79×10^{-2}	1.71

values. It can be seen that the theoretical values are about one order of magnitude lower than the lowest measured values. Part of the discrepancy is undoubtedly related to the use of an Einstein type effective frequency, the absolute value of which enters into D_0 as ν_e , as can be seen from equation (4). This conclusion stems from the fact that the calculated Einstein frequencies near the center of the perfect array were found to be lower than the more realistic experimentally derived Debye frequencies for the various metals by about a factor of 2. This however does not eliminate the discrepancy, which could depend on more fundamental shortcomings of the present simple approach. Apart from the experimental uncertainties inherent in a

precise determination of D_0 , there is one more possible source for the discrepancies. It has recently become apparent that the Arrhenius plots representing self diffusion in some f.c.c. metals show a measure of curvature. Recent theoretical investigations into the possible sources of this curvature [21–23] have shown that if single vacancy migration is assumed to be the only significant mechanism then the observed curvature is too large to stem from any intrinsic temperature dependence of the energy terms which make up the activation energy for self diffusion. Furthermore, if it is assumed that both mono and divacancies contribute to the diffusion flux, the curvature in the Arrhenius plot can be satisfactorily accounted for [24]. Such a justification of the curvature requires that D_{02} , the Arrhenius constant appropriate for vacancy pairs, be larger than D_{01} , the Arrhenius constant for single vacancies, and in addition that a significant diffusion flux be assigned to the motion of divacancies. Under these circumstances it is perhaps not too surprising that experimentally determined D_0 's are found to be higher than the theoretical values predicted on the assumption of a single vacancy diffusion mechanism.

Acknowledgements—The author is indebted to Drs. D. M. Barnett and N. A. Gjostein for helpful discussions during the course of this study. The valuable criticism of the manuscript by Drs. H. E. Cook and C. L. Magee is gratefully acknowledged.

REFERENCES

- HUNTINGTON H. B., SHIRN G. A. and WAJDA E. S., *Phys. Rev.* **99**, 1085 (1955).
- DIENES G. J., *Phys. Rev.* **89**, 185 (1953).
- GIRIFALCO L. A. and WELCH D. O., *Point Defects and Diffusion in Strained Metals*. Gordon and Breach, New York (1967).
- SCHOTTKY G., SEEGER A. and SCHMID G., *Phys. Status Solidi* **4**, 439 (1964).
- MCLELLAN R. B., *Trans. metall. Soc. A.I.M.E.* **245**, 379 (1969).
- ESHELBY J. D., In *Solid State Physics* Edited by F. Seitz and D. Turnbull, Vol. 3, pp. 79–144. Academic, New York (1956).
- WYNBLATT P. and GJOSTEIN N. A., *J. Phys. Chem. Solids* **28**, 2108 (1967).
- GIRIFALCO L. A. and WEIZER V. G., *J. Phys. Chem. Solids* **12**, 260 (1960).
- SHYU W.-M., BRUST D. and FUMI F. G., *J. Phys. Chem. Solids* **28** 717 (1967).
- SEEGER A. and MANN E., *J. Phys. Chem. Solids* **12**, 326 (1960).
- FLINN P. A. and MARADUDIN A. A., *Am. Phys.* **18**, 81 (1962).
- VINEYARD G. H., *J. Phys. Chem. Solids* **3**, 121 (1957).
- WYNBLATT P., *Acta Metall* **15**, 1453 (1967).
- DOYAMA M. and COTTERILL R. M. J., In *Lattice Defects and Their Interactions* (Edited by R. R. Hasiguti), p. 79. Gordon and Breach, New York (1967).
- WYNBLATT P., *J. Phys. Chem. Solids* **29**, 215 (1968).
- GIRIFALCO L. A. and WEIZER V. G., *Phys. Rev.* **114**, 687 (1959).
- See for example: NYE J. F., *Physical Properties of Crystals*. Oxford University Press, Oxford (1957).
- LAND P. L. and GOODMAN B., *J. Phys. Chem. Solids* **28**, 113 (1967).
- LITZMANN O., *Czech. J. Phys.* **8**, 521, 633 (1958).
- WERT C. and ZENER C., *Phys. Rev.* **76**, 1169 (1949).
- LEVINSON L. M. and NABARRO F. R. N., *Acta Metall.* **15**, 785 (1967).
- GIRIFALCO L. A., *Scripta Met.* **1**, 5 (1967).
- NOWICK A. S. and DIENES G. J., *Phys. Status Solidi* **24**, 461 (1967).
- SEEGER A. and SCHUMACHER D., *Mater. Sci. Engng.* **2**, 31 (1967).
- SIMMONS R. O. and BALLUFFI R. W., *Phys. Rev.* **129**, 1533 (1963).
- SIMMONS R. O. and BALLUFFI R. W., *Phys. Rev.* **117**, 52 (1960).
- ASKILL J., Rep. No. ORNL 3795. Oak Ridge Laboratory (1965).

EXCITON LUMINESCENCE IN LEAD IODIDE LIFETIME, INTENSITY AND SPECTRAL POSITION DEPENDENCE ON TEMPERATURE

R. KLEIM and F. RAGA†

Laboratoire de Spectroscopie et d'Optique du Corps Solide, associé au C.N.R.S., Institut de Physique,
Université de Strasbourg, France

(Received 16 July 1968; in revised form 5 March 1969)

Abstract—The emission spectrum of PbI_2 on the low energy side of the fundamental exciton absorption, is studied in the temperature range 4.2°–180°K. An emission spectrum composed of many lines, is observed. The lines are interpreted as free exciton, bound exciton, and phonon assisted recombination lines. Temperature dependence of the position of the free exciton line is studied. The experimental results are shown to agree with the hypothesis of a lattice expansion effect at low temperatures and an electron-lattice interaction at higher temperatures. A very short luminescence lifetime ($5 \cdot 10^{-10}$ sec) of the above lines is measured by the 'single photoelectron' technique.

1. INTRODUCTION

OPTICAL properties of Lead Iodide (PbI_2) have been studied by many authors[1–10]. Nikitine and coworkers[1–6] studied extensively the absorption spectrum and found at 4.2°K a series of strong lines, interpreted, according to the Elliott theory[11] and Nikitine[12] classification as a first class exciton spectrum.

On the other hand, recently Tubbs[13] tried to explain the absorption spectrum at 77°K according to the recent theory of Ralph[14], concerning excitons in anisotropic crystals (PbI_2 has a layer structure): the value found for the binding energy of the exciton (0.53 eV), differs considerably from Nikitine's value (0.062 eV) which is however previous to the theory of Ralph.

Other authors[15, 16] have been interested in the refractive index of PbI_2 ; Dugan and Henisch[16], based on their results on refractive index and dielectric constant, conclude that PbI_2 "is much less strongly ionic than hitherto supposed".

Works on the luminescence are much less conclusive: the origin of the numerous

emission lines observed at low temperature by several authors[3–8] is not yet explained.

The aim of the present work, on the spectral position, intensity and lifetime dependence on temperature of exciton fluorescence lines in PbI_2 , is to identify the transitions corresponding to the strongest lines and to obtain new experimental data. It is hoped that a better understanding of the optical properties of this compound is obtained.

2. EXPERIMENTAL PROCEDURES

(a) Samples

Lead Iodide crystallizes in an hexagonal Cadmium Iodide-like structure: atoms are located in layers of Pb and I perpendicular to the *c* axis in the succession I–Pb–I–I–Pb–I; on account of the Van der Waals bonding between the Iodine planes the cleavage of PbI_2 normal to the *c* axis is very easy. The crystals studied were obtained from cleavage of zone-refined single crystals; the *c* axis of the crystal was perpendicular to the examined surface of the samples. Owing to the extremely easy cleavage of PbI_2 perpendicular to the *c* axis, good surfaces parallel to the *c* axis have not been obtained. Samples were about half a millimeter thick: we preferred to study thick samples rather than thin ones, owing to

†Permanent address: Instituto de Fisica, Università di Cagliari, Italie, Gruppo Nazionale struttura della Materia del C.N.R.

the better reproducibility of the position of the emission lines [6] for thick samples.

(b) Experimental arrangement

Fluorescence spectrum was excited by the 3650 Å mercury line obtained from the light of a SP 500 Philips high pressure mercury lamp filtered with a UG 11 Schott glass filter (3 millimeter). Fluorescent light was examined in a suitable direction for the removal of the incident light reflected from the surface of the sample. In this way, we had no visible parasite light. Fluorescent light was analysed with a Spex monochromator (10 Å/mm). Spectra have been recorded between 4·2° and 180°K.

The measurements of the lifetime of the fluorescence are carried out using the 'single photoelectron' technique [17, 18].

The schematic diagram of Fig. 1 illustrates the principle of the method. The light pulses are generated using the gaseous discharge in air between two tungsten electrodes with a

gap width of 0·4 mm. The lamp is operated in a relaxation type of circuit. It provides nearly $2 \cdot 10^4$ flashes per sec, with a half-width of about 3 nsec. The maximum light output is located in the near u.v. part of the spectrum, and its intensity is sufficient to excite the luminescence of our crystals. The flash generates also short electrical pulses. The intensity of the light reaching the multiplier (type 56 AVP/03 Radiotechnique) is made so low that the probability of a photoelectron being produced from the multiplier cathode during a flash is less than 10 per cent. Under these circumstances the probability that more than one photoelectron will be emitted in any one flash is small.

The pulses from the multiplier are delayed 100 nsec and shaped by a discriminator so that the transmitted pulses are of the same duration and height. The electrical flash pulses, first shaped by a second discriminator, operate a gating circuit and permit the time-to-pulse-height converter to be started by the multiplier pulses. The stop input is supplied with the electrical flash pulses, previously delayed 300 nsec. The output pulses from the time-to-pulse-height converter are measured and recorded in a multichannel analyser. Replacing the crystal with a mirror, we obtain the time resolution curve $F(t)$ for the flash. This curve corresponds to the convolution of the time resolution function of the apparatus and the probability density of photon emission by the flash. If $L(t)$ is the curve obtained with the fluorescent crystal excited by the flash, the relation between $L(t)$ and $F(t)$ is simply given by the convolution integral:

$$L(t) = \int_{-\infty}^{+\infty} F(t-\theta) p(\theta) d\theta$$

where $p(\theta)$ is the normalized probability density of photon emission by the crystal.

Knowing $p(\theta)$, the evaluation of the lifetime τ is straight forward [19, 20]. For a simple exponential decay, $p(\theta) = 1/\tau e^{-\theta/\tau}$ and the lifetime τ is directly given by the displacement of the centroids of $L(t)$ and $F(t)$ curves [19].

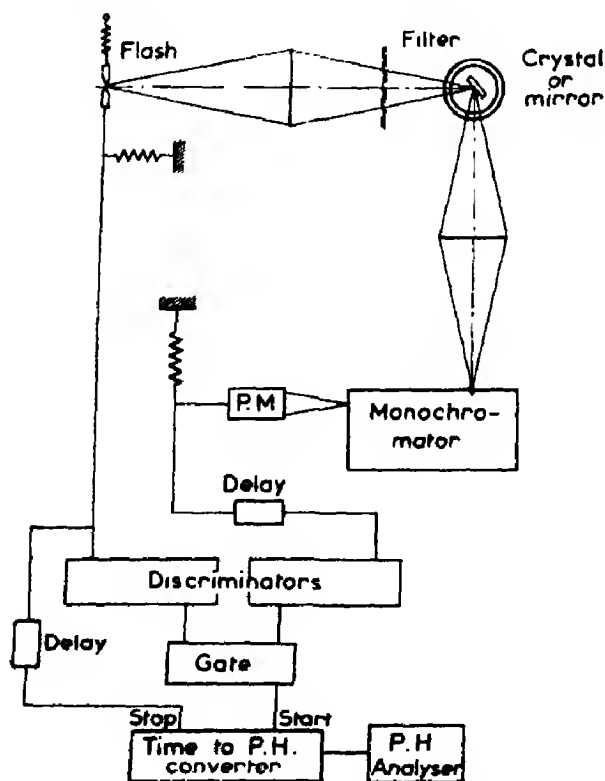


Fig. 1. Schematic diagram of apparatus for measurement of luminescence decay curves.

This method has been used for the determination of the very short lifetimes reported in this paper.

3. EXPERIMENTAL RESULTS

A typical fluorescence spectrum of Lead Iodide at 4.2°K is represented on Fig. 2. We will consider separately the group of lines between $20,300\text{ cm}^{-1}$ and $19,900\text{ cm}^{-1}$ and the complex band placed at wavenumbers lower than $19,900\text{ cm}^{-1}$. This distinction is useful in the description of the spectrum. It will be shown to have physical reasons later on.

(a) The emission spectrum at different temperatures

In Table 1, we give the spectral position at 4.2°K of observed luminescence lines and of the reflection anomalies observed on the same face of the sample, namely the missing ray (RM) and the residual ray (RR) corresponding to the state $n=1$ of the excitonic series observed in absorption by Nikitine *et al.* In the same table, the difference (in cm^{-1}) between some emission lines is given: all the

Table 1. The spectral position of the emission lines and reflection anomalies in PbI_2

Line	ν (cm^{-1})	$\Delta\nu$ (cm^{-1})
RM	20,317	
ν'_0	20,290	
RR	20,253	
ν''_0	20,238	95
ν_c	20,192	
ν_x	20,155	94
$\nu_0\text{-LO}$	20,143	
ν_y	20,123	105
$\nu_c\text{-LO}$	20,098	
$\nu_0\text{-2LO}$	20,038	98
$\nu_0\text{-3LO}$	19,940	

differences are very close to 100 cm^{-1} , which is the wavenumber of the longitudinal optical (LO) phonon recently measured [21]†.

†In a recent work, Dugan and Henisch [22] suggest the existence of 240 cm^{-1} optical phonon. Preliminary measurements, made in our laboratory by Dr Carabatos, show two strong Raman emission lines at ≈ 95 and 109 cm^{-1} , in agreement with the more rough value 100 cm^{-1} reported by Mon [21]. A phonon at 240 cm^{-1} has not yet been measured, but, at this state of our investigations, its existence cannot be entirely excluded.

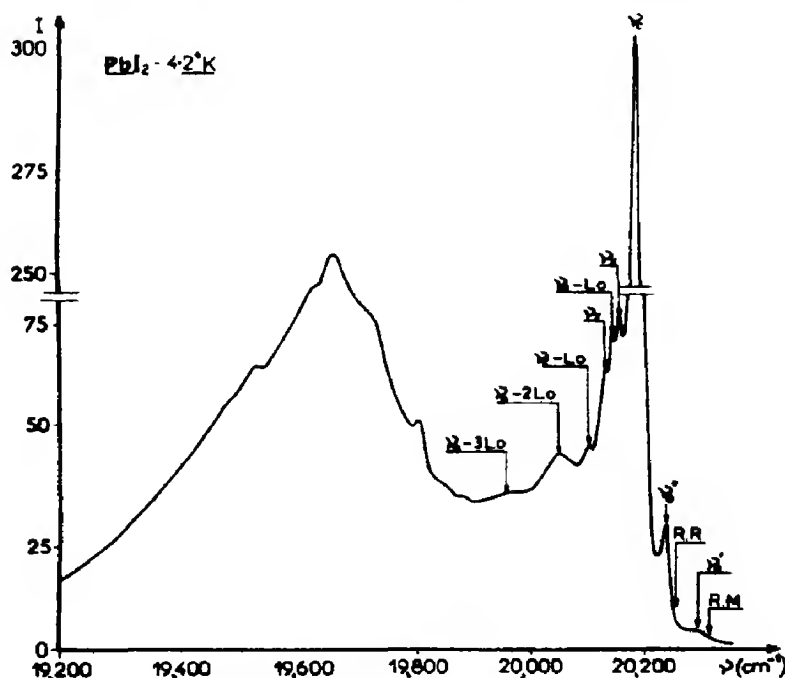


Fig. 2. Emission spectrum of PbI_2 at 4.2°K .

The emission spectrum has been observed at different temperatures. A representative example is shown in Fig. 3. The study of this temperature variation gives most helpful information.

The behaviour of ν'_0 and ν''_0 was considered with special attention: the analysis of the shape of the spectrum at different temperatures, especially between 50° and 90°K, suggests that ν'_0 and ν''_0 belong actually to the same emission line, which we shall call ν_0 , and that a strong self-absorption is responsible for the presence of these two maxima. Therefore they are suggested to be apparent maxima and do not correspond to discrete states.

In the emission spectrum the minimum

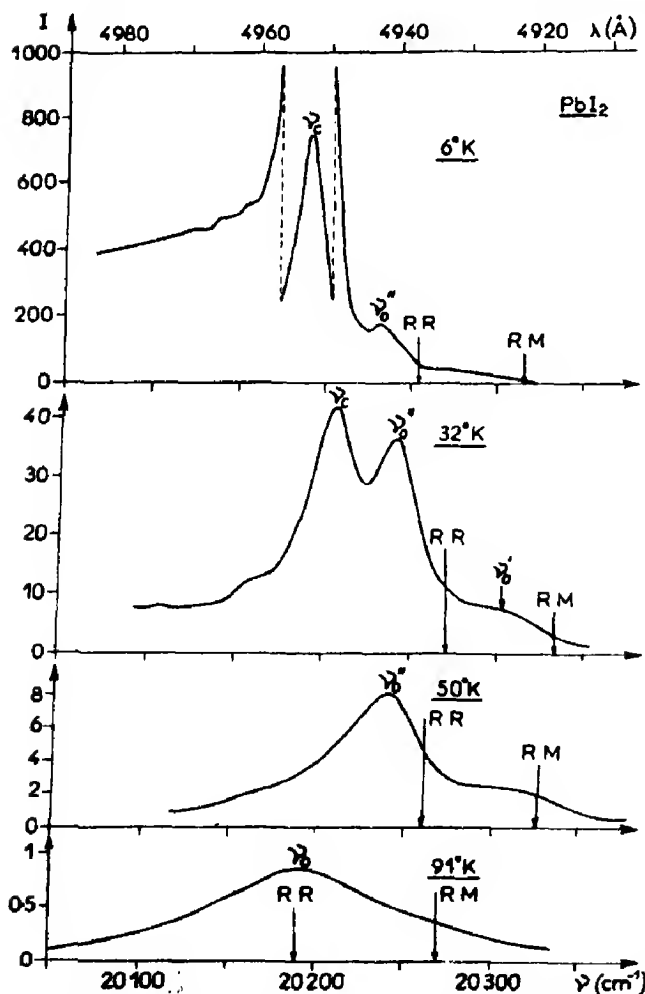


Fig. 3. Change of the exciton emission spectrum of PbI_2 at increasing temperatures.

between ν'_0 and ν''_0 is close in frequency to that of the strong exciton absorption line† $n = 1$. The wave length of excitation light used in our experiments is 3650 Å. The value of the absorption coefficient at this region of the spectrum is comparable to that of the line $n = 1$ [23]. Consequently, the depth of penetration of the excitation light in the crystal is comparable to that involved in the re-absorption of the emitted radiation.

It can easily be shown that the intensity of the emitted light is:

$$I(\lambda) = kI_0\theta_0 \frac{S(\lambda)}{n_\lambda^2(\alpha_\lambda + \alpha_0)} \quad (1)$$

where k is a constant, I_0 the intensity of the excitation light, θ_0 is the aperture angle of the beam emitted by the crystal (the angle must be small for the validity of (1)); $S(\lambda)$ is the shape of the emission line without self absorption, n_λ the refractive index, α_0 the absorption coefficient at excitation wavelength and α_λ the absorption coefficient at λ . This formula is valid if emission intensity is proportional to excitation intensity, which is true for the ν_0 line. If there are no absorption lines near the emission line, then α_λ and n_λ are constant and the emission is not deformed. For PbI_2 , considering the very rough values of the refractive index in the $n = 1$ absorption line, of the absorption coefficient and of the shape of this line, the minimum between ν'_0 and ν''_0 can immediately be explained as due to a self-absorption and it can be shown that the true maximum of the emission line ν_0 is shifted a few cm^{-1} (e.g. 10 cm^{-1}) towards high wave-numbers as compared to ν''_0 . A similar behaviour was observed in CuCl [24].

As regards the origin of the ν_0 line, its

†The absorption line is too strong to be observed in thick samples; on the other hand the spectral position of the absorption line, the residual ray and the emission line is different in thick and in very thin samples[5]. The position of the absorption line was therefore derived from the position of the missing and residual rays we measured in our crystals, considering that, in general[5], the absorption line is shifted about 15 cm^{-1} towards high wave-numbers compared to the residual ray.

spectral position suggests the hypothesis that there is a close connection to the excitonic absorption line $n = 1$, namely that it is the direct radiative annihilation of this excitonic state. A quantitative study of thermal dependence of the intensity of ν_0 and ν_c lines† supplied us with results easily explainable with this hypothesis.

The ν_c -LO line could arise from the same energy level as the ν_c line, however, with simultaneous emission of a LO phonon; ν_0 -LO, ν_0 -2LO, ν_0 -3LO lines are suggested to arise from the same exciton level responsible for ν_0 with simultaneous emission respectively of 1, 2, 3 LO phonons.

Most of the lines are observed only at very low temperatures. At 32°K only ν'_0 , ν''_0 , ν_c and ν_0 -LO are left; at 50°K only ν'_0 and ν''_0 .

(b) *The intensity dependence on temperature of the emission lines*

As it is shown in Fig. 4, the intensity of the ν_c line falls very rapidly when the temperature rises and it disappears at about 45°K.

†Of course, at temperatures below 80°K, on account of self-absorption, the measured intensity of ν_0 is a rough approximation.

The intensity of ν_0 , on the contrary, rises slightly until about 16°K and decreases then for higher temperatures; it disappears at about 180°K.

This result can easily be explained by the assumption that at low temperatures most of the excitons are bound by defects of the crystal (i.e. donor or acceptor centers) and that its radiative annihilation from this state gives rise to the ν_c line. The binding energy of this excitonic complex corresponds to the distance between the ν_0 and ν_c lines and is very low, about $7 \cdot 10^{-3}$ eV. When temperature rises bound excitons are thermally dissociated in free excitons and effects. This mechanism explains the rise at low temperatures, of the intensity of ν_0 , which occurs to the detriment of ν_c , and the fast decrease of the intensity of ν_c when the temperature rises. If, on the other hand, it is supposed that levels that originates the ν_0 and ν_c emission lines are quite independent, the ν_0 line, that corresponds to the less deep level, would disappear before the ν_c line, in contradiction with the experimental results.

At high temperatures ($T > 50^\circ\text{K}$) the decrease in the intensity of ν_0 must be ascribed to thermal dissociation of the

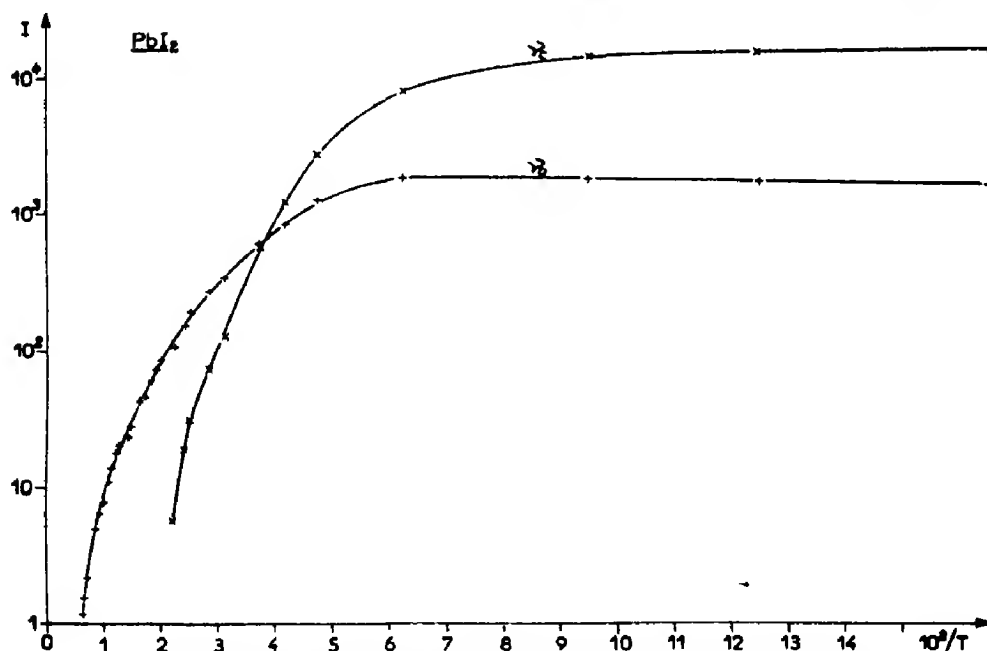


Fig. 4. Intensity dependence on temperature of the emission lines.

exciton which becomes more and more important.

If we plot the logarithm of the intensity of ν_0 against $1/T$, at high temperatures we obtain a straight line, from which can be deduced a dissociation energy of 0.04 eV (322 cm^{-1}) for the exciton. In spite of its lack of precision, this value can be compared to the value of 0.062 eV (506 cm^{-1}) that Nikitine *et al.*[5] deduced from the study of the excitonic series, especially considering that Nikitine's values were deduced at 4.2°K , whereas ours at about 150°K , and that at this temperature even a thermal excitation towards the $n = 2$ excitonic level causes an ionization: in this way the thermally deduced value of exciton dissociation energy may be below the true value. Our value of 0.04 eV is, on the contrary, in evident disagreement with the value of 0.53 eV proposed by Tubbs[13].

A quantitative study of the equilibrium free exciton + defect \rightleftharpoons bound exciton as a function of the temperature is very difficult, both from an experimental point of view owing to the self-absorption of ν_0 which is certainly temperature-dependent under 80°K , and from the point of view of interpretation. The radiative annihilation and the thermal dissociation of the free and the bound exciton are not the single possible mechanism of annihilation of an exciton in a crystal. The theoretical work of Trlifaj[25], on the ionization of donors and acceptors in a crystal by excitons and the work of Khàs[26] on the self-ionization of excitonic complexes should be remembered.

(c) Thermal dependence of the spectral position of the emission lines

The experimental values of the positions of the luminescence lines in PbI_2 as a function of temperature are shown in Fig. 5. We have studied only the lines ν_0 , ν_c and $\nu_0\text{-LO}$, all the other lines having practically disappeared at about 10°K . The lines ν_c and $\nu_0\text{-LO}$ both disappear very rapidly and only the ν_0 line

can be followed from 4.2° to 180°K . The dissociation energy of the exciton is weak in comparison to the width of the gap and it may be admitted that it varies little with the temperature, therefore the variation of the spectral position of the ν_0 line may be identified with the gap variation. An analogous hypothesis was adopted by Bleil and Broser[27] for CdS, by Mahan for CdTe[28] and by Grun, Sieskind and Nikitine for the excitonic line $n = 1$ of the yellow series of Cu_2O [29].

As can be seen in Fig. 5, the variation of the spectral position of the ν_0 line is very surprising in comparison to other semiconductors. In most of semiconductors the gap decreases with the increase in temperature[30]; several compounds such as CuCl[24], PbS, PbSe, PbTe[31] are known in which the energy gap increases with the temperature. For Lead Iodide we have found an intermediate behaviour: the ν_0 line energy (and thus the gap) increases up to a temperature of about 35°K and decreases at higher temperatures. The values of $\Delta E/\Delta T$ ($2 \cdot 10^{-4}\text{ eV}/^\circ\text{K}$ at 150°K) for the line ν_0 are, in our case, rather higher than the values of $\Delta E/\Delta T$ for the first absorption peak measured by Imai[7] at temperatures higher than 77°K .

Actually the two results are not comparable as the absorption spectra also are somewhat different. The higher values found by Tubbs[32] ($|\Delta E/\Delta T| = 5.25 \cdot 10^{-4}\text{ eV}/^\circ\text{K}$ between 100° and 500°K) and by Izvozchikov[33] ($|\Delta E/\Delta T| = 7.5 \cdot 10^{-4}\text{ eV}/^\circ\text{K}$ between 290° and 630°K) for the absorption edge temperature coefficient are compatible with our results: on one hand our measurements show that the quantity $|\Delta E/\Delta T|$ is, above 35°K , an increasing function of the temperature, on the other hand, as PbI_2 obeys Urbach's rule[34], the value of the thermal coefficient of the absorption edge depends on the absorption coefficient at the measured edge and, in general, it is higher than that relative to an absorption peak.

It is generally admitted[35] that gap varia-

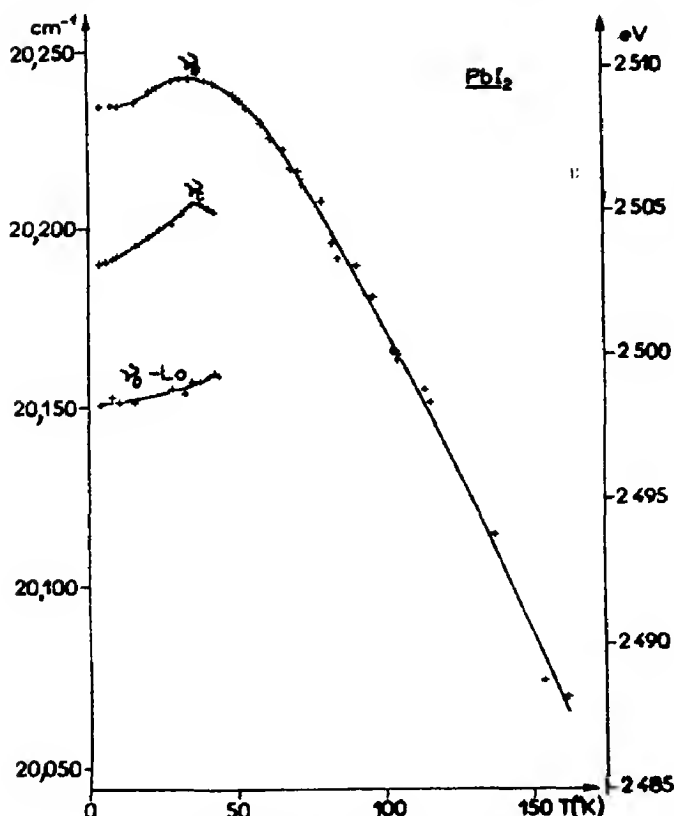


Fig. 5. Temperature dependence of the spectral position of the excitonic lines.

tion obeys the law:

$$E(T) - E(0) = (\Delta E)_v - \frac{\alpha}{\chi} \left(\frac{\Delta E}{\Delta R} \right)_T \quad (2)$$

where $\alpha = 1/V(dV/dT)_p$ is the cubic isobaric thermal expansion coefficient and χ the isothermal compressibility. The second term on the right is due to the variation of the lattice parameter with the temperature; it is positive or negative according to the compound studied. The first term $(\Delta E)_v$, calculated at a constant volume, is due to interaction of electrons and holes with phonons. Many authors [36–38] have theoretically and experimentally studied the $(\Delta E)_v$ variation with the temperature. It may be written:

$$(\Delta E)_v = (\Delta E)_v^{(1)} + (\Delta E)_v^{(2)}. \quad (3)$$

The term $(\Delta E)_v^{(1)}$ is due to the interaction of electrons and holes with optical phonons and

may be written [38]:

$$(\Delta E)_v^{(1)} = -\frac{A}{e^{h\nu/kT} - 1} \quad (4)$$

where ν is the longitudinal optical phonon frequency. The second term $(\Delta E)_v^{(2)}$ is owing to interaction with acoustical phonons and may be written [28]:

$$(\Delta E)_v^{(2)} = -MT^2 \quad \text{for } T < \theta \quad (5)$$

$$(\Delta E)_v^{(2)} = -NT \quad \text{for } T > \theta \quad (6)$$

where θ is the Debye temperature and M and N are positive, temperature independent constants. According to Varshni [30] formulae (5) and (6) can be replaced by:

$$(\Delta E)_v^{(2)} = -\frac{BT^2}{T + \theta}. \quad (7)$$

Thus the term $(\Delta E)_v$ always provide a negative contribution to $E(T) - E(0)$.

In general we may admit, for the energy gap variation with temperature, the relation:

$$E(T) = E(0) + C\alpha T - \frac{BT^2}{T+\theta} - \frac{A}{e^{\hbar\nu/kT} - 1} \quad (8)$$

where $C = -(1/\chi)(\Delta E/\Delta p)_T$ may be supposed temperature independent.

The lack of experimental values of many of the quantities which enter into the calculation of the coefficients A , B , C renders any precise numerical calculation of $E(T) - E(0)$ impossible. But we can try to determine the importance of the different contributions on the basis of the experimental data.

In our case is $(\Delta E/\Delta p)_T = 1.62 \cdot 10^{-2}$ eV/kbar [39] a value of χ is not available, but χ is of course positive; thus $C > 0$. For PbI_2 is $\alpha = 3\beta = 9 \cdot 10^{-5} \text{K}^{-1}$ at 300°K [40], but α depends on temperature and its variation for Lead Iodide is not known; for CdI_2 , α has been measured between 20° and 300°K [41]. Since PbI_2 and CdI_2 are isomorphic, and at 300°K , α is almost identical for the two compounds, we assume that its thermal dependence also is identical. The employed value of the Debye temperature, estimated from heat capacity [42] is $\theta = 150^\circ\text{K}$. The coefficients A , B and C have been determined by the method of least squares, and the following values were obtained: $A = 5.673 \cdot 10^{-2}$ eV; $B = 0$; $C = 1.784$ eV with $E(0) = 2.5085$ eV. The values of the mean square deviations are respectively $\sigma_A = 0.118 \cdot 10^{-2}$ eV for A and $\sigma_C = 0.067$ eV for C .

It may thus be concluded: (1) the positive value of $\Delta E/\Delta T$ for $T < 35^\circ\text{K}$ due to the term $C\alpha T$ of (8), is due to thermal expansion of the lattice. The compressibility deduced from experimental value of $(\Delta E/\Delta p)_T$ is $\chi = 10^{-12} \text{cm}^2/\text{dyn}$; (2) the negative value of $\Delta E/\Delta T$ at $T > 35^\circ\text{K}$ has presumably to be ascribed to **electron and hole interaction with optical phonons**. The contribution due to acoustical phonons can be neglected, since $B \approx 0$.

According to Fan's theory [38] we have:

$$A = \frac{e^2(e^*)^2}{2a^3 M \nu^{3/2} \pi^{1/2} \hbar^{1/2}} (\sqrt{m_e} + \sqrt{m_h}). \quad (9)$$

From this, with the preceding value for A , we deduce:

$$\left(\frac{e^*}{e}\right)^2 \left(\sqrt{\frac{m_e}{m_0}} + \sqrt{\frac{m_h}{m_0}}\right) < 0.013. \quad (10)$$

We have, for the excitonic reduced mass:

$$\frac{\mu}{m_0} = \frac{\kappa_0^2 R_e}{R_H} = 0.176^\dagger$$

that involves:

$$\sqrt{\frac{m_e}{m_0}} + \sqrt{\frac{m_h}{m_0}} > 1.18,$$

We may finally deduce from (10):

$$\frac{e^*}{e} < 0.43.$$

Lead Iodide thus seems to be a compound with little ionic character. This conclusion is in agreement with the results obtained by Dugan and Henisch [16] from the measurement of the refractive index and the dielectric constant.

As regards shifting of the other luminescence lines the temperature range is too limited to allow us to draw conclusions. It may however be noted that the ν_0 -LO line shifts parallel to ν_0 , while the ν_c line has thermal coefficient almost double which causes a decrease in distance between ν_0 and ν_c when the temperature increases. This behaviour can be understood by our hypothesis that the ν_c line is owing to the annihilation of a trapped exciton. The defect-exciton complex may have vibration levels [43]. When the temperature increases the higher levels may begin to fill up and the barycenter of the line may shift towards the higher energies. An alternative hypothesis is that in the neighbourhood of the center responsible for

[†] Values used: dielectric constant $\kappa_0 = 6.21$ [16]; $R_e \approx 0.062$ eV [5].

the bound exciton existence the value of the compressibility, of the thermal expansion and of the LO phonons are different from the measured macroscopic ones.

(d) Lines lifetime

We measured the lifetime of excitonic luminescence between 4.2° and 77°K. At 4.2°K, because of the very high intensity of ν_c in comparison to ν_0 and of partial reciprocal overlap, it was not possible to measure the lifetime of the two lines separately and thus measurements refer to the more intense of the two, that is ν_c . Figure 6 represents the decay curve of the ν_c line, its lifetime, calculated from the shift of the barycenter of the excitation and emission curves, is about $5 \cdot 10^{-10}$ sec. This value, constant between 4.2° and 20°K, is comparable to that already measured for CuCl[24] and HgI₂[44]. At 77°K, the measured lifetime is 10^{-9} sec; it refers to the ν_0 line which is the only line in the spectrum at this temperature; a very precise measurement is difficult since the line is very weak.

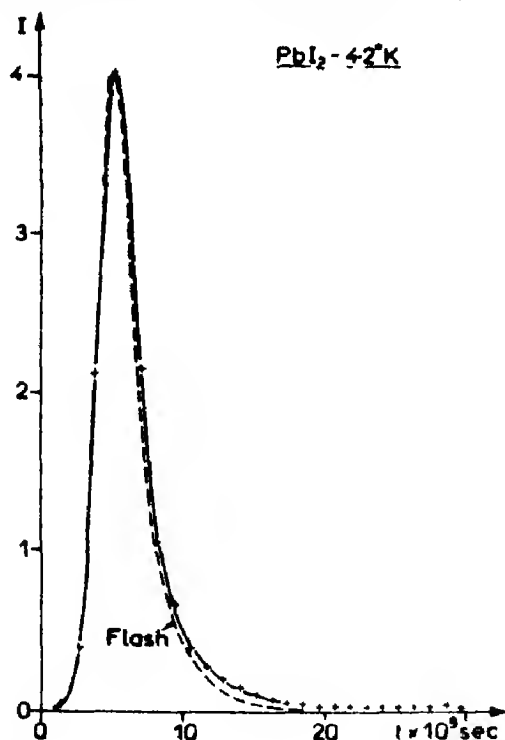


Fig. 6. Rise and decay of the ν_c line excited by a flash (dashed in figure).

Such a short lifetime may be understood by assuming that a recombination mechanism different from spontaneous emission contributes to the annihilation of the exciton. In the case of an exciton bound to a neutral donor or acceptor center (this may be the case of the ν_c line) a transfer of exciton energy by an Auger effect to the electron of the center may be considered[26, 45]. It is useful to emphasize here that the time necessary for electron and hole to thermalise before forming an exciton is very short (10^{-11} to 10^{-13} sec) compared to the resolving time of the electronic apparatus. Therefore it does not contribute appreciably to the measured lifetime.

(e) The emission band

We limited our study of the band having a maximum at $19,600 \text{ cm}^{-1}$ to spectral position variation with temperature and to lifetime measurements. Figure 7 shows the variation

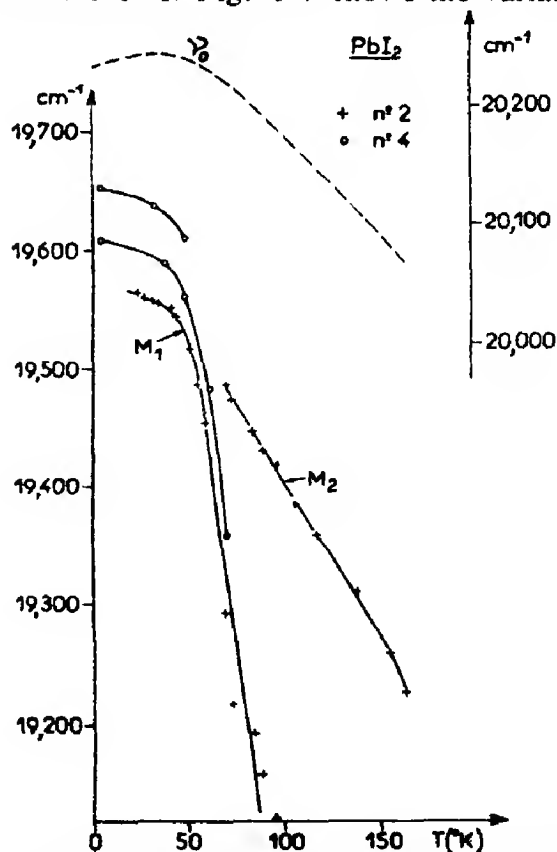


Fig. 7. Temperature dependence of the spectral position of several emission peaks of the band.

in position of its different components as a function of temperature for two different samples. The behaviour of the two samples is similar, but the relative intensity of the components is different. The band structure, rather complex at 4.2°K, is clearly simplified at about 20°K, when only one intense peak remains; it shifts with a thermal coefficient of $0.6 \cdot 10^{-4}$ eV/°K, towards the lower energies; at 40°K it splits into two components, M_1 and M_2 , which present a great difference in their thermal shift. M_1 is characterized by a very high thermal coefficient ($17 \cdot 10^{-4}$ eV/°K) and M_2 disappears at about 170°K and its thermal coefficient ($3.5 \cdot 10^{-4}$ eV/°K) is close to that of the ν_0 line.

A study of the lifetime of the M band shows, at 4.2°K two components respectively of $3.5 \cdot 10^{-9}$ sec (Fig. 8), and $20 \cdot 10^{-9}$; this fact is certainly related to the band splitting.

The great difference in the behaviour of the band and the lines is clear; this, on one hand gives value to the hypothesis of the difference

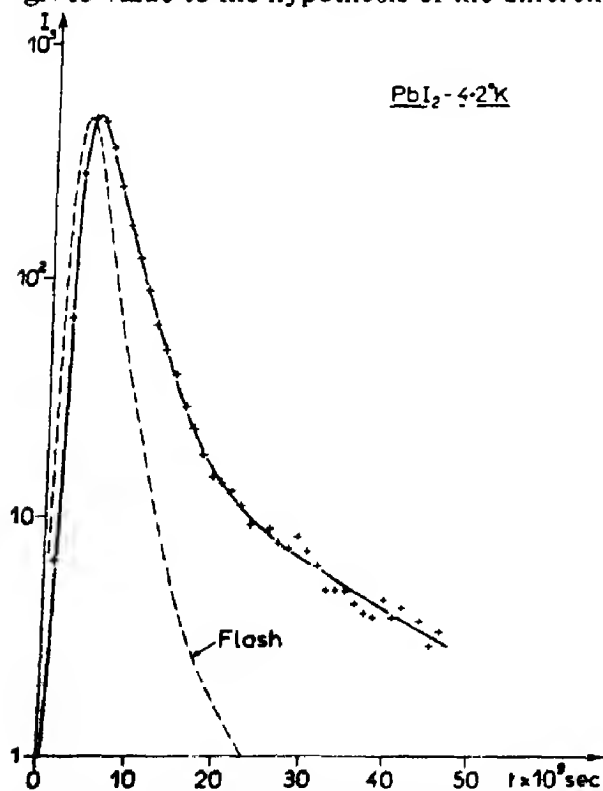


Fig. 8. Rise and decay of the luminescence of the band excited by a flash.

of their origin, on the other hand raises the interesting problem of the identification of this band and the understanding of its properties.

4. CONCLUSION

The experimental results and the above exposed arguments lead to identification of many of the observed emission lines. The ν'_0 and ν'' lines are two parts of the same self-absorbed ν_0 line arising from the direct recombination of an exciton; this line is shifted about 15 cm^{-1} from the absorption line position. The excitonic state responsible for the emission of ν_0 may originate the lines ν_0 -LO, ν_0 -2LO, ν_0 -3LO respectively, if annihilation occurs with a simultaneous emission of 1, 2, or 3LO phonons. The ν_c line arises from a bound exciton and the ν_c -LO line from the annihilation of this with emission of a LO phonon. Experimental data are insufficient for the identification of the ν_x and ν_y lines.

Emission spectrum of PbI_2 is thus similar to that of CuCl [24], HgI_2 [46] and CdS [47]. As in CdS , at 4.2°K, the transitions with phonon emission are stronger than direct excitonic recombination. This fact may be caused by the necessity of conserving the momentum of the exciton when it is radiatively annihilated, and this can occur with the emission of at least one LO phonon[48]. On the contrary momentum conservation is not applicable to a bound exciton because it is fixed to the lattice: we find, in fact, a high value for the ratio ν_c/ν_c -LO. We note that it follows from these facts, in the analogy of CdS , that in PbI_2 too, the exciton is free to move in the lattice.

We think that this very close analogy between CdS and PbI_2 is very interesting, owing to the great difference in the binding and in the structure; as recently shown[49], the excitons in PbI_2 are confined to the single layers I-Pb-I ; it is therefore interesting that these bidimensional excitons behave in the recombination processes in quite similar way to those of ordinary excitons. However, the

large width of the lines ($2.5 \cdot 10^{-3}$ eV for ν_c , $6 \cdot 10^{-3}$ eV for ν_0) in comparison to the II-VI semiconductors, must be noted. This fact may be due to the lower perfection of the lattice of PbI_2 which generally contains several polytypes; there is in fact some dispersion in the values of the axis ratio c/a [42]. In addition a partial inner cleavage can create some strain and stress with a consequent gap variation [6].

Acknowledgements—The authors would like to thank Professor S. Nikitine for helpful and stimulating discussions. They thank Dr Carabatos for communication of unpublished results, concerning the Raman spectrum of PbI_2 .

REFERENCES

1. NIKITINE S., *Helv. Phys. Acta* **28**, 308 (1955); *J. Phys. Radium, Paris* **17**, 817 (1956).
2. NIKITINE S. and PERNY G., *C.r. hebdom. Séanc. Acad. Sci., Paris* **240**, 64 (1955); *J. Phys. Radium, Paris* **16**, 136 (1955); *ibid.* **17**, 1017 (1956).
3. PERNY G., *Annls Phys.* **5**, 1683 (1960).
4. NIKITINE S., BURCKEL J., BIELLMANN J. and REISS R., *C.r. hebdom. Séanc. Acad. Sci., Paris* **251**, 935 (1960).
5. NIKITINE S., BURCKEL J., BIELLMANN J. and RINGEISSEN J., *J. Phys. Chem. Solids* **25**, 951 (1964).
6. NIKITINE S. and BIELLMANN J., *J. Phys. Suppl.* **27**, 95 (1966).
7. IMAI I., *J. Phys. Chem. Solids* **22**, 81 (1961).
8. GROSS E. F. and KAPLIANSKY A. A., *J. tech. Phys.* **25**, 1061 (1955).
9. TUBBS M. R. and FORTY A. J., *J. Phys. Chem. Solids* **26**, 711 (1965).
10. GORBAN I. S. and KOSAREV V. M., *Ukr. fiz. Zh.* **2**, 658 (1966).
11. ELLIOTT R., *Phys. Rev.* **108**, 1384 (1957).
12. NIKITINE S., *Prog. Semiconductors* **6**, 239 (1962).
13. TUBBS M. R., *Phys. Lett.* **22**, 13 (1966).
14. RALPH R. I., *Solid State Commun.* **3**, 303 (1965).
15. TUBBS M. R., *J. Phys. Chem. Solids* **27**, 1667 (1966).
16. DUGAN A. E. and HENISCH H. K., *J. Phys. Chem. Solids* **28**, 971 (1967).
17. PFEFFER G., LAMI H., LAUSTRIAT G. and COCHE A., *Congrès Electronique Nucléaire*, Publication O.C.D.E., p. 63, Paris (1965).
18. MORTON G. A., *Appl. Optics* **7**, 1 (1968).
19. BAY Z., *Phys. Rev.* **77**, 419 (1950).
20. WEAVER R. S. and BELL R. E., *Nucl. Instrum. Meth.* **9**, 149 (1960).
21. MON J. P., *C.r. hebdom. Séanc. Acad. Sci., Paris* **262B**, 493 (1966).
22. DUGAN A. E. and HENISCH H. K., *Phys. Rev.* **171**, 1047 (1968).
23. BRAHMS S., *C.r. hebdom. Séanc. Acad. Sci., Paris* **261**, 5052 (1965).
24. RAGA F., KLEIM R., MYSYROWICZ A., GRUN J. B. and NIKITINE S., *J. Phys. Suppl.* **28**, C3-116 (1967).
25. TRLIFAJ M., *Czech. J. Phys.* **B14**, 227 (1964).
26. KHÁSZ., *Czech J. Phys.* **B15**, 568 (1965).
27. BLEIL E. E. and BROSER I., *J. Phys. Chem. Solids* **26**, 751 (1965).
28. MAHAN G. D., *J. Phys. Chem. Solids* **26**, 751 (1965).
29. GRUN J. B., SIESKIND M. and NIKITINE S., *J. Phys. Chem. Solids* **19**, 189 (1961).
30. VARSHNI Y. P., *Physica* **34**, 149 (1967).
31. GIBSON A. F., *Proc. phys. Soc.* **B65**, 378 (1952).
32. TUBBS M. R., *Proc. Soc.* **A280**, 566 (1964).
33. IZVOZCHIKOV V. A., *Soviet Phys. solid St.* **8**, 2505 (1967).
34. DUGAN A. E. and HENISCH H. K., *J. Phys. Chem. Solids* **28**, 1885 (1967).
35. MOSS T. S., In *Optical properties of semiconductors*, p. 43. Butterworths, London (1959).
36. RADKOWSKI A., *Phys. Rev.* **73**, 749 (1948).
37. MUTO T. and OYAMA S., *Prog. theor. Phys.* **5**, 833 (1950).
38. FAN H., *Phys. Rev.* **82**, 900 (1951).
39. ZAHNER J. C. and DRICKAMER H. G., *J. Phys. Chem. Solids* **11**, 92 (1959).
40. EUCKEN A. and BUCHNER E., *Z. phys. Chem.* **27B**, 321 (1934).
41. KOVALEVSKAIA Y. A. and STRELKOV P. G., *Soviet Phys. solid St.* **8**, 1044 (1966).
42. PASCAL P., In *Nouveau Traité de Chimie Minérale*, Tome VIII, p. 549. Masson et Cie, Paris (1963).
43. NIKITINE S., MUNSCHY G., RINGEISSEN J. and KIRCH M., *J. Phys. Suppl.* **28**, C3-120 (1967).
44. NIKITINE S., KLEIM R., PFEFFER G. and MEYER B., *C.r. hebdom. Séanc. Acad. Sci., Paris* **261**, 682 (1965).
45. NELSON D. F., CUTHBERT J. D., DEAN P. J. and THOMAS D. G., *Phys. Rev. Lett.* **17**, 1262 (1966).
46. KLEIM R., RAGA F. and NIKITINE S., *Int'l Conf. on Luminescence*, Suppl. p. 179. Budapest (1966).
47. REYNOLDS D. C., LITTON C. W. and COLLINS T. C., *Phys. Status Solidi* **12**, 3 (1965).
48. GROSS E. F., PERMOGOROV S. and RAZBIRIN B., *J. Phys. Chem. Solids* **27**, 1647 (1966).
49. GREENAWAY D. L. and HARBEKE G., *J. phys. Soc. Japan, Suppl.* **21**, 151 (1966).

PHOTOLUMINESCENCE OF Ge-DOPED GaAs GROWN BY VAPOR-PHASE EPITAXY

W. SCHAIRER*

Physikalisches Institut, Universität Frankfurt/M.

and

W. GRAMAN

AEG-Telefunken Halbleiter Entwicklung, Heilbronn, Germany

(Received 4 March 1969)

Abstract—Ge-doped GaAs grown by vapor phase epitaxy was investigated by photoluminescence measurements between 1.8° and 20.3°K. Two bands caused by Ge-doping are found at about 1.476 and 1.480 eV. The bands are interpreted in terms of donor-acceptor recombination and free electron-acceptor transition. The binding energy of the acceptor is 42 ± 1 meV.

1. INTRODUCTION

IT IS WELL known that Ge is an amphoteric impurity in GaAs[1]. The ratio of Ge-donors on Ga-sites against Ge-acceptors on As-sites is strongly dependent on the conditions during crystal growth[2, 3]. Several values have been quoted for the binding energy of the Ge-acceptor: 30 and 43 meV when the specimen was grown from Ga-solution[3, 4] and 34 meV in GaAs grown by liquid phase epitaxy[5]. Williams[6] arrives at a binding energy of 39 meV. He points out, however, that this level should not be attributed to a chemical, but to a native defect introduced by Ge-doping. He finds an identical luminescence band in 'undoped' material, if the donor concentration is greater than 10^{16} cm^{-3} .

We have investigated the photoluminescence of Ge-doped GaAs obtained by vapor phase epitaxy (VPE). The technique of VPE presently provides the best crystals with lowest impurity content; such samples are therefore particularly suited for optical analysis[7, 8].

2. EXPERIMENTAL TECHNIQUE AND RESULTS

Crystals were immersed directly in liquid He or H₂. The luminescence was excited with a He-Ne laser of 30 mW power, excitation intensity 1.50 W/mm^2 . The spectrometer used was a Spex 0.75 m Czerny-Turner grating monochromator. The crystals investigated are described in Table 1. They were all grown by the Effer method[9] on (100)

Table 1

Sample	Doping	$N_d - N_a \text{ (cm}^{-3}\text{)}$ (295°K)	Thickness of layer (μ)	Substrate orientation
E 143		$2.5 \cdot 10^{13}$	11	(100)
E 124	Ge	$2 \cdot 10^{14}$	8	(100)
E 129	Ge	$7 \cdot 10^{14}$	14	(100)
E 139 b	Ge	$1 \cdot 10^{16}$	15	(100)

*Work done in partial fulfillment of the requirements for a "Dr. rer. nat."-degree.

oriented substrates, doped with $2 \cdot 10^{18} \text{ cm}^{-3}$ Te. The $N_d - N_a$ values listed were obtained by

the Schottky-Barrier capacitance method at room temperature. Doping was achieved by adding Ge into the Ga-source.

Figure 1 shows the luminescence spectrum of crystal E 129 at 1.8°K. The spectra of the other crystals are similar, except for sample E 143, where (a) in the region of 1.51 eV more structure is seen and (b) the band at 1.48 eV is very weak. The structure of the near-gap

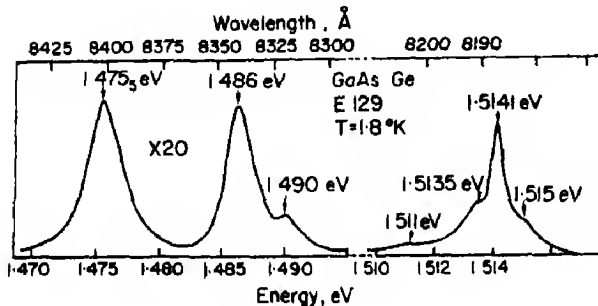


Fig. 1. Photoluminescence spectrum of Ge-doped GaAs (E 129, $N_d - N_a = 7 \cdot 10^{14} \text{ cm}^{-3}$) at 1.8°K.

band around 1.514 eV is typical for relatively pure GaAs[7, 8], and we shall not discuss it here. The two bands near 1.49 eV are attributed to Si, which was probably introduced inadvertently from the quartz tube; these bands have been reported and discussed in detail by Bogardus and Bebb[8].

Germanium introduces the band at 1.475 eV. This band, as well as the Si-bands, have two phonon replica at a distance of 36 and 72 meV, corresponding to the emission of one and two LO phonons.

Figure 2 shows details of the spectrum for crystal E 139 b in the region of 1.48 eV, taken at four different temperatures. We select this crystal because of its comparatively high luminescent intensity of the bands considered. It is clearly seen, that there are actually two bands 'A' and 'B', the one at high energies dominating at the higher temperatures. The excitation intensity in Fig. 2 is low.

The band shape and peak position of band B depend upon excitation intensity. Figure 3 shows the broadening and the shift to higher

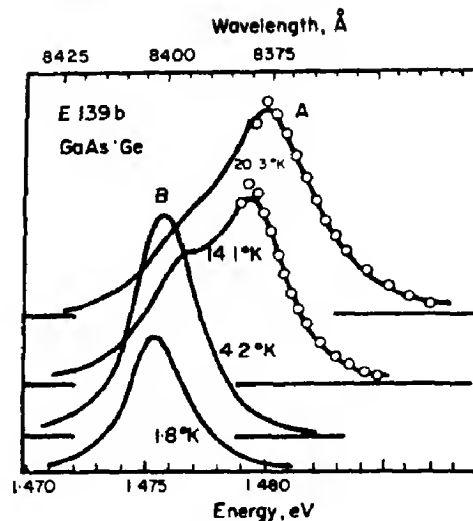


Fig. 2. Photoluminescence spectrum of Ge-doped GaAs (E 139 b, $N_d - N_a = 1 \cdot 10^{16} \text{ cm}^{-3}$) in the region of 1.48 eV at four different temperatures. The circles on band A are theoretical points after Eagles' theory for band-acceptor recombination. Band B is ascribed to donor-acceptor recombination.

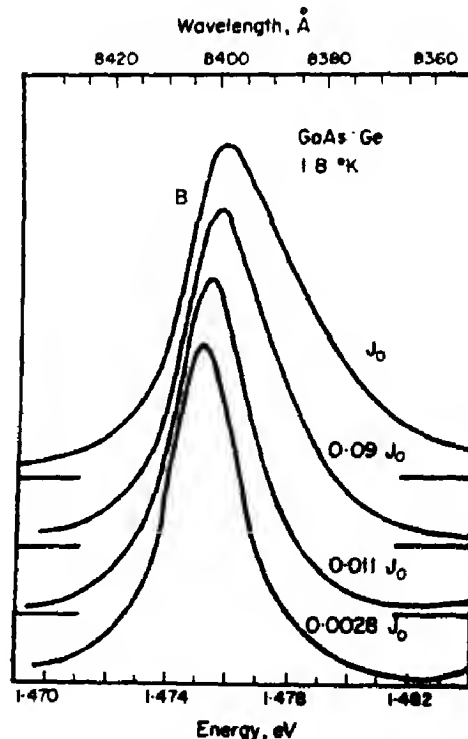


Fig. 3. Photoluminescence spectrum of Ge-doped GaAs (E 139 b, $N_d - N_a = 1 \cdot 10^{16} \text{ cm}^{-3}$) at 1.8°K and four different excitation intensities.

energies of band *B* (at 1.8°K), when the excitation intensity increases.

The energies of the luminescence peaks *A* and *B* as a function of the excitation intensity are depicted in Fig. 4. One can see, that the lower energy band *B* shifts as the excitation intensity increases, whereas the position of band *A* remains essentially unchanged.

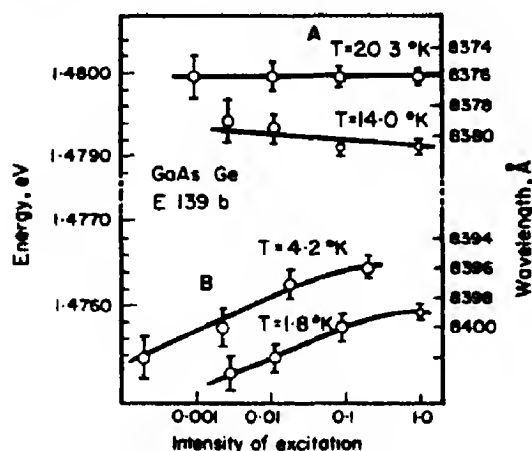


Fig. 4. The energetic position of bands *A* and *B* as a function of the excitation intensity at different temperatures.

3. DISCUSSION

We suggest to interpret the high energy band *A* as a free electron-acceptor recombination and the low energy band *B* as a donor-acceptor recombination. The following evidence supports this assignment.

The band shape of the high energy peak *A* was compared with the free electron-acceptor recombination model by Eagles[10]. He has derived the following theoretical band shape:

$$g(y) = y^{1/2} \exp(-y) \quad (1)$$

where $y = (\hbar\omega - E_g + E_{acc.})/kT$. The circles in Fig. 2 are theoretical values derived from the equation (1). The agreement with experimental data is good, if the excitation intensity is low (excitation intensity in Fig. 2 is 1/100 of the maximum excitation). At 14.1°K, the agreement around the maximum of the curve is improved if the excitation intensity is still lower. We found that temperature changes as small as 0.5°K lead to a detectable difference

between theoretical and experimental curves. At high excitation levels, the experimental band is broader than predicted by theory. We suggest that this discrepancy is probably caused by a rise of the quasi Fermi-level and not by an increase of the lattice temperature. An estimate of the energy dissipation on the basis of thermal conductivity and photon flux incident on the sample supports this suggestion.

The energy of the peak *A* is independent of the excitation intensity as shown in Fig. 4. This gives further support to the band-acceptor assignment. In this case, the peak position is given by

$$\hbar\omega_{max.} = E_g - E_{acc.} + (1/2)kT. \quad (2)$$

From the data of sample E 139 b we obtain

$$E_g - E_{acc.} = (1.4789 \pm 0.0003) \text{ eV}$$

at $T \leq 20.3^\circ\text{K}$. The data of all samples together yield an average energy of

$$E_g - E_{acc.} = (1.478_5 \pm 0.001) \text{ eV at } T \leq 20.3^\circ\text{K}.$$

With $E_g = 1.5202 \text{ eV}$ [7] we obtain the following value for the binding energy of the acceptor

$$E_{acc.} = (42 \pm 1) \text{ meV}.$$

The low energy band *B* broadens on the high energy side and shifts to higher energies if the excitation intensity increases, as is shown in Fig. 3. A similar broadening and shift to higher energies is reported for the broad donor-acceptor recombination band (unresolved pair recombination lines) in GaP[11, 12]. In our samples the shift is approximately 0.35 meV when the excitation intensity changes by a factor of 10. Somewhat larger shifts have been reported for the donor-acceptor recombination band at 1.492 eV in GaAs[13] and in GaP[12]. The energy shift in our samples is small, presumably because the Coulomb term $e^2/\epsilon r$ is small because of large average donor-acceptor separation due to low doping levels.

The energetic separation, ΔE , of the peaks of bands *A* and *B* is 3.7 meV at 1.8°K and at weak excitation level. ΔE , in a donor-acceptor recombination model, is given by

$$\Delta E = E_d - e^2/\epsilon\bar{r} + (1/2)kT. \quad (3)$$

With $E_d = 6$ meV [7], we obtain $\bar{r} = 500$ Å for the average separation of donors and acceptors. A rough estimate of the doping level is obtained, if one identifies this \bar{r} with the average donor separation. Our estimate for the average donor separation yields $N_d = 8 \cdot 10^{15} \text{ cm}^{-3}$ in fairly good agreement with the measured uncompensated impurity concentration of $N_d - N_a = 1 \cdot 10^{16} \text{ cm}^{-3}$ (Table 1).

We have made three further observations supporting our assignments of bands *A* and *B*:

- (1) the different shift of the two bands *A* and *B* with temperature.
- (2) the shift of band *B* with doping level and
- (3) the change of intensity with temperature.

These features, however, could not be studied in quantitative detail because all effects characteristic for donor-acceptor recombination are relatively small in high purity material, and because there is still a considerable overlap of the bands *A* and *B* at all temperatures, in spite of the low doping level.

(1) The energy shift of peak *B* with temperature is demonstrated in Fig. 4. Band *B* shifts to higher energy when the temperature is increased, as expected for a donor-acceptor recombination band.

The energy shift of peak *A* with temperature should be equal to $1/2 kT$ (equation (2)). Experimentally we observe a shift of about kT . However, this is difficult to determine, because the position of peak *A* at 14.1°K may be somewhat obscured by peak *B*.

(2) The energy shift of peak *B* with doping level at constant excitation intensity is rather small. A shift of about 1 Å towards higher energies is observed, when the doping level

is increased from $N_d - N_a = 2 \cdot 10^{14} \text{ cm}^{-3}$ to $1 \cdot 10^{16} \text{ cm}^{-3}$. This shift is, however, of the order of our experimental accuracy.

(3) The change of intensity with temperature is seen in Fig. 2. The intensity of band *A* increases between 14°K and 20°K while band *B* decreases. In this temperature range the equilibrium carrier concentration n changes from $n = 6 \cdot 10^{-3}(N_d - N_a)$ at 14°K to $n = 3 \cdot 10^{-2}(N_d - N_a)$ at 20°K if a donor binding energy of $E_d = 6$ meV is assumed. The number of ionized donors increases by a factor 5, which correlates roughly with the observed intensity changes.

A third band between bands *A* and *B* was observed in sample E 143 at 1.8°K. This sample is not intentionally doped with Ge, however, it has been grown subsequent to a run with Ge-doping. Consequently it may contain spurious Ge-impurities. These three bands resemble those found by Bogardus and Bebb [8] in the region of 1.49 eV, which were attributed to the Si-acceptor in GaAs. They suggest to interpret the low energy band as donor-acceptor recombination and the high energy band as band-acceptor transition, while the band between both is attributed to an exciton bound to the ionized Si-acceptor.

In our Ge-doped samples the separation between *A* and *B* is only about half as large as the one reported for Si-doping. Therefore the overlap of the three bands is rather large. In addition, the intensity of the bands is low. For these reasons we were not able to investigate the three bands in detail and to decide if they are analogous to the structure induced by Si.

Another explanation of our weak intermediate band would involve excited donor states as recently suggested by Shah *et al.* [14].

Williams [6] has reported a band at 1.482 eV in Ge-doped material ($N_d - N_a \geq 3 \cdot 10^{15} \text{ cm}^{-3}$) and in 'undoped' material ($N_d - N_a \geq 10^{16} \text{ cm}^{-3}$). We measured in addition to the samples quoted in Table 1 the luminescence of two Te-doped samples with $N_d - N_a = 2 \cdot 10^{15} \text{ cm}^{-3}$ and $N_d - N_a = 2 \cdot 10^{16} \text{ cm}^{-3}$. The lower

doped sample exhibited two bands in the region of 1.48 eV. These bands, however, cannot be identified with the bands *A* and *B* because of their rather large widths and temperature independent positions and intensity ratios. The higher doped sample showed two bands similar to bands *A* and *B*. In addition the spectra contain the emission bands found for the lightly doped sample as a background, which leads to rather uncertain values for peak positions. Further investigations are necessary to decide, whether impurities different from Ge (e.g. Te) may also induce defects responsible for emission bands similar to bands *A* and *B* described in this paper.

Acknowledgements — We wish to thank Professor Queisser and Professor Pilkuhn, as well as Dr. Goldbach for helpful discussions. The crystal growing effort at Heilbronn was supported by "Forschungsauftrag des Bundesministeriums der Verteidigung" and the optical investigations at Frankfurt were supported by the Fraunhofer Gesellschaft; the support is gratefully acknowledged.

REFERENCES

1. WHELAN J. M., STRUTHERS J. D. and DITZENBERGER J. A., *Metallurgical Soc. Conf.*, Vol. 5, p. 146. Interscience, New York (1960); McCALDIN J. O. and HARADA R., *J. appl. Phys.* **31**, 2065 (1960); VIELAND L. J. and SEIDEL T., *J. appl. Phys.* **33**, 2414 (1962).
2. SOLOMON R., NEWMAN R. and KYLE N. R., *J. electrochem. Soc.* **108**, 716 (1962).
3. KRESSEL H., HAWRYLO F. Z. and LEFUR P., *J. appl. Phys.* **39**, 4059 (1968).
4. CONSTANTINESCU Cr. and PETRESCU-PRAHOVA J., *J. Phys. Chem. Solids* **28**, 2397 (1967).
5. ROSZTOCZY F. E., ERMANIS F., HAYASHI J. and SCHWARTZ B., *Bull. Am. Phys. Soc., Ser. VI*, **13**, 375 (1968).
6. WILLIAMS E. W., *Solid State Commun.* **4**, 585 (1966).
7. GILLES M. A., BAILEY P. T. and HILL D. E., *Phys. Rev.* **174**, 898 (1968).
8. BOGARDUS E. H. and BEBB H. B., *Phys. Rev.* **176**, 993 (1968).
9. KNIGHT J. R., EFFER D. and EVANS P. R., *Solid-St. Electron.* **8**, 178 (1965).
10. EAGLES D. M., *J. Phys. Chem. Solids* **16**, 76 (1960).
11. THOMAS D. G., HOPFIELD J. J. and AUGUSTYNIAK W. M., *Phys. Rev.* **140A**, 202 (1965).
12. THOMAS D. G., GERSHENZON M. and TRUMBORE, *Phys. Rev.* **133A**, 269 (1964).
13. LEITE R. C. C. and DIGIOVANNI A. E., *Phys. Rev.* **153**, 841 (1967); YEE J. H. and CONDAS G. A., *J. appl. Phys.* **39**, 351 (1968); DINGLE R., *Appl. Phys. Lett.* **14**, 183 (1969).
14. SHAH J., LEITE R. C. C. and GORDON J. P., *Phys. Rev.* **176**, 938 (1968).

SPECTRA OF SYNTHETIC ZEOLITES CONTAINING TRANSITION METAL IONS—III. A SIMPLE MODEL CALCULATION OF THE SYSTEM ADSORBED MOLECULE—NiA ZEOLITE

R. POLÁK and K. KLIER

Institute of Physical Chemistry, Czechoslovak Academy of Sciences, Prague, Czechoslovakia, and
Center for Surface and Coatings Research, Lehigh University, Bethlehem, Pa. 18015, U.S.A.

(Received 28 February 1969)

Abstract—Adsorption on NiA zeolitic sites where the Ni^{2+} ions are surrounded by the neighboring ligands of the D_{3h} symmetry is treated as a transition to C_{3v} symmetry whereby the adsorbed molecule represents a perturbation whose ligand field strength is expressed as a function of variable parameters. The main feature of the corresponding spectral changes, namely a bathochromic shift of the main band in the visible region, leading to a change of color from yellow to pink during adsorption, and a band separation in the low energy region, are qualitatively explained by this model.

INTRODUCTION

IN THE PRECEDING work [1, 2] the electronic spectra of the dehydrated NiA molecular sieve were interpreted on a model of a Ni^{2+} cation surrounded by oxygen ligands having D_{3h} (D_{6h}) symmetry. Additionally, it was observed that the NiA spectrum is changed on adsorption of gases such as water, nitrous oxide, cyclopropane, ethylene, propylene, and acetylene [2]. Some main features of this change are common to all adsorbing molecules, namely the bathochromic shift of the $22,760\text{ cm}^{-1}$ NiA band and the appearance of new bands in the region between 6000 and $10,000\text{ cm}^{-1}$. Since all experimental evidence shows that the complexes formed contain one adsorbate molecule linked to one Ni^{2+} ion, it was suggested that a simplified treatment with the adsorbed molecule as a perturbation on the axis perpendicular to the plane of oxygen ligands, would explain the main features of the new spectra*.

ANALYSIS AND CALCULATIONS ON THE MODEL

The model of 'unoccupied site' is that of

*The resulting spectra resemble somewhat those of tetrahedrally coordinated Ni^{2+} . However, since the adsorbed molecules represent ligands of varying strengths, a slightly more general model is one in which one additional parameter is reserved for the adsorbate ligand field strength.

the Ni^{2+} ion in the center of an equilateral triangle of oxygen ions of the aluminosilicate skeleton and is best described by the values of the parameters $C/B = 4.5$, $K = G_2/G_4 = 7$, and $G_4/B = 3.1$, the meaning of these symbols being the same as in [1]. The unperturbed system of electrons in the following treatment is therefore described by functions obtained by diagonalization of the Hamiltonian of electrostatic interaction of the d^8 system with ligands of D_{3h} symmetry, using the above choice of parameters. The model of 'occupied site' is that of a negative perturbation placed on the z-axis perpendicular to the original plane of oxygen ligands. The symmetry is now C_{3v} , the relation between irreducible representations of these point groups and the change of the classification of the states being given by the following scheme.

$$\begin{aligned} \Gamma(D_{3h}) &\longrightarrow \Gamma'(C_{3v}) \\ \left. \begin{matrix} A_1' \\ A_2'' \end{matrix} \right\} &\longrightarrow A_1 \\ \left. \begin{matrix} A_2' \\ A_1'' \end{matrix} \right\} &\longrightarrow A_2 \\ \left. \begin{matrix} E' \\ E'' \end{matrix} \right\} &\longrightarrow E. \end{aligned} \quad (1)$$

Let us denote \hat{V}' the one-electron operator corresponding to the potential energy due to the additional perturbation by the adsorbed molecule. Then, using the notation of [1], the term energies of the perturbed system $E(\Gamma'_i)$ are given by

$$E(\Gamma'_i) = E(\Gamma_i) + \sum_{j=0}^2 a_j(\Gamma'_i) (j|\hat{V}'|j) \quad (2)$$

considering the first order perturbation contribution only. $E(\Gamma_i)$ is the unperturbed term energy of the d^8 system in D_{3h} symmetry, $a_j(\Gamma'_i)$ are the numbers following from Slater's rules applied to the calculation of the matrix elements, and

$$\begin{aligned} (0|\hat{V}'|0) &= \frac{8}{21} (K' + 1) G'_4/B \\ (1|\hat{V}'|1) &= \frac{8}{21} (3K' - 4) G'_4/B \\ (2|\hat{V}'|2) &= \frac{8}{21} (-6K' + 1) G'_4/B \end{aligned} \quad (3)$$

are the non-vanishing matrix elements of the one-electron operator of electrostatic interaction with the charge representing an adsorbed molecule. The symbols in (3) are taken from [3] and the matrix elements are calculated according to [4]. Since variations of $K' = G'_2/G'_4$ from 2 to 10 do not alter the qualitative character of the required information, relation (2) is graphically represented in Fig. 1 for one selected value of $K' = 4$ only.

Figure 2 represents the term scheme of the triplet states in which the Hamiltonian was exactly diagonalized within the d^8 configuration using the same set of parameters as before. It appears that as long as the 3A_2 term remains the ground state, the perturbation treatment in Fig. 1 describes the term scheme satisfactorily and the exact diagonalization is not necessary.

DISCUSSION

The unperturbed wave functions in the present treatment are very close to the strong field functions, as can be seen e.g. from Fig. 3 in [1] when using $G_4/B = 3.1$. The only terms significantly affected by the configuration

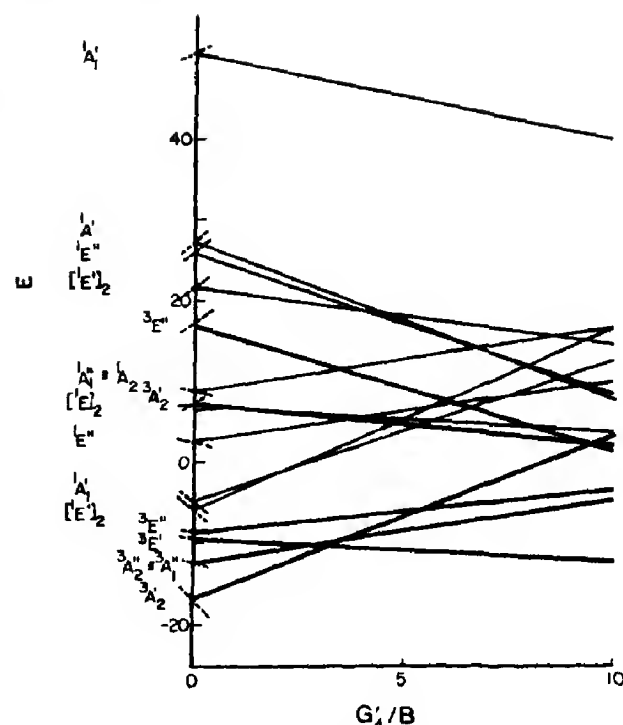


Fig. 1. Term scheme of the d^8 electron system in crystal field of C_{3v} symmetry as a function of G'_4/B . The calculation involves first order perturbation energy contributions only. Energy is in B units, $C/B = 4.5$, $K = 7$, $G_4/B = 3.1$, $K' = 4$. The unperturbed states are indicated as a function of G_4/B by dashed lines.

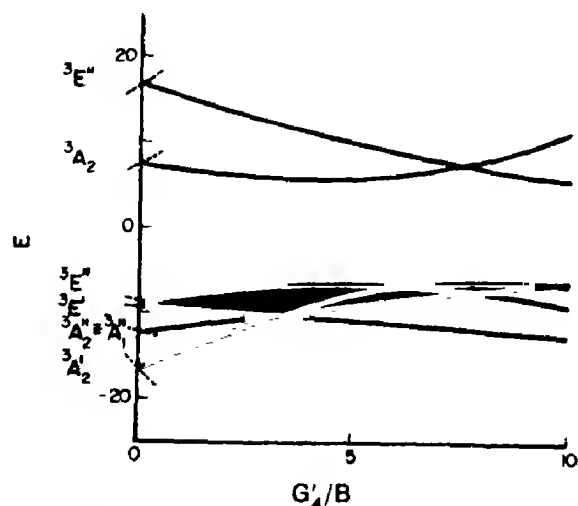
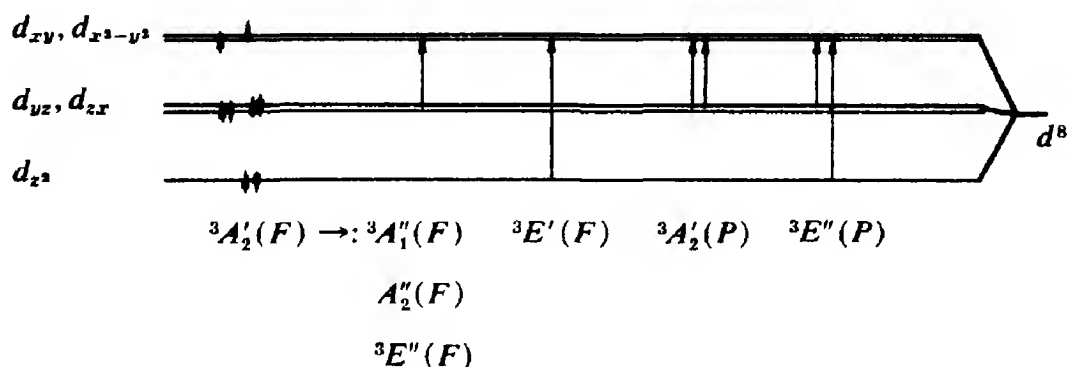


Fig. 2. Term scheme of triplet states of the d^8 electron system in a crystal field of C_{3v} symmetry as a function of G'_4/B . The calculation involves diagonalization of the complete Hamiltonian within the d^8 configuration. Values of parameters are the same as in Fig. 1. The unperturbed states are indicated as a function of G_4/B by dashed lines.

interaction are the ${}^3E''(F)$ and ${}^1A'_1(D)$, the deviations being unimportant for the overall interpretation of the spectra in [2]. In this case the spectra of the dehydrated molecular sieve NiA may be interpreted as one- and two-electron transitions among the real one-electron orbitals d_{xz} , d_{xy} , d_{yz} , d_{zx} and $d_{x^2-y^2}$, schematically represented for the triplet-triplet transitions in the following way:



and in an analogous way for the triplet-singlet transitions. Occupation numbers for the various terms were taken from Table 2 [1].

The effect of perturbation shown in Fig. 1 and Fig. 2 is easily understood as one facilitating the transitions of electrons from the d_{xz} , d_{zx} and d_{yz} orbitals into the in-plane orbitals d_{xy} and $d_{x^2-y^2}$. This includes the bathochromic shift of the ${}^3A'_2(F) \rightarrow {}^3A'_2(P)$ band in the visible region leading to an observable change of color from yellow to pink during adsorption of all molecules [2]. Moreover, transitions from the d_{xz} orbital are more affected than those from the d_{zx} and d_{yz} orbitals because of stronger electrostatic repulsion between the d_{xz} electrons and those of the adsorbing molecule, which leads to a larger separation of the originally close terms ${}^3E'(F)$ and ${}^3E''(F)$. We believe that the 'new bands' observed on adsorption in the region between

6000 and 10,000 cm^{-1} (Fig. 7 of [2]) are a manifestation of this effect, although complications may arise due to the presence of near-i.r. bands of the adsorbed molecules themselves [5].

It should be noted that the out-of-plane orbitals of the Ni^{2+} ions are fully occupied in the ground state and interact with the adsorbed molecule as a closed shell system.

Therefore, the present model is quite adequate to explain the spectral band shifts as due merely to electrostatic repulsion. More specific interactions may be expected with ions whose out-of-plane orbitals are partially filled, such as divalent cobalt and iron.

REFERENCES

1. POLÁK R. and ČERNÝ V., *J. Phys. Chem. Solids* **29**, 945 (1968).
2. KLIER K. and RÁLEK M., *J. Phys. Chem. Solids* **9**, 951 (1968).
3. HARTMANN H. and KÖNIG E., *Z. phys. Chem.* **28**, 425 (1961).
4. GRIFFITH J. S., *Theory of Transition Metal Ions*, p. 202. Cambridge University Press, Cambridge (1961).
5. Ethylene exhibits near i.r. bands at 4514, 4728, 11,470 and 11,800 cm^{-1} ; cyclopropane, at 4500, 7000 and 10,000 cm^{-1} , according to LANDOLT-BÖRNSTEIN, *Zahlenwerte und Funktionen*, Teil 2, pp. 345, 385. Berlin.

MAGNETIC SUSCEPTIBILITY AND EXCHANGE COUPLING IN THE MINERAL ARDENNITE*

A. N. THORPE, F. E. SENFTLE and G. DONNAY

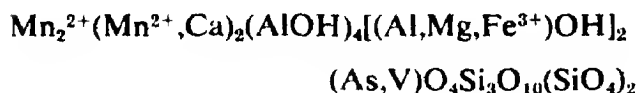
Howard University, U.S. Geological Survey, and Geophysical Laboratory,
Carnegie Institution of Washington, Washington, D.C. 20008, U.S.A.

(Received 27 February 1969)

Abstract—Ardennite, a rare silicate mineral, contains about 19 wt.% manganese. Some of the manganese atoms are in positions which are close enough to allow negative exchange and hence a reduction of the total magnetic susceptibility. It is shown that the susceptibility can be accounted for approximately by the treatment of Earnshaw and Lewis (1958) for $S = 5/2$ and a Hamiltonian $H = -2g\mu H_b - 2J S_1 \cdot S_2$.

INTRODUCTION

THE CRYSTAL structure of ardennite, a rare arsenic-vanadium silicate mineral having the formula



has recently been described[1]. Ardennite contains about 19 wt.% or about 9 at.% manganese pseudo-octahedrally coordinated with oxygen, and about 1 per cent ferric iron. The only other chemical elements present that have a magnetic moment are copper and chromium amounting to less than 0.5 wt.%. An investigation of the magnetic susceptibility of this mineral down to liquid helium temperature shows that the magnetic properties can be described if one allows for a local negative exchange coupling between manganese atoms at the centers of edge-sharing oxygen coordination polyhedra. The remaining manganese ions and all other ions with magnetic moments are considered to contribute a paramagnetic component to the total magnetic susceptibility. Ardennite is thus a mixed magnetic compound containing magnetic

ion pairs with negative exchange coupling and noninteracting magnetic ions contributing to the paramagnetism of the mineral.

Earnshaw and Lewis[2, 3] and others[4, 5] have considered the variation of magnetic susceptibility with temperature of polynuclear organic complexes containing iron or chromium. Many of these compounds contained small temperature-independent paramagnetic components of the Van Vleck type, as well as a temperature dependent magnetism. The magnetic properties of ardennite are due to significant contributions of magnetism caused by local exchange coupling as well as normal temperature dependent and temperature independent paramagnetism.

THEORETICAL DISCUSSION

(a) *The exchange coupling contribution*

Fe^{3+} , Cu^{2+} , and Cr^{3+} are separated widely in the structure, so that their magnetic contributions can only be assumed to be paramagnetic in character. Manganese, the principal magnetic atom in ardennite, occupies two 4-fold positions, 4(*f*), with point symmetry *m* in the space group Pnmm (D_{2h}^{13}) (Fig. 1). One of the positions, referred to as Mn_1 , is occupied by Mn atoms only; in the other position, Mn_2 , calcium atoms may substitute for manganese. Mn_1 has five nearest oxygen

*Publication authorized by the Director, U.S. Geological Survey.

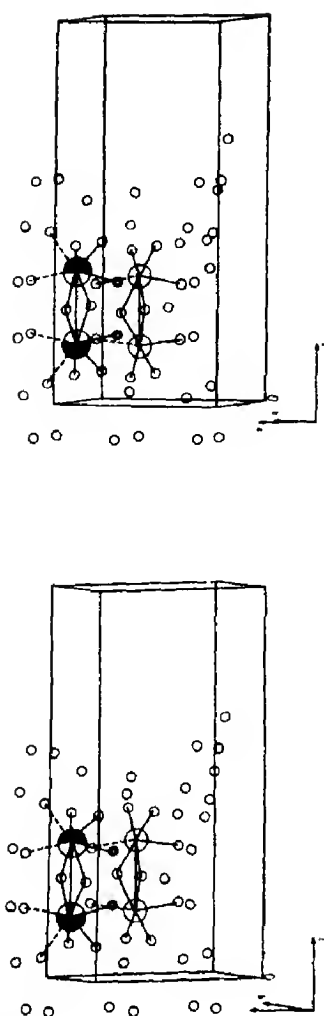


Fig. 1. Stereoview of part of the ardennite structure. Large clear circles: Mn_1 ; large partly filled circles: Mn_2 ; small circles: oxygen atoms; small double circles: hydroxyl ions. Dashed lines represent bonds considerably longer than the bonds represented by solid lines.

neighbors at an average distance of 2.20 Å and a sixth oxygen at 2.51 Å. The Mn_1 - Mn_1 distance across the shared oxygen edge is 3.33 Å. Exchange coupling can take place between the two manganese atoms through their shared oxygen atoms. Mn_2 has four nearest oxygen and one hydroxyl neighbor at an average distance of 2.24 Å, a sixth oxygen atom at 2.40 Å, and a seventh oxygen at 2.47 Å. The Mn_2 - Mn_2 distance across this shared edge is 3.50 Å. If both sites are occupied by manganese atoms, local exchange

coupling will take place as in the Mn_1 - Mn_1 case; if a calcium atom substitutes for one of the manganese atoms, Mn_2 - Mn_2 has to be replaced by Mn_2 - Ca_2 , and the remaining manganese atom will contribute a paramagnetic component only to the total magnetism of the crystal structure.

If we assume that the symmetry relation between the magnetic tensors of the coupled Mn atoms obeys the observed symmetry of the chemical structure, the spins must line up in antiparallel orientation along [010] according to the following symmetry reasoning: the atoms lie on mirrors perpendicular to [010] which requires their magnetic moments to line up parallel or antiparallel to [010]; they are related to each other by another mirror parallel to the [010] direction which results in an antiparallel relation between them[6]. Therefore in the ground state (0°K) the spins of the pair of ions (Mn,Mn) separated by the mirror plane parallel to the [010] direction are in opposite directions. No magnetic translation relation between unit cells can be expected. We may be dealing with short-range but not long-range magnetic ordering. We propose to represent the situation magnetically to a first approximation by assuming a Hamiltonian, H , as follows:

$$H = -2g\mu H_b - 2J S_1 \cdot S_2 \quad (1)$$

where the exchange integral, J , is negative, g is the spectroscopic splitting factor, H_b is the magnetic field in the [010] direction, and μ is the magnetic moment. This treatment is similar to the treatment used by others [2-5] in treating the magnetic properties of binuclear compounds. However, in the direction perpendicular to the y axis the Hamiltonian is different but, if J is found to be small, as it is in this case, the same theory can be used to fit the data approximately using a slightly different J .

In the case of ardennite $S = \frac{5}{2}$ for manganese. Earnshaw and Lewis give the following equation for the magnetic susceptibility,

$\bar{\chi}_I$, due to exchange coupling where $S = \frac{1}{2}$:

$$\bar{\chi}_I = \frac{3k}{T} \left[\frac{55 + 30\exp(10x) + 14\exp(18x) + 5\exp(24x) + \exp(28x)}{11 + 9\exp(10x) + 7\exp(18x) + 5\exp(24x) + 3\exp(28x)} + \exp(30x) \right] + N(\alpha)$$

$$= \frac{3k}{T} \cdot G + N(\alpha) \quad (2)$$

where $k = (g^2 N \beta^2)/3K$; $x = -J/KT = \theta/T$. In the above expression, g is the spectroscopic splitting factor, $N(\alpha)$ is the temperature-independent term, N is the number of paramagnetic atoms, β is the unit Bohr magneton, K is Boltzmann's constant, and T is the absolute temperature.

(b) The paramagnetic contribution

When Ca substitutes for Mn in the (Mn, Mn)₂ position, the spin of the remaining Mn contributes a temperature dependent paramagnetic component, χ_p , to the total susceptibility. Thus,

$$\chi_p = \frac{N\beta^2\mu^2}{3K} \cdot \frac{1}{T} = \frac{A}{T} \quad (3)$$

where the symbols have their usual meaning as given above.

The total magnetic susceptibility, $\bar{\chi}_T$, for the exchange coupling, the temperature dependent (paramagnetic) and temperature independent contributions can thus be written in the form

$$\bar{\chi}_T = [A + 3kG(\theta)] \frac{1}{T} + N(\alpha) \quad (4)$$

where $A = (N\beta^2\mu^2)/3K$ and k is defined above.

EXPERIMENTAL MEASUREMENTS

This investigation was made on single crystals from a hand specimen of ardennite from Salm-Chateau, Ardennes, Belgium. Their weight ranged from 0.7 to 12 mg. According to a chemical analysis on material from the same hand specimen [7], the manganese content is 19.62 wt.% or 8.65 at.%, and each formula unit contains 7.53 manganese

atoms, four of which always occur in the Mn₁ position. Hence there will be $4.00/7.53 \times 19.62$ or 10.42 per cent manganese in the Mn₁ position and 9.20 per cent in the Mn₂ position. The structure determination further shows that there are 4.02 Mn₂ atoms (i.e. Mn or Ca) per formula unit. Thus, the probability of a manganese atom occurring in one of the coordination polyhedra of this position is $(7.53 - 4.00)/4.02$ or 0.88, and hence the probability of two manganese atoms occurring together as a pair in adjacent coordination polyhedra is $0.88 \times 0.88 = 0.774$. Similarly, the probability of a single Mn atom occurring in a (Mn,Ca) site will be $0.88 \times 0.12 \times 2 = 0.211$ where 0.12 is the probability of a single Ca atom occupying the position. Adjusting the probabilities for the fact that there will be twice as many manganese in the (Mn,Mn)₂ sites as in the (Mn,Ca) sites, it can be shown that 8.10 per cent manganese is present in the (Mn,Mn)₂ sites and 1.10 per cent in the (Mn,Ca) sites (Table 1).

The magnetic susceptibility measurements (Figs. 2 and 3) from room temperature down to about 5°K were made in a magnetic field of 5000 Oe by the Faraday method using a quartz helical spring balance [8]. Above 16°K the temperature was determined with an Au-Co to Au-Ag thermocouple, and below this temperature with a calibrated carbon resistor. The errors of the measurements are all less than 2 per cent.

Crystals were oriented by X-ray diffraction procedures and magnetic susceptibility measurements were made with the magnetic field both parallel and perpendicular to the b axis. A small anisotropy occurs as shown by comparison of Figs. 2 and 3.

Table 1. Calculated data for ardennite

Ionic species	Atomic pairs	Magnetic ion concentration (wt. %)	No. of ions per gram ($\times 10^{20}$)	A ($\times 10^{-4}$)
Mn^{2+}	(Mn,Mn) ₁	10.42	11.42	
Mn^{2+}	(Mn,Mn) ₂	8.10	8.89	
Mn^{2+}	(Mn,Ca)	1.10	1.206	8.77
Cu^{2+}	(Cu,Ca)	0.37	0.35	0.217
Fe^{3+}	(Fe,Ca)	1.05	1.13	8.21
Cr^{3+}	(Cr,Ca)	0.08	0.09	0.296

DISCUSSION

Assuming that the proposed model as described by equation (4) is approximately correct, we have attempted to evaluate the constants. The paramagnetic term, A , in equation (4) is simply the sum of similar terms for each of the paramagnetic ions. From the known chemical data one obtains $A = 17.50 \times 10^{-4}$ e.m.u.-°K per gram (Table 1). Using the calculated values of N in the table for the number of manganese ions in the (Mn,Mn)₁ and (Mn,Mn)₂ positions, and letting $g = 2$, one obtains 50.6×10^{-4} e.m.u.-°K per gram for $3k$. By programming equation (4) on the computer, a best fit was made to determine θ and $N(\alpha)$. To get a good fit, it was found that the calculated values of A and $3k$ had to be adjusted slightly. The final values used in equation (4) are $A = 16.90 \times 10^{-4}$ e.m.u.-°K per gram, $3k = 45.7 \times 10^{-4}$ e.m.u.-°K per gram, $\theta_{||} = 1.50$, $\theta_{\perp} = 1.55$, and $N(\alpha) = 8.7 \times 10^{-6}$ e.m.u./g. The calculated curves (solid lines, Figs. 2 and 3) give reasonable agreement with the experimental data.

The fact that slightly lower than calculated values of A and $3k$ had to be used to best fit the experimental data can be accounted for in either one of two ways. The spectroscopic splitting factor, g , may be slightly lower than two. The anisotropy of the 'g' factor may also account for some of the anisotropy observed in the magnetic susceptibility. There may also be a little less manganese in this particular specimen than that given by the chemical analysis on an aliquot of the same sample. Electron probe scans for Mn in single crystals

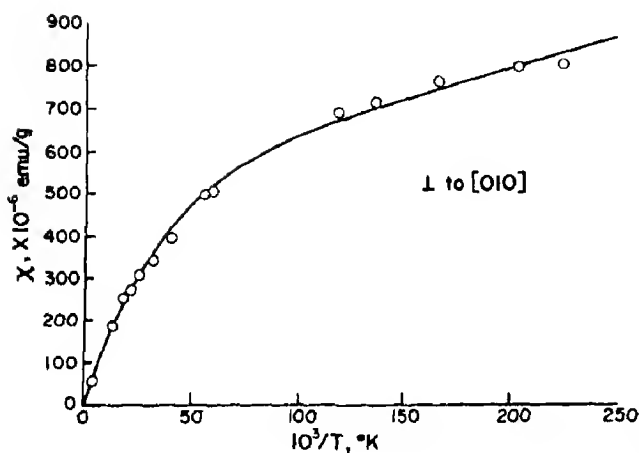


Fig. 2. The magnetic susceptibility of ardennite as a function of the reciprocal temperature perpendicular to the [010] direction.

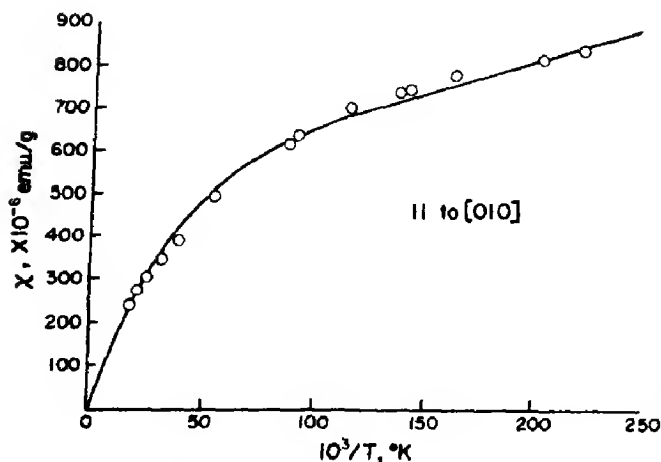


Fig. 3. The magnetic susceptibility of ardennite as a function of the reciprocal temperature parallel to the [010] direction.

of ardennite show variations of 1–2 wt.% in Mn content.

At temperatures in the vicinity of absolute zero one might expect the susceptibility to approach zero if all the magnetic atoms were coupled. In the case of ardennite, all of the atoms are not coupled because Ca substitutes for many of the Mn atoms, and other atoms, such as Fe and Cu, are present in noninteracting sites. Hence, one would expect a Curie law dependence at below 1°K. Preliminary measurements below 4°K support these expectations.

Acknowledgements—The authors are grateful to Dr. S. Geller of North American Rockwell Corporation and to Dr. Lester Corliss of Brookhaven National Laboratory for their helpful comments, and to Corrinne Alexander who assisted in making the measurements. Dr. Edgar

F. Meyer of Texas A. and M. University prepared the computer drawing of Figure 1 at Brookhaven National Laboratory. We also wish to thank Dr. H. Branson of the Department of Physics of Howard University for his interest in this work.

REFERENCES

1. DONNAY G. and ALLMAN R., *Acta crystallogr.* **B24**, 845 (1968).
2. EARNSHAW A. and LEWIS J., *Nature* **181**, 1262 (1958).
3. EARNSHAW A. and LEWIS J., *J. chem. Soc.* 396 (1960).
4. KAMBE K., *J. phys. Soc. Japan* **5**, 48 (1950).
5. YVON J., HOROWITZ J. and ABRAGAM H., *Rev. mod. Phys.* **25**, 165 (1953).
6. DONNAY G., CORLISS L., DONNAY J., ELLIOTT W. and HASTINGS J., *Phys. Rev.* **112**, 1917 (1958).
7. INGAMELLS C. O. See reference [1], p. 845, Table 1, column 3.
8. SENFTLE F. E. and THORPE A. N., *Trans. instrum. Soc. Am.* **2**, 117 (1963).

PRESSURE DERIVATIVES OF ELASTIC MODULI OF VYCOR GLASS TO 8 KBAR*

MURLI H. MANGHNANI and W. M. BENZING

Hawaii Institute of Geophysics, University of Hawaii, Honolulu, Hawaii 96822, U.S.A.

(Received 2 January 1969; in revised form 20 February 1969)

Abstract—Longitudinal- and shear-wave velocities in Vycor glass were measured to 8 kbar at 25°C, using the ultrasonic interferometry method. Corresponding bulk and shear moduli were also computed. The pressure derivatives of the shear-wave velocity and shear modulus at zero pressure were anomalously negative

$$\frac{dv_s}{dP} = -2.44 \times 10^{-2} \text{ km/sec/kbar and}$$

$$\frac{dG}{dP} = -2.67 \text{ kbar/kbar}$$

and constant throughout the 8 kbar range. On the other hand, the pressure derivatives of the longitudinal-wave velocity and bulk modulus, though also anomalously negative, ($dv_l/dP = -4.74 \times 10^{-2}$ km/sec/kbar and $dB/dP = -4.72$ kbar/kbar), tended to become normal (i.e. less negative) at pressures of about 4 kbar and higher. For the Vycor glass, $d\sigma/dP$ at zero pressure, where σ is the Poisson's ratio, is negative (-1.67×10^{-3} /kbar).

INTRODUCTION

THE STUDY of the anomalous elastic behavior of silica-rich noncrystalline materials at high pressures and temperatures has steadily gained recognition[1–4]. Recently[5], it was further shown that the anomalous behavior of fused quartz under pressure tends to become normal at about 5 kbar. The purpose of this paper is to report measurements of the elastic parameters of Vycor glass to 8 kbar, and to point out a normalizing tendency similar to that of fused quartz for this material under pressure. In our study, we used the ultrasonic interferometry ('pulse superposition') method which made it possible to obtain results accurate to within ± 0.04 per cent.

METHOD OF INVESTIGATION

Using the 'pulse superposition' method described by McSkimin[7] the longitudinal- and shear-wave velocities in Vycor glass

were measured to 8 kbar at 25°C. The Vycor glass specimen used was No. CGW7319 (supplied by F. J. Gray Co., Inc., Brooklyn, N.Y.) with optically parallel faces $\frac{3}{8}$ in. apart. Its chemical composition is 96.5% SiO₂, 3% B₂O₃, and 1% alkali oxides.

In brief, an r.f. pulse was applied to the transducer attached to the specimen, at an interval equal to the round-trip delay time of the waves in the specimen. Periodically, the pulses were gated so that the superimposed echoes could be observed. By adjusting the time interval (i.e. pulse-repetition frequency) between the applied signals, a maximum in the amplitude of the echo was obtained. The velocities and the elastic moduli were computed from the pulse-repetition frequency (p.r.f.) measurements to 4 kbar. Longitudinal- and shear-wave velocities were generated in the specimen by use of 30 mc X- and Y-cut quartz transducers, respectively.

Besides the ultrasonic interferometry equipment, the setup included a gas pressure

*Hawaii Institute of Geophysics Contribution No. 262.

generating system employing nitrogen as the pressure medium, and a vessel with a constant-temperature water jacket. The pressure was measured by means of a manganin pressure cell and a Carey-Foster potentiometric bridge, both calibrated to 4 kbar with a Harwood dead-weight tester. The temperature of the test specimen was maintained at $25 \pm 0.1^\circ\text{C}$ during the measurements.

RESULTS AND DISCUSSION

The basic measurements and the elastic parameters at 1 bar are given in Table 1. Figure 1 is a plot of the frequency ratio (f_n/f_0) vs. pressure, where f_0 is the p.r.f. at 1 bar and f_n is the p.r.f. at a given pressure. Velocities were computed from the relationship.

$$v = 2lf \quad (1)$$

where l is the length of the specimen and f is the p.r.f. The velocities at given pressures were obtained after correcting for specimen-length changes computed from Cook's[8] method, which also yields density ratios at given pressures.

As can be seen from the plots of the velocity ratios (v/v_0) in Fig. 2, both the longitudinal- and shear-wave velocities decrease with increasing pressure. Such anomalous behavior has also been reported[2, 7] for an obsidian—a natural glass containing 76% SiO_2 . As seen in the upper curve in Fig. 2, the density ratio

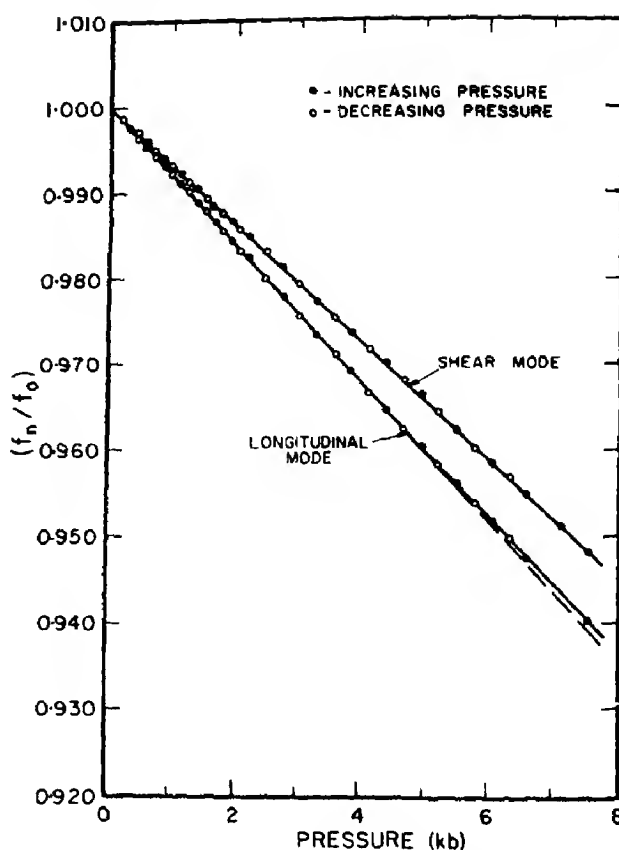


Fig. 1. Plots of (f_n/f_0) vs. pressure for longitudinal and shear modes in Vycor glass. The dashed line is the linear relationship.

(ρ/ρ_0) in Vycor glass increases at increasing rate with pressure (hence the concavity of the curve toward the ordinate). This implies an increase in compressibility with pressure.

The plots of the bulk and shear moduli (Fig.

Table 1. Elastic parameters of Vycor glass at 1 bar and 25°C

Parameter	Relationship	Units	Value
Length	l	mm	8.5207
p.r.f. (longitudinal mode)	f_p	cycles/sec	297,619
p.r.f. (shear mode)	f_s	cycles/sec	188,244
Longitudinal-wave velocity	$v_p = 2lf_p$	km/sec	5.0718
Shear-wave velocity	$v_s = 2lf_s$	km/sec	3.2076
Density	ρ	gm/cm ³	2.180
Adiabatic bulk modulus	$B_s = \rho(v_p^2 - \frac{1}{2}v_s^2)$	kbar	261.9
Adiabatic compressibility	$\beta_s = 1/B_s$	mbar ⁻¹	3.82
Shear modulus	$G = \rho v_s^2$	kbar	224.3
Poisson's ratio	$\sigma = \frac{1}{2} \left\{ \frac{(v_p/v_s)^2 - 2}{(v_p/v_s)^2 + 1} \right\}$		0.167

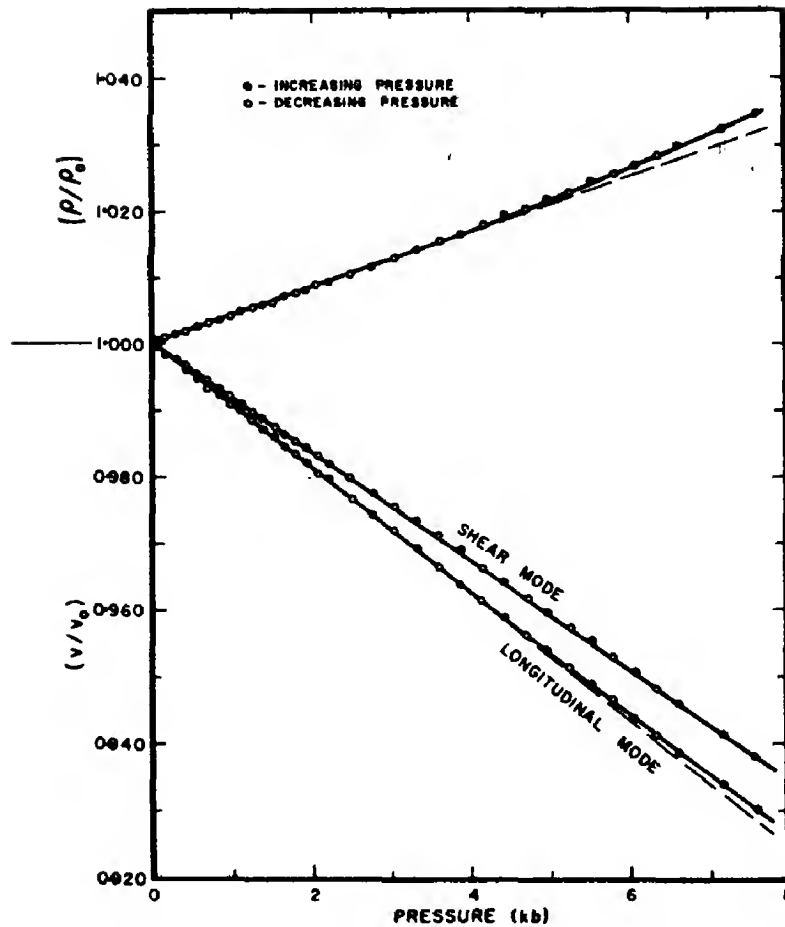


Fig. 2. Plots of velocity ratios (v/v_0) (lower set of data) and density ratios (ρ/ρ_0) (upper set of data) vs. pressure for Vycor glass. The dashed lines are the linear relationships.

3) show that both moduli decrease with pressure. The pressure derivative of the shear modulus (dG/dP) is negative (-2.67) and constant throughout the pressure range to 8 kbar, whereas that of the bulk modulus, also negative (-4.81), is constant to about 4 kbar, but, at this pressure, (dB/dP) becomes less negative and at some higher pressure it should become normal[1] (i.e. positive). Similar findings have also been reported for bulk and shear moduli of fused quartz by Peselnick[5] and of Pyrex glass by Manghnani[6].

A comparison of the pressure derivatives of the elastic parameters for Vycor and Pyrex glasses, and for fused quartz, is given in Table

2. Besides showing a correlation between the values of (dB/dP) and (dG/dP) and the silica content[6], the data suggest a relationship between the critical pressure and the silica content. For Pyrex glass (80.7% SiO_2) the critical pressure is lowest (3.0 kbar), and for fused quartz (100% SiO_2), highest (5.0 kbar).

It is interesting to note that ($d\sigma/dP$) for the Vycor glass is negative ($-1.63 \times 10^{-3}/\text{kbar}$). A comparison of the ($d\sigma/dP$) values for the Pyrex glass, Vycor glass and fused quartz shows that this quantity becomes more negative as the SiO_2 content increases.

In conclusion, it should be apparent that the behavior of (dB/dP) and (dG/dP) at given

Table 2. Pressure derivatives of the elastic parameters for Pyrex and Vycor glasses, and for fused quartz in the pressure range of the critical pressure; the latter is the pressure at which (dB/dP) tends to become less negative

Parameter	Relationship	Units	Pyrex glass (80.7% SiO ₂)	Vycor glass (96% SiO ₂)	Fused quartz (100% SiO ₂)
$\frac{dG}{dP}$	$2\rho v_s \left(\frac{dv_s}{dP} \right) + \frac{G}{B_s}$	kbar/kbar	-2.39	-2.67	-3.25*
$\frac{dB_s}{dP}$	$2\rho \left[v_p \left(\frac{dv_p}{dP} \right) - \frac{4}{3} v_s \left(\frac{dv_s}{dP} \right) \right] + (1 + \alpha\gamma T)^\dagger$	kbar/kbar	-4.05	-4.72	-6.15*
$\frac{dv_p}{dP}$		km/sec/kbar	-3.66×10^{-2}	-4.74×10^{-2}	-4.82×10^{-2}
$\frac{dv_s}{dP}$		km/sec/kbar	-2.10×10^{-2}	-2.44×10^{-2}	-2.48×10^{-2}
$\frac{d\sigma}{dP}$	$2(1 - \sigma)(1 - 2\sigma) \left[\frac{d \ln v_p}{dP} - \frac{d \ln v_s}{dP} \right]$	kbar ⁻¹	-0.50×10^{-1}	-1.63×10^{-1}	-1.67×10^{-1}
Critical pressure		kbar	3.0	3.8	5.0

* Data from reference [5].

† Quantity $\alpha\gamma T$, being small, was ignored in the computation.

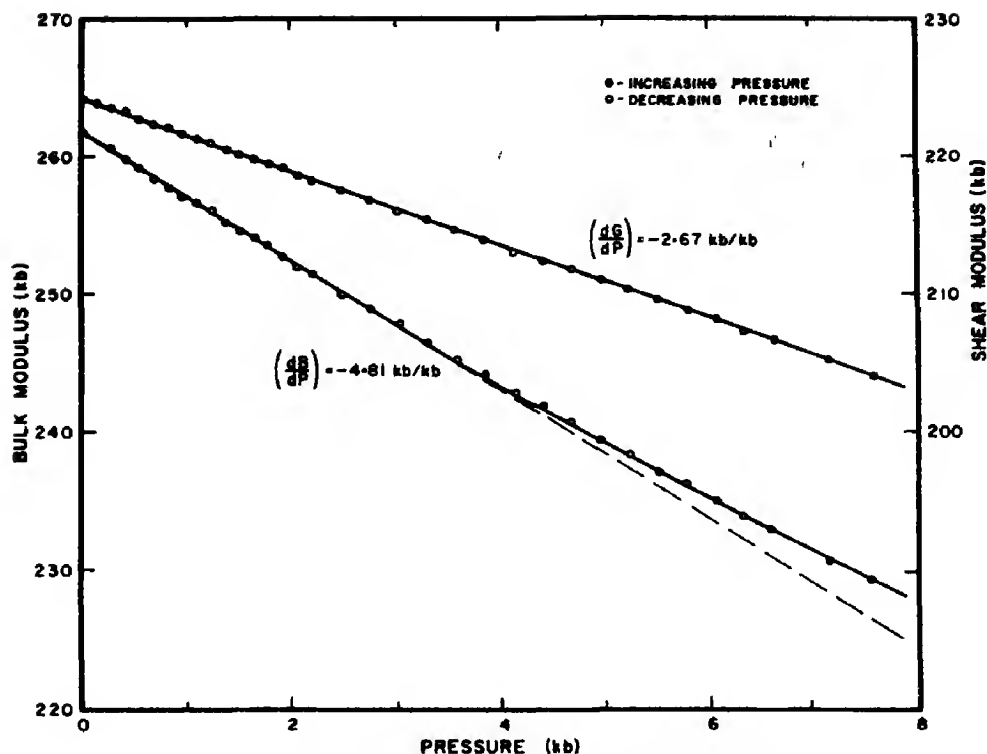


Fig. 3. Bulk and shear moduli vs. pressure for Vycor glass. The dashed line is the linear relationship.

pressures in silica-rich glasses deserves more study. Also of interest would be a study of critical pressures for various glasses of known composition-range to see whether the relationship reported here holds true.

Acknowledgements—The authors gratefully acknowledge the inspiration given by O. L. Anderson in suggesting this study. Thanks are also due to J. D. Layfield for maintaining the laboratory apparatus. This work has been supported in part by National Science Foundation grant GP-5584, and by Office of Naval Research contracts No. 3748(05) and No. 0014-67-A-0387-0005, NR 032-515.

REFERENCES

1. BRIDGMAN P. W., *Proc. Am. Acad. Arts Sci.* **76**, 55 (1948); BRIDGMAN P. W., *Am. J. Sci.* **10**, 359, (1925).
2. BIRCH F., *J. Geophys. Res.* **64**, 1083 (1960); BIRCH F. and BANCROFT D., *J. Geol.* **46**, 113 (1938); BIRCH F. and BANCROFT D., *Am. J. Sci.* **240**, 457, (1942).
3. ANDERSON O. L., *Progress in very high pressure research* (Edited by F. P. BUNDY, W. R. HIBBARD and H. M. STRONG), p. 225. Wiley, New York (1960); ANDERSON O. L. and DIENES G. J., In *Noncrystalline Solids* (Edited by V. D. FRECHETE), Chap. 18. Wiley, New York (1959).
4. BOGARDUS E. H., *J. appl. Phys.* **36**, 2504 (1965).
5. PESELNICK L., MEISTER R. and WILSON W. H., *J. Phys. Chem. Solids* **28**, 235 (1967).
6. MANGHNANI M. H., *Bull. Am. Ceram. Soc.* **44**, 434 (1969).
7. McSKIMIN H. J., *J. acoust. Soc. Am.* **33**, 12 (1961).
8. COOK R. K., *J. acoust. Soc. Am.* **29**, 445 (1957).
9. MANGHNANI M. H., SCHREIBER E. and SOGA N., *J. Geophys. Res.* **73**, 824 (1968).

THE KNIGHT SHIFT IN METALS: LIQUID ARSENIC

D.A. RIGNEY

The Ohio State University, Columbus, Ohio 43210, U.S.A.

and

J. A. BLODGETT*

University of Illinois, Urbana, Ill. 61803, U.S.A.

(Received 25 February 1969)

Abstract—Using high temperature NMR apparatus, we have measured the Knight shift of liquid arsenic. The resulting value of 0.318 ± 0.005 per cent is slightly low when compared with the Knight shifts of other polyvalent metals approximately normalized for period effects.

IN A RECENT publication[1], Rigney and Flynn have drawn attention to the dominant effect of valence in determining the Knight shift in non-transitional metals. When enhancement of the wave functions by core penetration is approximately eliminated from the problem by considering only the *relative* values of Knight shifts of metals in a given row of the periodic table, these relative Knight shifts fall into a well defined pattern. Two characteristics appear: first, the Knight shifts of any two polyvalent metals ($Z_1, Z_2 > 2$) with valence Z_1 and Z_2 in a given row of the periodic table are in a constant proportion to each other which is independent of the chosen row of the table; and second, the Knight shifts of metals with valence 1 or 2, when compared with those of higher valence metals from the same row, show a greatly increased scatter from row to row of the periodic table. These characteristics emerge most vividly in Fig. 1, which gives K_Z/K_3 plotted against Z for different metals. K_Z is the Knight shift of a metal of valence Z and K_3 is the Knight shift of the trivalent metal from the same row of the periodic table.

Rigney and Flynn[1] have explained these effects in terms of exchange correlation. In

higher valence metals the electron density is large enough for the exclusion principle to be dominant in limiting s -electron polarizability near the nucleus. Since the atomic volumes do not vary greatly, the relative Knight shifts simply measure the relative strengths of the exchange inhibition of polarizability at the nucleus, which evidently depends mainly on valence. On the other hand, monovalent and divalent metals have smaller s -wave components of the electron wave function in a cell; therefore exchange correlation exerts a lesser influence on the Knight shift, which then becomes sensitive to detailed features of the metallic structure.

In the present note we report a measurement of the Knight shift in liquid arsenic. We also draw attention to the recent work of Narath[2], who has measured the Knight shift in gold. Both results are included in Fig. 1.

The arsenic measurements were made at 7 mHz (9.6 kG) using a high temperature probe[3] and a conventional NMR bridge system feeding a signal averager[4]. ASARCO arsenic of 99.999 per cent purity was crushed in an alumina mortar to give powder of less than 325 mesh size. This was dispersed in alumina and encapsulated in a 10 mm O.D. (1 mm wall) fused quartz container under 1 atm. of argon at room temperature. The

*Present address: Naval Research Laboratory, Washington, D.C.

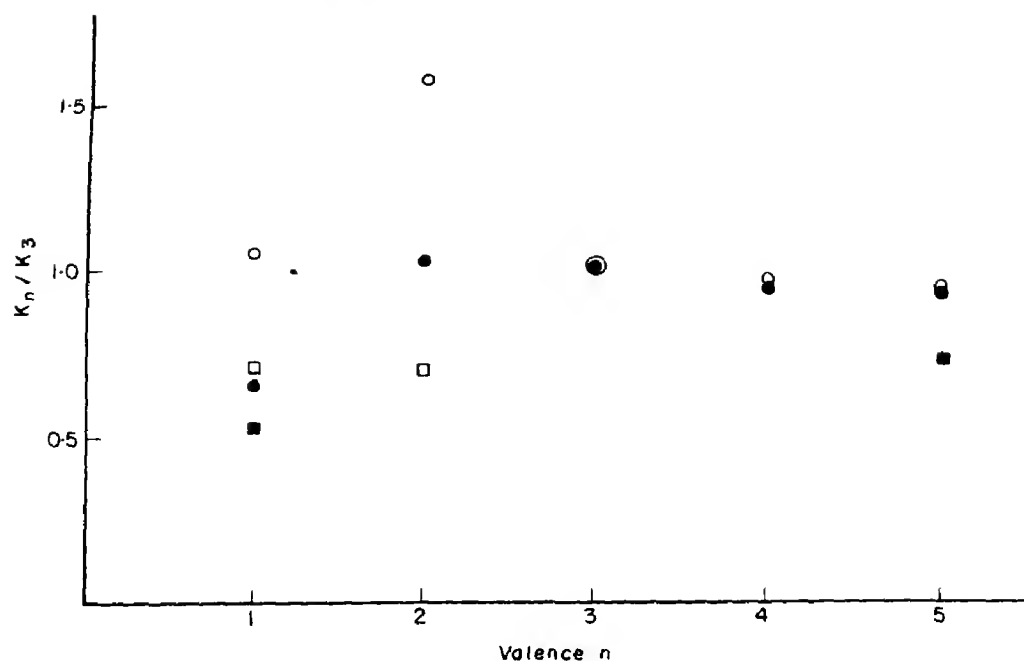


Fig. 1. Ratio of Knight shift for the valence plotted to that for the trivalent element from the same row of the periodic table. Data from Rowland[11], Narath[2], and the present work.
 □ Na, Mg, and Al; ■ Cu, Ga, and As; ● Ag, Cd, In, Sn, and Sb; ○ Au, Hg, Tl, Pb, and Bi.

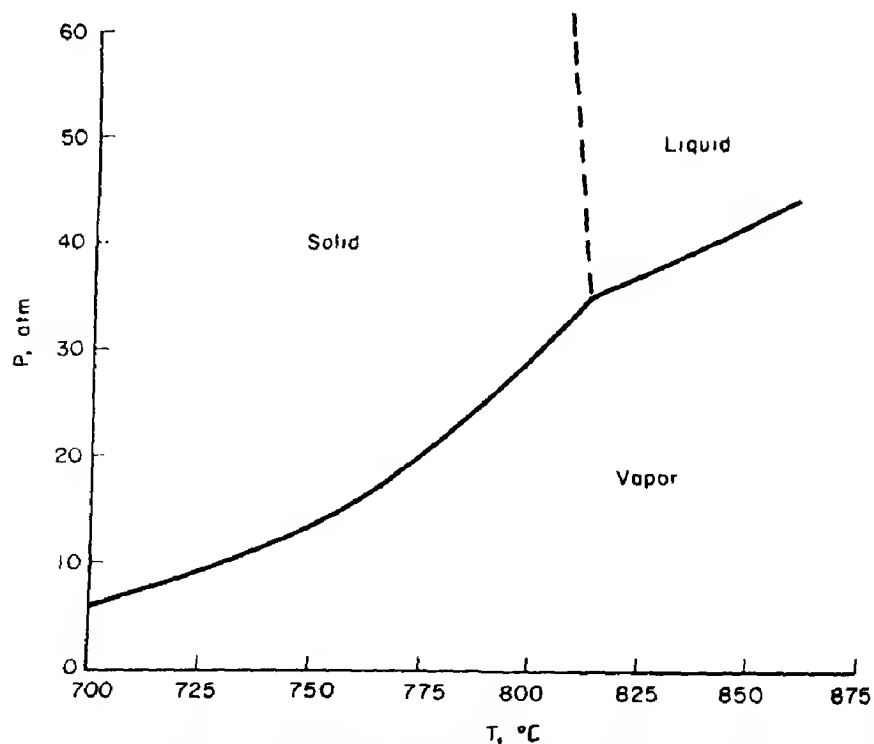


Fig. 2. Approximate pressure-temperature phase diagram for arsenic. Data taken from reference[5].

sample capsules proved strong enough to withstand the combined argon and arsenic pressures at the operating temperature of 870°C. (See Fig. 2 for approximate pressure-temperature phase diagram).

The ^{75}As resonance in liquid arsenic was observed to have a Knight shift of 0.318 ± 0.005 per cent relative to the arsenic resonance in $\text{Na}_2\text{HAsO}_4 + \text{NaOH}$ solution. The latter resonance has previously been reported [6, 7]. We also calculated the arsenic Knight shift by using liquid ^{27}Al at 13 mHz and 850°C as a reference. This could be done with the aid of published data on the Knight shift of liquid aluminum[8], together with standard chart values for the NMR frequencies of ^1H , ^{27}Al and ^{75}As at 10 KG[9]. Both procedures gave the same value for the Knight shift of liquid arsenic, indicating that errors from the temperature effects or from our use of an external proton probe were negligible.

Our result for the arsenic Knight shift is included in Fig. 1. Compared with the data on other polyvalent metals, the arsenic point lies somewhat low. Apparently, liquid arsenic is not as good a metal at 870°C as we had expected. It is possible that the Knight shift would increase at higher temperatures. Unfortunately, since we could not locate the resonance at 1000°C, we can not report that such a temperature dependence exists.

Also included in Fig. 1 is the Au Knight

shift[2], which like that of Hg, is rather large compared with Ag and Cu. As we have observed, scattered ratios for low valence metals are to be expected. The sharp distinction between the behavior of metals with valence 1 or 2 and higher valence metals confirms the suggestion[8, 1] that qualitative insight into these rather complex effects in metallic systems may be gained by analogy with the better understood mechanics of atomic systems.

Acknowledgements—We wish to thank Professors C. P. Flynn, C. Wert, and M. G. Fontana for their interest and for partial support in the course of this work.

REFERENCES

1. RIGNEY D. A. and FLYNN C. P., *Phil. Mag.* **15**, 1213 (1967).
2. NARATH A., *Phys. Rev.* **163**, 232 (1967).
3. ODLE R. L. and FLYNN C. P., *Rev. scient. Instrum.* **35**, 1611 (1964).
4. BLODGETT J. A., Ph.D. Thesis. University of Illinois. (1968).
5. *Handbook of Chemistry and Physics*, p. 2425. Chemical Rubber Publishing Co., Cleveland, Ohio.
6. TING Y. and WILLIAMS D., *Phys. Rev.* **89**, 595 (1953).
7. DHARMATTI S. S. and WEAVER H. E., Jr., *Phys. Rev.* **84**, 367 (1951).
8. KNIGHT W. D., BERGER A. G., and HEINE V., *Ann. Phys.* **8**, 173, (1959).
9. *NMR Table*, 4th Edn. Varian Associates (1964).
10. FLYNN C. P., In *Atomic and Electronic Structure of Metals*, p. 41. Am. Soc. Metals, Metals Park, Ohio (1967).
11. ROWLAND T. J., In *Progress in Materials Science*, Vol. 9, p. 1. Pergamon Press, Oxford (1961).

THE THERMAL CONDUCTIVITY OF FAST NEUTRON IRRADIATED GRAPHITE

R. TAYLOR

University of Manchester, Institute of Science and Technology, Manchester, England

and

B. T. KELLY and K. E. GILCHRIST

U.K.A.E.A. Reactor Materials Laboratory, Culcheth, Warrington, England

(Received 24 June 1968; in revised form 19 February 1969)

Abstract—Recent studies of changes in crystal dimensions and of crystal lattice parameters following fast neutron irradiation over a wide range of doses and temperatures have been interpreted in terms of two types of interstitial defect and three types of vacancy defect. It is now possible to estimate the concentration of interstitial atoms and vacancies in each type of defect as a function of neutron dose and irradiation temperature. The relative concentration of each type depends on the irradiation conditions, and in addition the annealing characteristics of each defect type are different.

Measurements have been made of the temperature dependence of the principal thermal conductivities of highly oriented pyrolytic graphite irradiated to selected doses at certain temperatures, and of changes in thermal conductivity during post-irradiation annealing. These changes are analysed in detail using a simplified theory of phonon scattering in the graphite lattice and the defect concentrations obtained from the analysis of dimensional changes. More detailed information has been published on the changes of thermal resistivity of reactor grade graphite at ambient temperature under the same conditions and this information is also successfully analysed by the theory. Analysis of these data yields meaningful scattering parameters and gives estimates of defect sizes in reasonable agreement with those obtained by other workers.

Considering the temperature dependence of the data on pyrolytic graphite, in the direction parallel to the basal planes at temperatures $> 300^\circ\text{K}$ the results can successfully be interpreted in terms of the parameters obtained from the reactor grade graphite analysis. At lower temperatures the resistance is found to increase with decreasing temperature. It is concluded that this is probably due to electron phonon scattering by electronic states associated with point defects. Parallel to the hexagonal axis approximate estimates are made of the thermal resistance changes due to each type of defect.

1. INTRODUCTION

THE CHANGES in properties of graphite when irradiated with fast neutrons are well documented[1,2] and recent work[3–5] has attempted to interpret property changes directly in terms of the different lattice defects introduced by irradiation. The interstitial atoms and vacancies produced during neutron irradiation are believed to form five distinct types of defect, the concentrations of atoms and vacancies in each type being deduced from lattice parameter and bulk crystal dimensional changes. The defects vary in their relative importance with the dose and temperature of irradiation. It is the purpose of this Report to attempt to interpret the

thermal resistance changes of nuclear and pyrolytic graphites under irradiation in terms of these same defects. The interpretation of these changes has been encouraged by the existence of a semi-continuum model of the lattice dynamics of graphite due to Komatsu[6,7], which recent work has shown to account rather well for the low-temperature conductivity of polycrystalline graphite[8]. It is possible, using these lattice dynamics, to make reasonable calculations of phonon scattering by various defects, and an approximate theory is given below for the defects introduced by fast neutron irradiation. A preliminary analysis of the effects of vacant lattice sites has already been shown to

explain many experimental observations[8a]. A further encouragement in attempting this analysis is the existence of data on very perfect pyrolytic graphite of high orientation with principal conductivities approaching those of mono-crystalline material, and we have irradiated a number of such samples to enable better comparisons to be made with the theory. These samples have been annealed at various temperatures in order to explore the interpretation of data further.

2. THEORY

The thermal conductivities of well oriented pyrolytic graphite in both principal directions and that of reactor grade graphite are dominated by the phonon contribution[9]. As a model for the lattice dynamics of graphite we use that due to Komatsu. In this model the individual graphite layer planes are replaced by thin elastic sheets which possess resistance to shearing, bending and stretching. Forces act between the sheets which resist their relative movements either parallel or perpendicular to the normal to the sheets. The frequency spectrum for the acoustic modes at the longer phonon wavelengths in this model agrees well with a detailed calculation due to Yoshimori and Kitano[10] using the Born-Von Karman method. The graphite lattice contains four atoms in the unit cell and there are therefore twelve vibrational modes, three acoustic and nine optical. In this work we consider the acoustic modes only, since the optical modes require a high temperature for their excitation and possess low group velocities. In the semi-continuum approximation the three acoustic modes separate into two polarised parallel to the layers known as 'in-plane' vibrations, and one polarised perpendicular to the layers known as the 'out-of-plane' vibration. The two in-plane modes further separate into longitudinal and transverse modes. The out-of-plane mode is longitudinal or transverse in special directions only.

The vibrational frequencies of the acoustic modes are

$$\left. \begin{aligned} \text{In-plane longitudinal } \nu_1 &= \left[v_l^2 \sigma_u^2 + \frac{\tau}{\pi^2 d^2} \sin^2 \pi d \sigma_z \right]^{1/2} \\ \text{In-plane transverse } \nu_2 &= \left[v_T^2 \sigma_u^2 + \frac{\tau}{\pi^2 d^2} \sin^2 \pi d \sigma_z \right]^{1/2} \\ \text{Out-of-plane } \nu_3 &= \left[4\pi^2 \delta^2 \sigma_u^4 + \frac{\mu^2}{\pi^2} \sin^2 \pi d \sigma_z + \tau \sigma_u^2 \right]^{1/2} \end{aligned} \right\} \quad (1)$$

σ_u and σ_z are wave number components parallel and perpendicular to the basal planes, d is the interlayer spacing, v_l ($= (C_{11}/\rho)^{1/2}$) is the longitudinal elastic wave velocity parallel to the basal planes, v_T ($= [\frac{1}{2} (C_{11} - C_{12})/\rho]^{1/2}$), is the transverse elastic wave velocity parallel to the layer planes, $\mu^2 = C_{33}/\rho d^2$, $\tau = C_{44}/\rho$, δ measures the resistance of a layer to bending, ρ is the density and the C_{ij} are the usual elastic constants.

The effect of each type of lattice defect on the principal conductivities of a graphite crystal is obtained by calculating the phonon mean free paths parallel and perpendicular to the hexagonal axis of the crystal for each vibrational mode p using the harmonic formula due to Ziman[11], which is valid in the limit of N -processes dominant[12], in determining the vibration spectrum.

$$\frac{1}{\Lambda_{ap}(T)} = \frac{v_{ap}(T)}{\rho C_p(T)} \int \frac{C_p(\sigma)}{\{v_p(\sigma)\}_\alpha \{\Lambda_p(\sigma)\}_\alpha} d\sigma \quad (2)$$

where $\{\Lambda_p(\sigma)\}_\alpha$ and $\{v_p(\sigma)\}_\alpha$ are the mean free path and velocity of a phonon of wave vector σ in direction α for the p 'th vibrational mode respectively.

$v_{ap}(T)$ is the average velocity of phonons in mode p at temperature T in direction α .

$C_p(T)$ is the specific heat/gm due to phonons in mode p at temperature T .

$C_p(\sigma)$ is the specific heat/unit volume due to phonons of wave vector σ in mode p .

The mean free paths in the principal crystallographic directions are obtained from the relaxation time $\tau_p(\sigma)$ for phonons in mode p , by

$$\left. \begin{aligned} \{\Lambda_p(\sigma)\}_a &= \tau_p(\sigma) \{v_p(\sigma)\}_a \\ \{\Lambda_p(\sigma)\}_c &= \tau_p(\sigma) \{v_p(\sigma)\}_c \end{aligned} \right\} \quad (3)$$

The quantities $C_p(T)$ [6, 7, 10] and $\{v_p(\sigma)\}_a$ [8(a,b)] are known, and thus it remains to estimate $\tau_p(\sigma)$ for each of the types of lattice defect in irradiated graphite.

The dimensional changes in irradiated graphite crystals have been interpreted in terms of five types of lattice defect as follows:

- (a) The sub-microscopic interstitial cluster. This cluster is too small to be visible in the electron microscope [13], but its existence and approximate size (4 ± 2 atoms) have been established by cold neutron scattering [14, 15] experiments. It is apparently associated with a free spin [16] and does not grow in size by capturing further interstitial atoms. The concentration of atoms in such clusters is denoted by $x(\gamma)$ after a dose γ n.cm⁻².
- (b) The interstitial loop. This defect has been studied by electron microscopy [13, 17]. It is essentially a new layer plane in a C position in the ABAB stacking sequence, which grows, following nucleation, by capturing further diffusing interstitials. The concentration of atoms in these defects is denoted by $C_i(\gamma)$.
- (c) The vacant lattice site, existing as singles, pairs or small groups. The concentration is denoted by $C_v(\gamma)$.
- (d) The collapsed line of vacant lattice sites. These defects have not been observed directly but their existence has been invoked to explain the continuous basal plane contraction of graphite crystals irradiated to high

doses [3, 17]. The concentration of vacancies in such collapsed lines is denoted by $C_{VL}(\gamma)$.

- (e) The vacancy loop. Electron microscope studies [18] have revealed vacancy loops in the basal planes of graphite crystals irradiated at temperatures of 650°, 900° and 1200°C, which are too small to have collapsed parallel to the hexagonal axis. The concentration of vacancies in loops is denoted by $C_{VL}(\gamma)$.

The phonon scattering by each of these defects is now examined in turn. It is important to note that accurate calculations of thermal resistance due to defects introduced parallel to the basal planes may be made by assuming the lattice to be dimensional, i.e. setting $C_{33} = C_{44} = 0$ for temperatures above 200°K.

Point defects

The sub-microscopic cluster and the vacancy may be regarded as point defects. According to Klemens [19] three effects must be taken into account in estimating the scattering of phonons by point defects: the change in mass due to the presence of the defect, the change in the interatomic bonds close to the defect and the elastic strain field around the defect. In a previous publication the scattering due to the mass defect of a vacancy in graphite was estimated assuming the lattice to be two dimensional, treating the vacancy as a circular hole of radius a , and then assuming that the strain field scattering has the same frequency dependence so that an adjustable scattering parameter S_1^2 was introduced by analogy with Klemens treatment of isotropic lattices. It was concluded that at irradiation temperatures of 200°, 250° and 350°C, the vacant lattice sites were the most important contributor to the radiation induced changes of thermal resistance in reactor graphite. Further, the two dimensional classical formula for scattering of waves by a cylinder given by Morse and Feshbach [20] led to good agreement with experiment at ambient temperatures and

above. The formula led to relaxation times for point defects proportional to σ_a^{-3} rather than the σ^{-4} obtained in isotropic lattices. Here we have derived an improved theory of point defect scattering.

Consider the addition or removal of a mass ΔM in the lattice in a region small compared to the appropriate mean phonon wavelengths. The phonon scattering is elastic, and in an isotropic lattice we would consider the scattering of a phonon of particular energy into states of equal energy in each of the three acoustic modes. However, according to Klemens[19] the scattering probability/unit time of a phonon contains the factor:-

$$C_{\sigma, \sigma'}^2 = (\Delta M / 2N_0)^2 w^2 w'^2 (\epsilon \cdot \epsilon')^2 \quad (4)$$

where N_0 is the number of atoms/unit volume, w, w' are the incident and scattered wave frequencies and ϵ, ϵ' are the corresponding polarisation vectors.

In graphite the in-plane polarisation vectors are perpendicular to the out-of-plane wave vector; thus as noted by Dreyfus and Maynard[21], in-plane waves are scattered into in-plane states and out-of-plane waves into out-of-plane states. This is, of course, an approximation but probably a good one.

Carruthers[22] has given a general expression for the phonon relaxation time for an arbitrary density of states $n(w)$ which we apply to the calculation of the relaxation times. Consider both types of in-plane waves together, with a mean velocity \bar{v}_a parallel to the basal planes given by:-

$$\frac{2}{\bar{v}_a^2} = \frac{1}{v_L^2} + \frac{1}{v_T^2} \quad (5)$$

and a density of states (neglecting the shear interaction between layers):-

$$n(w) = \frac{w}{\pi d \bar{v}_a^2} \quad (6)$$

For the in-plane phonons the average value of $(\epsilon \cdot \epsilon')^2$ in (4) is $\frac{1}{2}$, and the Carruthers

formula yields as the relaxation time for mass defect scattering by in-plane phonons.

$$\tau_{1+2}(w) = N_0 d / \pi \bar{v}_a \sigma_a^3 I \quad (7)$$

where $I = C(1-C)[\Delta M / \bar{M}]^2$, C is the defect concentration and \bar{M} the mean atomic mass. Substitution of equation (7) into (3) for the mean free paths leads to

$$\left. \begin{aligned} \{\Lambda_{1+2}(\sigma)\}_c &= \tau N_0 \sin 2\pi d \sigma_z / 2\pi^2 \bar{v}_a^2 \sigma_a^4 I \\ \text{and} \\ \{\Lambda_{1+2}(\sigma)\}_a &= N_0 d / \pi \sigma_a^3 I \end{aligned} \right\} \quad (8)$$

The wave number dependence of the second equations (8) is the same as that estimated from the classical formula, but its magnitude is about 22 times greater. There is no previous calculation corresponding to the first equation. The calculations for the out-of-plane mode are more complicated; as an approximation the density of states may be represented by

$$n(w) = \begin{cases} 1.8 w / 2\pi d \mu \delta & \text{for } w < 2\mu \\ 1.8 / \pi d \delta & \text{for } w > 2\mu \end{cases} \quad (9)$$

The value of $\epsilon \cdot \epsilon'$ is unity and Carruthers' formula is now (neglecting the shear interaction)

$$\left\{ \Lambda_3(\sigma) \right\}_a = \begin{cases} 8\pi \delta^3 \mu N_0 d \sigma_a^3 / 1.8 I \left\{ 4\pi^2 \delta^2 \sigma_a^4 + \frac{\mu^2}{\pi^2} \sin^2 \pi d \sigma_z \right\}^2 & \text{for } w < 2\mu \\ 8\pi^2 \delta^3 N_0 d \sigma_a^3 / 1.8 I \left\{ 4\pi^2 \delta^2 \sigma_a^4 + \frac{\mu^2}{\pi^2} \sin^2 \pi d \sigma_z \right\}^{3/2} & \text{for } w > 2\mu \end{cases} \quad (10)$$

When $w > 2\mu$, the terms containing μ^2 are insignificant[8] and the second equation of (10) becomes

$$\{\Lambda_3(\sigma)\}_a = N_0 d / 1.8 \pi \sigma_a^3 I \quad (11)$$

again agreeing in wave-number dependence with the classical formula, but about 12 times the magnitude. For the other crystal direction

$$\{\Lambda_3(\sigma)\}_c =$$

$$\left[\begin{array}{l} \frac{N_0 d \delta \mu^3 \sin 2\pi d \sigma_z}{3 \cdot 6 \pi^2 I \left\{ 4\pi^2 \sigma_a^4 + \frac{\mu^2}{\pi^2} \sin^2 \pi d \sigma_z \right\}^2} \text{ for } w < 2\mu \\ \frac{N_0 d^2 \mu^2 \delta \sin 2\pi d \sigma_z}{3 \cdot 6 \pi \left\{ 4\pi^2 \delta^2 \sigma_a^4 + \frac{\mu^2}{\pi^2} \sin^2 \pi d \sigma_z \right\}^{3/2}} \text{ for } w > 2\mu \end{array} \right] \quad (12)$$

Again, there is no previous calculation equivalent to (12).

The next contribution to scattering is that due to the strain field about the defect. Consider the single vacancy first. We can regard the vacancy as a circular hole in an isolated layer of radius a , with the boundary displaced inwards by $\epsilon_0 a$. The radial displacement U is given by:-

$$\frac{d}{dr} \left(\frac{du}{dr} + \frac{u}{r} \right) = 0 \quad (13)$$

with the general solution

$$u(r) = Ar + B/r. \quad (14)$$

The boundary conditions $u \rightarrow 0$ as $r \rightarrow \infty$, $u = \epsilon_0 a$ as $r \rightarrow a$ lead to a radial strain

$$e_{rr} = -\epsilon_0 a^2 / r^2. \quad (15)$$

The velocity of in-plane waves at radius r is assumed to be given by

$$v_a = v_a \left(1 \pm \gamma \epsilon_0 \frac{a^2}{r^2} \right) \quad (16)$$

where γ is an average anharmonic coefficient for the in-plane waves. The part of a homogeneous phonon flux in the mode scattered between r and $r+dr$ is proportional to

$(1 - \cos \phi) dr$ where ϕ is the angle of refraction. For small ϕ

$$(1 - \cos \phi) dr \approx \phi^2 / 2 \cdot dr = \frac{\gamma^2}{2} \left(\frac{\epsilon_0 a^2}{r^2} \right)^2 dr. \quad (17)$$

The fraction of the flux scattered is proportional to

$$f = \frac{\gamma^2 \epsilon_0^2 a^4}{2} \int_{r'}^{\infty} \frac{dr}{r^4} \approx \frac{\gamma^2 \epsilon_0^2 a^4}{6 r'^3} \quad (18)$$

Where $r' \sim \lambda \sim \sigma_a^{-1}$ is the smallest value of r for which this type of analysis is valid. Thus, for this mode the relaxation time and mean free path for both mass defect and strain field scattering are proportional to σ_a^{-3} as long as the strain field is two dimensional. The same results are found for the out-of-plane mode provided that $w > 2\mu$.

If we now consider the sub-microscopic interstitial cluster, it is a reasonable approximation to assume its elastic field as that due to a force doublet with the axis parallel to the hexagonal axis. The strain field of such a doublet in hexagonal elasticity has been calculated by Elliot [23]. The radial displacement for instance is given by:-

$$u(r, z) = M \left[\frac{r}{\nu_1^{1/2} (r^2 + z^2 \nu_1^{-1})^{3/2}} - \frac{r}{\nu_2^{1/2} (r^2 + z^2 \nu_2^{-1})^{3/2}} \right] \quad (19)$$

where M , ν_1 and ν_2 are constants. This strain field is clearly not two dimensional even on the plane $z = 0$, so that the σ_a^{-3} formula cannot be used unless the mass defect scattering dominates. Without knowledge of the anharmonic coefficients no further progress can be made theoretically, recourse must be made to experiment.

Vacancy loops

Using the two dimensional approximation on uncollapsed vacancy loop of radius r_0 is simply a circular hole in the layer plane and

the scattering cross section/unit length for two dimensional waves is $4r_0$ ($r_0 \gg (2\pi\sigma_a)^{-1}$) [20]. Thus for a single layer, the scattering cross section is

$$\sigma \times 4r_0d. \quad (20)$$

For N such loops/unit volume the mean free path parallel to the basal planes is

$$\Lambda = \frac{1}{4N r_0 d} = \frac{\pi r_0}{4 C_{r, \text{loop}}}. \quad (21)$$

On substituting this into equation (2) we get

$$\left[\begin{aligned} \left\{ \frac{1}{\Lambda_{1+2}(T)} \right\}_{\text{loop}} &= \frac{4 C_{v, \text{loop}}}{\pi r_0} \\ \left\{ \frac{1}{\Lambda_3(T)} \right\}_{\text{loop}} &= \frac{2v_3(T)}{\pi r_0 \delta^{1/2}} \left\{ \frac{\hbar}{kT} \right\}^{1/2} \\ &\times \frac{J_{3/2}(\theta_0/T)}{J_2(\theta_0/T)} C_{r, \text{loop}}. \end{aligned} \right] \quad (22)$$

Using the two dimensional formula [24]

$$K_v = \frac{1}{2} C_v(T) v_0 \Lambda_v \rho \quad (23)$$

then the thermal resistance change can be calculated from

$$\Delta(1/K_a) = \frac{1}{K_{1+2}(T) + K_3(T)}. \quad (24)$$

The scattering cross-section for waves propagating parallel to the hexagonal axis is $\sim \pi r_0^2$. It is to be expected that vacancy loops will have no effect on $\Delta(1/K_c)$ in any of the pyrolytic samples.

Vacancy lines

Although later analysis shows the effect of vacancy lines on the basal conductivity to be small it is worthwhile to discuss the effects which may be expected. Physically the collapsed line may be viewed as an edge dislocation dipole of length h one layer plane thick, so for h greater than the mean phonon

wavelength the component dislocations will scatter independently whilst at the other extreme the line will resemble a point defect.

Moss [25] has shown that the relaxation time τ_L for scattering may be obtained for unit length of dislocation from

$$1/\tau_L = 4\tau_D \sin^2[\pi\sigma_a \cdot h] \quad (25)$$

where τ_D is the relaxation time for scattering due to unit length of an edge dislocation. This is given by Ziman [12] as

$$(\tau_D)_p = \frac{1}{\pi N b^2 \sigma_a \{v_p\}_a \gamma_p^2} \quad (26)$$

where N is the number of dislocations/unit volume, b is the Burger's vector and γ_p is an average anharmonic coefficient for mode p . The mean free path parallel to the basal planes is thus

$$\{\lambda_L\}_p = \frac{1}{4N \gamma_p^2 b^2 \sigma_a \pi d \sin^2[\pi\sigma_a h \cos \phi]} \quad (27)$$

where ϕ is the angle between σ_a and h .

For short lines $\sin^2[\pi\sigma_a h \cos \phi] \rightarrow \pi^2 \sigma_a^2 h^2 \cos^2 \phi$ but for long lines $\sin^2[\pi\sigma_a h \cos \phi] \rightarrow 1$ and the integral for out-of-plane waves when it is substituted in equation (2) does not converge. A short line has a wave number dependence similar to a point defect so if the mean free paths for particular phonons scattered by lines and vacancies are compared we have

$$\left[\begin{aligned} \frac{\{\lambda_L\}_p}{\{\lambda_v\}_p} &= \frac{1}{N_v} \left\{ \frac{C_v}{C_{vL}} \right\} \frac{1}{\gamma_p^2} \text{ (short lines)} \\ \frac{\{\lambda_L\}_p}{\{\lambda_v\}_p} &= N_v \left\{ \frac{C_v}{C_{vL}} \right\} \frac{1}{\gamma_p^2} \cdot 4\pi^2 \sigma_a^2 10^{-16} \text{ (long lines)} \end{aligned} \right] \quad (28)$$

where N_v is the number of vacancies in a line ($h > 10 \text{ \AA}$).

Interstitial cluster

This is essentially a new layer plane so whilst phonon scattering is to be expected

from the strain field around the edge of the cluster it is not possible to calculate the magnitude—the experimental results show it to be insignificant however.

3. EXPERIMENTAL DETAILS

The experimental materials on which thermal conductivity data have been obtained are of two types, standard Pile Grade A reactor graphite as described by Bell and O'Driscoll[26] and highly oriented and perfect pyrolytic graphite. The latter material was obtained by annealing pyrolytic graphite deposits obtained at $\sim 2200^\circ\text{C}$ at a temperature of 3200°C , and was supplied through the courtesy of Dr. R. Diefendorf of the General

The furnace design varies somewhat with the required irradiation temperature, but all are basically similar to those described by Bell *et al.*[29]. One pair of pyrolytic samples was irradiated at each of four temperatures, 30° , 150° , 300° and 450°C . Irradiation temperatures were controlled to $\pm 2^\circ\text{C}$. at 30° , 150° and 300°C and $\pm 10^\circ\text{C}$. at 450°C . The pairs comprised one sample parallel and one perpendicular to the deposition plane, denoted by *A* and *C* directions respectively. The irradiation doses received were measured using the $^{58}\text{Ni}/n,p)^{58}\text{Co}$ reaction assuming a cross-section of 107 mb[30]. The doses received by the pyrolytic samples are tabulated below:

Samples	Temperature of irradiation ($^\circ\text{C}$)	Fast neutron dose (n/cm^2)
<i>A</i> , <i>C</i>	30	0.02×10^{20}
1 <i>A</i> , 1 <i>C</i>	150	0.83
2 <i>A</i> , 2 <i>C</i>	300	3.8
3 <i>A</i> , 3 <i>C</i>	450	4.85

Electric Co., U.S.A. The physical properties of this material are given by Kelly, Martin and Nettle[27]. In material of this perfection samples cut parallel or perpendicular to the plane of deposition reflect essentially the directions parallel or perpendicular to the basal planes of the component crystals.

Pyrolytic graphite samples were cut in the form of cylinders ~ 0.2 in. dia., the lengths of specimens cut parallel to the deposition plane being 0.5 in. and of those cut perpendicular to the deposition plane being 0.1–0.2 in. The thermal diffusivities α of these samples were measured using the heat pulse method described by Taylor[28], and converted to thermal conductivities using the relationship $K = \alpha \rho c$ (where ρ = density, c = specific heat).

The irradiations were carried out in specially designed constant-temperature furnaces located in hollow fuel elements in the Materials Testing Reactors Dido and Pluto at A.E.R.E.

The thermal conductivities of the irradiated specimens are shown in Figs. 1(a) and 2(a) for the *A* and *C* directions respectively. The unirradiated conductivities are included for comparison. A similar pair of pyrolytic graphite samples were also irradiated in the Dounreay Fast Reactor using a rig of the type described by Martin and Price[31] to a dose of $150 \times 10^{20} \text{ n}/\text{cm}^2$ Dido equivalent, at a Dido equivalent temperature of about 400°C . The spectrum of fast neutrons is very different in fast reactors to that in the M.T.R. and is of much greater intensity (10^{15} fast neutrons/ cm^2 sec compared with 5×10^{13} fast neutrons/ cm^2 sec) so that the temperatures and doses have been converted to those required to give the same effects in an M.T.R. using well established methods[1].

All the pyrolytic specimens (except *A* and *C*) irradiated in M.T.R.'s. were annealed, usually at 200°C intervals, at temperatures up to 2800°C [32]. The specimen was main-

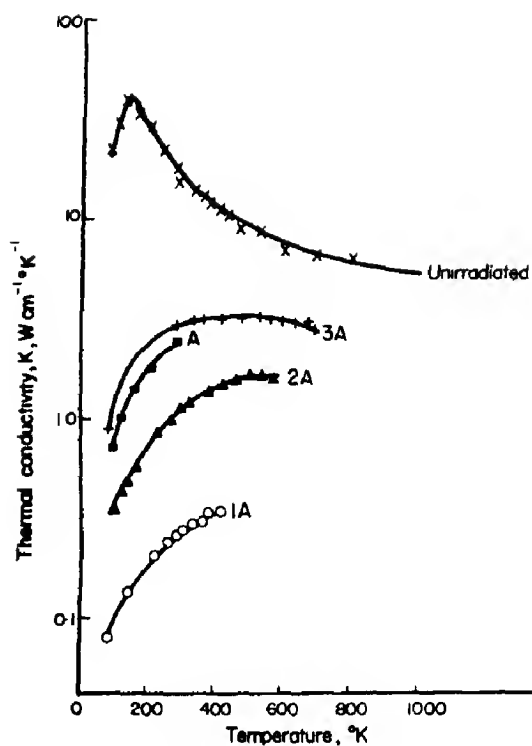


Fig. 1(a). Thermal conductivity of irradiated specimens of pyrolytic graphite measured parallel to the deposition plane.

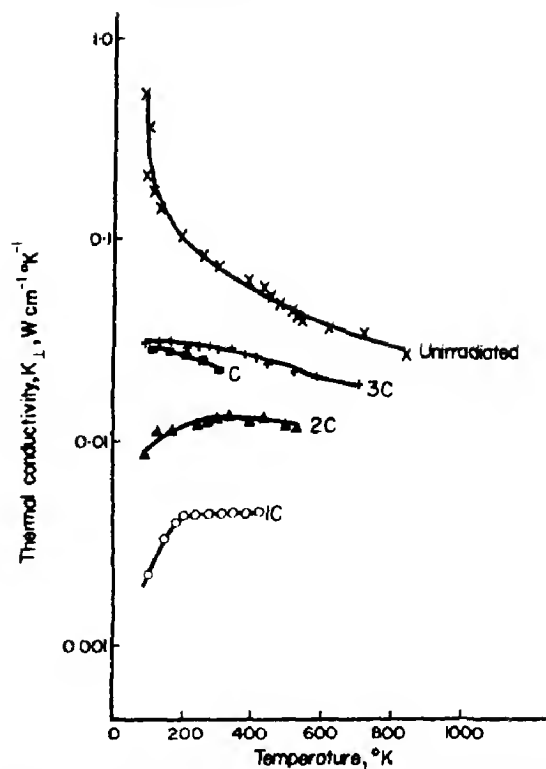


Fig. 2(a). Thermal conductivity of irradiated specimens of pyrolytic graphite measured perpendicular to the deposition plane.

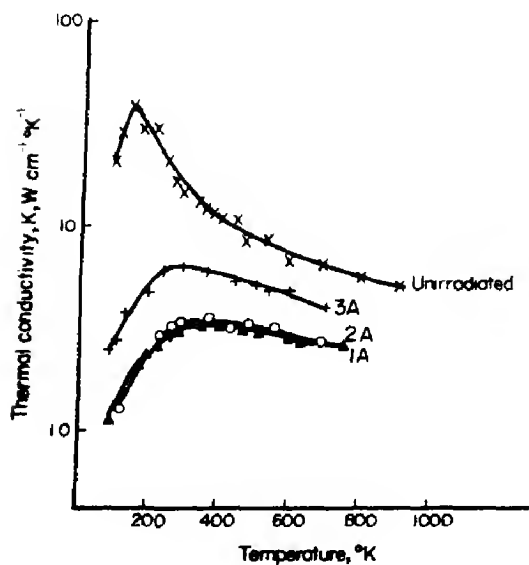


Fig. 1(b). Thermal conductivity of irradiated samples of pyrolytic graphite parallel to the deposition plane after annealing at 1200°C .

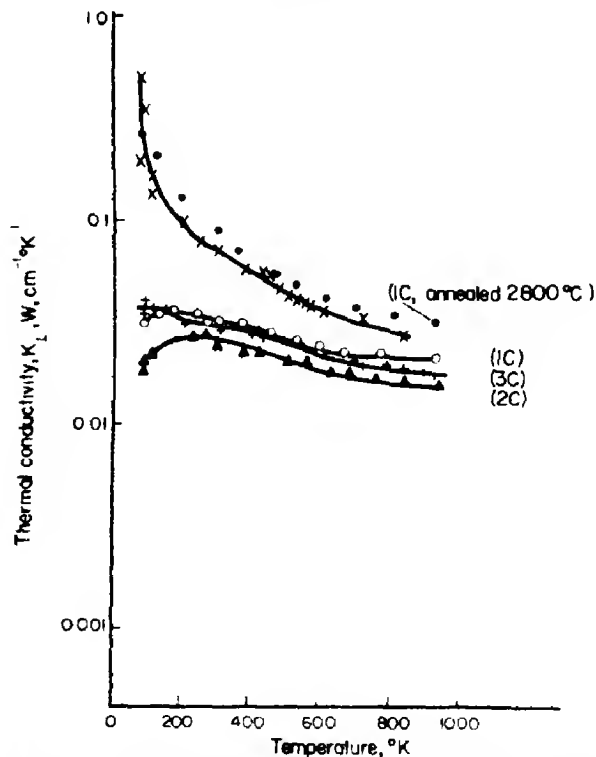


Fig. 2(b). Thermal conductivity of irradiated samples of pyrolytic graphite perpendicular to the deposition plane after annealing at 1200°C .

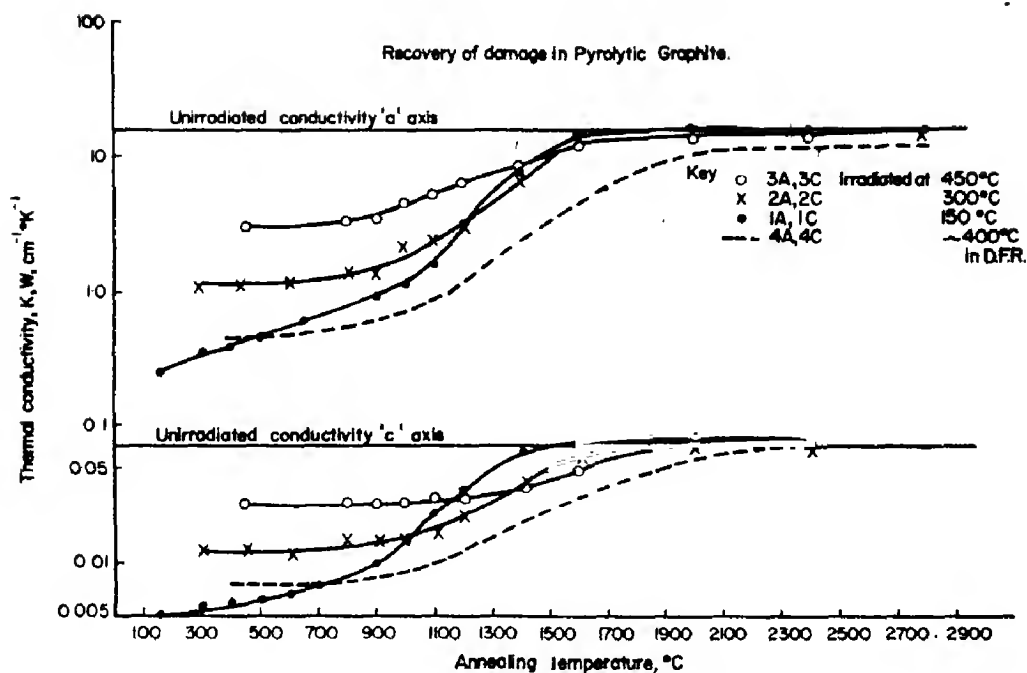


Fig. 3. Change in room temperature thermal conductivity during post irradiation annealing.

tained at each annealing temperature for a period of two hours. The thermal conductivity changes during annealing are plotted in Fig. 3. Only the thermal conductivity at room temperature (20°C) was measured after most anneals but after annealing at 1200°C the thermal conductivity of all specimens was measured from 90°–750°K. (Figs. 1(b) and 2(b)). The annealing programme carried out on the specimen irradiated in the D.F.R. was more limited in scope and specimens were only annealed at 1000°, 2000°, 2500° and 3000°C. The thermal conductivity was measured in each case from 90°–750°K and the results are shown in Fig. 4.

We also consider room temperature fractional changes in thermal resistance of Pile Grade A graphite irradiated at temperatures of 200°, 250°, 300°, 350°, 450°, 650°, 900° and 1350°C to neutron doses of 50×10^{20} n/cm² which have been reported elsewhere [31, 33]. These specimens were all irradiated under similar conditions and the temperature control was $\pm 2^\circ\text{C}$ for temperatures $< 300^\circ\text{C}$, $\pm 10^\circ\text{C}$ for temperatures between 300° and

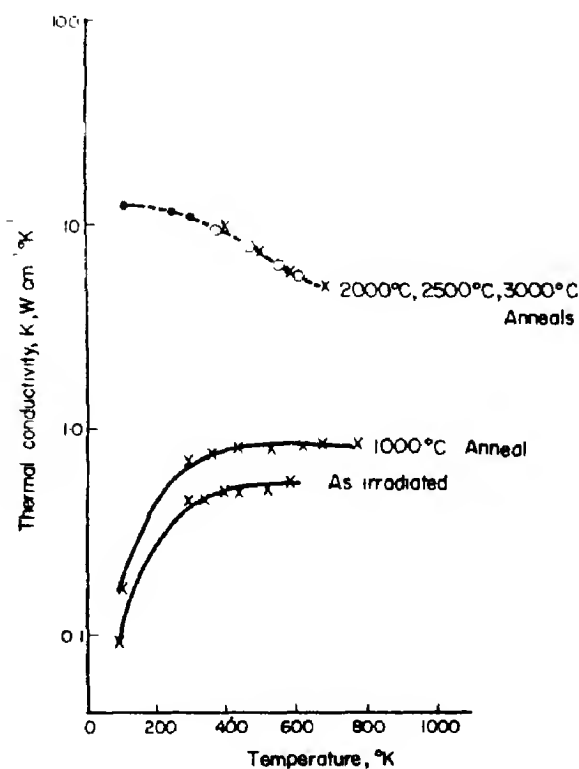


Fig. 4. Recovery of thermal conductivity of samples cut parallel to the deposition plane.

650°C, and $\pm 50^\circ\text{C}$ at 900°C and at 1350°C. Measurements were made using the Kohlrausch method[34] for which samples 3.00 in. long \times 0.250 in. dia. were employed.

4. DISCUSSION

Considerations of lattice parameter and dimensional changes of graphite crystals show that $x(\gamma)$ is insignificant at irradiation temperatures above 300°C and $C_{\text{rLoop}}(\gamma)$ is negligible at irradiation temperatures below 650°C. Post irradiation annealing of dimensional changes shows that by about 900°C $x(\gamma)$ is removed, $C_r(\gamma)$ is annealable in the range 1000°–2000°C and $C_{\text{rLoop}}(\gamma)$ is annealable in the range 2100°–2600°C. The defects comprising $C_i(\gamma)$ and $C_{vL}(\gamma)$ are little affected and do not anneal even at temperatures up to 3000°C [1, 35].

The thermal conductivity of porous polycrystalline graphite in direction x may be written[36].

$$K_x = K_a/\gamma_x \quad (29)$$

where $\gamma_x (> 1)$ is a factor allowing for porosity, orientation and K_a is the layer plane conductivity. Much data is available on reactor grade graphite so we will examine this first.

Reactor grade graphite – point defects

Previously Kelly[8(a)] has shown that data at 200°, 250° and 350°C could be accounted for by vacancies using a relaxation time $\propto \sigma_a^{-3}$ with only a small correction for the submicroscopic clusters. Although the theory outlined earlier indicates this to be valid for the vacancies above 200°K, it is not justified apparently for the submicroscopic cluster. However as we see later the two cannot be distinguished in the temperature dependence of the thermal resistivity they produce. So we assume the scattering formula in the classical approximation to be applicable to both defects and use separate scattering parameters S_i^2 and S_r^2 for the interstitial and vacancy defects respectively. It is further assumed that S_i^2 and S_r^2 are the same for in-plane and out-of-plane vibrations. The change in thermal resistance of polycrystalline graphite is

$$\Delta(1/K_x) = \gamma_x \Delta(1/K_a) = \beta \gamma_x (x S_i^2 + C_r S_r^2) \quad (30)$$

β is the appropriate numerical factor[8(a)], which at room temperature is 3.24×10^2 . This relation is tested in Fig. 5 where we plot $[\beta C_r K_a]^{-1} ((K_0/K) - 1)$ against (x/C_i) using data on Pile Grade A graphite irradiated at temperatures up to 450°C x and C_i are

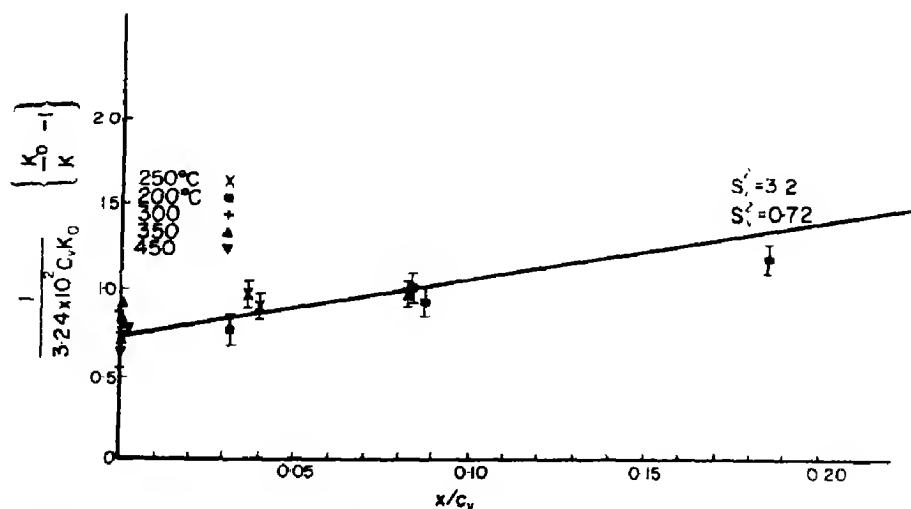


Fig. 5. Derivation of scattering parameters from point defect concentrations.

calculated from lattice parameter changes[4]. From the intercept we obtain $S_v^2 = 0.72$ and from the slope (S_i^2/S_v^2) we obtain $S_i^2 = 3.2$.

The value of S_v^2 is well defined by the data at 300°, 350° and 450°C where x is negligible, as being in the range $0.6 < S_v^2 < 0.9$. This is in reasonable agreement with the expectation that $S_v^2 \sim 1$ whereas the scattering strength S_i^2 of the cluster is roughly four times greater in rough accord with its being 4 ± 2 atoms in size[14, 15].

Reactor grade graphite – vacancy loops

Thermal resistance changes at temperatures above 650°C are all longer than can be accounted for by the vacancy content estimated from lattice parameter changes. Analysis of crystal dimensional changes indicates the presence of uncollapsed vacancy loops[18, 5]. In the presence of vacancy loops equation (30) may be written

$$\Delta(1/K_r) = \gamma_r \left[3.24 \times 10^2 S_r^2 C_r + 5.78 \times 10^{-6} \frac{C_{rloop}}{r_0} \right] \quad (31)$$

to allow estimate of room temperature thermal resistance changes. Using Simmons[33] data at 650°, 900° and 1350°C, r_0 may be estimated as a function of dose and temperature since C_r and C_{rloop} are known. The co-planer vacancy loop half-separation r_r is given by

$$C_{rloop}(\gamma) = (r_0/r_r)^2.$$

The results given in figure show that with increasing irradiation temperature the loops increase both in size and separation. It is to be noted that the radii are less than the value of 110 Å estimated for collapse by Tsuzuku [37] and agree with the incomplete collapse for loops of radii > 150 Å observed by Thrower[18].

Pyrolytic graphite parallel to the deposition plane

The pyrolytic graphite we use is high density highly oriented material so we assume

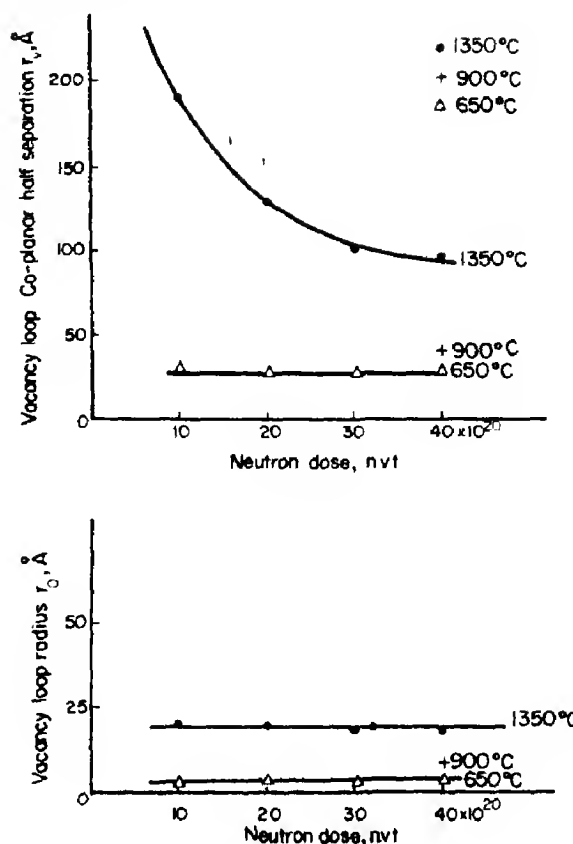


Fig. 6. Calculated vacancy loop radii and co-planar separations of loops.

that the conductivity parallel to the deposition plane $K_{||}$ is the intrinsic layer plane conductivity K_a . Applying the orientation conductivity relationship suggested by Klein[38] substantiates this assumption.

The four lower-dose samples were irradiated at 30°, 150°, 300° and 450°C; thus on the basis of the defect concentrations we expect the thermal resistance changes parallel to the basal planes to be dependent upon both the sub-microscopic clusters and vacancies in the 30° and 150°C samples and almost entirely due to vacancies in the other two samples. In Fig. 7 we show the increases in thermal resistance as a function of temperature in both the as-irradiated condition and after annealing at 1200°C. It is known from other annealing studies[35] that, from the irradiation temperature to about 900°C, the recovery of physical properties is due to the condensa-

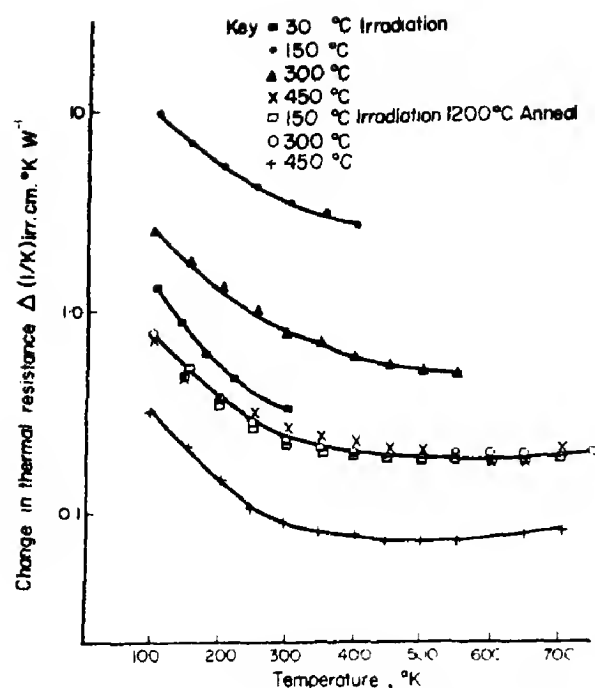


Fig. 7. Irradiation component of thermal resistance parallel to the deposition planes.

tion of sub-microscopic clusters into interstitial loops, either by diffusing to the existing loops or by aggregation. If these now cease to give observable scattering, then the residual resistivity should be wholly occasioned by the vacancies. In accord with our assumptions the 150°C sample recovers considerably by 900°C and the higher-temperature samples much less. If we calculate, using measured lattice parameter changes, the values of x and

C_v for the 150°C sample following Reynolds and Henson[4], then we can estimate the thermal resistance change at room temperature. If we further assume that the 900°C anneal removes the thermal resistance change due to sub-microscopic clusters without changing the vacancy content, then we can compare the separate effects of the two defects with estimates based on equation (30). The agreement in Table 1 is good. In Fig. 8 these are all normalised to unity at 300°K

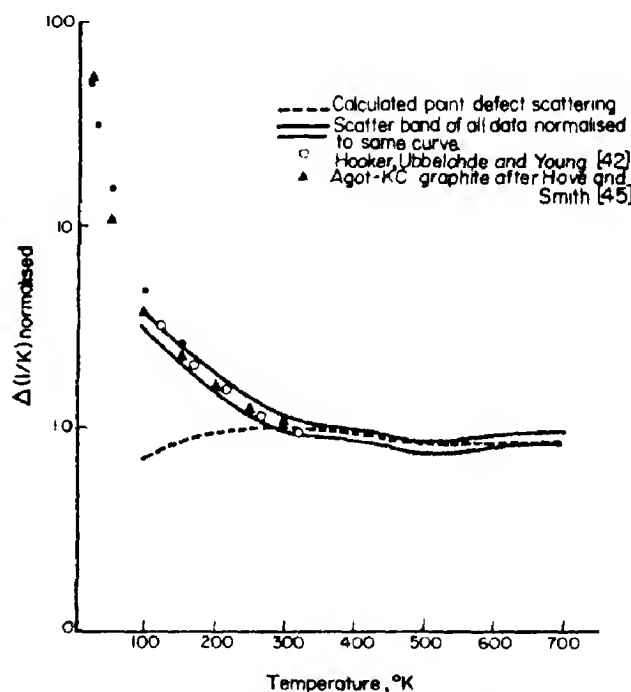


Fig. 8. Point defect scattering in irradiated graphite.

Table 1. Measured and predicted fractional changes in thermal resistance before and after annealing

Irrad. temp. (°C)	Neutron dose (n.v.t.)	Lattice parameter changes		Defect content		Thermal resistance changes $\left(\frac{K_0}{K} - 1\right)$			
		$\frac{\Delta a}{a}$ (%)	$\frac{\Delta c}{c}$ (%)	x (%)	C_v (%)	Before annealing		After annealing at 900°C	
						Calculated	Measured	Calculated	Measured
150	0.83×10^{20}	-0.45	+3.6	1.07	1.5	55	59.5	13.2	15.6
300	3.8	-0.175	+0.37	0.025	1.23	12	13.2	10.2	10.3
450	4.8	-0.07	+0.15	0.01	0.49	4.65	4.4	4.3	3.5

and compared with the theoretical calculation. It may be seen that the agreement is good for temperature $> 300^\circ\text{K}$, but below that temperature the theory predicts a decreasing thermal resistance while the observed one increases with decreasing temperature. It should be noted that the normalised curves seem to be the same whether the thermal resistance is due to vacancies alone or to both vacancies and sub-microscopic clusters.

The high-dose sample was irradiated with the object of examining the contribution to the thermal resistance of the collapsed lines of vacant lattice sites. This sample showed a basal plane contraction of ~ 9 per cent and thus contains ~ 18 per cent collapsed vacancies[3, 27]. The collapsed lines cannot be annealed out at temperatures below 3000°K , whereas all point defects disappear below 2400°K [35]. Thus this annealing study should isolate the effect of collapsed lines. It is found, however, that only a fractional change of thermal resistance equal to 0.34 can be attributed to this and large interstitial loops, the remainder annealing in the range $1100^\circ\text{--}2000^\circ\text{C}$ and therefore attributable to vacancies. The magnitude of the thermal resistance changes suggests $C_r \sim 3$ per cent which is in excellent agreement with estimates of $C_r \sim 3$ per cent from lattice parameter changes of polycrystalline graphite[5]. The temperature dependence of the additional thermal resistance also supports this conclusion. It is, therefore, possible to neglect the effect of collapsed lines and interstitial loops for analysis.

The temperature dependence of the thermal resistance changes contains two surprising features:

- (a) The temperature dependence of the excess thermal resistance is independent of the dominant defect, either the sub-microscopic cluster or the vacancy. In Fig. 8 we show data obtained by Hooker *et al.*[39] in irradiations of pyrolytic graphite with neutrons at 30°C , and also data obtained on reactor grade graphite irradiated at

30°C by Smith and Rasor[40]. At this temperature, the same basic dependence is observed although the interstitial defects clearly make a large contribution. De Combarieu[41] has observed the same behaviour in pyrolytic graphite irradiations at 80°K where again, roughly comparable interstitial/vacancy contributions are expected. It thus seems that the curve in Fig. 8 is characteristic of a point defect in graphite.

- (b) The thermal resistance increases with decreasing temperature. It is well established[14, 5] that we are dealing with point defects and it is to be expected on very general grounds that long-wavelength phonons would be scattered less than short-wavelength phonons by such defects (cf. Ziman[12]). The samples of bromine-doped graphite examined by Smith and Rasor[40], show a similar effect. If the entire temperature dependence of the scattering curve is to be explained, a scattering cross-section *independent* of wave number for small wave number is required, which seems incompatible with point defects, since for this to hold the defect dimensions must be greater than the phonon wavelength.

There are a number of possible explanations of these effects, either proposed previously or considered by us.

Hove and Smith[42] assumed that the defects were large compared with the phonon wavelength, suggesting as a possibility that tilt boundaries normally transparent to phonons trapped point defects and became frequency independent scatterers. However, our results demonstrate clearly that we are dealing with point defects, for which we obtain plausible parameters; it is also clear that the defects are similar in quantity and quality in the pyrolytic graphite and reactor graphite although the latter has many more tilt boundaries.

Dreyfus and Marnard[21] have shown that a defect which produces a coupling between

adjacent layer planes can account for such behaviour. This has previously been suggested for the sub-microscopic interstitial cluster [43], but seems much less likely for a vacancy. This cannot be entirely ruled out since the vacancy produces a surprisingly large c -axis contraction in its own right [4].

Fukuda [44] has shown that the introduction of a defect state in the graphite lattice changes the density of states at the Fermi-level. It is suggested that the new electronic states scatter phonons, and since they are proportional to the number of defects, this appears as an unusual defect scattering behaviour. The excess scattering compared with the σ_a^{-3} calculation gives a thermal resistance $\propto T^{-2}$. This scattering would be particularly effective for the in-plane longitudinal modes which are just those which lead to most of the discrepancy between theory and experiment at low temperatures [8]. The observation of the effect of bromine doping suggests that this may be correct. Hove and Smith [42] dismiss this possibility on the basis of unpublished theoretical work by Hove [45], and a comparison of bromination and irradiation [40]. The latter suggests that only $\sim \frac{1}{3}$ of the scattering in neutron irradiated graphite can be due to the electron phonon effect. Hove's calculations are based on a rigid band from which electrons are trapped and thus do not prove the inadequacy of this effect. It is our conclusion that this effect is the most likely source of the unusual behaviour, and requires further theoretical study.

Other possibilities considered were the existence of a maximum phonon wavelength dictated by the crystallite size, but the effect is clearly independent of L_a over a wide range (3000–30,000 Å); the effect may be due to N -processes coupling the in-plane and out-of-plane modes; or it may be a feature of the lattice in some way. One obvious feature is the sensitivity of C_{44} to lattice strain and its growing importance at long wavelengths.

Two further features of the basal conduc-

tivity are the insensitivity to the collapsed lines of vacant lattice sites and the reasonable estimate obtained of the vacancy loop sizes. At 650° and 900°C, however, the loop sizes obtained are rather small for the scattering cross-section to be independent of wavelength. At long phonon wavelengths the scattering obtained from equation (30) is comparable for lines and point defects for reasonable values of γ_p . In the event, however, any such effect is masked by the increase in the point defect scattering at low temperatures. As the temperature increases, the phonon wavelength decreases, the lines all become effectively long and the scattering is insignificant. In the sample irradiated in D.F.R., theory suggests a spectrum of line lengths of 10–150 Å. Assuming a mean line length of 75 Å, $C_r/C_L \sim 50$ –75, then using the experimental value $\{\Lambda_L\}/\{\Lambda_r\}_p \sim 100$ gives $\gamma_p \sim 0.1$, if a mean value q_a is assumed appropriate to $w \sim kT/\hbar$. Considering the crude approximations made this is in fair agreement with other estimates [46] of γ_p .

Pyrolytic graphite perpendicular to the deposition plane

Considering the graphite to be homogeneous and poreless as before and expressing the thermal conductivity K_\perp in terms of the conductivities K_a and K_c using Klein's [38] relationship suggests $K_\perp = K_c$ and this is also substantiated by Young [47]. However Klein [48] has concluded that cracks parallel to the basal planes act as barriers to heat flow and hence pyrolytic graphite is inadequate to study the c axis conductivity. In view of this uncertainty estimates of the absolute thermal resistance changes may not be reliable although temperature dependences and comparison of annealing changes should be valid.

The measurements of the room temperature changes in thermal resistance on annealing suggest that again we only need to examine the effects of the submicroscopic clusters and point vacancies. Making the same assumptions as before regarding the annealing behaviour

we may compare, at least approximately, the relative effects of the two types of defect. This is done in Table 2 for the low-dose samples.

Thus as regards the hexagonal axis direction the sub-microscopic cluster scatters about twice as much as the vacant lattice site.

In Fig. 9 the temperature dependences of the added thermal resistances are shown, while in Fig. 10 these are normalised at 300°K. The changes are practically temperature independent for $T > 300^\circ\text{K}$, but at lower temperatures there are differences, the thermal resistance increasing with decreasing temperature.

The analysis of crystal conduction published previously [8(b,c)] indicates that it is essentially the out-of-plane vibrations which give most of the hexagonal axis conductivity.

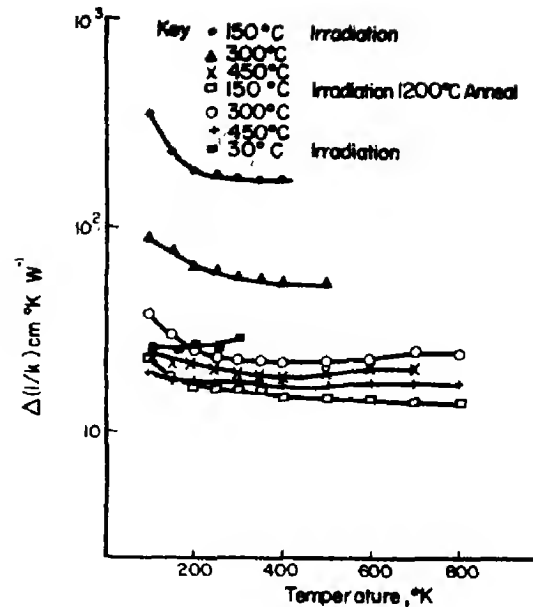


Fig. 9. Irradiation component of thermal resistance perpendicular to the deposition plane.

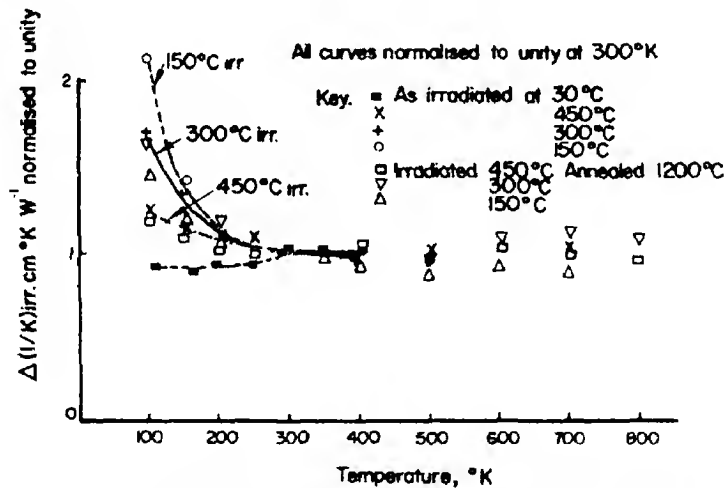


Fig. 10. Irradiation component of thermal resistance perpendicular to the deposition plane.

Table 2. Thermal resistance changes parallel to the hexagonal axis

Irradiation temp. (°C)	Defect content (%)		Fractional changes in thermal resistance			
	x	C_r	As irr.	After 900°C anneal	For unit C_r	For unit x
150	1.07	1.5	16.5	6.05	4.0	9.7
300	0.025	1.23	5.0	4.2	3.4	
450	0.01	0.49	1.65	1.6	3.2	

Equation (12) is adequate for the mass-defect scattering, but does not treat strain field effects—it is by no means clear that the presence of strain fields would simply modify the value of I , so that no analysis has been attempted. A further complexity in analysis is that the conductivity of the annealed 150°C specimen is, for $T > 100^\circ\text{K}$ some 10–15 per cent higher than the unirradiated conductivity.

5. CONCLUSIONS

The experimental data on pyrolytic graphite measured parallel to the deposition plane and polycrystalline graphite both refer to the changes in thermal resistance of the component crystals parallel to the basal planes. It is found that the changes are due to the sub-microscopic cluster, the vacant lattice site and the vacancy loop, and that the interstitial loop and the collapsed line can be neglected. The analysis is generally made on the assumption that the lattice is two-dimensional, which leads to reasonable results above 200°K[8]. The presence of the lattice defects increases the interlayer spacing, tending to make this approximation more valid[8(a)]. The most important contributor to the changes is the vacancy for which the analysis justifies the use of a σ_n^{-3} scattering formula for both strain field and mass-defect scattering in a two-dimensional approximation. It is uncertain whether these vacancies are single, or in the form of di-vacancies, tri-vacancies etc.; however, the classical formula with $S_v^2 = 1$ overestimates the scattering, while the more correct treatment given here shows that the strain field must be a significant part of the total scattering, as would be expected[19].

The value of S_v^2 depends upon the assumption that the lattice is two dimensional and it is clear that the strain field does not approximate to that of the vacancy. However, the same σ dependence is shown and this is substantiated by the very good agreement on the pyrolytic graphite specimen irradiated

at 150°C where comparable vacancy and interstitial effects are noted.

We have suggested a number of possibilities to explain the unexpected increase in thermal resistance with decreasing temperature and consider that the most probable effect is due to the creation of new electronic states as suggested by Fukuda. However, it is an affect associated with *both* the vacancy and the small interstitial cluster.

In the direction parallel to the hexagonal axis, it is apparent that the submicroscopic cluster and the vacancy are the important defects. Equation (14) could give an upper limit to the mean free path, but the lack of knowledge of the strain field, the anharmonic coefficients, and the differences in the normalised curves of Fig. 10 do not suggest that numerical analysis is worthwhile at present.

The data presented here and their analysis show that the changes in thermal conductivity of a graphite crystal parallel to the basal planes are readily understood in terms of the defects postulated to explain the crystal dimensional changes for temperatures $> 300^\circ\text{K}$. However, the lack of difference in the effects attributed to interstitials and vacancies is not understood for lower temperatures. The data show that the same defects are important for the hexagonal axis conductivity but an improved theory of point defect scattering is required to analyse this direction.

Acknowledgements—The authors would like to thank Drs R. Dietendorf and T. J. Clark of the U.S. General Electric Co. for supplying pyrolytic graphite samples. We are indebted to Prof. A. Dreyfus and Dr. A. de Combarieu for a preview of their unpublished work on pyrolytic graphite, to Dr. H. Ashcroft and Mr. M. Toes of the U.K.A.E.A. for programming calculations, and to Mr. J. H. W. Simmons and Dr. W. N. Reynolds of A.E.R.E. Harwell for many discussions.

REFERENCES

1. SIMMONS J. H. W., *Radiation Damage in Graphite*. Pergamon Press, Oxford (1965).
2. REYNOLDS W. N., *Chemistry and Physics of Carbon*, Vol. II. Merce! Dekker, New York (1967).

3. KELLY B. T., *Proc. 2nd Conf. Industrial Carbon and Graphite*, p. 483. Soc. of Chem. Ind., London (1966).
4. HENSON R. W. and REYNOLDS W. N., *Carbon* **3**, 287 (1965).
5. HENSON R. W., PERKS A. J. and SIMMONS J. H. W., U.K.A.E.A. Rep. No. A.E.R.E.-R 5489; *Carbon* **6**, 789 (1968).
6. KOMATSU K. and NAGAMIYA T., *J. phys. Soc. Japan* **6**, 438 (1951).
7. KOMATSU K., *J. phys. Soc. Japan* **10**, 346 (1955); *J. Phys. Chem. Solids* **6**, 380 (1958).
8. KELLY, B. T., (a) *Carbon* **5**, 247 (1967); (b) *Carbon* **6**, 485 (1968); (c) *Carbon* **6**, 571 (1968).
9. SLACK G. A., *Phys. Rev.* **127**, 694 (1962).
10. YOSHIMORI A. and KITANO Y., *J. phys. Soc. Japan* **11**, 352 (1956).
11. ZIMAN J. M., *Can. J. Phys.* **34**, 1257 (1956).
12. ZIMAN J. M., *Electrons and Phonons*. Clarendon Press, Oxford (1957).
13. REYNOLDS W. N. and THROWER P. A., *Phil. Mag.* **12**, 573 (1965).
14. MARTIN D. G. and HENSON R. W., *Phil. Mag.* **9**, 659 (1969); *Carbon* **5**, 313 (1967).
15. MARTIN D. G., U.K.A.E.A. Research Group Rep. No. A.E.R.E. R/R 5269. Vol. 1, p. 243 (1966).
16. HARKER H. and HORSLEY J. B., *Phil. Mag.* **16**, 23 (1967).
17. LIDIARD A. B. and PERRIN R., *Phil. Mag.* **14**, 433 (1966).
18. THROWER, P. A., U.K.A.E.A. Rep. No. A.E.R.E.-R 5296 (1967).
19. KLEMENS P. G., *Solid State Physics*, Vol. 7, p. 1. Academic Press, New York (1958).
20. MORSE P. M. and FESHBACH H., *Methods of Theoretical Physics*. McGraw-Hill, New York (1953).
21. DREYFUS B. and MAYNARD R., *J. Phys.* **28**, 955 (1969).
22. CARRUTHERS P., *Rev. mod. Phys.* **33**, 1, 92 (1961).
23. ELLIOTT H. A., *Phil. Soc., Cambridge* **44**, 4, 522 (1948).
24. HOOKER C. N., UBELLOHDE A. R. and YOUNG D. A., *Proc. R. Soc.* **276A**, 83 (1963).
25. MOSS M., *J. appl. Phys.* **36**, 10, 3308 (1965).
26. BELL J. C. and O'DRISCOLL W. G., *Mats. for Nucl. Eng.* p. 171. Temple Press, London (1960).
27. KELLY B. T., MARTIN W. H. and NETTLEY P. T., *Phil. Trans. R. Soc.* **260A**, 51 (1966).
28. TAYLOR R., *Br. J. appl. Phys.* **16**, 509 (1965).
29. BELL J. C., BRIDGE H., COTTRELL A. H., GREENOUGH G. B., REYNOLDS W. N. and SIMMONS J. H. W., *Phil. Trans. R. Soc.* **154A**, 361 (1962).
30. MARTIN W. H. and CLARE D. M., *Nucl. Sci. Engng* **18**, 468 (1964).
31. MARTIN W. H. and PRICE A. M., *J. nucl. Engng* **21**, 359 (1967).
32. KELLY B. T., JONES D. and JAMES A., *J. nucl. Mater.* **7**, 279 (1962).
33. SIMMONS J. H. W., Private communication.
34. REYNOLDS W. N., U.K.A.E.A. Rep. No. A.E.R.E. M/R 2821.
35. KELLY B. T., MARTIN W. H., PRICE A. M., DOLBY P. and SMITH K., *J. nucl. Mater.* **20**, 195 (1966).
36. TAYLOR R., GILCHRIST K. and POSTON J., *Carbon* **6**, 537 (1968).
37. TSUZUKU T., *J. phys. Soc. Japan* **16**, 407 (1961).
38. KLEIN C. A., *Chemistry and Physics of Carbon II*, p. 225. Marcell Dekker, New York (1964).
39. HOOKER C. N., UBELLOHDE A. R. and YOUNG D. A., *Proc. R. Soc.* **284A**, 17 (1965).
40. SMITH A. W. and RASOR N. S., *Phys. Rev.* **104**, 855 (1956).
41. De COMBARIEU A., *J. Phys.* **28**, 951 (1969).
42. HOVE J. E. and SMITH A. W., *Phys. Rev.* **104**, 892 (1956).
43. GOGGIN P., *Proc. 2nd Conf. Industrial Carbon and Graphite*. Soc. Chem. Ind., London (1966).
44. FUKUDA Y., *J. phys. Soc. Japan* **20**, 353 (1965).
45. HOVE J. E., North Amer. Aviation Rep. No. NAA-SR-1398 (1950).
46. NELSON J. B. and RILEY D. P., *Proc. phys. Soc.* **57**, 477 (1945).
47. YOUNG D. A., *Carbon* **6**, 135 (1968).
48. KLEIN C. A., Private communication.

ISOTOPE EFFECT OF CARBON DIFFUSION IN AN Fe-Si ALLOY

M. WUTTIG and E. T. YEN*

Department of Metallurgical Engineering, University of Missouri, Rolla, Mo. 65401, U.S.A.

(Received 29 January 1969)

Abstract—The isotope effect of carbon diffusion in dilute iron silicon alloys containing ^{28}Si and ^{30}Si has been measured below room temperature using the disaccommodation technique. The time dependence of the reluctivity has been analysed in terms of two relaxation processes which are due to the reorientation of carbon interstitials in Fe-Fe and Fe-Si sites respectively. The ratio of the relaxation times of the two carbon isotopes ^{13}C and ^{12}C τ_{13}/τ_{12} is 1.037 for the former and 1.007 for the latter process in the Fe- ^{28}Si alloy. The ratios of the relaxation times of the same carbon isotope ^{12}C contained in a dilute Fe- ^{30}Si and in a dilute Fe- ^{28}Si alloy respectively τ_{30}/τ_{28} are 0.995 and 1.020 for the two processes mentioned. These results demonstrate clearly the many body aspects of the diffusional process.

INTRODUCTION

THE AIM of studies of the isotope effect of diffusion is to help determine a diffusion mechanism. Generally such studies[1–10] yield the product of $f \cdot \Delta K$ of the correlation factor f and the fraction of the activation energy in the decompositional mode ΔK . In cases where this product is less than about 0.5 (AgBr[11], δ -Fe[12], Na[13]) so that the range of f embraces values corresponding to more than one mechanism the results of such studies alone do not lead to an unambiguous identification of the diffusion mechanism[14]. This difficulty does not exist if the mechanism of diffusion can be inferred from evidence other than isotope effect studies as is the case for interstitial diffusion. Here, the correlation factor is unity and isotope studies yield ΔK directly. Isotope studies of interstitial diffusion have shown that in an unrelaxed lattice $\Delta K = 1$ [2]. It is of interest to investigate how ΔK differs from one in the case of interstitial diffusion in a relaxed environment.

The extra anelastic effects[15–19] and disaccommodations[20, 21] observed in ternary iron based alloys are well known. They are

generally interpreted as being due to the reorientation of interstitials located next to substitutionals with respect to local stresses and the direction of the local spontaneous magnetization. As interstitials sitting next to a small substitutional reside in a relaxed environment a study of the isotope effect on the extra disaccommodation offers an opportunity to investigate the influence of the lattice relaxation on ΔK . This paper reports on studies of the isotope effect on the extra disaccommodation of Fe-Si-C alloys where the extra anelastic effects[17] and disaccommodations[20] are well established.

EXPERIMENTAL PROCEDURE AND RESULTS

The experimental approach consisted of preparing pairs of Fe-Si-C alloys matched as closely as possible except for the kinds of isotopes contained and measuring the disaccommodation under identical conditions, so that the expected small changes of the relaxation times could be determined reliably.

Two pairs of alloys were prepared by induction melting iron (99.9%) and silicon (99.999%) in alumina crucibles (99.7%) in an argon (99.995%) atmosphere at 600 mm Hg. The ingots were swaged, recrystallized, decarburized, and denitrided and recarburized

*Submitted in Partial Fulfillment of the Requirements for the M. S. Degree. Now at IBM, Fishkill, N.Y.

in a closed system. The methane used to prepare the Fe-²⁸Si-¹³C alloy contained 93.9% ¹³CH₄ and the actual isotopic composition of the ³⁰Si was 95.20% ³⁰Si, 0.53% ²⁹Si and 4.28% ²⁸Si. Natural isotope mixtures were used for ¹²C and ²⁸Si. The compositions of the matched alloy pairs are given in Table 1. The silicon content was determined by chemical analysis. No silicon concentration gradients could be detected along the length of the swaged rod. The carbon content was estimated from the disaccommodation amplitude.* The carbon was in solid solution as determined by measurements of the initial permeability of all specimens[22].

The disaccommodation was measured as described[23]. The samples were positioned as identically as possible in the center of the solenoid with a thermocouple in contact with the sample. The temperature at the position of this thermocouple would be controlled and reproduced to within 0.02°C. The disaccommodation measurements of pairs numbers 1 and 2 were carried out at -3°C and -14°C respectively. The results of a typical run are shown in Fig. 1.

The reluctivity data were analysed in terms of two independent[24] and two interdependent exponentials with the relaxation times

Table 1. Composition of investigated alloys

Matched pair (No.)	Isotope composition	Content of alloying elements (wt.%)	
		Si	C
1	Fe, ²⁸ Si, ¹³ C	1.40	0.003
	Fe, ²⁸ Si, ¹² C	1.40	0.003 ₂
2	Fe, ³⁰ Si, ¹² C	1.21	0.004
	Fe, ²⁸ Si, ¹² C	1.22	0.005

*This estimate is correct only to within a factor of three as the influence of the silicon on the disaccommodation amplitude is not known exactly. In the context of this paper, however, this information is sufficient to judge whether or not the difference of the carbon contents of a given pair of specimens can be neglected.

having a lognormal distribution around a mean time τ of half width β [25]. The value of the β 's for the first of the two exponentials with shorter τ due to the reorientation of carbon interstitials in Fe-Fe sites was set to 0.6 in accord with the half width of the Gaussian distribution of the published damping data in binary Fe-C alloys[26, 27]. The value of β_2 for the second of the two exponentials with larger τ due to the reorientation of carbon interstitials in Fe-Si sites was determined experimentally. Figure 2 shows the deviations of the data from the least square regressions and it can be seen that the deviations are smallest for $\beta_2 = 1.0$ especially for long times. The same information is contained in the variances listed in Tables 2 and 3 which give a summary of all results obtained. The oscillatory nature of the deviations can be traced back to the choice of the fully relaxed reluctivity which is discussed below. The analysis of the reluctivity data in terms of two interdependent exponentials made use of the facts that the ratio of the relaxation times for the reorientation of the ¹³C and ¹²C interstitials in Fe-Fe sites is known to be equal to the square root of the ratio of the isotopic masses[2] and that the relaxation times for the reorientation of the carbon interstitials in Fe-Fe sites should be independent of the isotopic mass of the silicon. Thus, the reluctivity data for the matched Fe-²⁸Si-¹²C, Fe-²⁸Si-¹³C pair were analysed simultaneously with the constraint $\delta_1 = \tau_{13-1}/\tau_{12-1} = 1.038$ while the data for the matched Fe-³⁰Si-¹²C, Fe-²⁸Si-¹²C pair were analysed simultaneously with the constraint $\Delta_1 = \tau_{30-1}/\tau_{28-1} = 1.000$. The results of these analyses are shown in Tables 2 and 3 and it can be seen that they are essentially the same for both modes of analysis.

The accuracy of the data depends on the reproducibility and control of the measuring temperatures and compositions of a matched pair as well as on the choice of the fully relaxed reluctivities $r(\infty)$. The temperature variations and reproducibility indicated above

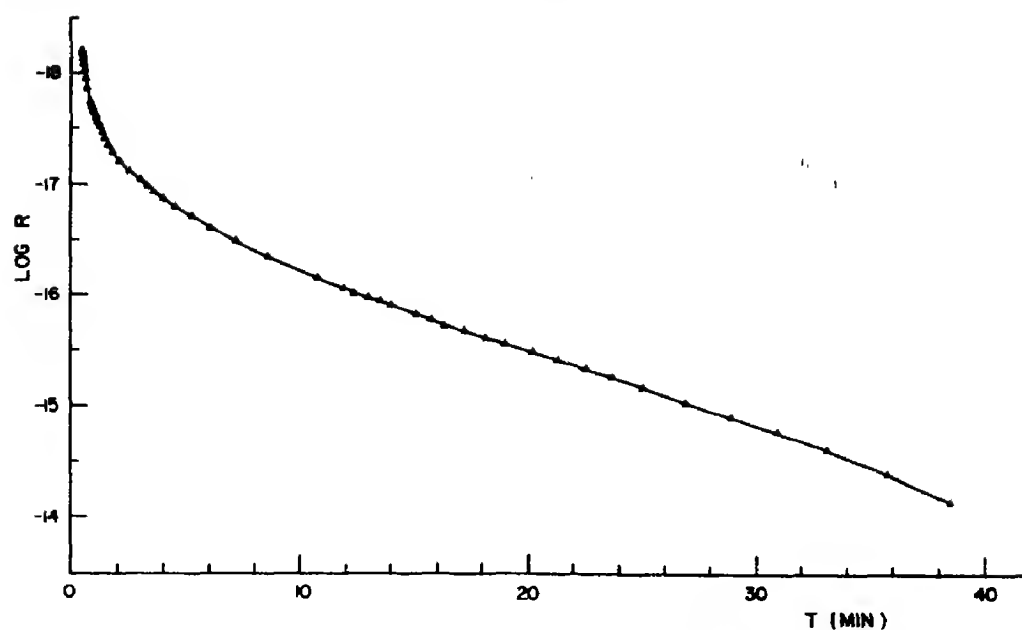


Fig. 1. Time dependence of the reluctivity r of a $\text{Fe}+^{28}\text{Si}+^{12}\text{C}$ alloy at -3.10°C .

Table 2. Carbon relaxation times τ , ratios of carbon relaxation times δ and variances for the matched pair of $\text{Fe}+^{28}\text{Si}+^{13}\text{C}$ and $\text{Fe}+^{28}\text{Si}+^{12}\text{C}$ alloys

Mode of analysis	β_1	β_2	τ_{111} (min)	τ_{121} (min)	τ_{132} (min)	τ_{122} (min)	δ_1	δ_2	Var_{13}	Var_{12}
Lognormal analysis	0.6	0.8	0.410	0.395	8.549	8.468	1.0373	1.0095	1.646	1.868
	0.6	1.0	0.382	0.368	7.593	7.541	1.0366	1.0069	1.242	1.288
	0.6	1.2	0.351	0.339	6.555	6.542	1.0368	1.0048	1.919	2.233
Lognormal analysis with constraint $\delta_1 = 1.0382$	0.6	0.75	0.417	0.401	8.770	8.67	1.0382	1.0106	1.701	1.900
	0.6	1.0	0.382	0.368	7.597	7.538	1.0382	1.0077	1.267	1.290
	0.6	1.25	0.344	0.331	6.293	6.262	1.0382	1.0048	1.899	2.241

Table 3. Carbon relaxation times τ , ratios of carbon relaxation times Δ and variances for the matched pair of $\text{Fe}+^{30}\text{Si}+^{12}\text{C}$ and $\text{Fe}+^{28}\text{Si}+^{12}\text{C}$ alloys

Mode of analysis	β_1	β_2	τ_{111} (min)	τ_{121} (min)	τ_{132} (min)	τ_{122} (min)	Δ_1	Δ_2	Var_{30}	Var_{28}
Lognormal analysis	0.6	0.4	2.364	2.377	40.77	40.15	0.994	1.016	1.267	1.145
	0.6	0.6	2.288	2.300	38.12	37.42	0.995	1.019	0.551	0.543
	0.6	0.8	2.189	2.200	34.61	33.85	0.995	1.022	0.228	0.581
	0.6	1.0	2.071	2.084	30.44	29.69	0.994	1.026	0.417	1.410
Lognormal analysis with $\Delta_1 = 1.000$	0.6	0.4	2.417	2.417	42.43	41.78	1.000	1.015 ₅	1.193	1.196
	0.6	0.6	2.303	2.303	38.50	37.80	1.000	1.018 ₇	0.578	0.585
	0.6	0.8	2.197	2.197	34.62	33.86	1.000	1.022 ₀	0.260	0.582
	0.6	1.0	2.011	2.011	28.93	28.21	1.000	1.025 ₄	0.553	1.494

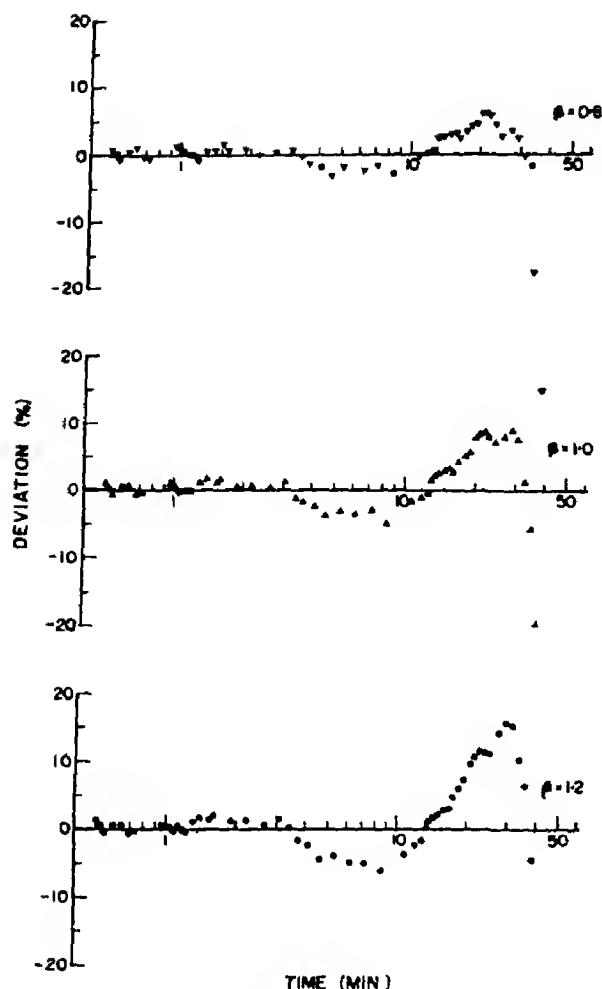


Fig. 2. Relative deviation of experimental reluctivity data from the fitted curve using the lognormal analysis with various half width β_2

yield an error of τ of ± 0.15 per cent for an activation energy of 0.9 eV. Compositional variations can be neglected on account of the large average spacing between carbon interstitials and the good reproducibility of the silicon contents (see Table 1). The influence of the choice of $r(\infty)$ was minimized by choosing $r(\infty) = r(t_\infty)$ where the same times $t_\infty \approx 5\tau$ were taken for a matched pair. In this case the deviations of δ_i and Δ_i from their true values due to the choice of $r(\infty)$ are less than -0.3 per cent as shown in the Appendix. Thus, the overall error ϵ of δ_i and Δ_i can be estimated to be within the

range $-0.3\% \leq \epsilon \leq +0.6\%$. The value obtained for Δ_i indicates that the errors of the experimentally determined ratios of the relaxation times are within this range.

DISCUSSION

The relaxation times $\tau_{0.1}$ for the reorientation of carbon interstitials in Fe-Fe sites are in good agreement with published data[28] as is the ratio δ_1 for pair number 1[2]. For instance, a value of $\tau = 0.41$ min is calculated from Wert's results which compares well with the value of $\tau_{13.1} = 0.38$ min listed in Table 2. As the mean isotopic masses of the ^{13}C and ^{12}C used in the experiment are 12.94 and 12.01 respectively the ratio of the square root of these mean masses is 1.038 which corresponds very well with the average $\delta_1 = 1.037$ obtained from Table 2. This result indicates that the decompositional mode of a carbon interstitial in iron is a local mode[14].

The isotope effect on the reorientation of carbon interstitials in Fe-Si sites $\delta_2 \approx \tau_{13.1}/\tau_{12.2}$ is remarkably different from δ_1 as can be seen from Table 2 (both analyses). From the value of $\delta_2 = 1.007$ and Mullen's[5] equation (8), it follows that $\Delta K \approx 0.19$ indicating that only 19 per cent of the kinetic energy in the decompositional mode is carried by the reorienting carbon interstitial. It must be concluded then that a major fraction of the kinetic energy of the decompositional mode is carried by the silicon substitutional adjacent to the reorienting carbon interstitial. Thus, a change of the mass of this silicon substitutional should change the relaxation time of a given carbon interstitial residing in an Fe-Si site. This is clearly demonstrated by the values of $\Delta_2 = \tau_{30.2}/\tau_{28.2}$ shown in Table 3.

As the ionic radius of silicon is smaller than the ionic radius of iron and since the lattice parameter of iron decreases upon the addition of silicon[29] it must be concluded that the unusually low value of δ_2 is due to the relaxation of the lattice around an Fe-Si interstitial site. It may be envisioned that the silicon substitutional has to 'move out of the

way' in order to enable the adjacent carbon to start moving toward a neighboring Fe-Si site. Consequently, the decompositional mode would trigger the motion of the carbon interstitial from the activated position to its 'new' Fe-Si site and the motion of the silicon back to its equilibrium site.

It remains to be seen how δ_2 and Δ_2 compare quantitatively. If it is assumed that all projections of the ionic displacements on the normal coordinate of the decompositional mode are zero except for the carbon and silicon displacements the effective mass m^* determining the isotope effect is given by [30]

$$m^* = m_C \cdot c^2 + m_{Si} (1 - c^2) \quad (1)$$

where m_C and m_{Si} are the actual mean masses of the carbon and silicon isotope mixtures, and c is the cosine of the projection angle of the carbon interstitial displacement on the normal coordinate of the decompositional mode. Using equation (1) and the measured value of δ_2 , Δ_2 is 'predicted' to be 1.024 which is slightly larger than Δ_2 for the minimum variance listed in Table 3. This would indicate that the projections of the displacements of the iron ions surrounding the Si-C pair on the normal coordinate of the decompositional mode are not equal to zero although they are small. Consequently the decompositional mode of the Si-C pair is only weakly influenced by its surroundings. Since only this mode is affected by the isotopic substitution [14] its nature can be analysed from the model shown in Fig. 3. This model results in two kinds of modes, a and b , as indicated in Fig. 3. The frequencies ω_a and ω_b of these modes are given by [31]

$$\omega_{a,b}^2 = k_2 / (2m_C) \{ 1 + \gamma + (1 + \Gamma) m_C / m_{Si} \mp [(1 + \gamma + (1 + \Gamma) m_C / m_{Si})^2 - 4(\gamma\Gamma + \gamma + \Gamma) m_C / m_{Si}]^{1/2} \} \quad (2)$$

where $\gamma = k_1/k_2$, $\Gamma = k_3/k_2$, k_i = spring constants as indicated in Fig. 3.

The ratios $\delta_{a,b} = \omega_{a,b,12} / \omega_{a,b,13}$ and $\Delta_{a,b}$

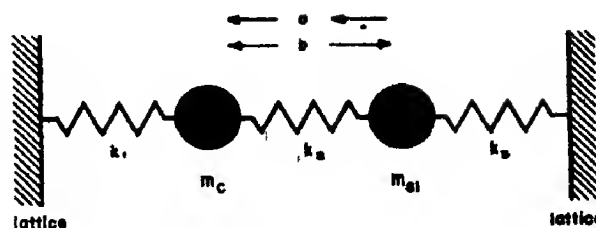


Fig. 3. Model for the analysis of the nature of the decompositional mode of the Si-C pair. See text for symbols.

$= \omega_{a,b,28} / \omega_{a,b,30}$ are shown in Figs. 4 and 5 respectively as a function of Γ with γ as a parameter. Also shown in these figures are the experimental values δ_2 and Δ_2 together with the estimated error limits. As can be seen from these figures, the values of δ_2 and Δ_2 agree both with the expected ratios δ_a and Δ_a of mode a if $\Gamma < 1$ and δ_b and Δ_b of mode b if $\Gamma > 1$. Since the case $\Gamma > 1$ has to be excluded because it is inconsistent with the assumption of a weak coupling it must be concluded that the decompositional mode resembles mode a . The uncertainty of δ_2 and Δ_2 does not permit quantitative conclusions on the ratios γ and Γ .

Throughout this discussion the assumption has been made that the activated state can be treated as an equilibrium state. While this assumption cannot be justified conceptually [32, 33] the results of this work are not in contradiction with it. It would appear that the corrections to the isotope effects investigated in this work to be made if the irreversibility of the diffusion process is taken into account are so small that they cannot be detected by the technique applied.

CONCLUSIONS

The conclusions to be drawn from this work are: The Si-C defect can be treated as a pair which is only weakly coupled to the iron lattice. The measured isotope effects can be rationalized within the framework of equilibrium statistical mechanics. The decompositional mode of the Si-C pair is a mode in which both constituents oscillate in the same direction.

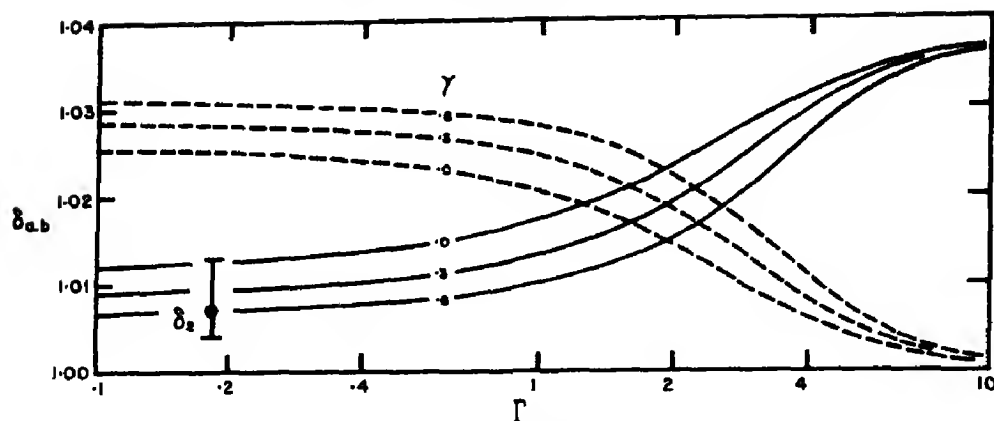


Fig. 4. Calculated ratios of the relaxation times $\delta_{a,b}$ as a function of the ratios of the spring constants γ and Γ . See text for symbols. — δ_a , mode a ; ---- δ_b , mode b .

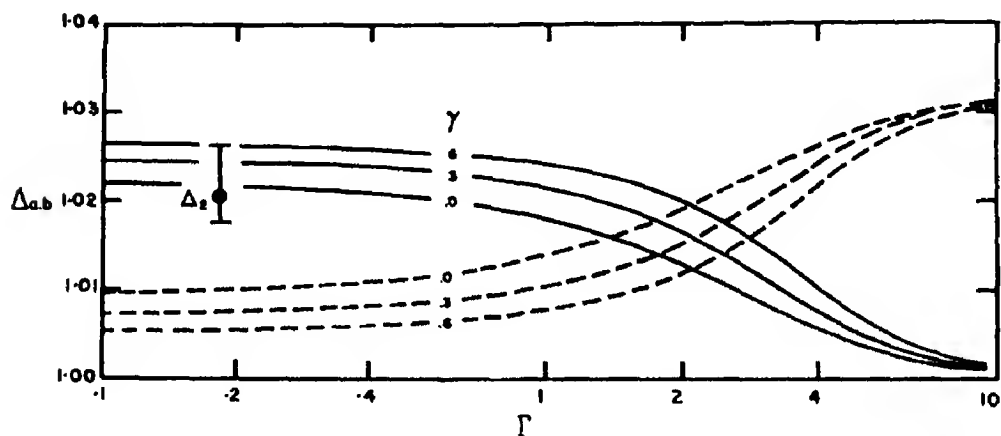


Fig. 5. Calculated ratios of the relaxation times $\Delta_{a,b}$ as a function of the ratios of the spring constants γ and Γ . See text for symbols. — Δ_a , mode a ; ---- Δ_b , mode b .

Acknowledgements—The authors would like to thank Mr. Robert Crosby of the United States Bureau of Mines, Rolla Metallurgical Research Center, for the preparation of Fe-Si alloys. They would also like to gratefully acknowledge the assistance of Bryce Shriver.* This work was supported by the National Science Foundation (grant No. GK 2678) and the American Iron and Steel Institute (Project No. 203).

REFERENCES

1. FRANK R. C., LEE W. L. and WILLIAMS R. L., *J. appl. Phys.* **29**, 898 (1958).
2. BOSMAN A. J., Thesis, Amsterdam University (1960).
3. EICHENANER W., LOSER W. and WITTE H., *Z. Metallk.* **56**, 287 (1965).
4. HEUMANN Th. and PRIMAS D., *Z. Naturf.* **21a**, 260 (1966).
5. MULLEN J. G., *Phys. Rev.* **121**, 1649 (1961).
6. PETERSON N. L., *Phys. Rev.* **136**, 568 (1964).
7. ROTHMAN S. J. and PETERSON N. L., *Phys. Rev.* **154**, 552 (1967).
8. PETERSON N. L. and ROTHMAN S. J., *Phys. Rev.* **154**, 558 (1967).
9. PETERSON N. L. and ROTHMAN S. J., *Phys. Rev.* **163**, 645 (1967).
10. COLEMAN M. G., Thesis, University of Illinois (1967).
11. PETERSON N. L. and BARR L. W., Private communication.
12. WALTER C. M. and PETERSON N. L., *Phys. Rev.* **178**, 922 (1969).
13. MUNDY J. N., BARR L. W. and SMITH F. A., *Phil. Mag.* **14**, 785 (1966).
14. LeCLAIRE A. D., *Phil. Mag.* **14**, 1271 (1966).
15. DIJKSTRA L. J. and SLADEK R. J., *Trans. AIME* **197**, 69 (1953).
16. DICKENSCHIED W. and SEEMANN H. J., *Rev. Met.* **55**, 872 (1958).
17. ENRIETTO J. F., *Trans. AIME* **224**, 1119 (1962).

*Partially supported by an Olin Summer Research Fellowship.

18. GLADMAN and PICKERING, *J. Iron Steel Inst.* **203**, 1212 (1965).
19. RITCHIE and RAWLINGS, *Acta. Metall.* **15**, 491 (1967).
20. HAMPE W. and WIDMAN D., *Z. angew. Phys.* **15**, 360 (1963).
21. GRAHAM R. H. and WUTTIG M., *Scripta Met.* **3**, 9 (1969).
22. WUTTIG M., STANLEY J. T. and BIRNBAUM H. K., *Phys. Status Solidi* (1968).
23. WUTTIG M. and BIRNBAUM H. K., *J. Phys. Chem. Solids* **27**, 225 (1966).
24. AARON H. B., WUTTIG M. and BIRNBAUM H. K., *Acta. Metall.* **16**, 269 (1968).
25. NOWICK A. S. and BERRY B. S., *IBM JI Res. Dev.* **5**, 297 (1961).
26. WERT C. A. and ZENER C., *Phys. Rev.* **76**, 1169 (1949).
27. SWARTZ J., Private communication.
28. WERT C., *Phys. Rev.* **79**, 601 (1950).
29. LIHL F. and EBEL H., *Arch. Eisenhüttenwesen* **32**, 489 (1961).
30. VINEYARD G. H., *J. Phys. Chem. Solids* **3**, 121 (1957).
31. See for instance SOMMERFELD A., *Mechanik*, p. 107. Akademic, Leipzig (1954).
32. PEGEL B., *Phys. Status Solidi* **22**, 223 (1967).
33. PEGEL B., *Phys. Status Solidi* **22**, K45 (1967).

APPENDIX

Consider the exponential relaxation of a quantity x

$$x(t) = x(0) \exp(-t/\tau). \quad (\text{A-1})$$

A relaxation time τ is obtained by fitting the experimental data $x(t_i) = x'(t_i) - x'(\infty)$ to equation (A-1). For this purpose it is necessary to determine $x'(\infty)$. In practice $x'(\infty)$ is approximated by $x'(t_\infty)$ where t_∞ is so large that $x(t_\infty) \ll x(0)$. In Fig. (A-1) it is shown how the ratio τ_a/τ depends on t_∞/τ . τ_a is the apparent relaxation time as obtained from the least-square fit analysis which was applied to the reluctivity data.

Consider now two relaxation processes numbers 1 and 2 characterized by the true relaxation times τ_1 and $\tau_2 = \tau_1(1 + \xi)$ where $\xi \leq 0.042$ as is the case for the isotope effects investigated. If the same time $t_{x2} = 5\tau_2$ is chosen for both processes as was done in the main body of this paper t_{x1} is given by $t_{x1} = 5\tau_1(1 + \xi)$. From Fig. (A-1) it follows then that $1.000 \geq \tau_{a2}/\tau_{a1} \cdot \tau_1/\tau_2 \geq 0.997$.

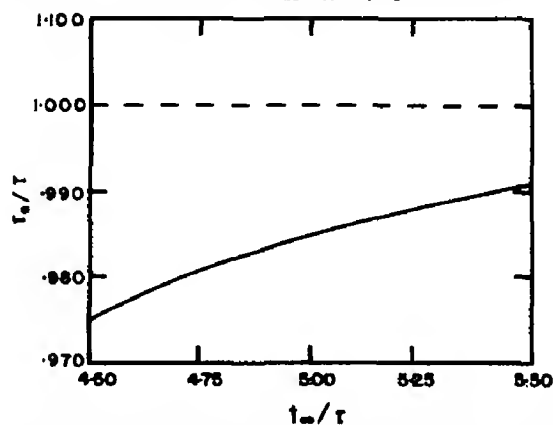


Fig A-1. Normalized apparent relaxation time as a function of the normalized time of termination of a relaxation measurement. See text for symbols.

ANISOTROPIE DE LA SUSCEPTIBILITÉ PARAMAGNÉTIQUE DES MONOCRISTAUX DE TERRES RARES: Gd, Tb, Dy, Ho et Er

R. ALEONARD, P. BOUTRON et D. BLOCH

Laboratoire d'Electrostatique et de Physique du Métal, Cedex 160, Grenoble, France

(Received 14 January 1969)

Résumé—On décrit l'appareillage expérimental mis au point afin d'étudier la susceptibilité paramagnétique d'un cristal en fonction de la direction du champ appliqué. On donne les principaux résultats obtenus pour Gd, Tb, Dy, Ho et Er. La susceptibilité varie sinusoïdalement avec la direction du champ appliqué, et l'anisotropie de la susceptibilité n'est fonction que du premier paramètre de champ cristallin. La mesure de la variation thermique de l'anisotropie de la susceptibilité fournit ainsi une méthode pour la détermination de la variation thermique du paramètre de champ cristallin. Cette variation est en accord avec celle prévue, en raison de la dilatation thermique, par le modèle des charges ponctuelles. Les paramètres de champ cristallin obtenus sont comparés à ceux fournis par la théorie de Kasuya ainsi qu'à ceux déduits des mesures d'aimantation à basse température.

Abstract—We describe the experimental techniques utilized to study the paramagnetic susceptibility of a crystal as a function of the applied field. We give the main results obtained for Gd, Tb, Dy, Ho and Er. The susceptibility varies sinusoidally with the direction of the applied field. The anisotropy of the susceptibility is a function only of the first crystalline field parameter. The measurement of the thermal variation of the anisotropy of the susceptibility thus provides a method for the determination of the thermal variation of the crystalline field parameter. This variation is in agreement with that given by a point charge model, due to the thermal dilatation. The crystalline field parameters obtained are compared to those given by the theory of Kasuya as well as those deduced from the measurement of the low temperature magnetization.

LES TERRES rares métalliques: Gd, Tb, Dy, Ho et Er possèdent la même structure cristalline, du type hexagonal compact. Les couches externes atomiques $5s$ et $5p$ sont pleines et restent localisées; les électrons $5d$ et $6s$ forment un nuage électronique au milieu duquel sont régulièrement disposés les ions terres rares positifs trivalents. Comme la couche interne $4f$ est incomplète, le moment magnétique du métal résulte essentiellement de la combinaison des moments orbitaux et de spin des électrons $4f$. Le couplage entre les moments magnétiques atomiques peut être attribué à des interactions d'échange à longue distance, via les électrons de conduction. La distribution des charges électriques donne lieu à un champ électrique cristallin qui contribue de manière importante aux propriétés magnétiques de ces matériaux. On leur attribue généralement l'origine de l'anisotropie

magnétocristalline. La possibilité récente d'obtenir d'une part les monocristaux avec des dimensions et une pureté suffisantes et d'autre part les champs magnétiques intenses nécessaires pour leur saturation a conduit à des progrès notables dans la description de leur comportement dans le domaine des températures où elles sont magnétiquement ordonnées. Les progrès de la théorie du champ cristallin et une meilleure compréhension des propriétés des électrons de conduction n'ont cependant pas encore permis de prévoir quantitativement les résultats obtenus. Aussi nous a-t-il semblé profitable d'entreprendre l'étude à la fois expérimentale et théorique des effets de l'anisotropie magnétocristalline dans le domaine paramagnétique. Nous décrivons, paragraphe 1, l'appareillage expérimental qui a été mis au point afin d'étudier la variation de la susceptibilité paramagnétique en fonction

de la température et de l'orientation du champ magnétique par rapport aux axes cristallins. Nous donnons, paragraphe 2, les principaux résultats obtenus pour Gd, Tb, Dy, Ho et Er. Nous établissons, paragraphe 3, les expressions théoriques de la variation thermique de la susceptibilité en fonction de la direction du champ appliqué. Nous analysons, paragraphe 4, les résultats expérimentaux au moyen des expressions ainsi établies et nous comparons les informations ainsi obtenues à celles déduites de l'analyse des courbes d'aimantation dans le domaine magnétiquement ordonné.

1. DISPOSITIF EXPERIMENTAL

Nous avons utilisé une balance de translation du type Foëx et Forrer[1] (Fig. 1). L'échantillon (1) est placé dans un champ magnétique non uniforme créé par un électro-aimant dont les pôles ont une forme appropriée. On le fixe au moyen d'une résine epoxy à l'extrémité inférieure d'une tige en alumine

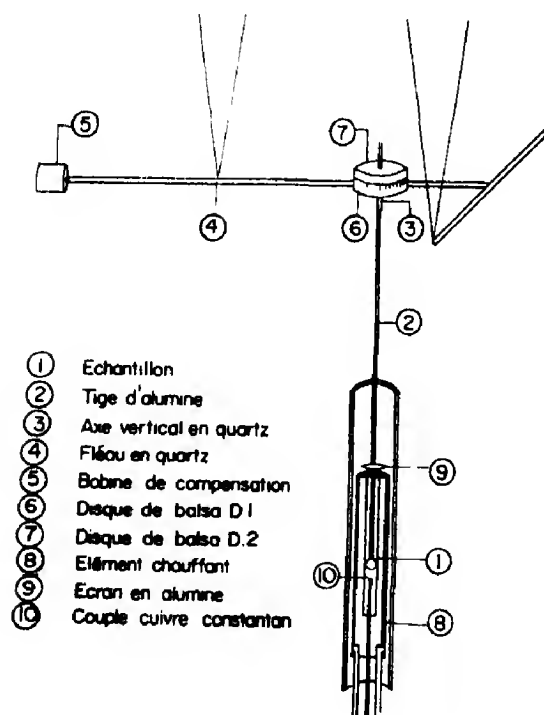


Fig. 1. Dispositif expérimental pour la mesure de l'anisotropie de la susceptibilité.

(2), qui coulisse à l'intérieur d'un cylindre en quartz (3) solidaire du fléau (4) de la balance. Le fléau est suspendu par cinq fils, ne lui accordant qu'un degré de liberté suivant la direction du gradient de champ. L'attraction de l'échantillon dans le champ non uniforme est équilibrée par l'attraction, dans le champ d'un aimant permanent, d'une bobine de compensation (5) parcourue par un courant ajustable. Un dispositif est prévu afin de permettre une rotation de l'échantillon autour de l'axe de la tige en alumine. Il est constitué par deux disques en balsa. Le premier (6), est solidaire du fléau de la balance, et le second (7) de la tige en alumine. Il s'appuie, par gravité, sur le premier. On fait tourner de cinq en cinq degrés l'échantillon en soulevant le disque (7) et en lui imprimant un mouvement de rotation. Les forces de frottement entre les disques de balsa permettent de compenser les forces d'anisotropie en présence du champ magnétique. L'échantillon est placé au centre d'une enceinte thermostatée (8) en matériau non magnétique, à température régulée à mieux de $1/10$ de degré entre 6° et 95°C , au moyen d'un fluide circulant dans un double enroulement en hélice. Des écrans en alumine (9) fixés sur la tige supportant l'échantillon, permettent de réduire l'importance des courants de convection. La température est mesurée au moyen d'un thermocouple préalablement étalonné (10) dont la soudure est placée au voisinage de l'échantillon. Le gradient de température auquel est soumis l'échantillon est négligeable. L'appareil est étalonné au moyen d'une substance de susceptibilité connue. Nous avons utilisé le pyrophosphate de manganèse comme substance étalon. Le support présente une susceptibilité qui se combine avec celle de l'échantillon et il y a lieu d'effectuer une correction. L'échantillon monocristallin taillé sous forme de sphère de 6 mm de diamètre est orienté en utilisant la méthode de Laue. Il est ensuite fixé sur le support en alumine suivant une direction choisie à l'avance. La précision angulaire est de l'ordre de un degré.

2. RESULTATS EXPERIMENTAUX

Les monocristaux de terres rares utilisés ont été achetés à Metals Research, à Cambridge (Angleterre). La pureté chimique annoncée est de 99,9%. Leur pureté cristallographique a été vérifiée aux rayons X. Ils ont été utilisés pour la détermination de l'effet de la pression hydrostatique sur les températures d'ordre magnétiques[2]. Leur comportement sous champ magnétique intense continu a fait l'objet d'études précises[3]. On a mesuré la susceptibilité paramagnétique dans le plan de base, perpendiculaire à l'axe c du cristal, ainsi que dans un plan perpendiculaire à l'axe a ou à l'axe b et contenant ainsi l'axe c . Les expériences ont été réalisées à diverses températures maintenues constantes. On s'est assuré par des mesures jusqu'à 2300 Oe (Gd) et 3600 Oe (Tb, Dy, Ho et Er) que la susceptibilité était, dans ces limites et à la précision des expériences, indépendante de la valeur du champ appliqué. Des mesures effectuées à 300°K (Dy, Ho, Er) et à 316°K (Gd) ont montré que l'anisotropie paramagnétique dans le plan de base était négligeable, la dispersion des points expérimentaux étant inférieure à 5 p.mille; aussi n'en avons nous pas tenu compte pour la suite. La variation angulaire de la susceptibilité, dans le plan contenant l'axe c a été analysée en série de Fourier[4]. Dans tous les cas la susceptibilité peut être décrite au moyen d'un terme constant et d'un terme harmonique de périodicité 180°. A la précision des expériences, la contribution des termes harmoniques de périodicité plus faible est négligeable.

(a) Gadolinium

Au voisinage du point de Curie l'axe de facile aimantation est l'axe c du cristal. Les mesures effectuées entre 302,7° et 361,4°K ne permettent pas de déterminer la constante de Curie du gadolinium, en raison de l'ordre à courte distance qui subsiste à une température notablement supérieure à la température de Curie ferromagnétique. Bien que l'anisotropie magnétocristalline soit faible, on note que la

susceptibilité paramagnétique est fonction de l'orientation du champ par rapport au cristal. Les courbes donnant (Fig. 2) l'inverse de la susceptibilité pour un champ appliqué parallèlement ou perpendiculairement à l'axe c présentent un écart de 0,7°K vers 300°K, au voisinage de la température de Curie paramagnétique. Il n'est plus que de 0,4° à 360°K, la différence $|1/\chi_{\parallel} - 1/\chi_{\perp}|$ entre les inverses des susceptibilités mesurées parallèlement et perpendiculairement à l'axe c décroît lorsque la température augmente.

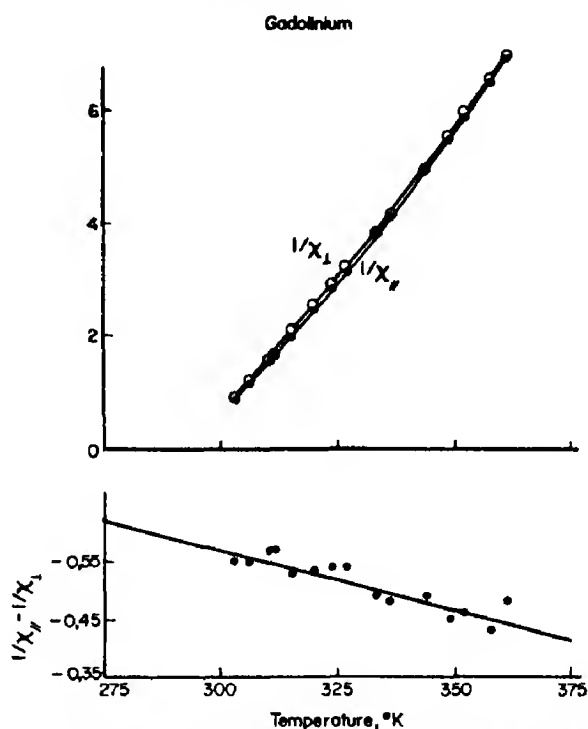


Fig. 2. Anisotropie de la susceptibilité paramagnétique du gadolinium.

(b) Terbium, dysprosium, holmium et erbium

L'axe c du cristal est de difficile aimantation pour Tb, Dy et Ho, mais axe de facile aimantation pour Er. L'inverse des susceptibilités mesurées parallèlement ou perpendiculairement à l'axe c présente une variation thermique linéaire dans l'intervalle de températures étudié, de 280° à 360°K. Elle a été analysée sous forme d'une 'température de Curie' et d'une 'constante de Curie' paramagnétiques. Cette façon de procéder est commode afin de

décrire les résultats expérimentaux. On notera plus loin cependant qu'elle présente une signification physique restreinte. La différence entre les 'températures de Curie' paramagnétiques suivant que le champ est appliqué perpendiculairement ou parallèlement à l'axe c est de 58°K pour le dysprosium, mais de -30°K pour l'erbium (Tableau 1). La différence $|1/\chi_{\parallel} - 1/\chi_{\perp}|$ est presque constante, indépendante de la température, pour chacun des cristaux de terre rare étudié. Un examen plus approfondi montre cependant qu'elle décroît lentement lorsque la température croît (Figs. 3-6). Nous avons analysé par la méthode des moindres carrés les résultats obtenus sous forme d'une variation thermique linéaire $1/\chi_{\parallel} - 1/\chi_{\perp} = A + BT$ où T est la température exprimée en degrés absolus. Les valeurs de A et de B ainsi obtenues sont données, Tableau 2. La susceptibilité est donnée en unités cgs. Elle est rapportée à un atome-gramme.

3. EXPRESSIONS THEORIQUES

L'anisotropie de la susceptibilité des substances magnétiques au-dessus du point d'ordre n'a été étudiée que dans des cas particuliers [9-12]. Nous donnerons ici une expression plus générale de la variation thermique de la susceptibilité paramagnétique d'un corps anisotrope en fonction de la direction du champ appliqué. Des études préliminaires ont fait l'objet de deux notes antérieures [13, 14]. Nous nous plaçons dans

Tableau 2

Elément	A (exper.)	$B \times 10^3$ (exper.)	$B \times 10^3$ (théor.)
Gd	0,120	-0,21	
Tb	4,88	-1,9	-0,42
Dy	4,31	-2,6	-1,3
Ho	1,12	-0,25	-0,24
Er	-2,45	1,2	1,2

le cadre de la théorie du champ moléculaire, et négligeons, pour l'instant, les contributions de l'échange anisotrope. Nous admettrons, et ceci constitue une bonne approximation dans le domaine des températures étudié, que la configuration des électrons 4f dans le métal est la configuration fondamentale des ions libres correspondants. L'Hamiltonien de l'ion magnétique s'écrit sous la forme:

$$\mathcal{H} = \mathcal{H}_0 + V - g_J \mu_B \mathbf{H}_{\text{eff.}} \cdot \mathbf{J} \quad (1)$$

où \mathcal{H}_0 est l'Hamiltonien de l'ion libre, V la contribution de l'environnement cristallin, g_J le facteur de Landé, μ_B le magnéton de Bohr et \mathbf{J} le moment cinétique total. Le champ effectif $\mathbf{H}_{\text{eff.}}$ est la somme du champ magnétique \mathbf{H} appliqué et du champ moléculaire \mathbf{H}_m . Le moment magnétique s'écrit alors, pour N ions identiques:

$$\mathbf{M} = \frac{-N \sum_i \nabla \mathbf{H}_{\text{eff.}} [W_i(\mathbf{H}_{\text{eff.}})] \exp(-W_i/kT)}{\sum_i \exp(-W_i/kT)} \quad (2)$$

Tableau 1

Elément	$\theta_{p,\perp}$ (°K)	$\theta_{p,\parallel}$ (°K)	$\theta_{p,\parallel} - \theta_{p,\perp}$ (°K)	C_{\parallel} (at.g)	C_{\perp} (at.g)	C_{spect} (at.g)
Tb	236 (239[5])	181 (195[5])	-55	12,5	12,3	11,8
Dy	167 (169[6])	109 (121[6])	-58	14,85	14,4	14,2
Ho	91,5 (88[7])	75 (73[7])	-16,5	15,2	15,1	14,1
Er	33 (32,5[8])	63 (61,7[8])	+30	12,4	12,6	11,5

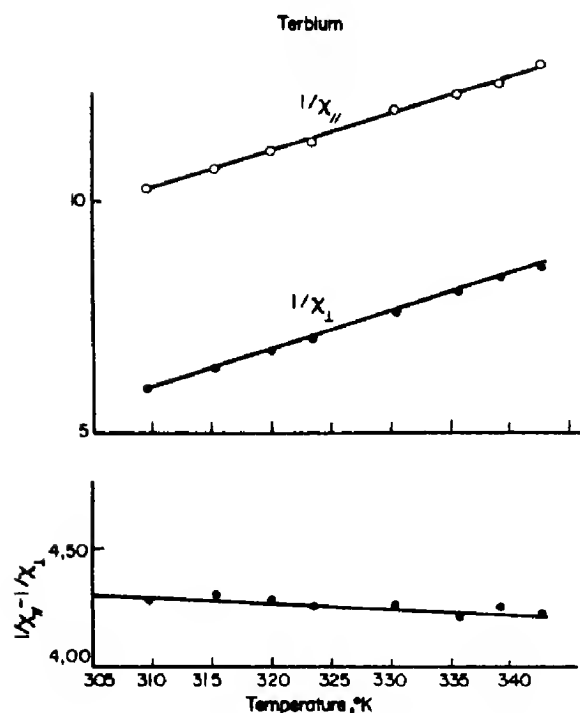


Fig. 3. Anisotropy of the paramagnetic susceptibility of terbium.

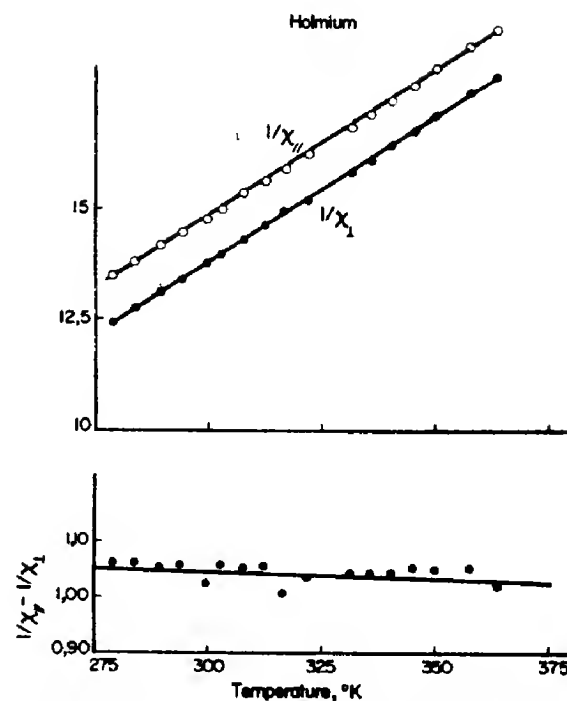


Fig. 5. Anisotropy of the paramagnetic susceptibility of holmium.

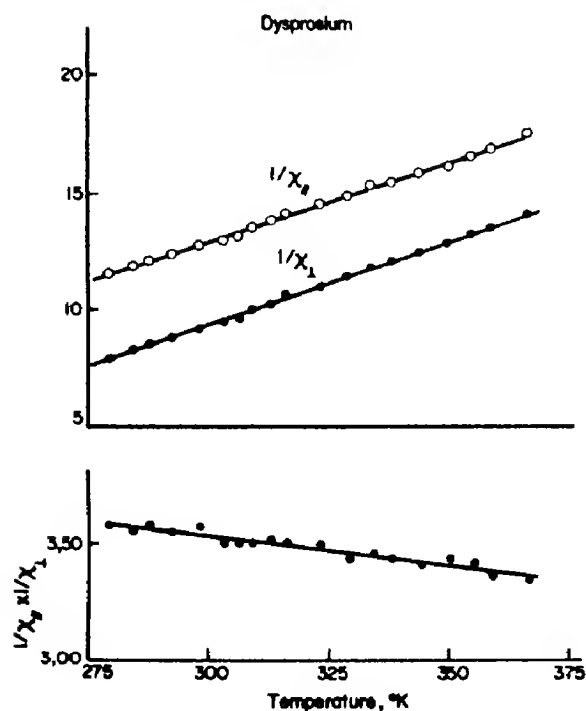


Fig. 4. Anisotropy of the paramagnetic susceptibility of dysprosium.

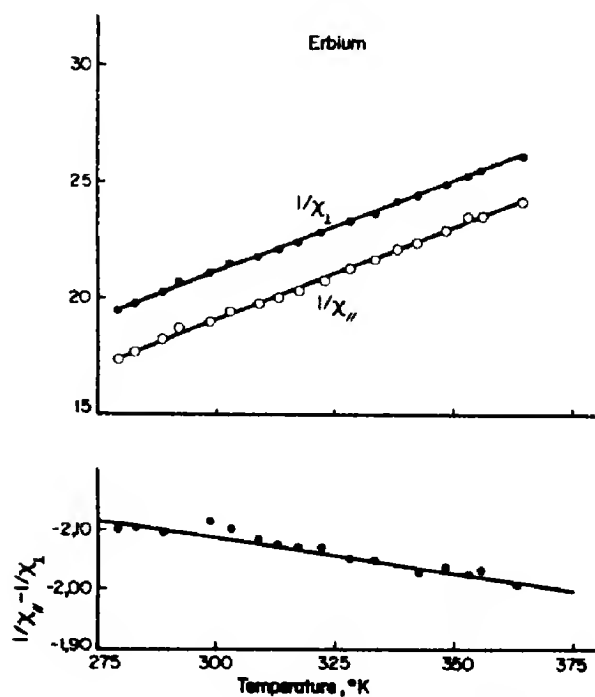


Fig. 6. Anisotropy of the paramagnetic susceptibility of erbium.

La sommation porte sur les états i du niveau fondamental d'énergie W_i de l'ion libre. L'aimantation M peut être développée en puissances croissantes de $1/T$. Dans le domaine paramagnétique, pour les champs magnétiques usuels, ce développement converge assez rapidement de sorte que l'on ne tiendra compte que du nombre de termes correspondant à la précision recherchée. La composante M_x de l'aimantation suivant un axe de symétrie Ox s'écrit:

$$M_x = \frac{N}{2kT(2J+1)} \sum_i \frac{\partial W_i^2}{\partial H_{\text{eff},x}} - \frac{N}{6k^2T^2(2J+1)} \sum_i \frac{\partial W_i^3}{\partial H_{\text{eff},x}} + \frac{N}{2k^2T^2(2J+1)^2} \left(\sum_i W_i \right) \left(\sum_i \frac{\partial W_i^2}{\partial H_{\text{eff},x}} \right) + O\left(\frac{1}{T^3}\right). \quad (3)$$

On peut obtenir aisément les expressions des diverses quantités $\sum_i W_i^2$ et $\sum_i W_i^3$. On en déduit:

$$M_x = \frac{CH_{\text{eff},x}}{T} \left\{ 1 - \frac{\text{Tr}[3VJ_x^2 - VJ(J+1)]}{kTJ(J+1)(2J+1)} \right\} + O\left(\frac{1}{T}\right) \quad (4)$$

quelle que soit la direction du champ appliqué. On obtiendrait des expressions équivalentes pour les composantes de l'aimantation suivant deux axes de symétrie Oy et Oz orthogonaux à Ox . On désigne par C la constante de Curie spectroscopique $Ng^2\mu_B^2J(J+1)/3k$.

On utilisera dans la suite la notion d'opérateur équivalent de Stevens $0_{\ell,\nu}^{m,\alpha}(J)$ proportionnel aux tesseral harmoniques vecteurs propres de la composante l_ν du moment cinétique orbital \mathbf{l} dans la direction ν [15]. On a ainsi:

$$0_{2,x}^0(J) = 3J_x^2 - J(J+1). \quad (5)$$

En utilisant la relation

$$\text{Tr}[0_{\ell_1}^{m_1,\alpha_1}(J) 0_{\ell_2}^{m_2,\alpha_2}(J)] \alpha \delta_{\ell_1-\ell_2} \delta_{m_1-m_2} \delta_{\alpha_1-\alpha_2} \quad (6)$$

et le développement en série du potentiel

cristallin:

$$V = \sum_{\ell=0}^{\infty} \sum_{m=-\ell}^{\ell} \sum_{\alpha} u_{\ell,x}^{m,\alpha} 0_{\ell,x}^{m,\alpha}(J) \quad (7)$$

l'expression (4) s'écrit simplement:

$$M_x = \frac{CH_{\text{eff},x}}{T} \left[1 - \frac{(2J-1)(2J+3)}{5kT} u_{2,x}^0 \right] + O\left(\frac{1}{T^3}\right). \quad (8)$$

A l'ordre considéré M_x ne dépendra de l'environnement cristallin que par le seul coefficient de champ cristallin $u_{2,x}^0$. Le champ effectif H_{eff} peut être exprimé sous la forme $nM + H$ où n est le coefficient de champ moléculaire et H le champ appliqué. On pose $\theta = nC$ où θ désigne la température de Curie paramagnétique en l'absence d'anisotropie magnétocristalline. L'inverse de la susceptibilité s'écrit, avec la même précision:

$$\frac{1}{\chi_x} = \frac{1}{C} \left[T - \theta + \frac{(2J-1)(2J+3)}{5k} u_{2,x}^0 \right]. \quad (9)$$

L'inverse de la susceptibilité paramagnétique selon les axes de symétrie du cristal est indépendante de la direction et de l'amplitude du champ appliqué. La somme $u_{2,x}^0 + u_{2,y}^0 + u_{2,z}^0$ étant nulle, deux paramètres suffisent, dans le cas général, à décrire l'anisotropie de la susceptibilité. Ces deux paramètres variant peu avec la température, les variations thermiques des mesures des susceptibilités paramagnétiques seront représentées en première approximation par des droites parallèles, de pente $1/C$. La susceptibilité dans la direction du champ appliqué est $M.H/H^2$. Elle a pour valeur:

$$\chi_H = \alpha_H^2 \chi_x + \beta_H^2 \chi_y + \gamma_H^2 \chi_z \quad (10)$$

où α_H , β_H et γ_H désignent les cosinus directeurs du champ appliqué. La susceptibilité, selon la direction du champ appliqué varie comme le carré des cosinus directeurs du champ, quelle que soit la symétrie du cristal. Lorsque l'environnement cristallin des atomes

magnétiques est de révolution autour de l'axe Oz , il vient alors:

$$\frac{1}{\chi_z} = \frac{1}{C} \left[T - \theta + \frac{(2J-1)(2J+3)}{5k} u_{2,z}^0 \right]. \quad (11a)$$

Suivant Ox , perpendiculairement à Oz , on a:

$$\frac{1}{\chi_x} = \frac{1}{C} \left[T - \theta - \frac{(2J-1)(2J+3)}{10k} u_{2,z}^0 \right]. \quad (11b)$$

L'anisotropie de la susceptibilité ne dépend plus alors de l'environnement cristallin que par le seul paramètre $u_{2,z}^0$ et la susceptibilité, dans la direction du champ appliqué s'écrit:

$$\chi_H = \chi_x + (\chi_z - \chi_x) \cos^2 \theta_H \quad (12)$$

θ_H étant l'angle entre l'axe Oz et la direction du champ magnétique. L'anisotropie de la susceptibilité est nulle, à l'ordre considéré, pour un environnement cubique, car on a alors: $u_{2,x}^0 = u_{2,y}^0 = u_{2,z}^0 = 0$. L'axe c des monocristaux de terre rare étant d'ordre 6, la susceptibilité dans le plan de base ne peut pas varier proportionnellement au carré des cosinus directeurs du champ magnétique. A l'ordre considéré on ne doit pas observer d'anisotropie de la susceptibilité dans ce plan.

Une étude plus systématique et plus générale de l'anisotropie de la susceptibilité paramagnétique est donnée dans un autre article [16].

4. EXPLOITATION DES RESULTATS EXPERIMENTAUX

On note tout d'abord que l'anisotropie dans le plan de base est nulle. L'axe c peut être considéré comme axe de révolution, de sorte que les expressions (11) et (12) seront applicables aux cas considérés. Dans les plans contenant l'axe c , les valeurs expérimentales des susceptibilités paramagnétiques sont décrites, avec une précision meilleure que 1 p. cent par les expressions (11) et (12); quelle que soit la direction du champ appliqué la susceptibilité paramagnétique peut être considérée comme résultant de la somme d'un terme constant et d'un terme sinusoïdal de période 180° . La différence $\theta_{p,\parallel} - \theta_{p,\perp}$ entre les 'températures de Curie' paramagnétiques mesurées parallèlement à l'axe c ou perpendiculairement à cet axe, est donnée par $-3(2J-1)(2J+3)u_{2,z}^0/10k$. On trouvera, Tableau 3, les valeurs $u_{2,z}^0$ (I) déduites de $\theta_{p,\parallel} - \theta_{p,\perp}$ au moyen de cette expression. Celles-ci peuvent être comparées aux valeurs 'théoriques' $u_{2,z}^0$ (II) déduites par Kasuya [17] à partir d'un modèle à charges ponctuelles écrantées. (Dans la notation de Kasuya, \bar{v}_2^0 est identique à $2u_2^0$.) L'accord obtenu est relativement satisfaisant. Il faut cependant noter qu'il n'a pas été tenu compte jusque là de la dilatation thermique. Celle-ci peut conduire, en raison de la variation des interactions d'échange et des paramètres de champ cristal-

Tableau 3

Elément J	Tb 6	Dy 15/2	Ho 8	Er 15/2
$u_{2,z}^0$ (I) $\times 10^{-16}$ erg (exper sans correction de dilatation)	+1,53	+1,06	+0,27	-0,55
$u_{2,z}^0$ (II) $\times 10^{-16}$ erg (théor. Kasuya) (273°K)	+1,48	+1,01	+0,35	-0,40
$u_{2,z}^0$ (III) $\times 10^{-16}$ erg (exper. avec correction de dilatation) (273°K)	+1,49	+0,96	+0,25	-0,48
$\beta \times 10^4$	-1	-3,6	-2,3	-5,6
$u_{2,z}^0$ (IV) $\times 10^{-16}$ erg (exper. aimantation) (0°K)	+2,73	+1,65	+1,08	

lin à des écarts assez importants entre la valeur théorique de la variation thermique de la susceptibilité à *volume constant* et la valeur expérimentale, déduite des mesures effectuées à *pression constante*. La valeur $u_{2,z}^0$ est proportionnelle à

$$\frac{Z'}{a} v_{2,z}^0 \frac{\bar{r}^2}{a^2} \text{ où } v_{2,z}^0 = -1,035 \left(1,636 - \frac{c}{a} \right).$$

Dans cette expression \bar{r}^2 désigne la valeur moyenne du carré du rayon de la couche $4f$, a et c les paramètres du cristal hexagonal et Z' la valeur de la charge ponctuelle efficace. On peut supposer raisonnablement que Z' comme \bar{r}^2 sont indépendants de la température. Il en résulte que l'on a:

$$\beta = \frac{\partial \log \theta_{2,z}^0}{\partial T} = \frac{(c/a)(\alpha_{\parallel} - \alpha_{\perp})}{c/a - 1,636} - 3\alpha_{\perp}. \quad (13)$$

On appelle α_{\parallel} et α_{\perp} les variations relatives $1/c \cdot dc/dT$ et $1/a \cdot da/dT$. On pourra considérer α_{\parallel} et α_{\perp} comme constants dans l'intervalle de températures où les mesures ont été effectuées. Le terme $3\alpha_{\perp}$ au second membre de l'équation (13) est généralement négligeable devant le premier terme au second membre. Les valeurs de β , déduites des mesures de c et a aux rayons X [18-20], sont données, Tableau 3. L'effet de la variation thermique de $u_{2,z}^0$ doit être pris en considération, étant donné les valeurs particulièrement importantes prises par β . Tout d'abord, des expressions (11), on déduit que β est égal à $\partial \log (1/\chi_{\parallel} - 1/\chi_{\perp}) / \partial T$. On a obtenu expérimentalement une variation de $1/\chi_{\parallel} - 1/\chi_{\perp}$ que l'on a analysée (Tableau 2) sous forme d'une variation linéaire $A + BT$. La valeur de B est donnée par $\beta(1/\chi_{\parallel} - 1/\chi_{\perp})$. A 273°K, $1/\chi_{\parallel} - 1/\chi_{\perp}$ est égal à 4,36 (Tb), 3,60 (Dy), 1,05 (Ho) et -2,12 (Er). Les valeurs de B 'théoriques' ainsi obtenues sont comparées, Tableau 2, aux valeurs expérimentales. Elles sont du même ordre de grandeur que celles déduites de l'expérience. On notera que l'accord est d'autant meilleur (Ho, Er) que les mesures ont été effectuées à des températures plus élevées au-dessus du

point d'ordre. La contribution à l'anisotropie de la susceptibilité du terme en $1/T$ dans le développement de l'inverse de la susceptibilité (expression (9)) ne permet pas d'interpréter la différence qui existe entre les valeurs expérimentale et théorique de B pour le dysprosium et le terbium (ce terme ne contribue que pour moins de 1/100 à l'anisotropie de la susceptibilité). Il faut sans doute attribuer cette différence à l'approximation de champ moléculaire.

Compte tenu de la dilatation thermique, l'écart obtenu expérimentalement entre les 'températures de Curie' paramagnétiques $\theta_{p,\parallel}$ et $\theta_{p,\perp}$ est donné par:

$$\theta_{p,\parallel} - \theta_{p,\perp} = - \frac{3(2J-1)(2J+3)}{10k} u_{2,z}^0 (1 - 273\beta) \quad (14)$$

la valeur de $u_{2,z}^0$ considérée étant celle à 273°K; on appellera $u_{2,z}^0(\text{III})$ les valeurs ainsi obtenues. On note (Tableau 3) que la dilatation thermique modifie assez largement les valeurs des paramètres cristallins déduites des résultats expérimentaux de mesure des susceptibilités. Les valeurs de $u_{2,z}^0$ peuvent également se déduire des mesures d'aimantation en champ fort continu [3]. On appelle $u_{2,z}^0(\text{IV})$ les valeurs ainsi obtenues à 0°K (Tableau 3). On notera le désaccord important qui existe entre ces valeurs et celles, $u_{2,z}^0(\text{III})$, à 273°K résultant des mesures de la susceptibilité paramagnétique. On notera cependant que ces diverses valeurs ne peuvent être comparées sans précautions. Il est probable en effet que l'on ne puisse pas tenir compte du couplage magnétocristallin, particulièrement important à basse température dans le cas de Tb, Dy, Ho et Er, par un simple calcul de perturbation. Par ailleurs les paramètres cristallins sont différents, en raison de la dilatation thermique, et le réseau cristallin n'a plus, à basse température, la symétrie hexagonale, en raison de la distorsion en dessous de la température de transition entre les phases antiferromagnétique hélicoïdale et ferromagnétique.

Remerciements—Les auteurs expriment à Messieurs J. L. Féron et R. Pauthenet, leurs remerciements pour des discussions nombreuses et pour la communication d'expériences et de résultats non publiés.

BIBLIOGRAPHIE

1. FOËX G. et FORRER R., *J. Phys. Rad.* **7**, 180 (1926).
2. BARTHOLIN H. et BLOCH D., *J. Phys. Chem. Solids* **29**, 1063 (1968).
3. FÉRON J. L., HUG G. et PAUTHENET R., *C.r. Colloque Intl du C.N.R.S. sur les Elements des Terres Rares*, Grenoble (1969).
4. On a utilisé un programme établi par M. Aubert pour l'ordinateur I.B.M. 7044. Les résultats détaillés sont donnés par ailleurs (ALÉONARD R. et PAUTHENET R.).
5. HEGLAND D. E., LEGVOLD S. et SPEDDING F. H., *Phys. Rev.* **131**, 158 (1963).
6. BEHREND D. R., LEGVOLD S. et SPEDDING F. H., *Phys. Rev.* **109**, 1544 (1958).
7. STRANDBURG D. L., LEGVOLD S. et SPEDDING F. H., *Phys. Rev.* **127**, 2046 (1962).
8. GREEN R. W., LEGVOLD S. et SPEDDING F. H., *Phys. Rev.* **122**, 827 (1961).
9. PENNEY W. G. et SCHLAPP R., *Phys. Rev.* **41**, 194 (1932).
10. ELLIOTT E. J. et STEVENS K. W. H., *Proc. R. Soc.* **219A**, 387 (1953).
11. CALLEN E. R., *Phys. Rev.* **124**, 1375 (1961).
12. LINES M. E., *Phys. Rev.* **137**, 982 (1965).
13. BOUTRON P., *C.r. hebd. Séanc. Acad. Sci., Paris* **263**, 892 (1966).
14. ALÉONARD R., BLOCH D. et BOUTRON P., *C.r. hebd. Séanc. Acad. Sci., Paris* **263**, 951 (1966).
15. HUTCHINGS M. T., *Solid State Physics* (F. Seitz et D. Turnbull, Editeurs), No. 16, p. 196. Academic Press, New York (1969).
16. BOUTRON P., *J. Phys.* **30**, 413 (1969).
17. KASUYA T., In *Magnetism II* B G. T. Rado et H. Suhl, Editeurs). Academic Press, New York (1966).
18. DARNELL F. J. et MOORE E. P., *J. appl. Phys.* **34**, 1337 (1963).
19. DARNELL F. J., *Phys. Rev.* **130**, 1825 (1963).
20. DARNELL F. J., *Phys. Rev.* **132**, 1098 (1963).

ELECTRICAL CONDUCTIVITY AND OPTICAL ABSORPTION CHANGES RELATED TO THE 3800 Å BAND OF CaO:Ca*

D. F. WINTERSTEIN and E. F. SIECKMANN

Physics Department, University of Idaho, Moscow, Idaho 83843, U.S.A.

(Received 5 August 1968; in revised form 13 January 1969)

Abstract—Simultaneous measurements of electrical current and optical absorption in CaO:Ca crystals as a function of temperature after light irradiation at liquid nitrogen temperature (LNT) have supported the view that an apparent upward shift of about 0.13 eV in the F' -band energy upon heating the crystal is actually caused by the formation of a new color center of unknown structure, labeled F_n . The apparent shift in the F' band occurred simultaneously with a change in the current vs. temperature slope. The F_n band was stable in the dark at room temperature and below, but bleached easily when the crystal was irradiated in the absorption band and when it was heated to $\sim 170^\circ\text{C}$.

INTRODUCTION

A MECHANISM for the $F \leftrightarrow F'$ photoreaction in CaO:Ca crystals has been proposed by Kemp *et al.*[1]. This mechanism differs from that proposed for the alkali halides[2] chiefly in that shallow impurity traps rather than electron-bare negative-ion vacancies collect the electrons ionized from the F' center. Thus irradiation in the F' band forms only one F center instead of two for each ionized electron, and $F \rightarrow F'$ occurs when the shallow traps are ionized by low-energy light ($\lambda > 5000 \text{ Å}$), permitting the F centers to regain electrons.

Extensive optical absorption studies in this laboratory of CaO:Ca for various irradiation treatments over a 300°C temperature range supported in general Kemp's proposed $F \leftrightarrow F'$ mechanism. However, following prolonged irradiation ($T \approx 1 \text{ hr}$) at LNT with an unfiltered Hg-arc lamp, the F' optical absorption band appeared to shift about 150 Å in the high-energy direction as the crystal was warmed to room temperature. The shift was reversible not with temperature but

with a certain sequence of tungsten-filament light treatments or with heat treatments. Van Doorn had observed a similar energy shift in the KCl M -center absorption following prolonged irradiation. He tentatively explained the shift in terms of local internal crystal strains[3]. Evidence from simultaneous optical absorption and electrical current measurements in conjunction with color center bleaching data, described below, suggests that in CaO:Ca the energy shift results not from local influences on an essentially unchanged F' center but from the formation of a completely different center, the F_n center, of as-yet undetermined structure.

EXPERIMENTAL PROCEDURE

The CaO crystals used were grown by fusing CaO powder with an electric arc in a cylindrical graphite crucible rotated on its axis at sufficient angular velocity to keep its contents thrown against the crucible walls and thus, by effectively melting the CaO in a crucible of CaO powder, eliminating chemical reaction of the CaO with the crucible. An N_2 gas jet passing through the graphite electrodes blew CaC_2 vapor, formed by reaction of carbon vapor with the melt, out the ends of the crucible to eliminate the electrodes as a source

*This research was supported in part by the Solid State Sciences Division of the Air Force Office of Scientific Research.

of carbon contamination. Optically clear CaO crystals several millimeters on an edge were then cleaved from the resulting polycrystalline mass.

Color centers were produced by heating crystals for approximately 30 min at 1700°C in carbon vapor. Crystals were cooled to LNT within 15 min of the coloring treatment. The resulting optical absorption bands closely resembled those obtained by Ward for crystals that were lightly colored by heating in Ca-metal vapor[5].

The procedure and apparatus for simultaneously measuring crystal optical absorption and electrical current followed approximately those used by Dutton and Maurer for similar measurements on KCl and KBr[6]. A dc field of about 2000 V/cm, supplied by dry cells, was applied across crystals of about 1 mm thickness. The crystal was sandwiched between two copper-plate electrodes having apertures for passage of a spectrophotometer beam. One of the copper plates contacted the cold tail of a cryostat. Teflon bolts held the crystal and the other plate to the cold plate. A copper-constantan thermocouple was soldered to the cold plate for approximate temperature monitoring. A nichrome resistance heater, wound around the cold tail and powered by storage batteries, provided sample temperature control. Crystal currents were measured with a Keithley Model 610B electrometer, while the optical absorption spectra were obtained with a Cary Model 14 spectrophotometer.

The data-gathering procedure consisted first of mounting the sample in its holder and cooling the cryostat to LNT. Once cooled, the crystal was irradiated for about an hour with the selected type of radiation (either light from an unfiltered, high-pressure, quartz-envelope Hg-arc lamp or light of $\lambda > 5630 \text{ \AA}$ from a tungsten-filament lamp). Then the cryostat with sample was placed into the spectrophotometer sample compartment and the voltage applied across the crystal. When electrical equilibrium was reached the heater was turned on and the sample holder warmed at a rate of 3–5°C/min. At close intervals (every 3–5 min) the crystal optical absorption was measured by scanning rapidly (25 Å/sec) the region between 6500–3000 Å. In this way, with the help of chart recorders, a nearly continuous correlation of sample optical absorption, temperature and electrical current was obtained. Although the spectrophotometer-beam light no doubt had some effect on the observed color-center changes, the final changes in optical absorption were identical in all major features with those obtained without intermediate scanning, so that the effect of the spectrophotometer light was considered negligible.

The rationale for the experiment is that crystal irradiation at low temperatures distributes ionized electronic charges on lattice

traps that are unstable at higher temperatures. Thus as the temperature rises, an increase in lattice energy ionizes the shallow traps, releasing a quantity of free charge whose motion can be picked up by the electrometer. When optical absorption changes correlate with current changes, each kind of change helps to interpret the other.

RESULTS

Figure 1 shows the optical absorption change, especially the 'F' energy shift,' which resulted from Hg-arc-light irradiation at LNT followed by heating to $\sim 100^\circ\text{C}$ and then recooling to LNT (to exclude the normal changes in optical absorption associated with

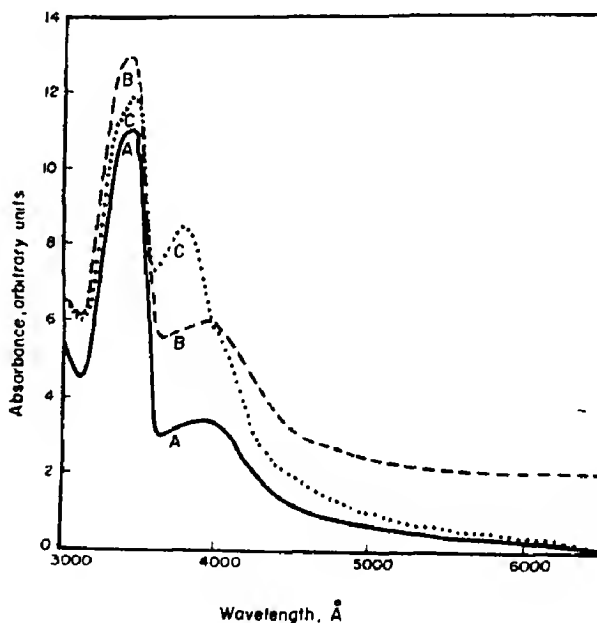


Fig. 1. 'F' shift' in CaO:Ca single crystal. Curve A indicates the optical absorption at LNT just prior to Hg-arc-light irradiation. Curve B shows the result of irradiating the crystal for 50 min at LNT with Hg-arc light, while curve C shows the changes (including the 'F' shift') after heating the crystal to 112°C and then recooling to LNT. The F band is at 3400 Å, the F' at 3950 Å. The apparent shift of F' to 3800 Å occurred near -17°C as the crystal temperature rose. (Note: Zero phonon lines, which appear on the F band at 3558 Å, have been omitted on all Figures except Fig. 7.)

a change in temperature)[5]. Figure 2 indicates the change in crystal current as the crystal warmed up on the same run. The current curve has two well-defined linear regions, resembling those associated with extrinsic and intrinsic ionic conductivity in insulators [7]. The '*F*' energy shift was found to occur at the knee in the current curve.

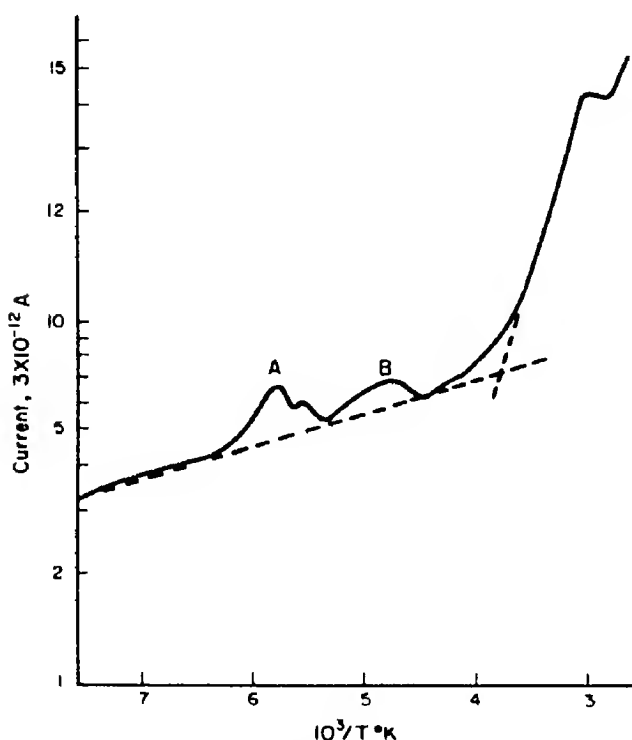


Fig. 2. Temperature dependence of the dc current in the CaO:Ca crystal following 50 min Hg-arc-light irradiation at LNT. The '*F*' shift occurred at the knee of the linear regions indicated by dashed lines. Current peak *A* resulted primarily from a flow of electrons, while peak *B* resulted from a flow of holes.

When the crystal was irradiated with long-wavelength light ($\lambda > 5630 \text{ Å}$) at LNT and then warmed to room temperature, almost exactly the same current curve resulted as is shown in Fig. 2 for Hg-arc irradiation. (Minor variations occurred partly as a function of previous crystal treatment.) However, virtually no change occurred in the final optical absorption spectrum other than what normally occurs simply as a result of change in temperature; no sign of the '*F*' energy shift appeared.

If the crystal received no irradiation at LNT, the characteristic current slopes remained but the small current peaks (*A* and *B*) on the low-temperature part of the curve disappeared.

The current curve for an irradiated, uncolored crystal exhibited current peaks similar to *A* and *B* (Fig. 2) but did not exhibit the marked change in slope near -17°C . However, repeated treatments of the uncolored crystal with unfiltered Hg-arc light produced current curves identical in all general features to the curve shown in Fig. 2. Thus the crystal defects responsible for the change in current slope appeared capable of being induced by the Hg-arc light. Low *F*-center concentrations, in fact, have been produced in CaO crystals with Hg-arc light in this laboratory.

The changes in optical absorption associated specifically with the small current peaks of Fig. 2 are shown in Fig. 3. These curves were selected from among those obtained over closely spaced time intervals as the temperature rose (see "Experimental Procedure"). Curve *A* shows the optical absorption at a temperature slightly lower than that at which the first small current peak (*A*) occurred. Curve *B* was obtained as current peak *A* dropped to its minimum, while curve *C* was obtained as current peak *B* reached its maximum.

DISCUSSION

According to the accepted *F*- and *F'*-center models[8] and the $F \leftrightarrow F'$ mechanism mentioned above, a simultaneous increase in the area under both the *F* and the *F'* peaks, as the temperature rises, requires either an increase in the total number of *F* and *F'* centers or the emergence of a new band underlying *F* and *F'*. Curve *B* of Fig. 3, corresponding to current peak *A* of Fig. 2, shows both peaks increasing simultaneously. Apparently, then, assuming no new bands arise here, current peak *A* represents primarily a flow of electrons, some of which become trapped on *F* centers and bare O^{2-} vacancies to increase the number and consequently the absorption

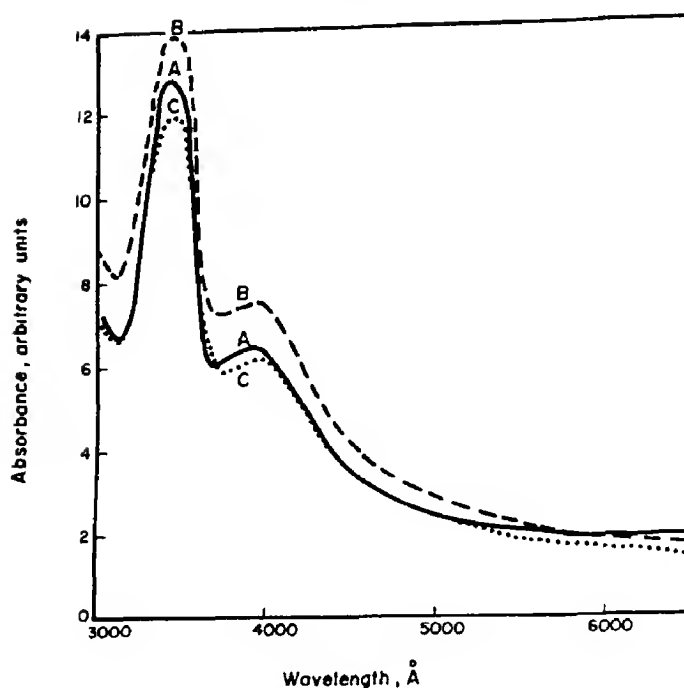


Fig. 3. Optical absorption changes in CaO:Ca crystal associated with current peaks *A* and *B* of Fig. 2. Curve *A* occurred for an abscissa value in Fig. 2 of $6.0 \times 10^{-3}^\circ\text{K}^{-1}$; curve *B* for $5.4 \times 10^{-3}^\circ\text{K}^{-1}$; curve *C* for $4.6 \times 10^{-3}^\circ\text{K}^{-1}$. The absorption changes reveal interaction of flowing charges with *F* and *F'* centers (see text).

of both kinds of center. Similarly, the decrease in area under both absorption peaks, associated with current peak *B*, indicates that this peak represents primarily a flow of holes, some of which annihilate with electrons orbiting O^{2-} vacancies to reduce total *F*, *F'* absorption.

The origin of the apparent energy shift of the *F'* band occurring at the knee of the current curve can at present be only partially elucidated. Kemp *et al.* have observed an optical absorption band at this shifted position (3800 \AA) in neutron irradiated CaO. On the basis of an EPR spectrum thought to originate from the same defect as the optical band at 3800 \AA , they interpreted the band as being due to an *M*-like center consisting of two O^{2-} vacancies orbited by two electrons[4]. (The center associated with the *M*-like EPR spectrum Kemp called '*F'*'. As this center may

not actually be related to the 3800 \AA optical absorption band of CaO crystals colored in carbon vapor, we label the center responsible for the 3800 \AA band '*F_n*' to avoid possible misunderstanding.) If an *M*-like center can exist in CaO at 3800 \AA , a possible explanation of the apparent *F'* shift would be that *M*-like centers formed from *F*-center coagulation as the temperature rose to -17°C and thus produced the observed shift. Rabin, in fact, has observed *M*-center formation in KCl under somewhat similar circumstances[11]. That the optical absorption shift did not reverse itself when the crystal was recooled to LNT favors the interpretation that the shift resulted, indeed, from the formation of a new color center rather than from a modification of *F'* center. Figure 7, showing the optical absorption of a CaO:Ca crystal in which two peaks—one at the shifted position and the

other at the usual F' position—are simultaneously resolved, further supports the concept that a new center, independent of F' , was created as the temperature rose. The bleaching data of Figs. 4–6, however, while supporting the formation of an independent center, argue against the possibility that the new center is a coagulation center formed from F and F' centers. A coagulation of F centers to produce an M -like center should reduce the F absorption two units for every unit increase in the coagulation-band absorption, while a bleaching of the coagulation band should increase F correspondingly. Figures 4 and 6 indicate that bleaching the new color center with light at LNT and with heat at 170°C, respectively, produced an apparent decrease in both F and F' . The F band increased somewhat on bleaching with light at room temperature, as Fig. 5 shows, but the magnitude of the increase is not sufficient to represent the breakdown of a coagulation center. (We assume that the rise in the long-wavelength tail that frequently accompanied bleaching is not a part of the F or

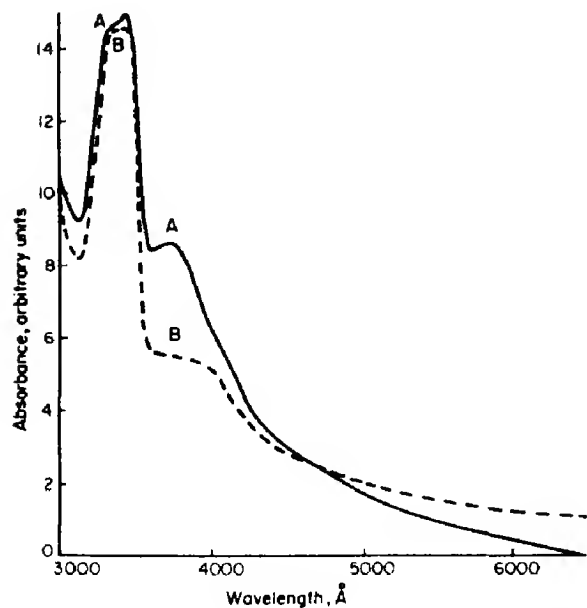


Fig. 4. Bleaching of F_n at LNT with 3500–3700 Å light applied for ~ 10 min. Curve A was obtained in the same way as curve C, Fig. 1. The total area under F , F' and F_n curves decreased after irradiation (curve B).

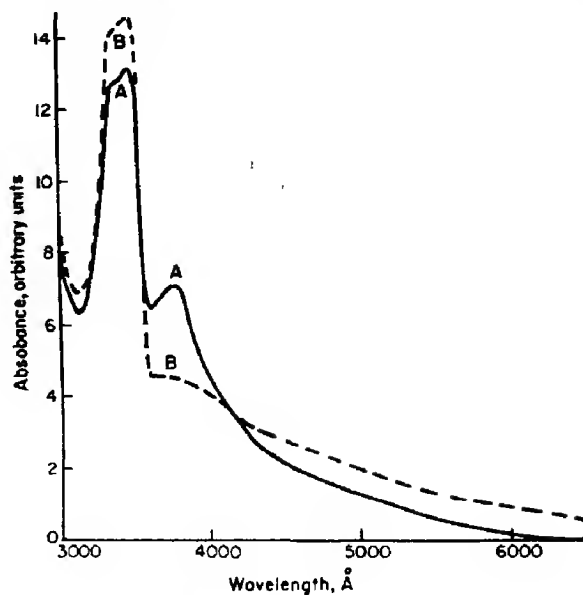


Fig. 5. Bleaching of F_n at room temperature with 3500–3700 Å light applied for 15 min. Curve A was obtained in the same way as curve C, Fig. 1. In contrast to the results obtained at LNT, the F band rose substantially as F_n bleached (curve B). Both curves were measured at LNT; it was noted that the F band of curve B decreased with successive measurements, suggesting that the configuration which was stable at room temperature was unstable at LNT.

F' absorption but represents a separate phenomenon: the formation of a broad band analogous in shape and relative location to the F' band in KCl.) The bleaching data thus suggest that the new color center is independent of both F and F' . The increase in F associated with room-temperature bleaching perhaps is nothing more than evidence of the $F' \rightarrow F$ photoconversion. An exaggerated example of such a conversion, combined with the bleaching of the F_n center, is depicted in Fig. 8. Here the $F \rightarrow F'$ reaction was produced in a crystal containing a large concentration of F_n centers by irradiating the specimen several hours with low-energy light ($\lambda > 5630$ Å), which is incapable of bleaching F_n centers. The $F' \rightarrow F$ reaction, combined with F_n bleaching, was then caused by irradiating the crystal with white light at room temperature for 30 min.

No attempt will be made here to relate the formation of F_n centers to the change

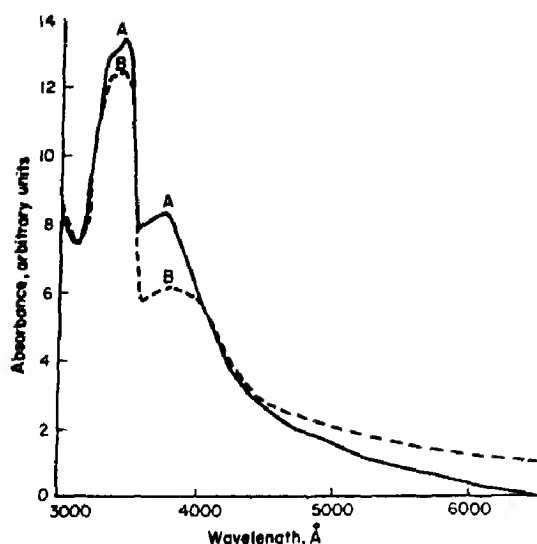


Fig. 6. Heat-bleaching of F_n , produced by holding the crystal near 170°C in the dark for 30 min. Curve A was obtained in the same way as curve C, Fig. 1; curve B shows the result of heating followed by rapid cooling to LNT. Both spectra were recorded at LNT. The drop in the F -center absorption was probably not due to thermal bleaching of F centers in the usual sense, as subsequent measurements on this crystal revealed a total F , F_n and F' absorption as large as that shown in curve A (i.e. thermal bleaching of F and F' centers ordinarily is irreversible, unless the coloring process is repeated. For CaO such bleaching is not efficient until $\sim 500^\circ\text{C}$).

in the current slope, both of which occurred in the same temperature region. However, if the two phenomena were related, as they appeared to be, an interpretation of the relationship should recognize that the major current slopes observed do not represent extrinsic and intrinsic regions. The general shape of the current curve resembles somewhat that obtained at higher temperatures by Dolloff in colored BaO[12]. Dolloff observed a conductivity maximum between 800°–900°K which resembles the drop in the current slope that appeared in colored CaO near 335°K (Fig. 2). Dolloff related the shape of his conductivity curves to donor and acceptor concentrations introduced in the coloring process. Possibly the same kind of reasoning applies to CaO as well, and may be relevant for future attempts to explain the formation of F_n centers.

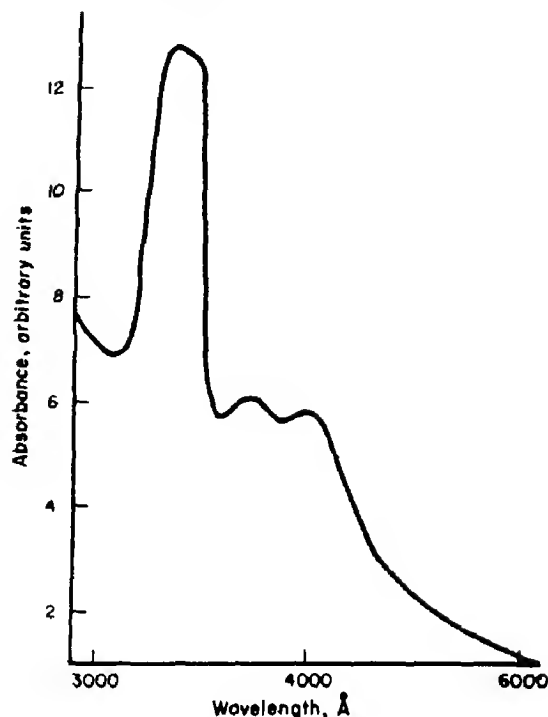


Fig. 7. Optical absorption of CaO:Ca single crystal showing F' and F_n peaks resolved simultaneously. This crystal appeared incapable of the behavior shown in Fig. 1: F_n could not be made to grow larger by Hg-arc irradiation at LNT followed by heating. Also, irradiation in the absorption band did not bleach F_n . A current vs. temperature measurement on this crystal indicated that the knee in the conductivity curve was very poorly defined: There were no truly linear regions. Optical and EPR spectra indicated a higher impurity concentration for this crystal than for the crystal used in the other figures.

Attempts to isolate exactly which Hg-arc wavelengths are responsible for the ' F ' shift' so far have not yielded conclusive results. Irradiation treatments using filters to select out several regions in the visible and u.v. as well as irradiation using a monochromator to isolate a few specific Hg-arc lines in the u.v. suggest that u.v. light is responsible; but so far no shifts approximating the magnitude of those obtained with the unfiltered Hg arc have been observed by these techniques, even when longer irradiation times were used.

CONCLUSIONS

More work needs to be done before the nature of the ' F ' shift' can be specified. The

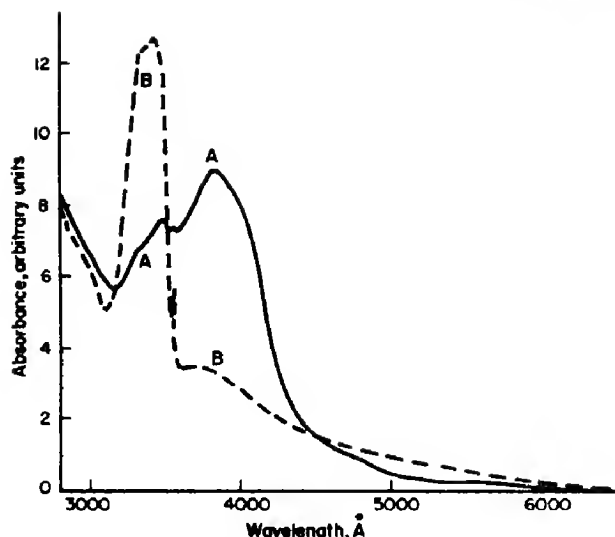


Fig. 8. Curve *A* shows the absorption configuration that resulted when a crystal having an absorption similar to that of curve *C*, Fig. 1, was irradiated at LNT several hours with light of $\lambda > 5630$ Å. The $F \rightarrow F'$ reaction greatly reduced the F band and caused F' and F_n to appear together as one large, asymmetric band. Curve *B* resulted from irradiating the crystal having the absorption of curve *A* with white light at room temperature for 30 min, then cooling to LNT. Note: F_n appears larger than F' in curve *B*. The spike at 3558 Å is the zero phonon line. The curves were arbitrarily joined at 6500 Å.

data presented here, it is believed, establish the independent existence of the center responsible for the F_n band and show that it is related to light irradiation treatments and crystal temperatures in an unusual manner. Its bleaching properties suggest that the center forms independently of both the F and the F' centers, and that it is thus probably not

a coagulation center. The relation of the F_n center to electrical conductivity as described above could be coincidental; yet for the small number of samples tested so far, there has been a one-to-one correspondence between a well-defined conductivity knee and the ability to undergo the ' F ' shift' (cf. caption, Fig. 6).

Acknowledgements—The authors wish to thank Dr. L. Johnston, D. Graham and A. Van't Hul for helpful discussions of experimental techniques; Dr. R. Porter for the loan of chart recorders; and the Agricultural Sciences Department for the use of the Cary spectrophotometer.

REFERENCES

1. KEMP J. C., ZINIKER W. M. and HENSLEY E. B., *Phys. Lett.* **25A**, 43 (1967).
2. SCHULMAN J. H. and COMPTON W. D., In *Color Centers in Solids*, pp. 107–112. Macmillan, New York (1962).
3. VAN DOORN C. Z., *Philips Res. Rep. Suppl.* **4** 17, 30, 81 (1962).
4. TANIMOTO D. H., ZINIKER W. M. and KEMP J. C., *Phys. Rev. Lett.* **14**, 645 (1965). Also, Private communication with KEMP.
5. WARD W. C., Ph. D. Thesis, University of Missouri, Columbia (1965).
6. DUTTON D. and MAURER R., *Phys. Rev.* **90**, 126 (1953).
7. *Handbuch Der Physik* (Edited by S. Flügge), Vol. 20, pp. 246ff. Springer, Berlin (1957).
8. SCHULMAN J. H. and COMPTON W. D., In *Color Centers in Solids*, pp. 52ff. Macmillan, New York (1962).
9. *Solid State Physics* (Edited by F. SEITZ and D. TURNBULL), Vol. 16, pp. 121ff. Academic Press, New York (1964).
10. MIYAKE S. and SUZUKI K., *J. phys. Soc. Japan* **9**, 802 (1954).
11. RABIN H., *Phys. Rev.* **129**, 129 (1963).
12. DOLLOFF R. T., *J. appl. Phys.* **27**, 1418 (1956).

THE PREPARATION OF NiO THIN FILMS AND THEIR USE IN OPTICAL MEASUREMENTS IN THE VISIBLE AND ULTRAVIOLET

CHARLES E. ROSSI

Westinghouse Corporation, Pittsburgh, Penna. 15235, U.S.A.

and

WILLIAM PAUL

Division of Engineering and Applied Physics, Harvard University, Cambridge, Mass. 02138, U.S.A.

(Received 13 January 1969)

Abstract—Several methods for producing NiO films for use in optical experiments are discussed including an indication of the significant problems encountered with each method. Transmission spectra between 2000 and 6000 Å are presented for films grown by both electron beam evaporation of nickel in an oxygen atmosphere and by reactive sputtering. The spectra appear to be consistent with one another as well as with the spectra of films grown on MgO by vapor deposition. The transmission spectra indicate that in addition to the absorption edge near 3700 Å, structure is present near 2300 Å. Electron reflection diffraction measurements indicate that films grown by electron beam evaporation and reactive sputtering on CaF₂ and LiF have at least some degree of crystalline order. Two films have been used to provide information on the shift of the NiO absorption edge with temperature, the results being -2.9 and $-4.2 \cdot 10^{-4}$ eV/°C. A Kramers Kronig analysis of the reflectivity of bulk NiO has been made and shows that the absorption of the films is consistent with the absorption constant derived from the reflectivity data. The reflectivities of a bulk sample and a film on MgO support the film transmission measurements in indicating structure near 2300 Å.

1. INTRODUCTION

MANY RECENT papers have indicated that the optical properties of thin epitaxial films of semiconducting materials are the same as those of bulk samples. This allows the use of film transmission to study the optical properties in the region above the fundamental absorption edge where reliable information was previously available only from reflectivity measurements. A number of workers for example, have reported the use of Ge, PbS, PbSe, PbTe, and Cd_xHg_{1-x}Te films to obtain reliable optical data in the transparent and highly absorbing regions [1–10].

The present work was initiated by the desire to extend the technique of epitaxial thin film growth to the transition metal oxides, NiO being an obvious first step. Since the ultimate goal was to investigate the electronic energy spectra from the optical behavior of these materials in the visible and ultraviolet at energies where they are quite absorbing, the deposited films had to be of a

good optical quality and have optical properties as nearly as possible identical to the properties of the bulk material.

In addition to using NiO as a test subject for the growth of epitaxial films of the transition metal oxides, we wished to learn more about the fundamental properties of NiO by interpreting the transmission spectrum in the ultraviolet. In NiO the five degenerate 3d orbitals of the Ni²⁺ ion are split by the crystal field into a doubly degenerate set and a triply degenerate set. Six electrons are in the lowest d levels and two in the upper levels. The Ni²⁺ magnetic moments are coupled such that NiO is antiferromagnetic below its Neel temperature T_N of 523°K. Above T_N , NiO is cubic whereas at low temperatures it is distorted by a contraction along one of the original cubic unit cell $\langle 111 \rangle$ axes. The low temperature structure is rhombohedral. The precise temperature at which the structure changes occurs is in question [12].

Since Ni²⁺ in NiO has an unfilled 3d shell,

simple band theory predicts NiO to be a conductor. Nevertheless, the purest available NiO has a specific resistivity greater than 10^{10} Ω -cm at room temperature. In non-stoichiometric or Li doped NiO the resistivity is lower by several orders of magnitude [12–15].

Many early workers [14–20] interpreted transport experiments (principally conductivity and thermoelectric measurements) in terms of models whereby holes moved through the crystal via thermally activated hopping. The low values for the mobility derived from a hopping model were consistent with the fact that no Hall effect could be detected.

Recently, however, measurements of the transport behavior of NiO including Hall effect experiments have pointed to a model where the activation energy is due to activation of carriers and the transport occurs in a narrow band [21–24]. The evidence [21–24] is inconsistent with a hopping model since it indicates that the mobility is not responsible for the activation energy occurring in the conductivity. It now appears that the transport in so-called pure NiO is determined by impurities and/or imperfections up to temperatures as high as room temperature. Adler [25] suggests the possibility that all observed transport data up to this time may be due to impurities and intrinsic conduction may not as yet have been observed in NiO. As possible evidence for this suggestion Adler quotes the optical results contained in References [26] and [27] which indicate an energy gap of ~ 4 eV, considerably higher than values obtained from recent transport experiments. Feinleib and Adler [28] have proposed that the conduction in NiO occurs by means of holes in the oxygen $2p$ band provided by acceptor impurities and have suggested a band structure to explain the transport and optical behavior.

Optical measurements on NiO have been reported by several workers [26, 27, 29–31]. The low energy region is dominated by lattice vibration effects [30, 31] and will not be discussed here. Newman and Chrenko [26]

measured the optical properties between 0.025 and 10 eV. Their samples consisted of single crystals grown by flame fusion and epitaxial films deposited on MgO by the vapor deposition method described by Cech and Alessandrini [32]. Between 1.0 and 3.5 eV there are several narrow absorption bands which Newman and Chrenko assign to transitions in Ni^{2+} as modified by the crystal field. At ~ 4 eV the NiO absorption increases rapidly to a plateau at higher energies. Since MgO absorbs strongly in the regions above 4 eV Newman and Chrenko used thin films of oxidized nickel for measurements between 4 and 5.8 eV. Their measurements showed no structure at energies above 4 eV. Newman and Chrenko measured the reflectivity of single crystal NiO between 0.025 and 10 eV. Between 0.1 and 10 eV only a single large peak at 4 eV corresponding to the rapid increase in absorption at about this energy was observed.

Ksendzov and Drobkin [27] observed a photocurrent in NiO which was small below 3 eV and which increased sharply between 3.5 and 4.0 eV. Furthermore, they interpreted their NiO conductivity as a function of temperature to indicate a forbidden band width of 3.7 eV.

As can be seen from the above brief summary of the measured properties of NiO, any experiments which might yield information on the band structure of NiO would be of considerable interest. The possibility of using thin films to obtain optical transmission data on NiO above the absorption edge was, thus, a strong motivation for our work.

2. EXPERIMENTAL

(A) Sample preparation

We wished to deposit NiO onto a substrate which was transparent far into the ultraviolet. The ideal substrate material was LiF which has the NaCl crystal structure, a lattice constant of 4.01 \AA [33] and is transparent to about 1040 \AA in the vacuum ultraviolet [34]. The lattice structure of LiF

appears to be quite compatible with NiO which is nearly cubic and has a lattice constant of 4.18 \AA [33]. Two other materials which are transparent into the vacuum ultra-violet also appeared promising— CaF_2 (lattice constant of 5.45 \AA and transparent to 1250 \AA [34]) and BaF_2 (lattice constant of 6.18 \AA and transparent to 1300 \AA [34]). These substances are less compatible with NiO since both are of the fluorite structure and cleave along (111) planes rather than (100).

In depositing NiO for use in optical experiments, we investigated six essentially different techniques:

1. Evaporation of NiO in a high vacuum
2. Flash evaporation of NiO
3. Oxidation of nickel films
4. Chemical transport and reaction via a gas
5. Electron beam evaporation of nickel in an O_2 atmosphere
6. Sputtering of nickel in an O_2 atmosphere.

The method of evaporation was quite similar to that given in [7]. NiO powder was heated by a tungsten boat in a vacuum of $2\text{--}3 \cdot 10^{-6} \text{ mm Hg}$. The substrates used were $1 \text{ cm} \times 1 \text{ cm} \times 3 \text{ mm}$ thick and were cleaved in air within a few minutes preceding an evaporation run. The substrates were attached to a tantalum plate which was heated by a tantalum wire heater located just above it. A thermocouple was attached to the tantalum plate in order to monitor the substrate temperature during evaporation. Nickel oxide evaporates at temperatures of the order of 1600°C . We found that with straightforward evaporation the NiO appeared to decompose and leave nickel behind to subsequently evaporate. In addition the nickel tended to alloy with the boat and cause it to burn out. In view of these difficulties we concluded that other deposition techniques would have to be used.

The chief problem in the ordinary evaporation of a compound such as NiO is that one or more elements may evaporate from the com-

pound more readily than the others. In flash evaporation one attempts to solve this problem by dropping small particles of the compound onto a surface held at a temperature sufficiently high to quickly evaporate all constituents [9]. In flash evaporation, NiO powder was dropped continuously onto the heated tungsten boat. The tungsten boat was held at $1800^\circ\text{--}2000^\circ\text{C}$ as measured by an optical pyrometer.

The flash evaporation procedure worked very well for evaporating epitaxial nickel films using nickel powder. Nickel films deposited on LiF held at 450°C were usually epitaxial, and photographs of the electron diffraction patterns were used as standards to give the spacing of the diffraction pattern for nickel. Similarly, photographs of the electron diffraction patterns of NiO films on MgO (the method of deposition will be discussed shortly) were used as standards giving the spacing of the diffraction pattern of known NiO.

From the spacing of the electron diffraction patterns of films obtained by flash evaporating NiO powder in a vacuum of $5 \cdot 10^{-6} \text{ mm Hg}$ we concluded that the flash evaporation of NiO powder, in general, yields nickel films. Flash evaporation of NiO powder in either air or O_2 at $2 \cdot 10^{-4} \text{ mm Hg}$ with LiF substrates at $500^\circ\text{--}550^\circ\text{C}$ in general yields films with at least a faint Laue pattern having the spacing of NiO. Usually the diffraction patterns also contain rings. The rings could very well be due to impurities evaporated along with the NiO. From the optical measurements we concluded that other materials (probably tungsten oxide) were evaporated along with NiO and distorted the transmission spectra.

We oxidized several films of nickel on LiF, starting with oriented nickel films rather than amorphous or polycrystalline ones. The nickel films were deposited both by direct evaporation and by flash evaporation, the substrate temperatures being 450°C . We oxidized one film in O_2 at approximately 300°C for three hours and a second in O_2 at approximately 500°C for eight hours. The diffraction pat-

terms of these films showed only rings. The optical results (to be discussed later) indicated that the oxidized films varied considerably in stoichiometry.

Cech and Alessandrini[32] have shown that epitaxial thin films of NiO can be grown on MgO by decomposition of nickel halide in an atmosphere of water vapor at a temperature of about 700°C. Films were grown by this method on MgO and used as standards of comparison in both the electron diffraction measurements and in the optical measurements. We made numerous attempts to extend the method to LiF substrates since MgO is not transparent at wavelengths less than 3500 Å. We found that the LiF reacted with the vapor given off in the chemical reaction at high substrate temperatures (700°–800°C) and no film could be deposited at low substrate temperatures ($\sim 300^\circ\text{C}$).

Evaporation by an electron beam has the advantage that the beam heats the material to be evaporated and not a crucible or boat of some foreign material. This reduces the possibility of evaporating impurities. In the use of the electron beam, nickel was evaporated from either an alumina or carbon crucible onto a substrate heated to 550°C (the substrate heater was identical to that used in the other evaporation techniques). During the evaporation of the nickel metal, O_2 was continuously bled into the system to maintain a pressure of $1 \cdot 10^{-4}$ mm Hg. For the electron beam evaporations, a Veeco Model VeB-6 electron beam gun was used at 11 kV.

Films of NiO were also deposited onto heated substrates (550°C) by reactive sputtering. For this, the R. D. Mathis Model SP210A sputtering module modified to contain a substrate heater was used. A Welch Model 3101A turbo-molecular pumping unit was used to evacuate the sputtering module. The sputtering gas was premixed O_2 -Ar.

Several films grown by electron beam evaporation and sputtering showed Laue patterns with the NiO spacing. The patterns will be shown in the following section.

(B) Optical measurements

The optical measurements were made using a Cary 14 spectrometer with its associated recording electronics and a McPherson Model 225 vacuum ultraviolet spectrometer. A hydrogen lamp with LiF window was attached to the entrance slit assembly of the McPherson spectrometer. The recording electronics consisted of a tuning fork chopper (200 cps) manufactured by American Time Products and fairly standard phase sensitive detection equipment composed of a P.A.R. JB-4 Lock-In Amplifier and a Model CR-4 pre-amplifier. An RCA 1P21 phototube with a sodium salicylate coated microscope slide in front of the cathode was used as a detector. The tube was rotated in front of the sample for transmission measurements. The sample was moved out of the beam when detecting I_0 .

3. RESULTS AND DISCUSSION

Figure 1 shows the transmission spectra of several films grown on LiF by flash evaporating

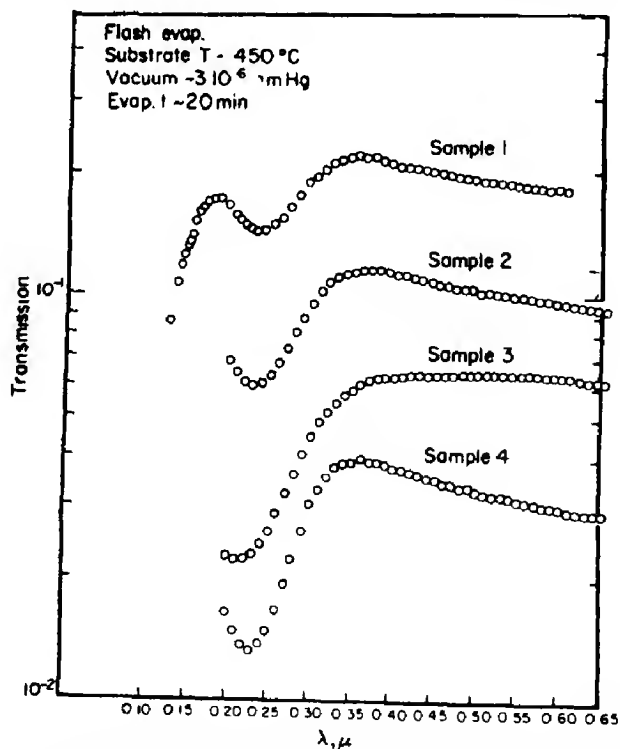


Fig. 1. Transmission spectra of several films grown on LiF by flash evaporating Ni powder in a vacuum of $\sim 3 \cdot 10^{-6}$ mm Hg.

Ni powder in a vacuum of $3 \cdot 10^{-6}$ mm Hg. The substrates were held at 450°C which in most cases gave epitaxial films. Only one (the thinnest) of the particular films in Fig. 1 was checked with the electron microscope and this film happened to be polycrystalline. All films were not checked because of the possibility of the electron beam coloring the substrates.

Figure 2 shows the transmission of three of the films in Fig. 1 after they were oxidized. The sample numbers in Figs. 1 and 2 are the

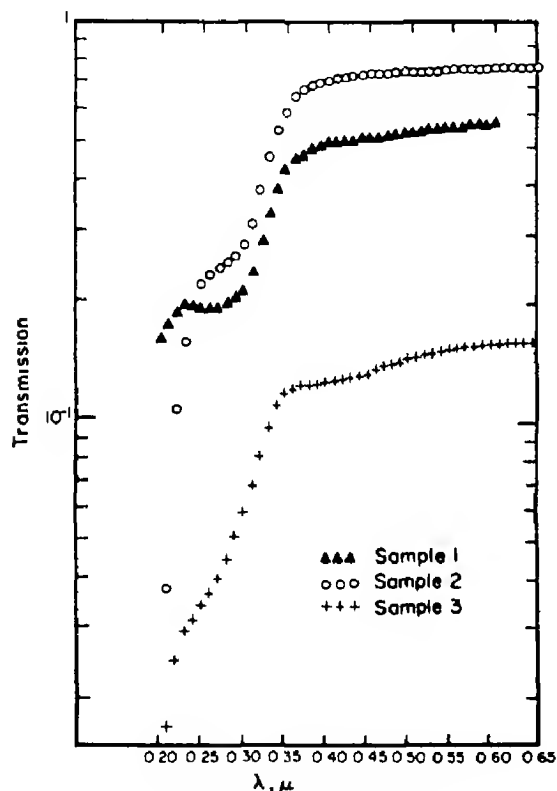


Fig. 2. Transmission spectra of samples 1 through 3 of Fig. 1 after oxidation. Sample 1 was oxidized for 2 hr at 550°C in O_2 at $2 \cdot 10^{-4}$ mm Hg and Samples 2 and 3 were oxidized for 3 hr at 300°C in O_2 at room pressure.

same. The three samples show an absorption edge beginning at 3500 to 3800 Å. The differences are probably due to variations in stoichiometry and imply that oxidized metal films can probably not be used to obtain accurate optical data for the metallic oxide. The technique of oxidizing Ni films had, however, been used to obtain NiO optical data by

several workers since better methods of producing sufficiently thin films were not available [28,31].

Figure 3 demonstrates a problem which occurred with the use of LiF substrates with electron beam gun evaporation and when sputtering onto LiF. The problem also occurred to some extent with CaF_2 substrates. In

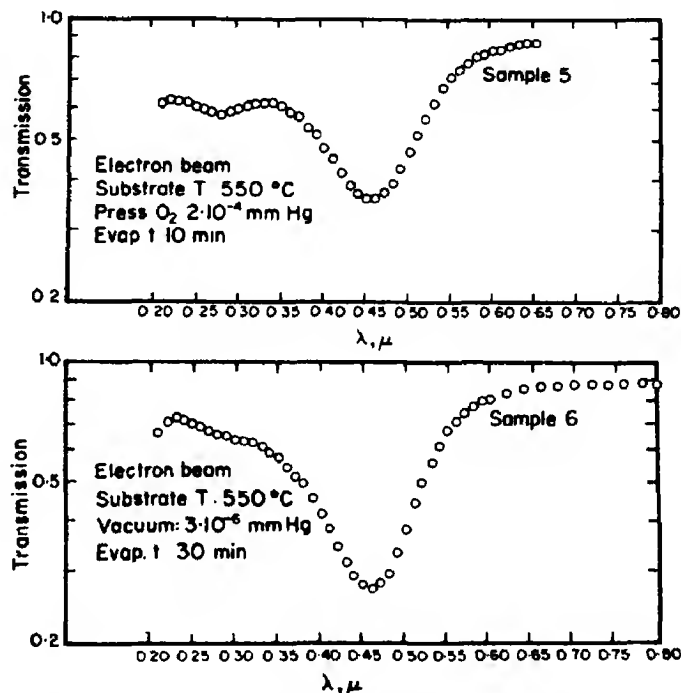


Fig. 3. Transmission spectra showing color center absorption encountered with LiF substrates when using electron beam evaporation.

Samples 5 and 6 the substrates were held at 550°C while the electron beam gun was directed onto the nickel source. In Sample 5 nickel was evaporated at a slow rate for ten minutes in an oxygen atmosphere of $2 \cdot 10^{-4}$ mm Hg whereas with Sample 6 the electron beam gun was operated in a vacuum of $3 \cdot 10^{-6}$ mm Hg at an intensity lower than that necessary to evaporate the nickel. In both cases the substrate surface was orange colored. By simultaneously depositing onto LiF, KCl, and glass, we determined that the coloring of the LiF was due to either X-rays created when the beam hit the source or due to electrons scattered onto the substrate by the source.

The coloring was not apparent in BaF_2 and seemed to be considerably less in CaF_2 when using the electron beam in an oxygen atmosphere. In depositing Ni in vacuum, CaF_2 was colored violet. The problem of color centers, which also existed when using the sputtering technique, makes it difficult to obtain u.v. optical data without, at a minimum, making measurements of films grown on several different substrate materials to separate out the effects of the color centers.

Figure 4 shows the electron diffraction pattern of one thin film grown by electron beam evaporation. The Laue spots were compared with those of known NiO and Ni films

and had the NiO spacing to within ~ 6 per cent, which is considered to be within the error in determining the electron diffraction pattern spacing. For comparison, the ratio of NiO to Ni lattice spacings is 0.842.

Figure 5 shows the results of transmission measurements made between successive evaporations onto the same CaF_2 substrate. The evaporations were made with the electron beam gun as previously described. The spectra show a sharp edge beginning between 3750 and 3700 Å which shifts with thickness due to interference. The two thinnest films showed small dips near 3800 Å which could be due to the d level absorption seen at this

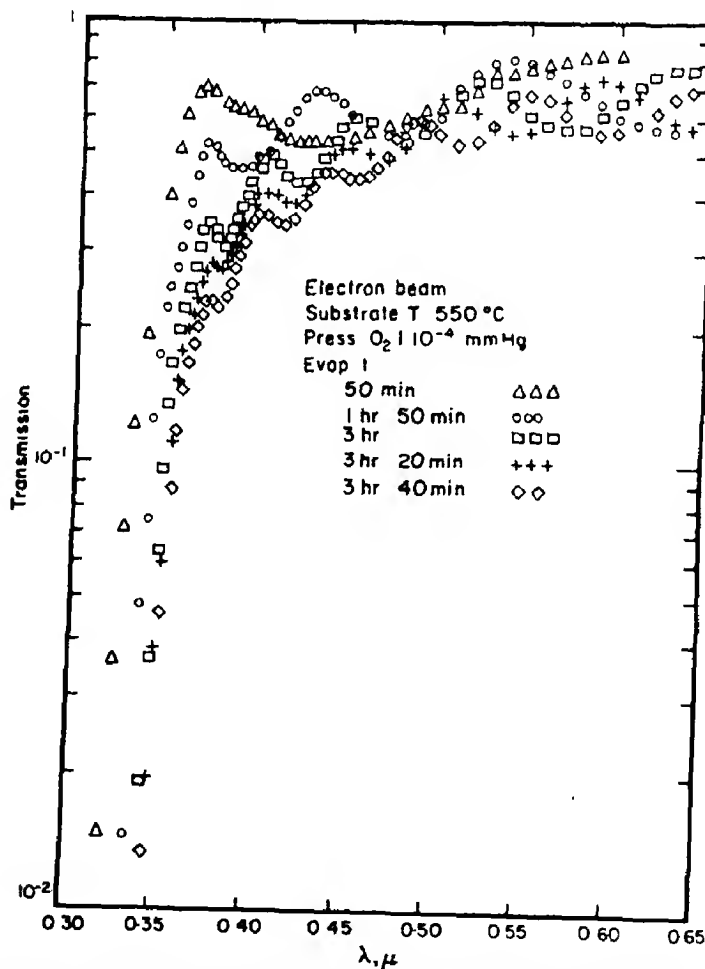


Fig. 5. Transmission measurements made between successive evaporations onto the same CaF_2 substrate. The evaporations were made using the electron beam to evaporate Ni in an O_2 atmosphere of 1.10^{-4} mm Hg.



Fig. 4. Electron diffraction pattern of a film grown on CaF_2 by electron beam evaporation of Ni in an O_2 atmosphere of 1.10^{-4} mm Hg. The evaporation time was eighteen minutes and the substrate temperature was 550°C .



Fig. 11. Electron diffraction pattern of the film of Fig. 10.

wavelength in films grown on MgO by vapor deposition ([26] and Fig. 6). Unfortunately the interference fringes made it impossible to determine whether there was an absorption at 3800 \AA in the thicker films. It should be noted that the films remained quite transparent at wavelengths greater than 4000 \AA as the film thickness was increased. Newman and Chrenko[26] have shown that the transparency of NiO at wavelengths greater than 4000 \AA is associated with good stoichiometry. The only electron diffraction measurement made on the films was made after the last evaporation and showed sharp rings.

Figure 6 compares the transmission spectrum of a film grown on MgO by vapor deposition with that of the thickest film of Fig. 5 and with a film grown on BaF_2 by electron beam evaporation in an oxygen atmosphere. Aside

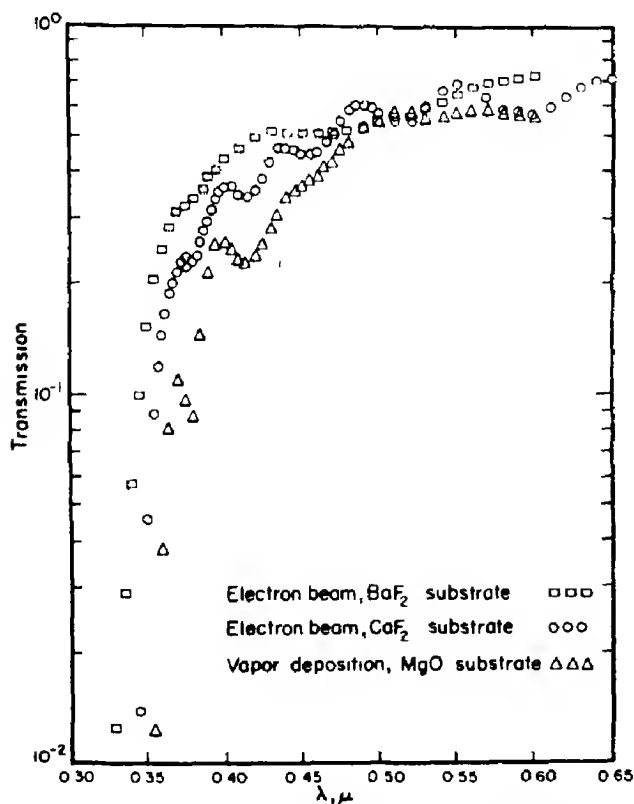


Fig. 6. Comparison of the transmission spectrum of a film grown on MgO by vapor deposition with that of the thickest film of Fig. 5 and with a film grown on BaF_2 (held at 550°C) by electron beam evaporation of Ni in an O_2 atmosphere of $1 \cdot 10^{-4} \text{ mm Hg}$.

from the interference fringes in the films grown by electron beam evaporation the transmission spectra are quite similar. Films grown on MgO showed quite good Laue patterns.

Figures 7-9 show the transmission spectra of one film of NiO on quartz and two on

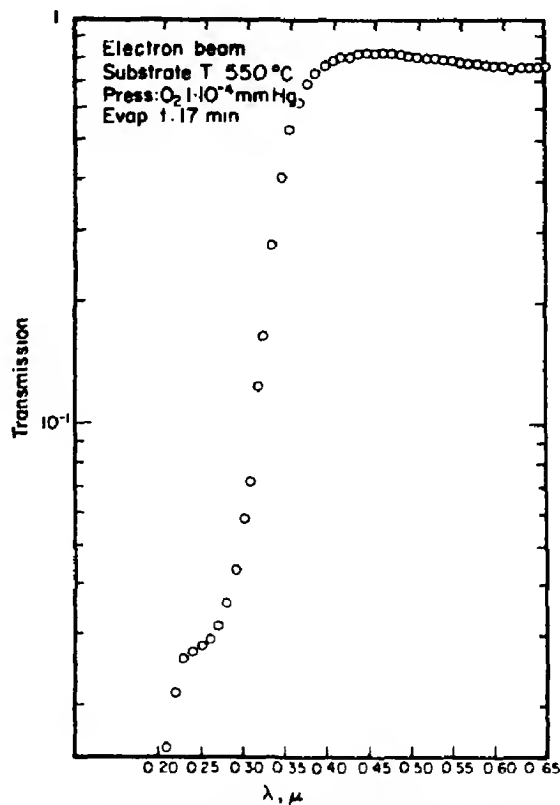


Fig. 7. Transmission spectrum of a film grown on quartz by electron beam evaporation of Ni in an O_2 atmosphere of $1 \cdot 10^{-4} \text{ mm Hg}$.

BaF_2 . The three films were all grown by electron beam evaporation of Ni in an O_2 atmosphere. The films of Fig. 7 and 8 were grown using an alumina crucible to hold Ni pellets. In depositing the film of Fig. 9, the Ni pellets were held in a crucible formed from nickel plate to insure no contamination from any foreign crucible material. The spectra of the three films are quite similar, all three showing an absorption edge near 3700 \AA , a plateau at about 2600 \AA , and a further increase in absorption near 2300 \AA .

Figure 10 shows the transmission spectrum

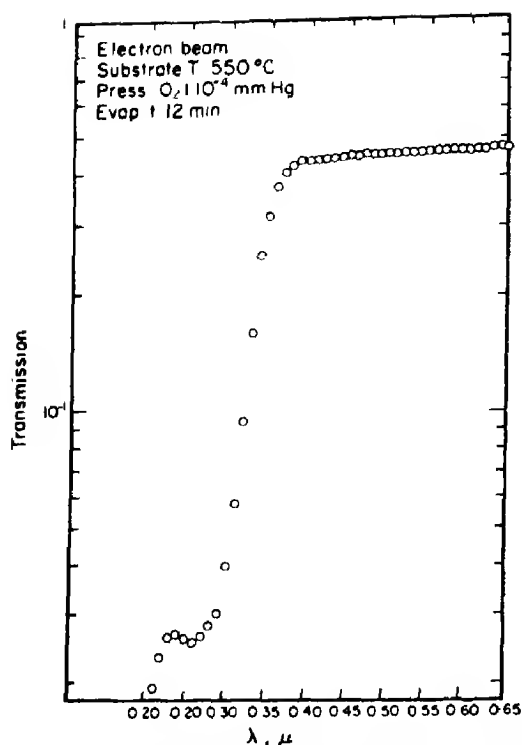


Fig. 8. Transmission spectrum of a film grown on BaF_2 by electron beam evaporation of Ni in an O_2 atmosphere of 1.10^{-4} mm Hg.

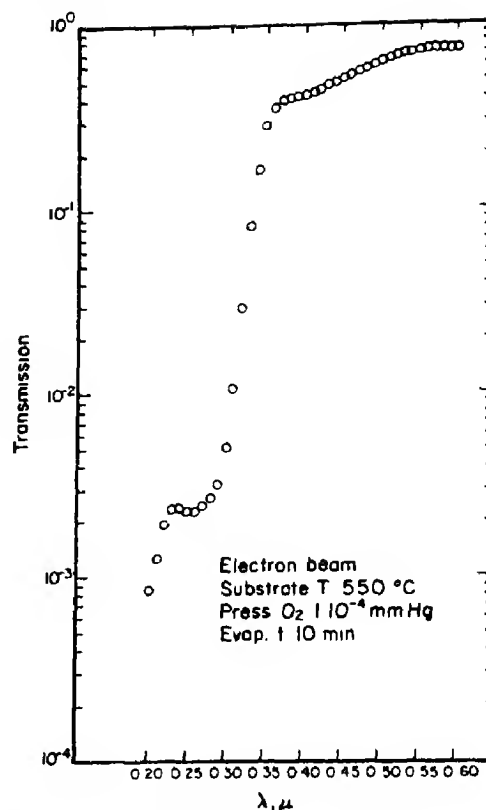


Fig. 9. Transmission spectrum of a film grown on BaF_2 by electron beam evaporation of Ni in an O_2 atmosphere of 1.10^{-4} mm Hg.

of a film grown on CaF_2 by sputtering Ni in a 20% O_2 , 80% A atmosphere. The absorption appears to be the same as that of the films in Figs. 7-9. Figure 11 shows the electron diffraction pattern of the sputtered film of Fig. 10. The pattern shows Laue spots which have the spacing of NiO to within 6 per cent.

Figure 12 shows the transmission spectrum of a film grown on quartz by sputtering Ni in a 10% O_2 , 90% A atmosphere.

Figure 13 shows the temperature shifts of the absorption edges of the films of Fig. 5 and 12 at liquid nitrogen temperature. The thickest of the films of Fig. 5 is shown. Room temperature scans of the film of Fig. 5 on CaF_2 were made before and after a scan at liquid nitrogen temperature. The room temperature scans agree to within about 15 Å. Only one room temperature scan was made of the film on quartz. The following temperature coefficients, which are necessarily very tentative and approximate because no corrections

have been made for thermal strains caused by the substrate, were computed for the absorption edges:

$$\text{Film on quartz, } \frac{dE_g}{dT} = -2.9 \cdot 10^{-4} \text{ eV/}^\circ\text{C}$$

$$\text{Film on CaF}_2, \frac{dE_g}{dT} = -4.2 \cdot 10^{-4} \text{ eV/}^\circ\text{C}$$

The transmission measurements described above were made using the Cary 14 spectrometer.

Figure 14 shows the reflectivity spectra of a bulk NiO sample and a NiO film on MgO . The spectra were taken using the McPherson spectrometer described earlier. In addition to the peak near 3100 Å previously observed by Newman and Chrenko[26] the samples both show structure near 2000 Å with a

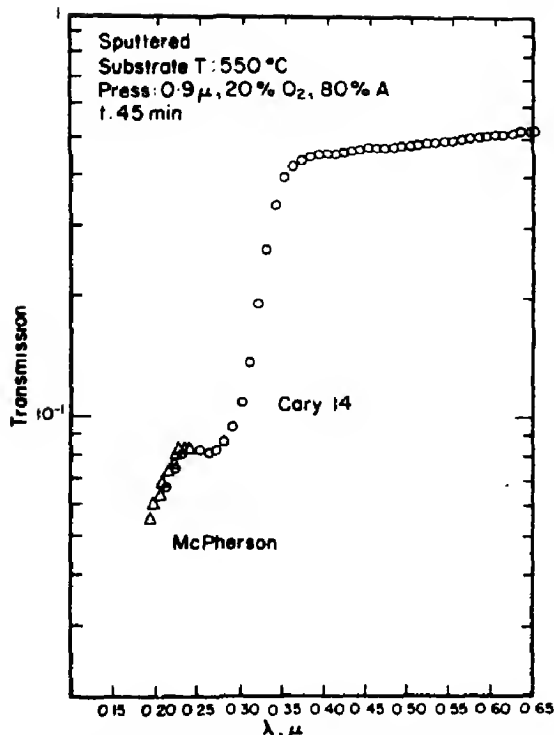


Fig. 10. Transmission spectrum of a film grown on CaF₂ by sputtering of Ni in a 20% O₂, 80% Ar atmosphere.

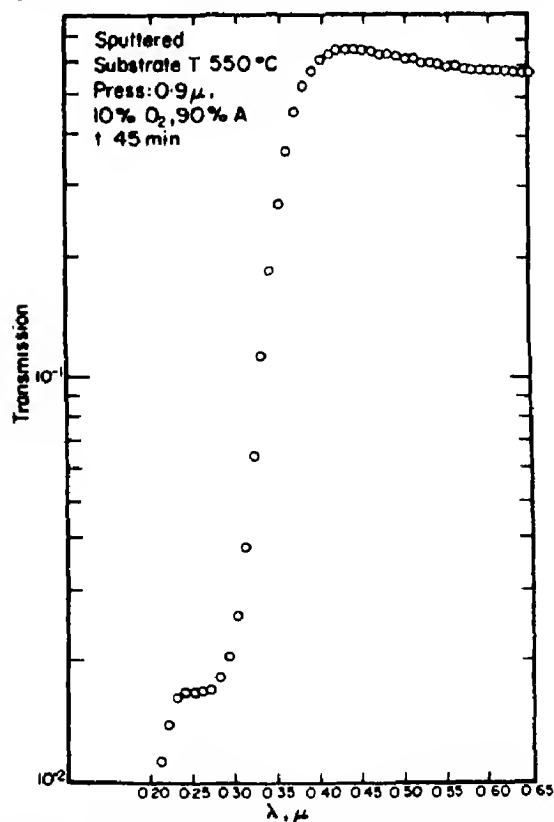


Fig. 12. Transmission spectrum of a film grown on quartz by sputtering Ni in a 10% O₂, 90% Ar atmosphere.

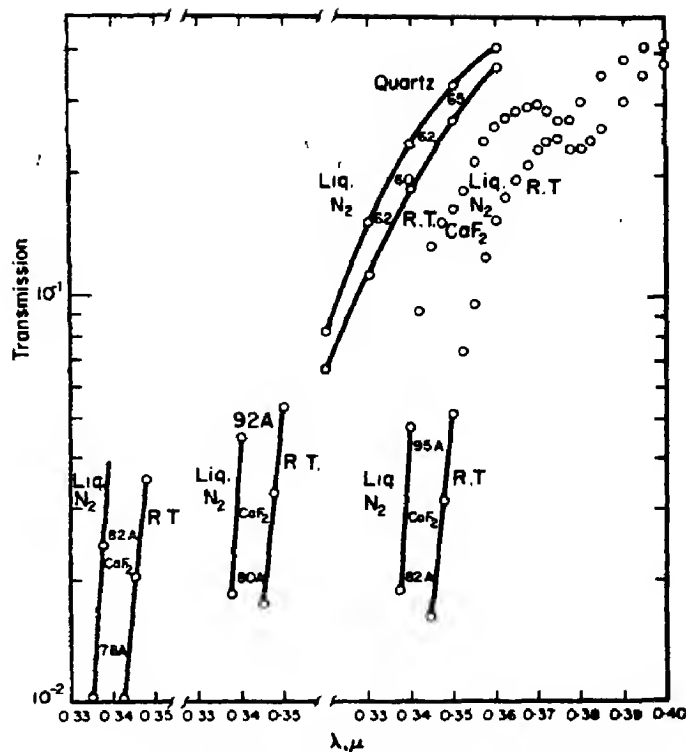


Fig. 13. Temperature shifts of the films in Figs. 5 and 12.

change in slope near 2350 Å. A Kramers Kronig analysis of the bulk reflectivity spectrum yielded the absorption constant shown in Fig. 15. At wavelengths shorter than 1250 Å the reflectivity in the Kramers Kronig analysis was extrapolated as $R_{\max}(E_{\max}/E)^p$ where R_{\max} is the reflectivity at 1250 Å, E_{\max} the energy corresponding to 1250 Å and E the energy. The absorption constant is shown for three values of P , $P = 2, 3$, and 4. At long wavelengths the reflectivity was assumed constant and equal to the value at 6000 Å.

The optical results discussed in this paper indicate that NiO films can be made by evaporating nickel in an O₂ atmosphere or by sputtering nickel in an O₂-Ar mixture. The transmission spectra of films grown by both the electron beam technique and by sputtering appear to be consistent with one another as well as with the spectra of films grown on MgO by vapor deposition. The film transmission spectra including the spectra of oxidized nickel films indicate that the absorption of NiO increases rapidly between 3700 Å

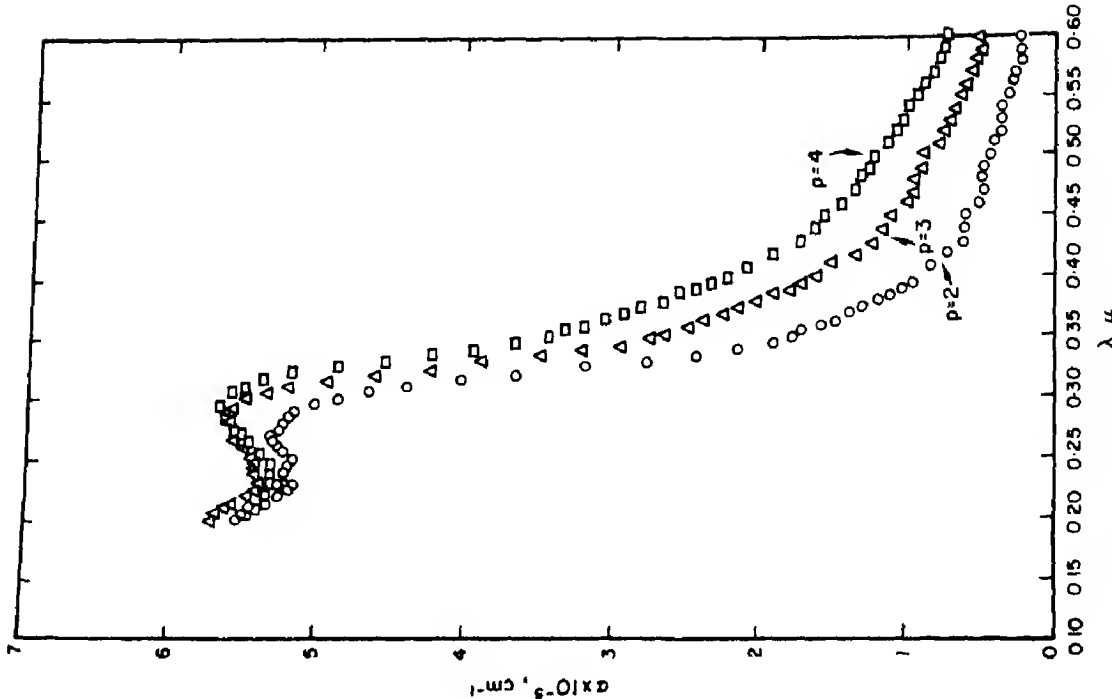


Fig. 15. The absorption constant obtained by a Kramers Kronig analysis of the bulk NiO reflectivity data shown in Fig. 14. The reflectivity was extrapolated at high energies as $R = R_{\max} (E_{\max}/E)^P$ where P is an adjustable parameter, R_{\max} the reflectivity at 1250 Å and E_{\max} the energy corresponding to 1250 Å. The absorption constant is shown for three extrapolation parameters, $P = 2, 3$ and 4.

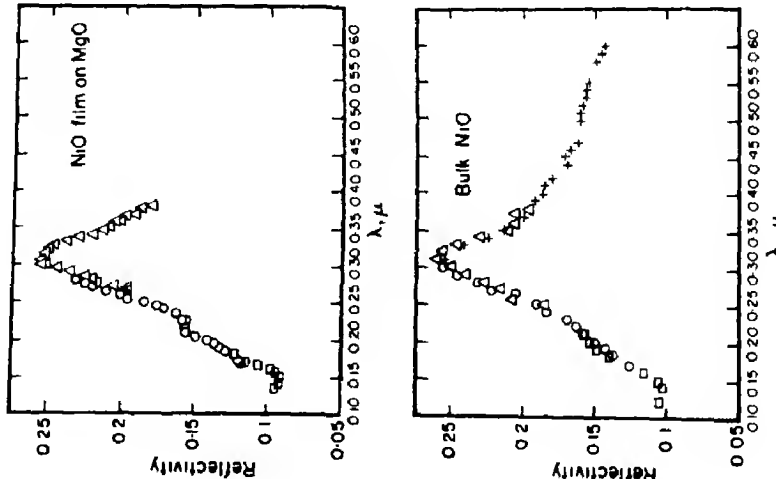


Fig. 14. Reflectivity spectra of a bulk NiO sample and a film on MgO. Different filters were used in different wavelength regions with overlap between the regions. A separate symbol has been used in the figure to designate data obtained with each filter.

(~ 3.3 eV) and 2600 \AA (~ 4.8 eV), levels off and then increases again near 2300 \AA (~ 5.4 eV). The absorption constant derived from the measured reflectivity of bulk NiO supports the behavior of the absorption inferred from the transmission of the films. The optical behavior is consistent with either two nearby band transitions or a transition to an exciton state followed by a band transition at a higher energy. A possible interpretation is the transition between the oxygen $2p$ levels and an exciton below the $4s$ band followed by a transition to the $4s$ band. Our results, however, are certainly not conclusive as to the precise transitions involved.

Acknowledgements—We should like to thank Dr. Fred Kahn and Dr. Peter Melz for help in completing the optical measurements on these films. Dr. Paul Grant and Dr. Rudolf Ludeke participated in many early discussions on the best procedure for their deposition, and contributed as well to an evaluation of methods for establishing the optical constants from film data. Mr. James Inglis and Mr. Albert Manning were responsible for the construction of apparatus. Mr. David McLeod not only made numerous contributions to improved ways of depositing samples but was also of great help in clearing up many of the final experimental details and in preparing this report for publication.

REFERENCES

- SCHOOLAR R. B., *Bull. Am. phys. Soc., Ser. II* **8**, 516 (1963).
- WESSEL P. R., DIXON J. R., ZEMEL J. N., SCHOOLAR R. B. and JENSEN J. D., *Bull. Am. phys. Soc., Ser. II* **8**, 517 (1963).
- RIEDL H. R. and SCHOOLAR R. B., *Phys. Rev.* **131**, 2082 (1963).
- MITCHELL D. L., PALIK E. D. and ZEMEL J. N., *Phys. Rev. A* **135**, 763 (1964).
- SCHOOLAR R. B. and DIXON J. R., *Phys. Rev. A* **137**, 667 (1965).
- WESSEL P. R., *Phys. Rev.* **153**, 836 (1967).
- ROSSI C. E. and PAUL W., *J. appl. Phys.* **38**, 1803 (1967).
- GRANT P. M. and PAUL W., *J. appl. Phys.* **37**, 3110 (1966).
- LUDEKE R. and PAUL W., *J. appl. Phys.* **37**, 3499 (1966).
- SEMILETOV S. A., VORONINA I. P. and KORTUKOVA E. I., *Soviet Phys. crystallogr.* **10**, 429 (1966).
- SLACK G. A., *J. appl. Phys.* **31**, 1571 (1960).
- VERNON M. W. and LOVELL M. C., *J. Phys. Chem. Solids* **27**, 1125 (1966).
- FEINLEIB J., Tech. Rep. No. HP-11, Gordon McKay Laboratory, Division of Engineering and Applied Physics, Harvard University (1963).
- VAN HOUTEN S., *J. Phys. Chem. Solids* **17**, 7 (1960).
- KOIDE S., *J. phys. Soc. Japan* **20**, 123 (1965).
- deBOER J. H. and VERWEY E. J. W., *Proc. phys. Soc.* **49**, 59 (1937).
- HEIKES R. R. and JOHNSTON W. D., *J. chem. Phys.* **26**, 582 (1957).
- MORIN F. J., *Phys. Rev.* **83**, 1005 (1951).
- MORIN F. J., *Phys. Rev.* **93**, 1195 and 1199 (1954).
- MORIN F. J., *Bell Syst. tech. J.* **37**, 1047 (1958).
- BOSMAN A. J. and CREVECOEUR C., *Phys. Rev.* **144**, 763 (1966).
- BOSMAN A. J., Van DAAL H. J. and KNUVERS G. F., *Phys. Lett.* **19**, 372 (1965).
- Van DAAL H. J. and BOSMAN A. J., *Phys. Rev.* **158**, 736 (1967).
- AUSTIN I. G., SPRINGTHORPE A. J., SMITH B. A. and TURNER C. E., *Proc. phys. Soc.* **90**, 157 (1967).
- ADLER D., To be published.
- NEWMAN R. and CHRENKO R. M., *Phys. Rev.* **114**, 1507 (1959).
- DSENDZOV Ta. M. and DROBKIN I. A., *Soviet Phys. solid St.* **7**, 1519 (1965).
- FEINLEIB J. and ADLER D., *Phys. Rev. Lett.* **21**, 1010 (1968).
- DOYLE W. P. and LONERGAN G. A., *Trans. Faraday Soc.* **26**, 27 (1958).
- MARSHALL R., MITRA S. S., GIELISSE P. J. and PLENDL J. N., *Proc. Intl Conf. Physics Semiconductors*, Paris (1964).
- GIELISSE P. J., PLENDL J. N., MANSUR L. C., MARSHALL R., MITRA S. S., MYKOLA-JEWYEZ R. and SMAKULA A., *J. appl. Phys.* **36**, 2446 (1965).
- CECH R. E. and ALESSANDRINI E. I., *Trans. Am. Soc. Metals* **51**, 150 (1959).
- Handbook of Chemistry and Physics*, Chemical Rubber Publishing Company, Cleveland (1955).
- Optovac Optical Crystals Bull. No. 50. Optovac Inc., North Brookfield, Mass. (1964).

THEORY OF DIELECTRIC SCREENING OF AN IMPURITY AT THE SURFACE OF AN ELECTRON GAS

J. W. GADZUK†

Department of Physics, Solid-State and Molecular Theory Group, and
Research Laboratory of Electronics,
Massachusetts Institute of Technology, Cambridge, Mass. 02139, U.S.A.

(Received 15 November 1968)

Abstract—A dielectric formalism is developed which is applicable to an electron gas with a surface. This formalism is then used to obtain a theory of static surface impurity screening. Expressions for the screening charge around the surface impurity are obtained and then numerically evaluated. It is found that there is considerably more structure to the surface impurity Friedel oscillations than to those of a volume impurity. Furthermore, the screened surface impurity seems to be of longer range than a volume impurity.

It is shown that this impurity theory is a reasonable model for ionic adsorption on metal surfaces. For ion-metal separations of the order of a Fermi wavelength, the classical image force arising from supposed surface polarization charge has no validity. One must consider volume polarization processes in which the unscreened impurity field penetrates into the imperfect conductor. Then it is shown why the image-force models have given reasonable numerical results in spite of the irrelevance of the model.

1. INTRODUCTION

ALTHOUGH the many-body theory of perfect, homogeneous, high-density electron gases has been quite well developed[1–4] theoretical ventures into the inhomogeneous electron gas, in which translation invariance does not exist, have been sparse.

Perhaps the first treatment of a problem in which absolute, as well as relative, electron coordinates played a significant role was the linear static dielectric screening of a point impurity immersed in an electron gas with a smeared out positive background of charge presented by Langer and Vosko[5]. Their work will be a fundamental building block in the present paper.

An obvious extension of a theory of impurities in electron gases was an attempt to apply many-body theory concepts in an extension of the theory of Thomas–Fermi atoms, with the hope of finally generating shell structure. It was thought that shell structure

could be regarded as a large-scale manifestation of the Friedel density oscillations seen around the ion core of a statically screened impurity in an electron gas. This problem has been investigated by Baraff and Borowitz[6] and by DuBois and Kivelson[7]. They found that a systematic utilization of density gradient expansion techniques was inadequate to conveniently describe electron gas effects caused by rapid density variations.

Without a doubt, the most significant contributions to the theory of inhomogeneous electron gases have been those of Kohn, Hohenberg and Sham[8–12]. Starting from a general theorem stating that all electron gas properties are related to the electron gas density by a unique, universal functional of the density, they present many examples of inhomogeneous electron gases in which this theorem is of use. Furthermore, computational methods are established for treating problems in which the density change is small over a distance comparable to a Fermi wavelength. The method involves expansions in powers and orders of density gradients. The rapid

†Present address: National Bureau of Standards, Washington, D.C. 20234, U.S.A.

convergence of such expansions can be guaranteed only for inhomogeneous electron gases in which the density variation is slow. For this reason, new techniques must be developed to treat problems in which the density change is significant over a Fermi wavelength, such as atoms, electron gases with periodic potentials, and surface effects.

In the examples just cited, a rapid density variation occurs as a result of imposing a boundary condition on the noninteracting single-electron wave functions. Rapid density changes result as the electrons try to screen out the effects of the well-localized force providing the boundary condition. Essentially, diffraction effects arise. To the present author, this seems to be a fundamentally different phenomenon from the type treated by the "density as a basic variable theory," a fact well recognized by Kohn *et al.* The point is that the density gradient method is really based on Thomas-Fermi type of thinking, in which the local density and potential are simply related. This is not the case in the inhomogeneous electron gas caused by a boundary condition.

With this general introduction we can now proceed to the more specific problem of interest in this paper, the many-body effects in the surface region of an electron gas. This is one of the examples of the rapidly varying inhomogeneous electron gas which should be considered beyond the density gradient method.

One of the more dramatic aspects of the surface problem is the recognition of collective oscillations of electrons in the surface region, surface plasma oscillations[12-14]. In the surface region, the electron density changes rapidly from its interior value to zero in a distance of the order of a Fermi wavelength. The electrons in this region can be regarded as a sort of polarization charge. Since the average density of this charge is less than the interior density, it is reasonable to expect the surface plasma frequency to be less than the volume plasma frequency, as indeed it is.

This problem has recently been considered by Fedders, who worked within the context of a linear response model[15].

In Section 2, a dielectric formalism is established, which enables problems related to the linear response of the surface electron gas to be handled with a bit more transparency than with the formalism of Fedders. By means of a new image technique, the response of an infinite electron gas is related to the response of a semi-infinite gas with a surface.

A many-body effect of considerable interest is concerned with the static dielectric screening of a massive charged particle in the surface region of an electron gas. This problem has been the subject of interest in some recent studies. Heine recognized the importance of ion screening in Auger processes at metal surfaces[16]. The author has presented a simple model of ionic adsorption at metal surfaces which displays the role of screening in adsorption[17]. Stern treated the case of an impurity polarizing a two-dimensional electron gas, the model for an inversion layer at a surface[18].

Section 3 is devoted to a formalism for treating static impurity screening in the surface region of an electron gas. This work is the final form of reported preliminary studies[19]. In this section expressions and numerical results for screening charge densities are presented. Surface impurity effects exist over a considerably longer range than volume impurity effects. The relevance of these studies to ionic adsorption theories is indicated.

2. DIELECTRIC FORMULATION WITH AN ARBITRARY NONINTERACTING ELECTRON BASIS

The central rallying point of many-body effects can be considered to be the time-dependent linear response function of the electron gas to a driving force. This response function is usually presented in the form of a dielectric function, susceptibility or polarizability. Among the most lucid derivations of

the RPA dielectric function for a homogeneous electron gas is the self-consistent field theory of Ehrenreich and Cohen (EC) [4], further elucidated by Brout and Carruthers [20].

We present a general derivation of the RPA self consistent screening charge for an inhomogeneous electron gas, within which the originally noninteracting electron wave functions are expandable with a plane-wave basis. In the limit in which each wave function is the 'sum' of only one plane wave, the homogeneous case, the derived dielectric properties reduce to the ordinary RPA result. With the aid of a new image technique, the inhomogeneous electron gas dielectric effects take on a simple form in the surface region also.

It is important to realize that the derivation presented below is not a derivation for the surface region of an electron gas. It is a dielectric formalism applicable to an infinite electron gas in which the electron wave functions are sine waves. The dielectric formalism is applicable to a semi-infinite electron gas with a surface only after the image technique presented below is introduced.

The motivation for the present approach is the following. As noted by Prange in work on Josephson tunneling [21], if one attempts to describe electrons confined to a semi-infinite half-space in terms of oscillating exponentials, then an unrealistically large number of high-energy components is required to achieve this spatial localization. If the phenomenon under study in the semi-infinite medium can be put into correspondence with some phenomenon in an infinite medium, then the problem of localizing electrons to a half-space vanishes. The present approach is to evaluate the dielectric function for an infinite electron gas in which the electrons are described by sine waves. The correspondence between the infinite and the semi-infinite gas will then be established.

Theoretical considerations

Following EC, we consider the Liouville

equation describing the time evolution of the single particle density matrix

$$i \frac{\partial \rho}{\partial t} = [H, \rho]. \quad (1)$$

The Hamiltonian for the system is written

$$H = H_0 + V(\mathbf{r}, t) \quad (2)$$

with $H_0 = KE + V_0(\mathbf{r})$ defining the complete set of noninteracting electron eigenfunctions $|\psi_k\rangle$, which are plane wave expandable. The exact eigenfunctions satisfy

$$H_0 |\psi_k\rangle = E(\mathbf{k}) |\psi_k\rangle. \quad (3)$$

with $|\psi_k\rangle = \sum_{\mathbf{r}} \Gamma_{\mathbf{k},\mathbf{r}} e^{i\mathbf{k}\cdot\mathbf{r}} = \sum_{\mathbf{k}'} \Gamma_{\mathbf{k},\mathbf{k}'} |\mathbf{k}'\rangle$, and Γ the coefficient matrix. The self-consistent potential $V(\mathbf{r}, t)$ is determined by the applied field plus the possibly time-dependent induced screening charge. The operator ρ , representing the single-particle density matrix is expanded as

$$\rho = \rho_0 + \rho_1 \quad (4)$$

so that

$$\rho_0 |\psi_k\rangle = f_0(E_k) |\psi_k\rangle \quad (5)$$

where f_0 is the Fermi function.

Considering that the noninteracting Liouville equation is

$$i \frac{\partial \rho_0}{\partial t} = [H_0, \rho_0] \quad (6)$$

and linearizing by neglecting the term $[V(\mathbf{r}, t), \rho_1]$ in the full commutator of equation (1), allows determination of the equation of motion for ρ_1 , the measure of departure from the equilibrium distribution. Substitution of equations (2), (4), and (6) in the linearized equation (1) yields

$$i \frac{\partial \rho_1}{\partial t} = [H_0, \rho_1] + [V(\mathbf{r}, t), \rho_0]. \quad (7)$$

Taking matrix elements of equation (7) between the time-independent states $|\psi_k\rangle$ and $|\psi_{k+q}\rangle$ and utilizing equations (3) and (5), we then obtain

$$i \frac{\partial}{\partial t} \langle \psi_k | \rho_1 | \psi_{k+q} \rangle = (E(k) - E(k+q)) \langle \psi_k | \rho_1 | \psi_{k+q} \rangle + (f_0(E_{k+q}) - f_0(E_k)) \langle \psi_k | V(r, t) | \psi_{k+q} \rangle. \quad (8)$$

In keeping with the sign convention of EC, the self-consistent potential is written

$$V(r, t) = \sum_q V(q, t) e^{-iq \cdot r}$$

and is related to the charge density through Poisson's equation

$$\nabla^2 V = -4\pi e^2 n$$

or, in momentum space,

$$V(q, t) = \frac{4\pi e^2}{q^2} n_q \quad (9)$$

with

$$n(r) = \sum_q n_q e^{-iq \cdot r}. \quad (10)$$

The expectation value of a single particle operator is given by

$$\langle \mathcal{O} \rangle = \text{Tr}(\rho \mathcal{O}),$$

where ρ is the density matrix, and Tr is the operation of taking the trace. In the present case we are interested in the density increment operator with $\rho = \delta(x_{op} - r)$. The trace is written as the sum of diagonal elements of the matrix of the operator between the exact single-particle states $|\psi_k\rangle$. Following this procedure, the density increment is

$$n(r) = \sum_k \langle \psi_k | \delta(x_{op} - r) \rho_1 | \psi_k \rangle.$$

Now inserting the exact eigenfunction representation of the unit operator

$$1 = \sum_k |\psi_k\rangle \langle \psi_k|$$

into equation (11) yields

$$n(r) = \sum_{k,k'} \langle \psi_{k'} | \delta(x_{op} - r) | \psi_k \rangle \langle \psi_k | \rho_1 | \psi_{k'} \rangle. \quad (12)$$

If we introduce a complete set of eigenfunctions of the position operator

$$1 = \int d^3y |y\rangle \langle y|,$$

then equation (12) becomes

$$n(r) = \int d^3y \sum_{k,k'} \langle \psi_{k'} | y \rangle \delta(y - r) \langle y | \psi_k \rangle \langle \psi_k | \rho_1 | \psi_{k'} \rangle \quad (13)$$

with the transformation functions

$$\langle y | \psi_k \rangle = \sum_{k''} \Gamma_{k,k''} e^{ik'' \cdot y}, \quad \langle \psi_{k'} | y \rangle = \sum_{k''} \Gamma_{k',k''}^* e^{-ik'' \cdot y}$$

Performing the y integration and using the transformation functions allows equation (13) to take the form

$$n(r) = \sum_{\substack{k,k' \\ k'',k'''}} \Gamma_{k',k''}^* \Gamma_{k,k'''} e^{i(k'' - k''') \cdot r} \langle \psi_{k'} | \rho_1 | \psi_k \rangle.$$

If we call $k' = k + q$ and replace the sum on k' by a sum on q , then

$$n(r) = \sum_q e^{iq \cdot r} \sum_{\substack{k,k'' \\ k'''}} \Gamma_{k+q,k''}^* \Gamma_{k,k'''} e^{i(k'' - k''') \cdot r} \langle \psi_k | \rho_1 | \psi_{k+q} \rangle. \quad (14)$$

For equations (10) and (14) to be compatible, it is required that $k'' - k''' + q = 0$. Thus the Fourier coefficient of the density increment is

$$n(q) = \sum_k \Gamma_{k+q,k}^* \Gamma_{k,k} \langle \psi_k | \rho_1 | \psi_{k+q} \rangle. \quad (15)$$

Returning to equation (8), if it is assumed that the time dependence of ρ_1 goes as $\rho_1 \sim e^{-i\omega t}$ and if we define the excitation frequency

$$E(k+q) - E(k) = \omega_q(k),$$

then

$$\langle \psi_k | \rho_1 | \psi_{k+q} \rangle = \frac{f_0(E_{k+q}) - f_0(E_k)}{\omega + \omega_q(k)} \langle \psi_k | V(r) | \psi_{k+q} \rangle. \quad (16)$$

The matrix element of the self-consistent potential is written with the kernel

$$\langle \psi_k | V(\mathbf{r}) | \psi_{k+q} \rangle = \sum_{\mathbf{k}', \mathbf{k}''} \Gamma_{\mathbf{k}, \mathbf{k}'}^* \Gamma_{\mathbf{k}+q, \mathbf{k}''} V(\mathbf{q}') \langle \mathbf{k}' | e^{-i\mathbf{q}' \cdot \mathbf{r}} | \mathbf{k}'' \rangle. \quad (17)$$

Since the plane wave matrix element is $\delta(\mathbf{k}'' - \mathbf{q}' - \mathbf{k}')$, equation (17) becomes

$$\langle \psi_k | V(\mathbf{r}) | \psi_{k+q} \rangle = \sum_{\mathbf{k}', \mathbf{q}'} \Gamma_{\mathbf{k}, \mathbf{k}'}^* \Gamma_{\mathbf{k}+q, \mathbf{k}'+\mathbf{q}'} V(\mathbf{q}'). \quad (18)$$

Combining equations (15), (16) and (18), and changing variables $\mathbf{k}'' \rightarrow \mathbf{k}'$ and $\mathbf{k}' \rightarrow \mathbf{k}''$, we obtain

$$n_q = \sum_{\mathbf{k}} \frac{f_0(E_{k+q}) - f_0(E_k)}{\omega + \omega_q(\mathbf{k})} \left\{ \sum_{\mathbf{k}', \mathbf{k}''} \Gamma_{\mathbf{k}+q, \mathbf{k}'}^* \Gamma_{\mathbf{k}, \mathbf{k}''} \Gamma_{\mathbf{k}, \mathbf{k}'}^* \Gamma_{\mathbf{k}+q, \mathbf{k}''+\mathbf{q}'} V(\mathbf{q}') \right\}. \quad (19)$$

It is a straightforward procedure, as outlined by EC, to go from the charge density n_q to the RPA dielectric function for a homogeneous electron gas. The result is

$$\epsilon(q) = 1 + v(q) \sum_{\mathbf{k}} B(q, \mathbf{k})$$

with

$$B(q, \mathbf{k}) = \frac{f_0(E_{k+q}) - f_0(E_k)}{\omega + \omega_q(\mathbf{k})}$$

and finally

$$\epsilon(q, 0) = 1 + \frac{p_F}{a_0 q^2} \left[1 + \frac{1}{p_F q} \left(p_F^2 - \frac{q^2}{4} \right) \ln \left| \frac{q + 2p_F}{q - 2p_F} \right| \right]$$

with a_0 = the Bohr radius. In the present case in which the wavefunctions are superpositions of plane waves, the dielectric function obtained from equation (19) is given by the integral equation

$$\epsilon(\mathbf{q}) = 1 + v(q) \sum_{\mathbf{k}, \mathbf{q}'} B(\mathbf{q}, \mathbf{k}) K(\mathbf{k}, \mathbf{q}') \frac{\epsilon(\mathbf{q})}{\epsilon(\mathbf{q}')} \quad (20)$$

$$K(\mathbf{k}, \mathbf{q}') = \sum_{\mathbf{k}', \mathbf{k}''} \Gamma_{\mathbf{k}+q, \mathbf{k}'}^* \Gamma_{\mathbf{k}, \mathbf{k}''} \Gamma_{\mathbf{k}, \mathbf{k}'}^* \Gamma_{\mathbf{k}+q, \mathbf{k}''+\mathbf{q}'} \quad (21)$$

This is a completely general result for the linear dielectric function of any electron gas, in which the noninteracting electron wave functions are expandable on a plane wave basis. If the kernel $K = \delta_{\mathbf{q}, \mathbf{q}'}$, then equation (20) would be the precise expression for the RPA dielectric function in a uniform electron gas. The utility of equation (20) depends upon the simplicity of the original noninteracting basis. Clearly, if the Γ matrix is complicated, requiring the superposition of many plane waves, then the resulting ϵ , if calculable, will be very complicated.

As has been constantly emphasized, the derivation, thus far, has no surface effects built into it, only the fact that the wave functions of the full infinite gas are sine waves. The fact that $\epsilon(\mathbf{q}, \omega)$ in equation (20) is not necessarily spherically symmetric, that is, it depends on \mathbf{q} and not just the magnitude of q , is a consequence of sine waves in the z direction and running waves in the x and y directions but is not a consequence of any surface effects, since the notion of a surface has yet to be introduced.

3. SURFACE IMPURITY SCREENING

(A) Theoretical considerations

One of the more interesting and experimentally relevant examples of an inhomogeneous electron gas occurs in the surface region of a metal. As is always the case in these kinds of problem, the destruction of translational invariance reduces the symmetry of the problem to the point where any quantitative theory can be attempted on highly idealized models that accentuate only the most dominant features of the physical system.

The problem of surface properties of electron gases has always been handled within the context of the following model [15, 19, 22].

A potential well with a perfectly reflecting infinite surface barrier perpendicular to the z direction is assumed. This allows one to work with the following noninteracting wave functions:

$$\Psi(\mathbf{r}) = \left(\frac{2}{\Omega}\right)^{1/2} \sin k_z z e^{i\mathbf{k}_\parallel \cdot \mathbf{r}_\parallel} \quad z \geq 0$$

$$\Psi(\mathbf{r}) = 0, \quad z \leq 0.$$

In general, people like to think of decaying exponential wave functions for $z \leq 0$. If, however, we consider the nodal plane $z = 0$ as a mathematical surface somewhere outside the physical surface, then the charge density given by the equation (22) wave functions,

$$n_0(\mathbf{r}) = \frac{4}{(2\pi)^3} \int_0^{\mu_F} \sin^2 k_z z \, d^3k = n_m \left(1 - 3 \left(\frac{\sin(2P_F r \cos \theta) - (2P_F r \cos \theta) \cos(2P_F r \cos \theta)}{(2P_F r \cos \theta)^4} \right) \right) \quad (23)$$

is not significantly different from that obtained with decaying exponentials and the physical surface at $z = \xi$, $\xi > 0$. As Bardeen has suggested[22], $\xi \sim O(1 \text{ \AA})$.

To proceed, we wish an expression for the dielectric function of this model. Goodman has devised an image technique for describing the lattice dynamics of surface atoms[23]. We shall now see how this approach can be modified to describe electronic surface properties. Briefly, Goodman realizes that a surface atom in the semi-infinite lattice responds to a point impulsive displacement from its equilibrium position in a manner that can be related to the infinite lattice response. In Fig. 1 the situation is illustrated. The response of the semi-infinite lattice to an initial surface atom displacement is exactly the same as the response of the infinite lattice to an equivalent displacement of two atoms on either side of the mathematical surface such that initially there is no net force across the surface plane. Clearly, it is much easier to calculate response functions for the infinite lattice, since one does not get into the problems of complicated Fourier transforms

involving high-energy Fourier components.

Goodman's thinking is also applicable to the surface electron gas response or dielectric function when appropriate modifications are performed. It is well known from any text

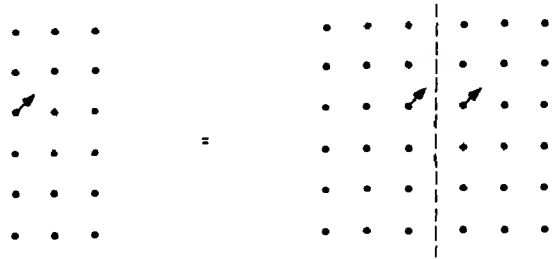


Fig. 1. Model for describing the lattice response of a surface atom in terms of the response of an atom in an infinite lattice.

on electromagnetism that the effects of a particular boundary condition in a dielectric or conducting medium can be reproduced by suitably choosing a finite number of discrete image charges that serve as sources producing the field required to satisfy the boundary condition[24]. In the present case of static dielectric screening of an impurity, in analogy with Goodman's lattice response theory, the relevant boundary condition to be satisfied is that at the plane $z = 0$, the normal component of the bare impurity electric field vanishes. This boundary condition can be satisfied by imaging the bare impurity potential as depicted in Fig. 2. As we shall see, for a pure metal or electron gas in which there is specular reflection of electrons at the surface, the response of a semi-infinite electron gas to some static perturbation a distance z' into the gas is exactly that of an infinite gas with the imaged perturbations such that no electric field lines cross the mathematical surface[25]. This sort of imaging in electron gas surface effects has also been used by Ritchie and Marusak when calculating surface plasmon dispersion relations[26]. By considering Fig. 3, a physical

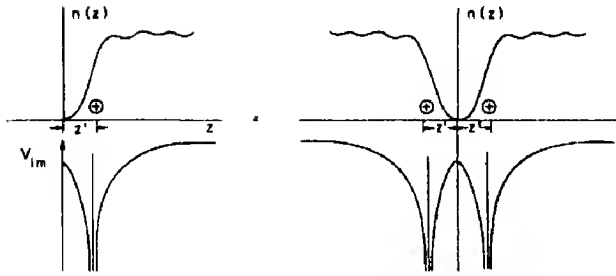


Fig. 2. Model for describing the dielectric response of an electron gas with a surface in terms of the response of an infinite gas.

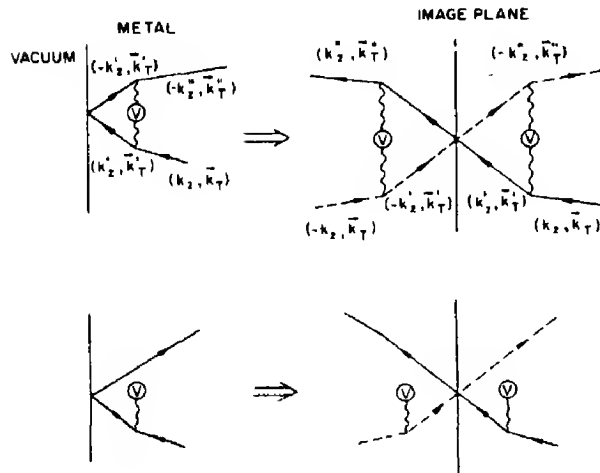


Fig. 3. Schematic diagrams showing the analogy between electrons scattering from an impurity in the surface region of a specularly reflecting surface and electrons scattering from imaged impurity potentials in the infinite electron gas.

picture of the image method can be seen. The surface problem, as shown on the left-hand side, involves electron scattering from the impurity, and then specular reflection at the surface. By using an imaged potential and an infinite sine-wave electron gas, the electron behavior in one of the half spaces has the same physical properties as a half-infinite electron gas with a specularly reflecting surface, as is seen in the right-hand side of Fig. 3.

The beauty of the infinite gas with a nodal plane at $z = 0$, as shown on the right-hand side of Fig. 2 is that the sine-wave functions

which are valid for all space, are easily built up from two plane waves. The Γ coefficients needed in equation (21) take the simple form

$$\Gamma_{\mathbf{k}+\mathbf{q},\mathbf{k}}^* = \frac{-1}{\sqrt{2}i} \left(\delta_{k_z+q_z, k_z} - \delta_{k_z+q_z, -k_z} \right) \delta_{\mathbf{k}_T+\mathbf{q}_T, \mathbf{k}_T}, \text{ etc.} \quad (25)$$

As usual, the subscript T signifies vector momentum transverse to the surface. It is important to realize that Kronecker delta functions are used and always implied hereafter, since at times we pass to the Dirac delta function limit without comment.

The major aim of the present study is to obtain expressions for the screening charge around a static impurity placed at $z = 0$. A consequence of the imaging technique is that the response of the semi-infinite gas to an impurity at $z = 0$ is exactly the same as the response of the infinite sinewave electron gas to an impurity at $z = 0$.

This problem should be of great interest for various reasons. First, it is of intrinsic interest in the general theory of inhomogeneous electron gases. A more practical and fundamental reason is that this model system is precisely a model for ionic adsorption on metal surfaces. The role of ion screening in the surface region has only recently been gaining recognition. An attempt to describe this phenomenon quantitatively is given here. Previous adsorption theories have treated the metal or electron gas in a very phenomenological sense. It has been assumed that the ion-metal interaction would have basically the same functional form as a classical image force, even at short distances where field penetration and bulk screening occur[27]. It will be seen why these theories have been so successful, in spite of their lack of rigor in treating the metal or electron gas.

The screening charge around the impurity is given by the inversion of equation (19),

$$\psi_{\mathbf{k}}(\mathbf{r}) = \left(\frac{2}{\Omega} \right)^{1/2} \sin k_z z e^{i\mathbf{k}_T \cdot \mathbf{r}_T} \quad (24)$$

$$\delta n(\mathbf{r}) = 2 \int \frac{d^3 q}{(2\pi)^3} n_{\mathbf{q}} e^{i\mathbf{q} \cdot \mathbf{r}} \quad (26)$$

with the factor of two entering because the normalization of the infinite sine wave gas is twice that of the semi-infinite gas. In equation (14), the self-consistent potential is

$$V(\mathbf{q}') = \frac{4\pi e^2}{q'^2 \epsilon(\mathbf{q}')} = \frac{v(q')}{\epsilon(\mathbf{q}')} \quad (27)$$

with $\epsilon(\mathbf{q})$ given by equation (20). Heine has suggested that the usual RPA dielectric function is probably the leading order term in an expansion of the true surface dielectric function [16] which is related to $\epsilon(\mathbf{q})$ given by equation (20). Due to the extreme difficulty in solving the integral equation, equation (20) we will take $K = \delta_{\mathbf{q}, \mathbf{q}'}$ in this first study of surface polarization effects with the hope and belief that this is a reasonable initial approximation.

Using the Γ coefficients of the form given by equation (25) and performing the \mathbf{k}' and \mathbf{k}'' sums of equation (19) yields:

$$n_{\mathbf{q}} = \sum_{\mathbf{k}} \frac{B(\mathbf{q}, \mathbf{k})}{4} \sum_{\mathbf{q}'} V(\mathbf{q}') \{ (\delta_{\mathbf{q}_z, \mathbf{q}_z'} \delta_{\mathbf{q}_\parallel, \mathbf{q}_\parallel'} + \delta_{\mathbf{q}_z, -\mathbf{q}_z'} \delta_{\mathbf{q}_\parallel, \mathbf{q}_\parallel'} - \delta_{\mathbf{q}_z, 2\mathbf{k}_z + \mathbf{q}_z'} \delta_{\mathbf{q}_\parallel, 2\mathbf{k}_\parallel + \mathbf{q}_\parallel'} - \delta_{\mathbf{q}_z, -2\mathbf{k}_z - \mathbf{q}_z'} \delta_{\mathbf{q}_\parallel, 2\mathbf{k}_\parallel + \mathbf{q}_\parallel'}) (1 - \delta_{\mathbf{q}_\parallel, -\mathbf{k}_\parallel}) \}. \quad (28)$$

We can take $1 - \delta_{\mathbf{q}_\parallel, -\mathbf{k}_\parallel} \approx 1$ because this delta function says to omit one non-singular point when summing over momentum space. Performing the \mathbf{q}' sum in equation (28) yields

$$n_{\mathbf{q}} = \sum_{\mathbf{k}} \frac{B(\mathbf{q}, \mathbf{k})}{4} \{ V(\mathbf{q}_T, q_z) + V(\mathbf{q}_T, -q_z) - V(\mathbf{q}_T, -2k_z - q_z) - V(\mathbf{q}_T, 2k_z + q_z) \}. \quad (29)$$

If we now use a form of the mean value theorem [29] in a manner similar to that of Wisner [30] for doing inhomogeneous electron gas problems, we can take

$$\sum_{\mathbf{k}} \frac{B(\mathbf{q}, \mathbf{k})}{4} V(\mathbf{q}_T, 2k_z + q_z) = V(\mathbf{q}_T, 2\zeta + q_z) \sum_{\mathbf{k}} \frac{B(\mathbf{q}, \mathbf{k})}{4}$$

with $0 < \zeta < p_F$. As an approximation $\zeta \approx \frac{1}{2} p_F$ is a reasonable average of the value of k_z . Using the standard RPA expression relating B and ϵ , and the mean value theorem result, equation (29) becomes

$$n_{\mathbf{q}} = \frac{1}{4} [(V(\mathbf{q}_T, q_z) + V(\mathbf{q}_T, -q_z)) - (V(\mathbf{q}_T, 2\zeta_z + q_z) + V(\mathbf{q}_T, -2\zeta_z - q_z))] \times \left(\frac{\epsilon(q)}{v(q)} - 1 \right).$$

Thus equation (26) takes the form

$$\delta n(\mathbf{r}) = \frac{1}{2} \int \frac{d^3 q}{(2\pi)^3} \left(\frac{\epsilon(q)}{v(q)} - 1 \right) e^{i\mathbf{q} \cdot \mathbf{r}} \times (V(\mathbf{q}_T, q_z) + V(\mathbf{q}_T, -q_z)) - \frac{1}{2} \int \frac{d^3 q}{(2\pi)^3} \left(\frac{\epsilon(q)}{v(q)} - 1 \right) e^{i\mathbf{q} \cdot \mathbf{r}} (V(\mathbf{q}_T, 2\zeta_z + q_z) + V(\mathbf{q}_T, -2\zeta_z - q_z)). \quad (30)$$

The first integral, upon substituting $-q_z \rightarrow q_z$ in V and in the exponential, a valid step since all other functions in the integrand are even in q_z and using equation (27) for V , gives

$$\delta n_1(\mathbf{r}) = \frac{1}{2} \int \frac{d^3 q}{(2\pi)^3} \left(1 - \frac{1}{\epsilon(q)} \right) e^{i\mathbf{q} \cdot \mathbf{r}} (e^{iq_z z} + e^{-iq_z z}).$$

Since the system is invariant with respect to reflection in the $z=0$ plane, letting $-z \rightarrow z$ in the second exponential yields

$$\delta n_1(\mathbf{r}) = \int \frac{d^3 q}{(2\pi)^3} \left(1 - \frac{1}{\epsilon(q)} \right) e^{i\mathbf{q} \cdot \mathbf{r}} \equiv \delta n_{LV}(r) \quad (31)$$

the result first obtained by Langer and Vosko [5]. Going through a similar procedure for the second integral of equation (30) in which first we transform $-2\zeta - q_z \rightarrow q_z$, and $2\zeta + q_z \rightarrow q_z$, and then invoke reflection symmetry, yields

$$\delta n_2(\mathbf{r}) = \frac{1}{2} \int \frac{d^3 q}{(2\pi)^3} \left(1 - \frac{1}{\epsilon(q)}\right) e^{i\mathbf{q} \cdot \mathbf{r}} (e^{-i2\zeta z} + e^{i2\zeta z}). \quad (32)$$

Combining equations (31) and (32) gives

$$\delta n(\mathbf{r}) = (1 - \cos 2\zeta z) \delta n_{LV}(r)$$

which with a simple trig identity becomes

$$\delta n(\mathbf{r}) = 2 \sin^2 \left(\frac{p_F z}{\sqrt{2}} \right) \delta n_{LV}(r). \quad (33)$$

This is just the Langer and Vosko result modified by the presence of the surface charge density variations. The resulting charge-density configuration has the form of a screened impurity with Friedel oscillations and superimposed surface-density variations and oscillations. This is not an unreasonable result and incidentally is the sort of result Kohn and Sham contemplated in problems of impurity screening in inhomogeneous electron gases [9, 10]. It is also interesting to note that this result is the same as that one obtained by the writer in a much more involved Green's function approach [31].

In the next section, numerical results are presented and discussed, and experimental suggestions made.

(B) Numerical results and discussion

Equation (33) has been evaluated numerically for several different electron gas densities along various radial lines emanating from the impurity. The results are displayed graphically in Figs. 4–6, for values of $r_s = 1.5$, 3 and 4.5.

Much can be said about these results of screening charge as a function of vector position from the impurity. We should first observe that these results are quite understandable. At $r = 0$, for any θ , the initial charge density is zero, because of the infinite barrier. Thus in the linearized model, there will be no polarization charge where initially there was no charge. As the weakly screened

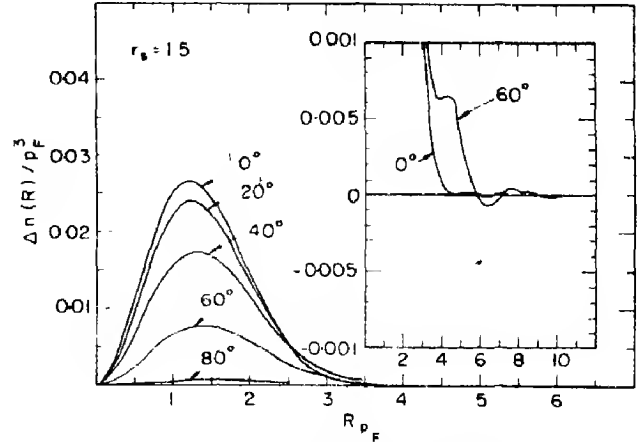


Fig. 4. Surface impurity screening charge density, $r_s = 1.5$.

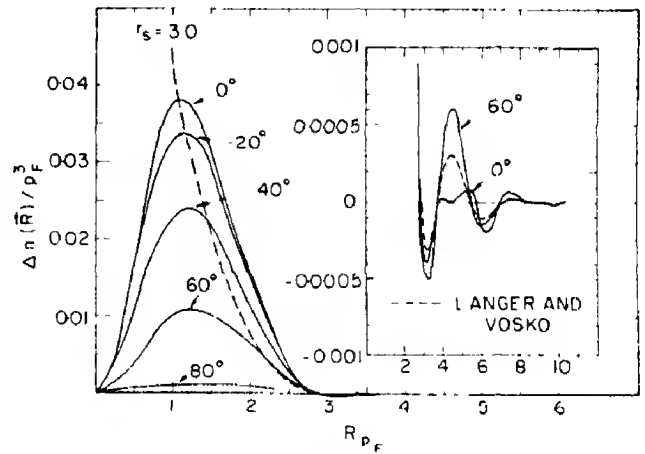


Fig. 5. Surface impurity screening charge density, $r_s = 3.0$.

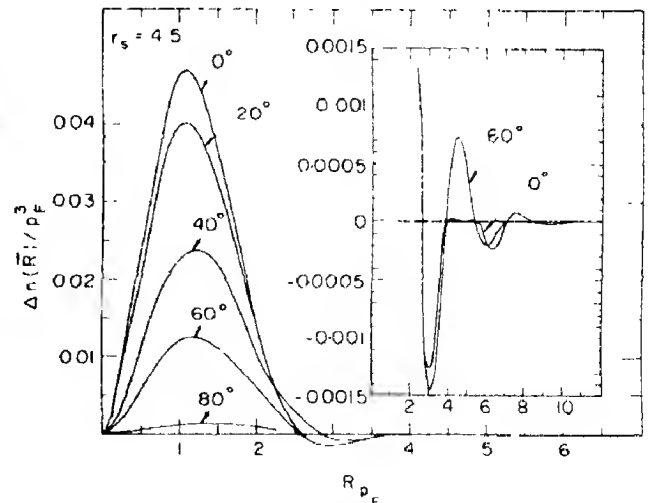


Fig. 6. Surface impurity screening charge density, $r_s = 4.5$.

field penetrates into the gas, polarization charge builds up as the unperturbed electron density increases. Farther into the electron gas past the point where the maximum screening charge density is seen, the screening becomes more effective and the polarization charge density decreases. Long-range Friedel oscillations, plotted on an expanded scale in the insets, are also present, although their structure is more complicated than volume impurity oscillations. This results from the fact that we are considering a phenomenon involving interferences between two diffraction patterns of different symmetries, that of the surface and that of the impurity. For a quantitative comparison with volume effects, the results obtained by Langer and Vosko for an impurity in a homogeneous electron gas of density $r_s = 3$ are also plotted in Fig. 5. It can be seen that the surface impurity screening is of a somewhat longer range than the volume impurity screening, as it must be. In the surface problem, the low-density region cannot provide enough electronic charge to do much screening. Hence the screening charge is less than in the volume case. To make up for this deficiency, as the relatively unscreened surface impurity field penetrates the metal, it must induce a larger long-range polarization charge than in the volume case, in order that the impurity be totally screened at large distances. Consequently, the surface impurity charge-density curves cross over the volume curves.

As we have mentioned, the structure of the oscillatory curves is more complicated for the surface impurity, at least in the intermediate region $4 \leq rP_F \leq 10$, where chaotic things are happening. As this chaos settles down, the longer range Friedel oscillations, say for $rP_F \geq 10$, become well-behaved in the sense of volume oscillations. Still there are longer range effects for the surface impurity than the volume impurity, as suggested in the preliminary theory of surface impurities [19]. This observation could be of experimental interest for a number of reasons. First, standard

magnetic resonance and Knight shift experiments are measuring effects occurring within the skin depth of metals. Since the conduction-band electron polarization around ion cores or impurities in the outer skin is different from that in the bulk, measurable events such as impurity-impurity interactions may be different than those inferred from standard theories using the customary expression for long-range polarization charge density. Second, the existence of different surface polarization properties from those in the bulk should offer encouragement for devising new resonance-type surface experiments to replace the rather dreary assemblage of present experiments. It should also be noted that in the case of an adsorbed partial monolayer, a distribution of surface impurities, there may be significant impurity-impurity interactions caused by the intermediary of the polarizable electron gas. Put another way, the long-range surface Friedel oscillations, for large angles, of one impurity may interact with the oscillations from a nearby impurity, thereby giving rise to an effective interaction that could not be intuited without considering the many-body screening effects. We see that the problem is much more subtle than would be guessed from the various oversimplified existing theories.

Returning to the numerical results, a few more comments are in order. As anticipated, we see that the screening charge increases more slowly as the transverse component of the radial line increases, since the unperturbed electron density doing the screening increases more slowly.

We also can observe the following structure in all curves. A maximum in the screening charge density is seen at $rP_F \sim 1.1$ and a minimum in charge density at $rP_F \sim 3$, corresponding to the first Friedel oscillation. The amount of screening charge in the first lobe decreases, however, as the electron gas density decreases. This means that in the lower density gas, more of the screening, and thus induced charge, appears farther into

the metal. For this reason, the classical image charge is not applicable to honestly describing surface impurity effects because the screening charge exists in the metal and not on the surface. This is a manifestation of the fact that the electron gas or real metal is not a perfect conductor, as must be assumed if the concept of an image charge is to contain any real meaning. In the case of a perfect conductor, $r_s = 0$. The total screening charge will appear within the first lobe with a maximum at $rP_F \sim 1.1$. But since $P_F = 3.64/r_s$, $\lim_{r_s \rightarrow 0} r \sim r_s \rightarrow 0$. Hence the screening charge appears either at the impurity site with $r = 0$ or in the $\theta = 90^\circ$ curve, in either case at $z = 0$. This is, then, a true surface polarization charge that is a consequence of the necessary conditions for having a perfect conductor. As the density is decreased to real metal densities, screening effects and their consequences must be considered from the volume polarization point of view. The fortuitous success that some, including the present author, have had in using the image force and surface polarization concepts absolutely does not mean that the approach is rigorously correct.

We may apply the present results to existing theories of ionic adsorption in the following manner. Essentially one is interested in the dipole moment formed by the point ion core or impurity and the resulting polarization charge, since the change in electron work function is given by $\Delta\phi_e = 2\pi\sigma M_0$, where σ is the density of dipoles, and M_0 is the dipole strength. As the author has stated in his paper on atom-metal interaction theory[27], the dipole strength is $M_0 = q(s + \mathcal{E}(s))$, with q the ion charge, s the ion-surface separation, which could be taken to be the ionic radius, and " $\mathcal{E}(s)$ is some effective location for the polarization charge of the positive ion core and has a numerical value greater than s for small s ." We should point out that assigning the value of the ionic radius for s must be taken somewhat with a grain of salt. Since this seems to be a convenient way of para-

meterizing the size of the adsorbate, however, the idea is introduced.

We can obtain a value for $\mathcal{E}(s)$ from the calculated screening charge densities as follows. Calculations of the dipole component of the polarization charge distribution

$$M_0 = q\langle z \rangle = \int z \delta n(\mathbf{r}) r^2 d\mathbf{r} d\Omega$$

have shown that a reasonable representation of the calculation for real metal densities[32], is given by

$$\langle z \rangle \approx 1.16/p_F = 0.32r_s \text{ \AA}.$$

Thus it is apparent that the strength of the effective dipole moment of an ion on a real metal surface is quite dependent upon the substrate properties, the free electron density. This observation has not previously been quantified and, with only a few exceptions, has not even been qualitatively recognized. To apply these ideas in real calculations, one must obtain the density of s -like and p -like conduction-band electrons, those electrons that participate in the screening. If one is dealing with noble or transition metals in which there is great hybridization between the free electronlike s and p bands and the tight-binding d bands, one must not include the electron densities coming from the d bands, since the d electrons do not contribute much to the true screening charge density.

In a typical system of experimental interest such as cesium on tungsten, sample parameters for theoretical calculations might be $s = r_i = 1.3 \text{ \AA}$ and $2 < r_s < 3$. With this choice of fundamental atomic and metallic parameters, the true dipole length or atom-metal separation would be

$$\frac{M_0}{q} = (r_i + 0.32 r_s) \approx 2 \text{ \AA}. \quad (34)$$

This is in accord with work-function data. The point to be made here is that in the author's other calculations[27], it had to be assumed that the dipole length was at least

4 Å or the atom-metal separation at least 2 Å in order to obtain meaningful results. This separation is, however, quite a bit greater than 1.3 Å, which must be used in an image-force picture. Now we see why the assumed 2 Å separation is the correct value, and not the 1.3 Å value that is required in a classical image-force model. The general rule is this: If the ion-metal separation becomes as small as a Fermi wavelength, then the average position of the screening charge will be deeper into the metal than the ion-metal separation. In this case, perfect conductor image forces have little quantitative significance. By using the simple approximate relation given by equation (34), we imagine that more realistic data correlation with relevant properties of both the ion and metal systems will be possible.

We should note that the implicit assumption has been made that the screening of an impurity that is a distance r_i from the real surface is basically the same as the screening of an impurity upon the mathematical surface of the infinite square well. This is a reasonable first approximation for several reasons. As we have noted, the charge density at $z = 0$ of the model calculation is quite similar to the charge density a finite distance of the order of 1 Å outside the surface of a real metal. Furthermore, in a convergent series expansion of the true screening charge around an impurity a finite distance from the mathematical surface, the leading term in the expansion will be that term given by equation (33) and drawn in Figs. 4–6. Work has been completed to calculate the higher order corrections and to obtain more accurate expressions for the dipole moment of an ionic impurity as a function of distance from the surface than those given by equation (34). Equation (34) should be a reasonable first approximation, however. These results will be published elsewhere [32].

We also feel that these considerations will permit an understanding of zero coverage work function and desorption energy studies

as a function of crystallographic face. Consider the dipole moment versus impurity position from the surface. At large distances where the classical image force is valid, the dipole varies linearly with the distance z from the surface. As the impurity is brought closer to the surface so that volume polarization occurs, the image dipole picture breaks down. The image picture predicts zero dipole length at $z = 0$, whereas the volume polarization picture indicates that $M_0(z = 0)/q \approx 0.32r_s \approx 1$ Å. As the impurity is removed from the surface, the M_0 curve eventually merges with the image dipole. Further quantitative studies of this effect have also been reported [32].

One final point to be made is concerned with the general trend of work-function changes with s and p electron densities. From equation (34), it would appear that the work-function change would be greatest for an ion adsorbed on a metal with the lowest electron density (r_s largest). But another competing trend must be reckoned with. In general, the bare work function of a metal decreases with decreasing electron density. Thus the position of the shifted broadened atomic level will overlap more of the occupied portion of the conduction band. Consequently, the atom-metal bond will become more metallic and thus less ionic in character [27]. In this case the effective charge on the adsorbate is reduced and the actual dipole moment $M_0 = q_{\text{eff}}(r_i + \langle z \rangle)$ will decrease [33].

There are thus two competing trends. As the electron density is decreased, $\langle z \rangle$ increases but q_{eff} decreases. Hence there exists an optimal electron gas density for the greatest work-function change, with a particular adsorbate used to specify the value of r_i . Put another way, it may be that cesium would produce the greatest work-function change in one metal, whereas potassium would produce the greatest change in some other metal, solely as a result of the different electron gas densities in the two metals.

We hope that considerations along the lines

outlined here will be given by workers doing numerical calculations of electronic surface properties, for it seems that if such considerations are not given, there can be little reason to expect a correspondence between what is calculated and what is occurring in physical reality.

Acknowledgements—The author gratefully acknowledges the help of Professor G. F. Koster whose clear physical insight always prevented plunges into mathematical obscurity rather than physics. Help in one way or another from Professors H. Ehrenreich and P. H. Cutler and Dr. E. O. Kane has been appreciated. Numerical computations were performed at the M.I.T. Computation Center. The work at the Research Laboratory of Electronics, M.I.T., was supported in part by the Joint Services Electronics Program (Contract DA28-043-AMC-02536 (E)).

REFERENCES

1. PINES D., *Elementary Excitations in Solids*, Benjamin, New York (1964).
2. GEIL-MANN M. and BRUECKNER K. A., *Phys. Rev.* **106**, 364 (1957).
3. DUBOIS D. F., *Ann. Phys.* **7**, 174 (1959); *ibid.* **8**, 24 (1959).
4. EHRENREICH H. and COHEN M. H., *Phys. Rev.* **115**, 786 (1959).
5. LANGER J. and VOSKO S. J., *J. Phys. Chem. Solids* **12**, 196 (1960).
6. BARAFF G. A. and BOROWITZ S., *Phys. Rev.* **121**, 1704 (1961).
7. DUBOIS D. F. and KIVELSON M. G., *Phys. Rev.* **127**, 1182 (1962).
8. HOHENBERG P. and KOHN W., *Phys. Rev.* **136**, B864 (1964).
9. KOHN W. and SHAM L. J., *Phys. Rev.* **137**, A1697 (1965); *ibid.* **140**, A1133 (1965).
10. SHAM L. J. and KOHN W., *Phys. Rev.* **145**, 561 (1966).
11. SHAM L. J., *Phys. Rev.* **150**, 720 (1966).
12. RITCHIE R. H., *Phys. Rev.* **106**, 874 (1957).
13. STERN E. A. and FERRELL R. A., *Phys. Rev.* **120**, 130 (1960).
14. KANEZAWA H., *Prog. theor. Phys.* **26**, 851 (1961).
15. FEDDERS P. A., *Phys. Rev.* **153**, 438 (1967).
16. HEINE V., *Phys. Rev.* **151**, 561 (1966).
17. GADZUK J. W., *Phys. Rev.* **154**, 622 (1967).
18. STERN F., *Phys. Rev. Lett.* **18**, 546 (1967).
19. GADZUK J. W., *Solid State Commun.* **5**, 743 (1967).
20. BROUT R. and CARRUTHERS R., *Lectures on the Many-Electron Problem*, Interscience, New York (1963).
21. PRANGE R. E., *Phys. Rev.* **131**, 1083 (1963).
22. BARDEEN J., *Phys. Rev.* **49**, 653 (1936).
23. GOODMAN F. O., *J. Phys. Chem. Solids* **23**, 1269 (1962); *ibid.* **23**, 1491 (1962); *ibid.* **26**, 85 (1965).
24. JACKSON J. D., *Classical Electrodynamics* p. 26, Wiley, New York (1962).
25. The author is grateful to KANE E. O. for some helpful suggestions with regard to the image technique.
26. RITCHIE R. H. and MARUSAK A. L., *Surface Sci.* **4**, 234 (1966).
27. GADZUK J. W., *Surface Sci.* **6**, 133 (1967); *ibid.* **159** (1967); see equation (23-1/2).
28. GADZUK J. W., NASA Tech. Rep. No. R-283 (1968).
29. WHITTAKER E. T. and WATSON G. N., *A Course of Modern Analysis*, p. 65, Cambridge University Press, Cambridge (1965).
30. WISER N., *Phys. Rev.* **138**, A452 (1965).
31. GADZUK J. W., *Solid State and Molecular Theory Group*, QPR.MIT, Vols. 68, 69 (1968).
32. GADZUK J. W., Theory of Metallic Adsorption on Real Metal Surfaces, To appear in *Proc. fourth Intl Materials Symp. Solid Surfaces*, Berkeley, California (1968).
33. BENNETT A. J. and FALICOV L. M., *Phys. Rev.* **151**, 512 (1966).

TECHNICAL NOTES

The effect of pressure on the isomer shift of $^{57}\text{Fe}(^{57}\text{Co})$ as an impurity in ZnSe, ZnTe and CdTe*

(Received 31 January 1969; in revised form 24 March 1969)

MÖSSBAUER resonance in ^{57}Fe has proved to be a useful tool for studying the effect of pressure on chemical bonding in insulators [1-3] and on the band structure of transition metals [4, 5]. The isomer shift measures the s electron density at the nucleus; however, since the $3s$ orbitals are significantly shielded from the nucleus by the $3d$ electrons, one can infer changes in energy or radial distribution of the $3d$ orbitals from changes in the isomer shift with pressure.

In this paper we show the effect of pressure on the isomer shift for ^{57}Fe (introduced as ^{57}Co) as an impurity in ZnSe, ZnTe, and CdTe. All three compounds have the zinc-blende structure at one atmosphere. Previous high pressure studies [6] have shown that ZnSe and ZnTe have first order phase transitions at about 165 and 135 kbar. The high pressure phase apparently has the NaCl structure [7] and is metallic or semimetallic [8]. CdTe has first order phase transitions at about 30 kbar and 100 kbar [6]. The phase at 30 kbar is NaCl [9, 10] and is semiconducting, while the high pressure phase is the diatomic analog of white tin [11] and is metallic [7].

The materials used in this work were those used in the electrical work [6, 7] or were reagent grade obtained from Pfaltz and Bauer. CoCl_2 was thermally diffused into the lattices at a temperature of 800°C . The maximum

concentration was 10^{-5} , and, in the case of CdTe it was very considerably less. The high pressure Mössbauer resonance techniques have been described elsewhere [12]. Figure 1 shows a typical spectrum for ZnTe at 90 kbar. The spectra were computer fit with Lorentzian peaks.

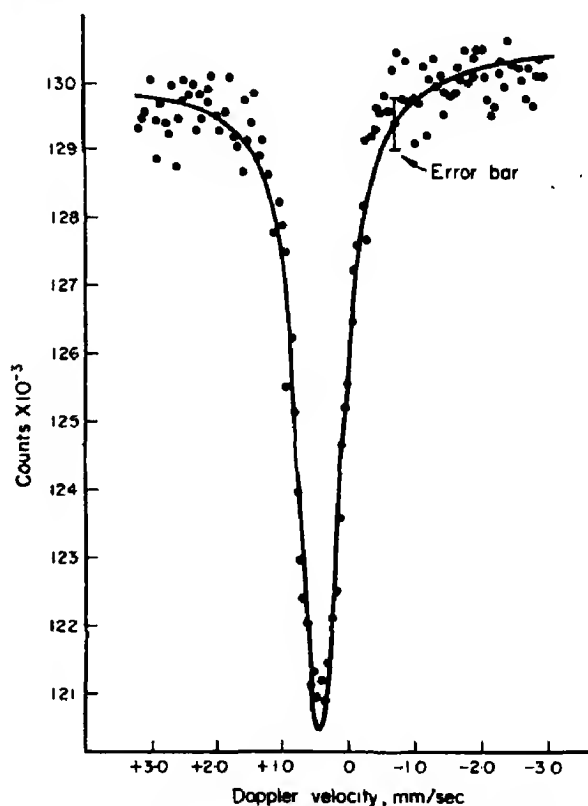


Fig. 1. Mössbauer spectrum of ZnTe at 90 kbar.

The results are shown in Fig. 2. The arrows represent the locations of the first order phase transitions observed electrically. (All isomer shifts are shown relative to metallic iron at one atmosphere.) The first point to be noted is that the atmospheric pressure isomer shifts are in the range 0.6 – 0.8 mm/sec. These are very close to the values observed for FeSe

*This work was supported in part by the United States Atomic Energy Commission.

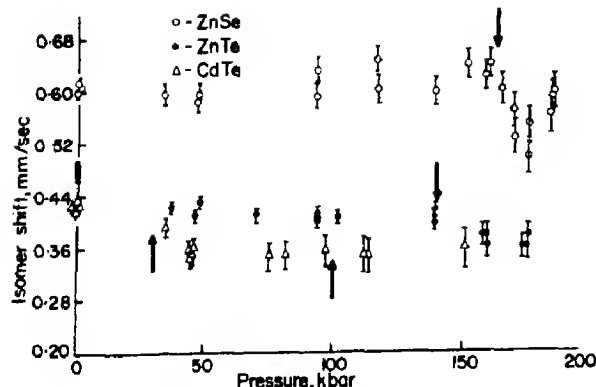


Fig. 2. Isomer shift vs. pressure—ZnSe, ZnTe and CdTe.

and FeTe[13], rather than near the typical ionic ferrous (1.2–1.4 mm/sec) or ferric (0.3–0.4 mm/sec) values. In the tellurides there was no sign of quadrupole splitting, but in ZnSe the peak was broadened sufficiently to imply a quadrupole splitting of about 0.75 mm/sec, which did not change significantly with pressure.

For ZnSe there is perhaps a slight increase in isomer shift (decrease in electron density at the nucleus) with increasing pressure in the zincblende phase. At the transition (165 kbar) there is a modest but distinct decrease in isomer shift, followed by a rise in the high pressure phase. ZnTe shows a small decrease in isomer shift with increasing pressure in the zincblende phase, and a small but measurable decrease at the transition (135 kbar). The CdTe isomer shift exhibits a distinct decrease at low pressure, probably associated with the 30 kbar transition. There appeared to be no effect associated with the 100 kbar transition, but with the very high dilution of ^{57}Co and the intense scattering by the heavy nuclei, a small change could easily be missed.

The most important feature of the results is the relatively small change in isomer shift at the phase transitions. Since the transitions

in ZnSe and ZnTe and the 100 kbar transition in CdTe involve not only a change in symmetry and coordination number, but also a semiconductor-to-metal transition with a change of resistivity of several orders of magnitude, there must be drastic modifications of band structure in the host. Yet the change electron density at the ^{57}Fe nucleus at the transition is much smaller than the change in electron density with compression observed in a typical ionic compound over a 50 kbar range[2]. The ^{57}Fe orbitals must be strictly localized so that there is little change in 4s occupation or in radial extent of the 3d orbitals, even though the surrounding atoms undergo a drastic rearrangement.

Departments of Chemistry,
Chemical Engineering
and Physics,
and Materials Research
Laboratory,
University of Illinois,
Urbana, Ill. 61803, U.S.A.

C.W. FRANK
G. de PASQUALI
H. G. DRICKAMER

REFERENCES

1. VAUGHAN R. W. and DRICKAMER H. G., *J. chem. Phys.* **47**, 468 (1967).
2. CHAMPION A. R., VAUGHAN R. W. and DRICKAMER H. G., *J. chem. Phys.* **47**, 2583 (1967).
3. CHAMPION A. R. and DRICKAMER H. G., *J. chem. Phys.* **47**, 2591 (1967).
4. INGALLS R. L., *Phys. Rev.* **155**, 157 (1967).
5. INGALLS R. L., DE PASQUALI G. and DRICKAMER H. G., *Phys. Rev.* **155**, 165 (1967).
6. SAMARA G. A. and DRICKAMER H. G., *J. Phys. Chem. Solids* **23**, 457 (1962).
7. FORSGREN K. F., Private communication.
8. MINOMURA S., SAMARA G. A. and DRICKAMER H. G., *J. appl. Phys.* **33**, 3196 (1962).
9. ROOYMANS G. J. M., *J. inorg. nucl. Chem.* **25**, 253 (1963).
10. MARIANO A. N. and WAREKOIS E. P., *Science* **142**, 672 (1963).
11. OWEN N. B., SMITH P. L., MARTIN J. E. and WRIGHT A. J., *J. Phys. Chem. Solids* **24**, 1519 (1963).
12. DEBRUNNER P., VAUGHAN R. W., CHAMPION A. R., COHEN J., MOYZIS J. and DRICKAMER H. G., *Rev. scient. Instrum.* **37**, 1310 (1966).
13. ONO K., ITO A. and HIRAHARA E., *J. phys. Soc. Japan* **17**, 1615 (1962).

J. Phys. Chem. Solids Vol. 30, pp. 2323-2325.

Dispersion effects in interference methods for the measurement of refractive index

(Received 12 December 1968; in revised form
24 March 1969)

THE WAVELENGTHS of transmission (or reflection) maxima and minima for a thin transparent crystal plate are given by [1]

$$4nt = m\lambda \quad (1)$$

where n is the index of refraction at wavelength λ , t the crystal thickness and m the order of interference, odd for minima and even for maxima. The spectral variation of refractive index may be determined using this equation if the order m can be found. This is usually done by preparing a specimen a few wavelengths thick which shows only one, or a few interference fringes in a very wide wavelength range so that unambiguous values of m can be assigned to the fringes. The approximate values of n obtained in this way are used to assign order numbers in successively thicker crystals whose thickness can be measured with increasing accuracy. This procedure is difficult to carry out and may be suspect since equation (1) fails for thin crystals with large dispersion [1]. The experimental difficulties include the preparation of thin specimens of adequate surface area or, in micro-transmission measurements [1, 2] on very small crystals, the problems involved in recording fringes over a suitably wide wavelength range.

Fortunately, it is possible to deduce the spectral variation of refractive index from measurements on the spacing of interference fringes in a limited wavelength range, usually near an absorption edge. For instance, if the dispersion is low, the order m appearing in

equation (1) may be eliminated between successive fringes occurring at λ_1, λ_2 to give

$$n^* = \frac{1}{2t} \frac{\lambda_1 \lambda_2}{(\lambda_1 - \lambda_2)} \quad (2)$$

where n^* is the apparent index for the region $\lambda_1 > \lambda > \lambda_2$ and is close to the true index when the dispersion is small. For dispersive media we write

$$\begin{aligned} 4n_1 t &= m\lambda_1 \\ 4n_2 t &= 4(n_1 + \Delta n) t = (m+2)(\lambda_1 - \Delta\lambda) \\ &= (m+2)\lambda_2 \end{aligned}$$

for two successive fringes to show that n^* exceeds n_1 by $\lambda_1(\Delta n/\Delta\lambda)$. For closely spaced fringes,

$$n^* = n - \lambda \frac{dn}{d\lambda}. \quad (3)$$

The apparent index n^* is larger than the true index n since $dn/d\lambda$ is negative on the long wave side of an electronic absorption edge. The true index for a specimen of convenient thickness may be derived from measurements of the apparent index in a limited wavelength range by integrating (3), to read

$$(n\nu^1)_a = \int_0^a n^* d\nu^1 \quad (4)$$

where ν^1 is the wave number and a the wave-number at which n is to be determined. Equation (3) shows that, if the refractive index varies linearly with wavelength in a small region of the spectrum ($n = a + b\lambda + \dots$), this will not affect the value of n^* . We should therefore add a constant (b) to the right hand side of equation (4) to allow for this. The constant will be equal to zero for the usual case of dispersion on the long wave side of an electronic absorption edge and has only been shown to have a non-zero value in one particular case [3] when electronic, free-

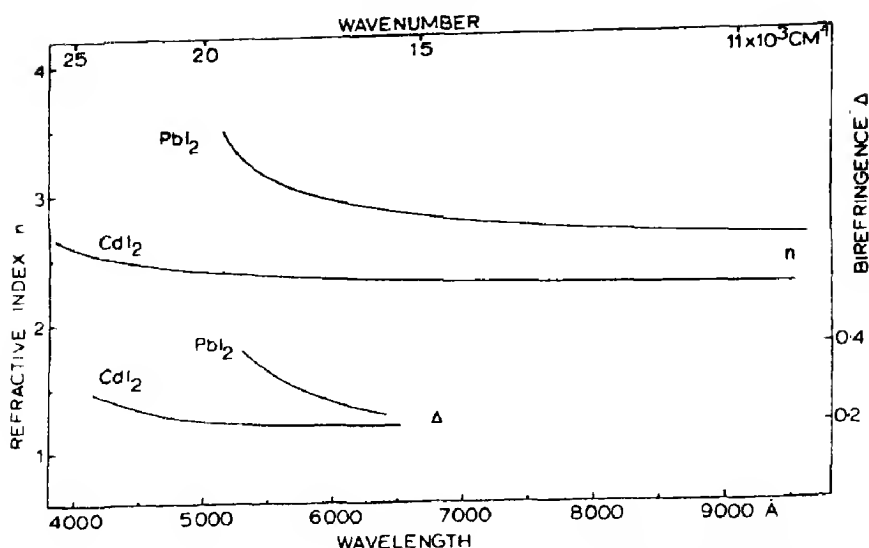


Fig. 1. The spectral variations of the ordinary refractive index (n) and the birefringence (Δ) for single crystals of PbI_2 and CdI_2 .

carrier and restrahl contributions to the refractive index combined to produce a linear term over a small region of the spectrum.

Measurements of the spectral variation of n^* for single crystals of PbI_2 and CdI_2 were reported in a previous paper[1]. In both cases, the measurements could be represented by:-

$$(n^*)^2 - 1 = \frac{A}{(\nu_0^1)^2 - (\nu^1)^2} \quad (5)$$

where ν_0^1 and A are constant for a particular material. Using (4) and (5) we can calculate values of the true index n from

$$(n\nu^1)_a = [(\nu_0^1)^2 + A]^{1/2} E(\theta, \phi) \quad (6)$$

where $E(\theta, \phi)$ is an elliptic integral of the second kind, fully tabulated in reference[4] and

$$\theta = \sin^{-1} \left(\frac{a}{\nu_0^1} \right), \phi = \frac{\nu_0^1}{[(\nu_0^1)^2 + A]^{1/2}}.$$

The spectral variations of the ordinary refractive index (n_0) for PbI_2 and CdI_2 have been calculated using (6) and the values of A ,

ν_0^1 reported previously[1]. These results are shown in Fig. 1 with values of the birefringence Δ calculated from measurements on interference figures[1]. Values of n^* and n are similar for CdI_2 over most of the visible region ($n \approx 2.4$, $n^* \approx 2.7$ at 5500 \AA) but are very different for PbI_2 near the absorption edge ($n \approx 3.1$, $n^* \approx 6$ at 5500 \AA) where $dn/d\lambda$ is comparable to n/λ . At long wavelengths n^* becomes equal to n since $dn/d\lambda$ is small at wavelengths far from the intrinsic absorption edge.

It is useful to compare values of n obtained by an interference method with values of n obtained using the microscope or transmission methods or from the reflectivity, $R = (n - 1/n + 1)^2$, in a non-absorbing region. This type of comparison also provides additional evidence for the absence of a linear variation of index with wavelength. Reflectivity measurements on freshly cleaved faces of PbI_2 and CdI_2 crystals (at wavelengths where there is sufficient absorption to eliminate spurious reflections from the back face of a specimen) give values of n that agree with those of Fig. 1 within the experimental errors of 10 and 5 per cent respectively. The values

of n calculated for PbI_2 and shown in Fig. 1 show excellent agreement with values obtained by the traditional method [5].

School of Physics,
University of Warwick,
Coventry,
England

M. R. TUBBS

REFERENCES

1. TUBBS M. R., *J. Phys. Chem. Solids* **27**, 1667 (1966).
2. TUBBS M. R., *J. scient. Instrum.* **43**, 698 (1966).
3. MOSS T. S., SMITH S. D. and HAWKINS T. D. F. *Proc. phys. Soc.* **70**, 776 (1957).
4. *Legendre's tables of complete and incomplete elliptic integrals* (Edited by K. Pearson). Cambridge University Press, Cambridge (1934).
5. DUGAN A. E. and HENISCH H. K., *J. Phys. Chem. Solids* **28**, 971 (1967).

J. Phys. Chem. Solids Vol. 30, pp. 2325-2327.

On the nature of the magnetic inclusions in EuF_2

(Received 17 March 1969)

AMONG THE significant results revealed by previous chemical and magnetic studies on EuF_2 were the characterization of the pure material as a paramagnet down to 1.6°K and the fact that magnetically ordered inclusions were observed in other single crystal specimens. This latter phenomenon initially led to the erroneous conclusion that EuF_2 ordered antiferromagnetically [1]. Subsequent work by Lee *et al.* [2], showed the ordering to be a result of an impurity phase of hexagon-shaped platelets precipitated throughout the EuF_2 matrix. From electron spin resonance experiments they characterized the platelets as simple uniaxial antiferromagnets with an ordering temperature of about 19°K. Further, based on rather indirect evidence, they assumed it to be a divalent europium oxy-

fluoride despite the fact that mass spectrographic analysis failed to detect the presence of oxygen in concentrations greater than 100 ppm. Thus, the question remained unanswered as to what is the composition and the source of the magnetically ordered precipitate. This note presents direct evidence showing it to be a europium sulfide, with the probable composition of EuS .

Recently we studied the conditions under which pure single crystals of EuF_2 can be grown and could find no relationship between the formation of the platelet precipitate and the water vapor or oxygen content of the growth atmosphere. Thus, it was unlikely to be an oxyfluoride. Further, electron microprobe analysis of the individual platelets showed them to contain sulfur rather than oxygen. More detailed microprobe studies, using an Applied Research Laboratory EMX-SM instrument, were then made on a number of other crystals containing the precipitate; these results will now be discussed.

The EuF_2 samples containing the inclusions were polished with 0-1 μ diamond paste using regular metallographic techniques. A large number of the platelets were oriented parallel to the (111) plane of the host crystal. By careful polishing at a slight angle to the (111) face it was, therefore, possible to expose an adequate area of the platelet for microscopic examination. It was quite easy, by using dark field illumination, to detect the surface-exposed inclusions. Since EuF_2 is a highly insulating crystal, it was necessary to coat the specimen with a thin conducting layer to prevent a surface charge from forming. Both carbon and gold layers were used, the latter being necessary to analyze for carbon and oxygen.

The results of a qualitative analysis of a number of inclusions showed europium and sulfur as the major constituents. Oxygen was not detected <5 wt. % and fluoride not detected <1 wt. %. Figure 1 is a photomicrograph of a typical hexagon-shaped inclusion which has been surface-exposed by polishing.

Figure 2 shows a scanning X-ray of the sulfur K_{α} output of the same inclusion. It is obviously a sulfur-rich phase. Similar micrographs (not shown) of the fluorine K_{α} output showed the area of the inclusion to be free of fluorine as contrasted to the high fluoride content of the matrix. A scan of the europium M_{β} output showed the Eu concentration to be about equal in both the inclusions and the host EuF_2 crystal. Since the europium content in EuF_2 and EuS differs by only 2.6 wt. % it is unlikely a difference could be observed. A further characterization of the inclusion phase was made by using the well-known shift, of the sulfur K_{α} wavelength with its oxidation state [3]. A comparison between the unknown inclusions and standard sulfur-containing compounds, i.e. K_2SO_4 for (S^{6+}) and EuS for (S^{2-}) was made. No shift was detected between the unknown and the EuS, but between it and K_2SO_4 a shift of $\sim 0.003 \text{ \AA}$ was observed. Since the reproducibility of the spectrometer is 0.0005 \AA , this observed shift is a real effect and suggests the sulfur is present in the inclusion phase as a sulfide (S^{2-}). When the X-ray counts for the europium M_{β} and the sulfur K_{α} for pure EuS were compared with the unknown, the following results were obtained:

Table 1

	$\text{Eu}M_{\beta}$	SK_{α}	$\frac{\text{Eu}M_{\beta}}{\text{SK}_{\alpha}}$ count ratio
Standard EuS	8415	10836	0.777
Inclusion	7982	10327	0.773

The counts were for 25 sec and represent the average of several determinations. In this study a primary electron energy of 5 kV was used in order to restrict the X-ray emitting depth to the size of the inclusion. This condition was established by the absence of fluorine K_{α} X-radiation. It should be pointed

out that in addition to analyzing our own crystals, Lee kindly supplied us with the crystals on which the original resonance data were taken. Identical results were obtained in both cases.

In addition to the electron microprobe results which suggest that the inclusions are EuS, the magnetic data of Lee *et al.*[2], is also consistent with this conclusion. The transition temperature of about 19°K, which they call Néel point since they assume anti-ferromagnetic order, fits well with the 15.6°K for the Curie temperature of ferromagnetic EuS[4]. The resonance they report can also be interpreted to show that the inclusions are ferromagnets. First, the ferromagnetic resonance (FMR) relation $(\omega/\gamma)^2 \approx 4\pi MS \cdot H_0$ (in the plane of the thin platelet and with $4\pi M \approx 13,500$ for EuS) gives a good fit for the reported resonance field vs. temperature data (for $H_0 \parallel \langle 111 \rangle$). Second, the reported frequency dependence of H_0 is not in good agreement with the AFMR relation suggested by Lee *et al.*, but does agree with the above FMR equation. Finally, the observed multiple resonances in the (111) plane are also consistent with FMR resonances in EuS platelets oriented with their planes \perp to the $\langle 111 \rangle$ direction. Thus, there is no disagreement between the resonance data of Lee *et al.*[2], and our own conclusions that the inclusions are ferromagnetic EuS.

As to the source of the sulfide in our crystals, we are certain that the graphite susceptor and the powdered carbon insulation used in our RF furnace contained sulfur as an impurity. When the carbon insulation and susceptor were replaced by outgassed molybdenum, sulfide-free crystals were obtained. However, under these carbon-free conditions we were able to produce similar hexagon-like platelet inclusions in our EuF_2 crystals by deliberately adding EuS. Although carbon crucibles were used in many of our runs, these were high purity and spectrographic analyses showed they could not be a source of sulfur. At the present time



Fig. 1. Photomicrograph of typical inclusion (250 \times).



Fig. 2. Scanning X-ray of sulfur K_{α} output of inclusion shown in Fig. 1.

we do not know the source of sulfur in Lee *et al's.*, crystals [2].

Acknowledgements—The authors would like to thank Dr. K. Lee for allowing us to examine his EuF_3 crystals, and Dr. D. E. Eastman for his analysis of the resonance data.

IBM Thomas J. Watson
Research Center,
Yorktown Heights, N.Y. 10598,
U.S.A.

M. W. SHAFER
J. D. KUPTSIS

REFERENCES

1. McGUIRE T. R., and SHAFER M. W., *J. appl. Phys.* **35**, 984 (1964).
2. LEE K., MUIR J. and CATALANO E., *J. Phys. Chem. Solids* **26**, 523 (1965).
3. CAESSLER A. and GOEHRING M., *Naturwissenschaften* **39**, 169 (1952).
4. VAN DER HOEVEN B. J. C., Jr., TEANEY D. T. and MORUZZI V. L., *Phys. Rev. Lett.* **20**, 719 (1968).

J. Phys. Chem. Solids Vol 30, pp 2327-2330

Temperature dependence of the hyperfine coupling of Mn^{2+} in CdS

(Received 11 February 1969)

IN THE COURSE of the last years the temperature dependence of hyperfine coupling of *S*-state ions in cubic crystals has been studied intensively [1]. The mechanism responsible for the observed decrease of hyperfine coupling with increasing temperature was first proposed by Šimánek and Orbach [2]. Their mechanism involves an admixture of the *s*-orbitals with the *3d*-orbitals caused by a dynamic phonon induced non-cubic field. These authors attempted to compute the temperature dependence of hyperfine field having used a Debye approximation for a cubic crystal with the six-fold coordination number and reached a good agreement with the experiment for $\text{MgO}:\text{Mn}^{2+}$. Their theory

is also satisfactory for many other impurity doped crystals when the *S*-state impurity ion is approximately of the same mass and ionic radius as that one being substituted in the lattice. When the mass or the ionic radius of the impurity and the lattice ion differs greatly a local or resonance vibrational mode of a large amplitude bound to the impurity appears. This local motion affects the temperature dependence of the hyperfine field not only quantitatively but also qualitatively. The qualitative course of this temperature dependence caused by a resonance mode was derived in [3] and a good agreement with the measurements on $\text{BaO}:\text{Mn}^{2+}$ and $\text{SrO}:\text{Mn}^{2+}$ was reached.

The CdS crystal doped by Mn^{2+} ions is a suitable object to study the temperature dependence of hyperfine coupling in the case of tetrahedral surrounding of the impurity ion. Though the crystal has a wurtzite structure, the deviation of CdS_4^{6-} tetrahedron from its regular form is very small and may be neglected. However, there is a great chance of appearing of the vibrational modes localized on the impurity due to the difference between impurity Mn^{2+} ion and original Cd^{2+} ion both in the mass and ionic radius. We would like to present our measurements of the temperature dependence of hyperfine coupling constant of Mn^{2+} ion in CdS. The interpretation of results is realized through the two vibrational modes localized on the Mn^{2+} ion.

The temperature dependence of hyperfine coupling was measured by an X-band electron spin resonance spectrometer. The magnetic field was determined by a temperature controlled Hall probe of InSb calibrated by the proton magnetic resonance. The relative accuracy of the magnetic field measurements was 10^{-4} . Cadmium sulphide were prepared by heating a mixture of powder cadmium oxide and sulphur. Manganese was not added and was observed in CdS as an accidental impurity. Powder samples of $\text{CdS}:\text{Mn}^{2+}$ pressed into pellets were used. To span the required range of temperature above the room temperature, the sample was arranged into a

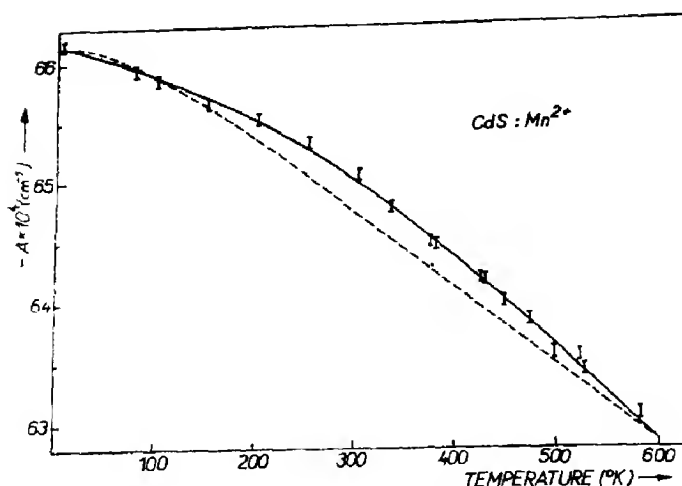


Fig. 1. The temperature dependence of the hyperfine coupling constant A of $\text{CdS}:\text{Mn}^{2+}$. The dashed line is the theoretical temperature dependence of A given by the interaction with the continuum phonon spectrum. The solid line is the theoretical dependence of A given by interaction with two local vibrational modes.

suitable furnace inserted directly into the cylindrical microwave cavity. This furnace consisting of Pt wire wound around the sample was placed in a fused silica tube covered with MgO powder. The temperature was measured by a thermocouple inserted directly inside the sample. To span the range of temperature between 77°K and a room temperature a special construction of Dewar vessel, made from a fused silica, was suggested. The finger of this vessel with the opening in its bottom was put through the cylindrical microwave cavity. The sample with a thermocouple inserted into the finger was fanned by a gas evaporated from the liquid nitrogen by which the Dewar vessel had been filled up. The temperature was kept on a required level by two heating resistors both placed inside a liquid nitrogen reservoir and a finger respectively.

The experimental results are plotted in Fig. 1. Corrections to the constant volume could not be performed but they are likely quite small[4]. The hyperfine coupling constant

decreases with the increasing temperature similarly as it is demanded in[2]. From the specific heat measurements[5] the Debye temperature of CdS is guessed to be about $\vartheta = 200^\circ\text{K}$. Having used this value of ϑ the temperature dependence of the hyperfine coupling

$$A(T) = A(T=0) \left[1 - CT^4 \int_0^{\vartheta/T} \frac{x^3 dx}{e^x - 1} \right] \quad (1)$$

derived by Šimánek and Orbach[2] has been computed. The parameter C appearing in (1) has been estimated by fitting the experimental value of $A(T)$ at $T = 600^\circ\text{K}$ and is equal to $C = 2.58 \cdot 10^{-13} \text{ }^\circ\text{K}^{-4}$. The theoretical expression (1) for $A(T)$ is plotted in Fig. 1. It can be seen that the departure of this theoretical $A(T)$ from the experimental values is greater than the experimental error. Thus obviously only strains induced by non-local phonons cannot explain entirely the observed course of the temperature dependence of $A(T)$ in

this case and local mode of vibration is under suspicion.

The temperature dependence of the hyperfine coupling given by the interaction with a local vibrational and/or resonance mode can be written in the form[3]

$$A(T) = A(T=0) \left[1 - C \cdot \left(\exp \frac{\hbar\omega}{kT} - 1 \right)^{-1} \right] \quad (2)$$

where ω is the frequency of the mode and C is a constant. It is evident from the course of the measured values in Fig. 1 that the curve $A(T)$ approximately consists of two straight lines with different slopes. At lower temperatures the line has smaller slope than that one at higher temperatures. Neither of two quoted expressions (1) and (2) gives an acceptable result. In trying to fit in the experimental and the theoretical curves, the linear superposition of both expressions (1) and (2) were used without success. Thus, evidently, the prevailing contribution to the temperature dependence of hyperfine coupling gives the interaction of electronic states of Mn^{2+} with two local modes. After using the linear superposition of two expressions of type (2), where four parameters C_1 , ω_1 , C_2 , ω_2 were varied so that the theoretical course should be merged in experimental data, the satisfactory results were reached. The theoretical temperature dependence of $A(T)$ for $C_1 = 1.6 \cdot 10^{-3}$, $\omega_1 = 4.25 \cdot 10^{14} \text{ sec}^{-1}$, $C_2 = 7.4 \cdot 10^{-2}$, $\omega_2 = 1.11 \cdot 10^{12} \text{ sec}^{-1}$ is plotted in Fig. 1. It can be seen that the departure from the experimental values are smaller than the experimental error $\pm 0.1 \cdot 10^{-4} \text{ cm}^{-1}$ in the determination of $A(T)$.

To simplify further consideration let us describe the local and/or the resonance vibrational mode bound to the impurity as a motion of the impurity ion and its nearest neighbours without respect to the motion of the more distant ions in the lattice. It means that the normal vibrational modes of octahedron or tetrahedron according to the respective lattice structure will be taken into account.

Let us consider conditions in the octahedron. Due to the inversion symmetry of the octahedron, its normal modes are of a defined parity. The three-dimensional vibrational motion of the impurity, if all other ions of the octahedron are fixed, gives a T_{1u} -normal mode of the odd parity. This T_{1u} -mode is not able to couple the d - and s -states of the impurity ion and thus it cannot contribute to the temperature dependence of the hyperfine field of this ion if the mechanism of s - d mixing[2] is supposed as decisive. These assumptions seem to be proved by the measurements of $A(T)$ in BaO and SrO doped by Mn^{2+} [3]. Here the temperature dependence of A is fully determined by the interaction with one resonance vibrational mode the frequency of which is below the lower limit of the optical vibrational band of the crystal. The odd T_{1u} -mode, given by the vibration of Mn^{2+} ion relative to the fixed oxygen ions of the octahedron, should have its frequency over the upper limit of the acoustical band owing to the smaller mass of Mn^{2+} ion in comparison with the Ba^{2+} and Sr^{2+} ions. Having observed no effect of a local mode of a frequency in this range, it is possible to conclude that the investigated effect is caused by another normal mode of octahedron, most probably of the even parity if the contribution of s - d -mixing is decisive.

The above mentioned restrictions are not valid in the case of tetrahedron-like surrounding of the impurity. The more covalent crystal is, the greater sp^3 hybridization of the impurity orbitals can be expected. These hybridized orbitals may be admixed into the d -orbitals by the interaction with the vibrational motion of the impurity ion relative to the fixed resting ions, which forms a normal T_2 -mode of the tetrahedron.

In the case of $\text{CdS}:\text{Mn}^{2+}$, where the mass of Mn^{2+} is smaller than that one of Cd^{2+} , the frequency of this T_2 -mode is over the lower frequency limit of the CdS optical band. On the other hand the presence of the resonance modes may not be excluded because Mn^{2+}

and Cd^{2+} differ in radius and this fact results in decreasing of the force constants coupling ions in MnS_4^{6-} in comparison with CdS_4^{6-} . (The $\text{Cd} \leftrightarrow \text{S}$ distance in CdS is 2.61 \AA and $\text{Mn} \leftrightarrow \text{S}$ distance in MnS is 2.43 \AA)[6]. The mode, arising in consequence of the sulphur ion's motion and motionless manganese ions, is able to cause the straight line dependence of $A(T)$ because its frequency is below the upper limit of the acoustic band of CdS . The second straight line dependence of $A(T)$ at higher frequencies is most probably caused by above mentioned T_2 -local mode. From this analysis it seems to be reasonable to suppose that the mechanism of s - d dynamic mixing is effective even in this case and the measured temperature dependence of $A(T)$ of Mn^{2+} in CdS caused by two vibrational modes localized on the Mn^{2+} impurity ion.

Acknowledgements—The authors are highly indebted to D. Nohavica for preparing the CdS -powder used in these measurements.

Institute of Radio
Engineering and Electronics,
Czechoslovak Academy
of Sciences
Prague,
Czechoslovakia

K. ŽĎÁNSKÝ
F. KUBEC

REFERENCES

1. WALSH W. M., JEENER J. J. and BLOEMBERGEN N., *Phys. Rev.* **139A**, 1338 (1965); ROSENTHAL J., YARMUS L. and BARTRAM R. H., *Phys. Rev.* **153**, 407 (1967); ROSENTHAL J. and YARMUS L., *J. chem. Phys.* **46**, 1217 (1967); ŽĎÁNSKÝ K., *Phys. Lett.* **24A**, 337 (1967); CALVO R. and ORBACH R., *Phys. Rev.* **164**, 284 (1967); CALVO R., *Phys. Lett.* **27A**, 713 (1968).
2. ŠIMÁNEK E. and ORBACH R., *Phys. Rev.* **145**, 191 (1966).
3. ŽĎÁNSKÝ K., *Phys. Status Solidi* **28**, 181 (1968).
4. WALSH W. M., Jr., JEENER J. and BLOEMBERGEN N., *Phys. Rev.* **139A**, 1338 (1965).
5. LANDOLT H. and BÖRNSTEIN R., *Phys.-chem. Tabellen*. Springer, Berlin (1958).
6. REMY H., *Lehrbuch der anorganischen Chemie* (Edited by L. Gees and K.-G. Portig). Leipzig (1957).

J. Phys. Chem. Solids Vol. 30, pp. 2330–2334.

Anomalous diffusion in beta zirconium, beta titanium and vanadium

(Received 15 October 1968; in revised form 6 January 1969)

A NUMBER of attempts[1–3] have been made to explain the non-linearity in the Arrhenius plots of $\log D$ vs. $1/T$ in the diffusion studies of β -Zr, β -Ti and vanadium. The first general interpretation[1] assumed the temperature dependence of diffusivity based on a single mechanism over the entire temperature range. Another explanation is on the basis of dual mechanisms[2, 3] operating simultaneously in the diffusion process and thus the diffusivity is expressed as

$$D = D_{01} \exp\left(-\frac{Q_1}{RT}\right) + D_{02} \exp\left(-\frac{Q_2}{RT}\right) \quad (1)$$

where D_{01} and Q_1 correspond to the mechanism operating at higher temperatures while D_{02} and Q_2 are the values for the mechanism at lower temperatures. The values of D_{01} and Q_1 for the self and impurity diffusion in β -Zr, β -Ti were normal and thus the vacancy mechanism seemed to be operative in these cases while the values of D_{02} and Q_2 for the low temperature region (below 1400°C) were found to be low compared to the respective self diffusion values. This led to different speculation for the mechanism of diffusion. According to Kidson[2], the low D_{02} and Q_2 values could arise as a result of enhancement of diffusivity through extrinsic vacancies by the presence of interstitially dissolved oxygen impurity (especially in β -Zr). LeClaire[4] has shown that a high binding energy for oxygen vacancy pairs is necessary if this model is applicable. The second proposed model[3] assumed the enhancement of lattice diffusivity (especially in β -Zr) due to the presence of randomly oriented dislocations where Kidson

[3] used Hart-Mortlock[5, 6] relations and showed qualitatively that if D_{02} and Q_2 represent the dislocation diffusion parameters, its dislocation density should be at least of the order of 10^9 – 10^{12} lines/cm².

Using random walk analysis and Hart-Mortlock[5, 6] relation similar to the previous work[7] an attempt has been made to extend it for the quantitative estimation of the enhancement of lattice diffusivity due to the presence of randomly oriented dislocations and to explain the anomalous behaviour in the self and impurity diffusion in β -Zr, β -Ti and vanadium.

Hart-Mortlock[5, 6] relation for self and impurity diffusion in metals is given by

$$(D/D_r) (\text{self}) = g(D_d/D_r) + 1 \quad (2)$$

$$(D/D_r) (\text{solute}) = g(D_d/D_r)K + 1 \quad (3)$$

where D is the apparent bulk diffusivity, D_r is the bulk diffusion coefficient in a crystal free from dislocations, D_d is the diffusion coefficient along dislocation, g is the fraction of the total time that the impurity atom spends in the dislocation and K is the segregation coefficient.

Evidently, to calculate quantitatively the enhancement terms, the values of D_d/D_r , K and g should be known. In absence of any data of (D_d/D_r) for β -Zr, β -Ti and V, the value of (D_d/D_r) as discussed earlier[7] was calculated from the known value of (D_d/D_r) for silver on the assumption that (D_d/D_r) should be the same for all the other metals at the same ratio of T/T_m where T and T_m are the absolute temperature for the diffusion anneal and melting points of the solvent. Cottrell has shown that for a small concentration of impurity in a solvent, the segregation coefficient $K \approx \exp(-W/RT)$ where W is the interaction energy of the impurity with dislocation core. The energy of interaction ' W ' arises as a result of the elastic and electrostatic interaction of impurity with dislocation and can be written as

$$W = W_1 + W_2 + W_3$$

where W_1 , W_2 are the elastic interaction terms of the impurity atom with dislocation core due to the difference in the size and elastic constants of the solute and solvent atoms respectively while W_3 takes into account the electrostatic interaction term. Ignoring the term W_3 , (which is very small and difficult to evaluate), W_1 and W_2 have been evaluated according to Friedel[8]. In absence of any data on the dislocation density in these metals, the value of ' g ' was calculated taking dislocation density of the order of 10^9 lines per cm². The value is definitely high for a well annealed single crystal. In view of the phase transformation of martensitic nature as reported by Fisher and Renken[9] and the possibility of the interlocking of the dislocations due to the presence of the dissolved impurities in β -Zr, β -Ti, a high dislocation density is possible. Even in vanadium an evidence of a polymorphic transformation[10] is available which also gives rise to high dislocation density.

The enhancement terms $(D_d/D_r)g$ and $(D_d/D_r)gK$ for the self and impurity diffusion in β -Zr, β -Ti and V have been calculated at different temperatures and a few values are given in Table 1. It is observed that the enhancement terms for the self and impurity diffusion in β -Zr, β -Ti and V is always greater than 1 below 1400°, 1300° and 1450°C respectively (Table 1). At higher temperatures (greater than 1450°C up to the melting point of the solvent) the contribution of the enhancement term due to dislocation becomes less pronounced and only lattice diffusion through normal vacancies seem to be operative. Hence it may be concluded that below the temperature of 1400°C or so, the diffusivity in β -Zr, β -Ti and V is enhanced by the presence of the randomly oriented dislocation and the experimental values of D_0 and Q obtained in the lower temperature region would thus represent the results along dislocations. Moreover, if diffusion along

Table 1. Enhancement terms for the self and impurity diffusion in beta zirconium, beta titanium and vanadium at few temperatures

Solvent	Temperature (°C)	$\frac{D_d}{D_v}g$				
			Zr[14]	Cb[14]	Cr	
	(°C)					
β -Zr		Zr[14]		Cb[14]	Cr[15]	Mo[16]
	900	4.31×10^2	3.03×10^3	7.19×10^4	7.45×10^3	
	950	1.94×10^2	1.26×10^3	2.70×10^3	2.98×10^3	
	1350	1.96	8.04	79.28	15.39	
	1400	1.29	5.08		9.82	
	1450	0.87	3.28		6.18	
	1600	0.30	1.02		1.83	
	1650	0.22	0.72		1.28	
β -Ti		Ti[20]		Cb[20]	Cr[20]	Mo[20]
	900	1.00×10^2	80.25	4.05×10^3	2.64×10^2	
	950	47.64	38.61	1.66×10^3	1.20×10^2	
	1350	0.68	0.58	9.90	1.37	
	1400	0.46	0.40	6.21	0.91	
	1600	0.12	0.11	1.22	0.22	
	1650	0.09	0.08	0.86	0.16	
V		V[21]		Fe[21]	Cr[21]	
	800	4.09×10^3	2.25×10^4	1.83×10^4		
	850	1.56×10^3	2.09×10^4	1.72×10^4		
	1450	1.16				
	1500	0.78				
	1850	0.09				

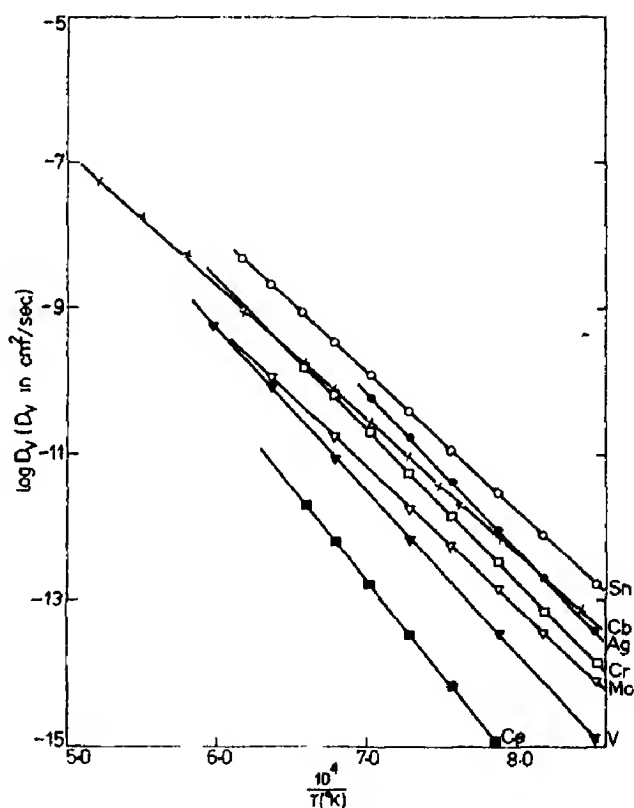
$\frac{D_d}{D_r}gK$					
Sn[17]	V[18]	Ag[19]	Ce[16]		
1.60×10^3	1.80×10^4	1.33×10^4	1.27×10^6		
6.85×10^2	7.03×10^3	5.21×10^3	4.17×10^3		
5.08	29.17	23.40	6.33×10^2		
			3.52×10^2		
			2.01×10^2		
			45.00		
			28.30		
Sn[20]	V[20]	Mn[20]	Fe[20]	Co[20]	Ni[20]
1.51×10^4	8.85×10^2	3.35×10^3	3.55×10^3	5.14×10^3	5.04×10^3
5.88×10^3	3.85×10^2	1.37×10^3	1.47×10^3	2.09×10^3	1.99×10^3
25.65	3.30	8.24	8.97	11.74	11.63
15.57	2.10	5.40	5.67	7.07	7.21
2.78	0.47	1.08	1.13	1.42	1.40
1.91	0.34	0.76	0.79	0.99	0.98

Table 2. Self diffusion parameters in beta zirconium, beta titanium and vanadium

Lattice	D_0 (cm ² /sec) (below 1400°C)	Q (kcal/mole)	D_0 (cm ² /sec) (above 1400°C)	Q (kcal/mole)	D_{0v} (cm ² /sec) (calculated)	Q_v (kcal/mole)	
β -Zr	8.50×10^{-8}	27.70	1.34	65.20	0.73	61.23	[14]
β -Ti	3.58×10^{-4}	31.20	1.09	60.00	3.80	62.15	[20]
V	0.36	73.65	2.14×10^2	94.14	1.42×10^4	114.25	[21]

dislocation is predominant, the plots of $\log D$ vs. $1/T$ in the lower temperature region should give straight lines. It is interesting to note that the self and impurity diffusion in β -Zr, β -Ti and V in the lower temperature region follow a simple Arrhenius relation. Furthermore the present results of quantitative analysis on the self and impurity diffusion in these systems also agree well with the proposed dual mechanism model of Kidson [3].

It was considered desirable to evaluate D_v , D_{0v} and Q_v (diffusion parameters in dislocation free single crystals). D_v was calculated using equations (2) and (3), and D_{0v} and Q_v were evaluated from the slopes of the plots of $\log D_v$ vs. $1/T$. In all these plots, fairly good straight lines are observed. A representative graph for the impurity diffusion in β -Zr is given in Fig. 1. For comparison, the least square values of D_{0v} and Q_v for the self diffusion in β -Zr, β -Ti and V along with the experimental values are given in Table 2. It is interesting to note that the least square values of Q_v for the self and impurity diffusion in β -Zr, β -Ti and V satisfy the empirical relations of the activation energy with melting point within 20 per cent. Therefore Q_v in general represent the activation energy corresponding to diffusion through normal lattice vacancies in dislocation free single crystals. The calculated value of D_{0v} in the case of vanadium (Table 2) is pretty high. Normally the values of D for face centred cubic systems, where vacancy mechanism is operative, lie within 0.1 – 10 cm²/sec, still a number of cases [11, 12] have been reported where D_0 is as high as 6.3×10^7 cm²/sec [13].

Fig. 1. Temperature dependence of ' D_v ' for impurity diffusion in β -zirconium.

In spite of some of the assumptions made in the above discussion, because of non-availability of the experimental data, it seems reasonable to assume that the apparent volume diffusivity is enhanced due to the existence of randomly oriented dislocations.

Bhabha Atomic Research Centre,
Chemistry Division,
Trombay, Bombay,
India

M. C. NAIK
R. P. AGARWALA

REFERENCES

1. GIBBS G. B., *Acta Metall.* **12**, 1303 (1964).
2. PEART R. F. and ASKILL J., *Phys. Status Solidi* **23**, 263 (1967).
3. KIDSON G. V., *Proc. Int. Conf. Gatlinburg, Tenn.*, p. 329. Am. Soc. Met. (1964).
4. LECLAIRE, A. D., *Proc. Int. Conf. Gatlinburg, Tenn.*, p. 1. Am. Soc. Met. (1964).
5. HART E., *Acta Metall.* **5**, 597 (1957).
6. MORTLOCK A., *Acta Metall.* **8**, 132 (1960).
7. NAIK M. C. and AGARWALA R. P., *Acta Metall.* **15**, 1521 (1967).
8. FRIEDEL J., *Dislocations*. Wesley, London (1964).
9. FISHER E. S. and RENKEN C. J., *Phys. Rev.* **135A**, 482 (1964).
10. SEYBOLT A. U. and SUMSION H. T., *J. Metals* **5**, 292 (1953).
11. ANDELIN R. L., KNIGHT J. D. and KAHN M., *Trans. Am. Inst. Min. Engrs* **233**, 19 (1965).
12. SPARK B., JAMES D. W. and LEAK G. M., *J. Iron Steel Inst.* **203**, 152 (1965).
13. VASILEV V. P. and CHERNOMORCHENKO S. G., *Zav. Lab.* **22**, 688 (1956).
14. FEDERER J. I. and LUNDY T. S., *Trans. Am. Inst. Min. Engrs* **227**, 592 (1963).
15. AGARWALA R. P., MURARKA S. P. and ANAND M. S., *Trans. metall. Soc. AIME* **233**, 986 (1965).
16. PAUL A. R., ANAND M. S., NAIK M. C. and AGARWALA R. P., *Intl Conf Vacancies Interstitials in Metals*, Julich (1968).
17. GRUZIN P. L., EMELYANOV V. S., RYABOVA G. G. and FEDOROV G. B., *2nd Intl Conf. Peaceful Uses of Atomic Energy, Geneva* **19**, 187 (1958).
18. AGARWALA R. P., MURARKA S. P. and ANAND M. S., *Acta Metall.* **16**, 61 (1968).
19. NAIK M. C. and AGARWALA R. P., *Proc. Nucl. Radiation Chem. Symp.*, p. 282. Waltair, India (1966).
20. GRAHAM D., *Proc. Intl Conf. Gatlinburg, Tenn.*, p. 27. Am. Soc. Met. (1964).
21. PEART R. F., *J. Phys. Chem. Solids* **26**, 1853 (1965).

J. Phys. Chem. Solids Vol. 30, pp. 2334-2336.

Compositional compensation points in magnetic garnets

(Received 12 November 1968)

VERY RECENT Mössbauer-effect spectroscopy measurements performed by Czerlinsky[1] on several Ga-substituted yttrium-iron garnets determined the distribution of the Ga^{3+} ions over the tetrahedral and the octahedral sites.

The experimental points of the fractional tetrahedral Ga ions, $f_t = x/t$, as a function of the total Ga substitution, t , in the formula $\text{Y}_3\text{Ga}_t\text{Fe}_{5-t}\text{O}_{12}$ are in excellent agreement with the theoretical curve derived from a previous treatment on the thermodynamics of solid solutions[2], $t = [2 + 3C - (C - 1)x]/[3C - (C - 1)x]$, with the value of the energy factor, $C = 6.5$.

Since the energy factor C is related by the formula $C = \exp \{-[\Delta\epsilon_M - \Delta\epsilon_{\text{Fe}}]/kT\}$ to $\Delta\epsilon_M$ and $\Delta\epsilon_{\text{Fe}}$, respectively the difference of the stabilization energy between tetrahedral and octahedral sites of the diamagnetic M cation and of Fe^{3+} , it gives a measure of the tetrahedral preference of M in iron-substituted garnets.

The chosen value is interesting if compared with $C = 3.0$ for Al^{3+} substitution[2], which has a weaker tetrahedral preference than Ga^{3+} [3-6].

We wish to point out in this note that also the magnetic moment compensation compositions of such garnets give a measure of the tetrahedral preference of diamagnetic substitutions in YIG and that this can easily be predicted by the theory. In fact, the magnetization compensation condition in a mono-substituted garnet $\{\text{Y}_3\} (\text{M}_x\text{Fe}_{3-x}) [\text{M}_{1-x}\text{Fe}_{2-t+x}]\text{O}_{12}$, $x = (1 + t)/2$, once substituted in the distribution equation provides the two roots: $t_{\text{comp.}} = (C + 1)/(C - 1)$ and $t = 5$; the first root is the compensation composition, the second one represents obviously the total diamagnetic substitution. The minimum value of $t_{\text{comp.}}$ is 1 and is obtained for $C = \infty$ (exclusive tetrahedral substitution); the maximum value, $t = 5$, is obtained for $C = 3/2$ but large t values require further discussion, as pointed out previously[2].

The value $C = 6.5$ leads to $t_{\text{comp.}} = 1.36$ for Ga-substituted garnets in very good agreement with $t = 1.3$ as reported by Geller *et al.* [7] and by Lüthi[8]. The value $C = 3$ leads to $t_{\text{comp.}} = 2.00$ for Al-substituted garnets in good agreement with $t \approx 2.1$ as measured by Geller *et al.*[3]. In Fig. 1 the curves f_t vs. t

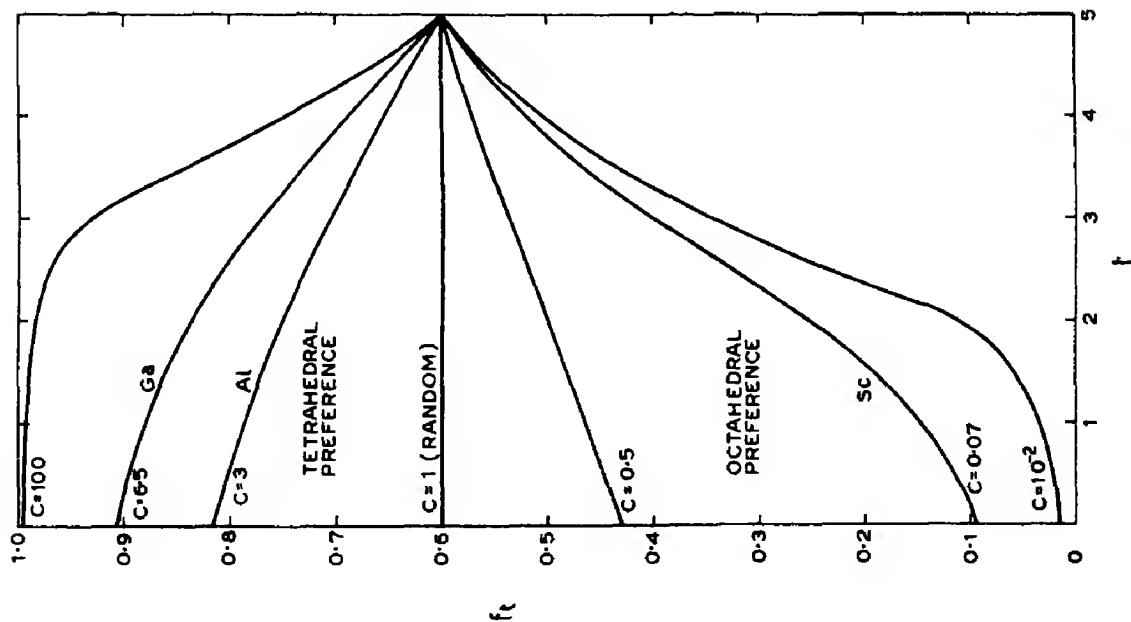


Fig. 1. Fraction of diamagnetic ions in tetrahedral sites f_t vs. total substitution t , for different values of the energy factors C . $C = 6.5$, 3.0 and 0.07 correspond to Ga, Al and Sc substitution, respectively.

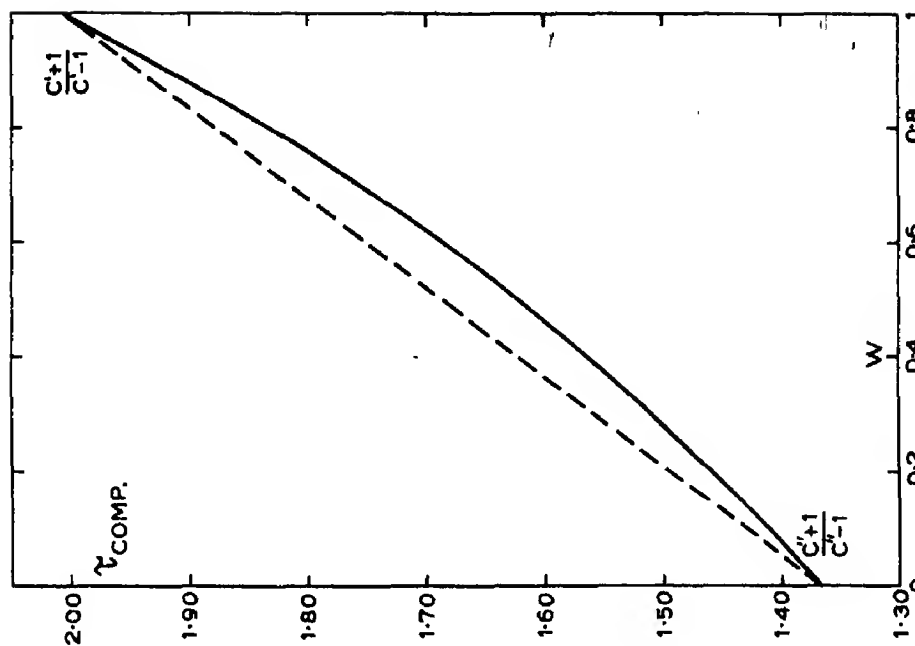


Fig. 2. Total substitutional compensation composition τ_{comp} in $Y_3(\text{Al}_w\text{Ga}_{1-w})\text{Fe}_3\text{O}_{12}$ as a function of the relative amount of Al ions per formula, w .

for different values of C are plotted. Also the curve for $C = 0.07$ is plotted which represents the distribution of the Sc^{3+} -substituted garnets. Sc^{3+} has a strong octahedral preference[3] and the given C -value provides a good agreement between theoretical and experimental magnetizations vs. total Sc substitutions.

In the case of YIG with double diamagnetic substitutes, e.g. Al and Ga, the formula can be written, following the bracket notation of Gilleo and Geller[9], $\{\text{Y}_3\}(\text{Al}_{\tau x}\text{Ga}_{\tau y}\text{Fe}_{3-\tau(x+y)})[\text{Al}_{\tau(w-x)}\text{Ga}_{\tau(1-w-y)}\text{Fe}_{2-\tau(1-x-y)}]\text{O}_{12}$, and the thermodynamic equilibrium conditions[2] are: $[3 - \tau(x+y)](w-x)C' = x[2 - \tau(1-x-y)]$ and $[3 - \tau(x+y)](1-w-y)C'' = y[2 - \tau(1-x-y)]$. The condition for a balance of the magnetic moments in the two sites, $x+y = (1+\tau)/2\tau$, gives the value of the total compositional compensation: $\tau_{\text{comp.}} = [w(C'-1)/(C'+1) + (1-w)(C''-1)/(C''+1)]^{-1}$. C'' and C' are the energy factors for Ga and Al, respectively. In Fig. 2, $\tau_{\text{comp.}}$ is plotted as a function of the relative amount of Al with respect to the total Ga+Al content per formula, w .

Accurate Mössbauer measurements of the kind performed by Czerlinsky would be desirable to check these results.

If the two substitutes have different site preferences like Ga^{3+} and Sc^{3+} (with respective energy factors C' and C'' and fractions w

and $1-w$ per formula) then a compensation composition appears for values $(3-2C'')/(C'+1)/5(C'-C'') \leq w < 1$ in correspondence of $5 > \tau_{\text{comp.}} \geq (C'+1)/(C'-1)$ that is, for the (Ga, Sc) case, $0.67 \leq w < 1$ and $5 > \tau_{\text{comp.}} \geq 1.36$.

Acknowledgements—We wish to thank Dr. E. Czerlinsky for communicating his results prior to publication and Dr. J. P. Remeika for sending a preprint of a paper on the distribution in (Y, Al, Ga) garnets.

Research Department,
Ceramic Laboratory,
Selenia S.p.A.,
Via Tiburtina Km 12,400,
00131 Roma, Italy

CAMILLO BORGHESE

REFERENCES

1. CZERLINSKY E., Presented at the *Conf. on Magnetism and Magnetic Materials*, New York (1968).
2. BORGHESE C., *J. Phys. Chem. Solids* **28**, 2225 (1967).
3. GELLER S., WILLIAMS H. J., ESPINOSA G. P. and SHERWOOD R. C., *Bell Syst. tech. J.* **43**, 565 (1964).
4. STREEVER R. L. and URIANO G. A., *Phys. Rev.* **139**, 305 (1965).
5. MAREZIO M., REMEIKA J. P. and JAYARAMAN A., *J. chem. Phys.* **45**, 1821 (1966).
6. MAREZIO M., REMEIKA J. P. and DERNIER P. D., *Acta crystallogr.* In press (1969).
7. GELLER S., CAPE J. A., ESPINOSA G. P. and LESLIE D. H., *Phys. Rev.* **148**, 522 (1966).
8. LÜTHI B., *Phys. Rev.* **148**, 519 (1966).
9. GILLES M. A. and GELLER S., *J. Phys. Chem. Solids* **10**, 187 (1959).

NOTES FOR CONTRIBUTORS

I. GENERAL

1. Submission of a paper to *The Journal of Physics and Chemistry of Solids* will be taken to imply that it represents original research not previously published (except in the form of an abstract or preliminary report), that it is not being considered for publication elsewhere, and that if accepted it will not be published elsewhere in the same form, in any language, without the consent of the Editor-in-Chief. It should deal with original research work in the field of the physics and chemistry of solids.

2. Papers should be submitted to the appropriate regional editor (all English-language papers to be sent to the U.S. editor).

3. Short communications may be published as "Technical Notes" and will receive somewhat more rapid handling than full length articles. Short communications requiring the maximum speed of publication should be submitted to one of the editors of "Solid State Communications."

II. SCRIPT REQUIREMENTS

1. **Papers** submitted should be concise and written in a readily understandable style. Scripts should be typed and double spaced with good margins on one side of the paper only and submitted in duplicate to facilitate refereeing.

It will be appreciated if authors clearly indicate any special characters used. An abstract not exceeding 200 words, should be provided in the language of the paper. French and German papers should be submitted with English abstract and titles, but if this is not possible the abstract will be translated by the publishers. To conserve space, **authors are requested to mark less important parts of the paper**, such as details of experimental technique, methods, mathematical derivations, etc. **for printing in small type**. The technical description of methods should be given in detail only when such methods are new. Authors will receive proofs for correction when their papers are first set, and **alterations must be restricted to printer's errors**. Other than these, any substantial changes may be charged to the authors.

2. **Illustrations** should not be included in the typescript of the paper, and legends should be typed on a separate sheet. Line drawings which require redrawing should include all relevant details and clear instructions for the draughtsman. If figures are already well drawn it may be possible to reproduce them direct from the originals, or from good photo-prints if these can be provided. It is not possible to reproduce from prints with weak lines. Illustrations for reproduction should normally be about twice the final size required. The lettering should be sufficiently large and bold to permit this reduction. Photographs should only be included where they are essential.

3. **Tables and figures** should be so constructed as to be intelligible without reference to the text. Every table and column should be provided with an explanatory heading. Units of measure must always be clearly indicated. The same data should not be published in both tables and figures. The following standard symbols should be used on line drawings since they are easily available to the printers: ○, ●, +, ×, □, ■, △, ▲, ◇, ◆, ▽, ▼.

4. **References** are indicated in the text by numbers on the line in brackets, and the full reference should be given in a list at the end of the paper in the following form:

1. BARNES R. G., BORSA F. and PETERSON D., *J. appl. Phys.* 36, 940 (1965).
2. KNIGHT W. D., In *Solid State Physics* (Edited by F. Seitz and D. Turnbull), Vol. 2, p. 93. Academic Press, New York (1957).

Abbreviations of journal titles should follow those given in *World List of Scientific Periodicals* (4th Edn.). It is particularly requested that authors' initials, and appropriate volume and page numbers, should be given in every case.

Footnotes, as distinct from literature references should be indicated by the following symbols—*, †, ‡, §, commencing anew on each page; they should not be included in the numbered reference system.

5. Due to the international character of the journal no rigid rules concerning notation and spelling will be observed, but each paper should be consistent within itself as to symbols and units.

CONTENTS

Y. ISHIBASHI and H. L. STADLER: Ferroelectric electroreflectance of gold films	2113
G. AMSEL, C. CHERKI, G. FEUILLADE and J. P. NADAI: The influence of the electrolyte on the composition of 'anodic oxide films' on tantalum	2117
M. CERTIER, C. WECKER and S. NIKITINE: Zeeman effect of free and bound excitons in CuCl	2135
T. M. SEARLE: Optical studies of the thermal dissociation of OH ⁻ ion aggregates in MgO	2143
B. OKAI, Y. ONODA, S. MINOMURA and S. NAKAMURA: Effect of pressure on the Knight shift in V ⁵¹ and β -Mn ⁵⁵ metals	2153
T. P. ABELES, W. G. BOS and P. J. OUSEPH: ¹⁶¹ Dy isomer shifts in dysprosium compounds	2159
P. LEONARD, M. C. CADEVILLE, J. DURAND and F. GAUTIER: Experimental proof for a two-band conduction in nickel alloys	2169
E. LÖFFLER and H. RAUCH: A neutron depolarization study on dysprosium and terbium	2175
A. R. ALLNATT and L. A. ROWLEY: The statistical mechanics of imperfect molecular crystals	2187
P. WYNBLATT: On the formation and migration entropies of vacancies in metals	2201
R. KLEIM and F. RAGA: Exciton luminescence in lead iodide lifetime, intensity and spectral position dependence on temperature	2213
W. SCHAIRER and W. GRÄMAN: Photoluminescence of Ge-doped GaAs grown by vapor-phase epitaxy	2225
R. POLÁK and K. KLIER: Spectra of synthetic zeolites containing transition metal ions—III. A simple model calculation of the system adsorbed molecule—NiA zeolite	2231
A. N. THORPE, F. E. SENFTLE and G. DONNAY: Magnetic susceptibility and exchange coupling in the mineral ardenite	2235
M. H. MANGHNANI and W. M. BENZING: Pressure derivatives of elastic moduli of Vycor glass to 8 kbar	2241
D. A. RIGNEY and J. A. BLODGETT: The Knight shift in metals: liquid arsenic	2247
R. TAYLOR, B. T. KELLY and K. E. GILCHRIST: The thermal conductivity of fast neutron irradiated graphite	2251
M. WUTTIG and E. T. YEN: Isotope effect of carbon diffusion in an Fe-Si alloy	2269
R. ALONARD, P. BOUTRON et D. BLOCH: Anisotropie de la susceptibilité paramagnétique des monocristaux de terres rares: Gd, Tb, Dy, Ho et Er	2277
D. F. WINTERSTEIN and E. F. SIECKMANN: Electrical conductivity and optical absorption changes related to the 3800 Å band of CaO:Ca	2287
C. E. ROSSI and W. PAUL: The preparation of NiO thin films and their use in optical measurements in the visible and ultraviolet	2295
J. W. GADZUK: Theory of dielectric screening of an impurity at the surface of an electron gas	2307
Technical Notes:	
C. W. FRANK, G. DE PASQUALI and H. G. DRICKAMER: The effect of pressure on the isomer shift of ⁵⁷ Fe(⁵⁷ Co) as an impurity in ZnSe, ZnTe and CdTe	2321
M. R. TUBBS: Dispersion effects in interference methods for the measurement of refractive index	2323
M. W. SHAFER and J. D. KUPTSI: On the nature of the magnetic inclusions in EuF ₂	2325
K. ŽDÁNSKÝ and F. KUBEC: Temperature dependence of the hyperfine coupling of Mn ²⁺ in CdS	2327
M. C. NAIK and R. P. AGARWALA: Anomalous diffusion in beta zirconium, beta titanium and vanadium	2330
C. BORGHESE: Compositional compensation points in magnetic garnets	2334

THE
JOURNAL OF
PHYSICS
AND
CHEMISTRY
OF SOLIDS
AN
INTERNATIONAL
JOURNAL

PERGAMON PRESS



NEW YORK • OXFORD • LONDON • PARIS

VOLUME 10

1949

OCTOBER 1949

Editor-in-Chief
HARVEY BROOKS
Cambridge, Mass.

Associate Editors

H. B. G. CASIMIR
Eindhoven

B. CHALMERS FRAZER
Brookhaven

JACQUES FRIEDEL
Paris

I. M. LIPSHITZ
Khar'kov

Spectrochimica Acta

This international journal for the rapid communication of original work dealing with atomic and molecular spectroscopy is published in two parts.

PART A MOLECULAR SPECTROSCOPY

Editors Prof. Sir Harold Thompson St. John's College Oxford
Prof. M. Kent Wilson National Science Foundation Washington DC

This journal deals particularly with qualitative and quantitative analysis, the determination of molecular parameters and general theory. Also included are papers on nuclear magnetic resonance spectra, electron spin resonance spectra, optical rotary dispersion, and the design and performance of instruments and components.

Papers recently published include:

M. J. HITCH and S. D. ROSS The infra-red spectra of 1:3- and 1:4- dithian and pentamethylene sulphide

C. L. HONEYBOURNE and G. A. WEBB A spectroscopic study of some N:N' disubstituted 1:3 di-imines

ULF BLINDHEIM and THOR GRAMSTAD Studies of hydrogen bonding-XX.

Hydrogen bonding ability of phosphoryl compounds containing N-P and S-P bonds

R. T. BAILEY Infrared and laser Raman spectra of methyl-cyclopentadienyl nickel nitrosyl

Published Monthly

PART B ATOMIC SPECTROSCOPY

Editors Dr. M. Margoshes Division of Block Eng. Maryland U.S.A.
Dr. K. Laqua Institut für Spektrochemie Dortmund Germany

Presents research papers on all regions of the electromagnetic spectrum, in so far as they have direct physicochemical interest. The main subjects include the determination of fundamental atomic data, new experimental procedures, and measurements or calculations of the properties of radiation sources or detectors.

Papers recently published include:

H. JÄGER Temperaturmessungen an Mischplasmen im 30 Amp Gleichstrombogen

J. O. KARTTUNEN and W. R. HARMON Determination of uranium in ores and in solution using a portable non-dispersive X-ray spectrograph

A. CARNEVALE and A. J. LINCOLN A computer program to determine photographic emulsion calibration curves

E. E. PICKETT and S. R. KOIRTYOHANN The nitrous oxide-acetylene flame in emission analysis - III. Aluminum, gallium, indium, thallium, germanium, and tin

Write for full details and an inspection copy of either part of the journal.
Details of other journals in the field can also be sent to you.



Pergamon Press

OXFORD · NEW YORK · LONDON · PARIS · SYDNEY



A NUCLEAR MAGNETIC RESONANCE STUDY OF GALLIUM SINGLE CRYSTALS—I. LOW FIELD SPECTRA*

M. I. VALIČ and D. LLEWELYN WILLIAMS

Physics Department, University of British Columbia, Vancouver 8, B.C., Canada

(Received 20 February 1969; in revised form 8 May 1969)

Abstract—The low magnetic field splitting of the quadrupole resonance in gallium metal has been studied in single crystal specimens. Precise determinations of the electric field gradient tensor have been made at 4.2°, 77° and 285°K. The results are only weakly temperature dependent and reveal two non-equivalent sites in the crystal which differ only in the relative orientation of their principal axes. An attempt at a decomposition of the electric field gradient tensor by subtracting the calculated ionic contribution is highly suggestive of a strong contribution in the direction of the nearest neighbour and possibly indicative of some covalency.

INTRODUCTION

A CONSIDERABLE improvement in the resolution of anisotropic effects in the nuclear magnetic resonance properties of metals has been achieved through their direct observation in single crystal specimens[1]. Gallium is one of the most anisotropic of metals and its nuclear magnetic properties can reveal useful information concerning its electronic properties. The measurable parameters are those of the electric field gradient (EFG) tensor at the nuclear site and the three describing the orientation dependence of the Knight shift in an orthorhombic crystal.

The EFG tensor in gallium single crystals has been previously studied at 4.2°K by Kiser [2] but the results obtained are considerably less accurate than ours particularly with regard to the orientation of the principal axes. The quadrupole resonance has also been studied in the polycrystalline sample by Knight, Hewitt and Pomerantz[3], Pomerantz[4] and Kiser and Knight[5] over a wide temperature range and also in the superconducting state by Hammond and Knight[6]. Some measurements on the pressure and temperature dependence of the

quadrupole frequency in powder samples have been undertaken by Kushida and Benedek[7].

The present study was initiated with the main aim of determining the Knight shift parameters in the solid with a view to understanding the temperature dependence of the spin-lattice relaxation time observed by Hammond, Wilkner and Kelly[8] and also in the hope that a comparison with the measurements in the liquid state[9] would clarify the interpretation of the liquid. The determination of these parameters however requires an accurate knowledge of the EFG tensor and the present paper is confined to the results obtained for the EFG tensor over the temperature range from 4.2° to 285°K. The Knight shift results are deferred to a second paper[10].

The relevant properties of gallium are summarized in Table 1 and the crystal structure is shown in Fig. 1. The crystal structure is orthorhombic with the unit cell dimensions $A = 4.5156$, $B = 4.4904$, $C = 7.6328$ at 4.2°K and atmospheric pressure[11]. The eight atoms in the unit cell are located at the sites [12]

$$\begin{aligned} & (u, 0, v) \quad (u + \tfrac{1}{2}, \tfrac{1}{2}, \bar{v}) \quad (\bar{u} + \tfrac{1}{2}, \tfrac{1}{2}, v) \quad (\bar{u}, 0, \bar{v}) \\ & (u, \tfrac{1}{2}, v + \tfrac{1}{2}) \quad (u + \tfrac{1}{2}, 0, \bar{v} + \tfrac{1}{2}) \quad (\bar{u} + \tfrac{1}{2}, 0, v + \tfrac{1}{2}) \\ & \quad \quad \quad (\bar{u}, \tfrac{1}{2}, \bar{v} + \tfrac{1}{2}) \end{aligned}$$

*Research supported by the National Research Council of Canada through Grant A-1873.

Table 1. Gallium magnetic resonance parameters

Isotope	Nuclear spin	Abundance (%)	Pure quadrupole frequency (285.3°K) (kc/sec)	NMR frequency in 10 kG (kc/sec)	Nuclear quadrupole moment ($\times 10^{-24}$ cm ²)
⁶⁹ Ga	3/2	60.8	10823.8	10218	0.19
⁷¹ Ga	3/2	39.2	6820.7	12984	0.12

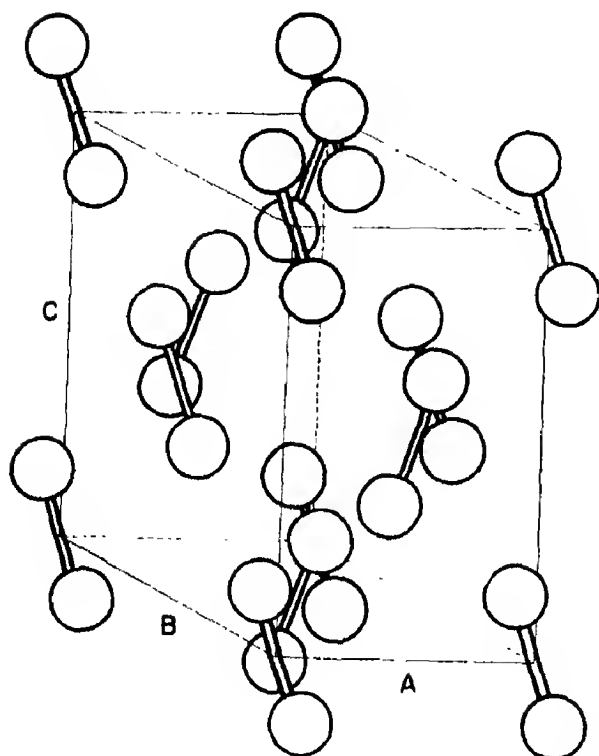
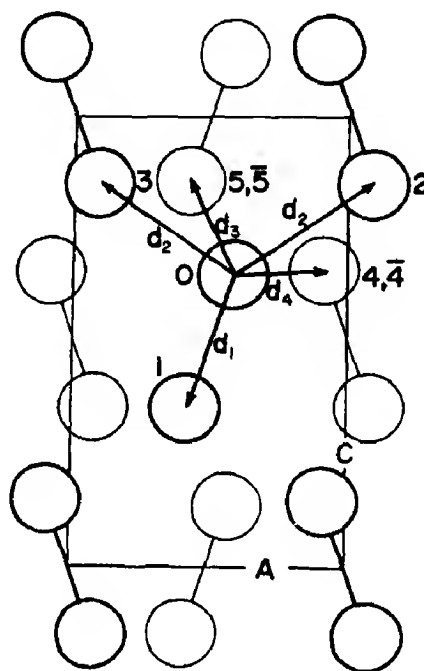


Fig. 1. Gallium crystal structure. The double lines connect nearest neighbours.

Fig. 2. Projection of the gallium unit cell onto the AC plane. Heavy lines correspond to atoms lying in one plane and light lines indicate atoms lying in planes $\frac{1}{2}B$ away. The various neighbours are indicated by the lettered vectors.

where $u = 0.0785$, $v = 0.1525$. The projection of the structure on to the AC plane is shown in Fig. 2. The structure may be visualized as a line of 'diatomic molecules' lying with their axes in the AC plane at an angle β of 16° to the C axis and displaced by half a lattice spacing along both B and C from the next line whose axes are rotated through 180° about the C axes.

Each atom has one nearest neighbour at 2.429 \AA and six others varying in distance between 2.709 \AA to 2.791 \AA . The two next nearest neighbours are considerably further away at a distance of 3.54 \AA .

THE QUADRUPOLEAR HAMILTONIAN

The Hamiltonian describing the interaction between a nuclear quadrupole moment and an electric field gradient together with the interaction between the magnetic dipole moment and a magnetic field H_0 [13, 14].

$$\mathcal{H} = A \{ 3I_z^2 - I(I+1) + \frac{1}{2}\eta(I_+^2 + I_-^2) \} + \hbar\nu_n \{ I_z \cos \nu + \frac{1}{2}(I_+ e^{-i\phi} + I_- e^{+i\phi}) \sin \theta \} \quad (1)$$

where

$$A = \frac{e^2 Q q_{zz}}{4I(2I-1)}; \eta = \frac{q_{yy} - q_{xx}}{q_{zz}}; |q_{xx}| \leq |q_{yy}| \leq |q_{zz}|. \quad (2)$$

I is the nuclear spin angular momentum, Q is the scalar nuclear quadrupole moment and $2\pi\nu_h = \gamma H_0$ is the Larmor frequency. The coordinate system chosen is that of the principal axes system of the EFG tensor which then only has the diagonal components q_{zz} , q_{yy} and q_{xx} . η is called the asymmetry parameter. θ and ϕ are the polar angles specifying the orientation of the external magnetic field with respect to the principal system.

The case of spin $I = \frac{3}{2}$ in the absence of an external magnetic field is characterized by a single resonance line corresponding to a transition between two doubly degenerate energy levels with a frequency separation

$$\nu_Q = \rho \nu_Q^0 \quad (3)$$

where $\rho = (1 + \frac{1}{3}\eta^2)^{1/2}$ and the pure quadrupole frequency $\nu_Q^0 = 6A/h$, which cannot serve to determine either A or η independently. The application of a magnetic field however removes the degeneracy and the dependence of the spectra upon crystal orientation reveals the principal axes and the components of the EFG tensor uniquely, assuming that Q is also known.

The frequencies for any value of η and correct to first order in the magnetic field are given by the expression [14]

$$\nu = \nu_Q \pm (m_1 \pm m_2) \nu_H \quad (4)$$

where

$$\begin{aligned} m_1 &= \frac{1}{2}\rho [(\rho + 1 - \eta)^2 \sin^2\theta \cos^2\phi + (\rho + 1 + \eta)^2 \\ &\quad \sin^2\theta \sin^2\phi + (2 - \rho)^2 \cos^2\theta]^{1/2} \\ m_2 &= \frac{1}{2}\rho [(\rho - 1 + \eta)^2 \sin^2\theta \cos^2\phi + (\rho - 1 - \eta)^2 \\ &\quad \sin^2\theta \sin^2\phi + (2 + \rho)^2 \cos^2\theta]^{1/2}. \end{aligned} \quad (5)$$

In general four resonance lines will be observed and of these the angular variation of

the 'inner pair' of lines (i.e. the lines which are least split from ν_Q by the magnetic field) contains sufficient information to determine accurately the required parameters. In particular we may note the following for the 'inner pair'.

H parallel to Z :

$$\nu = \nu_Q \pm \nu_H$$

H parallel to X :

$$\nu = \nu_Q \mp \nu_H(1 - \eta)/\rho. \quad (6)$$

Thus the mean frequency for both cases is the quadrupole frequency and the frequency splittings Δ_X and Δ_Z between the 'inner pair' may be combined to determine the asymmetry parameter from the result

$$\frac{\Delta_X}{\Delta_Z} = \frac{1 - \eta}{\rho}. \quad (7)$$

It should be noted that this result does not require a knowledge of the magnetic field provided it is small.

To obtain more accurate values of energy levels and frequencies we can solve the problem exactly. The Hamiltonian (1) in the representation that diagonalized I_z is given by the following matrix

$$\mathcal{H} = \frac{h\nu_H}{2} \begin{pmatrix} 3 \cos \theta + y\eta/\sqrt{3}y & \sqrt{3} \sin \theta e^{+i\phi} & 0 \\ \eta/\sqrt{3}y & -\cos \theta - y & 2 \sin \theta e^{-i\phi} & \sqrt{3} \sin \theta e^{+i\phi} \\ \sqrt{3} \sin \theta e^{-i\phi} & 2 \sin \theta e^{+i\phi} \cos \theta - y & \eta/\sqrt{3}y & \\ 0 & \sqrt{3} \sin \theta e^{-i\phi} & \eta/\sqrt{3}y & -3 \cos \theta + y \end{pmatrix} \quad (8)$$

where $y = \nu_H/\nu_Q^0$. In some cases, in particular $\theta = \phi = 0$ ($H_0 \parallel Z$) and $\theta = 90^\circ$, $\phi = 0$ ($H_0 \parallel X$) the matrix is exactly soluble in closed form, but in all cases may be diagonalized by computer.

EXPERIMENTAL DETAILS

The experiments were performed with a modified Pound-Knight spectrometer in magnetic fields produced by a rotateable

Varian electromagnet. The specimens were single crystals of gallium grown from high purity 79 grade gallium supplied by Eagle Picher Industries Ltd. Cylindrical crystals of approximately $\frac{3}{8}$ in. dia. by $\frac{3}{4}$ in. length were prepared by touching supercooled liquid gallium contained in a teflon mould with a seed crystal of the desired orientation. X-ray back reflection Laue photographs enabled an unambiguous determination of the crystal orientation [15] and the crystal was mounted in a coil of the spectrometer so that the magnetic field could be rotated in a plane containing two crystallographic axes. The coil was of No. 40 wire separated from the crystal surface by a layer of 0.0005 in. thick Mylar. This configuration was such that the oscillator could be made marginal at all temperatures. The applied magnetic field of 300 G was measured with a proton n.m.r. probe and a lower field of 60 G also used was determined by comparing the results with those obtained at the higher field. The experiments were carried out at the three temperatures 4.2°, 77° and 285°K. The former two

temperatures were obtained with liquid helium and liquid nitrogen respectively whereas the latter was obtained with a water bath whose temperature was regulated to better than 0.1°K in view of the rapid variation of the pure quadrupole resonance frequency with temperature close to the melting point of gallium. The magnetic field was modulated and the resonance signals observed with phase sensitive detection.

RESULTS

Figure 3 shows the observed ^{69}Ga resonance signals at the three temperatures. The signal shapes reveal a mixture of absorption and dispersion modes brought about by the phase shifts involved in the penetration of the radio frequency field into the bulk metal and they are also slightly distorted by the modulation amplitude used.

The resonance frequencies of the important lines for a rotation of the magnetic field in a plane perpendicular to the B crystallographic axis are shown in Fig. 4 and it is immediately seen from the occurrence of two sets of

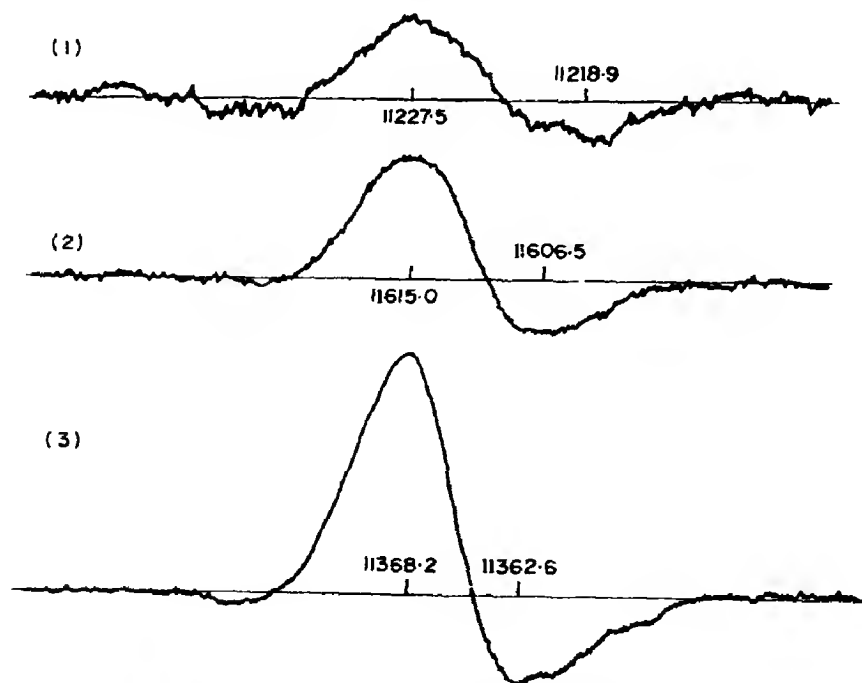


Fig. 3. ^{69}Ga resonance signals at (1) 285°K (2) 77°K and (3) 4.2°K. The numbers specify the frequency scale in kc/s.

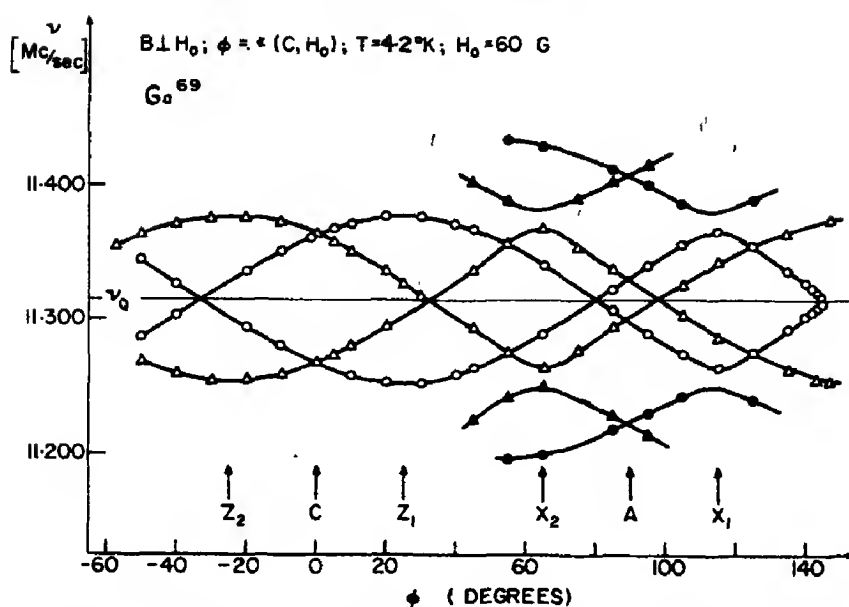


Fig. 4. ^{69}Ga spectrum as a function of orientation of the magnetic field H_0 in the AC crystal plane.

resonances that two physically non-equivalent sites exist in the crystal. Since the two sets of lines only differ in relative orientation it follows that the EFG tensors differ only in the orientation of their principal axes and have the same coupling constants and asymmetry parameters. The form of the orientation dependence together with considerations of crystal symmetry indicates the positions of the Z and X axes of the two EFG tensors shown in the figure. The positions of the two Z axes were determined more precisely in the following manner.

A calculation shows that the resonance frequency corresponding to the $(\frac{1}{2} \rightarrow -\frac{1}{2})$ transition for the case of the magnetic field parallel to the Z principal axis is given by the following expression which omits only a negligibly small term in η^4 .

$$\nu = \nu_H \left[1 - \frac{\eta^2}{3} \left(\frac{1}{1 - 4(\nu_H/\nu_Q^0)^2} \right) \right] \quad (9)$$

where $2\pi\nu_H = \gamma H_0(1 + K)$ and K is the Knight shift. A misalignment of the magnetic

field by a small angle θ from the Z axis causes a deviation J in the resonance frequency which is given by the following expression obtained by a perturbation calculation

$$\delta = \frac{3}{2} \frac{\nu_H}{1 - (\nu_H/\nu_Q^0)^2} \theta^2 \quad (10)$$

where θ is measured in radians. It is obvious from the expression that δ is highly sensitive to misalignment when ν_H is close to ν_Q , but can be made comparatively insensitive by a suitable choice of ν_H/ν_Q^0 . In principle, with the reasonable assumption that K is field independent, two sets of measurements at different magnetic fields would suffice to determine both K and the misalignment. Fortunately gallium has two isotopes with rather different quadrupole moments so that with the assumption that K is not isotopically sensitive it is possible to avoid extensively retuning the spectrometer and yet observe the ^{69}Ga and ^{71}Ga resonances under quite different conditions of equation (9). The angular variations are shown in Fig. 5 and are again displayed in Fig. 6 as a function of θ^2 . In practice the

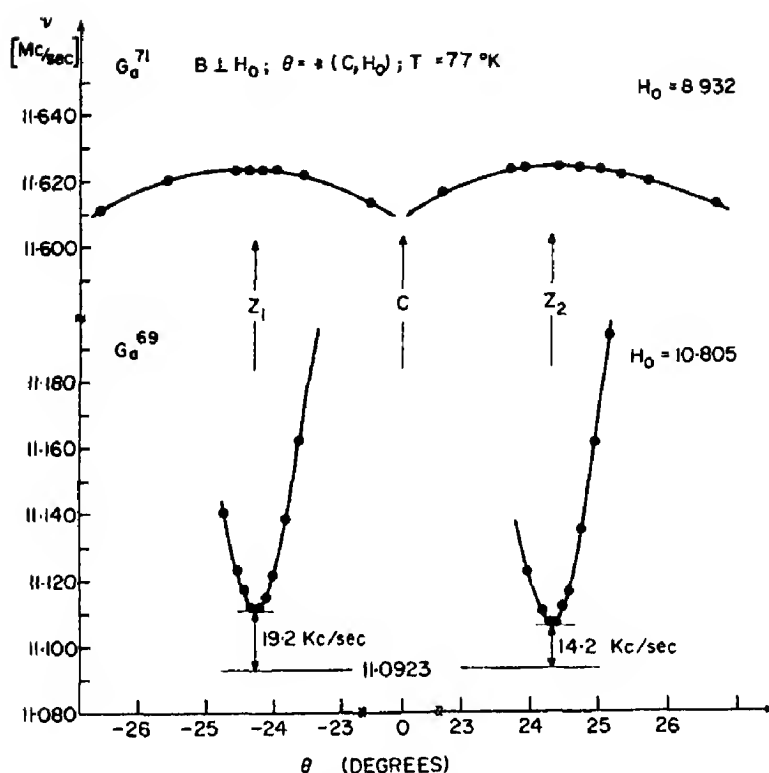


Fig. 5 High field angular dependence of ($\frac{1}{2} \rightarrow -\frac{1}{2}$) transition frequency close to the Z principal axes. The field strength H_0 is quoted in kg

Knight shift is initially determined from the slowly varying results on ^{71}Ga and is then used to predict the angular variation for ^{69}Ga . Because of the very rapid angular variation in the case of ^{69}Ga , first order perturbation theory is inadequate and an exact calculation is necessary. The misalignment determined is then used to correct the ^{71}Ga Knight shift and the procedure repeated for self-consistent results. In the results shown, a misalignment of 0.2° is observed but in the whole set of measurements the misalignment was never observed to exceed 3.5° . The values of K have been published in a preliminary note [19]. The results show that both Z principal axes lie in the AC plane of the crystal and enable a highly accurate determination of their relative orientation. It should be noted that the crystal has reflection symmetry in the AC plane which requires that the B axis of the crystal to be one of the principal axes and that

the other two axes lie in the AC plane. As is seen from the results the X and Z axes lie in the AC plane and the B axis is coincident with the Y principal axis for both crystal sites. This was checked experimentally by studying a crystal rotation in the AB plane. In this case the patterns from both sites are observed to coincide and the 'inner pair' splitting along the B axis is equal to that along the Z axes. Even though the magnetic field used was small, its influence on the determination of η from equation (7) was not entirely negligible and this is illustrated by the results and theoretical variation shown in Fig. 7. The fact that this correction was considered at all indicates the high precision of the results. The accuracy in the determination of η using equation (7) is governed by the measurement of the splittings Δ_X and Δ_Z which is unaffected by the distortions in the line shape due to modulation or the effect of

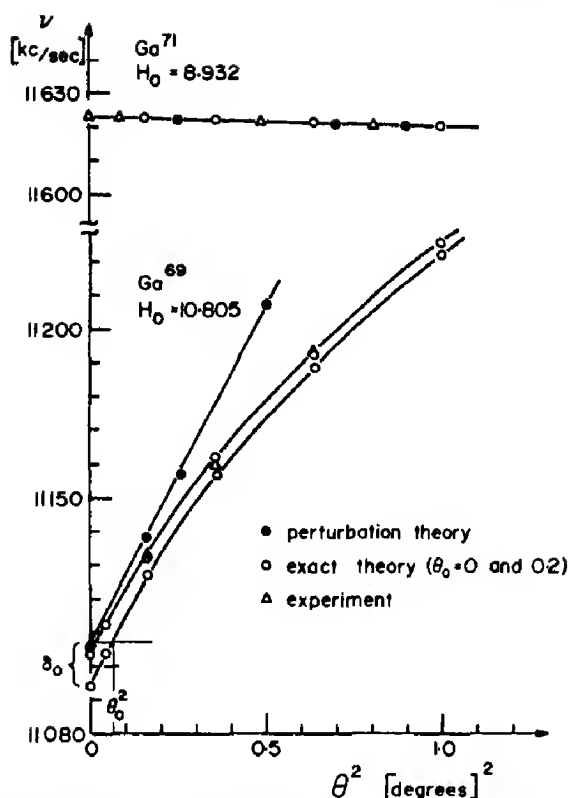


Fig. 6. Angular dependence of ($\frac{1}{2} \rightarrow -\frac{1}{2}$) transition frequency as a function of the square of the misalignment between the magnetic field and the Z principal axis.

the skin depth in mixing the modes. It is merely necessary to measure between any two equivalent points on the resonance lines. However the determination of the pure quadrupole frequency does require a line shape analysis to determine the true resonance frequency. The line was found to be well represented by a Gaussian absorption mode and the resonance frequency was determined by fitting the results to a modulation broadened superposition of dispersion and absorption modes. Figure 8 shows a comparison between the observed resonance at 77°K and the theoretical Gaussian line shape for an equal mixture of modulation broadened absorption and dispersion modes. The line shape at 4.2°K revealed a higher proportion of dispersion mode in contradiction to the predictions of Allen and Seymour[18]. This however merely reflects the fact that the anomalous skin effect theory is only strictly valid in zero magnetic field and we may infer from our result that the imaginary part of the surface impedance is dominant at this field strength. It is also possible for the line to be

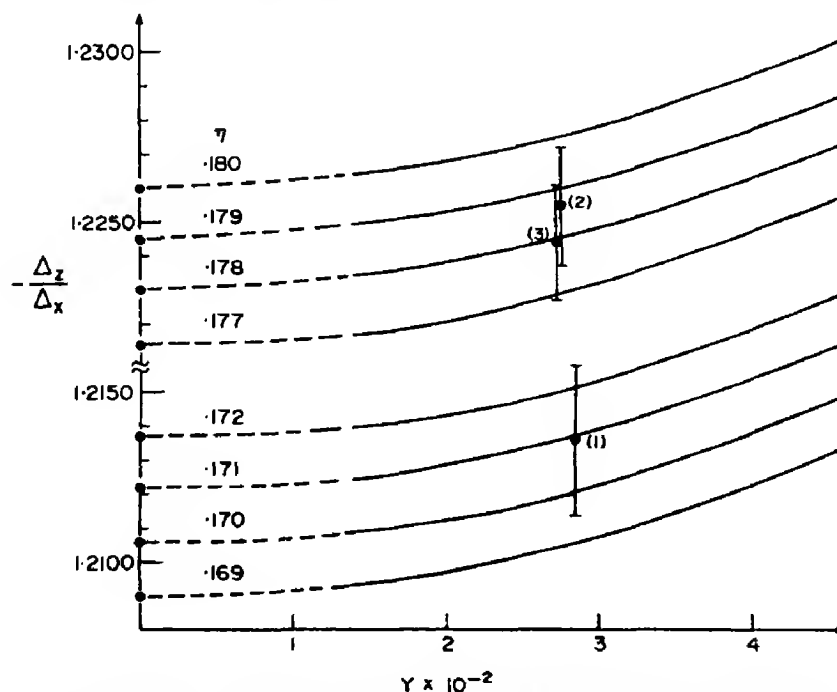


Fig. 7. Effect of the magnetic field on the determination of η . The experimental points correspond to the temperatures (1) 285°, (2) 77° and 4.2°K.

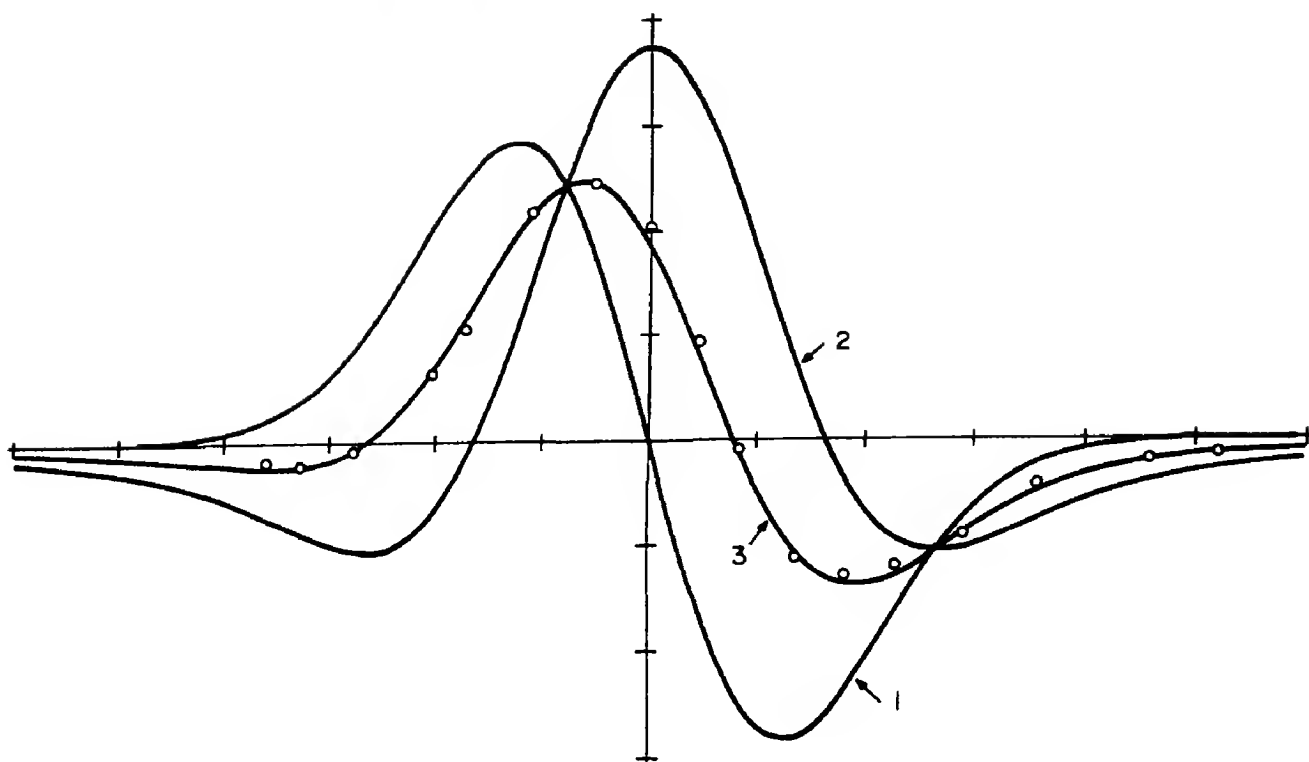


Fig. 8. Comparison between a theoretical Gaussian line shape and the experimental line at 77°K. 1. Absorption mode. 2. Dispersion mode. 3. Equal mixture. The points are taken from the experimental line.

influenced by saturation effects but the spin lattice relaxation time for gallium is probably sufficiently short that this may be disregarded.

The values of the parameters determining the EFG are tabulated in Table 2 and the orientation of the two sets of principal axes is shown in Fig. 9.

DISCUSSION

The EFG tensor in a metal at a particular nuclear site has been considered to arise from three sources[21], the first denoted by $Zq_{latt.}$ from the nuclear and electronic charges ex-

ternal to an atomic sphere around the nucleus in question (where Z is the normal valence of gallium) and second $q_{loc.}$ from the conduction electrons within the atomic sphere, and finally the third which results from the distortion of closed shell electrons at the atomic site may be accounted for in terms of Sternheimer antishielding factors γ_∞ and R_q so that the total EFG tensor q_{tot} is given by

$$q_{tot} = (1 - \gamma_\infty)Zq_{latt.} + (1 - R_q)q_{loc.} \quad (4.1)$$

We have evaluated $q_{latt.}$ for gallium in the

Table 2. Electric field gradient tensor results

Temperature (°K)	ν_Q^{89} (kc/sec)	η	2γ (deg)	c/a
4.2	11312.2 ± 0.4	0.179 ± 0.001	48.7 ± 0.2	1.6903
78	11253.2 ± 0.4	0.179 ± 0.001	48.6 ± 0.2	1.691
285.3	10877.2 ± 0.5	0.171 ± 0.002	48.2 ± 0.2	1.6955

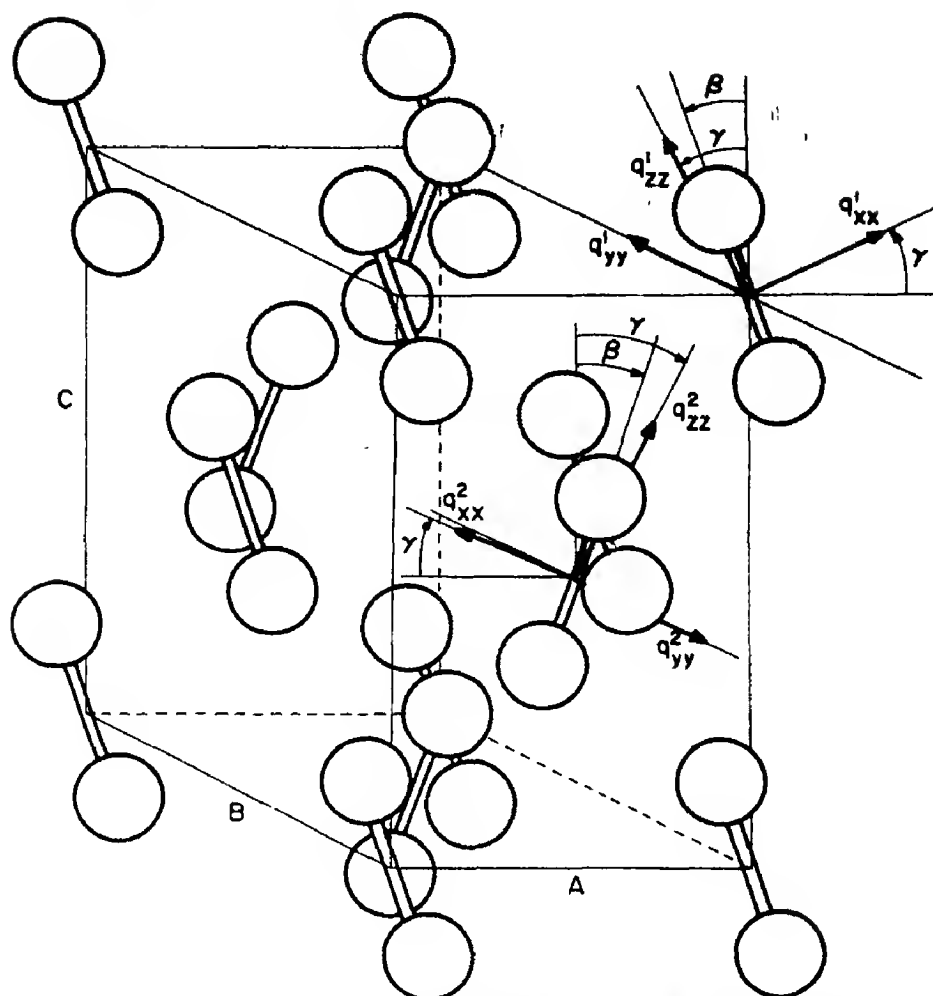


Fig. 9. Orientation of principal axes with respect to the crystal structure of gallium.

approximation of a uniform distribution of conduction electrons by direct machine summation of the expression

$$(\mathbf{q}_{\text{latt.}})_{ij} = \sum_{m=1}^8 \sum_{l_1, l_2, l_3=-N}^{+N} \times \frac{3x_m^i(l_1 l_2 l_3) x_m^j(l_1 l_2 l_3) - \delta_{ij} r_m^2(l_1 l_2 l_3)}{r_m^5(l_1 l_2 l_3)} \quad (12)$$

where the summation over m includes the eight atoms in the unit cell designated by (l_1, l_2, l_3) and the second summation includes all the atoms lying within a spherical volume of radius R which is a multiple of the shortest lattice parameter at a given temperature. The

atom at the origin is excluded from the summation. Indices i and j stand for any of three symbols A, B, C and $(\mathbf{q}_{\text{latt.}})_{ij}$ is the (ij) component of the $\mathbf{q}_{\text{latt.}}$ in the crystallographic coordinate system. From the calculations it follows that $(\mathbf{q}_{\text{latt.}})_{AB} = (\mathbf{q}_{\text{latt.}})_{CB} = 0$ and therefore the B crystallographic axis is one of the principal axes, which of course also follows from the symmetry of the unit cell. Instead of tabulating the calculated components $(\mathbf{q}_{\text{latt.}})_{AA}, (\mathbf{q}_{\text{latt.}})_{BB}, (\mathbf{q}_{\text{latt.}})_{CC}$ and $(\mathbf{q}_{\text{latt.}})_{AC}$ we present in Table 3 $\mathbf{q}_{\text{latt.}}$ in diagonalized form already.

N is the total number of contributing atoms inside the sphere of radius R in units of B . The lattice parameters used for this calcula-

Table 3. Ionic contribution to the EFG tensor as a function of number of atoms considered

R	N	$(q_{\text{latt.}})_{xx}$	$(q_{\text{latt.}})_{yy}$	$(q_{\text{latt.}})_{zz}$	$\beta_{\text{latt.}}$	$\eta_{\text{latt.}}$
3	532	-0.02147	-0.00329	0.02476	31.7	-0.734
15	66105	-0.02087	-0.00378	0.02464	30.0	-0.694
25	306450	-0.02094	-0.00374	0.02468	30.0	-0.697

tion are those from Table 4 at 4.2°K. The principal components of $q_{\text{latt.}}$ are all in the units of 10^{24} cm^{-3} . $\beta_{\text{latt.}}$ is the angle in degrees between the Z principal axis of $q_{\text{latt.}}$ and the C crystallographic axis. $\eta_{\text{latt.}}$ is its asymmetry parameter.

Table 4. Lattice parameters of gallium

T (°K)	A (Å)	B (Å)	C (Å)
4.2	4.5156	4.4904	7.6328
78	4.516	4.493	7.636
285.3	4.5195	4.5242	7.6618

Since the convergence of the sums is quite fast (in contrast to the case of indium, etc.), alternative methods for calculating $q_{\text{latt.}}$ have not been considered. In order to see to what extent our ionic model describes the crystal-line field gradient in gallium we compare in Table 5 the experimentally determined parameters characterizing the EFG at 4.2°K with those calculated assuming an antishielding factor of -9.50 for free ^{69}Ga ions 17 and $Z = 3$, from the relation.

$$v_Q = e^2 Q (1 - \gamma_\infty) Z (q_{\text{latt.}})_{zz} (1 - \frac{1}{3} \eta_{\text{latt.}}^2)^{1/2} / 2h. \quad (13)$$

In particular one should note that the X axis is parallel to the B axis in the ionic model rather than the Y axis in the experimental case which we have indicated by assigning a negative sign to it.

The most obvious feature of the experimental results is the very small temperature varia-

Table 5. Comparison of ionic calculation and experimental results for the EFG tensor

EFG	v_Q (Mc/sec)	$\beta_{\text{latt.}}$	$\eta_{\text{latt.}}$
Experiment	11.31	24.3	-0.179
Ionic	2.82	30.0	-0.697

tion of both the asymmetry parameter and the orientation of the principal axes. The quadrupole frequency exhibits the temperature variation shown in Fig. 10 and the results may be combined with the asymmetry parameter to give the changes in all EFG components between 285.3° and 4.2°K. We have calculated the temperature dependence of $q_{\text{latt.}}$ using the temperature dependent values of the lattice parameters from Table 4 and assuming the parameters u and v to be the same for all

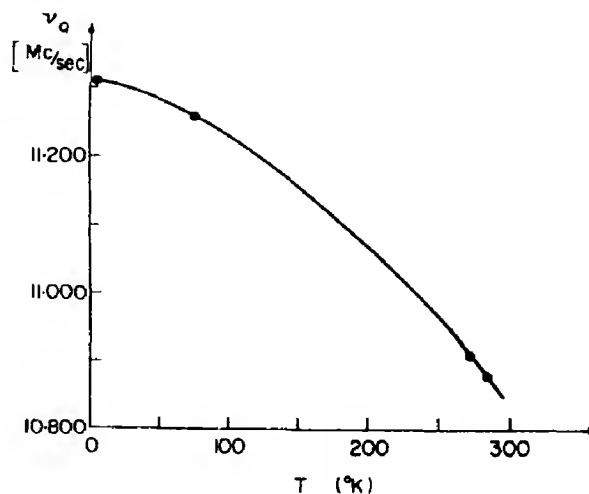


Fig. 10. The temperature dependence of the ^{69}Ga NQR frequency. The solid line represents the results of Pomerantz [4]; the experimental points are from the present work.

temperatures. Results for $R = 22$ are included in the Table 6. All the parameters remain practically constant over the whole temperature range so that thermal expansion alone does not explain the small changes observed. However the explicit temperature dependence of the quadrupolar interaction which arises from the influence of the lattice vibrations is generally the dominant effect[20] and it is possible that this could account for the whole temperature variation.

$q_{\text{exp.}}$ and obtain an alternative solution for $q_{\text{diff.}}$ with an angle $\beta_{\text{diff.}}$ of 31.6° and $\eta = 0.03$ and also sensibly temperature independent. However, in view of the close correlation between the angles mentioned above it is likely that our first value is the correct one.

In conclusion, our results suggest that the dominant contribution to the gradient is $q_{\text{loc.}}$. Watson, Gossard and Yafet[21] estimate that the main contribution to $q_{\text{loc.}}$ results from the interaction between the ionic and the

Table 6. Temperature variation of the ionic contribution to the EFG tensor

T (°K)	$(q_{\text{latt}})_{xx}$	$(q_{\text{latt}})_{zz}$	$(q_{\text{latt}})_{yy}$	$\beta_{\text{latt.}}$	$\eta_{\text{latt.}}$	ν_{qlatt} (Mc/sec)
4.2	-0.02090	-0.00373	0.02463	30.0	-0.697	2.77
78	-0.02086	-0.00377	0.02462	30.0	-0.694	2.77
285.3	-0.02063	-0.00453	0.02516	30.0	-0.640	2.80

We may now proceed in the spirit of the assumed model and determine the difference tensor

$$q_{\text{diff.}} = (1 - R_\varphi) q_{\text{loc.}} = q_{\text{exp.}} - (1 - \gamma_\infty) Z q_{\text{latt.}} \quad (14)$$

and the results are given in Table 7. It is very interesting to note that the angle $\beta_{\text{diff.}}$ is almost equal to the angle $\beta_{\text{pair.}}$ between the nearest neighbour direction and the C axis which is 15.9° . The temperature variation of $\beta_{\text{pair.}}$ is not available in the present literature and it would be of interest to see if its temperature variation is the same as $\beta_{\text{diff.}}$.

Since we can only determine the absolute value of $q_{\text{exp.}}$, we can reverse the sign of

Table 7. Temperature variation of $q_{\text{diff.}}$

T (°K)	$(q_{\text{diff.}})_{xx}$	$(q_{\text{diff.}})_{yy}$	$(q_{\text{diff.}})_{zz}$	$\beta_{\text{diff.}}$	$\eta_{\text{diff.}}$
4.2	1.210	2.123	-3.333	15.7	0.274
78	1.205	2.113	-3.318	15.6	0.274
285.3	1.115	2.059	-3.228	15.0	0.276

electron states at the Fermi Surface, but in view of the small temperature variation in contrast to the large variation of the Knight shift and the spin lattice relaxation time, and also the very small difference between normal and superconducting states, this seems unlikely. The close correlation between $\beta_{\text{diff.}}$ and $\beta_{\text{pair.}}$ is suggestive of a strong interaction in the direction of the nearest neighbour, and $\beta_{\text{pair.}}$ is suggestive of a strong interaction in the direction of the nearest neighbour, possibly an indication of covalency. In this connection it would be valuable to have more information on the temperature variation of $\beta_{\text{pair.}}$. Clearly a detailed theoretical treatment is required together with a measurement of the Knight shift tensor to provide additional information on the Fermi Surface states. The large difference between the Knight shift in solid and liquid gallium[19] is certainly indicative of a large p -electron contribution. Measurements on the Knight shift are presently in progress and preliminary measurement indicate a large anisotropy. We hope to further discuss these points in a subsequent paper when measurements are complete.

Acknowledgements—We wish to acknowledge our debt to Dr. E. P. Jones who first suggested the study of gallium to one of us (D.L.W) in 1964. At that time Dr. Jones had already made a preliminary observation of the spectrum at 4.2°K in one crystal plane, but was unable to complete his work in the time available. We are also grateful to Dr. S. N. Sharma for his assistance with the spectrometer and one of us (M.V.) is indebted to the University of British Columbia for a University Studentship and to the National Research Council of Canada for the subsequent award of an NRC Studentship.

REFERENCES

1. JONES E. P. and LLEWELYN WILLIAMS D., *Phys. Lett.* **1**, 109 (1962).
2. KISER S. R., Thesis. University of California, Berkeley (1965-unpublished).
3. KNIGHT W. D., HEWITT R. R., and POMERANTZ M., *Phys. Rev.* **104**, 271 (1956).
4. POMERANTZ M., Thesis. University of California, Berkeley (1955-unpublished).
5. KISER S. R. and KNIGHT W. D., *Am. Phys. Soc. Bull.* **7**, 613 (1962).
6. HAMMOND R. H. and KNIGHT W. D., *Phys. Rev.* **120**, 762 (1960).
7. KUSHIDA T. and BENEDEK G. B., *Am. Phys. Soc. Bull.* 167 (1958).
8. HAMMOND R. H., WILKNER E. G. and KELLY, G. M., *Phys. Rev.* **143**, 275 (1966).
9. CORNELL D. A., *Phys. Rev.* **153**, 208 (1967).
10. VALIČ M. I. and LLEWELYN WILLIAMS D., In preparation.
11. BARRETT C. S., *Advances in X-ray Analysis*, Vol. 5, p. 33 (1961).
12. BRADLEY A. J., *Z. Kristall.* **91A**, 302 (1935).
13. ABRAGAM A., *Principles of Nuclear Magnetism*, Chap. VII. Oxford University Press, Oxford (1961).
14. DAS T. P. and HAHN E. L., *Solid State Physics*, Suppl. 1, Chap. I. Academic Press, New York (1969).
15. DEAN C., *Phys. Rev.* **96**, 1053 (1954).
16. YAQUB M. and COCHRAN J. F., *Phys. Rev.* **137**, A1182 (1965).
17. CHAPMAN A. C., RHODES P. and SEYMOUR E. F. W., *Proc. phys. Soc.* **70**, 345 (1957).
18. ALLEN P. S. and SEYMOUR E. F. W., *Proc. phys. Soc.* **82**, 174 (1963).
19. VALIČ M. I., SHARMA S. N. and LLEWELYN WILLIAMS D., *Phys. Lett.* **26A**, 528 (1968).
20. KUSHIDA T., BENEDEK G. B. and BLOEMBERGEN N., *Phys. Rev.* **104**, 1364 (1956).
21. WATSON R. A., GOSSARD A. C. and YAFET Y., *Phys. Rev.* **140**, A375 (1965).
22. STERNHEIMER R. M., *Phys. Rev.* **130**, 1423 (1963).

SIZE EFFECTS ON PLASMON-PHONON MODES IN POLAR SEMICONDUCTORS

R. RUPPIN

Israel Atomic Energy Commission, Soreq Nuclear Research Centre, Yavne, Israel*

(Received 15 April 1969)

Abstract—The coupled plasmon-optical phonon modes in a finite sample of a degenerate polar semiconductor are studied in the long wavelength limit. The novel feature resulting from the finiteness of the crystal is the existence of surface modes. The manifestation of these modes in the infrared absorption spectra of small samples is discussed. The effects of the application of a magnetic field are also investigated.

INTRODUCTION

IN DOPED polar semiconductors the LO phonons and the plasmons are coupled by the macroscopic polarization field which is associated with both types of excitations. This coupling has been treated theoretically for the case of crystals which are subject to periodic boundary conditions[1, 2]. In such crystals the only type of phonons which set up macroscopic fields are the LO phonons. By discarding the periodic boundary conditions and taking into account the finite dimensions of the crystal, it can be shown[3] that in ionic crystals there also exist surface optical phonons which are not longitudinal and which do set up macroscopic fields. Similarly, a plasma confined to a finite volume can support surface plasma oscillations which are not longitudinal and whose frequency is different from the bulk plasma frequency[4]. These surface plasmons also create macroscopic fields. In doped polar semiconductors the surface phonons are coupled to the surface plasmons.

We first derive the normal plasmon-phonon modes of a finite semiconductor. We then discuss the i.r. absorption spectra of small samples, in which surface modes play a dominant role. Finally, the effects of applying

a constant magnetic field parallel to small cylindrical samples are discussed.

PLASMON-PHONON MODES OF A FINITE CRYSTAL

The eigenmodes of the system can be derived from the following equations of motion, which apply in the long wavelength limit for a diatomic polar semiconductor containing free electrons,

$$\mu \ddot{\mathbf{u}} = -\mu \omega_T^2 \mathbf{u} + e^* \mathbf{E} \quad (1)$$

$$m^* \ddot{\mathbf{x}} = e \mathbf{E}. \quad (2)$$

Here \mathbf{u} is the relative displacement of the two ions, μ is their reduced mass and e^* their effective charge; \mathbf{x} is the electronic displacement and m^* is the electronic effective mass.

The ionic and electronic displacements are coupled through the macroscopic electric field \mathbf{E} , which can be written in terms of the polarization in the form

$$\mathbf{E}(\mathbf{r}) = \text{grad div} \int \frac{\mathbf{P}(\mathbf{r}')}{|\mathbf{r} - \mathbf{r}'|} d^3 r' \quad (3)$$

where the integration is performed over the volume of the crystal. The polarization is a sum of independent contributions from the optical phonons, the free carriers and inter-band transitions:

$$\mathbf{P} = N e^* \mathbf{u} + n e \mathbf{x} + \frac{\epsilon_\infty - 1}{4\pi} \mathbf{E} \quad (4)$$

*Present address: Department of Physics, University of North Carolina, Chapel Hill, N.C. 27514, U.S.A.

where N is the number of unit cells per unit volume and n is the free carrier concentration.

Equations (1-4) can be solved simultaneously by choosing \mathbf{P} to be an eigenfunction, with eigenvalue ν , of the integral equation (3)

$$\text{grad div} \int \frac{\mathbf{P}(\mathbf{r}')}{|\mathbf{r}-\mathbf{r}'|} d^3r' = -4\pi\nu\mathbf{P}(\mathbf{r}) \quad (5)$$

in which case the equations of motion assume the form

$$\{[1 + \nu(\epsilon_\infty - 1)](\omega_T^2 - \omega^2) + \nu\epsilon_\infty\Omega^2\}\mathbf{u} + \nu \frac{m^*e^*}{\mu e} \epsilon_\infty \omega_p^2 \mathbf{x} = 0 \quad (6)$$

$$\nu\epsilon_\infty \frac{\mu e}{m^*e^*} \Omega^2 \mathbf{u} + \{\nu\epsilon_\infty \omega_p^2 - [1 + \nu(\epsilon_\infty - 1)]\omega^2\}\mathbf{x} = 0 \quad (7)$$

where $e^{-i\omega t}$ time dependence has been assumed and where

$$\Omega^2 = \frac{4\pi N e^{*2}}{\mu \epsilon_\infty} \equiv \omega_L^2 - \omega_T^2; \omega_p^2 = \frac{4\pi n e^2}{m^* \epsilon_\infty}.$$

Equating to zero the determinant of the coefficients of \mathbf{u} and \mathbf{x} in equations (6) and (7) we obtain the equation for the frequencies

$$\{[1 + \nu(\epsilon_\infty - 1)](\omega_T^2 - \omega^2) + \nu\epsilon_\infty\Omega^2\} \times \{\nu\epsilon_\infty\omega_p^2 - [1 + \nu(\epsilon_\infty - 1)]\omega^2\} - \nu^2\epsilon_\infty^2\omega_p^2\Omega^2 = 0$$

or

$$\epsilon_\infty \left(1 - \frac{\omega_p^2}{\omega^2} + \frac{\Omega^2}{\omega_T^2 - \omega^2}\right) = \frac{\nu - 1}{\nu}. \quad (8)$$

The expression on the l.h.s. is just the frequency dependent dielectric constant of the system, so that the eigenfrequencies equation can be written in the concise form

$$\epsilon(\omega) = \frac{\nu - 1}{\nu}. \quad (9)$$

There exist three types of eigenmodes, corresponding to the three types of solutions

which the integral equation (5) is known to have[3]:

$$(a) \nu = 0, \text{div } \mathbf{P} = 0.$$

These are transverse bulk modes. From (9) we find that their frequency is ω_T , which identifies them as the pure TO phonons.

$$(b) \nu = 1, \text{curl } \mathbf{P} = 0.$$

These are longitudinal bulk modes and from (9) we see that their frequencies are the zeros of the dielectric constant and are the roots of the equation

$$\omega^4 - (\omega_p^2 + \omega_L^2)\omega^2 + \omega_T^2\omega_p^2 = 0. \quad (10)$$

These are just the coupled plasmon-phonon modes discussed by Varga[1].

$$(c) 0 < \nu < 1, \text{div } \mathbf{P} = \text{curl } \mathbf{P} = 0.$$

These are surface modes and their frequencies depend on the particular shape of the specimen. In these modes the vibration amplitudes usually decrease with increasing distance from the surface of the sample. For each eigenvalue ν in the range $0 < \nu < 1$ there exist two roots of equation (9). One of the surface mode bands lies in the range $\omega < \omega_-$ and the second one in the range $\omega_T < \omega < \omega_+$, where ω_\pm are the frequencies of the longitudinal bulk modes i.e. the roots of equation (10).

For a spherical specimen, for example, the eigenvalues of the integral equation (5), which correspond to surface modes, are given by[3]

$$\nu = \frac{l}{2l+1}; l = 1, 2, 3, \dots \quad (11)$$

In Fig. 1 the bulk modes (solid curves[5]) and the lowest ($l=1$) surface modes (broken curves) of a spherical GaAs crystal are shown for different free carrier concentrations. In this case the two surface mode bands lie within the narrow range between the broken curves and the corresponding full curves.

I.R. ABSORPTION SPECTRA

Retardation effects, which have been neglected so far, have to be included if the interaction of the crystal with electromagnetic radiation is to be discussed. The retarded eigenmodes of the system are obtained by solving the vector Helmholtz equation which both the electric and the magnetic field obey

$$\left[\Delta + \epsilon(\omega) \frac{\omega^2}{c^2} \right] \mathbf{u} = 0 \quad (12)$$

where $\epsilon(\omega)$ is given by l.h.s. of (8) inside the crystal and $\epsilon(\omega) = 1$ outside it. The eigenfrequencies are then obtained by imposing the appropriate continuity conditions at the surface of the sample. Instead of carrying out this procedure we go over directly to discuss the infrared absorption properties of small spherical samples. We apply Mie's theory [6], according to which the absorption cross section of a spherical sample of radius R (in units of the geometric cross section) is given by

$$\sigma_a = \frac{2c^2}{\omega^2 R^2} \sum_{l=1}^{\infty} (2l+1) \times (-\text{Re } a_l - |a_l|^2 - \text{Re } b_l - |b_l|^2)$$

where the Mie coefficients a_l, b_l are defined by

$$a_l = -\frac{j_l(k^i R) [k^0 R j_l(k^0 R)]' - j_l(k^0 R) [k^i R j_l(k^i R)]'}{j_l(k^i R) [k^0 R h_l(k^0 R)]' - h_l(k^0 R) [k^i R j_l(k^i R)]'}$$

$$b_l = -\frac{j_l(k^0 R) [k^i R j_l(k^i R)]' - \epsilon_j j_l(k^i R) [k^0 R j_l(k^0 R)]'}{h_l(k^0 R) [k^i R j_l(k^i R)]' - \epsilon_j j_l(k^i R) [k^0 R h_l(k^0 R)]'}$$

Here $k^0 = \omega/c$, $k^i = \sqrt{\epsilon}\omega/c$; j_l and h_l are spherical Bessel and Neumann functions respectively.

We have calculated the absorption cross section of small spheres of GaAs. A damped dielectric function was used in the calculation

$$\epsilon(\omega) = \epsilon_{\infty} + \frac{\epsilon_0 - \epsilon_{\infty}}{1 - \left(\frac{\omega}{\omega_T}\right)^2 - i\Gamma \frac{\omega}{\omega_T}} - \frac{\omega_p^2 \epsilon_{\infty}}{\omega(\omega + i/\tau)}$$

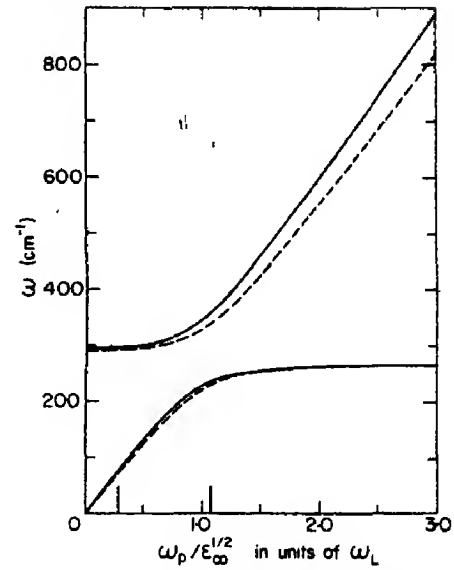


Fig. 1. Bulk and surface mode frequencies of a GaAs sphere. The vertical lines denote the ω_p values of the two samples whose absorption spectra are shown in Figs. 2 and 3.

with $\epsilon_{\infty} = 11.1$, $\epsilon_0 = 13.13$, $\omega_T = 269 \text{ cm}^{-1}$, $\Gamma = 0.007$. For the plasma frequency ω_p and the plasmon lifetime τ we have taken values given by Tell and Martin [5] for some of the samples which they have used in their Raman scattering experiments. The structure of the absorption spectra shown in Figs. 2 and 3 is in fact reminiscent of the Raman spectra which have been observed on large samples

[5, 7]. In both cases there appear three peaks, the middle one being due to the TO phonons. The other two peaks are due to the plasmon-phonon modes, bulk modes in the Raman experiment and surface modes in the absorption by small spheres. In the latter case, if the radius of the sphere is small compared with the wavelength the absorption frequencies are close to the non-retarded values obtained from (9) and (11), with $l = 1$. These

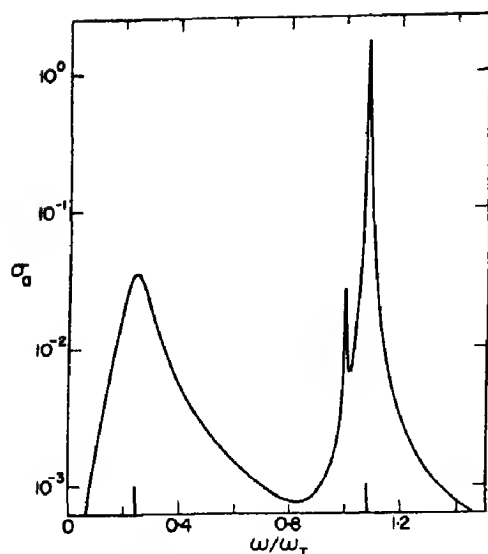


Fig. 2. Absorption cross section of a GaAs sphere of diameter 1μ ; $n = 5.1 \times 10^{16} \text{ cm}^{-3}$, $\tau = 17.7 \times 10^{-14} \text{ sec}$.

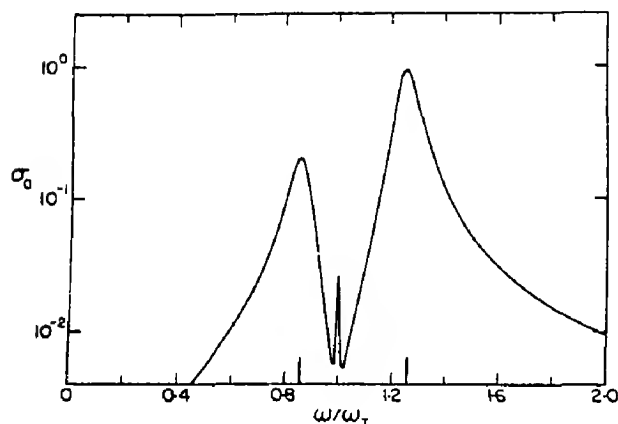


Fig. 3. Absorption cross section of a GaAs sphere of diameter 1μ ; $n = 8.6 \times 10^{17} \text{ cm}^{-3}$, $\tau = 11.4 \times 10^{-14} \text{ sec}$.

are denoted by vertical lines on the frequency axes in Figs. 2-4. The absorption frequencies of very small spheres thus follow the broken lines of Fig. 1 (whereas in the Raman experiment the solid lines are traced). Increasing the dimensions of the sample will increase the ratio to bulk to surface mode absorption. This is exemplified by Fig. 4 which is to be compared with Fig. 2.

Observation of the absorption of i.r. radiation by plasmon-phonons modes has been attempted by measuring the transmission

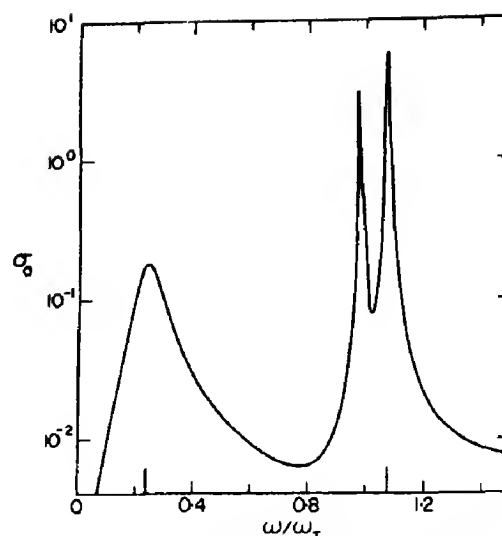


Fig. 4. Absorption cross section of a GaAs sphere of diameter 5μ ; $n = 5.1 \times 10^{16} \text{ cm}^{-3}$, $\tau = 17.7 \times 10^{-14} \text{ sec}$.

through thin slabs at oblique incidence [8]. In this experiment it was not possible to observe the low frequency phonon-plasmon bulk mode since, for the doping used, its frequency ω_- was close to ω_T and the strong absorption by the TO phonons masked the absorption at ω_- . In the measurement of absorption by fine powders this difficulty is avoided since the absorption at ω_T can be reduced considerably if small enough samples are available.

In our calculations we have taken for τ the 'bulk value' of the lifetime. This is correct only when the smallest dimension of the specimen is much greater than the electronic mean free path. Estimating the mean free path l by $v_F \tau$ where v_F is the Fermi velocity we find that l is of the order of 10^{-6} cm for the GaAs specimens discussed above. Thus l is indeed much smaller than the dimensions of the absorbing spheres, which are of the order of 10^{-4} cm .

EFFECTS OF MAGNETIC FIELD

In the presence of a magnetic field there exists a new type of collective bulk modes. These result from the coupling of the collective cyclotron excitations to the LO phonons through the macroscopic electric fields [8]. The

frequencies of the bulk modes are given by the two roots of the equation

$$\omega^4 - (\omega_p^2 + \omega_c^2 + \omega_L^2)\omega^2 + \omega_p^2\omega_T^2 + \omega_c^2\omega_L^2 = 0 \quad (13)$$

where $\omega_c = eH_0/m^*c$.

The coupled modes have been observed in the transmission spectra of thin slabs[9] (with the magnetic field in the plane of the slab).

We discuss the effects of a magnetic field on the plasmon-phonon surface modes in cylindrical samples with the magnetic field H_0 parallel to the axis of the cylinder (the z axis). The electromagnetic properties of a plasma in the magnetic field can be described by a complex, frequency dependent, tensor dielectric function[10]. By adding the scalar contribution of the optical lattice vibrations we find that the dielectric tensor ϵ of the doped semiconductor is given by

$$\epsilon_{xx} = \epsilon_{yy} = \epsilon_1, \epsilon_{zz} = \epsilon_3, \epsilon_{xy} = -\epsilon_{yx} = i\epsilon'$$

where (neglecting damping)

$$\epsilon_1 = \epsilon_\infty + \frac{\epsilon_0 - \epsilon_\infty}{1 - \omega^2/\omega_T^2} - \frac{\omega_p^2 \epsilon_\infty}{\omega^2 - \omega_c^2}$$

$$\epsilon_3 = \epsilon_\infty + \frac{\epsilon_0 - \epsilon_\infty}{1 - \omega^2/\omega_T^2} - \frac{\omega_p^2 \epsilon_\infty}{\omega^2}$$

$$\epsilon' = \frac{\omega_p^2 \omega_c \epsilon_\infty}{\omega(\omega^2 - \omega_c^2)}$$

With this dielectric constant and assuming $e^{-i\omega t}$ time dependence Maxwell's equations assume the form

$$\begin{aligned} \text{div } \mathbf{H} &= 0 \\ \text{div } \epsilon \cdot \mathbf{E} &= 0 \\ \text{curl } \mathbf{H} &= -i \frac{\omega}{c} \epsilon \cdot \mathbf{E} \\ \text{curl } \mathbf{E} &= i \frac{\omega}{c} \mathbf{H} \end{aligned} \quad (14)$$

The optical properties of the cylinder will be treated for the case of normal incidence (Voigt

geometry). Only normal modes which are independent of z will be involved. There exists two types of such normal modes[11] which can be excited independently by using beams which are polarized with the electric field either parallel or perpendicular to the axis of the cylinder: (a) modes with $\mathbf{E} \parallel z$. From (14) it is found that \mathbf{E} satisfies the following Helmholtz equation

$$\left(\Delta + \epsilon_3 \frac{\omega^2}{c^2}\right) \mathbf{E} = 0. \quad (15)$$

For these modes the medium is described by the dielectric constant $\epsilon_{||} = \epsilon_3$ which is independent of the magnetic field. This reflects the fact that for this polarization the electric field drives the electrons in the z direction i.e., parallel to the external magnetic field. (b) Modes with $\mathbf{E} \perp z$. In this case the time dependent magnetic field has only a z component, which satisfies the following Helmholtz equation

$$(\Delta + k^2) \mathbf{H} = 0 \quad (16)$$

where

$$k^2 = \frac{\omega^2}{c^2} \frac{\epsilon_1^2 - \epsilon'^2}{\epsilon_1}$$

For these modes the medium is described by the dielectric constant

$$\epsilon_{\perp} = \frac{\epsilon_1^2 - \epsilon'^2}{\epsilon_1}. \quad (17)$$

To solve the problem of absorption by cylindrical samples one has to write the external fields (the incident and the scattered waves) and the internal fields (solutions of (15) and (16)) in terms of cylindrical waves, so that the appropriate boundary conditions can be satisfied. Since for the parallel polarization no surface modes are excited[12] only the case of perpendicular polarization will be discussed. The dielectric constant ϵ_{\perp} has three resonances corresponding to bulk modes. One pole is at ω_T and the other two at

the roots of equation (13). For thin cylinders the strongest absorption peaks will lie at the frequencies of surface modes.

The absorption width (absorption cross section per unit length) of the cylinder is given by (in units of the geometric width)

$$C_a = \frac{-2}{k^0 R} \sum_{n=-\infty}^{\infty} (|b_n|^2 + \text{Re } b_n)$$

where

$$b_n = \frac{J_n(k^0 R) \Delta^n - \epsilon_{\perp}^{1/2} J_n(k^i R) J'_n(k^0 R)}{\epsilon_{\perp}^{1/2} J_n(k^i R) H'_n(k^0 R) - H_n(k^0 R) \Delta^n} \quad (18)$$

$$\Delta^n = J'_n(k^i R) + n \frac{\epsilon' J_n(k^i R)}{\epsilon_1 k^i R}$$

$$k^0 = \omega/c, \quad k^i = \sqrt{\epsilon_{\perp}} \omega/c.$$

The coefficients b_n have been derived by Platzman and Ozaki[13] (but their formula (13) seems to be misprinted). The frequencies of the surface modes can be deduced from (18) by equating to zero the denominator of this expression. For small specimens, $k^0 R \ll 1$, we find that the surface mode frequencies are given by

$$\epsilon_1(\epsilon_1 + 1) - \epsilon'(\epsilon' \mp 1) = 0 \quad (19)$$

where the upper (lower) sign corresponds to positive (negative) values of n . In the absence of a magnetic field $\epsilon' = 0$ and modes with $e^{\pm i n \phi}$ angular dependence are degenerate. The application of a magnetic field removes the degeneracy. Equation (19) has four pairs of solutions.

We have calculated the absorption by thin cylinders of InAs using the parameters given by Palik *et al.*[14] for the two samples on which they have performed bulk reflectivity measurements. (In their experiment they have observed the four reflectivity minima which appear at the frequencies at which ϵ_{\perp} is equal to one.) For the sample denoted 1-InAs: $\omega_p = 236 \text{ cm}^{-1}$, and the damping frequency of the free carriers $\gamma = 30 \text{ cm}^{-1}$. For the sample 2-InAs: $\omega_p = 90 \text{ cm}^{-1}$, $\gamma = 20 \text{ cm}^{-1}$. The other

parameters are $\omega_T = 219 \text{ cm}^{-1}$, $\omega_L = 243 \text{ cm}^{-1}$, $\epsilon_{\infty} = 11.8$ and the phonon damping frequency $\Gamma = 2 \text{ cm}^{-1}$. In Figs. 5-10 the absorption

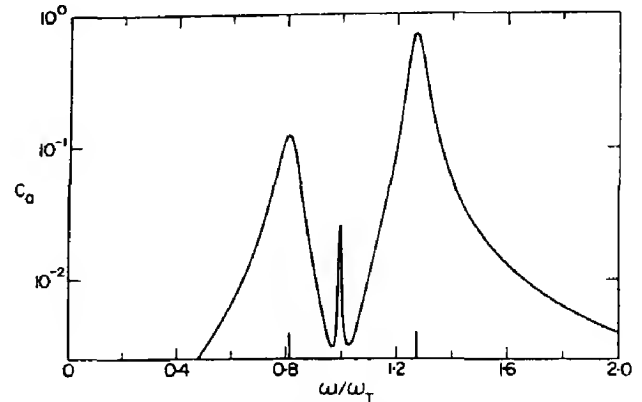


Fig. 5. Absorption width (absorption cross section per unit length) of a 1-InAs cylinder of diameter 1μ ; $\omega_c = 0$.

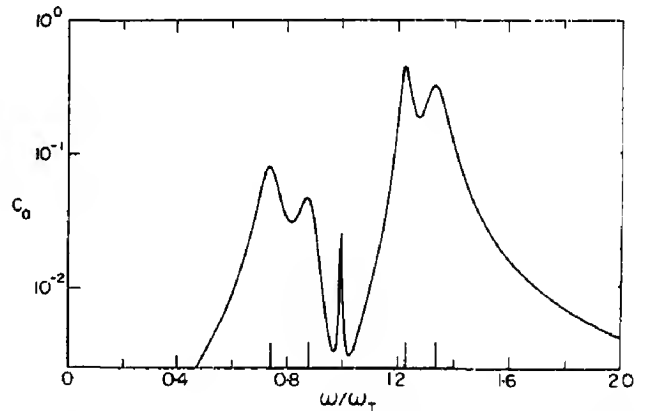


Fig. 6. Absorption width of a 1-InAs cylinder of diameter 1μ ; $\omega_c = 0.25 \omega_T$.

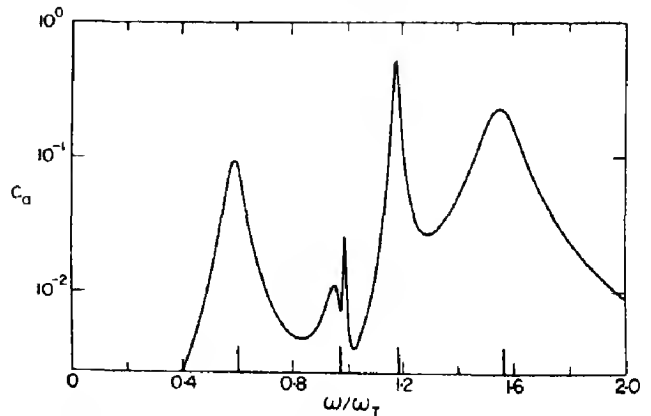


Fig. 7. Absorption width of a 1-InAs cylinder of diameter 1μ ; $\omega_c = 0.75 \omega_T$.

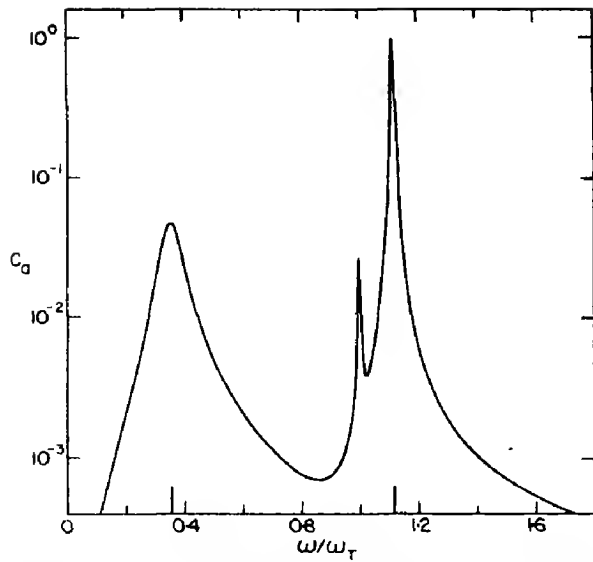


Fig. 8. Absorption width of a 2-InAs cylinder of diameter 1μ ; $\omega_c = 0$.

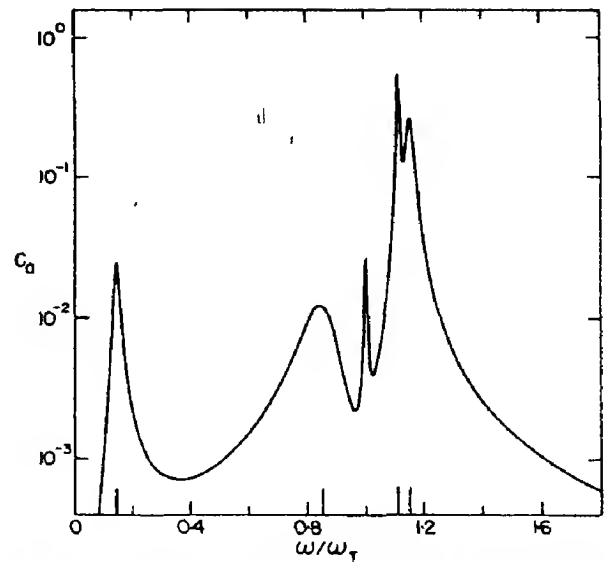


Fig. 10. Absorption width of a 2-InAs cylinder of diameter 1μ ; $\omega_c = 0.75 \omega_T$.

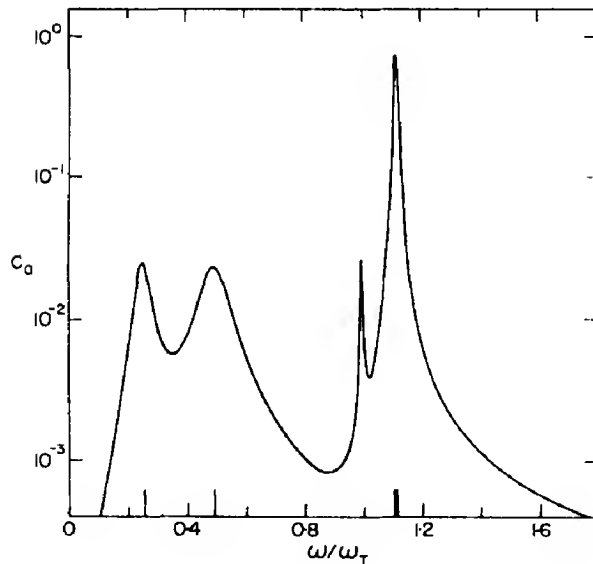


Fig. 9. Absorption width of a 2-InAs cylinder of diameter 1μ ; $\omega_c = 0.25 \omega_T$.

widths of cylinders of diameter 1μ in different magnetic fields are shown. The frequencies of the surface modes which cause the peaks in absorption are denoted by vertical lines on the frequency axis.

In zero magnetic field there appear three peaks, one at ω_T and the others at surface mode frequencies. In this case the spectrum

is very similar in structure to that of small spheres (Figs. 2-4). For a cylinder however, the surface mode absorption peaks are given by the equation $\epsilon(\omega) = -1$ whereas for a sphere the corresponding equation is $\epsilon(\omega) = -2$ [3]. The application of a magnetic field splits the surface mode absorption peaks. Since the magnetic field influences only the plasmon component of the mixed plasmon-phonon modes it is expected that the splitting will be larger for modes which are predominantly plasmon in character. Varga[1] has defined the phonon strength of plasmon-phonon bulk modes. Burstein *et al.*[15] have added an analogous definition of the plasmon strength. For 1-InAs, for which ω_p lies between ω_T and ω_L , both the high and the low frequency modes have comparable plasmon and phonon components. The plasmon strengths are $S(\omega_-) = 0.70$, $S(\omega_+) = 0.38$. The splitting of the corresponding high and low surface modes is indeed of the same order of magnitude (Figs. 6, 7). For 2-InAs ω_p is much lower than ω_T so that the low (high) frequency mode is mainly plasmon (phonon) in character. In terms of the plasmon strengths we have $S(\omega_-) = 1.09$, $S(\omega_+) = 0.01$. The splitting of the low frequency surface mode is

much larger than that of the high frequency one (Figs. 9, 10).

The effect of increasing the dimensions of the sample is demonstrated in Fig. 11, in which the absorption width of a 1-InAs cylinder of diameter 5μ is shown. Significant bulk mode absorption now appears (the peaks denoted B). The bulk mode frequencies (which are the poles of ϵ_{\perp}) are denoted by the two higher vertical lines on the frequency axis.

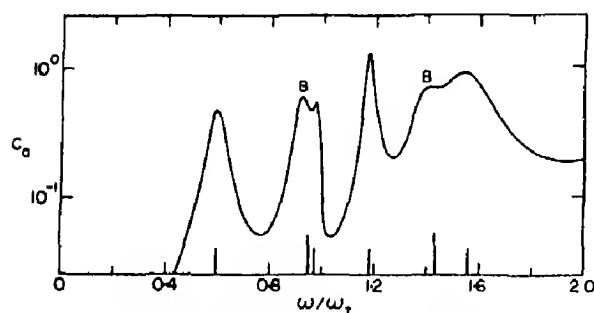


Fig. 11. Absorption width of a 1-InAs cylinder of diameter 5μ ; $\omega_r = 0.75\omega_T$.

CONCLUSION

Three types of normal modes were shown to exist in the finite plasmon-optical system. Transverse bulk modes of frequency ω_T ; longitudinal bulk modes (which result from the coupling of the LO phonons and the longitudinal bulk plasmons) and non longitudinal plasmon-phonon surface modes. The surface modes usually decay with increasing distance from the surface but, due to the existence of the long range Coulomb interaction, this decay is rather slow.

The i.r. spectra of small doped semiconductor samples were calculated. It was shown

that for small enough specimens the strongest absorption peaks occur at surface mode frequencies, whereas the absorption at ω_T is suppressed. This fact might prove useful for direct optical measurement of plasmon-phonon modes.

The application of a magnetic field parallel to small cylindrical samples was shown to cause a splitting of the surface mode absorption peaks. The splitting is most prominent for modes which have a high plasmon strength.

Acknowledgement—The author wishes to thank Professor R. Englman for criticism, suggestions and helpful discussions.

REFERENCES

1. VARGA B. B., *Phys. Rev.* **137A**, 1896 (1965).
2. SINGWI K. S. and TOSI M. P., *Phys. Rev.* **147**, 658 (1966).
3. ENGLMAN R. and RUPPIN R., *J. Phys. C., Proc. Phys. Soc.* **1**, 614 (1968).
4. RITCHIE R. H., *Phys. Rev.* **106**, 874 (1957).
5. TELL B. and MARTIN R. J., *Phys. Rev.* **167**, 381 (1968).
6. MIE G., *Annln Phys.* **25**, 377 (1908).
7. MOORADIAN A. and WRIGHT G. B., *Phys. Rev. Lett.* **16**, 999 (1966).
8. IWASA S., SAWADA Y., BURSTEIN E. and PALIK E. D., *J. phys. Soc. Japan, Suppl.* **21**, 742 (1966).
9. KAPLAN R., PALIK E. D., WALLIS R. F., IWASA S., BURSTEIN E. and SAWADA Y., *Phys. Rev. Lett.* **18**, 159 (1967).
10. GINZBURG V. L., *The Propagation of Electromagnetic Waves in Plasmas*. Pergamon Press, Oxford (1964).
11. EPSTEIN P. S., *Rev. mod. Phys.* **28**, 3 (1956).
12. ENGLMAN R. and RUPPIN R., *J. Phys. C., Proc. Phys. Soc.* **1**, 1515 (1968).
13. PLATZMAN P. M. and OZAKI H. T., *J. appl. Phys.* **31**, 1597 (1960).
14. PALIK E. D., HENVIS B. W. and STEVENSON J. R., *Solid State Commun.* **6**, 721 (1968).
15. BURSTEIN E., PINCZUK A. and IWASA S., *Phys. Rev.* **157**, 611 (1967).

INTERACTIONS BETWEEN OCTAHEDRALLY CO-ORDINATED E_g JAHN-TELLER IONS

PAVEL NOVÁK

Institute of Solid State Physics, Czechoslovak Academy of Sciences, Prague, Czechoslovakia

(Received 8 July 1968; in revised form 31 March 1969)

Abstract—A study is made of the interaction between octahedrally co-ordinated E_g Jahn–Teller ions. Simple expression of the interaction energy allows the analysis of the configurations of the isolated pair of Jahn–Teller ions. The method is illustrated by the numerical calculations for the host crystals of the rocksalt structure. The study is based on the assumption of the strong Jahn–Teller effect. The vibronic coupling between degenerate orbital and only one vibrational mode is considered.

1. INTRODUCTION

IF THE orbital level of the transition metal impurity in a given crystal lattice is degenerate some important phenomena, which are usually called the Jahn–Teller effect, can appear. Jahn–Teller effect can be explained as a consequence of the interaction between the electrons of the transition metal ion and the motion of the nuclei. As a base for study of the Jahn–Teller effect the model which takes into account only the nearest neighbours of the ion [1–3] has been frequently used. However since we are mainly interested in the interactions between Jahn–Teller ions, it is necessary to take into account the role of the whole crystal explicitly.

We shall limit ourselves to the study of statics of the Jahn–Teller effect. This restriction considerably simplifies the theory, but at the same time it requires the existence of the strong Jahn–Teller coupling (splitting of the orbital level much greater than zero point energy of the nuclear motion). It is believed, that strong Jahn–Teller coupling exists at least in some of the systems containing octahedrally co-ordinated E_g ions [4–6] and on such systems we shall focus our attention. The assumption of the strong Jahn–Teller coupling is not sufficient, as in this case Jahn–Teller effect can have not only static, but also a dynamic character [7]. We must therefore assume a stabilization of the particular configuration by either interaction between Jahn–Teller ions, or the intrinsic

stabilization of Jahn–Teller effect (static effect).

In the present paper the Jahn–Teller ion will be treated, using the methods of the theory of point defects. In part 2 the displacement field due to one Jahn–Teller ion in an infinite crystal lattice is studied. Simple formalism for the interaction energy of a pair of the Jahn–Teller ions will be developed in part 3. We shall then illustrate general results of parts 2 and 3 by a numerical calculation assuming the host crystal of the rocksalt structure (part 4). Finally in part 5 the lowest energy configurations of the isolated pair of Jahn–Teller ions will be determined.

Using the theory of pair interactions, an interesting consequence can be deduced for the cooperative Jahn–Teller effect. Owing to the complexity of the cooperative effect, another paper will be devoted to this problem.

2. DISPLACEMENT FIELD

Let us consider a transition metal ion placed in an infinite crystal on the lattice site with the symmetry O_h . As mentioned above we shall deal with the ions, which have doubly degenerated E_g orbital state in this symmetry.

The part of the energy of the system, which depends on displacement of ions from their positions in the undistorted crystal, can be expressed in the form (kinetic energy of nuclear motion is neglected):

$$W = V(\xi, \xi') + \Psi(\xi). \quad (1)$$

In this expression ξ is the vector of displacements (α -th component of the displacement of m -th ion in the l -th elementary cell will be denoted $\xi_{\alpha}^{(l)}(m)$), $V(\xi, \xi')$ includes the interactions between displaced ions, $\Psi(\xi)$ is that part of the potential energy of the Jahn-Teller ion, which arises as a consequence of the vibronic interactions.

$V(\xi, \xi')$ can be expressed in harmonic approximation, as the quadratic form:

$$V(\xi, \xi') = \frac{1}{2} \bar{\xi} v \xi \quad (2)$$

where v is the matrix with the elements

$$v_{\alpha\beta}^{(l, l')}(m, m') = \frac{\partial^2 V}{\partial \xi_{\alpha}^{(l)}(m) \partial \xi_{\beta}^{(l')}(m')}.$$

If only the linear coupling between E_g orbital and e_g vibrational mode of the octahedron is considered [1], the potential $\Psi(\xi)$ can be expressed in the form:

$$\Psi(\xi) = -\frac{1}{2} \alpha \sqrt{Q_2^2 + Q_3^2} \quad (3)$$

Q_2, Q_3 are the normal coordinates of the octahedron, which form the base of e_g representation of symmetry group O_h :

$$\begin{aligned} Q_2 &= \frac{1}{2} [\xi_x(1, 0, 0) - \xi_x(-1, 0, 0) \\ &\quad - \xi_y(0, 1, 0) + \xi_y(0, -1, 0)] \\ Q_3 &= \frac{1}{2\sqrt{3}} [2\xi_z(0, 0, 1) - 2\xi_z(0, 0, -1) \\ &\quad - \xi_x(1, 0, 0) + \xi_x(-1, 0, 0) - \xi_y(0, 1, 0) \\ &\quad + \xi_y(0, -1, 0)] \end{aligned} \quad (4)$$

where ions $(\pm 1, 0, 0)$; $(0, \pm 1, 0)$; $(0, 0, \pm 1)$ lie in the vertexes of the octahedron, in the centre of which the Jahn-Teller ion is placed. It is convenient to introduce polar coordinates in the Q_2, Q_3 space:

$$q = \sqrt{Q_2^2 + Q_3^2} \operatorname{tg} \Phi = \frac{Q_2}{Q_3} \quad (5)$$

The first problem which is to be solved, is the determination of the equilibrium deformation of the crystal, in which the Jahn-Teller ion is placed. It will be assumed, that the configuration of the octahedron of Jahn-Teller ion is specified by an arbitrary, but fixed angle ϕ .

The equilibrium equation $\partial W / \partial \xi = 0$ can be expressed with respect to (1) and (2) in the form:

$$\bar{\xi} v + \frac{\partial \Psi}{\partial \xi} = 0. \quad (6)$$

It is to be noted that the energy of system (and not the free energy) is minimized. The results therefore holds only for $T \rightarrow 0^\circ \text{K}$.

Expression (6) can be rewritten if the form (3) for potential Ψ is taken into account:

$$\bar{\xi} v - \frac{1}{2} \left(\cos \phi \cdot \frac{\partial Q_3}{\partial \xi} + \sin \phi \cdot \frac{\partial Q_2}{\partial \xi} \right) = 0.$$

As the angle ϕ is fixed, this equation is linear and the solution ξ_ϕ can therefore be expressed as a linear combination:

$$\xi_\phi = \xi^{(3)} \cdot \cos \phi + \xi^{(2)} \cdot \sin \phi. \quad (7)$$

$\xi^{(3)}$ resp. $\xi^{(2)}$ are the displacement fields corresponding to the configuration of the Jahn-Teller ion's octahedron, having Q_2 resp. Q_3 equal to zero. Moreover the displacement fields $\xi^{(2)}, \xi^{(3)}$ are not independent. From the symmetry of normal coordinates Q_2, Q_3 follows, that the substitution $\phi \rightarrow \phi + 2\pi/3$ interchanges only the coordinate axes ($x \rightarrow z, y \rightarrow x, z \rightarrow y$). Using expression (7), the following relation can be deduced:

$$\xi^{(3)}(z, x, y) = -\frac{1}{2} \xi^{(3)}(x, y, z) + \frac{\sqrt{3}}{2} \xi^{(2)}(x, y, z)$$

It is therefore sufficient to determine only the displacement field $\xi^{(3)}$.

As follows from (1) and (6), the change of the equilibrium energy of the crystal is

determined by the relation:

$$W(\xi_\phi) = \Psi(\xi_\phi) - \frac{1}{2} \xi_\phi \frac{\partial \Psi}{\partial \xi} \Big|_{\xi=\xi_\phi}. \quad (8)$$

It can be verified, by substitution of (3) and (7) in (8), that this energy does not depend on the angle ϕ . There is, analogously as in the case of the molecule XY_6 [1], a continuous series of nuclear configurations, which have the same energy (all these configurations have the same 'absolute value' of the deformation q). The nonlinearity of vibronic coupling [2] and (or) the anharmonicity of crystal lattice [3] will break this energy equivalence.

The dependence of the potential on the angle ϕ (corresponding term will be called anisotropy energy) can then be represented by the expression:

$$\epsilon_a = \frac{1}{2} K \cdot \cos 3\phi. \quad (9)$$

The anisotropy energy arises as a consequence of the higher order terms; therefore it will be assumed, that this energy is much smaller than the linear Jahn-Teller stabilization energy:

$$\epsilon_0 = -\frac{1}{2} \alpha q_0. \quad (10)$$

As follows from expression (9) anisotropy energy stabilizes three configurations having $\phi = k\pi/3$ ($k = 0; 2; 4$ if $K < 0$; $k = 1; 3; 5$ if $K > 0$). These configurations correspond to tetragonal compression or elongation of the octahedron of Jahn-Teller ion. It is believed, that if K is sufficiently large, the Jahn-Teller effect is static, which means that the system may be assumed frozen in one of the three potential energy minima.

3. INTERACTION POTENTIALS

If the two defects a and b are located in a crystal, their interaction energy can be defined as a difference:

$$\epsilon_i = W(\xi_e) - [W(\xi_a^0) + W(\xi_b^0)].$$

ξ_e is the equilibrium displacement field,

if both defects are placed in the lattice, $\xi_a^0(\xi_b^0)$ is the displacement field if only defect $a(b)$ is present. $W(\xi_e)$, $W(\xi_a^0)$, $W(\xi_b^0)$ are corresponding changes (1) in the energy of the crystal.

If it is supposed, that the displacement fields due to the defects a, b are independent (i.e. the relation $\xi_e = \xi_a^0 + \xi_b^0$ holds), then the interaction energy can be written in a simple form [8]

$$\epsilon_i = \frac{1}{2} \left(\frac{\partial \Psi_a}{\partial \xi} \Big|_{\xi=\xi_a^0} \cdot \xi_b^0 + \frac{\partial \Psi_b}{\partial \xi} \Big|_{\xi=\xi_b^0} \cdot \xi_a^0 \right). \quad (11)$$

Let us suppose, that the configuration of the octahedron of Jahn-Teller ion $a(b)$ is specified by an arbitrary, but fixed angle $\phi_a(\phi_b)$. With respect to the form (4) of the potential Ψ , the interaction energy (11) takes the form:

$$\epsilon_i = -\frac{1}{4} \alpha (Q_3^{ab} \cdot \cos \phi_a + Q_2^{ab} \cdot \sin \phi_a + Q_3^{ba} \cdot \cos \phi_b + Q_2^{ba} \cdot \sin \phi_b) \quad (13)$$

where Q_3^{ab} is the change of the normal coordinate Q_3 of the octahedron of ion a , which is caused by the displacement field of the ion b . Analogously are defined Q_2^{ab} , Q_2^{ba} and Q_3^{ba} . Expression (13) can be further rearranged, if the relation (7) for the displacement fields is used:

$$\epsilon_i = \sum_{\sigma\sigma'=2,3} J_{\sigma\sigma'}^{ab} S_\sigma^a S_{\sigma'}^b, \quad (14)$$

where $S_2^c = \sin \phi_c$, $S_3^c = \cos \phi_c$, $c = a, b$ and

$$J_{\sigma\sigma'}^{ab} = -\frac{1}{4} \alpha [Q_\sigma^{ab}(\sigma') + Q_{\sigma'}^{ba}(\sigma)], \sigma, \sigma' = 2, 3. \quad (15)$$

$Q_\sigma^{ab}(\sigma')$ is equal to Q_σ^{ab} if configuration of the octahedron of ion b is specified by angle $\phi_b = 0$ ($\sigma' = 3$) or $\phi_b = \pi/2$ ($\sigma' = 2$).

From the equivalence of the ions a, b follows, that the tensor $J_{\sigma\sigma'}^{ab}$ is symmetrical, and hence the three quantities J_{22}^{ab} , J_{33}^{ab} , J_{23}^{ab} are sufficient for the determination of the interaction energy.

We shall now analyse two mutual configura-

tions of the pair of Jahn-Teller ions (it is supposed, that ion a is placed in the origin).

Configuration $A(l)$ —ion b is placed in the lattice site with the radius vector $\mathbf{R}_b = R_0(l, l, 0)$; R_0 being the shortest cation-anion distance. In the rocksalt structure $l = 1$ corresponds to a, b being nearest neighbours in cations sublattice.

Configuration $B(l)$ —ion b in lattice site with $\mathbf{R}_b = R_0(0, 0, 2l)$. For $l = 1$ ions a, b are next nearest neighbours in the cation sublattice of the rocksalt structure. From symmetry of the displacement field it follows, that for both cases $J_{23}^{ab} = 0$. Notation $J_{22}^{ab} = J_2(l)$, $J_{33}^{ab} = J_3(l)$ will be used in the following analysis. For $l = 1$, it is not difficult to estimate the signs of the quantities $J_2(1)$, $J_3(1)$. The Jahn-Teller forces due to ion a and expected direction and magnitude of that part of the displacement field ξ_a^0 , which is necessary for the determination of $J_2(1)$ and $J_3(1)$ are shown in Fig. 1. From this figure, using the definition of the normal coordinate (4) and expression (15), following inequalities can be deduced:

$$\begin{aligned} J_2^A(1) < 0; J_3^A(1) < 0 \\ J_2^B(1) < 0; J_3^B(1) > 0 \\ |J_2^B(1)| \ll |J_3^B(1)|. \end{aligned} \quad (16)$$

The last inequality follows from the fact, that only $J_3^B(1)$ contains the big displacement of the nearest neighbour of the Jahn-Teller ion.

The inequalities (16) will be verified in

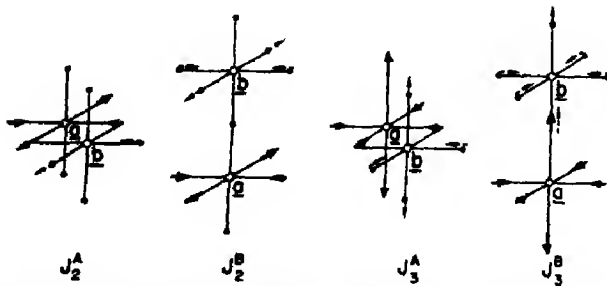


Fig. 1. The forces due to Jahn-Teller ion (full arrows) and the expected direction and magnitude of the part of the displacement field (dotted arrows).

the next section for a special structure of the host crystal.

4. JAHN-TELLER IONS IN A CRYSTAL WITH THE ROCKSALT STRUCTURE

The general theory will be in this section illustrated assuming the host crystal of the rocksalt structure. It is necessary first to specify the interaction $V(\xi, \xi')$ acting between the displaced ions. For simplicity it will be assumed, that the interaction between the two ions having the radius vectors $\mathbf{R}^{(l)}_m$, $\mathbf{R}^{(l')}_m$ and charges η_m , $\eta_{m'}$ can be written in the form:

$$v = -\frac{\eta_m \eta_{m'}}{|\mathbf{R}^{(l)}_m - \mathbf{R}^{(l')}_m|} + B \cdot e^{-|\mathbf{R}^{(l)}_m - \mathbf{R}^{(l')}_m|/\rho} \quad (17)$$

where the repulsion term is nonzero only for nearest neighbours.

It is convenient to solve the equilibrium equation for the crystal containing Jahn-Teller ion in the reciprocal space. The periodic Born conditions are introduced in the usual way, instead of one Jahn-Teller ion, it is supposed, that the superlattice of Jahn-Teller ions is placed in the crystal. Elementary translations in this superlattice are the N -multiple of the elementary translations in the original lattice.

It can be shown[9], that in the reciprocal space the equilibrium equation has the form:

$$\sum_{m'B} (\frac{mm'}{\alpha\beta}) Q_{\alpha}^m(-\mathbf{k}) = G_{\alpha}^m(\mathbf{k}) \quad (18)$$

where $Q_{\alpha}^m(\mathbf{k})$ are defined by the relation:

$$Q_{\alpha}^m(\mathbf{k}) = \sum_l \xi_{\alpha}^{(l)} e^{-2\pi i \mathbf{k} \mathbf{R}^{(l)}_m}$$

The matrix $(\frac{mm'}{\alpha\beta})$ is well known in lattice dynamics where it is called the dynamical matrix in the particular case that the mass of ions is set equal to unity.

$G_{\alpha}^m(\mathbf{k})$ is the component of the transformed force:

$$-G_{\alpha}^m(\mathbf{k}) = -\frac{1}{N^3} \sum_l \frac{\partial \Psi}{\partial \xi_{\alpha}^{(l)}_m} e^{2\pi i \mathbf{k} \mathbf{R}^{(l)}_m}$$

If $Q_\alpha^m(\mathbf{k})$ are known, the displacement field can be obtained by inverse Fourier transformation:

$$\xi_\alpha^{(l)} = \frac{1}{N^3} \sum_{\mathbf{k}} Q_\alpha^m(\mathbf{k}) e^{2\pi i \mathbf{k} \cdot \mathbf{R}^{(l)}} \quad (19)$$

Born periodic condition restrict the values of the wave vector \mathbf{k} . If \mathbf{k} is written in the form: $\mathbf{k} = k_1 \mathbf{b}_1 + k_2 \mathbf{b}_2 + k_3 \mathbf{b}_3$ ($\mathbf{b}_1, \mathbf{b}_2, \mathbf{b}_3$ being the elementary translations in the reciprocal lattice) then:

$$k_\alpha = \frac{n_\alpha}{N} \quad n_\alpha = 0, 1 \dots N \quad \alpha = 1, 2, 3$$

The equilibrium system (18) must therefore be solved for N^3 values of vector \mathbf{k} . This number can be however greatly reduced if the symmetry of the normal coordinates $Q_\alpha^m(\mathbf{k})$ is employed.

As shown in part 2 it is sufficient to determine the displacement field $\xi^{(3)}$ ($\phi = 0$). Assuming for the potential Ψ the form (3), transformed force G may be in this case expressed as follows:

$$\begin{aligned} G_x^{(1)} &= G_y^{(1)} = G_z^{(1)} = 0; \\ G_x^{(2)} &= A \cdot \sin(2\pi R_0 k_x); \\ G_y^{(2)} &= A \cdot \sin(2\pi R_0 k_y); \\ G_z^{(2)} &= -2A \sin(2\pi R_0 k_z). \end{aligned}$$

Where $A = i\alpha/N^3$; R_0 is the shortest cation-anion distance, $m = 1$ ($m = 2$) corresponds to the cation (anion) sublattice.

The repulsive part of the dynamical matrix can be easily determined using the form (17) for interaction between ions in crystal. For determination of the coulomb part of this matrix Ewald method can be used [10].

The problem, which includes the determination of the elements of the dynamical matrix, elements of transformed force, solution of equilibrium equation (18) and the determination of displacement field by summing (19), was solved numerically, using the Minsk 22 computer. In addition to the multiplicative factor, the results depend on the parameter $\kappa = R_0/\rho$ (ρ is the parameter in the repulsive

part of potential (17)) and on the size of the cell in the superlattice of Jahn-Teller ions, that means on N . With increasing N , the displacements of ions near to Jahn-Teller ion converge to their limits, which correspond to the displacements in an infinite crystal containing one Jahn-Teller ion. This convergence is fairly rapid (Fig. 2). In all following calculations values of N is taken so high, that the results are on this value practically independent.

The dependence of some components of the displacement field on the parameter κ is revealed by Fig. 3. It can be shown [14], that the singularity, which the displacement field exhibits for $\kappa \sim 5$ is connected with the zeros of the determinant of the dynamical matrix; therefore the singularity is connected with the choice of the form (18) of the potential acting between the ions in crystal.

The relation (15) was used for the determination of the quantities J_2, J_3 . The depen-

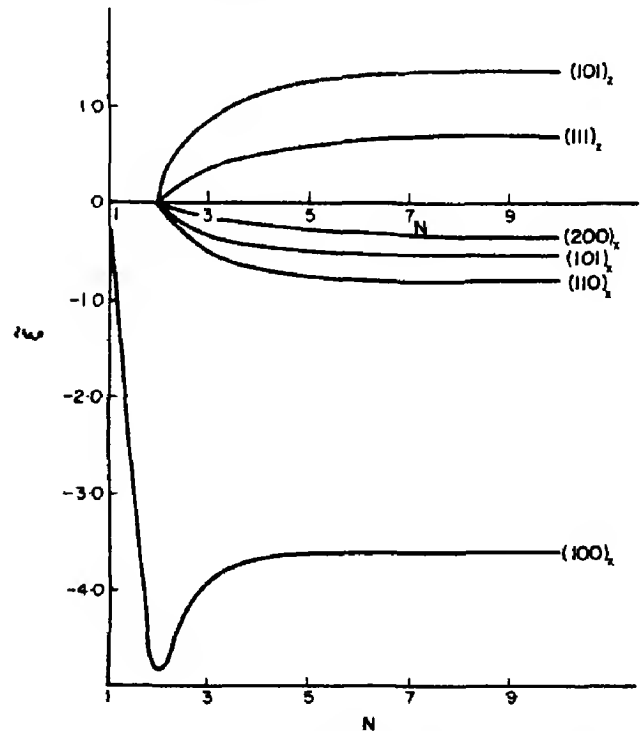


Fig. 2. Typical example of the convergence of the displacement field as a function of N . (Parameter $\kappa = 6$).

ξ is connected with ξ by the relation $\xi = \frac{R_0^3 \alpha}{\sqrt{3} \eta^3} \xi$.

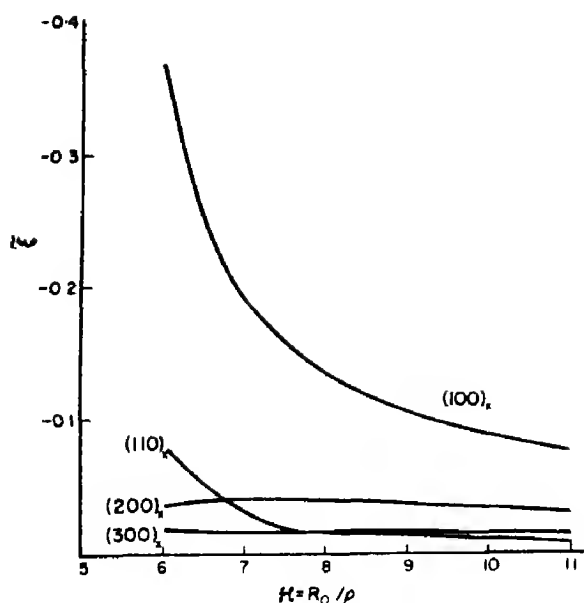


Fig. 3. Dependence of the displacement field on the parameter κ .

dence of the ratio $J_2(1)/|\epsilon_0|$, $J_3(1)/|\epsilon_0|$ (ϵ_0 being the linear Jahn-Teller stabilization energy (10)) on the parameter κ (Fig. 4) confirms the validity of the inequalities (16). To have an idea about the magnitude of the

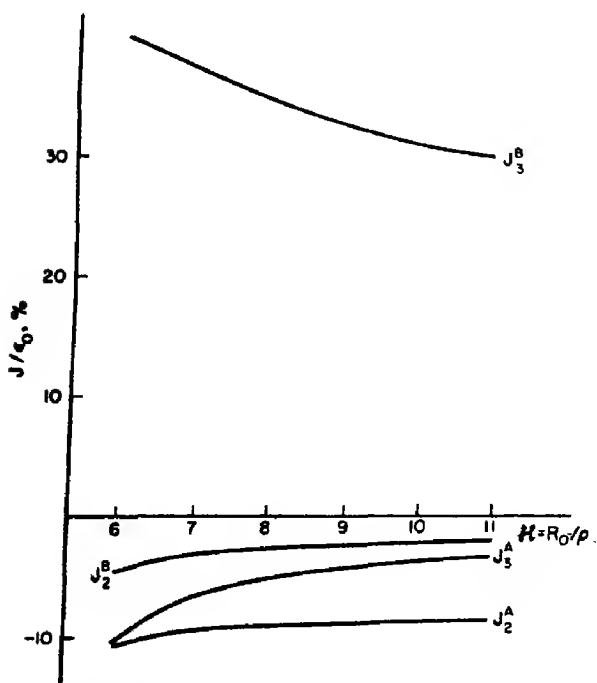


Fig. 4. Quantities J_2 , J_3 for $A(1)$ and $B(1)$ configurations.

displacement field and the interaction energy the system $\text{CaO}:\text{Cu}$ was considered. Stabilization Jahn-Teller energy ϵ^0 was, for this case determined by Höchli *et al.* [11] to be roughly 10^3 cm^{-1} . Values of the parameters ρ , R_0 were taken to be $\rho = 0.4 \text{ \AA}$; $R_0 = 2.4 \text{ \AA}$ [12]. Using Figs. 3, 4 following results were obtained:

$$\begin{aligned} |\xi_x(100)| &= 0.06 \text{ \AA} \\ J_2^A(1) &\approx J_3^A(1) = -100 \text{ cm}^{-1}; \\ J_2^B(1) &= -45 \text{ cm}^{-1}; J_3^B(1) = 400 \text{ cm}^{-1}. \end{aligned}$$

5. LOWEST ENERGY CONFIGURATIONS OF THE PAIR OF JAHN-TELLER IONS

Inequalities (16), which we expect to be valid independently on the structure of the host crystal, enable us to analyse the configurations of the pairs of Jahn-Teller ions. Let us consider first the case of the strong anisotropy (anisotropy energy (9) much greater than the interaction energy). Inequivalent pair's configurations $A(1)$, $B(1)$, which give the maximum gain of the anisotropy energy are shown, together with corresponding interaction energy in Fig. 5. It is interesting to compare our results, with the assumptions, which were made by Wojtowicz [13], who has studied the cooperative Jahn-Teller effect on the base of the strong anisotropy model. Using (16) it is easy to show, that

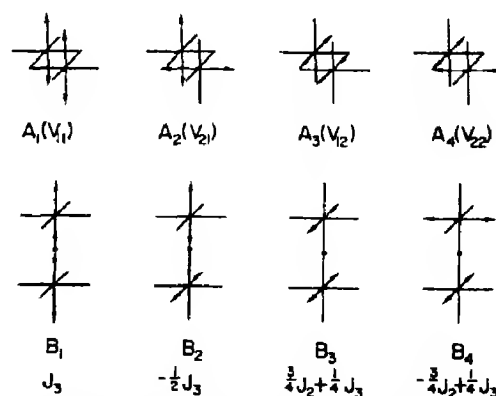


Fig. 5. Configurations, which minimise the anisotropy energy of the pair of the Jahn-Teller ions. Pair interaction energy is indicated below corresponding pictures. In brackets the Wojtowicz's notation of the interaction potentials is shown. Arrows indicate the axes of tetragonal distortions.

Wojtowicz assumption $V_{12} < V_{11} < V_{22} < V_{21}$ never holds, as for $|J_3^A(1)| > |J_2^A(1)|$ the sequence of the interaction potentials is $V_{11} < V_{12} < V_{22} < V_{21}$ while for $|J_2^A(1)| > |J_3^A(1)|$ inequality $V_{12} < V_{11} < V_{21} < V_{22}$ holds.

The lowest energy configurations of the pair may be determined, by minimizing the sum of the interaction and anisotropy energies of the pair. Configurations $A(1)$, $B(1)$ which may have lowest energy are shown in Fig. 6.

Energy of these configurations and the condition under which they will represent the ground state of the pair are summarized in Table 1.

6. CONCLUDING REMARKS

In order to keep the problem as simple as possible several quite important effects have been neglected. First only the coupling of the E_g orbital to one e_g vibrational mode was considered. This often used approximation is in our case equivalent to the assumption of the shortrange vibronic interactions (coupling of the electrons of Jahn-Teller ion with only nearest neighbours is taken into account).

Second important approximation is the neglect of the induced interaction, which represents the correction to the direct interaction energy (11). Induced interaction

Table 1. The conditions, under which configurations shown in Fig. 6 represent the ground state of the pair of Jahn-Teller ions. Corresponding energy gain is shown.

Denotation in Fig. 6	a	b	c	d	e
Represents ground state if	$ J_3^A > J_2^A $	$ J_2^A > J_3^A $ $K > \frac{1}{4} J_2^A - J_3^A $	$ J_2^A > J_3^A $ $K < \frac{1}{4} J_2^A - J_3^A $	$K < \frac{1}{2}J_3^B$	$K > \frac{1}{2}J_3^B$
Energy gain	$J_3^A - J$	$\frac{3}{4}J_2^A + \frac{1}{4}J_3^A - K$	J_2^A	$-J_3^B$	$-\frac{1}{2}J_3^B - K$

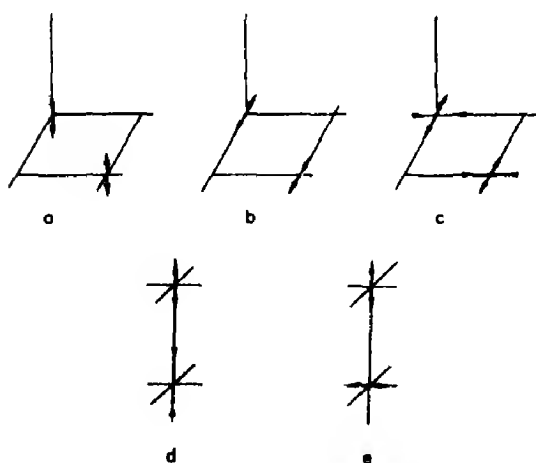


Fig. 6. Configurations, which may represent the ground state of the pair of the Jahn-Teller ions. For energy of the configurations and for the conditions, under which they represent the ground state see Table 1. Meaning of the symbols: \uparrow tetragonally elongated octahedron; \downarrow tetragonally compressed octahedron; \times rhombic deformation ($Q_3 = 0$).

may be especially important, if the concentration of the defects is high. The effect of the induced interaction will be considered in another paper in connection with the problem of the cooperative Jahn-Teller effect.

The Jahn-Teller ion located in the host crystal may evoke, in addition to the deformation having e_g symmetry, a totally symmetrical deformation (point symmetry group of the lattice site in which Jahn-Teller ion is placed is preserved). If analogously as for e_g deformation, only corresponding linear term in the potential energy of defect is considered, the superposition law holds for the displacement field:

$$\xi = \xi_0 + \xi_1$$

where ξ_0 is determined by relation (7). Totally

symmetrical component ξ_1 of the displacement field may be determined in the way analogous to the determination of the l_0 -like displacements. Also the expressions for interaction energy may be generalized to include the influence of the totally symmetrical deformation[14].

Finally it must be mentioned, that the magnetic coupling of the Jahn-Teller ions was entirely neglected.

Acknowledgements—I should like to thank Dr. S. Krupicka for suggesting the problem and for helpful discussions in the course of this work

REFERENCES

1. VAN VLECK J. H., *J. chem. Phys.* **7**, 472 (1939).
2. LIEHR A. D. and BALLHAUSEN C. J., *Ann. Phys.* **3**, 304 (1958).
3. ÖPIK U. and PRYCE M. H. L., *Proc. R. Soc.* **238A**, 425 (1957).
4. COFFMAN R. E., *J. chem. Phys.* **48**, 609 (1968).
5. LOHR L. L., *Inorg. Chem.* **6**, 1890 (1967).
6. BATES C. A. *et al.*, *J. Phys.* **1C**, 859 (1968).
7. O'BRIEN M. C. M., *Proc. R. Soc.* **281A**, 323 (1964).
8. HARDY J. R. and BULLOUGH R., *Phil. Mag.* **15**, 237 (1967).
9. KANZAKI H., *J. Phys. Chem. Solids* **2**, 24 (1957).
10. KELLERMAN E. W., *Phil. Trans.* **238A**, 513 (1940).
11. HÖCHLI U., MÜLLER K. A. and WYSLING P., *Phys. Lett.* **15**, 5 (1965).
12. HUGGINS M. L. and SAKAMOTO Y., *J. phys. Soc. Japan* **12**, 241 (1957).
13. WOJTOWICZ P. J., *Phys. Rev.* **116**, 32 (1959).
14. NOVÁK P., Thesis, Prague (1968).

THE EFFECT OF MAGNETIC AND CONFIGURATIONAL DISORDERING ON THE HIGH TEMPERATURE HEAT CAPACITY OF A Ni-50 AT. % Pd ALLOY*

R. E. BINGHAM† and C. R. BROOKS

Department of Chemical and Metallurgical Engineering, The University of Tennessee, Knoxville, Tenn. 37916, U.S.A.

(Received 6 November 1968; in revised form 24 March 1969)

Abstract—Heat capacity-temperature curves from 400° to 920°K for a Ni-50 at. % Pd solid solution alloy, measured after various heat treatments which were designed to alter the type of atom arrangements, are presented and discussed. Quite measurable deviations from a smooth reference heat capacity curve were observed. A rise in the heat capacity beginning below 400°K and terminating around 520°K is associated with ferromagnetic disordering; this part of the heat capacity curve is essentially the same for slow cooling and for quenching from 970°K. Anomalous behavior above 520°K clearly shows that nonrandom atom arrangements can be induced in the solid solution Ni-Pd alloy by heat treatment, although the exact type of ordering could not be determined.

1. INTRODUCTION

ALTHOUGH Ni and Pd are completely soluble in each other[1], the numerous physical properties which have been measured on Ni-Pd alloys[2-7] can be interpreted to indicate that the local atom configurational arrangements are non-random. Not included in these measurements is the high temperature (above 300°K) heat capacity, which for Cu-base[8] and Ni-base solid solutions[9] has been useful in interpreting configurational changes.

This paper reports measurements on the heat capacity of a Ni-50 at. % Pd alloy from 420° to 920°K for various initial heat treatments designed to vary the local atom arrangements. Measurements on this alloy are of further interest because the possibility exists that the effect of configurational arrangements on ferromagnetic disordering can be studied.

2. EXPERIMENTAL DETAILS

The heat capacity was measured by dynamic adiabatic calorimetry using the techniques described in detail elsewhere[10]. The reproducibility has been established to be about ± 0.7 per cent. The heat capacity is obtained from measurements at a constant energy input rate, which corresponds approximately to a constant heating rate. The specimen was about 2.0 cm in dia. and 7.5 cm long and weighed 287 g. It was prepared by melting 99.9 per cent pure Ni and 99.999 per cent Pd in a high-purity alumina crucible in vacuum. The specimen was homogenized for 2 weeks at 1320°K prior to measurements. Examination of the microstructure after homogenization using optical microscopy revealed no evidence of segregation or precipitation. The chemical analysis of the alloy was not obtained and the value 50 at. % Pd is based on the weighed starting materials.

3. RESULTS AND DISCUSSION

The specimen was initially heated to 920°K then cooled in vacuum at approximately 4°K/min; the resulting state will be referred

*Research sponsored by the United States Atomic Energy Commission under contract with the Department of Chemical and Metallurgical Engineering, The University of Tennessee, Knoxville, Tennessee.

†Present address: International Business Machines Corporation, Lexington, Kentucky, U.S.A.

to as the slowly cooled condition. The heat capacity obtained for this initial state is shown in Fig. 1. The peak at 448°K locates the Curie temperature and agrees closely with that given by Hansen[1]. The rise in the heat capacity between 620° and 720°K shows the existence of another energy absorbing process.

Because of the lack of data for the Ni-Pd system, equation (1) was used to calculate the reference C_p . The volume expansivity was estimated using an arithmetic average (on a volume basis) of the expansivity of non-magnetic Ni[12] and of Pd[13]. A Debye temperature of 318°K and an electronic heat

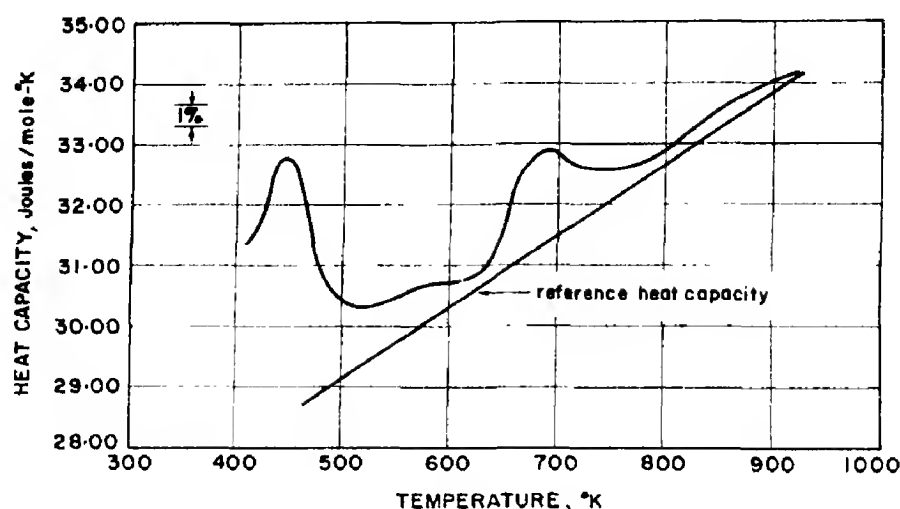


Fig. 1. The heat capacity of a Ni-50 at. % Pd alloy after slowly cooling from above 920°K. The energy input rate was 55 J/g-hr. or about 2.1°K/min at 870°K.

A proper analysis of the heat capacity results requires establishment of the heat capacity of the alloy in a non-magnetic and configurationally random state. This can be approximated by using the Debye heat capacity, characterized by a single Debye temperature, to which is added the electronic heat capacity approximated by a term linear with temperature. The sum of these two terms gives the heat capacity at constant volume, C_v , which can be converted to that at constant pressure, C_p , if the specific volume, volume expansivity, and isothermal compressibility are known at each temperature. If such data do not exist, an approximate conversion[11] is

$$C_p = C_v(1 + G\alpha T) \quad (1)$$

where α is the volume expansivity (temperature dependent), T is the absolute temperature, and G is Grueneisen's constant.

capacity coefficient of 0.0082 J/mole-°K² was obtained by interpolation from the low temperature heat capacity data of Mackliet and Schindler[14]; from these data C_v was calculated[11]. The experimental heat capacity at 920°K was then used to calculate G in equation (1); a value of 1.30 was obtained which was assumed to be constant over the entire temperature range. However, even with values of α and G , equation (1) may not represent adequately the dilation correction [11]. Also, the model for C_v is questionable as the Debye temperature and the electronic heat capacity coefficient used were obtained from low temperature measurements, and hence may be inappropriate for high temperatures. Thus it is emphasized that the calculated base heat capacity is a crude approximation; however, it does give a reference from which to interpret the results. The calculated, or reference, heat capacity is shown in Fig. 1,

and also on the subsequent graphs. It is to be noted that a Kopp-Neumann calculation (using the non-magnetic heat capacity of Ni) was not employed because of the excessively low heat capacity obtained.

As an introduction to the discussion of the results, a possible variation of the heat capacity with temperature illustrated schematically in Fig. 2 is discussed. The heat capacity of the alloy in a non-magnetic, configurationally random state (reference heat capacity) is shown overlaid separately with a heat capacity anomaly associated with ferromagnetic disordering and, at higher temperatures, an anomaly (curve A) associated with configurational randomization, which we shall refer to as configurational disordering. Consider an alloy initially in the slowly cooled condition. Upon heating, the experimental heat capacity follows the reference heat capacity until a temperature is reached at which magnetic disordering is detectable (T_d). If configurational exchanges can be suppressed, magnetic disordering is complete at temperature T_a , and the heat capacity returns to the reference curve. However, if

atom exchanges begin at temperature T_b for the fixed heating rate, then the additional heat effect reinforces that associated with the remaining magnetic disordering. The heat capacity does not return to the reference curve until about 920°K, when atom exchanges have completely randomized the alloy.

If the alloy were cooled rapidly (water quenched) from above 920°K a state approaching configurational randomness would be expected; in contrast the suppression of the ferromagnetic state may be difficult to predict. However, if ferromagnetic disordering is suppressed upon reheating, the heat capacity follows the reference curve until a temperature is reached (T_c) at which the atom exchanges begin to occur, which in this case causes a heat evolution, since the alloy is more random than for the equilibrium state; thus the heat capacity falls below the reference curve. Eventually a temperature is reached where the alloy begins to disorder, and the heat capacity rises above the reference curve. The preceding describes curve B in Fig. 2. Configurational changes occur at a lower temperature for the quenched

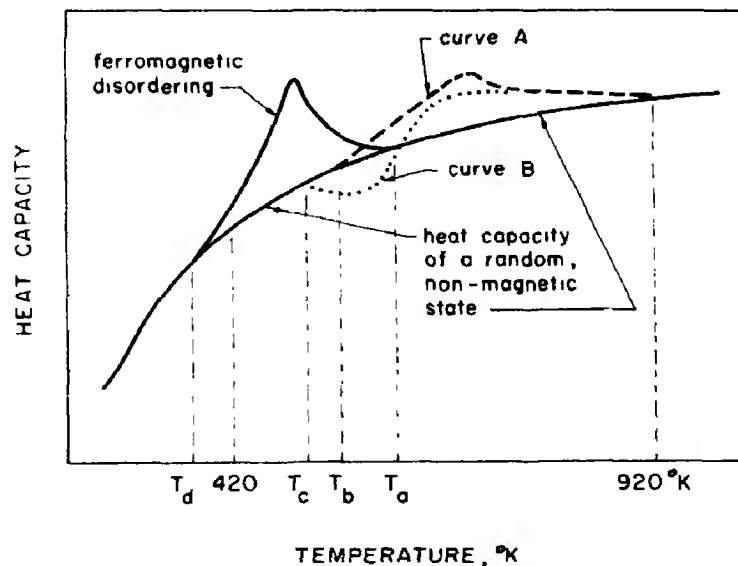


Fig. 2. Schematic representation of the effect of ferromagnetic disordering and configurational alterations on the heat capacity.

condition than for the slowly cooled condition because of the influence of quenched-in defects on the kinetics.

Nagasawa[15] has reported that a superlattice exists between 45 and 90 at. % Pd; this was based on an analysis of electron diffraction patterns from thin films. However, these results have been negated by the diffuse X-ray scattering measurements on single crystals of Ni-Pd alloys made by Spruiell and Lin[16]. Their results showed no evidence of long-range ordering, but for 50 at. % Pd alloy diffuse intensity maxima were observed, indicating the existence of some form of nonrandom local atom arrangements. Thus it is assumed that the rise in heat capacity in the range 620°–720°K for the 50 at. % Pd alloy is due to the randomization of the solid solution.

Further evidence that the heat capacity rise between 620° and 720°K is due to configurational randomization of the alloy is provided by the effect on the heat capacity of quenching into water after one hour at 920°K. The resulting heat capacity curve is shown in Fig. 3, where it is compared to the slowly cooled condition. The heat capacity

varies as described in discussing Fig. 2. The alloy first undergoes magnetic disordering, then beginning around 570°K undergoes some type of configurational ordering followed by disordering. The heat capacity associated with the magnetic disordering is almost identical for the slowly cooled and for the quenched condition.

It seems reasonable that a greater deviation from the random state over that induced by the slow cooling from above 870°K could be achieved by heat treating at sufficiently low temperatures. Thus the specimen, in the slowly cooled condition, was annealed for 7.5 hr at 620°K, and the heat capacity re-measured. The result, shown in Fig. 4, indicates that additional configurational disordering may have occurred as a consequence of the additional ordering during the low temperature heat treatment. However, the effect is very slight as the two curves lie almost within the reproducibility of the measurements.

Also, increasing the heating rate for a fixed initial condition should increase the temperature at which configurational disordering begins, whereas the kinetics of magnetic

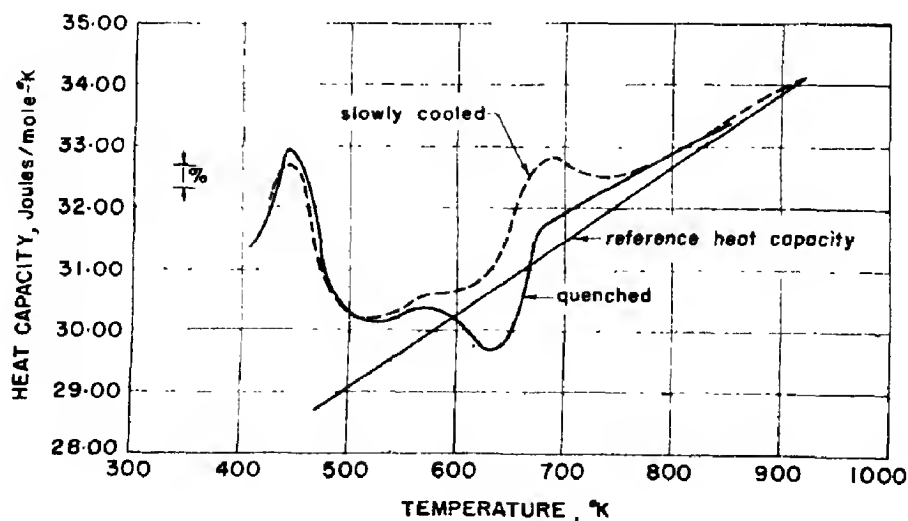


Fig. 3. The effect of water quenching from 970°K on the heat capacity of a Ni-50 at. % Pd alloy. The curve represents two sets of identical data; for one set, the energy input rate was 77 J/g-hr and for the other 73. Both correspond to about 3.1°K/min at 870°K.

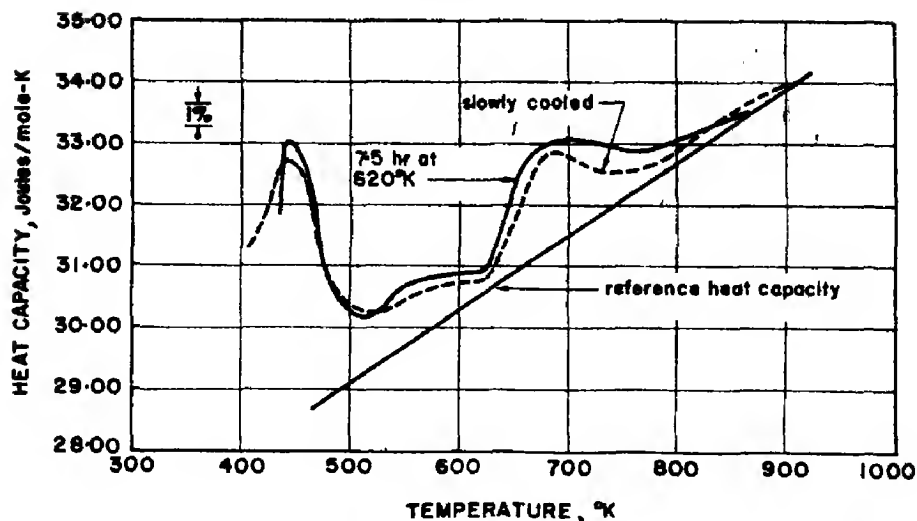


Fig. 4. The effect of annealing for 7.5 hr at 620°K after slow cooling on the heat capacity of a Ni-50 at. % Pd alloy. For this curve the energy input was 57 J/g-hr, or about 2.3°K/min at 870°K.

disordering may make that part of the heat capacity curve associated with this heat effect independent of the heating rate. Since the initial condition is identical and the final condition at 920°K (randomness) is identical for each heating rate, the heat capacity curves must shift to make the enthalpy change between 390° and 920°K the same. The effect

of heating rate on the heat capacity is shown in Fig. 5. The onset of configurational disordering shifts to higher temperature as the heating rate increases. Also, the enthalpy of disordering is identical for the various heating rates. The dependency of the heat capacity curve on the rate of heating in the region of magnetic disordering is unexpected, as

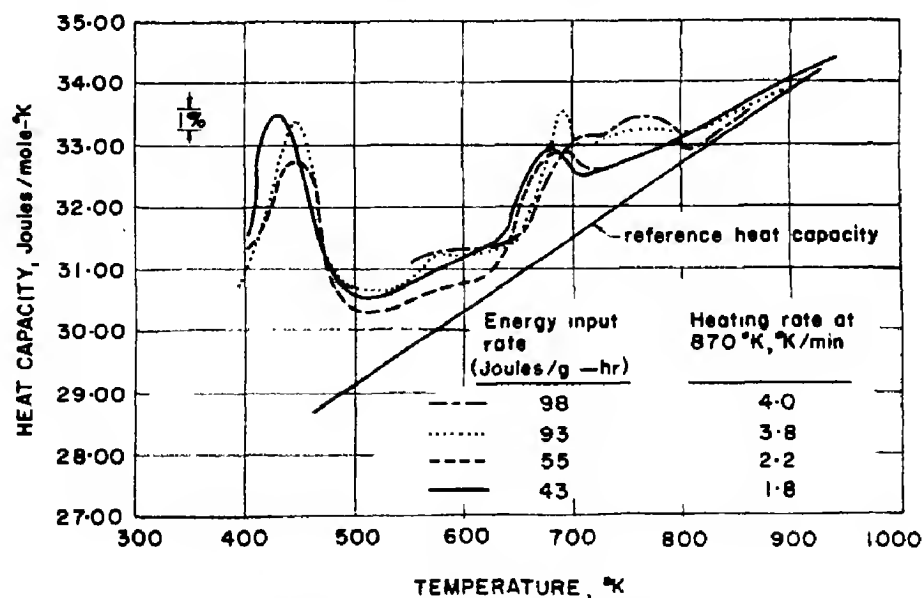


Fig. 5. Effect of heating rate on the heat capacity of a Ni-50 at. % Pd alloy initially in the slowly cooled condition.

this process should be unaffected by the heating rate. Although there are differences in the heat capacity curves in Fig. 5 between 400° and 480°K which lie outside of the reproducibility of the measurements, it is uncertain whether they are real, as the heat capacity curves during magnetic disordering for a slowly cooled and quenched condition are very similar (Fig. 3).

The unusual curvature in the heat capacity between 720° and 820°K in Fig. 5 for the higher heating rates must be associated with characteristics of the kinetics of atom exchanges involved in the disordering process.

Concerning that part of the heat capacity associated with configurational disordering, the behavior is identical to that reported for Cu-base[8] and Ni-base solid solutions[9], in which short-range ordering is involved. For the slowly cooled condition, the energy of configurational disordering in the Ni-50 at. % Pd alloy is approximately 910 J/mole. This is comparable to that obtained for binary, Ni-base, Ni-Cr and Ni-Mo alloys[9]. However, the onset of disordering in the slowly cooled condition for these alloys is about 770°K, whereas the temperature of about 620°K required for the Ni-Pd alloy shows that the atom exchanges are considerably easier in this Ni-Pd alloy.

Although the effect of heating rate (Fig. 5) and low temperature annealing (Fig. 4) on the heat capacity from 620° to 720°K is consistent with the explanation of configurational randomization, the evidence is not strong as the effects produced are slight. However, the effect of quenching on the heat capacity (Fig. 3) clearly establishes that local configurational ordering occurs in the Ni-50 at. % Pd alloy.

Comparing the heat capacity curves of the slowly cooled condition to that of the quenched condition indicates that either the temperature dependence of the absorption of heat during magnetic disordering is not sensitive to the degree or type of configurational ar-

range present, or the alloy in either of these heat treated conditions is almost random. This latter possibility is supported by Spruiell and Lin[16], who have interpreted their X-ray diffuse scattering measurements of Ni-Pd alloys to indicate that the degree of randomness is high even when heat treated at 620°K following quenching. It is also emphasized that they have not yet established the actual type of atom configurational arrangements involved.

Acknowledgements—This work was supported by the Atomic Energy Commission under Contract No. AT-(40-1)-3291. Appreciation is expressed to Professor J. E. Spruiell and Dr. W. Lin for allowing us to refer to their unpublished research, and to Professor E. E. Stansbury for reviewing the manuscript.

REFERENCES

1. HANSEN M., In *Constitution of Binary Alloys*, p. 1029. McGraw-Hill, New York (1958).
2. YAZLIEV S., *Russ. J. inorg. Chem.* **5**, 1182 (1960).
3. YAZLIEV S., *Russ. J. inorg. Chem.* **5**, 1185 (1960).
4. BIDWELL R. L. and SPEISER R., *Acta Metall.* **13**, 61 (1965).
5. SCHWERDTFEGGER K. and MUAN A., *Acta Metall.* **13**, 509 (1960).
6. SCHINDLER A. I., SMITH R. J. and SALKOVITZ E. I., *Phys. Rev.* **108**, 921 (1957).
7. ANNAEY R. G., MYALIKGULVEY G. and ORAZSAKHATOV A., *Inv. Akad. Nauk Turkm SSSR, Ser. Fiz-Hekhn., Khim. i Geol. Nauk* **6**, 19 (1963).
8. BROOKS C. R. and STANSBURY E. E., *Acta Metall.* **11**, 1303 (1963).
9. STANSBURY E. E., BROOKS C. R. and ARLEDGET L., *J. Inst. Metals* **94**, 136 (1966).
10. BROOKS C. R., NOREM W. E., HENDRIX D. H., WRIGHT J. W. and NORTHCUTT W. G., *J. Phys. Chem. Solids* **29**, 565 (1968).
11. BROOKS C. R., *J. Phys. Chem. Solids* **29**, 1377 (1968).
12. NIX F. C. and MACNAIR D., *Phys. Rev.* **60**, 597 (1941).
13. ZEMANSKY M. W., In *Heat and Thermodynamics*, 4th Edn, p. 256. McGraw-Hill, New York (1957).
14. MACKLIET C. A. and SCHINDLER A. I., *J. Phys. Chem. Solids* **24**, 1639 (1963).
15. NAGASAWA A., *J. phys. Soc. Japan* **21**, 1215 (1966).
16. SPRUIELL J. E. and LIN W., Unpublished research, University of Tennessee.

HIGH-FIELD AND QUANTUM OSCILLATORY EFFECTS IN THE MAGNETORESISTANCE OF AuSn*

D. J. SELLMYER†

Center for Materials Science and Engineering, Massachusetts Institute of Technology, Cambridge, Mass. 02139, U.S.A.

(Received 5 March 1969)

Abstract—High-field magnetoresistance measurements have been used to investigate the Fermi surface of the metallic compound AuSn. The maximum field used was 150 kG and the maximum resistance ratio of the single crystal samples was 157. The results indicate that AuSn is a compensated metal and that its Fermi surface supports open orbits along $[0001]$, $\langle 10\bar{1}0 \rangle$ and $\langle 11\bar{2}0 \rangle$ directions. Magnetoresistance oscillations periodic in inverse field were observed when the field was in the basal plane and when the current direction was not in the basal plane. Three sets of frequencies were measured in the basal plane and these agreed well with the de Haas-van Alphen results of other workers. The amplitude of the oscillations was approx. 0.1–1 per cent of the steady magnetoresistance. In the absence of a band structure calculation, the topological results are compared with a nearly-free-electron Fermi surface model in the single zone scheme. The experimental results are found to be consistent with the model and with the de Haas-van Alphen results insofar as open orbit directions are concerned. The possible influence of magnetic breakdown on the state of compensation and on the origin of the resistivity oscillations is discussed.

1. INTRODUCTION

DURING the past several years it has become increasingly clear that we are well along the way toward a quantitative theoretical understanding of the electronic structure of solids. Such calculational techniques as the augmented-plane-wave (APW), Korringa-Kohn-Rostoker (KKR), and orthogonalized-plane-wave (OPW), methods have given energy bands which are in reasonably good agreement with experiment for metals of every class in the periodic table[1]. These techniques have also been successfully applied to ionic crystals such as KCl[2].

When one considers more complicated solids, however, the level of understanding is much lower. Although several calculations have been attempted, the study of electronic energy levels in compounds is in its earliest stages. In compounds in which the binding is

neither purely ionic nor purely metallic, choosing the crystalline potential becomes quite critical and carrying the calculations to self-consistency would seem to be particularly important.

In the case of metallic compounds, there have been APW and/or KKR calculations on β' -CuZn[3, 4], β' -AgZn[5], and β' -PdIn[6], all having the simple cubic CsCl structure with two atoms per primitive cell. It has been possible to measure the de Haas-van Alphen (DHVA) effect in these alloys[7] and to measure the high-field magnetoresistance (MR) in β' -CuZn[8]. It is of considerable interest to extend the above-mentioned energy band methods to successively more complicated solids and in the case of *metallic* compounds, it is obviously desirable to have Fermi surface measurements for comparison with the theoretical calculations. The hexagonal nickel arsenide structure would appear to be a good choice for energy band calculations at the present time. There are four atoms per primitive cell in this structure but this number is within reach of the above energy band

*Research supported by the Advanced Research Projects Agency under contract SD-90.

†Visiting scientist at the Francis Bitter National Magnet Laboratory which is supported by the United States Air Force Office of Scientific Research.

methods [9]. There are many compounds having this structure and their properties cover the spectrum ranging from ionic to metallic.

The compound AuSn has the NiAs structure and has been the object of DHVA [10, 11] and transport [12] studies. A preliminary investigation showed that open orbit effects could be observed in its magnetoresistance in fields of 50 kG [13]. In the present paper we present the results of an investigation of the MR and quantum resistivity oscillations in AuSn in fields up to 150 kG. Because of the expected importance of relativistic effects and the relatively complex structure of AuSn, a serious energy band calculation for it would represent one of the most difficult such calculations attempted for a solid. Such a calculation is presently being undertaken for AuSn [14] and it is hoped, therefore, that the work reported herein and the DHVA work will provide a rather stringent test of present energy band calculational techniques.

2. THEORY

(A) High-field magnetoresistance

The high-field condition is defined to be $\langle \omega_c \tau \rangle_{av} > 1$, where ω_c is the cyclotron frequency and τ the electronic relaxation time. The theory of Lifshitz and coworkers [15, 16] has shown that, in the high-field limit, the galvanomagnetic properties of a metal are determined by its state of compensation and by topological properties of its Fermi surface. In an uncompensated metal (electron volume \neq hole volume), the transverse MR saturates for a general field direction and is proportional to $B^2 \cos^2 \gamma$ when there are open orbits making an angle γ with the current density \mathbf{J} . On the other hand, for compensated metals (electron volume = hole volume), quadratic behavior of the transverse MR is the general rule when the orbits are all closed; when there are open orbits the MR is proportional to $B^2 \cos^2 \gamma$ as above so that saturation is achieved essentially only when there are open orbits nearly perpendicular to \mathbf{J} . This indicates that in order to determine the field directions on a stereogram

for which there exist open orbits in a compensated metal, many samples having different current directions must be used if only *transverse* measurements are made. We wish to investigate explicitly the conditions under which open orbits may be detected in a compensated metal when non-transverse measurements are made.

Suppose that \mathbf{J} is not normal to the field \mathbf{B} as shown in Fig. 1. We must consider the re-

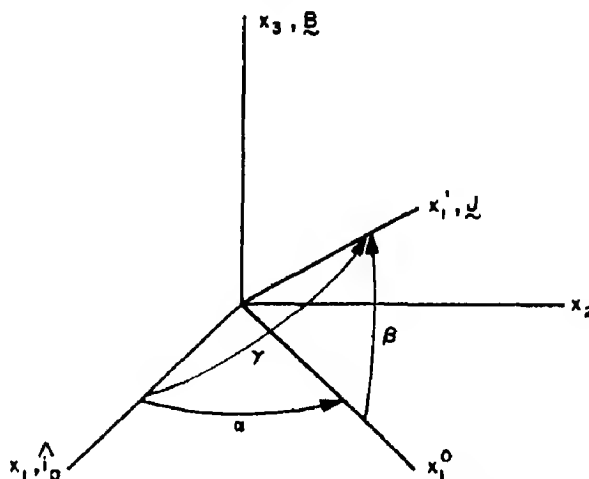


Fig. 1. Geometry of nontransverse magnetoresistance measurement. Some of the axes of the coordinate systems S , S^0 and S' are shown along with angles involved in the coordinate transformations. γ is the angle between the open orbit direction \hat{i}_0 and \mathbf{J} .

sistance, measured along the current axis of the sample, when there are open orbits along \hat{i}_0 (the x_1 direction), and when there are no open orbits along the x_1 axis or any other direction in planes normal to the x_3 axis. The three coordinate systems of Fig. 1 are $S(x_1, x_2, x_3)$, $S^0(x_1^0, x_2^0, x_3^0)$, and $S'(x_1', x_2', x_3')$. The S^0 system is derived from S by a rotation $R(\alpha)$ about x_3 and the S' system is derived from S^0 by a rotation $R(\beta)$ about x_2^0 . In system S , the matrix equation relating the electric field \mathbf{E} to the current \mathbf{J} is

$$\mathbf{E} = \rho \mathbf{J} \quad (1)$$

where ρ is the resistivity matrix. Then in S' we have

$$\mathbf{E}' = \rho' \mathbf{J}' \quad (2)$$

where the resistivity matrix in the S' system is given by

$$\rho' = R(\beta)R(\alpha)\rho R(\alpha)^{-1}R(\beta)^{-1}. \quad (3)$$

Equations (1-3) give the matrix element governing the resistance measured along the sample axis, i.e.

$$\begin{aligned} \rho'_{11} = & \rho_{11} \cos^2 \beta \cos^2 \alpha + \rho_{12} \cos^2 \beta \cos \alpha \sin \alpha \\ & + \rho_{13} \cos \beta \sin \beta \cos \alpha \\ \rho'_{11} = & + \rho_{21} \cos^2 \beta \cos \alpha \sin \alpha + \rho_{22} \cos^2 \beta \sin^2 \alpha \\ & + \rho_{23} \cos \beta \sin \beta \sin \alpha \\ & + \rho_{31} \cos \beta \sin \beta \cos \alpha \\ & + \rho_{32} \cos \beta \sin \beta \sin \alpha + \rho_{33} \sin^2 \beta. \end{aligned} \quad (4)$$

The procedure for determining the nature of a nontransverse MR rotation plot when the field direction sweeps through a one-dimensional region of open orbits is as follows. We assume that if \mathbf{B} is tipped infinitesimally away from the x_3 axis toward \hat{i}_0 , then the open orbits are lost while α and β remain fixed to first order. We then compare the *magnitude* of ρ'_{11} for the open orbit and closed orbit case. In the S system the high-field resistivity matrices for a compensated metal in the closed and open orbit cases are [17]:

$$\rho_c = \begin{pmatrix} a_{11}^c B^2 & a_{12}^c B^2 & a_{13}^c B \\ a_{21}^c B^2 & a_{22}^c B^2 & a_{23}^c B \\ -a_{13}^c B & -a_{23}^c B & a_{33}^c \end{pmatrix} \quad (5)$$

$$\rho_0 = \begin{pmatrix} a_{11}^0 B^2 & a_{12}^0 B & a_{13}^0 B \\ -a_{12}^0 B & a_{22}^0 & a_{23}^0 \\ -a_{13}^0 B & a_{32}^0 & a_{33}^0 \end{pmatrix} \quad (6)$$

where the coefficients a_{ij}^c and a_{ij}^0 are field independent but depend on the closed orbit and open orbit mobilities and relaxation times. If the field dependent part of the resistivity tensor is given by

$$\Delta\rho \equiv \rho(B) - \rho(0) \quad (7)$$

then equations (4-7) give

$$\begin{aligned} \Delta\rho'_{011} &= a_{11}^0 B^2 \cos^2 \beta \cos^2 \alpha \\ \Delta\rho'_{c11} &= B^2 \cos^2 \beta [a_{11}^c \cos^2 \alpha + a_{22}^c \sin^2 \alpha]. \end{aligned}$$

Furthermore, if the not unreasonable assumption is made that $a_{11}^c \cong a_{22}^c \equiv a^c$, then

$$\frac{\Delta\rho'_{011}}{\Delta\rho'_{c11}} = \frac{a_{11}^0}{a^c} \cos^2 \alpha. \quad (8)$$

Thus if $a_{11}^0 = a^c$ and $\alpha \neq 0$, a sharp dip in the MR would be expected as \mathbf{B} goes through a one-dimensional region of open orbits on the stereogram, i.e. becomes perpendicular to \hat{i}_0 . However, it would be possible to have a sharp peak as \mathbf{B} becomes perpendicular to \hat{i}_0 if $a_{11}^0 \cos^2 \alpha > a^c$. Evidence for both such types of behavior is presented below. In the high-field limit, the width of the extremum as \mathbf{B} crosses a one-dimensional open orbit region is inversely proportional to $\langle \omega_c \tau \rangle_{av}$ [16]. Thus the characteristic indicator of the presence of a one-dimensional open orbit region is a *narrow* extremum in the rotation plot.

(B) Quantum oscillations in the resistivity

Resistivity oscillations periodic in B^{-1} have been observed in several metals, semimetals, and degenerate semiconductors. Since these oscillations arise from two different, yet related, phenomena, we shall classify them here as either the Shubnikov-de Haas effect (SDH) or magnetic breakdown oscillations (MBO).

Adams and Holstein [18] and Lifshitz and Kosevich [19] have discussed the theory of the SDH effect, and Kahn and Frederikse [20] and Roth and Argyres [21] have reviewed theoretical and experimental work on the subject. While the SDH effect has been observed in many semimetals and semiconductors, to our knowledge it has not been reported in metals whose Fermi surfaces contain large pieces*. When a magnetic field is applied to a metal, the energies of the electrons are quantized into Landau levels, whose area

*See, however, Note added in proof.

in \mathbf{k} space is given by [22]

$$A_n = (n + \gamma) \frac{2\pi e B}{\hbar c} \quad (9)$$

where n is an integer and γ is a constant equal to $\frac{1}{2}$ for free electrons. As B is increased the various Landau levels successively burst through the Fermi surface and this causes the density of states at the Fermi level to oscillate periodically in B^{-1} . The SDH effect and oscillations in the susceptibility (the DHVA effect) are a direct result of the density of states oscillations. It follows from (9) that if A_0 is an extremal area of the Fermi surface normal to \mathbf{B} , then the period of the oscillation is given by

$$\Delta\left(\frac{1}{B}\right) = 2\pi e / \hbar c A_0 \equiv F^{-1} \quad (10)$$

where F is defined as the SDH or DHVA frequency. If the λ th Landau level is congruent with the Fermi surface at an extremum whose area is A_0 and a field B_λ ,

$$A_\lambda = A_0 = (\lambda + \gamma) \frac{2\pi e B_\lambda}{\hbar c}$$

or

$$\lambda + \gamma = \hbar c A_0 / 2\pi e B_\lambda.$$

Typical experimental values are $F = 10^8$ G and $B_\lambda = 10^5$ G giving $\lambda + \gamma = 10^3$ so we may put $\lambda \approx F/B_\lambda$. Now Pippard has shown with free electron theory that the amplitude of the conductivity oscillations is given approximately by [23].

$$\frac{\delta\sigma}{\sigma} \approx (2\lambda)^{-1/2}. \quad (11)$$

Thus the amplitude of the conductivity oscillations would be of the order of 1 per cent even at 100 kG. If in addition there are smaller pockets of electrons with frequencies much less than 10^8 G, λ for these small orbits will

decrease but it is unlikely that $\delta\sigma/\sigma$ will increase above about 1 per cent because the larger pieces of Fermi surface effectively short circuit the oscillations from the small pockets of electrons.

On the other hand, MBO have been observed exclusively in polyvalent metals such as Zn[24], Mg[25] and Sn[26]. These metals all possess some relatively small energy gaps so that electrons can tunnel from one band to another when high magnetic fields are present. The probability for magnetic breakdown is [27]

$$P = \exp(-B_0/B) \quad (12)$$

where, in a nearly free electron case, the characteristic breakdown field is given by

$$B_0 = K(\Delta\epsilon)^2 mc / \hbar e \epsilon_F. \quad (13)$$

K is a constant of order unity which depends on the geometry, $\Delta\epsilon$ is the energy gap between bands, m the free electron mass, and ϵ_F the Fermi energy.

The distinguishing feature of MBO is their large amplitude. In the three metals mentioned above $\delta\sigma/\sigma \approx \frac{1}{4}$ to $\frac{1}{2}$. Stark[24] suggested the following explanation for these large oscillations. As the field is increased, the quantized Landau levels cause the effective energy gap to oscillate which in turn causes P to oscillate and thus the resistivity to oscillate. The period of the oscillation is the same as that of the piece of Fermi surface involved in the new orbit caused by breakdown. $\delta\sigma/\sigma$ can be of the order of one because, for example, if $P \approx 0$, the resistivity may be essentially that of a Fermi surface with only closed orbits; if $P \approx 1$, the resistivity may be dominated by an open orbit caused by the breakdown. Stark and Falicov have recently reviewed theoretical and experimental aspects of magnetic breakdown in metals[28].

3. EXPERIMENTAL PROCEDURE

The preparation of the specimens is described in detail elsewhere[29]. We mention

here only that the pure metals used were ASARCO 'five-nines' gold and COMINCO 'six-nines' tin and that single crystals were grown by the Bridgman method and by zone refining. The purity of the crystals was determined by measuring their residual resistance ratios, $R \equiv \rho(295^\circ\text{K})/(4.2^\circ\text{K})$. It was found that the zone refined crystals and Bridgman crystals of large (~ 1 cm) diameter typically had $R \approx 15$ and this level of purity is insufficient to satisfy the high-field condition, $\langle\omega_c\tau\rangle_{\text{av}} > 1$. To get higher purity crystals it was necessary to grow long thin rods of diameter ~ 2 mm. The resistance ratio of these rods was measured as a function of length along them and it was invariably found that the initially solidified end had the higher resistance ratio. While giving sufficiently high purity crystals, this procedure had the disadvantage that one had to accept the 'as-grown' orientation for the current axis. Of the many crystals grown, three were selected for experimental study; Table 1 lists the crystals, their resistance ratios, and their current directions. Jan and Pearson[12] have determined that the AuSn phase exists from 50.0 to 50.5 at.% tin and have measured R as a function of concentration in this range for several crystals. By extrapolating a curve of R vs. composition constructed from their data, we estimate that for our purest sample, the deviation from the exact stoichiometry is approximately 60 ppm.

Because of the limited degree of purity of the samples, it was necessary to perform the experiments in very high magnetic fields. The measurements were made at the Francis

Bitter National Magnet Laboratory in a water-cooled solenoid providing a maximum field of 150 kG. The sample holder, which has been described in detail previously[30], had two degrees of freedom so the field could be pointed in any crystallographic direction for an arbitrary current direction. The angular and field dependence of the MR was determined by passing a constant current of one to two amps through the sample and measuring the magnetoresistive voltage $V(\mathbf{B})$ across the sample as the sample was rotated at constant field or as the field was swept at constant field direction. The voltages were measured with a Keithley Model 148 nanovoltmeter and recorded continuously as a function of angle or magnet current on an X-Y recorder.

Quantum oscillations in the MR were observed either in DC as above or with a field-modulation method with phase-sensitive detection. The frequency and amplitude of the modulation were 10 Hz and about 1 kG, respectively, with detection at the second harmonic.

4. RESULTS

(A) High-field magnetoresistance

Figure 2 shows the MR plots for two samples whose current directions are within 2° of the basal plane. Curves *a* and *b* are transverse rotation plots for which $\mathbf{B}(0^\circ)$ lies in the basal plane and $\mathbf{B}(90^\circ)$ is within two degrees of [0001]. Curve *c* is a longitudinal-to-transverse plot which shows a very small MR when $\mathbf{J} \parallel \mathbf{B}$ at 0° . The field dependence of the MR is shown at several angles of Fig. 2 in Fig. 3. Let the field dependence of the MR be expressed as

$$\frac{\Delta\rho}{\rho} \equiv \frac{\rho(B) - \rho(0)}{\rho(0)} = aB^m$$

where a is independent of field. Table 2 lists the values of the exponent m at the highest field, 150 kG.

The rotation plots of Fig. 2 indicate clearly that AuSn is a compensated metal; the MR is

Table 1. Specimen characteristics

Sample	θ^*	θ'^{\dagger}	Resistance ratio, R
I	7°	88°	62
II	12°	88°	157
III	4°	60°	84

* θ = angle between plane of [0001] and \mathbf{J} and {10 $\bar{1}$ 0}.

$\dagger\theta'$ = angle between [0001] and \mathbf{J} .

Table 2. Field dependence of the magnetoresistance

Sample	Curve and position of Figs. 2 and 3	m
II	$a(56^\circ)$	2.0
I	$b(56^\circ)$	1.6
II	$a(90^\circ)$	0.71
I	$b(90^\circ)$	1.0
II	$a(0^\circ)$	0.75
I	$b(0^\circ)$	0.61
I	$c(0^\circ)$	0.3

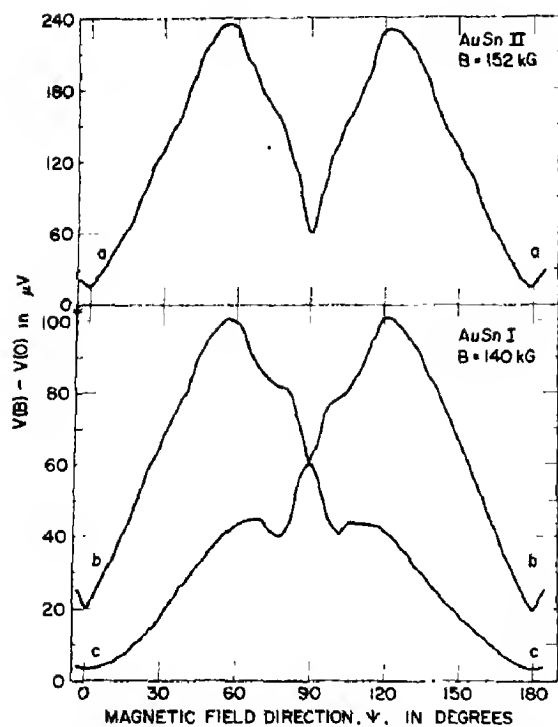


Fig. 2. (a) Transverse MR voltage for AuSn II: $B(0^\circ)$ is in (0001), 12° from $\langle 11\bar{2}0 \rangle$; $B(90^\circ)$ is 2° from [0001]. (b) Transverse MR voltage for AuSn I: $B(0^\circ)$ is in (0001), 7° from $\langle 11\bar{2}0 \rangle$; $B(90^\circ)$ is 2° from [0001]. (c) Longitudinal-to-transverse MR voltage for AuSn I: $B(0^\circ) \parallel J$; $B(90^\circ)$ is 2° from [0001].

approaching quadratic behavior everywhere except when B is in (0001) or nearly parallel to [0001]. The nearly complete saturation of $\Delta\rho/\rho$ when $J \parallel B$ indicates that the high-field condition is being satisfied, at least marginally, in the *least* pure sample, AuSn I. That m is equal to the theoretically expected 2.0 for curve $a(56^\circ)$ of Fig. 3 is a further indication

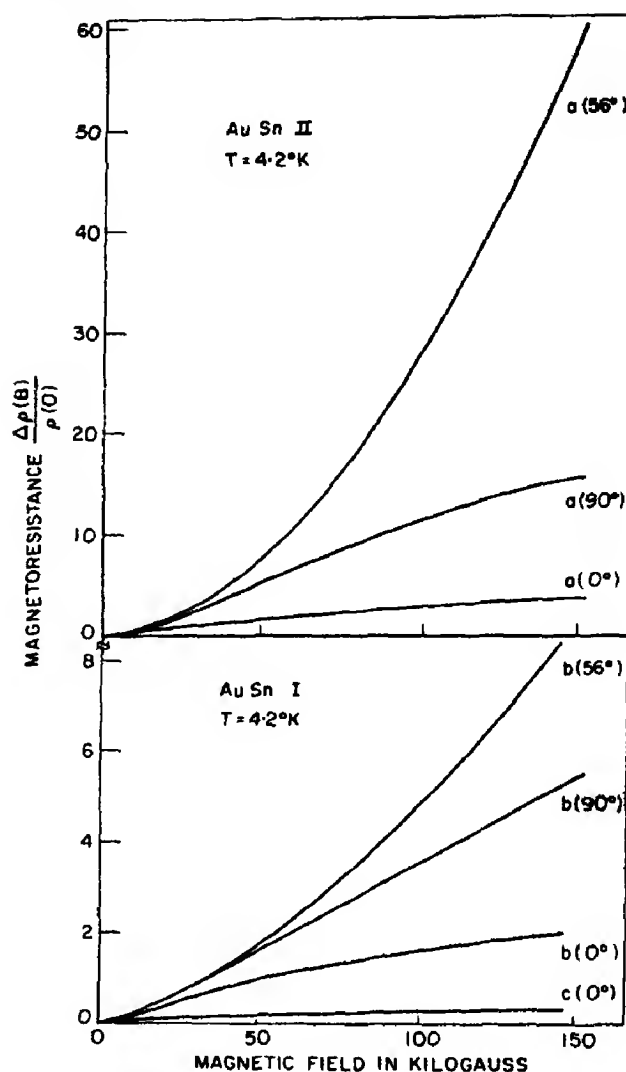


Fig. 3. The field dependence of the MR for AuSn I and AuSn II is shown at several field directions of the rotation plots of Fig. 2; each of the curves is labelled with the corresponding curve and angle of Fig. 2.

that $\langle \omega_c \tau \rangle_{av} > 1$. In compensated metals it is difficult to estimate $\langle \omega_c \tau \rangle_{av}$ but if we assume a (highly unrealistic) two-band model in which the mobilities and numbers of electrons and holes are equal, then $\Delta\rho/\rho = (\omega_c \tau)^2$. This model would then give a rough estimate of $\omega_c \tau \approx 8$ at 150 kG from Fig. 3, curve $a(56^\circ)$. The tendency toward saturation when B is in the basal plane implies that there exist open orbits along [0001]. Furthermore the weak tendency toward saturation ($m \approx 1$) when B is nearly parallel to [0001] suggests

that there may be open orbits somewhere in the basal plane. However, since the current axes of the two samples is no closer than 7° from a $\langle 11\bar{2}0 \rangle$ direction, one would not necessarily expect a definite saturation because $\gamma \neq 90^\circ$. We return to this question after presenting results on AuSn III.

Figure 4 is a photograph of transverse rotation plots for AuSn III at three different fields. Figure 5 shows the field directions (the dashed line marked $B \perp J$) for the rotation plot of Fig. 4. It is seen that, as the field increases, the dips occurring when B lies in high symmetry planes become increasingly sharp. As discussed in Section 2, these rather sharp dips indicate the presence of open orbits in the corresponding directions, viz. $\langle 10\bar{1}0 \rangle$ and $\langle 11\bar{2}0 \rangle$ directions. According to equation (8) and Fig. 1 the $(\bar{2}110)$ and

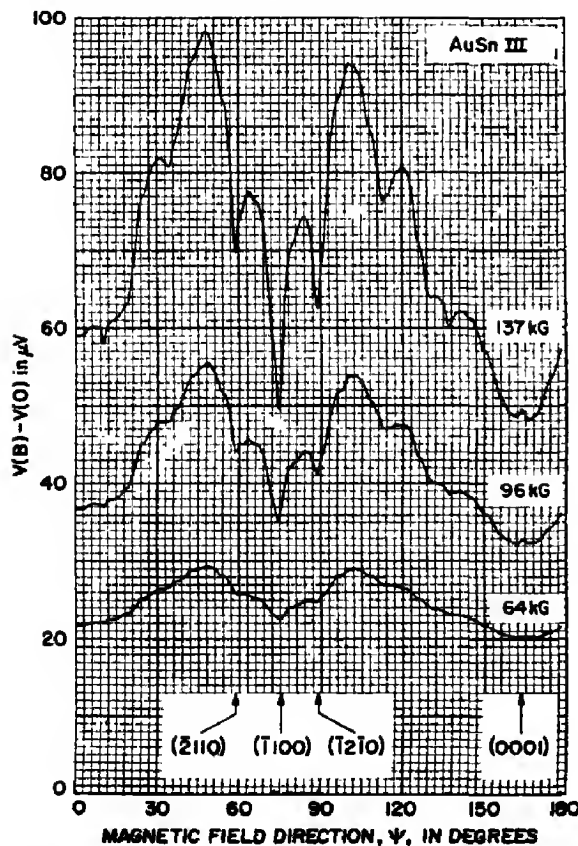


Fig. 4. Photograph of transverse MR voltages for AuSn III at three field values. The development of sharp dips due to open orbits is seen as B increases.

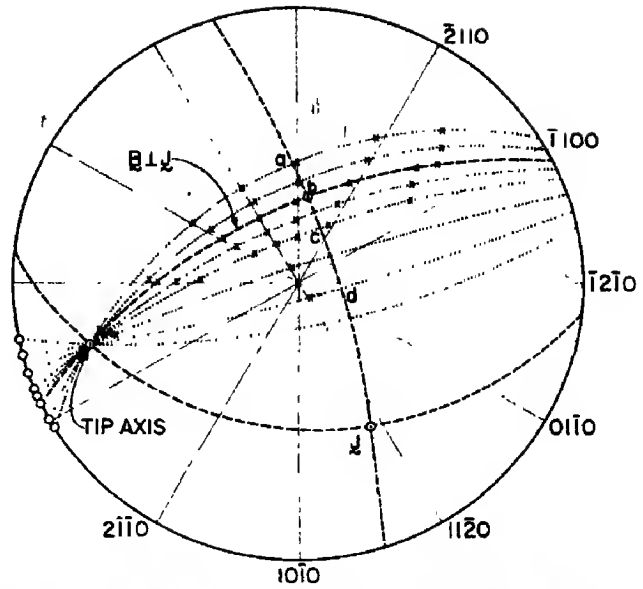


Fig. 5. Stereogram showing field directions for transverse rotation plots of Fig. 4 (dashed line labelled $B \perp J$), and nontransverse rotation plots of Fig. 6 (dotted lines labelled with corresponding curves of Fig. 6). The stereogram shows the positions of MR dips (X) and peaks (O).

$(\bar{1}2\bar{1}0)$ dips are less pronounced than the $(\bar{1}100)$ dip because in the former cases $\gamma = \alpha \approx 64^\circ$ and in the latter case $\gamma = \alpha = 86^\circ$. To further explore the existence of these $\langle 10\bar{1}0 \rangle$ and $\langle 11\bar{2}0 \rangle$ open orbits, a series of non-transverse rotation plots[31] were made on this sample and several of these are shown in Fig. 6. The loci of field directions for these plots also are shown in Fig. 5. It is clear that the dips when B is in $\{10\bar{1}0\}$ and $\{11\bar{2}0\}$ planes persist and the positions of these narrow minima are shown in Fig. 5. Figure 6 also shows how the $\{11\bar{2}0\}$ dips adjacent to the $(\bar{1}100)$ dip converge as the field rotation plane approach the $[0001]$ direction. As the angle between J and B becomes smaller, the dips become washed out and this is reasonable in terms of the discussion of Section 2. There are, in addition, some weaker dips in higher order planes but we have at present no explanation for them.

An interesting feature of Fig. 6 is the occurrence of relative maxima whenever B lies in the basal plane. These spikes appear to be the result of open orbits along the $[0001]$

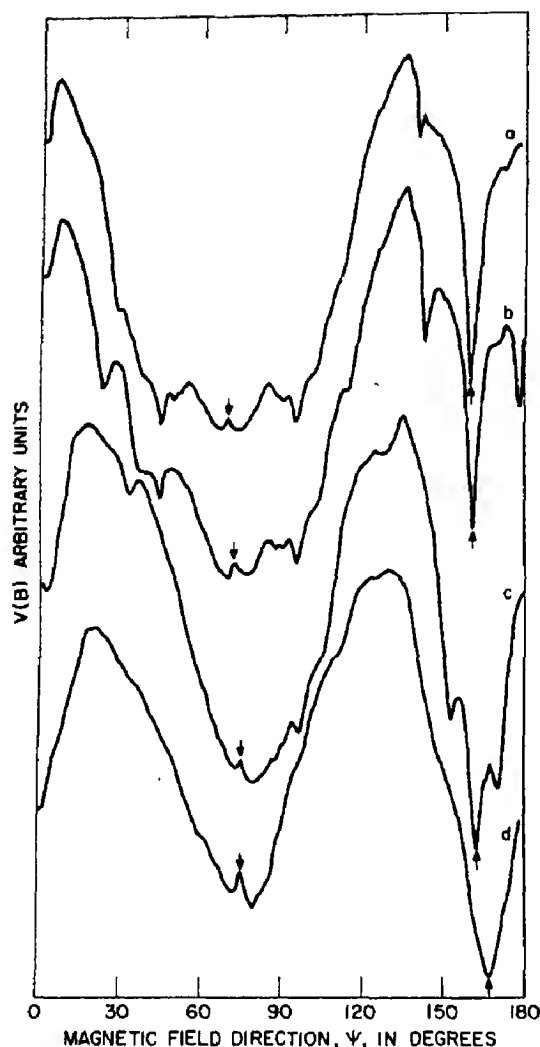


Fig. 6. Nontransverse MR rotation plots at 135 kG for AuSn III. The curves are labelled with the corresponding field directions of Fig. 5. The vertical positions of the curves are arbitrary. (\downarrow) denotes the peak when \mathbf{B} lies in (0001) and (\uparrow) denotes the dip when \mathbf{B} lies in $(\bar{1}100)$. Other pronounced minima occur in $\{11\bar{2}0\}$ and $\{10\bar{1}0\}$ planes.

direction. This would correspond to the situation discussed earlier in which $a_{11}0 \cos^2 \alpha > a^c$. No such spikes are seen in Fig. 2 when \mathbf{B} lies in the basal plane because for those samples, \mathbf{J} is very nearly perpendicular to the direction of open orbits, i.e. $\gamma = 88^\circ$. In the case of Fig. 6, $\gamma = 60^\circ$ so that a component of the open orbit electric field can be seen on the sample axis.

(B) Oscillatory effects

Quantum oscillations periodic in B^{-1} were discovered in the MR of AuSn but they were observed only under very special conditions, viz. when \mathbf{B} was in the basal plane and when \mathbf{J} was *not* in or close to the basal plane. Examples of d.c. and field-modulation data are shown in Fig. 7. Three sets of frequencies were observed and the angular dependence of these in the basal plane is shown in Fig. 8 along with some of the DHVA results of Edwards *et al.* [10]. No attempt was made to measure the temperature dependence of the amplitude of the oscillations because the signal-to-noise ratio was fairly small; the absolute amplitude of the ζ oscillation at $T = 1.3^\circ$ was only $\sim 0.06 \mu\text{V}$. Edwards *et al.* [10, 11] have measured DHVA frequencies in $\{10\bar{1}0\}$ and $\{11\bar{2}0\}$ planes as well as in (0001) so that, insofar as Fermi surface cross-sectional areas are concerned, our results merely corroborate some of their frequency determinations. However, there are two in-

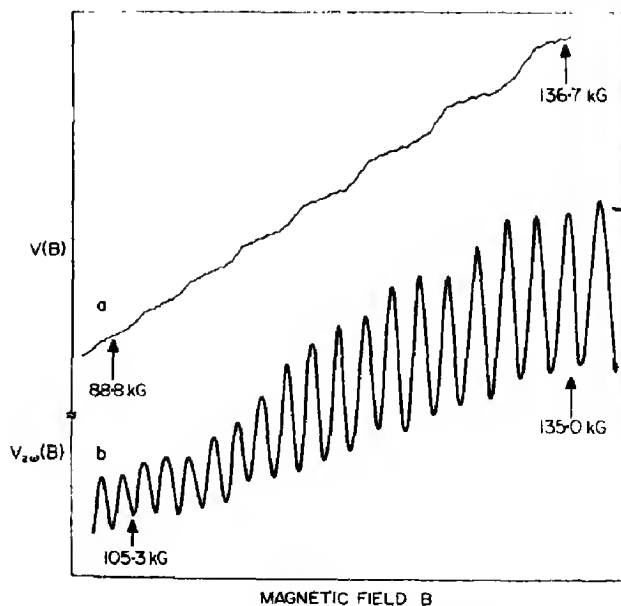


Fig. 7. Typical examples of magnetoresistance oscillations. (a) d.c. magnetoresistive voltage at $T = 1.25^\circ\text{K}$ showing δ frequency ($1.87 \times 10^6\text{G}$) and ϵ frequency ($1.32 \times 10^6\text{G}$). (b) Second harmonic signal $V_{2\omega}$ at $T = 1.22^\circ\text{K}$ showing enhancement of higher (ϵ) frequency. The voltages are in arbitrary units.

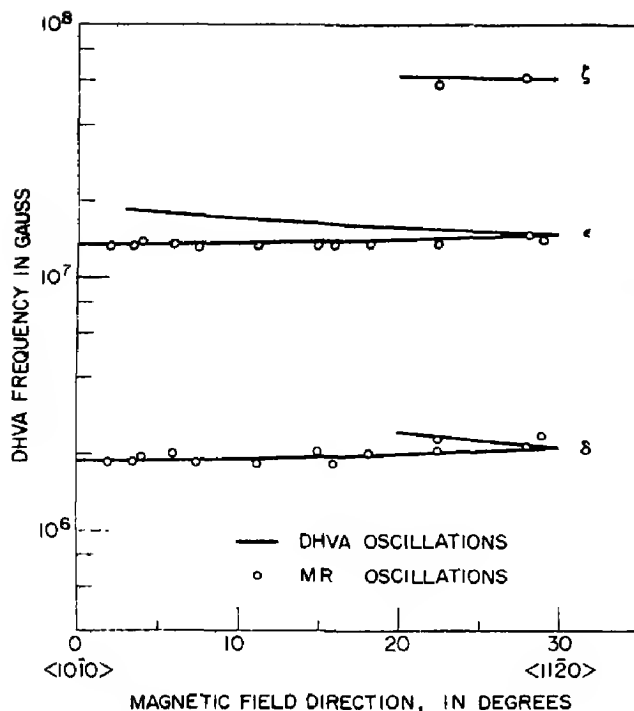


Fig. 8. Frequency of MR and DHVA oscillations in the basal plane. The labelling of the frequencies is that of [11]. The DHVA curves were constructed from the very finely spaced data points of [10].

interesting points regarding the MR oscillations: (1) the reason for their existence *only* when **B** lies in (0001), and (2) the question of whether their underlying cause is magnetic breakdown as opposed to the Shubnikov-de Haas effect. We return to these questions in the next section after discussing Fermi surface models and the correlation of the observed frequencies with particular orbits on the Fermi surface.

5. DISCUSSION

Since an energy band calculation for AuSn has not been completed as yet, we compare our results with a 1-OPW (nearly-free-electron) Fermi surface model[32]. It is by no means clear that such a model will give even a first approximation to the Fermi surface of such a compound. However, in AuSn one expects the conduction electrons to be essentially all *s* and *p* electrons rather than *d* electrons so that, extrapolating from the pure metal case, at least this necessary condition

for the validity of the 1-OPW approximation is met. Moreover, there is evidence that another group of compounds based on gold, *viz.* AuAl₂ and AuGa₂, does follow the 1-OPW model in a first approximation [33, 34].

In the case of elemental polyvalent metals having the hexagonal-close-packed structure, experience has shown that the 1-OPW model often gives a good first approximation to the Fermi surface. However, because of the screw axis parallel to [0001], the energy bands stick together on the hexagonal faces of the Brillouin zone in the absence of spin-orbit coupling. In this case the 1-OPW Fermi surface would have to be constructed in the double zone scheme as discussed by Harrison[32]. Even if there is a finite spin-orbit coupling which lifts the degeneracy on the hexagonal zone faces, it is possible that magnetic breakdown occurs in the high fields in which the experiments are done so that neighboring zones are again coupled together. Since gold and tin have moderately high atomic numbers it is likely that such splittings exist in AuSn as they do in the heavier h.c.p. elemental metals Cd and Tl[35]. One is then faced with the possibility of having, in effect, a low-field Fermi surface (double zone scheme), or an intermediate case in which there is only partial magnetic breakdown.

The 1-OPW Fermi surface model for AuSn is shown in Figs. 9.* Edwards, Springford and Saito[11] (hereafter referred to as ESS) made a detailed study of this surface and modifications of it in relation to their DHVA results. This model assumes that gold contributes one and tin four electrons to the conduction bands, giving a total of ten nearly free electrons per primitive cell. The double zone scheme, 1-OPW model is obtained trivially from Figs. 9 by stacking together the pieces of zones 3 and 4, 5 and 6, and 7 and 8, with due regard to symmetry. The result is a large closed 'dumbbell' in zone 3:4; a complicated,

*I am grateful to Drs. Edwards and Springford for providing figures similar to these.

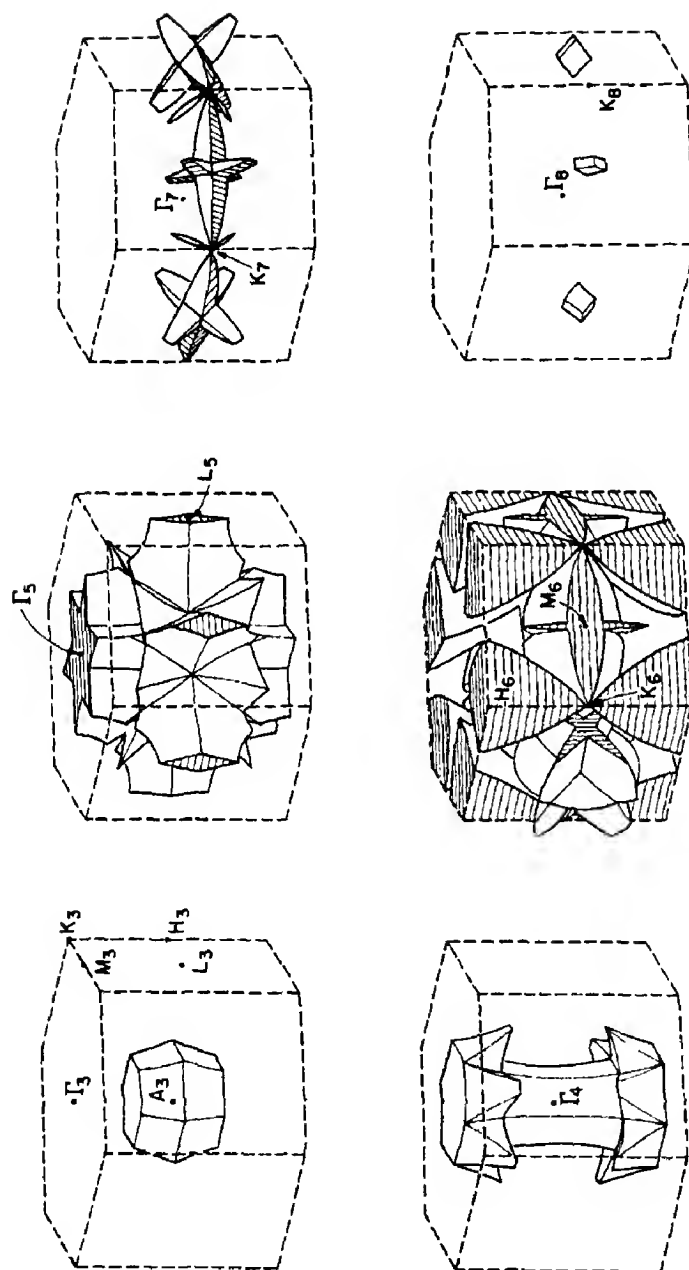


Fig. 9. 1-OPW Fermi surface for AuSn in the single-zone-scheme (after [11]). Several of the high symmetry points are labelled in the various zones; the subscripts denote the zone number. Certain pieces of Fermi surface which occur several times as a result of symmetry are not shown. A cut-off view of the 'butterflies' centered on M_6 is shown. These butterflies protrude inward and contact the large electron surfaces extending from H_6 toward K_6 .

multiply-connected surface in zone 5:6; and small, closed electron pockets and 'propellers' in zone 7:8. However, the MR results can be used to rule out this double zone scheme model immediately. The reason for this is that the nature of the sheets in zone 5 and 6 is hole and electron, respectively. If these two pieces of Fermi surface were connected together as in the double zone scheme, AuSn would lose its compensated nature, in contradiction to the MR measurements.

The 1-OPW model of Figs. 9 is also consistent with the MR results as regards open orbit directions. The zone 4 surface permits open orbits along $[0001]$ and the zone 5 surface supports open orbits along $\{0001\}$, $\langle 10\bar{1}0 \rangle$, and $\langle 11\bar{2}0 \rangle$. The topology of the zone 6 surface is rather complicated in that the 'butterflies' centered on M actually contact the large electron pieces extending from H towards K . This is shown in the cross-sections of Fig. 10.* The connectivity in

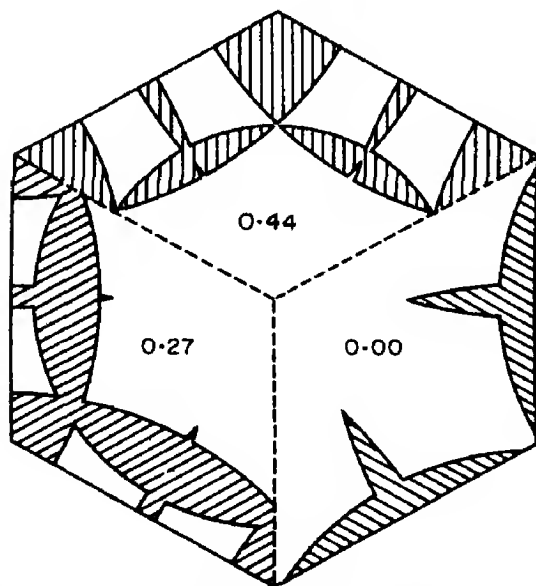


Fig. 10. Portions of three Fermi surface cross-sections parallel to (0001) in zone 6. The numbers shown are the distance of the cross-sections from the central Γ point, in units of ΓA (see Fig. 9). The 0.27 section shows how the butterflies contact the electron surface extending from H toward K (see Fig. 9).

*I am grateful to J. T. Longo and I. S. Goldstein for the Harrison construction computer program from which these plots were obtained.

question has been considered in detail by ESS who concluded that it does not, in fact, exist [11]. Since zones 4 and 5 already can account for the majority of our MR data, our results cannot shed further light on the correct connectivity in zone 6.

Additional support for the validity of the 1-OPW model can be obtained from our earlier Hall effect measurements [29]. The high-field Hall effect in a compensated metal gives essentially no information *except* when at least one sheet of Fermi surface is multiply-connected and when the field is along a high symmetry direction for which the normal state of compensation is destroyed. Such a field direction is called a *singular field direction* and the geometrical considerations which lead to the discompensation are explained in [17] and [29]. When the field is along the hexad axis, a consideration of Figs. 9 shows that there are only closed orbits and that in the hole sheet of zone 5, there are closed *electron* orbits running through three zones. This results in geometric discompensation and the detailed analysis [29] shows that the Hall coefficient measures the volume discompensation given by

$$\Delta V = A_{BZ}d$$

where A_{BZ} is the area of the hexagonal zone face and d is the minimum diameter, measured parallel to B , of the $\langle 10\bar{1}0 \rangle$ directed arms. The sign of the Hall coefficient at a singular field direction is opposite to the nature of the open sheet of Fermi surface giving rise to the discompensation. The measured Hall coefficient when $B \parallel [0001]$ was negative in agreement with the hole nature of the zone 5 sheet. Regarding the magnitude of d , Edwards [36] has fitted the DHVA results to a 4-OPW model in the vicinity of L_5 . His fit, the 1-OPW model, and the Hall effect give, respectively,

$$\begin{aligned} d(4\text{-OPW}) &= 0.16 \text{ a.u.} \\ d(1\text{-OPW}) &= 0.24 \text{ a.u.} \\ d(\text{Hall}) &= 0.21 \text{ a.u.} \end{aligned}$$

The Hall coefficient was measured with an accuracy of about 15 per cent. It is difficult to estimate the uncertainty in $d(4\text{-OPW})$ but an indication of it is contained in the statement that the 4-OPW fit gave a cross-sectional area about L_5 which agreed with the experimentally determined one to within 10 per cent[36]. Thus there is at least qualitative agreement between the 1-OPW and 4-OPW models, and the experimental results.

We now turn to a discussion of the origin of the resistivity oscillations. Since the oscillations are observed only when there are spikes in the rotation plots (Fig. 6) and are not observed when \mathbf{J} is in (0001), it is clear that the oscillations are observable under the same conditions necessary for detecting open orbits along [0001]. Thus it seems plausible that the oscillations are intimately connected with the open orbits along [0001]. This, in itself, however, does not imply that the oscillations are due to magnetic breakdown for the following reason. The coefficients a^0 and a^c in the high field conductivity tensor contain characteristic relaxation times τ_0 and τ_c for the open orbit and closed orbit electrons, respectively. The resistivity tensor is obtained by inverting the conductivity tensor and each term ρ_{ij} will, in general, depend in a complicated way on both τ_0 and τ_c when there are closed and open orbits present. Thus it seems possible that oscillations in the density of states could give rise to oscillations in τ_c as discussed by Pippard[23], and this in turn could cause ρ to oscillate even in the case when the monotonic part of ρ is dominated by the open orbits. In addition, the amplitude of the MR oscillations is not unreasonable in terms of the simple estimate of equation (11) for the amplitude of the SDH effect. If ξ_i is defined as the maximum fractional amplitude of the i th oscillation, then $\xi_0 = 1.2\%$, $\xi_c = 0.3\%$, and $\xi_t = 0.1\%$ at $T = 1.3^\circ\text{K}$. On the other hand, our samples are relatively impure compared with the pure metals in which MBO have been observed and this could have the effect of damping the amplitude of breakdown oscillations to the

rather small experimentally observed values. This behavior has already been observed in Mg[28]. One positive indication of the presence of magnetic breakdown is an anomalous field dependence of the quantum oscillatory effects. The quantitative theory of this has been discussed for several special cases by Falicov and coworkers[37]. While we have not been able to study amplitude effects in the MR oscillations, ESS have, in addition to their detailed DHVA frequency determinations, specifically studied the field dependence of selected frequencies in a search for magnetic breakdown effects. ESS have assigned the three frequencies we have observed to orbits on the 1-OPW model as follows: δ -orbits around arms at L_5 , ϵ -orbits around butterflies at M_6 , and ζ -orbits around the bellies centered on H_6 . No anomalous field dependences that could be associated with magnetic breakdown were observed for the ϵ and ζ frequencies, at least up to 100 kG, the maximum field used in their experiments. ESS observe that the δ oscillation is lost above about 40 kG when $\mathbf{B} \parallel \langle 1120 \rangle$. Our measurements of the δ oscillations in the basal plane, however, were in the field region from about 70 to 150 kG. The amplitude of the δ MR oscillation tends toward zero as \mathbf{B} approaches $\langle 1120 \rangle$ and it is barely visible at one degree away from $\langle 1120 \rangle$. Thus the oscillatory MR and DHVA results are in agreement that if there is magnetic breakdown involving the L_5 arms, it probably occurs only for a very restricted field range near the $\langle 11\bar{2}0 \rangle$ directions. Furthermore, the energy gap across the hexagonal zone face separating zones 5 and 6 is estimated by ESS from the cyclotron masses and difference in area of two orbits which would be degenerate in the 1-OPW model. They find that the energy gap obtained would predict a characteristic breakdown field B_0 (equations (12) and (13)) of about 250 kG which is well above the maximum field used in our experiments. Thus it appears that the evidence for magnetic breakdown is rather limited and, in terms of the Fermi surface model, there is no obvious

necessity to invoke breakdown across certain zone faces to explain the observed MR oscillations. These considerations suggest therefore that the MR oscillations are manifestations of the ordinary Shubnikov-de Haas effect. If this conclusion is, in fact, correct, it is rather surprising because it apparently would constitute one of the few observations of the SDH effect in a metal having large pieces of Fermi surface.

6. SUMMARY AND CONCLUSIONS

The present work has shown that AuSn is a compensated metal in agreement with its even number of electrons per primitive cell. Open orbits were discovered in the $[0001]$, $\langle 10\bar{1}0 \rangle$, and $\langle 11\bar{2}0 \rangle$ directions. These results are consistent with a 1-OPW Fermi surface model in the single zone scheme, a model which also has been used as a first approximation in explaining the DHVA results[11]. One of the features of this model is a multiply-connected hole surface in the fifth zone and Hall effect measurements for $B \parallel [0001]$ were used to estimate one dimension of the $\langle 10\bar{1}0 \rangle$ directed arms. This estimate was in qualitative agreement with a 4-OPW estimate[36]. Quantum oscillations in the resistivity were observed when the field was in the basal plane and the current was not in the basal plane. It was shown that these oscillations are observable under the same conditions as $[0001]$ directed open orbits are observable. Three sets of frequencies were measured in the basal plane and these agreed well with the DHVA results. An attempt was made to determine whether the oscillations were the ordinary Shubnikov-de Haas effect or had their origin in magnetic breakdown. Relying heavily on the DHVA work for the correlation of the observed frequencies with particular Fermi surface orbits and for the possible detection of magnetic breakdown, it was suggested that the oscillations are due to the ordinary Shubnikov-de Haas effect rather than magnetic breakdown,

but this conclusion must be regarded as tentative.

The DHVA and the present work, when taken together, indicate that AuSn may be added to the small, but growing, list of inter-metallic compounds for which the nearly-free-electron approximation forms a useful first approximation to the electronic structure.

Acknowledgements—I wish to thank Drs. G. J. Edwards and M. Springford for communicating their results prior to publication and for several illuminating discussions, and to thank Professor P. A. Schroeder for assistance in the early stages of the work. I am indebted to Professor B. L. Averbach for his interest and support and to the staff of the Francis Bitter National Magnet Laboratory for the use of its facilities. Support of this research by the Advanced Research Projects Agency through the Center for Materials Science and Engineering at MIT is gratefully acknowledged.

REFERENCES

1. See, for example, SLATER J. C., *Quantum Theory of Molecules and Solids*, Vol. 2. McGraw-Hill, New York (1965).
2. DECICCO P. D., *Phys. Rev.* **153**, 931 (1967).
3. JOHNSON K. H. and AMAR H., *Phys. Rev.* **139**, A760 (1965).
4. ARLINGHAUS F. J., *Phys. Rev.* **157**, 491 (1967).
5. AMAR H., JOHNSON K. H. and WANG K. P., *Phys. Rev.* **148**, 672 (1966).
6. CHO S. J., *Bull. Am. Phys. Soc.* **12**, 333 (1967).
7. JAN J.-P., PEARSON W. B. and SAITO Y., *Proc. R. Soc. A* **297**, 275 (1967).
8. SELLMYER D. J., AHN J. and JAN J.-P., *Phys. Rev.* **161**, 618 (1967).
9. JOHNSON K. H., Private communication.
10. EDWARDS G. J., SPRINGFORD M., PEARSON W. B. and SAITO Y., *Proc. 10th Intl. Conf. Low-Temperature Physics*, Moscow (1966).
11. EDWARDS G. J., SPRINGFORD M. and SAITO Y., To be published.
12. JAN J.-P., PEARSON W. B., KJEKSHUS A. and WOOD S., *Can. J. Phys.* **41**, 2252 (1963).
13. SELLMYER D. J. and SCHROEDER P. A., *Phys. Lett.* **16**, 100 (1965).
14. ARLINGHAUS F., Private communication.
15. LIFSHITZ I. M., AZBEL M. I. and KAGANOV M. I., *Zh. eksp. teor. Fiz.* **31**, 63 (1956); (English transl.: *Soviet Phys. JETP* **4**, 41 (1957)).
16. LIFSHITZ I. M. and PESCHANSKII V. G., *Zh. eksp. teor. Fiz.* **35**, 1251 (1958); *ibid.* **38**, 188 (1960); (English transl.: *Soviet Phys. JETP* **8**, 875 (1959); *ibid.* **11**, 137 (1960)).
17. FAWCETT E., *Advan. Phys.* **13**, 139 (1964).
18. ADAMS E. N. and HOLSTEIN T. D., *J. Phys. Chem. Solids* **10**, 254 (1959).

19. LIFSHITZ I. M. and KOSEVICH A. M., *J. Phys. Chem. Solids* **4**, 1 (1958).
20. KAHN A. H. and FREDERIKSE H. P. R., *Solid St. Phys.* **9**, 257 (1959).
21. ROTH L. M. and ARGYRES P. N., In *Semiconductors and Semimetals*, Edited by R. K. Willardson and A. C. Beer, Vol. 1, p. 159. Academic Press, New York (1966).
22. ONSAGER L., *Phil. Mag.* **43**, 1006 (1952).
23. PIPPARD A. B., In *The Dynamics of Conduction Electrons*, p. 109. Gordon and Breach, New York (1965).
24. STARK R. W., *Phys. Rev. Lett.* **9**, 482 (1962).
25. STARK R. W., In *Proc. 9th Intl. Conf. Low Temperature Physics*, Columbus, Ohio, 1964, p. 712. Plenum Press, New York (1965).
26. YOUNG R. C., *Phys. Rev.* **152**, 659 (1966).
27. BLOUNT E. I., *Phys. Rev.* **126**, 1636 (1962).
28. STARK R. W. and FALICOV L. M., In *Progress in Low Temperature Physics* (Edited by C. J. Gorter), Vol. V, p. 235. North-Holland, Amsterdam, The Netherlands (1967).
29. SELLMYER D. J., Ph.D. Thesis. Department of Physics and Astronomy, Michigan State University (1965).
30. SELLMYER D. J., *Rev. scient. Instrum.* **38**, 434 (1967).
31. The geometry of rotating the crystal when \mathbf{J} is not perpendicular to \mathbf{B} is explained, with reference to our sample holder, by SELLMYER, AHN and JAN in [30] and [8].
32. See, for example, HARRISON W. A., *Pseudopotentials in the Theory of Metals*. Benjamin, New York (1966).
33. LONGO J. T., SCHROEDER P. A. and SELLMYER D. J., *Phys. Lett.* **25A**, 747 (1967) and *Phys. Rev.*, in press.
34. JAN J.-P., PEARSON W. B., SAITO Y. and TEMPLETON I. M., *Phil. Mag.* **12**, 1271 (1965).
35. COHEN M. H. and FALICOV L. M., *Phys. Rev.* **130**, 92 (1963).
36. EDWARDS G. J., Ph.D. Thesis, Department of Physics, University of Sussex (1967).
37. FALICOV L. M. and STOCHOWIAK H., *Phys. Rev.* **147**, 505 (1966); FALICOV L. M., PIPPARD A. B. and SIEVERT P. R., *Phys. Rev.* **151**, 499 (1966).
38. TOBIN P. J., SELLMYER D. J. and AVERBACH B. L., *Phys. Lett.* **28A**, 723 (1969).

Note added in proof—With reference to the comment in Section 2(B) concerning the observation of the SDH effect in metals with large pieces of Fermi surface, MR oscillations have been reported recently in lead and have been interpreted as being due to the SDH effect rather than MBO[38].

OPTICAL PROPERTIES OF ELECTRON AND HOLE TRAPS IN Ag-DOPED ALUMINOBORATE GLASS*

AMAL K. GHOSH

Argonne National Laboratory, Argonne, Ill. 60439, U.S.A.,
and Itek Corporation, Lexington, Mass. 02173, U.S.A.

(Received 16 January 1969; in revised form 5 March 1969)

Abstract—From a wide variety of experiments on silver doped aluminoborate glass which include thermoluminescence, thermal bleaching and enhancement of radiation induced absorption and emission spectra, after glow spectra, luminescence and absorption spectra of the unirradiated glass, and effects due to dopants other than silver, a number of Ag^0 and Ag^{2+} -like centers were identified in the irradiated glass. The Ag^+ ions in aluminoborate glass act as both electron and hole traps. The after-glow and thermoluminescence emissions are attributed to thermal release of trapped electrons and their recombination with some Ag^{2+} centers; this results in emissions characteristic of Ag^+ ions. The possible transitions associated with Ag^+ , Ag^0 , and Ag^{2+} centers in glass are discussed.

INTRODUCTION

THE ABSORPTION and emission spectra of Ag-doped glasses, before and after gamma-ray exposure, are of both experimental and theoretical interest. A considerable amount of work has been reported for Ag-doped phosphate glass, but many aspects of the results are still not understood[1-5]. Earlier studies[1-3] indicated the presence of a radiation induced absorption band at about $340\text{ m}\mu$ and fluorescence bands at $480\text{ m}\mu$ (weak) and $640\text{ m}\mu$ (strong), all attributed to Ag^0 centers. Recent experimental results of Lell and Kreidl[5] indicate that the radiation induced absorption and emission spectra of Ag-doped phosphate glass could be quite complex. They do not observe the absorption and emission bands attributed to the Ag^0 center, but find a completely new set of bands due to Ag^{2+} -like centers as described in Table 1. No explanation has been presented to account for this difference. Further, there is doubt about the nature of some of the centers. In the irradiated silver doped silicate glass, no absorption or emission bands

due to silver centers similar to phosphates have been observed[5, 7]. It was thus concluded that the radiation induced bands of silver doped phosphate glass are characteristic of the phosphate glass structure. EPR spectra [4] of the irradiated phosphate glass indicates the possible presence of both Ag^0 and Ag^{2+} centers. Unfortunately, no work correlating EPR and optical studies, similar to that for KCl: Ag [6], has been reported. The present work on aluminoborate glass indicates for the first time that the radiation induced centers related to silver are not characteristic of the phosphate glass structure. Both Ag^0 and Ag^{2+} -like centers were detected in a single composition of aluminoborate glass. This was done by correlating a wide variety of experiments which include thermoluminescence and thermal bleaching or enhancement of radiation induced absorption and emission bands. A few of the absorption and emission bands are similar to those reported for phosphates and could be related to similar centers. No correlation work of the type described in the present paper has been reported for phosphates. Some of the possible transitions associated with Ag^+ , Ag^0 , and Ag^{2+} centers in glass are discussed.

*Based on work performed under the auspices of the United States Atomic Energy Commission when the author was at Argonne National Laboratory.

Table 1. Color centers in silver doped phosphate glass and KCl

Center	Luminescence ($m\mu$)		Absorption ($m\mu$)	Remarks
	Excitation λ	Emission		
AgA	254	290		Due to Ag^+ ions ^(a)
AgB	365	590	390	Trapped hole ^(a)
AgB'	315			
AgB'	365	475		Nature of center not known ^(a)
AgC	365	435	285(?)	Trapped hole ^(a)
AgD	315	485	318(?)	Trapped hole ^(a)
Ag ⁰	340	480	340	Silver atom in phosphate glass ^(b)
Ag ⁰		640		
in KCl			197	Silver atom in KCl ^(c)
			425	
Ag ²⁺				The Ag^{2+} ions form a square planar complex in KCl ^(c)
or			338	
$AgCl_4^{2-}$			460	
in KCl				
Ag ⁺ in KCl		275	below 230 $m\mu$	Attributed to Ag^+ ions in KCl ^(d)

^(a)LELL E. and KREIDL N. J., In *Interaction of Radiation with Solids*, p. 199. Plenum Press, New York (1967). Composition—50 $Al(PO_3)_3$: 50 $LiPO_3$: 4 $AgPO_3$ (weight), the absorptions marked (?) have not been definitely identified with the corresponding emission bands.

^(b)SCHULMAN J. H., SHURCLIFF W., GINTHER R. J. and ATTIX F. H., *Nucleonics* 11, 52 (1953). Composition 50 $Al(PO_3)_3$: 25 $Ba(PO_3)_2$: 25 KPO_3 (about 8 w.% of $AgPO_3$).

^(c)DELBECQ C. J., HAYES W., O'BRIEN M. C. M. and YUSTER P. H., *Proc. R. Soc.* 271A, 243 (1963).

^(d)ETZEL H. W. and SCHULMAN J. H., *J. chem. Phys.* 22, 1549 (1954).

EXPERIMENTAL RESULTS

The experimental methods are the same as those reported in earlier publications [8–10]. The samples are 0.5 mm thick unless specified otherwise.

Absorption and emission spectra of the Ag doped glass prior to irradiation

The optical absorption due to Ag in glass is shown in Fig. 1. The glass composition was 1 Al_2O_3 : 4.5 B_2O_3 : 1 K_2O : n Ag_2O , where n is 0.0005 for curve (a), 0.001 for (b) and 0.003 for (c). To find the shape of the absorption bands due to silver, the optical absorption of the base glass has been subtracted from that containing Ag. The Ag bands are broad and overlap with one another.

The fluorescence spectrum due to 2537 Å

excitation is shown in Fig. 2. The emission band peaks at about 296 $m\mu$. The spectrum is not corrected for the spectral response of the recording apparatus, which consists of a Bausch and Lomb Monochromator 33–86–25–01, with a grating blazed at 250 $m\mu$ and a 6255S EMI photomultiplier. The intensity of the 296 $m\mu$ band increases with increasing silver concentration.

Radiation induced effects

(a) *Absorption spectra.*—The radiation induced absorption spectra for a glass with 0.001 Ag_2O is shown in Fig. 3. The exposures were (a) 3×10^5 r, (b) 9×10^5 r, and (c) 6.3×10^6 r. Note, there are bands with peaks roughly at 310, 340, 350, and 450–500 $m\mu$. Some of the peaks are not well defined, and there are some overlapping bands which

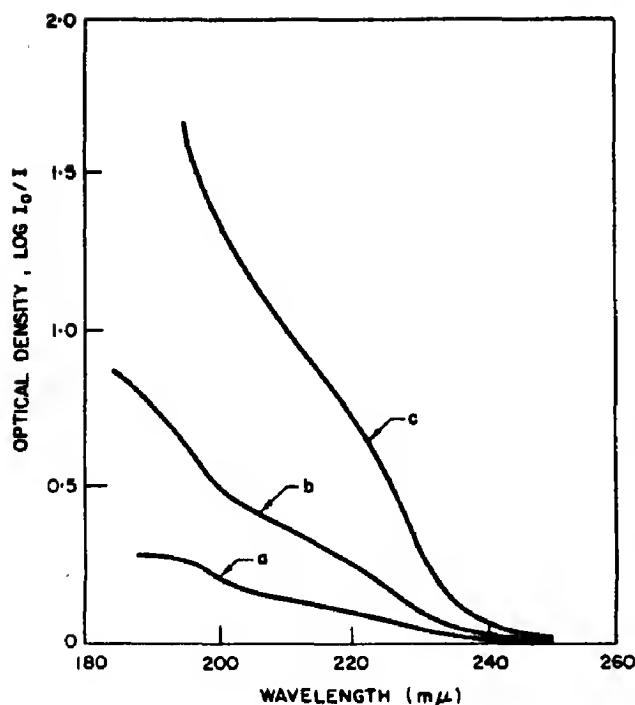


Fig. 1. The absorption spectra of Ag^+ ions in aluminoborate glass as a function of Ag_2O concentration.

are not evident at all. The position of these bands, as it will be subsequently shown in Fig. 6, are approximately at 260, 280 and 380 $m\mu$. The absorption characteristic of the undoped glass for equivalent dose is small[9]. Silver acts as both electron and hole trap, and as a result, this is expected to further reduce the radiation induced absorption characteristic of the base glass. In general, the intensity of the different bands for the same dose increases with increasing silver concentration. For 0.003 Ag_2O and exposures $\sim 6.3 \times 10^6 \text{r}$, the 310 $m\mu$ increases more than the other bands. This is shown later in Fig. 6 (25°C curve).

(b) *Afterglow spectrum.*—There is only one band in the afterglow. It is the same as the 296 $m\mu$ band, one observes due to 2537 Å excitation before irradiation. The afterglow spectrum of the glass due to other dopants (Ce, Cu, Tl, etc.) were also studied, and it is found to be always characteristic of the dopant. Along with the afterglow, there is

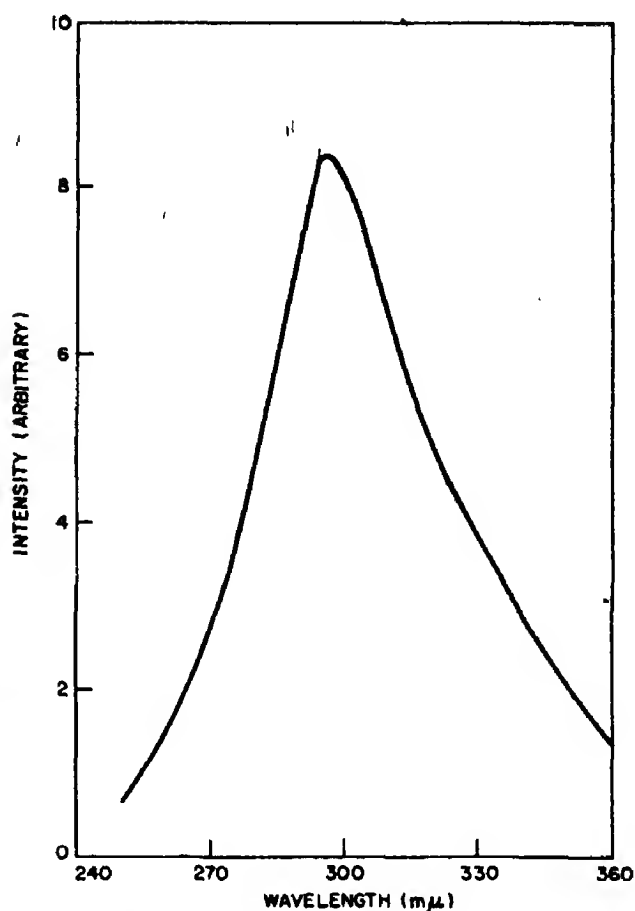


Fig. 2. The fluorescence spectrum of Ag^+ ions in aluminoborate glass.

partial bleaching of the radiation induced bands with time, even if the irradiated glass is left in the dark.

(c) *Thermoluminescence.*—On heating the irradiated glass, one observes thermoluminescence glow peaks roughly at $65^\circ \pm 5^\circ\text{C}$ and $165^\circ \pm 10^\circ\text{C}$. The peak position of the 165°C glow is not well defined. Glow peaks at similar temperatures have been observed in the base glass and with other dopants. This is shown in Fig. 4. Like the afterglow spectrum, the thermoluminescence spectrum is always found to be characteristic of the dopant. For Ag-doped glass, one observes the 296 $m\mu$ band in both glow peaks.

(d) *Thermal bleaching of absorption bands.*—During the thermoluminescence emissions, there are changes in the radiation

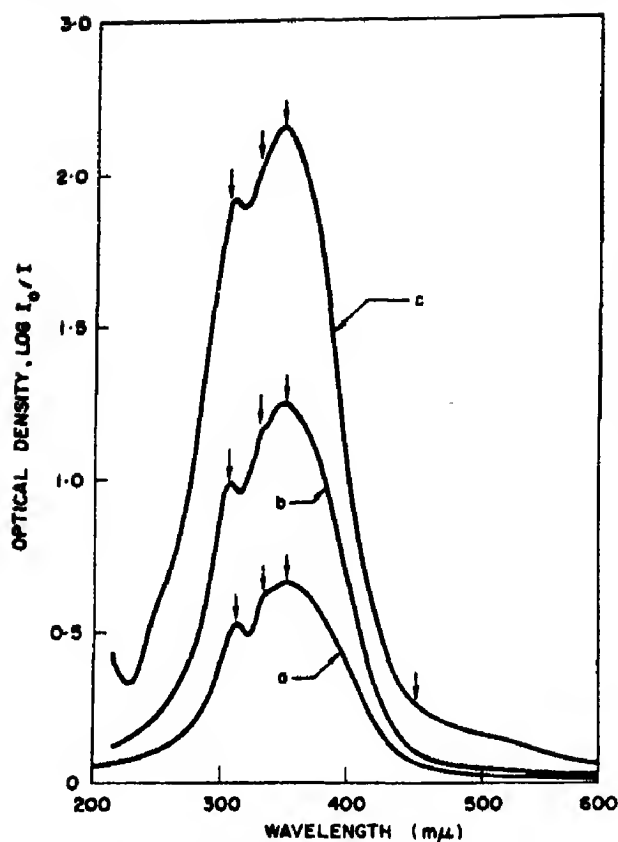


Fig. 3. The radiation-induced absorption spectra of Ag-doped aluminoborate glass as a function of exposure.

induced absorption bands. The rate of change of optical density at 350 $m\mu$ with temperature ($\Delta OD/\Delta T$), as a function of temperature is shown in Fig. 5. Similar curves are obtained for the other bands that bleach. In the bleaching curve, there are peaks at about $80^\circ \pm 10^\circ\text{C}$ and $165^\circ \pm 10^\circ\text{C}$. The change in optical density was recorded after the irradiated glass was subjected to a sawtooth annealing process. The specimen was raised to a particular temperature for five minutes by placing it in a preheated furnace, cooled to room temperature, and the absorption spectrum recorded. The amount of bleaching (ΔOD) is estimated from the difference in optical density and the difference in annealing temperatures gives ΔT . Several bands contribute to the optical density at 350 $m\mu$ band, and so the bleaching should not be

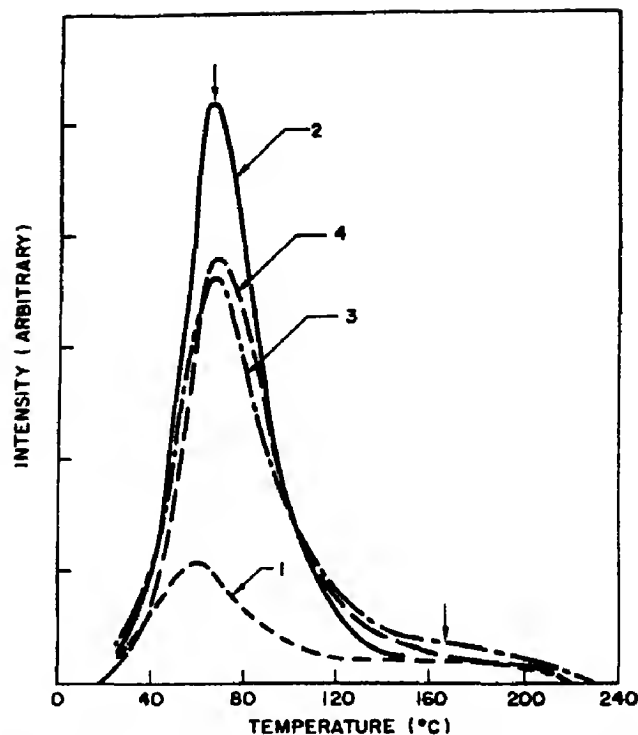


Fig. 4. Thermoluminescence glow curve of aluminoborate glass doped with different impurities (1) base glass (2) Ag (3) Cu (4) Ce.

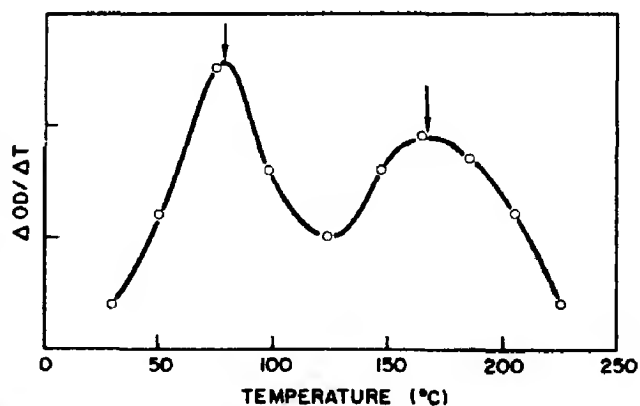


Fig. 5. The rate of change of optical density at 350 $m\mu$ with temperature.

attributed to the destruction of the 350 $m\mu$ band alone. The changes in the radiation induced absorption spectra, due to sawtooth annealing at various temperatures and cooling the glass to room temperature, are shown in Fig. 6. Absorption spectra for only a few of the annealing temperatures are shown.

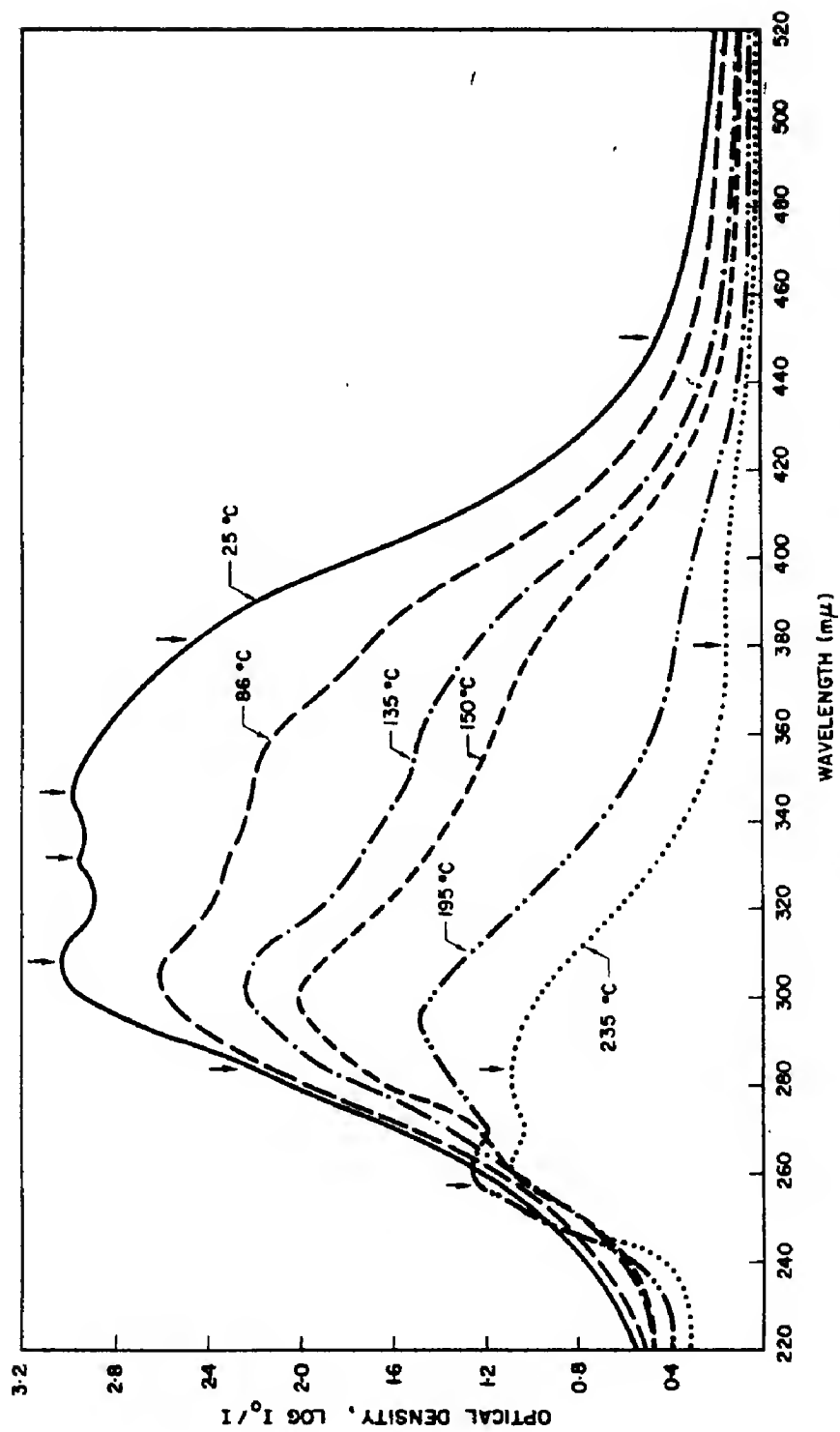


Fig. 6. Changes in the radiation-induced absorption bands due to annealing the irradiated glass at different temperatures.

It is difficult to analyze in detail the effect of temperature on each individual band because they overlap with one another. In the range of the first glow peak, there is bleaching of all absorption bands. The bleaching in the region 220–300 $m\mu$ is small as compared to other regions of the spectra. In heating through the second glow peak, there is bleaching of absorption bands at 310, 350, 380 and 450 $m\mu$, and bands roughly at 260, 280 and 380 $m\mu$ which were not evident on irradiation, become prominent. The bleaching of absorption bands is better evident if the difference curves are plotted. This is shown in Fig. 7. The 260 $m\mu$ band increases in intensity during the second

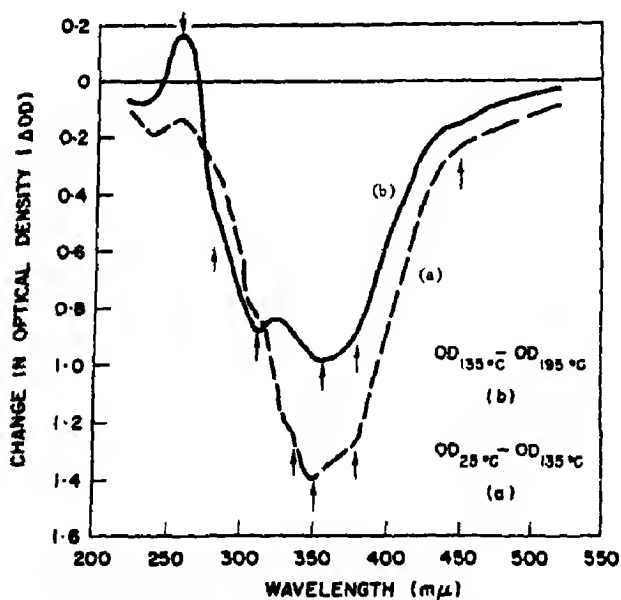


Fig. 7. Difference spectra after annealing the glass at different temperatures.

glow peak. With increase of annealing temperature, along with bleaching of the 310 $m\mu$ band, there is an apparent shift in its peak position to shorter wavelengths. With the disappearance of the 310 $m\mu$ band, the 260 and 280 $m\mu$ bands become prominent. The apparent shift in the peak position of the 310 $m\mu$ band is possibly due to the difference in bleaching rate of the 280 and 310 $m\mu$

bands. The 280 $m\mu$ band is thermally more stable than the 310 $m\mu$ band. In Fig. 7(a), the difference in the optical density of a sample annealed at 25° and 135°C is shown. Figure 7(b) shows the thermal bleaching of absorption bands around the second glow temperature. It is the difference in optical density of a sample annealed at 135° and 195°C. As described earlier, during the second glow peak, the 280, 310, 350, 380 and 450 $m\mu$ bands bleach, while the 260 $m\mu$ band increases in intensity. Because of overlapping of the bands, some of the peaks are displaced, and it is also difficult to resolve some of them. At the first glow peak temperature, the bands described earlier along with a band at 340 $m\mu$ is found to bleach.

(e) *Evidence to prove that electrons are released from traps during second glow peak.*—The radiation induced absorption spectra of aluminoborate glass of composition 1 Al_2O_3 : 4.5 B_2O_3 : 1: K_2O : 0.05 PbO (1 cm thick. Dose $\sim 2.25 \times 10^{16}r$) is shown in Fig. 8. The peaks at 835 and 970 $m\mu$ are due to Pb^{+} ions[10]. On heating the irradiated glass to 65°C for about ten minutes and cooling it to room temperature, the peak intensities do not change. But, on heating the glass to 165°C for ten minutes and cooling

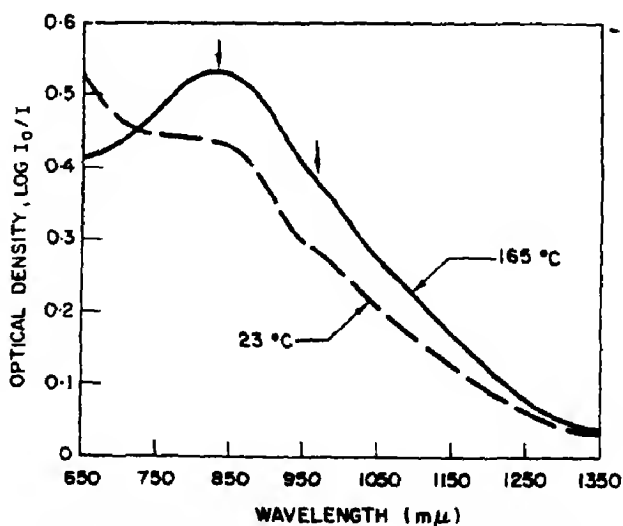


Fig. 8. Changes in the intensity of Pb^{+} ions at 165°C in irradiated Pb doped aluminoborate glass.

it to room temperature, the intensity of both the peaks increase, indicating an increase in Pb^{+} concentration.

(f) *Fluorescence spectra of irradiated glass.*—The irradiated glass fluoresces and the emission is different from that observed prior to irradiation. The fluorescence spectra depends on the excitation wavelength. The spectra due to excitation with 2537, 3131 and 3650 Å light from an Hg lamp is shown in Fig. 9. Though there is an absorption band at 340 $m\mu$, similar to that reported for phosphate glass, no emission corresponding to the 640 $m\mu$ band was detected. This is possibly because the spectrophotometer sensitivity is low at such wavelengths.

The changes in fluorescence spectra (due to excitation with 3131 Å light), after annealing the glass at various temperatures are

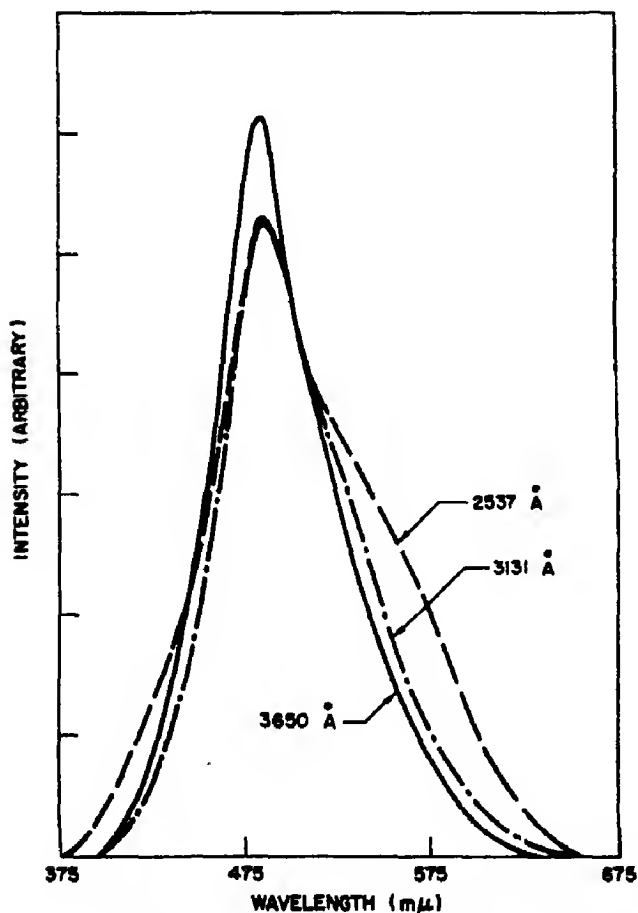


Fig. 9. The fluorescence spectra of the irradiated glass.

shown in Fig. 10. The peak around 485 $m\mu$ reaches its maximum intensity during the second glow peak.

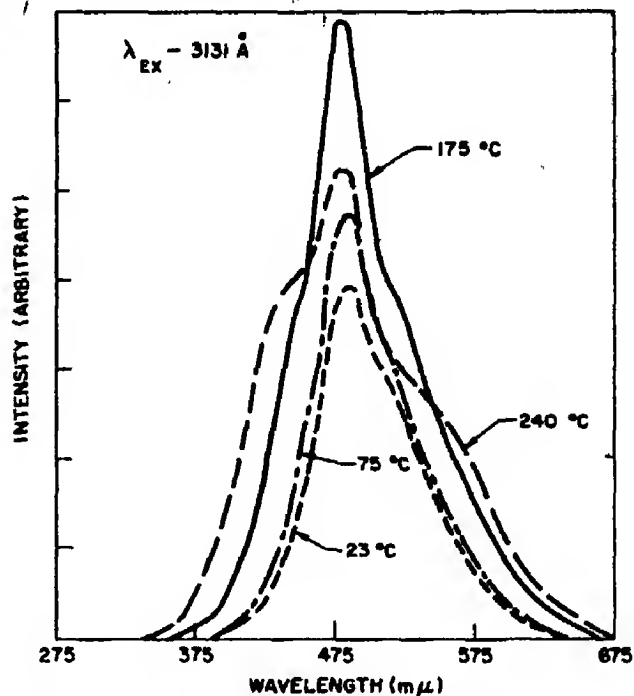


Fig. 10. Changes in the fluorescence spectra after annealing the irradiated glass at different temperatures.

Figure 11 shows the fluorescence spectra due to 2537 and 3341 Å excitation after the irradiated sample was annealed at 240°C and cooled to room temperature. The same emission bands prior to heating are observed though the relative intensities of the bands are now different.

None of the fluorescence spectra have been corrected for the spectral response of the recording apparatus. In general, there seems to be three bands in the emission. The peak position of the bands are roughly at 430, 485 and 530 $m\mu$. There is some doubt about the exact location of the peak for the 530 $m\mu$ band.

DISCUSSIONS

The absorption and emission spectra of Ag^{+} ions in glass

The absorption spectra in Fig. 1 and the emission band at 296 $m\mu$ in Fig. 2 are

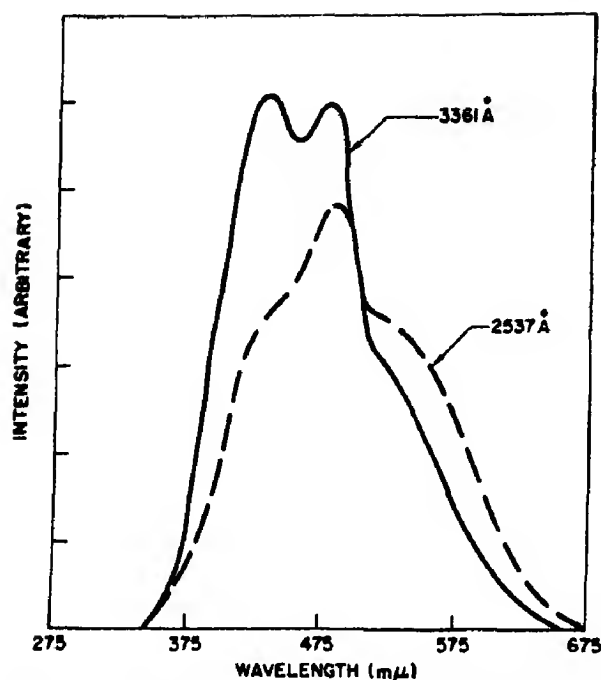


Fig. 11. The fluorescence spectra after annealing the irradiated glass at 240°C.

all attributed to Ag^+ ions in the aluminoborate glass. In analogy with the results of Ag-doped alkali halide crystals, the absorption bands are attributed to $4d^{10}-4d^95s$ transitions [11]. The transitions are forbidden in the free ion by parity selection rule, but are somewhat allowed in crystals and glass, possibly because of mixing of states due to the surrounding crystal field. The emission band at 296 $m\mu$ in aluminoborate glass and the 290 $m\mu$ in phosphate glass possibly corresponds to the 275 $m\mu$ emission observed in KCl: Ag [12].

The nature of radiation induced absorption and emission centers

The radiation induced absorption and emission bands in silver-doped aluminoborate glass are attributed to different silver centers in the glass. The nature of the different centers was found by correlating the thermoluminescence glow peak around 165°C with the thermal bleaching and enhancement of

radiation induced absorption and emission bands.

The thermoluminescence glow peak temperatures are independent of the dopant, though the emission spectrum is characteristic of it. Based on such a result, it is concluded that the traps involved are characteristic of the base glass. The thermoluminescence and afterglow emissions are both attributed to recombination luminescence. Electrons freed from traps recombining with Ag^{2+} ions result in emissions characteristic of Ag^+ ions. The emission due to silver and the other dopants can be described by the process $X^+ + e \rightarrow (X^+)^* \rightarrow X + h\nu$, where X^+ represents Ce^{4+} , Ag^{2+} or Cu^{2+} ions and $h\nu$ the characteristic Ce^{3+} , Ag^+ and Cu^+ emissions. The nature of the traps involved have been discussed in an earlier report [9]. Further confirmation of thermal release of electrons from traps, at least for the 165° glow peak, is evident from the increase in the concentration of Pb^+ ions (due to Pb^{2+} ions capturing electrons). The transitions responsible for the Pb^+ ion absorption has been discussed earlier [10]. The bleaching of the absorption bands at 280, 310, 350, 380 and 450 $m\mu$ at the second glow peak temperature suggest that these bands are related to hole centers, possibly Ag^{2+} ions in different structural sites. A single center may have more than one band associated with it. More than a single form of Ag^{2+} -like center could be responsible for the characteristic Ag^+ emission observed in the afterglow and thermoluminescence emissions. The increase in the 260 $m\mu$ absorption band around 165°C suggests that it is due to an Ag^0 -like center. We believe that the 260 $m\mu$ band is present on irradiation, but we cannot detect it without annealing because it is masked by other overlapping bands. The Ag^+ ions in aluminoborate glass act as both electron and hole trap, and thus on irradiation, both Ag^0 and Ag^{2+} -like centers are formed.

The kinetics of the thermoluminescence

emission and thermal bleaching process during the low-temperature glow peak is complicated. We believe that both electrons and holes become free at this temperature. The reason for arriving at such a conclusion has been described in earlier papers [9, 10]. The $340\text{ m}\mu$ band is apparently bleached during the first glow peak. In phosphate glass, an absorption band at $340\text{ m}\mu$ has been attributed to Ag^0 centers, and it is quite possible that the $340\text{ m}\mu$ band in aluminoborate glass is also related to Ag^0 centers.

There are three absorption and three emission bands after annealing the glass at 240°C . The relative intensities of the fluorescence bands depend on the excitation wavelength. In general, while most absorption bands (with the exception of the $260\text{ m}\mu$ peak) decrease in intensity at the second glow peak temperature, the fluorescence intensity of the different bands increases. There are many overlapping absorption bands, and for a given excitation wavelength, the excitation energy may be divided between centers which fluoresce and those which do not. Thus, if non-fluorescent centers bleach at a faster rate than the fluorescent centers, it is possible to observe an apparent increase in emission intensity for a center which bleaches. The $485\text{ m}\mu$ band, along with the other emission bands, can be excited with 2537, 3131 and 3650 \AA light, thus indicating that the absorption bands associated with the different emission centers are spread over the u.v. region. The $485\text{ m}\mu$ emission band, like the $260\text{ m}\mu$ absorption band, reaches maximum intensity during the 165°C glow peak and is attributed to an Ag^0 -like center. It should be mentioned that the $485\text{ m}\mu$ emission in phosphate glass has been attributed to an Ag^{2+} -like center by Lell and Kreidl [5], while earlier studies indicated that an emission at $480\text{ m}\mu$ is due to an Ag^0 center [1-3]. The other emission bands in the present glass are attributed to Ag^{2+} -like centers and are possibly related to the 280 and $380\text{ m}\mu$ absorption bands. Some of the other radiation

induced absorption and emission bands in aluminoborate glass are very similar to those reported for phosphate glass. It is quite possible that a number of similar silver centers are present in both glass systems.

The nature of some of the optical transitions associated with the radiation induced centers

The $425\text{ m}\mu$ band due to Ag^0 centers in KCl is attributed [6] to a transition from the ground $4d^{10}5s, {}^2S$ state to the first excited state $4d^{10}5p, {}^2P$. It is quite possible that the $340\text{ m}\mu$ band if associated with Ag^0 centers corresponds to this transition. The exact nature of the electron transition giving rise to the absorption band at $260\text{ m}\mu$ is not known. This could not correspond to the transition described above, because it is at a higher energy than the corresponding transition in the free atom.

The Ag^{2+} ion has a $4d^9$ configuration as compared to $3d^9$ for Cu^{2+} ion. The energy levels of ions with d^9 configuration split into 2T_3 and 2T_2 states in octahedral symmetry. Ions with a 1A_1 ground state are subject to large Jahn-Teller distortions. In most cases, a strong tetragonal distortion is encountered, the limit of which is a square planar complex. In Cu^{2+} complexes with small tetragonality, or three bands are observed in the near infrared and visible. In complexes with strong tetragonality, only one band is observed because the three excited levels lie close together and the absorption bands are superimposed [13-15]. In Cu-doped aluminoborate glass, an absorption band at $760\text{ m}\mu$ associated with Cu^{2+} ions could not be resolved into three gaussian shaped bands. In analogy with the results of silicate glasses [16, 17], it is concluded that Cu^{2+} ions in aluminoborate glass are in octahedral symmetry with a strong tetragonal distortion. The oscillator strength of the $760\text{ m}\mu$ band for Cu^{2+} ion in aluminoborate glass was found to be about 2.9×10^{-4} . The radiation induced bands attributed to hole centers are roughly estimated to have oscillator strengths several

orders of magnitude higher. Thus, the absorption bands due to the hole centers if related to Ag^{2+} ions in octahedral sites are not due to the transitions due to splitting of the d-level in a ligand field. The absorption bands are strong and could be due to charge transfer transitions similar to those suggested for AgCl_4^{2-} complexes[6].

Acknowledgements—Thanks are due to K. R. Ferguson for his interest in the work and to C. H. Sowers for technical assistance.

REFERENCES

1. WEYL W. A., SCHULMAN J. H., GINTHER R. J. and EVANS L. W., *J. electrochem. Soc.* **95**, 70 (1949).
2. SCHULMAN J. H., GINTHER R. J., KLICK C. C., ALGER R. S. and LEVY R. A., *J. appl. Phys.* **22**, 1479 (1951); SCHULMAN J. H., SCHURCLIFF W., GINTHER R. J. and ATTIX F. H., *Nucleonics* **11**, 52 (1953).
3. SCHULMAN J. H., KLICK C. C. and RABIN H., *Nucleonics* **13**, 30 (1955).
4. TUCKER R. F., In *Advances in Glass Technology*, Vol. 1, p. 113. Plenum Press, New York (1962).
5. LELL E. and KREIDL N. J., In *Interaction of Radiation with Solids*, p. 199. Plenum Press, New York (1967).
6. DELBECQ C. J., HAYES W., O'BRIEN M. C. M. and YUSTER P. H., *Proc. R. Soc.* **271A**, 243 (1963).
7. YOKOTA R., In *Advances in Glass Technology*, Vol. 1, p. 424. Plenum Press, New York (1962).
8. GHOSH A. K., *J. chem. Phys.* **44**, 535 (1966).
9. GHOSH A. K., *J. chem. Phys.* **44**, 541 (1966).
10. GHOSH A. K., *J. Phys. Chem. Solids* **29**, 387 (1968).
11. SEITZ F., *Rev. mod. Phys.* **23**, 328 (1951).
12. ETZEL H. W. and SCHULMAN J. H., *J. chem. Phys.* **22**, 1549 (1954).
13. BJERRUM J., BALLHAUSEN C. J. and JORGENSEN C. K., *Acta chem. scand.* **8**, 1275 (1954).
14. JORGENSEN C. K., *Acta chem. scand.* **11**, 73 (1957).
15. HOLMES O. G. and McCLURE D. S., *J. chem. Phys.* **26**, 1686 (1957).
16. KUMAR S., In *Cent. Glass Ceram. Res. Inst. Bull.* **6**, 99 (1959).
17. BATES T., In *Modern Aspects of the Vitreous State*, Vol. 2, p. 250. Butterworths, New York (1962).

CALCULATION OF THE ENTROPIES OF LATTICE VACANCIES

LEONARD DOBRZYNSKI*

Section d'Etudes des Interactions Gaz-Solides, CEN, Saclay, France

(Received 27 December 1968; in revised form 4 March 1969)

Abstract—The vibrational entropy of formation of a vacancy in a crystal is calculated at high temperatures and compared with experimental data. The method used, has a pedagogical value by its simplicity, and can be applied to all kinds of lattice defects. The Einstein model is thus justified.

IN THE harmonic approximation, the time independent equations of motion of a crystal atom assume the form:

$$(\mathbf{D} - \omega^2 \mathbf{I})\mathbf{u} = 0 \quad (1)$$

where we introduce the dynamical matrix \mathbf{D} which depends on the details of the microscopic forces between atoms; ω is the frequency of the motion, \mathbf{I} the identity matrix and \mathbf{u} a $3N$ column vector, which gives the displacements of the N atoms from their equilibrium position.

Let \mathbf{D} and \mathbf{D}' denote the dynamical matrix respectively of an initial crystal and of the same crystal with added defects. We separate the dynamical matrices \mathbf{D} and \mathbf{D}' into two parts, one part \mathbf{d} and \mathbf{d}' which is diagonal and the non-diagonal remaining parts, \mathbf{R} and \mathbf{R}' . We write:

$$\mathbf{D} = \mathbf{d} + \mathbf{R}$$

$$\mathbf{D}' = \mathbf{d}' + \mathbf{R}'$$

One may then derive an expansion in inverse powers of the absolute temperature T for the change in entropy ΔS associated with the introduction of defects in the initial crystal [1, 8]. We can write:

$$\begin{aligned} \frac{\Delta S}{k} = & 3(N' - N) \left(1 - \ln \frac{\hbar}{kT} \right) \\ & - \frac{1}{2} [Tr \ln \mathbf{d}' - Tr \ln \mathbf{d}] \\ & + \sum_{n=1}^{\infty} \left[K_n + 0 \left(\frac{1}{T^{2n}} \right) \right] \end{aligned} \quad (2)$$

where N and N' are respectively the number of atoms in the two crystals, \hbar and k are the Planck and Boltzmann constants and

$$K_n = \frac{(-1)^n}{2n} Tr [(\mathbf{d}'^{-1}\mathbf{R}')^n - \mathbf{d}^{-1}\mathbf{R})^n] \quad (3)$$

$$0 \left(\frac{1}{T^{2n}} \right) = (-1)^{(n-1)} \frac{2n-1}{2n(2n)!} \Delta \mu_{2n} B_{2n} \left(\frac{\hbar}{kT} \right)^{2n} \quad (4)$$

where B_{2n} is the Bernoulli number and

$$\Delta \mu_{2n} = Tr[\mathbf{D}'^n - \mathbf{D}^n] \quad (5)$$

the variation of the 'moments' of the density of states [2]. The traces in these formulae are conveniently evaluated by using the Cyrot-Lackmann [2] method.

The expansion (2) has already been used for the calculation of the phonon entropy of clean [1] and contaminated [3] surfaces and will be applied here to the case of the vibrational entropy of formation of a vacancy as announced in a recent review paper [4]. This problem has received in the past a large amount of experimental [5] and theoretical [6] attention.

*Formerly at the Service de Physique des Solides, I.S.E.N., 59-Lille, France, where part of this calculation was done.

The vibrational entropy S_f of formation of a vacancy is the variation in entropy when an atom is taken out of its bulk position and added on to a surface kink. It is possible to imagine this operation in two steps: migration from the bulk to the gas (ΔS_0) and adsorption of a gas atom on to a surface kink (ΔS_1). We write:

$$\Delta S_f = \Delta S_0 + \Delta S_1. \quad (6)$$

In the last operation, the number of the crystal atoms is increased but the surface configurations remain unchanged (only the length of the surface step is increased).

Huntington *et al.*[6], representing the ion-core interaction by an exponential potential of the Born-Mayer type, have calculated $S_f (= 1.85 k)$ using an Einstein model. An inward radial displacement of about 0.015 of the equilibrium interatomic distance for the twelve nearest neighbors gave a contribution of $-0.16 k$; the contribution arising from regions somewhat remote from the defect was $+0.13 k$ and was evaluated by an elastic theory approach. The surface effect was also evaluated from an elastic theory point of view and gave a contribution of $-0.44 k$ to S_f . The Einstein model disregards the normal modes of the lattice in treating the vibrations of the atoms as uncoupled. To gain an idea of the seriousness of this shortcoming Huntington *et al.*[6] investigated a two-dimensional analog, namely a hexagonal ring of atoms with and without a central atom and computed as an indication of the size of this coupling term a contribution of $0.09 k$ to S_f . This last effect is given easily in our approach on the microscopic model of the crystal.

The expansion (2) has also the advantage of giving rapidly the variation of phonon entropy for models with detailed microscopic forces between atoms and for any kind of lattice defect. However in the vacancy case, S_f is known experimentally[5] with a precision of about 30 per cent only for Au, Ag, Al, Cu and like Huntington *et al.*[6] we

will consider in what follows only the interactions between nearest neighbors.

If

$$u(\mathbf{l}) = (u(\mathbf{l}), v(\mathbf{l}), w(\mathbf{l}))$$

is the displacement from equilibrium of the atom in a lattice site \mathbf{l} of the perfect crystal, then the potential energy term in the Hamiltonian is assumed here to have the form

$$V = \text{Const.} + \frac{1}{2}\beta \left\{ \sum_{\mathbf{l}} \sum_{\delta} [u(\mathbf{l}) - u(\mathbf{l} + \delta)]^2 + [v(\mathbf{l}) - v(\mathbf{l} + \delta)]^2 + [w(\mathbf{l}) - w(\mathbf{l} + \delta)]^2 \right\}. \quad (7)$$

The nearest neighbors of the atom in lattice site \mathbf{l} are the atoms in lattice site $\mathbf{l} + \delta$; β is the force constant between nearest neighbors. We may introduce a Debye temperature T_D using the definition

$$kT_D = \hbar\omega_M \quad (8)$$

where ω_M is the maximum frequency of the bulk phonon branch.

With the potential energy given by (7), one obtains a three fold degenerate phonon branch with ω_M^2 equal to $16\beta/M$ for f.c.c. crystals.

The Cyrot-Lackmann[2] method gives directly the phonon contribution to ΔS_0 defined in (6), by using the expansion (2):

$$\frac{\Delta S_0}{k} = -3 \left[1 + \ln \left(\frac{4}{3} \right)^{1/2} \frac{T}{T_D} \right] + 18 \ln \frac{12}{11} - \frac{3}{16} \left(\frac{T_D}{T} \right)^2 + O \left(\frac{1}{T^4} \right). \quad (9)$$

Due to the symmetry in ΔS_0 , $\sum_{n=1} K_n = 0$ (equation (3)). Therefore the $O(1/T^{2n})$ term gives us the error on ΔS_0 made, by truncating the expansion (2) and gives the magnitude of the coupling term for which Huntington *et al.*[6] gave a value of $0.09 k$.

In the same manner, by considering the

adsorption of a gas atom on a kink of a [100] step of a (001) surface, we obtain:

$$\frac{\Delta S_1}{k} = 3 \left[1 + \ln \left(\frac{4}{3} \right)^{1/2} \frac{T}{T_D} \right] + \frac{1}{48} + K_4 + \dots + \frac{3}{32} \left(\frac{T_D}{T} \right)^2 + O \left(\frac{1}{T^4} \right). \quad (10)$$

The $\sum_{n=1}^{\infty} K_n$ (equation (3)) may be expected to be a few times greater than K_2 ($= 1/48$), by analogy with the free surface entropy calculation [1, 7]. ΔS_1 has exactly the same value as the entropy of a bulk atom. This is quite clear, for, the number of neighbors of a kink atom is half of the neighbors of a bulk atom, and this can be rapidly checked on the high temperature expansion for the entropy. ΔS_1 is not to be compared with what Huntington *et al.* [6] called the surface effect. They attributed this effect to a term, in the elastic solution for a center of pressure, corresponding to a uniform contraction which is introduced to fit the boundary conditions at the surface of zero pressure. They calculated this term using experimental results for the effect of pressure on the elastic constants. In our simple model we do not have relaxation of atoms in the neighborhood of the vacancy and therefore no uniform contraction.

Finally, equations (6), (9) and (10) give us the vibrational entropy of formation of a vacancy in f.c.c. crystals:

$$\Delta S_{f1}/k = 1.57 + 0.02 + K_4 - 0.09 (T_D/T)^2 + O(1/T^4). \quad (11)$$

The principal errors in (11) are probably due to the fact that we choose the simplest force model and neglect relaxation. However for the experimental values given with a precision of 30 per cent we have shown that the Einstein model is justified, and that with p first neighbors ($p \gg 1$, [4]):

$$S_{f1} \approx \frac{3}{2} k p \ln \frac{p}{p-1} \approx \frac{3}{2} k. \quad (12)$$

We also checked numerically that the result (12) is an approximation as good for simple cubic and b.c.c. as for f.c.c. structures.

Similar computations [4] show that the entropy of vibration S_{f1} for a divacancy should be nearly equal to the one of two isolated vacancies: for example for f.c.c. crystals:

$$S_{f2} - S_{f1} = 3k \left(4 \ln \frac{11}{10} - \ln \frac{12}{11} \right) \approx 0.89k.$$

The comparison of the theoretical values (11) and (12) with the experimental results given in the Table show a good agreement; the accuracy of the measured values is about 30 per cent.

Table 1. Experimental results for the entropy of formation of vacancies

	S_f/k	Reference
Au	1	[5(a)]
Ag	1.5	[5(b)]
Cu	1.5	[5(c)]
Al	2.4	[5(d)]
Al	1.76	[5(e)]

The application of the method used here for a vacancy to other kinds of lattice defects such as bulk impurities, adsorbed atoms, is underway.

Acknowledgements—We are much grateful to Professor J. Friedel for the physics contained in this paper, to Drs. P. Lengart and G. Thibaudier who pointed out the applicability of the 'moment method' to the problem of point defects, to Professor E. Bonnier, Drs. Y. Adda and Y. Quéré who gave us some references, and to Professor D. Lazarus who helped us through many interesting comments on the manuscript.

REFERENCES

1. DOBRZYNSKI L. and FRIEDEL J., *Surface Sci.* 12, 469 (1968).
2. CYROT-LACKMANN F., *J. Phys. Chem. Solids* 29, 1235 (1968).
3. DOBRZYNSKI L., *Colloque de Physique des Surfaces dans les Gaz Raréfiés*, To be published, I.N.S.T.N., Saclay (1969).

4. FRIEDEL J., *Jülich Symp. Interlattices and Vacancies* (1968).
5. See for example: SIMMONS R. O. and BALUFFI R. W., (a) *Phys. Rev.* **125**, 862 (1962); (b) *ibid.* **119**, 600 (1960); (c) *ibid.* **129**, 1533 (1963); (d) *ibid.* **117**, 52 (1960); (e) BLANCHI G., MALLE JAC D., JANOT C. and CHAMPIER G., *C. r. hebd. Seanc. Acad. Sci., Paris* **263**, 1404 (1966); (f) ADDAY. and PHILIBERT J., *Diffusion dans les Solids*. Tome 1, Presses Universitaires de France (1966).
6. See for example: HUNTINGTON H. B., SHIRN G. A. and WAJDA E. S., *Phys. Rev.* **99**, 1085 (1955).
7. DOBRZYNSKI L. and LEMAN G., *J. Phys.* **30**, 116 (1969).
8. SALTER L., *Proc. R. Soc.* **233A**, 418 (1956).

MAGNETIC STUDIES ON DYSPROSIUM ETHYL SULPHATE SINGLE CRYSTALS

A. MOOKHERJI and S. P. CHACHRA

Physics Laboratory, The University, Burdwan, W. Bengal, India

(Received 6 February 1969)

Abstract—Principal magnetic susceptibilities of $\text{Dy}(\text{C}_2\text{H}_5\text{SO}_4)_3 \cdot 9\text{H}_2\text{O}$ have been determined from 300° to 90°K. It has been observed that the interaction between electronic states and phonons lowers the overall stark splitting and increases the splitting of a few low lying stark levels. Consequently correlation between optically observed stark levels and those deduced from static magnetic susceptibility data becomes difficult. Distortions of 5*p* and 5*s* orbitals make the effective field on Dy^{+3} ion weaker. A variety of field parameters may exist which makes a state lowest to give almost the same value of the spectroscopic splitting factor.

INTRODUCTION

IN SOME recent papers [1–4] it has been shown that the static magnetic susceptibility data from 300° to 90°K of rare earth ions in crystals can be explained on the assumption of a single suitable crystal field different for different ions acting on the rare earth ions and that this field is influenced by magnetic dilution and by the distortion of closed shells of electrons about the rare earth ion.

To a first approximation only and not precisely this field could explain the stark levels as obtained from optical absorption studies of concentrated salts.

It is well-known that any time-dependent variations of the crystal lattice caused by thermal vibrations will be averaged out and the lattice may be taken as a static one. But this will not be true if there are low frequency modes of vibrations. Hence in rare earth ions lattice vibrations may be responsible for the observed deviation between the stark levels as deduced from static magnetic susceptibility data and those from optical absorption data.

This communication reports the results of magnetic anisotropy and absolute susceptibility measurements on $\text{Dy}(\text{C}_2\text{H}_5\text{SO}_4)_3 \cdot 9\text{H}_2\text{O}$ single crystals in the range 300°–90°K and discussed in the light of the above findings.

EXPERIMENTAL

Dysprosium Ethyl Sulphate was prepared from its spec. pure oxide supplied by Johnson and Matthey Co. Ltd., London, by the usual procedure.

Crystals were grown out of aqueous solution by evaporation in a desiccator under reduced pressure. The crystals so obtained were checked for twining under a polarizing microscope.

The method and procedure in the magnetic anisotropy and absolute magnetic susceptibility measurements have been described by Krishnan *et al.* [5] and by Mookherji and Mookherji [16].

RESULTS

The results of measurements are collected in Table 1. $\text{Dy}(\text{C}_2\text{H}_5\text{SO}_4)_3 \cdot 9\text{H}_2\text{O}$ crystals are hexagonal with two magnetically equivalent complexes in the unit cell of the crystal.

If the gram molecular susceptibility along the hexagonal axis of the crystal is represented by X_{\parallel} and that for directions normal to it by X_{\perp} ; then

$$X_{\perp} - X_{\parallel} = K_{\perp} - K_{\parallel}$$

where K_{\parallel} and K_{\perp} are the gram ionic susceptibilities of the complexes for directions along

Table 1. Temperature variation of K and μ values

Temp. (°K)	$10^4 K$	μ
300	7526	108.4
280	8110	107.8
260	8760	107.5
240	9710	107.4
220	10820	107.1
200	12430	107.0
180	15340	106.9
160	18490	106.6
140	23010	105.9
120	28360	105.5
100	34500	104.2
90	38070	102.6

and normal to the axis of symmetry. The mean effective moment $\mu = 2.84(\sqrt{X'T/q})$, where $X' = X'_{\parallel} + 2X'_{\perp}/3 = K =$ mean gram molecular susceptibility corrected for diamagnetism and q is the number of rare earth ions.

The following diamagnetic corrections were adopted[6, 7]

Dy^{+3}	$(\text{C}_2\text{H}_5\text{SO}_4)^{-1}$	H_2O
-24.9	-63.8	-13.0

Susceptibility is expressed as 10^{-6} c.g.s. electromagnetic units.

STARK SPLITTING OF THE GROUND STATE

The ground state, $4f^9 6H_{15/2}$ of Dy^{+3} ion is separated from its next excited state by 3500 cm^{-1} and hence its contribution to magnetism may be neglected.

According to group theoretical considerations[8] the ground state under a crystal field of C_{3h} symmetry breaks into eight levels denoted by the irreducible representations $3\Gamma_7 + 2\Gamma_8 + 3\Gamma_9$.

The complete Hamiltonian for Dy^{+3} ion under a crystal field of C_{3h} symmetry is

$$\mathcal{H} = \mathcal{H}_0 + V_c + \mathcal{H}_2$$

where \mathcal{H}_0 denotes the Hamiltonian for the free ion,

V_c denotes the crystal potential.

For C_{3h} symmetry, $V_c = A_2^0 V_2^0 + A_4^0 V_4^0 + A_6^0 V_6^0 + A_8^0 V_8^0$, the symbols having the usual meanings.

\mathcal{H}_2 is the effect of the external magnetic field H and is given by $\beta g' JH$ (g' = effective Lande splitting factor, β = the Bohr magneton number)

MATRIX ELEMENTS

The diagonal and off diagonal matrix elements inside the manifold of states spanned by $J = 15/2$ using operator equivalent method of Elliot and Stevens[9] and Stevens[10] are as follows:

$$\begin{aligned} A_1 &= \langle \pm 15/2 | V | \pm 15/2 \rangle \\ &= -0.6667 B_2^0 - 0.09697 B_4^0 + 0.9324 B_6^0 \\ A_2 &= \langle \pm 13/2 | V | \pm 13/2 \rangle \\ &= -0.4000 B_2^0 + 0.3232 B_4^0 - 1.6784 B_6^0 \\ A_3 &= \langle \pm 11/2 | V | \pm 11/2 \rangle \\ &= -0.1714 B_2^0 + 0.7850 B_4^0 - 0.5599 B_6^0 \\ A_4 &= \langle \pm 9/2 | V | \pm 9/2 \rangle \\ &= 0.01905 B_2^0 + 0.7139 B_4^0 + 0.8463 B_6^0 \\ A_5 &= \langle \pm 7/2 | V | \pm 7/2 \rangle \\ &= 0.1714 B_2^0 + 0.3387 B_4^0 + 1.2481 B_6^0 \\ A_6 &= \langle \pm 5/2 | V | \pm 5/2 \rangle \\ &= 0.2857 B_2^0 - 0.08178 B_4^0 + 0.6455 B_6^0 \\ A_7 &= \langle \pm 3/2 | V | \pm 3/2 \rangle \\ &= 0.3619 B_2^0 - 0.4582 B_4^0 - 0.3586 B_6^0 \\ A_8 &= \langle \pm 1/2 | V | \pm 1/2 \rangle \\ &= 0.4000 B_2^0 - 0.6713 B_4^0 - 1.0759 B_6^0 \end{aligned}$$

$$\begin{aligned} B_1 &= \langle \pm 15/2 | V | \pm 3/2 \rangle = 0.02636 B_6^0 \\ B_2 &= \langle \pm 13/2 | V | \pm 1/2 \rangle = 0.05402 B_6^0 \\ B_3 &= \langle \pm 11/2 | V | \mp 1/2 \rangle = 0.08167 B_6^0 \\ B_4 &= \langle \pm 9/2 | V | \mp 3/2 \rangle = 0.1038 B_6^0 \\ B_5 &= \langle \pm 7/2 | V | \mp 5/2 \rangle = 0.1160 B_6^0 \end{aligned}$$

Now setting up the sixteen by sixteen matrix, it breaks into four 3×3 matrices and two 2×2 matrices. The secular determinant breaks into two cubic equations and one quadratic is given as follows:

$$\lambda^3 - (A_1 + A_4 + A_7)\lambda^2 + (A_1A_4 + A_4A_7 + A_7A_1 - B_1^2 - B_4^2)\lambda - (A_1A_4A_7 - A_1B_4^2 - A_4B_1^2) = 0$$

$$\lambda^3 - (A_2 + A_3 + A_8)\lambda^2 + (A_2A_3 + A_3A_8 + A_8A_2 - B_2^2 - B_3^2)\lambda - (A_2A_3A_8 - A_2B_3^2 - A_3B_2^2) = 0$$

$$\lambda^2 - (A_5 + A_6)\lambda + A_5A_6 - B_5^2 = 0.$$

Comparison of optical absorption data and magnetic susceptibility data

Hufner[11] have fitted the optical absorption data of the concentrated salt of Gramberg [12] with the following parameters.

$$B_2^0 = 124.0 \text{ cm}^{-1}; B_4^0 = -79.0 \text{ cm}^{-1};$$

$$B_6^0 = -31.0 \text{ cm}^{-1} \text{ and } B_6^6 = 492 \text{ cm}^{-1}.$$

In order to test whether the above parameters can explain also the observed magnetic susceptibility data, we have calculated K and K using them. These parameters give the following stark levels and wave functions.

Substituting these in Van Vleck's[13] formula K_{\parallel} and K_{\perp} are calculated from which $K_{\perp} - K_{\parallel} = \Delta K$ and $\bar{\mu}^2$ are deduced. These are included in Table 2 along with our observed values for comparison.

The agreement between the observed values and those deduced from optical absorption data is extremely poor. This disagreement suggests that the interaction between the phonons and the rare earth electronic states might be effective in this case.

Effect of lattice vibrations

It has been mentioned in the introduction that all the optical absorption lines may not be due to transition between stark levels but are produced by the excitation of lattice waves. In order to avoid this interaction between the electronic states and phonons Hill and Wheeler[14] arranged for direct observations of transitions between Stark and Zeeman split ground J manifolds in earth ethyl sulphates; from such observations they

Energy in cm^{-1}	Wave functions	(1)
$W_1^0 = -96.8$	$0.0631 \pm 15/2\rangle - 0.2984 \pm 3/2\rangle + 0.9523 \mp 9/2\rangle$	
$W_2^0 = -78.3$	$0.8689 \pm 7/2\rangle - 0.4951 \mp 5/2\rangle$	
$W_3^0 = -73.6$	$0.0992 \pm 13/2\rangle - 0.1887 \pm 1/2\rangle + 0.9770 \mp 11/2\rangle$	
$W_4^0 = -35.8$	$-0.9876 \pm 15/2\rangle + 0.0686 \pm 3/2\rangle + 0.0789 \mp 9/2\rangle$	
$W_5^0 = -27.0$	$-0.9781 \pm 13/2\rangle + 0.1446 \pm 1/2\rangle + 0.1494 \pm 11/2\rangle$	
$W_6^0 = 54.4$	$0.8689 \pm 15/2\rangle + 0.4951 \mp 7/2\rangle$	
$W_7^0 = 109.1$	$0.6560 \pm 15/2\rangle + 0.7237 \pm 3/2\rangle + 0.1767 \mp 9/2\rangle$	
$W_8^0 = 147.7$	$0.1512 \pm 13/2\rangle + 0.9716 \pm 1/2\rangle + 0.1828 \mp 9/2\rangle$	

Now taking the magnetic field perturbation on the crystal field splitting the values of the Zeeman energies along and normal to the direction of H are given below:

H parallel to Z	H perpendicular to Z
$W_1^0 \pm 3.918 G - 0.01449 G^2$	$W_1^0 + 0 - 1.1020 G^2$
$W_2^0 \pm 2.029 G - 0.05020 G^2$	$W_2^0 \pm 3.019 G + 0.6246 G^2$
$W_3^0 \pm 5.168 G - 0.07319 G^2$	$W_3^0 \pm 0.6522 G + 0.2911 G^2$
$W_4^0 \pm 7.465 G - 0.15048 G^2$	$W_4^0 + 0 - 0.4279 G^2$
$W_5^0 \pm 6.101 G + 0.0630 G^2$	$W_5^0 \pm 0.6896 G + 0.5731 G^2$
$W_6^0 \pm 1.029 G + 0.0502 G^2$	$W_6^0 \pm 3.1904 G + 0.1078 G^2$
$W_7^0 \pm 3.884 G + 0.16497 G^2$	$W_7^0 + 0 - 0.2699 G^2$
$W_8^0 \pm 0.4369 G + 0.01019 G^2$	$W_8^0 \pm 3.922 G + 0.4188 G^2$

where $G = g'\beta H$

Table 2. ΔK and $\bar{\mu}^2$ values compared

Temp. (°K)		300	200	140	100	90
$\Delta K \cdot 10^6$	Observed	7526	12430	23010	34500	38070
	Calculated	23740	41030	47950	57100	58750
$\bar{\mu}^2$	Observed	108.4	107.1	105.9	104.2	102.6
	Calculated	110.0	109.8	106.4	103.5	103.00

suggested the following set of field parameters for Dy^{+3} ion in ethyl sulphate lattice.

$$B_2^0 = 143 \text{ cm}^{-1}, N_4^0 = -85 \text{ cm}^{-1}, \\ B_6^0 = -332 \text{ cm}^{-1} \text{ and } B_6^6 = 535.4 \text{ cm}^{-1}.$$

In order to verify this hypothesis we have calculated the stark energy levels and hence ΔK and $\bar{\mu}^2$ using these parameters following the procedure as discussed earlier. The energy levels and their corresponding wave functions are given below. ΔK and $\bar{\mu}^2$ values along with our observed values are given in Table 3 for comparison.

The ΔK values agree satisfactorily up to 140°K but there is a considerable deviation as the temperature is lowered. This disagreement can be removed by adjusting the parameters of Hill and Wheeler slightly.

Thus it may be concluded that the hypothesis of coupling the lattice waves to the electronic states has some substance in it.

The stark levels as modified by this coupling effect are shown in Table 4a.

It is seen that the effect of coupling is to decrease the overall splitting and to increase the separation between a few lowlying levels. It is further seen from equations (1) and (2)

Energy in cm^{-1}	Wave functions
$W_1^0 = -101.47$	$0.0559 \pm 15/2\rangle - 0.2659 \pm 3/2\rangle + 0.9624 \mp 9/2\rangle$
$W_2^0 = -96.67$	$0.2154 \pm 13/2\rangle - 0.4679 \pm 1/2\rangle + 0.8606 \mp 11/2\rangle$
$W_3^0 = -82.62$	$0.8693 \pm 7/2\rangle - 0.4943 \mp 5/2\rangle$
$W_4^0 = -45.28$	$-0.9942 \pm 15/2\rangle + 0.0635 \pm 3/2\rangle + 0.0865 \mp 9/2\rangle$
$W_5^0 = -26.49$	$0.9908 \pm 13/2\rangle + 0.0976 \pm 1/2\rangle + 0.2603 \mp 11/2\rangle$
$W_6^0 = -61.97$	$0.8693 \mp 5/2\rangle + 0.4943 \pm 7/2\rangle$
$W_7^0 = 119.24$	$0.0831 \pm 15/2\rangle + 0.9619 \pm 3/2\rangle + 0.2603 \mp 9/2\rangle$
$W_8^0 = 171.33$	$0.1405 \pm 13/2\rangle + 0.9746 \pm 1/2\rangle + 0.1745 \mp 11/2\rangle$

(2)

Table 3. ΔK and $\bar{\mu}^2$ values with Hill and Wheeler's parameters

Temp. (°K)		300	200	140	100
$\Delta K \cdot 10^6$	Observed	7526	12435	23010	34500
	Calculated	7494	14013	22573	27292
$\bar{\mu}^2$	Calculated	106.9	105.2	104.0	101.9
	Observed	108.4	107.1	105.0	104.1

Table 4a. Stark levels compared

Modified	0, 18, 23, 42, 69, 150, 205, 243 in cm^{-1}
Corrected	0, 4.8, 18.9, 56.1, 75, 163, 220, 273 in cm^{-1}

that the wave functions (2) and (3) are interchanged. The coupling effect drastically alters the values of K but leaves the mean moment values near about the observed values. The K value at 300°K is nearly three times the observed value and nearly 1.5 times at 90°K where phonons are less effective.

Effect of shielding and distortion

It has been observed[15] that the distortion of $5p$ and $5s$ orbitals in rare earth ions in crystals makes the effective crystalline field weaker. Consequently the magnetic moment of an ion in a crystal field of lower symmetry will be higher than that for the same ion in a field of higher symmetry. This has been verified in case of Yb^{+3} ion in a hexagonal and a tetragonal field. From Table 4b it is seen that the state of affairs is also the same with Dy^{+3} ion.

Table 4b. $\bar{\mu}^2$ values under field of different symmetry

Temp. (°K)	Symmetry	
	Hexagonal	Tetragonal
300	108.4	112.6
200	107.1	112.0
140	105.2	110.9
100	104.2	109.2

Spectroscopic splitting factor:

A comparison of the wave functions as given in expressions (1) and (2) shows that the (2) and (3) interchange their relative position. g -values deduced from these sets are given in Table 5.

All the workers deduced almost the same value of g and g for the lowest stark levels, whereas g -values for (2) and (2) levels differ considerably. The value for the fourth level both the workers give almost the same value.

Thus it is clear that a variety of field parameters may exist which make a state lowest and give almost the same g -value. Hence an attempt to deduce field parameters from observed g -values may often lead to wrong results. These also agree with the findings of Mookherji and Mookherji[16] and Mookherji[17].

Acknowledgements—The work was carried out under a C.S.I.R. Scheme. The authors wish to express their thanks to the Council for financial support.

REFERENCES

1. NEOGY D., *Physica* **29**, 974 (1963).
2. NEOGY D. and MOOKHERJI A., *Proc. phys. Soc.* **20**, 1332 (1965); *Physica* **31**, 1325 (1965).
3. CHACRA S. P., *Ind. J. Pure Appl. Phys.* **3**, 459 (1965).
4. MAHALANABIS A. and CHACHRA S. P., *Ind. J. Pure Appl. Phys.* **6**, 55 (1968).
5. KRISHNAN K. S., MOOKHERJI A. and BOSE A., *Phil. Trans.* **A238**, 125 (1939).
6. JAGANADHAN A. V., *Proc. Raj. Acad. Sci.* **1**, 6 (1950).
7. SEELWOOD P. W., *Magneto-chemistry*. Interscience, New York (1956).
8. BETHE H., *Ann. In. Phys.* **3**, 133 (1929).
9. ELLIOT R. J. and STEVENS K. W. H., *Proc. R.*

Table 5. Spectroscopic splitting factor

Stark levels	1		2		3		4	
	g_{\parallel}	g_{\perp}	g_{\parallel}	g_{\perp}	g_{\parallel}	g_{\perp}	g_{\parallel}	g_{\perp}
Gramberg	10.76	0	5.60	7.28	12.50	3.90		
Huffner	10.45	0	5.41	8.51	13.76	1.75	19.90	0
Hill and Wheeler	10.77	0	10.39	5.14	5.42	8.49	19.69	0

- Soc. A218*, 553 (1952); *Proc. R. Soc. A219*, 387 (1953).
10. STEVENS K. W. H., *Proc. phys. Soc. A65*, 209 (1952).
11. HUFNER S., *Z. Phys.* **169**, 417 (1962).
12. GRAMBERG G., *Z. Phys.* **159**, 125 (1960).
13. VAN VLECK J. H., *Electric and Magnetic Susceptibilities*. Oxford University Press, Oxford (1932).
14. HILL J. C. and WHEELER R. C., *Phys. Rev.* **152**, 482 (1966).
15. MOOKHERJI A. and MOOKHERJI T., *Proc. phys. Soc.* **22**, 525 (1967).
16. MOOKHERJI T. and MOOKHERJI A., *Ind. J. Pure Appl. Phys.* **4**, 43 (1966).
17. MOOKHERJI T., D. Phil thesis. Burdwan University, W. B. (1965).

THE PRESSURE DEPENDENCE OF THE LATTICE PARAMETERS OF CrTe and CrSb

HIROSHI NAGASAKI, IPPEI WAKABAYASHI and SHIGERU MINOMURA

The Institute for Solid State Physics, The University of Tokyo, Roppongi, Minato-ku, Tokyo, Japan

(Received 13 January 1969)

Abstract—The effect of pressure up to 150 kbar has been measured at the room temperature on the lattice parameters of CrTe and CrSb. The initial compressibilities are $(1/a_0)(da/dp) = 4.1 \times 10^{-4} \text{ kbar}^{-1}$, $(1/c_0)(dc/dp) = 8.4 \times 10^{-4} \text{ kbar}^{-1}$ in CrTe (extrapolated); $(1/a_0)(da/dp) = 3.9 \times 10^{-4} \text{ kbar}^{-1}$, $(1/c_0)(dc/dp) = 6.7 \times 10^{-4} \text{ kbar}^{-1}$ in CrSb. The pressure dependence of the Curie temperature of CrTe was discussed in relation to interatomic distances and bonding angle, and compared with the changes of the Curie temperature by chemical substitution. CrSb exhibits an anomalous compression both in a and c axes in the pressure range from 80 to 100 kbar; c axis expands rapidly with increasing pressure while a axis contracts. The fact suggests that the second order magnetic transition from antiferromagnetic to nonmagnetic state occurs at 100 kbar, and that the large exchange magnetostriction vanishes rapidly at the transition.

INTRODUCTION

IN A PREVIOUS PAPER[1], we reported the pressure dependence of the lattice parameters of ferromagnetic MnSb and antiferromagnetic MnTe. The pressure dependences of their magnetic transition temperatures have been discussed by the change of exchange magnetostriction.

For providing further data for similar discussions, we measured in this work the lattice parameters of CrTe and CrSb at pressure up to 150 kbar. Both compounds belong to a group of magnetic materials of NiAs-type structure as MnSb and MnTe. CrTe is a ferromagnet with the Curie temperature 340°K, which decreases with hydrostatic pressure by the rate $-5.5 \times 10^{-3} \text{ deg bar}^{-1}$ [2]. CrSb, on the other hand, an antiferromagnet with the Néel temperature 720°K, the pressure dependence of which has not been measured.

EXPERIMENTAL

Powder photographs of CrTe and CrSb were taken at quasihydrostatic pressure and room temperature using a Drickamer-type

high pressure X-ray cell[3, 4]. The materials were diluted about 5 times by weight with boron powder for reduction of X-ray absorption, and small amount of NaCl was added as pressure marker. Pressure was determined by NaCl compressibility data[5, 6]. Maximum pressure was 120 kbar in CrTe and 150 kbar in CrSb.

Powder samples of CrTe and CrSb were obtained from Kaneko of Tohoku University. The X-ray diffraction patterns obtained at the atmospheric pressure show that they are in single phase, and have the lattice parameters as follows; $a = 3.99 \text{ Å}$, $c = 6.22 \text{ Å}$, $c/a = 1.56$ for CrTe; $a = 4.11 \text{ Å}$, $c = 5.45 \text{ Å}$, $c/a = 1.33$ for CrSb.

The lattice parameters at high pressures were calculated from the diffraction lines (101), (102) and (110) both for CrTe and CrSb. The errors of the parameters at each pressure are within 0.02 Å in a , 0.04 Å in c and 0.01 in c/a .

RESULTS

(a) CrTe

The Curie temperature of CrTe, 70°C at

the atmospheric pressure, decreases with pressure at the rate of -5.5×10^{-3} deg bar $^{-1}$ and it descends beneath the room temperature at the pressure above 10 kbar. As our X-ray cell does not yield us the exact data at lower pressures than 10 kbar, the detailed pressure dependence of lattice parameters below 10 kbar (in the range of ferromagnetic state) was not known. Above 10 kbar, there are no anomalies in the compression curves of a , c and c/a . They decrease almost linearly with pressure up to 100 kbar. The smooth data of a/a_0 , c/c_0 and $(c/a)/(c/a)_0$ are listed in Table 1.

(b) CrSb

In Fig. 1, lattice parameters a and c of hexagonal CrSb are plotted vs. pressure, and in Fig. 2 an axial ratio c/a vs. pressure. Fig. 3 is a plot of relative change in volume V/V_0 vs. pressure. In these figures, lattice parameters are calculated assuming the same unit cell of NiAs-type through all pressure range.

The pressure dependence of a and c are very anomalous; the compressibility of a becomes almost zero at about 80 kbar. Then a decreases rapidly again above 80 to 100 kbar, and decreases more slowly above 100 kbar. In c axis, it decreases more slowly than that of the other NiAs-type compounds and above

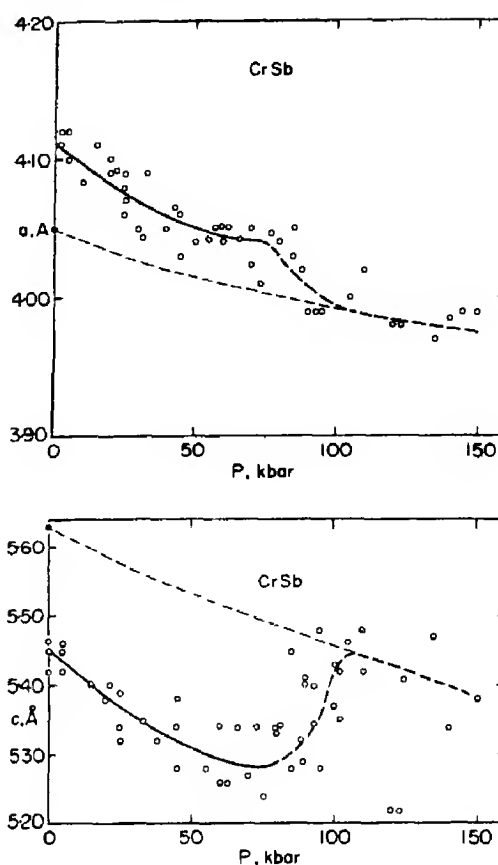
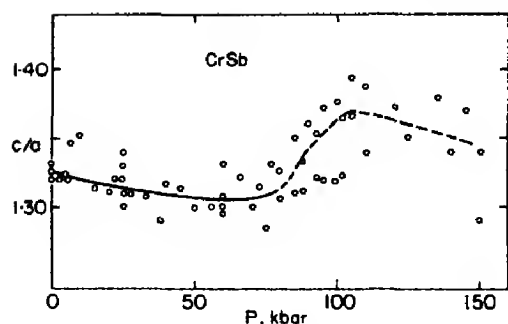
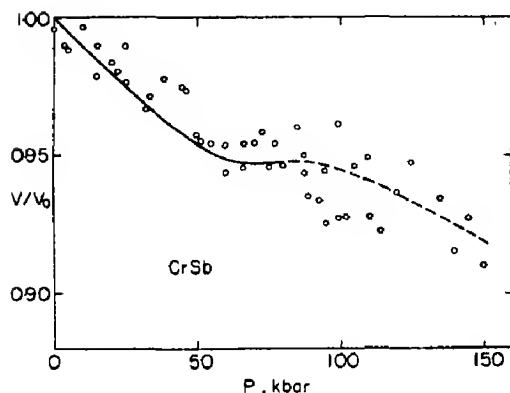


Fig. 1. (a) a (b) c vs. pressure in CrSb. The black points are the lattice parameters of fictitious paramagnetic CrSb extrapolated from those above the Néel temperature.

80 kbar it increases rapidly. Above 100 kbar, c decreases monotonically, as in the case of the

Table 1. Smoothed values of a/a_0 , c/c_0 and $(c/a)/(c/a)_0$ in CrTe and CrSb

P (kbar)	CrTe			CrSb		
	a/a_0	c/c_0	$(c/a)/(c/a)_0$	a/a_0	c/c_0	$(c/a)/(c/a)_0$
0	1.000	1.000	1.000	1.000	1.000	1.000
10	0.996	0.991	0.995	0.996	0.993	0.996
20	0.992	0.983	0.990	0.993	0.987	0.993
30	0.988	0.975	0.985	0.990	0.982	0.989
40	0.985	0.967	0.979	0.988	0.978	0.987
50	0.982	0.959	0.974	0.985	0.974	0.985
60	0.979	0.951	0.969	0.984	0.971	0.985
70	0.976	0.943	0.964	0.983	0.970	0.985
80	0.973	0.936	0.959	0.981	0.971	0.990
90	0.970	0.928	0.955	(0.975)	(0.976)	(1.011)
100	0.967	0.920	0.950	(0.972)	(0.994)	(1.026)

Fig. 2. c/a vs. pressure in CrSb.Fig. 3. V/V_0 vs. pressure in CrSb.

a axis. Consequently, a similar anomaly is seen in c/a and V/V_0 .

We could not detect any first order phase transition above 100 kbar, in so far as our X-ray apparatus could resolve. Dotted lines above 80 kbar in Figs. 3–5 mean that the lattice parameters were calculated assuming the same unit cell as that of the lattice below 80 kbar. The smooth data of a/a_0 , c/c_0 and $(c/a)/(c/a)_0$ up to 100 kbar are given in Table I.

DISCUSSION

(a) CrTe

It is well known that the magnetic transition temperatures in NiAs-type compounds depend largely on the interatomic distances. Interatomic distances of a NiAs-type magnetic compound can be changed by two different methods; (i) substituting its non-magnetic atoms by other ones. (ii) compression by

hydrostatic pressure. It is shown [1, 7], however, that the two methods of changing interatomic distances do not affect the Curie temperatures of ferromagnetic manganese compounds of NiAs-type in the same way.

The similar discrepancy is found also in the NiAs-type chromium compounds. In Fig. 4, the Curie temperature of ferro-

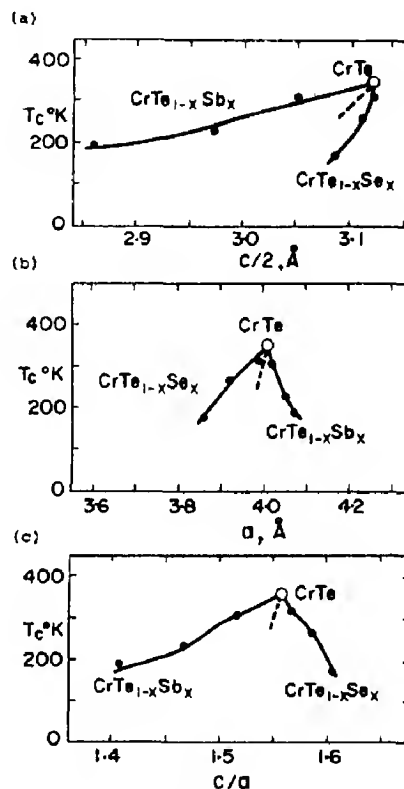


Fig. 4. The Curie temperature T_c vs. (a) $c/2$ (b) a (c) c/a in $\text{CrTe}_{1-x}\text{Se}_x$ ($0 \leq x \leq 0.5$) and $\text{CrTe}_{1-x}\text{Sb}_x$ ($0 \leq x \leq 0.6$), drawn by \bullet — \bullet parameter of x ; ----- parameter of pressure.

magnetic $\text{CrTe}_{1-x}\text{Sb}_x$ ($0 \leq x \leq 0.6$) and $\text{CrTe}_{1-x}\text{Se}_x$ ($0 \leq x \leq 0.5$) [8] are plotted vs. (a) first neighbor distance of Cr atoms ($c/2$), (b) second neighbor distance a , and (c) an axial ratio c/a which corresponds to the bonding angle between two Cr atoms and a nonmagnetic atom. The corresponding changes with pressure up to about 10 kbar are shown in dotted lines in the same figure.

These interaction curves, drawn by implicit parameters of components and pressures,

show that the Curie temperatures in NiAs-type chromium compounds depend on the atomic separations not only of magnetic atoms, but also of nonmagnetic atoms. The fact suggests that the indirect exchange interaction is important along with direct one in the ferromagnetic chromium compounds of NiAs-type.

(b) CrSb

The compression curves of a and c axes of CrSb are very anomalous in the pressure range from 80 to 100 kbar. We would interpret the fact assuming a second order magnetic transition at about 100 kbar and at the room temperature. If the transition is that from antiferromagnetic state to paramagnetic state, it would accompany the anomalous compressibility of a and c axes. The lattice distortion of CrSb due to the antiferromagnetic ordering (exchange magnetostriction) is very large, that is, $\Delta a/a_0 = +1.5$ per cent and $\Delta c/c_0 = -3.3$ per cent at the room temperature and the atmospheric pressure [9, 10]. The lattice parameters of fictitious paramagnetic CrSb at the room temperature and the atmospheric pressure are shown in Fig. 1. The distortion should vanish rapidly near the transition point; a decreases and c increases. Whereas the rapid changes of a and c axes in the range from 80 to 100 kbar shown in Fig. 1 are about -0.8 per cent and $+3$ per cent, respectively. Therefore, it could be considered that the large exchange magnetostriction of antiferromagnetic CrSb vanishes at 100 kbar and that the normal compressibility of paramagnetic lattice is found above 100 kbar both in a and c axes. In Fig. 1, the extrapolated lattice parameters of paramagnetic CrSb at the room temperature and the atmospheric pressure are connected with the compression curves above 100 kbar by the fine dotted lines, which would be the compression curves of a fictitious paramagnetic CrSb below the transition pressure.

If the Néel temperature T_N (720°K at the

atmospheric pressure) descends to the room temperature at 100 kbar, it means that the average value of dT_N/dp is about -5 deg kbar $^{-1}$. This is not an abnormal value compared with those of other NiAs-type magnetic compounds. But unfortunately, the pressure dependence of the Néel temperature has not been measured. It could be predicted by Ehrenfest's relation for a second order phase transition;

$$\frac{dT_N}{dp} = \frac{\Delta\chi}{\Delta\alpha}$$

where $\Delta\chi$ is the change of compressibility and $\Delta\alpha$ is the change of thermal expansion coefficient at the Néel point. The compressibility data at the room temperature exhibit $\Delta\chi = \chi_2$ (above 100 kbar) $-\chi_1$ (below 100 kbar) $= 5 \times 10^{-4}$ kbar $^{-1}$ as shown in Fig. 3. The X-ray data [9] at the atmospheric pressure exhibit $\Delta\alpha = \alpha_2$ (above 720°K) $-\alpha_1$ (below 720°K) $= -7 \times 10^{-5}$ deg $^{-1}$. Consequently,

$$\frac{dT_N}{dp} = -7 \text{ deg kbar}^{-1}.$$

In conclusion, we would interpret that the transition from the antiferromagnetic state to the paramagnetic state occurs at 100 kbar and that the anomalous compressibility is accompanied by the transition.

Acknowledgement—We wish to thank Dr. T. Kaneko of Tohoku University for providing us the materials of our experiments.

REFERENCES

1. NAGASAKI H., WAKABAYASHI I. and MINOMURA S., *J. Phys. Chem. Solids* **30**, 329 (1969).
2. IDO H., KANEKO T. and KAMIGAI K., *J. phys. Soc. Japan* **22**, 1418 (1967).
3. PEREZ-ALBUERNE E. A., FORSGREN K. F. and DRICKAMER H. G., *Rev. scient. Instrum.* **35**, 29 (1964).
4. NAGASAKI H. and MINOMURA S., *J. phys. Soc. Japan* **19**, 1496 (1964).
5. BRIDGMAN P. W., *Proc. Am. Acad. Arts Sci.* **76**, 1 (1945).
6. PEREZ-ALBUERNE E. A. and DRICKAMER H. G., *J. chem. Phys.* **43**, 1381 (1965).
7. LYNCH R. W., *J. chem. Phys.* **47**, 5180 (1967).
8. LOTGERING F. K. and GORTER E. W., *J. Phys. Chem. Solids* **3**, 238 (1957).
9. SNOW A. I., *Rev. mod. Phys.* **25**, 127 (1953).
10. WILLIS B. T. M., *Acta crystallogr.* **6**, 425 (1953).

STUDY OF THE NEUTRAL VACANCY IN SEMI-CONDUCTORS*

M. LANNOO and P. LENGART

Laboratoire de Physique des Solides, Institut Supérieur d'Electronique du Nord,
3, rue François Baes, 59 Lille, France

(Received 7 October 1968)

Abstract—The neutral vacancy in semi-conductors is studied by using the Green's operator method combined with the tight-binding approximation. A simple model for the band structure with only one resonance integral between first neighbours is used. First a two-band linear semi-conductor, where analytical solutions are obtained, is studied and then the method is applied to diamond. In both cases bound states are obtained whose extension is discussed. Application is made to the calculation of the formation energy of the vacancy in diamond which is found to be about 9 eV without taking relaxation into account.

1. INTRODUCTION

THE FIRST theoretical study of the vacancy in diamond has been made by Coulson and Kearsley[1] in order to interpret the GR1 optical absorption band observed by Clark *et al.*[2]. They considered the first neighbours of the vacancy as forming a molecule and they used a molecular orbital treatment by taking combinations of the sp^3 hybrid orbitals pointing from each atom towards the center of the vacancy. A similar study has been made by Yamaguchi[3] and another by Stoneham[10] using the point-ion approximation.

On the basis of a simple molecular Hartree model, Watkins[4] has given a very successful interpretation of his EPR experiments in silicon. He has identified two spectra with the simple positive and negative vacancies.

Contrasting with those molecular models, other calculations have been made by Bennemann[5] and Callaway[6] who have both made use of the Green's function method. Such studies are not easily comparable with Coulson and Kearsley's.

We want here to connect the molecular and band descriptions for defects. The simplest

way to do it is to use the tight-binding approximation which involves the same approximations as Coulson and Kearsley's model. We have simplified the problem by considering only one resonance integral between first neighbours. Clearly this is an oversimplification but we obtain the first significant correction to a molecular approach and the results are useful for discussion. This will also serve as a basis for future work including resonance integrals up to second nearest neighbours and taking electron-electron interactions into account.

2. GENERAL CONSIDERATIONS

We use here the Green's operator method combined with the tight-binding approximation. In cases where the vacancy produces a short-range perturbation potential, this leads to very simple calculations.

(A) Mathematical formulation

We first choose a one-band system to detail the theory with maximum simplicity. Let H be the perfect crystal Hamiltonian and $|\phi\rangle$ its solutions. We may write:

$$H|\phi\rangle = E|\phi\rangle. \quad (1a)$$

In the tight-binding approximation $|\phi\rangle$ is

*Cet article constitue une partie de ma thèse de Doctorat d'Etat en Sciences Physiques enregistrée au C.N.R.S. sous le no. A.O. 2646.

a linear combination of the N atomic orbitals (N is the number of atoms), i.e.:

$$|\phi\rangle = \frac{1}{\sqrt{N}} \sum_j e^{i\mathbf{R}_j} |j\rangle \quad (1b)$$

where $|j\rangle$ is the atomic orbital on site \mathbf{R}_j .

If we now create a vacancy at the origin the new Hamiltonian is H' and the wave functions $|\psi\rangle$, but $|\psi\rangle$ is now a combination of $N-1$ atomic orbitals only, because the atomic potential and wave functions of the central atom are missing:

$$|\psi\rangle = \sum_{j \neq 0} a_j |j\rangle. \quad (2a)$$

An easy way of joining the perturbed crystal to the unperturbed one is to write $|\psi\rangle$ in the following form:

$$|\psi\rangle = |\phi\rangle + GV|\psi\rangle \quad (2b)$$

where

$$G = \lim_{\eta \rightarrow 0} \frac{1}{E - H + i\eta}$$

is the Green's operator of the perfect crystal and V the perturbative potential. If the atomic orbitals are assumed to be orthogonal, the relation (2) leads to:

$$\langle 0|\psi\rangle = 0. \quad (3)$$

This condition is obvious from another point of view. H can be represented by a $N \times N$ matrix using the atomic orbitals as a basis and H' by a $(N-1) \times (N-1)$ one. To relate the two problems we must write H' as a $N \times N$ matrix by adding a row and a column of zeros corresponding to $\langle 0|H'|m\rangle$ elements. In this way we obtain a condition on the perturbative potential, i.e.:

$$\langle 0|V|m\rangle = -\langle 0|H|m\rangle. \quad (4)$$

Equations (3) and (4) are equivalent.

(B) Study of bound states

For the bound state energy there is no solution of H . The bound state wave function is then given by:

$$|\psi\rangle = GV|\psi\rangle. \quad (5)$$

If we project on the atomic orbitals we obtain easily the set of equations

$$l \neq 0; \langle l|\psi\rangle = \sum_{j \neq 0}^m G_{lm} V_{mj} \langle j|\psi\rangle \quad (6)$$

and the supplementary condition:

$$\langle 0|\psi\rangle = \sum_{j \neq 0}^m G_{0m} V_{mj} \langle j|\psi\rangle = 0. \quad (7)$$

Equation (6) is a set of $N-1$ linear and homogeneous equations with $N-1$ unknowns which are the $\langle j|\psi\rangle$. To obtain solutions, the determinant of this set of equations must vanish. The energies obtained in this way must also satisfy condition (7) to represent bound states of the vacancy. We can notice that (6) and (7) satisfy the usual condition for bound states which is

$$\det(I - GV) = 0; (N \times N). \quad (8)$$

(C) Extension to many-band systems

It is possible to simplify the study of such systems by taking symmetry into account. Let us assume for instance that the central atom (which will be removed to create the vacancy) has m atomic orbitals. These orbitals form a representation of the point group of the crystal. In a similar way the orbitals on the j th neighbours of the central atom transform into each other under operations of the point group. They also form representations which can be reduced by taking linear combinations of the orbitals.

Now G and V are totally symmetric and can mix only basis functions of the same row of the same irreducible representation. In the simple case where the representation of the point group of the crystal induced by the m atomic orbitals on the center contains only once each irreducible representation, it is possible to factorize the problem into m parts. For each part the equations for the bound states will have the same form as (6) and (7).

As we want first to apply the theory to

deep levels in semi-conductors, we shall first consider a simple linear model and then extend the treatment to diamond.

3. ONE-DIMENSIONAL MODEL SEMI-CONDUCTOR

We consider a linear chain with two orbitals of s and p type by atom. We can build hybridised orbitals by taking their sum and their difference. We take the notation $|j, j+1\rangle$ for the orbital centered on atom j and pointing towards atom $j+1$ (Fig. 1).

(A) Band structure

We shall take a quite simple approximation in order to obtain easily the essential features of the problem. We can write a Bloch function of the perfect problem

$$|\phi\rangle = \frac{1}{\sqrt{N}} \sum_j e^{ikja} [A |j, j+1\rangle + B |j, j-1\rangle]. \quad (9)$$

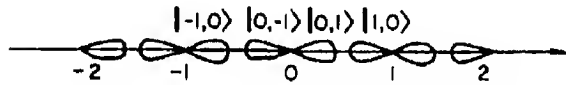


Fig. 1. Linear chain with two orbitals per atom.

If now we define $2\epsilon = E_p - E_s$ and $x = E - (E_s + E_p)/2$ where E_s and E_p are the free atom energy values, we obtain for A and B the set of equations

$$\begin{aligned} xA + (\epsilon + \lambda e^{ika})B &= 0 \\ xB + (\epsilon + \lambda e^{-ka})A &= 0 \end{aligned} \quad (10)$$

when we take only into account the resonance integral

$$-\lambda = \langle j, j+1 | V_j | j+1, j \rangle.$$

The two energy bands are given by:

$$x = \pm (\epsilon^2 + \lambda^2 + 2\epsilon\lambda \cos ka)^{1/2}. \quad (11)$$

The gap is given by $2|\lambda - \epsilon|$, but in the physical case of interest where $\lambda \gg \epsilon$, we obtain $2(\lambda - \epsilon)$ and the width of one band is 2ϵ

(B) The vacancy

To use symmetry considerations we form two types of functions:

Symmetric:

$$\begin{aligned} |j\rangle &= \frac{|j, j-1\rangle + |-j, -j+1\rangle}{\sqrt{2}} \\ |j'\rangle &= \frac{|j, j+1\rangle + |-j, -j-1\rangle}{\sqrt{2}} \end{aligned} \quad (12)$$

Antisymmetric:

$$\begin{aligned} |j\rangle &= \frac{|j, j-1\rangle - |-j, -j+1\rangle}{\sqrt{2}} \\ |j'\rangle &= \frac{|j, j+1\rangle - |-j, -j-1\rangle}{\sqrt{2}} \end{aligned}$$

Let us solve first the symmetric case. With the preceding approximations for the band structure the perturbative potential has very simple matrix elements, taking $(E_s + E_p)/2$ as the zero of energy:

$$V_{0'0'} = \epsilon V_{0'1} = \lambda. \quad (13)$$

Applying equation (7) we readily find the simple condition for bound states:

$$G_{0'0'} = 0. \quad (14)$$

This condition is satisfied when $x = 0$, i.e. at the center of the gap.

The same result holds for the antisymmetric bound state. (For details see Appendix A).

This result is physically evident because the two half chains are independent and the levels must be twofold degenerate.

(C) The wave function of the bound state

If we apply (6) to both symmetric and antisymmetric bound states we find for $l \neq 0$

$$\langle l | \psi \rangle = G_{l0, \lambda} \langle l | \psi \rangle. \quad (15)$$

For that state it is possible to determine rapidly the Green's functions which turn out to be:

$$G_{0j'} = 0, G_{0j} = \frac{1}{\lambda} \left(\frac{-\epsilon}{\lambda} \right)^{j-1}. \quad (16)$$

We find easily that the contribution of orbitals $|j\rangle$ and $|j'\rangle$ to the bound state wave function will be:

$$|\langle j'|\psi\rangle|^2 = 0 \quad |\langle j|\psi\rangle|^2 = \left(\frac{\epsilon}{\lambda} \right)^{2(j-1)} (1 - \epsilon^2/\lambda^2). \quad (17)$$

This provides very useful information in comparing that method to a local molecular treatment.

(D) Comparison with a molecular model

A local molecular model of the vacancy would consist in building a molecule with the first neighbours of the vacancy. In that case, if we put:

$$-\gamma = \langle j, j+1 | V_j | j+2, j+1 \rangle$$

we obtain two eigenstates ψ_A and ψ_S (Fig. 2) with a splitting of 2γ .

$$\begin{aligned} \psi_A &= \frac{|1,0\rangle - |-1,0\rangle}{\sqrt{2}} \\ \psi_S &= \frac{|1,0\rangle + |-1,0\rangle}{\sqrt{2}}. \end{aligned} \quad (18a)$$

In our model a careful treatment would consist in including γ in the band structure calculation but it is possible to have immediately an order of magnitude of the result for small γ by perturbation theory. To first order we can see immediately that introducing interaction between second neighbours by γ affects only the first neighbours of the vacancy

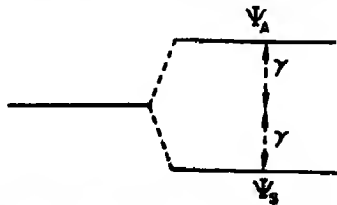


Fig. 2. Local molecular model for the linear chain.

and gives a shift in the energy:

$$-\gamma \left(1 - \frac{\epsilon^2}{\lambda^2} \right) \text{ for the symmetric state} \quad (18b)$$

and

$$+\gamma \left(1 - \frac{\epsilon^2}{\lambda^2} \right) \text{ for the antisymmetric one.}$$

Instead of 2γ we shall find $2\gamma(1 - \epsilon^2/\lambda^2)$. The difference is due to the fact that the zeroth order wave function is spreading out of the molecule. We find the local molecular result in the limit where $\epsilon/\lambda \rightarrow 0$.

4. DIAMOND CASE

We shall apply exactly the same method to the diamond structure except that it is necessary to calculate one of the Green's functions numerically.

(A) Band structure

We use the model of Leman and Friedel[7] which leads to analytical results. The only integral involved in this calculation is:

$$\lambda = -\langle \alpha | V_\alpha | \beta \rangle \quad (19)$$

where α and β are sp^3 hybrid orbitals centered on first neighbours and pointing towards each other.

The essential features of their results are the density of states curve $\nu_0(E)$ (Fig. 3),

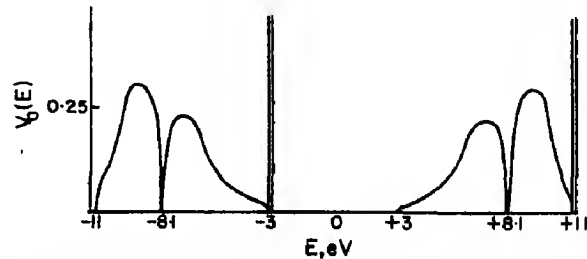


Fig. 3. Density of states per atom $\nu_0(E)$ for diamond with $\lambda = 7$ eV and $4\epsilon = 8$ eV. If we divide λ and 4ϵ by the same factor η , we have to multiply $\nu_0(E)$ and divide the energies by η . The 8 functions are representing zero width bands which occur in the simple model we have used. These bands have totally p character. The zero of energy is $(E_s + E_p)/2$ and the broad bands are symmetric with respect to that origin.

the gap E_g and the valence band width E_v which are given by the formulae:

$$\begin{aligned} E_g &= 2\lambda - 4\epsilon \\ E_v &= 4\epsilon \end{aligned} \quad (20)$$

4ϵ being the promotional energy, $4\epsilon = E_p - E_s$, where E_s and E_p are the atomic energies.

When we take the numerical values of Leman and Friedel

$$\lambda = 7 \text{ eV}; \quad 4\epsilon = 8 \text{ eV} \quad (21a)$$

we find a cohesive energy per atom

$$E_c = \int_{v_B} \nu_0(E) E dE \quad (21b)$$

which is of the order of 23 eV to be compared to the experimental value which is believed to be 7.5 eV. As in the following we shall use this model to calculate the formation energy of the vacancy, we think it is better to fit the value of the cohesive energy to the observed one. So we divide the values of λ and 4ϵ by 3 and take

$$\lambda = 2.3 \text{ eV}; \quad 4\epsilon = 2.7 \text{ eV} \quad (21c)$$

(B) The vacancy

Here we must make some conventions. We label the atoms as in Fig. 4 and design the sp^3 hybrid orbitals (Fig. 5) by

$$|00'\rangle |01'\rangle |02'\rangle |03'\rangle |0'0\rangle |1'0\rangle |2'0\rangle |3'0\rangle. \quad (22a)$$

To use the symmetry properties we use the

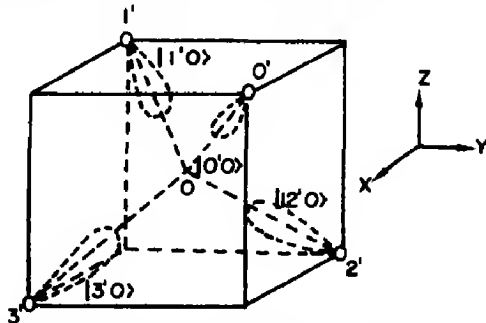


Fig. 4. The vacancy with its four neighbours in the diamond lattice.

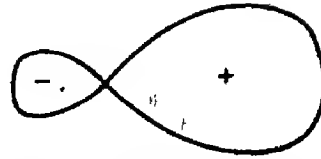


Fig. 5. Schematic representation of a sp^3 hybrid for carbon.

following combinations of (22a)

$$\begin{aligned} |s\rangle &= \frac{1}{2} (|00'\rangle + |01'\rangle + |02'\rangle + |03'\rangle) \\ |x\rangle &= \frac{1}{2} (|00'\rangle - |01'\rangle - |02'\rangle + |03'\rangle) \\ |y\rangle &= \frac{1}{2} (|00'\rangle - |01'\rangle + |02'\rangle - |03'\rangle) \\ |z\rangle &= \frac{1}{2} (|00'\rangle + |01'\rangle - |02'\rangle - |03'\rangle) \end{aligned} \quad (22b)$$

and $|v\rangle$, $|t_x\rangle$, $|t_y\rangle$, $|t_z\rangle$ which are the same combinations of the $|n'0\rangle$.

As shown before, the conditions for bound states are written very simply as

$$\begin{aligned} \langle s|G|s\rangle &= 0; \quad \langle x|G|x\rangle = 0; \quad \langle y|G|y\rangle = 0; \\ \langle z|G|z\rangle &= 0. \end{aligned} \quad (23)$$

The last three conditions are identical giving a threefold degenerate state (T_2), the first one a non-degenerate state (A_1). With the numerical values chosen in (21c) we find that all levels are located practically at the same energy which is about +0.7 eV from the center of the gap. To explain the fact that the (A_1) state and the (T_2) states are nearly degenerate we cannot divide the crystal in four independent parts as for the linear case, but if the states are strongly localized these interactions will be very weak so that these states will be nearly degenerate.

(C) The bound state wave function

We have here a great similarity with the linear chain. The calculation is not so simple but we find that, for the energy of the bound state

$$\langle s|G|v\rangle = \frac{1}{\lambda}, \quad \langle x|G|t_x\rangle = \frac{1}{\lambda}. \quad (24)$$

From this we find (Appendix B) that the con-

tribution of $|\psi\rangle$ to the symmetric bound state, i.e. $|\langle\psi|v\rangle|^2$ is about 0.7. We obtain the same value for the contribution of $|t_x\rangle$, $|t_y\rangle$, $|t_z\rangle$ to the T_2 bound state.

In order to compare with the linear model we have also calculated the contribution of $|v'\rangle$ to the symmetric bound state wave function $|\psi\rangle$ being determined by taking the sum of the three hybrid orbitals other than $|j'0\rangle$ on a first neighbour $|j'\rangle$ and then summing over j' . We find it to be about 0.03 which is negligibly small compared to 0.7. We obtain similar values for the T_2 case. From the similarity with the linear problem we may think that most of the remaining charge will be on the second nearest neighbours.

(D) Comparison with a molecular model

If we build a local molecule with the first neighbours of the vacancy and if we define:

$$\gamma = -\langle 0'0|V_0|1'0\rangle \quad (25)$$

it is easy to see that the splitting between the A_1 (v) level and the T_2 (t_x, t_y, t_z) level is 4γ as shown in Fig. 6.

To compare with this model, we must still use perturbation theory as in the linear case. To first order the shift would be given by:

$$\langle\psi|V|\psi\rangle \quad (26)$$

where $|\psi\rangle$ is the wave function of the bound state and V the perturbative potential which introduces second neighbours interaction. Expression (26) cannot be calculated exactly, but from the similarity with the linear case, we can take for $|\psi\rangle$ only the contribution from the first neighbours which would give a

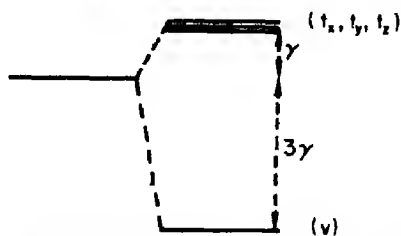


Fig. 6. Local molecular model for the diamond vacancy.

splitting of about $0.7 \times (4\gamma)$. This can be justified in the following way: if we assume that $|\psi\rangle$ extends only up to second nearest neighbours, then all the matrix elements of V vanish except between the first neighbours of the vacancy and if $|\psi\rangle$ extends more, further contribution would be negligible.

To conclude this section we can say that the main features of this Hartree model are:

the existence of bound states

their nearly degeneracy

their strong localization

results quite similar to those of a local molecular treatment when taking into account interaction between second nearest neighbours in first-order perturbation theory.

5. FORMATION ENERGY OF THE VACANCY IN DIAMOND

In principle such a model must give easily the formation energy E_F by summing the energies which are necessary to take one atom out of the crystal and then replace it on the surface.

(A) Simple estimation of E_F

We shall follow Friedel[8] by saying that the valence band is built from bonding orbitals which are the sums of sp^3 hybrid orbitals centered on first neighbours and pointing towards each other. The valence band is filled when we put two electrons in each bond. When forming a bond we gain an energy of 2λ .

We can evaluate the cohesive energy per atom in the following way: to dissociate the whole crystal it is necessary to cut two bonds per atom, i.e. to spend an energy of 4λ per atom, but the atoms are still in their sp^3 state. The cohesive energy per atom is then approximately given by [7, 8]

$$E_c \approx 4\lambda - 4\epsilon \quad (27)$$

which is about 6.5 eV with the numerical values of (21c). This expression (27) would be rigorous if the valence band would be symmetric[7].

Now to create a vacancy, we have to cut four bonds, i.e. to spend 8λ . If we put the corresponding atom on the surface, we create two new bonds and gain 4λ . In this simple way we obtain the formation energy of the vacancy as:

$$E_F \approx 4\lambda = 9.2 \text{ eV.} \quad (28)$$

(B) Numerical calculations

We have seen before (21b) that the exact value of E_c can be calculated and we have fitted this value to 7.5 eV which is the experimental one.

To create a vacancy we have to take one atom out of the crystal which needs an energy ΔE ; to replace it on the surface which needs $-E_c$. The problem is to calculate ΔE . It is given by:

$$\Delta E = \int \delta n(E) E dE \quad (29)$$

where $\delta n(E)$ is the total variation of the density of states between the crystal with the vacancy and the perfect crystal, and the integration is made on occupied states.

To know the limits of integration we must fill the new states with electrons. Before creating the vacancy the crystal contained $2N$ atoms and $8N$ valence electrons. Now there are $2N-1$ atoms, i.e. $8N-4$ possible states. As there are 4 bound states, only $8N-8$ states remain for the band and particularly $4N-4$ for the valence band. As we have $8N-4$ electrons, we can put $8N-4$ into the valence band and 4 into the bound states. Then:

$$\Delta E = \int_{VB} \delta n(E) E dE + 4 E_B \quad (30a)$$

where E_B is the energy of the bound states.

We can write:

$$\delta n(E) = \frac{1}{\pi} \frac{d}{dE} \left[\text{Arc tg} \frac{\text{Im det}(I - GV)}{\text{Re det}(I - GV)} \right]. \quad (30b)$$

This allows us to calculate ΔE (Appendix B) and we find:

$$\Delta E \approx 16.4 \text{ eV.} \quad (31)$$

Then we obtain for the formation energy:

$$E_F \approx 8.9 \text{ eV.} \quad (32)$$

The main conclusion from the simple study is that E_F is greater than the cohesive energy but of the same order of magnitude. We must notice here that this value of the formation energy must be reduced by relaxation. This could perhaps give for E_F a value smaller than for E_c .

6. CHARGED STATES AND RELAXATION

(A) Charged states

Let us first consider the neutral state. As for the band structure we write

$$H' = T + \sum_{l \neq 0} V_l \quad (33)$$

where T is the kinetic energy and V_l are the same Hartree potentials as in H . In this way it is quite easy to define the matrix of the perturbative potentials to solve the problem numerically.

Now we can see very easily the difference between the charged states. As there are more or less electrons than in the neutral case the one-electron potentials will not be the same. One way to determine them could be to do a self-consistent calculation, i.e. to express the new potentials as a function of the electronic density, then to calculate the electronic density deduced from those values, and finally to equal the values.

(B) Relaxation

It is easy to see that relaxation can formally be studied by changing some integrals between the first neighbours of the vacancy or more if we want a better description. If relaxation is not too large it is possible to develop the matrix elements to first order in the normal coordinates of the system. We can calculate the

mean energy of the system as a function of these normal coordinates, add the elastic energy and minimise the total energy with respect to all the coordinates. This will give the new atomic configurations and the gain in energy due to relaxation and distortion (Jahn-Teller effect)[9].

CONCLUSION

We have seen that the Green's function method combined with the tight binding approximation can lead to straightforward and physically interesting results in the model we have used.

In a first part, we have studied a completely analytical model (linear chain) which gave the following results: two degenerate bound states exist in the gap and their localization depends on the ratio of the promotional energy to the resonance integral between first neighbours; when this ratio is weak we find results similar to a local molecular treatment.

We have then studied the physically important case of the neutral vacancy in diamond in the same approximation. We find bound states of (A_1) and (T_2) symmetry in the gap, which are nearly degenerate and strongly localized (0.7 of the population on the first neighbours). We conclude that a local molecular model is well justified in that approximation. A calculation of the formation energy of the vacancy gives about 9 eV when the parameters of the band structure λ and 4ϵ are determined to fit the cohesive energy per atom to the experimental value 7.5 eV. This value must be reduced by relaxation.

The first step for a better treatment including the relaxation would be to study the neutral vacancy in a better description of the band structure. Another point of interest would be to compare our model to Coulson and Kearsley's when taking electron-electron interaction into account, and also to do a self-consistent calculation for the charged states.

Acknowledgements—We wish to thank Professor J. Friedel for his helpful encouragement and Dr A. M. Stoneham and Dr. G. Leman for stimulating discussions.

REFERENCES

1. COULSON C. A. and KEARSLEY M. J., *Proc. R. Soc.* **241A**, 433 (1957).
2. CLARK C. D., DITCHBURN R. W. and DYER H. E., *Proc. R. Soc.* **234A**, 363 (1956); *ibid* **237A**, 75 (1956).
3. YAMAGUCHI T., *J. phys. Soc. Japan* **17**, 1359 (1962).
4. WATKINS G. D., In *Proc. Intl Conf. Physics of Semiconductors, Paris, 1964*, Vol. 3, p. 97. Academic Press, New York (1965).
5. BENNEMANN K. H., *Phys. Rev.* **137A**, 1497 (1965).
6. CALLAWAY J. and HUGHES A. J., *Phys. Rev.* **156**, 3, 860 (1967).
7. LEMAN G. and FRIEDEL J., *J. appl. Phys. (Suppl)* **33**, 281 (1962); LEMAN G., *Ann. Phys.* **7**, 505 (1962).
8. FRIEDEL J., *Remarques sur la Structure Électronique des Défauts d'Irradiation dans les Solides Covalents*. Orsay (1967).
9. LANNOO M., Thèse de 3ème cycle. Orsay, unpublished; FRIEDEL J., LANNOO M. and LEMAN G., *Phys. Rev.* **164**, 1056 (1967).
10. STONEHAM A. M., *Proc. phys. Soc.* **88**, 135 (1966).

APPENDIX A

Green functions in the linear model

We have seen that, outside the bands:

$$G = \sum_{k,\nu} \frac{|\phi_k^\nu\rangle \langle \phi_k^\nu|}{E - E_\nu(k)} = \sum_{k,\nu} \frac{|\phi_k^\nu\rangle \langle \phi_k^\nu|}{x - x_\nu(k)}. \quad (\text{A.1})$$

This allows us to calculate very simply the matrix elements $\langle 0'|G|j\rangle$ and $\langle 0'|G|j'\rangle$ in the symmetric case:

$$\langle 0'|G|j\rangle = \frac{1}{2N} \sum_{k,\nu} \frac{(A+B)(A e^{-ikja} + B e^{ikja})}{x - x_\nu(k)} \quad (\text{A.2})$$

$$\langle 0'|G|j'\rangle = \frac{1}{2N} \sum_{k,\nu} \frac{(A+B)(A e^{ikja} + B e^{-ikja})}{x - x_\nu(k)}$$

and in the antisymmetric one:

$$\langle 0'|G|j\rangle = \frac{1}{2N} \sum_{k,\nu} \frac{(A-B)(A e^{-ikja} - B e^{ikja})}{x - x_\nu(k)} \quad (\text{A.3})$$

$$\langle 0'|G|j'\rangle = \frac{1}{2N} \sum_{k,\nu} \frac{(A-B)(A e^{ikja} - B e^{-ikja})}{x - x_\nu(k)}$$

Bound states

The conditions for symmetric and antisymmetric bound states are:

$$\langle 0'|G|0'\rangle = 0. \quad (\text{A.4})$$

From equations (10) A and B are complex conjugate and from normalization of the wave function we have:

$$|A| = |B| = 1/\sqrt{2}. \quad (\text{A.5})$$

We can then put:

$$A = 1/\sqrt{2} e^{i\theta}, \quad B = 1/\sqrt{2} e^{-i\theta}. \quad (\text{A.6})$$

With those notations it is easy to write:

$$\langle 0' | G | 0' \rangle \text{ symmetric} = \frac{1}{2N} \sum_{k,v} \frac{1 + \cos 2\theta}{x - x_v(k)} \quad (\text{A.7})$$

$$\langle 0' | G | 0' \rangle \text{ antisymmetric} = \frac{1}{2N} \sum_{k,v} \frac{1 - \cos 2\theta}{x - x_v(k)}.$$

These expressions allow us to show the relation

$$G_{0',0'} \text{ sym.}(x) = -G_{0',0'} \text{ antisym.}(-x). \quad (\text{A.8})$$

When there is a symmetric bound state at energy x , there is also an antisymmetric one at $-x$.

In the symmetric case we have, treating \sum_k as an integral on k

$$G_{0',0'} = \frac{1}{2\epsilon} \left[1 - \sqrt{\frac{(x-\epsilon)^2 - \lambda^2}{(x+\epsilon)^2 - \lambda^2}} \right]. \quad (\text{A.9})$$

We immediately see that the solution is $x = 0$ in this case; from (A.8) it is also a solution for the antisymmetric one.

Calculation of other Green's functions

We shall do it only in the symmetric case because there are similar relations in the antisymmetric one.

From (10), (A.2) and the fact that $\lim_{E \rightarrow \infty} E \langle 0' | G | j \rangle$ and $E \langle 0' | G | j' \rangle$ with $j' \neq 0'$ is zero, we can easily deduce the relations:

$$\begin{aligned} G_{0',1} &= \frac{1}{\lambda} [1 - (x + \epsilon) G_{0',0'}] \\ G_{0',1'} &= -\frac{1}{\epsilon} [x G_{0',1} + \lambda G_{0',0'}] \\ G_{0',J} &= -\frac{1}{\lambda} [x G_{0',J-1} + \epsilon G_{0',J-1'}] \\ G_{0',J'} &= -\frac{1}{\epsilon} [x G_{0',J} + \lambda G_{0',J-1'}]. \end{aligned} \quad (\text{A.10})$$

For the bound states $x = 0$ and we find

$$G_{0',1} = \frac{1}{\lambda}; G_{0',1'} = 0; G_{0',J} = \frac{1}{\lambda} \left(\frac{-\epsilon}{\lambda} \right)^{J-1}; G_{0',J'} = 0. \quad (\text{A.11})$$

From (15) we see that the contribution of the orbitals $|j\rangle$ and $|j'\rangle$ to the bound state wave function is:

$$\begin{aligned} |\langle j' | \psi \rangle|^2 &= 0 \\ |\langle j | \psi \rangle|^2 &= \left(\frac{\epsilon}{\lambda} \right)^{2(J-1)} |\langle 1 | \psi \rangle|^2. \end{aligned} \quad (\text{A.12})$$

From normalization of the wave function we find

$$|\langle 1 | \psi \rangle|^2 = 1 - \frac{\epsilon^2}{\lambda^2}. \quad (\text{A.13})$$

APPENDIX B

Green functions for diamond

In the work of Leman and Friedel the Bloch functions of the perfect crystal were written

$$|\phi\rangle = \frac{1}{C\sqrt{2N}} \sum_j e^{ik_j R} \sum_n (A_n |\psi_{jn}\rangle + A_n^* |\psi'_{jn}\rangle) \quad (\text{B.1})$$

where diamond is considered to have two sublattices, $|\psi_{jn}\rangle$ being centered on the atoms of the first sublattice, $|\psi'_{jn}\rangle$ on the atoms of the other one. The index n refers to the direction in which point the sp^3 hybrid orbitals $|\psi_{jn}\rangle$ and $|\psi'_{jn}\rangle$. The equations which relate the coefficient are:

$$xA_m + \epsilon \sum_{m=0}^3 A_m + \lambda \alpha_m A_m^* = 0; \quad m = 0, 1, 2, 3 \text{ with } x = E - E_p \quad (\text{B.2})$$

and their complex conjugates. The α_m are defined in the following way:

$$\alpha_0 = 1; \alpha_1 = e^{-i a/2 (k_x + k_y)}; \alpha_2 = e^{-i a/2 (k_x + k_z)}; \alpha_3 = e^{-i a/2 (k_y + k_z)} \quad (\text{B.3})$$

a being the crystalline parameter.

Bound states

We start from the expression of G in the gap

$$G = \frac{V}{(2\pi)^3} \sum_v \int \frac{|\phi^v\rangle \langle \phi^v|}{x - x_v(k)} d^3 k \quad (\text{B.4a})$$

V being the volume of the crystal.

We can define for the symmetric case a new coefficient:

$$C_s = \frac{\sum_{n=0}^3 A_n}{2C}. \quad (\text{B.4b})$$

This coefficient represents the proportion of s character in the total wave function. The symmetric matrix element of G on the center can be written:

$$G_{ss} = \frac{1}{2} \int \frac{C_s^2(E') n(E') dE'}{E - E'}. \quad (\text{B.4c})$$

This expression can be calculated numerically and we find that it vanishes at 0.7 eV from the center of the gap (with λ and ϵ given by (21c)).

In the same way we can define the three other independent combinations of the A_n which we call C_x , C_y and C_z . We have the relation:

$$C_s^2 + C_x^2 + C_y^2 + C_z^2 = 1. \quad (\text{B.5})$$

We can express

$$G_{xx} = \frac{1}{2} \int \frac{C_x^2(E') n(E') dE'}{E - E'}. \quad (\text{B.6})$$

A numerical calculation also gives the x type bound state at +0.7 eV.

Extension of the bound state

We treat only the symmetric case, the other cases being quite identical to it. We shall try to calculate the contribution of the first neighbours to the bound state wave function. We find easily from normalization

$$|\langle v|\psi\rangle|^2 = -\frac{1}{\lambda^2 \frac{d}{dE} G_{ss}} \approx 0.7. \quad (\text{B.7})$$

If we go further, i.e. if we consider the orbital $|\psi'\rangle$ formed from the sum of the three other hybrid orbitals on the first neighbours, we find:

$$|\langle v'|\psi\rangle|^2 \approx 0.03 \quad (\text{B.8})$$

which is quite negligible.

Formation energy

We detail here the calculation of ΔE given by (29). We have to determine:

$$\int_{v,b} \delta n(E) E dE = \int_{x1}^{x2} \delta n(E) E dE. \quad (\text{B.9})$$

It is easier to calculate the variation of the total number of states having an energy smaller than E , which is:

$$\delta N(E) = \int^E \delta n(E') dE' = \frac{1}{\pi} \text{Arc tg} \left[\frac{\text{Im det}(I - GV)}{\text{Re det}(I - GV)} \right]. \quad (\text{B.10})$$

We then express (B.9) under the form

$$E_x \delta N(E_x) \sim \int_{E_1}^{E_2} \delta N(E) dE. \quad (\text{B.11})$$

The algebraic calculation of (B.10) gives

$$\delta N(E) = \frac{1}{\pi} \left[\text{Arc tg} \frac{\text{Im } G_{ss}}{\text{Re } G_{ss}} + 3 \text{Arc tg} \frac{\text{Im } G_{xx}}{\text{Re } G_{xx}} \right]. \quad (\text{B.12})$$

In Fig. 7 we give the shape of the real part of G_{ss} and G_{xx} and in Fig. 8 we give the result of the calculation of $\delta N(E)$ from formula (B.12).

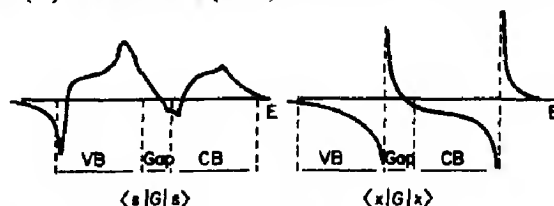


Fig. 7. Shape of the Green's function $\langle s|G|s \rangle$ and $\langle x|G|x \rangle$ for diamond inside the valence (VB) and conduction (CB) bands, and in the gap.

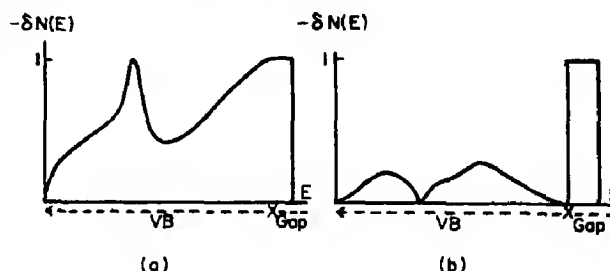


Fig. 8. Curves representing $-\delta N(E)$, where $\delta N(E)$ is the variation of the total number of states due to the vacancy (a) for the symmetric states (b) for one of the T_2 states. These quantities tend to 1 at the valence band edge but fall to zero at the bound state energy. They will rise again to 1 at the conduction band edge, showing that four states have been removed.

ESR-RESONANCES IN DOPED GaAs and GaP*

S. HARALDSON† and C-G. RIBBING

Solid State Division, Institute of Physics, University of Uppsala, Uppsala, Sweden

(Received 6 May 1969)

Abstract—ESR-signals from GaP:Sn, GaP:Si and GaAs:Si, GaAs:Te are reported. GaP:Sn crystals give two isotropic signals. The larger one of them with g -value 1.998 is attributed to bound donor electrons. No definite conclusion about the origin of the other line with $g = 2.131$ is presented. The system GaP:Si gave only one line with $g = 1.985$, which we also attribute to bound donor electrons. GaAs:Si and GaAs:Te give each one very broad isotropic signal with $g = 2.07$ and $g = 2.06$ respectively. These values do not agree with earlier measurements on GaAs. They also disagree with theoretical values for shallow donors obtained by application of Roth's formula for g -factors. It is concluded that these signals are not likely to come from shallow donor electrons. The problems of treating impurity-levels in GaAs and GaP within the effective mass formalism are discussed. It is pointed out that a calculation following the Koster-Slater-method might be valuable in those cases of relatively deep donors.

INTRODUCTION

SINCE Fletcher *et al.*[1] reported the first spin resonance measurement from bound donor electrons, the field of ESR in impurity semiconductors has grown very rapidly. Plenty of information about the detailed nature of these defects has been gathered, most of which is available in survey-articles by Ludwig and Woodbury [2] and Feher [3].

In 1967 Title [4] reported spin-resonance lines from the donors Si, Se and Te in GaP. Within the experimental error he got the same g -factor 1.9976 in all cases. The result that the g -factor is independent of the dopant is in agreement with the effective mass approximation developed by Luttinger and Kohn [5], and the main result of Roth's [6] calculation. She obtained, by introducing spin-orbit coupling to first order and using a two-level approximation of the band-structure, comparatively simple formulas for the g -factors of conduction electrons in Si and Ge. The numerical results were in fair agreement with

the measured ones and an earlier, similar calculation for the extreme case of conduction electrons in InSb [7] gave a good agreement with the experimental result reported later by Bemski [8].

On the other hand, Title's straight-forward application of Roth's formula to the case of GaP gave not a very good numerical agreement with his experimental g -factor. Title discusses several causes to this numerical discrepancy among which we quote three: (1) donor levels in GaP are so deep, that the effective mass approximation may break down. (2) the relevant effective masses in GaP are not known, so an average has to be used. (3) the two-level approximation in Roth's calculation may be insufficient for GaP as for the earlier treated case of Si.

The purpose of this paper is to report some further ESR-signals from two III-V-compounds, mainly doped with group IV-elements, and discuss their origin. The problems connected with the application of Roth's formulae to these compound semiconductors will be pointed out.

EXPERIMENTAL

The experiments were carried out on a standard Varian 4500 X-band ESR spectro-

*This work has been supported in part by the United States Air Force Office of Scientific Research under Contract AF 61(052)-937 and in part by the Swedish Natural Science Research Council.

†Present address: Kenya Science Teachers College, P.O. Box 30 596, Nairobi, Kenya.

meter equipped with a multipurpose rectangular cavity and a 100 kHz-modulation-unit. In all measurements reported here the klystron frequency was ≈ 9.4 GHz.

The measurements had to be carried out at low temperatures. In all cases but one we had to go down to 4.2°K. Principally two methods are possible to achieve this cooling: Either to immerse the whole cavity with the sample and part of the wave-guide in the liquid helium, or to introduce a quartz-finger-dewar with the sample inside it, into the cavity. In the first case you cannot use the modulation-coils in the cavity-walls since this causes too much Joule-heating, i.e. you lose the enhanced sensitivity obtained by the 100 kHz-modulation. In the second case the boiling of the liquid is bound to be rather violent since there is no space for an outer liquid nitrogen jacket around the finger, which cannot even be silvered to protect against radiation.

We have chosen the latter way, often called the cold-finger method, mainly because it allowed us to benefit from the increased sensitivity through the 100 kHz-modulation. Details of the arrangement have been described elsewhere[9]. The four crystal-systems investigated were GaP doped with Sn and Si, GaAs doped with Si and Te*. GaP:Sn, GaAs:Si and GaAs:Te were single crystals, GaP:Si polycrystalline of high purity produced at the Bell Telephone Laboratories. Doping concentration was of the order of 10^{17} cm $^{-3}$ and the doped samples give Si-Si pair spectra in contrast to the undoped ones whose Si-concentration is believed to be $\ll 10^{18}$ cm $^{-3}$. The GaAs:Si crystal was pulled horizontally according to the Bridgman technique. The Si-concentration was about 10^{18} cm $^{-3}$. The GaAs:Te crystal was made by floating zone purification and

the Te-conc. also of the order 10^{18} cm $^{-3}$. Some acceptor impurities were probably present in the last two samples. The Sn-concentration in GaP:Sn was estimated to be in the range 10^{17} – 10^{18} cm $^{-3}$.

To ensure good accuracy of the values of the magnetic field, NMR-technique was used to fix certain field-points between which interpolation could be done. We estimated that errors in the determination of the magnetic field could be neglected compared to other errors such as asymmetry in line-shape, variation in klystron-frequency etc.

RESULTS AND DISCUSSION

The *g*-values and line-widths of the ESR-signals for the investigated crystal-systems are given in Table 1 and Fig. 1. In the table are included some related results reported by other authors. The figures show the standard 1st derivative representation of microwave-absorption vs. magnetic field strength. Among our samples only GaP:Sn gave significant signals already at 77°K. The strength of these signals increased about 100 times when the temperature was lowered to 4.2°K.

To ensure that the signals were caused by the doping of the crystals we made similar measurements on the corresponding undoped samples in the cases of GaP:Sn and GaP:Si. In neither case did the signals from the doped samples appear.

The ESR-spectrum from GaP:Sn consisted of two strong isotropic lines and five, much weaker anisotropic lines. The *g*-value and crystalline field splitting parameter obtained for the five lines made it possible to identify Fe $^{3+}$ as an unwanted impurity in our sample. The details of this are reported in [9]. The larger of the isotropic lines with *g*-value 1.998 can certainly be attributed to bound donor electrons from the Sn-dopant. The numerical values: *g*-factor and linewidth, agree with those reported by Title[4]. The puzzling feature is however the second isotropic line with such a high positive *g*-shift as 0.129. The possibility that this strong signal origin-

*We gratefully acknowledge the helpfulness of Dr. C. J. Frosch, Bell Telephone Lab. New Jersey for providing the GaP-Si samples and Tekn. lic. H. Nettelblad, HAFO-institute, Stockholm for giving us the GaAs:Si and Te crystals.

Table 1. Observed g -factors and approximate line-widths Δ in g , for different dopants in GaP and GaAs. Unless otherwise specified $T = 4.2^\circ K$

Dopant Host	Zn	Cd	Si	Sn	S	Se	Te
g			$1.985 \pm 0.003^{(a)}$	$1.998 \pm 0.001^{(a)}$			
GaP				2.131 ± 0.001		$1.9976 \pm 0.0008^{(b)}$	
Δ			70	55		77°K	
	$\perp 8.1^{(c)}$	$\perp 6.7^{(c)}$	$2.07 \pm 0.02^{(a)}$	25		45-60	$2.06 \pm 0.01^{(a)}$
		$\parallel 3.4^{(d)}$					
GaAs		77K					
g							
Δ	20	300 ^(d)	170				160

(a) Our result, cf. [9].

(b) Title 1967 [4].

(c) Title 1963 [10].

(d) Fedotov *et al.* 1968 [11]. \perp : B orthogonal to stress; \parallel : B parallel to stress.

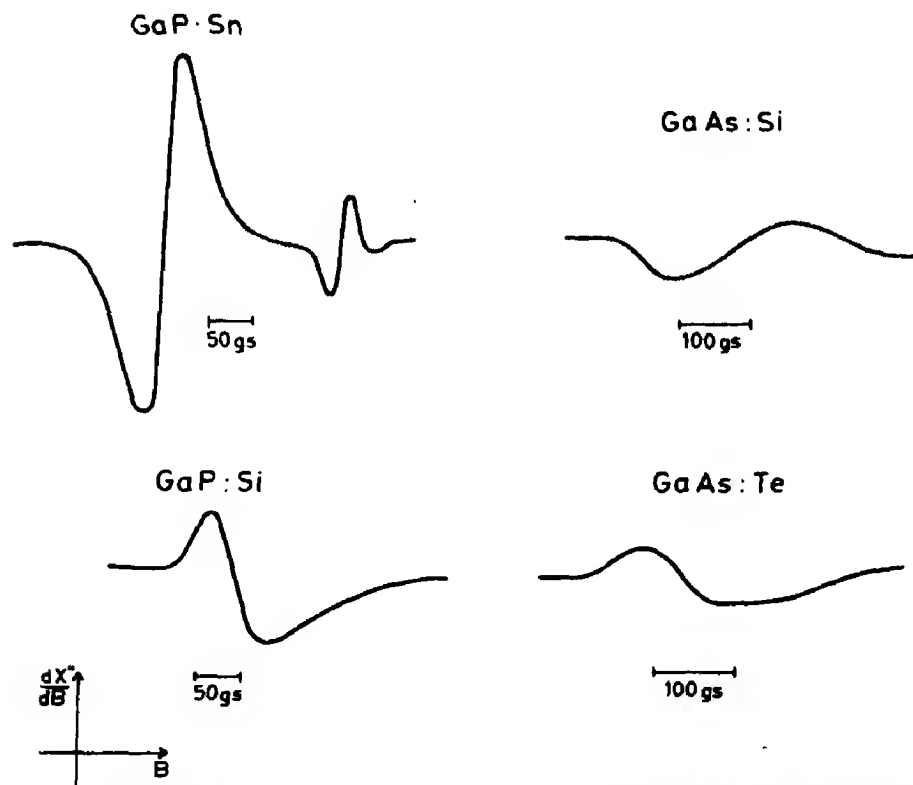


Fig. 1. The signals obtained from the four crystal systems at $4.2^\circ K$ in the standard first derivative representation of magnetic susceptibility χ' vs. magnetic field B (no quantitative intensity-comparisons should be made, since the signals have been recorded with different amplifications).

ates from another unwanted impurity can not be ruled out completely. Due to it's isotropic character however, it would have appeared even in the polycrystalline undoped sample

if the impurity belonged to the matrix material. We consider it unlikely that such a high concentration of an unwanted impurity should be caused only by the Sn-doping. Finally,

if the doping introduced another impurity, it remains to explain the high g -value of the signal. Oxygen and sulphur are common impurities in the GaP but are both group VI donors and should give signals in accordance with Title's results[4]. It would be tempting to assume that Sn could substitute both for Ga and P-atoms in the lattice, thus acting both as donor and acceptor. The second line should then be due to transitions between Zeeman-levels of a hole bound to an acceptor. However, acceptor-holes should not give rise to EPR-signals according to earlier experiments and theoretical considerations. Kohn[12] argues that the width of the energy-level of an acceptor is larger than the transition energy $h\nu$ in X-band experiments. The reason for this large energy-spread could be the electron-lattice interactions. Kohn also suggests that random internal stresses, due to dislocations, lift the degeneracy of the valence band, which in turn broadens the signal beyond detection. The second argument was tested by Feher, Hensel and Gere[13] who applied an uniaxial pressure to boron-doped silicon and only then detected an ESR-signal. A similar experiment on GaAs doped with Cd, was later made by Title[10] which also confirmed Kohn's second suggestion. The other communication on Cd-doped GaAs, by Fedotov *et al.*[11], reported however an acceptor-line obtained without applying any external stress. The authors did not claim that their results contradicted those mentioned—they believed that the mechanical treatment of the crystal had caused such a large uniaxial strain that it overcame the random strains due to dislocations.

These considerations make it difficult to reach a definite conclusion about the origin of the isotropic line with $g = 2.131$ in GaP-Sn. We suggest that, either a deep donor of unknown origin, or a combined impurity center with Sn and perhaps with the Fe^{3+} -ions, could give rise to a signal of this nature. We believe that careful optical measurements

and analysis might give valuable information for the solution of this problem.

The line obtained from GaP:Si we consider to have an easily conceived origin. There are good reasons to believe that it is caused by electrons bound to the Si-donors. However, there is a small significant difference of the g -value for this resonance and our donor-resonance in GaP-Sn.

It has been suggested by Thomas, Gershenson and Trumbore[14] that Si enters GaP as a shallow acceptor, which would violate the interpretation just given. In contrast to this Lorenz and Pilkuhn[15] conclude from their optical data that Si dominantly enters as a shallow donor in GaP-crystals, but that the presence of Si also introduces a deep acceptor about 0.25 eV above the valence band. It seems as if our results support the interpretation of Lorenz and Pilkuhn that Si enters GaP as a shallow donor. This argument is based on the fact that an acceptor would not be seen in ESR-measurements unless an uniaxial pressure is applied, as discussed above.

At the first glance the signals from the two GaAs-crystals offer no complications: the g -values do not differ significantly in accordance with the effective mass theory, and their line-widths are also similar. It is thus easily supposed that the group IV-element Si and VI-element Te in a similar way act as shallow donors in GaAs. The first objection, however, arises from the complete disagreement with earlier experimental results. Duncan and Schneider[16] report for n -type GaAs two lines with: $g = 0.5228$ and 1.2. We failed to reproduce the signal with $g = 1.2$, though several attempts were made both at 77° and 4.2°K. Duncan and Schneider used the formula for the g -factor of conduction electrons in InSb derived by Roth[7]:

$$g \approx 2 \left[1 - \left(\frac{m}{m^*} - 1 \right) \frac{\Delta}{3E_g + 2\Delta} \right]$$

where all parameters: m^*/m = effective mass

ratio, E_g = bandgap and Δ = spin-orbit splitting of the valence band, refer to the Γ -point of the Brillouin-zone.

Since GaAs is also a polar semiconductor with the absolute conduction band minimum at the Γ -point this application might constitute a reasonable first approach. The resulting g -factor is between +0.28 and +0.56, into which range the lower g -value of Duncan and Schneider falls.

Cardona[17] published the same year an extensive amount of experimental and theoretical results for semiconductors with diamond and ZnS-structure. He calculates the effective g -factor at conduction-band-minima at the Γ - and L -points, taking into account, not only the spin-orbit-splitting of the valence-band as was done by Roth, but also the splitting of the conduction-band. It is typical for polar materials that such a splitting appears. He obtains an expression for $g(\Gamma_{1c})$ in band-energies which are experimentally determined. The values used are slightly different from those of Duncan and Schneider: $m^*/m = 0.07$ instead of 0.074, $E_g = 1.55$ instead of 1.53 eV, $\Delta = 0.35$ instead of 0.33 eV, which changes the result. To show that Cardona's refined calculation gives a significant difference for the case of GaAs we used his experimental values in equation (8) of [17] which is equivalent to Roth's formula. This gives $g(\Gamma_{1c}) \approx 0.17$ instead of Cardona's own value of 0.32.

These considerations, however, have not shed any light on the origin of our signals in GaAs with g -factors 2.07 and 2.06. Provided that Roth's calculation is valid for GaAs, we can conclude that it is not likely that these signals come from electrons bound at shallow donors. The possibility of a deep donor or a combined impurity center should be considered in this case as well as for GaP. With such a model the similarity of the g -factors for the two different donors becomes the most remarkable feature.

For the sake of explicitness we write down Roth's formulae[16] for g -shifts in Ge:

$$\Delta g_{\parallel} \approx -\frac{\delta}{\epsilon'_{13}} \left(\frac{m}{m_t} - 1 \right)$$

$$\Delta g_{\perp} \approx -\frac{\delta}{\epsilon'_{13}} \left(\frac{m}{m_l} - 1 \right) + \Delta g'_{\perp}$$

where m_t , m_l are the transverse and longitudinal effective masses at the k -point of the conduction-band minimum, ϵ'_{13} is the bandgap and δ the spin-orbit-splitting of the valence-band at the same point. $\Delta g'_{\perp}$ is a correction, the value of which is not really decided upon.

If the signal is isotropic the g -value measured is the spherical average: $g = \frac{1}{3}g_{\parallel} + \frac{2}{3}g_{\perp}$;

The application of these results to GaP, as is done by Title[4] raises some problems. First, the absence of inversion-symmetry in the GaP-structure might complicate the derivation. Secondly, the conduction-band edges are not at the corresponding k -points in the Brillouin-zone. In GaP the conduction-band minimum is on the $\langle 100 \rangle$ -axis, probably at the boarder[18] i.e. the X_1 -point, while for the Ge the edge is at the L -point on the $\langle 111 \rangle$ -axis. The assumption made by Title (as by Roth) about the relation of the spin-orbit-splitting of the valence-band at the k -point of the conduction-band minimum: δ , to the splitting at the center of the zone: Δ , $\delta \approx \frac{1}{3}\Delta$ can be questioned. A quantitative argument for this can be found in a later article by Cardona and Greenaway[19] on the reflectivity of Gray Tin. The spin-orbit splitting at the L -point is there demonstrated to be about $\frac{1}{3}$ of the splitting at the Γ -point. The assumption that this relation approximately holds for Ge is supported by experimental data in Table 1 of [19] where $\Delta(\Gamma) = 0.30$ eV and $\Delta(L) = 0.18$ eV are given. We feel, however, that the use of the same relation between the spin-orbit-splitting at the Γ - and X -points instead of the Γ - and L -points in GaP needs some further justification.

We would like to conclude this discussion of g -factors and their calculation within the effective mass formalism by stressing that in

numerous cases the fact that the donor level is deep may make this formalism inapplicable. It is argued by Tittle[4] that the group VI-donors he has studied are as deep as about 0.1 eV, which within the hydrogenic approximation gives the bound donor electrons a 'Bohr radius' of 7\AA , which is not very large in comparison with the lattice constant 5.4\AA . It thus seems desirable with a calculation for deep donor states which takes account of the spin-orbit coupling in the central cell. A method for such a calculation was presented early by Elliot[20]. He uses Wannier-functions instead of Bloch-functions and due to their localized properties, the contribution from the central Wigner-Seitz cell to the spin-orbit coupling is obtained in closed form. In his actual calculations thereafter he had to refer to the tight-binding approximation which gave a result proportional to the atomic spin-orbit-splitting.

During the same period the Koster-Slater method[21] for calculating impurity-levels of isolated impurities was presented. Although this method has great advantages, realistic applications have been very few, due both to numerical and theoretical difficulties. It seems, however, that some of the complications encountered can now be handled. Two recent publications by Callaway and Hughes [22] and Faulkner[23] present extensive calculations on realistic multiband systems following the Koster-Slater approach. In both these cases as well as in earlier calculations, the final results, the energy-levels of the impurity-electron, depend on at least one parameter expressing the strength of the perturbing potential. This parameter is used to fit the calculated values to the experimental ones. We suggest that an independent check on such a calculation could be done in the following way: When the parameter in the potential is fixed, an expression for the impurity-electron wavefunction is defined as a linear combination of Wannier-functions for the perfect lattice. With this wave-function one can perform a calculation of the g -

factor for the impurity electron along the line suggested by Elliot in [20], without referring to the tight-binding approximation. In favorable cases this g -factor can be compared directly with an experimental value.

It should be noted that such a calculation has the advantage of being designed specifically for an impurity level. The essence of the effective mass approximation is on the contrary to treat for instance a shallow donor level, as a linear combination of conduction band minima. That this approximation corresponds to a measurable difference in g -value also for the relatively favourable case of donor-doped silicon has been shown by Feher[24]. He demonstrates the difference between the g -factors of bound donor electrons and conduction electrons. He also showed that this difference increases with increasing ionization energy of the donor. From the values given in Table 4 of [24] one could guess that a donor state as deep down in the bandgap as 0.1 eV would be dangerous to treat as a conduction state. On the other hand, the value of ionization energy where the effective mass approximation brakes down must be related to the bandgap.

We believe that important progress could be made by a calculation of g -factors as outlined above. Our application of the Koster-Slater method[25] is though planned to be different from that of Callaway and Faulkner. Instead of transforming the Bloch-functions of the unperturbed lattice to Wannier-functions it was suggested to approximate them directly by Löwdin's[26] Orthogonalized Atomic Orbitals.

Finally a comment on the rather shocking line-widths which we give in Table 1 and which can also be inferred from Fig. 1. The first thing to say is that a rather large line-width is to be expected from unresolved hyperfine splitting at the donor nuclei as well as at the neighbouring lattice atoms. The donors Sn, Si and Te all have isotopes possessing a nuclear spin of $I = \frac{1}{2}$. The natural abundance is however only 15.5 and 8 per

cent respectively. All isotopes of Ga, As and P have nuclear spins $I = \frac{3}{2}$, $\frac{5}{2}$ and $\frac{1}{2}$ respectively. We doubt however that this can be the only reason for the extremely large line-widths observed. Additionally the high doping concentration might cause broadening of the signals by interactions between the donor electrons as discussed by Title[4]. He estimates this hopping mechanism to be effective for doping-concentrations about 10^{18} cm^{-3} in GaP giving Lorentzian-type tails to the signals. Finally there is a more technical reason for the large line-width put forward by Goldstein[27], who fears that high local strains may be present in compound semiconductors, thus broadening all ESR-signals.

CONCLUSIONS

In this work ESR-resonances of Sn- and Si-donors in GaP are reported and identified. A second signal from GaP:Sn and other signals from Si- and Te-doped GaAs are reported and possible origins discussed. The difficulties in using existing theoretical results for the g -values in doped GaP and GaAs are stressed. Finally an alternative to the effective mass approach is outlined which should work also for the calculation of g -factors of deep donor-electrons.

Acknowledgements—The work reported here has been carried out within the Solid State Group, Uppsala University, and we gratefully acknowledge assistance and cheerful support from it's Members and Technical Staff. We are also indebted to Professor Norman March, Sheffield, for valuable comments on the manuscript.

REFERENCES

1. FLETCHER R. C., YAGER W. A., PEARSON G. L., HOLDEN A. N., READ W. T. and MERRIT F. T., *Phys. Rev.* **94**, 1392 (1954).
2. LUDWIG G. W. and WOODBURY H. H., In *Solid State Physics* (Edited by F. Seitz and D. Turnbull), Vol. 13, p. 223. Wiley, New York (1962).
3. FEHER G., In *Paramagnetic Resonance, Jerusalem Conference* (Edited by W. Low), Vol. II, p. 715. (1963).
4. TITLE R. S., *Phys. Rev.* **154**, 668 (1967).
5. LUTTINGER J. M. and KOHN W., *Phys. Rev.* **97**, 869 (1955). KOHN W. and LUTTINGER J. M., *Phys. Rev.* **97**, 1721 (1955). KOHN W. and LUTTINGER J. M., *Phys. Rev.* **98**, 915 (1955).
6. ROTH L., *Phys. Rev.* **118**, 1534 (1960).
7. ROTH L. M., LAX B. and ZWERDLING S., *Phys. Rev.* **114**, 90 (1959).
8. BEMSKI G., *Phys. Rev. Lett.* **4**, 62 (1960).
9. BRIZZI J., HARALDSON S. and RIBBING C-G, Uppsala University Institute of Physics, UIUP Rep. No. 582 (1968).
10. TITLE R. S., *IBM J. Res. Dev.* **7**, 68 (1963).
11. FEDOTOV S. P., PRESNOV U. A. and BAZHENOV V. R., *Soviet Phys. solid St.* **9**, 2620 (transl. from *Fiz. Tverd. Tela* **9**, 3332).
12. KOHN W., In *Solid State Physics* (Edited by F. Seitz and D. Turnbull), Vol. 5, p. 319. Wiley, New York (1957).
13. FEHER G., HENSEL J. C. and GERE E. A., *Phys. Rev. Lett.* **5**, 309 (1960).
14. THOMAS D. G., GERSHENZON M. and TRUMBORE F. A., *Phys. Rev.* **133**, A269 (1964).
15. LORENZ M. R. and PILKUHN M. H., *J. appl. Phys.* **38**, 61 (1967).
16. DUNCAN W. and SCHNEIDER E. E., *Phys. Lett.* **7**, 23 (1963).
17. CARDONA M., *J. Phys. Chem. Solids* **24**, 1543 (1963).
18. COHEN M. L. and BERGSTRESSER T. K., *Phys. Rev.* **141**, 789 (1966).
19. CARDONA M. and GREENAWAY D. L., *Phys. Rev.* **125**, 1291 (1962).
20. ELLIOT R. J., *Phys. Rev.* **96**, 266 (1954).
21. KOSTER G. F. and SLATER J. C., *Phys. Rev.* **95**, 1167 (1954); KOSTER G. F., *Phys. Rev.* **95**, 1436 (1954); KOSTER G. F. and SLATER J. C., *Phys. Rev.* **96**, 1208 (1954).
22. CALLAWAY J. and HUGHES A. J., *Phys. Rev.* **156**, 860 (1967).
23. FAULKNER R. A., *Phys. Rev.* **175**, 991 (1968).
24. FEHER G., *Phys. Rev.* **114**, 1219 (1959).
25. RIBBING C-G., CALAIS J-L. and HARALDSON S., Preliminary Research Rep. No. 226 (Nov. 1968), Quantum Chemistry Group, Uppsala University, Uppsala.
26. LOWDIN P-O., *Ark. Mat. Astr. Fys.* **35A**, No. 9 (1947); LÖWDIN P-O., *J. Chem. Phys.* **18**, 365 (1950).
27. GOLDSTEIN B., In *Semiconductors and Semimetals* (Edited by R. K. Willardson and A. C. Beer), Vol. 2, p. 200. Academic Press, New York (1966).

THE KINETICS OF CLUSTERING AND SHORT-RANGE ORDER IN STABLE SOLID SOLUTIONS

H. E. COOK

Metallurgy Department, Scientific Research Staff, Ford Motor Company, Dearborn, Mich. U.S.A.

(Received 2 December 1968; in revised form 14 April 1969)

Abstract—The kinetics of clustering and short-range order in stable solid solutions are examined from the viewpoint of a recent lattice diffusion theory. It is found that short-range order kinetics can be approximated by a single relaxation time but that clustering kinetics display a wide spectrum of relaxation times. For a regular solution, the short-range order relaxation time is

$$\tau = \frac{a^2}{32D} \left[\frac{T + \beta T_c}{T - T_c} \right]$$

where a is the lattice parameter, D is the chemical or interdiffusion coefficient, T is the temperature, T_c is the critical temperature, and

$$\beta = \begin{cases} 1 & \text{b.c.c. lattice} \\ 3 & \text{f.c.c. lattice.} \end{cases}$$

Consequently, if the interdiffusion coefficient shows Arrhenius type behavior when $T \gg T_c$, the relaxation time will also show this behavior and have the same activation energy. As $T \rightarrow T_c$, the interdiffusion coefficient generally deviates somewhat from Arrhenius type behavior; the relaxation time, however, will show a much stronger deviation due to the singularity at $T = T_c$.

1. INTRODUCTION

IT IS NOW well-established that the diffuse, short-range order intensity changes with temperature [1-3], indicative of changes in the statistical arrangement of solute and solvent atoms. After a sudden change in temperature, the new intensity distribution will not, of course, arise instantaneously because atomic migration is required. The purpose of this paper is to consider the time dependence of the intensity. Little theoretical development will be needed here since it is only necessary to show how a recent lattice diffusion theory [4] can be extended to this problem. The main effort will be analytical: calculations of the relaxation times for several systems will be given to illustrate its variation with temperature and to contrast its variation between clustering and ordering systems. The primary impetus for considering this problem are the recent measurements by Radelaar [5, 6] of the

resistivity relaxation times for binary solid solutions, and we will compare the short-range order relaxation time for the gold-silver system, for which the assumptions used here are strictly obeyed, with his results [6].

2. THEORY

When the diffuse intensity, $I(h, t)$, is somewhat larger than its equilibrium value, we may assume that its rate of decay can be written as

$$\frac{\partial I(h, t)}{\partial t} = R(h) - \tau^{-1}(h) I(h, t) \quad (1)$$

where t is the time, $R(h)$ is the rate when $I(h) = 0$, and $\tau(h)$ is the relaxation time for the intensity at position (h) in reciprocal space reached by the diffraction vector

$$s(h) = (S - S_0)/\lambda_R,$$

where S_0 and S are unit vectors in the direc-

tion of the incident and diffracted beams, respectively, and λ_R is the wavelength of the radiation. The relaxation time is assumed to have a non-zero, positive value as the single-phase solid solution is assumed to be stable. Therefore, at equilibrium (i.e. at $t = \infty$) we have by definition that

$$\left. \frac{\partial I(h, t)}{\partial t} \right|_{t=\infty} = 0,$$

which from equation (1) yields:

$$R(h) = \tau^{-1}(h) I(h, \infty). \quad (2)$$

On replacing $R(h)$ in equation (1) by its value given by equation (2), we find that the solution to equation (1) is

$$I(h, t) = [I(h, 0) - I(h, \infty)] \times \exp[-\tau^{-1}(h)t] + I(h, \infty). \quad (3)$$

We can obtain the expression for the relaxation time, $\tau(h)$, valid for any site (h) in the reciprocal space for cubic crystals, from the lattice diffusion theory where it was shown that the Fourier amplitudes of the composition modulation in a solid solution obeyed the equation[4]

$$A(h, t) = A(h, 0) \exp[\alpha(h)t]$$

where $\alpha(h)$ is an 'amplification factor' which depends on the thermodynamic properties of the crystal, the atomic mobility, and crystal lattice. Since the intensity in Laue units is given by

$$I(h, t) = A(h, t) A^*(h, t) N/c(1-c)$$

where N is the number of atoms and c is the atomic fraction of component two in a binary substitutional solid solution, the intensity expression according to the lattice diffusion theory is

$$I(h, t) = I(h, 0) \exp[2\alpha(h)t]. \quad (4)$$

This expression differs from equation (3) by the omission of the terms in $I(h, \infty)$. For stable, single-phase solutions, this omission can be attributed to neglect of the composition fluctuations at equilibrium. The diffusion theory is, therefore, strictly valid (for stable, single-phase solutions) only when $I(h, t) \gg I(h, \infty)$ and yet not so large that non-linear effects must be considered. (It should be pointed out that in the satellite decay studies [7, 8], relaxation times were obtained from the slope of logarithmic plots of $[I(h, t) - I(h, \infty)]/[I(h, 0) - I(h, \infty)]$ versus time which is the proper plot according to equation (3).) On comparing equation (4) with (3) for the case where $I(h, t) \gg I(h, \infty)$ we see that the reciprocal relaxation time is simply twice the negative value of the amplification factor:

$$\tau^{-1}(h) = -2\alpha(h). \quad (5)$$

Substituting for $\alpha(h)$ from equation (12) of reference [4] we find that

$$\tau^{-1}(h) = [2DB^2(h)/f''] [f'' + 2KB^2(h)]. \quad (6)$$

The function D is the interdiffusion coefficient [9] given by

$$D = [\Omega c(1-c)f''/k_B T] [cD_1 + (1-c)D_2] \quad (7)$$

where Ω is the atomic volume, f'' is the second derivative of the Helmholtz free energy per unit volume with respect to the concentration, c , and D_1 and D_2 are the tracer diffusivities of components one and two, respectively. The term k_B is Boltzmann's constant and T is the temperature. The parameter K represents the gradient-energy coefficient of the Cahn-Hilliard theory[10] and has been measured for two clustering systems where it is positive[11, 12] and for two ordering systems where it is negative[7, 8]. The function $B^2(h)$ is simply a lattice transform of the type:

$$B^2(h) = (1/a^2) \sum_r [1 - \cos \mathbf{k}(h) \cdot \mathbf{x}(r)] \quad (8)$$

over nearest neighbor sites reached by the vector $\mathbf{x}(r)$ in which a is the lattice parameter of a cubic crystal and $\mathbf{k}(h)$ is the wave vector:

$$\mathbf{k}(h) = 2\pi(h_1\mathbf{b}_1 + h_2\mathbf{b}_2 + h_3\mathbf{b}_3)$$

where \mathbf{b}_1 , \mathbf{b}_2 and \mathbf{b}_3 are the reciprocal lattice vectors and the symbol (h) , denoting the reciprocal space coordinates, is shorthand for (h_1, h_2, h_3) . It is evident from the equation for $B^2(h)$ that this function, when $|\mathbf{k}(h)|$ is large, causes $\tau^{-1}(h)$ to depend on the lattice geometry; when the wave vector is small, it reduces to $|\mathbf{k}(h)|^2$.

A physical interpretation can be given to equation (1) if we substitute for $\tau^{-1}(h)$ its value given by equation (6) and substitute for $I(h, \infty)$ its value given by fluctuation theory [13, 14] which, in Laue units, is given by

$$I(h, \infty) = \frac{k_B T}{c(1-c)\Omega[f'' + 2KB^2(h)]} \quad (9)$$

following the notation used in reference [4]. On substituting into equation (1) and rearranging, we obtain

$$\frac{\partial I(h, t)}{\partial t} = M(h) \left\{ [f'' + 2KB^2(h)]I(h) - \frac{k_B T}{\Omega c(1-c)} \right\} \quad (10)$$

In this form, the equation readily lends itself to the "rate-equals-mobility-times-driving-force" interpretation where

$$M(h) = 2DB^2(h)/f''$$

represents the mobility and

$$F(h) = [f'' + 2KB^2(h)]I(h)$$

the driving force which is proportional to the free energy associated with the Fourier coefficient of wave vector $\mathbf{k}(h)$ [4]. The remain-

ing term in braces, $k_B T/\Omega c(1-c)$, can be considered as a driving force resulting from thermal energy which tends to move the system away from a hypothetical equilibrium given by $I(h) = 0$. The two 'forces' are balanced at $t = \infty$.

3. APPLICATION TO ORDERING SYSTEMS

β -Brass

The negative free energy associated with the negative gradient energy coefficient found in ordering systems and proportional to $2KB^2(h)$ is offset in the stable, single-phase region above the critical temperature, T_c , by the second derivative of the Helmholtz free energy, f'' , which is positive. However, at T_c the sum of these two free energy terms is zero for the Fourier coefficients which produce order [4] i.e. those with wavelengths equal to the lattice parameter, and for temperatures near but above T_c , this sum is quite small. As a result, there are large fluctuations in short range order near T_c .

The diffuse scattering associated with these fluctuations, critical opalescence, was first observed in solid solutions by Walker and Keating [2] who measured, over a range of temperatures above T_c ($= 741^\circ\text{K}$), the diffuse neutron intensity scattered by a β -brass crystal. The fluctuation intensity for this system according to equation (9) is shown in Fig. 1 for $T = T_c + 25$ and $+75^\circ\text{K}$. For the calculations, the gradient energy coefficient and the second derivative of the free energy were obtained from equations based on regular solution theory which for b.c.c. crystals are [4]

$$K = -k_B T_c / 2a$$

and

$$f'' = 4k_B(T + T_c)/\Omega$$

For demonstrating the kinetic theory, let us consider the intensity for $T = T_c + 75$ in Fig. 1 as the initial condition for isothermal aging at $T = T_c + 25$. The changes in intensity with time and the approach to the equilibrium

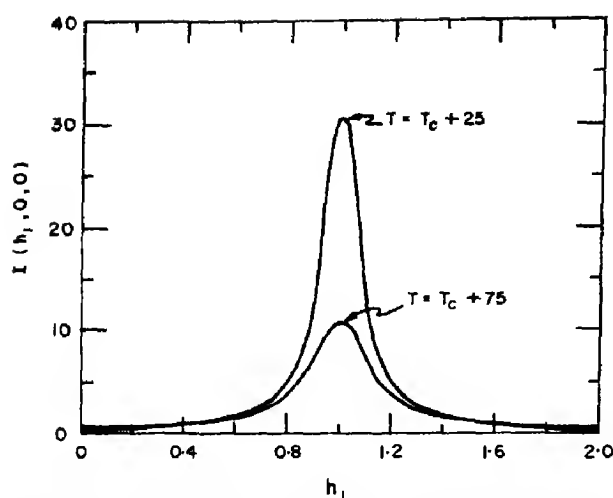


Fig. 1. The diffuse intensity along the [100] direction of β -brass determined from equation (9) for two temperatures above the critical point.

intensity distribution can be obtained from equation (3). The behavior with time of $I(1, 0, 0)$, the intensity of the ordering Fourier coefficient, is shown in Fig. 2. The relaxation time, $\tau(1, 0, 0)$, for this intensity was calculated from equation (6) using the regular solution values for K and f'' and the tracer diffusivities reported by Kuper, Lazarus, Manning and Tomizuka [15].

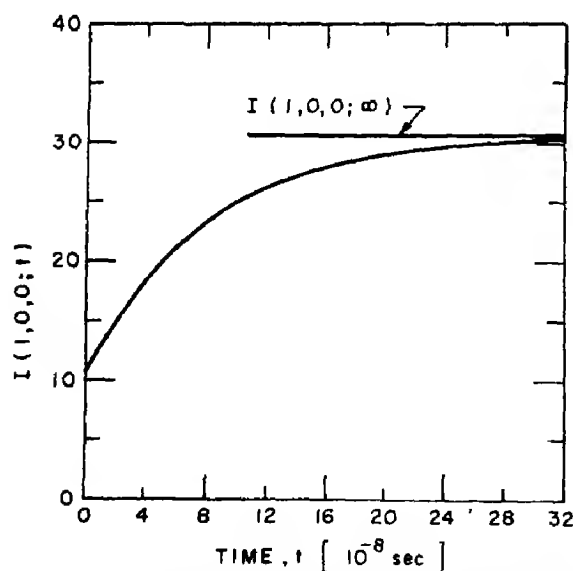


Fig. 2. The approach of the intensity at the superlattice position for β -brass to its equilibrium value at $T = T_c + 25$. The initial value is the equilibrium intensity at $T = T_c + 75$.

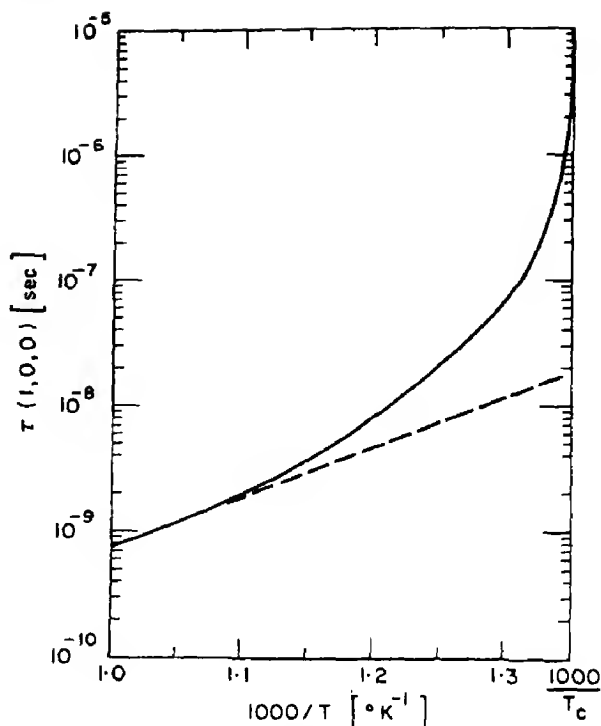


Fig. 3. The behavior of the relaxation time $\tau(1, 0, 0)$ for the intensity at the superlattice position of β -brass as a function of the reciprocal temperature. A positive deviation from linear, Arrhenius type behavior is observed as $1/T \rightarrow 1/T_c$.

The variation of the relaxation time with temperature is shown in the Arrhenius plot of Fig. 3. The pronounced positive deviation from the straight line results from the driving force (free energy) for the ordering Fourier coefficient approaching zero as $T \rightarrow T_c$ from above. The very short relaxation times, even when T is very near T_c , explains the impossibility of retaining short-range order in this system on quenching [16]. Although the relaxation times for this alloy are much too fast to be measured by resistivity techniques [5, 6, 17], the deviation of $\tau(h_1, 0, 0)$ from linear Arrhenius type behavior near T_c is a general result. We will return to a discussion of this behavior in Section 5.

Gold-silver system

Although the gold-silver phase diagram shows a single-phase solution at all temperatures below the solidus, the negative heat of

mixing[15] indicates that an order-disorder transition might be thermodynamically feasible at some low temperature. It has been suggested by Norman and Warren[19] on interpreting on their short-range order measurements with Cowley's theory[20] that the composition Ag_3Au should order at 160°K. The recent measurement of a negative gradient energy coefficient for this system[7] is further support that an order-disorder reaction is thermodynamically feasible.

From Radelaar's recent work[5, 6], it is evident that the resistivity relaxation time is associated with that for short-range order. The simplest assumption for this correlation is that the resistivity relaxation time is equal to that for the intensity $I(1, 0, 0)$ at the superlattice position. To check the validity of this, we have compared the relaxation time $\tau(1, 0, 0)$, determined from equation (6), with Radelaar's results. The values for the tracer diffusivities were obtained by extrapolating (analytically) the values measured at high temperatures[17]. The second derivative of the free energy[7] was obtained from tabulated thermodynamic functions[18]:

$$f'' = 4640 - 1970c$$

$$- \{1.13 - [0.814/c(1-c)]\} T \times 10^7 \frac{\text{erg}}{\text{cm}^3} \quad (11)$$

We have treated K as an adjustable parameter in fitting $\tau(1, 0, 0)$ to the relaxation time measured by Radelaar for the 45.1 at.% Au alloy at 473°K as shown in Fig. 4. A fit should be necessary at only one point since the gradient energy coefficient is insensitive to temperature and composition changes[7, 10]. A value of $K = -2.1 \times 10^{-6} \text{ erg/cm}$ gives a good fit and lies at the lower limit of the experimentally measured value of $K = -2.6 \pm 0.5 \times 10^{-6} \text{ erg/cm}$. [7]. In fact, it is a more reasonable value for K than the mean value measured experimentally if we consider the critical temperature, T_c , at which

$$f'' + 2KB^2(1, 0, 0) = 0. \quad (12)$$

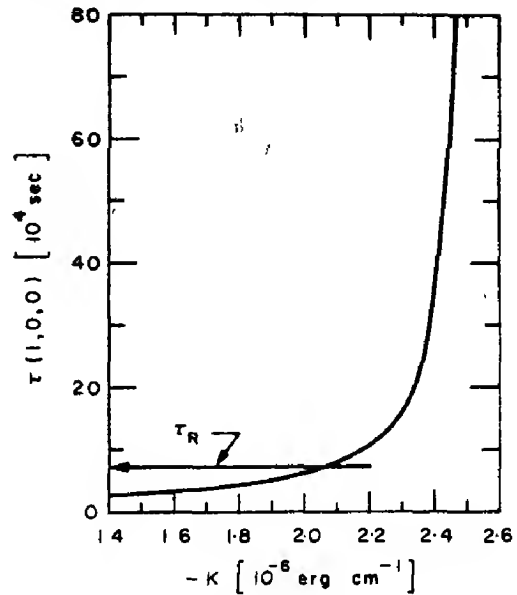


Fig. 4. The variation of the relaxation time $\tau(1, 0, 0)$ for the intensity at the superlattice position of Ag 45.1 at.% Au at 473°K as a function of the gradient energy coefficient, K . The resistivity relaxation time, τ_R , measured by Radelaar[6] is given by the horizontal line.

On substituting for f'' from equation (11), we obtain the dependence of the critical temperature on the gradient energy coefficient shown in Fig. 5 for the 45.1 at.% Au alloy. We see for $K = -2.6 \times 10^{-6} \text{ erg/cm}$ that the critical

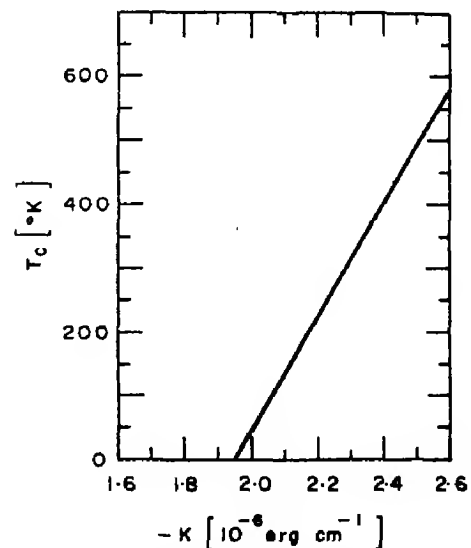


Fig. 5. The linear variation of critical temperature, T_c , for Ag 45.1 at.% Au as a function of the gradient energy coefficient, K .

Table 1. A comparison of the resistivity relaxation times [6] with the relaxation time of the ordering intensity $I(1, 0, 0)$: gold-silver system

Temperature (°K)	Alloy composition (at. % Au)					
	45.1		50.0		56.1	
	τ_R (10^3 sec)	$\tau(1, 0, 0)$ (10^3 sec)	τ_R (10^3 sec)	$\tau(1, 0, 0)$ (10^3 sec)	τ_R (10^3 sec)	$\tau(1, 0, 0)$ (10^3 sec)
473	72.0	80.0	55.0	75.0	27.0	59.0
500	5.7	6.6	4.5	6.2	2.6	4.8
550	0.126	0.121	0.071	0.115	0.072	0.091
600	0.005	0.0044	0.0031	0.0042	0.0032	0.0033

temperature is 580°K which is obviously incorrect since the solution is known to be stable at this temperature. The value of $K = -2.1 \times 10^{-6}$ erg/cm; however, yields a critical temperature of 145°K which is nearer the value suggested by Norman and Warren [19].

The resistivity relaxation times, τ_R , obtained by Radelaar are compared with the calculated values of $\tau(1, 0, 0)$ in Table 1. Both relaxation times can be fitted by linear Arrhenius plots with the activation energies shown in Table 2. The activation energies for $\tau(1, 0, 0)$ are somewhat higher than those for τ_R . A similar deviation has been observed between the calculated activation energies for interdiffusion [7], which from equation (6) are approximately that for $\tau(1, 0, 0)$, and the measured values in this temperature range for the gold-silver system [7].

Before leaving our discussion of this system, it is worthwhile to check the assumption of a single relaxation time, $\tau(1, 0, 0)$, for short-range order. To do this it is necessary to consider the distribution of relaxation times in the vicinity of the superlattice position. Calculated values of $\tau(h_1, 0, 0)$ for the 50 at.% Au alloy at 473°K are shown in Fig. 6 below the diffuse intensity calculated from equation (9). At this temperature, we see that there is a small peak in $\tau(h_1, 0, 0)$ at the superlattice position but that the variation time of the

Table 2. A comparison of activation energy for the resistivity relaxation time with that for $I(1, 0, 0)$: gold-silver system

Composition (at.% Au)	Q (kcal/mole)	
	For τ_R [6]	For $\tau(1, 0, 0)$
45.1	42.3	43.2
50.0	41.4	42.5
56.1	40.0	42.5

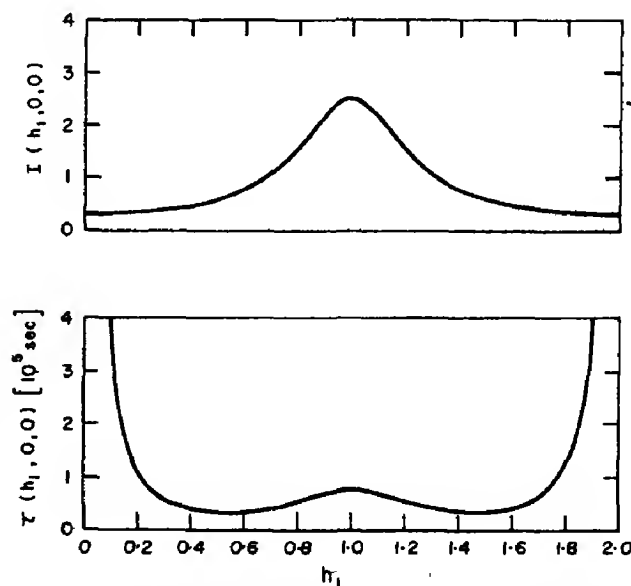


Fig. 6. The calculated diffuse intensity and relaxation times for Ag 50 at.% Au along the [100] direction at 473°K.

relaxation time over the range $h_1 = 0.25$ to 1.0 is relatively small. From the half-width of the diffuse short-range order peak, it seems that the relaxation time for short-range order should be a weighted average over the range $h_1 = 0.8$ to 1.0 . Then according to these arguments the value for $\tau(1, 0, 0)$ should be a slight overestimate, roughly 15 per cent, of the effective relaxation time for short-range order. As the temperature is decreased towards T_c , the peak in the relaxation time at $h_1 = 0$ becomes more pronounced. However, the diffuse short-range order peak also becomes more pronounced and decreases in width. Thus the weighted average of the $\tau(h_1, 0, 0)$ values in the vicinity of the superlattice position will still be approximately equal to $\tau(1, 0, 0)$ even though there is a wider distribution of relaxation times about this position.

4. APPLICATION TO CLUSTERING SYSTEMS

The changes in diffuse intensity with time according to equation (3) for a clustering system is shown in Fig. 7. The intensity behavior is similar in several respects to that for spinodal decomposition[11, 22]. The calculated behavior in Fig. 7, however, is for the

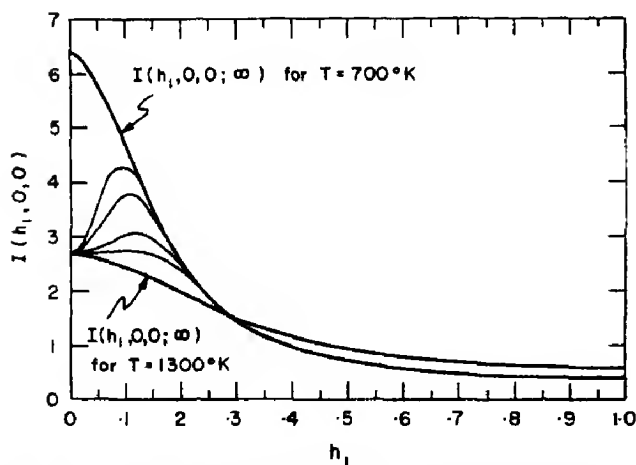


Fig. 7. The approach to equilibrium of the diffuse intensity for a clustering system above the spinodal. The calculations are for Cu 67 at. % Ni at 700°K. The initial distribution is equal to the calculated equilibrium intensity at 1300°K. The four intermediate intensity profiles are for aging times, at 700°K, of 5, 10, 30, and 60×10^3 sec.

copper-nickel system *above* the spinodal. The choice of this system for a sample calculation is due to the fact that it lends itself to the ingenious experimental technique devised by Mozer, Keating and Moss[23] of preparing a 'null alloy', the use of which for clustering systems is quite advantageous because the diffuse peak at the Bragg positions, e.g. at $(h) = (2, 0, 0)$, is not superimposed on the Bragg, Huang, and thermal diffuse intensities which are present in alloys when the mean scattering length (or the mean scattering factor for X-rays) is non-zero.

The alloy composition for the calculation is 67 at.% Ni. The second derivative of the free energy, f'' , was obtained from the tabulated thermodynamic functions[18]:

$$f'' = (-1.82 \times 10^3 + 3.44 T) \times 10^7 \text{ erg/cm}^3$$

which equals zero when $T \approx 530^\circ\text{K}$. This temperature agrees with the critical temperature for this composition suggested by Mozer, Keating and Moss[23]. The value for K was obtained from the heat of mixing at $c = 0.5$ using the assumption of nearest neighbor interactions[10, 11]:

$$K = 3.85 \times 10^{-6} \text{ erg/cm}$$

The tracer diffusivities were obtained from the results of Monma, Suto and Oikawa[24].

The intensities shown by Fig. 7 represent the approach to equilibrium at 700°K; the initial intensity distribution is that given by equation (9) for 1300°K. As is well known from the theory of spinodal decomposition [22], the intensities at small values of h_1 grow slowly because the diffusion distances associated with these intensities are large, proportional to $1/h_1$. The gradual shift in the intensity maximum during the isothermal anneal makes it impossible to describe clustering kinetics, even approximately, by a single relaxation time in contrast to short-range order kinetics. The decay at larger values of h_1 , i.e. for $h_1 > 0.3$, can be attributed to the

positive gradient energy coefficient which gives a rather large 'incipient surface energy' [22] for the Fourier coefficients of large wave number, small wavelength. Thus on going to lower temperatures, their fluctuation intensity decreases.

5. DISCUSSION

The rise in relaxation time near T_c

A noticeable result of the lattice diffusion theory is the pronounced deviation of the relaxation time from linear Arrhenius behavior in the vicinity of the critical temperature, Fig. 3. This is caused by a rapid fall-off in the thermodynamic driving force as the critical temperature is approached. In fact, the critical temperature represents a singularity in the relaxation time. This is best seen by substituting the expressions from regular solution theory for f'' and K into equation (6) for the reciprocal relaxation time at the superlattice position which yields*

$$\tau^{-1}(1, 0, 0) = \frac{32}{a^2} D \left[\frac{T - T_c}{T - \beta T_c} \right] \quad (13)$$

where

$$\beta = \begin{cases} 1 & \text{b.c.c.} \\ 3 & \text{f.c.c.} \end{cases}$$

Thus, the relaxation time is equal to $a^2/32 D$ when $T \gg T_c$ but approaches infinity as $1/(T - T_c)$ near the critical temperature.

An appreciable deviation from linear Arrhenius behavior has been observed by Radelaar and Ritzen[25] for the resistivity relaxation time of Au_3Cu above its critical

temperature. The qualitative agreement between this observed behavior and the theoretical prediction† is strong support for Radelaar's conclusion that the resistivity relaxation time is directly related to the short-range order relaxation time[26].

The explanation given by Radelaar and Ritzen[25] for the anomalous rise in relaxation time differs somewhat from that given here. They revived the concept, given much earlier by Borelius[27], of small ordered regions in a disordered matrix which must surmount a potential barrier between the ordered and disordered states to reach equilibrium. If small ordered regions do exist with a potential (free energy) barrier, then they must be considered as a second phase which is not in equilibrium with the matrix. However, the relaxation experiments of Radelaar and Ritzen were performed on specimens having only a small departure from equilibrium and the possibility of a second phase must, therefore, be discounted. Moreover, to make the small ordered region mechanism viable, it was necessary to postulate that the free energy barrier between the two states increases as the critical temperature is approached which seems contrary to the principle that the chemical potentials in the 'disordered' (short-range ordered) and ordered states must be equal at the critical temperature. In fact, it is the decrease in the difference in free energy between the disordered and ordered states as the critical temperature is approached which causes the rise in relaxation time according to the phenomenological theory proposed here.

It is now established both experimentally [15] and theoretically[28] that the self-diffusion coefficients also deviate from linear Arrhenius behavior near T_c due to the dependence of vacancy formation and migration energies on the degree short-range order. As a result, this effect will also contribute to the

*The steps for deriving equation (13) were as follows: first equation (6) was written explicitly for $\tau^{-1}(1, 0, 0)$ yielding

$$\tau^{-1}(1, 0, 0) = \frac{32D}{a^2} \left[1 + \frac{32K}{a^2 f''} \right]$$

on replacing $B^2(1, 0, 0)$ by its value $16/a^2$ [4]. Next the regular solution parameters were substituted for f'' and K , equations (16) and (17), respectively, of reference [4]. The interaction energy, v , was then solved for in terms of the critical temperature, T_c , using equation (12).

†The assumptions of solely nearest-neighbor interactions and of no size difference between solute and solvent atoms do not permit a quantitative comparison for the copper-gold system.

rise in relaxation time since the interdiffusion coefficient, D in equation (7), is a linear combination of the self diffusivities. This second contribution, however, should generally be minimal compared to the contribution from the singularity in the driving force at T_c . For disordered β -brass, the self-diffusivities do not begin to deviate from an extrapolated line through the Arrhenius plot of the high-temperature measurements until the reciprocal temperature $(1000/T) = 1.3$ is reached [15]. At this same reciprocal temperature, the calculated value for $\tau(1, 0, 0)$ for β -brass, Fig. 3, is already an order of magnitude higher than its value given by a linear extrapolation. There is a further point regarding the critical temperature which needs clarification. The pertinent critical temperature for the kinetic theory is the temperature at which equation (12) is obeyed where a second order phase transformation is predicted. For β -brass, the critical opalescence observed by Walker and Keating [2] strongly suggests that the transformation is second order. However, the order-disorder reaction in Cu_3Au and, apparently, in Au_3Cu is first order [29]. Therefore, for these alloys, the critical temperature for the kinetic theory will be a metastable one lying below the temperature at which the first order reaction occurs.

Time dependence of the Warren short-range order parameters

Recently, Welch [30] has developed a theory for the kinetics of short-range order in which he obtained an expression for the time dependence of the Warren short-range order parameter, $\alpha(r, t)$, for nearest neighbors. Radelaar [31] has independently developed a similar theory for short-range order kinetics.

The solution to Welch's linearized kinetic theory for the short-range order parameter is

$$\alpha(r, t) = \Delta\alpha \exp(-t/\tau') + \alpha(r, \infty) \quad (14)$$

where $\Delta\alpha = \alpha(r, 0) - \alpha(r, \infty)$ and τ' is the relaxation time for the short-range order par-

ameter, $\alpha(r, t)$. The argument (r) represents one of the nearest neighbor sites of the origin, (0). Welch's theory predicts that the reciprocal relaxation time will be directly proportional to the diffusivity of the faster component if the two self-diffusivities are widely different. This same qualitative result holds for $\tau(h)$, equation (6).

Important quantitative differences do exist, however. To see this, it is necessary to write the expression for $\alpha(r, t)$ according to the lattice diffusion theory. This is obtained by substituting the expression for $I(h, t)$, equation (3), into the defining equation for $\alpha(r, t)$ given by the integral

$$\alpha(r, t) = \frac{1}{z} \int \int \int I(h, t) \times \exp[i\mathbf{k}(h) \cdot \mathbf{x}(r)] d\mathbf{h}_1 d\mathbf{h}_2 d\mathbf{h}_3 \quad (15)$$

over the Brillouin zone in which z is the number of atoms in the unit cell. It is readily seen on inspecting equations (3) and (15) that the lattice diffusion theory does not yield an exponential time dependence and a single relaxation time for the short-range order parameter in contrast to Welch's result, equation (14). Indeed, diffusion theory [32] predicts that it is the X-ray intensity at a point in reciprocal space and not the Fourier transform of the intensity, $\alpha(r, t)$, which shows exponential time dependence. Significantly, both exponential decay and growth of the intensity have been verified by experiment [7, 8, 11, 33].

Limitations of the theory

Because the diffuse intensity is conserved*, the increase in intensity of a diffuse peak during isothermal annealing must be compensated by a decrease in the 'background' intensity in regions of h -space away from the peak. This result is shown in Figs. 1 and 7 for systems

*The integrated value of $I(h, t)$ over the Brillouin zone is independent of time and equal to the number of atoms in the unit cell.

with short-range order and clustering, respectively. For the calculations, however, the intensity is only approximately conserved because the fluctuation equation used to obtain $I(h, \infty)$, equation (9), is strictly valid only when $T \gg T_c$. Instead of equation (9), for example, the more rigorous (and considerably more complex) fluctuation theory of Zernike[34], which agreed admirably with the measurements of Walker and Keating[2] for all $T > T_c$, could be used. However, the thermodynamic approximations which yield equation (9) are identical to those used in obtaining the driving force equation for the kinetic theory which is, likewise, only strictly valid when $T \gg T_c$. Consequently, the equations given here represent a synthesis of two theories, a fluctuation theory and a diffusion theory, which are valid to the same approximations.

As the critical temperature is approached, the theory will become less accurate because of large fluctuations. For β -brass, the diffuse intensity given by equation (9) agrees with the short-range order intensity measured by Walker and Keating[2] for temperatures above $T_c + 20^\circ\text{C}$. Consequently, we expect that the kinetic theory will, likewise, be valid for temperatures greater than $\approx T_c + 20^\circ\text{C}$. Since the theory is not valid at T_c , the value of infinity for the relaxation time should not be taken literally.

There are further limitations on the theory. The approximations limit the theory to only small departures from equilibrium. Furthermore, the equations are written solely for binary, substitutional alloys of cubic symmetry[4] and are strictly correct only when the solute and solvent atoms are of the same size. The lattice diffusion theory has, however, been extended[35] to all Bravais lattices including interactions between more distant neighbors and the elastic free energy[36] resulting from the size difference between solute and solvent atoms. This more complete theory should be used to study the distribution of relaxation times in the α -brass[17] and

copper-gold systems[25] where the size difference is large. It does not, however, change the results, both quantitative and qualitative, obtained here since these assumptions are adequately obeyed for the gold-silver and copper-nickel systems. The equations are also valid for the β -brass system for relaxation times and intensities in the vicinity of a superlattice position since the elastic free energy associated with Fourier coefficients having wave vectors near $k(1, 0, 0)$ is small for the b.c.c. lattice[36].

6. SUMMARY

We have shown that the lattice diffusion theory[4] can be used to study kinetics of solute rearrangement in stable, single-phase solid solutions. The principal findings are:

- (1) The kinetics of short-range order can be approximated by a single relaxation time; whereas, the kinetics of clustering cannot.
- (2) The relaxation time for short-range order deviates from linear Arrhenius behavior in the vicinity of the critical temperature at which the free energy associated with the ordering Fourier coefficient vanishes.
- (3) For temperatures considerably above the critical, the activation energy for the short-range order relaxation time should correspond to that for the interdiffusion coefficient.
- (4) The calculated short-range order relaxation times for the gold-silver system agreed reasonably well with the resistivity relaxation times measured by Radelaar[6] for a gradient energy coefficient of -2.1×10^{-6} erg/cm. This value is at the lower limit of the range determined experimentally, $\pm 2.6 \pm 0.5 \times 10^{-6}$, from diffusion studies in layered, gold-silver thin films[7].

Acknowledgements—The author has benefited from several discussions with Drs. G. F. Bolling, C. L. Magee and H. Sato and is indebted to Dr. Magee for a critical review of the manuscript.

REFERENCES

1. COWLEY J. M., *J. appl. Phys.* **21**, 24 (1950).
2. WALKER C. B. and KEATING D. T., *Phys. Rev.* **130**, 1726 (1963).
3. MOSS S. C., *J. appl. Phys.* **35**, 3547 (1964).
4. COOK H. E., DE FONTAINE D. and J. E. HILLIARD, *Acta Metall.* **17**, 765 (1969).
5. RADELAAR S., *J. Phys. Chem. Solids* **27**, 1375 (1966).
6. RADELAAR S., *Phys. Status Solidi* **27**, K63 (1968).
7. COOK H. E. and HILLIARD J. E., *J. appl. Phys.* **40**, 2198 (1969).
8. PHILOFSKY E. and HILLIARD J. E., *J. appl. Phys.* **40**, 2198 (1969).
9. DARKEN L. S., *Trans. Am. Inst. Min. Engrs.* **175**, 184 (1948).
10. CAHN J. W. and HILLIARD J. E., *J. chem. Phys.* **28**, 258 (1958).
11. RUNDMAN K. B. and HILLIARD J. E., *Acta metall.* **15**, 1025 (1967).
12. ERB D. and HILLIARD J. E., To be published.
13. LANDAU L. D. and LIFSHITZ, In *Statistical Physics* (Translated by E. Peierls and R. F. Peierls), pp. 366-369. Addison-Wesley, Reading (1958).
14. KRIVOGLAZ M. A., *Soviet Phys. JETP* **5**, 1115 (1957).
15. KUPER A. B., LAZARUS D., MANNING J. R. and TOMIZUKA C. T., *Phys. Rev.* **104**, 1536 (1956).
16. MARTIN M. C. and KOLLEN W., *J. appl. Phys.* **39**, 4336 (1968).
17. DAMASK A. C., *J. appl. Phys.* **27**, 610 (1956).
18. HULTGREN R., ORR R. L., ANDERSON P. D. and KELLEY K. K., *Selected Values of Thermodynamic Properties of Metals and Alloys*. Wiley, New York (1963).
19. NORMAN N. and WARREN B. E., *J. appl. Phys.* **22**, 483 (1951).
20. COWLEY J. M., *Phys. Rev.* **77**, 669 (1950).
21. MALLARD W. C., GARDNER A. B., BASS R. F. and SLIFKIN L. M., *Phys. Rev.* **129**, 617 (1963).
22. CAHN J. W., *Acta metall.* **9**, 795 (1961).
23. MOZER B., KEATING D. T. and MOSS S. C., *Phys. Rev.* **175**, 868 (1968).
24. MONMA K., SUTO H. and OIKAWA H., *J. Japan Inst. Metals* **28**, 188 (1964).
25. RADELLAR S. and RITZEN J. M. J., *Phys. Status Solidi* **31**, 277 (1969).
26. RADELAAR S., Thesis, Technische Hogeschool, Delft (1967).
27. BORELIUS G., *J. Inst. Metals* **74**, 17 (1947).
28. SCHOJET M. and GIRIFALCO L. A., *J. Phys. Chem. Solids* **29**, 481 (1968); *ibid.* **29**, 497 (1968); *ibid.* **29**, 911 (1968).
29. GUTTMAN L., *Solid St. Phys.* **3**, 145 (1956).
30. WELCH D. O., *Mater. Sci. Engng.* **4**, 9 (1969).
31. RADELAAR S., To be published.
32. DU MOND J. and YOUTZ J. P., *J. appl. Phys.* **11**, 357 (1940).
33. DINKLAGE J. and FRERICHS R., *J. appl. Phys.* **34**, 2633 (1963).
34. ZERNIKE F., *Physica* **7**, 565 (1940).
35. DE FONTAINE D. and COOK H. E., To be published.
36. COOK H. E. and DE FONTAINE D., *Acta metall.* **17**, 915 (1969).

$$x^2 + y^2 = 1$$

ON THE SOLUTION OF THE EQUATION OF DIFFUSION PROCESSES DURING THE UPTAKE OF EXCESS CALCIUM BY CALCIUM FLUORIDE

C. F. LEE

Department of External Studies, University of Queensland, Brisbane, Queensland 4067, Australia

(Received 22 November 1968; in revised form 1 April 1969)

Abstract—This paper presents an iteration method for the solution of a generalized diffusion equation derived from the theory of diffusion process during the uptake of excess calcium by calcium fluoride. The iteration process can be carried out by a digital computer to obtain a numerical integration of the diffusion equation with estimated accuracy. By using a GE-225 computer it takes, on the average, no more than 2 min to obtain a solution of the diffusion equation to within 1 per cent error. To demonstrate the general applicability of the method numerical solutions for a wide range of the parameter have been worked out.

INTRODUCTION

A STUDY has been made by Wagner[1] on the theory of diffusion process during the uptake of excess calcium by calcium fluoride. When calcium fluoride is heated in calcium vapor, additional layers of the CaF_2 lattice are formed at its surface due to outward diffusion of F^- ions and inward diffusion of electrons, e^- . During this process it assumes a dark color due to the electrons trapped at anion vacancies, i.e. color centers.

The diffusion process is determined by a diffusion equation derived from Fick's second law. Concentration distributions can then be calculated with the solution of the diffusion equation.

If the calcium excess is very low, the diffusion coefficient is independent of concentration and the classical solutions suffice.

However, if the calcium excess is moderately high it has been shown[1] that the diffusion coefficient is dependent on concentration, and the classical solution no longer applies. In this case to obtain concentration distributions the solution of a differential equation governing the concentration of color centers has to be sought. The differential equation contains a modified diffusion coefficient which

is dependent on the concentration. Analytic solutions of the equation subject to the required boundary conditions are not available and even numerical solutions are difficult to obtain.

This paper presents a method which, with the aid of a medium size digital computer, would take no more than a few minutes to obtain a numerical solution of the diffusion equation with prescribed practical accuracy. It is suggested that the method also applies to the solutions of other diffusion equations involving concentration-dependent coefficients.

DIFFUSION EQUATION AND ITS TRANSFORMATION

Consider a semi-infinite sample of CaF_2 with its surface exposed to Ca vapor (Fig. 1).

Following Kröger's notations[2] let n_e , concentration of free electrons; n_{e^*} , concentrations of color centers (trapped electrons); D , diffusion coefficient for counter-diffusion of F^- ions and electrons; t , time; x , distance from the surface.

When calcium excess is moderately high electronic conduction dominates[1]. The differential equations governing the concentration of free and trapped electrons:

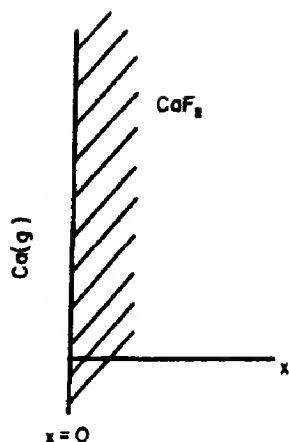


Fig. 1.

$$\frac{\partial(n_{e'} + n_{e_F}^*)}{\partial t} = \frac{\partial}{\partial x} \left(D \frac{\partial n_{e'}}{\partial x} \right) \quad (1)$$

can then be converted to a diffusion equation governing the concentration of the color centers

$$\frac{\partial n_{e_F}^*}{\partial t} = \frac{\partial}{\partial x} \left(D_m \frac{\partial n_{e_F}^*}{\partial x} \right) \quad (2)$$

where D_m is the modified diffusion coefficient

$$D_m = \frac{D_m^0}{1 + \alpha n_{e_F}^*} \quad (3)$$

$$D_m^0 = \frac{D_{e'}}{1 + K_1^{1/2} K_2}$$

$$\alpha = \frac{u_{e'}}{u_{F_i} + u_{v_F}} \frac{1}{K_1 K_2} > 0$$

$D_{e'}$, diffusivity of electrons; K_1 , constant of internal equilibrium between F^- interstitials and anion vacancies; K_2 , constant of equilibrium between the color centers and the anion vacancies and mobile excess electrons; $u_{e'}$, u_{F_i} , u_{v_F} , electrochemical mobilities of the mobile excess electrons, the interstitial fluoride ions and the anion vacancies respectively.

Assuming that a constant concentration $n_{e_F}^0$ of color centers is maintained by a definite

partial pressure of calcium vapor at the surface $x = 0$ and initially no excess of calcium is present in the calcium fluoride, the initial-boundary conditions for the diffusion equation (2) are then

$$n_{e_F}^* = n_{e_F}^0 \quad \text{at} \quad x = 0, \quad t > 0 \quad (4)$$

and

$$n_{e_F}^* = 0 \quad \text{at} \quad x > 0, \quad t = 0 \quad (5)$$

Equation (2) with conditions (4) and (5) is a one-dimensional diffusion in a semi-infinite sample. Following [3], we assume that $n_{e_F}^*$ is a function of the variable

$$\lambda = \frac{1}{2} x / (D_m^0 t)^{1/2} \quad (6)$$

only and introduce the dimensionless ratio

$$\gamma = \frac{n_{e_F}^*}{n_{e_F}^0} \quad (7)$$

Equation (2) can then be reduced to

$$-2\lambda \frac{d\gamma}{d\lambda} = \frac{d}{d\lambda} \left(\frac{1}{1 + A\gamma} \frac{d\gamma}{d\lambda} \right) \quad (8)$$

where

$$A = \alpha n_{e_F}^0 > 0 \quad (9)$$

and accordingly (4) and (5) become two-point boundary conditions

$$\gamma = 1 = \gamma_0 \quad \text{at} \quad \lambda = 0 \quad (10)$$

and

$$\gamma = 0 = \gamma_\infty \quad \text{at} \quad \lambda = +\infty \quad (11)$$

Now following [4] and [5], we introduce and substitute the new variable

$$s = \log(1 + A\gamma) \quad (12)$$

into equation (8), conditions (10) and (11), and obtain

$$\frac{d^2s}{d\lambda^2} = -2\lambda e^s \frac{ds}{d\lambda} \quad (13)$$

$$s = \log(1+A) = s_0 \quad \text{at} \quad \lambda = 0 \quad (14)$$

and

$$s = 0 = s_\infty \quad \text{at} \quad \lambda = +\infty. \quad (15)$$

Note that from equation (12) we have

$$\gamma = \frac{1}{A} (e^s - 1) \quad (16)$$

and

$$\frac{dy}{d\lambda} = \frac{e^s}{A} \frac{ds}{d\lambda}. \quad (17)$$

SOLUTION BY THE ITERATION METHOD

A formal solution of the diffusion equation with equation (8) as a special case has been obtained [6]. A method for obtaining a numerical solution of equation (8) with conditions (10) and (11) through interpolations of some tabulated values, corresponding to certain values of a parameter, of λ and γ has been worked out [1]. A method involving step function approximation [7] may also be applied to obtain a numerical solution of equation (8).

In what follows an iteration method with one simple programme for a computer to obtain a numerical integration of equation (8) subject to conditions (10) and (11) is presented. In this method the iterations converge rapidly and the error in each iteration can be estimated.

Comparing with the former approaches, the advantage of this method is its speed and its obtaining a numerical integration of equation (8) for any given value of parameter A with prescribed estimated accuracy without resorting to any tabulation or any interim manipulation.

Notice that if the initial gradient corresponding to the solution of equation (8) with the two-point boundary conditions (10) and (11) can be evaluated, then as an initial

condition problem the numerical integration of equation (8) can be readily performed by a computer. We shall evaluate the initial gradient by the iteration method. For this purpose we first derive an approximate differential equation of equation (13) as follows.

It is obvious from equation (13) with conditions (14) and (15) that $d^2s/d\lambda^2 > 0$ for $0 < \lambda < +\infty$, and for small λ , $d^2s/d\lambda^2 \ll 1$ and hence $ds/d\lambda$ changes slowly. Thus taking into consideration condition (14) we replace the term $ds/d\lambda$ on the right-hand side of equation (13) by the term

$$\frac{s - s_0}{\lambda} \quad (18)$$

and obtain an approximate equation of (13):

$$\frac{d^2s}{d\lambda^2} = 2e^s(s_0 - s). \quad (19)$$

Equation (19) is equivalent to

$$\frac{d}{ds} \left(\frac{ds}{d\lambda} \right)^2 = 4e^s(s_0 - s) \quad (20)$$

which can be integrated with condition (14):

$$\left(\frac{ds}{d\lambda} \right)^2 = s_0'^2 + 4\{e^s(1 + s_0 - s) - e^{s_0}\} \quad (21)$$

where

$$s_0' = \left(\frac{ds}{d\lambda} \right)_{\lambda=0}. \quad (22)$$

Equation (21) gives

$$\frac{ds}{d\lambda} = - (s_0'^2 + 4\{e^s(1 + s_0 - s) - e^{s_0}\})^{1/2} \quad (23)$$

and

$$s_0' = - \left(\left\{ \frac{ds}{d\lambda} \right\}^2 + 4\{e^{s_0} - e^s(1 + s_0 - s)\} \right)^{1/2} \quad (24)$$

where the choice of negative values is evident.

We note that condition (15) under equation (13) implies

$$\frac{ds}{d\lambda} = 0 \quad \text{at} \quad s = s_{\infty} = 0. \quad (25)$$

As first approximation we evaluate the initial gradient $s_0^{(1)}$ from (24) by assuming

$$\frac{ds}{d\lambda} = 0 \quad \text{at} \quad s = s_*^{(1)} = s_{\infty}.$$

Thus

$$s_0^{(1)} = -2(e^{s_0} - 1 - s_0)^{1/2}. \quad (26)$$

From (17) we obtain the corresponding initial gradient for equation (8)

$$\gamma_0^{(1)} = \left(\frac{d\gamma}{d\lambda} \right)_{\lambda=0}^{(1)} = \frac{e^{s_0}}{A} s_0^{(1)} \quad (27)$$

which together with (10) can be used as initial conditions to obtain by a computer a numerical integration of equation (8), from which the asymptotic value

$$\gamma = \gamma_{\infty}^{(1)} \quad \text{at} \quad \lambda = +\infty \quad (28)$$

can be approximately obtained. The difference

$$R_1 = \gamma_{\infty} - \gamma_{\infty}^{(1)} \quad (29)$$

between the asymptotic values (11) and (28) gives the error estimate of the first approximation.

Note that from (12) we obtain the corresponding asymptotic value for the solution of equation (13)

$$s_{\infty}^{(1)} = \log(1 + A\gamma_{\infty}^{(1)}) \quad (30)$$

between which and the asymptotic value (15) the difference

$$r_1 = s_{\infty} - s_{\infty}^{(1)} \quad (31)$$

will be used as a correction term for the next iteration.

As second approximation we again evaluate the initial gradient $s_0^{(2)}$ from (24) by assuming

$$\frac{ds}{d\lambda} = 0 \quad \text{at} \quad s = s_*^{(2)} = s_*^{(1)} + r_1.$$

Thus

$$s_0^{(2)} = -2\{e^{s_0} - e^{s_*^{(2)}}(1 + s_0 - s_*^{(2)})\}^{1/2}. \quad (32)$$

Then with (17) we calculate the corresponding initial gradient for equation (8)

$$\gamma_0^{(2)} = \frac{e^{s_0}}{A} s_0^{(2)} \quad (33)$$

which together with (10) can be used as initial conditions to obtain a numerical integration of equation (8), which yields approximately the asymptotic value

$$\gamma = \gamma_{\infty}^{(2)} \quad \text{at} \quad \lambda = +\infty. \quad (34)$$

The error of the approximation can then be estimated by the difference

$$R_2 = \gamma_{\infty} - \gamma_{\infty}^{(2)}. \quad (35)$$

The correction term for the next iteration is given by

$$r_2 = s_{\infty} - s_{\infty}^{(2)} \quad (36)$$

where $s_{\infty}^{(2)}$ can be evaluated with equation (12):

$$s_{\infty} = \log(1 + A\gamma_{\infty}^{(2)}). \quad (37)$$

Generally the k^{th} iteration proceeds as follows.

(i) Calculate

$$s_*^{(k)} = s_*^{(k-1)} + r_{k-1}. \quad (38)$$

(ii) By assigning

$$\frac{ds}{d\lambda} = 0 \quad \text{at} \quad s = s_*^{(k)} \quad (39)$$

to (24) evaluate

$$s_0^{(k)} = -2\{e^{s_0} - e^{s_0^{(k)}}(1 + s_0 - s_0^{(k)})\}^{1/2} \quad (40)$$

and then

$$\gamma_0^{(k)} = \frac{e^{s_0}}{A} s_0^{(k)}. \quad (41)$$

(iii) Use (10) and $\gamma_0^{(k)}$ as initial conditions to perform numerical integration of equation (8) and hence obtain approximately the asymptotic values

$$\gamma = \gamma_\infty^{(k)} \quad \text{at } \lambda = +\infty. \quad (42)$$

(iv) Compare the error estimate

$$R_k = \gamma_\infty - \gamma_\infty^{(k)} \quad (43)$$

with the prescribed value R .

(v) If $|R_k| > R$ and therefore further iteration is required, calculate

$$s_\infty^{(k)} = \log(1 + A\gamma_\infty^{(k)}) \quad (44)$$

and the correction term

$$r_k = s_\infty - s_\infty^{(k)} \quad (45)$$

for the next iteration.

The above iteration process, together with A, γ_∞ and the prescribed estimated accuracy R as input data, can be put into one simple programme to be executed by a computer.

By using a GE computer with the programme solutions of equation (8) with conditions (10) and (11) for a wide range of the parameter A have been worked out. The time taken by the computer from data input to solution printed was 1–2 min. The numerical integrations were calculated by Runge-Kutta method. Asymptotic values of the solutions were assumed after $|d\gamma/d\lambda| < 0.01$. The prescribed estimated accuracy was $R = 0.01$.

The numerical solutions obtained are listed in the following table.

Table 1. Results, obtained by iteration method, of numerical integration of equation (8)

$A = \alpha n_0^0$	0.500	1.000	2.000	4.000	6.000
Number of iterations required	6	6	6	10	12
$-(d\gamma/d\lambda)_{\lambda=0}$	1.483	1.787	2.305	3.158	3.835
λ	γ	γ	γ	γ	γ
0.0	1.000	1.000	1.000	1.000	1.000
0.1	0.856	0.830	0.788	0.725	0.679
0.2	0.723	0.680	0.615	0.524	0.464
0.3	0.602	0.551	0.476	0.381	0.324
0.4	0.495	0.441	0.368	0.279	0.230
0.5	0.402	0.350	0.283	0.206	0.166
0.6	0.323	0.276	0.217	0.153	0.122
0.7	0.256	0.215	0.166	0.114	0.090
0.8	0.200	0.166	0.126	0.084	0.067
0.9	0.154	0.127	0.095	0.063	0.050
1.0	0.117	0.096	0.072	0.046	0.038
1.1	0.088	0.071	0.054	0.034	0.029
1.2	0.065	0.052	0.040	0.025	0.022
1.3	0.047	0.038	0.029	0.018	0.017
1.4	0.033	0.027	0.021	0.013	0.013
1.5	0.023	0.019	0.016	0.009	0.010
1.6	0.016	0.013	0.011	0.006	0.008
1.7	0.010	0.009	0.008	0.004	0.007
1.8	0.007	0.006	0.006	0.003	0.006
1.9	0.004	0.004	0.005	0.002	
2.0	0.002	0.002	0.004		
2.1	0.001	0.001			

Runge-Kutta integration step size $\Delta\lambda = 0.01$

$A = \alpha n_0^0$	10.00	25.00	50.00	100.0	200.0
Number of iterations required	18	40	3	2	7
$-(d\gamma/d\lambda)_{\lambda=0}$	4.986	8.021	11.71	16.73	23.67
λ	γ	γ	γ	γ	γ
0.00	1.000	1.000	1.000	1.000	1.000
0.05	0.786	0.672	0.565	0.452	0.340
0.10	0.608	0.463	0.340	0.235	0.153
0.15	0.479	0.330	0.220	0.139	0.085
0.20	0.382	0.243	0.151	0.091	0.053
0.25	0.308	0.184	0.108	0.063	0.036
0.30	0.250	0.143	0.080	0.046	0.026
0.35	0.206	0.113	0.061	0.034	0.020
0.40	0.171	0.091	0.048	0.026	0.016
0.45	0.142	0.075	0.038	0.021	0.012
0.50	0.120	0.062	0.030	0.016	0.010
0.55	0.101	0.052	0.025	0.013	0.008
0.60	0.086	0.044	0.020	0.011	0.007
0.65	0.073	0.037	0.016	0.009	0.006
0.70	0.063	0.032	0.013	0.007	0.005
0.75	0.054	0.027	0.011	0.006	0.005
0.80	0.046	0.024	0.009	0.005	0.004
0.85	0.040	0.021	0.007	0.004	
0.90	0.034	0.018	0.006	0.003	
0.95	0.030	0.016	0.005	0.003	

Table 1 (cont.)

$A = \alpha n_{eF}^0$	10.00	25.00	50.00	100.0	200.0
Number of iterations required	18	40	3	2	7
$-(dy/d\lambda)_{\lambda=0}$	4.986	8.021	11.71	16.73	23.67
λ	γ	γ	γ	γ	γ
1.00	0.026	0.014	0.003	0.002	
1.05	0.022	0.013	0.003		
1.10	0.019	0.012	0.002		
1.15	0.017	0.010	0.001		
1.20	0.015	0.009	0.001		
1.25	0.013	0.008	0.000		
1.30	0.011	0.008			
1.35	0.010	0.007			
1.40	0.009	0.007			
1.45	0.008				
1.50	0.007				
1.55	0.006				
1.60	0.006				
1.65	0.005				
Runge-Kutta integration step size $\Delta\lambda = 0.01$					
$A = \alpha n_{eF}^0$	500.0	1000.0	1500.0		
Number of iterations required	7	4	4		
$-(dy/d\lambda)_{\lambda=0}$	37.59	55.93	68.90		
λ	γ	γ	γ		
0.00	1.000	1.000	1.000		
0.02	0.487	0.355	0.289		
0.04	0.267	0.160	0.117		
0.06	0.164	0.086	0.059		
0.08	0.110	0.052	0.034		
0.10	0.078	0.034	0.021		
0.12	0.059	0.023	0.014		
0.14	0.046	0.017	0.010		
0.16	0.036	0.012	0.007		
0.18	0.030	0.009	0.005		
0.20	0.025	0.007	0.003		
0.22	0.021	0.005	0.002		
0.24	0.018	0.004	0.002		
0.26	0.016	0.003	0.001		
0.28	0.014	0.002	0.001		
0.30	0.012	0.002	0.001		
0.32	0.011	0.001	0.000		
0.34	0.010	0.001	0.000		
0.36	0.009	0.001			
0.38	0.008	0.000			
0.40	0.008	0.000			
0.42	0.007				
0.44	0.007				
0.46	0.006				
0.48	0.006				
0.50	0.005				
0.52	0.005				
0.54	0.005				
0.56	0.005				
0.58	0.004				
0.60	0.004				
Runge-Kutta integration step size $\Delta\lambda = 0.005$.					

CONCLUDING DISCUSSIONS

As it has been pointed out in [1] that solutions for $\alpha n_{eF}^0 > 1$ are characterized by a high negative gradient at $\lambda = 0$. However the present method would still be applicable even if $A = \alpha n_{eF}^0$ is very large. As shown in the table numerical solution of equation (8) has been obtained by the present approach even for $A = \alpha n_{eF}^0 = 1.500$.

From the above tabulated values it can be seen that for the same value of λ the values of γ are decreasing with increasing values of the parameter A . This shows that with increasing initial concentration the diffusion of color centers in terms of the ratio of local concentration to initial concentration is slowed down in a manner described quantitatively by the present method.

It has been noted [8] that the value of $(dy/d\lambda)_{\lambda=0}$ for a particular value of the parameter A could be estimated by means of interpolation with the tabulated values. Plotting $(dy/d\lambda)_{\lambda=0}$ vs. $(1+A)^{1/2}$ one obtains nearly a straight line so that interpolations is feasible, bearing a rather small error. Assuming such approximation the initial gradient $(dy/d\lambda)_{\lambda=0}$ is linearly increasing with $(1+A)^{-1/2}$, inverse square root of the local diffusion coefficient at $\lambda = 0$, in accord with the general conclusion [1] that local concentration gradient is inversely proportional to the local diffusion coefficient. Actually the quotient

$$\frac{\left(\frac{dy}{d\lambda}\right)_{\lambda=0} - \left(\frac{dy}{d\lambda}\right)_{\lambda=0, A=0}}{(1+A)^{1/2} - 1}$$

increases from about 1.58 to about 1.73 over the total range of A between 0 and 1500. Hence strictly speaking the graph is not a straight line, but concave upward.

In many instances [5,9] the study of diffusion process in solid states often leads to the problem of solution of a diffusion equation involving concentration-dependent diffusion-coefficient, subject to initial-boundary conditions similar to (4) and (5).

Without modifications the above method applies to the solution of such equations. It has been pointed out[1] such would be the case with the diffusion process during the uptake of excess alkali metal by alkali halides.

Acknowledgements—The author is indebted to Professor C. Wagner for his communication and useful discussion. The author wishes to thank Professor L. Bass and Professor I. Lauder for their criticism and to thank Mr. I. Oliver for his advice on programming of the computer.

REFERENCES

1. WAGNER C., To appear in *J. Phys. Chem. Solids*, (1969).
2. KRÖGER F. A., *The Chemistry of Imperfect Crystals*. North-Holland, Amsterdam (1964).
3. BOLTZMANN L., *Wiedem. Ann. Phys.* **53**, 801 (1894).
4. EYRES N. R. HARTREE D. R., INGHAM J., JACKSON R., SARJART A. J. and WAGSTAFF S. M., *Phil. Trans. R. Soc. A* **240**, 1 (1946).
5. CRANK J., *Mathematics of Diffusion*. Oxford (1967).
6. FUJITA H., *Text. Res. J.* **24**, 234 (1954).
7. PHILIP J. R., *Trans. Faraday Soc.* **51**, 885 (1955).
8. WAGNER C., Private communication.
9. BARRIER R. M., *Diffusion in and through Solids*. Cambridge (1941).

LOW TEMPERATURE ELECTROLUMINESCENCE OF ZnSe:Cu:Br*

GEORGE A. SAUM, RICHARD H. GLAENZER and JAMES E. DUEKER

McDonnell Research Laboratories, McDonnell Douglas Corporation, St. Louis, Mo. 63166, U.S.A.

(Received 28 March 1969)

Abstract—The electroluminescent (EL) properties of zinc selenide doped with copper and bromine have been measured at various frequencies of the applied operating voltage and as a function of temperature. The samples measured were prepared with different doping concentrations and firing schedules. Two EL emission bands have been observed, at ~ 5300 and ~ 6300 Å. The relative intensities of these two bands were found to depend upon how the samples were prepared. The observed characteristics are in agreement with models which have been proposed to explain reported photoluminescence and photoconduction experiments.

1. INTRODUCTION

OUR ORIGINAL interest in ZnSe was to use it as an electroluminescent phosphor for visible displays held at liquid nitrogen temperature. Experiments undertaken to determine the electroluminescent properties of ZnSe:Cu:Br revealed two electroluminescent emission bands at ~ 5300 and 6300 Å. This observed electroluminescent emission can be explained on the basis of the same models which have been proposed for photoluminescence and photoconduction experiments[1,2]. Should the shorter wavelength emission predominate when the phosphor is cooled to liquid nitrogen temperature, this would be a useful phosphor, since the green (5300 Å) band in ZnSe:Cu is near the peak of the eye's sensitivity[3] and thus has potentialities for greater apparent brightness. So far, ZnSe has not proven superior in brightness to a more commonly used phosphor ZnS which when cooled shifts its emission to the deep blue, away from the peak of eye response, resulting in low sensitivity to the human eye.

2. EXPERIMENTAL PROCEDURES

Samples were prepared from slurries of ZnSe, $\text{Cu}(\text{NO}_3)_2$, and ZnBr_2 in alcohol and

then dried at 200°C . In some samples, NH_4Br was added after drying. Firing was done in a tight, but not sealed, quartz ampoule in a quartz tube furnace with helium flushing gas. Firing times were 20 min, and the samples were rapidly withdrawn to the cool zone. The materials were then ground, etched with aqueous sodium cyanide, washed, dried, mixed with epoxy[4], and bladed in layers $50\text{ }\mu\text{m}$ thick on brass substrates. A transparent gold layer ($300\text{ }\Omega/\square$) was used as one contact. The brass substrates were tightly screwed to the cooling block of a vacuum optical dewar. The EL spectra were measured with a monochromator (Bausch and Lomb High Intensity Monochromator Model 2) and a photomultiplier (RCA 7326, S-20 response).

3. ELECTROLUMINESCENT PROPERTIES

Measurements of the photoluminescent properties of ZnSe:Cu by Morehead[1] have shown two prominent emission bands at 1.97 eV (6300 Å) and 2.34 eV (5300 Å). These same two bands have now been observed in electroluminescent spectra. The relative intensities of these two EL bands can be established by the processing techniques used and somewhat by the operating parameters (frequency and temperature). The following paragraphs discuss how these bands

*This research was conducted under the McDonnell Douglas Corporation Independent Research and Development Program.

are controlled and how they behave in response to thermal quenching.

General dependence of processing

The relative intensities of the 1.97 and 2.34 eV bands can be controlled by the amount of Cu cation and Br anion added and by the firing temperature. When only Cu ion is added to the ZnSe powder, a single EL band at 2.34 eV is obtained. As the bromine ion content is increased, a band at 1.97 eV develops and increases, as shown in Fig. 1.

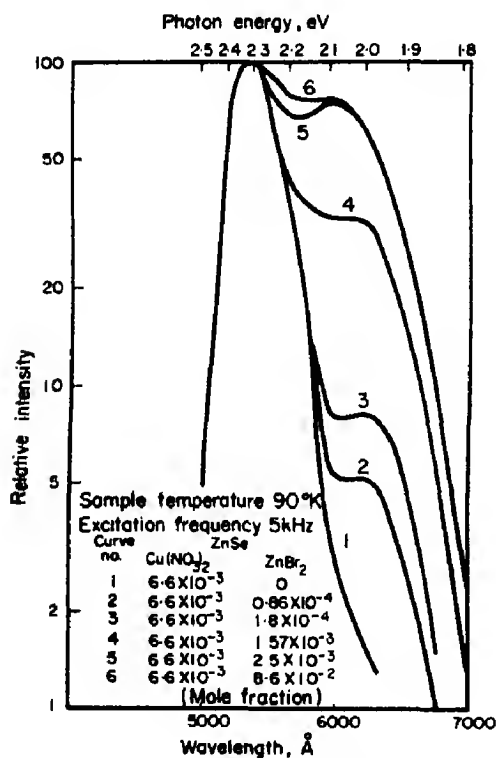


Fig. 1. Spectral electroluminescence brightness for various bromine ion concentrations.

The 1.97 eV band seems to become saturated with about 2.5×10^{-3} mole fraction Br ion added. Whether this saturation is due to rapid volatilization during firing of the ZnBr₂ in the mix, hence restricting the level of bromine ion concentration, or whether it may be a consequence of the limited solubility of bromine ion in ZnSe at 950°C as indicated below is not known. Both possibilities exist.

By varying the firing temperature, the intensity of the 1.97 eV band can also be controlled as shown in Fig. 2. Our samples

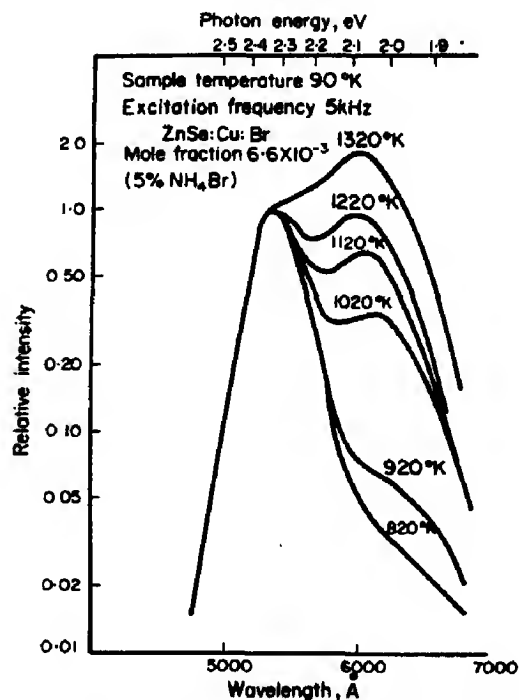


Fig. 2. Spectral electroluminescence brightness for various firing temperatures.

all had excess Br ion (5 per cent NH₄Br), so the increasing brightness of the 1.97 eV band reflects either the increased solubility of bromine ion with temperature or an increase in sites for Br ion resulting from selenium vacancies generated at the firing temperature.

The energy of the 1.97 eV band changes with preparation methods, shifting ~ 0.1 eV (to 2.07 eV) at higher bromine ion concentrations or higher firing temperatures. For convenience, it is still called the 1.97 eV band.

Dependence of operation parameters

The overall EL brightness of two typical samples as a function of temperature is shown in Fig. 3. In the one sample (ZnSe:Cu:Br), two broad maxima are observed during cooling from room temperature. The first maximum is predominantly red (1.97 eV) in color, and the second is predominantly green

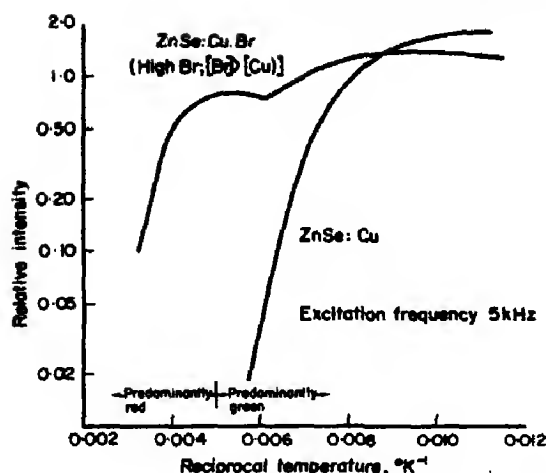


Fig. 3. Electroluminescence intensity for various temperatures.

(2.34 eV). The crossover between these two is at about 200°K. The other sample (ZnSe:Cu) was doped to have green emission only and did not show the first maximum.

The spectral output at various temperatures shows more explicitly what happens during cooling. In Fig. 4, the 1.97 eV emission

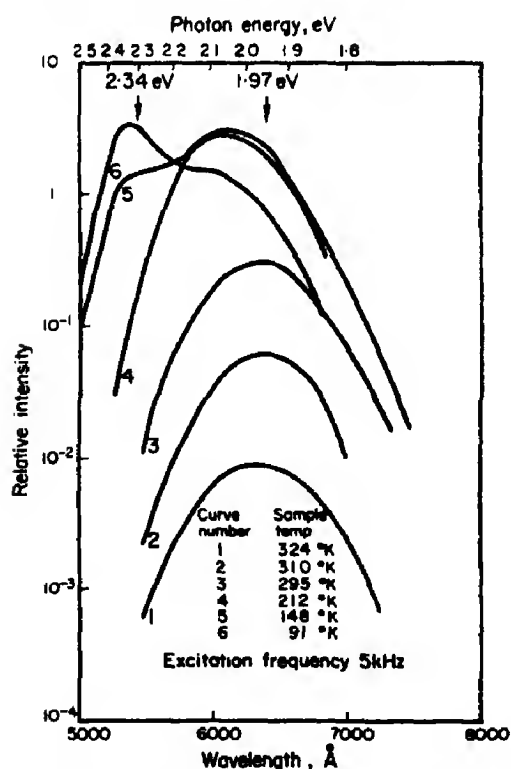


Fig. 4. Spectral electroluminescence brightness for various temperatures.

develops rapidly as the sample is cooled from 324° to 200°K, and then the 2.34 eV band develops below 200°K.

The relative intensity of these two bands can be varied with change in excitation frequency, as is shown in Fig. 5. As the frequency is increased, the high energy band (2.34 eV) increases faster than the low energy band (1.97 eV) similar to the behavior of the

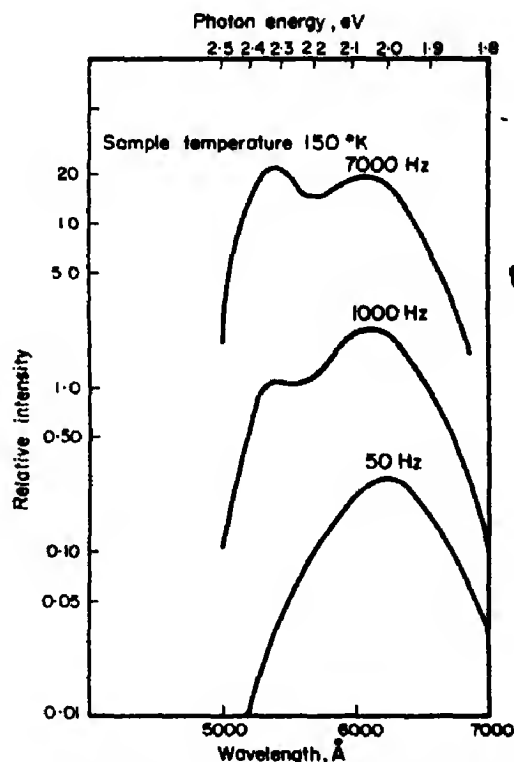


Fig. 5. Spectral electroluminescence brightness for various excitation frequencies.

two bands in ZnS phosphors[5]. These measurements were made at 150°K, the temperature at which the holes have a chance to escape from the green centers and become trapped on red centers during one cycle of excitation. At higher or lower temperatures, the spectra are relatively insensitive to frequency of excitation.

Temperature quenching of EL

Samples were prepared to show predominantly the 1.97 eV band or 2.34 eV band

so that the brightness of one particular band could be measured as a function of temperature with a minimum of interference from the other band. The intensity of the green band, as a function of $1/T$, for several excitation frequencies, is shown in Fig. 6. Three main

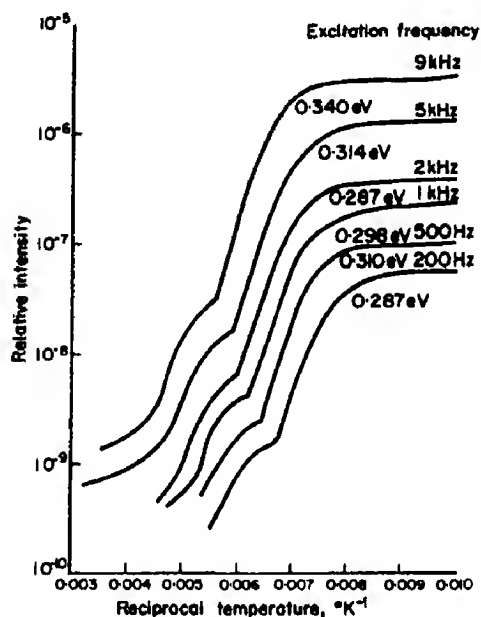


Fig. 6. Electroluminescence intensity of 2.34 eV photons as a function of temperature and excitation frequency.

features are noted: a constant intensity region at low temperature; a region of thermal quenching of the emission, with quenching activation energy of approx. 0.3–0.35 eV; and a 'shoulder' on the quenching portion of the curve. Spectral measurements show no shift in wavelength of the green band (2.34 eV) when this shoulder appears, but observations of the brightness wave (Fig. 7) show that a secondary brightness maximum occurs when the shoulder appears. This secondary maximum has been proposed as being either the release of trapped electrons[6] or the return (during a later portion of the voltage pulse) of conduction electrons which missed the luminescent centers on the first transit through the crystallite[7]. A plot of the $1/T$ position of this shoulder versus frequency gave an activation energy of 0.27 eV. This is so close to the

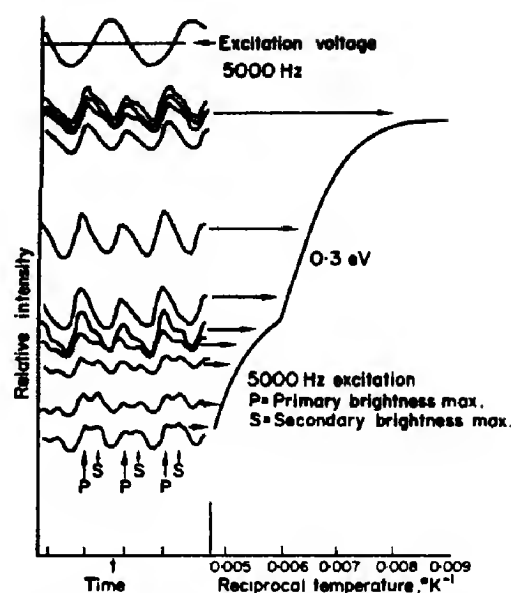


Fig. 7. Relative intensity of 2.34 eV band vs. $1/T$ and brightness wave form at various intensities.

quenching activation energy (0.3 eV) that an unambiguous interpretation is difficult.

The ~ 0.3 eV quenching of EL red band is to be compared to the ~ 0.4 eV value of quenching of overall photoluminescence observed by Morehead[1].

The temperature quenching characteristics of the 1.97 eV band are shown in Fig. 8. This curve gives an indication of the expected 0.7 eV slope, which is predicted from the ZnSe:Cu model[1], though a long, linear slope is not demonstrated as clearly as might be desired before the curve falls into a 1.35 eV (or greater) slope. The simplest interpretation for this steep slope which is not expected from the model for the Cu ion centers in the ZnSe is the presence of a radiationless recombination center with an activation energy 1.35 eV, which competes with the luminescent center for the free electrons at higher temperatures. (This same slope was also found using u.v. rather than EL excitation, so this steep portion is not due to the EL excitation process.) A few experiments such as adding large quantities of selenium or NH_4Br to the charge in order to more effectively expel

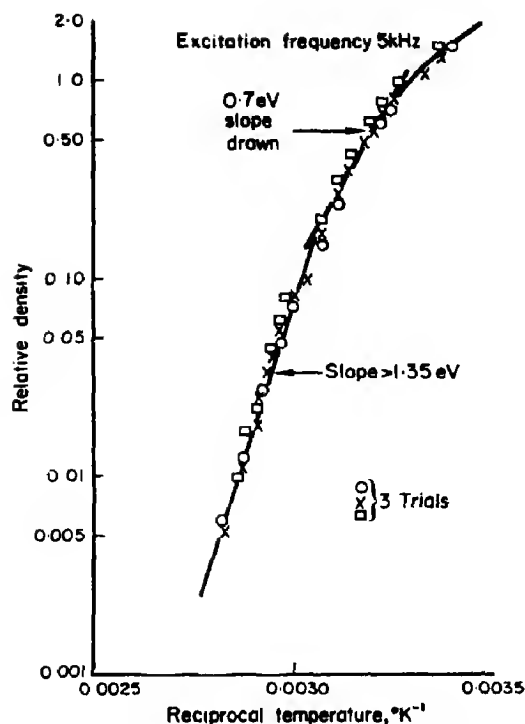


Fig. 8. Electroluminescence intensity of 1.97 eV photons for various temperatures.

residual oxygen have had no noticeable effect on this quenching energy.

4. DISCUSSION

ZnSe:Cu:Br can be prepared to show either a predominant red (1.97 eV) or green (2.34 eV) EL band by varying the bromine ion concentration and firing temperature. The two EL bands show thermal quenching with about 0.7 and 0.3 eV activation energy, respectively. The electroluminescent characteristics of these two bands can be explained by the 2 energy level model for ZnSe:Cu proposed by Morehead[1] and Stringfellow and Bube[2] shown in Fig. 9. The copper ion alone produces a center ~ 0.3 eV above the valence band (or 2.4 eV below the conduction band)

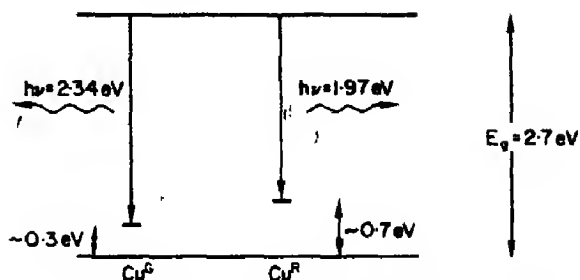


Fig. 9. Simplified energy band diagram of ZnSe doped with copper ion.

and is responsible for the 2.34 eV emission. As bromine ion is added to the sample, the first Cu ion level becomes compensated (or associated with Br ion) and the second Cu level, ~ 0.7 eV above the valence band (or 1.97 eV below the conduction band), appears, giving rise to the 1.97 eV emission. The extra shoulder on the 2.34 eV quenching curve can be interpreted either as release of electrons from traps 0.27 eV deep, or as the return of free electrons to the luminescent center later in the voltage cycle. The extremely large quenching activation energy (> 1.35 eV) for the 1.97 eV band at higher temperatures can be attributed to a competing recombination center, the source of which was not demonstrated in these experiments.

REFERENCES

1. MOREHEAD F. F., *J. Phys. Chem. Solids* **24**, 37 (1963).
2. STRINGFELLOW G. B. and BUBE R. H., *Phys. Rev.* **171**, 903 (1968).
3. BORN B. and WOLF E., *In Principles of Optics*, p. 184. Pergamon Press, Oxford (1965).
4. Hysol R9-2039 with H3840 Hardener, Hysol Corporation, Olean, New York.
5. IVEY H. F., *In Electroluminescence and Related Effects*, p. 50. Academic Press, New York (1963).
6. IVEY H. F., *In Electroluminescence and Related Effects*, p. 90. Academic Press, New York (1963).
7. IVEY H. F., *In Electroluminescence and Related Effects*, p. 94. Academic Press, New York (1963).

MAGNETIC SUSCEPTIBILITIES AND NMR PROPERTIES OF V-Ru ALLOYS

M. BERNASSON, P. DESCOUTS, P. DONZÉ and A. TREYVAUD
Institute of Experimental Physics, University of Geneva, Geneva, Switzerland

(Received 20 March 1969)

Abstract—NMR and magnetic susceptibility properties of the multiphase V-Ru alloy system have been measured between room and liquid helium temperatures. The Knight shift of the ^{51}V behaves similarly as in some other previously investigated cubic V-X alloys for the same c/a ratio. Taking into account the recent specific heat and the present magnetostatic results, obtained in the same V-Ru samples, the NMR data are analysed.

THE SPECIFIC heat, susceptibility and NMR properties have been extensively studied for the alloys of vanadium with the 3d and 4d transition elements[1-4]: Ti, Cr, Fe, Nb and Tc. Generally the rigid band model has been used to explain the similarity in behaviour.

In this article we report the measurements of the magnetic properties of vanadium-ruthenium alloys whose specific heats and superconducting transition temperatures have been already studied[5].

The bulk samples are the same that were used for the measurements of the thermal properties. They were prepared from 3N vanadium and 5N ruthenium by arc-melting under argon pressure and initially no annealing was performed. The alloys compositions were deduced from the weighed charges before melting; X rays studies have confirmed the structures given in reference[6]: V and Ruthenium at high temperature form solid solutions progressing continuously through the structures b.c.c., CsCl, tetragonal, to hexagonal as the percentage of V is increased.

The powders for NMR measurements were obtained by filing and ball-milling: the particle size was under 40 μ .

Magnetic susceptibilities were obtained by measuring the force acting on small specimens (about 100 mg) in constant H dH/dy magnetic configuration, from room tempera-

tures down to 1.5°K, and in fields ranging between 2 and 17 kOe.

Figure 1 shows the molar susceptibility χ_m (at 20°C) of the $\text{V}_{1-x}\text{Ru}_x$ alloy system with dependence in Ru concentration. A close similarity in the general aspect appears by comparing this susceptibility plot with the respective curves for the electronic specific heat coefficients and superconductivity transition temperatures[5].

In good agreement with the nearly temperature independent behaviour observed for the NMR Knight shift (see later), susceptibility measurements have shown no important variation as a function of temperature. After corrections for the parasitic magnetic impurities, all the investigated V-Ru alloys exhibit changes in susceptibility less than 1-10 per cent between room and liquid He temperatures.

From [7] each Fe atom dissolved in $\text{V}_{1-x}\text{Ru}_x$ with $0.3 < x \leq 0.5$ is known to have an associated localized magnetic moment with effective value ranging between 1 and 2.5 μ_B . The purity of the V used to prepare the ingots was not better than 3N, major impurity being Fe. As expected, an appreciable Curie-like susceptibility term was observed in low temperature measurements for the alloys in the Ru concentration range where we have to deal with localized Fe moments. Therefore the χ_m vs. T curves were corrected with a

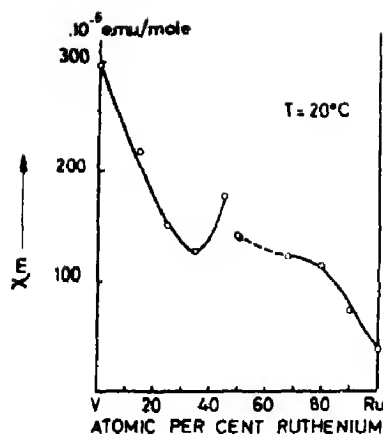


Fig. 1. Magnetic susceptibility of V-Ru alloys as a function of composition.

Curie or Curie-Weiss law contribution in such a way that $d\chi_m^{\text{alloy}}/dT = 0$ at extrapolated 0°K temperature, as usually performed. The Fe impurities content can be estimated to about 1000 ppm. The corrected molar susceptibilities at 0°K for all 'pure' alloys $\chi_m^{\text{alloy}}(0^\circ\text{K})$ are to be found in the Table 1.

Knight shift measurements were performed with a modified Varian NMR spectrometer: a laboratory built crossed coils probe with a balancing system similar to that designed by Drain[8] was adapted to the Varian spectro-

meter for the measurements at nitrogen and helium temperature. The metal dewar used for the low temperature measurements was of standard commercial type. The magnetic field of the 12 in. Varian magnet was monitored with a marginal oscillator using deuteron or proton resonances.

Figure 2 shows the Knight shift at 10 Mhz, referred to pure vanadium dissolved in nitric acid, as a function of composition. Within the limit of error the Knight shift can be considered independent of the temperature. The very small increase with field, almost indepen-

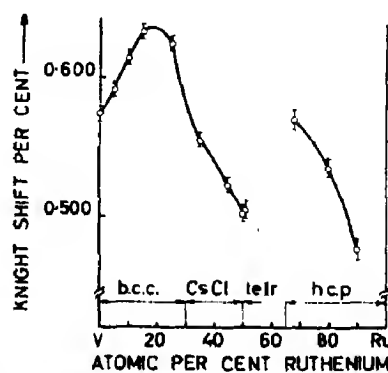


Fig. 2. The Knight shift of the ^{51}V magnetic resonance in V-Ru alloys as a function of composition measured at 10 Mc/s.

Table 1. V-Ru data table

	$\chi_m^{\text{alloy}}(0^\circ\text{K})$ (i)	χ_m^{dia}	γ (ii)	$\chi_m^{\text{spin}}(\gamma)$	χ_m^{cv}	θ_D (ii)	T_c (ii)	λ	γ^* (iii)	$\chi_m^{\text{spin}}(\gamma^*)$	$\chi_m^{* \text{vt}}$
V	303 (iv)	- 9	9.9	135	177	399	5.3	0.599	6.19	85	227
Ru _{0.15}	221	- 11	3.95	54	178	351	< 1				
Ru _{0.25}	149	- 12	1.93	26	135	460	< 1				
Ru _{0.35}	125	- 13	1.93	26	112	460	< 1				
Ru _{0.45}	182	- 14	7.40	101	95	413	4.0	0.552	4.77	65	131
Ru _{0.50}	125	- 15	3.55	48	92	420	< 1				
Ru _{0.51}	122	- 15	3.75	51	86	427	< 1				
Ru _{0.58}	111	- 17	4.4	60	68	417	4.0	0.552	2.84	39	89
Ru _{0.80}	106	- 19	3.82	52	73	475	2.8	0.497	2.55	35	90
Ru _{0.90}	68	- 20	3.23	44	44	500	1.2	0.426	2.27	31	57
Ru	38 (iv)	- 21	3.0	41	18	550	0.49	0.375	2.18	30	29

- (i) Measured total molar susceptibilities extrapolated at 0°K and corrected for parasitic Fe impurities. All susceptibilities are to be found in this table in 10^{-6} e.m.u./mole units.
- (ii) Results of Flükiger, Heiniger and Muller[5]. The electronic specific heat coefficients are expressed in $\text{mJ}/^\circ\text{K}^2 \text{ mole}$. The Debye θ_D and transition T_c temperatures are in °K.
- (iii) All quantities marked with an asterisk are related to McMillan theory[11].
- (iv) Our susceptibility results on pure V are in good agreement with the other data to be found in the recent literature. The Ru magnetic data are taken from WEISS and KOHLHAAS, *Z. angew. Phys.* 23, 175 (1967).

dent of composition, can be attributed to a second order quadrupole effect.

For the CsCl type alloys the indicated Knight shift has been measured at helium temperature, where the line shape is normal. At nitrogen and room temperature, these samples show an assymmetric line broadening, and satellites appear in the high field side of the main resonance (Fig. 3). The satellites shift being proportional to the field prevents their observation at field lower than 8 kG and shows that they are not the result of a second-order quadrupole effect, but of magnetic origin.

Annealing of these samples at 800°C for 24 hr completely changed the line shapes: the satellites in the high field side of the resonance vanished and new satellites again field dependent appeared in the low field side (Fig. 3). The same behaviour was observed

with a bulk sample which was annealed for 10 hr at 1400°C and then powdered. Such phenomena could be the result of ordering in CsCl structure and further investigations of this effect are in progress.

We have verified that annealing of the other samples at 800°C causes a difference of less than one per cent in susceptibility and Knight shift measurements. The linewidth, defined as the separation of the absorption peaks, was measured for all the samples at different fields and temperatures. In the b.c.c. and hexagonal structures, the linewidth is independent of temperature, except for a small increase at helium temperature, which is almost certainly the result of impurity effect. For the CsCl structure where the high temperature line shape does not allow us to define a linewidth the reported values were taken at helium temperature.

The linewidth shows a marked dependence on the field and varies with composition (see Fig. 4); the extrapolated value for $H = 0$ gives the field independent value which is of the same order as the estimated theoretical linewidth (as calculated with the Van Vleck formula assuming a Gaussian line shape).

For the field dependent contribution we can distinguish between the behaviour of the b.c.c. structure and that of the hexagonal structure. In the first case (Fig. 5) the linewidth increases with the field, independently

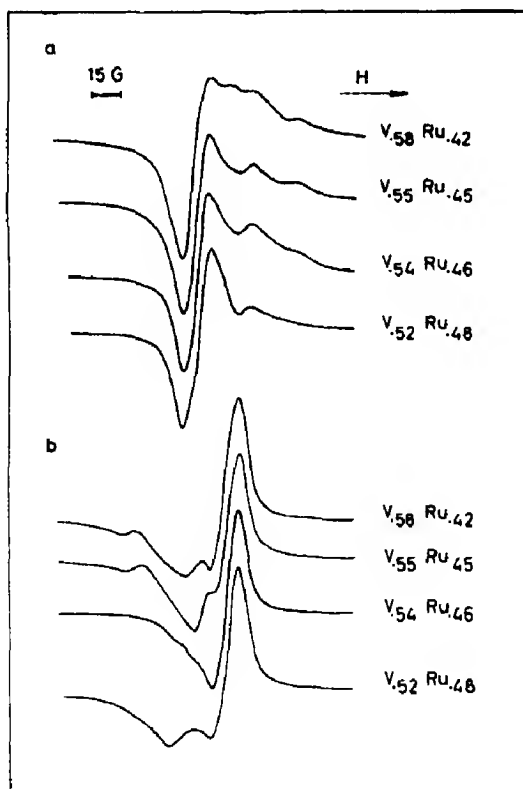


Fig. 3. Typical NMR absorption derivative curves of ^{51}V in V-Ru alloys with CsCl structure; (a) unannealed, (b) annealed at 800°C.

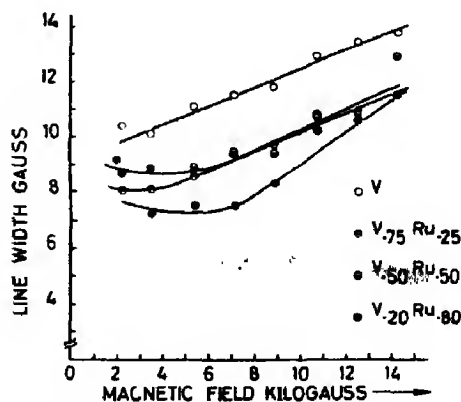


Fig. 4. The field dependence of ^{51}V resonance linewidth of some V-Ru alloys.

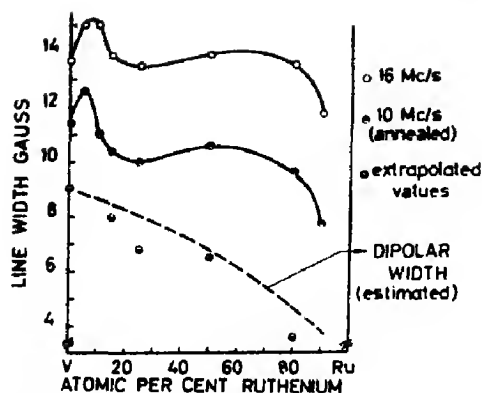


Fig. 5. Linewidth of ^{51}V magnetic resonance in V-Ru alloys as a function of composition.

of composition: it could be in part the result of the demagnetization field arising from the bulk magnetism of the particles (of order 1 g) and in part to Knight shift effects caused by local fluctuations in concentration or anisotropic shift. For h.c.p. case the variation of the linewidth with field shows a minimum (see Fig. 5) in high fields the linear dependence on field is more marked than in the b.c.c. structures: this is probably caused by an increase of the anisotropic shift, as confirmed by the asymmetry of the line. At low field the increase of the linewidth is the result of a second order quadrupole effect as expected with the hexagonal structure and the minimum is obviously the combination of the two effects.

The similarity in behaviour of the Knight shift of VCr, VFe, VTc and VRu in b.c.c. phase as a function of electron-atom ratio (see Fig. 6) suggests an analysis of the results on the basis of a rigid-band model. Such an analysis has been done for VCr [1, 3, 4].

The susceptibility data can be crudely analysed to estimate the orbital contribution of the Van Vleck type χ_m^{vv} in this alloy system:

$$\chi_m^{vv} = \chi_m^{\text{alloy}} - \chi_m^{\text{dia.}} - \chi_m^{\text{spin}}(\gamma).$$

For the diamagnetic contribution $\chi_m^{\text{dia.}}$ of the closed-shell ions we took linearly interpolated values between the average value of

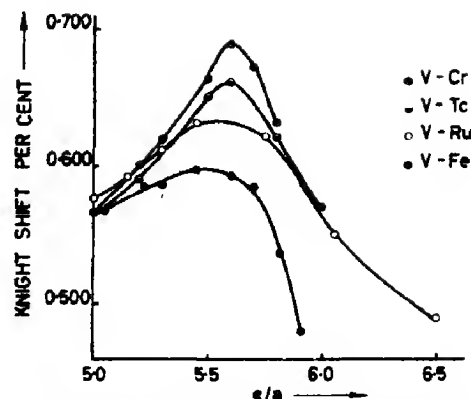


Fig. 6. Knight shift of ^{51}V in V-Cr, V-Fe, V-Tc and V-Ru alloys as a function of e/a .

$-9 \cdot 10^{-6}$ e.m.u./mole for V and the one of $-21 \cdot 10^{-6}$ for Ru atoms. The very small Landau diamagnetic susceptibility arising from s electrons was neglected. In a first attempt to estimate χ_m^{vv} we have calculated the unenhanced Pauli spin susceptibility for s and d electrons $\chi_m^{\text{spin}}(\gamma)$ from the specific heat results of Heiniger [5]. These values are given in Table 1.

The Knight shift was then calculated

$$K = K_s + K_d + K_{vv} \\ = a\chi_s + b\chi_d + c\chi_{vv}$$

using the Clogston [9, 10] values of the coupling coefficients a , b and c : the result of this analysis for the cubic alloys is in qualitative agreement with the data of Fig. 2 (see Fig. 7).

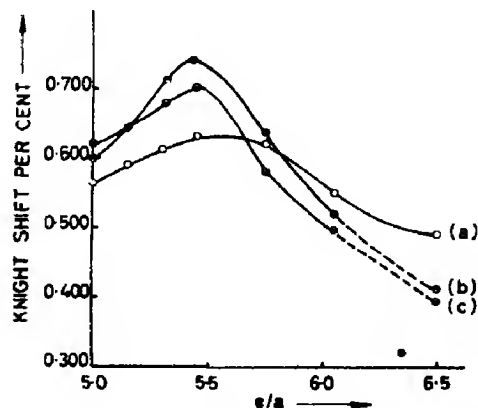


Fig. 7. Knight shift of ^{51}V in V-Ru alloys as a function of e/a in the cubic range; (a) measured, (b) estimated using χ_m^{spin} specific heat (c) estimated using χ_m^{spin} with MacMillan correction.

A possible origin of the quantitative discrepancy could be a poor estimation of the spin susceptibility caused by ignoring the electron-phonon interaction in density of states and/or the exchange enhancement of the spin susceptibility. For the samples in the hexagonal range of structure, some qualitative agreement between the susceptibility and the Knight shift was obtained, but the basis of a quantitative analysis is for the present uncertain.

The electron-phonon contribution to the specific heat coefficient, γ , can be computed, using the theory of McMillan [11].

Taking his semi-empirical electron-electron coupling constant $\mu^* = 0.13$ (more or less appropriate for transition metal alloys as shown by McMillan) we can compute the electron-phonon coupling constant λ with the help of the measured [5] transition temperatures, T_c , and Debye temperatures θ_D . Thus we calculate the electronic heat capacity coefficient γ^* corrected for the electron-phonon interaction; γ^* and γ are related by the enhancement factor $(1 + \lambda)$. Again from γ^* we can obtain values for χ_m^{spin} (γ^*) and hence for χ_m^{*ev} (see the data Table 1).

With the help of this McMillan correction we reanalyse the Knight shift data in the cubic range. It is impossible to make direct use of the McMillan theory because of the lack of T_c data. However assuming the same λ value as in the CrV system for the same e/a ratio one finds some improvement over the uncorrected estimates, as shown in Fig. 7 but the results are not in precise quantitative agreement. Further studies are planned to

obtain the required data on T_c and to test the rigid band model in more detail by nuclear spin lattice relaxation measurements. However the rough agreement may be a result of the fact that the relatively large and dominant orbital contribution to the estimated Knight shift is only slightly modified by the other contributions.

Acknowledgements—The authors wish to thank Dr. F. Heiniger for the V-Ru samples, Dr. L. E. Drain for informations about his NMR apparatus, and A. Dupanloup for technical assistance. They are indebted to Professor J. Muller and Dr. F. Heiniger for numerous discussions and helpful suggestions throughout the course of this work. Special thanks are due to Professor A. Heeger for reading and commenting on the manuscript prior to publication. This work was financially supported by the Swiss National Science Foundation.

REFERENCES

1. DRAIN L. E., *J. Phys. Radium* **23**, 745 (1962).
2. VAN OSTENBURG D. O., LAM D. J., TRAPP H. D. and MACLEOD D. E., *Phys. Rev.* **128**, 1550 (1962).
3. SHIMIZU M., TAKAHASHI T. and KATSUKI A., *J. phys. Soc. Japan* **18**, 1192 (1963).
4. BUTTERWORTH J., *Proc. phys. Soc.* **83**, 71 (1964).
5. FLÜKIGER R., HEINIGER F. and MÜLLER J., *11th Conf. Low Temperature Physics*, p. 1021 (1968).
6. RAUB E. and FRITZCHE W., *Z. Metallk.* **54**, 21 (1963).
7. CLOGSTON A. M., MATTHIAS B. T., PETER M., WILLIAMS H. J., CORENZWITT E. and SHERWOOD R. C., *Phys. Rev.* **125**, 541 (1962).
8. DRAIN L. E., *Discuss. Faraday Soc.* **19**, 200 (1955); Private communication.
9. CLOGSTON A. M., GOSSARD A. C., JACCARINO V. and YAFET Y., *Phys. Rev. Lett.* **9**, 262 (1962).
10. DRAIN L. E., *Proc. phys. Soc.* **83**, 755 (1964).
11. MCMILLAN W. L., *Phys. Rev.* **167**, 331 (1968).

DIFFUSION OF NICKEL INTO LEAD TELLURIDE BETWEEN 200° AND 400°C*

T. D. GEORGE† and J. B. WAGNER, Jr.

Department of Materials Science Northwestern University Evanston, Ill. 62201, U.S.A.

(Received 11 March 1969)

Abstract—The diffusion of nickel into lead telluride has been studied between 200° and 400° as a function of crystal composition and doping. Even at these temperatures, the diffusion of nickel is very dependent on the composition of the crystal. For the most part the nickel distribution profiles, as determined using radiotracer techniques, cannot be described by a simple solution of the diffusion equation. Except in crystals containing a large concentration of cation vacancies, the nickel distribution profiles are best fit by two overlapping curves, each of which is a solution of the diffusion equation with different values of the diffusion coefficient. Diffusion into crystals containing a large cation vacancy concentration can be described by a simple solution of the diffusion equation. The range of compositions which can be studied at these temperatures is restricted by the retrograde solubility of lead and tellurium in PbTe.

INTRODUCTION

IT HAS BEEN evident for sometime that impurities such as copper, nickel, and silver have unusually large diffusion coefficients in semiconducting materials. Copper has been shown to diffuse rapidly into PbS[1], germanium[2], silicon[3] and GaAs[4], while nickel diffuses rapidly into PbS[5] and germanium[6]. Bloem and Kröger[1, 5] found that in the temperature range 100°–500°C both nickel and copper behave as donors in PbS. By measuring the migration of the *p-n* junction into initially *p*-type PbS, they determined the diffusion coefficients of Cu and Ni into PbS to be,

$$D_{\text{Cu}} = 5 \times 10^{-5} \exp(-7130/RT) \quad (1)$$

and

$$D_{\text{Ni}} = 17.8 \exp(-22,000/RT). \quad (2)$$

In the studies on lead sulfide[1, 5] the

migration of nickel or copper was followed by electrical methods, not by radiotracers and the variable of initial crystal composition was not studied. It is the purpose of the present paper to report an investigation of the low temperature diffusion of nickel into PbTe using radiotracer techniques. Particular attention has been given to the initial composition of the PbTe crystals and its effect on the migration of nickel.

EXPERIMENTAL

Single crystals of PbTe used in this investigation were grown by the Bridgeman technique. Crystals were sawed from the ingot, polished, and equilibrated at 700°C as previously described[7, 8]. The initial compositions of the crystals equilibrated at 700°C were those defined by the lead telluride-lead phase limit (9.7×10^{17} electrons/cm³), the minimum total pressure (2.0×10^{18} holes/cm³), and the lead telluride-tellurium phase limit (6.4×10^{18} holes/cm³). As will be discussed in the next section, the retrograde solubility of lead and tellurium makes these compositions unstable at the lower temperatures used for diffusion anneals.

The counting procedures and the method

*Taken in part from the Ph.D. thesis of T. D. George, Northwestern University (1968). Work supported by a grant from the Army Research Office-Durham.

†Formerly a NASA Trainee at Northwestern University. Present address: Central Analytical and Characterization Laboratory, Texas Instruments, Inc., Dallas, Texas.

by which the nickel concentrations were estimated have been previously described [7, 8]. All diffusion anneals were carried out in sealed, evacuated ampoules of approximately 2 cm³ total volume.

Precipitation phenomena

The first study of the aging behavior of lead telluride at low temperatures was that of Scanlon[9]. He equilibrated crystals at 700°C containing approximately 3×10^{18} holes/cm³ and aged them at temperatures ranging from 200° to 400°C. By following the change in Seebeck coefficient with time, he was able to determine the kinetics of aging and concluded that crystals containing excess tellurium precipitated the excess at dislocations until the composition of the matrix crystal corresponded to the limit of solid solubility of tellurium in PbTe at the aging temperature. The time necessary to reach the new 'equilibrium' state increased with decreasing temperature, and the carrier concentration of the aged crystals decreased with decreasing temperature. At 400°C the precipitation of excess tellurium required approximately two hours and the 'equilibrium' carrier concentration was 2×10^{18} holes/cm³, whereas at 300°C, fifty hours were required for complete precipitation and the carrier concentration was 4.5×10^{17} holes/cm³. At 200°C the time required to precipitate the excess tellurium was on the order of five hundred hours and the final carrier concentration was 2×10^{17} holes/cm³. The equilibration times were independent of sample dimensions.

The precipitation phenomenon was checked in the present investigation on all crystals used for diffusion studies by measuring the room temperature Seebeck coefficient of crystals aged for various lengths of time at various temperatures. Room temperature Hall measurements were also made. At 300°C the Seebeck coefficient ceases to change after about sixty hours on crystals initially containing 2×10^{18} holes/cm³. The carrier

concentration of *p*-type undoped crystals aged 72 hr at 300°C was 6.4×10^{17} holes/cm³ as compared to 4.5×10^{17} holes/cm³ reported by Scanlon[9]. The carrier concentration of crystals aged 72 hr at 300°C was the same for crystals pre-equilibrated at the tellurium phase limit (6.4×10^{18} holes/cm³ initially after quenching from 700°C) as those pre-equilibrated under argon (2×10^{18} holes/cm³ initially after quenching from 700°C). Crystals pre-equilibrated at the lead telluride-lead phase boundary (9.7×10^{17} electrons/cm³) showed no change in their Seebeck coefficient when aged for seventy-two hours at 300°C. It was concluded that excess lead precipitates more slowly than tellurium. Since diffusion times did not exceed 24 hr, crystals containing excess lead were used as quenched from 700°C. Silver doped crystals containing 1×10^{19} Ag/cm³ and 5×10^{18} holes/cm³ initially after quenching from 700°C also showed a change in their Seebeck coefficient when they were aged at 300°C. At equilibrium at 300°C, these silver doped crystals contained 3×10^{18} holes/cm³. This aging of silver-doped crystals agrees with the aging studies of sodium-doped PbTe as reported by Crocker and Dorning[10]. Bismuth doped crystals also age at 300°C. Crystals whose initial Seebeck coefficient was $-275 \mu\text{V}/^\circ\text{C}$ ($\sim 9.7 \times 10^{17}$ electrons/cm³) had a carrier concentration of 3×10^{17} electrons/cm³ after aging at 300°C. While undoped *p*-type and Ag-doped crystals became less *p*-type upon aging, Bi-doped crystals became less *n*-type. This behavior is consistent with a model involving a decrease in cation vacancies during aging.

At 400°C, crystals pre-equilibrated at the lead telluride-tellurium phase limit, show a decrease in carrier concentration from 6.4×10^{18} holes/cm³ to 2×10^{18} holes/cm³. Crystals initially containing 2×10^{18} holes/cm³ showed no change in carrier concentration when aged at 400°C. One set of Bi-doped crystals (*n*-type) and one set of undoped *n*-type crystals converted to *p*-type after

72 hr at 400°C. These crystals were not used for diffusion studies as the Seebeck coefficient of these aged crystals showed a large amount of scatter from sample to sample. None of the crystals showed any change in their Seebeck coefficients when aged at 72 hr at 200°C. Since diffusion times did not exceed 28 hr, crystals used for diffusion studies at 200°C were used as quenched from 700°C. Several crystals were aged at 300° and 400°C before diffusing at 200°C. In this way more compositions could be studied at one temperature. At both 300° and 400° the composition range which can be studied is obviously quite restricted due to retrograde solubility.

RESULTS

Diffusion at 400°C

Diffusion anneals at 400°C were carried out only on crystals containing excess tellurium. All crystals contained 2×10^{18} holes/cm³ which corresponds to the limit of solid solubility of tellurium in PbTe at this temperature[9]. Crystals initially containing 6.4×10^{18} holes/cm³ at 700°C were first aged in a closed vacuum at 400°C before the diffusion was carried out. Crystals equilibrated at 700°C under argon contain 2×10^{18} holes/cm³ and were used without aging. Typical results on the aged crystals are shown in Fig. 1. The results obtained on unaged crystals containing 2×10^{18} holes/cm³ (crystals annealed under argon at 700°C and quenched) were similar except that the diffusion coefficients were generally higher by a factor of two. This difference may indicate that the aging treatment at 400°C removes thermal defects in addition to defects due to deviations from stoichiometry. Thus a crystal may be produced with the same carrier concentration but fewer lattice defects which yields a smaller diffusion coefficient.

As can be seen in Fig. 1, the nickel distribution profiles cannot be described in terms of a simple solution of the diffusion equation.

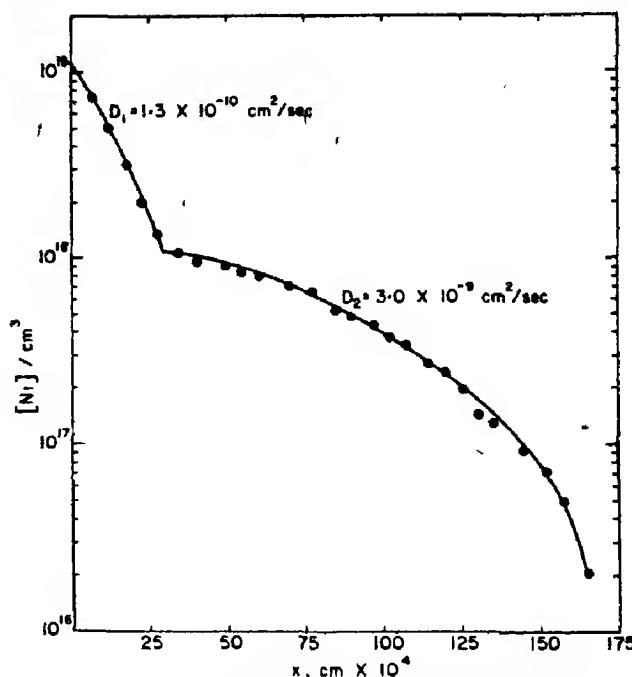


Fig. 1. Nickel distribution profile at 400°C; 2×10^{18} holes/cm³, 2 hr.

The curves can, however, be fit by two overlapping curves each of the form

$$C(x) = C_0 \exp(-x^2/4Dt) \quad (3)$$

where $C(x)$ is the nickel concentration of x cm below the initial surface, C_0 is the value of the nickel concentration at $x=0$ (extrapolated in the case of the faster component of nickel diffusion), t is the diffusion time in seconds, and D is the diffusion coefficient in cm²/sec. The values of D were evaluated from slopes of the straight lines resulting from $\log C(x)$ vs. x^2 plots.

Diffusion at 300°C

At 300°C several compositions were studied. Crystals containing excess lead (9.7×10^{17} electrons/cm³) showed no indication of precipitation when aged and were used as quenched from 700°C. Undoped p -type PbTe was aged for at least 72 hr before carrying out the diffusion anneal. Doped crystals, both Ag- and Bi-doped, were also

aged before diffusing in nickel. The final equilibrium states have already been described.

Typical results for *p*-type undoped crystals are shown in Figs. 2 and 3. Again the distribution profiles of nickel cannot be described in terms of a simple solution of the diffusion equation. Similar nickel distribution profiles were obtained for undoped crystals containing excess lead and Ag-doped crystals. The diffusion coefficients for these undoped, *n*-type and Ag-doped crystals were about an order of magnitude higher than those obtained for undoped, *p*-type crystals. The diffusion coefficient of nickel in Bi-doped crystals was also higher than for undoped *p*-type crystals, but the nickel distribution did not have a break as shown in Fig. 2.

As mentioned earlier, the retrograde nature of the phase field of PbTe severely limits the compositional range which can be studied at low temperatures. In order to investigate the behavior of nickel in undoped crystals containing greater than 6.4×10^{17} holes/cm², several diffusion anneals were carried out on undoped, *p*-type crystals

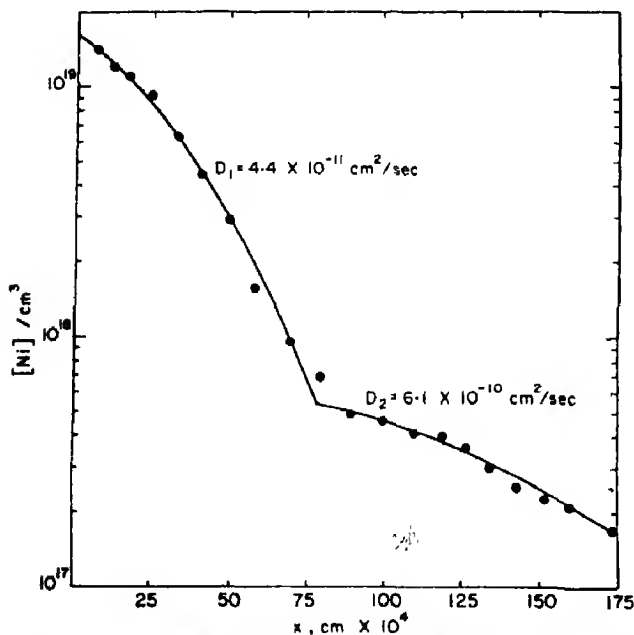


Fig. 2. Nickel distribution profile at 300°C; PbTe, aged, 6.4×10^{17} holes/cm², 24 hr.

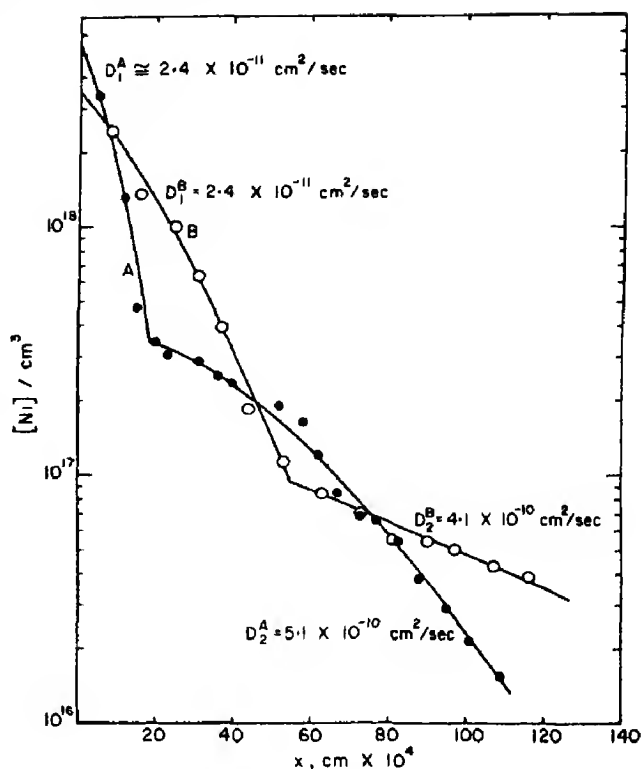


Fig. 3. Nickel distribution profiles at 300°C; PbTe/Te, aged 6.4×10^{17} holes/cm² ●—5 hr, ○—24 hr.

containing initially 2×10^{18} holes/cm³. During the diffusion anneal the carrier concentration in these crystals decreased due to the simultaneous precipitation of tellurium. The nickel distribution profiles which resulted were time dependent and could not be adequately described by equation (3). Several of the profiles obtained in this way are shown in Fig. 4. The diffusion coefficients indicated have been approximated from the slopes of the solid lines shown. It is evident that the apparent diffusion coefficient of nickel migration decreases with increasing time of the diffusion anneal and therefore with decreasing carrier concentration. From values of the changing Seebeck coefficients determined in a separate series of experiments, the apparent nickel diffusion coefficient has been correlated with the electronic state of the crystal. This correlation is shown in Fig. 5. The values of the Seebeck

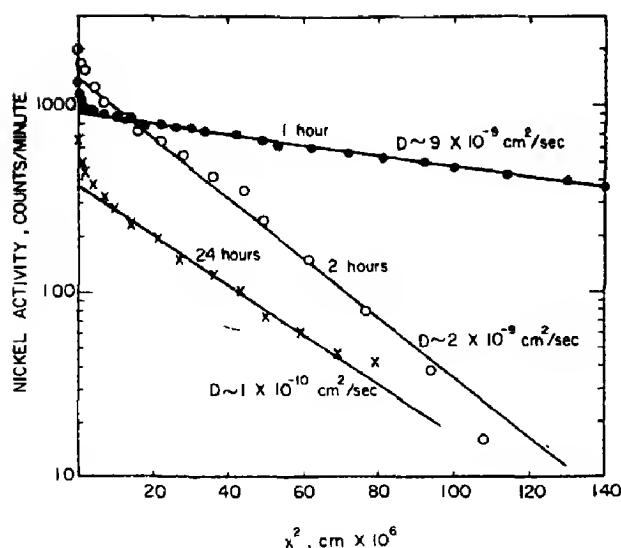


Fig. 4. Nickel distribution profiles on unaged crystals at 300°C. Initial carrier concentration 2×10^{18} holes/cm³.

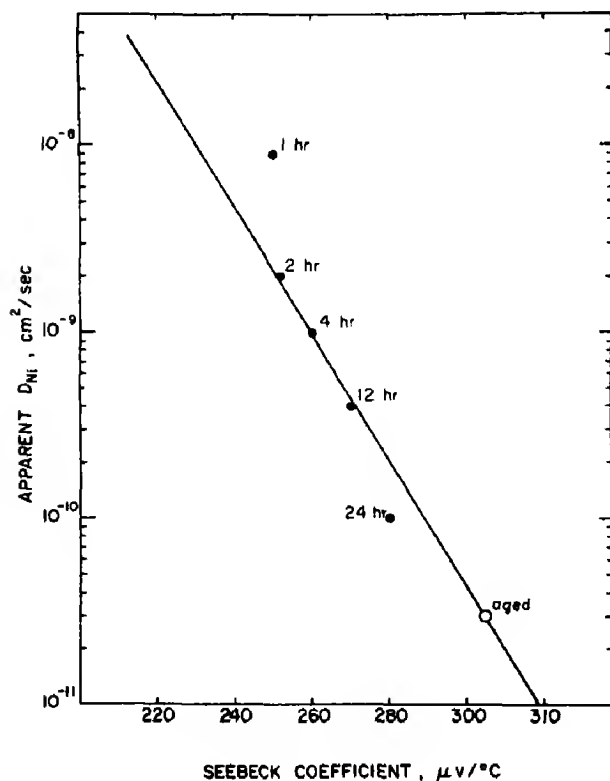


Fig. 5. Correlation between apparent D_{Ni} and Seebeck coefficient at 300°C. The open circle marked 'aged' denotes a sample whose Seebeck coefficient attained a constant value with time.

coefficients used were the ones obtained by aging undoped crystals for the times indicated. Diffusion anneals were carried out for the same length of time. The point shown by the open circle is the value of D_{Ni} obtained on a fully aged crystal and corresponds to the slower component of nickel diffusion shown in Fig. 2.

Diffusion at 200°C

According to Scanlon[9], the time required to reach equilibrium through precipitation of excess Te at 200°C is on the order of 500 hr. Crystals of several compositions aged for 48 hr at 200°C did not show any change in their Seebeck coefficients. Since diffusion times did not exceed 28 hr, crystals could be used as quenched from 700°C. Several crystals were, however, aged at 300° or 400°C prior to diffusion at 200°C in order to provide additional compositions.

In general the results obtained at 200°C agree with those obtained at the higher temperatures. Crystals containing excess Pb, Ag-doped crystals, and undoped, *p*-type crystals containing less than 2×10^{18} holes/cm³ show a break in the nickel diffusion profile. Bismuth-doped crystals and undoped crystals containing 6.4×10^{18} holes/cm³ do not exhibit a break in the nickel profile, and the nickel diffusion coefficient was found to be higher in these crystals than in crystals containing 2×10^{18} hole/cm³.

DISCUSSION

Retrograde solubility of the constituents of lead telluride places certain restrictions on the study of any phenomena at low temperatures. Most notable in the case of diffusion studies is the limitation placed on the effect of composition on the diffusion of impurities. Because of retrograde solubility, the composition range which can be conveniently investigated is considerably less than that which can be obtained at 700°C. Nevertheless, within the limitations imposed by the system,

the dependence of the diffusion of nickel on composition has been demonstrated.

The diffusion of nickel in PbTe cannot be explained in terms of a single mechanism. The results suggest that there are at least two processes occurring during the diffusion of nickel. Diffusion curves with 'breaks' similar to those reported here (Figs 1 and 2) have been observed for the diffusion of silver in cadmium sulfide[11] and of manganese into gallium arsenide[12]. Lead telluride crystals containing excess Pb, silver doped crystals, and undoped crystals containing up to 2×10^{18} holes/cm³ yield nickel profiles which exhibit a break. Both components of the nickel distribution profile appear to depend on composition in the same way, with the diffusion coefficients for both components being highest in crystals saturated with lead. Of the compositions studied, the smallest nickel diffusion coefficients were found in undoped, p-type crystals containing 6.4×10^{17} holes/cm³.

At this time no mechanism can be verified for the diffusion of nickel in PbTe at low temperature. Several observations can be made which may help in understanding the phenomena. Those compositions in which nickel appears to migrate via a dual process contain fewer cation vacancies or more cation interstitials than do those crystals which produced a single, smooth nickel profile. This result suggests that interstitial migration of nickel is occurring. Bloem and Kröger[5] first suggested that nickel migrates interstitially in lead sulfide based on their measurements of *p-n* junction migration. In contrast to the lead sulfide work[5], in the present case both *n* and *p* type crystals retained their original carrier sign after the nickel diffusion. Even *p*-type crystals with carrier concentrations as low as 6×10^{17} /cm³ retained their *p*-type carrier sign after the nickel diffusion. Moreover, it was also shown that the nickel diffusion coefficient in PbTe is composition dependent. The diffusivity decreases with decreasing lead

concentration. Secondly, the two processes involved in the diffusion of nickel appear to be of the same nature. Both components of nickel diffusion vary in the same direction with changes in crystal composition. Finally the two components of nickel diffusion appear to be simultaneous events. Were this not the case, the break in the curve would be expected to occur at some particular nickel concentration. A time-dependent study at one composition indicated that the position of the break in the nickel profile depended only on the time of the diffusion anneal (See Fig. 3).

That crystals containing a large vacancy concentration, excess Te or Bi-doped crystals, do not show a break in the nickel distribution profile suggests that a different diffusion mechanism is operative in these crystals. At this time nothing more can be said about nickel diffusion in these crystals.

The overall composition dependence of nickel diffusion at these low temperatures is striking. It is generally assumed that lattice defects are relatively immobile in the lead salts at these low temperatures[5]. The precipitation studies of Scanlon[9] illustrated that under certain conditions, at least, lattice defects can be made to migrate at low temperatures. The nickel diffusion results shown in Fig. 4 illustrate that the migration of defects and their concentration play an important role in the diffusion of nickel. Defects in the lead salts are probably much more mobile than previously thought. The general trends established here for the variation of nickel diffusion follows that expected for cation self-diffusion in a solid having a Frenkel defect structure. That is the diffusion coefficient is higher at both phase boundaries than at intermediate compositions. Since the diffusion coefficient for nickel does not change continuously in the same direction across the phase field, it is unlikely that a single diffusion mechanism can be invoked.

SUMMARY AND CONCLUSIONS

Diffusion of nickel into PbTe at low temperatures (200°–400°C) shows that even at these temperatures the diffusion of nickel is very dependent on the composition of the crystal. For most of the compositions studied the diffusion profiles of nickel can be described in terms of two overlapping curves each of which is a solution of the diffusion equation but with different values of the diffusion coefficient. In general the diffusion coefficients for each component of nickel diffusion differ by an order of magnitude. Crystals containing excess lead (9.7×10^{17} electrons/cm³) and silver-doped crystals have higher diffusion coefficients than do undoped *p*-type crystals (6.4×10^{17} holes/cm³) at 300°C. Undoped crystals containing more than 6.4×10^{17} holes/cm³ are not stable at 300°C and excess Te precipitates during annealing. A study of the diffusion behavior of nickel in *p*-type crystals while the precipitation of tellurium was occurring simultaneously indicates that the diffusion coefficient of nickel increases with increasing hole concentration above 6.4×10^{17} holes/cm³. Experiments at 200°C where the precipitation of tellurium is much slower confirm this

dependence of the nickel diffusion coefficient on composition. Further, the distribution profile of nickel in bismuth doped crystals and undoped crystals containing 6.4×10^{18} holes/cm³ at 200°C can be described by a simple solution of the diffusion equation. All of the crystals, *n*- or *p*-type, retained their original carrier sign after the diffusion with nickel.

REFERENCES

1. BLOEM J. and KRÖGER F. A., *Philips Res. Rep.* **12**, 281 (1957).
2. FULLER C. S. and STRUTHERS J. D., *Phys. Rev.* **87**, 526 (1952).
3. BOLTAKS B. I. and SOZINOV I., *Zh. Tech. Fiz.* **28**, 3 (1958).
4. HALL R. N. and RACETTE J. H., *J. Appl. Phys.* **35**, 379 (1964).
5. BLOEM J. and KRÖGER F. A., *Philips Res. Rep.* **12**, 303 (1957).
6. VAN DER MAESEN F. and BRECKMAN J. A., *Philips Res. Rep.* **9**, 225 (1954).
7. GEORGE T. D. and WAGNER J. B., Jr., *J. electrochem. Soc.* **115**, 956 (1968).
8. GEORGE T. D. and WAGNER J. B. Jr., *J. electrochem. Soc.* **114**, 848 (1969).
9. SCANLON W. W., *Phys. Rev.* **126**, 509 (1962).
10. CROCKER A. J. and DORNING D. F., *J. Phys. Chem. Solids* **29**, 155 (1968).
11. WOODBURY H. H., *J. appl. Phys.* **36**, 2287 (1965).
12. SELTZER M. S., *J. Phys. Chem. Solids* **26**, 243 (1965).

STRUCTURE MAGNETIQUE A TROIS SOUS-RESEAUX DANS L'APPROXIMATION DU CHAMP MOLECULAIRE

B. BOUCHER*, R. BUHL† et M. PERRIN†

Service de Physique du Solide et de Résonance Magnétique, Centre d'Etudes Nucléaires de Saclay,
BP n° 2-91, Gif-sur-Yvette, France

(Received 4 February 1969)

Résumé—On considère un corps dans lequel les moments magnétiques se groupent en trois sous-réseaux, les ions appartenant à un même sous-réseau ayant leurs moments parallèles. On suppose l'anisotropie négligeable. Le calcul fait dans l'approximation du champ moléculaire, montre qu'il peut exister deux sortes de structures: soit une structure colinéaire (ferro-ou ferrimagnétique) soit une structure dite 'en étoile'. On détermine les conditions de stabilité de ces différents types de configuration. On étudie enfin l'évolution d'une structure 'en étoile' vers un arrangement colinéaire, obligatoire quand la température croît ainsi que les différents types de variation de l'aimantation des sous-réseaux et de leur résultante générale. Ces deux derniers points sont traités en partie par le calcul algébrique, en partie par le calcul numérique.

Abstract—We are considering a compound in which the magnetic moments are divided into three sublattices, ions belonging to the same sublattice having their moments parallel. Anisotropy is supposed to be negligible. Calculations made in the approximation of molecular field theory, show that two kinds of structure may exist: either a collinear structure (ferro or ferrimagnetic) or a 'star' structure. We determine the stability conditions of these various configurations. Finally we study the evolution of a 'star' structure to a collinear arrangement which always occurs when temperature increases and also the different types of variation of the sublattice magnetizations and of the net moment. These two latest points are treated partly by algebraic, partly by numerical calculation.

INTRODUCTION

SOIT UN oxyde métallique comportant trois cations magnétiques de nature différente. Nous supposons: (1) que les ions de même nature occupent dans le cristal un site cristallographique unique qu'ils garnissent en totalité (nous repérons chacun des sites cristallographiques, ainsi que les ions qui l'occupent par les indices 1, 2, 3); (2) que dans l'état magnétiquement ordonné, les moments magnétiques de tous les ions d'un même type forment un arrangement *ferro-magnétique*: les ions du type i ont tous le même moment magnétique μ_i . L'aimantation du sous-réseau i dans le cristal est donc $M_i = n_i \mu_i$, où n_i est le nombre d'ions i dans le

cristal; (3) que le couplage spin-réseau, c'est-à-dire l'anisotropie, peut être négligée. De plus les interactions d'échange seront isotropes, les coefficients de champ moléculaire seront donc des scalaires.

Reprenant la méthode de calcul, employée par Néel [1] dans le cas de deux sous-réseaux, nous allons chercher, dans le cas de 3 sous-réseaux, quelles sont les solutions des équations de champ moléculaire et déterminer parmi ces solutions celles qui correspondent à des structures stables à une température $T < T_c$. Nous étudierons ensuite l'évolution de ces structures en fonction de la température.

A. STRUCTURE A UNE TEMPERATURE $T < T_c$

1. Solution des équations de champ moléculaire

Avec les hypothèses faites ci-dessus les équations de champ moléculaire s'écrivent:

*Partie de la thèse de doctorat d'état, Paris le 2 décembre 1968.

†L.M.P.S.-C.N.R.S. Bellevue.

$$\mathbf{h}_1 = \delta \mathbf{M}_1 + \gamma \mathbf{M}_2 + \beta \mathbf{M}_3 \quad (1)$$

$$\mathbf{h}_2 = \gamma \mathbf{M}_1 + \epsilon \mathbf{M}_2 + \alpha \mathbf{M}_3 \quad (2)$$

$$\mathbf{h}_3 = \beta \mathbf{M}_1 + \alpha \mathbf{M}_2 + \zeta \mathbf{M}_3 \quad (3)$$

δ, ϵ, ζ étant les constantes de champ moléculaire relatives aux interactions 1-1, 2-2, 3-3 respectivement et α, β, γ celles relatives aux interactions 2-3, 3-1, 1-2 (Fig. 1).

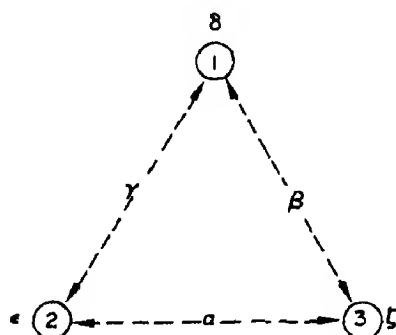


Fig. 1.

Il faut bien remarquer que l'hypothèse que nous faisons au départ, à savoir que les moments magnétiques des ions d'un même type forment un arrangement ferromagnétique, peut être remise en cause si les constantes δ, ϵ, ζ sont fortement négatives, c'est-à-dire s'il existe de fortes interactions antiferromagnétiques entre ions de même type (cf. plus loin).

En l'absence d'anisotropie, les moments μ_i (donc \mathbf{M}_i) doivent être parallèles au champ moléculaire \mathbf{h}_i . Il existe donc d'après (1-3) une relation linéaire homogène entre les moments μ_1, μ_2, μ_3 , qui par suite sont coplanaires. Nous appelons respectivement ψ et θ les angles $(\mathbf{M}_1, \mathbf{M}_2)$ et $(\mathbf{M}_2, \mathbf{M}_3)$ (Fig. 2).

L'énergie libre du système s'écrit:

$$F = E(\mathbf{M}_i, \theta, \psi) + kT \int_0^{x_i} \mathcal{B}_i^{-1}(x_i) dx_i \quad (4)$$

avec $x_i = M_i(T)/M_{i0}$. $\mathcal{B}^{-1}(x)$ est la fonction inverse de la fonction de Brillouin. M_{i0} et $M_i(T)$ représentent les aimantations du sous-réseau i à 0°K et à T °K.



Fig. 2. Différents types de structures.

Le premier terme correspond à l'énergie interne:

$$E = -\frac{1}{2} \sum_i \mathbf{h}_i \cdot \mathbf{M}_i = -\left[\frac{1}{2} (\delta M_1^2 + \epsilon M_2^2 + \zeta M_3^2) + \gamma M_1 M_2 \cos \psi + \alpha M_2 M_3 \cos \theta + \beta M_1 M_3 \cos (\theta + \psi) \right]. \quad (5)$$

A une température donnée, F dépend de θ, ψ et M_i . La minimisation de F par rapport à ces variables donne l'état d'équilibre.

Nous avons:

$$\gamma M_2 \sin \psi + \beta M_3 \sin (\theta + \psi) = 0 \quad (6)$$

$$\gamma M_1 \sin \psi - \alpha M_3 \sin \theta = 0 \quad (7)$$

et

$$M_i(T) = M_{i0} \mathcal{B} \left(\frac{h_i \cdot M_{i0}}{kT} \right). \quad (8)$$

Les solutions des équations (6) et (7) sont:

(1) $\sin \psi = \sin \theta = 0$, solution ferro-ou ferri-magnétique.

$$(2) \quad \cos \psi = \frac{-\alpha^2 \beta^2 M_1^2 - \alpha^2 \gamma^2 M_2^2 + \alpha^2 \beta^2 M_3^2}{2 \gamma^2 \alpha \beta M_1 M_2} = \frac{-m_1^2 - m_2^2 + m_3^2}{2 m_1 m_2} \quad (9)$$

de même

$$\cos \theta = \frac{\beta^2 \gamma^2 M_1^2 - \alpha^2 \gamma^2 M_2^2 - \alpha^2 \beta^2 M_3^2}{2 \alpha^2 \beta \gamma M_2 M_3} = \frac{m_1^2 - m_2^2 - m_3^2}{2 m_2 m_3} \quad (10)$$

avec

$$m_1 = \gamma \beta M_1, m_2 = \alpha \gamma M_2, m_3 = \alpha \beta M_3. \quad (11)$$

Cette solution correspond à une structure dite 'en étoile' déjà signalée par Niessen[2]. (La structure Yafet-Kittel[3] est un cas particulier de la structure 'en étoile').

Les configurations correspondantes à ces solutions sont représentées sur la Fig. 2.

2. Condition d'existence et stabilité des différentes structures

(1) *Structure 'en étoile'*. Nous aurons une structure 'en étoile' si les deux conditions (A et B) suivantes sont remplies simultanément:

Condition A: Il faut que simultanément les expressions des cosinus (equations (9, 10)) soient en module inférieures à l'unité.

Ceci revient à écrire, dans le cas des deux expressions (9) et (10), une seule inégalité soit:

$$[m_1^2 - (m_2 + m_3)^2][m_1^2 - (m_2 - m_3)^2] < 0 \quad (11)$$

ou en développant la formule

$$(m_1 + m_2 + m_3)(m_1 - m_2 - m_3)(m_1 - m_2 + m_3)(m_1 + m_2 - m_3) < 0. \quad (11')$$

Autrement dit le module de tout m_i doit être compris entre les modules de la somme et de la différence des deux autres m_i .

De plus nous voyons (que les cosinus tendent simultanément vers ± 1 ; la structure 'en étoile' peut donc évoluer de façon continue vers une structure colinéaire.

Condition B: Il faut que l'énergie magnétique d'une telle configuration soit inférieure à l'énergie magnétique correspondant à une structure colinéaire (ferro-ou ferrimagnétique).

Nous avons cinq configurations possibles appelées respectivement F , N_1 , N_2 , N_3 (Fig. 2). L'énergie de chacune des ces configurations se calcule aisément à partir de l'expression (5). Nous avons:

$$E^* = \frac{1}{2\alpha\beta\gamma} (m_1^2 + m_2^2 + m_3^2) - K \quad (12)$$

$$E_{\text{col.}} = -\frac{1}{\alpha\beta\gamma} (u_1 m_1 m_2 + u_2 m_2 m_3 + u_3 m_3 m_1) - K \quad (13)$$

avec

$$K = \frac{1}{2}(\delta M_1^2 + \epsilon M_2^2 + \zeta M_3^2)$$

u_1 , u_2 , u_3 représentent respectivement la valeur limite (± 1) des cosinus de θ , $\theta + \psi$ et ψ . Nous avons donc pour une structure du type:

$$F \quad u_1 = u_2 = u_3 = +1$$

$$N_1 \quad u_2 = u_3 = -1 \quad u_1 = 1$$

$$N_2 \quad u_1 = u_3 = -1 \quad u_2 = 1$$

$$N_3 \quad u_1 = u_2 = -1 \quad u_3 = 1.$$

La différence $(F^* - F_{\text{col.}}) = (E^* - E_{\text{col.}})$ se présente toujours sous la forme du produit du carré d'une fonction linéaire de m_1 , m_2 , m_3 par le facteur $1/2\alpha\beta\gamma$. Elle est donc du signe du produit $\alpha\beta\gamma$.

La condition B sera $\alpha\beta\gamma < 0$. Donc si le produit $\alpha\beta\gamma$ est négatif (condition B) et si $\cos \theta$ et $\cos \psi$ existent (condition A) la structure 'en étoile' présente l'énergie la plus basse. Ceci confirme le résultat déjà trouvé avec les structures Yafet et Kittel et les structures en hélice à savoir: si une structure non colinéaire existe et si les interactions sont antiferromagnétiques, la structure non colinéaire est la plus stable.

(2) *Structure colinéaire* (dans le cas $\alpha\beta\gamma < 0$). Si le produit $\alpha\beta\gamma$ est négatif, mais que la condition A n'est pas satisfaite, nous aurons une structure colinéaire. Il est aisé à partir de la formule (13) de déterminer la structure stable.

(3) Le Tableau 1 résume la discussion dans le cas $\alpha\beta\gamma < 0$. Dans chaque combinaison possible des signes de α, β, γ , le tableau indique les signes des quatre expressions de la forme $(m_1 + m_2 + m_3) \dots$ (inégalité 11') quand la structure est du type 'en étoile'; quand la structure est colinéaire, trois de ces quatre expressions gardent la même signe

que dans le cas de la structure 'en étoile' la 4ème change de signe; cette dernière est indiquée dans la 2ème colonne et son signe dans les colonnes suivantes. Enfin certaines structures ne sont jamais stables: la case correspondante est vide.

Tableau 1

	Signe des constantes	α, β, γ	α, β, γ	α, β, γ	α, β, γ
		---	---	---	---
E	$m_1 + m_2 + m_3$	+	-	-	-
	$m_1 - m_2 - m_3$	-	+	-	-
	$-m_1 + m_2 - m_3$	-	-	+	-
	$-m_1 - m_2 + m_3$	-	-	-	+
F	$m_1 + m_2 + m_3$		+	+	+
N ₁	$m_1 - m_2 - m_3$	+		+	+
N ₂	$-m_1 + m_2 - m_3$	+	+		+
N ₃	$-m_1 - m_2 + m_3$	+	+	+	

(4) Quand $\alpha\beta\gamma$ est positif nous avons une structure colinéaire dont le type se détermine sans difficulté.

Remarque

L'état stable doit correspondre à une configuration magnétique dont les moments sont non seulement parallèles (extremum de l'énergie) au champ moléculaire, mais de même sens (minimum de l'énergie). Nous écrivons cette condition pour h_1 (equation (1)) dans le cas d'une structure 'en étoile'.

$$h_1 = \delta M_1 + \gamma M_2 + \beta M_3;$$

la valeur algébrique de h_1 comptée sur M_1 positif est:

$$h_1 = \delta M_1 + \gamma M_2 \cos \psi + \beta M_3 \cos (\theta + \psi)$$

$$h_1 = \delta M_1 + \frac{1}{\alpha} (-m_1) = \left(\delta - \frac{\beta\gamma}{\alpha} \right) M_1. \quad (14)$$

L'état stable correspond donc, dans le cas d'une structure 'en étoile' ($\alpha\beta\gamma < 0$), à:

$$\left(\delta - \frac{\beta\gamma}{\alpha} \right) > 0 \text{ et de même, } \left(\epsilon - \frac{\alpha\gamma}{\beta} \right) > 0,$$

$$\left(\zeta - \frac{\alpha\beta}{\gamma} \right) > 0. \quad (15)$$

Il peut exister une interaction antiferromagnétique à l'intérieur d'un sous-réseau, mais il faut qu'elle soit assez faible, sinon la répartition en sous-réseaux que nous avons supposée au départ ne serait pas correcte.

Nous limiterons donc notre étude par les trois conditions (15).

3. Valeur de l'aimantation

(1) Cas d'une structure 'en étoile' (Fig. 3). Si nous avons une structure 'en étoile', l'aimantation spontanée est donnée par la formule:

$$I = [M_1^2 + M_2^2 + M_3^2 + 2 M_1 M_2 \cos \psi + 2 M_2 M_3 \cos \theta + 2 M_3 M_1 \cos (\theta + \psi)]^{1/2}. \quad (16)$$

Nous voyons que pour un système d'ions magnétiques donnés l'aimantation peut prendre des valeurs très différentes suivant la valeur des angles θ et ψ . Notamment ces valeurs peuvent devenir très faibles par rapport à celles qui seraient obtenues avec une structure colinéaire pour le même système d'ions magnétiques.

Cette aimantation est évidemment dans le plan des moments magnétiques. Sa direction dépend des différents paramètres (constantes de champ, valeur des pins...). Sauf cas

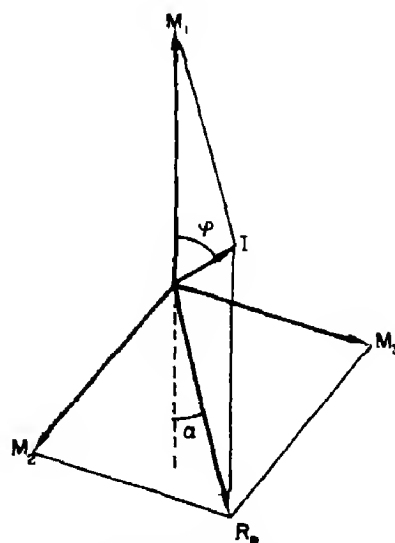


Fig. 3. Schéma de la structure 'en étoile'.

particuliers, elle ne sera alignée avec aucun des moments. L'angle φ que fait cette aimantation avec l'un des moments du motif, par exemple μ_1 est donné par la formule:

$$\tan \varphi = \frac{M_2 \sin \psi + M_3 \sin (\theta + \psi)}{M_1 + M_2 \cos \psi + M_3 \cos (\psi + \theta)}. \quad (17)$$

(2) *Cas d'une structure colinéaire* (Fig. 2). L'aimantation, qui évidemment est alignée avec les moments, a la valeur bien connue qui peut s'écrire:

$$I = |u_1 M_1 + u_2 M_2 + u_3 M_3| \quad (18)$$

B. EVOLUTION EN FONCTION DE LA TEMPERATURE D'UNE STRUCTURE MAGNETIQUE EN 'ETOILE'

Nous avons défini les conditions de stabilité d'une structure 'en étoile'. Nous supposons maintenant qu'une telle structure est stable à 0°K dans un corps donné. Nous allons étudier l'évolution de cette structure avec la température.

1. Lois de variation des aimantations des sous-réseaux en fonction de T

En remplaçant dans l'équation (8), h_i par son expression en fonction des M_i (equations (1-14)) nous obtenons:

dans le cas d'une structure 'en étoile'

$$M_1 = M_{10} \mathcal{B}_{J_1} \left[\frac{M_{10}}{kT} M_1 \left(\delta - \frac{\beta\gamma}{\alpha} \right) \right] \quad (19)$$

$$M_2 = M_{20} \mathcal{B}_{J_2} \left(\frac{M_{20}}{kT} M_2 \left(\epsilon - \frac{\alpha\gamma}{\beta} \right) \right) \quad (20)$$

$$M_3 = M_{30} \mathcal{B}_{J_3} \left[\frac{M_{30}}{kT} M_3 \left(\zeta - \frac{\alpha\beta}{\gamma} \right) \right] \quad (21)$$

dans le cas d'une structure alignée

$$M_1 = M_{10} \mathcal{B}_{J_1} \left[\frac{M_{10}}{kT} |\delta M_1 + u_3 \gamma M_2 + u_2 \beta M_3| \right] \quad (22)$$

$$M_2 = M_{20} \mathcal{B}_{J_2} \left[\frac{M_{20}}{kT} |u_3 \gamma M_1 + \epsilon M_2 + u_1 \alpha M_3| \right] \quad (23)$$

$$M_3 = M_{30} \mathcal{B}_{J_3} \left[\frac{M_{30}}{kT} |u_2 \beta M_1 + u_1 \alpha M_2 + \zeta M_3| \right]. \quad (24)$$

Ainsi dans le cas d'une structure alignée la valeur de l'aimantation d'un sous-réseau dépend des valeurs des aimantations des deux autres sous-réseaux. Par contre dans le cas d'une structure 'en étoile' les aimantations des sous-réseaux varient indépendamment les unes des autres.

Nous tirons de cette dernière propriété deux conséquences: l'aimantation $M_i(T)$ d'un sous-réseau est toujours décroissante quand la température croît, à chaque sous-réseau correspond une température de Curie:

$$T_c^i = \frac{J_i + 1}{3J_i} \frac{M_{i0}^2}{3k} \left(\delta - \frac{\beta\gamma}{\alpha} \right). \quad (25)$$

Quand T croît et se rapproche de la plus petite température de Curie T_c^i , l'aimantation d'un des sous-réseaux devient suffisamment petite pour que les expressions des cosinus θ et ψ deviennent égales en module à l'unité (equations (9) ou (10)). La structure en étoile devient alors colinéaire. Nous appellerons T_1 la température à laquelle ce changement de phase magnétique a lieu. Nous avons obligatoirement $0 < T_1 < T_c$, où T_c est la température de Curie du corps. A $T = T_1$, les trois sous-réseaux présentent une aimantation non nulle.

2. Variation des aimantations des sous-réseaux à $T = T_1$

A $T = T_1$ la structure 'en étoile' devient colinéaire. Il y a continuité des aimantations $M_i(T)$, h_i étant le même à cette température, que l'on se place dans la phase 'en étoile' ou dans la phase colinéaire. Mais la loi de variation de l'aimantation $M_i(T)$ change: l'aimantation peut décroître plus vite après

T_1 qu'avant T_1 (nous appellerons ce cas le '1er cas') ou au contraire moins vite après T_1 qu'avant T_1 (nous disons le '2ème cas') (Fig. 4). Nous allons déterminer comment varie l'aimantation de chacun des sous-réseaux.

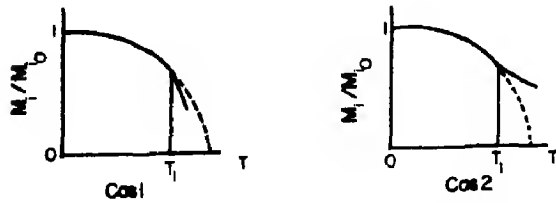


Fig. 4. Les deux types possibles de variation en fonction de la température de l'aimantation réduite d'un sous-réseau d'une structure 'en étoile'.

Appelons P_i la pente de la courbe $M_i(T)$ à $T = T_1$ du côté des basses températures et P'_i celle du côté des hautes températures. Il est possible de calculer des rapports P'_i/P_i . Nous obtenons:

$$1 - \frac{P'_1}{P_1} = \frac{\frac{1}{\alpha} (\beta\gamma P_1 + u_3 \alpha\gamma P_2 + u_2 \alpha\beta P_3) T_1}{\left(\delta - \frac{\beta\gamma}{\alpha}\right) M_1 D} \quad (26)$$

$$1 - \frac{P'_2}{P_2} = \frac{\frac{1}{\beta} (u_3 \gamma\beta P_1 + \alpha\gamma P_2 + u_1 \alpha\beta P_3) T_1}{\left(\epsilon - \frac{\alpha\gamma}{\beta}\right) M_2 D} \quad (27)$$

$$1 - \frac{P'_3}{P_3} = \frac{\frac{1}{\gamma} (u_2 \gamma\beta P_1 + u_1 \alpha\gamma P_2 + \alpha\beta P_3) T_1}{\left(\zeta - \frac{\alpha\beta}{\gamma}\right) M_3 D} \quad (28)$$

où D est une quantité toujours positive dépendant des constantes de champs des aimantations $M_i(T_1)$ et des dérivées $P_i(T_1)$.

La courbe $M_i(T)$ sera du type '1er cas' si $1 - P'_i/P_i < 0$ et du type '2ème cas' si $1 - P'_i/P_i > 0$.

Avec les hypothèses faites: $\alpha\beta\gamma < 0$,

$(\delta - \beta\gamma/\alpha) > 0$, $(\epsilon - \alpha\gamma/\beta) > 0$ et $(\zeta - \alpha\beta/\gamma) > 0$, les dénominateurs des rapports figurant au second membre des équations (26-28) sont toujours positifs.

Les signes des numérateurs de ces rapports nous renseignent donc directement sur la forme des courbes d'aimantations $M_i(T)$. Ces numérateurs peuvent s'écrire:

$$\frac{T_1}{\alpha} \frac{d}{dT} (m_1 + u_3 m_2 + u_2 m_3) \quad (29)$$

$$\frac{T_1}{\beta} \frac{d}{dT} (u_3 m_1 + m_2 + u_1 m_3) \quad (30)$$

$$\frac{T_1}{\gamma} \frac{d}{dT} (u_2 m_1 + u_1 m_2 + m_3). \quad (31)$$

Dans le cas d'une structure colinéaire donnée u_1, u_2, u_3 sont tels (Paragr. A-2) que les trois expressions entre parenthèses sont identiques au signe près. Ces expressions changent de signe à $T = T_1$. Ce signe est donné au paragr. A (Tableau 1). Le signe des dérivées par rapport à la température de ces expressions à $T = T_1$ est donc parfaitement connu. Par suite nous pouvons construire le Tableau 2 qui donne, en fonction du signe des constantes de champ et du type de

Tableau 2

		α	β	γ	α	β	γ	α	β	γ	α	β	γ
		+	-	+	+	+	-	-	+	+	-	-	-
		cas			cas			cas			cas		
F	M_1	2			2			1					
	M_2	1			2			2					
	M_3	2			1			2					
N_1	M_1	2			2						1		
	M_2	2			1						2		
	M_3	1			2						2		
N_2	M_1				1			2			2		
	M_2				2			2			1		
	M_3				2			1			2		
N_3	M_1	1						2			2		
	M_2	2						1			2		
	M_3	2						2			1		

structure colinéaire vers lequel évolue la structure 'en étoile', la forme des courbes $M_i(T)$ à $T = T_1$.

La lecture du Tableau 2 montre que, *quelque soit le cas envisagé, l'aimantation d'un sous-réseau décroît plus vite quand la structure est devenue colinéaire ('1er cas') et deux aimantations de sous-réseaux décroissent moins vite ('2ème cas')*. Quand α , β et γ sont négatifs l'aimantation qui décroît plus vite dans la phase colinéaire correspond au sous-réseau dont l'aimantation est opposée à celle des deux autres.

Parmi les 2 sous-réseaux dont les aimantations obéissent à la loi du type 2, on remarque que l'aimantation de l'un d'entre eux peut croître à $T > T_1$. Il n'est pas possible de démontrer algébriquement cette propriété, mais par contre il est possible de montrer que *seule une* des deux aimantations peut croître. En effet les conditions nécessaires pour que les aimantations des deux sous-réseaux croissent simultanément avec T s'excluent.

En résumé on peut dire:

- (1) Quand $T < T_1$, l'aimantation de chaque sous-réseau décroît avec T .
- (2) On passe de façon continue d'une structure 'en étoile' à une structure colinéaire à $T = T_1$.
- (3) A cette température l'aimantation d'un des trois sous-réseaux décroît plus vite au-delà de T_1 qu'avant T_1 .
- (4) L'aimantation des deux autres sous-réseaux décroît moins vite au-delà de T_1 qu'avant T_1 .
- (5) L'une des deux dernières aimantations peut être alors une fonction croissante de la température, mais pas les deux.

3. Mise en évidence de différentes formes de courbes par le calcul numérique

A partir de valeurs de constantes de champ moléculaire, que nous nous donnons, nous avons calculé les fonctions $M_i(T)$, $I(T)$, $\theta(T)$, $\psi(T)$, $\varphi(T)$ pour montrer la diversité

d'allure des courbes représentatives qu'il est possible de rencontrer. Les calculs ont été faits avec un ordinateur IBM 7094.

Nous avons calculé les fonctions pour tous les signes possibles de α , β , γ ($\alpha\beta\gamma < 0$). Nous retrouvons toujours les mêmes types. Nous ne présenterons donc que des courbes correspondantes à α , β , γ , tous trois négatifs, et du même ordre de grandeur (si l'une des constantes est très petite ou très grande par rapport aux autres, la température T_1 est proche de 0°K et il n'est pas possible d'examiner la forme de la courbe).

Nous avons pris les constantes δ , ϵ , ζ , soit nulles, soit positives, plus rarement négatives (les conditions $(\delta - \alpha\gamma/\beta) > 0 \dots$ étant respectées).

En général pour simplifier nous avons posé: $\mu_{10} = \mu_{20} = \mu_{30} = 4\mu_B$, sauf dans quelques cas où nous avons pris $\mu_{10} = \mu_{20} = 4\mu_B$, $\mu_{30} = 2\mu_B$ (avec les valeurs de J correspondantes).

Parmi toutes les courbes calculées nous n'avons gardé que celles qui présentaient quelques particularités. Le Tableau 3 donne les valeurs des différentes constantes correspondant aux courbes publiées (dans les calculs seuls les rapports des constantes de champ intervenant, β est pris arbitrairement égal à -1). Il indique de plus les valeurs des quantités

$$A = \frac{J_1 + 1}{J_1} \left(\delta - \frac{\beta\gamma}{\alpha} \right) M_{10}^2;$$

$$B = \frac{J_2 + 1}{J_2} \left(\epsilon - \frac{\alpha\gamma}{\beta} \right) M_{20}^2;$$

$$C = \frac{J_3 + 1}{J_3} \left(\zeta - \frac{\alpha\beta}{\gamma} \right) M_{30}^2.$$

Nous savons que les températures de Curie des trois sous-réseaux de la structure 'en étoile' sont respectivement proportionnelles à A , B , C .

Toutes les courbes que nous avons calculées vérifient le résultat obtenu précédemment concernant la variation de $M_i(T)$ à

Tableau 3

Figs. 5	Courbes	α	β	γ	δ	ϵ	ζ	μ_{10} μ_B	T_c^1			Structure à $T_1 < T < T_c$
									A	B	C	
(a)	I	-1,35	-1	-0,88	0	0	0	4,4,4	0,65	1,19	1,53	N_3
(b)	II	-0,92	-1	-1,14	0	1,88	0	4,4,4	1,24	2,93	0,80	N_2
(c)	III	-0,78	-1	-1,03	0	0	0	4,4,2	1,32	0,80	0,25	N_1
(d)	IV	-1,29	-1	-0,94	1,73	-0,12	-0,68	4,4,2	2,46	1,04	0,23	N_2
(e)	V	-0,78	-1	-1,33	0	3	1,7	4,4,4	1,7	4,04	2,29	N_2
(f)	VI	-1,05	-1	-1,12	0	2,3	1,9	4,4,4	1,07	3,48	2,84	N_2

$T = T_1$: deux aimantations de sous-réseaux décroissent moins vite avec T au-delà de T_1 qu'avant T_1 .

Sur la Fig. 5(a) nous avons prolongé la première partie de la courbe (equations (19-21)) jusqu'à T_c^1 , pour mettre en évidence cette propriété.

La courbe II (Fig. 5(b)) montre qu'avec des valeurs de constantes de champ physiquement raisonnables, l'aimantation d'un sous-réseau peut croître à T ($T_1 < T < T_c$). Nous savons qu'un seul des trois sous-réseaux peut présenter cette propriété.

Les variations des angles θ , ψ et φ correspondant à ces deux cas, représentent assez

bien le type de variation que nous avons trouvé pour l'ensemble des courbes calculées: variation assez lente de θ et ψ en fonction de T (avec ou non changement de sens de variation) puis variation beaucoup plus rapide.

L'ensemble des Figs 5(a-f) montrent la diversité d'allure des courbes d'aimantation $I(T)$ du corps. Nous observons dans la phase 'en étoile' ($0 < T < T_1$)

$I(T)$ toujours décroissante (Figs. 5(a-d))

$I(T)$ toujours croissante (Fig. 5(f))

$I(T)$ croissante puis décroissante (Fig. 5(e)).

Dans la phase colinéaire les courbes $I(T)$

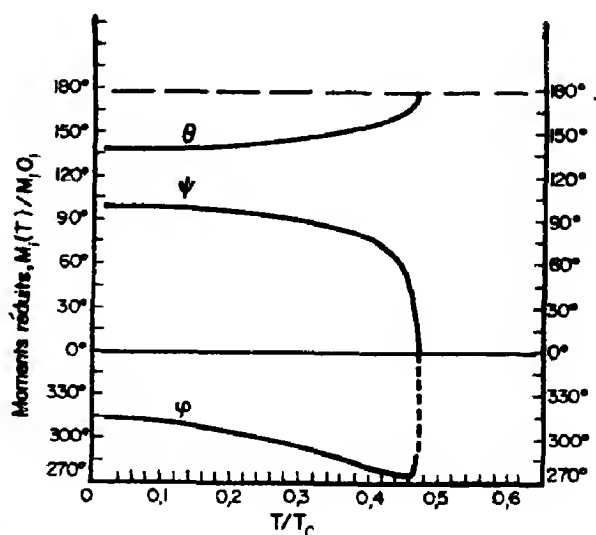
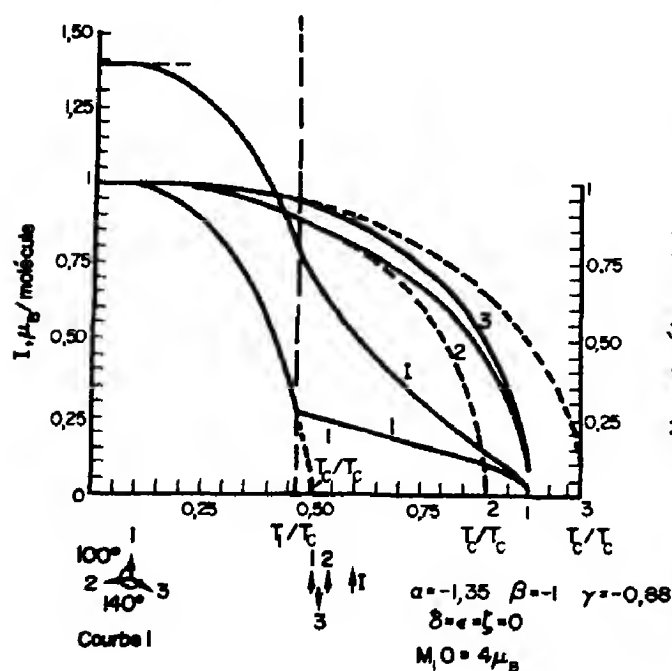


Fig. 5(a).

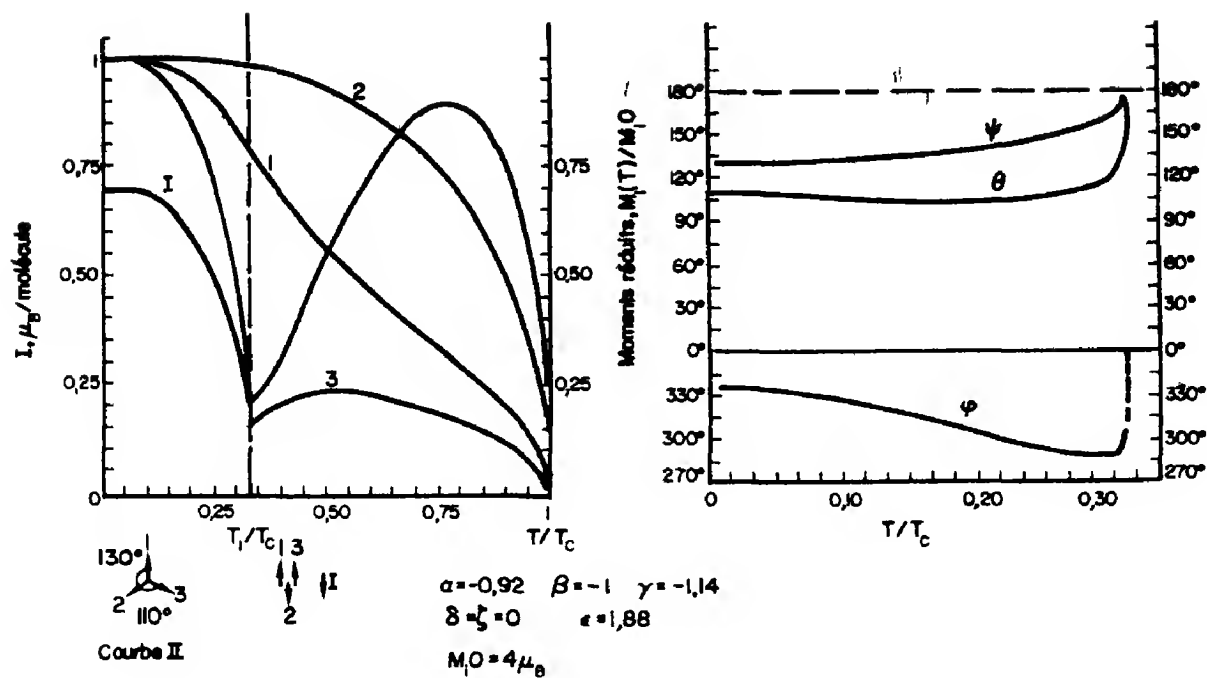


Fig. 5(b).

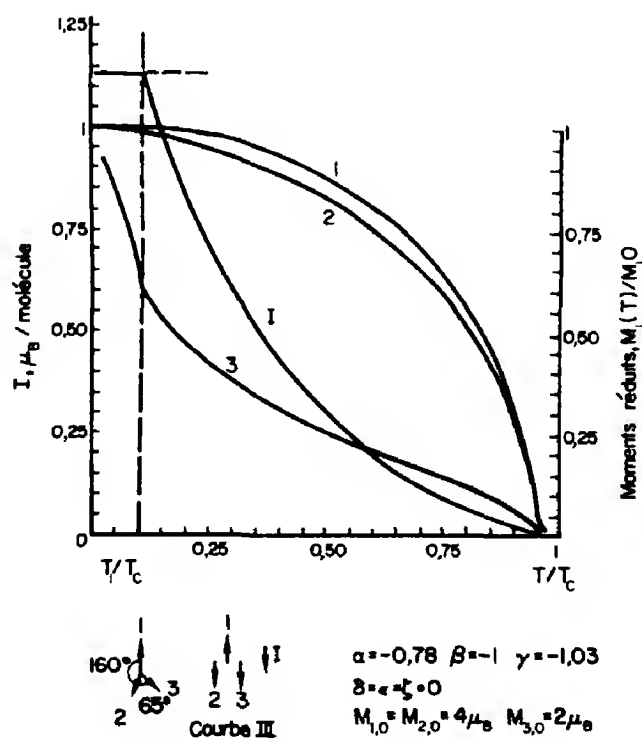


Fig. 5(c).

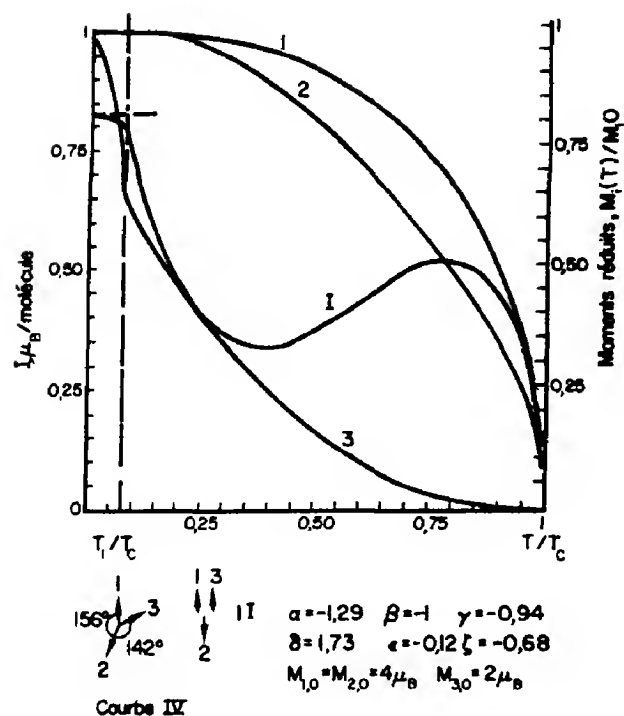


Fig. 5(d).

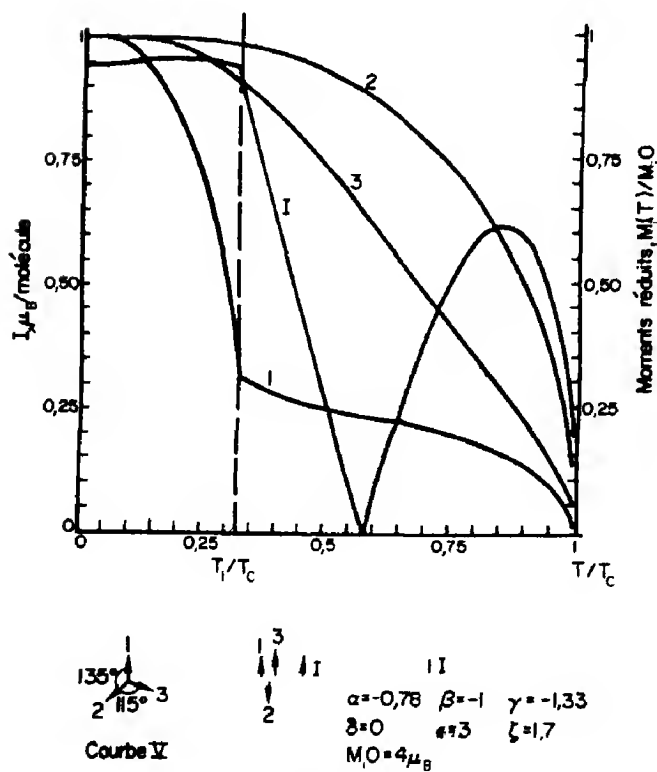


Fig. 5(e).

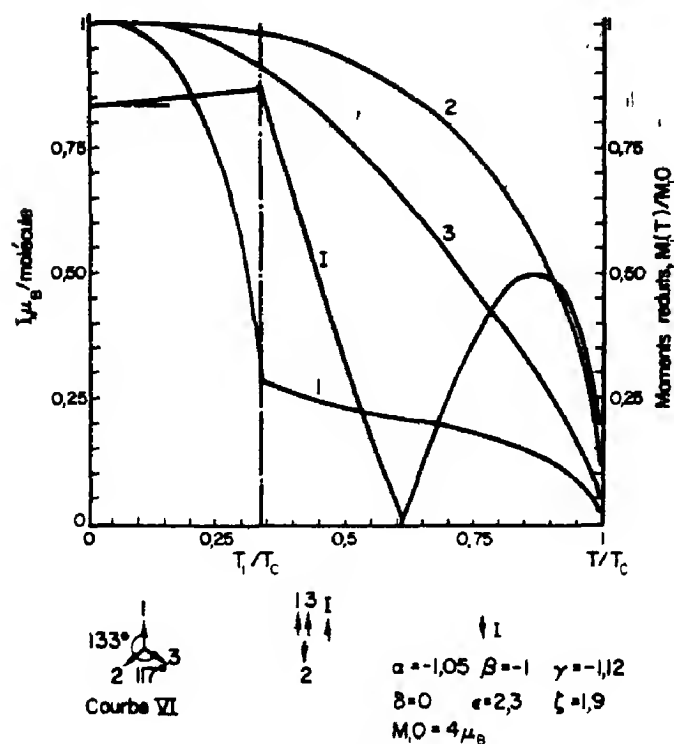


Fig. 5(f).

Fig. 5. Variation en fonction de la température réduite des aimantations réduites des sous-réseaux, de l'aimantation du corps et des angles que forment entre elles les aimantations des sous-réseaux.

peuvent avoir les formes les plus diverses présentant ou non un minimum ou un point de compensation; $I(T)$ peut croître ou décroître très rapidement quand la température croît.

CONCLUSION

Nous avons mis en évidence l'existence d'une structure 'en étoile' dans le cas d'un corps où existent trois interactions différentes entre ions magnétiques. Cette structure devient colinéaire à une température $T < T_C$. Nous avons étudié les variations de l'aimantation des trois sous-réseaux en fonction de la température et donné quelques courbes types.

Dans un prochain article[4] nous montrerons, par des mesures de diffraction de neutrons, que ce type de structure existe effectivement dans $MiMn_2O_4$ et suit bien l'évolution thermique prévue par la théorie.

Remerciements—Nous remercions vivement M. le Professeur Herpin qui a suivi de près ce travail ainsi que M. P. Meriel qui nous a aidés par de nombreuses discussions.

REFERENCES

1. NEEL S., *Ann. Phys.* **3**, 137 (1948).
2. NIESSEN K. F. *Physica* **19**, 1035 (1953).
3. YAFET Y. and KITTEL C., *Phys. Rev.* **87**, 290 (1952).
4. BOUCHER B., BUHL R. et PERRIN M., *J. Phys. Chem. Solids* (à paraître).

TECHNICAL NOTES

Knight shift measurements in liquid alloys of Al, Cu and Mn

(Received 5 March 1969; in revised form 7 May 1969)

THE PURPOSE of this paper is to give a brief preliminary report of measurements of ^{27}Al Knight shift changes in liquid Al-Cu alloys doped with Mn, currently in progress in our laboratory. When dissolved in pure Cu, Mn impurity atoms possess a localized magnetic moment[1] while in Al, by the same criteria, they do not[2]. By alloying Al and Cu it becomes possible, in effect, to investigate the influence of variations of the Fermi energy of the matrix on the formation of localized moments. Similar experiments have been carried out previously in solid alloys[3], but metallurgical considerations drastically limit the possible variations in the composition of the matrix. In the liquid state no such problems arise, Al and Cu being miscible in all proportions, and it is possible to study the magnetic behavior of transition metal impurities in a matrix of any desired composition. Recent work with liquid alloys has shown that the properties of the impurity state are not strongly dependent upon the state of the matrix in which the impurity is dissolved [1, 4(a)]. Thus, general conclusions about the impurity state based on work with liquid metal systems should be pertinent to solid alloys as well. It is perhaps the possibility of obtaining a better understanding of certain solid state phenomena that provides the major incentive for research on liquid metals.

The alloys used for the measurements described below were prepared by melting the constituents in capped purified alumina crucibles under an atmosphere of purified argon. Magnetic susceptibility measurements

on these same alloys have been previously reported[5]. The apparatus used for the NMR work is essentially that described by Odle and Flynn[4(b)].

We have measured the change in Knight shift of the ^{27}Al nucleus as a function of temperature in liquid Al, relative to that at the melting point. The change was observed to be small, $0.0032\%/^{\circ}\text{C}$ over the temperature range 660° to 1100°C . If we set the Knight shift of the ^{27}Al nucleus in pure liquid Al near the melting point equal to 0.164 per cent, the value obtained by Knight, Berger and Heine[6], the data is closely represented by the line shown in Fig. 1.

The temperature dependence of the Knight shift of the same nucleus in liquid $\text{Al}_{80}\text{Cu}_{20}$, $\text{Al}_{60}\text{Cu}_{40}$, and $\text{Al}_{40}\text{Cu}_{60}$ has been determined relative to pure liquid Al at the same temperature. Use of the value 0.164 per cent for the Knight shift of ^{27}Al in pure liquid Al permits the determination of the fractional shift, relative to a non-conducting reference compound, of the ^{27}Al resonance in the liquid binary alloys at the temperature of the measurement. This fractional shift is denoted by the symbol K_a , and the results of our experiments are presented in Fig. 1. We emphasize that the values shown there represent a fractional shift relative to a suitable reference compound, and not a shift relative to pure liquid Al. As is clear from this diagram, increasing the Cu content of the alloys results in a monotonic decrease in the fractional shift of the ^{27}Al nuclear resonance.

Measurements were also carried out on alloys of the same composition, containing sufficiently small quantities (2 at. %) of Mn to preclude the appearance of any indication of magnetic coupling between the Mn atoms.

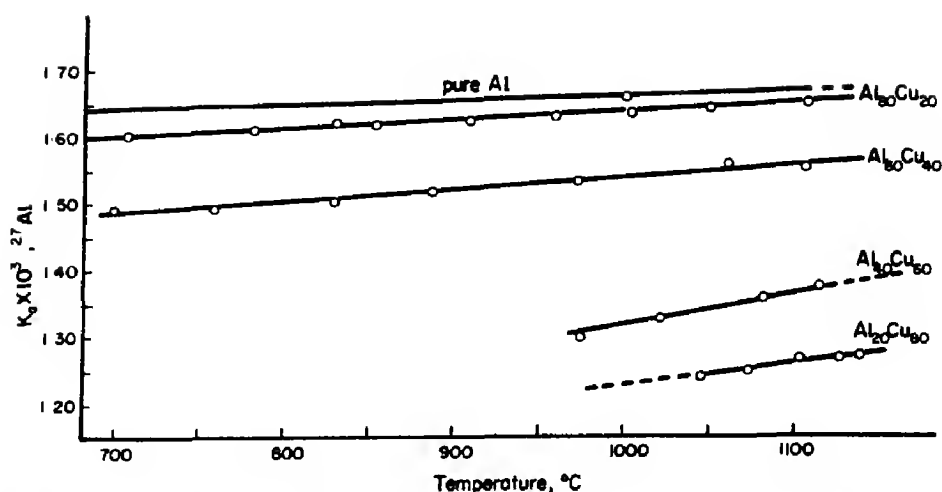


Fig. 1. The temperature dependence of the fractional frequency shift of the ^{27}Al NMR line in pure Al and in binary alloys of Al and Cu.

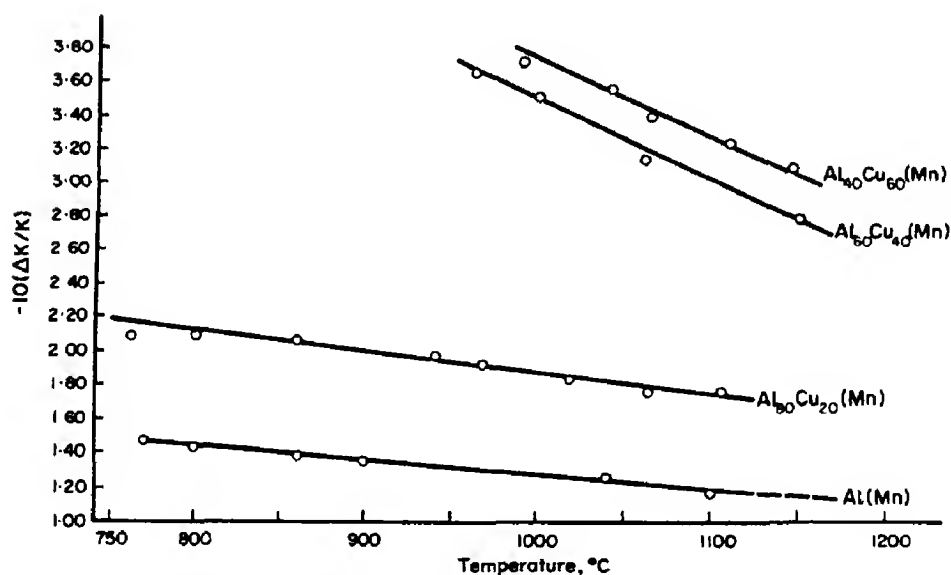


Fig. 2. The temperature dependence of the fractional change in Knight shift of the ^{27}Al NMR line in binary alloys of Al and Cu doped with 2 at.% Mn.

The results of these measurements are reported in Fig. 2. There, the numbers given are calculated from the equation

$$\frac{\Delta K}{K} = \frac{K'_a - K_a}{K_a} \quad (1)$$

where K'_a is the fractional shift of the ^{27}Al nucleus in the doped alloy.

In the one-electron approximation the relative change in Knight shift due to an atomic fraction c of magnetic impurities in a liquid metal, is given[1] by the rather

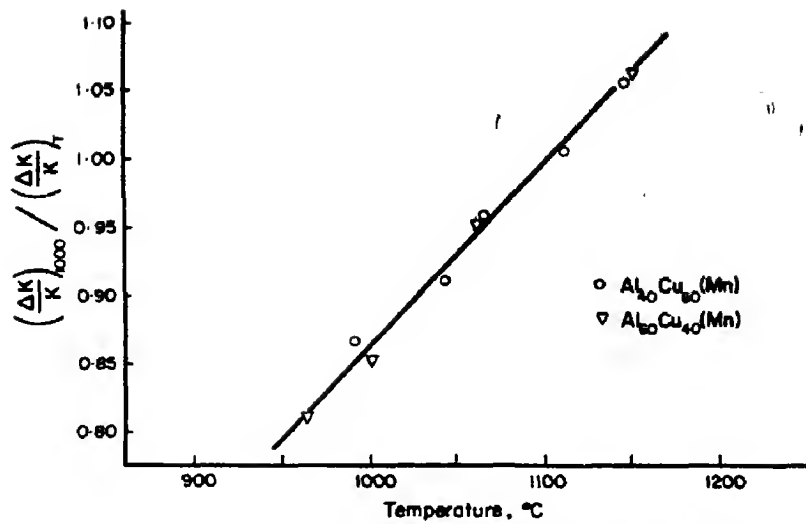


Fig. 3. Reciprocal of the fractional change in the ^{27}Al Knight shift versus temperature for Mn impurities in binary alloys of Al and Cu. $\Delta K/K$ is scaled to unity at 1100°C for purposes of comparison.

cumbersome expression

$$\Gamma = \frac{1}{K} \cdot \frac{\partial K}{\partial c} = \frac{(n+2)E_F}{3k_B(T-\theta)\rho(k_F)k_F^3} \int_0^{k_F} k^2 \rho(k) dk \{A_2[\sin^2 \eta \uparrow(k) - \sin^2 \eta \downarrow(k)] + B_2[\sin 2\eta \uparrow(k) - \sin 2\eta \downarrow(k)]\} \quad (2)$$

where

$$A_2 = 5 \int_0^\infty [n_2^2(kr) - j_2^2(kr)] d(r) dr$$

$$B_2 = -5 \int_0^\infty n_2(kr) j_2(kr) d(r) dr.$$

Here E_F is the Fermi energy of the alloy, n is the difference in occupation of the spin-up and spin-down sub-bands, k_B is Boltzmann's constant, θ is the Curie temperature of the alloy, $\rho(k)$ is the density of electrons at the nuclear-sites with wave vector k , $n_2(kr)$ and $j_2(kr)$ are, respectively, the spherical Neumann and Bessel functions of order, 2, $\eta_i(k)$ are the d wave phase shifts for the two spin sub-bands, and $d(r)$ is the radial distribution function appropriate to the matrix. In view of the complexity of this equation and the un-

known or difficult-to-estimate parameters required, we have for the time being made no attempt to compute numerical values for Γ . Rather, we make use of this expression to provide a criterion for the presence or absence of a localized magnetic moment, i.e. in the event that $1/\Gamma$ is linear in T over the available temperature range, the impurities are assumed to possess a local moment, otherwise not.

In Fig. 3 we plot

$$\frac{\left(\frac{\Delta K}{K}\right)_{1100^\circ\text{C}}}{\left(\frac{\Delta K}{K}\right)_T}$$

vs. temperature for the alloys containing 40 at.% and 60 at.% Cu. The two sets of data have been arbitrarily normalized to unity at 1100°C and cluster quite closely about a straight line.

The data for the alloys containing 20 at.% Cu cannot be fitted to this graph, nor can the data for a 20 at.% Cu alloy doped with Fe.

According to the criterion given above, a substantial localized magnetic moment develops on the Mn atoms in the concentration

range 20 at.% Cu to 40 at.%. The transition from the non-magnetic to the magnetic state is rather abrupt, the magnitude of the Knight shift change and local moment varying only slowly for concentrations of Cu greater than 40 at.%.

Friedel[7, 8] has given a rough criterion for the formation of a localized magnetic moment which can be applied to the alloys investigated here. He finds that an impurity should possess a local moment if

$$W \leq p \cdot \Delta E \quad (3)$$

where p is the number of unpaired atomic spins, ΔE is the average difference in energy between two atomic d -electrons with spins parallel and anti-parallel, and $W \approx 1/3 E_F$ is the width of the virtual bound d level.

For Mn, $p = 5$ and ΔE is estimated from atomic data to be about 0.8 eV for all 3- d -transition-metals from Sc to Ni. Using these numerical values and estimates of the Fermi energy of the Al-Cu alloys, Friedel's criterion suggests that the onset of a magnetic moment should occur in the vicinity of 40 at.% Cu, as is indeed observed.

Schrieffer[9] has suggested that it may be possible to interpret the behavior of these alloys in terms of a very high Kondo temperature, which, in the case of the non-magnetic alloys would exceed the temperature at which the measurements are performed. In this case a quasi-bound state is formed between the impurity spin and the average spin of the conduction electrons in the neighborhood of the impurity so that the net spin of the complex vanishes. In the transition region (between 20 at.% Cu and 40 at.% Cu for the alloys studied here) the Kondo temperature would be of approximately the same magnitude as the temperature at which the experiments are performed, i.e. $\sim 1000^\circ\text{C}$. However, a detailed elucidation of any relationship between the results reported here and the Kondo effect in the same alloys awaits theoretical clarification and more experimental data. At the present

time we are extending our measurements to alloys with concentrations between 20 at.% Cu and 40 at.% Cu, as well as to binary alloys of Al and Cu containing transition metal impurities other than Mn.

Acknowledgements—The authors wish to express their gratitude to Professor E. Lüscher, in whose laboratory this work was carried out, and to O. Gruber, who provided the alloys used for these measurements.

Physik-Department,
Technische Hochschule,
München,
Germany

R. L. ODLE
G. BECKER
S. SOTIER

REFERENCES

1. GARDNER J. A. and FLYNN C. P., *Phil. Mag.* **15**, 1233 (1967).
2. FLYNN C. P., RIGNEY D. A. and GARDNER J. A., *Phil. Mag.* **15**, 1255 (1967).
3. COLLINGS E. W., HEDGCOCK F. T., MUIR W. B. and MUTO Y., *Phil. Mag.* **10**, 159 (1967).
4. ODLE R. L. and FLYNN C. P., (a) *Phil. Mag.* **13**, 699 (1966); (b) *Rev. scient. Instrum.* **35**, 1611 (1964).
5. GARDNER J. A., ODLE R. L. and GRUBER O., *Bull. Am. Phys. Soc.* **13**, 411 (1968).
6. KNIGHT W. D., BERGER A. C. and HEINE V., *Ann. Phys.* **8**, 173 (1959).
7. FRIEDEL J., (a) *Nuovo Cim. (Suppl. 2)* **7**, 287 (1958); (b) *J. Phys. Radium, Paris*, **23**, 692 (1962).
8. DANIEL E. and FRIEDEL J., *Proc. IXth Intl. Conf. on Low Temp. Phys.* (part B), 933 (1965).
9. SCHRIEFFER J. R., (a) *12th Annual Conf. on Magnetism and Magnetic Mat.*, Washington (1966); (b) *J. appl. Phys.* **38**, 1143 (1967).

J. Phys. Chem. Solids Vol. 30, pp. 2482–2484.

Dislocation pits in α -silicon carbide by heating

(Received 22 January 1969; in revised form 6 May 1969)

WELL-DEFINED pits at the sites of dislocations in α -silicon carbide could be produced chemically[1–4] so far only on the (0001) plane i.e. the A face as a consequence of the polar structure of the crystal. The authors[5], how-

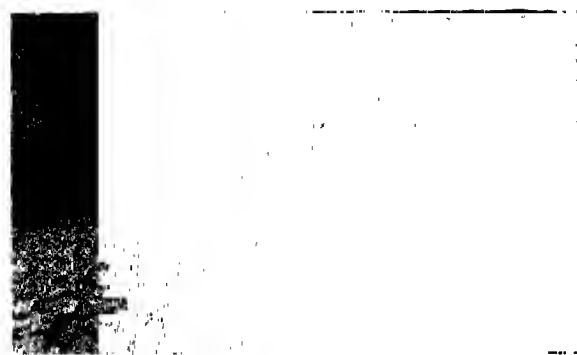


Fig. 1. General etch pattern produced on a habit $\{0001\}$ face by heating in the carbon arc ($\times 262.5$).



Fig. 2(a).



Fig. 2(b).

Figs. 2(a,b). Etch patterns produced on a pair of matched $\{00001\}$ cleavage by heating ($\times 122.5$).

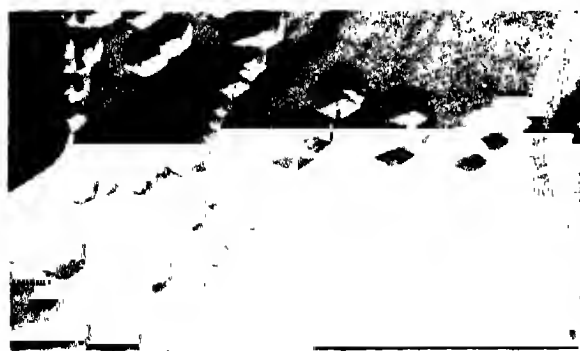


Fig. 3(a). The etch patterns on a $(000\bar{1})$ face by heating ($\times 122.5$).



Fig. 3(b). The patterns produced on the complementary (0001) face of Fig. 5(a) by etching in Na_2O_2 at 480°C ($\times 122.5$).

ever, could produce well-defined hexagonal pits on both the $\{0001\}$ planes by etching them in controlled conditions in a mixture of molten $K_2CO_3 + Na_2CO_3$ (1:3)[1] at $920^\circ C$ for $1\frac{1}{2}$ min and in molten NaOH[3] at $650^\circ C$.

SiC has no congruent melting point[6, 7] and oxidation takes place readily at $1700^\circ C$ [8]. Volatile oxides of Si are formed at this temperature[9] and Faust[3] suggests that volatile SiO and CO should constitute an etch for SiC. It was, therefore, considered that if SiC crystals are heated to a temperature of the order of $2000^\circ C$ etching might take place. Savitskii *et al.*[10] have reported the effects of thermovacuum etching on chemically etched A faces of SiC.

For etching, SiC crystals were heated to the required temperature in a carbon arc for 30 to 45 sec, keeping the crystals in a cavity drilled in one of the carbon rods. Thus the carbon electrode functioned as a furnace. The crystals were kept sufficiently below the flame with the faces to be etched away from it to avoid the formation of a carbon coating over the faces. The accurate measurement of the temperature at which the thermal etching took place was not, however, possible.

Figure 1 shows the etch patterns on a habit $\{0001\}$ face of SiC, produced by this method. It is similar to the usual chemically etched figures, with randomly distributed hexagonal point bottomed pits with sides parallel to $\langle 11\bar{2}0 \rangle$ directions. The results obtained on the fractured basal cleavages were similar to those in Fig. 1.

To determine whether the pits produced by this technique, originate at the sites of dislocations $\{0001\}$ matched cleavages were simultaneously etched in the arc as shown in Figs. 2(a) and 2(b). The pits have a perfect correspondence in number, position and orientation on the two complementary cleavages, though the cleavage lines have moved due to preferential etching. Notice the indistinguishability of the (0001) face from the $(000\bar{1})$ face. The formation of pits at the sites of dislocations was confirmed by etching one part of a

cleavage thermally and the counterpart chemically in molten Na_2O_2 . The exact correspondence of pits are shown in Figs. 3(a) and 3(b) respectively.

The results shown in Figs 1–3 suggest that the pits are formed at the sites of dislocations.

Unlike in the chemical etching the thermal attack on (0001) and $(000\bar{1})$ faces appears to be similar, and this gives an advantage to thermal method over chemical etching. Though the mode of evaporation in thermal etching is not understood, it can be considered that SiC dissociates into Si and C atoms with a rich Si vapor. Both Si and C react with oxygen at high temperatures to form volatile SiO and CO. A balance between the amount of rich SiO and less CO will be obtained from the production of CO from the burning of carbon rods. These volatile oxides in balance attack the A layer with Si on top[11] and the B layer with C on top similarly. This process of etching appears to be different from the chemical etching where SiC molecules are removed as single units enabling each face to keep its own identity. Here also an A face will end up as an A face after thermal etching because as soon as Si is dissociated from the surface the C atom will also escape immediately since its bond is weakened. The process is two stage.

This method can easily and successfully be applied to study the dislocation contents in other non-centrosymmetric crystals whose opposite faces chemically react differently.

Acknowledgements—K. J. M. wishes to acknowledge the C.S.I.R. Government of India for the award of a Jr. Research Fellowship.

Department of Physics,
Sardar Patel University,
Vallabh Vidyanager,
Gujarat State,
India

A. R. PATEL
K. JOHN MATHAI

REFERENCES

1. HORN F. H., *Phil. Mag.* **43**, 1210 (1952).
2. GEVERS R., AMELINCKX S. and DEKEYSER D., *Naturewissenschaften* **39**, 448 (1952).
3. FAUST, Jr., J. W., In *Silicon Carbide* p. 403. Pergamon Press, Oxford (1960).

4. AMELINCKX S., STRUMANE G. and WEBB W. W., *J. appl. Phys.* **31**, 1359 (1960).
5. PATEL A. R. and JOHN MATHAI K., *Indian J. Pure and Appl. Phys.* To be published.
6. KNIPPENBERG W. F., *Philips Res. Rep.* **18**, 161 (1963).
7. SCACE R. I. and SLACK G. A., *J. chem. Phys.* **30**, 1551 (1959).
8. WIEBKE G., *Ber. Deut. Keram. Ges.* **37**, 219 (1960).
9. ELMER J. H. and HOSHUBA W. J., *Nepa Division Rep. No. 1770*, Oak Ridge Tennessee (1951) (Unclassified).
10. SAVITSKII K. V., ILUSCHENKOV M. A., BURNAKOV K. K. and HYKONNYA A. F., *Soviet Phys. Crystallogr. (English)* **11**, 309 (1966).
11. BRACK K., *J. appl. Phys.* **36**, 3560 (1965).

J. Phys. Chem. Solids Vol. 30, pp. 2484-2486.

X-ray determination of the thermal expansion of calcium molybdate

(Received 9 April 1969)

INTRODUCTION

IN CONNECTION with a programme of X-ray investigations, undertaken to obtain detailed information on the temperature variation of the lattice parameters, the coefficients of thermal expansion and the position and thermal parameters of the atoms in the unit cell of some Scheelite (CaWO_4) type crystals, we have previously reported the results on the thermal expansion of KIO_4 [1] and NaIO_4 [2]. Results of a similar X-ray study on calcium molybdate (CaMoO_4) are being presented here.

EXPERIMENTAL AND RESULTS

A synthetic single crystal of CaMoO_4 obtained from Dr. W. S. Brower of the National Bureau of Standards, Washington, D.C. was crushed to fine powder form and filled in the specimen holder of the back

reflection focussing Camera. X-ray powder pictures were obtained at eight different temperatures using CuK_α radiation. The details of the experimental set up have been described earlier by Sirdeshmukh[3].

Unambiguous indexing of the powder lines was achieved with the help of the space group conditions and the fact that in these compounds the expansion along the c -axis is larger than that along the a -axis. Thirteen lines, $(3, 3, 10)_{a_1a_2}$, $(604)_{a_1}$, $(620)_{a_1a_2}$, $(536)_{a_1a_2}$, $(1, 1, 14)_{a_1a_2}$, $(634)_{a_1a_2}$, and $(448)_{a_1a_2}$ recorded in the back reflection region were used in evaluating the lattice parameters at different temperatures using Cohen's[4] analytical method in combination with the error function, $\phi \tan \phi$. Independent measurements and calculations were made on each film and the average values obtained therefrom, are given in Table 1. The standard errors calculated by the method of Jette and Foote[5] are also tabulated.

Table 1. Values of the lattice parameters of CaMoO_4 at different temperatures

Temp. (°C)	a (Å)	c (Å)
33	5.2266 ± 0.0001	11.4352 ± 0.0004
75	5.2292 ± 0.0001	11.4420 ± 0.0004
110	5.2304 ± 0.0002	11.4483 ± 0.0005
158	5.2332 ± 0.0002	11.4577 ± 0.0005
215	5.2358 ± 0.0002	11.4668 ± 0.0005
265	5.2385 ± 0.0003	11.4769 ± 0.0009
312	5.2415 ± 0.0002	11.4893 ± 0.0007
355	5.2431 ± 0.0001	11.4937 ± 0.0009

The values of the principal coefficients of expansion at different temperatures were determined by the procedure suggested by Deshpande and Mudholkar[6] and the following expressions were obtained by the usual method of statistical treatment:

$$\alpha_a = 7.20 \times 10^{-6} + 15.96 \times 10^{-9}t - 1.54 \times 10^{-12}t^2$$

and

$$\alpha_c = 11.17 \times 10^{-6} + 22.99 \times 10^{-9}t + 16.14 \times 10^{-12}t^2.$$

Here α_a and α_c are the coefficients of expansion at $t^\circ\text{C}$, parallel to the a and c axes respectively. The values calculated at different temperatures using the above expressions are shown in Fig. 1 along with the observed values. The mean coefficients of expansion, over the range $30^\circ\text{--}350^\circ\text{C}$, were found to be $\alpha_a = 10.13 \times 10^{-6}/^\circ\text{C}$ and $\alpha_c = 16.54 \times 10^{-6}/^\circ\text{C}$.

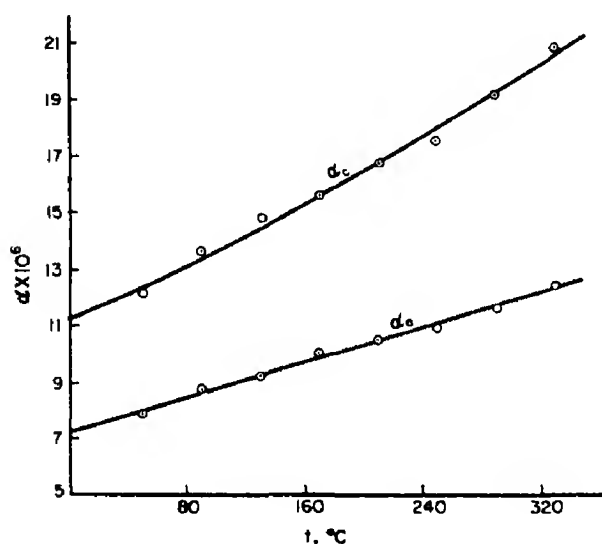


Fig. 1. Temperature variation of the coefficients of thermal expansion of calcium molybdate.

DISCUSSION

The values of the lattice parameters of CaMoO_4 obtained at room temperature in the present study, are compared in Table 2 with those available in literature.

There is good agreement between the values obtained in the present investigation and those reported by Swanson *et al.*[9]. The values of the expansion coefficients are also in good accord with those of Brower[10], who reports $\alpha_a = 10.71 \times 10^{-6}/^\circ\text{C}$ and $\alpha_c = 16.17 \times 10^{-6}/^\circ\text{C}$ in the range $30^\circ\text{--}350^\circ\text{C}$ as obtained by an interferometric method.

Table 2. Comparison of the lattice parameters of CaMoO_4 at room temperature

Authors	a (Å)	c (Å)
Vegard[7]	5.23	11.44
Sillen and Nylander[8]	5.213	11.426
Swanson <i>et al.</i> [9]	5.226	11.43
Present study	5.2266	11.4352

A comparison of the principal coefficients of expansion at 30°C for a few crystals having the Scheelite structure, is made in Table 3.

Table 3. Thermal expansion coefficients of a few Scheelite type crystals at 30°C

Substance	$\alpha_a \times 10^6$	$\alpha_c \times 10^6$
KIO_4 [1]	25.35	56.62
NaIO_4 [2]	38.17	54.87
CaWO_4 [11]	6.35	12.38
SrWO_4 [12]	5.86	13.21
BaWO_4 [13]	4.43	18.35
CdMoO_4 [11]	6.85	15.13
CaMoO_4	7.67	11.88

It is seen that all these crystals exhibit same type of anisotropy. For any of these compounds, the value of the thermal expansion coefficient along the tetragonal axis, is larger than that along the a -axis and remains larger at all temperatures. However in the periodates, numerical values of the expansion coefficients and the rates of their temperature variation are higher than the corresponding quantities in the tungstates and the molybdates. That the melting points of the tungstates and the molybdates are much higher than those of periodates[14–17] is also a fact, worth a mention in this context.

Structurally all these ABO_4 type crystals belong to the space $I 4_1/a$ of the tetragonal system. They are known to have a complex layer structure, the layers being perpendicular

to the c -axis [18]. Each layer has a two-dimensional CsCl type arrangement of A^{n+} and BO_4^{n-} ions ($n = 1$ or 2). Each ion is surrounded by eight ions of the other sign, four at the corners of a square, lying in the layers and the other four situated tetrahedrally around it. The reasoning given earlier by Deshpande *et al.* [1, 2] to explain the results of periodates, also holds good for calcium molybdate and other crystals of this group. The ionic interactions between any ion and the four ions of opposite sign lying in the same layer give rise to binding forces essentially along the layers and the interaction between this ion and the four ions of opposite sign situated at the corners of a tetrahedron provide binding forces with components along the layers as well as in perpendicular directions. It follows from this that the binding between neighbouring atoms in the layers of the lattice is stronger than that along the c -axis and so the coefficients of expansion along the a -axis can be expected to be smaller than that along the c -axis.

Acknowledgements—The authors wish to thank Dr. W. S. Brower for supplying them with the synthetic crystals of Calcium molybdate used in the present investigation. One of us (S.V.S.) thanks the Ministry of Education, Government of India for financial assistance.

V. T. DESHPANDE
S. V. SURYANARAYANA

Physics Department,
Osmania University, Hyderabad-7,
India

REFERENCES

1. DESHPANDE V. T., PAWAR R. R. and SURYANARAYANA S. V., *Curr. Sci.* **36**, 513 (1967).
2. DESHPANDE V. T., SURYANARAYANA S. V. and PAWAR R. R., *Acta crystallogr.* **A24**, 398 (1968).
3. SIRDESHMUKH D. B., Ph.D. Thesis. Osmania University (1963).
4. COHEN M. U., *Rev. scient. Instrum.* **6**, 68 (1935).
5. JETTE E. R. and FOOTE F., *J. chem. Phys.* **3**, 605 (1935).
6. DESHPANDE V. T. and MUDHOLKAR V. M., *Ind. J. Phys.* **35**, 434 (1961).
7. VEGARD L., *Skr. Norske Vid. Akad. Oslo* nr 11 (1925).
8. SILLEN L. G. and NYLANDER A. L., *Ark. Kemi Geol.* **17A**, 4 (1943).
9. SWANSON H. E., GILFRICH N. T. and COOK M. I., Standard X-ray diffraction patterns, NBS Circ. No. 539, 6 (1956).
10. BROWER W. S., Private Communication (1968).
11. DESHPANDE V. T. and SURYANARAYANA S. V., Unpublished results.
12. DESHPANDE V. T. and SURYANARAYANA S. V., *J. meter. Sci.* To be published (1969).
13. DESHPANDE V. T. and SURYANARAYANA S. V., *J. appl. Phys.* To be published (1969).
14. CHANG LUKE L. Y., SCROGER M. G. and PHILLIPS B., *J. Am. Ceram. Soc.* **49**, 385 (1966).
15. NASSAU K. and VAN UITERT L. G., *J. appl. Phys.* **31**, 1508 (1960).
16. BRIXNER L. H., *Electrochem. Tech.* **6**, 88 (1968).
17. *Handbook of Chemistry and Physics* (Edited by C. D. HODGMAN), pp. 545, 571. Chemical Rubber, Cleveland, Ohio (1950).
18. ARBEL A. and STOKES R. J., *J. appl. Phys.* **36**, 1460 (1965).

J. Phys. Chem. Solids Vol. 30, pp. 2486–2490.

Coloration of LiF produced by 3.0 MeV ^{40}Ar ions

(Received 28 March 1969)

EXTENSIVE studies have established that the exposure of alkali halide crystals to ionizing radiation results in the production of color center bands. These studies have been restricted for the most part to irradiations by u.v. rays, X-rays, gamma rays, electrons, protons and neutrons. Little information has been reported, however, as to the color center bands produced by energetic massive ions. Since the penetration depth of the massive ions is quite small it is possible to investigate color center, e.g. the F -center, concentrations in crystals which are otherwise too opaque for ordinary optical measurements.

LiF was used in this investigation since preliminary coloration studies with various alkali halides exposed to energetic argon ions indicated that the damage was quite stable in LiF at room temperature. The dominant color

centers produced by ionizing radiation in LiF at room temperature have been identified as F and F -aggregate center bands[1] and the damage has been found to be independent of irradiation flux[2]. Thus the color centers produced by ionizing radiation in LiF could be used as a basis for comparison to the color centers produced by the 3.0 MeV argon ions. The crystals* were first hardened by very brief exposure to Co^{60} (10^6R) gamma rays to facilitate cleaving. Samples were then cleaved ($\sim 6 \times 6 \times \frac{1}{2}\text{mm}^3$) and annealed for several hours at 450°C to remove the damage induced by the gamma-ray irradiation.

The NRL 5 MV Van de Graaff accelerator was used to produce the 3.0 MeV beam of ^{40}Ar ions. The ion beam was magnetically analyzed before striking the target and the beam current on target was measured and integrated in a Faraday cup arrangement which had a negatively biased guard ring located at its entrance to suppress secondary electrons. Tests were made for the presence of a neutral beam component which would produce damage in the target but not be measured as an electrical current. The neutral beam component introduced a correction of about 3 per cent to the dose delivered to the target. The beam spot ($\sim 25\text{mm}^2$) was scanned electrostatically over an area somewhat larger than the sample size in order to ensure uniform irradiation over the target. Slits were used to limit the beam scan to a well defined rectangular area which was larger than the crystal samples which were irradiated. The area bombarded was measured and used together with the integrated beam charge in calculating the total number of ions per cm^2 incident on the sample. Irradiations consisted of repeated short runs with beam intensities of $6 \times 10^{-9}\text{A}$ or less into target areas of approximately 1cm^2 . The coloration produced was measured at room temperature

with a Cary 14 optical spectrophotometer several hours after irradiation.

The F -center growth curve (plotted as F -centers/ cm^2 v. incident ions/ cm^2) obtained from the 3.0 MeV ^{40}Ar ion bombardment is shown in Fig. 1. In order to convert the optical density measurements of the F band (247 nm) to F centers/ cm^2 , Smakula's equation[3,4] was employed using an oscillator strength of unity and a half-width for the F band of 0.70 eV. The data are presented as a log-log plot since it covers several orders of magnitude in both parameters. The F -center growth curve shown in Fig. 1 is linear up to approximately 5×10^{14} F centers/ cm^2 . Farge *et al.*[5] have reported that a log-log plot of the F -center growth curve from X-ray irradiated LiF should have a slope of $\frac{1}{2}$. Extrapolation of the linear portion intersects the abscissa at 1.7×10^{13} F centers/ cm^2 . A linear F to M -center relationship is observed over the dose range examined.

An estimate of the corresponding F -center concentration (F centers/cc) at which the growth curves begins to become nonlinear can be obtained by assuming uniform coloration within the damaged layer. Preliminary damage profile curves, obtained by etching, have indicated that deviations from uniform coloration are not large. The nuclear and electronic stopping powers of 3.0 MeV ^{40}Ar in Li and F were calculated using the theory of Lindhard *et al.*[6]. The projected range for 3.0 MeV ^{40}Ar in LiF was calculated to be 1.64μ . Taking into account the penetration depth of the ^{40}Ar yields an initial concentration of negative ion vacancy sources for LiF crystals prehardened and annealed of about 9.5×10^{16} F centers/cc, which is in range of the value usually observed. The F -center concentration at which the growth curve becomes nonlinear is estimated to be 2.8×10^{18} F centers/cc. This nonlinear section occurs at a dose of about 2×10^{11} ions/ cm^2 . Saturation of the F -center concentration occurs at about 4.25×10^{19} F centers/cc. Pooley[7] has obtained a saturation for the F -center con-

*The samples were cleaved from a single block of LiF purchased from the Harshaw Chemical Co., Cleveland, Ohio, U.S.A.

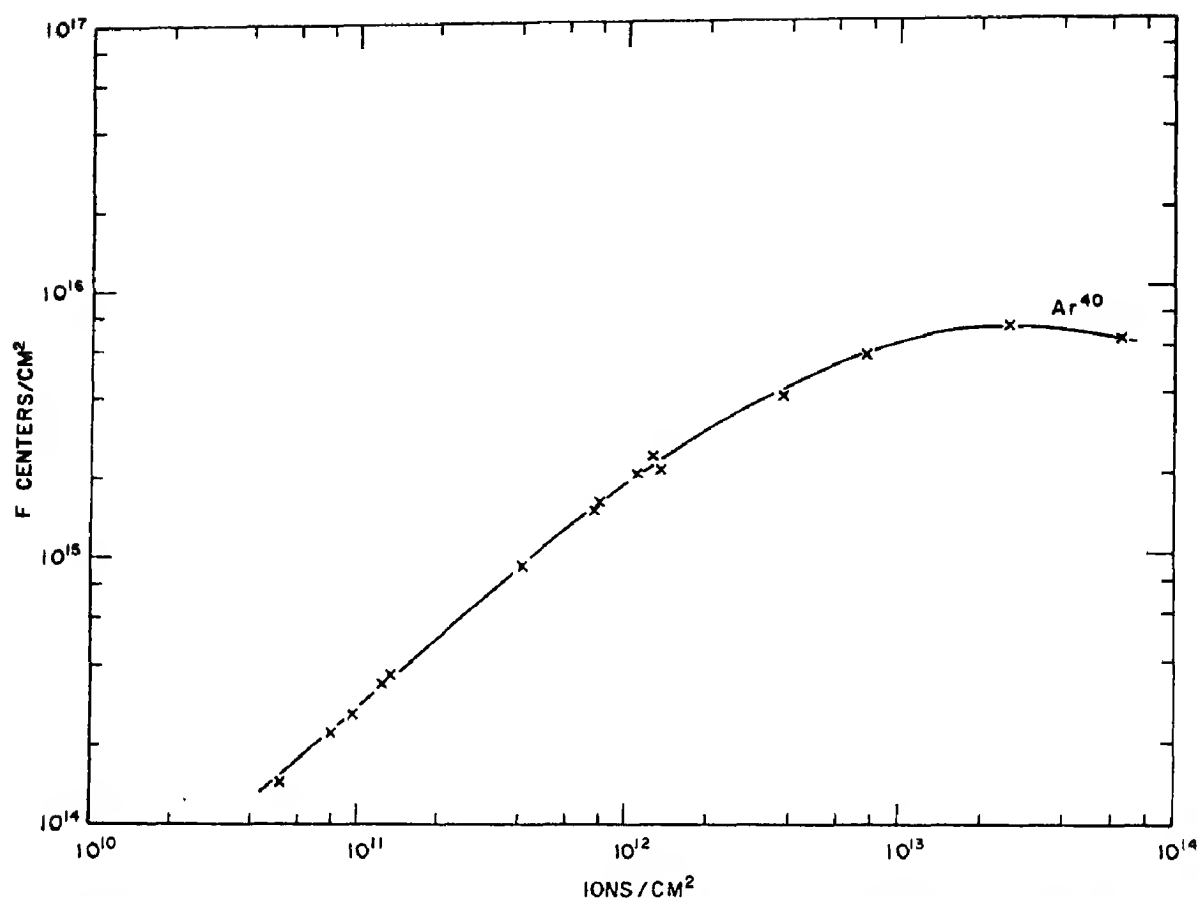


Fig. 1. Log-log plot of the *F*-center growth curve in LiF produced by 3.0 MeV ^{40}Ar ion bombardment.

centration in KCl subjected to 300 keV proton irradiation of about 0.8×10^{19} *F*-centers/cc.

For the linear portion of the growth curve an accurate determination of the number of *F* centers produced per incident ion can be obtained. It is found that 2600 *F* centers are created per ^{40}Ar ion. Since each ion has an incident energy of 3.0 MeV, an average energy of 1150 eV is expended per *F* center produced. This efficiency can be compared to values ranging from 850 eV/*F* center to 3800 eV/*F* center for irradiation of LiF at liquid-helium temperature by 2.0 MeV electrons and X-rays of various energies[8]. The relative magnitude of the efficiency for ^{40}Ar in the present study is consistent with the X-ray and electron liquid-helium study in that for

irradiations with high track ionization densities, the efficiency decreases as the ionization density increases. Such comparisons are not very meaningful, however, due to the differences in sample temperatures.

In addition to the *F* band (247 nm) the absorption spectra produced by the ^{40}Ar bombardment contained additional bands in the *M*-band (445 nm) region. In an effort to catalog the new color center bands the spectra produced was quantitatively resolved with a computer into individual Gaussian bands and compared to a similarly resolved spectrum obtained from a sample which had received gamma-ray irradiation. A general computer program designed to perform at least squares analysis for nonlinear functions[9] was

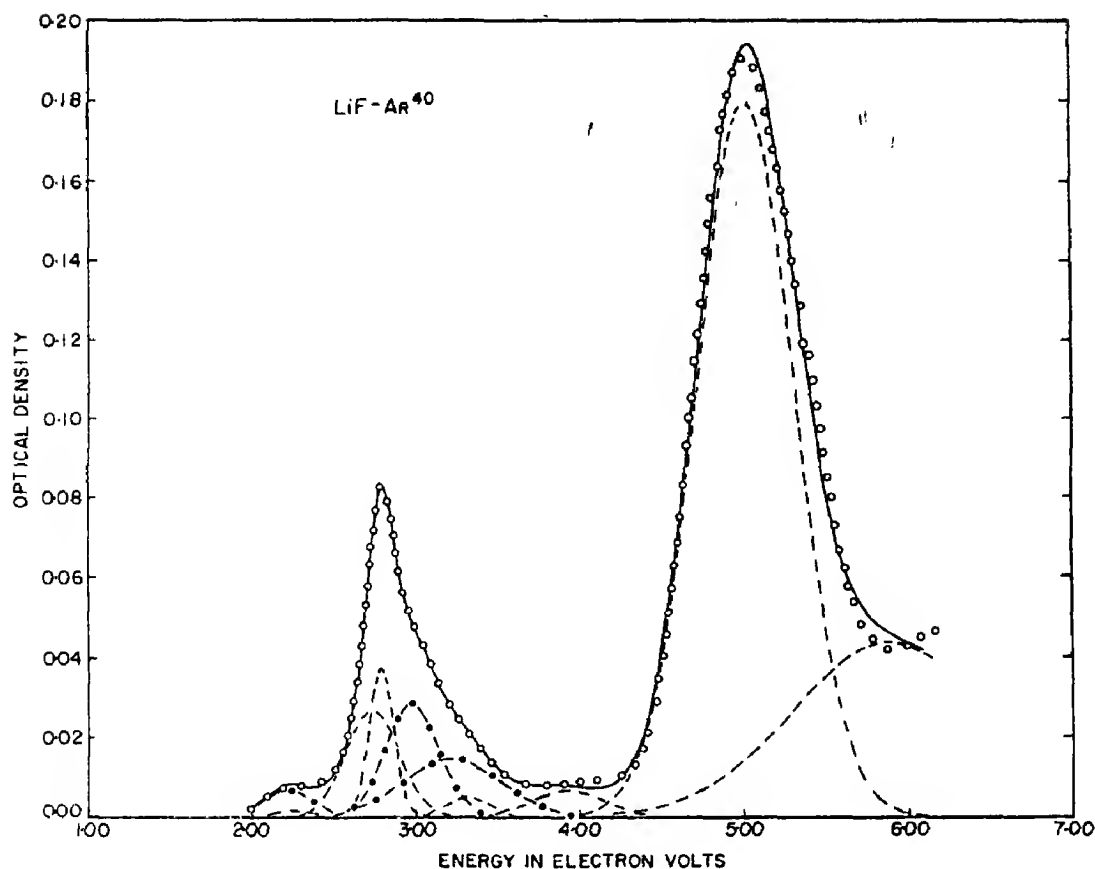


Fig. 2. Resolved spectrum of a LiF sample bombarded by 3.0 MeV ^{40}Ar ions with a dose of 3.8×10^{12} ions/cm². The data is represented by open circles, the resolved individual Gaussians by the broken lines, the fit by the solid line. The new bands are represented by the dash-dot curves.

employed to decompose the optical absorption spectrum into its component Gaussian bands. The program input consisted of (1) the data points, taken at intervals of 1 nm, from the continuous spectrum furnished by the Cary spectrophotometer, (2) initial guesses as to the Gaussians present, i.e. the number present, their height in optical density, the positions of the band maxima, and the bandwidths at half maximum, and (3) which, if any, of the three parameters per Gaussian were to be held fixed. The spectrum of a gamma-ray (10^7 R) irradiated crystal was analyzed by estimating the parameters of the six dominant *F* and *F*-aggregate color-center bands known to exist in gamma-ray

irradiated LiF, i.e. the *F*, *M*, *R*₁, *R*₂, *R*_N[10], and *F*₃⁺[11] bands. To analyze the spectra produced by the ^{40}Ar ions the positions and bandwidths of the standard bands (*R*, *M* and *F*₃⁺ bands) were held fixed and only their heights were allowed to vary.

The fit for an ^{40}Ar (3.8×10^{12} ions/cm²) produced spectrum is shown in Fig. 2. The data are represented by open circles, the resolved individual Gaussians by broken lines, the fit by the solid curve, and the new bands by the dash-dot curves. The assignment of bands at 3.21, 2.97 and 2.22 eV, resulted in a particularly good fit to the data. It is assumed in this analysis that the rate of growth of these bands, as well as their cor-

responding half-widths, remains constant over the dose range studies. An enlarged view of both the known bands and the three new bands are shown in Fig. 3.

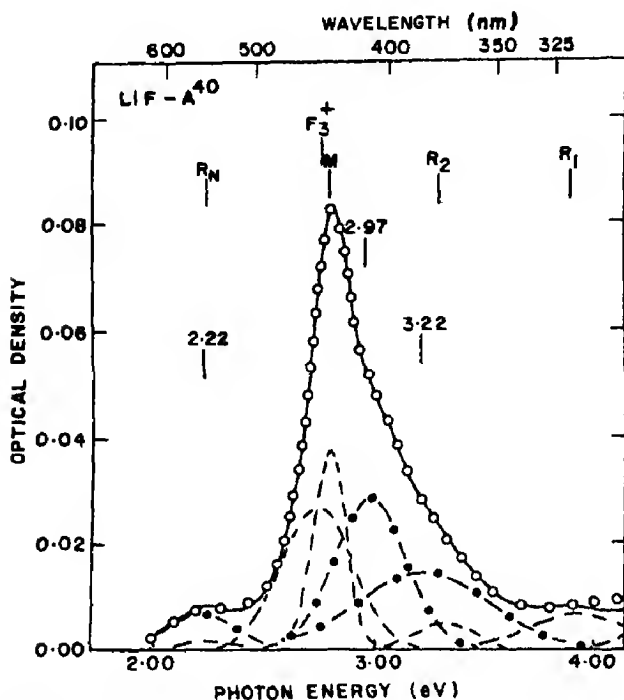


Fig. 3. Enlargement of the *M*-band region shown in Fig. 2 indicating the positions of the three new bands at 2.22, 2.97 and 3.22 eV.

Support for the assignment of the three bands unobserved in previous studies in the ^{40}Ar produced spectrum was sought by extending the study to include other massive ions. LiF crystals were therefore bombarded with 3.0 MeV ^{84}Kr and 2.0 MeV ^{129}Xe ions. Preliminary spectra produced by these ions were then analyzed following the procedure used with the ^{40}Ar results. Similarly the spectra resulting from the ^{84}Kr and ^{129}Xe irradiations required three additional Gaussian bands in order to obtain a good fit. The positions and half-widths of the bands agreed quite well, with one exception in ^{84}Kr .

In conclusion, we have found that in addition to the known color centers created in

LiF by irradiation with electromagnetic rays or light particles, bombardment by energetic massive ions produces additional damage. The centers created by 3.0 MeV ^{40}Ar ions exhibit bands near 3.22, 2.97 and 2.22 eV. The ^{40}Ar produced *F*-center growth curve is linear up to approximately 2.8×10^{18} *F* centers/cc. From the slope of the linear portion of the growth curve it is determined that 2600 *F* centers are created per incident ^{40}Ar ion, which yields an efficiency of 1150 eV per *F* center. Saturation of the *F*-center concentration in LiF due to the 3.0 MeV ^{40}Ar irradiation at room temperature occurs at approximately 4.25×10^{19} /cc.

Acknowledgements—It is a pleasure to thank Dr. B. J. Faraday for his interest and many helpful discussions. We wish to thank Mr. J. Halpin for his help with the computer analysis and Drs. M. N. Kabler and V. Ritz for their valuable comments.

K. L. VAN DER LUGT*
J. COMAS
E. A. WOLICKI

Naval Research Laboratory,
Washington, D.C. 20390,
U.S.A.

REFERENCES

1. COMPTON W. D. and RABIN H., *Solid State Physics* (Edited by F. Seitz and D. Turnbull), Vol. 16. Academic Press, New York (1964).
2. WHAPHAM A. D. and MAKIN M. J., *Phil. Mag.* **5**, 237 (1960).
3. SMAKULA A., *Z. Phys.* **59**, 603 (1930).
4. DEXTER D. L., *Phys. Rev.* **101**, 48 (1956).
5. FARGE Y., DURAND P. and LAMBERT M., *Intl Symp. on Color Centers, Rome, 1968*, Abstract 58.
6. LINDHARD J., SCHARFF M. and SCHIOTT H. E., *Mat. Fys. Medd. Dan. Vid. Selsk.* **33**, No. 14 (1963).
7. POOLEY D., *Br. J. appl. Phys.* **17**, 855 (1966).
8. RITZ V. H., *Phys. Rev.* **133**, A1452 (1964).
9. DANIELS W. E., *General Least Squares with Statistics*, Tech. Rep. No. 579, University of Maryland (1966).
10. VANDER LUGT K. L. and KIM Y. W., *Phys. Lett.* **22**, 50 (1966).
11. NAHUM J. and WIEGAND D. A., *Phys. Rev.* **154**, 817 (1967).

*NMR Postdoctoral Associate. Present address: Augustana College, Sioux Falls, S.D. 57102, U.S.A.

Stacking faults in $\text{GaAs}_{1-x}\text{P}_x$ alloys*(Received 21 March 1969)*

THE OCCURRENCE of stacking faults in epitaxial semiconducting layers, notably Si, [1-3] has been widely reported and well described. Their presence in III-V compounds has also been reported [4, 5] but their characterization has been less complete than for Si. This correspondence reports the occurrence of intrinsic stacking faults in doped $\text{GaAs}_{1-x}\text{P}_x$ alloys.

The epitaxial layers were grown by a vapor-phase technique [6] on damage-free GaAs substrates in the [100] direction. The growth rate was approximately $0.4 \mu \text{ min}^{-1}$. Two general cases were examined: *p*-type GaAs, and *n*-type $\text{GaAs}_{1-x}\text{P}_x$. The latter included a compositionally graded region between the substrate and constant composition layer. In all of the latter cases, the compositional gradient, $(\Delta C/\Delta X)$, was found to be a constant using electron beam microprobe analysis [7]. The doping was done directly from the vapor-phase during growth. Specimens obtained from these layers and thinned by ion bombardment [8] were examined by transmission electron microscopy in an RCA-EMU-3G electron microscope.

For *p*-type GaAs, seven homoepitaxial Zn-doped GaAs layers were prepared on Te-doped substrates ($n = 1-2 \times 10^{18} \text{ cm}^{-3}$), with $3 \times 10^{18} \leq p \leq 1 \times 10^{20} \text{ cm}^{-3}$. Stacking faults were observed in only the most highly doped crystal for which $p = 1 \times 10^{20} \text{ cm}^{-3}$. This crystal also contained precipitates, which were identified as Zn_3As_2 by transmission electron diffraction. A complete account of precipitation in Zn-doped GaAs will be published separately.

The experimental results for the *n*-type samples of $\text{GaAs}_{1-x}\text{P}_x$ are presented in

Table 1. The carrier concentration for all the doped samples in Table 1 equalled $1-2 \times 10^{18} \text{ cm}^{-3}$. It is seen that faults were observed only when the epitaxial layer was doped (samples 2, 5, 7, and 9). Neither doping in the substrate (samples 1, 4, 6, and 8), the magnitude of $(\Delta C/\Delta X)$ (compare sample 7 and 8), nor the final composition of a constant composition layer could be correlated with the occurrence of faulting.

We had previously observed [9] Ga_2Se_3 precipitates in GaAs doped with Se to $n \geq 1 \times 10^{18} \text{ cm}^{-3}$. In all cases when stacking faults were observed, the dopant concentrations for both Se and Zn were high enough for precipitates to have formed. Furthermore, the faults form continuously during growth since the faults had a wide distribution in length. Further, as shown above, they are not introduced from the substrate. This suggests that the faults might be nucleated at precipitate sites. If this is true, it is implied that reduction of the doping in the vapor-grown layers will reduce the probability of stacking fault intersections, and thus decrease the formation of stair-rod dislocations. This is of importance since stair-rod dislocations can be electrically active [10].

The faults were invariably intrinsic and were bounded by Shockley partial dislocations. A typical fault is shown in Fig. 1 for different diffraction conditions. By inspection of Figs. 1(a) and 1(b) the plane of the fault is determined as $(\bar{1}\bar{1}1)$. Figure 1(a) was taken under two-beam bright-field conditions, using $\bar{g}_{0\bar{2}2}$; $s = 0$ [11], while Fig. 1(b) was taken in dark field using $\bar{g}_{0\bar{2}2}$; $s = 0$. From the fact that the two images are pseudo-complementary at the bottom foil surface [12], the fault plane can be specified with the aid of the diffraction pattern. The sense of the inclination of the fault plane was confirmed by additional dark-field experiments were $s \neq 0$ using the techniques described by Bell and Thomas [13]. Figures 1(e) and 1(f) were obtained in dark-field, using $\bar{g}_{0\bar{2}2}$ with $s < 0$ and $s > 0$, respectively. Under these condi-

Table 1. Dependence of stacking fault occurrence on growth parameters of GaAs_{1-x}P_x alloys. S = substrate; G = compositionally graded layer; C = constant composition layer

Sample	Compositional gradient (% P/ μ)	Final composition (% P)	Doping			Specimen origin	Stacking faults observed	
			S	G	C		G	C
1	0	0	Te		none	C		no
2	0	0	Te		Se	C		yes
3	0.21	20	none	none		G	no	
4	1.15	45	Te	none	none	G, C	no	no
5	1.57	20	Te	none	Se	G, C	no	yes
6	1.74	50	Te	none	none	G, C	no	no
7	3.14	40	Te	Se	Zn	G	yes	
8	3.74	50	Si	none		G	no	
9	5.00	100	Te	Se	Se	G, C	yes	yes

tions, the image contrast is greatest at the top of the foil for $s < 0$, and greatest at the bottom of the foil for $s > 0$. It can be seen from either Figs. 1(e) or 1(f) that the sense of the inclination of the fault agrees with that determined from Figs. 1(a) and 1(b).

The nature of the fault was determined in the following way. With reference to the dark field image ($s = 0$) in Fig. 1(b), it is observed that if the origin of the operative reciprocal lattice vector, \bar{g}_{022} , is placed at the center of the fault, \bar{g}_{022} is directed away from the bright fringe. This is sufficient to indicate that the fault is intrinsic [14].

Since the stacking fault in Fig. 1 is intrinsic, its displacement vector $\bar{R} = -\frac{1}{3}[\bar{1}\bar{1}\bar{1}]$. The phase angle [15] $\alpha = 2\pi\bar{g}\cdot\bar{R} = -2\pi/3$, which implies the edge fringes in the bright field image will be dark, as observed in Fig. 1(a). When $\alpha = 0$, there is no fringe contrast. This is shown in the bright field image of Fig. 1(c), where $\bar{g} = 022$.

Figures 1(a), 1(c) and 1(d) which show the bright field images of the fault for \bar{g}_{022} , \bar{g}_{022} , and \bar{g}_{040} , respectively, can be used to determine the types of partial dislocations bounding the stacking fault. The invisibility criterion for partial dislocations is $\bar{g}\cdot\bar{b} = 0$ or $\pm\frac{1}{2}$. It can be seen that both partials are out of contrast for

\bar{g}_{022} and that they are both in contrast for \bar{g}_{022} and \bar{g}_{040} . Reference to Table 2, which shows $\bar{g}\cdot\bar{b}$ values for the partial dislocations which can lie in the $(\bar{1}\bar{1}\bar{1})$ plane of the fault,

Table 2. Values of $\bar{g}\cdot\bar{b}$ for partial dislocations (foil normal $[100]$ parallel to electron beam)

\bar{b}	$\bar{g}\cdot\bar{b}$			
	\bar{g}	$0\bar{2}2$	022	$0\bar{4}0$ 004
$\frac{1}{6}[\bar{1}12]$	$\frac{1}{6}$	1	$-\frac{1}{2}$	$\frac{1}{2}$
$\frac{1}{6}[\bar{1}\bar{2}1]$	$-\frac{1}{6}$	1	$-\frac{1}{2}$	$\frac{1}{2}$
$\frac{1}{6}[\bar{2}\bar{1}\bar{1}]$	$\frac{1}{6}$	0	$\frac{1}{2}$	$\frac{1}{2}$
$\frac{1}{6}[\bar{1}\bar{1}\bar{1}]$	$-\frac{1}{6}$	0	$-\frac{1}{2}$	$-\frac{1}{2}$

indicates that dislocations having Burgers vectors equal to $(1/6)[112]$ and $(1/6)[\bar{1}\bar{2}1]$ would be invisible for \bar{g}_{022} . Although which of the two partial dislocations is associated with which Burgers vector cannot be specified, it can be said that both partials are of the Shockley type and that neither is a Frank partial. A Frank partial (see Table 2, $\bar{b} = \frac{1}{6}[\bar{1}\bar{1}\bar{1}]$) should be visible for \bar{g}_{022} , but invisible for \bar{g}_{040} .

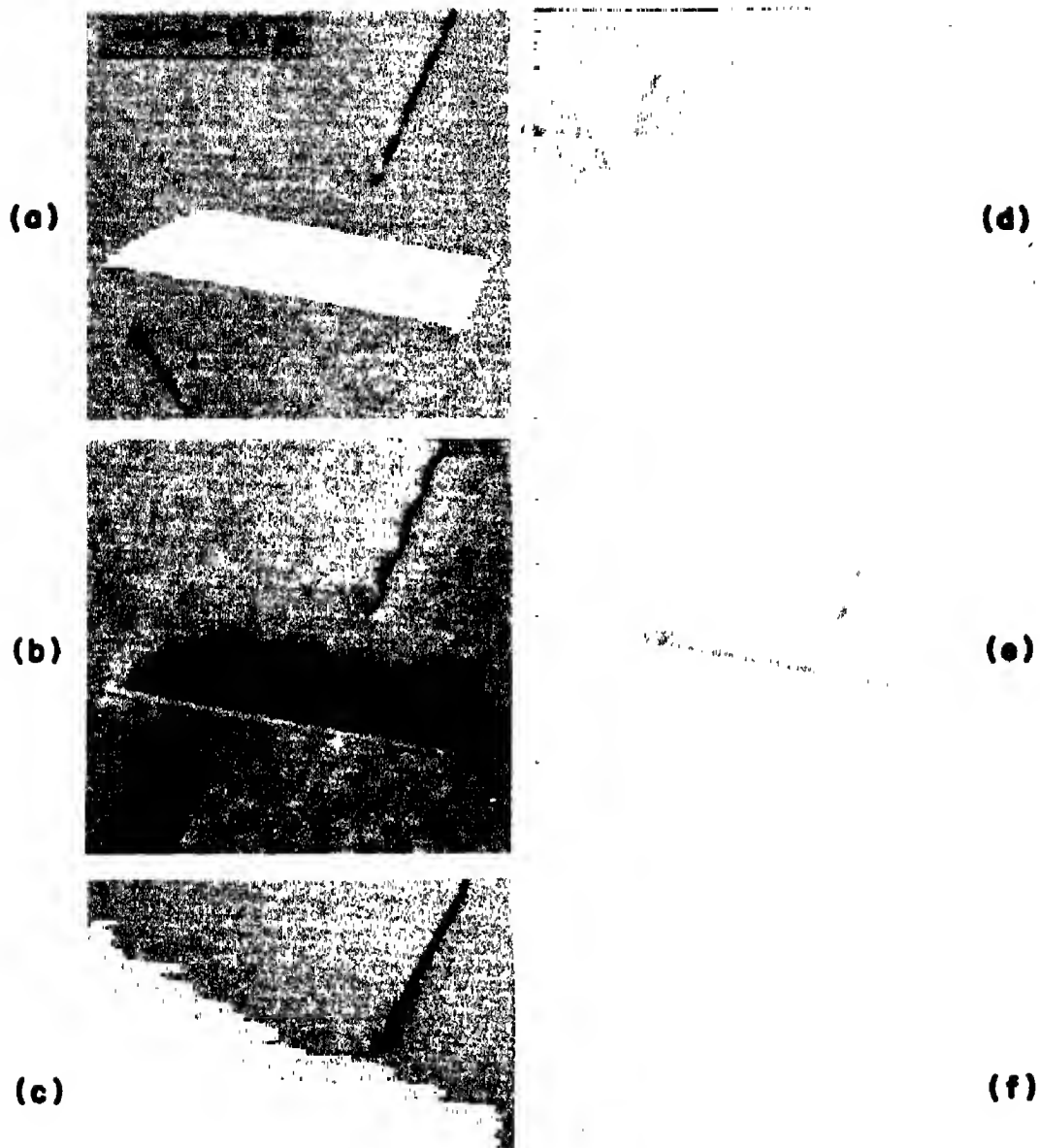


Fig. 1. Intrinsic stacking fault in Se-doped $\text{GaAs}_{1-x}\text{P}_x$.
 (a) BF, g_{012} , $s = 0$; (b) DF, g_{012} , $s = 0$; (c) BF, g_{022} ,
 $s = 0$; (d) BF, g_{040} , $s \approx 0$; (e) DF, g_{021} , $s < 0$; (f) DF,
 g_{012} , $s > 0$. BF = bright field; DF = dark field.

RCA Laboratories,
Princeton, N.J. 08540,
U.S.A.

M. S. ABRAHAMS
J. J. TIETJEN

REFERENCES

1. MENDELSON S., *J. appl. Phys.* **35**, 1570 (1964).
2. BOOKER G. R. and UNVALA B. A., *Phil. Mag.* **11**, 109 (1965).
3. JOSHI M. L., *Acta Metall.* **14**, 1157 (1966).
4. ABRAHAMS M. S. and BUIOCCHI C. J., *J. Phys. Chem. Solids* **28**, 927 (1967).
5. WILLIAMS F. V., *Trans. AIME* **239**, 702 (1967).
6. TIETJEN J. J. and AMICK J. A., *J. electrochem. Soc.* **113**, 724 (1966).
7. FORNOFF M., RCA, Lancaster, Pa.
8. ABRAHAMS M. S., BUIOCCHI C. J., and COUTTS M. D., *Rev. scient. Instrum.* **39**, 1944 (1968).
9. ABRAHAMS M. S., BUIOCCHI C. J. and TIETJEN J. J., *J. appl. Phys.* **38**, 760 (1967).
10. QUEISSER H. J. and GOETZBERGER A., *Phil. Mag.* **8**, 1063 (1963).
11. \vec{g}_{hkl} is the operative reciprocal lattice vector; s is the magnitude of the vector drawn from \vec{g}_{hkl} to the Ewald sphere. See HIRSCH P. B. *et al.*, In *Electron Microscopy of Thin Crystals*, p. 440. Butterworths, Washington, (1965).
12. HASHIMOTO H., HOWIE A. and WHELAN M. J., *Proc. R. Soc. A* **269**, 80 (1960).
13. BELL W. L. and THOMAS G., *Phys. Status Solidi* **12**, 843 (1965).
14. GEVERS R. ART A. and AMELINCKX S., *Phys. Status Solidi* **3**, 1563 (1963).
15. HIRSCH P. B., *et al.*, *Electron Microscopy of Thin Crystals*, p. 261. Butterworths, Washington, (1965).

J. Phys. Chem. Solids Vol. 30, pp. 2493-2494.

Some comments on "On the magnetic anisotropy and susceptibility of $\text{CoF}_2 \cdot 5\text{HF} \cdot 6\text{H}_2\text{O}$ and $\text{NiF}_2 \cdot 5\text{HF} \cdot 6\text{H}_2\text{O}$ "*

(Received 4 March 1969)

THE AUTHORS of the above paper, Dutta Roy and Ghosh (abbreviated as DR & G) report a phase transition in $\text{CoF}_2 \cdot 5\text{HF} \cdot 6\text{H}_2\text{O}$ at 246°K which is shown to be very similar to that observed in $\text{CoSiF}_6 \cdot 6\text{H}_2\text{O}$ by Majum-

dar and Datta[1]. The fluosilicate belongs to the trigonal system and is isomorphous (at the room temperature) with $\text{FeSiF}_6 \cdot 6\text{H}_2\text{O}$ the detailed structure of which was worked out by Hamilton[2] (cf. also the X-ray structure of $\text{NiSnCl}_6 \cdot 6\text{H}_2\text{O}$ by Pauling[3]). There is one $\text{Co}(\text{H}_2\text{O})_6^{2+}$ ion in the unit cell which has trigonal symmetry, the symmetry axis coinciding with that of the crystal (referred to here as the c axis).

The hydrofluorides reported by DR & G apparently have quite different chemical composition and detailed data on their chemical preparation and analysis (or a reference to the relevant literature) seem very desirable. No X-ray data have been reported except that the crystal contains one molecule in the unit cell. Nothing has been stated about the space group or the cell dimensions. An octahedrally coordinated $\text{Co}(\text{H}_2\text{O})_6^{2+}$ ion is assumed to be present in the crystal from the "presence of a strong absorption band at $19,800\text{ cm}^{-1}$ " in the optical spectrum, the justification for which is open to question. Even then, the structural similarity between this crystal and the fluosilicate is not sufficiently well established so that the assumed analogy in the magnetic and phase transition properties does not seem very meaningful.

After the phase transition in $\text{CoSiF}_6 \cdot 6\text{H}_2\text{O}$ was first reported by Majumdar and Datta[1], Ray[4] of the same laboratory published preliminary X-ray data of this crystal at low Ohtsubo[5] reported the unpublished X-ray temperatures which indicated a monoclinic phase below the transition temperature. data of Watanabe and his group at Osaka University as showing that the low temperature phase is "monoclinic or triclinic, with less possibility." Ohtsubo assumed the presence of two kinds of $\text{Co}(\text{H}_2\text{O})_6^{2+}$ ions at low temperatures and proposed a "spin structure" in which the two ions are tilted in opposite directions, in order to explain his observed weakly ferromagnetic properties of the crystal at 1°K. It appears, therefore, that the frequent reference by DR & G to "Watanabe's

*DUTTA ROY S. K. and GHOSH B., *J. Phys. Chem. Solids* **29**, 1511 (1968).

X-ray data" really refers to Ohtsubo's spin structure.

It was observed[1] that during the phase transition in $\text{CoSiF}_6 \cdot 6\text{H}_2\text{O}$ (a) the principal magnetic anisotropy, $\chi_{\parallel} - \chi_{\perp}$ (\parallel and \perp are with reference to the c axis of the crystal) increases sharply; (b) an anisotropy appears in the plane normal to the c axis and (c) the colour of the crystal changes from pink to orange yellow, accompanied by changes in the optical spectra. DR & G report similar changes in the hydrofluoride (no spectral data are given except mentioning the position of the main band at room temperature) and proceed on the basis of the assumption that the two $\text{Co}(\text{H}_2\text{O})_6^{2+}$ ions are tilted by an angle ϕ with respect to the c axis below the transition temperature. They have not considered an alternative possibility, namely that the clusters do not appreciably change in orientation but become distorted to a lower symmetry. Objections against DR & G's assumption are the following: (1) the changes in the optical spectra of the fluosilicate, especially the appearance of a new band at $19,000\text{ cm}^{-1}$, indicate a change in the ligand field symmetry[†]; (2) the g -values for the Co^{2+} ion calculated from the susceptibility data[1, 5] and $\phi = 12^\circ$, as deduced by DR & G, would come out as $g_{\parallel} = 6.8$ and $g_{\perp} = 2.6$ which are widely different from the values $g_{\parallel} = 5.82$ and $g_{\perp} = 3.44$ as reported by Bleaney and Ingram[6] from the e.s.r. measurements on the diluted crystal where the trigonal symmetry of the *bulk crystal* does not change at low temperatures (for discussions on the weak subsidiary lines of g_{\parallel} and g_{\perp} values of 6.6 and 2.6, respectively, see [1]; DR & G's remark that "it is evident from the magnetic data of Majumdar and Datta[1] that on dilution the phase transformation disappears" is not quite correct,

since measurable anisotropy has been observed in the plane normal to the c axis at low temperatures in a 1:1 diluted crystal; see Table 2(b), p. 423 of [1]); (3) the easy cleavage of the crystals along the c axis, the close-packed columnar structure of the $\text{Co}(\text{H}_2\text{O})_6\text{-SiF}_6$ chains which are difficult to break (Pauling[3]), and the fact that in such transitions there are normally only small changes in lattice parameters with a tendency for "persistence of axes" (Ubbelohde[7]), would preclude any large change in the orientation of the clusters; (4) Ohtsubo[5] concludes from his data that the spin axes are tilted by only about 1° while the crystal field axes are canted "a little more than this value" but are still "nearly along" the c axis of the room temperature form.

Two other minor points in regard to DR & G's paper deserve comment: (i) the source of the "experimental results" on $\text{CoSiF}_6 \cdot 6\text{H}_2\text{O}$ (Table 2) is not stated. Apparently they refer to [1]; however, no experimental data have been presented in the latter paper at rounded off temperatures; and (ii) the split components of 4F should be quartets in spin and not triplets, as given by DR & G (p. 1516, col. 2, line 3 from bottom).

There are a few typographical errors; e.g. "Mazumdar and Dutta Roy[1]" occurring twice (in the text and in the list of references) should read "Majumdar and Datta[1]".

Department of Chemistry,
Presidency College,
Calcutta,
India

S. K. DATTA

REFERENCES

1. MAJUMDAR M. and DATTA S. K., *J. chem. Phys.* **42**, 418 (1965).
2. HAMILTON W. C., *Acta crystallogr.* **15**, 353 (1962).
3. PAULING L., *Z. Kristallogr.* **72**, 482 (1930).
4. RAY S., *Indian J. Phys.* **38**, 176 (1964).
5. OHTSUBO A., *J. phys. Soc. Japan* **20**, 82 (1965).
6. BLEANEY B. and INGRAM D. J. E., *Proc. R. Soc. A* **208**, 143 (1951).
7. UBBELOHDE A. R., *Br. J. appl. Phys.* **7**, 313 (1956).

[†]Note added in proof: Professor A. G. McLellan of the University of Canterbury, New Zealand, has reported (To be published) that two sharp peaks of the i.r. band of the fluosilicate centered at $1.45\text{ }\mu$ abruptly diminish in intensity as the temperature of the crystal is raised across 250°K .

ERRATA

I

L. M. AMZEL and L. N. BECKA: A model for the evaluation of thermodynamic properties for the solid-solid and melting transitions of molecular crystals. *J. Phys. Chem. Solids* **30**, 521 (1969).

THE PRINTER regrets that several of the expressions in the published paper should be changed to the following correct formulations:

- (i) On page 523, column 1, 4th line from top; in the expression for E the upper limits of the summations are missing, and should be ' D ' in the first and ' i ' in the second summation, respectively.
- (ii) On page 523, column 1, 6th line from top; in the expression for γ there are factorial signs and brackets missing; the true expression is

$$\gamma = \left\{ \frac{N!}{[NQ]![N(1-Q)]!} \right\}^2$$

$$\left\{ \frac{[NQ]!}{[NQS_1]! \prod_{i=2}^D [NQS_i]!} \right\} \left\{ \frac{[N(1-Q)]!}{[N(1-Q)S_1]! \prod_{i=2}^D [N(1-Q)S_i]!} \right\}$$

- (iii) On page 523, column 1; in equation (1) the variable S_1 has to be replaced by S_r , with $S_r = 1 - S_1$.
- (iv) On page 523, column 1, in equation (2) the brackets are misplaced and the variable S_1 has to be replaced by S_r , with $S_r = 1 - S_1$, so that equation (2) should have read

$$\log (Q/(1-Q)) = \{(zW/2kT) - (z'W'/kT)S_r[1 - (DS_r/(2D-2))]\}(2Q-1). \quad (2)$$

- (v) On page 524, column 2, in equation (3) the variable S_1 has to be changed to S_r , with $S_r = 1 - S_1$.

The calculations and discussions presented in the paper were based on the above, correct expressions.

II

N. G. EROR and J. B. WAGNER, Jr.: Electrical conductivity and thermogravimetric studies of single crystalline cobaltous oxide. *J. Phys. Chem. Solids* **29**, 1597 (1968).

THE AUTHOR regrets that in Table 3 on page 1608 the activity of oxygen in cobaltous oxide was denoted as a_{O_2} . It should be a_O . The standard state oxygen pressures, $P_{O_2}^0$, were omitted from Table 3. They are: 4.98×10^{-3} , 2.83×10^{-3} and 1.72×10^{-3} (atm) for 1000°, 1100° and 1200°C, respectively. In addition, the value for the activity of cobalt at $N_O/N_{Co} = 1.006$ is 0.112. This value of N_O/N_{Co} was inadvertently omitted from Table 3. The activity of cobalt at $N_O/N_{Co} = 1.00643$ was not calculated.

NOTES FOR CONTRIBUTORS

I. GENERAL

1. Submission of a paper to *The Journal of Physics and Chemistry of Solids* will be taken to imply that it represents original research not previously published (except in the form of an abstract or preliminary report), that it is not being considered for publication elsewhere, and that if accepted it will not be published elsewhere in the same form, in any language, without the consent of the Editor-in-Chief. It should deal with original research work in the field of the physics and chemistry of solids.

2. Papers should be submitted to the appropriate regional editor (all English-language papers to be sent to the U.S. editor).

3. Short communications may be published as "Technical Notes" and will receive somewhat more rapid handling than full length articles. Short communications requiring the maximum speed of publication should be submitted to one of the editors of "Solid State Communications."

II. SCRIPT REQUIREMENTS

1. **Papers** submitted should be concise and written in a readily understandable style. Scripts should be typed and double spaced with good margins on one side of the paper only and submitted in duplicate to facilitate refereeing.

It will be appreciated if authors clearly indicate any special characters used. An abstract not exceeding 200 words, should be provided in the language of the paper. French and German papers should be submitted with English abstract and titles, but if this is not possible the abstract will be translated by the publishers. To conserve space, **authors are requested to mark less important parts of the paper**, such as details of experimental technique, methods, mathematical derivations, etc. **for printing in small type**. The technical description of methods should be given in detail only when such methods are new. Authors will receive proofs for correction when their papers are first set, and **alterations must be restricted to printer's errors**. Other than these, any substantial changes may be charged to the authors.

2. **Illustrations** should not be included in the typescript of the paper, and legends should be typed on a separate sheet. Line drawings which require redrawing should include all relevant details and clear instructions for the draughtsman. If figures are already well drawn it may be possible to reproduce them direct from the originals, or from good photo-prints if these can be provided. It is not possible to reproduce from prints with weak lines. Illustrations for reproduction should normally be about twice the final size required. The lettering should be sufficiently large and bold to permit this reduction. Photographs should only be included where they are essential.

3. **Tables and figures** should be so constructed as to be intelligible without reference to the text. Every table and column should be provided with an explanatory heading. Units of measure must always be clearly indicated. The same data should not be published in both tables and figures. The following standard symbols should be used on line drawings since they are easily available to the printers: ○, ●, +, ×, □, ■, △, ▲, ◇, ◆, ▽, ▼.

4. **References** are indicated in the text by numbers on the line in brackets, and the full reference should be given in a list at the end of the paper in the following form:

1. BARNES R. G., BORSA F. and PETERSON D., *J. appl. Phys.* 36, 940 (1965).
2. KNIGHT W. D., In *Solid State Physics* (Edited by F. Seitz and D. Turnbull), Vol. 2, p. 93. Academic Press, New York (1957).

Abbreviations of journal titles should follow those given in *World List of Scientific Periodicals* (4th Edn.). It is particularly requested that authors' initials, and appropriate volume and page numbers, should be given in every case.

Footnotes, as distinct from literature references should be indicated by the following symbols—*, †, ‡, §, commencing anew on each page; they should *not* be included in the numbered reference system.

5. Due to the international character of the journal no rigid rules concerning notation and spelling will be observed, but each paper should be consistent within itself as to symbols and units.

CONTENTS

M. I. VALLO and D. LLEWELYN WILLIAMS: A nuclear magnetic resonance study of gallium single crystals—I. Low field spectra	2337
R. RUFFIN: Size effects on plasmon-phonon modes in polar semiconductors	2349
P. NOVÁK: Interactions between octahedrally co-ordinated E_g Jahn-Teller ions	2357
R. E. BINGHAM and C. R. BROOKS: The effect of magnetic and configurational disordering on the high temperature heat capacity of a Ni-50 at.% Pd alloy	2365
D. J. SELLMYER: High-field and quantum oscillatory effects in the magnetoresistance of AuSn	2371
A. K. GHOSH: Optical properties of electron and hole traps in Ag-doped aluminoborate glass	2385
L. DOBRZYŃSKI: Calculation of the entropies of lattice vacancies	2395
A. MOOKHERJEE and S. P. CHACHRA: Magnetic studies on dysprosium ethyl sulphate single crystals	2399
H. NAGASAKI, I. WAKABAYASHI and S. MINOMURA: The pressure dependence of the lattice parameters of CrTe and CrSb	2405
M. LANNOO and P. LENGART: Study of the neutral vacancy in semi-conductors	2409
S. HARALDSON and C-G. RIBBING: ESR-resonances in doped GaAs and GaP	2419
H. E. COOK: The kinetics of clustering and short-range order in stable solid solutions	2427
C. F. LEE: On the solution of the equation of diffusion processes during the uptake of excess calcium by calcium fluoride	2439
G. A. SAUM, R. H. GLAENZER and J. E. DUEKER: Low temperature electroluminescence of ZnSe:Cu:Br	2447
M. BERNASSON, P. DESCOUTS, P. DONZÉ and A. TREYVAUD: Magnetic susceptibilities and NMR properties of V-Ru alloys	2453
T. D. GEORGE and J. B. WAGNER, JR.: Diffusion of nickel into lead telluride between 200° and 400°C	2459
B. BOUCHER, R. BUHL et M. PERRIN: Structure magnétique a trois sous-réseaux dans l'approximation du champ moléculaire	2467
 Technical Notes:	
R. L. ODLE, G. BECKER and S. SOTIER: Knight shift measurements in liquid alloys of Al, Cu and Mn	2479
A. R. PATEL and K. J. MATHAI: Dislocation pits in α -silicon carbide by heating	2482
V. T. DESHPANDE and S. V. SURYANARAYANA: X-ray determination of the thermal expansion of calcium molybdate	2484
K. L. VAN DER LUGT, J. COMAS and E. A. WOLICKI: Coloration of LiF produced by 3.0 MeV ^{40}Ar ions	2486
M. S. ABRAHAM and J. J. TIETJEN: Stacking faults in $\text{GaAs}_{1-x}\text{P}_x$ alloys	2491
S. K. DATTA: Some comments on "On the magnetic anisotropy and susceptibility of $\text{CoF}_2\cdot 5\text{HF}$, $6\text{H}_2\text{O}$ and $\text{NiF}_2\cdot 5\text{HF}$, $6\text{H}_2\text{O}$ "	2493
Errata	2495

THE
JOURNAL OF
PHYSICS
AND
CHEMISTRY
OF SOLIDS

AN
INTERNATIONAL
JOURNAL

BERGAMON PRESS



NEW YORK • OXFORD • LONDON • PARIS

VOLUME 20

NOVEMBER 1963

Editor in Chief
HARVEY BROOKS
Cambridge, Mass.

Associate Editors

H. B. G. CASIMIR
Brindhaven

B. CHALMERS FRAZER
Brøokhaven

JACQUES FRIEDEL
Paris

I. M. LIFSHITZ
Khar'kov

THE JOURNAL OF PHYSICS AND CHEMISTRY OF SOLIDS

Editors

PROF. HARVEY BROOKS (*Editor-in-Chief*), 217 Pierce Hall, Harvard University, Cambridge 38, Mass., U.S.A.

PROF. DR. H. B. G. CASIMIR, *N.V. Philips' Gloeilampenfabrieken, Eindhoven, The Netherlands*

DR. B. CHALMERS FRAZER, *Brookhaven National Laboratory, Upton, Long Island, New York, U.S.A.*

PROF. JACQUES FRIEDEL, *Laboratoire de Physique des Solides, Bâtiment 210, Faculté des Sciences, 91-Orsay, France*

PROF. I. M. LIFSHITZ, *Physico-Technical Institute, Academy of Science, Yumorskii tupik, Khar'kov, U.S.S.R.*

Editorial Advisory Board

U.S.A.

E. N. ADAMS, White Plains, N.Y.
D. ALPERT, Urbana, Ill.
L. APKER, Schenectady, N.Y.
J. BARDEEN, Urbana, Ill.
D. S. BILLINGTON, Oak Ridge, Tenn.
R. G. BRECKENRIDGE, Canoga Pk., Calif.
LEO BREWER, Berkeley, Calif.
E. BURSTEIN, Philadelphia, Penn.
J. A. BURTON, Murray Hill, N.J.
N. CABRERA, Charlottesville, Va.
G. C. DANIELSON, Ames, Iowa
G. J. DIENES, Long Island, N.Y.
J. C. FISHER, Schenectady, N.Y.
F. G. FUMI, Chicago, Ill.
H. K. HENISCH, University Park, Penn.
F. HERMAN, San Jose, Calif.
C. HERRING, Murray Hill, N.J.
A. R. VON HIPPEL, Cambridge, Mass.
J. H. HOLLOMON, Washington, D.C.
W. V. HOUSTON, Houston, Texas
H. B. HUNTINGTON, Troy, N.Y.
H. M. JAMES, Lafayette, Ind.
C. KITTEL, Berkeley, Calif.
W. KOHN, La Jolla, Calif.
J. A. KRUMHANS, Ithaca, N.Y.
A. W. LAWSON, Riverside, Calif.
H. W. LEVERENZ, Princeton, N.J.
O. T. MARZKE, Pittsburgh, Penn.
B. T. MATTHIAS, La Jolla, Calif.
L. R. MAXWELL, Silver Spring, Md.
J. E. MAYER, La Jolla, Calif.
J. W. MITCHELL, Charlottesville, Va.
E. W. MONTROLL, Rochester, N.Y.
D. PINES, Urbana, Ill.

M. H. L. PRYCE, Los Angeles, Calif.
G. T. RADO, Washington, D.C.
H. REISS, Thousand Oaks, Calif.
J. R. REITZ, Dearborn, Mich.
A. ROSE, Princeton, N.J.
R. A. SMITH, Cambridge, Mass.
R. SMOLUCHOWSKI, Princeton, N.J.
F. H. SPEDDING, Ames, Iowa
D. TURNBULL, Cambridge, Mass.
J. H. VAN VLECK, Cambridge, Mass.
B. E. WARREN, Cambridge, Mass.
E. P. WIGNER, Princeton, N.J.
B. H. ZIMM, La Jolla, Calif.

Canada

R. E. BURGESS, Vancouver
W. B. PEARSON, Ottawa

United Kingdom

M. BORN, Bad Pyrmont
A. CHARLESBY, Shrivenham, Berks.
W. J. DUNNING, Bristol
F. C. FRANK, Bristol
H. JONES, London
A. B. PIPPARD, Cambridge
O. C. SIMPSON, Baldock, Herts.
K. W. H. STEVENS, Nottingham
F. C. TOMPKINS, London

Czechoslovakia

J. TAUC, Praha

France

E. F. BERTAUT, Grenoble
J. BOK, Paris

B. DREYFUS, Grenoble
A. GUINIER, Orsay
A. HERPIN, Gif-sur-Yvette
B. JACROT, Grenoble
LOUIS NÉEL, Grenoble

Germany

ULRICH DEHLINGER, Stuttgart
R. HILSCH, Göttingen
G. LEIBFRIED, Aachen
E. MOLLWO, Erlangen
H. PICK, Stuttgart
W. WELKER, Erlangen

Israel

I. ESTERMANN, Haifa

Italy

F. G. FUMI, Palermo

Japan

TOSHINOSUKE MUTO, Tokyo

The Netherlands

A. MICHELS, Amsterdam
G. W. RATHENAU, Eindhoven

Sweden

J. O. LINDE, Stockholm
PER-OLOF LÖWDIN, Uppsala

Switzerland

G. BUSCH, Zurich
P. SCHERRER, Zurich

U.S.S.R.

G. S. ZHDANOV, Moscow

Publishing Offices

American Continent: Pergamon Press Inc., Maxwell House, Fairview Park, Elmsford, N.Y. 10523.

Rest of the World: Pergamon Press Ltd., 84-86 Malahide Road, Coolock, Dublin 5.

Published monthly. Annual subscription for libraries, research establishments and all other multiple-reader institutions, £60 (\$150.00); private individuals, whose departmental libraries subscribe, may obtain this Journal for their personal use at a reduced price of £6 (\$15.00) per annum, including postage. All subscription enquiries are to be addressed to The Manager, Subscriptions Department, Pergamon Press, Headington Hill Hall, Oxford OX3 0BW, England. Back issues are available, write for Back Issues Price Lists.

Copyright © 1969 Pergamon Press Ltd.

PERGAMON PRESS INC.

MAXWELL HOUSE, FAIRVIEW PARK, ELMSFORD, N.Y. 10523
HEADINGTON HILL HALL, OXFORD OX3 0BW

THE PERGAMON TRANSLATION SERVICE



backed by the Pergamon Group's resources producing 200 learned and technical journals and over 600 books a year.

copies of articles on scientific, technical and educational subjects published in the open literature of any country can be obtained for TRANSLATION.

TRANSLATION of articles appearing in Pergamon Publications into any required language can be provided.

Fees are moderate.

Enquiries should be addressed to:
PERGAMON PRESS LIMITED
—TRANSLATION SERVICE,
MAXWELL HOUSE,
348/350 GRAY'S INN ROAD,
LONDON, W.C.1.

Telephone: 01-837-6484

Design of Resonant Piezoelectric Devices *by Richard Holland and E. P. EerNisse*

The primary goal of the work is to introduce and explicate general concepts. For this reason, the authors have organized their book so that many of the discussions pertain to ferroelectric ceramics, which form the piezoelectric material symmetry class that is the simplest to represent analytically. This minimizes the risk of losing the reader in a morass of details. In almost every case where specific results are restricted to ferroelectric ceramics, the general concepts are in no way so restricted, and the engineer who is working with more complicated materials will be able to apply these concepts in an appropriate form to his own design problems. **\$12.50**

Physics of Strength and Plasticity *edited by Ali S. Argon*

Professor Ali Argon felt that the retirement of Professor Egon Orowan from the M.I.T. faculty was an appropriate occasion to take stock of the developments in the immediate past and to produce a needed synthesis of this technologically important field. For this purpose he invited 37 of the world's leading figures in the field to contribute theoretical papers of original work. The 17 papers on the Physics of Plasticity fall into two categories: (1) Individual Dislocations and Basic Deformation Mechanisms, and (2) Hardening Mechanisms and Dislocation Dynamics. The 10 papers on the Physics of Strength concentrate on (1) Cracks and Fracture, and (2) Geology. **\$12.50**

Atomic Order:

An Introduction to the Philosophy of Microphysics
by Enrico Cantore

The intention of *Atomic Order* is to encourage and contribute to the dialogue between philosophers and scientists by discussing a concrete example of scientific discovery according to a method acceptable and understandable to both sides.

The book consists of two parts. The first part is devoted to the problem of atomic order as discovered and verified by physics, from the speculations of Dalton to the consequences of modern quantum mechanics. The second part analyzes the presuppositions, guiding principles, and implications that made possible the development of atomic physics and that impart a humanistic meaning to it. **\$12.50**

The MIT Press

Massachusetts Institute of Technology
Cambridge, Massachusetts 02142

new books
FALL '69

Spectrochimica Acta

This international journal for the rapid communication of original work dealing with atomic and molecular spectroscopy is published in two parts.

PART A MOLECULAR SPECTROSCOPY

Editors Prof. Sir Harold Thompson St. John's College Oxford
Prof. M. Kent Wilson National Science Foundation Washington DC

This journal deals particularly with qualitative and quantitative analysis, the determination of molecular parameters and general theory. Also included are papers on nuclear magnetic resonance spectra, electron spin resonance spectra, optical rotary dispersion, and the design and performance of instruments and components.

Papers recently published include:

M. J. HITCH and S. D. ROSS The infra-red spectra of 1:3- and 1:4- dithian and pentamethylene sulphide

C. L. HONEYBOURNE and G. A. WEBB A spectroscopic study of some N:N' disubstituted 1:3 di-imines

ULF BLINDHEIM and THOR GRAMSTAD Studies of hydrogen bonding-XX.

Hydrogen bonding ability of phosphoryl compounds containing N-P and S-P bonds

R. T. BAILEY Infrared and laser Raman spectra of methyl-cyclopentadienyl nickel nitrosyl

Published Monthly

PART B ATOMIC SPECTROSCOPY

Editors Dr. M. Margoshes Division of Block Eng. Maryland U.S.A.
Dr. K. Laqua Institut für Spektrochemie Dortmund Germany

Presents research papers on all regions of the electromagnetic spectrum, in so far as they have direct physicochemical interest. The main subjects include the determination of fundamental atomic data, new experimental procedures, and measurements or calculations of the properties of radiation sources or detectors.

Papers recently published include:

H. JÄGER Temperaturmessungen an Mischplasmen im 30 Amp Gleichstrombogen

J. O. KARTTUNEN and W. R. HARMON Determination of uranium in ores and in solution using a portable non-dispersive X-ray spectrograph

A. CARNEVALE and A. J. LINCOLN A computer program to determine photographic emulsion calibration curves

E. E. PICKETT and S. R. KOIRTYOHANN The nitrous oxide-acetylene flame in emission analysis - III. Aluminum, gallium, indium, thallium, germanium, and tin

Write for full details and an inspection copy of either part of the journal.
Details of other journals in the field can also be sent to you.



Pergamon Press

OXFORD · NEW YORK · LONDON · PARIS · SYDNEY



A LINEAR INTERPOLATION OF THE ELECTRONIC LEVELS OF f^2 -SYSTEM IN OCTAHEDRAL COORDINATION

H. U. RAHMAN

Department of Mathematics, Heriot-Watt University, Edinburgh, Great Britain

(Received 22 April 1969)

Abstract—The transition from LS to jj coupling within the f^2 configuration is shown schematically as a function of ζ/F_2 , and the composition of levels in the intermediate coupling is given at $\zeta/F_2 = 4.2, 8.4$ and 12.6 . Also, the energy levels of f^2 -system in an octahedral crystal-field were calculated by diagonalizing complete Coulomb, spin-orbit and crystal-field interaction matrices for a range of values of the parameters $F_2, F_4, F_6, \zeta, A_4\langle r^4 \rangle$ and $A_6\langle r^6 \rangle$. The eigenvalues were expanded by Taylor series, and a linear interpolation to describe the variation of the energy levels as a function of these parameters is presented. The accuracy of this interpolation is indicated.

1. INTRODUCTION

IN RECENT YEARS it has been realized that, for actinide ions in crystals, the spin-orbit and crystal-field interactions are large and of comparable size [1, 2]. It is, therefore, desirable to calculate the energy levels by simultaneously diagonalizing these interactions with the electrostatic interaction within the $5f^2$ configuration. In these ions, the crystal-field cannot be treated as a first-order perturbation on the free-ion J levels because the levels are not usually grouped in clusters of levels associated with a particular free-ion J level [3] as is the case in lanthanide with smaller crystal-fields. But even when the crystal-field is small as in Pr^{3+} , there are many good reasons for performing complete calculations. For those spectra in which many of the levels have been identified, such calculations will, apart from testing the theory, help in assessing the need for other interactions such as exchange interaction and the configuration interaction.

Satten *et al.* [1] did such complete calculations for the f^2 configuration and obtained a set of values of the parameters $F_2, F_4, F_6, \zeta, A_4\langle r^4 \rangle, A_6\langle r^6 \rangle$ by fitting the calculated levels to the absorption spectra of U^{4+} in crystals containing UCl_2^{2-} complexes. This work made useful assessment of the size of the crystal-fields in salts of UCl_2^{2-} . However, if one wants

to change the parameters to study other ions of f^2 configuration embedded in crystals of octahedral symmetry, one profits very little from this work, since the interaction matrices have to be set up and diagonalized again.

In the first part of this paper, the case of a free-ion of f^2 configuration in the intermediate coupling is considered, and then the effect of crystal-field is included. The eigenvalues of complete interaction matrices (Coulomb, spin-orbit and crystal-field) are expanded by Taylor series, and a linear interpolation is given from which energy levels can be calculated, if the variation in the six parameters $F_2, F_4, F_6, \zeta, A_4\langle r^4 \rangle$ and $A_6\langle r^6 \rangle$ is small, without having to set up and diagonalize the interaction matrices.

2. FREE-ION CALCULATIONS

Using the tensor operator methods of Racah [4], the matrix elements of the spin-orbit $\zeta_{nl} \sum_i (s_i \cdot l_i)$ in an l^N configuration can be expressed as

$$\begin{aligned} \langle l^N \alpha S L J M | \zeta_{nl} \sum_i (s_i \cdot l_i) | l^N \alpha' S' L' J M \rangle \\ = \zeta_{nl} (-1)^{L+S'+J} [l(l+1)(2l+1)]^{1/2} \\ \times \begin{Bmatrix} L & L' & 1 \\ S' & S & J \end{Bmatrix} \langle l^N \alpha S L || V^{[11]} || l^N \alpha' S' L' \rangle \end{aligned}$$

Nielson and Koster[5] have calculated the reduced matrix elements of $V^{(11)}$ for the configurations p^N , d^N and f^N . They have also given the electrostatic matrices for these configurations.

Assuming that the $5f$ radial wave functions is hydrogenic, the following relations between F_k were obtained by Judd[6, p. 226]*

$$F_4/F_2 = 0.142, F_6/F_2 = 0.0161. \quad (1)$$

These relations were used to show, in Fig. 1, the transition from LS to jj coupling by plotting energy levels for different values of ζ/F_2 ($\zeta = \zeta_{nf}$). For $\zeta = 0$, the energies of the multiplets of f^2 configuration lies between -32.45 and 115.74 (in units of F_2) if hydro-

genic ratios (1) are used, while in the jj coupling limit ($F_2 = 0$) f^2 is split into three equally spaced levels at -4.0 , -0.5 and 3.0 (in units of ζ). Following a scheme of Condon and Shortley[8, p. 271], transition is shown by taking $\chi/(1+\chi)$ as the abscissas where

$$\chi = \frac{1}{21} \zeta/F_2 (\zeta = \zeta_{nf})$$

The factor $\frac{1}{21}$ is introduced to make the total splitting nearly the same at the two ends of the diagram.

Since for lanthanide and actinide the ratio $\frac{1}{21} \zeta/F_2$ is likely to be near the left hand side of the Fig. 1, composition of the levels in the intermediate coupling is given, in Table 1, at $\chi = 0.2, 0.4$ and 0.6 .

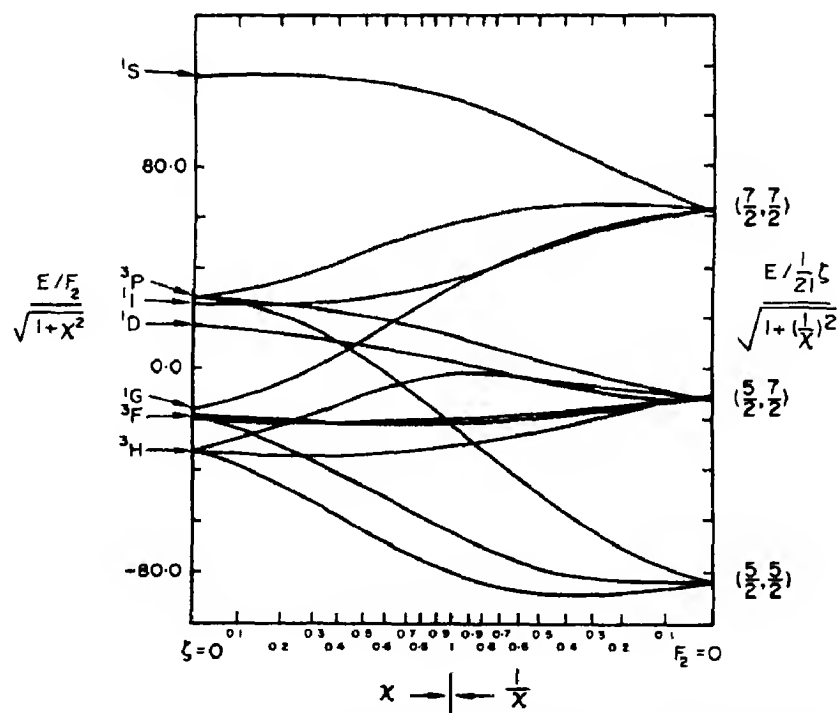


Fig. 1. The f^2 configuration in the intermediate coupling. The arrangement of levels at the left-end of the diagram ($\zeta = 0$) will be altered if different F_k ratios are chosen.

*Judd corrected a slight arithmetic error in his earlier work (Elliott *et al.* [7]) where they are given as

$$F_4/F_2 = 0.145, F_6/F_2 = 0.0164.$$

3. CRYSTAL-FIELD CALCULATIONS

The cubic crystal-field for the f electrons may be expressed in terms of spherical har-

Table 1. Composition of levels in the intermediate coupling for $\chi = 0.2, 0.4$ and 0.6

Level	Composition ($\chi = 0.2$)	Composition ($\chi = 0.4$)	Composition ($\chi = 0.6$)
3H_4	$0.967 ^3H_4\rangle - 0.246 ^1G_4\rangle + 0.058 ^3F_4\rangle$	$0.939 ^3H_4\rangle - 0.331 ^1G_4\rangle + 0.094 ^3F_4\rangle$	$0.922 ^3H_4\rangle - 0.371 ^1G_4\rangle + 0.113 ^3F_4\rangle$
3F_2	$0.975 ^3F_2\rangle + 0.222 ^1D_2\rangle + 0.032 ^3P_2\rangle$	$0.935 ^3F_2\rangle + 0.344 ^1D_2\rangle + 0.080 ^3P_2\rangle$	$0.903 ^3F_2\rangle + 0.413 ^1D_2\rangle + 0.117 ^3P_2\rangle$
3H_3	3H_3	3H_3	3H_3
3F_4	$-0.215 ^3H_4\rangle - 0.681 ^1G_4\rangle + 0.700 ^3F_4\rangle$	$-0.308 ^3H_4\rangle - 0.687 ^1G_4\rangle + 0.658 ^3F_4\rangle$	$-0.352 ^3H_4\rangle - 0.679 ^1G_4\rangle + 0.643 ^3F_4\rangle$
3F_3	3F_3	3F_3	3F_3
3H_6	$0.994 ^3H_6\rangle - 0.105 ^1I_6\rangle$	$0.969 ^3H_6\rangle - 0.247 ^1I_6\rangle$	$0.911 ^3H_6\rangle - 0.411 ^1I_6\rangle$
3P_0	$0.988 ^3P_0\rangle - 0.154 ^1S_0\rangle$	$0.963 ^3P_0\rangle - 0.271 ^1S_0\rangle$	$0.936 ^3P_0\rangle - 0.352 ^1S_0\rangle$
1D_2	$0.212 ^3F_2\rangle - 0.864 ^1D_2\rangle - 0.458 ^3P_2\rangle$	$0.322 ^3F_2\rangle - 0.737 ^1D_2\rangle - 0.594 ^3P_2\rangle$	$0.385 ^3F_2\rangle - 0.657 ^1D_2\rangle - 0.648 ^3P_2\rangle$
1G_4	$0.133 ^3H_4\rangle + 0.690 ^1G_4\rangle + 0.712 ^3F_4\rangle$	$0.153 ^3H_4\rangle + 0.647 ^1G_4\rangle + 0.747 ^3F_4\rangle$	$0.162 ^3H_4\rangle + 0.633 ^1G_4\rangle + 0.757 ^3F_4\rangle$
3P_1	3P_1	3P_1	3P_1
1I_6	$0.105 ^3H_6\rangle + 0.994 ^1I_6\rangle$	$0.247 ^3H_6\rangle + 0.969 ^1I_6\rangle$	$0.411 ^3H_6\rangle + 0.911 ^1I_6\rangle$
3P_2	$0.074 ^3F_2\rangle - 0.453 ^1D_2\rangle + 0.889 ^3P_2\rangle$	$0.145 ^3F_2\rangle - 0.582 ^1D_2\rangle + 0.800 ^3P_2\rangle$	$0.190 ^3F_2\rangle - 0.631 ^1D_2\rangle + 0.752 ^3P_2\rangle$
1S_0	$0.154 ^3P_0\rangle + 0.988 ^1S_0\rangle$	$0.271 ^3P_0\rangle + 0.963 ^1S_0\rangle$	$0.352 ^3P_0\rangle + 0.936 ^1S_0\rangle$

monics, and can be expressed as the sum of the 4th order and 6th order potentials,

$$V = V_4 + V_6 = (16/3)\pi^{1/2}A_4 \sum r^4 [Y_4^0 + (5/14)^{1/2}(Y_4^4 + Y_4^{-4})] + 32(\pi/13)^{1/2}A_6 \times \sum r^6 [Y_6^0 - (7/2)^{1/2}(Y_6^4 + Y_6^{-4})] \quad (2)$$

where Y_l^m are the normalized spherical harmonics and the summation is over all the electrons. A_4 and A_6 are the function of the lattice, and in the matrix elements of V they always appear multiplied by $\langle r^4 \rangle$ and $\langle r^6 \rangle$ for a single f electron. In view of the uncertainty of the values of $\langle r^4 \rangle$ and $\langle r^6 \rangle$, coupled with the fact that A_4 and A_6 are not given by a point-charge model calculation because of the possible shielding effect etc., $A_4\langle r^4 \rangle (=A)$ and $A_6\langle r^6 \rangle (=B)$ are treated as empirical parameters. Satten and Margolis[9] have calculated the matrices of the potential (2) for the f^2 configuration in the basis $|LSJ\Gamma_i\rangle$, where i indicates the irreducible representation of the octahedral group. The matrices are 7×7 , 3×3 , two 9×9 and 12×12 for Γ_1 , Γ_2 , Γ_3 , Γ_4 and Γ_5 (in Bethe's notation) or A_1 , A_2 , E , T_1 and T_2 (in Mulliken's notation) respectively.

4. LINEAR INTERPOLATION

If the variation in the parameters is small, the energy levels can be calculated by Taylor series expansion of the eigenvalues of the complete interaction matrices. The energy of a level depends on six parameters F_2 , F_4 , F_6 , ζ , A and B . If we let

$$F_2 = F_2' + \delta F_2, F_4 = F_4' + \delta F_4, \text{ etc.}$$

and neglect squares and products of δF_2 , δF_4 , etc., the energy of a level j can be expanded as

$$E_j = E_j^0 + \sum_{i=1}^6 \left[\frac{\partial E_j}{\partial P_i} \right]_0 \delta P_i \quad (3)$$

where E_j^0 is the zero-order energy of the level j calculated at P_i' which are F_2' , F_4' , etc.;

$\left[\frac{\partial E_j}{\partial P_i} \right]_0$ are the partial derivatives calculated at F_2' , F_4' , etc.; P_i are the parameters F_2 , F_4 , F_6 , ζ , A , B for $i = 1, 2, 3, 4, 5$ respectively.

It is difficult to calculate the partial derivatives analytically. However, numerical calculations can be done by changing the parameters slightly from the values F_2' , F_4' , etc. and calculating the difference of the eigenvalues from E_j^0 . Once the partial derivatives are calculated, the first-order energy can be obtained from equation (3).

The crystal-field matrices were combined with the corresponding matrices of electrostatic and spin-orbit interactions, and diagonalized for $F_2' = 190$, $F_4' = 34$, $F_6' = 3.5$, $\zeta' (= \zeta_{\text{eff}}) = 1800$, $A' = 1000$ and $B' = 55$ (all in units of cm^{-1}) to obtain E_j^0 . These zero-order values of the parameters seem reasonable from previous works, e.g. by Pappalardo and Jørgensen[10], Satten *et al.*[1]. The interaction matrices were rediagonalized, by varying F_6 by $\pm 0.5 \text{ cm}^{-1}$ and the other parameters by $\pm 1 \text{ cm}^{-1}$, to obtain the values of $\left[\frac{\partial E_j}{\partial F_2} \right]_0$, $\left[\frac{\partial E_j}{\partial F_4} \right]_0$, etc. When an f^2 -ion is surrounded by an octahedral crystal-field, the energy levels are derived from the splitting and mixing of J -manifolds, and are labelled by the irreducible representations of the site symmetry group. The results are given in Table 2. Apart from a few low-lying levels, the wavefunctions involve considerable mixture of $|SLJ\rangle$ states.

In order to estimate the contribution from the higher-order terms (omitted in equation (3)) in the Taylor series expansion, the parameters were changed by certain percentage c (i.e. $\delta P_i = c\%P_i'$) and the mean square-error, μ , between the exact results and those given by equation (3), was computed. μ is defined in the usual way as

$$\mu = \left[\sum_i \Delta_i^2 / (n - k) \right]^{1/2}$$

where Δ_i are the differences between the exact calculations and those given by equation (3), n

Table 2. The zero-order energy E_j^0 and the partial derivatives $(\partial E_j/\partial F_2)_0$, $(\partial E_j/\partial F_4)_0$, etc. The lowest A_1 -level is taken as zero on the scale

Level	E_j^0, cm^{-1}	$(\partial E_j/\partial F_2)_0$	$(\partial E_j/\partial F_4)_0$	$(\partial E_j/\partial F_6)_0$	$(\partial E_j/\partial \zeta)_0$	$(\partial E_j/\partial A)_0$	$(\partial E_j/\partial B)_0$
T_1	929.3	-0.76	-1.39	7.71	0.07	0.87	1.77
E	1241.1	0.59	-0.39	-9.32	0.07	0.76	5.12
T_2	2490.9	1.36	-6.23	-16.73	0.27	2.09	-1.55
T_2	4970.6	14.62	-7.86	-102.29	0.84	1.03	5.07
E	5223.9	11.98	-7.89	-123.75	1.22	1.71	-4.78
T_1	6336.7	0.31	-12.51	-11.31	3.29	0.61	3.92
T_1	7214.4	4.39	-3.41	-82.44	3.37	0.70	0.21
T_2	7216.6	3.76	-15.16	-19.53	2.79	2.03	0.31
E	8006.0	3.97	2.15	-51.06	2.73	2.21	4.15
A_1	8255.7	6.95	46.39	-69.33	3.44	-0.69	2.56
T_2	9431.4	11.60	8.17	-205.58	3.47	1.18	4.72
T_1	9480.4	4.34	20.81	-52.65	3.52	1.76	1.57
A_2	9953.4	12.98	-0.90	-239.29	3.60	1.36	9.30
E	10029.3	4.88	19.43	-62.82	4.20	0.95	3.31
T_1	10353.6	10.36	13.97	-192.31	3.37	2.41	0.86
T_2	11105.7	5.73	0.46	-71.73	4.78	1.64	0.84
E	11502.0	1.41	12.81	1.82	4.74	2.21	0.41
T_2	11601.8	6.47	18.08	-98.80	4.13	2.59	0.44
A_2	12263.8	3.58	-12.17	-21.09	5.37	2.13	4.37
T_2	13079.2	5.22	-6.48	-22.33	5.09	3.04	3.09
A_1	13325.3	-0.90	28.48	32.47	5.85	1.64	4.49
T_1	13453.8	2.73	6.19	-5.14	5.22	3.14	3.49
A_1	14732.5	34.03	44.83	-378.61	4.34	0.04	5.55
T_1	15626.4	16.95	45.46	-163.28	6.08	0.27	3.48
E	15837.1	24.64	37.14	-201.56	5.21	1.52	-2.72
T_2	16436.3	43.95	-12.49	13.4	3.54	2.18	0.92
E	17327.2	35.85	14.96	-155.19	4.29	2.73	0.37
A_1	17418.4	55.32	56.94	-784.84	2.32	3.07	6.14
T_2	17778.2	11.22	63.86	-46.92	6.31	2.19	0.66
T_1	19498.7	64.07	60.63	-1018.04	3.47	2.64	2.27
T_2	20140.1	39.57	39.78	22.73	5.01	1.83	5.39
A_1	20179.6	32.21	41.22	14.80	5.55	2.61	-0.77
T_1	20351.2	36.05	42.13	-144.94	5.28	2.66	2.13
A_2	21269.0	46.25	39.02	18.92	4.57	2.83	-0.15
T_2	22111.6	45.91	46.04	-130.71	4.81	3.41	4.55
E	22282.0	46.73	43.43	-81.80	4.65	3.60	3.84
T_2	23720.6	55.84	21.70	-497.46	6.17	2.53	3.56
E	25148.2	52.40	2.26	-250.73	6.55	3.73	4.75
A_1	41058.4	82.28	219.73	1513.39	5.47	2.56	3.25

is the number of levels and k is the number of the parameters. The results are given in Table 3.

Table 3

Change in parameters (%)	μ
3	3.2
5	5.3
8	8.5
10	10.7
15	16.1

REFERENCES

1. SATTEN R. A., SCHREIBER C. L. and WONG E. Y., *J. chem. Phys.* **42**, 162 (1965).
2. RAHMAN H. U. and RUNCIMAN W. A., *J. Phys. Chem. Solids* **27**, 1833 (1966).
3. JOHNSTON D., SATTEN R. and WONG E., *J. chem. Phys.* **44**, 687 (1966).
4. RACAH G., *Phys. Rev.* **62**, 438 (1942); *ibid.* **63**, 367 (1943).
5. NIELSON C. W. and KOSTER G. F., *Spectroscopic Coefficients for the pⁿ, dⁿ and fⁿ Configurations*, M.I.T. Press, New York (1963).
6. JUDD B. R., *Operator Techniques in Atomic Spectroscopy*, McGraw-Hill, New York (1963).

7. ELLIOTT J. P., JUDD B. R. and RUNCIMAN W. A., *Proc. R. Soc. A* **240**, 509 (1957).
8. CONDON E. U. and SHORTLEY G. H., *The Theory of Atomic Spectra*. Cambridge University Press, Cambridge (1964).
9. SATTEN R. A. and MARGOLIS J. S., *J. chem. Phys.* **32**, 573 (1960); Errata, *ibid.* **33**, 618 (1960).
10. PAPPALARDO R. and JØRGENSEN C. K., *Helv. Phys. Acta* **37**, 79 (1964).

LATTICE THEORY OF ALKALI HALIDE SOLID SOLUTIONS—I.*

HEAT OF FORMATION

D. L. FANCHER

Materials Research Laboratory, The Pennsylvania State University,
University Park, Penn. 16802, U.S.A.

and

G. R. BARSCH

Materials Research Laboratory and Department of Physics, The Pennsylvania State University,
University Park, Penn. 16802, U.S.A.

(Received 4 April 1969)

Abstract—A statistical theory for the composition dependence of the heat of formation of alkali halide solid solutions has been developed on the basis of the substitutional impurity model of Dick and Das. Numerical results are presented for all pairs of binary alkali halide systems. Good agreement with experimental values is found over the entire composition range for seven out of eight systems for which experimental data are available. The overall agreement is better than for any of the previously developed theories of other authors.

1. INTRODUCTION

THE CLASSICAL theory of ionic crystals of Born[1], Born and Mayer[2] and Huggins and Mayer[3] has been quite successfully applied to the calculation of the formation energy of point defects in alkali halides. It has been shown that, although the results depend markedly on the particular choice of the short range potential and the sets of parameters used, good agreement with experiment can be obtained for some potential forms with suitable parameters[4–6]. Most of this work deals, however, with vacancies and interstitials, but for substitutional defects and solid solutions over the entire composition range the sufficiency of the Born–Mayer theory is still subject to question. As no extra charge is introduced and the elastic strain field is only due to the size difference of two ions, a substitutional defect represents only a minor

perturbation of the crystal lattice and the formation energies amount generally only to about one-tenth of the formation energy of Schottky defects. It is not clear whether the smallness of the perturbation acts in favor of, or against the applicability of the Born–Mayer theory. On the one hand, one may expect that the simple theory can account more easily for the energy change due to a small change in configuration. On the other hand, however, the formation energy for substitutional defects amounts only to about one per cent of the cohesive energy, and it is conceivable that the small difference between the solid solution and the solid mixture depends more sensitively on the details and on possible deviations from the two-body central-force potential. This expectation seems to be supported by a recent treatment of this subject by Tosi and Doyama[7] who find very good agreement between theory and experiment for the formation energy of Schottky defects and for the migration energies of vacancies in alkali halides,

*This work was supported by the National Science Foundation.

whereas for substitutional defects discrepancies up to 50 and 100 per cent occur.

It is the purpose of this paper to demonstrate that good agreement between theory and experiment can be obtained with a very simple model over the entire composition range for the heat of formation of seven out of eight alkali halide systems for which experimental data are available. The entire composition range is considered because it is believed that this permits a more severe test of the theory than the treatment of an isolated defect only. Also the reliability and accuracy of experimental data is higher for the composition dependence of the heat of formation over the entire composition range than for the initial slope only. The second objective of this paper is to calculate the heat of formation over the entire composition range for all alkali halide systems because these data will be used in a subsequent paper for calculating the temperature dependence of the solid solubility.

The present treatment avoids some of the shortcomings or limitations of previous approaches which will be briefly assessed and summarized below. Essentially, the quality of any treatment of the individual defect problem is determined by two factors, namely the form of the interatomic potential used, and the approximations made in calculating the atomic displacements around the defect. For large defect concentrations the problems connected with defect interaction and cluster effects enter as a third factor. For vacancies and charged interstitials in ionic crystals the displacement field gives rise to long range elastic and dielectric polarization effects, but for monovalent substitutional defects in alkali halides it has been shown by Dick and Das[4] that over 99 per cent of the relaxation energy arises from the displacement of 24 ions surrounding the defect.

While the contribution from farther distant ions may therefore be safely omitted it is not at all possible to neglect the relaxation altogether, or to consider too small an environment in which the relaxation is taken into account. This is illustrated by all theoretical treatments prior to Dick and Das[4]. In the first three of these [8-10] the relaxation is neglected, resulting in rather poor agreement with experiment. Grimm and Herzfeld[8] considered a potential consisting of a Coulomb and an inverse power law repulsive term and determined the repulsive exponent from experimental heat of formation data. The values obtained in this way are much smaller than those obtained from empirical compressibility data. The approach of Tobolsky[9] amounts in effect to ignoring the repulsive contribution which is, however, important for the defect formation energy. For this reason the heats of formation values obtained by Tobolsky are

smaller than the experimental data by a factor of about two. In the theory of Wallace[10] the repulsive energy is properly taken into account and even van der Waals interaction included, but ionic displacements are still neglected, resulting in theoretical data which are too large by a factor of about two. Subsequently two equivalent theories were developed independently by Wasastjerna[11] and Hovi[12], and by Durham and Hawkins[13] who did allow for the relaxation of one common ion, i.e. the X ion between two second nearest neighbor A and B ions in a solid solution of the form $A_xB_{1-x}X$. The interaction potential used by Wasastjerna and Hovi is assumed to be of the two-body central-force type, but is not specified because only its second derivative is retained which is determined from the compressibility. The potential used by Durham and Hawkins is composed of Coulomb, van der Waals and exponential repulsive terms between first and second neighbors. Wasastjerna and Hovi also included the effect of local order which reduces the heat of formation. Although Wasastjerna and Hovi[12] find very good agreement with experiment for the two systems KCl-KBr and KCl-RbCl, the theoretical values of Durham and Hawkins[13] are too small by about 30 per cent for $KCl_{0.5}Br_{0.5}$ and $K_{0.5}Rb_{0.5}Cl$. Later Lister and Meyers[14] concluded on the basis of their careful experimental data for six alkali halide solid solution systems that neither of these two theories can account for the experimental data of all systems over the entire composition range, even if suitable adjustments of the input parameters are made.

In the more elaborate theory of Dick and Das[4] the relaxation of 24 ions surrounding the defect is taken into account, and the electrostatic interaction of the dipole moments induced in the displaced ions is included in addition to the short range van der Waals and exponential repulsive interaction. These authors investigate the effect of changes in the potential on the heat of formation of individual substitutional cation and anion impurities. They consider the Huggins-Mayer form of the repulsive potential in connection with (a) no van der Waals interaction, (b) van der Waals interaction with the constants from Mayer, and (c) van der Waals interaction with iso-electronic van der Waals constants. In addition, the simple potential of Born and Huang[15] consisting only of Coulomb and exponential repulsive interaction between first nearest neighbors is considered with the repulsive parameters obtained by Born and Huang[15] from the compressibilities. For all four cases mentioned the electrostatic dipole interaction is calculated for the two sets of polarizability data of Sternheimer[16] and of Tessman, Kahn and Shockley[17]. It is found that the heat of formation and the displacements and especially the induced dipole moments which minimize the relaxation energy depend on the potential and the choice of the parameters. For the heat of formation the values obtained differ by as much as a factor of three. Comparison with experimental data for NaCl-Br and NaBr-Cl indicated that the best agreement is obtained for (a) the Huggins-Mayer potential with iso-electronic van der Waals constants and Sternheimer's polarizability values, and for (b) the Born-Huang potential without van der Waals interaction with the polarizability values of Tessman,

Kahn and Shockley. These conclusions are based on the experimental data of Fineman and Wallace[18] for the system NaCl–NaBr. If one considers in addition the experimental data of Lister and Meyers[14] (which are listed below in Table 3), one may conclude by comparison with the four cases NaCl–Br, NaBr–Cl, KBr–Na, NaBr–K, for which Dick and Das have calculated the theoretical values for all different models mentioned that the Born–Huang potential in connection with the Tessman–Kahn–Shockley polarizabilities is superior to any of the other potential models. For these reasons the defect model of Dick and Das with the Born–Huang potential and the Tessman–Kahn–Shockley polarizabilities is adopted as the basis and starting point of the present work.

The present paper is devoted to calculating the heat of formation of all alkali halide solid solutions over the entire composition range. Whereas in the limit of small defect concentrations this amounts to a mere numerical application of the model of Dick and Das, the extension to large defect concentrations is based on a new statistical model which will be developed in Section 3.

The starting point is the definition of the heat of formation Q_F ('heat of mixing') of a solid solution as the difference of the internal energies of the solid solution, U_{ss} , and of a solid mixture of the components 1 and 2,

$$Q_F = U_{ss} - (x_1 U_1 + x_2 U_2) \quad (1.1)$$

where x_1 , x_2 denote the mole fractions and U_1 , U_2 the internal energies of the two components, respectively ($x_1 + x_2 = 1$). Since zero point and thermal energy amount at most only to a few parts per thousand of the internal energy, and since only deviations of the thermal energy of the solid solution from a linearly interpolated dependence of the two end components enter according to (1.1), it is sufficient for all practical purposes to replace in (1.1) the internal energy U by the cohesive energy ϕ of the static lattice. All additional assumptions will be mentioned below in the two following sections.

2. THE MODEL OF DICK AND DAS

In this section the single substitutional defect model of Dick and Das[4] is described

and the pertinent equations are presented. The intention is not only to make this paper self-contained and to explain the nomenclature, but especially to provide the basis for the application and extension of this model to large defect concentrations.

Figure 1 shows the types of ions which are allowed to relax in the model of Dick and Das upon substitution of a monovalent impurity in an alkali halide with the rock salt structure.

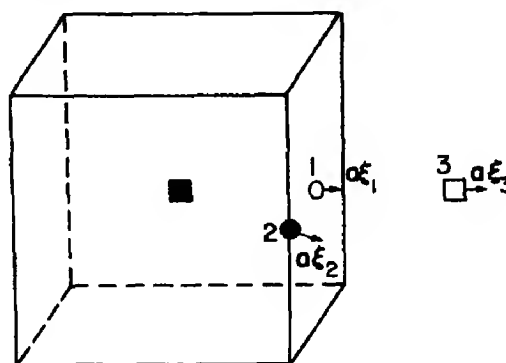


Fig. 1. The three types of ions allowed to relax around a substitutional impurity in the rocksalt structure. There are six type '1' ions (open circle), twelve type '2' ions (filled circle), and six type '3' ions (open square) displaced by the impurity (filled square). (The ions of type '3' are not third nearest neighbors of the impurity.)

The ξ_i ($i = 1, 2, 3$) represent the displacements of the ions in terms of a , the nearest neighbor distance of the pure host crystal. The displacements ξ_i are assumed to be in a radial direction with respect to the impurity. The ions 1, 2, and 3 are also allowed to polarize. The electronic dipole vectors are also assumed to be radially directed and are denoted by μ_i ($i = 1, 2, 3$) in units of ea , where e denotes the electronic charge. The rest of the ions are assumed to be undisplaced and unpolarized. As mentioned in the introduction, Dick and Das[4, 19] have shown that this assumption is justified.

The change in the lattice energy, ΔE , due to the introduction of the single substitutional impurity can be separated into four parts: repulsive, electrostatic, electronic dipole self-energy, and van der Waals. The zero of energy is taken to be the energy of the host crystal. The change in zero-point energy of the lattice vibrations is neglected.

Nearest neighbor repulsive interactions only are considered in calculating the repulsive part of ΔE . This will be denoted by ΔE_r . The repulsive energy due to an anion-cation interaction in the pure host crystal is assumed to be $A \exp(-r/\rho)$ if the two ions are separated by a distance r . $B \exp(-r/\sigma)$ describes the repulsive energy between an impurity ion and its nearest neighbor. The change in repulsive energy to second order in the displacements, ξ_i , is the following (reference [4], equation (1)):

$$\begin{aligned} \Delta E_r = & 6[B \exp(-a/\sigma) - A \exp(-a/\rho)] \\ & + 6[(a/\rho)A \exp(-a/\rho) - (a/\sigma)B \exp(-a/\sigma)]\xi_1 \\ & + 6[(a^2/2\rho^2) - (2a/\rho)A \exp(-a/\rho) \\ & + (a^2/2\sigma^2)B \exp(-a/\sigma)]\xi_1^2 \\ & + 6[(a^2/\rho^2) - (2a/\rho)A \exp(-a/\rho)](2\xi_2^2 + \xi_3^2) \\ & + 12\sqrt{2}(a/\rho)A \exp(-a/\rho)\xi_1\xi_2 \\ & - 6(a^2/\rho^2)A \exp(-a/\rho)\xi_1\xi_3. \end{aligned} \quad (2.1)$$

Here a denotes the nearest neighbor distance.

Dick and Das investigated the case of second nearest neighbor repulsive interactions and found their effect to be small for a Br^- defect in NaCl .

The electrostatic part is calculated by superimposing both a fictitious positive and negative unit electronic charge at the normal lattices sites of the 1, 2, and 3 type ions. One of these charges will restore the correct charge to that lattice site vacated by the displaced ion. The remaining charge and the displaced ion can be treated as a dipole at the undisplaced site. Calculating the dipole-dipole interactions to second order in ξ_i and μ_i gives (reference [4], equation (3)):

$$\begin{aligned} \Delta E_e = & \frac{e^2}{a} (7.113M_1^2 + 16.245M_2^2 + 0.8895M_3^2 \\ & + 9.705M_2M_3 + 8.955M_1M_3 - 27.44M_1M_2) \end{aligned} \quad (2.2)$$

where

$$M_i = q\xi_i \pm \mu_i, \quad (+ \text{ for } i = 1; - \text{ for } i = 2, 3) \quad (2.3)$$

with $q = +1$ for an anion impurity and $q = -1$ for a cation impurity. The electrostatic part of the energy change does not contain the interaction of the dipoles with the perfect cubic lattice as the interaction is zero due to the field being zero at the perfect cubic lattice sites.

The electronic dipole self-energy ΔE_s becomes (reference [4], equation (4)):

$$\Delta E_s = e^2 a \left(\frac{3\mu_1^2}{\alpha_1} + \frac{6\mu_2^2}{\alpha_2} + \frac{3\mu_3^2}{\alpha_3} \right) \quad (2.4)$$

where α_1 , α_2 , and α_3 are the electronic polarizabilities of the 1, 2, and 3 ions. Since ion 2 and 3 are of the same kind, it is $\alpha_2 = \alpha_3$.

As the van der Waals energy term contributes a very small amount to the total energy, the van der Waals term will be omitted. As is well known (see e.g. [15]), this is no serious deficiency at all, first because the van der Waals contribution to the cohesive energy amounts to about one per cent or less, and second, because the repulsive parameters are determined from empirical compressibility data which naturally include the van der Waals interaction.

The total change in energy due to a single substitutional defect can be written as

$$\Delta E = \Delta E_r + \Delta E_e + \Delta E_s \quad (2.5)$$

Minimizing this expression with respect to the six variables ξ_i and μ_i ($i = 1, 2, 3$) gives the minimum value ΔE_{\min} .

The value ΔE_{\min} for the system $AX-B$ represents the difference between the energy of a B ion at an A site in the AX host crystal and the energy of an A ion at an A site in the AX host crystal. In order to obtain the heat of formation as defined in equation (1.1) a term ΔE_0 must be added to ΔE_{\min} , where ΔE_0 is the difference between the energy of an A ion at an A site in an AX crystal and the energy of a B ion at a B site in a BX crystal:

$$Q_F = \Delta E_{\min} + \Delta E_0 \quad (2.6)$$

where

$$\begin{aligned} \Delta E_0 = & \left[-\frac{e^2\alpha}{a} + 6A \exp(-a/\rho) \right] - \left[-\frac{e^2\alpha}{b} \right. \\ & \left. + 6B \exp(-b/\sigma) \right]. \end{aligned} \quad (2.7)$$

Here a and b are the nearest neighbor distances in the two crystals AX and BX , respectively, and α is Madelung's constant.

3. COMPOSITION DEPENDENCE OF THE HEAT OF FORMATION

The purpose of this section is to develop a statistical model for the lattice energy of binary solid solutions of alkali halides over the entire composition range. To this end, the lattice energy will be assumed to be associated with certain lattice sites rather than with unit cells as commonly done. This is similar to summing over the bond energies of all pairs of ions and dividing by two to find the lattice energy. In this approach the total lattice energy per mole is obtained by summing the energy per lattice site over the N lattice sites of either the anion or the cation sublattice of the crystal ($N = \text{Avogadro's number}$):

$$\phi = \sum_i \epsilon_i^* \quad (3.1)$$

Here ϵ_i^* is the energy associated with the i th lattice site and depends on the type of site and on the kind of ion at that site. It will be calculated on the basis of the Dick and Das model with due allowance to be made for the

surroundings and the lattice constant of each site which determine its nature. All N sites of either of the two sublattices are considered to contain defects.

The sites are characterized by the configuration of the second nearest neighbors, and there are 13 different types of sites assumed in this model. Since the six nearest neighbors of any possible defect site are always ions of opposite sign to the occupant of the site under consideration, the site type designation is made after considering the 12 second nearest neighbors of the given site. Assume the host crystal to be an AX crystal and B ions to be the defects. Site types are designated by the number m of A ions as second nearest neighbors ($m = 12, 11, \dots, 1$, or 0). Thus there are 13 site types.

There are 26 different site energies which must be taken into account since either an A ion or B ion can occupy each of the 13 different types of sites. They are denoted by ϵ_{IJ}^m where m denotes the number of A ions as second nearest neighbors ($m = 12, 11, \dots, 1, 0$) and I denotes the type of ion occupying the site ($I = A, B$). The index J is redundant and indicates whether the site is predominantly an A site or a B site ($J = A, B$). By definition, a site is called a J site if it has more than six second nearest neighbors of type J . Thus it is $J = A$ for $m = 7, 8, \dots, 12$ and $J = B$ for $m = 1, 2, \dots, 6$. For $m = 6$ the site is considered as an A site if occupied by an A ion, and as a B site if occupied by a B ion, thus $J = I$ for $m = 6$.

Now let $P^{(m)}$ ($m = 12, 11, \dots, 1, 0$) denote the probability that a site has m ions of type A as second neighbors, and P_I ($I = A, B$) the probability that the site is occupied by an ion of type I . Then the summation in (3.1) can be written as

$$\phi = N \sum_{m=0}^{12} P^{(m)} [P_A \epsilon_{AJ}^m + P_B \epsilon_{BJ}^m]. \quad (3.2)$$

Assuming complete random distribution of defects the probability factors P_I ($I = A, B$) are given by

$$\begin{aligned} P_A &= x_A = 1 - x \\ P_B &= x_B = x. \end{aligned} \quad (3.3)$$

The probability factors $P^{(m)}$ ($m = 0, 1, \dots, 12$) and the site energies ϵ_{IJ}^m are listed in Table 1. The probability factors are obtained from the combinatorial factors for each configuration. The site energies shown reflect the fact that when a site is occupied by an A ion and has from 6 to 12 second nearest neighbor A ions, a site is called an A site so that all site energies are referred to the lattice energy corresponding to the composition AX , whereas for coordination numbers smaller than six the site becomes a B site and the site energies refer to the composition BX along with the the corresponding energy difference $\Delta E_{AB}''$ for replacing a B ion occupying a B site with $(12-n)$ second nearest B -neighbors by an A ion. The nomenclature has been chosen so that the superscript refers again to the number of A ions in the second coordination sphere, resulting in the factor $(12-n)$.

The site energies are evaluated explicitly as follows. When a single substitutional defect B is put into a host crystal AX , a change in energy ΔE_{BA}^0 arises. At high concentrations of defects one would not be substituting a B ion in a pure A site but the substitution would be in a modified A site and hence an energy change different from ΔE_{BA}^0 would result. For example, assuming that the B ion is larger than the A ion, it would require less energy to squeeze the B ion into an expanded A site than it would be to squeeze the B ion into a pure A site. An expanded A site is caused by some B ions as second nearest neighbors. Likewise, an A ion in a modified A site would have an energy different from ϵ_{AA}^{12} .

In evaluating the various site energies, it is assumed that the energy of an A site (as defined above) is given by the same expression for the lattice energy as that corresponding to a pure AX crystal, except that for the nearest neighbor distance an intermediate value corresponding to Vegard's law is used:

Table 1. The site energies ϵ_{ij}^m associated with the different types of sites and their occupation probabilities $P^{(m)}$

m	Site type (2nd n.n. filled by)	Probability $P^{(m)}$ of site type occurring	Site energy when site occupied by an A ion ($I = A$)	Site energy when site occupied by a B ion ($I = B$)
12	12A 0B	$(1-x)^{12}$	ϵ_{AA}^{12}	$\epsilon_{BA}^{12} = (\Delta E_{BA}^{12} + \epsilon_{AA}^{12})$
11	11A 1B	$12(1-x)^{11}x$	ϵ_{AA}^{11}	$\epsilon_{BA}^{11} = (\Delta E_{BA}^{11} + \epsilon_{AA}^{11})$
10	10A 2B	$66(1-x)^{10}x^2$	ϵ_{AA}^{10}	$\epsilon_{BA}^{10} = (\Delta E_{BA}^{10} + \epsilon_{AA}^{10})$
9	9A 3B	$220(1-x)^9x^3$	ϵ_{AA}^9	$\epsilon_{BA}^9 = (\Delta E_{BA}^9 + \epsilon_{AA}^9)$
8	8A 4B	$495(1-x)^8x^4$	ϵ_{AA}^8	$\epsilon_{BA}^8 = (\Delta E_{BA}^8 + \epsilon_{AA}^8)$
7	7A 5B	$792(1-x)^7x^5$	ϵ_{AA}^7	$\epsilon_{BA}^7 = (\Delta E_{BA}^7 + \epsilon_{AA}^7)$
6	6A 6B	$924(1-x)^6x^6$	ϵ_{AA}^6	ϵ_{BB}^6
5	5A 7B	$792(1-x)^5x^7$	$\epsilon_{AB}^5 = \Delta E_{AB}^5 + \epsilon_{BB}^5$	ϵ_{BB}^5
4	4A 8B	$495(1-x)^4x^8$	$\epsilon_{AB}^4 = \Delta E_{AB}^4 + \epsilon_{BB}^4$	ϵ_{BB}^4
3	3A 9B	$220(1-x)^3x^9$	$\epsilon_{AB}^3 = \Delta E_{AB}^3 + \epsilon_{BB}^3$	ϵ_{BB}^3
2	2A 10B	$66(1-x)^2x^{10}$	$\epsilon_{AB}^2 = \Delta E_{AB}^2 + \epsilon_{BB}^2$	ϵ_{BB}^2
1	1A 11B	$12(1-x)x^{11}$	$\epsilon_{AB}^1 = \Delta E_{AB}^1 + \epsilon_{BB}^1$	ϵ_{BB}^1
0	0A 12B	x^{12}	$\epsilon_{AB}^0 = \Delta E_{AB}^0 + \epsilon_{BB}^0$	ϵ_{BB}^0

$$\epsilon_{AA}^m = -\frac{\alpha e^2}{a_m} + 6A \exp(-a_m/\rho), \quad (m = 0, 1, \dots, 12). \quad (3.4)$$

Here a_m is the nearest neighbor distance of the site determined from Vegard's law by considering the concentration to be set by the occupants of the 12 second nearest neighbors, i.e.

$$a_m = \frac{m}{12} a_0 + \frac{(12-m)}{12} b_0, \quad (m = 0, 1, \dots, 12) \quad (3.5)$$

where a_0 and b_0 are the nearest neighbor distances for the compositions AX and BX , respectively.

Likewise, the energy for the B sites is assumed to be of the form:

$$\epsilon_{BB}^m = -\frac{\alpha e^2}{b_m} + 6B \exp(-b_m/\rho), \quad (m = 0, 1, \dots, 12) \quad (3.6)$$

where b_m is determined in the same manner as a_m .

Vegard's law then takes the form of a series of successive step functions. It is an atomistic Vegard's law which is used to determine the site size—atomistic in the sense that the second nearest neighbor configuration fixes

the site size. It should be noted, however, that for any given defect concentration x all 13 values of the lattice constant occur according to the probability with which the 13 types of sites are present.

ΔE_{BA}^m is the change in energy due to a single substitutional impurity B in an AX host crystal with a nearest neighbor distance of a_m and ΔE_{AB}^m is the change in energy due to a single substitutional impurity A in a BX host crystal with a nearest neighbor distance of b_m .

Consider, for example, the energy ϵ_{AB}^0 associated with an A ion in a site with no A ions as second nearest neighbors:

$$\epsilon_{AB}^0 = \Delta E_{AB}^0 + \epsilon_{BB}^0. \quad (3.7)$$

The energy ΔE_{AB}^0 due to replacing a B ion in a pure BX crystal by an A ion may be split up as a sum of two terms,

$$\Delta E_{AB}^0 = 6[A \exp(-b_0/\rho) - B \exp(-b_0/\sigma)] + D. \quad (3.8)$$

The first term denotes simply the change in repulsive energy for constant nearest neighbor distance b_0 , and the second term D arises from the relaxation of the surrounding ions.

Therefore, from equations (3.6) and (3.8),

$$\epsilon_{AB}^0 = -\frac{\alpha e^2}{b_0} + 64 \exp(-b_0/\rho) + D. \quad (3.9)$$

This form illustrates the fact that the relaxation term D occurs in the site energy ϵ_{AB}^0 as an additive correction to the lattice energy of the pure BX crystal, given by the first two terms in (3.9) and therefore appears as a property of the defect site.

According to Fig. 1, the ions labelled as 2 and 3 are the same kind as the reference ion. In the case of an anion defect, 18 of the 24 ions which relax are, therefore, anions with large polarizabilities. Hence, the ΔE calculated in the anion defect case is significantly affected by the polarizabilities of its second nearest neighbors. This requires a modification of the procedure used for evaluating the site energies as described below. In fact, this method has been used in arriving at the numerical results listed in Section 4.

Consider, for example, the energy ϵ_{AB}^5 associated with an A anion in a site with five A ions as second nearest neighbors; according to Table 1 it consists of ΔE_{AB}^5 and ϵ_{BB}^5 . Now ΔE_{AB}^5 represents the change in energy due to a single A ion being substituted in a BX crystal with a nearest neighbor distance given by b_5 , but with the 12 second nearest neighbors as B ions. A better estimate of ϵ_{AB}^5 would be the following:

$$\epsilon_{AB}^5 = \frac{7}{12} (\Delta E_{AB}^5 + \epsilon_{BB}^5) + \frac{5}{12} \epsilon_{AA}^5. \quad (3.10)$$

This would account for the five A ions among the second nearest neighbors. In general,

$$\begin{aligned} \epsilon_{AB}^m &= \frac{(12-m)}{12} (\Delta E_{AB}^m + \epsilon_{BB}^m) + \frac{m}{12} \epsilon_{AA}^m, \\ &\quad (m = 1, 2, \dots, 5) \\ \epsilon_{AB}^m &= \frac{m}{12} (\Delta E_{AB}^m + \epsilon_{AA}^m) + \frac{(12-m)}{12} \epsilon_{BB}^m, \\ &\quad (m = 7, 8, \dots, 12). \end{aligned} \quad (3.11)$$

For a cation defect, the polarization plays a

less significant role as the polarizabilities are smaller. It was found numerically that only the following values of ϵ_{ij}^n need to be adjusted:

$$\begin{aligned} \epsilon_{AB}^5 &= \frac{7}{12} (\Delta E_{AB}^5 + \epsilon_{BB}^5) + \frac{5}{12} \epsilon_{AA}^5 \\ \epsilon_{AB}^4 &= \frac{8}{12} (\Delta E_{AB}^4 + \epsilon_{BB}^4) + \frac{4}{12} \epsilon_{AA}^4. \end{aligned} \quad (3.12)$$

Finally, the heat of formation over the whole composition range is given by the following expression:

$$Q_F = \Phi - N[(1-x)\epsilon_{AA}^{12} + x\epsilon_{BB}^0]. \quad (3.13)$$

The numerical data were calculated from (3.13) by using the improved site energies according to (3.11) and (3.12) for calculating Φ and are presented in the following section.

4. NUMERICAL RESULTS AND DISCUSSION

Equation (2.5) was minimized with respect to the six variables ξ_i and μ_i ($i = 1, 2, 3$), and the heat of formation corresponding to 1 per cent defect concentration calculated from (2.6). The repulsive parameters of Born and Huang[15] (Table 9) that were calculated from the lattice constants and compressibilities were used together with the polarizability data of Tessman, Kahn and Shockley[17].

Results were obtained for 96 alkali halide host crystal and defect combinations and are tabulated in Tables 2(a) and 2(b). Table 2(a) contains 48 systems with cation defects and is arranged so that systematic comparisons can be made easily. Adjacent entries across in the first and second columns are the opposite end components of a single solid solution system. The same is true for adjacent entries in the third and fourth columns. Each group of four entries going down a column is also a series such that comparisons are easily made. Table 2(b) contains 48 systems with anion defects and is arranged similar to Table 2(a). The data in Tables 2(a) and 2(b) illustrate an intuitively obvious trend first stated by Bruni

Table 2(a). Heat of formation for 1 per cent cation defect concentration (in cal/mole)

LiF-Na	49.3	NaF-Li	133	LiF-K	510	KF-Li	369
LiCl-Na	37.2	NaCl-Li	28.6	LiCl-K	263	KCl-Li	119
LiBr-Na	30.2	NaBr-Li	23.8	LiBr-K	194	KBr-Li	102
LiI-Na	22.1	NaI-Li	17.5	LiI-K	141	KI-Li	75.4
LiF-Rb	834	RbF-Li	463	NaF-K	118	KF-Na	73
LiCl-Rb	412	RbCl-Li	164	NaCl-K	63.6	KCl-Na	39.4
LiBr-Rb	302	RbBr-Li	143	NaBr-K	47.2	KBr-Na	34.2
LiI-Rb	244	RbI-Li	110	NaI-K	34.1	KI-Na	24.6
NaF-Rb	243	RbF-Na	127	KF-Rb	13.3	RbF-K	11.2
NaCl-Rb	128	RbCl-Na	70.7	KCl-Rb	9.36	RbCl-K	4.59
NaBr-Rb	95.9	RbBr-Na	63.4	KBr-Rb	5.50	RbBr-K	6.46
NaI-Rb	77.5	RbI-Na	48.2	KI-Rb	5.70	RbI-K	5.16

Table 2(b). Heat of formation for 1 per cent anion defect concentration (in cal/mole)

LiF-Cl	233	LiCl-F	205	LiF-Br	466	LiBr-F	257
NaF-Cl	226	NaCl-F	116	NaF-Br	442	NaBr-F	176
KF-Cl	164	KCl-F	83.8	KF-Br	293	KBr-F	134
RbF-Cl	129	RbCl-F	69.1	RbF-Br	226	RbBr-F	115
LiF-I	973	LiI-F	256	LiCl-Br	14.5	LiBr-Cl	10.5
NaF-I	849	NaI-F	255	NaCl-Br	12.6	NaBr-Cl	10.6
KF-I	620	KI-F	208	KCl-Br	10.5	KBr-Cl	7.21
RbF-I	530	RbI-F	185	RbCl-Br	8.74	RbBr-Cl	6.91
LiCl-I	96.1	LiI-Cl	35.9	LiBr-I	24.3	LiI-Br	14.3
NaCl-I	82.9	NaI-Cl	46.6	NaBr-I	24.1	NaI-Br	16.7
KCl-I	67.9	KI-Cl	37.7	KBr-I	18.9	KI-Br	14.6
RbCl-I	63.2	RbI-Cl	36.1	RbBr-I	16.9	RbI-Br	14.6

[20] according to which the energy for the formation of the solid solution increases with increasing degree of deformation required. For instance, KBr-Na has a lower heat of formation than NaBr-K as it is easier to put a small ion in a large 'hole' than it is to put a large ion in a small 'hole.' Also, a series such as KCl-Na, KBr-Na, KI-Na shows a decrease in their respective heats of formation. This is the anticipated result as the 'hole' in which the Na ion is inserted increases in size as one goes through this sequence of solid solutions. The physical parameters that enter the theory are lattice constants, the electronic polarizabilities, and the repulsive parameters which describe the size of the ions and their compressibilities.

Table 3 contains a comparison of known experimental data for the initial slopes of heat of formation and the theoretical values of Table 2 together with theoretical values of several other authors. The experimental values listed in Table 3 were obtained by estimating the slopes of the measured curves and hence a certain amount of uncertainty is introduced in addition to the rather large experimental error that is reflected by the discrepancies among the experimental values of different authors.

It is apparent that for the three alkali halide systems for which more than one theoretical value is available the data calculated here from the model of Dick and Das agree within an estimated error of 10-15 per cent with the

Table 3. Comparison of experimental and theoretical heats of formation (in cal/mole) for 1 per cent defect concentration

x	$\text{Na}_x\text{K}_{1-x}\text{Cl}$	$\text{Na}_x\text{K}_{1-x}\text{Br}$	$\text{K}_x\text{Rb}_{1-x}\text{Cl}$	$\text{K}_x\text{Rb}_{1-x}\text{I}$	$\text{NaCl}_x\text{Br}_{1-x}$	$\text{NaBr}_x\text{I}_{1-x}$	$\text{KCl}_x\text{Br}_{1-x}$	$\text{KBr}_x\text{I}_{1-x}$
0.99	Experiment	46 ^(c) 55 ^(d)	46 ^(c)	26 ^(e)	14.3 ^(b) 10.8 ^(e)	22 ^(e)	8.5 ^(a)	15 ^(e)
	Theory	63.6 ^(f)	47.2 ^(f)	34.1 ^(f)	12.6 ^(f)	24.1 ^(f)	10.5 ^(f) 7.9 ^(g) 8.2 ^(h)	18.9 ^(f)
		53 ⁽ⁱ⁾						
0.01	Experiment	39 ^(e) 46 ^(d)	34.5 ^(e)	22 ^(e)	12.5 ^(b) 10.5 ^(e)	18 ^(e)	8.3 ^(a)	16.5 ^(e)
	Theory	39.4 ^(f)	34.2 ^(f)	24.6 ^(f)	10.6 ^(f)	16.7 ^(f)	7.2 ^(f) 8.5 ^(g) 6.9 ^(h)	14.6 ^(f)
		60 ⁽ⁱ⁾						

^(a)Hovi[21].^(b)Fineman and Wallace[18].^(c)Fontell, Hovi and Hyvonen[22].^(d)Barrett and Wallace[23].^(e)Lister and Myers[14].^(f)Dick and Das model (present work).^(g)Hovi[12].^(h)Durham and Hawkins[13].⁽ⁱ⁾Tosi and Doyama[7].

experimental data, with the exception of the slope at the Rb-rich end of the system KCl-RbCl, where the theoretical slope is 40 per cent too small. None of the other theoretical data provide as good overall agreement for all systems, although some of the other theoretical data agree better with the experimental values for one system or one of the two slopes of the system. For the remaining 5 systems where no other theoretical data are available the theoretical data presented here agree within experimental error with the experimental values, except for NaI-K and KBr-I, where the theoretical values are 31 per cent and 26 per cent too large, respectively.

Thus it must be asserted that the theoretical data presented here differ noticeably from the experimental values for only 3 out of the 16 heat of formation data listed in Table 3.

The heat of formation was calculated over the whole composition range from the theoretical model presented in Section 3 for all alkali halide solid solution systems. The results are listed in Tables 4(a) and 4(b) for all systems containing a common anion or cation, respectively. The tables are arranged so that the values going across represent increasing composition of the component listed second, e.g. NaF for LiF-NaF. Those systems that on the basis of ideal entropy of

Table 4(a). *Heats of formation (in cal/mole) of alkali halide solid solutions containing a common anion**

Mole per cent of second compound	10	20	30	40	50	60	70	80	90
(LiF-NaF)	1530	2303	2550	2665	2864	2986	2761	2155	1256
LiCl-NaCl	337	540	643	698	730	717	632	480	275
LiBr-NaBr	286	457	545	592	619	609	538	410	235
LiI-NaI	205	329	393	428	449	442	391	298	172
(LiF-KF)	6337	8918	9180	8925	8997	8979	8158	6346	3646
(LiCl-KCl)	2243	3425	3856	3901	3803	3562	3074	2322	1319
(LiBr-KBr)	1701	2613	2962	3027	2978	2804	2423	1827	1037
(LiI-KI)	1231	1904	2178	2242	2217	2092	1809	1368	780
(LiF-RbF)	9175	11948	13500	13900	13200	10800	9191	7827	4603
(LiCl-RbCl)	3459	5193	5712	5604	5301	4875	4191	3177	1808
(LiBr-RbBr)	2605	3942	4381	4359	4184	3882	3341	2522	1428
(LiI-RbI)	2072	3148	3519	3516	3372	3116	2671	2016	1145
(NaF-KF)	1045	1633	1893	1992	2026	1953	1704	1288	737
NaCl-KCl	583	920	1077	1148	1179	1145	1004	763	440
NaBr-KBr	433	685	807	865	894	872	764	579	332
NaI-KI	312	495	584	627	650	635	559	426	246
(NaF-RbF)	2117	3244	3661	3718	3646	3430	2964	2244	1287
(NaCl-RbCl)	1154	1796	2067	2148	2147	2042	1772	1344	773
(NaBr-RbBr)	869	1360	1576	1650	1661	1585	1376	1042	598
NaI-RbI	694	1086	1259	1321	1332	1274	1108	840	483
KF-RbF	125	200	238	260	275	273	242	185	108
KCl-RbCl	69	112	133	146	156	156	139	106	62
KBr-RbBr	57	91	109	120	128	128	114	87	51
KI-RbI	53	86	102	112	120	120	107	82	48

*Those systems that are not likely to form solid solutions at any temperature are included in parentheses.

Table 4(b). *Heats of formation (in cal/mole) of alkali halide solid solutions containing a common cation**

Mole per cent of second compound	10	20	30	40	50	60	70	80	90
(LiF-LiCl)	4261	6692	7375	6752	5563	4641	4077	3381	2049
(NaF-NaCl)	2143	3584	4360	4510	4182	3612	2959	2197	1221
(KF-KCl)	1575	2658	3272	3441	3254	2856	2359	1749	967
(RbF-RbCl)	1246	2116	2623	2782	2657	2355	1952	1449	801
(LiF-LiBr)	6808	10353	11028	9488	6840	4578	3625	3384	2383
(NaF-NaBr)	4053	6603	7756	7628	6637	5428	4375	3311	1882
(KF-KBr)	2739	4522	5423	5518	5028	4279	3479	2578	1429
(RbF-RbBr)	2140	3560	4310	4445	4118	3556	2908	2149	1186
(LiF-LiI)	11631	16220	14877	11061	7771	5403	3428	2287	1874
(NaF-NaI)	7552	11865	13103	11509	8409	5843	4742	4133	2623
(KF-KI)	5547	8854	10161	9721	8198	6532	5218	3962	2250
(RbF-RbI)	4759	7636	8840	8592	7411	6019	4811	3595	2009
LiCl-LiBr	141	248	317	346	339	306	256	191	107
NaCl-NaBr	135	240	318	363	364	328	271	200	111
KCl-KBr	85	150	194	216	217	202	173	130	72
RbCl-RbBr	70	123	159	177	180	167	143	108	60
(LiCl-LiI)	920	1562	1895	1881	1593	1227	934	698	405
(NaCl-NaI)	838	1430	1769	1844	1704	1457	1185	884	497
KCl-KI	620	1064	1330	1416	1350	1191	984	732	407
RbCl-RbI	574	984	1232	1317	1264	1122	931	692	384
LiBr-LiI	263	458	575	606	561	476	384	284	159
NaBr-NaI	248	433	550	595	576	514	428	319	178
KBr-KI	198	347	443	486	480	438	369	276	154
RbBr-RbI	190	333	426	468	465	426	361	270	150

*See footnote of Table 4(a).

mixing are not expected to form solid-solid solutions at any temperature are shown in parentheses.

For the eight alkali halide systems for which experimental data are available the theoretical results of Table 4 are plotted in Figs. 2-9. Also shown are the curves according to the theories of Wasastjerna and Hovi[11, 12] and of Durham and Hawkins[13] that, for the systems shown in Figs. 2-7 were calculated by Lister and Meyers[14]. It can be seen that the present theory gives better overall agreement with the experimental data than does either of the two older theories. For some systems some of the other theories provide, however, better agreement over certain parts of the composition range. The only

serious failure of the present theory occurs for the system KCl-RbCl. There is no explanation why this should happen for this particular system.

The present theory does not fit the experimental data perfectly. In some cases the maximum of the theoretical curve does not coincide with the maximum experimental value in height and the composition location of the maxima of the two curves do not always agree. The reason for the discrepancies is that in the middle sector of the composition range, i.e. for high defect concentration, it is very difficult to account for the clustering of large groups of ions. Also, the method of using the atomistic Vegard's law approach is not rigorous enough to obtain complete agreement

with experiment. In addition, for those systems for which the theoretical curve lies above the experimental data the discrepancy could be explained by a small degree of ordering which so far has been taken into account only in the theory of Wasastjerna and Hovi [11, 12].

While the present theory is not entirely satisfactory it is a step in the right direction. This is, among other things, reflected by the fact that according to equations (3.2), (3.3) and Table 1, the heat of formation is a polynomial of 13th degree in the variable x . Apparently a polynomial of this high a degree

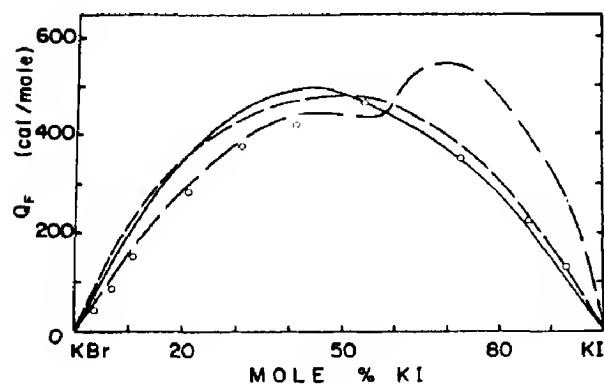


Fig. 2.

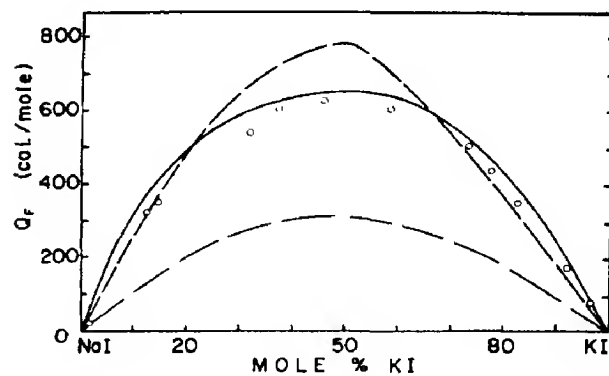


Fig. 5.

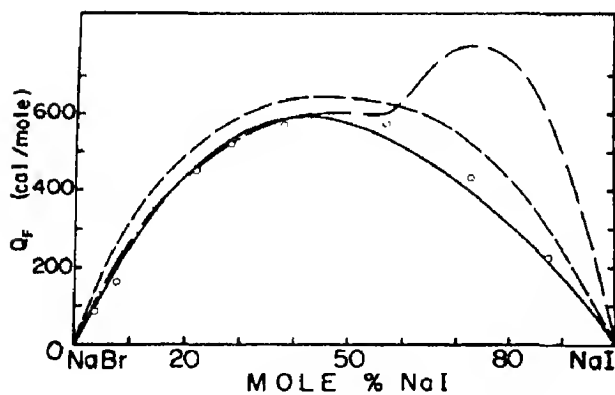


Fig. 3.

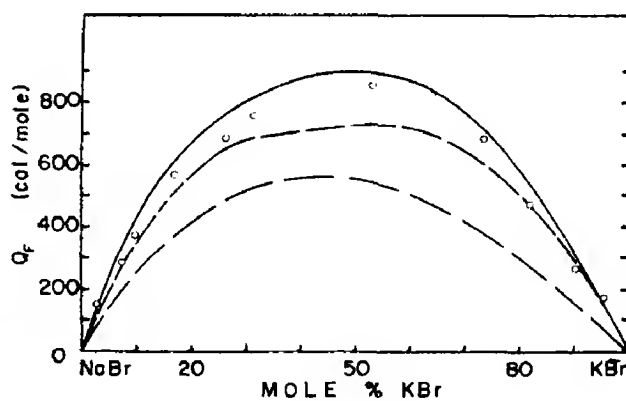


Fig. 6.

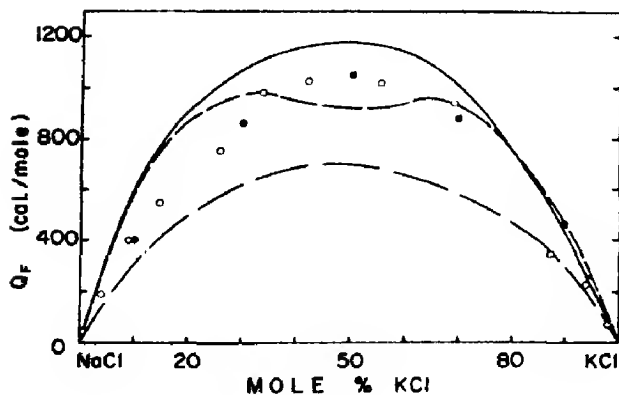


Fig. 4.

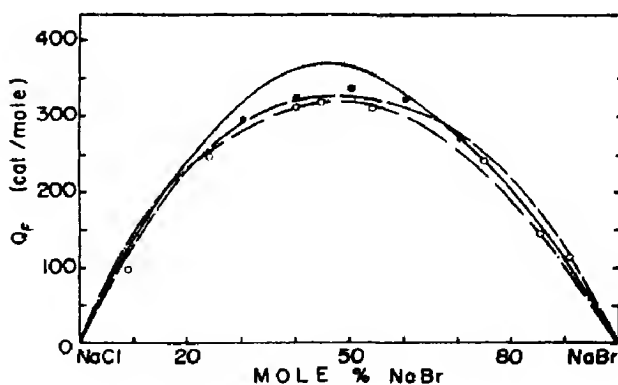


Fig. 7.

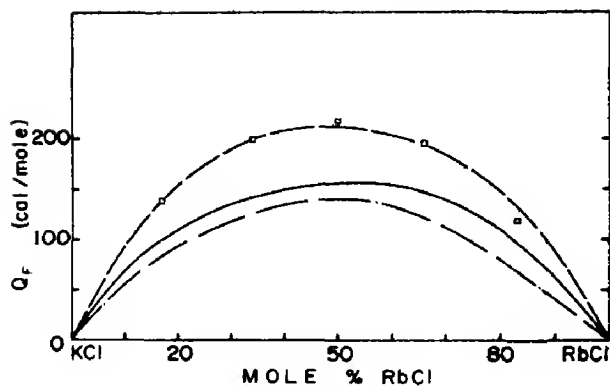


Fig. 8.

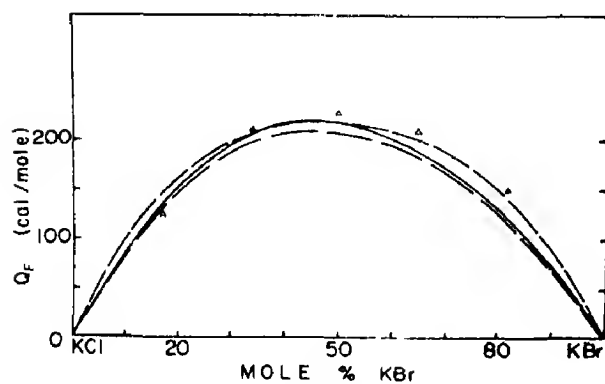


Fig. 9.

Figs. 2-9. Heats of formation of eight alkali halide solid solution systems according to present theory (solid curve), Wasastjerna and Hovi's theory [11, 12] (dashed curve), and Durham and Hawkins's theory [13] (dash-dot curve). Experimental points from Lister and Myers [14] (open circles); Hovi [21] (open triangles); Fineman and Wallace [18] (filled squares); Fontell *et al.* [22] (open squares); Bassett and Wallace [23] (filled circles).

is necessary for describing the composition dependence in alkali halides because it was found that the simple functional form $x(1-x)$ which is typical for the elementary treatment of metallic solid solutions with short range forces and without relaxation is not sufficient.

Of fundamental importance in calculating the heat of formation over the entire composition range was the extension of the Dick and Das isolated defect model to evaluate energy changes at high defect concentration levels. This was accomplished with the assumption of an atomistic Vegard's law for determining nearest neighbor distances. No explicit allowance was made for the clustering of

defects at high concentrations. However, the success of the present theory in its agreement with experimental data may be considered the justification for the present method of handling high defect concentrations.

The apparent superiority of the present theory over the previous theoretical attempts of Wasastjerna and Hovi and of Durham and Hawkins seems to be due to the fact that in the model of Dick and Das the displacements around the defect are handled more appropriately (not only is the number of ions that are allowed to be relaxed larger, but also all ions around the defect are taken into account, rather than only the 'common ion'), and that the electrostatic interaction of the induced electronic dipoles is included.

Recently, there has been much interest in the theory of off-center displacements in ionic crystals. Experimental work [24-26] along with theoretical work [27-29] has revealed that in systems with a large ionic size difference, e.g. KCl-Li, the small ion possibly does not reside on the normal lattice site but is slightly displaced in either a (100) or (111) direction. The present theory minimized the energy change due to a substitutional defect by assuming the defect was at a normal lattice site. Because of the small difference in ionic radii this seems to be justified for the eight systems of Figs. 2-9. However, for systems with a large ionic size mismatch there may exist a lower energy minimum if the defect is slightly displaced from the normal lattice site and is smaller than the original host ions. The associated energy change is of the order of 2 cal/mole per cent [30] so that for these systems the data in Table 2 may be expected to be too high by an amount of this order of magnitude. Also, for very small cation-anion radius ratios one has to expect correction terms arising from second neighbor anion-anion contributions.

The fact that the agreement of the Dick and Das model with experiment is best for the exponential repulsive law with the parameters of Born and Huang and without van der Waals interaction is surprising. In fact, for Schottky defects, Boswarva and Lidiard [6] arrive at the opposite conclusion. A possible explanation for this discrepancy is the smallness of the perturbation for substitutional defects which could result in a smaller sensitivity to the details of the potential. Also, in the Huggins-Mayer form of the repulsive potential the parameters are determined from the compressibilities and therefore fit exactly

the second derivatives of the potential that enter the expression (2.1) for the relaxation energy.

5. CONCLUSIONS

The following conclusions about the present theory may be drawn. First, the present work gives better overall agreement with experimental data than do previous theories. Second, Dick and Das' model for the substitutional defect is realistic, since it gives agreement not only for the initial slope, but, with extensions, also for the shape of the curve over the entire composition range. Third, this good agreement is achieved with a small number of input parameters; the nearest neighbor distances, two repulsive parameters for the Born-Mayer potential, and the electronic polarizabilities. Fourth, from the good agreement one may conclude that the assumption of random defect distribution over the entire composition range is justified, or that only a very small degree of order should exist. This supports the conclusions of Barrett and Wallace[31] from their experimental work that no local order is present in alkali halide solid solutions.

Acknowledgements—One of the authors (D.L.F.) would like to thank the National Science Foundation for a Traineeship.

REFERENCES

1. BORN M., *Atomtheorie des festen Zustandes*. Teubner, Berlin (1923).
2. BORN M. and MAYER J. E., *Z. Phys.* **75**, 1 (1932).
3. HUGGINS M. L. and MAYER J. E., *J. chem. Phys.* **1**, 643 (1933).
4. DICK B. G. and DAS T. P., *Phys. Rev.* **127**, 1053 (1962); *J. appl. Phys.* **33**, 2815 (1962).
5. TOSI M. P., *Calculation of the Properties of Vacancies and Interstitials*, p. 1. N.B.S. Misc. Publ. No. 287, Washington (1966).
6. BOSWARVA I. M. and LIDIARD A. B., *Phil. Mag.* **16**, 805 (1967).
7. TOSI M. P. and DOYAMA M., *Phys. Rev.* **151**, 642 (1966).
8. GRIMM H. G. and HERZFELD K. F., *Z. Phys.* **16**, 77 (1923).
9. TOBOLSKY A. V., *J. chem. Phys.* **10**, 187 (1942).
10. WALLACE W. E., *J. chem. Phys.* **17**, 1095 (1949).
11. WASASTJERNA J. A., *Soc. Sci. Fennica, Comm. Phys.-Math.* **14**, No. 3, 1 (1948); *ibid.* **14**, 1 (1948); *ibid.* **15**, No. 3, 1 (1949).
12. HOVI V., *Soc. Sci. Fennica, Comm. Phys.-Math.* **15**, No. 12, 1 (1950); *Ark. Fys.* **5**, 6 (1952).
13. DURHAM G. S. and HAWKINS J. A., *J. chem. Phys.* **19**, 149 (1957).
14. LISTER M. W. and MEYERS N. F., *J. phys. Chem.* **62**, 145 (1958).
15. BORN M. and HUANG K., *Dynamical Theory of Crystal Lattices*. Oxford University Press, Oxford (1954).
16. STERNHEIMER R. M., *Phys. Rev.* **96**, 951 (1954); *ibid.* **107**, 1565 (1957).
17. TESSMAN J. R., KAHN A. K. and SHOCKLEY W., *Phys. Rev.* **92**, 890 (1953).
18. FINEMAN M. and WALLACE W. E., *J. Am. chem. Soc.* **70**, 4165 (1948).
19. DICK B. G., *Phys. Rev.* **145**, 609 (1966).
20. BRUNI G., *Chem. Rev.* **1**, 345 (1925).
21. HOVI V., *Ann. Acad. Sci. Fennica AI*, No. 55, 1 (1948).
22. FONTELL N., HOVI V. and HYVONEN L., *Ann. Acad. Sci. Fennica AI*, No. 65, 1 (1949).
23. BARRETT W. T. and WALLACE W. E., *J. Am. chem. Soc.* **76**, 366 (1954).
24. LOMBARDO G. and POHL R. O., *Phys. Rev. Lett.* **15**, 291 (1965).
25. SACK H. S. and MORIARTY M. C., *Solid State Commun.* **3**, 93 (1965).
26. BYER N. E. and SACK H. S., *Phys. Rev. Lett.* **17**, 72 (1966).
27. BOWEN S. P., GOMEZ M., KRUMHANSL J. A. and MATTHEW J. A. D., *Phys. Rev. Lett.* **16**, 1105 (1966).
28. DIENES G., HATCHER R., SMOLUCHOWSKI R. and WILSON W., *Phys. Rev. Lett.* **16**, 25 (1966).
29. QUIGLEY R. J. and DAS T. P., *Phys. Rev.* **164**, 1185 (1967).
30. LIDIARD A. B., *Calculation of the Properties of Vacancies and Interstitials*, p. 61. N.B.S. Misc. Publ. No. 287, Washington (1966).
31. BARRETT W. T. and WALLACE W. E., *J. Am. chem. Soc.* **76**, 370 (1954).

LATTICE THEORY OF ALKALI HALIDE SOLID SOLUTIONS—II.*

ENTROPY OF MIXING AND SOLID SOLUBILITY

D. L. FANCHER

Materials Research Laboratory, The Pennsylvania State University,
University Park, Penn. 16802, U.S.A.

and

G. R. BARSCH

Materials Research Laboratory and Department of Physics, The Pennsylvania State University,
University Park, Penn. 16802, U.S.A.

(Received 4 April 1969)

Abstract—Solid solubility curves are calculated for six alkali halide systems from theoretical heat of formation data. Fair to good agreement with experimental data is found for the two systems for which these are available. The vibrational contribution to the entropy of mixing is found to be important and can be adequately calculated from the Debye approximation. The composition dependence of the elastic constants required for the calculation of the Debye temperature of the solid solution can be successfully determined from a simple interpolation formula based on Vegard's law for the volume under pressure.

1. INTRODUCTION

ALTHOUGH for metallic alloys theory and experiment have advanced more uniformly, a striking imbalance between knowledge and understanding exists for solid solutions of ionic crystals. An enormous amount of empirical solubility data has been accumulated for nonmetallic systems[1], but theoretical approaches have been scarce, and even for the simplest case of alkali halide solid solutions only very few and approximate theoretical attempts have been made[2, 3]. Fineman and Wallace[2] calculated the solid solubility of NaCl-NaBr from experimental heat of formation data by using the entropy for ideal mixing, but no experimental data are available for this system that would permit verification of the theory. For the system NaCl-KCl Barrett and Wallace[3] compared the experimental entropy of mixing (determined from experimental heat of formation and solid solubility data) with the theoretical entropy corresponding to (a) ideal mixing, (b) partial order as

calculated from the theory of Wasastjerna[4] and Hovi[5], and (c) ideal mixing plus the contribution arising from Schottky defects. These authors found fair agreement of the experimental data with the theoretical data of (c). This implies that no local order is present and no vibrational contribution arises.

It is well known that for metallic alloys the solid solubility cannot be explained in terms of the entropy of ideal mixing, and that the vibrational contribution is crucial in accounting for deviations from the entropy of ideal mixing [6]. The question arises whether this is not true more generally, and whether, for example, in alkali halide solid solution the vibrational contribution may be important. This contribution can be calculated from the composition dependence of either the heat capacity or of the Debye temperature for the solid solution. However, experimental data for alkali halides do not seem to be available, and rigorous theoretical calculations for the vibrational spectra of disordered solids encounter great difficulties that have not been completely solved even for simpler metallic systems[7, 8].

*This work was supported by the National Science Foundation.

For metals, estimates of the vibrational contribution based on the Debye approximation have been very successful[6]. The only input data required are the elastic constants over the entire composition range. For alkali halide systems experimental data are available only for KCl-KBr[9], but for this system the exsolution dome has not been measured. For the two systems (NaCl-KCl and LiCl-NaCl) for which the exsolution domes are known experimentally, no elastic constant data are available, however. Although a general theory for the composition dependence of the elastic constants is available[10] no application to alkali halide systems has been made that would permit a purely theoretical calculation of the vibrational entropy contribution.

The objective of the present paper is to discuss several interpolation formulas for the composition dependence of the elastic constants that can be derived from simple ad hoc assumptions. It will be shown (a) that the experimental data for the KCl-KBr system can be well represented by an interpolation formula, and (b) that for NaCl-KCl and LiCl-NaCl the vibrational entropy calculated in the Debye approximation from the interpolation formula for the elastic constants leads to fair to good agreement between theoretical and experimental solid solubility curves. The solid solubility curves are calculated for altogether six alkali halide systems and it is found that the vibrational entropy contribution is important in all cases and may result in a lowering of the exsolution domes by as much as 450°C from the value calculated from the entropy of ideal mixing.

2. COMPOSITION DEPENDENCE OF ELASTIC CONSTANTS

Experimental data for the composition dependence of the elastic constants of alkali halide solid solutions are available for only one system, KCl-KBr[9]. The elastic constants c_{12} and c_{44} vary linearly with composition, but c_{11} 'hangs' up to two percent below the straight line joining the values of c_{11} for the

end components. The same is true also for the bulk modulus $B = (1/3)(c_{11} + 2c_{12})$. Thus if the composition dependence of the bulk modulus is known theoretically it can be used in connection with the linear composition dependence of c_{12} and c_{44} to calculate the nonlinear composition dependence of the constant c_{11} also.

It is convenient to describe the composition dependence of the bulk modulus $B(x)$ in terms of the deviation $\Delta B(x)$ from a linear composition dependence:

$$\Delta B(x) = B(x) - [B_0(1-x) + B_1x] \quad (2.1)$$

where $B_i = B(i)$ ($i=0,1$), and x is the mole fraction of component 1. In this section, three alternative expressions for $\Delta B(x)$ will be derived and compared with the experimental data for KCl-KBr.

In Fig. 1 the experimental data of $\Delta B(x)$ for KCl-KBr calculated from [9] are plotted and suggest a functional dependence of the form

$$\Delta B(x) = Dx(1-x). \quad (2.2)$$

The constant D can be expressed by differentiation of (2.1) and (2.2) in terms of the

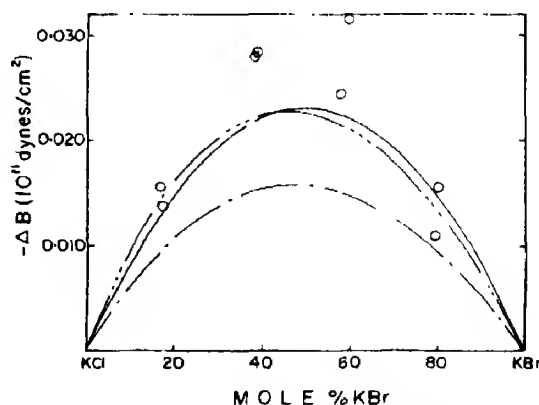


Fig. 1. Composition dependence of deviation $-\Delta B$ of bulk modulus from linear law for KCl-KBr (0 experimental data of Slagle and McKinstry[9]); — calculated from equation (2.2); - - - calculated from Vegard's law for volume, equations (2.9a) and (2.9b); - · - calculated from Vegard's law for lattice constant, equations (2.9a) and (2.9c).

slopes $(\partial B/\partial x)_{x=0} = (\partial B/\partial x)_0$ and $(\partial B/\partial x)_{x=1} = (\partial B/\partial x)_1$ as follows:

$$D = \frac{1}{2} \left[\left(\frac{\partial B}{\partial x} \right)_0 - \left(\frac{\partial B}{\partial x} \right)_1 \right]. \quad (2.3)$$

The slopes can be obtained by differentiating the equation defining the bulk modulus

$$\frac{1}{B(x)} = -\frac{1}{V(x)} \left(\frac{\partial V(x, p)}{\partial p} \right)_{p=0} \quad (2.4)$$

with respect to composition:

$$\begin{aligned} \left(\frac{\partial B}{\partial x} \right) &= \frac{B(x)}{V(x)} \left(\frac{\partial V(x, p)}{\partial x} \right)_{p=0} + \frac{B^2(x)}{V(x)} \\ &\quad \times \left(\frac{\partial^2 V(x, p)}{\partial p \partial x} \right)_{p=0}. \end{aligned} \quad (2.5)$$

Assuming that the volume depends linearly on composition for arbitrary pressure ('generalized Vegard's law'),

$$V(x, p) = V(0, p) (1-x) + V(1, p) x \quad (2.6)$$

gives upon differentiation:

$$\left(\frac{\partial V}{\partial x} \right)_{p=0} = V_1 - V_0 \quad (2.7a)$$

$$\left(\frac{\partial^2 V}{\partial p \partial x} \right)_{p=0} = - \left(\frac{V_1}{B_1} - \frac{V_0}{B_0} \right). \quad (2.7b)$$

Here $V_i = V(i, 0)$ ($i=1, 2$) are the zero pressure values of the molar volumes of the two end components. Both quantities in (2.7) are independent of the composition. The constant D follows then from (2.3), (2.5) and (2.7) as

$$D = \frac{[(B_0 V_1)^2 - (B_1 V_0)^2] (B_1 - B_0)}{2 B_0 B_1 V_0 V_1}. \quad (2.8)$$

Thus the deviation $\Delta B(x)$ is in this approximation determined by the bulk moduli and the volumes of the two end components.

An alternative expression for $\Delta B(x)$ can be derived from the generalized Vegard's law (2.6) without assuming a particular functional form as in (2.2). One obtains directly from (2.6) in connection with (2.4) and (2.1)

$$\Delta B(x) = \frac{(B_1 - B_0)E}{1 + Ex} x(1-x) \quad (2.9a)$$

where

$$E = \frac{V_1 B_0}{V_0 B_1} - 1. \quad (2.9b)$$

Comparison with (2.2) shows that the constant D is replaced by a composition dependent factor. Actually, equation (2.2) is nothing but a symmetrical form of (2.9a) in which this factor is replaced by a constant that is determined from the average initial slopes according to (2.3).

The composition dependence according to (2.9) and (2.1) has been derived before by Liu and Takahashi and successfully used for describing the composition dependence of the bulk modulus in solid solutions of almandite and pyrope[11].

A third interpolation formula is obtained if Vegard's law at arbitrary pressure is assumed to hold for the lattice constant, instead of the volume:

$$a(x, p) = a(0, p) (1-x) + a(1, p) x. \quad (2.10)$$

Since for cubic crystals the bulk modulus is given by

$$\frac{1}{B(x)} = -\frac{3}{a(x, 0)} \left(\frac{\partial a(x, p)}{\partial p} \right)_{p=0} \quad (2.11)$$

one obtains in connection with (2.1) again equation (2.9a); however, with E replaced by

$$E' = \frac{a_1 B_0}{a_0 B_1} - 1.$$

The composition dependence of the deviation ΔB of the bulk modulus from a linear

relationship has been calculated for the three cases mentioned for the system KCl-KBr by using the experimental data for the molar volume and for the bulk modulus listed in Table 1. The results are plotted in Fig. 1 and show that the symmetrized formula (2.2) and equation (2.9a) in connection with (2.9b) based on Vegard's law for the volume both agree fairly well with the experimental data. The agreement is not perfect, but this may be partly due to the large experimental error which is reflected in the large scatter of the experi-

justified a posteriori by the success of this formula in correctly accounting for the entropy of mixing.

In addition, it will be assumed that for all other alkali halide systems the elastic constants c_{12} and c_{44} also vary linearly with composition, as is the case for KCl-KBr. It then follows immediately that the deviation of the elastic constant c_{11} from a straight line also follows a law of the form (2.2),

$$\Delta c_{11}(x) = Ax(1-x) \quad (2.12)$$

Table 1. Molar volume $V(\text{cm}^3/\text{mole})$, elastic constants (10^{11} dynes/cm²) and bulk modulus (10^{11} dynes/cm²) of six alkali halides at 300°K

	LiCl	NaCl	KCl	KBr	KI	NaBr
$V^{(a)}$	20.50	26.84	37.19	43.02	52.81	31.91
c_{11}	4.94 ^(b)	4.94 ^(b)	4.069 ^(c)	3.468 ^(c)	2.74 ^(b)	4.01 ^(b)
c_{12}	2.28 ^(b)	1.29 ^(b)	0.711 ^(c)	0.580 ^(c)	0.45 ^(b)	1.09 ^(b)
c_{44}	2.46 ^(b)	1.27 ^(b)	0.631 ^(b)	0.507 ^(c)	0.37 ^(b)	0.99 ^(b)
$B^{(d)}$	3.167	2.506	1.831	1.543	1.213	2.063

^(a)Calculated from the lattice constants tabulated in [12].

^(b)Haussühl[3].

^(c)Slagle and McKinsty[9].

^(d)Calculated from c_{11} and c_{12} .

mental data. It must be kept in mind that according to (2.1) ΔB is the difference of two large numbers, and that $\Delta B/B$ amounts only to less than 2 per cent. The difference between the symmetric form (2.2) and equation (2.9a) with (2.9b) based on Vegard's law for the volume is smaller than the experimental error and may be neglected for practical purposes. For the values calculated from equation (2.9a) in connection with (2.9c) based on Vegard's law for the lattice constant, much larger discrepancies with the experimental data occur.

As the symmetric law (2.2) gives as good agreement with the experimental data as equations (2.9a) and (2.9b) the former will be used subsequently because of its greater simplicity. Encouraged by the success of this formula for KCl-KBr it will be applied below to other alkali halide systems. This extension will be

where

$$A = 3D \quad (2.13)$$

and D is given by (2.8).

Numerical values of the constant A were calculated for six alkali halide systems from the input data of Table 1 and are listed in Table 2. Also shown are the equimolar values of the relative deviation of c_{11} from the linear dependence corresponding to a solid mixture of the components, $c_{11}^{MIX}(x) = c_{11}(0)(1-x) + c_{11}(1)x$. For the systems considered this deviation ranges from about 2 to 8 per cent.

3. THEORY OF SOLID SOLUBILITY

The solid solubility is determined by the excess Gibbs free energy G^* of the solid solution over the solid mixture. At zero pressure it is [14]

Table 2. The constant A according to equation (2.13) and (2.8) (10^{11} dynes/cm²) and the relative deviation $(\Delta c_{11}/c_{11}^{mix})_{x=0.5}$ (per cent) of the elastic constant c_{11} from a linear dependence for equimolar solutions of six alkali halide systems

	LiCl-NaCl	NaCl-KCl	NaBr-KBr	NaCl-NaBr	KCl-KBr	KBr-KI
A	-1.131	-1.377	-0.915	-0.501	-0.278	-0.447
$(\Delta c_{11}/c_{11}^{mix})_{x=0.5}$	-5.7	-7.6	-6.1	-2.8	-1.8	-3.6

$$G^* = Q_F - T\Delta S \quad (3.1)$$

where

$$Q_F = U^{ss} - U^{mix} \quad (3.2)$$

is the excess internal energy of the solid solution over the mixture of the components (heat of formation), ΔS is the corresponding excess entropy (entropy of mixing), and T is the absolute temperature. It will be assumed that the excess entropy is additively composed of the entropy of ideal mixing and of the vibrational contribution:

$$\Delta S = \Delta S^{ID} + \Delta S^{VIB}. \quad (3.3)$$

The entropy of ideal mixing per mole is given by [15]

$$\Delta S^{ID} = -R[x \ln x + (1-x) \ln (1-x)] \quad (3.4)$$

where R is the gas constant. The vibrational contribution is in the Debye approximation and in the high temperature limit ($T > \theta$) given by [6]

$$\Delta S^{VIB} = -3R(\Delta\theta(x)/\theta^{ss}(x)). \quad (3.5)$$

Here $\Delta\theta(x) = \theta^{ss}(x) - \theta^{mix}$ is the deviation of the Debye temperature of the solid solution, $\theta^{ss}(x)$, from that for the solid mixture, $\theta^{mix}(x) = \theta_0(1-x) + \theta_1x$, where θ_i ($i=1, 2$) denotes the Debye temperatures of the end components.

For metals, additional entropy terms due to differences in electronegativity and valence contribute to ΔS [6], but may be neglected for

alkali halide solid solutions. In addition, contributions from defects, especially Schottky defects, may arise and may not be entirely negligible for alkali halides [3]. This point will be discussed below.

If the composition dependence of the heat of formation Q_F and of the entropy of mixing ΔS are known, the solid solubility limits x_1 and x_2 can be obtained for each temperature T from the excess free energy (3.1) by solving the two equations $(\partial G^*/\partial x)_1 = (\partial G^*/\partial x)_2$, and $G_2^* - G_1^* = (\partial G^*/\partial x)_1(x_2 - x_1)$ (method of equal tangents) [14].

The composition dependence of the heat of formation has been investigated in a previous paper ([16], subsequently referred to as I), and the theoretical results obtained for $Q_F(x)$ have been used to calculate solid solubility data which are presented in the following section.

The Debye temperature $\theta^{ss}(x)$ of the solid solution was calculated by the method of Quimby and Sutton [17] from the equation

$$\theta^{ss}(x) = (h/k) (3s/4V_z(x))^{1/3} [(c_{11}(x) - c_{44}(x))/\rho(x)]^{1/2} J(C(x), K(x)) \quad (3.6)$$

where h and k denote Planck's and Boltzmann's constant, respectively, $V_z(x)$ is the volume of the unit cell, s is the number of atoms in $V_z(x)$, and $\rho(x)$ is the density. The factor $J(C(x), K(x))$ is a function of the combinations of elastic constants $C = c_{44}/(c_{11} - c_{44})$ and $K = (c_{12} + c_{44})/(c_{11} - c_{44})$, and is available in graphical form [18].

Since only $(\Delta\theta(x)/\theta(x))$ is of interest, most factors in (3.6) cancel out approximately, ex-

cept the factor containing $(c_{11} - c_{44})^{1/2}$. Consequently, the excess entropy term is related to the deviation of the elastic constants of the solid solution from a linear interpolation of the elastic constants of the end components. In calculating the vibrational entropy from (3.5) the composition dependence of the elastic constants was described by the formulae described in Section 2.

4. NUMERICAL RESULTS AND DISCUSSION

The solubility curves were calculated from the theoretical heat of formation $Q_F(x)$ according to equation (3.13) of I for six alkali halide systems with and without the vibrational entropy term in (3.3). The results are plotted in Figs. 2-7 together with experimental data.

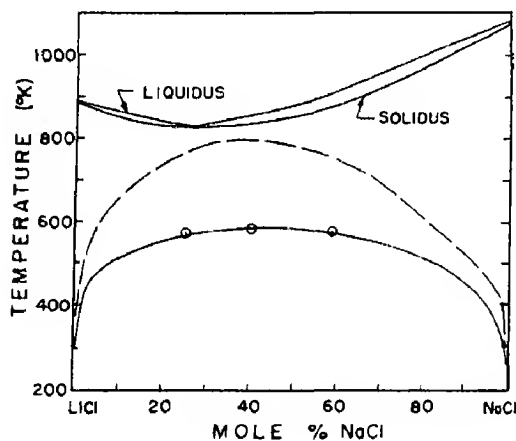


Fig. 2.

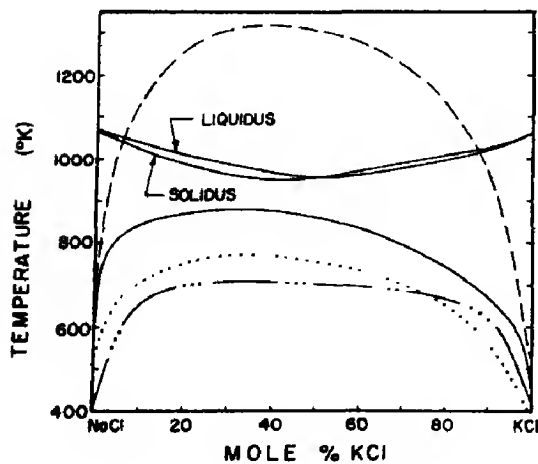


Fig. 3.

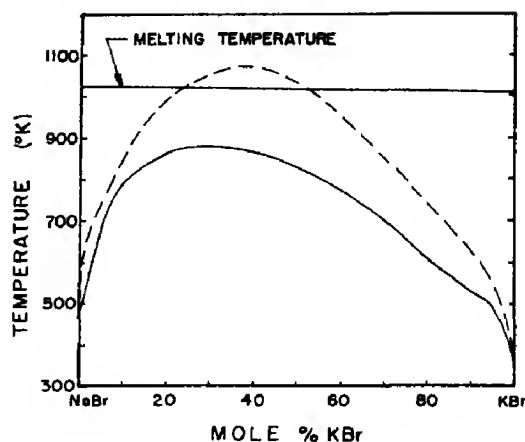


Fig. 4.

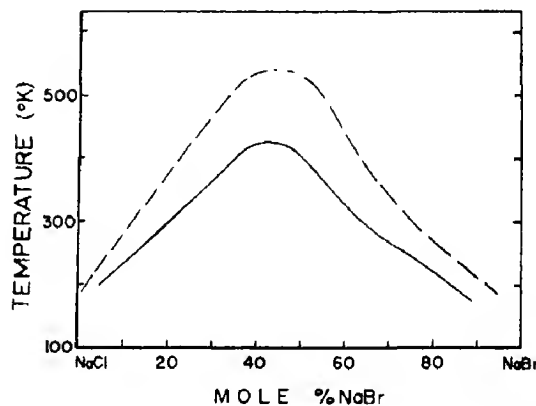


Fig. 5.

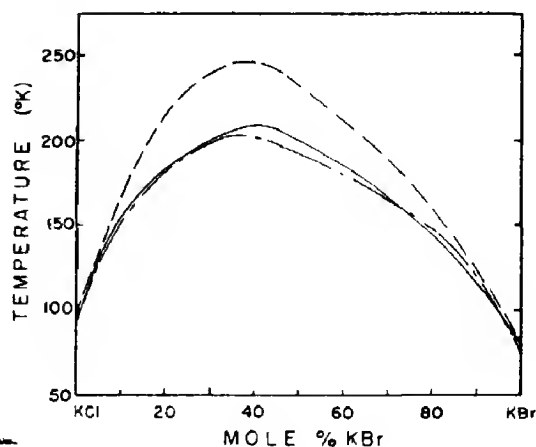


Fig. 6.

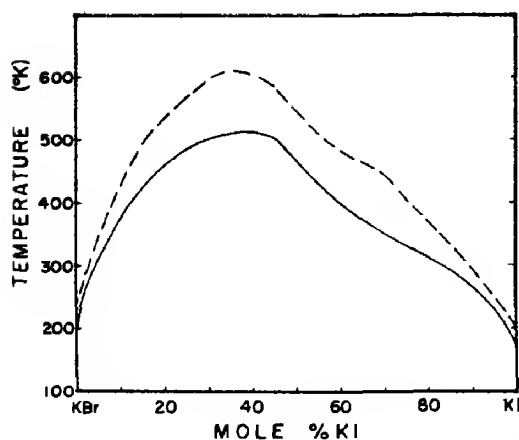


Fig. 7.

Figs. 2-7. Solid solubility curves for alkali halide systems: (---) theoretical curve, calculated with ΔS^{ID} only; (—) theoretical curve, calculated with ΔS^{ID} and ΔS^{VIB} ; (— · — · —) semi-theoretical curve, calculated from experimental heat of formation with ΔS^{ID} and ΔS^{VIB} ; (· · · · ·) semi-theoretical curve, calculated with ΔS^{ID} and ΔS^{VIB} , where experimental data on composition dependence of elastic constants were used; (○) experimental data from [19]; (□) experimental data from [20].

where available. In all cases the solid solubility curve is drastically shifted to lower temperatures if the vibrational entropy term is included. Whenever the melting curve is not shown it lies well above the temperature range of the figures.

Figures 2 and 3 for the systems NaCl-KCl and LiCl-NaCl show that the exsolution domes calculated with both the entropy of ideal mixing and the additional entropy contribution from the vibrational factor are much closer to the experimental exsolution domes than the exsolution domes calculated with ΔS^{ID} only. The agreement between the experimental and the theoretical exsolution domes for LiCl-NaCl is very good.

For NaCl-KCl there is still some disagreement between the theoretical exsolution dome calculated with both ΔS^{ID} and ΔS^{VIB} and the experimental exsolution dome. Since, according to Fig. 4 of I the theoretical heat of formation curve is for this system somewhat higher than the experimental data, the solid solubility curve was also calculated (including both ΔS^{ID}

and ΔS^{VIB}) from an experimental heat of formation curve obtained by drawing a best curve through the experimental data. Because of the large scatter of the experimental data this was not possible without ambiguity. The result is also plotted in Fig. 3 and agrees better with the experimental data than the purely theoretical curve. However, the solubility curve calculated from the experimental heat of formation data falls about 50°C below the experimental solubility curve. This would mean that the actual heat of formation curve lies between the theoretical and experimental curves of Fig. 4 of I. A part of the discrepancy between the theoretical and experimental solubility curves of Fig. 3 could possibly also be accounted for by considering the entropy contribution due to the presence of vacancies. Barrett and Wallace[3] pointed out that a positive contribution to the excess entropy is also possible due to the existence of vacancies in the lattice. They determined from density measurements[21] the number of vacancies (Schottky defects) for their samples of NaCl-KCl. The amount of vacancies was quite large, corresponding to a maximum of about one percent. Barrett and Wallace estimated the additional entropy due to the empty lattice sites. This additional positive contribution to the entropy, if included, would also lower the purely theoretical exsolution dome and bring it in closer agreement with the experimental exsolution dome.

Table 3 gives the various entropy contributions in calories per mole at $x=0.5$ for all the solid solutions studied. The value listed for the entropy contribution due to vacancies, ΔS^{VAC} , for NaCl-KCl was estimated by Barrett and Wallace[3]. The term ΔS^{VAC} was not taken into account in the calculations of the results shown in Fig. 3.

It is unlikely that the number of vacancies in a system such as KCl-KBr is large enough to give any appreciable entropy contribution due to the lower temperatures and smaller size misfit involved in this system as compared to NaCl-KCl.

Table 3. Contributions to entropy of mixing (cal/mole) for $x=0.5$

	LiCl-NaCl	NaCl-KCl	NaBr-KBr	NaCl-NaBr	KCl-KBr	KBr-KI
ΔS^{ID}	1.38	1.38	1.38	1.38	1.38	1.38
ΔS^{VIB}	0.28	0.34	0.25	0.32	0.20	0.20
ΔS^{VAC}		0.19 ^(a)				

^(a)Barrett and Wallace[3].

The effect of the defect concentration on the solid solubility illustrates that the absolute value of the solid solubility curve should depend on the number of vacancies present in the sample. If a sample is grown at a high temperature and then quenched to a lower temperature for measurement, the configuration of the higher temperature is 'frozen' into the sample.

In order to verify the quality of the interpolation formulae used for the elastic constants for the system KCl-KBr the vibrational entropy was also calculated from a smooth curve drawn through the experimental elastic constant data as a function of composition. The result is also shown in Fig. 6 and is seen to deviate by a small amount only from the solubility curve calculated with the interpolation formula for the elastic constants.

A possible objection to the calculation of solid solubilities presented here is that a special analytical form has been used, according to equation (3.13) of 1, for the composition dependence of the heat of formation. That this argument must be discarded can be seen as follows. Supposing the heat of formation had the simple form, as usually assumed in elementary treatments of alloys, $Q_F = Hx(1-x)$, where H depends on the differences in lattice energies of the two end members, the corresponding exsolution dome would lie lower than the theoretical one calculated with ΔS^{ID} only. In the first place, however, this special composition dependence does not fit the experimental data because of the asymmetry and the quantitatively different shape of the heat of formation vs. composition curve. Moreover, it can be shown that the lowering of the exsolution dome that can be achieved in this manner is not large enough for NaCl-KCl, so that only the use of the entropy for ideal mixing can account for this failure.

Consider, for example, the system NaCl-KCl. Using the experimental heat of formation from [3], one obtains for the constant H a value of 4200 (cal/mole). Assuming the form $Hx(1-x)$ for the heat of formation and using the entropy of ideal mixing, the Gibbs free energy function

becomes $G^* = 4200x(1-x) - T\Delta S^{ID}$. The maximum temperature of the exsolution dome can then be calculated by finding the temperature at which the second derivative of G^* with respect to composition for $x=0.5$ is equal to zero. One obtains a value of 1050°K, as compared with 1310°K for the theoretical curve calculated with ΔS^{ID} only. The value of 1050° is still almost 300°K above the maximum temperature of the experimental solubility curve. In this connection it must be emphasized again that the work in 1 shows that the simple form (4.1) is entirely inadequate to describe the experimental heat of formation data, but that a much higher order polynomial is needed. Also, the exsolution dome calculated from $Q_F = Hx(1-x)$ consists of a much sharper peak than is observed experimentally.

The good agreement of the theoretical and experimental exsolution domes of LiCl-NaCl and the relatively good agreement of the theoretical and experimental exsolution domes of NaCl-KCl, in addition to the reasonable agreement of the experimental and theoretical results for the composition dependence of the bulk modulus and the elastic constants justifies to a large extent the assumptions made in the present work.

5. CONCLUSIONS

For the two alkali halide systems for which experimental solid solubility curves are available (LiCl-NaCl and NaCl-KCl), the theoretical curves presented here agree quite well with the experimental data. This implies that the assumptions made in these calculations are approximately valid. These assumptions are (a) that the entropy of mixing deviates markedly from that of ideal mixing, (b) that the deviation from ideal mixing is primarily due to the vibrational contribution, (c) that the vibrational contribution to the heat of mixing can be adequately calculated (i.e. within the relatively large bounds of experi-

mental error) from the Debye approximation, (d) that the composition dependence of the elastic constants is linear for c_{12} and c_{44} and nonlinear for c_{11} , and (e) that the nonlinear composition dependence for c_{11} can be calculated from a simple interpolation formula for the bulk modulus that is based on the assumption of Vegard's law for the pressure dependence of the volume. Conclusions (d) and (e) are supported independently by direct experimental data on the composition dependence of the elastic constants for the only one alkali halide system (KBr-KCl) for which experimental data are available.

Acknowledgements—The authors are indebted to Professor T. Takahashi for a copy of the thesis of L. S. Liu prior to publication. One of the authors (D.L.F.) would like to thank the National Science Foundation for a Traineeship.

REFERENCES

1. LEVIN E., ROBBINS G. and McMURDIE H., *Phase Diagrams for Ceramists*. American Ceramic Society, Columbus, Ohio (1964).
2. FINEMAN M. and WALLACE W. E., *J. Am. Chem. Soc.* **70**, 4165 (1948).
3. BARRETT W. T. and WALLACE W. E., *J. Am. chem. Soc.* **76**, 370 (1954).
4. WASASTJERNA J. A., *Soc. Sci. Fennica, Comm. Phys.-Math.* **14**, No. 3, 1 (1948); *ibid.* **14**, No. 7, 1 (1948); *ibid.* **15**, No. 3, 1 (1949).
5. HOVI V., *Soc. Sci. Fennica, Comm. Phys.-Math.* **15**, No. 12, (1950); *Ark. Fys.* **5**, 6 (1952).
6. KLEPPA O. J., In *Metallic Solid Solutions* (Edited by J. Friedel and A. Guinier). Benjamin, New York (1963).
7. NARDELLI G. F. and TETTAMANZI N., *Phys. Rev.* **126**, 2059 (1962).
8. MATTHEW J. A. D., *Proc. phys. Soc.* **89**, 683 (1966).
9. SLAGLE O. D. and MCKINSTRY H. A., *J. appl. Phys.* **38**, 446 (1967).
10. LUDWIG W., *Calculation of the Properties of Vacancies and Interstitials*. N.B.S. Mis. Publ. No. 287, p. 151. Washington (1966).
11. LIU L. G. and TAKAHASHI T., To be published (1969); LIU L. G., M. S. Thesis (Geology), University of Rochester, Rochester, N.Y. (1968).
12. LANDOLT BÖRNSTEIN, *Zahlenwerte und Tabellen*, Vol. 1, Part 4. Springer, Berlin (1955).
13. HAUSSÜHL S., *Z. Phys.* **159**, 223 (1960).
14. DARKEN L. S. and GURRY R. W., *Physical Chemistry of Metals*. McGraw-Hill, New York (1953).
15. SLATER J. C., *Introduction to Chemical Physics*, McGraw-Hill, New York (1963).
16. FANCHER D. L. and BARSCH G. R., *J. Phys. Chem. Solids* **30**, 2503 (1969).
17. QUIMBEY S. L. and SUTTON P. M., *Phys. Rev.* **91**, 1122 (1953).
18. LEIBFRIED G., *Handbuch der Physik*, Vol. 7, p. 252. Springer, Berlin (1955).
19. SMITS A., ELGERSMA J. and HARDENBERG H. V., *Rec. Trav. Chim.* **43**, 671 (1924).
20. SCHEIL E. and STADELMAIER H., *Z. Metallk.* **43**, 227 (1952).
21. BARRETT W. T. and WALLACE W. E., *J. Am. chem. Soc.* **76**, 366 (1954).

THE FERMI SURFACE OF AuSn*

G. J. EDWARDS† and M. SPRINGFORD

University of Sussex, School of Mathematical and Physical Sciences, Brighton, Falmer, Sussex, England

and

Y. SAITO‡

Division of Pure Physics, National Research Council of Canada, Ottawa, Canada

(Received 10 March 1969)

Abstract—De Haas–van Alphen oscillations in the low-temperature, magnetic susceptibility have been investigated in fields up to 100 kG for the hexagonal, intermetallic compound AuSn at the equi-atomic composition. Results are presented for the frequency measurements in the {0001}, {1010} and {1120} planes, together with cyclotron effective masses and Dingle ‘scattering temperatures’. The 1-OPW model, extending into eight zones, the first two of which are filled, has been constructed according to both the single and double zone schemes, and the extremal cross-sectional areas have been computed. Spin-orbit effects are found to be important in AuSn and the experimental results are interpreted in terms of a model for the Fermi surface based on the single zone scheme, but with limited magnetic breakdown. Between zones 3 and 4, breakdown is complete at magnetic fields > 30 kG, but no major breakdown phenomena were observed below 100 kG between zones 5 and 6. An estimate of 0.16 eV is obtained for the spin-orbit gap relevant to the latter case, corresponding to a breakdown field of ~ 250 kG. The derived model for the Fermi surface indicates that in the absence of breakdown between zones 5 and 6, AuSn is a compensated metal supporting open orbits along (001), (1010) and (1120). These conclusions are in agreement with the high-field, galvanomagnetic properties of AuSn.

I. INTRODUCTION

DE HAAS–van Alphen (dHvA) oscillations in the low temperature, magnetic susceptibility provide direct experimental information on the extremal cross-sectional areas, cyclotron masses and average relaxation times relating to the Fermi surface. In recent years, improvements in experimental techniques and in crystal preparation have enabled studies of the effect, previously restricted to high purity metallic elements, to be extended to a number of intermetallic compounds [2–6] and ordered alloy phases [7, 8]. In particular, the effect has been examined in a series of ordered intermetallic compounds [2–6] containing a noble metal in combination with group IIb metals (CuZn, AgZn) [7, 8] and group IIIa metals

(AuAl₂, AuGa₂ and AuIn₂) [9]. The present study of the hexagonal, intermetallic compound AuSn at the equiatomic composition is an extension of this work.

AuSn crystallizes in the NiAs structure. This phase forms an important link between compounds which are non-metallic (ionic or covalent) and those which are truly metallic. Apart from AuSn, all known compounds with this structure consist of a transition metal in combination with a metalloid or group B element. Typically they exhibit wide ranges of homogeneity and a variety of bonding, ranging from predominantly ionic for c/a near to 1.63 to mainly metallic for low axial ratios (the order of 1.3).

AuSn has been fairly extensively investigated. The structural, thermal, electrical and magnetic properties have been studied by Jan *et al.* [10, 11] and the high-field, galvanomagnetic properties by Sellmyer and

*Work supported by the S.R.C.

†Present address: Department of Physics, Michigan State University, Mich. 48823, U.S.A.

‡Present address: Tohoku University, Sendai, Japan.

Schroeder[12]. AuSn is known to be a superconductor with a transition temperature of 1.25°K[13]. To explain the transport properties, models for the Fermi surface have been proposed[10, 12] and the present study was motivated by the existence of strong dHvA signals in AuSn, enabling the geometry of the Fermi surface to be investigated. A preliminary report of this investigation has been given elsewhere[14].

In Section 2 the essential theory of the dHvA effect is summarized. The experimental procedure is described in Section 3, followed by a discussion of the nearly-free-electron model for AuSn in Section 4. Sections 5 and 6 discuss the experimental results and their interpretation to yield a model for the Fermi surface. This model is discussed and compared with the results of other workers on AuSn in Section 7.

2. DE HAAS-VAN ALPHEN EFFECT

It may be shown that for a metal the free energy F and the magnetization $M = -\partial F/\partial H$ are periodic functions in H^{-1} , the reciprocal magnetic field. The fundamental frequency f of these oscillations is related to an extremal, cross-sectional area A of the Fermi surface (FS) by the Onsager relation

$$A = (2\pi e/c\hbar) f.$$

Lifshitz and Kosevich[16] have derived an expression for the free energy of a system of electrons having an arbitrary dispersion relation. Incorporating the factor derived by Dingle[17] to account for electron scattering the expression for the fundamental term in the magnetization becomes

$$M = M_0(H, T) \sin\left(\frac{c\hbar A}{eH} \pm \frac{\pi}{4} - 2\pi\theta\right) \quad (2.1)$$

$$M_0(H, T) = \frac{2kTA}{\pi} \left(\frac{e}{c\hbar H}\right)^{1/2} |A''|^{-1/2} \times e^{-\alpha(T+T_D)/H} \cos\left(\frac{\pi g m^*}{2m}\right) \quad (2.2)$$

Here, the usual approximation, $2\pi f \gg \alpha(T+T_D) \gg H$, has been made. T_D is the Dingle 'scattering temperature', A'' is the curvature of the FS evaluated at the extremum. θ is a phase constant which is $\frac{1}{2}$ for a quadratic dispersion law and $\alpha = 2\pi^2 c k m^*/e\hbar$. The last term in equation (2.2) was derived by Lifshitz and Kosevich from considerations of the electron spin, with the assumption that the spin splitting is much less than the Landau level separation. Under conditions where this criterion is not valid[18], the expression must be modified[19].

In this work, the low frequency modulation technique developed by Shoenberg and Stiles[20] was used. The dHvA effect is observed by surrounding the specimen by a small pick-up coil, the e.m.f. (V) induced in the coil being given by

$$V = C \frac{dM}{dt}. \quad (2.3)$$

Here, C is a factor depending on the coil geometry etc. The specimen is placed in a high magnetic field H_0 on which is superimposed an alternating field $h \cos(\omega t)$ of small magnitude. For small field ranges, we may write for M

$$M = M_0 \sin(2\pi f' H)$$

where $f' = f/H^2$ and $H = H_0 + h \cos \omega t$. We thus obtain

$$M = M_0 \sin[2\pi f' H_0 + \pi\beta \cos \omega t] \quad (2.4)$$

where $\beta = 2f'h$.

Expansion of equation (2.4) leads to a d.c. term plus oscillatory terms with frequencies of $\omega, 2\omega, \dots, n\omega, \dots$. The coefficients of these terms are Bessel functions[21] J_n . In this work, detection of the second harmonic (2ω) signal was employed. From equations (2.3) and (2.4) the amplitude of the dHvA oscillations for 2ω detection is given by

$$V = B\omega TH^{-1/2}J_2(2\pi fh/H^2) \\ \times \exp[-\alpha(T + T_D)/H] \quad (2.5)$$

where

$$B = \frac{8CkA}{\pi} \left(\frac{e}{ch}\right)^{1/2} \cos\left(\frac{\pi gm^*}{2m}\right).$$

Two assumptions have been made in this derivation. Firstly, that h is constant over the specimen dimensions, and secondly, that ω is sufficiently low to ensure complete penetration of the specimen by the modulation field.

From equation (2.5) it is seen that measurements of $\ln(V/T)$ as a function of T at constant field will give the effective masses for the various dHvA frequencies while measurements of $\ln[VH^{1/2}/J_2(2\pi fh/H^2)]$ as a function of H^{-1} will yield the Dingle temperatures T_D .

3. EXPERIMENTAL PROCEDURE

The AuSn ingot from which the specimens were cut was grown by Beck[22]. The alloy was prepared in an evacuated silica tube from equiatomic quantities of spectrographically pure tin and gold supplied by the Johnson Matthey Company. After an initial melt, the ingot was subjected to approximately 30 zone passes to prepare a single crystal of homogeneous composition. Five crystals (I-V) were spark-machined from the ingot, crystals III, IV and V on a particularly fine range in

view of the difficulty encountered in etching crystals for orientation by X-ray techniques. The specimens were cylinders of length 5 mm and diameter 2 mm. The cylinder was, in each case, oriented along a crystal symmetry direction to within 1° of that specified in Table 1.

The residual resistance ratios of the specimens were measured using the eddy current decay technique devised by Bean *et al.*[23]. To facilitate measurements, we have employed a repetitive rather than a pulsed method[24, 25]. The resistance ratios were reproducible to 3 per cent.

The orientations and residual resistance ratios are given in Table 1. For three of the crystals, two sets of resistance ratio measurements were made within an interval of approximately 18 months. The second set showed consistently higher values than the first, reflecting a slow annealing phenomenon at room temperature.

The dHvA effect was investigated in a 100 kG superconducting magnet at temperatures between 1.14° and 4.2°K. The modulation frequency was 5 KHz with phase-sensitive detection at 10 KHz. The residual noise level referred to the pick-up coil of approximately 200 turns linked to the specimen was $4 \cdot 10^{-9}$ V r.m.s. for a 2.5 Hz bandwidth. Signal levels of this same order were detectable, although vibration was troublesome at these low levels.

It is well known that superconducting

Table 1. Crystallographic orientations and measured residual resistance ratios for specimens of AuSn. The two sets of data were obtained with an interval of 18 months

Specimen	Orientation	Resistance ratio 1	Resistance ratio 2
I	$\langle 0001 \rangle$		42.4
II	$\langle 1\bar{1}00 \rangle$		40.8
III	$\langle 0001 \rangle$	34.9	38.2
IV	$\langle 1\bar{1}00 \rangle$	39.6	43.3
V	$\langle 11\bar{2}0 \rangle$	35.2	43.8

magnets constructed of niobium-tin exhibit pronounced hysteresis effects between the magnetic field and the energizing current. In this work, the magnetic field was continuously monitored with the aid of a copper coil used as a magnetoresistance. The device was calibrated using N.M.R. and interpolation to any magnetic field was achieved by means of a curve-fitting programme. The details of this technique are described elsewhere[26]. Due to a small systematic error in the field calibration during the course of this investigation, the accuracy of the dHvA measurements is 1 per cent.

4. SINGLE-OPW FERMI SURFACE FOR AuSn

In many metallic elements, with the notable exception of the transition metals, the Fermi surface is rather closely related to that derived according to the single orthogonalized-plane-wave (1-OPW) or 'empty lattice' approximation. The reasons for this agreement have been clarified in recent years by the work of Phillips and Kleinman[27], Heine[28], Harrison[29] and others.

It is expected that, as for metallic elements, the 1-OPW Fermi surface will be a reasonably good approximation to the real Fermi surface in the field of metallic compounds and ordered intermetallic phases. Recent experiments have confirmed this[7-9], although the presence of a noble metal will somewhat weaken the expectation in the case of AuSn.

AuSn has the hexagonal NiAs ($B8_1$) structure (Fig. 1) with $c = 5.5230 \text{ \AA}$, $a = 4.3218 \text{ \AA}$ and $c/a = 1.278$ at room temperature[11]. The gold atoms reside on a simple hexagonal lattice and the tin on hexagonal close-packed hcp sites. The crystal structure belongs to the space group $P6_3/mmc$ (D_{6h}^4), and contains four atoms per primitive cell. This corresponds to ten valence electrons, which in our model are assumed free.

The first Brillouin zone for the structure (Fig. 2) is a hexagonal prism. For hcp lattices, however, there is the complication that in the

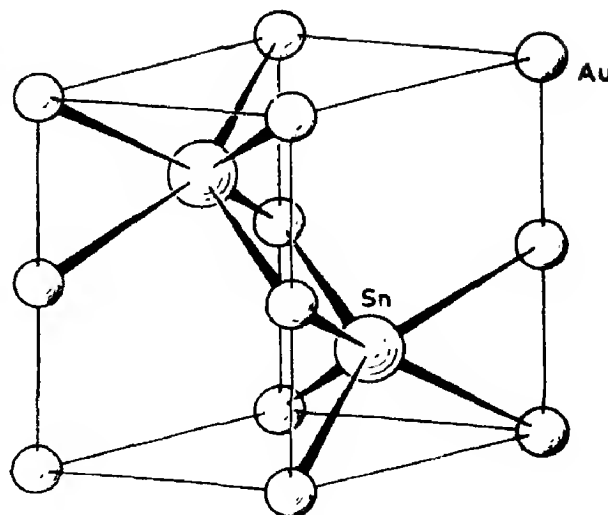


Fig. 1. Crystal structure of AuSn (NiAs, $B8_1$ structure) showing the hexagonal unit cell.

absence of spin-orbit coupling the energy bands are degenerate across the hexagonal face of the first Brillouin zone. Spin-orbit coupling removes this degeneracy everywhere except along the lines R (Fig. 2), the effect of the interaction being greatest at H .

In general, the spin-orbit interaction is small enough to allow a reasonable possibility of magnetic breakthrough at experimentally attainable magnetic fields. In the limiting case of high magnetic fields and complete breakthrough, all the electrons move on orbits which exist continuously over two bands and it is convenient to introduce the concept of the 'double zone'. Zones 1 and 2 coalesce to form a zone of double the volume of each separately and similarly for zones 3 and 4 etc. The electrons now move on orbits contained entirely in a repeated set of double zones.

In AuSn, the magnitude of the spin-orbit coupling is only approximately known. Since in the hcp metal thallium, with a very similar atomic number to that of gold, magnetic breakthrough has been observed at fields well below 100 kG, the 1-OPW Fermi surface for AuSn was constructed according to both the single and double zone schemes, using the method of Harrison[32]. The calculated

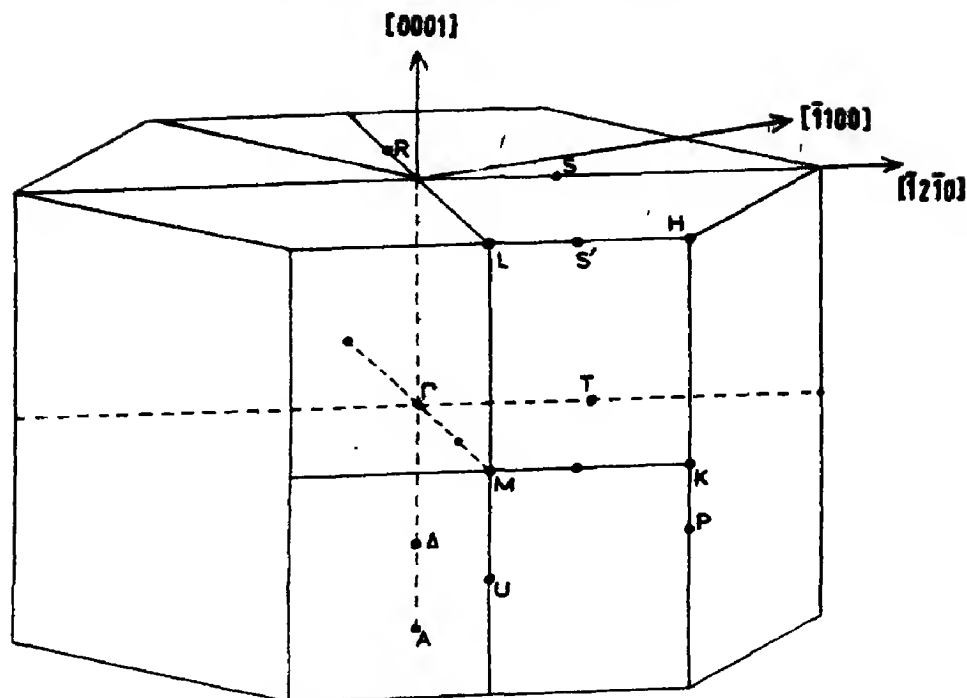


Fig. 2. First Brillouin zone for the hexagonal close-packed structure, showing points and lines of symmetry.

Fermi radius, corresponding to ten valence electrons, is 0.789 a.u.*

Extremal cross-sectional areas of these surfaces have been computed† for the principal crystallographic planes $\{0001\}$, $\{10\bar{1}0\}$ and $\{11\bar{2}0\}$. These results are shown in Fig. 3 in which extremal orbits are labelled by a letter referring to the symmetry points about which the orbit is centred in the reduced zone and a subscript indicating the zone number.

The 1-OPW Fermi surface extends into eight zones of which the first two are filled. A construction of the Fermi surface in the remaining partially occupied six zones is shown in Figs. 4-6 and is briefly discussed.

*In these calculations, the room temperature values for the lattice parameters have been employed. In consequence, a small correction to account for lattice dilation is relevant.

†We are indebted to Dr. R. Taylor of the Division of Pure Physics, N.R.C., Ottawa, Canada, for making available to us a computer program developed by him to undertake these calculations and those of effective mass.

Zone 3 contains a single, closed hole surface which supports an extremal orbit A_3 . The 4th zone hole surface is open along $\langle 0001 \rangle$ with extremal sections A_4 and Γ_4 for certain field orientations. In zone 5 the hole surface is multiply connected, being topologically equivalent to a set of arms connected at Γ and directed both in the $\langle 0001 \rangle$ and $\langle 10\bar{1}0 \rangle$ directions. Possible extremal orbits in this zone are H_5 , L_5 , Γ_5 , M_5 and A_5 . The electron surface of zone 6 has two main features; 'humbugs' situated at H with the general form of trigonal bipyramids, and complex winged electron pockets or 'butterflies' at M . These latter surfaces are shown truncated in Fig. 4(d) to demonstrate their form more clearly. The humbugs and butterflies contact each other in the manner depicted in Fig. 5. In zone 6 at least two extremal orbits (H_6 and M_6) exist. There are 'propellor'-shaped features in zone 7 situated at M_7 and giving the extremal section M_7 , and small electron pockets in the eight zone corresponding to M_8 .

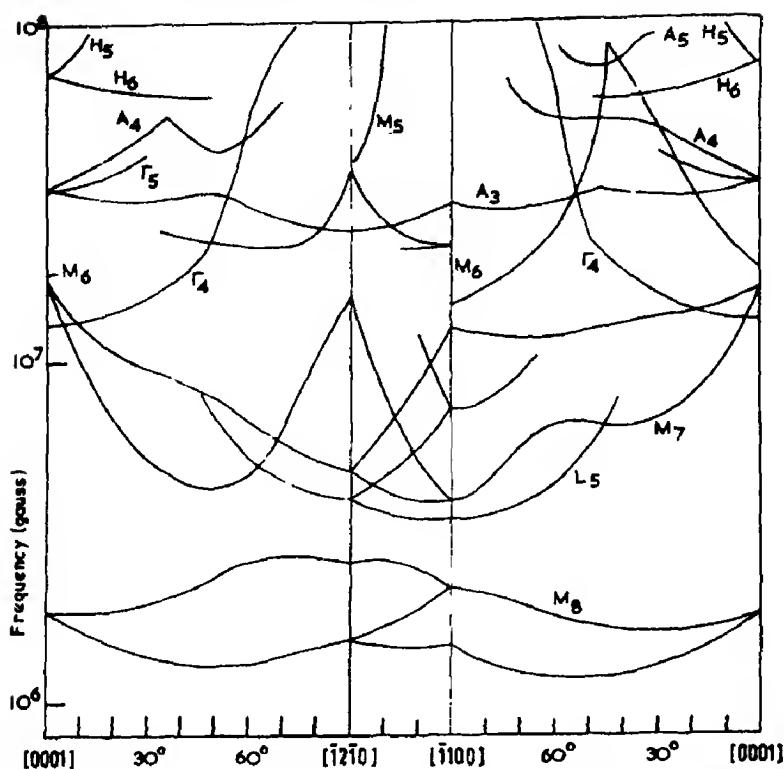


Fig. 3. Computed curves showing the angular variation of the dHvA frequencies for the Fermi surface of AuSn in the 1-OPW approximation with strong spin-orbit coupling (single-zone model). The curves are labelled by a letter and a number, the latter giving the reduced zone in which the orbit exists and the former indicating the symmetry point in the zone about which the orbit is centred.

In the double zone scheme, a closed hole surface is formed in zone 3,4 (the double zone formed by the coalescence of zones 3 and 4), but in zone 5,6 only three extremal orbits, Γ_5 , M_5 and M_6 remain of those which existed for zones 5 and 6 separately. The surfaces present in zones 7 and 8 remain unchanged and consequently have not been reconstructed in the double zone scheme.

With 10 electrons per primitive cell, AuSn is compensated according to the single zone scheme. However, this compensation is destroyed if complete magnetic breakdown occurs between zones 5 and 6.

5. EXPERIMENTAL RESULTS

The dHvA effect was investigated as the direction of the magnetic field was varied in

the principal crystallographic planes $\{0001\}$, $\{1\bar{1}00\}$ and $\{11\bar{2}0\}$. Of the eleven frequencies observed, eight could be studied over an extended angular range. The results are summarized in Fig. 7 and reproduced in detail in Figs. 8–13.

The α oscillations (Fig. 8) were the lowest frequencies observed. The branch is centred about $\langle 0001 \rangle$ and the angular variation of frequency is identical, within experimental error, in both the $\{11\bar{2}0\}$ and $\{1\bar{1}00\}$ planes. This indicates that the α oscillations may be associated with a FS feature having cylindrical symmetry about the $\langle 0001 \rangle$ axis. The results may in fact be fitted closely to a hyperboloid surface defined by

$$r^2 - az^2 = b$$

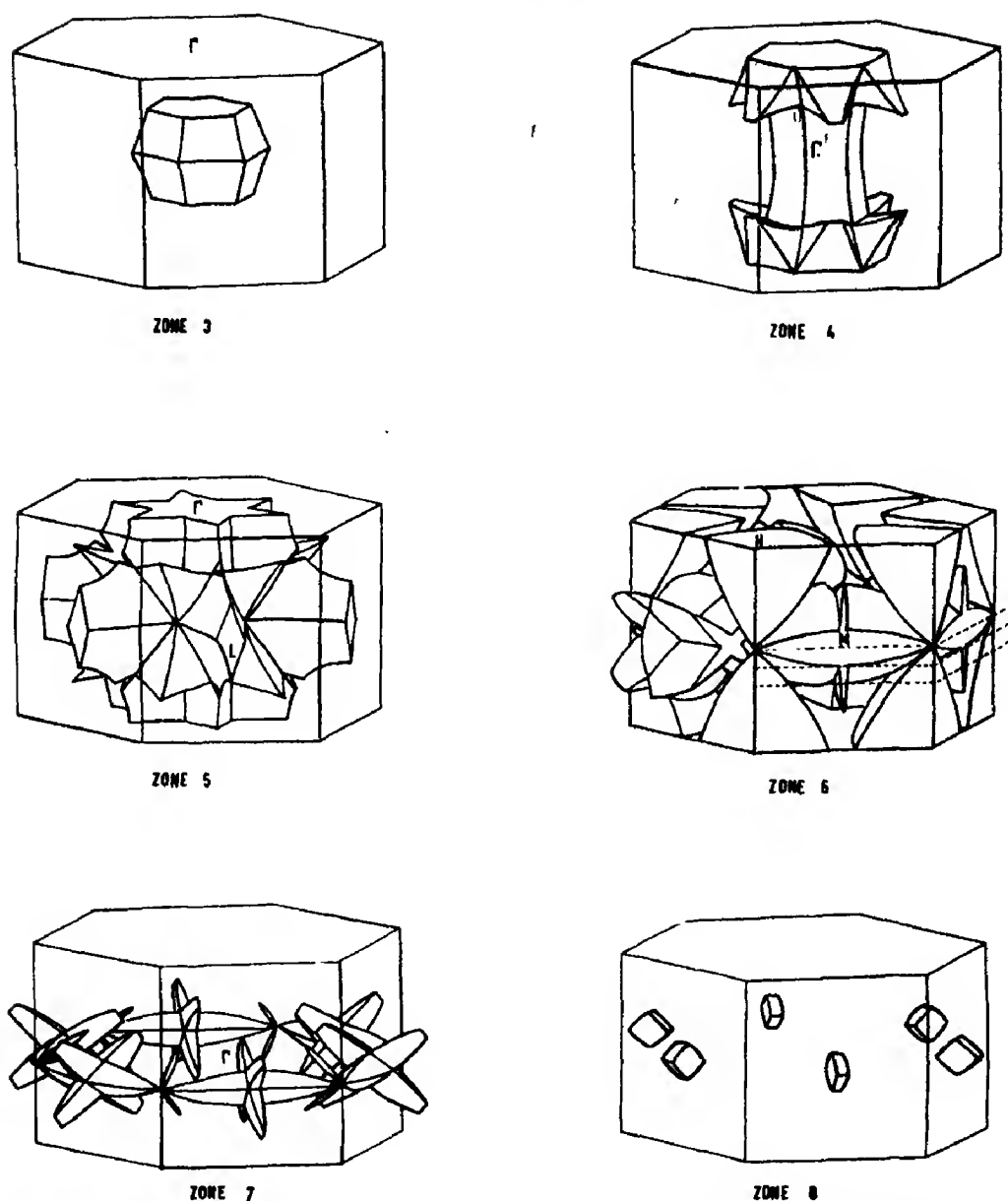


Fig. 4. Fermi surface of AuSn in the 1-OPW approximation with strong spin-orbit coupling (single zone model). Zones 1 and 2 are full. The electron pockets ('butterflies') centred at M in zone 6 are shown truncated to exhibit more clearly their form. Note that the zone centre has been shifted in zones 3 and 5.

where z and r are distances, in units of $(G)^{1/2}$, measured along and normal to $\langle 0001 \rangle$ respectively. A best fit is achieved with $a = 0.756$ and $b = 2.26 \cdot 10^5$ G, as shown in Fig. 8.

The β and ν oscillations (Fig. 9) have closely similar frequencies ($1.49 \cdot 10^7$ and $1.54 \cdot 10^7$ G respectively along $\langle 0001 \rangle$) and

for certain field orientations close to $\langle 0001 \rangle$ there was some evidence for a third frequency of similar magnitude.

The γ oscillations (Fig. 10) form a single branch of frequency $6.14 \cdot 10^7$ G at $\langle 0001 \rangle$. The angular range of observation terminates abruptly at $5(\pm \frac{1}{2})^\circ$ from $\langle 10\bar{1}0 \rangle$ and at

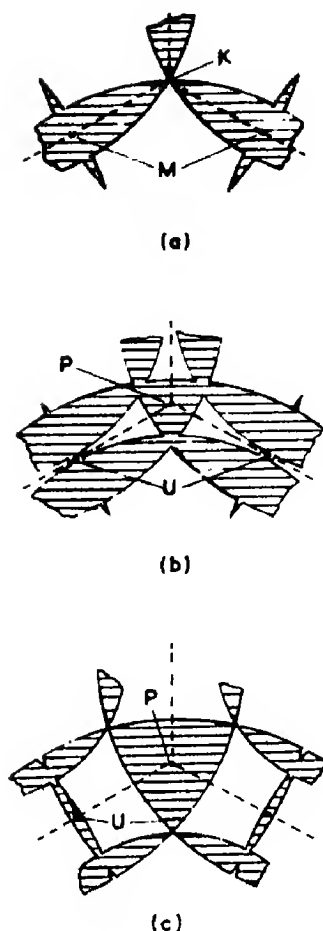
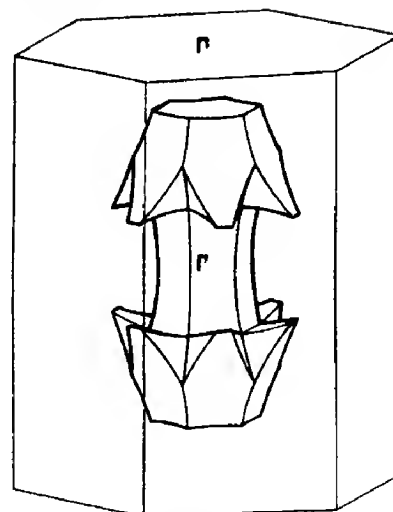


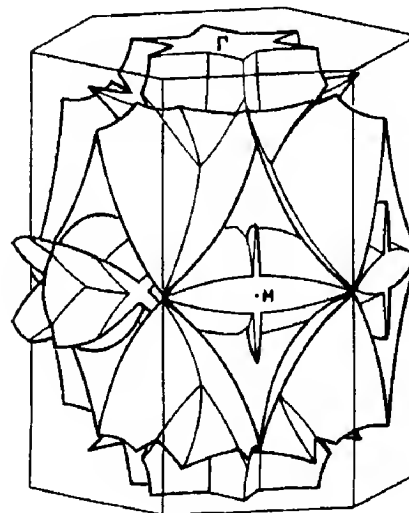
Fig. 5. Sections of the 6th zone parallel to (0001), showing the form and connectivity of the Fermi surface about symmetry point K . The three sections a , b and c correspond to those indicated in Fig. 4(d). Dotted lines are Brillouin zone boundaries.

$17(\pm 1)^\circ$ from $\langle 11\bar{2}0 \rangle$ in the $\{11\bar{2}0\}$ and $\{1\bar{1}00\}$ planes respectively, indicating that the angular range of existence of the γ branch is determined by geometrical features of the FS rather than by intrinsic amplitude factors.

Experimentally, the δ oscillations (Fig. 11) were visible as a low frequency ripple on the ϵ oscillations. At $\langle 10\bar{1}0 \rangle$, the δ oscillations were visible up to 100 kG with a frequency of $1.86 \cdot 10^6$ G. Along $\langle 11\bar{2}0 \rangle$ however, they were observed only for magnetic fields below a value which varied between 35 kG and 50 kG in different experiments. At higher fields up to 100 kG, a new set of oscillations



ZONE 3,4



ZONE 5,6

Figs. 6(a, b). Fermi surface of AuSn in the 1-OPW approximation with weak spin-orbit coupling (double zone model). Zones 7 and 8 (Figs. 4(e) and 4(f)) remain unaffected in the presence of magnetic breakdown and consequently have not been reconstructed here.

(ξ) became visible. These were only observed along $\langle 11\bar{2}0 \rangle$ and two determinations of their frequency made in different experiments, gave the values $3.32 \cdot 10^6$ G and $2.96 \cdot 10^6$ G, a discrepancy too great to be attributable to

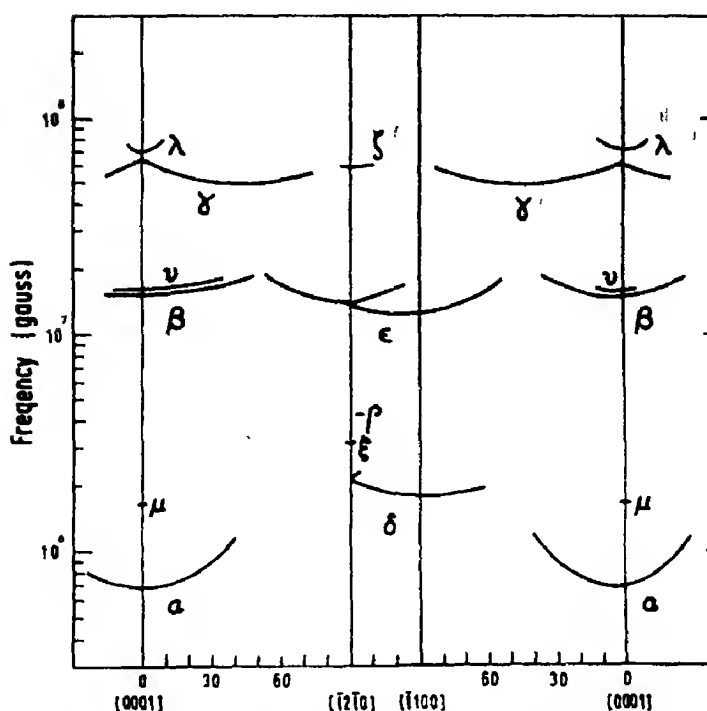


Fig. 7. Summary of the dHvA frequency results obtained for AuSn in the three principal crystallographic planes. Although indicated by continuous lines, the data were in fact taken at discrete orientations.

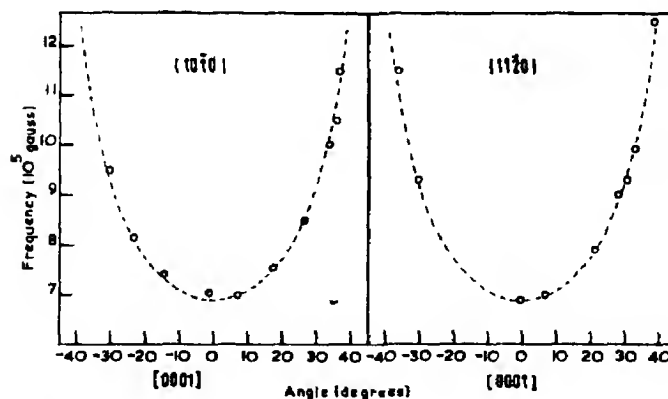


Fig. 8. Angular variation of dHvA frequency for the α oscillations. The dotted line shows the result of fitting the data to an hyperboloid shaped piece of Fermi surface (see Section 5).

experimental errors. This phenomenon will be mentioned in 6.

The ϵ oscillations (Fig. 12) have frequencies of $1.40 \cdot 10^7$ and $1.31 \cdot 10^7$ G at $\langle 11\bar{2}0 \rangle$ and $\langle 1\bar{1}00 \rangle$ respectively. No experimental

evidence could be found for ϵ and β being part of the same branch of frequencies.

As seen in Fig. 13, the ζ oscillations were only visible within $8(\pm 1)^\circ$ from $\langle 11\bar{2}0 \rangle$ in the (0001) plane, the frequency at $\langle 11\bar{2}0 \rangle$ being

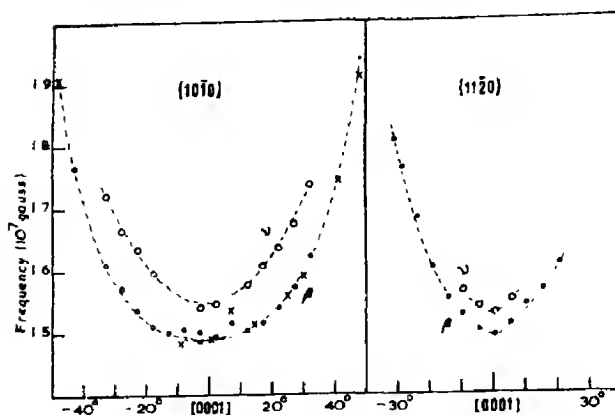


Fig. 9. Angular variation of dHvA frequency for the β and ν oscillations.

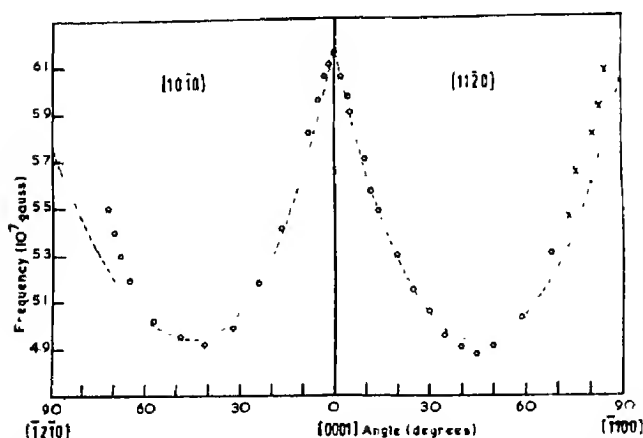


Fig. 10. Angular variation of dHvA frequency for the γ oscillations. The dotted lines are derived from a model based on the 6th zone 'humbugs' of the 1-OPW, single zone scheme (cf. Section 6).

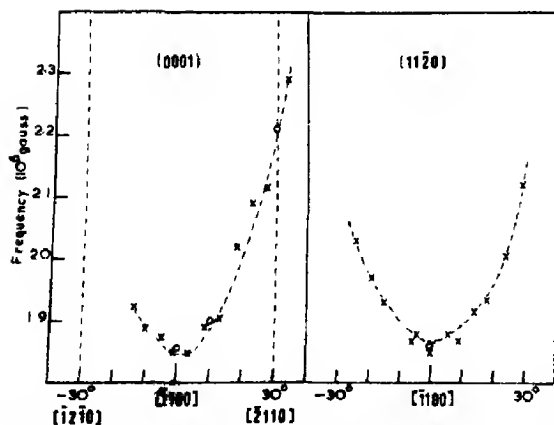
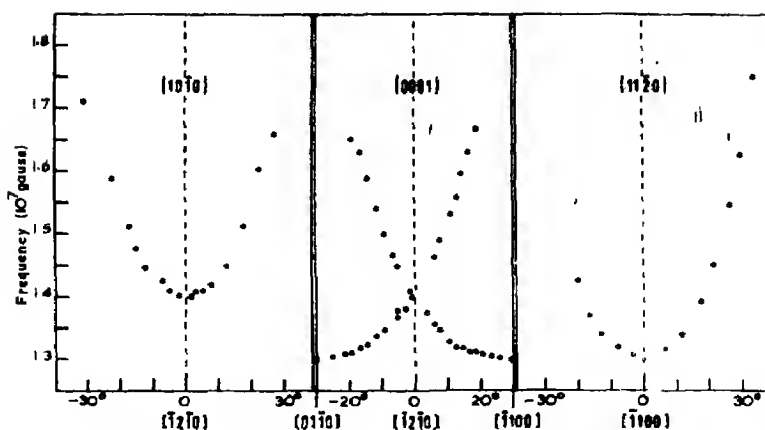
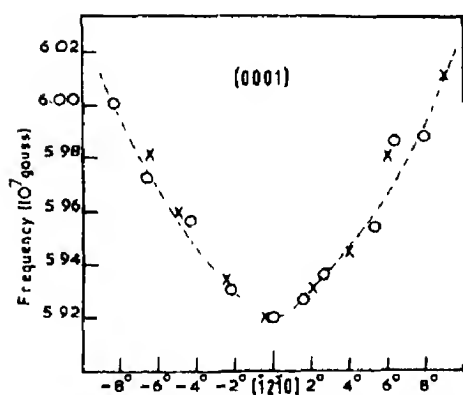


Fig. 11. Angular variation of dHvA frequency for the δ oscillations.

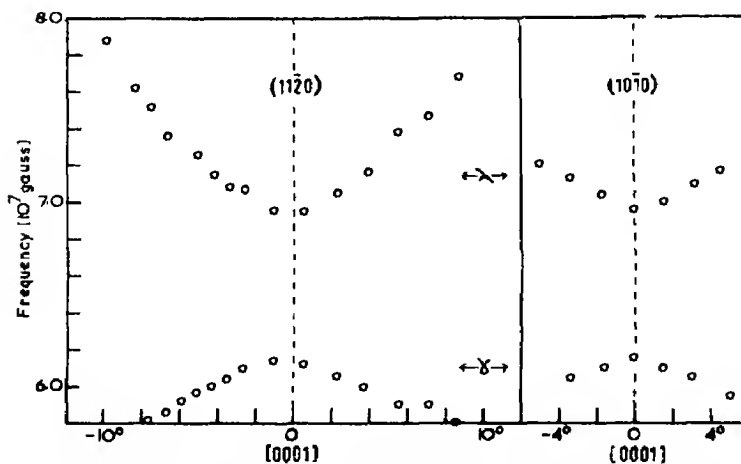
$5.92 \cdot 10^7$ G. Observations of the λ oscillations too were limited to a small angular range close to $\langle 0001 \rangle$, as shown in Fig. 14. The frequency along $\langle 0001 \rangle$ is $6.96 \cdot 10^7$ G and increases very rapidly as the field inclines away from the symmetry direction.

The μ oscillations were of low amplitude and were only visible along $\langle 0001 \rangle$. Similarly, the ρ oscillations were only seen for field orientations very close to $\langle 11\bar{2}0 \rangle$.

From the temperature dependence of the amplitude of the dHvA oscillations, effective mass values were obtained for the α , β , γ , ϵ and λ frequencies along symmetry directions.

Fig. 12. Angular variation of dHvA frequency for the ϵ oscillations.Fig. 13. Angular variation of dHvA frequency for the ζ oscillations.

The measurements were made in the temperature range 4.2° – 1.14°K but, as illustrated in Fig. 15, which typifies the experimental results, a few points at the high temperature end were, in each case, consistently above the straight line extrapolated from the low temperature data. Because no plausible explanation for this phenomenon could be found, the effective masses were determined from the experimental points between 1.14° and 3.5°K . This procedure is somewhat arbitrary and some doubt is thereby cast on the calculated mass values. The cyclotron effective masses, frequencies and other parameters are collected in Table 2.

Fig. 14. Angular variation of dHvA frequency for the λ oscillations showing also part of the γ branch.

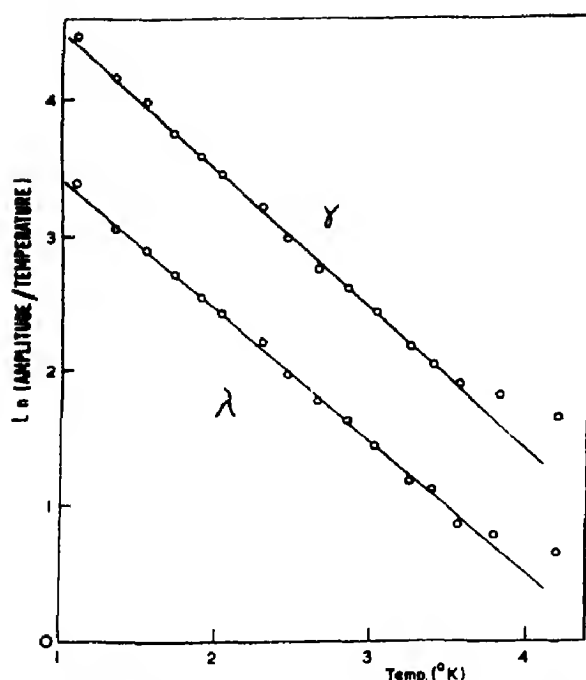


Fig. 15. Data taken along $\langle 0001 \rangle$ showing the variation of dHvA amplitude as a function of temperature for the γ and λ oscillations. These results typify the data obtained for all sets of oscillations. In all cases, a few high temperature points lie above the line extrapolated from the linear portion of the graph.

As a preliminary to measuring the Dingle temperature T_D , the validity of the Bessel function $J_2(2\pi fh/H^2)$ in equation (2.5) was checked. The agreement between the computed curve for J_2 , inserting the details of the coil geometry, and the experimental curve, was surprisingly good in view of the fact that the Bessel function in equation 2.5 is strictly valid only for a uniform modulation field. The theoretical expression in equation (2.5) was thus employed to evaluate T_D , and from this analysis of the experimental results, values for T_D of $5.0(\pm 0.2)^\circ\text{K}$ and 5.4°K were obtained along $\langle 0001 \rangle$ for the α and γ oscillations respectively.

A particularly interesting behaviour has been observed with regard to the magnetic field dependence of the ϵ oscillations.

The original amplitude measurements on the ϵ oscillations were made along $\langle 10\bar{1}0 \rangle$ and the results for two temperatures are shown in Fig. 16. There is a marked deviation of the graphs from linear behaviour. These deviations were reproducible in different experiments and for three different crystals and hence are

Table 2. Experimentally measured dHvA frequencies and effective masses, together with the associated orbits and frequencies in the 1-OPW model

Experimental results				1-OPW model	
Frequency branch	Orientation	Frequency (10^6 G)	Effective mass ratio	Orbit	Frequency (10^6 G)
α	$\langle 0001 \rangle$	0.711	0.108	K_6	— ^(a)
β	$\langle 0001 \rangle$	14.9	0.340	M_6	18.3
γ	$\langle 0001 \rangle$	61.4	0.636	H_6	73.6
δ	$\langle 11\bar{2}0 \rangle$	2.20		L_5	3.96
δ	$\langle 1\bar{1}00 \rangle$	1.86		L_5	3.41
ϵ	$\langle 11\bar{2}0 \rangle$	14.0		M_6	— ^(a)
ϵ	$\langle 1\bar{1}00 \rangle$	13.1	0.3 ^(d)	M_6	14.6
ζ	$\langle 11\bar{2}0 \rangle$	59.4		H_6	73.6
λ	$\langle 0001 \rangle$	69.6	0.604	H_5	73.6
μ	$\langle 0001 \rangle$	1.65		Γ_4	13.0
ν	$\langle 0001 \rangle$	15.4		Γ_5	32.8
ξ	$\langle 11\bar{2}0 \rangle$	3.32 2.96 ^(b)		M_7	16.7
ρ	$\langle 11\bar{2}0 \rangle$	4.25 ^(c)		M_7	16.7

^(a) No extremal orbit present in the 1-OPW model.

^(b) Results of two measurements.

^(c) Measured at 4° from $\langle 11\bar{2}0 \rangle$.

^(d) This figure represents only an approximate estimate of the effective mass ratio.

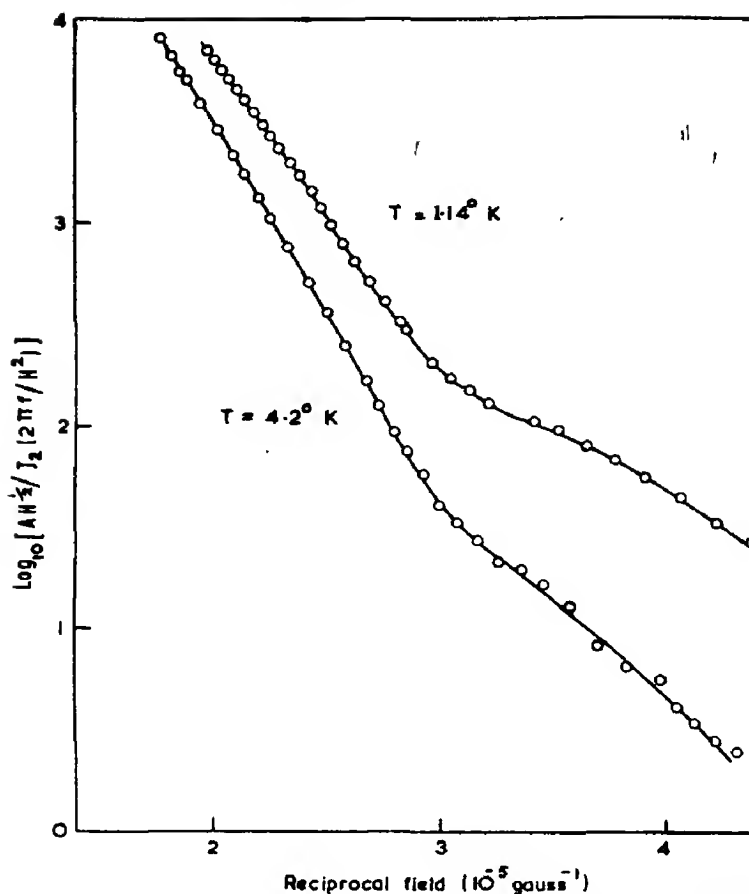


Fig. 16. Data taken along $\langle 10\bar{1}0 \rangle$ showing the variation of amplitude of the ϵ dHvA oscillations as a function of reciprocal magnetic field at two temperatures.

not caused by the peculiarities of a particular specimen. Further experiments showed that the anomalous field dependence of amplitude of the ϵ oscillations existed for all field orientations studied in the basal plane. A second example is shown in Fig. 17 for the magnetic field inclined at 9.5° from $\langle 11\bar{2}0 \rangle$, where two branches of ϵ are visible as a beating waveform.

Several possible explanations of this behaviour have been examined. The graphs of Fig. 16 have the wrong general shape, that is abruptly increasing slope with increasing field at about 30 kG, for the effect to be explained in terms of magnetic breakdown. The same remark is true if the measurement frequency were such that incomplete penetra-

tion of the specimen by the modulation field took place. To check this point, however, the experiment was repeated at a modulation frequency of 429 Hz and the previous results were closely reproduced.

The most probable explanation of the phenomenon was eventually found to be in terms of two very similar frequencies present in the ϵ oscillations, as demonstrated by the following analysis. Assume we have two frequencies present whose amplitudes are defined by

$$V_1^1 = V_1 H^{1/2} / J_2(\pi\beta) = a_1 e^{-\varphi_1/H} \sin(2\pi f/H)$$

$$\begin{aligned} V_2^1 &= V_2 H^{1/2} / J_2(\pi\beta) \\ &= a_2 e^{-\varphi_2/H} \sin(2\pi(f + \Delta f)/H). \end{aligned}$$

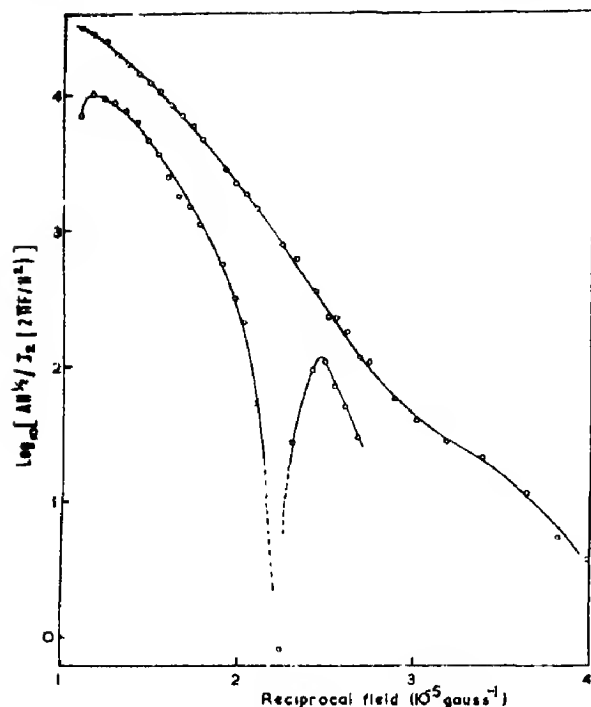


Fig. 17. Data taken at 9.5° from $\langle 11\bar{2}0 \rangle$ in the (0001) plane, showing the variation of amplitude with reciprocal magnetic field for the ϵ dHvA oscillations at 1.2°K . The upper curve pertains to the lower frequency of the two comprising the ϵ waveform at this orientation, and vice versa.

Here we have assumed that the two frequencies are in phase at the origin of reciprocal magnetic field and that Δf is small enough such that we can assume $\beta_1 = \beta_2 = \beta$. The quantities a_1 and a_2 are constants while $\varphi_1 = \alpha_1(T + T_{D1})$ and similarly for φ_2 . The resultant signal is $V_R^1 (= V_1^1 + V_2^1)$ defined by

$$\begin{aligned} V_R^1 &= a_2 \left[e^{-2\varphi_2/H} + \left(\frac{a_1}{a_2} \right)^2 e^{-2\varphi_1/H} \right. \\ &\quad \left. + 2 \frac{a_1}{a_2} e^{-(\varphi_1 + \varphi_2)/H} \cos(2\pi\Delta f/H) \right]^{1/2} \\ &\quad \times \sin(2\pi f/H) \\ &= a_2 V_0 \sin(2\pi f/H). \end{aligned} \quad (5.1)$$

The quantities involved in the expression for V_0 were estimated as follows. The high and low field portions (above and below about

30 kG) of the results in Fig. 16 were fitted separately and approximately to a straight line. The gradients of these lines gave the estimates for φ_1 and φ_2 respectively. The ratio a_1/a_2 was taken to be the ratio of the amplitudes obtained by extrapolating the lines to the origin of reciprocal field. This procedure gave $\varphi_1 = 3.7 \cdot 10^5 \text{ G}$, $\varphi_2 = 2.4 \cdot 10^5 \text{ G}$ and $a_1/a_2 = 50$. Using these values, V_0 was computed as a function of H for various values of Δf . The results are shown in Fig. 18 where it is seen that the curves reproduce, in a semi-quantitative manner, the experimental results of Figs. 16 and 17. In particular the results along $\langle 10\bar{1}0 \rangle$ appear to agree most closely with the theory for $\Delta f/f \sim 1.5 \cdot 10^{-4}$ while the lower of the two curves in Fig. 18 agrees approximately with the curve having $\Delta f/f \sim 1.2 \cdot 10^{-3}$. No attempt was made to fit the

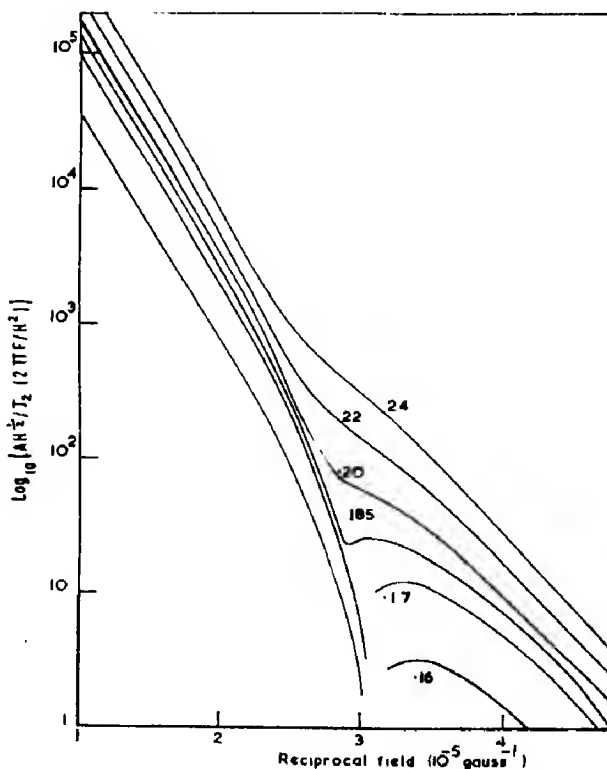


Fig. 18. Computed curves of dHvA amplitude as a function of reciprocal magnetic field for a hypothetical waveform composed of two very similar frequencies. The figures labelling the curves are the values of Δf in units of 10^5 G (see equation (5.1) and text).

experimental results exactly by equation (5.1) as this would involve the adjustment of four parameters in each case. However, the correspondence between the theoretical and experimental curves is strong evidence for the oscillations being composed of two very similar frequencies.

Further evidence for this explanation comes from a separate experiment in which the frequency of the ϵ oscillations was measured along $\langle 10\bar{1}0 \rangle$ as a function of the magnetic field. This was done by comparing the frequency of ϵ with the frequency of the neck orbit in gold over small identical field intervals, thus eliminating any systematic errors in the magnetic field calibration or from other causes. The results indicated a small but systematic increase in frequency for ϵ with decreasing field. The total increase between 70 and 20 kG is about 0.3 per cent, consistent with the frequency differences estimated above. This also indicates that the high field portion in Fig. 16 comes predominantly from the lower of the two frequencies present.

The origin of these two frequencies cannot be associated with a crystal defect such as a twinned specimen. The form of the curves precludes this explanation while the fact that different specimens give identical results is a cogent factor against such an association. A possible origin for the effect is discussed in 6 in connection with the model for the FS.

6. INTERPRETATION OF EXPERIMENTAL RESULTS

It is convenient to investigate firstly whether large features of the FS, corresponding to the high dHvA frequencies, might be recognizable distortions of their 1-OPW counterparts. We therefore discuss the origin of the γ oscillations.

The γ frequency branch is single-valued and is abruptly terminated, as discussed in 5, at particular field orientations, suggesting that the relevant surface is not closed. These considerations limit possible interpretations

to A_4 , $A_{3,4}$ and to H_6 . A consideration of Fig. 3 shows that H_6 , an electron orbit around the humbugs, bears a close resemblance to the curves for γ , whereas the other two do not.

In the 1-OPW model, contact between the humbugs and butterflies limits the angular range of H_6 to a region within approximately 45° from $\langle 0001 \rangle$ in both symmetry planes. Experimentally γ is seen over almost the whole of the $(11\bar{2}0)$ plane, indicating a modification of the form of the contact and it was assumed as a first approximation that the humbugs are closed surfaces. A convenient model for this hypothesis was constructed by neglecting all the 'Fermi spheres' in the Harrison construction of the FS except for those six which define any one of the humbugs. The frequency vs. angle curves for the model were calculated and these curves, which are identical with those for H_6 over the angular range of existence of the latter in the 1-OPW model, are shown, scaled in frequency by a factor 0.833, with the results for γ in Fig. 10. The close agreement shown between the theoretical and experimental curves indicates, with little doubt, that the γ branch is in fact derived from the humbug surfaces.

Such a closed surface, however, would predict that the γ oscillations would be visible for all field orientations. The humbugs must in fact be connected in the region of K to other surfaces or amongst themselves. Two possible models for this connectivity have been considered and these are shown by sections in the plane of the zone side in Fig. 19. Model (a) is topologically equivalent to the 1-OPW case, the humbugs being joined to the butterflies. Model (b) is topologically different; the humbugs are connected along $\langle 0001 \rangle$ by small necks, leaving the butterflies as isolated surfaces. The essential distinction between the two cases is that in (b), orbits about the butterflies are possible when the field is along $\langle 10\bar{1}0 \rangle$ (perpendicular to the plane of the construction in Fig. 19), as also are orbits about the necks when the field is along $\langle 0001 \rangle$. In model (a) neither of these orbits is

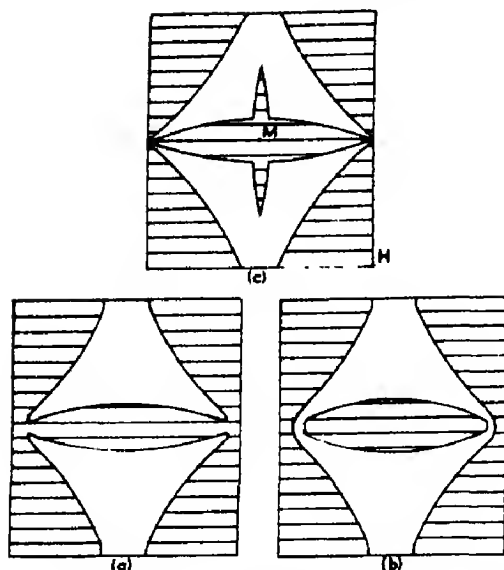


Fig. 19. $\{10\bar{1}0\}$ sections of the 6th zone, in the plane of the zone face. Figure 19(c) shows the form of the Fermi surface in the 1-OPW, single zone approximation. Figures 19(a) and (b) show schematically two possible models for the connectivity of the surface in the real metal.

possible, allowing us to distinguish experimentally between the two alternatives.

The size of the necks (K_6) in model (b) may be estimated from the orientations at which the γ oscillations cease to become visible. In the $\{11\bar{2}0\}$ plane, planes containing the extremal orbits pass through H by symmetry. Hence, when such a plane becomes tangential to the necks, extremal orbits must cease to exist. This consideration, together with the fact that γ ceases at $5(\pm\frac{1}{2})^\circ$ from $\langle 10\bar{1}0 \rangle$ defines a neck 'radius' along $\langle 10\bar{1}0 \rangle$ of 0.026 ± 0.0003 a.u. In the $\{10\bar{1}0\}$ planes, planes containing extremal orbits no longer contain H . However, since the main bulk of the humbugs still appears to be reasonably 1-OPW-like, the positions of such planes may be assumed to be approximately as in the 1-OPW model. This approximation together with the experimental observation that the γ oscillations disappear at 17° from $\langle 11\bar{2}0 \rangle$ leads to a neck 'radius' along $\langle 11\bar{2}0 \rangle$ of $0.029(\pm 0.003)$ a.u. It is reasonable to expect that because of its small size the neck will be

approximately circular in cross-section and hence these two estimates are consistent. Model (b) is thus capable of accounting quantitatively for the angular range of γ .

From the radii quoted, the neck frequency at $\langle 0001 \rangle$ is estimated as $7.80 (\pm 1.8) 10^5$ G. Reference to Fig. 7 shows that only α falls within this range and is probably derived from the neck orbit if model (b) is correct. Further points consistent with this interpretation are: Firstly, the area of the neck cross-section should increase faster than that for a cylinder in accordance with the observations for α ; secondly, semi-quantitative estimates indicate that the neck orbits are not likely to exist for field orientations greater than 55° from $\langle 0001 \rangle$, which is consistent with the experimental range for α .

The above arguments strengthen the validity of model (b) as a representation of the FS and lead to a consideration of the butterflies M_6 . In the 1-OPW model, M_6 orbits are possible only at certain orientations because of the presence of the humbugs. In model (b) they are possible at all orientations and hence a process identical to that for the humbugs was performed whereby only the spheres defining any one of the butterflies in the Harrison construction were used and the frequency versus angle curves for the resultant figures were constructed. It then appears probable that the orbits M_6 give rise to both the ϵ and β oscillations for the following reasons. Firstly, the existence of two ϵ branches in the basal plane limits the origin of ϵ , for reasons of symmetry, to M_6 , M_7 , M_8 or L_5 . The first and last possibilities may be eliminated as their 1-OPW frequencies are too low and are expected to be even lower for the real FS. M_7 also appears an unlikely interpretation for several reasons. Secondly, the 1-OPW frequencies of M_6 at $\langle 10\bar{1}0 \rangle$ and $\langle 0001 \rangle$ are $1.46 \cdot 10^7$ and $1.82 \cdot 10^7$ G respectively compared with the ϵ and β values at $\langle 10\bar{1}0 \rangle$ and $\langle 0001 \rangle$ of $1.31 \cdot 10^7$ and $1.49 \cdot 10^7$ G. Thirdly, the combined ϵ - β curves exhibit the basic features of the butterflies. The frequency

maxima in the $(11\bar{2}0)$ and $(10\bar{1}0)$ planes occur as the orbits pass over the 'wings' of the butterflies. Practically, as mentioned in Section 5, it was not possible to observe oscillations at or near this maximum. This may be understood in terms of the relatively high curvature for the FS at this orientation. Also, the frequencies of the maximum as extrapolated from the β and ϵ curves on either side are considerably less than in the 1-OPW model,

an observation which is consistent with the expected modifications in the presence of the finite lattice potential.

The foregoing arguments favour the connectivity of the model (b) for the FS and lead to the construction for the FS in the 6th zone depicted in Fig. 20. This model also explains the existence of the ζ oscillations, in terms of orbits about the humbugs. Along $(11\bar{2}0)$ the planes containing extremal orbits do not pass

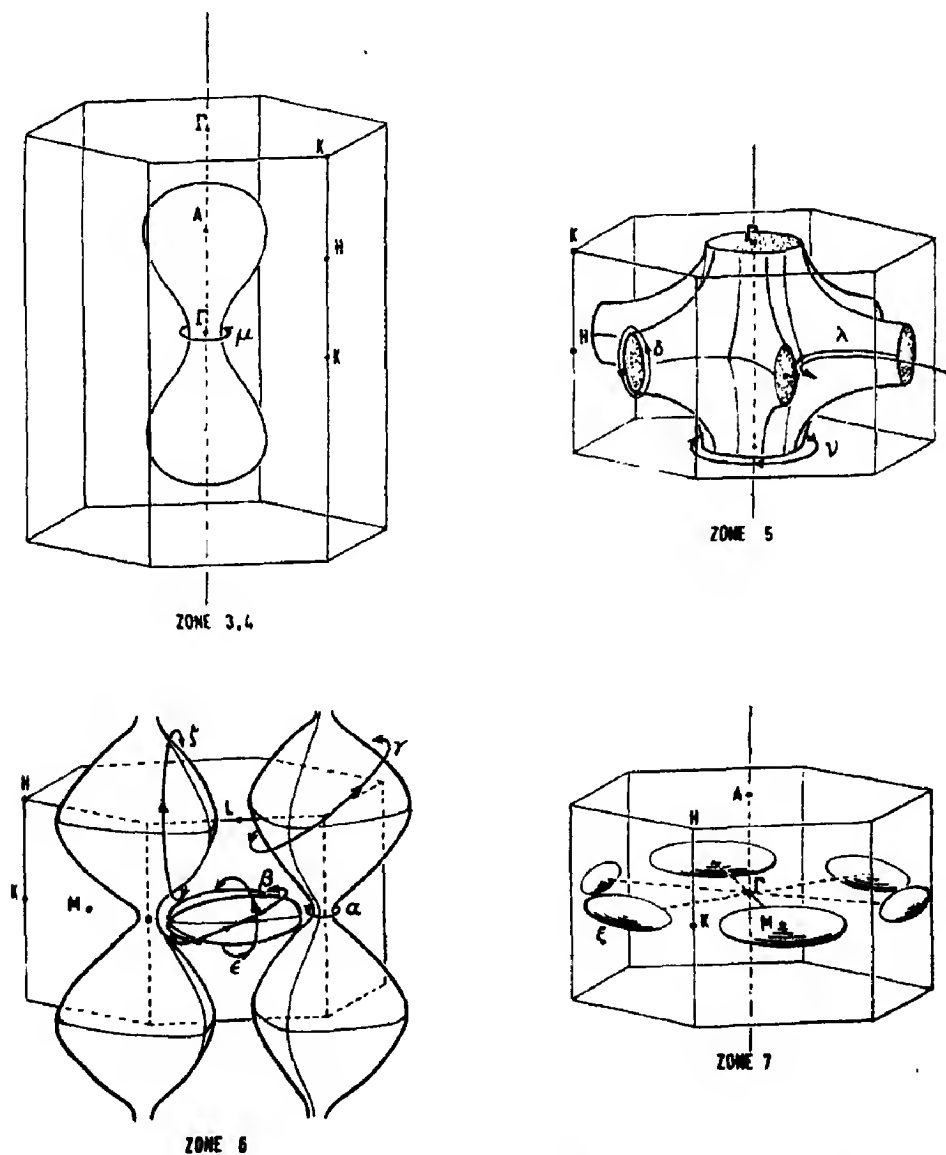


Fig. 20. Proposed model for the Fermi surface of AuSn, showing the origins of the various frequencies found experimentally.

through H and such orbits may exist in our model. As the field is rotated from $\langle 11\bar{2}0 \rangle$ the range of ζ is determined by the angle at which the plane becomes tangential to the necks, K_6 . Estimates show that ranges determined in this way are in agreement with those observed.

The observation of 6th zone orbits experimentally indicates that magnetic breakdown is not important between zones 5 and 6 in fields up to 100 kG. Further, two branches may be associated with 5th zone extremal orbits. H_5 exists between the $\langle 10\bar{1}0 \rangle$ directed arms and along $\langle 0001 \rangle$ is degenerate in frequency with H_6 in the 1-OPW model. The natural interpretation is in terms of the λ oscillations whose limited range and rapid frequency increase away from $\langle 0001 \rangle$ are consistent with this model. The 1-OPW frequency for H_5 ($7.36 \cdot 10^7$ G) agrees reasonably well with the value of $6.96 \cdot 10^7$ G for λ . Orbits L_5 around the arms give rise to the δ oscillations, for which we can find no other equally plausible interpretation. The branching of δ in the basal plane is consistent with the symmetry at L and the measured frequency along $\langle 10\bar{1}0 \rangle$ ($1.86 \cdot 10^6$ G) is in reasonable agreement with the 1-OPW value of $3.41 \cdot 10^6$ G.

The ν oscillations are difficult to interpret unambiguously. The fact that they closely parallel the β curves, suggests that ν may, like β , be derived from the butterflies. This suggestion is reinforced by a possible interpretation of the ϵ amplitude anomaly and is mentioned in Section 7. Other possible sources of ν are A_4 and Γ_5 ($3.36 \cdot 10^7$ and $3.28 \cdot 10^7$ G respectively at $\langle 0001 \rangle$).

The ξ and ρ oscillations were only visible at or very close to $\langle 11\bar{2}0 \rangle$. On the basis of the 1-OPW model and the interpretations so far, only the orbits A_3 , M_8 and M_7 offer possible interpretations. M_7 has a frequency at $\langle 11\bar{2}0 \rangle$ of $4.78 \cdot 10^6$ G which agrees reasonably well with the experimental data. Furthermore, the rapid variation of frequency with angle near $\langle 11\bar{2}0 \rangle$ in the 1-OPW model offers a possible solution to the two different measurements of ξ in terms of small differ-

ences in orientation between experiments. It is thus proposed that both ρ and ξ originate from orbits about the seventh zone surfaces.

Finally, there is the observation of μ along $\langle 0001 \rangle$. Assuming that zone 8 is empty, M_7 and Γ_4 are both possible sources.

7. FERMI SURFACE OF AuSn

The previous section has shown that a consistent interpretation of the experimental results is possible in terms of a FS based on the 1-OPW model. Of the observed frequencies, seven may be unambiguously associated with features of this model, whilst the remaining four (ν , ρ , μ , ξ) have less certain interpretations. This arises because of an excess rather than a lack of possible explanations.

The single zone model has been used for zones 5 and 6, implying that spin-orbit effects in AuSn are large. For γ , the magnetic field dependence of the dHvA amplitude shows no signs of the effects of magnetic breakdown up to 95 kG. An estimate of the energy gap across the $\{0001\}$ face applicable to γ and λ may be made from the effective masses of these orbits. We have

$$m^*/m_0 = (\hbar^2/2\pi) \partial A / \partial E \approx (\hbar^2/2\pi) \Delta A / \Delta E.$$

From Table 2 the average of the two similar effective mass ratios is 0.62 and from the experimental frequency difference between γ and λ along $\langle 0001 \rangle$, a value for ΔE of 0.16 eV is obtained. From the expression of Blount[33] relating breakdown field H_0 and energy gap we obtain $H_0 = 250$ kG. This figure is approximate since ΔE would not be expected to be constant around these orbits. It is, however, consistent with the lack of breakdown phenomena in the observations on γ . Further, in the $\langle 11\bar{2}0 \rangle$ plane, γ orbits pass through the characteristic line S' at a point P such that $LP:PH \sim 1:4$. Since the spin-orbit gaps are zero at L and a maximum at H , the implication is that the breakdown field at H must be high, probably several hundred kilogauss at least. Estimates based on the atomic spin-splitting

parameters indicate a value for H_0 of 2.5 . 10⁶ G, although it is doubtful whether such estimates are reliable for heavy metals such as gold and tin.

The δ oscillations were visible along $\langle 10\bar{1}0 \rangle$ up to 100 kG whereas at $\langle 11\bar{2}0 \rangle$ they disappeared for fields higher than approximately 40 kG. The assignation of δ to L_3 means that this phenomenon may be understood in terms of magnetic breakdown. Such an explanation implies that the breakdown field H_0 is varying rapidly across that region of the (0001) face which is of interest here. Thus, the observed variations in the breakdown field at $\langle 11\bar{2}0 \rangle$ (35–50 kG) were very possibly caused by slight differences of orientation between experiments.

In zones 3 and 4 there is little direct evidence of the form of the FS apart from the tentative assignment of μ to Γ_4 . The lack of observation of any frequency that could be associated with the 3rd zone hole surface is somewhat surprising. This surface is fairly isotropic in form and is a feature one would normally expect to observe. The most probable explanation is that breakdown occurs at relatively low fields (< 30 kG). The surface is centred at A where H_0 is theoretically zero and the orbits A_3 probably encounter energy gaps considerably smaller than in the case of the γ orbits. Based on these observations, it is proposed that, for fields greater than ~ 30 kG the FS in the 3rd and 4th zones is as depicted in Fig. 20.

In the light of the source of the ϵ oscillations, it is possible to propose an explanation of the anomaly in the ϵ amplitude. This anomaly was analysed in terms of two similar frequencies which appeared to remain within 0.3 per cent of each other over an angular region extending to 45° from $\langle 10\bar{1}0 \rangle$. The higher frequency of the two was found to have the lower amplitude at limitingly high fields indicating a higher value for the appropriate FS curvature (A'' in 2.5). It is possible to interpret this phenomenon in terms of two extremal orbits about the butterflies. In the

1-OPW model the central orbits M_0 are minima for fields along $\langle 10\bar{1}0 \rangle$ and $\langle 0001 \rangle$ showing that non-central extremal orbits with a maximal area must exist. If this remains true for the real FS then it is possible that the oscillations composing ϵ are derived from these two extrema. This theory is strengthened by the fact that the higher frequency experimentally has the higher value of A'' , as might be expected. Similarly the β and ν oscillations might be explicable in these terms, the β frequency being derived from the central orbit and ν from the non-central one.

In connection with the work pertaining to the FS in AuSn, Jan and Pearson[10] have observed a pronounced anisotropy in their measurements of the thermoelectric power of AuSn. Along $\langle 10\bar{1}0 \rangle$ there is a maximum in the thermopower at 25°K, a feature which is almost absent from measurements along $\langle 0001 \rangle$. It has been noted that a possible explanation for this phenomenon, attributed to anisotropic phonon-drag, is the existence in AuSn of a FS consisting of undulating cylinders with their axes along $\langle 0001 \rangle$ [10]. In the $\{0001\}$ plane, these cylinders would be close enough to allow Umklapp processes for phonons of wave vector greater than a minimum q . It is interesting to note that such features are present in the model proposed here for the FS. In zone 6 the interconnected humbugs form undulating cylinders along $\langle 0001 \rangle$. Estimates made from the closest distance of approach of two such cylinders along $\langle 10\bar{1}0 \rangle$ show that semi-quantitatively these features could produce positive phonon-drag peaks in the temperature region measured by Jan and Pearson[10].

Sellmyer and Schroeder[12] and Sellmyer[1] have investigated the magnetoresistance of AuSn in magnetic fields up to 150 kG. Their work shows AuSn to be a compensated metal which supports open orbits along the three symmetry directions $\langle 11\bar{2}0 \rangle$, $\langle 10\bar{1}0 \rangle$ and $\langle 0001 \rangle$. From the results of the present study, since magnetic breakdown is not important between zones 5 and 6

in fields up to 100 kG, the FS also represents a compensated metal. Furthermore, primary open orbits along the three symmetry directions are possible in zone 5. Those along $\langle 0001 \rangle$ exist for all field directions in the basal plane while $\langle 11\bar{2}0 \rangle$ and $\langle 10\bar{1}0 \rangle$ orbits are possible only for certain field orientations. As evident from Fig. 20, zone 6 will also support open orbits along $\langle 0001 \rangle$ for all field directions in the basal plane. The proposed model for the FS is thus topologically consistent with the high field galvanomagnetic properties of AuSn.

Acknowledgements—We wish gratefully to acknowledge the assistance of members of the low temperature group of the Division of Pure Physics, N.R.C. of Canada, with whom we have been in close association during the course of this investigation. In particular we wish to thank W. B. Pearson and J. P. Jan for illuminating discussions. A. Beck for growing the single crystals and R. Taylor for developing the programme for the 1-OPW calculations. We should also like to thank P. Schroeder for his helpful comments on the manuscript and D. J. Sellmyer for details of his work on AuSn prior to publication. The experimental assistance of G. B. Scott and J. R. Stockton is also gratefully acknowledged.

REFERENCES

1. SELLMYER D. J., *J. Phys. Chem. Solids* **30**, 2371 (1969).
2. THORSEN A. C. and BERLIN COURT, T. G. *Nature* **192**, 959 (1961).
3. SAITO Y., *J. phys. Soc. Japan*, **17**, 716 (1962).
4. VEAL B. W. and RAYNE J. A., *Phys. Lett.* **6**, 12 (1963).
5. BECK A., JAN J.-P., PEARSON W. B. and TEMPLETON I. M., *Phil. Mag.* **8**, 351 (1963).
6. JAN J.-P., PEARSON W. B. and SPRINGFORD M., *Can. J. Phys.* **42**, 2537 (1964).
7. JAN J.-P., PEARSON W. B. and SPRINGFORD M., *9th Intl Conf. on Low Temperature Physics* (1964).
8. JAN J.-P., PEARSON W. B. and SAITO Y., *Proc. R. Soc. A* **297**, 275 (1967).
9. JAN J.-P., PEARSON W. B., SAITO Y., SPRINGFORD M. and TEMPLETON, I. M., *Phil. Mag.* **12**, 1271 (1965).
10. JAN J.-P. and PEARSON W. B., *Phil. Mag.* **8**, 911 (1963).
11. JAN J.-P., PEARSON W. B., KJEKSHUS A. and WOODS S. B., *Can. J. Phys.* **41**, 2252 (1963).
12. SELLMYER D. J. and SCHROEDER P. A., *Phys. Lett.* **16**, 100 (1965).
13. HAMILTON D. A., RAUB CH. J., MATTHIAS B. T., CORERZWIET E. and HULL G. W., *J. Phys. Chem. Solids* **26**, 665 (1965).
14. EDWARDS G. J., PEARSON W. B., SAITO Y. and SPRINGFORD M., *10th Intl Conf. on Low Temperature Physics* (1966).
15. ONSAGER L., *Phil. Mag.* **43**, 1006 (1952).
16. LIFSHITZ I. M. and KOSEVICH A. M., *J. exp. theor. Phys.* **2**, 636 (1955).
17. DINGLE R. B., *Proc. R. Soc. A* **211**, 517 (1952).
18. COHEN M. H. and BLOUNT E. I., *Phil. Mag.* **5**, 115 (1960).
19. O'SULLIVAN W. J. and SCHIRBER J. E., *Phys. Rev. Lett.* **16**, 691 (1966).
20. SHOENBERG D. and STILES P. J., *Proc. R. Soc. A* **281**, 62 (1964).
21. GOLDSTEIN A., WILLIAMSON S. J. and FONER S., *Rev. scient. Instrum.* **36**, 1356 (1965).
22. These crystals were prepared by BECK A. at the N.R.C. of Canada, Ottawa.
23. BEAN C. P., DE BLOIS R. W. and NESBITT L. B., *J. appl. Phys.* **30**, 1976 (1959).
24. STERN R., LEVY M., KAGIWADA R. and RUDNICK I., *Appl. Phys. Lett.* **2**, 80 (1963).
25. EDWARDS G. J., DARBY C. and SPRINGFORD M., To be published.
26. SCOTT G. B., SPRINGFORD M. and STOCKTON J. R., *J. scient. Instrum.* **1**, 925 (1968).
27. PHILIPS J. C. and KLEINMAN L., *Phys. Rev.* **116**, 287 (1959); *ibid.* **118**, 1153 (1960).
28. HEINE V., *Proc. R. Soc. A* **240**, 340, 354, 361 (1957).
29. HARRISON W. A., *Phys. Rev.* **126**, 497 (1962).
30. COHEN M. H. and FALICOV L. M., *Phys. Rev. Lett.* **5**, 44 (1960).
31. PRIESTLEY M. G., *Phys. Rev.* **148**, 580 (1966).
32. HARRISON W. A., *Phys. Rev.* **116**, 555 (1959).
33. BLOUNT E. I., *Phys. Rev.* **126**, 1636 (1962).

MODEL BAND STRUCTURES IN NONLINEAR OPTICS

K. C. RUSTAGI

Tata Institute of Fundamental Research, Bombay, India

(Received 17 September 1968; in revised form 5 March 1969)

Abstract—Calculation of linear and nonlinear optical susceptibilities is considered in the band theory formulation. A simple two band model is found to be useful in the discussion of $\chi^{(1)}$ and $\chi^{(3)}$, the first and third order susceptibilities respectively and unsuitable for a description of the second order susceptibility $\chi^{(2)}$. The restrictions placed on the two band and three band models by the general results of band theory are discussed and the role of space inversion symmetry is assessed.

It is shown that Kane's model for the band structure of small gap III-V compounds provides a suitable basis for a discussion of $\chi^{(2)}$. Proper inclusion of the spin orbit coupling is found to be crucial for this purpose, and a direct relationship between the k -linear terms in the valence bands and $\chi^{(2)}$ is established in this model. The agreement of rough estimates of the magnitudes of the k -linear terms based on the observed values of $\chi^{(2)}$ with Dresselhaus' estimate of these terms seems to support our basic assumptions. It is apparent from our results that a refined calculation of the imaginary part of $\chi^{(2)}$ and its comparison with the suggested experiments will yield quantitative determination of parameters depending directly on the inversion asymmetric part of the crystal potential.

1. INTRODUCTION

THE LINEAR and nonlinear electromagnetic response of a solid can, in principle, be understood (we ignore many body effects) if we know the eigenstates of the one electron Hamiltonian \mathcal{H} of the system. Including spin orbit (s.o.) coupling one can write [1]

$$\mathcal{H} = (p^2/2m) + V(\mathbf{x}) + (\hbar/4m^2c^2)(\boldsymbol{\sigma} \times \nabla V) \cdot \mathbf{p} \quad (1.1)$$

where $V(\mathbf{x})$ is the periodic potential, \mathbf{p} is the electron momentum and the components σ_i of $\boldsymbol{\sigma}$ are the Pauli spin matrices. The general eigenstates of \mathcal{H} are expressed in the Bloch form as

$$\psi_{\mathbf{k}}(\mathbf{x}) = \frac{1}{\sqrt{N}} e^{i\mathbf{k} \cdot \mathbf{x}} u_{\mathbf{k}}(\mathbf{x}) \quad (1.2)$$

where N is the number of unit cells in the sample, r is the band index and the wave vector \mathbf{k} lies in the first Brillouin zone. $u_{\mathbf{k}}$ is the lattice periodic Pauli spinor which is separable into its space and spin parts only if the s.o. coupling is neglected. The general expressions for the linear and nonlinear

current-densities (or susceptibilities) are given by several authors[2]. Usually, it suffices to consider only the long wavelength limit of the susceptibilities. In Section 2 of the present paper we briefly mention the general properties of Bloch states and write the expressions for various susceptibilities in a suitable form. Throughout this paper we work in the *long-wavelength limit* and also neglect the *Umklapp processes*.

As is well known[3] a large fraction of our information about Bloch states in various solids is obtained by studying the fundamental optical spectra. In principle, it is clear from the general expressions for higher order optical susceptibilities that a study of these will yield important information (not available from the linear data) about the electronic eigenstates of the solid[4]. In practice, however, because of the accompanying increase in the complexity of the experiments and the theoretical analysis involved, nonlinear optical methods have rarely been used to infer the band structure properties of the solid[5]. The most notable exception is the direct study of the nonparabolicity of the conduction band of many *n*-type semiconductors by performing

third order optical mixing experiments[6, 7]. An accurate determination of nonparabolicity is made possible by separation of $\chi^{(3)a}$ and $\chi^{(3)b}$ the conduction and bound electron contributions to the third order susceptibility. $\chi^{(3)a}$ provides the most direct measurement of the nonparabolicity of the conduction band because it vanishes if the conduction band is parabolic. Similarly, the study of $\chi^{(2)}$, the second order susceptibility, should provide direct information about band structure parameters which vanish for centrosymmetric solids, since $\chi^{(2)}$ vanishes in the long wavelength (dipole) limit for centrosymmetric solids. A calculation of $\chi^{(2)}$ and $\chi^{(3)b}$ from the general expressions[2] is very difficult because our knowledge of the Bloch states is not adequate for most materials of interest. In view of this, two approaches were used in the past.

Simple model band structures[8-10] have been used with some success to calculate the optical response. Such models have also been used in the study of Bloch electrons in d.c. electric and magnetic fields[11, 12]. In Section 3 of the present paper we study the second and third order susceptibilities in simple two band and three band models, employing the general properties of Bloch states and the f -sum rule to relate the various parameters involved in a consistent manner. The limitations and the uses of such models then become evident.

Because of the difficulties mentioned above some recent papers have abandoned[7, 13, 14] the basis provided by the general expressions for susceptibilities in terms of Bloch states. These theories calculate the low frequency limit of $\chi^{(2)}$ for III-V compounds in terms of bonding orbitals and bond polarizabilities. Although the rough agreement between theory and experiments is generally encouraging, such an approach has obvious shortcomings e.g. the neglect of dispersion in the higher order susceptibilities and difficulties in application to the more ionic solids. Further, these calculations do

not provide any *quantitative* information about the electronic eigenstates of the solid. In Section 4 of the present paper we show that Kane's model[15] for the band structure of InSb can be used successfully to discuss the second order susceptibilities of small band gap III-V compounds. In these compounds with zinc blende structure, we find that $\chi^{(2)}$ is related to the k -linear terms in the valence bands in a direct manner. We find an adequate inclusion of the s.o. coupling crucial to our discussion since even for non-centrosymmetric solids the k -linear terms vanish because of time reversal invariance, when the s.o. coupling is neglected[16]. The connection between $\chi^{(2)}$ and the k -linear terms is very important since no experimental information is yet available about the k -linear terms in the valence bands of III-V compounds. However, it is believed[17] that a detection of k -linear terms should be feasible in extremely accurate magneto-optical experiments.

It should be remarked that approximations in our calculation are related to those in the bonding orbital calculations of $\chi^{(2)}$. We assume that it suffices to consider the 4 band complex consisting of a doubly degenerate s -band and three doubly degenerate p -bands while the bonding orbital calculations consider the s - p tetrahedral bonding orbitals. In Section 5 we discuss this connection and the possible refinements in our calculation in view of the suggested experimental investigations.

2. BLOCH STATES AND SUSCEPTIBILITY TENSORS

(a) General properties of Bloch states

For every k in the 1 Brillouin Zone the Bloch states occur in pairs $\psi_{k\uparrow}$ and $\psi_{k\downarrow}$ with $E_{k\uparrow}$ and $E_{k\downarrow}$ as the corresponding energies. We omit the band index here for the sake of clarity. Time reversal invariance of the Hamiltonian gives

$$-(\psi_{-k\downarrow}, \sigma_z \psi_{-k\downarrow}) = (\psi_{k\uparrow}, \sigma_z \psi_{k\uparrow}) (\geq 0) \quad (2.1)$$

and

$$E_{\mathbf{k}\uparrow} = E_{-\mathbf{k}\downarrow}. \quad (2.2)$$

Thus, in general $\psi_{\mathbf{k}\uparrow}$ and $\psi_{\mathbf{k}\downarrow}$ refer to a pair of different bands which are degenerate at $\mathbf{k} = 0$. If $V(\mathbf{x})$ has a center of inversion the bands are doubly degenerate throughout the Brillouin zone such that

$$E_{\mathbf{k}\uparrow} = E_{\mathbf{k}\downarrow} = E_{-\mathbf{k}\uparrow} = E_{-\mathbf{k}\downarrow} \quad (2.3)$$

and

$$KJ\psi_{\mathbf{k}\uparrow}(\mathbf{x}) = \psi_{\mathbf{k}\downarrow}(\mathbf{x}) \quad (2.4)$$

apart from an unimportant phase factor, where K is the time reversal operator and J denotes the space inversion operator.

Including the s.o. coupling, the kinetic momentum operator π is defined by

$$\pi = \mathbf{p} + (\hbar/4mc^2)\boldsymbol{\sigma} \times \nabla V(\mathbf{x}). \quad (2.5)$$

Time reversal invariance of \mathcal{H} gives

$$\begin{aligned} \langle r_0, \rho, \mathbf{k} | \pi | s_0, \rho', \mathbf{k}' \rangle \\ = -\langle r_0, -\rho, -\mathbf{k} | \pi | s_0, -\rho', -\mathbf{k}' \rangle^* \end{aligned} \quad (2.6)$$

apart from an unimportant phase factor. Here, r_0 and s_0 denote the pairs of bands and ρ and ρ' are the spin indices (\uparrow, \downarrow). We use the notation

$$\begin{aligned} \langle r_0, \rho, \mathbf{k} | \theta | s_0, \rho', \mathbf{k}' \rangle \\ = \int_{\text{entire crystal}} \psi_{r_0, \rho, \mathbf{k}}^+(\mathbf{x}) \theta \psi_{s_0, \rho', \mathbf{k}'}(\mathbf{x}) d^3x \end{aligned} \quad (2.7)$$

and

$$\begin{aligned} \langle r_0, \rho, \mathbf{k} | \theta | s_0, \rho', \mathbf{k}' \rangle \\ = \int_{\text{unit cell}} u_{r_0, \rho, \mathbf{k}}^+(\mathbf{x}) \theta u_{s_0, \rho', \mathbf{k}'}(\mathbf{x}) d^3x \end{aligned} \quad (2.8)$$

where θ is any operator. Orthonormality and completeness properties of Bloch states and of the lattice periodic spinors $u_{r\mathbf{k}}$ lead to some very important results [18]. Denoting the pair

(r_0, ρ) of indices by a single band index r we have†

$$\begin{aligned} \frac{\hbar}{m} \langle r\mathbf{k} | \pi^\mu | s\mathbf{k} \rangle = \delta_{r,s} \left[-(E_{r\mathbf{k}} - E_{s\mathbf{k}}) \left(r\mathbf{k} \left| \frac{\partial}{\partial \mathbf{k}^\mu} \right| s\mathbf{k} \right) \right. \\ \left. + \delta_{r,s} \frac{\partial E_{r\mathbf{k}}}{\partial k^\mu} \right]. \end{aligned} \quad (2.9)$$

Allowing only for a certain type of degeneracies, one can prove the f -sum rule

$$\begin{aligned} \frac{1}{\hbar^2} \frac{\partial^2 E_{r\mathbf{k}}}{\partial k^\mu \partial k^\nu} = \frac{1}{m} \delta^{\mu, \nu} \\ + \sum_r \frac{\pi_{rs}^\mu \pi_{sr}^\nu + \text{complex conjugate (c.c.)}}{m^2 \hbar \omega_{rs}} \end{aligned} \quad (2.10)$$

where,

$$\pi_{rs}^\mu = \langle r\mathbf{k} | \pi^\mu | s\mathbf{k} \rangle \quad (2.11)$$

and

$$\hbar \omega_{rs} = E_{r\mathbf{k}} - E_{s\mathbf{k}}. \quad (2.12)$$

For brevity the \mathbf{k} dependence of π_{rs}^μ and ω_{rs} is not written explicitly. The prime on the summation in equation (2.10) denotes that the terms corresponding to $\omega_{rs} = 0$ are excluded. The type of degeneracies allowed are those for which $\psi_{r\mathbf{k}}(\mathbf{x})$ still form a complete set of orthonormal states and the differentiability of $\psi_{r\mathbf{k}}$ with respect to \mathbf{k} can be assumed. Degeneracies due to time reversal invariance and space inversion symmetry are thus expected to be allowed degeneracies. We close this subsection with the remark that when s.o. coupling is neglected we can treat the Bloch states $\psi_{r\mathbf{k}}(\mathbf{x})$ as one component functions with the proviso that each state (r, \mathbf{k}) can be occupied by two electrons.

†The Greek indices denote cartesian components. The differentiability of $\psi_{r\mathbf{k}}$ with respect to \mathbf{k} , is assumed, which is justified in most cases. See [18] for an elaborate discussion of this point.

(b) *General expressions for susceptibility tensors*

In the electric dipole approximation for the electromagnetic field the n th order susceptibility tensor $\chi_{\mu\alpha_1\alpha_2\ldots\alpha_n}^{(n)}(\omega_1, \omega_2, \ldots, \omega_n)$ can be defined by

$$J_\mu^{(n)}(\omega_1 + \omega_2 + \ldots + \omega_n) = -i(\omega_1 + \omega_2 + \ldots + \omega_n) \times \chi_{\mu\alpha_1\alpha_2\ldots\alpha_n}^{(n)}(\omega_1, \omega_2, \ldots, \omega_n) \times \epsilon_{\alpha_1}(\omega_1)\epsilon_{\alpha_2}(\omega_2)\ldots \times \epsilon_{\alpha_n}(\omega_n) + \text{terms obtained by taking distinct permutations of frequencies } \omega_1, \omega_2, \ldots, \omega_n, \quad (2.13)$$

where we have followed the convention [7] of Jha and Bloembergen to expand the current density $J(t)$ and the electric field $\epsilon(t)$ as

$$J(t) = \sum_{\omega} e^{-i\omega t} J(\omega) \quad (2.14)$$

and

$$\epsilon(t) = \sum_{\omega} e^{-i\omega t} \epsilon(\omega) \quad (2.15)$$

where

$$\epsilon(-\omega) = \epsilon^*(\omega) \quad (2.16)$$

and

$$J(-\omega) = J^*(\omega). \quad (2.17)$$

Using time reversal invariance of \mathcal{H} one can show that the linear susceptibility tensor can be written as

$$\chi_{\mu\alpha}^{(1)}(\omega) = -\frac{e^2}{m\omega^2} \sum_{r,s,k} \times f(r, \mathbf{k}) \left[\delta^{\mu,\alpha} + f_{r,s}^{\mu,\alpha} \cdot \frac{\omega^2}{\omega_{rs}^2 - \omega^2} \right] \quad (2.18)$$

where $f(r, \mathbf{k}) \equiv f(E_{r\mathbf{k}})$ is the Fermi occupation number at the energy $E_{r\mathbf{k}}$ and the oscillator strength tensor, $f_{r,s}^{\mu,\alpha}(\mathbf{k})$ defined by

$$f_{r,s}^{\mu,\alpha}(\mathbf{k}) = \frac{\pi_{rs}^{\mu}\pi_{sr}^{\alpha} + \text{c.c.}}{m\hbar\omega_{rs}} \quad (2.19)$$

is related to the effective mass tensor $(1/\hbar^2)(\partial^2 E_{r\mathbf{k}})/\partial k^\mu \partial k^\alpha$ and $(1/\hbar^2)(\partial^2 E_{s\mathbf{k}}/\partial k^\mu \partial k^\alpha)$.

The separation of $\chi_{\mu\alpha}^{(1)}$ into intra- and inter-band contributions is straightforward and leads to the familiar definition of the optical effective mass. The expressions for the second and third order susceptibility tensors can be written as

$$\chi_{\mu\alpha\beta}^{(2)}(\omega_1, \omega_2) = \frac{-e^3}{4im^3\hbar^2\omega_1\omega_2\omega_{12}} \sum_p P(\alpha\omega_1, \beta\omega_2) \times (1 + \zeta) \sum_{rst\mathbf{k}} (f(r\mathbf{k}) - f(s\mathbf{k})) \times \frac{\pi_{rs}^{\alpha}\pi_{st}^{\beta}\pi_{tr}^{\mu} - \text{c.c.}}{(\omega_{rs} - \omega_1)(\omega_{rt} - \omega_{12})} \quad (2.20)$$

and

$$\chi_{\mu\alpha\beta\gamma}^{(3)}(\omega_1, \omega_2, \omega_3) = \frac{e^4}{6m^4\omega_1\omega_2\omega_3\omega_{123}\hbar^3} \times \sum_p P(\alpha\omega_1, \beta\omega_2, \gamma\omega_3) \times (1 + \zeta) \sum_{rstu\mathbf{k}} (f(r\mathbf{k}) - f(s\mathbf{k})) \times \text{Re} \left[\frac{\pi_{rs}^{\alpha}\pi_{st}^{\beta}}{(\omega_{rs} - \omega_1)(\omega_{rt} - \omega_{12})} \times \left(\frac{\pi_{tu}^{\gamma}\pi_{ur}^{\mu}}{(\omega_{ru} - \omega_{123})} - \frac{\pi_{tu}^{\mu}\pi_{ur}^{\gamma}}{(\omega_{ut} - \omega_{123})} \right) \right] \quad (2.21)$$

where $\omega_{12} = \omega_1 + \omega_2$, $\omega_{123} = \omega_1 + \omega_2 + \omega_3$ etc. $P(\alpha\omega_1, \beta\omega_2, \gamma\omega_3)$ are the permutation operators of objects $\alpha\omega_1, \beta\omega_2, \gamma\omega_3$ and the operator ζ takes the complex conjugate and changes all ω_i to $-\omega_i$ ($i = 1, 2, 3$). We have made use of the time reversal invariance of \mathcal{H} (expressed in equations (2.2) and (2.6)) in writing the above expressions for $\chi_{\mu\alpha\beta}^{(2)}$ and $\chi_{\mu\alpha\beta\gamma}^{(3)}$ which can be easily shown to be equivalent to those written by Butcher and Mclean [2]. The above form seems more suitable for actual computation of $\chi_{\mu\alpha\beta}^{(2)}$ and $\chi_{\mu\alpha\beta\gamma}^{(3)}$ since the presence of $(f(r\mathbf{k}) - f(s\mathbf{k}))$ reduces the number of values s could take for a given r .

It is important to notice here that when we include the s.o. coupling in our discussion we always have some energy gaps which vanish at $\mathbf{k} = 0$ apart from the degeneracy at other points of special symmetry. Therefore, it becomes necessary to show that the low frequency limit is a well defined limit. To do this we first put $\omega_1 = \omega_2 = \omega_3 = \omega$ and then rewrite $\chi_{\mu\alpha\beta}^{(2)}$ and $\chi_{\mu\alpha\beta\gamma}^{(3)}$, after some simplification, as

$$\chi^{(2)} = \sum_{r\mathbf{k}} (f(r\mathbf{k}) - f(s\mathbf{k})) \times \left(\frac{\mathbf{Q}_{rs}^{(1)}(\mathbf{k})}{\omega_{rs}^2 - \omega^2} + \frac{\mathbf{Q}_{rs}^{(2)}(\mathbf{k})}{\omega_{rs}^2 - 4\omega^2} \right) \quad (2.22)$$

and

$$\chi^{(3)} = \frac{1}{\omega^3} \sum_{r\mathbf{k}} (f(r\mathbf{k}) - f(s\mathbf{k})) \times \left(\frac{\mathbf{Q}_{rs}^{(3)}(\mathbf{k})}{\omega_{rs}^2 - \omega^2} + \frac{\mathbf{Q}_{rs}^{(4)}(\mathbf{k})}{\omega_{rs}^2 - 4\omega^2} + \frac{\mathbf{Q}_{rs}^{(5)}(\mathbf{k})}{\omega_{rs}^2 - 9\omega^2} \right) \quad (2.23)$$

where the functions \mathbf{Q}_{rs} involve summations over intermediate states and are all real, frequency independent and odd under the interchange of r and s . The equation (2.22) is essentially a generalized form of equation (1) of Chang *et al.*[4] for χ_{14} in crystals with ZnS structure. One excludes those points in the \mathbf{k} -summation for which the factors \mathbf{Q}_{rs} have poles. From equations (2.22) and (2.23) it is evident that only those r and s are included in the sum for which $\omega_{rs} \neq 0$ so that the low frequency limit is essentially valid when $(\omega/\omega_{rs}) \ll 1$. It should also be remarked that equation (2.22) shows that the second order susceptibility goes to a constant value as $\omega \rightarrow 0$.

In general, the second order susceptibility can be separated into two parts: a two band part in which the band index t in equation (2.20) equals one of the two unequal band indices r and s , and a three band part in which all the indices r, s, t are unequal. Similarly,

$\chi_{\mu\alpha\beta\gamma}^{(3)}$ can be separated into 3 parts, a four band part, a three band part and a two band part.

3. GENERAL TWO BAND AND THREE BAND MODELS

The basic premise of a calculation of optical properties based on a model band structure involving a small number of bands is that the set of bands considered interact mainly amongst themselves. The model band structures considered in this section are general in the sense that no particular crystal symmetry is assumed. We do not assume the crystal to possess inversion symmetry since $\chi^{(2)}$ vanishes for centrosymmetric solids in the dipole approximation. For noncentrosymmetric solids the s.o. coupling generally removes the double degeneracy due to spin at a general \mathbf{k} so that the simplest model band structure including s.o. coupling has 4 bands doubly degenerate in pairs at $\mathbf{k} = 0$. In this section we consider the two band and three band models and neglect the s.o. coupling for reasons stated above.

As was remarked in Section 2, $u_{r\mathbf{k}}$ are now considered as one component functions and we can choose the phase convention such that

$$u_{r\mathbf{k}}(\mathbf{x}) = u_{r-\mathbf{k}}^*(\mathbf{x}). \quad (3.1)$$

Equation (2.6) simplifies to

$$(r\mathbf{k}|p^\mu|s\mathbf{k}) = -(r-\mathbf{k}|p^\mu|s-\mathbf{k})^* \quad (3.2)$$

and one can easily show that

$$\langle r\mathbf{k}|p^\mu|s\mathbf{k}' \rangle = \delta_{\mathbf{k},\mathbf{k}'} \left\{ (m/\hbar) \delta_{r,s} \frac{\partial E_{r\mathbf{k}}}{\partial k^\mu} + (1 - \delta_{r,s}) (r\mathbf{k}|p^\mu|s\mathbf{k}) \right\}. \quad (3.3)$$

The matrix elements $\langle r\mathbf{k}|p^\mu|s\mathbf{k} \rangle$, ($r \neq s$) are still complex in general being purely imaginary at $\mathbf{k} = 0$. We define the *modulus* $p_{rs}^\mu(\mathbf{k})$ and the phase $\varphi_{rs}^\mu(\mathbf{k})$ of the matrix element $\langle r\mathbf{k}|p^\mu|s\mathbf{k} \rangle$ by

$$\langle r\mathbf{k}|p^\mu|s\mathbf{k} \rangle = p_{rs}^\mu(\mathbf{k}) \exp(i\varphi_{rs}^\mu(\mathbf{k})). \quad (3.4)$$

One can easily verify the relations

$$p_{rs}^{\mu}(\mathbf{k}) = p_{rs}^{\mu}(\mathbf{k}) = p_{rs}^{\mu}(-\mathbf{k}) \quad (3.5)$$

and

$$\varphi_{rs}^{\mu}(\mathbf{k}) = -\varphi_{sr}^{\mu}(\mathbf{k}) = -\varphi_{rs}^{\mu}(-\mathbf{k}) \\ + \text{an odd multiple of } \pi. \quad (3.6)$$

The f -sum rule (2.10) can now be written as

$$\frac{1}{\hbar^2} \frac{\partial^2 E_{\mathbf{k}}}{\partial k^{\mu} \partial k^{\nu}} - \frac{1}{m} \delta^{\mu\nu} \equiv \alpha_r^{\mu\nu}(\mathbf{k}) \\ = \frac{1}{m} \sum_s f_{rs}^{\mu\nu}(\mathbf{k}) \\ = \sum_s \frac{2 \cos(\varphi_{rs}^{\mu} - \varphi_{rs}^{\nu}) p_{rs}^{\mu} p_{rs}^{\nu}}{m^2 \hbar \omega_{rs}}. \quad (3.7)$$

In a model with only two bands denoted by indices c and v with $\hbar \omega_{cv}$ representing the band gap, the sum in equation (3.7) involves only one term so that the oscillator strength tensor is directly related to the inverse effective mass tensor $\alpha_r^{\mu\nu}$. Using equations (3.2)–(3.7) in equations (2.20)–(2.21) we find

$$\chi_{\mu\alpha\beta}^{(2)}(\omega_1, \omega_2) = \frac{e^3}{2\hbar\omega_1\omega_2\omega_{12}} \sum_p P(\alpha\omega_1, \beta\omega_2) \sum_{\mathbf{k}} \\ \times \frac{f(c\mathbf{k}) - f(v\mathbf{k})}{\omega_{cv}^2 - \omega_1^2} \omega_{cv}^2 \\ \times \left\{ \frac{1}{\omega_{12}} \tan(\varphi^{\alpha} - \varphi^{\beta}) \alpha_c^{\alpha\beta} \frac{\partial \omega_{cv}}{\partial k^{\mu}} \right. \\ \left. + \frac{2\omega_1 + \omega_2}{\omega_{cv}^2 - \omega_{12}^2} \tan(\varphi^{\alpha} - \varphi^{\mu}) \alpha_c^{\mu\alpha} \right. \\ \left. \times \frac{\partial \omega_{cv}}{\partial k^{\beta}} \right\} \quad (3.8)$$

and

$$\chi_{\mu\alpha\beta\gamma}^{(3)}(\omega_1, \omega_2, \omega_3) = \frac{e^4}{6\hbar^2\omega_1\omega_2\omega_3\omega_{123}} \\ \times \sum_p P(\alpha\omega_1, \beta\omega_2, \gamma\omega_3)$$

$$\times \sum_{\mathbf{k}} \frac{f(c\mathbf{k}) - f(v\mathbf{k})}{\omega_{cv}^2 - \omega_1^2} \omega_{cv}^2 \\ \times \left[\frac{\partial \omega_{cv}}{\partial k^{\beta}} \frac{\partial \omega_{cv}}{\partial k^{\mu}} \alpha_c^{\alpha\gamma} \right. \\ \times \frac{2\omega_1 + \omega_2}{(\omega_{cv}^2 - \omega_{12}^2) \omega_{123}} \\ \left. + \frac{\partial \omega_{cv}}{\partial k^{\beta}} \frac{\partial \omega_{cv}}{\partial k^{\gamma}} \alpha_c^{\mu\alpha} \right. \\ \times \frac{(\omega_{cv}^2 + \omega_1\omega_{12} + \omega_1\omega_{123} + \omega_{12}\omega_{123})}{(\omega_{cv}^2 - \omega_{12}^2)(\omega_{cv}^2 - \omega_{123}^2)} \\ \left. + \alpha_c^{\alpha\beta} \alpha_c^{\gamma\mu} (\tan(\varphi^{\alpha} - \varphi^{\beta}) \tan(\varphi^{\gamma} - \varphi^{\mu}) - 1) \right. \\ \left. \times \frac{\hbar \omega_{cv} (\omega_{cv}^2 + (\omega_1 - \omega_2)\omega_{12} - \omega_2^2)}{(\omega_{cv}^2 - \omega_2^2)(\omega_{cv}^2 - \omega_{123}^2)} \right] \quad (3.9)$$

where $\varphi^{\mu} = \varphi_{cv}^{\mu}$ and the \mathbf{k} -dependence of the phase φ^{μ} , the inverse mass tensor $\alpha_c^{\mu\alpha}$ and the energy gap ω_{cv} is not explicitly written. The following results are evident from the above expressions in our general two band model.

(a) The second order susceptibility vanishes even for noncentrosymmetric solids when the inverse effective mass tensor is an isotropic tensor† i.e.

$$\frac{1}{\hbar^2} \frac{\partial^2 E_{c\mathbf{k}}}{\partial k^{\alpha} \partial k^{\beta}} = \frac{1}{m^*} \delta^{\alpha\beta}. \quad (3.10)$$

The above difficulty in the two band model is actually due to the fact that a two band model with isotropic inverse effective mass tensor is not consistent with the f -sum rule. It can be shown that it is not possible to find a vector \mathbf{p}_{cv} such that

$$(p_{cv}^{\alpha} p_{cv}^{\beta*} + \text{c.c.}) = \frac{2}{3} |p_{cv}|^2 \delta^{\alpha\beta} \quad (3.11)$$

unless all the components p_{cv}^{α} vanish. The sum of the tensors $(p_{cv}^{\alpha} p_{cv}^{\beta*})$ over the star of \mathbf{k} is, however, isotropic for all cubic crystals [19].

†A spherical energy band i.e. one for which $E(\mathbf{k}) = E(|\mathbf{k}|)$ implies equation (3.10) as $\mathbf{k} \rightarrow 0$ if $E(|\mathbf{k}|)$ does not contain terms linear in $|\mathbf{k}|$.

(b) For all beams polarized in the same plane, the third order current density is independent of the phase factors $\varphi^\mu(\mathbf{k})$. This is in agreement with the fact that the third order optical mixing experiments[6] do not distinguish the solids possessing a center of inversion from those lacking it. For beams polarized differently we expect a small contribution from the term involving φ^μ 's. This result is, in general, true for the two band contribution to $\chi^{(3)}$ even when we include all pairs of bands.

(c) Equations (2.18) and (3.9) provide some justification for the use of an isotropic effective mass tensor for calculating the linear and third order response of a solid when the incident beams are polarized in the same plane. The isotropic effective mass can now be assumed as an approximation to achieve simplification of the integrations involved.

(d) In a $\mathbf{k} \cdot \mathbf{p}$ two band model with band extrema at $\mathbf{k} = 0$, one can show† that the eigenvalues and eigenfunctions are given by

$$E_{ck} = \frac{1}{2}\hbar^2 k^2/m + \frac{1}{2}E_g \sec \theta_k \quad (3.12)$$

$$E_{ck} = \frac{1}{2}\hbar^2 k^2/m - \frac{1}{2}E_g \sec \theta_k \quad (3.13)$$

$$\psi_{ck}(\mathbf{x}) = \frac{1}{\sqrt{N}} e^{i\mathbf{k} \cdot \mathbf{x}} \times (\cos \frac{1}{2}\theta_k u_{10} - i \sin \frac{1}{2}\theta_k u_{20}) \quad (3.14)$$

and

$$\psi_{ck}(\mathbf{x}) = \frac{1}{\sqrt{N}} e^{i\mathbf{k} \cdot \mathbf{x}} (-i \sin \frac{1}{2}\theta_k u_{10} + \cos \frac{1}{2}\theta_k u_{20}) \quad (3.15)$$

where

$$\tan \theta_k = \frac{2\hbar}{mE_g} \mathbf{k} \cdot \mathbf{p}_{cv}^0 \quad (3.16)$$

u_{10} and u_{20} are the band edge eigenfunctions, $(i\mathbf{p}_{cv}^0)$ is the interband momentum matrix

element at $\mathbf{k} = 0$ which is purely imaginary in our phase convention. The band gap at the center of the zone is denoted by E_g . In this model we obtain

$$\langle c\mathbf{k}|\mathbf{p}|\nu\mathbf{k}\rangle = \cos \theta_k (i\mathbf{p}_{cv}^0) \quad (3.17)$$

so that the phases $\varphi^\mu(\mathbf{k})$ are independent of the index μ which implies vanishing of $\chi_{\mu\alpha\beta}^{(2)}(\omega_1, \omega_2)$. It was pointed out by Kelley[8] that the term linear in \mathbf{k} in the tensor $\langle c\mathbf{k}|\mathbf{p}^\alpha|\nu\mathbf{k}\rangle \langle \nu\mathbf{k}|\mathbf{p}^\beta|c\mathbf{k}\rangle$ (and hence $\chi^{(2)}$ to that order) vanishes if we calculate it in a two (parabolic) band model. Our result is thus a generalization of Kelley's result, to all orders in \mathbf{k} . For $\chi_{\mu\alpha\beta\gamma}^{(3)}$, the results obtained by using energies given in equations (3.12) and (3.13) are same as those obtained in Jha's work[10] for a centrosymmetric solid.

In a three band model, both the two band and the three band contributions appear. The two band terms can again be written in terms of the oscillator strength tensors $f_{rs}^{\alpha\beta}(\mathbf{k})$ and the phases $\varphi_{rs}^\mu(\mathbf{k})$ of the matrix elements $\langle r\mathbf{k}|\mathbf{p}^\mu|s\mathbf{k}\rangle$. Using the f -sum rule, the three oscillator strengths involved are then expressed in terms of the three inverse effective mass tensors and one oscillator strength. Each three band term involves a product of three different matrix elements which is related to the third order derivative of the band energies with respect to \mathbf{k} . In a $\mathbf{k} \cdot \mathbf{p}$ three band model the parameters involved are the two band gaps and the 9 parameters determining the 9 matrix elements of p_x, p_y, p_z . The number of parameters can be considerably reduced by relating these quantities to the various derivatives of band energies. In fact, it can be shown that a three band model with energy extrema at $\mathbf{k} = 0$ cannot have strictly parabolic bands near $\mathbf{k} = 0$. We do not give the detailed expressions in this case since no interesting features appear.

To summarise, the models considered in this section have not made use of the group theoretical results for various crystal struc-

†These results are obtained by a simple generalization of Jha's results in [10].

tures. The inclusion of s.o. coupling doubles the number of bands, in general. An increase in the number of bands included in the model rapidly increases the number of parameters. But the symmetry of the crystal demands certain inter-relationships, thus reducing the number of parameters. This is done, for example, in Kane's $\mathbf{k} \cdot \mathbf{p}$ procedure. In the next section we discuss a calculation based on this for III-V compounds with small band gaps.

4. $\chi^{(2)}$ IN KANE'S MODEL BAND STRUCTURE

In this section we focus our attention on the second order susceptibility tensor $\chi_{\mu\alpha\beta}^{(2)}(\omega_1, \omega_2)$ for III-V compounds. These compounds crystalize in the zinc-blende structure whose point group symmetry is given by the tetrahedral point group. By general symmetry considerations [20] one knows that for these compounds $\chi_{xuz}^{(2)}(\omega_1, \omega_2) = \chi_{xzu}^{(2)}(\omega_1, \omega_2) = \chi_{uzx}^{(2)}(\omega_1, \omega_2) = \chi_{zux}^{(2)}(\omega_1, \omega_2) = \chi_{zxy}^{(2)}(\omega_1, \omega_2) = \chi_{zyx}^{(2)}(\omega_1, \omega_2)$ and that all other components of $\chi_{\mu\alpha\beta}^{(2)}(\omega_1, \omega_2)$ are zero.

The information obtained on the basis of symmetry considerations is an essential ingredient of Kane's model for the band structure of III-V compounds with small band gap at Γ . The model treats the conduction and valence band interactions exactly in a $\mathbf{k} \cdot \mathbf{p}$ calculation of the band structure near Γ . The interactions of these bands with other bands can be treated in a perturbation theory but we will neglect all other bands in our present discussion. Neglecting the \mathbf{k} -dependent spin orbit coupling one obtains 4 doubly degenerate spherical bands, one conduction band c and 3 valence bands v_1, v_2 and v_3 . The lattice periodic parts of the doubly degenerate eigenfunctions are given by

$$\begin{aligned} |i, m\rangle &= a_i |iS \downarrow\rangle' + b_i [(X - iY) \uparrow / \sqrt{2}]' \\ &\quad + c_i |Z \downarrow\rangle' \\ |i, n\rangle &= a_i |iS \uparrow\rangle' + b_i [-(X + iY) \downarrow / \sqrt{2}]' \\ &\quad + c_i |Z \uparrow\rangle' \end{aligned}$$

$$\begin{aligned} |v_1, m\rangle &= [(X + iY) \uparrow]'/\sqrt{2} \\ |v_1, n\rangle &= [(X - iY) \downarrow]'/\sqrt{2} \end{aligned} \quad (4.1)$$

where a_i, b_i, c_i are real coefficients, the index i refers to the bands c, v_2 and v_3 and spin indices m and n serve to distinguish the two degenerate orthonormal eigenfunctions. The primes denote that the eigenfunctions for a general \mathbf{k} -direction with spherical polar angles (θ, φ) are rotated according to

$$\begin{pmatrix} \uparrow' \\ \downarrow' \end{pmatrix} = \begin{pmatrix} e^{-i\varphi/2} \cos \theta/2 & e^{i\varphi/2} \sin \theta/2 \\ -e^{-i\varphi/2} \sin \theta/2 & e^{i\varphi/2} \cos \theta/2 \end{pmatrix} \begin{pmatrix} \uparrow \\ \downarrow \end{pmatrix} \quad (4.2)$$

$$\begin{pmatrix} X' \\ Y' \\ Z' \end{pmatrix} = \begin{pmatrix} \cos \theta \cos \varphi & \cos \theta \sin \varphi & -\sin \theta \\ -\sin \varphi & \cos \varphi & 0 \\ \sin \theta \cos \varphi & \sin \theta \sin \varphi & \cos \theta \end{pmatrix} \begin{pmatrix} X \\ Y \\ Z \end{pmatrix} \quad (4.3)$$

and

$$S' = S \quad (4.4)$$

where the functions S and (X, Y, Z) transform like the atomic S and (p_x, p_y, p_z) functions respectively under the rotations of the tetrahedral point group. In the language of group theory S and (X, Y, Z) transform according to Γ_1 and Γ_4 irreducible representations of the tetrahedral group T_d . \uparrow and \downarrow are the two spin states.

The matrix elements of p^μ in the eigenstates (4.1) are listed below

$$\begin{aligned} (i, m | p^\mu | j, m) &= (i, n | p^\mu | j, n) \\ &= P(a_i c_j + c_i a_j) R_{z\mu}, \\ (i, m | p^\mu | j, n) &= P(b_i a_j - a_i b_j) \\ &\quad \times (R_{x\mu} + i R_{y\mu}) / \sqrt{2}, \\ (i, n | p^\mu | v_1, m) &= (i, m | p^\mu | v_1, n)^* \\ &= P a_i (R_{x\mu} + i R_{y\mu}) / \sqrt{2}, \\ (v_1, m | p^\mu | v_1, m) &= (v_1, n | p^\mu | v_1, n) \\ &= (v_1, m | p^\mu | v_1, n) \\ &= (v_1, n | p^\mu | v_1, m) \\ &= (i, m | p^\mu | v_1, m) \\ &= (i, n | p^\mu | v_1, n) = 0 \end{aligned} \quad (4.5)$$

where

$$P = -i\langle S | p_z | Z \rangle \quad (4.6)$$

and $R_{\mu\nu}$ are the elements of 3×3 matrix in equation (4.3). It is evident from these matrix elements that the product $\text{Im}(\pi_{rs}^a \pi_{st}^b \pi_{tr}^c)$ vanishes for all possible choices of r, s and t when we neglect the $\sigma \times \nabla V$ term in π . It should be remarked that we have to consider only those combinations of r, s and t for which the bands r and s are neither both filled nor both empty. We consider the bands v_1, v_2 and v_3 completely full and c completely empty. The effect of the conduction band c being partially filled is simply to reduce the range of k -integration. At this stage one could make a hasty conclusion that the region near Γ , where Kane's theory is valid, does not contribute appreciably to the second order susceptibility. This seems highly unlikely from the close resemblance between the dispersion of linear and second order susceptibility [4]. We believe that the actual cause of the above result is the inadequate inclusion of s.o. coupling in our discussion. The calculation of the matrix elements of π including the $\sigma \times \nabla V$ term is very complicated in general but that of the matrix elements in $k = k\hat{z}$ states is relatively simple. One finds that the matrix elements near Γ with k along the z axis are given by

$$\begin{aligned} (i, m | \pi | j, m) &= (i, n | \pi | j, n) \\ &= \hat{z} \{ P(a_i c_j + c_i a_j) \\ &\quad - \sqrt{2} Q(a_i b_j + b_i a_j) \}, \end{aligned}$$

$$\begin{aligned} (i, m | \pi | v_1, m) &= (i, n | \pi | v_1, n) \\ &= \hat{z} R c_i \sqrt{2}, \end{aligned}$$

$$(v_1, m | \pi | v_1, m) = (v_1, n | \pi | v_1, n) = 0,$$

$$\begin{aligned} (i, m | \pi | j, n) &= (\hat{x} + i\hat{y}) \{ (b_i a_j - a_i b_j) \\ &\quad \times (P + Q) / \sqrt{2} \\ &\quad + (a_i c_j - c_i a_j) Q \} \\ &\quad - (\hat{x} - i\hat{y}) R \\ &\quad \times \{ b_i b_j + (c_i b_j + b_i c_j) / \sqrt{2} \}, \end{aligned}$$

$$\begin{aligned} (i, m | \pi | v_1, n) &= (\hat{x} + i\hat{y}) R c_i / \sqrt{2} \\ &\quad + (\hat{x} - i\hat{y}) (P - Q) a_i / \sqrt{2}, \end{aligned}$$

$$\begin{aligned} (i, n | \pi | v_1, m) &= -(\hat{x} - i\hat{y}) R c_i / \sqrt{2} \\ &\quad + (\hat{x} + i\hat{y}) (P - Q) a_i / 2, \end{aligned}$$

$$\begin{aligned} (v_1, m | \pi | v_1, n) &= (v_1, n | \pi | v_1, m)^* \\ &= -R(\hat{x} - i\hat{y}) \end{aligned} \quad (4.7)$$

where

$$Q = \frac{\hbar}{4mc^2} \left\langle S \left| \frac{\partial V}{\partial z} \right| Z \right\rangle. \quad (4.8)$$

and

$$R = \frac{\hbar}{4mc^2} \left\langle X \left| \frac{\delta V}{\delta y} \right| Z \right\rangle. \quad (4.9)$$

In the appendix we list the values of $\text{Im}(\pi_{rs}^x \pi_{st}^y \pi_{tr}^z)$ for all relevant r, s and t so that we could now write $\chi_{zxy}^{(2)}(\omega_1, \omega_2)$ in terms of band energies, neglecting the k -dependence of momentum matrix elements.

It is important to note that the parameters P and Q will be common to zinc-blende and diamond structures while R is nonvanishing only for the zinc-blende structure. It determines the k linear terms in the valence band energies when we include the k -dependent s.o. interaction in perturbation theory. A rough estimate of this parameter by Dresselhaus [16] gives $R \approx 2.5 \times 10^{-22} \text{ g cm sec}^{-1}$ for InSb. The parameter Q is relatively insignificant since it always comes with P and its magnitude is expected to be small in view of the good fit obtained for the optical absorption by Kane using only P . A theoretical estimate of Q can be made in terms of P and Δ , the spin orbit splitting if we assume that \mathbf{p} does not connect the states, X, Y, Z to those outside the s - p complex of bands. One obtains

$$Q \approx -\frac{1}{3}(m\Delta/P) \quad (4.10)$$

so that for InSb where $P \approx 1.36 \times 10^{-19} \text{ g cm sec}^{-1}$ and $\Delta \approx 0.9 \text{ eV}$ we obtain $Q \approx 3 \times 10^{-21} \text{ g cm sec}^{-1}$ which is about $0.02 P$. Thus, for InSb and by a similar calculation for InAs

one can either neglect Q or use its above approximate value. This enables us to calculate, to a good approximation, the contribution of the region near Γ to $\chi^{(2)}$. This, however, cannot be directly compared with the experimentally observed $|\chi^{(2)}|$ since no region of k -space is singled out for the real part of $\chi^{(2)}$. This difficulty is exactly the same as in the calculation of $\epsilon_1(\omega)$ the real part of linear dielectric constant. In the linear case we know that the imaginary part $\epsilon_2(\omega)$ receives the major contribution from a very small region of k -space which is singled out by the frequency ω . A comparison of $\epsilon_2(\omega)$ obtained experimentally and calculated theoretically, near the critical points provides useful information about the band structure of the solid. In the bilinear case also the contribution to $\chi_2^{(2)}(\omega, \omega)$, the imaginary part of $\chi^{(2)}(\omega, \omega)$ comes from a small region of k space singled out by the frequency ω . We do not discuss the evaluation of $\chi_2^{(2)}(\omega, \omega)$ since no experimental information is available yet. It must be emphasized here that the possibility of determining $\chi_2^{(2)}$ by performing second harmonic interference experiments has been demonstrated [21] by Chang *et al.* and Simon and Bloembergen.

An extrapolation of the available experimental data gives $\chi_{z,xy}^{(2)} \approx 3 \times 10^{-6}$ e.s.u. in the low frequency limit. To obtain a rough estimate of R from this data we note that in the low frequency limit

$$\begin{aligned} \chi_{z,xy}^{(2)} \approx & -(e^3/m^3\hbar^2) \sum_{\mathbf{k}, \mathbf{r}, \mathbf{s}, t} (f(\mathbf{rk}) - f(\mathbf{sk})) \\ & \times \mathcal{J}(r_0, s_0, t_0) \omega_{rs}^{-4} \omega_{rt}^{-4} \\ & \times (\omega_{rt}^3 + 2\omega_{rs}\omega_{rt}^2 + 4\omega_{rs}^2\omega_{rt} + 8\omega_{rs}^3) \quad (4.11) \end{aligned}$$

where we have neglected the k -dependence of the momentum matrix elements. Equation (4.11) is obtained from equation (2.20) and the expansion

$$\frac{1}{\omega_G - \omega} = \frac{1}{\omega_G} + \frac{\omega}{\omega_G^2} + \frac{\omega^2}{\omega_G^3} + \frac{\omega^3}{\omega_G^4} + \dots$$

and using the various symmetries of $\chi_{\mu\alpha\beta}^{(2)}(0, 0)$. The function $\mathcal{J}(r_0, s_0, t_0)$ is defined in the appendix. The summation over \mathbf{k} in equation (4.11) can be evaluated using the calculated band structure. In view of our several approximations, however, it seems appropriate to replace ω_{rs} and ω_{rt} by their 'average' values defined by

$$\omega_{rs} = \frac{1}{2} \left(\frac{\omega_{rs}(\Gamma) + \omega_{rs}(X)}{2} + \frac{\omega_{rs}(\Gamma) + \omega_{rs}(L)}{2} \right).$$

For InSb we put $\hbar\bar{\omega}_{cv_1} = \hbar\bar{\omega}_{cv_2} = 1.5$ eV and $\hbar\bar{\omega}_{cv_3} = 3.5$ eV. Corresponding to the experimental value of $\chi^{(2)}$ we then obtain $R \approx 3 \times 10^{-21}$ g cm sec⁻¹ which compares well with Dresselhaus' estimate since both the estimates are very rough. It should be mentioned that we obtain a lower limit for $R \approx 4 \times 10^{-25}$ g cm sec⁻¹ when we use the minimum energy gaps and put $\hbar\bar{\omega}_{cv_1} = \hbar\bar{\omega}_{cv_2} = 0.22$ eV and $\hbar\bar{\omega}_{cv_3} = 1.1$ eV.

5. CONCLUSIONS

We have considered the nonlinear optical response of solids on the basis of the band theory. A two band model which provides a good qualitative picture for the linear and third order response is found unsuitable for the description of second order optical response. It is shown that the consistency with general properties of Bloch states imposes important restrictions on such two band and three band models. An important difference between the calculations of the linear and nonlinear response is that the inclusion of group theoretical selection rules is much more involved in the nonlinear case. While constructing model band structures to describe nonlinear optical response of a solid, the symmetry properties of the bands must be specified in the beginning. This is done in Kane's model for the band structure of III-V compounds. The assumption about the small band gap at Γ appears to be more valid for InSb ($E_g = 0.22$ eV) and InAs ($E_g =$

0.35 eV) than for GaAs ($E_g = 1.4$ eV) and GaSb ($E_g = 0.8$ eV).

We have shown that the inclusion of s.o. coupling is crucial to the calculation of $\chi^{(2)}$. This should in fact be expected from our knowledge of band theory. The only qualitative difference between the band structures of III-V and IV-IV semiconductors is that in the latter all the bands must always be doubly degenerate throughout the Brillouin Zone, while in the III-V compounds this degeneracy can be lifted by the s.o. coupling in the Hamiltonian. Near Γ , small \mathbf{k} -linear terms are predicted in the valence band energies of III-V compounds[16]. These terms originate from the \mathbf{k} -dependent s.o. interaction in the Schrodinger equation for the lattice periodic spinor $u_{\mathbf{k}}(\mathbf{x})$, and they vanish for the IV-IV semiconductors because of equation (2.3). It should be noted that the inclusion of the \mathbf{k} -dependent s.o. interaction in the Schrodinger equation for $u_{\mathbf{k}}(\mathbf{x})$ and that of the $(\boldsymbol{\sigma} \times \nabla V)$ term in π both give rise to terms involving R , but at $\mathbf{k} = 0$ only the latter enters into our calculation. As we go away from Γ we expect $\text{Im}(\pi_{rs}^x \pi_{st}^y \pi_{tr}^z)$ to vary slowly with respect to $|\mathbf{k}|$ and the dependence on the direction of \mathbf{k} can be averaged. The averaging over all directions of \mathbf{k} may be important in an accurate calculation of $\chi^{(2)}$. The effect of including the \mathbf{k} -linear terms in energies is expected to be quite small so that their neglect is justified.

The main difficulties in a complete calculation of $\chi^{(2)}$ are similar to those in a complete calculation of $\epsilon(\omega)$. Our result shows that a critical point analysis of $\chi_{\mu\alpha\beta}^{(2)}(\omega, \omega)$ will provide important information about the band structure parameters which distinguish the noncentrosymmetric solids from the corresponding symmetric ones. Our results also demonstrate an advantage of the $\mathbf{k} \cdot \mathbf{p}$ approach to band structure compared to other calculations. In the $\mathbf{k} \cdot \mathbf{p}$ method the wavefunctions are more reliable than in most other methods of band structure calculation. The full zone $\mathbf{k} \cdot \mathbf{p}$ theory[23] of Cardona and

co-workers can be used to extend our calculations in two directions. Firstly, the 'not so small' gap compounds can be treated; secondly \mathbf{k} values away from the critical points can be suitably incorporated.

The approximation of neglecting all other bands in Kane's model corresponds to the neglect of core electrons in the bonding orbital theories. The main advantage of our approach based on band theory is the ready inclusion of dispersion in $\chi_{\mu\alpha\beta}^{(2)}(\omega_1, \omega_2)$ and the possibility of obtaining quantitative information about those aspects of the band structure which depend directly on the lack of inversion symmetry of the solid. In addition to this the tensorial character of the various susceptibility tensors is always correctly represented in the band theory calculations. Inadequate representation of the tensorial character of $\chi_{\mu\alpha\beta\gamma}^{(3)b}$ is an important drawback of the presently available bonding orbital calculations. The major difficulty in the band theory calculations is our inadequate knowledge of the band structure and the corresponding eigenfunctions throughout the Brillouin Zone. The most appropriate way to overcome this, as already pointed out, is to consider the imaginary part of $\chi_{\mu\alpha\beta}^{(2)}$ separately in small frequency ranges near the critical points. Assuming $\text{Im}(\pi_{rs}^x \pi_{st}^y \pi_{tr}^z)$ as constant throughout the Brillouin Zone and using the calculated band structures to perform the \mathbf{k} -sum over the entire zone may be a good approximation to start with a calculation of the real part of $\chi_{\mu\alpha\beta}^{(2)}$. The validity of the various approximations can be checked by first calculating the linear dielectric constant with the same approximations. It is hoped that improved band theory calculations and more thorough determinations of the imaginary parts of $\chi_{\mu\alpha\beta}^{(2)}$ will provide important information about the inversion asymmetric part of the potential in III-V compounds.

Acknowledgements—The author is indebted to Dr. A. K. Rajagopal for his constant encouragement and valuable help throughout the course of this work. He is very

grateful to Dr. Sudhanshu S. Jha for many important suggestions and for making available his work in reference [10]. His grateful thanks are due to Dr. Chanchal K. Majumdar and Dr. Chindhu S. Warke for their help in preparing the manuscript.

REFERENCES

1. KITTEL C., In *Quantum Theory of Solids*, Chap. IX. Wiley, New York (1963).
2. BLOEMBERGEN N., *Nonlinear Optics*. Benjamin, New York (1965); BUTCHER P. N. and McLEAN T. P., *Proc. phys. Soc.* **81**, 219 (1963); *ibid.* **83**, 579 (1964); JHA S. S. and WARKE C. S., *Nuovo Cim.* **53B**, 120 (1968).
3. PHILLIPS J. C., In *Solid State Physics* (Edited by F. Seitz and D. Turnbull), Vol. 18, p. 56. Academic Press, New York (1966).
4. CHANG R. K., DUCUING J. and BLOEMBERGEN N., *Phys. Rev. Lett.* **15**, 415 (1965).
5. PERSHAN P. S., In *Semi Conductors and Semi Metals* (Edited by R. K. Willardson and A. C. Beer), Vol. 2, p. 283. Academic Press, New York (1966).
6. PATEL C. K. N., SLUSHER R. E. and FLEURY P. A., *Phys. Rev. Lett.* **17**, 1011 (1966); WYNNE J. J., *Phys. Rev.* **178**, 1295, (1969). See also other references in this paper.
7. JHA S. S. and BLOEMBERGEN N., *Phys. Rev.* **171**, 891 (1968).
8. KELLEY P. L., *J. Phys. Chem. Solids* **24**, 1113 (1963).
9. RUSTAGI K. C., *Nuovo Cim.* **53B**, 346 (1968).
10. JHA S. S., Unpublished.
11. WOLFF P. A., *J. Phys. Chem. Solids* **25**, 1057 (1964).
12. RUSTAGI K. C., JHA S. S. and WARKE C. S., *Nuovo Cim.* **58B**, 93 (1968); ZAWADZKI W. and LAX B., *Phys. Rev. Lett.* **16**, 1001 (1966); For other references see DRESSELHAUS G. and DRESSELHAUS M. S., *Proc. Intl. Sch. Physics. Enrico Fermi Course XXXIV*, (Edited by J. Tauc), p. 198. Academic Press, New York (1966).
13. ROBINSON F. N. H., *Bell. Syst. tech. J.* **46**, 913 (1967).
14. FLYTZANIS C. and DUCUING J., *Phys. Lett.* **26A**, 315 (1968); *Phys. Rev.* **178**, 1218, (1969).
15. KANE E. O., *J. Phys. Chem. Solids* **1**, 249 (1956).
16. DRESSELHAUS, *Phys. Rev.* **100**, 580 (1955); see also KANE E. O., In *Semiconductors and Semi Metals* (Edited by R. K. Willardson and A. C. Beer), Vol. 1, p. 75. Academic Press, New York (1966).
17. BLINOWSKI J. and GRYNBERG M., *Phys. Rev.* **168**, 882 (1968).
18. BLOUNT E. I., In *Solid State Physics* (Edited by F. Seitz and D. Turnbull), Vol. 13, p. 306. Academic Press, New York (1963).
19. ADLER S. L., *Phys. Rev.* **126**, 413 (1962).
20. BUTCHER P. N., Bull. No. 200, Engineering Experiment Section, Ohio State University, Columbus (1965) (Unpublished).
21. CHANG R. K., DUCUING J. and BLOEMBERGEN N., *Phys. Rev. Lett.* **15**, 6 (1965); SIMON H. J. and BLOEMBERGEN N., *Phys. Rev.* **171**, 1104 (1968).
22. BLOOM S. and BERGSTRASSER T. K., *Solid State Commun.* **6**, 465 (1968).
23. CARDONA M., McELROY P., POLLAK F. H. and SHAKLEE K. L., *Solid State Commun.* **4**, 319 (1966).

APPENDIX

Equations (4.7) show that the only states connected by π_z are those with the same spin index while π_x , π_y connect only states with unequal spin indices. Further since the energies do not change under the interchange of spin indices m, n , it is appropriate to consider

$$\begin{aligned} \mathcal{J}(r_0, s_0, t_0) = & \text{Im} (\langle r_0 m | \pi^x | s_0 n \rangle \langle s_0 n | \pi^y | t_0 m \rangle \\ & \times \langle t_0 m | \pi^z | r_0 m \rangle \\ & + \langle r_0 n | \pi^x | s_0 m \rangle \langle s_0 m | \pi^y | t_0 n \rangle \langle t_0 n | \pi^z | r_0 n \rangle). \end{aligned} \quad (\text{A.1})$$

Using a_i , b_i , c_i given by equation (16) of reference [15] we obtain the values of $\mathcal{J}(r_0, s_0, t_0)$ for all admissible r_0 , s_0 and t_0 i.e. such that r_0 and s_0 are neither both occupied nor both empty. The nonvanishing elements $\mathcal{J}(r_0, s_0, t_0)$ are listed below.

$$\begin{aligned} -\mathcal{J}(c, v_1, v_2) &= \mathcal{J}(c, v_2, v_2) = -\mathcal{J}(v_1, c, v_2) \\ &= \mathcal{J}(v_2, c, v_1) = \frac{1}{2}(P-Q)^2 R, \end{aligned} \quad (\text{A.2})$$

$$\begin{aligned} -2\mathcal{J}(c, v_1, v_3) &= -2\mathcal{J}(c, v_2, v_3) = \mathcal{J}(c, v_3, v_2) \\ &= \mathcal{J}(v_1, c, v_3) = -\mathcal{J}(v_3, c, v_1) \\ &= \frac{1}{2}(P-Q)(P+2Q)R. \end{aligned} \quad (\text{A.3})$$

Note added in proof

In general the estimate of the matrix element R from the low frequency limit of $|\chi_{14}^{(2)}(\omega, \omega)|$ is more accurate than that obtained by approximating all energy denominators in $|\chi_{14}^{(2)}(\omega, \omega)|$ by a constant energy $\hbar\omega_0 \approx 1$ eV and comparing with the experimental value at $\hbar\omega \approx 1$ eV (see RUSTAGI K. C., *Phys. Lett.* **29A**, 185 (1969)). Very recently, however, Van Tran and Patel have reported (see, VAN TRAN N. and PATEL C. K. N., *Phys. Rev. Lett.* **22**, 463 (1969)) a value of $\chi_{14}^{(2)}$ at $\hbar\omega \approx 2 \times 10^{-3}$ eV which is considerably lower than the low frequency limit used by us in section 4. This again emphasizes the importance of dispersion of $\chi^{(2)}$ in the sense that the linear extrapolation (usually found in the literature) of the data in the infrared and visible region does not yield the correct low frequency limit.

OPTICAL AND ELECTRICAL PROPERTIES OF THIN FILMS OF α -LEAD AZIDE

HARRY D. FAIR, Jr. and ARTHUR C. FORSYTH

Explosives Laboratory, Feltman Research Laboratories, Picatinny Arsenal, Dover, N.J. 07801, U.S.A.

(Received 28 August 1968; in revised form 28 February 1969)

Abstract—The optical absorption spectrum of α -lead azide was measured in the region 185–700 m μ at room, liquid nitrogen and liquid helium temperatures. Absorption coefficients were determined from the diffuse reflectance of powders and from transmission measurements on thin films. The spectral response of photoconductivity of thin films was determined from room temperature down to 77°K. The thin films of lead azide were prepared by vacuum depositing a thin film of metallic lead on either quartz or sapphire substrates followed by exposure of the lead film to gaseous hydrazoic acid. The results indicate that the fundamental absorption is at shorter wavelengths than indicated previously. Structure not previously reported has been found in the optical absorption and photoconductivity data and has been interpreted in terms of fundamental exciton structure.

1. INTRODUCTION

OF ALL THE inorganic azides, lead azide has been utilized the most extensively as a commercial and military initiating explosive and as a consequence, its macroscopic physical and explosive properties are relatively well characterized. Little is actually known, however, about its fundamental optical and electrical properties. This lack of basic information is due in part to the experimental difficulties encountered in performing measurements on explosive materials which are extremely sensitive to heat, light and impact, but in addition to the non-availability of lead azide in the form of large single crystals.

It is the purpose of this paper: (1) to report the preparation of thin films of pure α -lead azide of good optical quality by the reaction of metallic lead with gaseous hydrazoic acid, (2) to present the experimental results of optical absorption measurements performed on these films at temperatures down to 13°K and the results of room temperature diffuse reflectance measurements performed on pure α -lead azide powders, (3) to present experimental spectra of thin film photoconductivity obtained from room temperature down to 77°K, (4) to present a possible interpretation of structure observed in both the absorption

and photoconductivity spectra in terms of fundamental exciton structure.

2. EXPERIMENTAL METHOD

(A) Diffuse reflectance

Diffuse reflectance measurements were performed on powder samples using a Perkin Elmer Model 350 spectrophotometer equipped with a diffuse reflectance attachment. Pure lead azide powder was prepared by reacting aqueous solutions of lead nitrite and hydrazoic acid and was determined by X-ray analysis to be the α -phase of lead azide. The powders were screened to obtain uniform particle sizes and were spread evenly over the bottom of a quartz sample holder constructed in the form of a cup with a 2 in. dia. quartz window serving as the bottom. The lead azide was held in place in the cup by firmly wedging a soft rubber stopper against the powder. An identical holder was filled with magnesium carbonate which served as the reflectance standard. The window of the sample holder completely covered the exit port of the spectrophotometer integrating sphere so that reflectance from equal-sized portions of lead azide powder and magnesium carbonate were compared. The powder samples were

greater than 2 mm thick so that even for the largest particles used, negligible radiation penetrated to the back of the sample holder.

(B) Thin film optical transmission

Optical transmission measurements were performed on thin films of lead azide using a Cary 14-R spectrophotometer. A liquid helium dewar was mounted on an adjustable platform on a hydraulic equipment jack. A sapphire disc containing the lead azide film was attached to a copper mask containing two identical slots and was positioned so that the lead azide film completely covered only one of the slots. The mask was then bolted to the cold finger of a liquid helium dewar and the dewar was evacuated to 10^{-6} Torr. using a liquid nitrogen trapped oil diffusion system. A simple translation of the dewar platform permitted either slot to be positioned in the optical path of the spectrophotometer. In all cases, care was taken to prevent exposure of the thin films to short wavelength visible or u.v. light prior to the optical measurement to prevent photolytic decomposition. The sample temperature was determined by a platinum resistance thermometer attached to the sample holder. Sample temperatures down to 13°K were obtained by this technique.

(C) Photoconductivity

Photoconductivity spectra of lead azide thin films were measured on a vibrating reed electrometer at field strengths ranging up to 2000 V/cm obtained from a d.c. power supply. Monochromatic light from a 150 W Xenon Arc and high intensity monochromator was passed through a sapphire window in the tail of a liquid nitrogen dewar and focused on the lead azide film which was attached to the cold finger of the dewar. The electrometer head was mounted directly in one window of the nitrogen dewar tail and permitted photo-currents to be detected down to the 10^{-16} A limit of the electrometer.

3. EXPERIMENTAL RESULTS

(A) Diffuse reflectance

The room temperature diffuse reflectance spectrum of pure α -lead azide power screened to an average particle size of 28μ appears in Fig. 1. The purity of the lead azide was determined by mass spectrometric analysis which indicated that no impurities were present in concentrations greater than one part per million with the exception of Cl and Br which were present as 100 and 40 ppm respectively. The threshold for optical absorption appears to be at 4200 Å.

An analysis[1] using the particle size and spectral response of the diffuse reflectance gives a minimum estimate of the absorption coefficient at 3800 Å to be at least 10^3 cm^{-1} .

(B) Thin film optical transmission

It has been impossible at this point to obtain single crystals of α -lead azide of sufficient size and quality for refined optical transmission measurements. Previous measurements[2] on a single crystal of α -lead azide indicate that the absorption edge is in the region of 4000 Å.

In general, thin films can be used for these measurements; however, film preparation using evaporation techniques requires that the substance be reasonably soluble and unfortunately such a solvent is not known for lead azide. Other film techniques such as deposition or sublimation cannot be used because of the decomposition of the azide.

Lead azide is very slightly soluble in water; however, numerous attempts to obtain thin films by slow evaporation from aqueous solutions proved to be largely unsuccessful. It was found, however, that thin films of excellent optical quality were obtained by reacting vacuum deposited layers of metallic lead with gaseous hydrazoic acid for several hours[3].

Thin films of metallic lead were vacuum deposited on quartz or sapphire substrates.

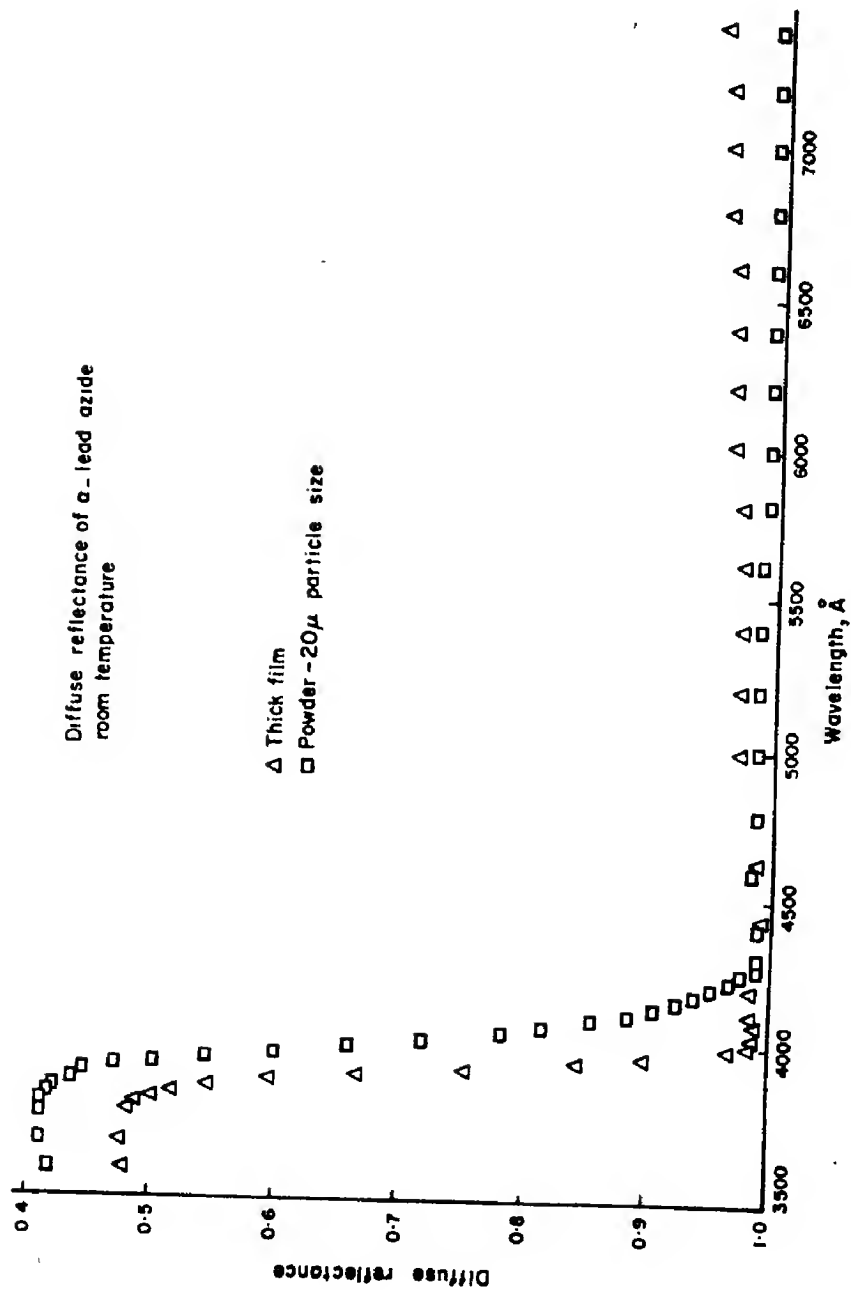


Fig. 1. Spectral dependence of the diffuse reflectance of α -lead azide at room temperature.

The substrates were in the form of discs 0.5 in. dia. and 0.02 in. thick. The films which were used in the absorption measurements were prepared by shielding half of the disc from the lead during the deposition so that the resulting lead film was in the form of a half moon. The films were then placed in a teflon holder inside a light tight desiccator which was attached to the output of a hydrazoic acid generator[4]. The desiccator was flushed continuously with hydrazoic acid in a nitrogen carrier gas.

After several hours of exposure to hydrazoic acid, the top surface of the metallic lead film became white. The lead surface next to the substrate appeared to be grey when observed through a microscope. Upon further exposure, the grey areas disappeared and the lead films became either completely white or transparent depending upon the thickness of the initial lead film. Lead films up to 150–200 Å thick became transparent after 5–8 hr of exposure to hydrazoic acid. Thicker films reacted more slowly and tended to become white. Figure 2 shows the sequence of reaction of a 100 Å thick metallic lead film with hydrazoic acid to become lead azide. A 100 Å metallic film is just at the threshold of having a metallic appearance (Curve 1). Continued exposure to HN_3 (Curve 3) increased the optical quality of the film until after 4 hr of exposure (Curve 4) the film was transparent to visible light. The most dramatic change in the visible part of the spectrum occurred shortly after the sample was exposed to hydrazoic acid.

The film thickness was determined first by measuring the unreacted lead metal thickness with a multiple beam interferometer. The azide film thickness was then calculated by assuming that the number of lead atoms in the metal film was equal to the number of lead azide molecules in the reacted film. It was also assumed that the area of the metallic film does not change appreciably during the volume change accompanying the reaction. The lead azide film thickness, t_{azide} is then

$$t_{\text{azide}} = \frac{(\text{mol. wt})_{\text{azide}} \times \text{density}_{\text{lead}}}{(\text{mol. wt})_{\text{lead}} \times \text{density}_{\text{azide}}} t_{\text{lead}} \\ = 3.4 t_{\text{lead}}.$$

The room temperature absorption spectrum showed a plateau at approximately 3750 Å. At liquid nitrogen temperature additional small peaks are observed at approximately 3300, 3000 and 2800 Å, and the peak at 3750 Å was more clearly resolved. At 13°K (Fig. 3) there was further resolution of this peak and an additional peak was observed at 3700 Å. The peak at 3750 Å was clearly observed in over twenty different lead azide films on either quartz or sapphire substrates. These films varied in thickness from 350–1500 Å. The lead azide films were prepared from 6-nine purity lead metal and spectroscopically pure hydrazoic acid. In addition, the absorption edge of the films as determined by diffuse reflectance appeared at slightly shorter wavelengths and was sharper than that of the spectroscopically pure lead azide powder. Thus, we conclude that the structure observed in the transmission data is most probably not due to impurities in the lead azide films but rather the absorption spectra arise from the fundamental absorption of the pure lead azide.

We cannot be as definite about the stoichiometric composition of the thin films. Lead films between 50 and 100 Å thick react in HN_3 to give a flat absorption in the visible. However, films of greater thickness often exhibit a long wavelength tail which extends through the visible. This tail fits a $1/\lambda^4$ dependence and could be due to Rayleigh scattering of small particles of unreacted lead. Further reaction of the films in gaseous hydrazoic acid reduces the amount of scattering or absorption in the visible and it was possible to obtain thicker films which showed no absorption in the visible region of the spectrum, however, it was not possible to determine absolutely the stoichiometric composition during any phase of the reaction and it is

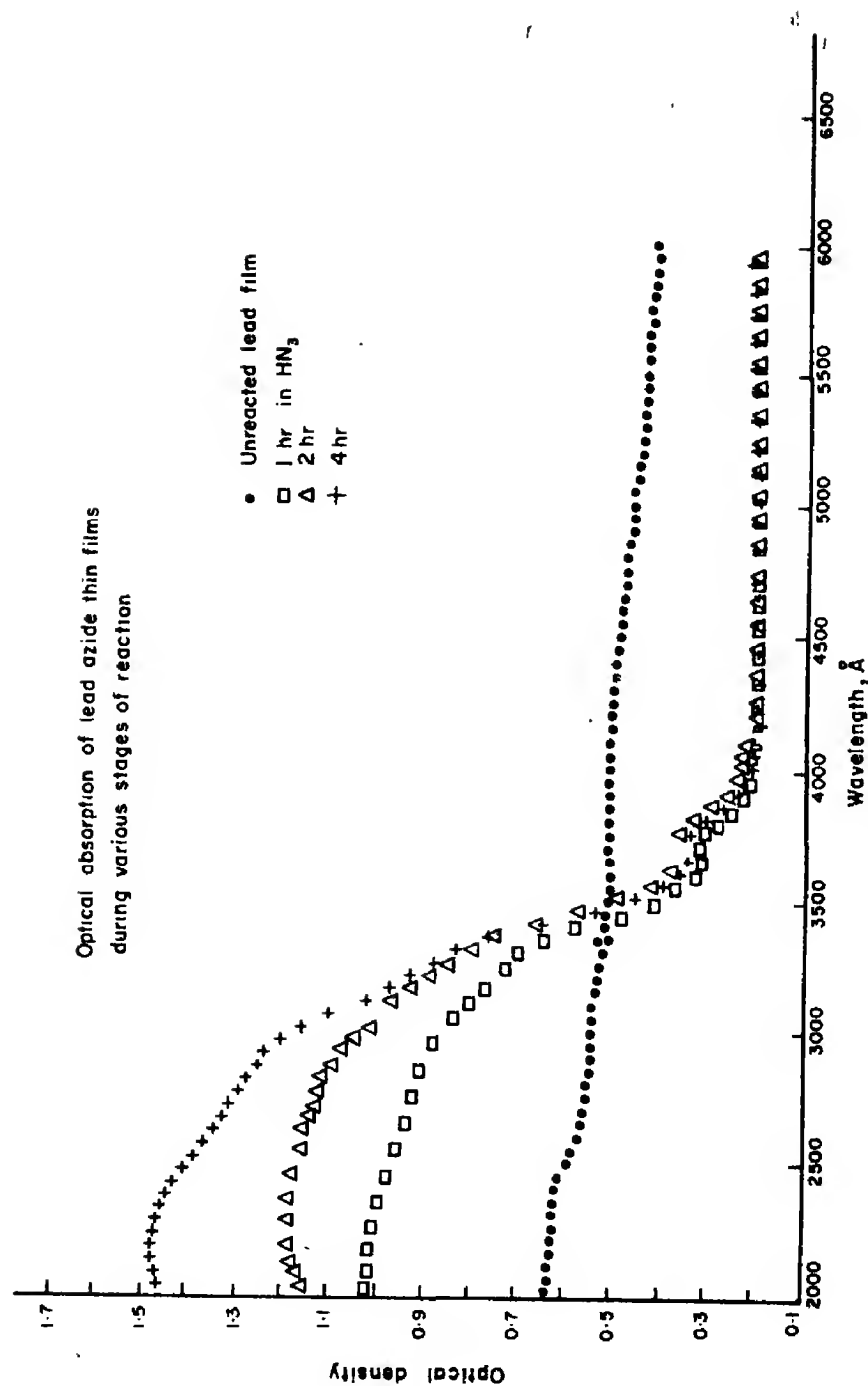


Fig. 2. Optical absorption of α -lead azide thin films during various stages of reaction in hydrazoic acid.

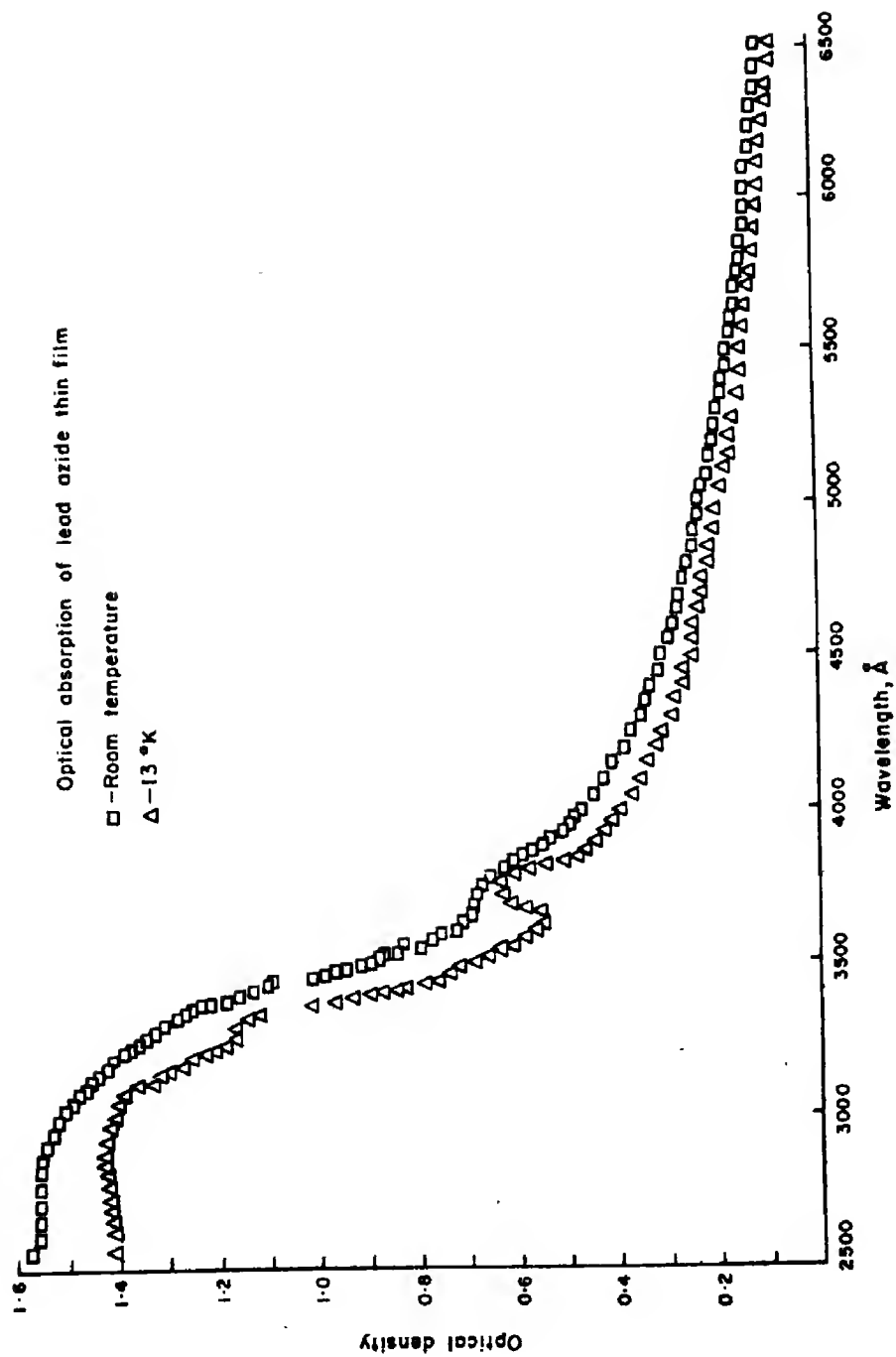


Fig. 3. Optical absorption of α -lead azide thin films at room temperature and at 13°K.

quite possible that the 'completely' reacted films could contain an excess of lead.

Since lead azide decomposes appreciably above 250°C it was not possible to anneal the thin films, however, there is some indication that the optical quality of the film increases when the films are stored for long periods of time in hydrazoic acid. It is in fact rather surprising that films of this quality are obtained by a gas-solid reaction in which the density changes from 11.3 for lead to 4.71 for lead azide. The intense peak at 3750 Å appears to shift slightly at a given temperature from one sample to another. At 15°K, this peak was observed at wavelengths ranging from 3700 to 3790 Å. This shift in peak position is due in part to a difference in sample thickness since there is an accompanying difference in intensity of the background absorption on which the peak is located. However, in several films observed at 15°K, this peak is further resolved (as indicated in Fig. 4) into two peaks at 3760 and 3725 Å. The ambiguity in the position of this first strong absorption peak could be due then to differences in intensity of the two rather poorly resolved absorption peaks at 3760 and 3725 Å.

Since the additional structure is not as clearly resolved, ten lead azide films, of slightly different thickness, were observed at room, liquid nitrogen and liquid helium temperatures. The two peaks described above as well as additional poorly resolved absorption peaks at shorter wavelengths occur in all the thin films. It is surprising that there is no marked temperature dependence of any of the observed line positions.

(C) Photoconductivity

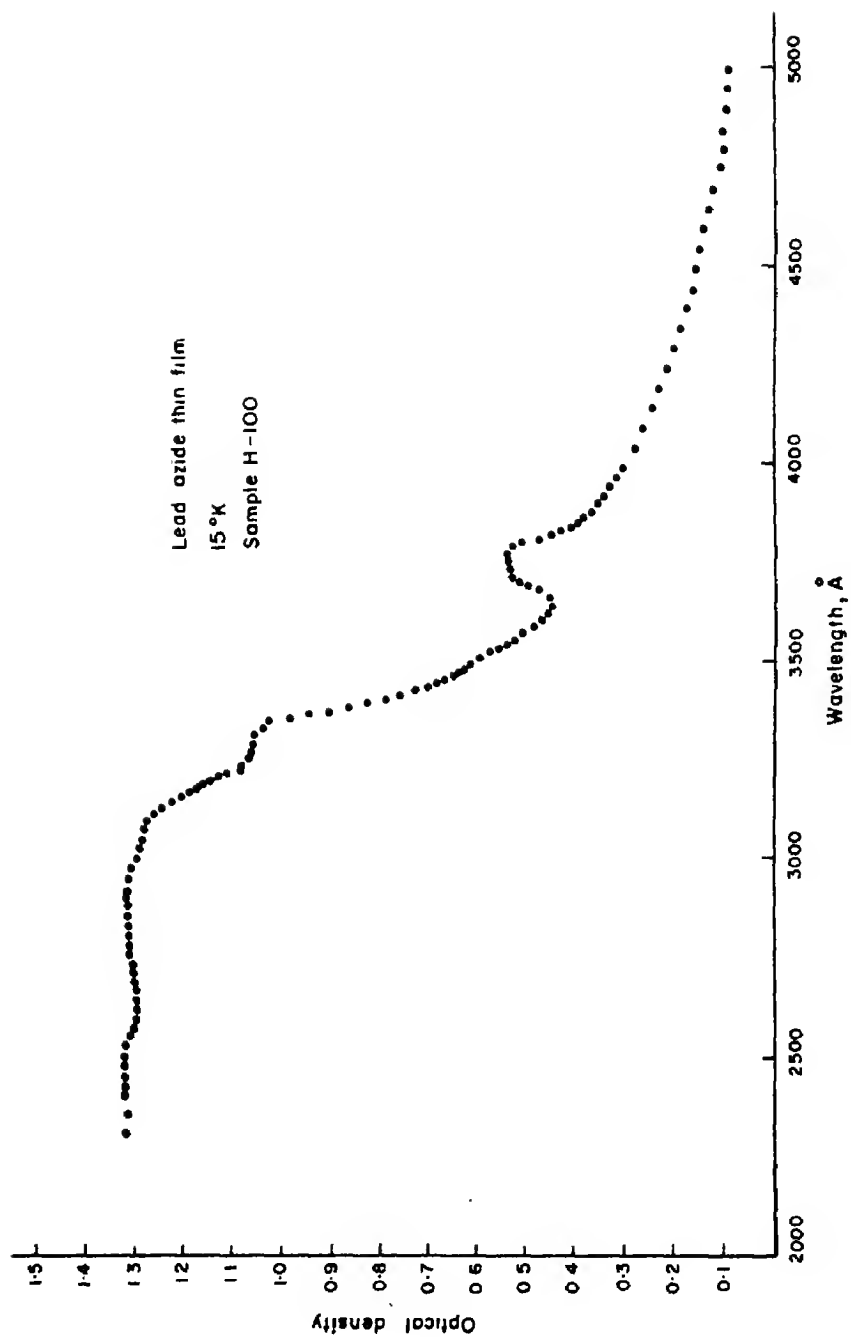
Photoconductivity spectra were obtained on thin films of α -lead azide in which the thickness of the initial metallic lead films was between 500 and 1000 Å. Several types of evaporated metal electrodes were used including gold, silver and aluminum, however, a mercury-indium amalgam was found to be

quite satisfactory and added much in convenience in mounting. Since most of these metals were found to be essentially non-reactive in the gaseous HN_3 atmosphere, the films for these measurements were prepared by first depositing a lead film on one side of a sapphire disc (0.5 in. dia. and 0.02 in. thick) and then shielding a central strip approximately 2–3 mm thick, the appropriate electrode material was vacuum deposited on the remainder of the lead film. The metal film was then placed in the HN_3 reaction chamber as described above. This technique proved to be more satisfactory than depositing the metal electrodes on the lead azide films after they had been reacted.

Previous measurements of the photoconductivity of single crystals[5] and pressed pellets[6] of lead azide showed photoconductivity throughout the visible region of the spectrum and a peak at approximately 4100 Å which has been alternately ascribed to interstitial nitrogen atoms and to the first peak of an exciton series.

The spectral response of photoconductivity [7] for a 1000 Å thick film of lead azide at room temperature is shown in Fig. 5. The photocurrent is normalized for a constant number of incident photons. No detectable photocurrent was obtained in the visible portion of the spectrum, however, two peaks were observed in the near ultraviolet at 3820 and 3545 Å. The relative intensities of these peaks varied slightly from sample to sample. At 103°K the photocurrents were reduced in intensity by more than an order of magnitude. The dependence of the 3820 Å peak on exciting intensity I , was measured using neutral density filters and the photocurrent was found to be proportional to the lamp intensity. A reliable measurement of the intensity dependence of the 3545 Å peak could not be obtained due to the low magnitude of this peak.

The observed photocurrents could in principle arise from band to band transitions, from impurity to band transitions, or they

Fig. 4. Optical absorption of α -lead azide thin film at 15°K.

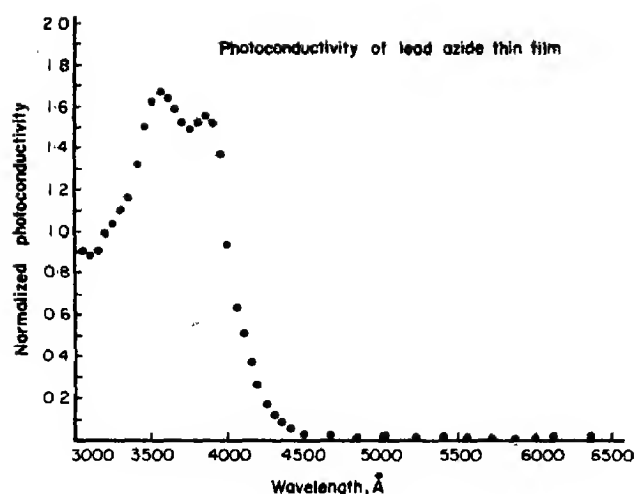


Fig. 5. Spectral response of the photoconductivity of α -lead azide thin film observed at room temperature.

could arise from excitons by any of several mechanisms, for example:

- (1) Dissociation of excitons through phonon interaction.
- (2) Dissociation of excitons through interaction with impurities, defects or other excitons.

It is interesting to consider two cases for the rate of change of free carriers for a thermally assisted process. For a bimolecular process at constant temperature, the photocurrent varies as the square root of the lamp intensity. However, if for any reason (for example, dissociation of the exciton on which one carrier is captured by an impurity and the remaining carrier released to valence or conduction band, etc.) one of the charge carrier concentrations changes very little, the process is monomolecular and the photocurrent is proportional to the lamp intensity.

As mentioned above, the observed photocurrent in lead azide at 3820 Å was found to be approximately proportional to the first power of the lamp intensity at constant temperature. The temperature dependence of the two photoconductivity peaks was

measured over a limited range from room temperature down to 103°K and the activation energy of the photocurrent found to be approximately $E_i = 0.02$ eV.

4. DISCUSSION

The structure in the absorption and photoconductivity spectra of lead azide may reflect the non-uniform density of states in band to band transitions, or may be due to impurity to band transitions, or may be due to any of several kinds of excitons. It is interesting to compare the spectral response of photoconductivity in Fig. 5 with the optical absorption. The minimum in the photocurrent occurs at approximately 3750 Å which is essentially the same wavelength as the first strong absorption peak. The photocurrents could then arise from band to band transitions in which the simultaneous occurrence of a strong absorption peak and photocurrent minimum may be attributed to a competing process occurring for the production of photoelectrons at 3750 Å. Such a competing process could be a transition involving either impurities or the creation of excitons.

It may be useful at this point to consider the types of excitons possible in lead azide and to estimate their creation energies. Of the localized or Frenkel type exciton in lead azide, there is the possibility of extremely localized intra anion or intra cation excitons which are describable in terms of excited atomic states of N_3^- or Pb^{+2} , in addition to the localized charge transfer excitons.

A weak absorption at 2300 Å has been observed [8] in numerous azides (Na, K, Rb, Cs) and has been ascribed to "a low lying excited state of the azide ion". This absorption can also be interpreted in terms of transitions which create excited states of an (N_3^-) intra anion exciton. Because of the extreme localization, the transition energy of the intra-anion exciton in lead azide should not differ greatly from that observed in the alkali azides and thus the transitions to these intra anion exciton states in lead azide would

be expected to occur in the neighborhood of 2300 Å.

The lowest excited free ion states of Pb^{+2} occur at 7.49, 7.98, 9.79 and 11.82 eV, corresponding to transitions from the $^1S6s^2$ configuration to the 3P and 1P states on the $6s\ 6p$ configuration. The transition energies of these excited states in solid lead azide will be reduced by the lead azide crystalline field. Optical absorption ascribed to Pb^{+2} has been observed in several alkali halides [9] in the region 2500 to 2700 Å (5.0 to 3.4 eV) and recently [10], absorption has been observed between the ground state and the sublevels of the 3P states of Pb^{+2} in KCl at 4.49 and 4.53 eV.

If the crystalline field of lead azide reduces the free ion states of Pb^{+2} by as much as a factor of 2.2 for example, the Pb^{+2} transitions mentioned above would be reduced to 3.30 eV (3700 Å), 3.61 eV (3430 Å), 4.43 eV (2800 Å) and 5.35 eV (2310 Å). Thus depending on the strength of the lead azide crystal field, the transitions described in terms of excited states of intra-cationic Pb^{+2} excitons may have transition energies which lie in the spectral region of the observed optical absorption data for lead azide.

The transition energy to create a Frenkel charge transfer exciton in lead azide is calculated by determining the energy required to remove an electron from an azide ion and place it at a neighboring lead ion. The total lattice energy of lead azide has been calculated [11] from thermo chemical quantities using an extended Born-Haber cycle and found to be 18.8 eV. The first excited state of the charge transfer exciton is then estimated to be 7.0 eV. This estimate of the transition energy has neglected other than coulombic contributions to the lattice energy and has not included the effects of lattice polarization. The total lattice energy contains contributions from quadrupole effects, the zero point energy and others, however, the Madelung term is the dominant contribution and is most probably within 1–2 eV of the total lattice

energy. Attempts to account for the lattice polarization in alkali halides has given values ranging from 1.2 eV for Pb Cl_2 to 2.2 eV for Li I and the polarization energy of lead azide would be expected to be on this order of magnitude.

Including these two corrections, the estimate of the charge transfer energy is then reduced to approximately 4–6 eV. To the extent that lead azide is partially covalent, this transition energy would be even further reduced since the Pb^{+2} states would be pulled closer to the states of N_3^- .

Finally, Wannier excitons in lead azide are describable in terms of perturbed band states in the framework of effective mass theory. The valence band is assumed to be synthesized from states of the azide ion and to be p -like since the free azide ion [12] has a Σ^+ ground state with the electron configuration

$$1\sigma g^2\ 1\sigma u^2 - - 1\pi u^4\ 1\pi g^4$$

It is observed that the long wavelength lines in PbN_3 can, in fact, be represented by three hydrogenic series:

$$\nu'_A = 28172\text{ cm}^{-1} - \frac{1576}{n^2}\text{ cm}^{-1}; n = 1, 2, \dots, \infty$$

$$\nu'_B = 29145\text{ cm}^{-1} - \frac{2299}{n^2}\text{ cm}^{-1}; n = 1, 2, \dots, \infty$$

$$\nu'_C = 32227\text{ cm}^{-1} - \frac{1924}{n^2}\text{ cm}^{-1}; n = 1, 2, \dots, \infty.$$

The three most intense absorption lines are assumed to correspond to the $n = 1$ transitions of the three exciton series. The degeneracy of the p -like valence bands should be completely lifted in orthorhombic α -lead azide due to the non-isotropic crystal field as well as the spin-orbit interaction. The three exciton series observed in lead azide could then be made up of an electron and a hole from each one of the valence bands.

The exciton series limits, reduced effective masses, exciton radii and ionization energies were determined for each of the exciton series and are shown in Table 1 (the electron and hole effective masses are assumed equal and low frequency dielectric constant $k = 4$ taken to be isotropic). It can be seen from the table that the excitons in lead azide are relatively small for effective mass excitons so that a central cell correction should probably be included.

The line breadth of the strong $n = 1$ line of the first series is approximately 70 \AA , which indicates a life time $\tau = 1.0 \times 10^{-16} \text{ sec}$. The line widths can be sensitive to the quality of the sample and therefore this value is representative of the order of magnitude only. It should be emphasized that the structure occurring at wavelengths shorter than 3700 \AA is masked by a large background absorption and the corresponding line positions and intensities are somewhat indeterminate.

In summary, structure has been observed in the low temperature optical absorption and photoconductivity of α -lead azide thin films. A minimum in the photoconductivity is observed in coincidence with the first strong absorption peak which can be interpreted

in terms of competing processes for the production of photoelectrons via impurities or the creation of excitons.

Due to the high purity of the thin films, we attribute the structure in the absorption spectra to any of several types of excitons. Intra-anion excitons are most probably not responsible for the long wavelength structure since these transitions have been observed at much shorter wavelengths in a variety of azides. However, the transition energies of either the Frenkel inter-cation excitons, $(\text{Pb}^+)^*$, or the localized charge transfer excitons may be reduced by the lead azide crystal field and by partial covalent effects to give optical transition energies in the region of the observed optical absorption structure. On the other hand, the long wavelength optical absorption structure seems to fit three separate hydrogen exciton series explicable in terms of Wannier exciton transitions involving holes from each one of three valence bands.

Unfortunately, it is not possible at this point to distinguish the exact type of electronic transition responsible for the observed structure in the optical absorption and photoconductivity of lead azide. Additional theoretical and experimental work will be required for a more complete understanding of the band structure of this very complex material.

Table 1. Energies and effective masses for the three Wannier-type exciton series in α -lead azide, where μ^* is reduced effective mass and $r^{(1)}$ is the exciton radius with $n = 1$

	Exciton series		
	A	B	C
ν' Gap	28172 cm^{-1} 3.49 eV	29145 cm^{-1} 3.61 eV	32227 cm^{-1} 3.99 eV
μ^*	0.23 m_0	0.34 m_0	0.28 m_0
m^*	0.46 m_0	0.68 m_0	0.56 m_0
$r^{(1)}$	9.2 \AA	6.2 \AA	7.6 \AA
$E_{\text{ionization}}$	0.20 eV	0.29 eV	0.24 eV

Acknowledgements—We are indebted to Mr. N. Palmer, Dr. O. Haase of Fairleigh Dickinson University and Dr. D. J. Berets of the American Cyanamid Company for vacuum deposition of the metallic films, Mr. V. I. Siele for production of the hydrazoic acid and Mr. M. Blas for help with the photoconductivity measurements. We gratefully acknowledge informative discussions with Dr. W. H. Taylor and Dr. J. Sharma of the Explosives Laboratory and we are particularly indebted to Professor F. E. Williams of the University of Delaware for his suggestions and helpful discussions on the various possible models of the band structure.

REFERENCES

1. JOHNSON P. D., *J. opt. Soc. Am.* **42**, 978 (1952); *J. appl. Phys.* **35**, 334 (1964).
2. YOFFE A. D., In *Developments in Inorganic Nitrogen Chemistry*, Vol. I, p. 72 London (1966).

3. FAIR H. D. and FORSYTH A. C., *Bull. Am. phys. Soc.* **12**, 895 (1967).
4. REITZNER B. and MANNO R., *Nature* **198**, 991 (1963).
5. DEDMAN A. J. and LEWIS T. J., *Trans. Faraday Soc.* **62**, 881 (1966).
6. COOK M. A., KEYES R. T., PITT C. H. and ROLLINS R. R., *Am. Chem. Soc. Symp. Explosives and Hazards and Testing of Explosives* (1963).
7. A more complete discussion of the photoconductivity of pure lead azide thin films and single crystals appears in; TAYLOR W. H. and BLAIS M., *Bull. Am. phys. Soc.* **13**, 466 (1968).
8. DEB S. K., *J. chem. Phys.* **35**, 2122 (1961).
9. EPPLER R. A., *Chem. Rev.* **61**, 523 (1961); SIBLEY W. A., SONDER E. and BUTLER C. T., *Phys. Rev.* **136**, 537 (1964); Lebl M., *Czech J. Phys.* **B16**, 902 (1966); *ibid.* **B16**, 898 (1966).
10. KOEZE P. and VOLGER J., *Physica* **37**, 467 (1967).
11. GRAY and WADDINGTON, *Proc. R. Soc.* **A235**, 481 (1956).
12. CLEMENTI E. and McLEAN A.D., *J. chem. Phys.* **39**, 323. (1963); KEMNEY P. J., MATTERN P. L. and BARTRAM R. H., *Bull. Am. phys. Soc.* **13**, 373 (1968).

THEORY OF THE KINETICS OF SHORT, RANGE ORDER*†

M. SCHOLJET

Physics Department, Temple University, Philadelphia, Pa. 19122, U.S.A.

(Received 6 February 1969)

Abstract—The theory of kinetics of short range order for an *AB* alloy containing vacancies of Kidin and Shtremel is criticized and an alternative set of equations of motion for the probabilities of atom-atom pairs and atom-vacancy pairs is proposed. Formulae are derived for the equilibrium probabilities which are consistent with the quasi-chemical theory and it is shown that the equilibrium state of atom-atom pairs implies the equilibrium state of atom-vacancy pairs. The integration of the equations of motion for the case of a quenching experiment in which the degree of short range order increases with time shows that the approach to equilibrium cannot be described by a simple exponential, in qualitative agreement with experiment. The study of the initial relaxation times gives also results in qualitative agreement with experiment. It is proposed that restrictive conditions that relate the equilibrium energy parameters to the energy of motion parameters should apply if the system is ever going to reach the state of thermodynamic equilibrium.

1. INTRODUCTION

IN A PAPER published in 1961 Kidin and Shtremel have studied the kinetics of the variations of short range order in a f.c.c. alloy [1] using a model which is based on Vineyard's model for the kinetics of an alloy. In Vineyard's theory [2] only long range order is considered but the model takes into account all possible configurations around the pair formed by the jumping atom and the vacancy. However, his treatment is in error because he considers that the height of the barrier the jumping atom has to go over between initial and final positions is a constant.

In the treatment of Kidin and Shtremel the jump rate for a given configuration is controlled by the difference in configurational energies between initial and final positions as in Vineyard's treatment. An extra term is added, however, to account for the order dependence of the potential energy barrier seen by the

jumping atom. But in defining this term the authors assume that both the atoms which are nearest neighbors at the saddle point and the atoms which are nearest neighbors before and after the jump contribute equally to this term. This seems incorrect to us because it assumes that interaction energies between nearest neighbors at the saddle point are equal to interaction energies for atoms in normal equilibrium positions. If we neglect relaxation a very simple calculation shows us that in a face centered cubic structure the distance of nearest approach at the saddle point is $\sqrt{\frac{2}{3}}a$ where $2a$ is the cube edge length while the normal equilibrium distance is $\sqrt{2}a$; i.e. the ratio of distances is $\sqrt{3}/2 \sim 0.86$. It is well known that interatomic forces increase steeply with distance, so that a difference of 14 per cent in distance may imply a large increase in the interaction energy.

We are going to investigate again the problem studied by Kidin and Shtremel. We will assume that the jump rate in a given configuration is determined by the height of the barrier and that the configuration of nearest neighbors of the saddle point plays the most important role in determining the jump

*Most of this work was carried out in partial fulfillment of the requirements for the Ph.D. in Metallurgy and Materials Science, University of Pennsylvania.

†This work is in part a contribution of the Laboratory for Research on the Structure of Matter, University of Pennsylvania, sponsored by the Advanced Research Projects Agency, Department of Defense.

rate. We will consider all possible configurations of atoms around the pair formed by the vacancy and the jumping atom. We will find out that a theory developed along these lines leads to a quasichemical equilibrium state. We will also find out that several other aspects of the Kidin and Shtremel treatment are probably also in error.

We will use to some extent the equations developed by Kidin and Shtremel which relate the temporal development of the *a posteriori* probabilities for atom pairs to the *a posteriori* probabilities for vacancy-atom pairs. In doing so we are going to show that some of the Kidin and Shtremel equations are wrong and suggest alternative equations.

Finally we will try to calculate the rates of approach to the equilibrium degree of short range order in a quenching experiment in which both the initial and final temperature are above the critical temperature of the alloy. Before we start the development of the equations of motion we will review briefly the experimental facts on the kinetics of short range ordering in alloys.

2. SUMMARY OF EXPERIMENTAL RESULTS

Although X-ray experiments give the most direct information about the state of short range order of an alloy it is certainly not the most preferred experimental method for studying the kinetics of ordering. The kinetics may also be inferred from the changes of specific heat, magnetic susceptibility, electrical resistivity, or some other physical property. The method most widely used for the study of the kinetics of ordering is the measurement of variations of the electrical resistivity caused by changes in the degree of order.

The appearance of short range order without the existence of long range order may cause either an increase or a decrease of resistivity.

An increase of resistivity with increasing short range order was observed in alloys of Cu and Au of several compositions with Cu

between 14 and 1.5 per cent by Korevaar[3]. For Cu₃Au Damask observed the same behavior[4] and similar results have been reported for AuAg alloys[5]. On the other hand decreases of resistivity for increasing short range order were reported in α -CuAl[6], FeCo[7], CoPt[8] and Ni₃Mn[9].

All the experimental work that has been published on the kinetics of short range order, and which we are going to review briefly, consists of measurements of the electrical resistivity during ordering. In interpreting the changes of electrical resistivity it is assumed that the change in electrical resistivity during isothermal annealing is proportional to the change in short range order.

A justification for this assumption and for the fact that the resistivity does either increase or decrease for an increase of short range order is given in the work of Beal[10]. There has been no quantitative investigation, however, on the limits of validity of this assumption, i.e. over how large of a temperature interval would this assumption be valid. Neither have other related problems been considered in Beal's work. For instance, it is possible that the change in short or long range order should cause a change in electrical resistivity via a change of the elastic constants of the crystal, which are related to the Debye temperature. A qualitative discussion of this point has been given by the author in another publication[11].

In comparison with the amount of experimental work quoted on the kinetics of long range order there is a very small amount for the kinetics of short range order, all of it very recent. There is no work that we know of about the kinetics of short range order in Cu₃Au. There are three experimental papers published, one on the kinetics of a Cu-Al (14.9 at.%) alloy by Radelaar[6] and one on the kinetics of Cu-Al and AuAg by Van den Beukel *et al.*[12] and one on kinetics in AuAg by Iyer and Asimow[5].

Radelaar measured the resistivity changes on strips of CuAl (85-15) alloy caused by a

sudden change in temperature. The temperature of the strip was kept constant by a heat bath and the change in temperature was achieved by changing the values of a d.c. current that was circulated through the strips. In this way down-quenches of approximately 10°C and up-quenches of 2°C were obtained in times smaller than one second. The plot of the time dependent resistivity change $\Delta\rho$ vs. time t could rather accurately be described by a simple exponential law.

$$\frac{\Delta\rho}{\Delta\rho_0} = \exp(-t/\tau). \quad (1)$$

Assuming τ to obey an Arrhenius type equation

$$\tau = \tau_0 \exp(Q/kT) \quad (2)$$

values of Q and τ_0 were obtained. The value of $Q = 1.70 \pm 0.05$ eV is not far from an activation energy for diffusion obtained by Childs and Le Claire [13] from internal friction experiments. The values of τ obtained in the up-quench experiments lie on the same $1/T$ curve than the down-quench values of τ , although it is possible to suspect from the scatter of points that a more careful study would show that the values of τ for the up-quench are consistently higher. Because the temperature changes are so small the vacancy concentration in this experiment is practically the equilibrium vacancy concentration. The temperature range investigated is rather small (between 200° and 325°C). Therefore no conclusions on whether Q may or may not have an order dependent term can be made.

Van den Beukel *et al.* followed the establishment of short range order in the alloys AuAg and CuAl (85, 15) by measuring the electrical resistivity of quenched wires. The wires were quenched from temperatures in the range from 800° to 400°C down to room temperature and the isothermal changes of resistivity after the quench were measured. Van den Beukel defines $\Delta\rho_\infty$ as the change of resistivity for

time tending to infinity as not necessarily equal to the change in resistivity for the system to reach the equilibrium state $\Delta\rho_e$. For AuAg the final value of $\Delta\rho$ after annealing at one temperature was measured as a function of the quenching temperature T_q . Up to $T_q = 800^\circ\text{C}$ $\Delta\rho_\infty$ increases; for $T_q > 800^\circ\text{C}$ it remains constant. The isothermal change of resistivity $\Delta\rho/\Delta\rho_\infty$ as a function of time cannot be fitted to an equation of the type

$$\frac{d\Delta\rho}{dt} = A(\Delta\rho_e - \Delta\rho)n_v e^{-E_M/kT}.$$

(where n_v is the number of vacancies) in other words it does not fit a single exponential. If an attempt is made to fit different segments of the curve to an exponential for each segment, i.e. assuming a curve

$$Ae^{-t/\tau}$$

where τ is not constant but a function of time, it is found that τ increases between two and eight times its initial value between the beginning and the end of annealing. This form of non-simple exponential decay is attributed by Van den Beukel *et al.* to an increase in the value of E_M with increasing short range order (see equation (1)). The total increase of E_M is estimated as 0.05 eV. The variation of $\Delta\rho_\infty$ with quenching temperature is attributed to a decay in the number of excess vacancies present during the quench. If vacancies disappear fast enough they will be gone before short range order equilibrium is established, and the values of $\rho_\infty < \rho_e$ tell us that the final state is not an equilibrium state. Van den Beukel *et al.* find the value of E_M for CuAl from a plot of $\ln[1/\rho_e(d\Delta\rho/dt)]_{t \rightarrow 0}$ vs. $1/T$, i.e. the initial values of τ at time $t = 0$ for different annealing temperatures.

The experimental points fall on a straight line and the value of E_M is in good agreement with results of other authors. Unfortunately the range of annealing temperatures is rather narrow (approximately 300°–370°K).

An important piece of work has been carried out by Iyer and Asimow[5]. The authors report quenching samples of $\text{Au}_{0.5}\text{Ag}_{0.5}$ alloy from different quenching temperatures for the same annealing temperature. They assume an equation

$$\frac{d\Delta\rho}{dt} = -\exp\left(-\frac{E_r}{kT_a}\right)f(\Delta\rho) \quad (3)$$

where the exponential is the vacancy concentration and $f(\Delta\rho)$ contains the information about the final state, and plot the resulting values of $\log(\ln(\Delta\rho_0/\Delta\rho))$ vs. $[\log t + A(T_Q)]$, where $A(T_Q)$ is a parameter used to take care of the shift in the values of $\log t$ caused by the different vacancy concentrations at different quenching temperatures. As can be seen (Fig. 1), the data all lie on the same curve, irrespective of T_Q . This verifies the initial assumption that the vacancy concentration during the anneal remains essentially constant. The curve is not a straight line, thus confirming that short range order kinetics is not adequately described by $f(\Delta\rho) \propto \Delta\rho$. The authors conclude that vacancy annealing is not a significant factor in the short range order kinetics in this alloy for quenches from 450°C and above, thus disagreeing with Van den Beukel *et al.* In support of this argument the authors also mention that in pure gold, i.e. for a case of vacancy annealing only, the time for the resistivity to reach one half the value of the final resistivity increment is of the order of hundreds of hours[14], i.e. one order of magnitude larger than the largest equivalent time in their experiments. Since there is no reason to believe that the number of jumps made by a vacancy before it anneals out is significantly different in the alloy, this supports their argument.

Iyer and Asimow also criticise the method of measurement of Van den Beukel *et al.* The latter measures the changes of resistivity from the as-quenched value. The as-quenched value is thought to be dependent on reordering during the quench. Therefore, Iyer and

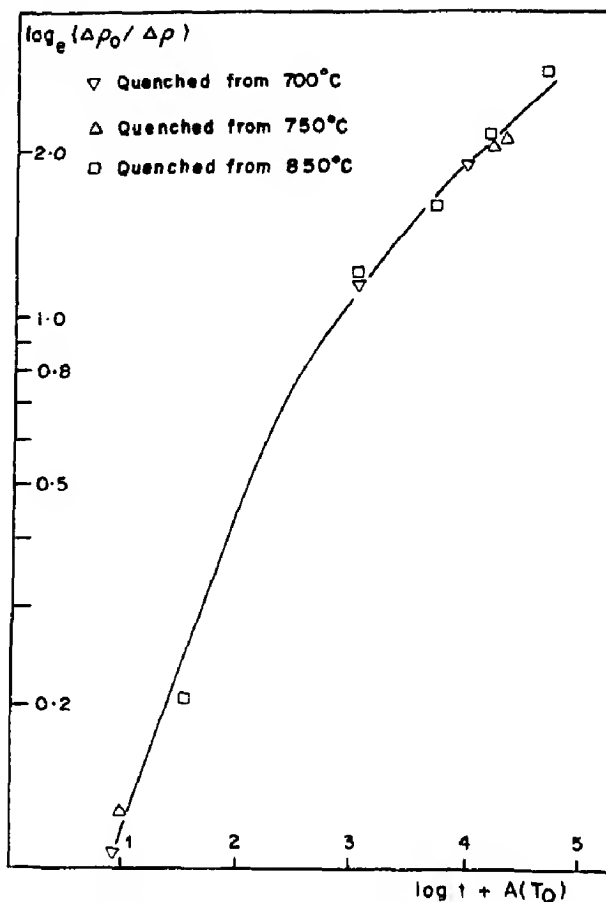


Fig. 1. $\log_{10}(\log_e(\Delta\rho_0/\Delta\rho))$ vs. $\log t$ in a quenching experiment for a short range ordered 0.50 Ag 0.50 Au alloy (according to Iyer and Asimow).

Asimow measure the deviations from the final value of the resistivity.

3. DEFINITION OF PROBABILITIES AND INTERCHANGE PROCESSES

We consider a short range ordered alloy without long range order and nearest neighbor atom-atom interactions only. c_A and c_B are the atomic concentrations. c_v is the vacancy concentration. Since c_v is assumed to be small we can write

$$c_A + c_B = 1.$$

p_{BA} , p_{AA} are *a posteriori* probabilities that when an A atom is at a given position a nearest neighbor position is occupied by

either a B or an A atom. For an f.c.c. alloy and neglecting vacancy-vacancy pairs of nearest neighbors the *a posteriori* probabilities are defined by the equations

$$p_{XY} = Q_{XY}/12Nc_X \quad (4)$$

$$p_{XX} = 2Q_{XX}/12Nc_X, (X, Y = A, B). \quad (5)$$

N is the total number of lattice sites; Q_{XY} is the number of XY pairs of nearest neighbors.

The *a posteriori* probabilities satisfy a consistency condition that comes about through the requirement that the number of AB pairs be the same irrespective of whether it is counted from A atoms or from B atoms

$$c_A p_{BA} = c_B p_{AB}. \quad (6)$$

Some other relations involving the *a posteriori* probabilities are given by

$$p_{AA} + p_{BA} = 1 \quad (7)$$

$$p_{BB} + p_{AB} = 1. \quad (8)$$

In writing (7) and (8) we neglected p_{VA} and p_{VB} , which is acceptable, since the vacancy concentration c_v is small compared to the atom concentrations c_A and c_B .

Let us consider a vacancy and an A atom that is a n.n. of the vacancy. There are

iB atoms n.n. of the vacancy only ($0 \leq i \leq 7$)

kB atoms n.n. of the A atom only ($0 \leq k \leq 7$)

jB atoms n.n. of both the A atom and the vacancy (saddle point neighbors) ($0 \leq j \leq 4$).

The probability of a configuration with iB atoms around the vacancy is given by

$$q_{BV}^{(i)} \equiv C_7^i p_{BV}^i (1 - p_{BV})^{7-i} \quad (9)$$

where the C_7^i are binomial coefficients.

The probability of a configuration with kB atoms around the jumping A atom is given by

$$q_{BA}^{(k)} \equiv C_7^k p_{BA}^k (1 - p_{BA})^{7-k} \quad (10)$$

where the C_7^k are binomial coefficients.

The probability of a saddle point configuration with jB atoms is given by

$$\begin{aligned} C_4^j (p_{BA} p_{BV})^j (p_{AA} p_{AV})^{4-j} \\ = C_4^j (p_{BA} p_{BV})^j [(1 - p_{BA})(1 - p_{BV})]^{4-j}. \end{aligned}$$

Kidin and Shtremel write instead of $(1 - p_{BA})(1 - p_{BV})$ a term $(1 - p_{BA} p_{BV})$ which we believe to be incorrect. Besides neither the above expression nor Kidin and Shtremel's are normalized probabilities. To normalize the probabilities of saddle point configurations we have to divide over the summation of this expression over j , i.e.

$$\begin{aligned} \sum_{j=0}^4 C_4^j (p_{BA} p_{BV})^j [(1 - p_{BA})(1 - p_{BV})]^{4-j} \\ = [1 + p_{BA}(2p_{BV} - 1) - p_{BV}]^4. \end{aligned}$$

Then we can define the normalized probability as

$$q_{B(AV)}(j) \equiv \frac{C_4^j (p_{BA} p_{BV})^j [(1 - p_{BA})(1 - p_{BV})]^{4-j}}{[1 + p_{BA}(2p_{BV} - 1) - p_{BV}]^4}. \quad (11)$$

The probability that given an AV pair it will have a configuration of nearest neighbors given by i, j and k can be defined as

$$Q_{i,j,k}^{(A)} \equiv q_{BV}(i) q_{BA}(k) q_{B(AV)}(j). \quad (12)$$

The rate of interchange of a given configuration defined by j and k is written as

$$R_{VA}(j, k) = \nu \exp(-E_A^M(j, k)/kT) \quad (13)$$

where ν is a frequency factor and we define the migration energy as

$$\begin{aligned} E_A^M(j, k) &\equiv -jv_{AB}^* - (4-j)v_{AA}^* - [-jv_{AB} \\ &\quad - (4-j)v_{AA} - kv_{AB} - (7-k)v_{AA}] \\ &= -4v_{AA}^* + 11v_{AA} - j[(v_{AB}^* - v_{AA}^*) \\ &\quad - (v_{AB} - v_{AA})] + k(v_{AB} - v_{AA}). \end{aligned} \quad (14)$$

We assume that $E_A^M(j, k)$ is always positive. Therefore, the implicit assumption in (14) is that the saddle point energies v_{AB}^\ddagger and v_{AA}^\ddagger are negative. Let us remember that in the current order-disorder theory the equilibrium interaction energies v_{AB} , v_{AA} , v_{BB} , are assumed to be positive. The justification for the saddle point energies having a negative sign is that the interatomic forces increase steeply and change sign for distances smaller than the equilibrium distance, like the distance between the jumping atom and its nearest neighbors when the jumping atom is at a saddle point position.

4. DEVELOPMENT OF THE KINETIC EQUATIONS.

For an AV pair with a neighbors configuration (i, j, k) where iB atoms are saddle point neighbors, kB atoms are nearest neighbors of the A atom and iB atoms are nearest neighbors of the vacancy only, if A and V interchange places the numbers of pairs of the crystal is going to change by

$$\Delta Q_{AB} = -\Delta Q_{AA} = \Delta Q_{VA} = -\Delta Q_{VB} = i - k. \quad (15)$$

From this Kidin and Shtremel proceed to write

$$\left(\frac{dQ_{VA}}{dt}\right)_{VA} = \left(\frac{dQ_{AB}}{dt}\right)_{VA} \quad (16)$$

$$\left(\frac{dQ_{VA}}{dt}\right)_{VB} = -\left(\frac{dQ_{AB}}{dt}\right)_{VB} \quad (17)$$

where t is the time variable and the subscripts VA and VB mean because of VA interchange and because of VB interchange.

At this point we are in disagreement with Kidin and Shtremel. Equations (16) and (17) contain implicit assumptions which have not been clarified by the authors.

The implicit assumption is that if a system is initially in a non-equilibrium state, equilibrium will be attained through many independent interchange processes. This means that if, let

us say, in the equilibrium state there are more AB and AV pairs than in the initial state, the increase in the number of AB and AV pairs will be attained in such a way that the AB and AV pairs created in individual interchange processes while the system is approaching equilibrium are not destroyed in other interchange processes before the system reaches the final state. In other words, equations (16) and (17) are true for times of the order of the average time that elapses between successive interchange processes for a single vacancy.

The assumption that the atom-atom pairs of a given kind that are created as the system does change towards equilibrium are not affected again after the elementary interchange by which they have been created seems reasonable. But the equivalent assumption for atom-vacancy pairs is incorrect. The reason is that there are of the order of c_v^{-1} more atom-atom pairs than atom-vacancy pairs. Therefore, the same number of elementary interchange processes that creates a given number of atom-atom pairs, creates a number of atom-vacancy pairs roughly c_v times smaller. While the system changes towards equilibrium a given atom may participate only once in an elementary interchange (or not participate at all), but each vacancy will participate in a large number of elementary interchange processes. Vacancy-atom pairs will constantly be created and destroyed. Therefore, we may expect that fluctuations in the atom-vacancy *a posteriori* probabilities are much larger than in the atom-atom *a posteriori* probabilities.

We therefore propose as an alternative to equations (16) and (17)

$$c_v^{-1}(dQ_{VA}/dt)_{VA} = (dQ_{AB}/dt)_{VA} \quad (18)$$

$$c_v^{-1}(dQ_{VA}/dt)_{VB} = -(dQ_{AB}/dt)_{VB}. \quad (19)$$

It should be emphasized that this is an approximation that cannot be completely accurate. The number of vacancies available for VA interchanges is not equal to the number

of vacancies available for VB interchanges, because in general $q_{BV}(i) \neq q_{AV}(i)$. Moreover, there will be vacancies completely surrounded by A atoms that cannot participate in VB interchanges and vacancies completely surrounded by B atoms that cannot participate in VA interchanges. A more accurate formulation of the theory would replace (18) and (19) by a set of equations with two equations for each value of i , containing explicitly the vacancy concentrations for given environments $c_v(i)$. If, on the other hand, the kinetics is affected by the trapping of vacancies, as we shall see later, the analysis of this process would require explicit consideration of the time dependence of each $c_v(i)$.

The change in the *a posteriori* probability of AB pairs will be given by

$$\frac{dp_{BA}}{dt} = \frac{\left(\frac{dQ_{AB}}{dt}\right)_{VA}}{12Nc_A} + \frac{\left(\frac{dQ_{AB}}{dt}\right)_{VB}}{12Nc_v} \quad (20)$$

since there are zNc_Ap_{BA} AB pairs radiating from A atoms ($z = 12$, coordination number); N is the total number of sites, approximately equal to the total number of atoms.

There are zNc_vp_{AV} pairs formed by a vacancy and a nearest neighbor A atom radiating from Nc_v vacancies, so that in a unit time the number of interchanges taking place is given by

$$zNc_vp_{AV} \sum_i \sum_j \sum_k Q_{i,j,k}^{(A)} R_{VA}(k, j).$$

In each of these interchanges the number of AB pairs does change by $\Delta Q_{AB} = i - k$. Then the rate of variation of Q_{AB} due to AV interchanges is given by

$$\left(\frac{dQ_{AB}}{dt}\right)_{VA} = zNc_vp_{AV}\Sigma^{(A)} \quad (21)$$

where

$$\Sigma^{(A)} = \sum_{j=0}^4 \sum_{k=0}^7 \sum_{i=0}^7 (i-k) Q_{i,j,k}^{(A)} R_{VA}(j, k). \quad (22)$$

Then (20) can be written as

$$\frac{dp_{BA}}{dt} = \frac{c_v}{c_A} p_{AV} \Sigma^{(A)} + \frac{c_v}{c_B} p_{BV} \Sigma^{(B)}. \quad (23)$$

The environment of the vacancy will vary at the rate

$$\frac{dp_{AV}}{dt} = \frac{\left(\frac{dQ_{VA}}{dt}\right)_{VA}}{12Nc_v} + \frac{\left(\frac{dQ_{VA}}{dt}\right)_{VB}}{12Nc_v}. \quad (24)$$

Using (18), (19), (21) and the expression similar to (20) for VB interchanges we obtain

$$\frac{dp_{AV}}{dt} = c_v p_{AV} \Sigma^{(A)} - c_v p_{BV} \Sigma^{(B)}. \quad (25)$$

Equations (23) and (25) are two coupled differential equations which govern the temporal development of the system.

$\Sigma^{(B)}$ plays the same role for the migration of B atoms as $\Sigma^{(A)}$ does for the A atoms. For $\Sigma^{(B)}$ the numbers i, j , and k refer to unlike atoms again (i.e. A atoms in this case).

For the equilibrium state we should have

$$dp_{BA}/dt = 0 \quad (26)$$

$$dp_{VA}/dt = dp_{VB}/dt = 0. \quad (27)$$

Since neither c_v , c_A , c_B , p_{AV} , p_{BV} are zero this implies that in the equilibrium state

$$\Sigma^{(A)} = \Sigma^{(B)} = 0. \quad (28)$$

Let us now try to calculate $\Sigma^{(A)}$ and $\Sigma^{(B)}$ using the definitions (9) to (14) in (22). We have

$$\begin{aligned} \Sigma^{(A)} = & e^{(4i_A^{\frac{1}{2}} - 11v_{AA})/kT} \sum_{i=0}^7 \sum_{k=0}^7 \sum_{j=0}^4 (i-k) C_7^i p_{BV}^k \\ & \times (1-p_{BV})^{7-i} C_7^k p_{BA}^j (1-p_{BA})^{7-k} a_A^k \\ & \times \frac{C_A^j (p_{BA} p_{BV})^j [(1-p_{BA})(1-p_{BV})]^{4-j} b_A^j}{[1 + p_{BA}(2p_{BV} - 1) - p_{BV}]^4} \end{aligned} \quad (29)$$

$$v_A \equiv v_{AB} - v_{A\cdot}; v_A^\dagger \equiv v_{AB}^\dagger - v_{AA}^\dagger$$

$$a_A^\dagger \equiv \exp[(v_A^\dagger - v_{A\cdot})/kT]; a_A \equiv \exp(-v_A/kT)$$

$$\begin{aligned} \Sigma^{(A)} &= \exp\left(\frac{4v_{AA}^\dagger - 11v_{AA}}{kT}\right) \\ &\times [S_A(k)S_A(j) \sum_{i=0}^7 iC_7^i p_{BV}^i (1-p_{BV})^{7-i} \\ &\times S_A(i)S_A(j) \sum_{k=0}^7 kC_7^k p_{BA}^k (1-p_{BA})^{7-k} a_A^k]. \end{aligned} \quad (30)$$

$$\begin{aligned} S_A(k) &\equiv \sum_{k=0}^7 C_7^k (p_{BA} a_A)^k (1-p_{BA})^{7-k} \\ &= [1 + p_{BA}(a_A - 1)]^7. \end{aligned} \quad (31)$$

$$\begin{aligned} S_A(j) &\equiv \frac{\sum_{j=0}^4 C_4^j (p_{BA} p_{BV})^j [(1-p_{BA})(1-p_{BV})]^{4-j} a_A^j}{[1 + p_{BA}(2p_{BV} - 1) - p_{BV}]^4} \\ &= \left[\frac{p_{AV} + p_{BA}(p_{BV} a_A - p_{AV})}{1 + p_{BA}(2p_{BV} - 1) - p_{BV}} \right]^4. \end{aligned} \quad (32)$$

$$S_A(i) \equiv \sum_{i=0}^7 C_7^i p_{BV}^i (1-p_{BV})^{7-i} = 1. \quad (33)$$

In order to evaluate the next summations we are going to use the formula

$$\sum_{l=0}^n iC_n^l \alpha^l \gamma^{n-l} = n\alpha(\alpha + \gamma)^{n-1}.$$

With this formula we obtain

$$\sum_{i=0}^7 iC_7^i p_{BV}^i (1-p_{BV})^{7-i} = 7p_{BV}. \quad (34)$$

$$\begin{aligned} \sum_{k=0}^7 kC_7^k (p_{BA} a_A)^k (1-p_{BA})^{7-k} \\ = 7p_{BA} a_A [1 + p_{BA}(a_A - 1)]^6. \end{aligned} \quad (35)$$

Now replacing (31)–(35) into (30)

$$\begin{aligned} \Sigma^{(A)} &= 7 \exp\left(\frac{4v_{AA}^\dagger - 11v_{AA}}{kT}\right) \\ &\times \left[\frac{p_{AV} + p_{BA}(p_{BV} e^{(v_A^\dagger - v_A)/kT} - p_{AV})}{1 + p_{BA}(2p_{BV} - 1) - p_{BV}} \right]^4 \\ &\times [1 + p_{BA}(a_A - 1)]^6 \\ &\times \{[1 + p_{BA}(a_A - 1)]p_{BV} - p_{BA}a_A\}. \end{aligned} \quad (36)$$

For the equilibrium state we should have $\Sigma^{(A)} = 0$. Equating the last bracket to zero we obtain

$$p_{BV}^0 = \frac{p_{BA}^0 a_A}{1 + p_{BA}^0 (a_A - 1)} \quad (37)$$

where the zero refers to the equilibrium value of p_{BV} and p_{BA} .

This last equation is identical with the result already obtained from a kinetic quasi-chemical approach for a crystal with vacancies [15].

We can obtain similar results for $\Sigma^{(B)}$ by defining a VB pair in which i, j , and k are the number of A atoms nearest neighbors of the vacancy only, of both vacancy and B atom and of B atom only. $\Sigma^{(A)}$ and $\Sigma^{(B)}$ will have the same functional form and all derivations for $\Sigma^{(A)}$ will be valid for obtaining $\Sigma^{(B)}$ if we replace p_{BA} by p_{AB} , p_{BV} by p_{AV} , v_{AA} and v_{AA}^\dagger by v_{BB} and v_{BB}^\dagger .

5. RESULTS OBTAINED FROM THE STUDY OF THE KINETIC EQUATIONS

From inspection of (23) and (25) for the case of a stoichiometric alloy ($c_A = c_B = \frac{1}{2}$) several conclusions can be drawn.

(a) The values of the parameters that enter into the equations cannot be independent

There are several reasons for this. The first is a physical reason. Assume that vacancy interactions are negligible and that the deviation from the equilibrium state is large

enough so that for the system to reach the equilibrium state each vacancy must perform several jumps, let us say ten. Assume also that the contribution of VA interchanges is larger than the contribution of VB interchanges by one order of magnitude. Then for a vacancy that starts with a given value of $i = i_0$ neighbors unlike the jumping atom, if the vacancy makes a jump that increases the degree of order then $(i-k) > 0$, therefore $i_1 \equiv k$, we will have $i_1 < i_0$ and successive VA interchanges will make $i_n < i_{n-1} \dots i_1 < i_0$. When $i_n = 0$ the process cannot continue and the vacancy will get trapped in a configuration of A atoms as only nearest neighbors. Thus, the vacancy would become ineffective for further increase in the degree of order. Therefore, only the small amount of vacancies that would escape trapping through VB interchanges would contribute to ordering and the VB interchange rate would determine the rate of ordering. If we want to avoid this situation we have to accept that both terms on the r.h.s. of (23) and (25) are of the same order of magnitude. This in turn requires that the values of the parameters $(4v_{AA}^\ddagger - 11v_{AA})$, $(v_A^\ddagger - v_A)$ be not very different from $(4v_{BB}^\ddagger - 11v_{BB})$, $(v_B^\ddagger - v_B)$ respectively, so that the first term in (23) should be of the same order of magnitude of the second term over the whole range of temperatures considered. It should be noted that the parameters $-(4v_{AA}^\ddagger - 11v_{AA})$ and $-(4v_{BB}^\ddagger - 11v_{BB})$ represent the migration energies of an A atom in an environment of A atoms only and the migration energy of a B atom in an environment of B atoms only, in a nearest neighbors model. Therefore, if our model of first neighbor interactions only would be valid, and if trapping of vacancies does not play a significant part, a condition for the equations of motion (23) and (25) to be applicable in their present form would be that the migration energies of atoms in pure A and pure B be approximately equal.

A relation between the equilibrium parameters v_A and v_B and the kinetic parameters considered above can also be deduced.

Suppose that we have

$$(v_{AA} - v_{BB}) > 0.$$

From the definitions of v_A and v_B it follows that

$$v_A < v_B$$

and according to the result for the atom-vacancy probability (37) and using $p_{BV} + p_{AV} = 1$ we find that p_{AV}° will be a decreasing function for decreasing temperature. Let us imagine a quenching experiment between an initial temperature T_i and a final temperature T_f . At time $t = 0$ we have $p_{AV} = p_{AV,i}^\circ$ (where the superscript denotes the equilibrium state) and for time $t \rightarrow \infty$, $p_{AV} \equiv p_{AV,f}^\circ$. Since p_{AV} would be decreasing this requires

$$p_{AV}\Sigma^{(A)} < p_{BV}\Sigma^{(B)}. \quad (38)$$

The most straightforward way to satisfy this requirement would be to have

$$|4v_{AA}^\ddagger - 11v_{AA}| > |4v_{BB}^\ddagger - 11v_{BB}| \quad (39)$$

$$|v_A^\ddagger - v_A| > |v_B^\ddagger - v_B|. \quad (40)$$

We have assumed $v_{AA} > v_{BB}$. The inequality (39) is consistent with the possibility that

$$v_{AA}^\ddagger = kv_{AA}; v_{BB}^\ddagger = kv_{BB}$$

but this would not be consistent with (40). However, since most probably the behavior of $\Sigma^{(A)}$ and $\Sigma^{(B)}$ would be dominated by $\exp((4v_{AA}^\ddagger - 11v_{AA})/kT)$ and $\exp((4v_{BB}^\ddagger - 11v_{BB})/kT)$, (38) could be satisfied without (40) being satisfied.

Let us suppose that (38) is not satisfied. Then $(dp_{AV}/dt)_{t=0}$ would be positive and the p_{AV} vs. t function would have to be required to have a maximum at some intermediate time and then decrease towards its final value. In other words $p_{AV}\Sigma^{(A)}$ would be initially larger than $p_{BV}\Sigma^{(B)}$ and after some time the

situation would be reversed. This in turn would require that $(dp_{BA}/dp_{AV})_{t=0}$ be positive and then change sign at some intermediate value of time, i.e. the non-equilibrium curve p_{BA} vs. p_{AV} would have the form shown in Fig. 2 where the equilibrium curve is also shown. Considering this and the form of the equations we think that this is rather difficult to accept. If we take smaller temperature intervals between the initial and the final temperature, i.e. we tend to make the transformation reversible the non-equilibrium curve would have to tend towards the equilibrium curve and this would be in contradiction with the initial positive slope of p_{AV} vs. t .

The line of reasoning we have developed above makes it necessary for the system to reach the equilibrium state to have the inequality (38) and therefore also inequality (39) satisfied. However it should be stated that the inequality (39) does not tell us that both

terms in (23) and (25) have to be of the same order of magnitude. In other words if $(v_{AA} - v_{BB}) > 0$ and the migration energies are such that VA interchanges occur more frequently than VB interchanges the system will never reach the state of equilibrium in a quenching experiment. But if the migration energies are different enough and their relative magnitudes are reversed for the situation to be reversed in such a way that VB interchanges occur much more frequently than VA interchanges the system will still be able to reach the state of thermodynamic equilibrium by a process of vacancy trapping in an environment of B atoms and release of the trapped vacancies through VA interchanges. With enough vacancies trapped the rate of ordering would be governed by the rate of escape of trapped vacancies and therefore controlled by the migration energies of the slowest moving atoms (A atoms). If such a situation occurs we should expect that equations (23) and (25) would no longer be adequate to describe the process, at least not in their present form.

The possibility of trapping needs to be explored in detail. It is possible that this would require that we include the probabilities of vacancies with given specific environments. We are not going to attempt such a detailed analysis here but we will try to draw a simple qualitative picture. For the case of a quenching experiment in an alloy that has $(v_{AA} - v_{BB}) > 0$, if the migration energies make VB interchanges much more frequent than VA interchanges we could imagine the following stages in the process of approaching the equilibrium state: (1) a first stage (fast) dominated by VB interchanges. (2) An intermediate stage (slow) in which the kinetics would be dominated by the rate of escape of vacancies surrounded by a majority of B atoms through VA interchanges. (3) A last stage in which the vacancies would tend to get back to their normal environment.

Quite obviously, this picture would only apply to large deviations from equilibrium.

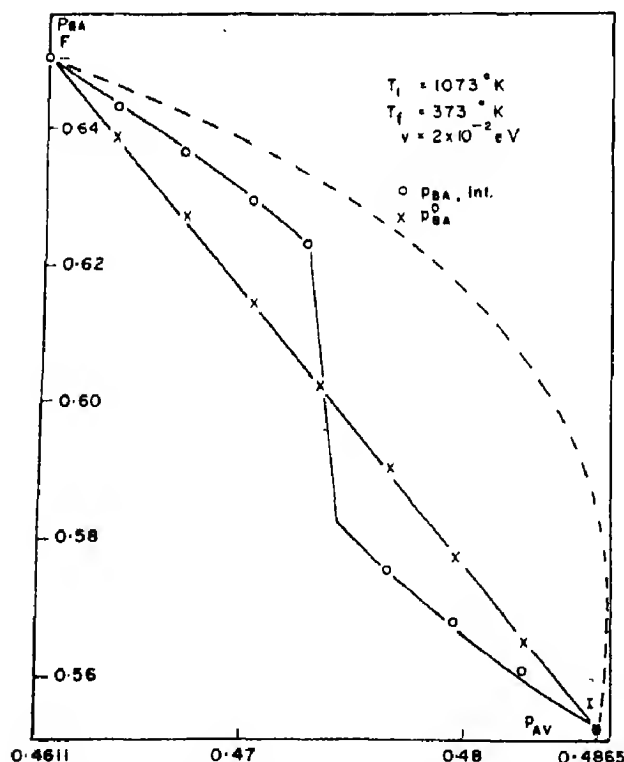


Fig. 2. Equilibrium and non-equilibrium p_{BA} vs. p_{AV} curves; p_{BA}^0 equilibrium curve; $p_{BA, int.}$ tangent interpolation scheme; dashed line, unlikely p_{BA} vs. p_{AV} curve.

Quite naturally, a process that involves several stages, which are dominated by different migration energies, would not be described by a simple exponential, thus giving a simple qualitative explanation of the observed experimental results.

If we have an alloy in which $(v_{AA} - v_{BB}) < 0$ and thus p_{AV} increases for decreasing temperature the same arguments could be applied to reverse the sign of the inequality (39). Therefore our model tells us that from the fact that an alloy is formed for a given pair of metals, if a pairwise interactions scheme is valid, we should be able to derive some restrictive conditions on the form of the pairwise interaction potentials of the atoms. Another consequence of the theory would be that if we could determine the migration energies of the atoms from experimental results we could from there obtain information on the relative values of the equilibrium interaction energy parameters.

(b) *The initial relaxation times*

When deviations from the equilibrium state become large the function $p_{BA} = f(t)$ can no longer be represented by a single exponential as shown by the experimental results[5, 12]. However, we can accept that for small time intervals near $t = 0$ the function tends towards an exponential. The relaxation time τ_0 associated with this zero time exponential will be given by

$$\tau_0 = -(dp_{BA}/dt)_{t=0}^{-1} \cdot \Delta p_0 \quad (41)$$

where

$$\Delta p_0 \equiv p_{BA,f} - p_{BA,i}$$

We tried to obtain the form of the function τ_0 vs. $1/T_f$ that would result from a series of experiments in which a number of samples in equilibrium at an initial temperature of 1273°K would be subjected to a sudden temperature drop of a given value for each sample. The following values were adopted for the parameters: $v = 4 \times 10^{-2}$ eV; $v_A =$

3×10^{-2} eV; $v_B = 5 \times 10^{-2}$ eV; $v_A^* = 0.18$ eV; $v_B^* = 0.20$ eV; $4v_{AA}^* - 11v_{AA} = -0.945$ eV; $4v_{BB}^* - 11v_{BB} = -0.86$ eV; $v = 10^{13}$ /sec; $c_v = 10^{-6}$.

The curve obtained is shown in Fig. 3.

The $\log \tau_0$ vs. $1/T_f$ curve appears to be linear over a temperature range of several hundred degrees. We also obtained values for a series of experiments in which the parameters v , v_A , and v_B were half the values given before, and the parameters v_A^* , v_B^* , $(4v_{AA}^* - 11v_{AA})$, $(4v_{BB}^* - 11v_{BB})$ had the same values. For this series of experiments we took the initial temperature $T_i = 1073^\circ\text{K}$ and the final temperatures varied in steps of 50° down to 373°K . A plot of the curve $\log \tau_0$ vs. $1/T_f$ still appeared to be linear over several hundred degrees but a calculation of the slope of

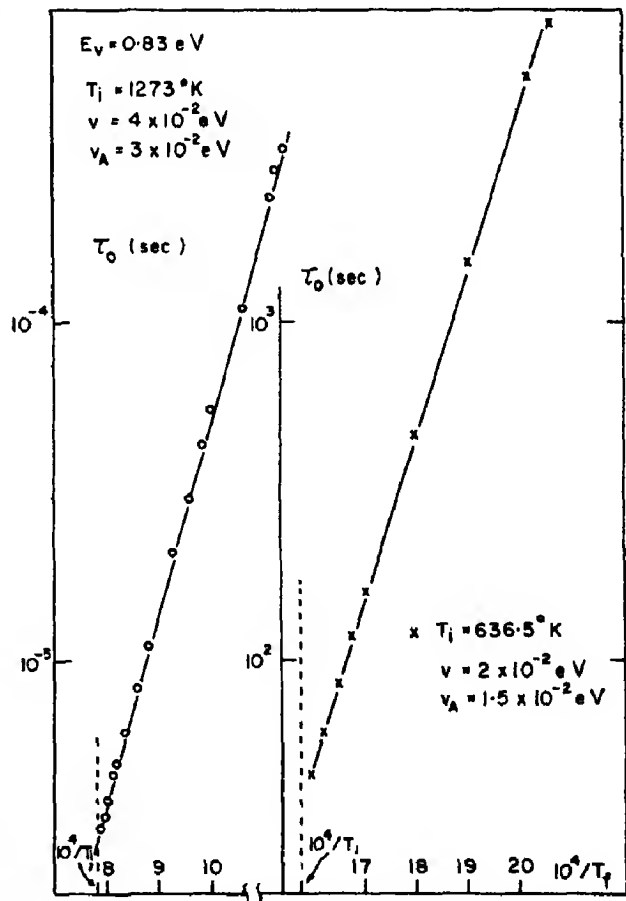


Fig. 3. τ_0 vs. $1/T_f$ for a series of quenching experiments.

$\log \tau_0$ vs. $1/T_f$ from the first two points of the curve gave a value slightly higher than the slope obtained from the last two points. The ratio of the difference in slopes to the slope at the lowest temperature values was of the order of 12 per cent. This is such a small deviation for a range of temperatures of 800°K that is is not surprising at all that it has not been observed in the experiments of Van den Beukel *et al.*[12]. Moreover, the annealing temperatures in the experiments of Van den Beukel were in all cases 400°C below the quenching temperatures, i.e. the range of temperatures investigated is smaller than ours, so this would make it even more difficult to observe.

We also investigated how the initial values of the relaxation times would change for a series of experiments in which in each experiment the quenching temperature is different but the temperature drop is the same, for temperature drops of 5°, 50° and 100°C. We get straight lines if we plot $\log \tau_0$ vs. $1/T_f$, over temperature ranges of several hundred degrees. This is in agreement with the experimental results of Radelaar[6].

(c) *A comment on the initial slopes of the equilibrium and non-equilibrium dp_{BA}/dp_{AV} curves*

The initial slope at $t=0$ of (dp_{BA}/dp_{AV}) will not, in general, tend to the value of the slope of dp_{BA}^0/dp_{AV}^0 , even in the case of small temperature changes. The reason is that the slope of the equilibrium curve is determined by the equilibrium parameters v and v_A only, while the slope obtained from the equations of motion depends on the relative values of the migration energies. We could have two limiting cases for the kinetic slope: if the two terms in the r.h.s. of the equations of motion are of the same order of magnitude (assuming $v_A < v_B$) then the initial slope will tend to minus infinity; if the second term of the r.h.s. is much larger the initial slope will tend to $-\frac{1}{2}$.

For values of v and v_A of 2×10^{-2} eV and

1.5×10^{-2} eV a simple calculation using the quasichemical equation

$$\frac{(p_{BA}^0)^2}{p_{AA}^0 p_{BB}^0} = e^{2v/kT}$$

and (37) for p_{AV}^0 shows that for values of T in the range 1000°–400°K the equilibrium slope is in the order of -3 , i.e. within the range of allowed values of the kinetic slope.

In the integration of the kinetic equations we will see that for the values of the parameters we chose the kinetic slope lies below the equilibrium slope. This may be interpreted as meaning that in a first stage the vacancies will tend to come in equilibrium with their environment faster than the atoms reach an equilibrium with their environment of other atoms, and also that this two stage process will be operating even for small deviations from equilibrium. There is, however, the possibility that we would consider values of the migration energies that would make the slope of $|(dp_{BA}/dp_{AV})_{t=0}| > |dp_{BA}^0/dp_{AV}^0|$. This would imply that the atomic environment changes faster than the vacancy environment.

In the limiting case of $(dp_{BA}/dp_{AV})_{t=0} \rightarrow -\frac{1}{2}$, i.e. the case in which the initial stage is dominated by VB interchanges, a natural extension of the theory would be to include a time dependent number of vacancies available for VB interchanges in (19) instead of c_v . This would reduce the second term in the r.h.s. of (23) and (25), thus reducing the value of dp_{BA}/dp_{AV} for $t > 0$.

(d) *Integration of the kinetic equations*

The main difficulty with equations (23) and (25) is that in order to integrate (23) and get the function $p_{BA} = f(t)$, so that we could compare it with experimental results, we have to know how p_{AV} changes as a function of p_{BA} for the non-equilibrium situation. We know the equilibrium curve between initial and final values, i.e. the series of successive values of p_{AV} that would occur if the trans-

formation would take place through a series of infinitely small temperature drops. We can take the equilibrium curve as a first order approximation to the true $p_{AV} = f(p_{BA})$. Taking a trial function in order to perform the integration implies that if we get $p_{AB} = f_1(t)$ from (23) we also know $p_{AV} = f_2(t)$ from (23). If we proceed to obtain from there $df_2(t)/dt$ this function should be expected to be different from dp_{AV}/dt given by (25) unless the trial function is the correct function. We used several types of trial function. Instead of working with $p_{AV} = f(p_{BA})$ we used p_{BA} as a function of p_{AV} , which is an equally valid approach; i.e. we divided the interval between initial and final values of p_{AV} in 408 equal segments and for each value of p_{AV} tried to find a correction term to the corresponding value of p_{BA}^0 . First we tried a term of the form $c(p_{AV,i} - p_{AV})(p_{AV} - p_{AV,f})$. A much better result was obtained with a correction term of the form

$$c \cdot \sin(2\pi(p_{AV,i} - p_{AV})/(p_{AV,i} - p_{AV,f})).$$

Equation (23) was integrated using an IBM 360 computer for the case of an *AB* alloy

quenched from 1373° down to 673°K using the values of the parameters stated before. $p_{BA,i}$ was 0.583 and $p_{BA,f} = 0.666$. We obtained $p_{BA} = f_1(t)$ by integrating (23) for a series of 408 pairs of values of p_{BA} and p_{AV} at equally spaced intervals of p_{AV} . From the results of integrating (23) and the p_{AV} vs. p_{BA} used in the integration we obtained $p_{AV} = f_2(t)$ and $df_2(t)/dt$ for seven values of p_{AV} intermediate between $p_{AV,i}$ and $p_{AV,f}$. The values of dp_{AV}/dt from (25) were then compared with the values of $df_2(t)/dt$ for the same values of p_{AV} . The differences between the two functions is shown in Fig. 4 for the best fit obtained. The largest difference is in the first and last points and it is of the order of 35 per cent, for the other points it varies between 20 and -0.1 per cent, for a correction term of the sine form with $c = 4 \times 10^{-3}$. Since the difference between the initial and final values of p_{BA} is of the order of 8×10^{-2} , the correction term is of the order of 5 per cent.

The results of integrating (23) for both $c = 0$ and $c = 4 \times 10^{-3}$ are shown in Fig. 5. We can see that the difference between both curves is negligible. The $\log(\log((p_{BA,f} - p_{BA,i})/(p_{BA,f} - p_{BA})))$ vs. $\log t$ deviates from

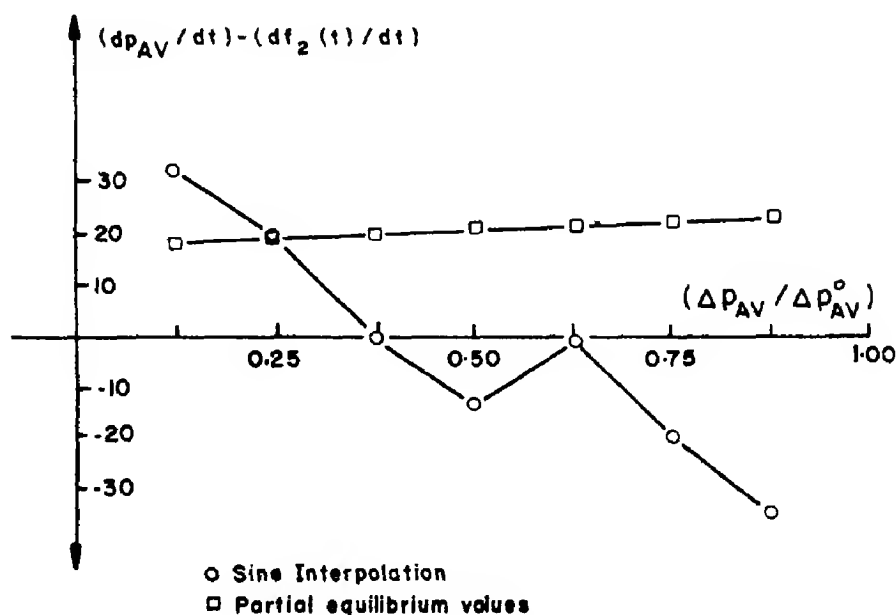
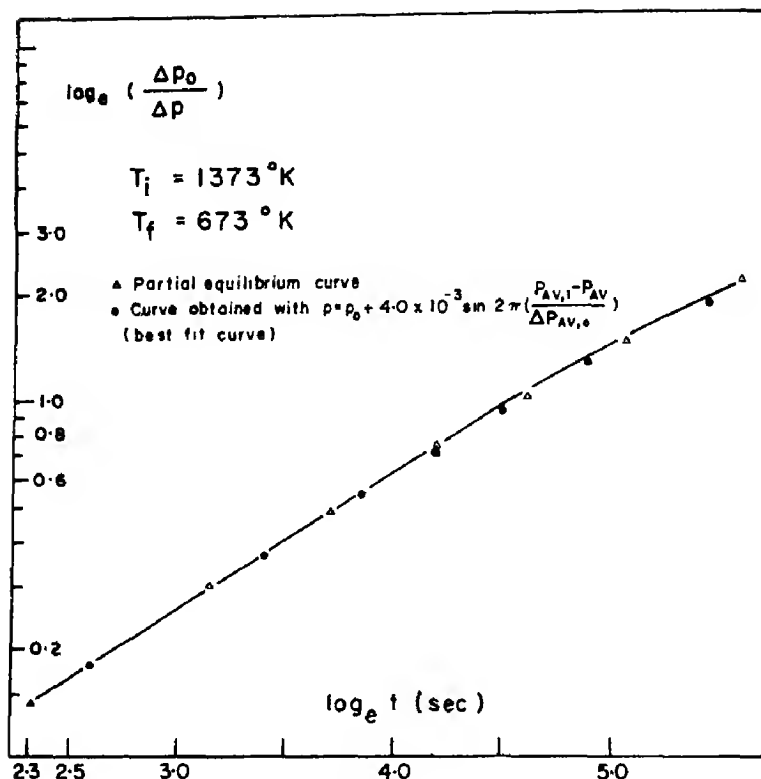


Fig. 4. Difference between (dp_{AV}/dt) and (df_2/dt) (per cent) vs. $(\Delta p_{AV}/\Delta p_{AV}^0)$.

Fig. 5. $\log_{10} (\log_e (\Delta p_0 / \Delta p))$ vs. $\log_e t$.

linearity in a way qualitatively similar to the experimental results of Van den Beukel *et al.*[12] and Iyer and Asimow[5].

Finally we tried another scheme for the function $p_{AV} = f(p_{BA})$ which we would call the 'extreme points tangent scheme'. We know exactly the values of the derivatives (23) and (25) at the initial point, i.e. for $t = 0$, since the values of p_{BA} and p_{AV} that enter into the equations are the equilibrium values. Hence we can find the values of

$$\begin{aligned} & ((dp_{BA}/dt)_{t=0} / (dp_{AV}/dt)_{t=0}) \\ & = (dp_{BA}/dp_{AV})_{t=0}. \quad (42) \end{aligned}$$

Let us assume now that the point of final equilibrium, i.e. for $t \rightarrow \infty$, is not a singular point. Then, for a value of p_{AV} close to $p_{AV,f}$ let us say $p_{AV,f} + \Delta$, where $\Delta \equiv (p_{AV,t} - p_{AV,f})/408$, let us find the corresponding value of p_{BA} from the equilibrium curve of p_{AV} vs. p_{BA} . We then replace these two values of p_{AV} and

p_{BA} in (23) and (25) and assume that their ratio gives us the derivative equivalent to (42) for $t \rightarrow \infty$. We then write $p_{BA}(1) = p_{BA,i}$; $p_{BA}(2) = p_{BA}(1) + \Delta(dp_{BA}/dp_{AV})_1$. Now that we have $p_{BA}(2)$ and $p_{AV}(2) = p_{AV}(1) + \Delta$, we can calculate the derivatives (23) and (25) for the second point of the p_{BA} vs. p_{AV} curve. Forming the ratio of the derivatives at the second point we can write $p_{BA}(3) = p_{BA}(2) + \Delta \cdot (dp_{BA}/dp_{AV})_2$. In a similar way we can obtain further successive points of the p_{BA} vs. p_{AV} curve. Now, if our procedure were exact the final point would coincide with the final equilibrium values of $p_{BA,f}$ vs. $p_{AV,f}$. Since this is very unlikely to happen, and it does not actually happen we can repeat the procedure starting with the final equilibrium values and go backwards towards the initial values. We thus have two branches of an approximate p_{BA} vs. p_{AV} curve. The next problem is how to join the two branches. We first attempted to make the function dis-

continuous at a point halfway between the initial and final values of p_{AV} . By using this discontinuous p_{BA} vs. p_{AV} function we integrated equation (23) using the IBM 360 computer. We obtained $p_{BA} = f_1(t)$ and from there $p_{AV} = f_2(t)$. By comparing the function $f_2(t)$ with dp_{AV}/dt as given by equation (25) we found that the difference between the two was small for a quenching experiment between $T_i = 1073^\circ\text{K}$ and $T_f = 373^\circ\text{K}$ with values of the parameters $v = 2 \times 10^{-2}$ eV, $v_A = 1.5 \times 10^{-2}$ eV, $v_B = 2.5 \times 10^{-2}$ eV and the other parameters having the same values as before. The difference was less than 1.1 per cent over the whole range of values of the variables. However, the $\log_e (\Delta p / \Delta p_0)$ where $\Delta p \equiv p_{BA,f} - p_{BA}$ and $\Delta p_0 \equiv p_{BA,f} - p_{BA,i}$ shows an inflection point in the region of the discontinuity of the function p_{BA} vs. p_{AV} which is probably due to the crude nature of the approximation, i.e. assuming a discontinuity in the p_{BA} vs. p_{AV} curve.

We therefore tried to improve the approximation by carrying out the 'tangent scheme' from the initial point of p_{BA} vs. p_{AV} up to a value of $p_{AV} = p_{AV,i} + 190 \cdot \Delta$ and from the final value $p_{AV,f}$ back to $p_{AV,f} - 190 \cdot \Delta$ and used a linear interpolation for the central part of the curve, so that now the p_{BA} vs. p_{AV} approximate function would be a continuous function with two discontinuities in the first derivative. As a result of this improved approximation the inflection point in the $\log_e (\Delta p / \Delta p_0)$ vs. t curve disappeared but the difference between the dp_{AV}/dt given by (25) and the equivalent function obtained from $p_{BA} = f_1(t)$, although remaining smaller than 1 per cent over 90 per cent of the values of $\log (\Delta p / \Delta p_0)$ climbed to 91 per cent in the central region corresponding to the linear interpolation. The difference between the non-equilibrium values of p_{BA} and the equilibrium values, for a given value of p_{AV} , using this interpolation scheme, was nowhere larger than 16 per cent of the value of Δp_0 .

Using this last approximation for the function p_{BA} vs. p_{AV} we have tried to reproduce

the $\log_e (\Delta p / \Delta p_0)$ vs. time curves that would be obtained in a series of experiments like the experiments by Iyer and Asimow [5]. We put $T_f = 373^\circ\text{K}$ and the values of the parameters v , v_A , v_B , etc. were the same as above. The vacancy concentration was normalized to a value $c_v = 10^{-6}$. We obtained the curves $\log_{10} (\log_e (\Delta p / \Delta p_0))$ vs. $\log_e t$ for the following values of the initial temperatures, $T_i = 1073^\circ$, 873° and 673°K . The results are shown in Fig. 6. In our case we obtain curves that are slightly shifted one with respect to the other, the curves that represent an experiment with lower T_i appearing shifted towards the right of those with higher T_i , the shift decreasing in magnitude for the part of the curves which represent the state of approaching equilibrium. In the experiments of Iyer and Asimow the spread of experimental points is such that it appears impossible to draw separate curves for the different experiments. It is possible, therefore, that the shift of the curves towards the right for decreasing values of T_i was obscured by experimental errors in the work of Iyer and Asimow and that more careful experiments would detect such a shift.

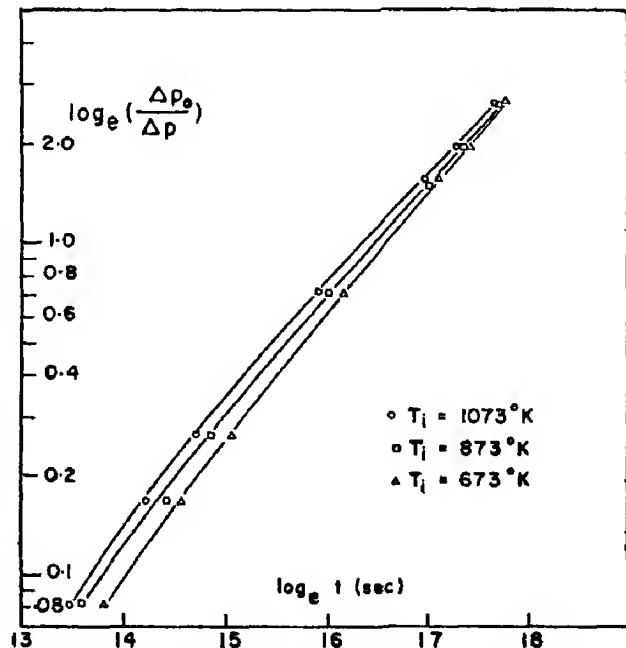


Fig. 6. Simulation of the Iyer and Asimow experiments.

The curves also exhibit the non-exponential character that was reported by both Van den Beukel *et al.*[12] and Iyer and Asimow[5]. Defining an 'effective relaxation time' as $\tau \equiv t \times \log_e (\Delta p_0 / \Delta p)$, which would be the constant relaxation time for a single exponential process, the 'effective relaxation time' for the nearly complete reaction (for $\Delta p / \Delta p_0 \sim 7$ per cent) increases up to three times the value of the initial relaxation time for a $T_i = 1073^\circ$ and $T_f = 373^\circ\text{K}$. For a smaller temperature drop, for instance $T_i = 473^\circ\text{K}$, $T_f = 373^\circ$, the 'effective relaxation time' increases only by 26 per cent, i.e. in the limit of small temperature changes, i.e. for small changes of short range order the curves tend to become exponentials.

The amount of change in the 'effective relaxation time' was not reported by Iyer and Asimow. However, from the form of the curves one might suspect that it should be considerably larger than the value we found. On the other hand Van den Beukel *et al.* report a change in the value of τ for the AuAg alloy of the order two to eight times the initial value. It would require further work to find out whether changing the parameters we have been using would yield a higher value of the ratio of final to initial relaxation times.

The curve of $\log_e (\Delta p / \Delta p_0)$ vs. time obtained by integrating the kinetic equations using the equilibrium values of $p_{B,1}$ vs. $p_{A,1}$ shows a very small difference with the curve obtained using a sine correction term. This comparison was carried out for the case of a quenching experiment for $T_i = 1373^\circ$, $T_f = 673^\circ$, $v = 4 \times 10^{-2}$, $v_A = 3 \times 10^{-2} \text{ eV}$, $v_B = 5 \times 10^{-2} \text{ eV}$ and all the other parameters with the same values as above. The differences in $dp_{A,1}/dt$ obtained from the values of $p_{B,1}$ vs. time and the values obtained by replacing directly in (25) vary between 18 and 24 per cent for different points of the $(\Delta p / \Delta p_0)$.

It should be mentioned that if we plot the curves of $\log \tau_0$ vs. $1/T_f$ for a series of quenching experiments with given T_i and variable T_f and then we plot the curves of τ for a given

fixed value of $(\Delta p / \Delta p_0)$, such that the change in short range order is nearly complete, there is an increase in the slope of $\log \tau$ vs. $1/T_f$ relative to $\log \tau_0$ vs. $1/T_f$. Such an increase of slope was calculated for $\tau_{(0.037)}$ for a temperature drop of the order of 800°C and an initial temperature of 1073°K . The change in slope is of the order of 13 per cent and for a simple picture in which $\tau \sim c \exp (Q/kT_f)$ it can be imagined as an increase in an 'effective activation energy' that results from the increase in the degree of short range order, thus agreeing with the picture we developed for the case of diffusion above the critical temperature using the Kirkwood second moment approximation[16, 17].

In conclusion, the integration of the kinetic equations gives good qualitative agreement with experiment. The $\log_e (\Delta p / \Delta p_0)$ vs. time curves show a non-exponential character and an increase in 'effective relaxation time' as the short range order increases at constant annealing temperature, as observed. The curves obtained from a simulation of the Iyer and Asimow experiments are in reasonable agreement with the experimental results. The theory predicts a new result, namely the shift of the curves for a series of experiments with constant T_f and variable T_i .

From studying the initial slopes of the curves for different cases we get results in agreement with the experimental results of Radelaar[7] and Van den Beukel *et al.*[12]. We also predict a small deviation of linearity in the curve of $\log \tau_0$ vs. $1/T_f$ for a rather large range of values of T_f , which is probably too small to be detected by experiment.

6. SUMMARY OF RESULTS AND DISCUSSION.

Our theory starts in a way parallel to the work of Kidin and Shtremel[1] but significant modifications are introduced. In the work of Kidin and Shtremel like in Vineyard's[2] the jump rate is controlled by the difference in configurational energy between initial and final positions of the atom but an extra term is added for the order dependence of the

potential barrier. For this term Kidin and Shtremel assume that both the atoms which are nearest neighbors at the saddle point and the nearest neighbors before and after the jump contribute equally to the height of the barrier. Instead of this our migration energy is defined by the saddle point neighbors and the other nearest neighbors before the jump.

We found the kinetic equations of Kidin and Shtremel to be incorrect, because they contained an implicit assumption that would be verified only in the limit of very small deviations from equilibrium or very large vacancy concentrations. We proposed an alternative set of equations which did not require, as Kidin and Shtremel's equations did, that the vacancy environment should come into instantaneous equilibrium in a quenching experiment. We also found that our equations led to expressions for the vacancy-atom *a posteriori* probabilities in agreement with the result the author derived previously using the quasichemical approach for the short range order crystal containing vacancies [15] and in disagreement with the results of Kidin and Shtremel.

Our results on the atom-vacancy *a posteriori* probabilities have the implication that Kidin and Shtremel's assumption about the vacancy environment reaching instantaneous equilibrium in a quenching experiment cannot be correct, since the equilibrium values of the vacancy-atom pair probabilities imply the equilibrium values of the atom-atom pair probabilities, in other words we cannot have the system in a state in which the atom-vacancy pairs have attained their equilibrium state while the atom-atom pairs have not. On the other hand using (42) we have calculated the slope of $(dp_{BA}/dp_{AV})_{t=0}$. As it is shown in Fig. 2 the tangent at $t=0$ lies below the tangent to the equilibrium curve of p_{BA} vs. p_{AV} , i.e. in the neighborhood of $t=0$ for a given decrease in p_{AV} the atom-atom probability will increase *less* than what it would if the system would follow the equilibrium p_{BA} vs. p_{AV} curve. In other words, for the values of

the parameters we used, the vacancy environment will change faster than the atom environment in the initial stage of a quenching experiment.

From inspection of the kinetic equations it was concluded that the values of the parameters that enter into the equations cannot be independent. The reason derives from the form of the equations and the necessity that the probabilities follow the equilibrium curves in the limit of small deviations from equilibrium. This leads to the requirement that if $v_{AA} > v_{BB}$ then

$$|4v_{AA}^* - 11v_{AA}| > |4v_{BB}^* - 11v_{BB}|$$

if the system is ever going to reach the equilibrium state. In other words, for a given state of short range order to be observed in an alloy it is not enough that the pairwise interaction potentials make the ordered state a state of lower free energy, but also that the equilibrium and saddle point interaction energies verify some restrictive conditions.

The possibility that the kinetics is dominated by a process of trapping of vacancies by an unfavorable environment and release by vacancy-atom interchanges of vacancies and slower moving atoms was discussed. If such processes are operating the equations of motion we developed are probably not adequate to describe them.

The values of the initial relaxation times for a series of quenching experiments with a given quenching temperature and different annealing temperatures followed the behavior observed in [12]. The values of $\log \tau_0$ vs. $1/T_f$ follow the behavior observed by Radelaar [6] for experiments with a constant difference between quenching and annealing temperature.

From integration of the kinetic equations it was found that $\log (\Delta p_0/\Delta p)$ vs. time deviate from a simple exponential behavior in the same way as observed in the experimental results [5, 12].

The deviations from a simple exponential behavior occurs for quenches of several

hundred degrees. The results also lead us to believe that the hypothesis of partial equilibrium between atom-atom and atom-vacancy pairs during the process of approaching the equilibrium state, in other words that the p_{AV} vs. p_{BA} equilibrium curve is followed by the system in its evolution towards equilibrium, is a good approximation even for the case of large deviations from equilibrium.

In conclusion we believe that there are several areas that deserve to be explored further and that the theory we have developed contains the elements required for further development. One problem is to clarify the relation between kinetics and diffusion in a short range ordered alloy. We have stated before that an increase in the slope of $\log \tau_0$ vs. $1/T$, should be expected for a series of quenching experiments with different values of T_f . It is quite possible to expect that a similar behavior could occur for the values of $\log D$ vs. $1/T$ in diffusion experiments. We should find out how the values of activation energies derived from kinetics compare with those to be expected in diffusion experiments.

We also think that a further development of the theory is necessary in order to find out the detailed behavior in which the system approaches equilibrium, in other words what the function p_{AV} vs. p_{BA} is for that part of the curve near the state of final equilibrium. This could require linearization of the equations (23) and (25) for values of p_{BA} and p_{AV} near the values of the final equilibrium state. By way of speculation, we suspect that for a cyclic process (i.e. for instance first a downquench and then an upquench to get the system back in its initial state) the p_{BA} vs. p_{AV} non-equilibrium curve would show a hysteresis effect.

Finally, our theory could possibly be extended to include diffusion and kinetics in a system with long range order. Neither is

there a fundamental difficulty in extending this treatment to body centered cubic structures, except that probably the algebra would become more involved because of the fact that we have both first neighbors and second neighbors at the saddle point.

Acknowledgements—The author is indebted to his Thesis advisor, Dr. L. A. Girifalco for useful discussions in the course of this work. The author also had useful discussions with Dr. J. Van den Syde of the Department of Metallurgy and Materials Science, University of Pennsylvania. The idea that a trapping mechanism for vacancies should be investigated was pointed out by Professor N. Cabrera of the Instituto Politecnico Nacional, Mexico City, Mexico. In the integration of the kinetic equations the author was helped by Mrs. Amanda Poor of the computer staff of the University City Science Center, Philadelphia, Pa. Dr. R. M. Asimow and Mr. V. K. Iyer kindly sent their results to the author before publication.

REFERENCES

1. KIDIN I. I. and SHTREMEL M. A., *Phys. Metals Metallogr.* **11**, 1 (1961).
2. VINEYARD G. H., *Phys. Rev.* **102**, 981 (1956).
3. KOREVAAR B. M., Thesis, Delft (1960).
4. DAMASK A., *J. Phys. Chem. Solids* **1**, 23 (1956).
5. IYER V. K. and ASIMOW R. M., *Scripta Metall.* **2**, 231 (1968).
6. RADELAAR S., *J. Phys. Chem. Solids* **27**, 1375 (1966).
7. SIEGEL S. and MCGREARY R., *Phys. Rev.* **65**, 347 (1944).
8. NEWKIRK J. B., SMOLUCHOWSKI R., GEISLER A. H. and MARTIN D. L., *J. appl. Phys.* **22**, 290 (1951).
9. THOMPSON N., *Proc. phys. Soc.* **52**, 217 (1940).
10. BEAL M. T., *J. Phys. Chem. Solids* **15**, 72 (1960).
11. SCHOUJET M., Ph.D. Thesis, University of Pennsylvania (1968).
12. VAN DEN BEUKEL A., COREMANS P. C. J. and VRIJHOEF M. M. A., *Phys. Status Solidi* **19**, 177 (1967).
13. CHILDS B. G. and LeCLAIRE A. D., *Acta Metall.* **2**, 718 (1954).
14. BAUERLE J. and KOEHLER J., *Phys. Rev.* **107**, 1493 (1967).
15. SCHOUJET M., *Phys. Status Solidi* (In press).
16. SCHOUJET M. and GIRIFALCO L. A., *J. Phys. Chem. Solids* **29**, 497 (1968).
17. SCHOUJET M. and GIRIFALCO L. A., *J. Phys. Chem. Solids* **29**, 911 (1968).

THEORETICAL DETERMINATION OF n -SITE CONFIGURATION PROBABILITIES FROM PAIR CORRELATIONS IN BINARY LATTICES

PHILIP C. CLAPP

Ledgemont Laboratory, Kennecott Copper Corporation, Lexington, Mass. 02173, U.S.A.

(Received 5 February 1969)

Abstract—A new variational method is presented for determining configuration probabilities of three or more sites in partially ordered binary lattices from pair correlation data. The method is tested for several cases where the exact solution is known by independent means, and it is shown to yield the correct result in each case. It is suggested but not proven that the method is exact for all applications where the configurational energy of the lattice remains constant during the variational procedure. Comparison is made with the Superposition Approximation of Kirkwood and with Monte Carlo studies. In addition, the method is shown to bear an inverse relationship to the Cluster Variation Method. It is concluded that this new variational procedure should be quite useful for obtaining a more complete microscopic description of a partially ordered lattice than is presently available with the pair configurations picture.

1. INTRODUCTION

A BINARY lattice is defined here as any regular lattice whose sites are occupied in one of two ways (e.g. a binary alloy, a lattice gas, or a spin $\frac{1}{2}$ magnetic lattice). A complete description of the lattice configuration is possible only when the lattice is perfectly ordered. At finite temperatures the lattice contains some degree of disorder and since the state of the lattice is now an average over some ensemble of configurations only a statistical description of the lattice arrangement is possible. When only short range order (SRO) is present the usual description of the lattice is based upon the pair correlations (i.e. the Warren SRO parameters in alloys, spin-spin correlations in magnetic systems) which are normally all that can be experimentally measured.* This however gives a very incomplete picture of the state of the lattice because it focuses on only two sites of the lattice at a time. It is

clear that a knowledge of the probabilities for larger cluster configurations (triplets, quadruplets, etc.) would provide a much more complete description of the lattice structure at the atomic level.

We shall propose here a general theoretical method for inferring these higher order cluster probabilities from the pair probability data. To give it a name we shall call it the Probability Variation Method (PVM). Our scheme is very closely allied to the Cluster Variation Method (CVM) which has been extensively developed by Kikuchi[1] and collaborators. It may be described in some ways as an inverse of the CVM as we show below.

This inverse operation appears to be new, except for a calculation made by Kikuchi[2] for soap-bubble configurations. Although the CVM as normally used to calculate the configuration entropy of a system is known to be approximate in most cases[3], the inverse application to determine n -site probabilities is not similarly limited and in fact may be exact in all circumstances where one condition is satisfied. This condition is that the configurational energy of the lattice depend only upon the pair correlations that are held

*Recent work by COWLEY J. M. (*Acta crystallogr.* **A24**, 557 (1968)) on kinematical diffraction from solid solutions and field ion microscopy studies by GOLD E. and MACHLIN E. S. on Au-Pt and Ni-Pt alloys (*Phil. Mag.* **18**, 453 (1968)) indicate that it may be possible to obtain larger cluster correlations experimentally in some cases.

constant during the calculation. The exposition of the method is given in Section 2 and it is shown in Section 3 that in the several cases where the exact result for larger cluster probabilities is known, the PVM produces the correct answer.

Previously the work on obtaining the configuration probabilities of larger clusters has taken two paths. The first is also an analytic method first proposed by Kirkwood[4] which yields an approximate value for the triplet correlations in terms of the pair correlations. This technique is known as the Superposition Approximation (SA) and although the SA can be extended to higher order correlations there is some ambiguity in the procedure. We shall demonstrate below that at least for the applications of interest here the SA gives results for the triplet case which are not self-consistent and are often grossly in error in comparison to the exact number.

The second approach is more recent and has been made possible by the advent of high speed digital computers. This is the use of the Monte Carlo method (MCM) to generate configurations of a large number of sites (10^2 – 10^4) by letting the computer shuffle site occupations according to either a set of hopping probabilities[5] or until the configuration arrived at by the computer satisfies the observed pair correlations of a real system[6]. This method has the great advantage of demonstrating explicitly the configuration of a large number of sites in a partially ordered lattice. There is the difficult question, however, of establishing whether the single configuration map presented by the computer is truly representative of the majority of the millions of other configurations that would also satisfy the constraints. More to the point, perhaps, is the question of which properties of this configuration are typical and which are peculiar to it alone (or to a minority set) and should thus be ignored. We shall return to this problem later when we compare results of our calculations to that of the MCM.

In comparison with the MCM the present

approach is limited in regards to the size of cluster which can be handled. The practical computational limit is of the order of ten sites. However, it has the advantage of providing cluster probabilities which are a statistical average over the entire ensemble of configurations of the infinite lattice that satisfy the pair correlation data. Also, the calculations are simpler to perform than the Monte Carlo procedures and if all that is needed are these smaller cluster probabilities then the present method should be completely satisfactory.

2. THEORY

(A) The Probability Variation Method (PVM)

We assume that the lattice composition and the pair correlations (or SRO parameters) for some range of the intersite distance are known. The problem is to determine the most probable frequency distribution for clusters of a given kind that will be consistent with the above data. The theory is most easily described by presenting an example and then generalizing to other order clusters. Consider a triplet cluster as shown in Fig. 1.

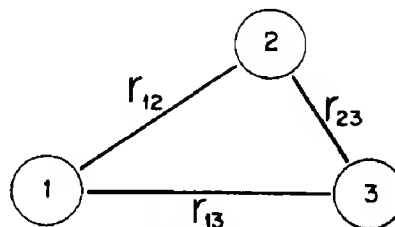


Fig. 1. A triplet.

We shall use the notation and some results developed in a previous paper[7] that presented exact expressions for triplet probabilities in the special case of equal composition binary lattices. If site i of the lattice is occupied by an (A, B) object we assign the occupation number σ_i the value $(+1, -1)$. Thus a specification of the σ_i 's (for $i=1, N$) completely describes the configuration of all N sites of the lattice. There will be N triplets of the kind shown in Fig. 1 obtained by letting site 1

successively be each of the N lattice sites while sites 2 and 3 maintain their same relative position and orientation to site 1. Periodic boundary conditions are assumed. There are eight possible configurations for a triplet. Each configuration type is identified by an index k and they are listed in Table 1 along with the values of various σ products in each

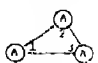
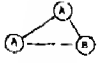
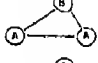
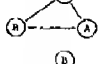
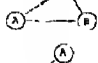
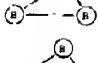
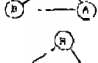
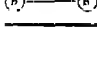
$$\sum_k [\sigma_1 \sigma_2]_k P_k = \langle \sigma_1 \sigma_2 \rangle \quad (2e)$$

$$\sum_k [\sigma_2 \sigma_3]_k P_k = \langle \sigma_2 \sigma_3 \rangle \quad (2f)$$

$$\sum_k [\sigma_3 \sigma_1]_k P_k = \langle \sigma_3 \sigma_1 \rangle \quad (2g)$$

$$\sum_k [\sigma_1 \sigma_2 \sigma_3]_k P_k = \langle \sigma_1 \sigma_2 \sigma_3 \rangle \quad (2h)$$

Table 1. Coefficients for triplet sum rules

Cluster type	k	$[\sigma_1]_k$	$[\sigma_2]_k$	$[\sigma_3]_k$	$[\sigma_1 \sigma_2]_k$	$[\sigma_2 \sigma_3]_k$	$[\sigma_3 \sigma_1]_k$	$[\sigma_1 \sigma_2 \sigma_3]_k$
	1	+1	+1	+1	+1	+1	+1	+1
	2	+1	+1	-1	+1	-1	-1	-1
	3	+1	-1	+1	-1	-1	+1	-1
	4	-1	+1	+1	-1	+1	-1	-1
	5	+1	-1	-1	-1	+1	-1	+1
	6	-1	+1	-1	-1	-1	+1	+1
	7	-1	-1	+1	+1	-1	-1	+1
	8	-1	-1	-1	+1	+1	+1	-1

cluster. Let the fraction of N triplets of type k be P_k . Then the lattice average of any occupation number product is given by the identity:

$$\begin{aligned} \langle \sigma_1 \sigma_2 \dots \sigma_n \rangle &\equiv \frac{1}{N} \sum_{j=0}^{N-1} \sigma_{1+j} \sigma_{2+j} \dots \sigma_{n+j} \\ &= \sum_k [\sigma_1 \sigma_2 \dots \sigma_n]_k P_k \quad (1) \end{aligned}$$

and for our example we can write the following set of sum rules:

$$\sum_k P_k = 1 \quad (2a)$$

$$\sum_k [\sigma_1]_k P_k = \langle \sigma_1 \rangle = c \quad (2b)$$

$$\sum_k [\sigma_2]_k P_k = \langle \sigma_2 \rangle = c \quad (2c)$$

$$\sum_k [\sigma_3]_k P_k = \langle \sigma_3 \rangle = c \quad (2d)$$

where $c \equiv m_A - m_B$ and (m_A, m_B) are the fraction of (A, B) objects in the lattice. The coefficients of the P_k 's in equation (2(a-h)) are all known by inspection of the cluster types and the values are listed in Table 1.

Strictly speaking, the averages on the right hand side (r.h.s) of equations (2(b-h)) are for a single lattice configuration, but we shall use the experimentally determined values of these quantities instead, which represent thermodynamic averages over a large ensemble of lattice configurations. However, since it is known from statistical mechanics that an overwhelming number of the states of the lattice which contribute to the average of a macroscopic quantity do not depart significantly from the ensemble average (except in the vicinity of critical points) this

ensures that we are studying the configurational properties of a 'typical' lattice state. Hence the r.h.s. of equations (2(b-d)) are known from the composition, and the r.h.s. of equations (2(e-g)) are assumed known from diffraction data. $\langle \sigma_i \sigma_j \rangle$ in alloys may be calculated from the Warren short range order parameter α_{ij} by the relation: $\langle \sigma_i \sigma_j \rangle = (1 - c^2)\alpha_{ij} + c^2$. Clearly a knowledge of $\langle \sigma_1 \sigma_2 \sigma_3 \rangle$ would make the set of equations determinate and the P_k 's could then be obtained. Symmetry considerations make a theoretical evaluation of $\langle \sigma_1 \sigma_2 \sigma_3 \rangle$ possible for the special case of $c = 0$ [7] but for $c \neq 0$ such arguments are no longer valid.

It is convenient at times to have the complementary set of identities which give a particular P_k in terms of occupation number lattice averages. For this purpose we use the projection numbers introduced in [7] and defined as follows:

$$\sigma_i^A \equiv \frac{1}{2}(1 + \sigma_i) = (1, 0) \text{ if } (A, B) \text{ is on site } i \quad (3a)$$

$$\sigma_i^B \equiv \frac{1}{2}(1 - \sigma_i) = (0, 1) \text{ if } (A, B) \text{ is on site } i. \quad (3b)$$

Then the probability that a cluster will be occupied in a particular manner is given by the lattice average of the corresponding projection numbers, e.g.

$$\begin{aligned} P_{12}^{AB} \cdots_n^B &= \frac{1}{N} \sum_{j=0}^{N-1} \sigma_{1+j}^A \sigma_{2+j}^B \cdots \sigma_{n+j}^B \equiv \langle \sigma_1^A \sigma_2^B \cdots \sigma_n^B \rangle \\ &= \frac{1}{2^n} \langle (1 + \sigma_1)(1 - \sigma_2) \cdots (1 - \sigma_n) \rangle \end{aligned} \quad (4)$$

which can then be multiplied out and reduced to a sum of occupation number averages. Explicit examples will be given in the next section.

A priori it might be expected that the possible range of $\langle \sigma_1 \sigma_2 \sigma_3 \rangle$ is +1 to -1 but the reality condition that all P_k 's are positive semi-definite in the linear equations limits $\langle \sigma_1 \sigma_2 \sigma_3 \rangle$ to a much smaller range. This is

also manifested by a narrowing of the allowable range of the individual P_k 's. An example of this effect will be seen in Section 3(C) below. In essence the linear equations for the P_k 's confine the possible P_k values to a small volume in P_k space (a linear manifold in the case of triplets). This important fact has previously been noted and emphasized by Gehlen and Cohen [6] in their Monte Carlo study of local order in alloys. The volume of the subspace depends upon the particular values of c and the $\langle \sigma_i \sigma_j \rangle$'s. It is largest when the $\langle \sigma_i \sigma_j \rangle$'s are that of a completely disordered alloy (i.e. $\langle \sigma_i \sigma_j \rangle = c^2$) and the volume reduces to a single point when the $\langle \sigma_i \sigma_j \rangle$ values are those of a fully ordered structure. The P_k 's then become completely determined.

Regarding P_k as the probability of finding, by random selection, a cluster of type k in the lattice, Information Theory [8] can be used to make a 'best choice' for the values of the P_k 's. Since the situation is one of incomplete knowledge (the P_k 's are only known within the limits imposed by the linear equations), Information Theory states that the most unbiased value for the P_k 's within this range is that set which maximizes the 'ignorance' function $I(P_k)$ given by:

$$I(P_k) = - \sum_k P_k \ln P_k. \quad (5)$$

Information Theory shows that any other choice would imply that there is more information about the P_k 's than has been given. More information of a very complicated kind may, in fact, be present due to overlapping cluster conditions that we shall now consider.

This choice can also be interpreted in more familiar terms as a principal of maximum entropy. $I(P_k)$ is proportional to the configurational entropy $W_{\text{CVM}}(P_k)$ obtained by placing NP_1 clusters of type 1, NP_2 clusters of type 2, etc. on a lattice of N sites in all possible ways *without worrying about incompatible overlaps*. This is given by the combinatorial factor:

$$W_{\text{CVM}}(P_k) = \frac{N!}{\prod_k [NP_k]!} \cong N \left[- \sum_k P_k \ln P_k \right] \quad (6)$$

and is recognizable as the combinatorial factor of the Cluster Variation Method (CVM) using this particular cluster as a basis.

Let us assume for the moment that equation (6) correctly evaluates the number of lattice configurations for a given set of P_k 's, and also assume that the configurational energy depends only on the $\langle \sigma_i \sigma_j \rangle$'s that are being held constant. Then maximizing $W(P_k)$ with respect to the P_k 's (and subject to the constraints of equations (2(a-g))) will yield the most probable value for the P_k 's. Furthermore, as the size of the lattice increases, the statistical law [9] of large numbers states that the fraction of lattice configurations having any value of the P_k 's other than this optimum set becomes vanishingly small.

We now examine the two assumptions that we have used. It is known from work on the CVM that equation (6) considerably overestimates the number of lattice configurations of given P_k because it includes many configurations containing incompatible cluster placements such as the one shown in Fig. 2. Here we have chosen an equilateral triangle

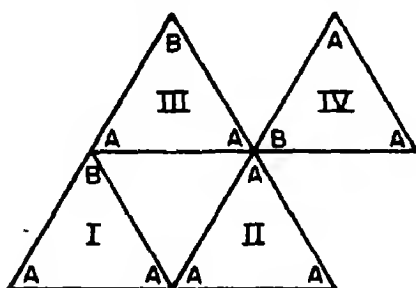


Fig. 2. Superposition of triplets in a lattice.

as the cluster and illustrate only a small region of the lattice. Although clusters I and II are in agreement on the occupation of their common vertex, I and III are incompatible and IV is incompatible with both II and III. Thus W_{CVM} counts not only all the possible lattice configurations but a much larger num-

ber which are impossible on a real lattice. If $W(P_k)$ is just the subset of compatible configurations then obviously $W(P_k) \leq W_{\text{CVM}}(P_k)$.

However, it is clear that for our purposes we do not need to know the magnitude of $W(P_k)$. All that is required is a knowledge of the P_k values which maximize it! Thus we can reduce our first assumption to a much simpler one, namely that if P_k is changed such that $W_{\text{CVM}}(P_k)$ increases (decreases), the subset of compatible configurations $W(P_k)$ also increases (decreases). At this point we are unable to prove the assumption generally but only argue its plausibility on the grounds that increasing the total number of configurations should increase the chance of compatible configurations occurring. The postulate in simplest form is:

Postulate I: In any given subregion of P_k space the maximum of $W_{\text{CVM}}(P_k)$ and $W(P_k)$ coincide.

The second assumption required in order that the variational calculation be exact is that the configurational energy of the lattice depends only upon quantities that are being held constant, i.e. the composition and pair correlations spanned by the cluster.

Postulate II: The configurational energy of the lattice is constant over the subregion of P_k space defined by the linear constraints.

We can compare the present procedure with the Cluster Variation Method as it is normally applied to illustrate the inverse relationship that they bear to each other. In the CVM the pair correlations are not assumed known but instead are the quantities to be predicted, while the P_k 's are used as intermediary variables to accomplish the calculation. A certain size of cluster is chosen, as we have done, and the same linear relationships are written between the P_k 's and the pair correlations. The entropy of the system for a particular set of values of the pair correlations is then deduced from equation (6) by maximizing W_{CVM} with respect to the P_k 's. This leaves W_{CVM} a function of just the pair correlations which are to be varied later when W_{CVM}

is inserted in a free energy expression. For this process to give the correct result it is necessary that the maximum of W_{CVM} agree with the true $W(P_k)$ not only in location but in magnitude as well (apart from a constant scale factor) over the entire P_k space. This is necessary in order that W (and hence the free energy) have the correct functional dependence on the pair correlations. This latter requirement is the principal cause of error in the Cluster Variation Method and is obviated in the present analysis by taking the pair correlations from measurements, i.e. we stay strictly within a micro-canonical ensemble and proceed in the reverse direction to determine the P_k 's from the pair correlations.

(B) The Superposition Approximation

Kirkwood's Superposition Approximation [4] and variants of it have been used by many writers to obtain rough estimates of higher order correlations in analytic form. The general formula is:

$$P(\sigma_1 \sigma_2 \cdots \sigma_n) = C \prod_{1 \leq i < j \leq n} P(\sigma_i \sigma_j) \quad (7)$$

where C is a normalization constant which is adjusted to make the sum of n -site probabilities add up to unity. $P(\sigma_1 \sigma_2 \cdots \sigma_n)$ is the probability of occurrence of the configuration σ_1 for site 1, σ_2 for site 2, \cdots , σ_n for site n . For triplets, which is the most frequent application of the SA, equation 5 is:

$$P(\sigma_1 \sigma_2 \sigma_3) = C P(\sigma_1 \sigma_2) P(\sigma_1 \sigma_3) P(\sigma_2 \sigma_3) \quad (8a)$$

and for a 4-site cluster, the SA expression is:

$$P(\sigma_1 \sigma_2 \sigma_3 \sigma_4) = C P(\sigma_1 \sigma_2) P(\sigma_1 \sigma_3) P(\sigma_1 \sigma_4) \\ \times P(\sigma_2 \sigma_3) P(\sigma_2 \sigma_4) P(\sigma_3 \sigma_4) \quad (8b)$$

It is generally recognized that for weakly correlated systems the SA is a good approximation (at least for triplets) but for non-dilute lattices at temperatures where the pair correlations are finite the SA is rather poor and, in fact, will give results that show serious in-

consistencies with the input values of the pair correlations.

3. EXACT RESULTS

(A) Linear chain

The simplest system in lattice statistics is the infinite one-dimensional chain (see Fig. 3) with nearest neighbor interactions, generally

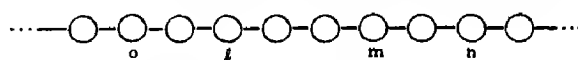


Fig. 3. The one-dimensional lattice.

referred to as the Ising linear chain. In 1925 Ising[10] exactly calculated a number of statistical properties of this lattice including the pair correlation functions. The pair correlation for n th neighbors on the chain is:

$$\langle \sigma_i \sigma_{i+n} \rangle = t^n \quad (9)$$

where $t \equiv \tanh(-\beta V)$, $\beta \equiv 1/kT$ and V is the nearest neighbor interaction. The triplet correlation function $\langle \sigma_i \sigma_{i+m} \sigma_{i+n} \rangle$ is zero for symmetry reasons and thus all triplet probabilities are completely determined from the pair correlations[7]. The quadruplet correlation function $\langle \sigma_i \sigma_{i+l} \sigma_{i+m} \sigma_{i+n} \rangle$ (or simply $\langle \sigma_o \sigma_l \sigma_m \sigma_n \rangle$) has some value q which we shall attempt to determine by our method. The sixteen quadruplet probabilities can be written in terms of the pair and quadruplet correlation functions by use of equation 4 and inserting the values of the pair correlations from equation 9 gives:

$$\begin{aligned} AAAA &= BBBB = (1 + t^l + t^{m-l} + t^{n-m} \\ &\quad + t^m + t^{n-l} + t^n + q)/16 \\ AABB &= BBAA = (1 + t^l - t^{m-l} + t^{n-m} \\ &\quad - t^m - t^{n-l} - t^n + q)/16 \\ ABAB &= BABA = (1 - t^l - t^{m-l} - t^{n-m} \\ &\quad + t^m + t^{n-l} - t^n + q)/16 \\ ABBA &= BAAB = (1 - t^l + t^{m-l} - t^{n-m} \\ &\quad - t^m - t^{n-l} + t^n + q)/16 \\ AAAB &= BBBA = (1 + t^l + t^{m-l} - t^{n-m} \\ &\quad + t^m - t^{n-l} - t^n - q)/16 \\ \sim AABA &= BBAB = (1 + t^l - t^{m-l} - t^{n-m} \\ &\quad - t^m + t^{n-l} + t^n - q)/16 \end{aligned}$$

$$\begin{aligned} ABAA &= BABB = (1 - t^l - t^{m-l} + t^{n-m} \\ &\quad + t^m - t^{n-l} + t^n - q)/16 \\ AB BB &= BA AA = (1 - t^l + t^{m-l} + t^{n-m} \\ &\quad - t^m + t^{n-l} - t^n - q)/16 \end{aligned} \quad (10)$$

where $AAAA$ represents P_{1234}^{AAAA} , etc. Each of the 16 P_k 's is now a linear function of the single variable q and maximizing equation 5 with respect to q yields:

$$\frac{\partial I(q)}{\partial q} = 0 = \frac{\partial}{\partial q} \left\{ - \sum_{k=1}^{16} P_k(q) \ln P_k(q) \right\} \quad (11)$$

which gives upon calculation:

$$\frac{(AAAA)(AABB)(ABAB)(ABBA)}{(A A A B)(A A B A)(A B A A)(A B B B)} = \frac{(XYZ + Q)(X\bar{Y}Z + Q)(\bar{X}\bar{Y}\bar{Z} + Q)(\bar{X}\bar{Y}\bar{Z} + Q)}{(XY\bar{Z} - Q)(X\bar{Y}\bar{Z} - Q)(\bar{X}\bar{Y}Z - Q)(\bar{X}\bar{Y}Z - Q)} = 1 \quad (12)$$

where $X = 1 + t^l$, $\bar{X} = 1 - t^l$, $Y = 1 + t^{m-l}$, $\bar{Y} = 1 - t^{m-l}$, $Z = 1 + t^{n-m}$, $\bar{Z} = 1 - t^{n-m}$, $Q = q - t^{n-m+l}$. Equation (12) has but one real root which is $Q = 0$ or:

$$q \equiv \langle \sigma_0 \sigma_l \sigma_m \sigma_n \rangle = t^{n-m+l} \quad (13)$$

$\langle \sigma_0 \sigma_l \sigma_m \sigma_n \rangle$ can also be evaluated exactly by the complete summation of a diagrammatic expansion with the same result. For comparison, the Superposition Approx. gives via equation (8(b)) expressions for the quadruplet probabilities which are correct only to lowest order in t , e.g.

$$(AAAA)_{S.A.} = C(1 + t^l)(1 + t^{m-l})(1 + t^{n-m})(1 + t^m)(1 + t^{n-l})(1 + t^n)/16$$

so that the SA does yield the correct high temperature weak correlation limit but is increasingly in error with increasing correlation. Paradoxically the SA also gives the correct result at the zero temperature perfectly ordered limit so that we conclude that the SA is most in error for states of partial order for this example.

(B) Triplets in AB alloys

The exact formulae for triplet cluster proba-

bilities in AB binary lattices with pairwise interactions is known[7]. Thus we can test the present method on a more realistic three dimensional problem. Employing equation (4) we may write the eight triplet probabilities of an arbitrary cluster as:

$$\begin{aligned} AAA &= (1 + 3c + \langle \sigma_1 \sigma_2 \rangle \\ &\quad + \langle \sigma_2 \sigma_3 \rangle + \langle \sigma_3 \sigma_1 \rangle + \tau)/8 \\ BBA &= (1 - c + \langle \sigma_1 \sigma_2 \rangle \\ &\quad - \langle \sigma_2 \sigma_3 \rangle - \langle \sigma_3 \sigma_1 \rangle + \tau)/8 \\ ABB &= (1 - c - \langle \sigma_1 \sigma_2 \rangle \\ &\quad + \langle \sigma_2 \sigma_3 \rangle - \langle \sigma_3 \sigma_1 \rangle + \tau)/8 \\ BAB &= (1 - c - \langle \sigma_1 \sigma_2 \rangle \\ &\quad - \langle \sigma_2 \sigma_3 \rangle + \langle \sigma_3 \sigma_1 \rangle + \tau)/8 \end{aligned} \quad (14)$$

$$\begin{aligned} BBB &= (1 - 3c + \langle \sigma_1 \sigma_2 \rangle \\ &\quad + \langle \sigma_2 \sigma_3 \rangle + \langle \sigma_3 \sigma_1 \rangle - \tau)/8 \\ AAB &= (1 + c + \langle \sigma_1 \sigma_2 \rangle \\ &\quad - \langle \sigma_2 \sigma_3 \rangle - \langle \sigma_3 \sigma_1 \rangle - \tau)/8 \\ BAA &= (1 + c - \langle \sigma_1 \sigma_2 \rangle \\ &\quad + \langle \sigma_2 \sigma_3 \rangle - \langle \sigma_3 \sigma_1 \rangle - \tau)/8 \\ ABA &= (1 + c - \langle \sigma_1 \sigma_2 \rangle \\ &\quad - \langle \sigma_2 \sigma_3 \rangle + \langle \sigma_3 \sigma_1 \rangle - \tau)/8 \end{aligned}$$

where BBA represents P_{123}^{BBA} etc., τ is the value of the triplet correlation $\langle \sigma_1 \sigma_2 \sigma_3 \rangle$, and we note that for an equi-composition alloy $\langle \sigma_i \rangle \equiv c = m_A - m_B = 0$. Assuming only pairwise interactions in the lattice implies that the con-

figurational energy is dependent only on the pair correlations so that varying τ subject to fixed values of $\langle \sigma_i \sigma_j \rangle$, etc. will ensure that Postulate II is satisfied. Varying equation (5) with respect to τ yields

$$\frac{\partial I(\tau)}{\partial \tau} = \frac{\partial}{\partial \tau} \left\{ - \sum_{k=1}^8 P_k(\tau) \ln P_k(\tau) \right\} = 0 \quad (15)$$

which gives:

$$\frac{(AAA)(BBA)(ABB)(BAB)}{(BBB)(AAB)(BAA)(ABA)} = 1. \quad (16)$$

This equation has but one real solution: $\tau = 0$, which is also the prediction of the exact theory. This result clearly depends on Postulate II being satisfied for if the system contained three body interactions as well τ would be expected to have a non-zero value.

(C) Triplets in Monte Carlo experiments

The Monte Carlo work that has most relevance to the present study is that carried out by Gehlen and Cohen[6]. Using Moss's experimental data[11] for the first, second, and third neighbor pair correlations in Cu_3Au at 450°C they used a computer to shuffle atomic configurations on 4000 sites. They used two starting configurations: perfectly random, and perfectly ordered and allowed the computer to change configurations only if the new configuration was more consistent with the pair correlation data. The process was stopped when the computer configuration had values for the pair correlations sufficiently close to the experimental data. A number of properties of the final computer configurations were then measured, in particular the various fractions of nearest neighbor triplets and quadruplets. Although these few computer configurations undoubtedly represent but a very small fraction of the ensemble of 4000 site configurations that would have the same pair correlations, it is safe to assume that the values for the triplet probabilities derived from the computer configurations are typical of the ensemble for two reasons. First, since there are 32,000 triplets of this kind in a single configuration, the statistical averaging is of a high order. This would not be true of some larger feature of the configuration such as the shape of an antiphase boundary involving several hundred atoms. Second, the results for the triplet numbers varied by insignificant amounts among different final configurations. As a consequence it is practically certain that their Monte Carlo values for the triplet and quadruplet proba-

bilities are very close to the exact values for the Cu_3Au lattice at this temperature. There is, of course, the implicit assumption in their operation that the configurational energy depends on no more than the three pair correlations that were used as input.

Our method is easily applied to the calculation of the triplet probabilities by using equations (14) and (15) which again yield equation (16) but the solution is now different from $\tau = 0$ because $c \neq 0$. We write equation (16) as

$$\frac{(D_1 + X)(D_2 + X)(D_3 + X)(D_4 + X)}{(D'_1 - X)(D_2 - X)(D_3 - X)(D_4 - X)} = 1 \quad (17)$$

with

$$\begin{aligned} X &= \tau - c \\ D_1 &= 1 + \langle \sigma_1 \sigma_2 \rangle + \langle \sigma_2 \sigma_3 \rangle + \langle \sigma_3 \sigma_1 \rangle + 4c \\ D'_1 &= 1 + \langle \sigma_1 \sigma_2 \rangle + \langle \sigma_2 \sigma_3 \rangle + \langle \sigma_3 \sigma_1 \rangle - 4c \\ D_2 &= 1 + \langle \sigma_1 \sigma_2 \rangle - \langle \sigma_2 \sigma_3 \rangle - \langle \sigma_3 \sigma_1 \rangle \\ D_3 &= 1 - \langle \sigma_1 \sigma_2 \rangle + \langle \sigma_2 \sigma_3 \rangle - \langle \sigma_3 \sigma_1 \rangle \\ D_4 &= 1 - \langle \sigma_1 \sigma_2 \rangle - \langle \sigma_2 \sigma_3 \rangle + \langle \sigma_3 \sigma_1 \rangle \end{aligned}$$

Equation (17) reduces to a cubic, $X^3 + a_2 X^2 + a_1 X + a_0 = 0$ with $a_2 = c(D_2 + D_3 + D_4)$, $a_1 = ((D_1 + D'_1)(D_2 D_3 + D_3 D_4 + D_2 D_4) + 2D_2 D_3 D_4)/8$, $a_0 = cD_2 D_3 D_4$. This has one real root, which can be proven by assuming there is more than one and showing that this implies negative values for some of the P_k 's. The single real root is extracted by the standard cubic solution method. At this point the solution is applicable to any kind of triplet on a lattice of arbitrary composition. The D_i 's are evaluated for Cu_3Au nearest neighbor triplets by setting $c = \frac{1}{2}$ and $\langle \sigma_1 \sigma_2 \rangle = \langle \sigma_2 \sigma_3 \rangle = \langle \sigma_3 \sigma_1 \rangle = (1 - c^2)\alpha_1 + c^2$ where α_1 is the measured Warren short range order parameter for nearest neighbors. The three pair correlations are equal because the triplet under consideration has each site a nearest neighbor of the other two. The numerical results are listed in Table 2.

The allowed range for the triplet probabilities has been found from equation (14) by putting in the known values for c and the $\langle \sigma_i \sigma_j \rangle$'s and then determining the range of τ for which all the probabilities remain positive.

Table 2. Nearest neighbor triplet probabilities in Cu_3Au at 450°C

Triplet type	Range allowed by linear equations at $T = 450^\circ$	Monte Carlo [6] $N = 4000$		This calculation (PVM)	Superposition approx.
		Ordered start	Random start		
Cu-Cu-Cu	0.302-0.328	0.3273	0.3275	0.3271	0.3474*
Cu-Cu-Au	0.672-0.594	0.5962	0.5956	0.5964	0.5676*
Cu-Au-Au	0.000-0.078	0.0758	0.0761	0.0759	0.0840*
Au-Au-Au	0.026-0.000	0.0007	0.0007	0.00067	0.0011

*Note that these values are outside the allowed range.

The result is that τ has a lower bound at -0.396 and an upper bound at -0.188 . The first values in the table correspond to the lower bound of τ and the second values to the upper, so that by imposing this reality condition alone, the values of the triplet probabilities are already known reasonably well. The PVM solution is $\tau = -0.1941$.

It is apparent from Table 2 that the agreement between the Monte Carlo numbers and the PVM predictions are very good. It suggests that the PVM values are probably the exact results for the infinite lattice ensemble.

Although the SA would appear to give a reasonable estimate of the triplet probabilities, three of the values are impossible because they lie outside the range allowed by equation (14). This means that if the SA probabilities were used to determine τ , each one of the linear equations would give a different τ and the inconsistency could not be resolved.

Alternatively, if the SA probabilities are fed back into equation (2) the values of c and α_1 so determined are in error by 2 and 23 per cent respectively. In fact, an arbitrary choice of τ anywhere within the allowed range of τ would be better than using the SA, for this at least would produce a set of values for the triplet probabilities consistent with the known alloy data.

4. SUMMARY AND CONCLUSIONS

We have introduced a new way to determine the statistical probabilities of clusters of more than two sites from pair correlation data in any binary lattice. This approach has

been called the Probability Variation Method (PVM) to indicate its kinship to an older method which has been employed in pair correlation determinations, the Cluster Variation Method. The PVM was compared with the Superposition Approximation and Monte Carlo results. It was shown to be more accurate than the former and more easily applied than the latter. A plausibility argument was presented that the PVM represents an exact calculation of the cluster probabilities for lattices where the configurational energy remains constant as the cluster probabilities are varied. The PVM was shown to yield the exact result for all the cases that could be calculated by alternate means. Thus the PVM should become a very useful tool for obtaining a more complete microscopic picture of partially ordered lattices.

In a subsequent paper we shall give results of the PVM applied to larger clusters consisting of a central site surrounded by all its nearest neighbor sites in two and three dimensional lattices. We shall also indicate various calculation short cuts and working techniques that can be employed in these more complex operations.

Acknowledgements—The author would like to thank Professor J. B. Cohen for a conversation and correspondence about cluster probabilities and the Monte Carlo work that were quite informative. He is also indebted to Professor J. M. Cowley for originally stimulating his interest in this subject and to Professor S. C. Moss and Dr. C. B. Walker for valuable discussions.

REFERENCES

1. KIKUCHI R., *Phys. Rev.* **81**, 988 (1951); *J. chem. Phys.* **19**, 1230 (1951).

2. KIKUCHI R., *J. chem. Phys.* **24**, 861 (1956).
3. KURATA, M., KIKUCHI R. and WATARI T., *J. chem. Phys.* **21**, 434 (1953).
4. HILL T. L., In *Statistical Mechanics*, pp. 195, 278. McGraw-Hill, New York (1956).
5. FOSDICK L. D., *Phys. Rev.* **116**, 565 (1959); GUTTMAN L., *J. chem. Phys.* **34**, 1024 (1961).
6. GEHLEN P. C. and COHEN J. B., *Phys. Rev.* **139**, A844 (1965).
7. CLAPP P. C., *Phys. Rev.* **164**, 1018 (1967).
8. KATZ A., In *Principles of Statistical Mechanics*, p. 18. Freeman, San Francisco (1967); also, BRILLOUIN L., *Science and Information Theory*. Academic Press, New York (1962).
9. GUGGENHEIM E. A., In *Thermodynamics*, 4th Edn., p. 63. North-Holland, Amsterdam (1959).
10. ISING E., *Z. Phys.* **31**, 253 (1925).
11. MOSS S. C., *J. appl. Phys.* **12**, 3547 (1964).

LE METATITANATE DE MAGNESIUM, NOUVELLE MATRICE POUR L'ETUDE DE LA FLUORESCENCE DE L'ION Mn^{4+} . PREPARATION ET PROPRIETES DE LUMINESCENCE

G. VILLELA, Y. SAÏKALI*, A. LOUAT, J. PÂRIS et F. GAUME-MAHN

Laboratoire de Spectroscopie et de Luminescence, Laboratoire de la chaire de Chimie Minérale,
Université de Lyon-Villeurbanne, France

(Received 31 January 1969; in revised form 2 May 1969)

Résumé— $MgTiO_3(Mn^{4+})$ a été préparé par décomposition à l'air d'un tartrate mixte de magnésium et de titane contenant du tartrate de manganèse. Cette méthode permet d'obtenir, par des recuits appropriés, une phase pure dans le domaine de stabilité du manganèse tétravalent. $MgTiO_3(Mn^{4+})$ présente une fluorescence rouge à 77°K. Les spectres d'excitation et d'émission de l'ion Mn^{4+} sont particulièrement nets. Dans l'approximation d'un champ cristallin cubique avec une déformation trigonale, symétrie correspondant au site C_3 de l'activateur, une interprétation de ces spectres a pu être donnée, en bon accord avec l'expérience.

Abstract— $MgTiO_3(Mn^{4+})$ was prepared by firing in air a magnesium–titanium complex tartrate including manganese tartrate. This method gives, by suitable annealings, a pure phase in the temperature field in which tetravalent manganese is stable. $MgTiO_3(Mn^{4+})$ has a red fluorescence at 77°K. The excitation and emission spectra of the Mn^{4+} ion are particularly clear. They have been interpreted, with a good experimental agreement, in the approximation of a cubic crystal field with a trigonal component, corresponding to the activator symmetry site C_3 .

INTRODUCTION

L'INFLUENCE du champ cristallin sur les niveaux d'énergie des ions $3d^n$ a fait l'objet des travaux théoriques de Tanabe et Sugano. On sait tout l'intérêt qui s'attache à l'ion Cr^{3+} dont les transitions optiques, en absorption et en émission, ont été étudiées expérimentalement et interprétées dans de nombreux composés. L'ion isoélectronique Mn^{4+} est moins connu. Certes, plusieurs sels oxygénés de magnésium activés par Mn^{4+} (germanate, fluorogermanate, arséniate, antimoniate, titanate, niobate, tantalate) sont bien connus depuis longtemps en raison de leur fluorescence rouge intense utilisée dans l'éclairage, notamment pour les lampes à vapeur de mercure à couleur corrigée. Cependant, la complexité de ces matrices d'une part, et la difficulté de stabiliser le manganèse tétravalent dans des matrices

plus simples d'autre part, ont limité les possibilités d'interprétation du spectre de fluorescence de l'ion Mn^{4+} .

C'est pourquoi il nous a paru intéressant d'essayer de stabiliser cet ion dans une phase unique de structure assez symétrique, d'étudier son spectre de fluorescence et d'en donner une interprétation. Des travaux préliminaires ont orienté notre choix vers le titanate $MgTiO_3$ de structure ilménite.

PREPARATION DE $MgTiO_3$ PUR ET ACTIVE PAR Mn^{4+}

(1) Préparation à haute température suivie d'un recuit

Un essai d'obtention de $MgTiO_3(Mn^{4+})$ a été réalisé tout d'abord selon la méthode de Kröger[4]: addition de carbonate de magnésium en proportion calculée à une solution contenant $TiCl_4$ et $MnCl_2$ (2.10^{-3} mole de MnO par mole de $MgTiO_3$), coprécipitation des hydroxydes, séchage, calcination très

*Boursier du Centre national de la Recherche Scientifique du Liban.

lente du produit jusqu'à 1 200°C, puis recuit de plusieurs heures à l'air à 550°C. Les diagrammes de rayons X montrent que la phase MgTiO_3 se forme bien et qu'elle est pure. Cependant, elle ne présente pas d'émission rouge, ni à 293°K, ni à 77°K. L'aspect blanc et l'analyse chimique du produit indiquent qu'il contient bien du manganèse, mais uniquement à l'état bivalent.

Il est apparu alors nécessaire de réaliser une préparation du titanate MgTiO_3 à une température relativement basse de manière à pouvoir conserver le manganèse au degré de valence quatre.

(2) Préparation à basse température

L'un d'entre nous [2] ayant montré tout le profit que l'on pouvait tirer de la pyrolyse de complexes organiques mixtes convenablement choisis pour obtenir, à des températures inférieures à 1000°C, un certain nombre d'oxydes mixtes et leurs solutions solides, nous avons envisagé l'application d'une telle méthode à la préparation du titanate MgTiO_3 pur d'une part et à l'activation de cette matrice par du manganèse tétravalent d'autre part.

L'oxyde MgTiO_3 résulte de la pyrolyse d'un complexe tartrique, selon une technique précédemment décrite [3] à propos de la préparation des métatitanates de structure ilménite correspondant à la formule générale MTiO_3 ($M = \text{Mg, Zn, Co, Ni et Mn}$). Dans le présent travail, nous avons plus spécialement étudié la préparation et la thermolyse du tartrate mixte de magnésium et de titane.

Des quantités équimoléculaires d'oxyde hydraté de titane IV et de magnésie sont dissoutes dans une solution renfermant des proportions d'acide tartrique telles que le rapport acide tartrique sur titane IV soit égal à 2. Par addition d'alcool à la solution ainsi obtenue, on aboutit à un solide blanc dont la composition, déterminée par analyse chimique, correspond à la formule:



Ce complexe mixte a une stabilité relativement peu importante car il se décompose légèrement au cours de la précipitation et conduit à un solide renfermant un léger excès de titane par rapport au magnésium ($\text{Ti/Mg} = 1,03$). Il est donc préférable de procéder à une évaporation lente de la solution en ajoutant un excès d'acide tartrique qui stabilise le complexe mixte; le solide obtenu dans ces conditions est constitué par du tartrate mixte renfermant des proportions rigoureusement équimoléculaires de magnésium et de titane et par une petite quantité d'acide tartrique.

La pyrolyse de ce complexe a été étudiée à la thermobalance. Par chauffage progressif à l'air, on observe (Fig. 1) une décomposition entre 50 et 600°C. Le résidu de la thermolyse effectuée à 600°C correspond bien à la formule MgTiO_3 ; toutefois, l'organisation cristalline n'est pas encore suffisante pour provoquer des phénomènes de diffraction par les rayons X. C'est seulement sous l'effet de recuits, réalisés dans des conditions appropriées, que la taille des cristallites augmente progressivement fournissant un seul système de raies attribuables à la phase ilménite MgTiO_3 . L'amélioration de l'état cristallin se traduit par un amincissement des raies de diffraction des produits traités à 600°C pendant des durées variables (Fig. 2).

Il importe de remarquer que le produit

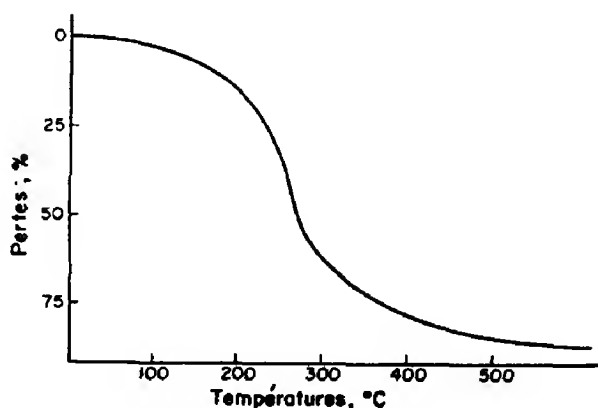


Fig. 1. Thermogramme du tartrate mixte de magnésium et de titane.

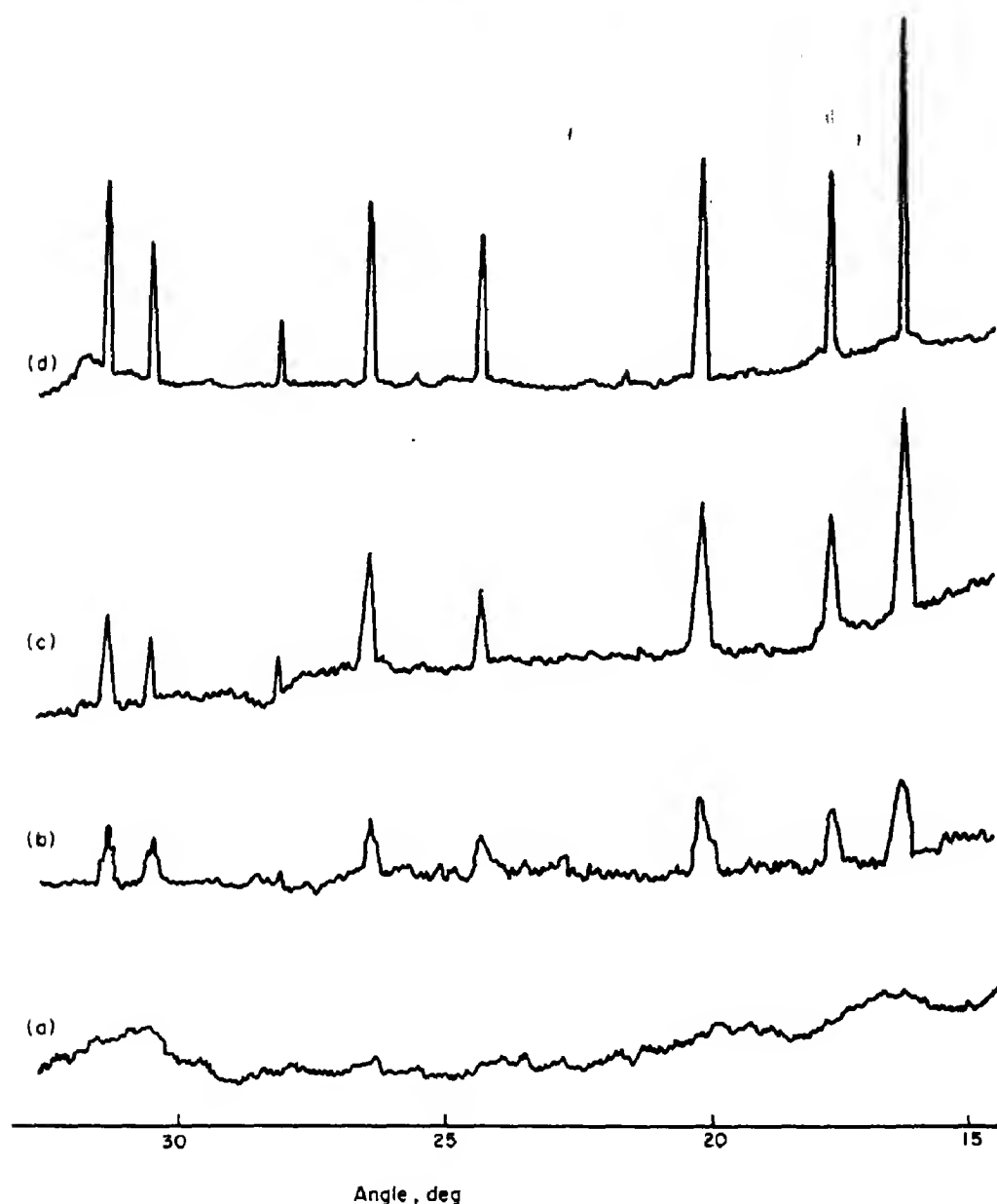


Fig. 2. Spectres de diffraction de rayons X d'échantillons de titanate MgTiO_3 :
(a) porté à 600°C ; (b) recuit 4 h à 600°C ; (c) recuit 20 h à 600°C ; (d) recuit
6 h à 1000°C .

organique obtenu par précipitation à l'alcool ou évaporation lente doit être considéré comme un complexe mixte et non comme un mélange de sels organiques. En effet, comme nous avons pu le vérifier, un mélange de tartrate de magnésium et de tartrate de titane (IV) obtenu par broyage se décompose à 600°C en oxyde de titane et magnésie; la

réaction complète entre ces deux oxydes n'intervient qu'à des températures supérieures à 1000°C . Au contraire, le complexe mixte donne, dès 600°C , une véritable combinaison dont le réseau s'organise peu à peu.

L'activation du métatitanate MgTiO_3 a été réalisée en calcinant à l'air le solide

provenant de l'évaporation lente d'une solution renfermant le tartare mixte de magnésium et de titane et du tartrate de manganèse bivalent. On obtient ainsi, à 600°C, un produit de couleur rose violacé.

ETUDE DE L'EMISSION DE FLUORESCENCE

Après préparation, à 600°C, $\text{MgTiO}_3(\text{Mn}^{4+})$ présente une faible émission rouge à 77°K, mais le rendement de cette fluorescence augmente fortement après recuit. Cette émission a été testée à l'aide d'un monochromateur à prisme, d'assez faible dispersion (300 Å/mm à 7000 Å) sous excitation par la radiation $\lambda = 3650$ Å. On observe alors deux bandes à 6990 et 7115 Å (Fig. 3).

(1) Influence des traitements thermiques

Les échantillons préparés par la méthode précédemment exposée ont subi une série de recuits à l'air de durée variable et à des températures différentes. Après chacun des traitements, on a déterminé le spectre

de rayons X et l'intensité I_0 du pic principal de fluorescence à 6990 Å.

On vient de voir que l'état cristallin du produit s'améliore par recuit (Fig. 2). Par contre, l'intensité I_0 passe par un maximum pour un traitement de 20 h à 600°C ou de 1 h à 700°C. Le rendement de fluorescence baisse ensuite rapidement (Tableau 1). Cette variation dans le rendement est à rapprocher de celle obtenue par Kröger pour Mg_2TiO_4 [4].

Tableau 1

Recuit		
Température	Temps	I_0
(°C)	(h)	(unités arbitraires)
600	4	490
600	8	815
600	16	1010
600	20	1030
700	1	1180
800	1	590
900	1	170

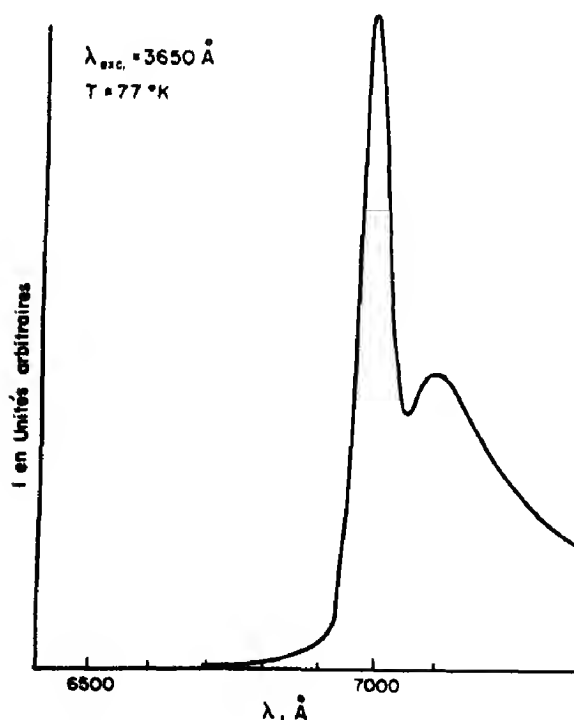


Fig. 3. Spectre d'émission de $\text{MgTiO}_3(\text{Mn}^{4+})$ (dispersion de 300 Å/mm).

La disparition de l'émission au-dessus de 700°C peut être attribuée à l'instabilité de l'ion Mn^{4+} . En effet, le produit rose violacé obtenu à 600°C se décolore rapidement lorsqu'il est porté à des températures supérieures à 700°C. Cette constatation est confirmée par des dosages de manganèse tétravalent qui ont été effectués selon la méthode de Kröger [4]. On trouve respectivement $1,2 \cdot 10^{-6}$, $2,4 \cdot 10^{-6}$ et 0 pour des échantillons recuits 4 h à 600°C, 20 h à 600°C et 1 h à 900°C.

Pour l'étude spectrale, on a choisi le produit recuit 1 h à 700°C.

(2) Influence de l'excitation

(a) *Produit activé.* Le spectre d'excitation est obtenu en irradiant l'échantillon entre 2000 et 5000 Å, avec le rayonnement d'un tube à hydrogène de puissance 3 kVA dispersé par un monochromateur à optique de quartz; l'émission de fluorescence, observée par réflexion, est reçue par un photomultiplicateur E.M.I. 9558, très

sensible dans le rouge. L'échantillon est placé dans un cryostat dont on peut faire varier la température de 77° à 600°K.

Le spectre d'excitation de $\text{MgTiO}_3(\text{Mn}^{4+})$ comprend deux bandes principales, caractéristiques de l'activateur (Fig. 4). On peut les attribuer, comme les bandes analogues d'autres composés activés par Mn^{4+} [5, 6], aux transitions ${}^4A_2 \rightarrow {}^4T_1$ et ${}^4A_2 \rightarrow {}^4T_2$ d'un ion $3d^3$ dans l'approximation d'un champ cristallin de symétrie cubique. Cependant, on voit sur la Fig. 5 que la bande ${}^4A_2 \rightarrow {}^4T_1$ comprend deux maximums secondaires. La symétrie du site de l'activateur dans MgTiO_3 étant C_3 , on peut les attribuer,

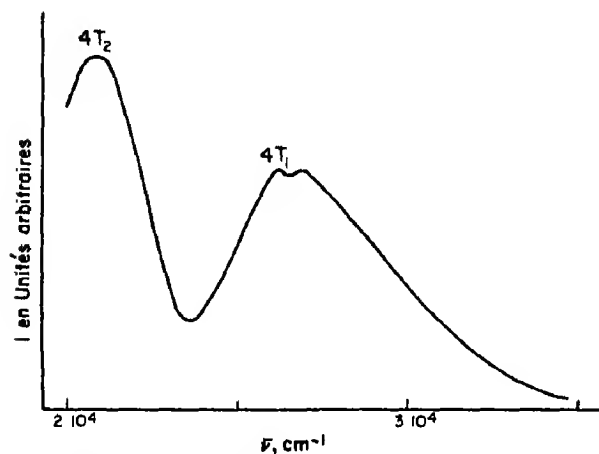


Fig. 4. Spectre d'excitation de $\text{MgTiO}_3(\text{Mn}^{4+})$.

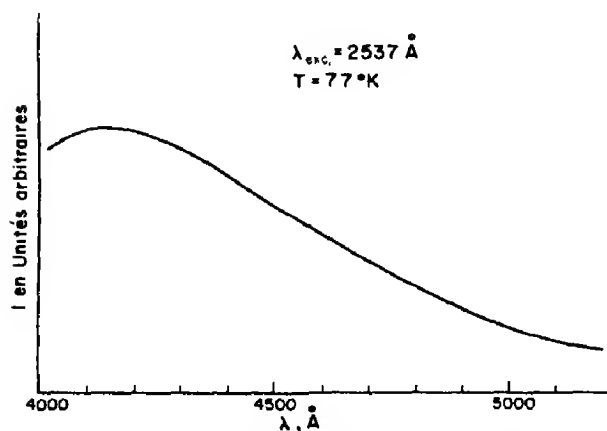


Fig. 5. Spectre d'émission de MgTiO_3 non activé (dispersion de 200 Å/mm).

comme on le verra plus loin, à une déformation trigonale du champ cubique.

Quelle que soit l'excitation, en 4T_1 ou en 4T_2 , l'émission reste inchangée.

(b) *Produit pur.* Excité par 2537 Å, MgTiO_3 ne contenant pas d'activateur possède une large bande d'émission bleue à 77°K (Fig. 5). Cette bande présente une analogie avec celle de Mg_2TiO_4 . Il semble, d'après Kröger, qu'on puisse attribuer cette fluorescence à des ions titane tétravalents, car on l'observe dans un grand nombre de composés du titane [4].

SPECTRE D'EMISSION EN GRANDE DISPERSION

La structure fine de l'émission de Mn^{4+} a été étudiée, à 77°K, à l'aide d'un monochromateur à réseau (Monospek 1000 Hilger) dont la dispersion est 8 Å/mm. Le spectre est représenté Fig. 6. On y distingue plusieurs éléments:

(1) *Deux raies fines et intenses* (14322 et 14291 cm^{-1}) correspondant à la bande principale des essais précédents. Ces raies peuvent être attribuées à la transition ${}^2E \rightarrow {}^4A_2$. Dans un champ parfaitement cubique, cette transition ne devrait faire apparaître qu'une raie. En réalité, l'environnement cubique n'est qu'une approximation et, dans toutes les matrices activées par Mn^{4+} déjà étudiées [6-8], le champ cristallin possède une composante de symétrie plus basse, ce qui a pour effet, compte tenu du couplage spin-orbite, de lever la dégénérescence du niveau 2E et de faire apparaître deux raies. Cette attribution se justifie par les arguments suivants: (a) Les raies sont fines, en accord avec la faible variation d'énergie du niveau 2E en fonction de l'intensité du champ cristallin [9]. (b) Le rapport des intensités I_2/I_1 de ces deux raies indique un équilibre de Boltzmann comme on doit l'attendre de deux raies provenant de la scission d'un même niveau. En effet, leur écart expérimental à 77°K est 31 cm^{-1} , valeur égale à celle calculée par la formule $I_2/I_1 = \exp. (\Delta E/kT)$.

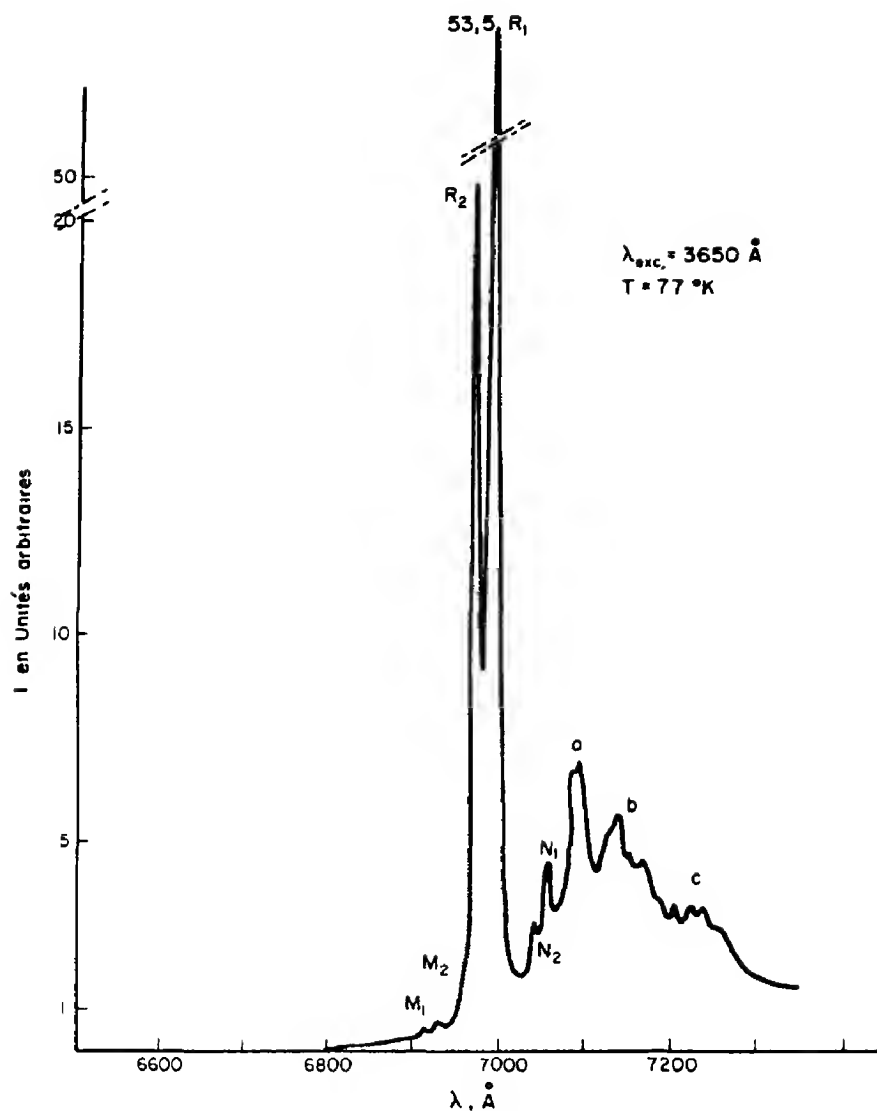


Fig. 6. Spectre d'émission de $\text{MgTiO}_3(\text{Mn}^{4+})$ (dispersion de 8 Å/mm).

De plus, la déformation trigonale envisagée pour expliquer la scission du niveau 2E et compatible avec un site de symétrie C_3 agit aussi sur le niveau excité 4T_1 . On a vu au paragraphe précédent qu'en effet la bande d'excitation ${}^4A_2 \rightarrow {}^4T_1$ possède deux maximums; si K représente l'intensité de la déformation trigonale, ils sont distants de $3K/2 \text{ cm}^{-1}$. Le paramètre K doit alors être relié à l'écart ΔE entre les raies R_1 et R_2 par la relation:

$$\frac{K}{\Delta E} = \frac{W_{2E} - W_{2T_2}}{4\zeta} \quad (10)$$

où ζ est la constante de couplage spin-orbite et $W_{2E} - W_{2T_2}$ la différence d'énergie des niveaux 2E et 2T_2 . Or, ζ et $W_{2E} - W_{2T_2}$ restent du même ordre de grandeur pour les ions $3d^3$ [7, 9]. Il doit donc en être de même pour leur rapport, donc pour $K/\Delta E$. C'est bien ce que montre l'examen du Tableau 2. Il semble donc qu'on puisse envisager valablement la présence d'une composante trigonale du champ.

(2) Une bande large, de faible intensité, s'étendant de 14200 à 13500 cm^{-1} . Il est possible qu'elle corresponde à la transition

${}^4T_2 \rightarrow {}^4A_2$, ainsi que le suggèrent les résultats de Kemeny et Haake sur le fluorogermanate de magnésium[11] et ceux de Dittmann sur les titanates spinelles[12], bien que les matrices employées ne soient pas les mêmes et que ces auteurs attribuent la totalité de l'émission à ${}^4T_2 \rightarrow {}^4A_2$. Il existerait alors un fort décalage de Stokes entre l'excitation et cette émission mais il pourrait s'expliquer par la variation importante de l'énergie du niveau 4T_2 avec l'intensité du champ cristallin.

(3) *Plusieurs raies dans la bande large.* Deux d'entre elles, N_2 et N_1 , à 14190 et 14160 cm^{-1} , dont le comportement thermique semble analogue à celui des raies R_1 et R_2 , pourraient correspondre à la transition $2E \rightarrow {}^4A_2$ de l'ion Mn^{4+} sur un autre site de symétrie voisine.

Les raies a , b et c peuvent être attribuées à des satellites vibroniques des deux groupes de raies N et R , car leurs écarts énergétiques avec ces raies fines correspondent à des fréquences caractéristiques de phonons.

(4) *Deux raies faibles, M_1 et M_2 , proches des raies R mais situées vers les courtes longueurs d'onde (14468 et 14429 cm^{-1}).* Il ne semble pas qu'elles soient de nature vibronique car elles sont très proches des raies R . Par contre, selon la suggestion d'Ibuki, Awazu et Hata dans le cas de $\text{As}_2\text{O}_5-6\text{MgO}(\text{Mn}^{4+})$ [13], il serait possible de les attribuer à la transition ${}^2T_1 \rightarrow {}^4A_2$. L'action simultanée du champ trigonal et du couplage spin-orbite scinde le niveau 2T_1 en trois composantes; on devrait donc observer trois raies.

Tableau 2

Composé	$\text{Al}_2\text{O}_3(\text{Cr}^{3+})$	$\text{Al}_2\text{O}_3(\text{Mn}^{4+})$	$\text{MgTiO}_3(\text{Mn}^{4+})$
Référence	[10]	[7]	
$-K(\text{cm}^{-1})$	330	700	700
$\Delta E(\text{cm}^{-1})$	29	82	31
$-K/\Delta E$	11	9	21

Il est possible, cependant, que l'une d'entre elles soit trop faible ou masquée par le reste de l'émission pour être observable.

CONCLUSION

Les résultats précédents soulignent l'intérêt d'une bonne définition de la matrice et des conditions de stabilité de l'activateur pour l'étude du spectre d'émission de l'ion Mn^{4+} .

La méthode de décomposition à l'air d'un tartrate mixte de magnésium et de titane a permis de réaliser une matrice de métatitanate de magnésium dans laquelle la fluorescence de l'ion Mn^{4+} a été mise en évidence. Cette émission a pu être interprétée, en bon accord avec l'expérience, dans l'approximation d'une symétrie cubique et d'une déformation trigonale du champ cristallin.

BIBLIOGRAPHIE

1. KRÖGER F. A., Brevet d'invention 62, 12 Cl. 8, no. 926. 859, Philips Gloeilampen Fabriken Pays-Bas (1947).
2. PÂRIS J. et PÂRIS R. A., *Bull. Soc. chim. Fr.* **4**, 1138 (1965).
3. SAÏKALI Y. et PÂRIS J., *C.r. hebdomadaire Séances Acad. Sci., Paris* **265C**, 1041 (1967).
4. KRÖGER F. A., *Some Aspects of the Luminescence of Solids*. Elsevier, Amsterdam (1948).
5. LOUAT A. et GAUME-MAHN F., *C.r. hebdomadaire Séances Acad. Sci., Paris* **265B**, 1199 (1967).
6. LOUAT A., Thèse de Doctorat-ès-Sciences, Lyon (1968).
7. GESCHWIND S., KISLIUK P. et KLEIN M., *Phys. Rev.* **126**, 1685 (1962).
8. LOUAT A. et GAUME-MAHN F., *C.r. hebdomadaire Séances Acad. Sci., Paris* **266**, 1128 (1968).
9. TANABE Y. et SUGANO S., *J. Phys. Soc. Japan* **9**, 766 (1954).
10. STURGE M. D., *Phys. Rev.* **130**, 639 (1963).
11. KEMENY G. et HAAKE C., *J. chem. Phys.* **33**, 783 (1960).
12. DITTMANN R. et HAHN D., *Z. Phys.* **207**, 484 (1967).
13. IBUKI S., AWAZU K. et HATA T., *Int. Conf. on Luminescence*. Budapest (1966).



ELECTROMIGRATION AND THERMOMIGRATION IN GAMMA-URANIUM†

J. F. D'AMICO‡§ and H. B. HUNTINGTON

Department of Physics, Rensselaer Polytechnic Institute, Troy, N.Y. 12181, U.S.A.

(Received 2 January 1969; in revised form 28 April 1969)

Abstract—Atom transport produced by large direct currents (electromigration) and thermal gradients (thermomigration) was measured in gamma-uranium by observation of local dilatations induced in high purity rods which were heated with a.c. or d.c. in a vacuum of 10^{-6} Torr, or better. Both radial and longitudinal dimensional changes, the latter obtained from displacements of surface markers, were measured in order to determine the atom flux. Rates of dimensional change were observed constant during the 8–12 days duration of the experiments. In the d.c. experiments, where the electromigration effect dominated, mass transport was observed toward the anode with Z^*/f equal to -1.6 ± 0.1 ; here f is the tracer diffusion correlation factor. The small negative value for Z^* , the effective charge, indicates a dominance of the electron 'wind' force over the combined forces of the hole 'wind' and the electrostatic field. In the a.c. experiments mass transport was observed toward the cooler regions with Q^*/f equal to $+4.7 \pm 0.5$ kcal/mole. If one adopts the Wirtz model for a vacancy mechanism, the thermomigration results imply a relatively large migration enthalpy and a correspondingly small formation enthalpy; the latter leads to a vacancy fraction at melting of about 2.7 per cent. Semi-log plots of DZ^*/f and DQ^*/f vs. $1/T$ were found linear with 'activation energies' of 27.2 ± 0.6 and 23.0 ± 1.6 kcal/mole, respectively. The former agrees with the activation energy obtained from tracer experiments while the latter is slightly less. A possible explanation is that Q^* has some temperature dependence, which is not too surprising in view of the large absolute thermoelectric power of gamma-uranium.

1. INTRODUCTION

ELECTROMIGRATION and thermomigration refer to processes in which matter transport is induced by application of electrical and thermal potential gradients, respectively. We have studied these processes in high-purity gamma-uranium by observing macroscopic dimensional changes produced in our specimens as a result of the induced atom motions. In the method employed here, cylindrical specimens were resistively heated for prolonged periods by a.c. or d.c. in high vacuum.

Our selection of gamma-uranium for these experiments was prompted by the 'anomalous' diffusion behavior of this metal, a characterization that has also been applied to β -Zr, β -Ti

and γ -Hf. These polymorphic b.c.c. transition metals deviate from the pattern of diffusion behavior observed in many other metals of various structure. Briefly, the 'anomalous' metals differ in that their Arrhenius plots for self and impurity diffusion show a definite curvature [1] and their self-diffusion activation energies are found to have a value about one-half that predicted by several widely-applicable empirical correlations, for example, the 'melting point rule' [1]. In addition, the measured values for the diffusion constant pre-exponential factor D_0 in the anomalous metals are significantly less than those of other metals. In terms of the Wert-Zener model [2], such values imply appreciably negative values for the total defect activation entropy, a situation which is difficult to understand in terms of our present knowledge of diffusion theory. This problem has already been discussed at length in the literature [1, 3–9] where several explanations have been offered. These fall into categories which

†Supported by U.S. Atomic Energy Commission.

‡Present address: Western Electric Engineering Research Center, Princeton, New Jersey, U.S.A.

§This paper is based on a thesis submitted to the Department of Physics and Astronomy at Rensselaer Polytechnic Institute in partial fulfillment of the requirements for the degree of Doctor of Philosophy.

attribute the anomaly to either: (i) extrinsic factors, e.g. temperature-independent vacancy concentrations resulting from a strong vacancy-impurity interaction[3], or dense dislocation networks stable at high temperature, or (ii) to a true bulk diffusion having temperature dependent parameters, e.g. temperature dependent Q and D_0 , or the simultaneous operation of two different intrinsic mechanisms. On reviewing this problem in the literature, one will probably conclude that no single, clear-cut explanation has yet been offered to explain all aspects of this anomaly.

It was with the idea of extending our knowledge of diffusion in these 'anomalous' metals that quantitative electro- and thermomigration experiments on them were begun, first on β -Zr by Campbell[8, 9], followed by those described here on γ -U. (The earlier experiments of Feller and Wever[10] were essentially qualitative. More recently, electro- and thermomigration experiments in β -Ti and β -Zr have also been reported by Dübler and Wever[11].) The study of diffusion in the presence of external forces supplements the information obtained from tracer experiments and presents some additional features which could aid in determining the diffusion mechanism. An advantage of our technique is that effects due to long-term annealing or gaseous impurity pickup are readily detectable so that the contribution of such effects to the 'anomalous' behavior can be observed. An added incentive for the selection of γ -U was that the electro- and thermomigration parameters, Z^* and Q^* respectively, were still completely undetermined. The extremely low vapor pressure of γ -U near its melting point, thus negligible metal evaporation, offered reasonable assurance that precise measurements of dimensional changes could be made in this metal in spite of operation at high temperature in high vacuum.

2. BASIS FOR ANALYSIS

In electro- and thermomigration experi-

ments in solids in which diffusion occurs by a vacancy mechanism, the presence of an electric field and/or a temperature gradient biases the normally random distribution of atom jumps into vacant lattice sites, thereby inducing a matter flux which can be determined by measuring the local dilatation rate in the specimen under study. In such a system, the atom drift velocity V_A is related to the mean applied force per atom F by the Nernst-Einstein equation

$$V_A = \frac{D_A F}{kT} \quad (1)$$

where k is the Boltzmann constant, T the absolute temperature, and D_A the diffusivity appropriate to the mechanism of the atom drift.

(A) Electromigration

The mean force per atom F_E due to an applied electric field E can be written as

$$F_E = Z^* |e| E \quad (2)$$

where e is the magnitude of the electronic charge, and the dimensionless parameter Z^* indicates the strength of the electromigration force. F_E is the resultant of the forces due to (i) the electric field acting directly on the valence charge of the lattice ions, and (ii) the momentum exchange forces produced by ion-charge carrier interactions[12, 13]. Substituting equation (2) into equation (1) and writing $E = J \cdot \rho(T)$ where J is the current density and $\rho(T)$ the resistivity gives

$$D_A Z^* = \frac{V_A k T}{J \rho(T) |e|} \quad (3)$$

In equation (3), D_A refers to the uncorrelated atom diffusivity since the atom (or vacancy) current determined from dilatation measurements is that due to the total atom (or vacancy) flux through the given volume element. Although D_A cannot be independently deter-

mined in the type of experiment described here, it can be evaluated from tracer diffusion studies in the same system, since then $D_A = D/f$, where D is the tracer diffusivity and f the correlation factor for the tracer diffusion. Thus

$$\frac{DZ^*}{f} = \frac{V_A kT}{J\rho(T)|e|}. \quad (4)$$

In the experiments described here, V_A , T and J were measured, while $\rho(T)$ was obtained from the literature[14]. In an experiment where both electro- and thermomigration occur due to the simultaneous presence of both electrical and thermal driving forces, as is the case in our d.c. experiments, V_A in equation (4) refers to the symmetric portion of the total atom velocity vs. position graph, the antisymmetric part being the result of thermomigration. We can also write

$$D = D_0 e^{-Q/RT} \quad (5)$$

where Q is the self diffusion activation energy and R the molar gas constant. From equations (4) and (5), then

$$\begin{aligned} \ln(DZ^*/f) &= \ln\left(\frac{D_0 Z^*}{f}\right) - Q/RT \\ &= \ln\left(\frac{V_A kT}{J\rho(T)|e|}\right). \end{aligned} \quad (6)$$

If Z^* and f are temperature independent, a semi-log plot of DZ^*/f vs. $1/T$ will be linear with slope $-Q/R$.

(B) Thermomigration

The thermomigration force F_T used here will be written as

$$F_T = -\left(\frac{Q^*}{N_A}\right) \frac{\nabla T}{T} \quad (7)$$

where N_A is Avogadro's number and Q^* , the heat of transport, is defined as the heat flow per mole that must be supplied in steady state

to maintain unit molar flow. (The Q^* used here equals $Q_A^* - H_f$, where H_f is the molar enthalpy of vacancy formation, and Q_A^* is the 'reduced heat flow' per unit atom current[15].) When the mass flow is by a vacancy mechanism, a counter flow of vacancies is implicit, and their enthalpy of formation appears as a negative term in the evaluation of Q^* . The physical significance of Q^* has been discussed at length in the literature[16-21]. For a vacancy mechanism, it has generally been concluded that Q^* in large part is given by

$$Q^* = \beta H_m - H_f \quad (8)$$

where H_m and H_f are the vacancy molar enthalpies of migration and formation and β is a dimensionless factor with a value somewhere near but less than 1. The complete evaluation of Q^* requires an analysis of all the factors inducing thermomigration, e.g. the phonon and charge carrier fluxes, Thomson heat, and the thermoelectric power. A unified treatment of the respective roles of these factors has been attempted elsewhere[21] by one of us (HBH).

By substituting equation (7) into equation (1) and rearranging, we obtain

$$DQ^*/f = -V_A RT^2/\nabla T. \quad (9)$$

Repeating the steps in Section 2(A)

$$\begin{aligned} \ln\left(\frac{DQ^*}{f}\right) &= \ln\left(\frac{D_0 Q^*}{f}\right) - Q/RT \\ &= \ln(-V_A RT^2/\nabla T). \end{aligned} \quad (10)$$

For temperature independent Q^* and f , we again anticipate that a semi-log plot of DQ^*/f vs. $1/T$ will be linear with slope $-Q/R$.

(C) Determination of atom drift velocity

By measuring local volume changes which occur in the specimens wherever the divergence of the vacancy flux is non-zero, the flow of matrix atoms (or the counterflow of

vacancies) can be calculated, provided there is no appreciable void formation or gaseous contamination. For the cylindrical specimens used in this work, the determination of V_A required measurement of both radial and longitudinal dimensional changes as a function of position and time. For any given volume element, we can equate the local dilatation rate to the net matter influx (or efflux) and thus obtain the atom drift velocity V_A (relative to the local lattice) as a function of position x along the specimen axis:

$$V_A(x) = - \int_{x_0}^x [\dot{\epsilon}_{xx}(x') + 2\dot{\epsilon}_{rr}(x')] dx'. \quad (11)$$

The term in brackets represents the volume dilatation rate $\dot{\Delta}$. We shall refer to $\dot{\epsilon}_{xx}$ as the longitudinal 'strain' rate, where $\dot{\epsilon}_{xx} = dV_m/dx$ and V_m is the velocity of a surface marker. Likewise $\dot{\epsilon}_{rr}$ will be referred to as the radial 'strain' rate, where $\dot{\epsilon}_{rr} = (1/R)dR/dt$, with R the specimen radius and t the time. The symbol x_0 denotes the position of the reference marker where all strains are zero. The physical interpretation of equation (11) is that the mass flow through a cross section of the specimen will be observed as a dilation elsewhere in the specimen. Now since

$$\int_{x_0}^x \dot{\epsilon}_{xx}(x') dx' = V_m(x), \quad (12)$$

equation (11) can be re-written:

$$V_A(x) = -V_m(x) + 2 \int_{x_0}^x \dot{\epsilon}_{rr}(x') dx'. \quad (13)$$

In earlier work[22,23], the ratio of the longitudinal strain to the total dilatation was defined as the isotropy factor α , $\epsilon_{xx}/(\epsilon_{xx} + 2\epsilon_{rr}) \equiv \alpha$, which was found to be very nearly constant over the length of a specimen. For such a situation

$$V_A(x) = -V_m(x)/\alpha \quad (13)$$

so that once α was determined, the total atom

flux could be completely determined from the surface marker velocities. In the elastic-plastic theory developed by Penney[22], $\frac{1}{2} \leq \alpha \leq 1$, the lower limit denoting the case of completely isotropic deformations. In γ -U, however, and to some extent in β -Zr[8,9], we have observed a pronounced position dependence in α , requiring measurement of both radial and longitudinal strains at every point in order to evaluate $V_A(x)$. Furthermore, we have noted that in a majority of our runs, the mean α has been decidedly less than $\frac{1}{2}$, indicating that radial strains are preferred in γ -U. A somewhat similar result has been observed in electromigration experiments in single crystals of zinc[24]. (A more detailed discussion of this point may be found in[25].)

3. EXPERIMENTAL PROCEDURE

(A) Material characterization and specimen preparation

The uranium rods used in our experiments were furnished by the Metallurgy Division of the Argonne National Laboratory and were drawn from ingots prepared and purified by a technique developed by Blumenthal and Noland[26]. The spectrochemical impurity analysis of the two ingots from which the specimens were taken was supplied by Argonne as stated in Table 1. Following a 1-2 hr electrolysis[27] to remove surface

Table 1. Impurity content of uranium specimens

Element	Analysis (ppm by wt.) (average of top and bottom of ingot)	
	Ingot HPX-43	Ingot HPX-136
Al	5	1
Fe	5	1
C	5	28
N	11	15
O	33	33
Mg	2	3
Si	10	10
H	1-2	(not analyzed)
(all other elements below spectrochemical detection)		

oxide, markers (razor scratches) were scribed along the specimen axis. Then specimens were re-electrolyzed to remove freshly formed oxide and immediately mounted in the vacuum chamber which was sealed and pumped down as quickly as possible. The color of the specimen after pumpdown indicated that no appreciable oxidation had occurred after the final electrolysis. However, subsequent to bake out in moderate vacuum (about 10^{-7} Torr.) the specimen color invariably turned to a uniform golden brown indicating the re-formation of an oxide layer.

(B) Apparatus

All experiments were carried out in a glass-stainless steel vacuum chamber which was designed and built by Campbell for similar experiments on β -Zr [8, 9]. Specimens were mounted horizontally in the chamber between two water-cooled copper clamps, one being fixed while the other was floated in liquid metal to facilitate free movement while maintaining electrical and thermal contact. On application of either d.c. or a.c. (for electro- or thermomigration experiments respectively) a nearly parabolic temperature distribution with the temperature maximum at the specimen center was induced. Experiments were performed in high vacuum to minimize specimen contamination, γ -U being a well-known 'getter' of gaseous constituents at high temperatures.

Specimen dimensional changes, both longitudinal and radial, were measured with a Gaertner travelling microscope of $1\ \mu$ resolution. This instrument was installed so that it could view the specimen through a horizontal quartz window. With this arrangement continuous measurement of marker positions to within $\pm 2\ \mu$ was obtained. Radial measurements were measured with similar precision by use of a filar micrometer mounted in the microscope. A CdS photoresistor (CL 605 L, Clairex Corp., New York, N.Y.) mounted in the microscope in place of the eyepiece was

used to measure the temperature distribution in the specimen. Details related to this technique of temperature measurement are given by Hehenkamp [28].

(C) Measurements

1. *Initiation of experimental runs.* After preparation and mounting of a specimen, the vacuum chamber was pumped down, then baked out for 12–14 hr to outgas the system. On cooling, the pressure was generally in the range $0.7\text{--}1.4 \times 10^{-8}$ Torr. Except for some pressure pulses of several minutes duration during the initial specimen heatup, the pressure was unaltered by the heating of the specimen.

The initial heating of the specimens was done at the rate of about 600°C/hr up to the α - β transition at 660°C , at which point the rate was reduced to about 100°C/hr to minimize strains which may have been induced by rapid motion of the phase boundaries. After obtaining the desired temperature, a 12–24 hr annealing was performed before making measurements.

2. *Temperature measurement.* (a) *Calibration of photoresistor.* Temperature calibration was accomplished by simultaneously measuring photoresistance vs. thermocouple output with both devices reading at the same position but on opposite sides of the specimen. All calibration measurements were made at the specimen center, the position of zero temperature gradient. The thermocouple was tungsten-rhenium (3 per cent) vs. tungsten-rhenium (25 per cent) made from 0.005 in. dia. wires supplied and calibrated by Engelhard Co., Newark, J.J.

Separate calibrations were made for each diameter specimen. In addition, melting point checks were run on each calibration as a test of the absolute accuracy of the temperature measurements. In the calibrations used for the $\frac{1}{8}$, $\frac{1}{16}$, and $\frac{1}{32}$ in. dia. specimens, the thermocouple reading at the onset of melting gave temperature values of 1129° , 1116° and 1127°C , respectively. (The melting point of

uranium is given as 1129°C[29].) In several attempts to run the experiments with a thermocouple on the specimen, melting occurred at temperatures as low as 1080°C after 2–3 days operation, apparently due to an appreciable alloying of the thermocouple and the specimen. This, we think, is the cause of the slightly reduced value for the melting point check of the $\frac{1}{8}$ in. dia. calibration, which was run over a longer time interval than the others.

We also observed a shift in specimen emissivity, and thus in the temperature calibration, after the initial heating of the specimen to high temperature. By performing several experiments with off-center thermocouples, we observed that once the temperature (at the hottest point) was above 1000°C for several hours, this emissivity change occurred over the entire gamma-phase of the specimen, irrespective of the actual temperature at any individual position. Thus a time- and temperature-independent calibration was obtained by heating the specimen to 1050°C (at the center) for several hours before establishing the temperature calibration. (b) *Determination of T and ∇T .* T and ∇T were determined in all computations from a computer least squares fit of mean temperature vs. position data to a polynomial of 2nd degree. Temperature vs. position readings at $\frac{1}{2}$ or 1 mm intervals along the specimen axis were taken at the beginning and end of each run, and several times in between.

3. *Measurement of dilatations.* With a few exceptions, all dilatation measurements were made with the specimen in place and at temperature in the vacuum chamber. Marker positions were measured daily to determine the rate of longitudinal strain. Markers on the colder side in the α -phase at the fixed clamp were used as a reference for the laboratory coordinates.

Measurements of radial strain rate were made with the filar micrometer by periodically recording specimen diameter at the exact position of each marker. This procedure

insured that successive measurements were made at exactly the same position on the specimen, thus reducing errors due to local or systematic variations in diameter. In the d.c. runs where the dimensional changes were relatively large, the radial measurements were generally made daily, whereas in the a.c. runs, they were made on alternate days.

4. RESULTS

(A) Electromigration

The electromigration results were obtained from four d.c. runs, two on specimens of $\frac{3}{32}$ in. and two on specimens of $\frac{1}{8}$ in. dia. In Fig. 1, we have plotted marker velocity V_m and rate of diameter change $\Delta\dot{D}$ vs. position x for Run 9A, which was performed on a $\frac{3}{32}$ in. dia. specimen at a current density of 2680 A/cm². The V_m were determined from linear fits to marker displacement vs. position plots, the $\Delta\dot{D}$ by difference between final and initial radial measurements. The asymmetry in V_m and $\Delta\dot{D}$ vs. x is due to the simultaneous presence of both electro- and thermomigration

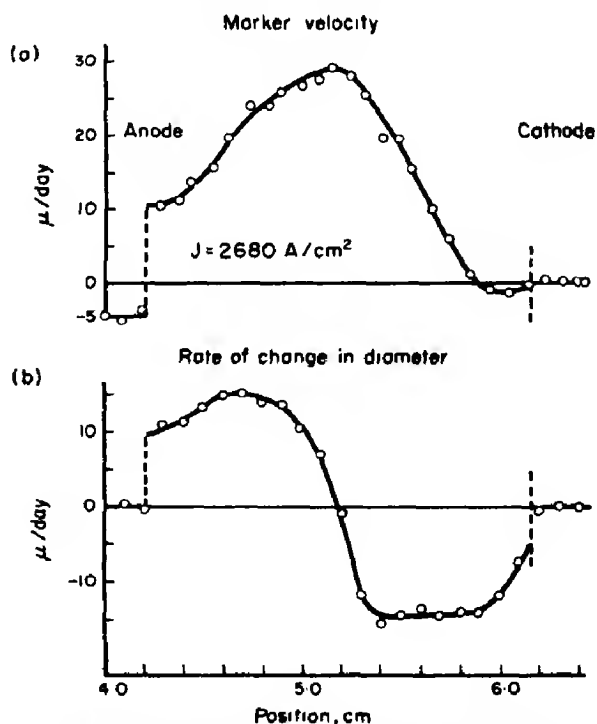


Fig. 1. Marker velocity and rate of change in diameter vs. position for d.c. Run 9A.

in d.c. runs. The positive values of $\Delta\dot{D}$ and slope of V_m vs. x on the anode side show that mass flow is from cathode to anode, i.e. Z^* is negative. The dashed lines indicate the locations of the β - γ phase boundaries where we observe a discontinuity in the atom flux. This effect is due to the greatly reduced diffusivity of the atoms in the colder phases[30]. The convention used here to denote the sign of the marker velocity is as follows: motion toward the fixed end (the cathode here) is positive. In Run 9A, the specimen expanded at the rate of about $4.5 \mu/\text{day}$ as indicated by the negative marker velocity at the free (anode) end.

In Fig. 2 we have plotted the total dilatation rate $\dot{\Delta}$ vs. x . Graphical integration of $\dot{\Delta}(x)$ vs. x (see equation (11)), gives $V_A(x)$ which is plotted in the lower half of Fig. 2. Here $V_A(x)$ represents the net atom drift due to both electro- and thermomigration. Separation into symmetric and antisymmetric components gives the electro- and thermomigration velocities respectively. These are also shown in Fig. 2.

Values of DZ^*/f , computed using equation

(4) are plotted semi-logarithmically vs. $1/T$ in Fig. 3 for each of the d.c. runs. The lines drawn are linear least-squares fits for each

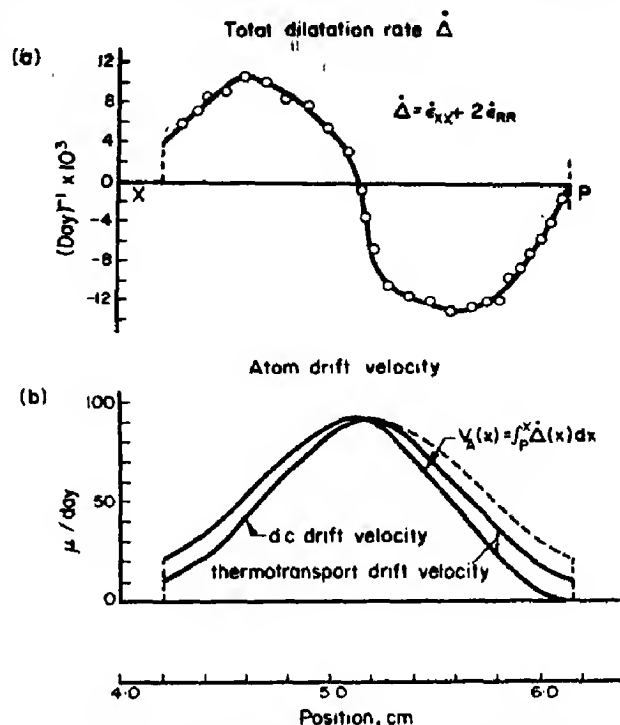


Fig. 2. Total dilatation rate and atom drift velocity vs. position for d.c. Run 9A.

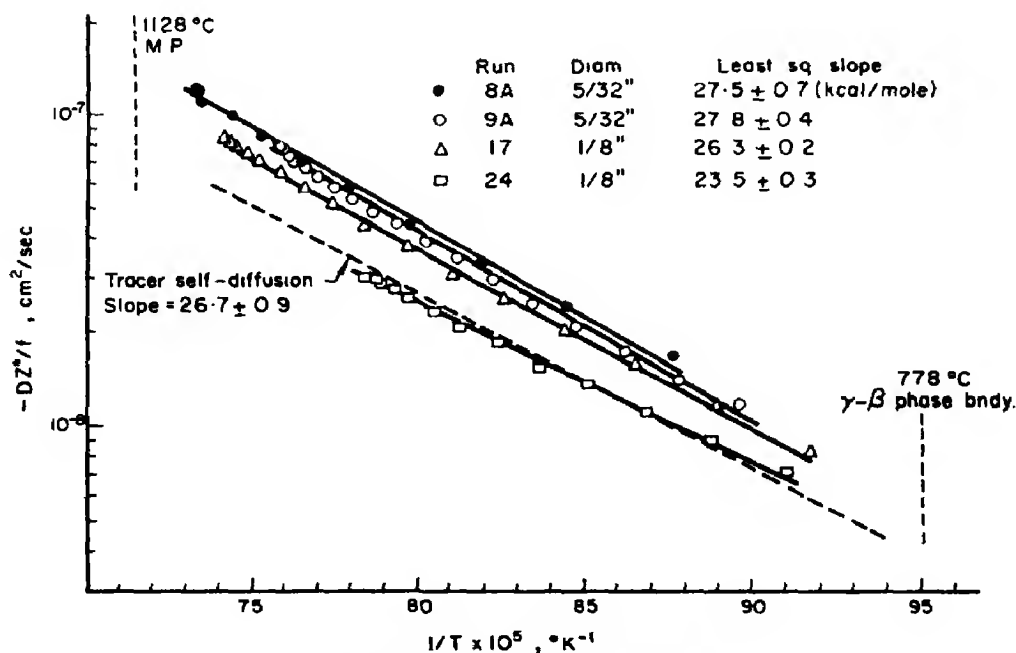


Fig. 3. $-DZ^*/f$ vs. $1/T$ (all d.c. runs).

run. Their slopes, which should be equal to the self-diffusion activation energy for temperature independent Z^*/f , are also stated in the figure. For comparison, a least-squares fit of the tracer data of Bochvar, Kuznetsova and Sergeyev[31], Adda and Kirianenko[32], and Rothman, Lloyd and Harkness[33] is also shown.

A summary of the electromigration results is presented in Table 2. The deviations in activation energy for each run are the standard deviations in the fitted slopes, whereas the deviation of the average activation energy is the mean deviation of the single run values from the mean of all runs. Values of Z^*/f in Table 2 were computed using D values from the least-squares fit of the tracer data cited above.

Table 2. Summary of electromigration results

Run	Activation energy Q (kcal/mole)	Z^*/f^\dagger
8A	27.5 ± 0.7	-1.7
9A	27.8 ± 0.4	-1.6
17	26.3 ± 0.2	-1.4
24	23.5 ± 0.3	-1.0
Average	26.3 ± 1.4	-1.4 ± 0.2
Average (excluding Run 24)	27.2 ± 0.6	-1.6 ± 0.1

$^\dagger f$ = tracer diffusion correlation factor.

(B) Thermomigration

The thermomigration results were obtained from four a.c. runs, three on specimens of $\frac{1}{8}$ in. and one on a specimen of $\frac{1}{16}$ in. dia. In Fig. 4, we have plotted V_m and $\Delta \dot{D}$ vs. x for Run 16. The negative slope of V_m vs. x and negative values of $\Delta \dot{D}$ at the specimen center indicate mass transport down the temperature gradient, i.e. positive Q^* . In Run 16 the specimen expanded continuously at the rate of about $20.4 \mu/\text{day}$ as seen on the left side of the marker velocity plot. Phase boundary discontinuities in V_m and $\Delta \dot{D}$ are observed as in Fig. 1. In Fig. 5, we show \dot{A} vs. x for Run

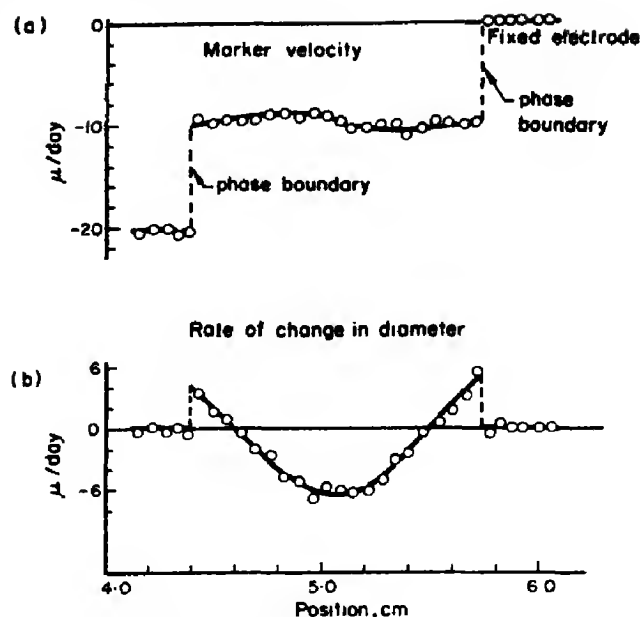


Fig. 4. Marker velocity and rate of change in diameter vs. position for a.c. Run 16.

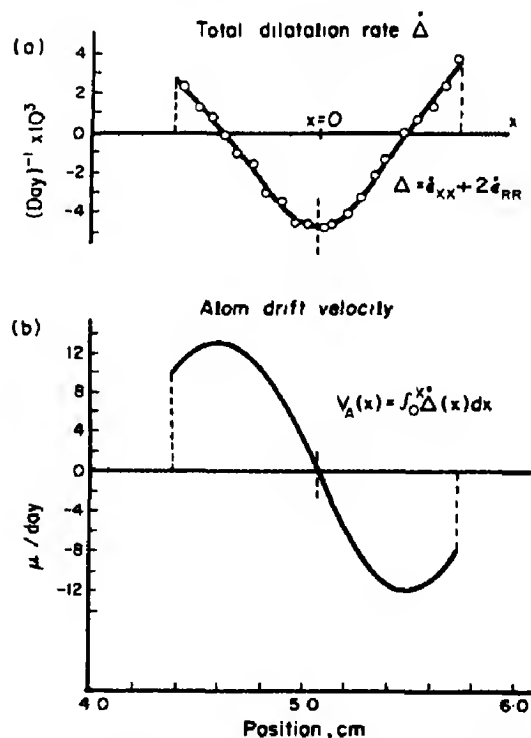
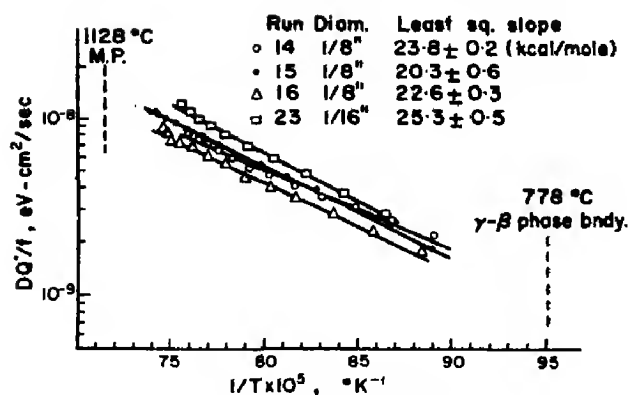


Fig. 5. Total dilatation rate and atom drift velocity vs. position for a.c. Run 16.

16, as well as the total atom velocity obtained by integration of the dilatation rate. In Fig. 6

Fig. 6. DQ^*/f vs. $1/T$ (all a.c. runs).

values of DQ^*/f calculated from equation (9) are plotted semilogarithmically vs. $1/T$. Linear least-squares fits to the data for each run are shown here, and thermomigration results are presented in Table 3. All deviations in Table 3 have the same meaning as those in Table 2. Values of Q^*/f were computed using the same D values used to compute Z^*/f .

Table 3. Summary of thermomigration results (a.c. runs only)

Run	Activation energy Q (kcal/mole)	Q^*/f^\dagger (kcal/mole)
14	23.8 ± 0.2	+4.7
15	20.3 ± 0.6	+4.6
16	22.6 ± 0.3	+3.7
23	25.3 ± 0.5	+5.6
Average	23.0 ± 1.6	$+4.7 \pm 0.5$

$^\dagger f$ = tracer diffusion correlation factor.

Values for DQ^*/f from the d.c. runs were found to agree within experimental error with those from the a.c. runs. However, the d.c. thermomigration data are less precise than the a.c. data primarily because of the anti-symmetrization required to separate the thermomigration velocity component $(V_A)_{\text{asym.}}$ from the total atom velocity (where $V_A = (V_A)_{\text{sym.}} + (V_A)_{\text{asym.}}$). Under the conditions in our d.c. runs, $V_A \approx (V_A)_{\text{sym.}}$ so that the fractional error in $(V_A)_{\text{asym.}}$ is rather large whereas that in $(V_A)_{\text{sym.}}$ is about equal to that

in V_A . The d.c. results therefore were not included in the final determination of Q^*/f .

(C) Search for annealing effects, impurity pickup and void formation

The effect on diffusivity caused by prolonged annealing of defects should be observed in our experiments as a change in the dilatation rate, for example, by observation of curvature in the marker displacement vs. time plots. In the first several hours of a run, however, rate changes due to annealing cannot be separated from those due to (1) relaxation of the specimen in the apparatus or (2) temperature fluctuations which the annealing induces. Our comments in regard to annealing, therefore, refer only to effects which occur after the initial 12–24 hr period. In Fig. 7, marker displacement vs. time is plotted for markers near the center of the specimens of Runs 9A and 16. The displacements in Run 9A are seen to be slightly non-linear in the

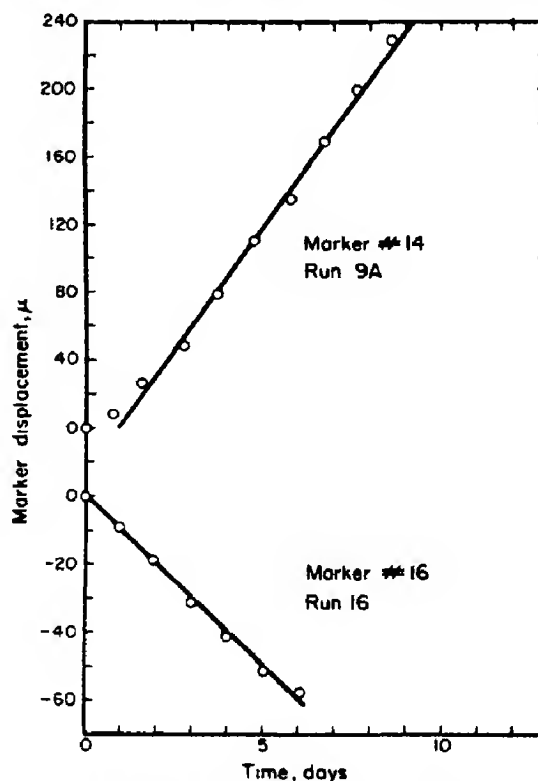


Fig. 7. Typical marker displacement vs. time plots, Runs 9A and 16.

first day of the run, probably due to a slow settling of the specimen in the apparatus. In this run there was some difficulty due to a bend in the specimen which occurred during the initial heating. If this initial effect is excluded, we observed that the displacements in both runs are quite linear. In general, no curvature after annealing was observed in any of the other runs.

In order to determine the extent of specimen contamination by gaseous impurities during our runs, several specimens were weighed on an analytical balance of $\pm 30 \mu\text{g}$ precision before and after running. The results of these weighings, given in Table 4, show that the loss of weight due to outgassing exceeds weight increase due to gaseous pickup. A rough estimate of weight increase due to pickup gives about $80 \mu\text{g}$ per week for oxygen, on the assumption that all molecules that collide with the surface are absorbed.

Table 4. Measured weight change of specimens

Run	Wt. before (g)	Wt. after (g)	Wt. change (μg)
3	9.48793	9.48748	-450
8A	10.24558	10.24522	-360
9A	11.06559	11.06560	-10

To observe void formation, specimens from both a.c. and d.c. runs were mounted in epoxy resin and hand-polished with alumina of particle size down to 0.1μ , followed by a 2-hr electropolish[27]. When examined under a $100\times$ microscope, the specimen showed no evidence of void formation. The appearance of the heated regions was identical to that of the material that was under the water-cooled clamps during the run. Some small voids were observed delineating the position of the β - γ phase boundary during the run, but these were not extensive and are estimated to represent very small volume changes, probably less than a few per cent of the total volume

change in the phase boundary region. The conclusion that void formation is negligible is further supported by the correlation of the observed marker velocity discontinuities at the phase boundaries (at which point $V_m = V_A$) with values of V_A determined from the dilatation measurements.

5. DISCUSSION

(A) Electromigration

1. *Experimental data.* The simultaneous presence of both electro- and thermomigration in d.c. runs is evident from the asymmetry of V_m vs. x in Fig. 1. The discontinuity in V_m vs. x at the anode side phase boundary is due to the difference in diffusivity between the high and low temperature phases of uranium mentioned earlier. At the anode phase boundary, the observed discontinuity is the result of contributions from both electro- and thermomigration to the total mass flux. On the cathode side, the induced fluxes are opposed, and apparently cancel in this particular run. The rate of diameter change in Fig. 1 also show a discontinuity at the phase boundary, with no radial changes observed in the colder phases. This result was found valid without exception, indicating that the atom current at the phase boundary was entirely longitudinal, i.e. $\alpha = 1$. Since the atom velocity is effectively zero in the colder phases, the magnitude of the velocity discontinuity at the phase boundary equals the total atom velocity V_A at this point. This conclusion, made originally by Campbell[8, 9] for β -Zr, also appears valid in β -Ti[34].

In examining the plots of DZ^*/f vs. $1/T$ in Fig. 3 one should note that the plotted points do not represent raw data but are obtained by computing the dilatation rate integral at arbitrarily selected positions along the specimen axis. However, the linear density of points plotted in Fig. 3 is very nearly equal to the density of measurements made on the specimen, so that fitting the line to the plotted points is still meaningful. The scatter in these points, however, has been markedly reduced

over that in the raw data by the integration. On the other hand, systematic errors in the data could introduce some curvature into these plots. The lack of precision in these measurements prevents a physical interpretation of the slight curvature observed in some of the plots in Fig. 3.

2. *Estimates of experimental error.* The random error in DZ^*/f may be obtained by differentiation of equation (4). From estimates for random error in velocity, temperature and current density of 5, $\frac{1}{2}$ and 2 per cent respectively, the r.m.s. error in DZ^*/f is approximately $5\frac{1}{2}$ per cent. The mean error in activation energy (Table 2) is about $1\frac{1}{2}$ per cent, indicating that the overall effect of the random errors is not very significant here. On the other hand, the intercept shifts in the lines in Fig. 3 must be due to systematic errors, most probably due to run-to-run shifts in the pyrometer temperature scale. From an analysis of temperature calibration runs, we would anticipate a maximum run-to-run shift in the temperature scale of about $\pm 8^\circ\text{K}$. This would explain the difference between Runs 8A, 9A and 17, but could not explain the results of Run 24 which appear to be appreciably affected by an additional systematic error of unknown origin. It is also possible that the run-to-run shifts in intercept are due to small differences in material since Runs 8A and 9A (the 2 upper lines) were done on specimens of slightly different impurity content and mechanical preparation than those used in Runs 17 and 24 (the 2 lower curves). However, the thermomigration results obtained from specimens of identical material show the same intercept shifts. The most consistent explanation is that this effect is due to temperature error in both d.c. and a.c. experiments.

In determining the r.m.s. error in Z^*/f , we have included, in addition to the random errors already mentioned, errors in resistivity ρ and in diffusivity D . The resistivity error, estimated at 7 per cent is introduced because results were calculated using literature values

of ρ [14] in the absence of any measurements on the Argonne uranium. The error value used reflects the scatter in the published resistivity values. The r.m.s. error in D is estimated to be $13\frac{1}{2}$ per cent. In computing this value, we used the Rothman estimate [33] of 7 per cent for the tracer experiment error and a value of 11 per cent for the error produced by our 1 per cent overall temperature uncertainty. The r.m.s. error in Z^*/f is approximately 21 per cent.

3. *Temperature dependence of Z^* .* Excluding Run 24, the mean electromigration activation energy of 27.2 ± 0.6 kcal/mole is not significantly different from the value of 26.7 ± 0.9 kcal/mole obtained from fits to the available tracer data for self-diffusion. Thus within the limits of error, the temperature dependence of DZ^*/f appears entirely due to that of D so that Z^* may correctly be considered constant. However, we should point out that although the deviation from linearity is quite small, the precision of the measurements and the smallness of the temperature range do not positively rule out the possibility that Z^* may have a weak temperature dependence, e.g. $Z^*(T) = Z_0^*(1 + aT^2)$ where $|aT^2| \ll 1$. Such a dependence would not produce an observable curvature but would slightly alter the slope of the fitted line. In Fig. 3 we also observe a slight upward curvature in points near the specimen center. This cannot be a real temperature effect since the curvature occurs at the specimen center regardless of the temperature at this point. This effect must be due to a systematic error in the measurement of atom velocity or perhaps temperature.

4. *Significance of Z^* .* For a single band metal, Z^* can be used to calculate specific defect resistivity, ρ_d/N_d [12]:

$$Z^* = Z_{ES} - z \left(\frac{\rho_d}{N_d} \right) \left(\frac{N}{\rho} \right) \frac{m^*}{|m^*|} \quad (14)$$

where Z_{ES} is the effective atom charge during the jump, z the number of charge carriers per

atom, ρ_d and ρ the respective defect and matrix atom resistivities, N_d and N the respective defect and atom densities, and m^* the effective mass of the charge carriers. However for a multi-band metal such as uranium [35], an additional term analogous to the 2nd term on the right but of opposite sign must be included in equation (14) to account for defect interactions with the other type of carriers. Thus Z^* in the multiband case is a measure of the difference in effectiveness of the electron 'wind' force and that due to the sum of the direct field and the hole 'wind' forces. The small negative value of Z^*/f measured in γ -U indicates that these two opposing forces are very nearly equal, with the electron 'wind' dominating slightly.

(B) Thermomigration

1. *Experimental data.* The phase boundary discontinuity mentioned in the discussion of electromigration results is also readily observable in the thermomigration data in Fig. 4. Here, however, the two discontinuities should be equal since the mass flow is symmetric about the temperature maximum at the specimen center. In Fig. 4 we observe that the slopes of V_m vs. x are quite small relative to the magnitude of the radial changes indicating that in Run 16 the dilatation was mostly radial. (The mean α for Run 16 was 0.14. In general the α values in this work were surprisingly low. In terms of our present concepts, values much below $\frac{1}{2}$ cannot be convincingly explained.) In Fig. 4 we also observe run-to-run shifts in the intercepts of the fitted lines as well as some curvature in the fits of the data to the lines. The comments made in the electromigration discussion of these effects are also relevant here.

2. *Estimates of experimental uncertainty.* By procedures similar to those referred to in Section 5(A)2, the r.m.s. error in DQ^*/f is estimated at 9 per cent. Here we have used values of 9, $\frac{1}{2}$ and 1 per cent for the respective random errors in velocity, temperature, and temperature gradient. From the previously

cited value for the error in D , the r.m.s. error in Q^*/f is estimated to be about 17 per cent. Mean error in the activation energy (Table 3) is 1.7 per cent again indicating the unimportance of the random errors. The intercept shifts in Fig. 6 can be accounted for by a run-to-run error in the temperature scale as previously mentioned.

3. *Temperature dependence of Q^* .* From equation (10) we expect that for temperature-independent Q^* the slope of $\ln(DQ^*/f)$ vs. $1/T$ should equal $-Q/R$. The mean value of Q obtained in the a.c. runs is 23.0 ± 1.6 kcal/mole whereas the self-diffusion value is 26.7 ± 0.9 kcal/mole. These values thus differ slightly, the difference being just beyond the estimated limits of error, suggesting that Q^* may be somewhat temperature dependent. This is not completely surprising since it has been shown [21] that the Thomson field and the action of the electrons and holes as heat carriers can give rise to additional terms in Q^* varying as T^2 . Such terms would be significant in metals having a large absolute thermoelectric power as is the case for γ -U [36]. We can write the temperature dependence of Q^* as

$$Q^*(T) = Q_0^*[1 - \gamma T^2] \quad (15)$$

where Q_0^* equals $\beta H_m - H_f$ and $Q^*(T)$ is the measured heat of transport. The parameter γ is approximately temperature independent in the model being used here, and has a positive sign by virtue of the positive absolute thermoelectric power in uranium. Although a first principles evaluation of γ in this metal is not possible here, an estimate of the term $\gamma Q_0^* T^2$ can be made by assuming that the activation energy of our thermomigration results differs from the self-diffusion value solely due to the temperature dependence of the heat of transport. In the temperature range involved, a value of $\gamma = 0.2 \times 10^{-6} (^\circ K)^{-2}$ was found to adequately describe the temperature dependence of $Q^*(T)$. For the cited γ value, $(1 - \gamma T^2)$ in

the center of the temperature range has a value of about 0.7, indicating that the temperature independent part of the heat of transport, $Q_0^* = \beta H_m - H_f$, exceeds the measured value $Q^*(T)$ by about 30 per cent. Under the assumptions made here, $Q_0^*/f = 4.4/0.7 = 6.7$ kcal/mole.

4. *Defect migration and formation enthalpies.* Although the diffusion mechanism in γ -U is not positively known, the experiments of Peterson and Rothman[37] show a defect mechanism to be operative, most probably, in their opinion, the single vacancy. For diffusion by a vacancy mechanism, $Q = H_m + H_f$ and using equation (8)

$$H_m = (Q^* + Q)/(1 + \beta) \quad (16)$$

$$H_f = Q - H_m. \quad (17)$$

The value of β is not known for γ -U but should be near unity. For $\beta = 0.9$, $Q = 26.7$ kcal/mole, and $f = 0.73$ for b.c.c. structures, our value of $Q^*/f = 6.7$ kcal/mole gives vacancy enthalpies: $H_m = 16.6$ kcal/mole and $H_f = 10.1$ kcal/mole. There are no reported values for these enthalpies to which these results may be compared.

We use H_f to estimate the vacancy fraction n_v at the melting point:

$$n_v(T_m) \approx \exp [-H_f/RT_m]$$

where we have set the entropy term equal to 1 as a lower limit, assuming a positive entropy of formation. On evaluation we obtain $n_v(T_m) \approx 2.7 \times 10^{-2}$, a value a few orders of magnitude larger than that observed in several other b.c.c. metals, for example, 1.1×10^{-4} in tungsten[38] or 7.5×10^{-4} in sodium[39]. In the f.c.c. noble metals[40], $n_v(T_m)$ is found to be $1-2 \times 10^{-4}$.

(C) *Effects due to annealing or contamination*

The observed constant dilatation rates indicate that the diffusion parameters measured

in these experiments are representative of γ -U that is well annealed and has a time independent defect concentration. If the anomalous behavior of uranium is due to a large density of phase transformation-induced dislocations, then such dislocations are evidently very stable and cannot be removed by annealing even at very high temperatures for extremely long times. This conclusion is in agreement with that of Peterson and Rothman[37] who observed no change in the diffusivity of cobalt tracer in γ -U after pre-annealing their uranium specimens for 19.5 hr at a temperature 30°C from the melting point. The effective annealing times in our experiments, however, are on the order of 10-15 days. Our results also exclude the possibility that specimen contamination by gaseous impurities from the ambient has any measurable effect on the diffusivity.

6. CONCLUSIONS

Within experimental error, the measured temperature dependence of DZ^*/f and DQ^*/f were found to be identical to the temperature dependence of D from self-diffusion measurements, from which we conclude that the same mechanism is operative in both types of experiments. The diffusion mechanism in γ -U has been discussed at length by Peterson and Rothman[37] who, on considering all the available diffusion data, concluded the most likely mechanism in γ -U to be the single vacancy. This conclusion was based on their analysis of the self and impurity diffusion data, Kirkendall experiments in dilute uranium alloys, and experiments in which the effect of high temperature pre-annealing of the uranium specimens was observed. The Peterson-Rothman conclusion, while not completely convincing, appears to us to be the most probable. The transport experiments which we have reported here do not, in the final analysis, add much in the way of new insights into the uranium diffusion mechanism. However, they appear to be in basic agree-

ment with the earlier diffusion work in γ -U. In addition to the agreement in activation energies, our results support the conclusion that diffusion along transformation-induced dislocations was not responsible for the anomalous behavior in γ -U. Peterson and Rothman's pre-anneal of their uranium specimens for 20 hr at a very high temperature showed no change in Co tracer diffusivity so that the high dislocation density required in the dislocation model was assumed not to be possible. Our experiments in essence confirm this result but extend the annealing time to 10 to 15 days with still no alteration of diffusivity observed. A similar comment pertains to effects caused by the pickup of gaseous impurities. If indeed very numerous dislocations exist in γ -U, they must have rather negligible mobility in this metal. We also have obtained reasonable values for H_f and H_m when interpreting the thermomigration results in terms of the vacancy mechanism. The overall behavior of γ -U which we have observed indicates that relative to electro- and thermomigration parameters it is rather different from β -Zr and β -Ti, both of which evinced substantial thermomigration toward the high temperature end and had small positive Z^* s.

The small values of α noted in many runs indicated deformations in the radial directions proportionally larger than in the longitudinal. There seems to be no ready explanation for this effect at this time, particularly since the specimen radius was presumably many times the vacancy life path. The vacancy formation enthalpy H_f obtained from the thermomigration results gives an estimate of vacancy fraction at melting of about 2-7 per cent, a value rather large compared to that previously measured in several other b.c.c. metals, e.g. W, Mo, Na, or in many f.c.c. metals. The thermomigration results also indicate that Q^* has some temperature dependence, which is not surprising in view of the relatively large absolute thermoelectric power in γ -U.

The small value of Z^*/f , -1.6 , indicates a

slight dominance of the 'wind' force due to atom-electron interactions over the sum of the direct field force and that due to atom-hole interactions.

Acknowledgements—The authors would like to thank the Metallurgy Division of the Argonne National Laboratory for supplying the uranium, especially to Dr. S. J. Rothman for his assistance in procuring the specimens and for helpful suggestions related to their preparation and use, to Dr. M. B. Brodsky who also helped in procuring the specimens, and to Mr. F. J. Karasek who rolled the uranium rods. We would also like to acknowledge many helpful discussions with Mr. M. D. Feit and Mr. H. R. Patil.

REFERENCES

1. See for example, LE CLAIRE A. D., In *Diffusion in Body-Centered Cubic Metals*, p. 3. ASM, Metals Park, Ohio (1965).
2. WERT C. and ZENER C., *Phys. Rev.* **76**, 1169 (1949).
3. KIDSON G. V., *Can. J. Phys.* **41**, 1563 (1963).
4. FEDERER J. and LUNDY T., *Trans. AIME* **227**, 592 (1963).
5. PEART R. F. and ASKILL J., *Phys. Status Solidi* **23**, 263 (1967).
6. LAZARUS D., In *Diffusion in Body-Centered Cubic Metals*, p. 155. ASM, Metals Park, Ohio (1965).
7. KIDSON G. V., In *Diffusion in Body-Centered Cubic Metals*, p. 329. ASM, Metals Park, Ohio (1965).
8. CAMPBELL D. R., Doctoral Thesis, Rensselaer Polytechnic Institute, Troy, New York (1967).
9. CAMPBELL D. R. and HUNTINGTON H. B., *Phys. Rev.* **179**, 601 (1969).
10. FELLER H. and WEVER H., *J. Phys. Chem. Solids* **24**, 969 (1963).
11. DÜBLER H. and WEVER H., *Phys. Status Solidi* **25**, 109 (1968).
12. HUNTINGTON H. B. and GRONE A. R., *J. Phys. Chem. Solids* **23**, 123 (1962).
13. FIKS V. B., *Soviet Phys. Solid St.* **1**, 14 (1959).
14. *Handbook of Thermophysical Properties of Solid Materials* Vol. 1. (Edited by A. Goldsmith, T. E. Waterman and H. J. Hirschhorn. Macmillan, New York (1961).
15. See, for example, HOWARD R. E. and LIDIARD A. B., *Rep. Prog. Phys.* **27**, 161 (1964).
16. SHEWMON P. G., *Diffusion in Solids*. McGraw-Hill, New York (1963).
17. LE CLAIRE A. D., *Phys. Rev.* **93**, 344 (1954).
18. BRINKMAN J. A., *Phys. Rev.* **93**, 345 (1954).
19. SHEWMON P. G., *J. chem. Phys.* **29**, 1032 (1958).
20. ORIANI R. A., *J. chem. Phys.* **34**, 1773 (1961).
21. HUNTINGTON H. B., *J. Phys. Chem. Solids* **29**, 1641 (1968).
22. PENNEY R., *J. Phys. Chem. Solids* **25**, 335 (1964).
23. HOP P. S., *J. Phys. Chem. Solids* **27**, 1331 (1966).

24. ROUTBORT J. L., *Phys. Rev.* **176**, 796 (1968).
25. D'AMICO J. F., Doctoral Thesis, Rensselaer Polytechnic Institute, Troy, New York (1968).
26. BLUMENTHAL B. and NOLAND R. A., *Progress in Nuclear Energy, Series V (Metallurgy and Fuels)* (Edited by H. M. Finniston and J. P. Howe), pp. 62-80. McGraw-Hill, New York (1956).
27. MOTT B. W., MEMBER M. A. and HAINES H. R., *J. Inst. Metals* **80**, 621 (1951-2).
28. HEHENKAMP T., *Rev. scient. Instrum.* **33**, 229 (1962).
29. BAUMRUCKER J. E. and CHISWIK H. H., Metallurgy Division Quarterly Report (Oct.-Dec. 1953); USAEC Rep. No. ANL-5234, Argonne National Laboratory (1953), reported in HOLDEN A. N., *Physical Metallurgy of Uranium*, Addison-Wesley, Reading, Mass. (1958).
30. BOCHVAR A. A., KUZNETSOVA V. G., SERGEEV V. S. and BATRA F. P., *Third United Nations Intl Conf. on the Peaceful Uses of Atomic Energy, A/Conf. Vol. 28*, p. 333 (1964).
31. BOCHVAR A. A., KUZNETSOVA V. G. and SERGEYEV V. S., *Trans. 2nd Geneva Conf. on Peaceful Uses of Atomic Energy*, Vol. VI, p. 68. United Nations, Geneva (1958).
32. ADDA Y. and KIRIANENKO A., *C.r. hebdom. Séanc Acad. Sci., Paris* **247**, 744 (1958).
33. ROTHMAN S. J., LLOYD L. T. and HARKNESS A. L., *Trans. AIME* **218**, 605 (1960).
34. D'AMICO J. F., Experiments in progress. RPI, Troy, N. Y.
35. FRIEDEL J., *J. Phys. Chem. Solids* **1**, 175 (1956).
36. WYMAN L. L. and BRADLEY J. F., Rep. No. KAPL-852 (1952), Thermal Electromotive Force of Uranium, Titanium and Zirconium.
37. PETERSON N. L. and ROTHMAN S. J., *Phys. Rev.* **136A**, 842 (1964).
38. SCHULTZ H., In *Lattice Defects in Quenched Metals* (Edited by R. M. J. Cotterill, M. Doyama, J. J. Jackson and M. Meshii), p. 763. Academic Press, New York (1965).
39. FEDER R. and CHARBNAU H. P., *Phys. Rev.* **149**, 465 (1966).
40. See, for example, DAMASK A. C. and DIENES G. J., *Point Defects in Metals*, p. 195. Gordon and Breach, New York (1963).



ON SHOULDER BANDS OF THE U BAND*

H. L. ARORA, C. K. MAHUTTE and S. WANG

Department of Physics, University of Waterloo, Waterloo, Ontario, Canada

(Received 2 December 1968; in revised form 25 April 1969)

Abstract—Two shoulder bands of the U band are theoretically investigated by computing absorption energies for optical transitions from the ground state of the U center to its high excited singlet states. The calculation is done by using the polaron model developed in a recent paper. The comparison of theoretical results with experimental results of the two shoulder bands shows that (a) one of the two shoulder bands (the U_a band) arises from the optical transition to the $1s3p$ -like singlet excited state and (b) the other (the U_b band) arises from the optical transitions to the $1snp$ -like singlet excited states with $n \geq 4$ modified by the crystal field.

1. INTRODUCTION

THE WORK of Timusk and Martienssen[1] has shown that the U band in an alkali halide containing a small amount of hydrogen has, under certain conditions, a shoulder on its high energy side. This shoulder band, according to the work of Goto *et al.*[2] consists of two absorption bands, which they designated as U_a and U_b from the low energy side. We shall adhere to this terminology in this paper. These authors suggested that the shoulder of the U band is due to optical transitions to higher excited states of the U center, which consists of a substitutional H^- ion located at a negative ion vacancy. Rockstad[3] has also observed U_a and U_b -like bands on the high energy side of the U band in KBr containing a small amount of KH.

The absorption maximum of the U band was first calculated by Gourary[4] using the point-ion approximation and the model that the U band is due to the transition from the ground state of the substitutional H^- ion to its $1s2p$ -like state. Rampacher[5] has calculated both the width and peak position of the U band for NaCl, KCl and RbBr using an approach based on the point-ion approxima-

tion. Wood and Öpik[6] have applied the extended ion method of Wood to the U centers in KCl, KBr and KI.

To our knowledge, there exists only one theoretical study, by Spector *et al.*[7], on the higher excited states of the U center. Their calculations, based on the point-ion approximation, show the energy difference between the $1s3p$ state and $1s2p$ state in the singlet state group of the U center to be much greater than the observed energy difference between the U_a and U bands in an alkali halide (e.g. for KBr, 1.52 eV versus the observed value of 0.50 eV). Thus, the optical absorption processes giving rise to the U_a and U_b bands are not yet well understood theoretically. To find the origin of the U_a and U_b bands, we have applied the polaron model [8], developed in a recent paper for a color center having two trapped electrons, to calculate the ground state and singlet excited states of the U center. The calculation and theoretical results are given in Section 2. The comparison of theoretical results with the experimental results of the U_a and U_b bands in KCl, NaCl and KBr is given in the last section. This comparison shows that the U_a band is due to the optical transition from the singlet ground state of the U center to its $1s3p$ -like singlet state modified by the crystal field and that the U_b band may be due to

*Supported by the National Research Council of Canada.

optical transitions to $1snp$ -like singlet states of the U center, where $n \geq 4$.

2. CALCULATION

(A) Effective Hamiltonian

In the polaron model developed in reference [8], the Hamiltonian including the electronic polarization of the crystal for the U center can be written as

$$H = \sum_{i=1}^2 H_i + \frac{e^2}{r_{12}} + H_v + V_{q-v} \quad (1)$$

where H_i takes the form

$$H_i = \frac{P_i^2}{2m_e} + \sum_{\alpha}' V(\mathbf{r}_i - \mathbf{R}_{\alpha 0}) - \frac{e^2}{r_i}, \quad |\mathbf{r}_i| < R_e \quad (2)$$

and

$$H_i = \frac{P_i^2}{2m_e} + \sum_{\alpha}' V(\mathbf{r}_i - \mathbf{R}_{\alpha 0}) - \frac{e^2}{r_i} + V_{e_i-v}, \quad |\mathbf{r}_i| > R_e \quad (3)$$

where R_e is the radius of a spherical region drawn about the trapping center within which the i th trapped electron does not polarize the core electrons of the ions making up the crystal. The second term in (1) is the interaction between the two trapped electrons of the U center. $P_i^2/2m_e$ is the kinetic energy of the i th trapped electron. $V(\mathbf{r}_i - \mathbf{R}_{\alpha 0})$ is the interaction of the i th trapped electron with the α th ion, when all the nuclei are at their equilibrium positions (which corresponds to the ground state of the crystal). The sum is over all ions except the trapping center q consisting of a proton located at a negative ion vacancy, as is indicated by the prime on the sum. $-(e^2/r_i)$ is the interaction between the i th trapped electron and the proton. H_v , V_{q-v} and V_{e_i-v} are the same as those in references [8] and [9] and represent the Hamiltonian of virtual excitons, the interaction of the virtual excitons with the trapping center q , and the interaction of the virtual exciton with the i th trapped electron, res-

pectively. Since the present system is equivalent to a perfect alkali halide plus a unit positive charge and a proton at the position q , the effective charge z of the trapping center is nearly two.

Making a simple canonical transformation as in reference [8] for H_v , V_{q-v} and V_{e_i-v} , which are written in terms of creation and annihilation operators for longitudinal excitons of wave vector \mathbf{w} in the polaron model, we then obtain the effective Hamiltonian

$$H_{\text{eff}} = \sum_{i=1}^2 \mathcal{H}_{\text{eff},i} + \frac{e^2}{\epsilon r_{12}} \quad (4)$$

where $\mathcal{H}_{\text{eff},i}$ is of the form

$$\mathcal{H}_{\text{eff},i} = \frac{P_i^2}{2m_e} - \frac{Me^2}{d} - \frac{e^2}{r_i}, \quad |\mathbf{r}_i| < R_e \quad (5)$$

$$\mathcal{H}_{\text{eff},i} = \frac{P_i^2}{2m_e} - \frac{Me^2}{d} - \frac{e^2}{r_i} + \frac{2e^2}{r_i} \left(1 - \frac{1}{\epsilon_{\infty}}\right) + \langle F_i | H_{\text{ex},i} | F_i \rangle, \quad R_e < |\mathbf{r}_i| < R_m \quad (6)$$

$$\mathcal{H}_{\text{eff},i} = \frac{P_i^2}{2m} - \frac{2e^2}{r_i} + \frac{2e^2}{r_i} \left(1 - \frac{1}{\epsilon_{\infty}}\right) + \langle F_i | H_{\text{ex},i} | F_i \rangle, \quad |\mathbf{r}_i| > R_m \quad (7)$$

In obtaining (4) from (1), the static field of the crystal, i.e. the second term in (2) is replaced by the Madelung energy $-Me^2/d$; and that in (3) is replaced by the Madelung energy for $R_e < |\mathbf{r}_i| < R_m$ and is taken into account by the effective mass approximation (i.e. $p^2/2m_e + \sum_{\alpha}' V(\mathbf{r}_i - \mathbf{R}_{\alpha 0}) = p^2/2m - V(\mathbf{r}_i - \mathbf{R}_{\nu 0})$, where $-V(\mathbf{r}_i - \mathbf{R}_{\nu 0})$ is the interaction of the i th trapped electron with the effective charge of the negative ion vacancy) for $|\mathbf{r}_i| > R_m$. Here, R_m is defined as the radius of another spherical region drawn about the trapping center and should be determined such that the effective mass approximation holds for $|\mathbf{r}_i| > R_m$. As in the semi-continuum and polaron model calculations of the F center, R_m can be set numerically equal to the Mott-Littleton radius (e.g. for KCl 0.85 times the

lattice constant) for typical alkali halides. We shall adopt this approximation in the following calculation. The ϵ in the last term of (4), as described in reference[9], is introduced to account for the exchange effect of the excitons surrounding the two trapped electrons. The ϵ_∞ is the usual high-frequency dielectric constant of the crystal. $H_{\text{ex},i}$ has the same form as (38) of reference[9] and is the Hamiltonian of virtual excitons surrounding the i th trapped electron plus the electron-exciton interaction. Thus $\langle F_i | H_{\text{ex},i} | F_i \rangle$ is interpreted as the self-energy of the i th trapped electron due to its own exciton cloud in the state F_i (see section 3 of reference[9]). Note that a constant energy resulting from the canonical transformation mentioned above is omitted in (4).

In this work we expect that the ground state of the system in question is so deep that the trapped electrons move very quickly and that they do not polarize the lattice because the ions making up the lattice cannot follow the electronic motion. In contrast, the trapping center may polarize the lattice because the trapping center moves slowly about its site and its motion can be followed by the ions. Consequently, there is an interaction between the trapping center and the virtual phonons. As in the case of the electronic polarization, this interaction can be transformed to a constant energy in the Hamiltonian. This constant energy (self energy of the trapping center) remains virtually unchanged during the optical absorption process, because the phonon state remains nearly unchanged during that process (Franck-Condon principle). Hence we shall omit the effect of ionic polarization in this work. This omission may not affect the theoretical results of absorption energies very much.

Since constant energies resulting from canonical transformations for virtual excitons and virtual phonons are omitted in (4), the eigenenergy of $\mathcal{H}_{\text{eff},i}$, i.e. the one-electron energy involved in this calculation is measured from the bottom of the conduction band

which includes polarizations, while the corresponding one-electron energy in the usual point-ion model calculation is measured from the bottom of the bare conduction band (see, e.g. [4]).

(B) Determination of R_e

We shall now use the electron paramagnetic resonance (EPR) data of the U_3 center, i.e. the hydrogen atom located at a negative ion vacancy, and the $1s$ hydrogenic wave function as the trial wave function for the U_3 electron to determine the R_e involved in the present problem. According to the formalism given in Section 2(a), the ground state energy of the U_3 center is given by $E_g(\alpha, R_e) = \langle \phi_{1s} | \mathcal{H}_{\text{eff}} | \phi_{1s} \rangle$, where α is the variational parameter in the trial wave function $\phi_{1s} = (\alpha^3/\pi)^{1/2} e^{-\alpha r}$, and \mathcal{H}_{eff} has the same form as $\mathcal{H}_{\text{eff},i}$ in Section 2(a). Thus, if α_g , being the value of α corresponding to the minimum of E_g , is known, then R_e can be determined in a similar way as in Section 3 of reference[8] from the equation $(\partial E_g / \partial \alpha)_{\alpha=\alpha_g} = 0$. α_g may be determined as follows. The Fermi interaction of the electron and the proton may be written as $a_0 = (-16\pi \mu_b \mu_0 |\phi_{1s}(0)|^2) / 3I_0$ (cf. equation (2) of reference[10]) where μ_b is the Bohr magneton, I_0 is the nuclear spin of the proton, μ_0 is the magnetic moment of the proton and $|\phi_{1s}(0)|^2$ is the electronic density at the proton. a_0 may be determined from the separation of lines, A , in the EPR spectrum of the U_3 center. From the observed EPR data of Hayes and Hody [11] for A (in units of frequency) for the U_3 centers in KCl and NaCl, we determine a_0 from the relation $a_0 = 2\pi\hbar A$. The values of α_g determined in this way for KCl and NaCl are 1.866 and 1.862 \AA^{-1} , respectively. Using these values for α_g and a method given in Section 3 of reference[8], we find R_e to be 0.430 \AA for KCl and 0.429 \AA for NaCl. Since these are nearly the same and since no EPR data are available for the U_3 center in KBr, we shall use $R_e = 0.4295 \text{ \AA}$ for KBr. Note that R_e determined in this way also includes a host of small corrections, such as the elec-

tron correlation energy and the effective mass approximation for the trapped electron etc., and is nearly the same as R_e involved in the U center.

In addition, we have also calculated the ground state energy of the U_3 centers. The calculated results, measured from the thermal bottom of the lowest conduction band, are given in Table 1. The theoretical value for KCl is obviously greater than the band gap between the lowest conduction band and the valence band in KCl (approximately 7.5 eV) and thus, the ground state of the U_3 center in the crystal considered lies below its valence band. In view of this and a discussion given

a hydrogen-like $2p$ state modified by the crystal field.

(C) Ground and optically excited states

From the form of the effective Hamiltonian given by equation (4), the U center may be regarded as an H^- -like ion modified by the crystal field. Thus we take

$$\psi_u(\mathbf{r}_1, \mathbf{r}_2) = N[\phi_\alpha(\mathbf{r}_1)\phi_\beta(\mathbf{r}_2) + \phi_\alpha(\mathbf{r}_2)\phi_\beta(\mathbf{r}_1)] \quad (8)$$

which was first proposed by Chandrasekhar [12] for the free H^- ion, as the trial electronic wave function for the ground state. Here N is the normalization factor and ϕ_α and ϕ_β are the hydrogen $1s$ wave functions, but represent different $1s$ orbitals. We have followed the method used in Section 4 of reference [8] and calculated $E_u = 2\langle\psi_u|\mathcal{H}_{\text{eff},1}|\psi_u\rangle + e^2/\epsilon_\infty \langle\psi_u|1/r_{12}|\psi_u\rangle$ for the U centers in KCl, NaCl and KBr. The calculated E_u and the corresponding variational parameters α and β are summarized in Table 2. The difference between the present ground state energy calculation and that by the point-ion model is discussed in detail in the last section.

In the consideration of the excited states of the U center, we shall only consider the $lsnp$ -like singlet excited states, because the optical transitions from the ground state (a singlet state) to any of these excited states occur with a large probability. Therefore, we take

$$\psi_{nc}(\mathbf{r}_1, \mathbf{r}_2) = \frac{1}{\sqrt{2}} [\phi_{1s}(\mathbf{r}_1)\phi_{np}(\mathbf{r}_2) + \phi_{1s}(\mathbf{r}_2)\phi_{np}(\mathbf{r}_1)] \quad (9)$$

Table 1. Values of α_g in \AA^{-1} , R_e in \AA and E_g in eV (measured with respect to the thermal bottom of the conduction band) for the U_3 centers in KCl, NaCl and KBr*

	α_g	R_e	E_g
KCl	1.866	0.430	-9.41
NaCl	1.862	0.429	-9.74
KBr		0.4295	-8.01

*Since no EPR data were available for KBr, α_g was not determined (see Section 2(b)).

in the last section of reference [8] for the excited state of the U_2 center, the first excited state to which the U_3 transition can be made from the ground state of the U_3 center is not

Table 2. Theoretical energies for the ground and optically excited states of the U centers in KCl, NaCl and KBr in eV and the corresponding variational parameters in \AA^{-1}

	KCl			NaCl			KBr		
	Minimum energy	α	β	Minimum energy	α	β	Minimum energy	α	β
$E_g(1s1s)$	-13.25	2.0	0.70	-14.17	2.0	0.80	-11.40	2.0	0.70
$E_{2p}(1s2p)$	-7.72	1.3	0.48	-8.14	1.2	0.56	-6.42	0.9	0.48
$E_{3p}(1s3p)$	-7.23	1.3	0.27	-7.57	1.2	0.30	-5.96	0.9	0.27
$E_{4p}(1s4p)$	-7.06	1.3	0.19	-7.41	1.2	0.20	-5.81	0.9	0.19
$E_I(\alpha)$	-6.87	1.3	0.00	-7.21	1.2	0.00	-5.62	0.9	0.00

as trial electronic wave functions for excited states of interest, where ϕ_{1s} is the hydrogen *1s* wave function and ϕ_{np} represents the hydrogen *np* wave function. The ϕ_{np} functions used here are as follows

$$\phi_{2p}(r) = \left(\frac{\beta^5}{\pi}\right)^{1/2} r e^{-\beta r} \cos \theta \quad (10)$$

$$\phi_{3p}(r) = \left(\frac{2\beta^5}{3\pi}\right)^{1/2} (2 - \beta r) r e^{-\beta r} \cos \theta \quad (11)$$

$$\phi_{4p}(r) = \left(\frac{\beta^5}{5\pi}\right)^{1/2} (\beta^2 r^2 - 5\beta r + 5) r e^{-\beta r} \cos \theta. \quad (12)$$

We have adopted an approach used in Section 5(b) of reference[8] and calculated $E_{ne} = \langle \psi_{ne}(\mathbf{r}_1, \mathbf{r}_2) | H_{\text{eff}} | \psi_{ne}(\mathbf{r}_1, \mathbf{r}_2) \rangle + e^2/a(1 - 1/\epsilon_\infty)$ for the optically excited states of the *U* center, where the last term is added such that E_g and E_{ne} in the present calculation are measured from the same reference point (see reference[9] for detail). The calculated E_{ne} and the corresponding values of the variational parameter α in the *1s* wave function and β in the *np* wave function are also summarized in Table 2.

The functional form of the energy of any optically excited state can be written as the sum of $E(\alpha)$, $E(\beta)$ and $E(\alpha, \beta)$. The function $E(\beta)$ vanishes as β approaches zero. Thus the energy of the optically ionized state (i.e. the optically excited state for $\beta = 0$) is given by $E_I(\alpha) = E(\alpha) + E(\alpha, 0)$. These values are calculated for KCl, NaCl and KBr and are also given in Table 2.

From the theoretical energies of the ground state and the excited states given in Table 2, the theoretical absorption energies for the optical transitions of interest are given in Table 3. The observed band maxima in KCl, NaCl and KBr are summarized in Table 4 for comparison.

3. DISCUSSION AND CONCLUSION

The *U* band has been believed to be due to the optical transition from the *1s1s*-like state

Table 3. Theoretical absorption energies of the *U* centers in KCl, NaCl and KBr in eV

	KCl	NaCl	KBr
$E_{2e} - E_g$	5.52	6.03	4.98
$E_{3e} - E_g$	6.02	6.60	5.44
$E_{4e} - E_g$	6.19	6.76	5.59
$E_I - E_g$	6.38	6.96	5.78

Table 4. Experimental band maxima (expressed as transition energies in eV) of the *U*, *U_a* and *U_b* absorption bands in KCl, NaCl and KBr

	KCl	NaCl	KBr
<i>U</i>	5.79*	6.46*	5.43*
<i>U_a</i>	6.43‡	6.89-7.61‡	5.93†
<i>U_b</i>	6.53-7.30‡	6.89-7.61‡	5.97-6.36§

*Reference[14].

†Reference[3].

‡Reference[2].

§Reference[15].

of the *U* center to its *1s2p*-like excited state. By comparing the present theoretical absorption energy for the transition *1s1s*-*1s2p* with the observed band maximum of the *U* band, we find that the present calculation underestimates the absorption energy of the *U* transition by 5 per cent for KCl, 6 per cent for NaCl, and 8 per cent for KBr. Here, we expect that the possible errors involved in the calculation of absorption energies for optical transitions to higher excited singlet states are of the same order as those given above, because the calculation is done by using the same method and wave functions of the same character. Obviously, the error just mentioned arises from (a) the method employed and (b) the approximate wave function used.

Let us now compare the calculated absorption energies for transitions to higher states with the observed band maxima of the *U_a* and *U_b* bands. As can be seen from Tables 3 and 4, the agreement between the calculated absorption energies of $E_{3e} - E_g$ and the observed band maxima of the *U_a* bands in the

crystals considered is as good as the agreement of the calculated absorption energies with the observed band maxima for the U bands in these crystals. Furthermore, the energy differences between the $1s3p$ and $1s2p$ singlet states compare very well with the experimental differences of the band maxima of the U_a and U bands for the crystals considered (cf. Table 5). Thus, we conclude that the U_a band is due to the optical transition from the ground state of the U center to its $1s3p$ -like singlet state modified by the crystal.

Table 5. Theoretical energy difference between the E_{3e} and E_{2e} states, and the experimental difference between the band maxima of the U and U_a bands in eV

	KCl	NaCl	KBr
$E_{3e} - E_{2e}$	0.49	0.57	0.46
$U_a - U$	0.64	0.43-1.15	0.50

We expect that the calculation for the optical transition to the $1s4p$ -like singlet state underestimates the corresponding absorption energy by ~ 5 per cent for KCl, ~ 6 per cent for NaCl, and ~ 8 per cent for KBr (see a discussion given previously for the possible errors involved in the calculation). Therefore, the true absorption energy for the optical transition to the $1s4p$ -like singlet state is about 6.50 eV for KCl, 7.17 eV for NaCl, and 6.07 eV for KBr. These values are in fairly good agreement with lower limits of observed band maxima of the U_b bands summarized in Table 4. In view of this and the comparison of the theoretical results with the experimental results, given in Table 6, we may conclude that the U_b band could be due to the optical transitions from the ground state of the U center to its $1snp$ -like singlet states modified by the crystal field, where $n \geq 4$. Hence, the U_b band has the same character as the K band, which is believed to be due to the optical

Table 6. Theoretical energy difference between E_{4e} and E_{2e} and that between E_1 and E_{2e} , and the experimental difference between the band maxima of the U and U_b bands in eV

	KCl	NaCl	KBr
$E_{4e} - E_{2e}$	0.66	0.73	0.61
$E_1 - E_{2e}$	0.85	0.93	0.80
$U_b - U$	0.74-1.51	0.43-1.15	0.54-0.93

transitions from the ground state of the F center to its np -like states, where $n \geq 3$ [13].

It is instructive to make a rough estimate of the influence of electronic polarization on the ground state energy of the U center. If the electronic polarization is omitted, then equation (1) may be reduced to

$$H_0 = h + \sum_{i=1}^2 \sum_{\alpha} V(\mathbf{r}_i - \mathbf{R}_{\alpha 0}) \quad (13)$$

where h has the same form as the Hamiltonian of the free H^- ion and $\sum_{\alpha} V(\mathbf{r}_i - \mathbf{R}_{\alpha 0})$ is the interaction of the i th trapped electron with the static field of the crystal in question and is replaced by the Madelung energy $-(Me^2/d)$, for $|\mathbf{r}_i| < R_m$ in the above calculation. Here, we expect from the calculated values listed in Table 2 for the two variational parameters in the ground state wave function ψ_g that the two trapped electrons spend most of their time inside the spherical region of radius R_m . Thus, the ground-state energy of the U center, based on H_0 given by (13), is approximately given by

$$E_0 = \langle \psi_g(\mathbf{r}_1, \mathbf{r}_2) | h | \psi_g(\mathbf{r}_1, \mathbf{r}_2) \rangle - 2 \frac{Me^2}{d} \quad (14)$$

where the first term in (14) may be regarded as the ground-state energy of the free H^- ion, which is of the order of -14.4 eV [16] and the second term is about -16 eV for KCl. Hence $E_0 \approx -30.4$ eV. This estimate compares well with that of the usual point-ion model calculation in which polarization effects are

omitted. This is because the potential of a trapped electron due to the crystal field in the point-ion model is nearly the same as that used here, i.e. $-(Me^2/d)$, in the spherical region of radius R_m [17] within which the ground state wave function is most predominant. On the other hand, using (4) for the effective Hamiltonian which includes electronic polarization caused by both the *trapping center* and the trapped electrons, and the wave function given by (8), the ground state energy of the *U* center in KCl is found to be -13.2 eV. This is about 17.2 eV above the E_0 , which does not include the contribution from electronic polarization. This difference comes mainly from twice (for two trapped electrons) the sum of the contributions of last two terms in (6) to the total energy. The fourth term in (6) results from the canonical transformation for the interaction of a trapped electron with the electronic polarization field caused by both the *trapping center* and the trapped electron. This term may be interpreted as the repulsive Coulomb interaction resulting from the exchange of virtual excitons between a trapped electron and the trapping center. The last term in (6) is the interaction of the i th trapped electron with its own exciton cloud (i.e. self energy) and takes the form $-e^2/r_i (1 - 1/\epsilon_\infty) + e^2/r_i (1 - 1/\epsilon_\infty) f_i(r_i)$ (see, for detail, (42) in [8]) where the second term contributes a relatively small positive energy to the total energy. As a result, the sum of the last two terms in (6) becomes $e^2/r_i (1 - 1/\epsilon_\infty) + e^2/r_i (1 - 1/\epsilon_\infty) f_i(r_i)$, whose contribution to the total energy in the calculation of the ground state is positive, and large because the average value of r_i is very small.

The above analysis leads us to conclude that the repulsive Coulomb interaction due to the exchange of virtual excitons between the trapping center and the trapped electrons is more dominant than the contribution from the self energy of the two trapped electrons (this is not the case in the *F* center problem) in the present problem and hence the inter-

action of the electronic polarization field with the trapping center and the trapped electrons contributes a positive energy as large as the order of 20 eV. This is somewhat reduced by the attractive Coulomb energy arising from the exchange of virtual excitons surrounding the two trapped electrons.

From the above discussion, we can make a remark about the binding energy of a substitutional H^- ion in a typical alkali halide crystal, say KCl. The net effect of the electronic polarization is to reduce its binding energy by about 17 eV and, on the other hand, the interaction of the two trapped electrons with the static crystal field (Madelung energy) increases the binding energy by about 16 eV. Accordingly, the binding energy of the substitutional H^- ion is less than that of the free H^- ion by a small amount.

Acknowledgement—We are very grateful to Dr. H. K. Rockstad for sending us some unpublished information which was very helpful to this work.

REFERENCES

1. TIMUSK T. and MARTIENSSEN W., *Z. Phys.* **176**, 305 (1963).
2. GOTO T., ISHII T. and UETA M., *J. phys. Soc. Japan* **18**, 1422 (1963).
3. ROCKSTAD H. K., *Phys. Rev.* **140**, A311 (1965).
4. GOURARY B. S., *Phys. Rev.* **112**, 337 (1958).
5. RAMPACHER H., *Z. Naturf.* **18a**, 777 (1963).
6. WOOD R. F., and ÖPIK U., *Phys. Rev.* **162**, 736 (1967).
7. SPECTOR H. N., MITRA S. S. and SCHMEISING H. N., *J. chem. Phys.* **46**, 2676 (1967).
8. WANG S. F., *Phys. Rev.* **170**, 799 (1968).
9. ARORA H. L. and WANG S. F., *J. Phys. Chem. Solids* **30**, 1649 (1969).
10. MIMURA H. and UEMURA Y., *J. phys. Soc. Japan* **14**, 1011 (1959).
11. HAYES W. and HODBY J. W., *Proc. R. Soc. A* **294**, 359 (1966).
12. CHANDRASEKHAR S., *Astrophys. J.* **100**, 176 (1944).
13. SMITH D. Y. and SPINOLO G., *Phys. Rev.* **140A**, 2121 (1965).
14. SCHULMAN J. W. and COMPTON W. D., *Color Centers in Solids*. MacMillan, New York (1962).
15. ROCKSTAD H. K., Private communication.
16. HEINRICH L. R., *Astrophys. J.* **99**, 59 (1943).
17. GOURARY B. S. and ADRIAN F. J., In *Solid State Physics* (Edited by F. Seitz and D. Turnbull), Vol. 10. Academic Press, New York 1960.

A QUASI-CHEMICAL TREATMENT OF INTERSTITIAL SOLID SOLUTIONS: IT APPLICATION TO CARBON AUSTENITE

REX B. McLELLAN and WILLIAM W. DUNN

Department of Mechanical and Aerospace Engineering and Materials Science, William Marsh Rice University, Houston, Texas 77001, U.S.A.

(Received 11 March 1969)

Abstract—A first order quasi-chemical treatment of binary interstitial solid solutions has been given. The enumeration of the nearest neighbor pairs is simplified by only considering those pairs whose number depends on the atomic configuration of the solution. Simple expressions have been derived for the partial Gibbs free energy and thermodynamic activity of an interstitial solute atom in terms of the pairwise interaction energy between two nearest neighbor solute atoms. It is shown that the equations yield the appropriate results in the limits when the binding energy between solute pairs becomes zero or infinite. Finally the equations are shown to be compatible with the known activity of carbon in austenite and a computer fitting technique has been used to derive the value of the solute-solute binding energy concomitant with the closest fit of the experimental data to the theoretical activity equation.

INTRODUCTION

WITH THE exception of many hydrogen-metal solid solutions, the majority of interstitial solid solutions for which thermodynamic data are available exhibit regular mixing statistics. Their configurational entropy is ideal. The notable exception is f.c.c. iron containing carbon (austenite). This solution shows large departures from Henrian behavior even at low solute concentrations and many models have been proposed to explain this departure.

Speiser and Spretnak[1] proposed a model in which the repulsive interaction between C-atoms in austenite is manifested by each C-atom excluding an integral number of nearest neighbor interstitial sites from occupancy by further C-atoms. This simple model is in reasonably good agreement with the thermodynamic data. The blocking model has been applied by Kaufman, Radcliffe and Cohen[2] to a study of the austenite-ferrite transformation, and McLellan, Garrard, Horowitz and Sprague[3] have considered the overlapping of sites excluded by more than one solute atom. Furthermore, the large increase in the diffusivity of C in austenite

with increasing C-concentration has been explained in terms of the site exclusion model [4].

However, despite the successes of the exclusion model, the concept of a C-atom nearest neighbor pair having an infinite repulsive interaction for certain orientations and essentially a zero potential energy for other equivalent orientations is not realistic. The exclusion model should be considered as involving an ensemble average non-integral number of excluded sites due to a finite repulsive interaction.

Darken and Smith[5] set up a model in which a C-atom located in its octahedral site has either one or no neighboring C-atoms and a C-atom does not interact with another solute atom located at a greater distance than the first shell of interstitial sites.

Recently Aaronson, Domian and Pound[6] (ADP) have compared the models discussed above as well as an equation derived by Fowler and Guggenheim[7] and by Lacher[8] which is based on a quasi-chemical treatment of surface adsorption. ADP show that all of these models are in reasonable agreement with

the data but they point out that the complex equation for the carbon activity deduced from the Lacher-Fowler-Guggenheim (LFG) treatment does not give the correct expression in the limit when the pairwise interaction energy $\omega\gamma$ between C-atoms becomes infinite. Furthermore, they showed that the LFG model fits the known activity data only if $\omega\gamma$ is strongly dependent on temperature.

In this paper a quasi-chemical treatment of interstitial solid solutions is given. An equation for the free energy of the solute is derived which yields the appropriate expressions in the limits when the pairwise interaction energy tends both to zero (ideal mixing) and infinity (complete blocking). The model is shown to be consistent with the activity data for carbon in austenite within certain limitations governed by the adequacy of the known data.

THEORETICAL MODEL

The calculation is based on the quasi-chemical or first order formalism given by Guggenheim[9] in which the total energy of the solution is given in terms of pairwise interaction energies between nearest neighbors.

The solid solution is represented schematically in Fig. 1; the squares represent the octahedral sites (E) in the f.c.c. solvent lattice and the black circles are solute atoms (u -atoms). The solvent (v) atoms are represented by the white circles. Since the number of v - v and u - v pairs remains constant for a given composition for all configurations, we can describe the thermodynamics of the solution

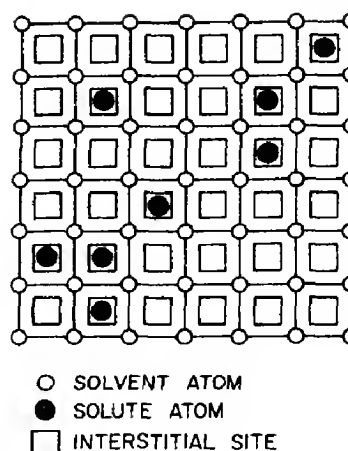


Fig. 1. Schematic representation of interstitial solution.

by just considering the lattice gas of u -atoms on the lattice of octahedral sites. The coordination number Z is the same for E -sites and solute atoms. The number of solute atoms is N_u , the number of solvent atoms is N_v , and the number of octahedral sites is then $N_v\beta$. In the f.c.c. lattice $\beta = 1$ for the octahedral sites and $\beta = 2$ for the tetrahedral sites. In this treatment we assume that the solute atoms occupy only the octahedral sites. Let the number of E - u (and u - E) nearest-neighbor pairs in some configuration be $Z\lambda$; the numbers of the other relevant pairs and their assigned energies given in Table 1 in terms of λ . (The energy zero is that of atoms at rest in a vacuum so that all the above energies are numerically negative.)

The configurational partition function for the lattice gas subassembly is

Table 1

Kind of pair	No. of such pairs	Energy per pair	Total energy
$E-E$	$\frac{1}{2}Z(N_v\beta - N_u - \lambda)$	0	0
$E-u$	$Z\lambda$	ϵ_u	$Z\lambda\epsilon_u$
$u-E$			
$u-u$	$\frac{1}{2}Z(N_u - \lambda)$	ϵ_{uu}	$\frac{1}{2}Z(N_u - \lambda)\epsilon_{uu}$
Total No. of all pairs	$\frac{1}{2}ZN_v\beta$		$Z\left[\lambda\epsilon_u + \frac{(N_u - \lambda)}{2}\epsilon_{uu}\right]$

$$\Omega_{\text{LGC}} = \sum_{\lambda} g(\lambda, N_u, N_v) \exp \left\{ -Z \left[\lambda \epsilon_u + \frac{(N_u - \lambda)}{2} \epsilon_{uu} \right] / kT \right\} \quad (1)$$

where $g(\lambda, N_u, N_v)$ is the number of distinguishable configurations. Assuming that the various pairs do not interact leads to a value of $g(\lambda, N_u, N_v)$ given by

$$\frac{\{\frac{1}{2}ZN_v\beta\}!}{\{\frac{1}{2}Z(N_v\beta - N_u - \lambda)\}! \{\frac{1}{2}Z(N_u - \lambda)\}! [\{\frac{1}{2}\lambda Z\}]^2}$$

where the squared term arises from the distinguishability of $u-E$ and $E-u$ pairs. Summing this expression over all λ does not give the correct total number of pairs. This problem can be eradicated, following Guggenheim[9], by inserting a normalizing factor $h(N_u, N_v)$ which can be determined from the restriction that the summation of $g(\lambda, N_u, N_v)$ over all λ must equal the total number of possible configurations of the atoms in the crystal.

$$\sum_{\lambda} \frac{h(N_u, N_v) \{\frac{1}{2}ZN_v\beta\}!}{\{\frac{1}{2}Z(N_v\beta - N_u - \lambda)\}! \{\frac{1}{2}Z(N_u - \lambda)\}! [\{\frac{1}{2}\lambda Z\}]^2} = \frac{\{N_v\beta\}!}{\{N_v\beta - N_u\}! N_u!}$$

The summation in the preceding expression can be replaced with sufficient accuracy by its largest term[9]. Differentiating this expression with respect to λ , we find that λ^* , the value of λ giving the largest term, is determined by

$$\lambda^* = N_u - \frac{N_u^2}{N_v\beta}$$

This is exactly the value λ would have in a completely random solution. Thus, $g(\lambda, N_u, N_v)$ is given by

$$g(\lambda, N_u, N_v) = \frac{\{N_v\beta\}!}{\{N_v\beta - N_u\}! N_u!} \cdot \frac{\{\frac{1}{2}Z(N_v\beta - N_u - \lambda^*)\}! \{\frac{1}{2}Z(N_u - \lambda^*)\}! [\{\frac{1}{2}Z\lambda^*\}]^2}{\{\frac{1}{2}Z(N_v\beta - N_u - \lambda)\}! \{\frac{1}{2}Z(N_u - \lambda)\}! [\{\frac{1}{2}Z\lambda\}]^2}$$

This value can then be placed in equation (1) for the partition function. Again we can re-

place the summation in equation (1) by its largest term (that for which $\lambda = \bar{\lambda}$). Differentiating with respect to λ shows that $\bar{\lambda}$ is determined by

$$\frac{(\bar{\lambda})^2}{(N_v\beta - N_u - \bar{\lambda})(N_u - \bar{\lambda})} = e^{-\Delta\epsilon/kT} \quad (2)$$

where $\Delta\epsilon = 2\epsilon_u - \epsilon_{uu}$, the binding energy of a $u-u$ nearest neighbor pair. This is the equation of quasi-chemical equilibrium.

Since we wish to assume that the interactions between the u -atoms are repulsive, $\Delta\epsilon$ must be numerically negative. Since the concentration of solute atoms $\theta = N_u/N_v$ is much less than unity, the discriminant of the quadratic equation (2) is positive and less than unity. The appropriate solution is

$$\bar{\lambda} = \frac{N_v\beta}{2\sigma} \left\{ 1 - \left[1 - 4\sigma \frac{\theta}{\beta} \left(1 - \frac{\theta}{\beta} \right) \right]^{1/2} \right\}$$

where

$$\sigma = 1 - e^{\Delta\epsilon/kT}.$$

Taking the limit when $\Delta\epsilon \rightarrow 0$ ($\sigma \rightarrow 0$), and using the expansion of $(1-x)^{1/2}$ for $x \ll 1$, it is easy to show that we get the random solution value for λ .

$$\lim_{\Delta\epsilon \rightarrow 0} \bar{\lambda} = \lambda^* = N_u - \frac{N_u^2}{N_v\beta}$$

If the repulsive interaction is infinite, $\sigma \rightarrow 1$, and it is easily shown that

$$\lim_{\Delta\epsilon \rightarrow -\infty} \bar{\lambda} = N_u.$$

This is the expected result since the number of $u-E$ and $E-u$ pairs should then be ZN_u .

The expression for the configurational partition function becomes

$$\Omega_{LGC} = \frac{\{N_v\beta\}!}{\{N_v\beta - N_u\}!N_u!} \frac{\{\frac{1}{2}Z(N_v\beta - N_u - \lambda^*)\}! \{\frac{1}{2}Z(N_u - \lambda^*)\}! [\{\frac{1}{2}Z\lambda^*\}]^2}{\{\frac{1}{2}Z(N_v\beta - N_u - \bar{\lambda})\}! \{\frac{1}{2}Z(N_u - \bar{\lambda})\}! [\{\frac{1}{2}Z\bar{\lambda}\}]^2} \times \exp \left\{ -Z \left(\bar{\lambda}\epsilon_u + \frac{(N_u - \bar{\lambda})\epsilon_{uu}}{2} \right) / kT \right\}. \quad (3)$$

Consequently, the configurational free energy and chemical potential are given by

$$F_{LGC} = -kT \ln \Omega_{LGC}$$

$$\mu_{LGC} = -kT \left\{ \frac{\partial \ln \Omega_{LGC}}{\partial N_u} \right\}_{N_v, T} \quad (4)$$

From equations (3) and (4) we get

$$\mu_{LGC} = -kT \ln \frac{\{\theta/\beta/(1-\theta/\beta)\}^{(Z-1)}}{\{(N_u - \bar{\lambda})/(N_v\beta - N_u - \bar{\lambda})\}^{Z/2}} + \frac{Z\epsilon_{uu}}{2}.$$

This can be re-written in the form

$$\mu_{LGC} = -kT \ln \left(\frac{\theta/\beta}{1-\theta/\beta} \right)^{(Z-1)} \left(\frac{1-\theta/\beta-\phi}{\theta/\beta-\phi} \right)^{Z/2} + Z\epsilon_u - \frac{Z\Delta\epsilon}{2} \quad (5)$$

where

$$\phi = \frac{1 - \{1 - 4(1 - e^{\Delta\epsilon/kT})\theta/\beta(1-\theta/\beta)\}^{1/2}}{2(1 - e^{\Delta\epsilon/kT})}.$$

Note that all the partial energy and configurational entropy terms are contained in equation (5). Assuming the partial excess entropy \bar{S}_u^v is constant and does not depend on composition, we have

$$\mu = \mu_{LGC} - T\bar{S}_u^v.$$

Inserting the term $-T\bar{S}_u^v$ in equation (5) and

$$\mu = Z\epsilon_u - T\bar{S}_u^v + kT \ln \frac{\theta/\beta}{1-\theta/\beta} - \frac{ZkT}{2} \ln \left(\frac{\theta/\beta}{1-\theta/\beta} \right)^2 \left(\frac{1-\theta/\beta-\phi}{\theta/\beta-\phi} \right) e^{\Delta\epsilon/kT}.$$

It is easy to show that as $\Delta\epsilon \rightarrow 0$, this formula gives the correct expression for μ^∞ , the chemical potential of an infinitely dilute interstitial solution

$$\mu^\infty = Z\epsilon_u - T\bar{S}_u^v + kT \ln \frac{\theta/\beta}{1-\theta/\beta}.$$

Thus we see that $Z\epsilon_u = \bar{E}_u$, the partial energy of the solute atoms in the infinitely dilute solution. Thus we can finally write

$$\mu = \bar{E}_u - T\bar{S}_u^v + kT \ln \frac{\theta/\beta}{1-\theta/\beta} - \frac{ZkT}{2} \ln \left(\frac{\theta/\beta}{1-\theta/\beta} \right)^2 \left(\frac{1-\theta/\beta-\phi}{\theta/\beta-\phi} \right) e^{\Delta\epsilon/kT}. \quad (6)$$

The deviation from Henrian behavior is all contained in the last term so that

$$\mu = \mu^\infty - \frac{ZkT}{2} \ln \left(\frac{\theta/\beta}{1-\theta/\beta} \right)^2 \left(\frac{1-\theta/\beta-\phi}{\theta/\beta-\phi} \right) e^{\Delta\epsilon/kT}.$$

Now if we put $\Delta\epsilon \rightarrow -\infty$, the limiting value of μ can be shown to be

$$\mu = \bar{E}_u - T\bar{S}_u^v + kT \ln \frac{\theta/\beta}{1-\theta(Z+1)/\beta}.$$

This is the correct expression for an interstitial solution in which all nearest neighbors of a

given solute atom are excluded from occupancy by other solute atoms [10].

Finally from the definition of the activity of the activity of the solute, α_u ,

$$\mu = E_u^0 - TS_u^0 + kT \ln \alpha_u$$

and equation (6), we can write

$$\alpha_u = \frac{\theta/\beta}{1-\theta/\beta} \cdot e^{\Delta\bar{G}_u/kT} \left\{ \left(\frac{\theta/\beta}{1-\theta/\beta} \right)^2 \left(\frac{1-\theta/\beta-\phi}{\theta/\beta-\phi} \right) \right\}^{-Z/2} e^{-Z\Delta\epsilon/2kT}. \quad (7)$$

In terms of the activity of the infinitely dilute solution α_u^∞ ,

$$\alpha_u = \alpha_u^\infty \cdot \left\{ \left(\frac{\theta/\beta}{1-\theta/\beta} \right)^2 \left(\frac{1-\theta/\beta-\phi}{\theta/\beta-\phi} \right) \right\}^{-Z/2} \times e^{-Z\Delta\epsilon/2kT}.$$

In these equations E_u^0 and S_u^0 are the energy and entropy per atom of the pure solute in its standard state and

$$\begin{aligned} \Delta\bar{G}_u &= \bar{E}_u - E_u^0 - T(\bar{S}_u^v - S_u^0) \\ &= \Delta\bar{E}_u - T\Delta\bar{S}_u^v \end{aligned}$$

where $\Delta\bar{E}_u$ and $\Delta\bar{S}_u^v$ are the relative partial energy and non-configurational entropy of a solute atom in solution with respect to the pure solute.

In the next section equation (7) is compared with the measured α -data for C in austenite and a computer fitting technique is used to find the best value of $\Delta\epsilon$ concomitant with the closest fit of the experimental data to equation (7).

COMPARISON WITH EXPERIMENTAL DATA

For carbon in austenite the most extensive activity data have been measured at 1000°C. The data of six authors [11-16] is given in Fig. 2 in the form of a plot of the C-activity α with respect to graphite against the atom ratio

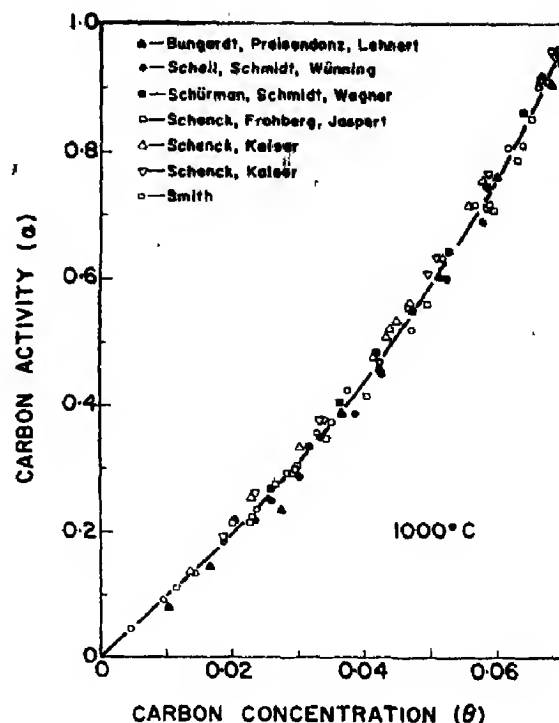


Fig. 2. Activity of carbon in austenite at 1000°C.

θ . It can be seen that the several sets of data are generally in good agreement and the data points are extensive in the region of low concentration where the departure from Henrian behavior is too small to be detected experimentally.

The activity data can be expressed in functional form,

$$\alpha = b_1\theta + b_2\theta^2 + b_3\theta^3 + \dots \quad (8)$$

Note that the constant term, b_0 , does not appear since $\theta = 0, \alpha = 0$ is a valid data point. A least squares computer program, using Cramer's Rule [17], was written to determine the coefficients at 1000°C. Comparison with the error sum of squares of higher order expressions showed that a third order expression, with coefficients given in Table 2 was suitable. Two data points were omitted due to their obvious inconsistency with the remaining 87.

Table 2. Coefficients for activity data at 1000°C

$b_1 = 9.1056$
$b_2 = 22.138$
$b_3 = 640.94$

The only unknown quantity appearing in equation (7) is $\Delta\epsilon$. The coordination number Z is 12, $\beta = 1$, and $\Delta\bar{G}_u$ was obtained from a least-squares fit of the activity data of Fig. 2 in the low concentration regular solution range (up to $\theta = 0.02$) using the coefficients of Table 2. There are nine data points in this range. The value of $\Delta\bar{G}_u$ found was 5626.0 cal/mole. Using this value of $\Delta\bar{G}_u$, the square of the difference between the α_u -values in the whole concentration range given by equation (8) and those given by equation (7) were determined for many different $\Delta\epsilon$ -values stepped in intervals of 10.0 cal. The best value of $\Delta\epsilon$ was determined from the distinct minimum in the error sum of squares. This value was found to be $\Delta\epsilon = -1.05$ kcal/mole. The degree of agreement between the experimental activity data (represented by equation (8) and equation (7) with $\Delta\epsilon = -1.05$ kcal is shown in Fig. 3. The solid line represents equation (8) and the points were taken from equation (7). The lower curve represents the activity of the Henrian solution having the same $\Delta\bar{G}_u$ as the austenite.

The activity of C in austenite has also been determined at 800°C by several authors [12, 13, 15, 16] and at 925° and 1050°C by Ellis, Davidson and Bodsworth [18]. All of these data show large departures from Henrian behavior. Those for 800°C are shown in Fig. 4. Unfortunately, the data fitting technique used for the 1000°C cannot be applied to these sets of data with much confidence since the corresponding $\Delta\bar{G}_u$ -values are not accurately determinable. At 800°C, excluding the two obviously inconsistent points, there are only four data points in the low concentration range. A similar situation pertains for the data of Ellis, Davidson, and Bodsworth

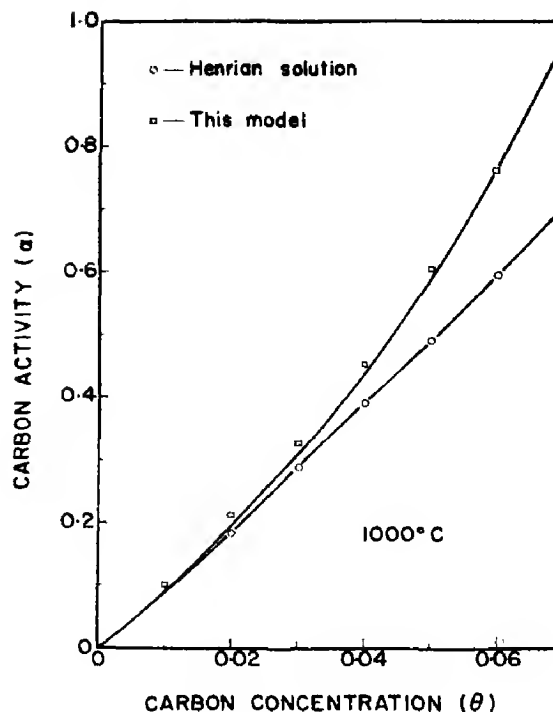


Fig. 3. Comparison of measured C-activity in austenite and that calculated from equation (7) with $\Delta\epsilon = -1.05$ kcal/mole. The continuous curve is the curve-fit representation of the data.

and in addition, there is a large degree of scatter in the data for 925°C. However, graphical means were used to estimate the slope of the α - θ plots for these sets of data in the low θ -range and the $\Delta\bar{G}_u$ -values thus estimated were used in the computer fitting program to estimate $\Delta\epsilon$ from the measured data and equation (7). Values of -1.4, -2.2, and -3.5 kcal were obtained for the 800°, 925° and 1050°C data respectively. However, little significance can be placed in these numbers since the values of $\Delta\bar{G}_u$ did not show a reasonable variation with temperature.

CONCLUSIONS

A first order model for interstitial solid solutions based on the quasi-chemical methodology of Guggenheim [9] has been set up. The resulting equation for the partial free energy of the solute atoms contains one unknown parameter $\Delta\epsilon$ the solute-solute pair

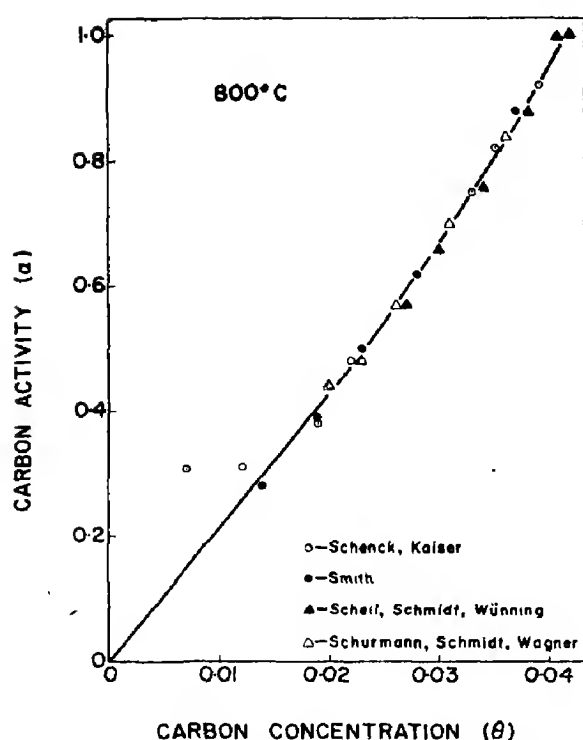


Fig. 4. Activity of carbon in austenite at 800°C.

binding energy. The relative partial free energy of the infinitely dilute solution, $\Delta\bar{G}_u$, can be regarded as an experimentally determined quantity. It is shown that in the two limiting cases where $\Delta\epsilon \rightarrow 0$, the model becomes equivalent to the case of regular mixing and in the limit where $\Delta\epsilon \rightarrow -\infty$, the model becomes equivalent to the well-known approximation where all the interstitial sites nearest neighbor to a given solute atom are excluded from occupancy by further solute atoms.

A data fitting technique has shown that this model is compatible with the known activity of carbon in austenite at 1000°C and the value of the C-C pair binding energy determined from this fit is -1.05 kcal/mole.

It must be remembered, however, that in reality the approximation made that the partial excess non-configurational entropy is constant may not be justified and there may be a small difference between the vibrational entropies of two isolated solute atoms and two nearest

neighbor solute atoms. Thus, $\Delta\epsilon$ should really be a free energy and may be temperature-dependent due to the $T\Delta S$ term. This may be a reason why activity data for carbon in austenite measured at various temperatures could not be fitted to the theoretical equation for α with a single constant value of $\Delta\epsilon$. However, at this time it is believed that only at 1000°C is the data really adequate to determine $\Delta\bar{G}_u$ with sufficient accuracy.

Acknowledgement—The authors are grateful for the support of the Robert A. Welch Foundation.

REFERENCES

1. SPEISER R. and SPRETNAK J. W., *Trans. Am. Inst. Min. Engrs* **47**, 493 (1955).
2. KAUFMAN L. S., RADCLIFFE S. V. and COHEN M., In *Decomposition of Austenite by Diffusion Controlled Processes* (Edited by V. F. Zackay and H. I. Aaronson), p. 313. Interscience, New York (1963).
3. McLELLAN R. B., GARRARD T. L., HOROWITZ S. J. and SRAGUE J. A., *Trans. Am. Inst. Min. Engrs* **239**, 528 (1967).
4. SILLER R. H. and McLELLAN R. B., *Trans. Am. Inst. Min. Engrs* (1969).
5. DARKEN L. and SMITH R. P., *J. Am. chem. Soc.* **68**, 1173 (1946).
6. AARONSON H. I., DOMIAN H. A. and POUND G. M., *Trans. Am. Inst. Min. Engrs* **236**, 753 (1966).
7. FOWLER R. H. and GUGGENHEIM E. A., In *Statistical Thermodynamics*, p. 442. Cambridge University Press, New York (1939).
8. LACHER J. R., *Proc. Camb. Phil. Soc.* **33**, 518 (1937).
9. GUGGENHEIM E. A., *Mixtures*. Oxford University Press, Oxford (1952).
10. McLELLAN R. B., In *Phase Stability in Metals and Alloys* (Edited by P. S. Rudman, J. Stringer and R. I. Jaffee), p. 393. McGraw-Hill, New York (1967).
11. SMITH R. P., *J. Am. chem. Soc.* **68**, 1163 (1946).
12. SCHENCK H., FROBERG M. G. and JASPERT E., *Arch. Eisenh.* **9**, 683 (1956).
13. SCHENCK H. and KAISER H., *Arch. Eisenh.* **31**, 227 (1960).
14. SCHEIL E., SCHMIDT T. and WÜNNING J., *Arch. Eisenh.* **13**, 251 (1961).
15. SCHÜRMANN E., SCHMIDT T. and WAGNER H., *Giesserei, techn.-wiss. Beih.* **16**, 91 (1964).
16. BUNGARDT K., PREISENDANZ H. and LEHNERT G., *Arch. Eisenh.* **35**, 999 (1964).
17. GRONE W. E., *Brief Numerical Methods*. Prentice-Hall, Englewood Cliffs, New Jersey (1966).
18. ELLIS T., DAVIDSON I. M. and BODSWORTH C., *J. Iron. Steel. Inst.* **2203**, 582 (1962).

2000

2000

2000

2000

2000

2000

2000

2000

2000

2000

2000

NOTES FOR CONTRIBUTORS

I. GENERAL

1. Submission of a paper to *The Journal of Physics and Chemistry of Solids* will be taken to imply that it represents original research not previously published (except in the form of an abstract or preliminary report), that it is not being considered for publication elsewhere, and that if accepted it will not be published elsewhere in the same form, in any language, without the consent of the Editor-in-Chief. It should deal with original research work in the field of the physics and chemistry of solids.

2. Papers should be submitted to the appropriate regional editor (all English-language papers to be sent to the U.S. editor).

3. Short communications may be published as "Technical Notes" and will receive somewhat more rapid handling than full length articles. Short communications requiring the maximum speed of publication should be submitted to one of the editors of "Solid State Communications."

II. SCRIPT REQUIREMENTS

1. **Papers** submitted should be concise and written in a readily understandable style. Scripts should be typed and double spaced with good margins on one side of the paper only and submitted in duplicate to facilitate refereeing.

It will be appreciated if authors clearly indicate any special characters used. An abstract not exceeding 200 words, should be provided in the language of the paper. French and German papers should be submitted with English abstract and titles, but if this is not possible the abstract will be translated by the publishers. To conserve space, **authors are requested to mark less important parts of the paper**, such as details of experimental technique, methods, mathematical derivations, etc. **for printing in small type**. The technical description of methods should be given in detail only when such methods are new. Authors will receive proofs for correction when their papers are first set, and **alterations must be restricted to printer's errors**. Other than these, any substantial changes may be charged to the authors.

2. **Illustrations** should not be included in the typescript of the paper, and legends should be typed on a separate sheet. Line drawings which require redrawing should include all relevant details and clear instructions for the draughtsman. If figures are already well drawn it may be possible to reproduce them direct from the originals, or from good photo-prints if these can be provided. It is not possible to reproduce from prints with weak lines. Illustrations for reproduction should normally be about twice the final size required. The lettering should be sufficiently large and bold to permit this reduction. Photographs should only be included where they are essential.

3. **Tables and figures** should be so constructed as to be intelligible without reference to the text. Every table and column should be provided with an explanatory heading. Units of measure must always be clearly indicated. The same data should not be published in both tables and figures. The following standard symbols should be used on line drawings since they are easily available to the printers: ○, ●, +, ×, □, ■, △, ▲, ◇, ◆, ▽, ▼.

4. **References** are indicated in the text by numbers on the line in brackets, and the full reference should be given in a list at the end of the paper in the following form:

1. BARNES R. G., BORSA F. and PETERSON D., *J. appl. Phys.* **36**, 940 (1965).
2. KNIGHT W. D., In *Solid State Physics* (Edited by F. Seitz and D. Turnbull), Vol. 2, p. 93. Academic Press, New York (1957).

Abbreviations of journal titles should follow those given in *World List of Scientific Periodicals* (4th Edn.). It is particularly requested that authors' initials, and appropriate volume and page numbers, should be given in every case.

Footnotes, as distinct from literature references should be indicated by the following symbols—*, †, ‡, §, commencing anew on each page; they should *not* be included in the numbered reference system.

5. Due to the international character of the journal no rigid rules concerning notation and spelling will be observed, but each paper should be consistent within itself as to symbols and units.

CONTENTS

H. U. RAHMAN: A linear interpolation of the electronic levels of f^2 -system in octahedral coordination	2497
D. L. FANCHER and G. R. BARSCH: Lattice theory of alkali halide solid solutions—I. Heat of formation	2503
D. L. FANCHER and G. R. BARSCH: Lattice theory of alkali halide solid solutions—II. Entropy of mixing and solid solubility	2517
G. J. EDWARDS, M. SPRINGFORD and Y. SAITO: The Fermi surface of AuSn	2527
K. C. RUSTAGI: Model band structures in nonlinear optics	2547
H. D. FAIR, JR. and A. C. FORSYTH: Optical and electrical properties of thin films of α -lead azide	2559
M. SCHOIJET: Theory of the kinetics of short range order	2571
P. C. CLAPP: Theoretical determination of n -site configuration probabilities from pair correlations in binary lattices	2589
G. VILLELA, Y. SAIKALI, A. LOUAT, J. PÂRIS et F. GAUME-MAHN: Le métatitanate de magnésium, nouvelle matrice pour l'étude de la fluorescence de l'ion Mn^{4+} . Préparation et propriétés de luminescence	2599
J. F. D'AMICO and H. B. HUNTINGTON: Electromigration and thermomigration in gamma-uranium	2607
H. L. ARORA, C. K. MAHUTTE and S. WANG: On shoulder bands of the U band	2623
R. B. McLELLAN and W. W. DUNN: A quasi-chemical treatment of interstitial solid solutions: its application to carbon austenite	2631


JOURNAL OF
PHYSICS
AND
CHEMISTRY
OF SOLIDS

AN
INTERNATIONAL
JOURNAL

PERGAMON PRESS



NEW YORK • OXFORD • LONDON • PARIS

VOLUME 30

NUMBER 1

DECEMBER 1969

Editor-in-Chief
HARVEY BROOKS
Cambridge, Mass.

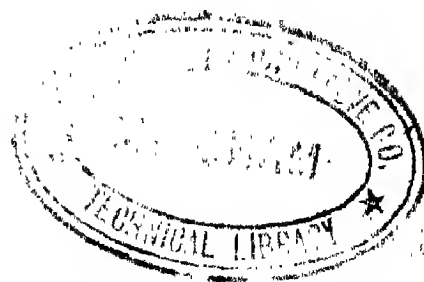
Associate Editors

H. B. G. CASIMIR
Eindhoven

B. CHALMERS FRAZER
and
DAVID E. COX
Brookhaven

JACQUES FRIEDEL
Paris

I. M. LIFSHITZ
Khar'kov



THE JOURNAL OF PHYSICS AND CHEMISTRY OF SOLIDS

Editors

PROF. HARVEY BROOKS (*Editor-in-Chief*), 217 Pierce Hall, Harvard University, Cambridge 38, Mass., U.S.A.

PROF. DR. H. B. G. CASIMIR, *N.V. Philips' Gloeilampenfabrieken, Eindhoven, The Netherlands*

DR. B. CHALMERS FRAZER and DR. DAVID E. COX (*Assistant Editor*), Brookhaven National Laboratory, Upton, Long Island, New York, U.S.A.

PROF. JACQUES FRIEDEL, *Laboratoire de Physique des Solides, Bâtiment 210, Faculté des Sciences, 91-Orsay, France*

PROF. I. M. LIFSHITZ, *Physico-Technical Institute, Academy of Science, Yumorskii tupik, Khar'kov, U.S.S.R.*

Editorial Advisory Board

U.S.A.

E. N. ADAMS, White Plains, N.Y.
D. ALPERT, Urbana, Ill.
L. APKER, Schenectady, N.Y.
J. BARDEEN, Urbana, Ill.
D. S. BILLINGTON, Oak Ridge, Tenn.
R. G. BRECKENRIDGE, Canoga Pk., Calif.
LEO BREWER, Berkeley, Calif.
E. BURSTEIN, Philadelphia, Penn.
J. A. BURTON, Murray Hill, N.J.
N. CABRERA, Charlottesville, Va.
G. C. DANIELSON, Ames, Iowa
G. J. DIENES, Long Island, N. Y.
J. C. FISHER, Schenectady, N.Y.
F. G. FUMI, Chicago, Ill.
H. K. HENISCH, University Park, Penn.
F. HERMAN, San Jose, Calif.
C. HERRING, Murray Hill, N.J.
A. R. VON HIPPEL, Cambridge, Mass.
J. H. HOLLOWOM, Washington, D.C.
W. V. HOUSTON, Houston, Texas
H. B. HUNTINGTON, Troy, N.Y.
H. M. JAMES, Lafayette, Ind.
C. KITTEL, Berkeley, Calif.
W. KOHN, La Jolla, Calif.
J. A. KRUMHANS, Ithaca, N.Y.
A. W. LAWSON, Riverside, Calif.
H. W. LEVERENZ, Princeton, N.J.
O. T. MARZKE, Pittsburgh, Penn.
B. T. MATTHIAS, La Jolla, Calif.
L. R. MAXWELL, Silver Spring, Md.
J. E. MAYER, La Jolla, Calif.
J. W. MITCHELL, Charlottesville, Va.
E. W. MONTROLL, Rochester, N.Y.
D. PINES, Urbana, Ill.

M. H. L. PRYCE, Los Angeles, Calif.
G. T. RADO, Washington, D.C.
H. REISS, Thousand Oaks, Calif.
J. R. REITZ, Dearborn, Mich.
A. ROSE, Princeton, N.J.
R. A. SMITH, Cambridge, Mass.
R. SMOLUCHOWSKI, Princeton, N.J.
F. H. SPEDDING, Ames, Iowa
D. TURNBULL, Cambridge, Mass.
J. H. VAN VLECK, Cambridge, Mass.
B. E. WARREN, Cambridge, Mass.
E. P. WIGNER, Princeton, N.J.
B. H. ZIMM, La Jolla, Calif.

B. DREYFUS, Grenoble
A. GUINIER, Orsay
A. HERPIN, Gif-sur-Yvette
B. JACROT, Grenoble
LOUIS NÉEL, Grenoble

Germany

ULRICH DEHLINGER, Stuttgart
R. HILSCH, Göttingen
G. LEIBFRIED, Aachen
E. MOLLWO, Erlangen
H. PICK, Stuttgart
W. WELKER, Erlangen

Israel

I. ESTERMANN, Haifa

Italy

F. G. FUMI, Palermo

Japan

TOSHINOSUKE MUTO, Tokyo

The Netherlands

A. MICHELS, Amsterdam
G. W. RATHENAU, Eindhoven

Sweden

J. O. LINDE, Stockholm
PER-OLOF LÖWDIN, Uppsala

Switzerland

G. BUSCH, Zurich
P. SCHERRER, Zurich

U.S.S.R.

G. S. ZHDANOV, Moscow

Canada

R. E. BURGESS, Vancouver
W. B. PEARSON, Ottawa

United Kingdom

M. BORN, Bad Pyrmont
A. CHARLESBY, Shrivenham, Berks.
W. J. DUNNING, Bristol
F. C. FRANK, Bristol
H. JONES, London
A. B. PIPPARD, Cambridge
O. C. SIMPSON, Baldock, Herts.
K. W. H. STEVENS, Nottingham
F. C. TOMPKINS, London

Czechoslovakia

J. TAUC, Praha

France

E. F. BERTAUT, Grenoble
J. BOK, Paris

Publishing Offices

American Continent: Pergamon Press Inc., Maxwell House, Fairview Park, Elmsford, N.Y. 10523.

Rest of the World: Pergamon Press Ltd., 84-86 Malahide Road, Coolock, Dublin 5.

Published monthly. Annual subscription for libraries, research establishments and all other multiple-reader institutions, £60 (\$150.00); private individuals, whose departmental libraries subscribe, may obtain this Journal for their personal use at a reduced price of £6 (\$15.00) per annum, including postage. All subscription enquiries are to be addressed to The Manager, Subscriptions Department, Pergamon Press, Headington Hill Hall, Oxford OX3 0BW, England. Back issues are available, write for Back Issues Price Lists.

Copyright © 1969 Pergamon Press Ltd.

PERGAMON PRESS INC.

MAXWELL HOUSE, FAIRVIEW PARK, ELMSFORD, N.Y. 10523
HEADINGTON HILL HALL, OXFORD OX3 0BW

new from pergamon



**International Tables
of Selected
Constants
Volume 16.
Metals: 1.
Thermal and
Mechanical Data**

252 pages £12 10s \$33.00

Edited by **Simonne Allard**

Constants reported in this Table have been selected on one hand for the precision of the measurements and on the other hand in respect to the purity of the metal.

Contents: Ch. I—Atomic Heat; Ch. II—Phase changes and vapor pressure; Ch. III—Elastic Constants; Ch. IV—Data for plasticity properties; Ch. V—Internal Friction; Ch. VI—Data for liquid metals close to the melting point.

**The Physics of
Selenium and
Tellurium**

404 pages £7 \$18.50

W. Cooper *Noranda Research Centre, Quebec*

The Proceedings of an International Symposium held in Montreal, Canada, under the sponsorship of the Selenium-Tellurium Development Association. This publication is particularly significant since it gathers together for the first time in one volume important advances which have been made in recent years in the Physics of selenium and tellurium, and can be considered as an up to date account of progress in this field.

Contents: Section 1—Band structure; Section 2—Crystal growth and characterization; Section 3—Optical properties; Section 4—Electrical properties.

**Introduction to
Superconductivity**

244 pages 70s \$9.50

A. C. Rose-Innes and E. H. Rhoderick
University of Manchester Institute of Science and Technology

A clear discussion of the basic phenomena and concepts of superconductivity, this book will be of value to graduate physics students who need a real *Introduction* to the subject.

Contents: Part 1. Type I Superconductors: Zero resistance; Perfect diamagnetism; Electrodynamics; The critical magnetic field; Thermodynamics of the transition; The intermediate state; Transport currents in superconductors; The superconducting properties of small specimens; The Microscopic theory of superconductivity; Tunnelling and the energy gap; Quantum Interference; Part 2. Type II Superconductors: The Mixed state; Critical currents of type II superconductors; Appendices.

**Progress in Materials
Science
Volume 14
Parts 2 & 3**

44 pages 18s \$2.25
flexi-cover

78 pages 25s \$3.25
flexi-cover

Edited by **Bruce Chalmers and W. Hume-Rothery (deceased)**

Contributions published in this series review specialised aspects of materials science which are of current interest.

Part 2

Contents: Introduction; Phase transformations in metals under pressure; Phase stability in binary systems; Alternative viewpoint of the stability of metallic phases; Summary; References.

Part 3

Contents: Part A: Electron Theory of Pure Metals; Part B: Fermi Surface and Physical Properties of Some Real Metals.

pergamon press



Pergamon Press Limited,
Headington Hill Hall,
Oxford, OX3 0BW

Maxwell House,
Fairview Park, Elmsford,
New York, 10523

Spectrochimica Acta

This international journal for the rapid communication of original work dealing with atomic and molecular spectroscopy is published in two parts.

PART A MOLECULAR SPECTROSCOPY

Editors Prof. Sir Harold Thompson St. John's College Oxford
Prof. M. Kent Wilson National Science Foundation Washington DC

This journal deals particularly with qualitative and quantitative analysis, the determination of molecular parameters and general theory. Also included are papers on nuclear magnetic resonance spectra, electron spin resonance spectra, optical rotary dispersion, and the design and performance of instruments and components.

Papers recently published include:

M. J. HITCH and S. D. ROSS The infra-red spectra of 1:3- and 1:4- dithian and pentamethylene sulphide

C. L. HONEYBOURNE and G. A. WEBB A spectroscopic study of some N:N' disubstituted 1:3 di-imines

ULF BLINDHEIM and THOR GRAMSTAD Studies of hydrogen bonding-XX.

Hydrogen bonding ability of phosphoryl compounds containing N-P and S-P bonds

R. T. BAILEY Infrared and laser Raman spectra of methyl-cyclopentadienyl nickel nitrosyl

Published Monthly

PART B ATOMIC SPECTROSCOPY

Editors Dr. M. Margoshes Division of Block Eng. Maryland U.S.A.
Dr. K. Laqua Institut für Spektrochemie Dortmund Germany

Presents research papers on all regions of the electromagnetic spectrum, in so far as they have direct physicochemical interest. The main subjects include the determination of fundamental atomic data, new experimental procedures, and measurements or calculations of the properties of radiation sources or detectors.

Papers recently published include:

H. JÄGER Temperaturmessungen an Mischplasmen im 30 Amp Gleichstrombogen

J. O. KARTTUNEN and W. R. HARMON Determination of uranium in ores and in solution using a portable non-dispersive X-ray spectrograph

A. CARNEVALE and A. J. LINCOLN A computer program to determine photographic emulsion calibration curves

E. E. PICKETT and S. R. KOIRTYOHANN The nitrous oxide-acetylene flame in emission analysis - III. Aluminum, gallium, indium, thallium, germanium, and tin

Write for full details and an inspection copy of either part of the journal.
Details of other journals in the field can also be sent to you.



Pergamon Press

OXFORD · NEW YORK · LONDON · PARIS · SYDNEY



HIGH TEMPERATURE TRANSPORT PROCESSES IN LITHIUM NIOBATE*

PAUL J. JORGENSEN

Stanford Research Institute, Menlo Park, Calif. 94025, U.S.A.

and

ROBERT W. BARTLETT

Stanford University, Palo Alto, Calif. 94305, U.S.A.

(Received 27 May 1969; in revised form 9 July 1969)

Abstract—The electrical conductivity of single crystal lithium niobate (LiNbO_3) was determined as a function of temperature for various oxygen partial pressures. The electrical conductivity is proportional to $P_{\text{O}_2}^{-1/4}$ which can be explained by a defect equilibrium involving singly ionized oxygen vacancies and electrons.

Measurements of electrical transport numbers at 1000°K show the electrical conductivity of LiNbO_3 to be ionic at one atmosphere of oxygen and electronic at low oxygen partial pressures.

Thermoelectric measurements indicate that LiNbO_3 at low oxygen partial pressures is *n*-type and that the concentration of electrons at 1000°K and in an atmosphere of 50% $\text{CO}/50\% \text{CO}_2$ is $4 \times 10^{17}/\text{cm}^3$ with a mobility of $1.7 \text{ cm}^2/\text{V sec}$.

The diffusion of oxygen in LiNbO_3 was determined as a function of temperature at an oxygen partial pressure of 70 Torr. by measuring $\text{O}^{18}/\text{O}^{16}$ isotope exchange with the gas phase as a function of time. The diffusion data may be represented by $D = 3.03 \times 10^{-8} \exp(-29.4 \text{ kcal mole}^{-1}/RT) \text{ cm}^2/\text{sec}$. Consideration of the Nernst-Einstein relation for oxygen and the variation in conductivity with Li_2O activity indicate that the ionic conduction is caused by transport of lithium ions.

1. INTRODUCTION

LITHIUM niobate (LiNbO_3), rhombohedral $R3c$, has important potential applications in laser modulation and laser frequency doubling because of its nonlinear optical coefficients [1–3]. The major obstacle to the use of LiNbO_3 crystals in laser applications is the generation of light scattering inhomogeneities during service. These inhomogeneities are referred to as radiation damage[4] and the extent of the damage increases with the intensity and duration of the light exposure. The nature of the damage mechanism is not well understood, but it may result from the formation of traps at oxygen vacancies. This investigation was designed to study the defect structure of LiNbO_3 by obtaining data on the electrical conductivity as a function of temperature and oxygen pressure, and by in-

vestigating thermoelectric power and oxygen diffusion as functions of temperature at selected oxygen partial pressures. The electronic and ionic transport numbers were also determined as a function of oxygen partial pressure at 1000°K. Bergmann[5] has recently measured the electrical conductivity of LiNbO_3 and found that the conductivity is proportional to $P_{\text{O}_2}^{-1/4}$ which indicates the formation of singly ionized oxygen vacancies.

2. EXPERIMENTAL

All measurements in this investigation were made on Czochralski grown single crystals (Supplied by Crystal Technology, Inc., Mountain View, Calif.) free of gaseous inclusions and prominent low-angle grain boundaries. The starting materials for crystal growth were 99.999% pure Li_2CO_3 and 99.999% pure Nb_2O_5 . Crystals were aligned by X-ray diffraction and cut in specific low-index orientations. Both poled and unpoled

*This work was supported by the Office of Naval Research.

crystals were used. In order to minimize any small random variations, the specimens used in this study were cut from a minimum number of large LiNbO_3 boules.

A. Electrical conductivity

A four-point probe method was used to measure electrical conductivity in rectangular bars, typically $3 \times 3 \times 15$ mm, with dimensions uniform within ± 0.01 mm. The two current leads were 0.020 in. platinum wires inserted in holes located within 1 mm of each end of the specimen. Each current lead was wrapped around the crystal at the end, and the two current leads suspended the crystal free of any other support. Two Pt-Pt, 10% Rh thermocouples (0.010 in. dia.) inserted in holes located 2.5 mm from each end served to measure both temperature and electrical potential. All holes in the specimens were drilled ultrasonically, which resulted in a slight taper. The thermocouple beads were tightly wedged into the tapered holes by pulling the lead wires through the smaller opening of the hole, which had been drilled through the crystal. The test crystal was mounted from the end of an alumina fixture inserted in a silicon carbide-heated tube furnace. A proportional temperature controller was used.

The electrical conductivity was determined by measurement of the potential drop between the two thermocouple/potential leads for known electrical currents passed through the crystal. The current was determined from the voltage drop measured across a $1000\ \Omega$ precision resistor connected in series with the crystal sample. A variable frequency a.c. generator was used as the current source to prevent possible electrochemical dissociation of the crystal, and the frequencies were kept low, approximately 50 Hz, to minimize capacitance contribution to the impedance.

Both the current measuring voltage and the voltage drop across the crystal were fed into the dual trace amplifier circuit of a 1 M Ω CRT Tektronix Type 561 oscilloscope. This provided a differential reading of the

potential drop across the crystal without any reference to ground or other potential sources. The dual voltage display in effect permitted determination of crystal resistance and allowed ready evaluation of capacitance contributions to the impedance. Corrections were made for the internal impedance of the oscilloscope at high crystal impedances and the oscilloscope was periodically calibrated against precision resistors to ensure accurate measurements. Electrical noise was minimized by using shielded cables outside the furnace and a grounded nickel sheath surrounding the furnace tube in which the crystal was located.

A dynamic gas atmosphere was used to control the oxygen partial pressure above the LiNbO_3 crystal. The oxygen partial pressure was varied from 1 atm to 10^{-27} atm by using oxygen, argon, and mixtures of CO and CO_2 or H_2 and H_2O . The CO/ CO_2 gases were purchased as pre-mixed gases while the $\text{H}_2/\text{H}_2\text{O}$ mixture was obtained by saturating H_2 with H_2O at a specified temperature. The oxygen pressure of these gases was checked at 800°C using an oxygen sensor containing a Pt; $\text{ZrO}_2(\text{CaO})$; Ni/NiO Pt cell. The attainment of equilibrium between the LiNbO_3 and the surrounding atmosphere was assured by heating the crystal in a given atmosphere for 24 hr at $1000^\circ\text{--}1100^\circ\text{C}$.

A series of measurements was then made at different temperatures. After each temperature change, sufficient time was allowed for equilibrium to occur before a conductivity reading was taken. Data taken after the temperature was raised were compared for convergence with data taken after the temperature was lowered to the measurement temperature.

B. Thermoelectric power measurements

Thermoelectric power data were obtained by placing the crystal in a temperature gradient of approximately $10^\circ\text{C}/\text{cm}$ and then measuring the potential and the temperature difference developed between the thermo-

couple/potential leads. The potential was determined by means of a Keithley 600 B high impedance electrometer.

Thermoelectric data were taken as a function of temperature between 700°C and 1150°C using a 50% CO/50% CO₂ atmosphere.

C. Oxygen diffusion

Measurements of oxygen diffusion rates in LiNbO₃ were made by monitoring the ratio of ³⁴O₂ to ³²O₂ as a function of time in a limited volume of well mixed gas surrounding the specimen.

Oxygen that analyzed 99.6 atom% ¹⁸O was purchased from the Bio-Rad Laboratories, Richmond, California and was diluted with normal oxygen to yield an ¹⁸O to ¹⁶O ratio of between 5 and 10 per cent. Samples of the gas phase were taken periodically during the diffusion experiments and analyzed with a Consolidated Electrodynamic Corporation mass spectrometer, Type 21-103C.

A plane sheet geometry was used for the LiNbO₃ single crystal samples. The solution of the one-dimensional nonsteady state diffusion equation for this type of system is [6]

$$\frac{M_t}{M_\infty} = 1 - \sum_{n=1}^{\infty} \frac{2\alpha(1+\alpha)}{1+\alpha+\alpha^2q_n^2} \exp\left(-\frac{Dq_n^2t}{l^2}\right) \quad (1)$$

where M_t is the total amount of diffusing ¹⁸O that enters the sheet in time t , and M_∞ is the quantity of ¹⁸O that enters in infinite time. α is the ratio of the total number of moles of oxygen in the gas phase to the number of moles of oxygen in the solid. D is the diffusion coefficient, $2l$ equals the thickness of the sheet, and the q_n 's are the nonzero positive roots of

$$\tan q_n = -\alpha q_n \quad (2)$$

M_t was calculated from the oxygen isotope ratios using the following equation:

$$M_t = M_g \left(\frac{r_0}{1+r_0} - \frac{r}{1+r} \right) \quad (3)$$

where M_g is the number of moles of oxygen in the gas phase and r_0 and r are the ratios of ¹⁸O to ¹⁶O at time zero and at time t , respectively. The ¹⁸O to ¹⁶O ratio, r , is related to the ³⁴O₂ to ³²O₂ ratio, R , by the relationship $r = R/2 + R$, and M_∞ is given by

$$M_\infty = M_g \left(\frac{r_0}{1+r_0} - 0.002 \right) \left(\frac{M_s}{M_s + M_g} \right) \quad (4)$$

where M_s is the number of moles of oxygen in the solid phase. Equation (4) includes a term to account for the 0.2% ¹⁸O content of the oxygen in the specimen. The diffusion coefficient can be calculated by comparing the experimentally observed M_t/M_∞ with curves of M_t/M_∞ vs. $(Dt/l^2)^{1/2}$ calculated from equation (1).

Lithium niobate sheets were cut from a single crystal boule so that the diffusion direction was along the c axis of the crystal. The sheets were then lapped to obtain parallel faces and polished using 1- μ diamond grit. Several sheets of constant thickness were used in each run, so that final fractional uptake of ¹⁸O was always greater than 50 per cent. Annealing of the LiNbO₃ in natural oxygen prior to the diffusion experiments did not alter the calculated oxygen diffusion coefficients within experimental error.

The experimental apparatus used for the diffusion anneals consisted of a fused silica heating chamber and a Pyrex glass vacuum system with a total working volume of 345.2 cm³. A pump was used to circulate the gas continuously during the experiment to ensure that isotopic concentration gradients did not occur in the gas phase. Preliminary isotope exchange experiments were conducted to determine the extent of oxygen exchange with the walls of the diffusion apparatus. A temperature of 1000°C was selected since this was the highest diffusion temperature used in this study. The amount of oxygen exchange which occurred for times in excess of those used in the diffusion runs was negligible compared to the amount of exchange when LiNbO₃ samples were placed in the system.

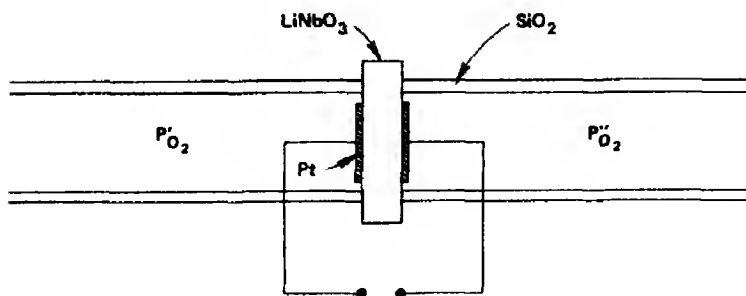


Fig. 1. A schematic representation of the O_2 Pt; $LiNbO_3$; Pt, O_2 cell used in the measurement of electrical transport numbers.

D. Transport numbers

An emf method of measuring the electrical transport number was used in this study. Wagner[7] has shown that the total ionic contribution to the electrical conductivity is given by the ratio of measured and thermodynamic voltages, i.e.

$$\frac{V}{V_0} = \tau_i \quad (5)$$

where

$$V_0 = \frac{RT}{nF} \ln \frac{P'_{O_2}}{P''_{O_2}} \quad (6)$$

and where V is the voltage measured across a crystal due to the difference in oxygen partial pressure, τ_i is the ionic transport number, P'_{O_2} and P''_{O_2} represent the oxygen partial pressures on opposite sides of the crystal. F is Faraday's constant, n is the number of equivalents involved in the ionic transport process, R is the gas constant and T is the absolute temperature. Figure 1 is a schematic representation of the apparatus used to measure the transport numbers in $LiNbO_3$. The output from the cell was monitored with a Hewlett-Packard digital voltmeter, Model Number 3430A.

3. RESULTS

The results of the electrical conductivity measurements are shown in Fig. 2 for $LiNbO_3$ in the as-grown condition. These data were obtained on $LiNbO_3$ bars cut perpendicular to the c direction of the equivalent hexagonal

lattice. Electrical conductivity data were also measured on $LiNbO_3$ crystals cut perpendicular to the a (prismatic) direction; however, the differences in conductivity between the two crystallographic directions were within experimental error.

Schmalzried[8] has pointed out that, in ternary ionic crystals, two independent variables in addition to pressure and temperature must be taken into account in order to unambiguously define the thermodynamic state of the system. For each datum point presented in Fig. 2 only three variables were fixed, i.e. pressure, temperature, and the chemical ac-

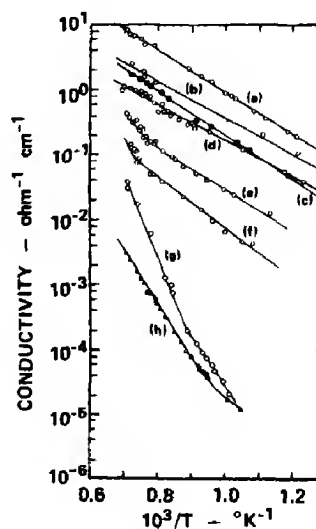


Fig. 2. Electrical conductivity of $LiNbO_3$ as a function of reciprocal temperature for various gaseous atmospheres (a, 99CO/1CO₂; b, 90CO/10CO₂; c, 4.28H₂/1H₂O; d, 50CO/50CO₂; e, 10CO/90CO₂; f, 1CO/99CO₂; g, argon, h, oxygen).

tivity of oxygen. In order to establish the chemical activity of another component in this system, we placed Li_2O in a platinum boat just beneath the LiNbO_3 crystal, and the level of the Li_2O was adjusted so that a distance of 3 mm existed between the Li_2O and the LiNbO_3 . The Li_2O extended upstream and the gas flow was reduced to a minimum in order to allow equilibration by vapour exchange between LiNbO_3 and Li_2O .

The addition of Li_2O to the system and equilibrating at temperatures between 1000° and 1300°K had no measurable effect on the conductivity at oxygen pressures less than 10^{-6} atm but produced large changes in the electrical conductivity values measured in oxygen at one atm as shown in Fig. 3. The upper curve shows the equilibrium electrical conductivity values obtained in the presence of Li_2O , and has an apparent activation energy of 43.7 kcal/mole. The lower group of parallel solid lines shown in Fig. 3 represent conductivity measurements without Li_2O being present. They illustrate the variation in electrical conductivity obtained by using LiNbO_3 samples cut from three different crystal boules, each having a slightly different lithium content. The sensitivity of electrical conductivity to Li_2O

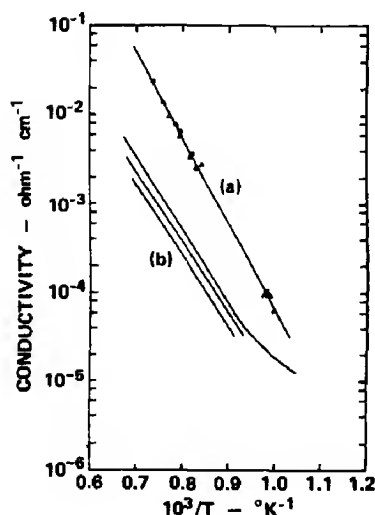


Fig. 3. Variation in the electrical conductivity of lithium niobate in 1 atm of Oxygen (a) equilibrated in Li_2O and (b) as grown crystals.

activity at oxygen pressures of 1 atm is consistent with a cationic conduction model that will be discussed later in the paper. The insensitivity of electrical conductivity to Li_2O activity at low oxygen pressures is caused by the dominance of electronic conduction arising from a defect equilibrium that is to a first approximation independent of the Li_2O activity.

The oxygen partial pressures below 10^{-6} atm resulting from CO/CO_2 mixtures and $\text{H}_2/\text{H}_2\text{O}$ mixtures depend on gas phase equilibria. Equilibrium constants for these equilibria were obtained from JANAF [5] tables, and the oxygen partial pressures were calibrated for various temperatures in order to obtain a plot of electrical conductivity vs. oxygen partial pressures, which is shown in Fig. 4. The electrical conductivity in LiNbO_3 depends on

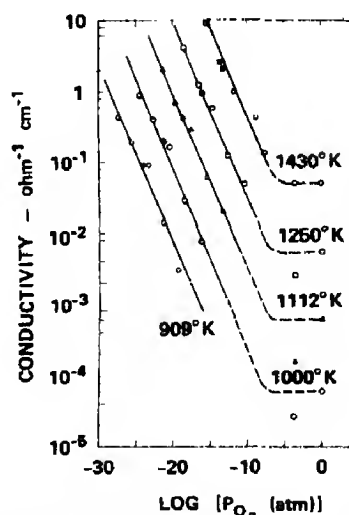
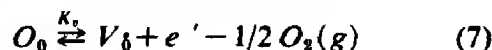


Fig. 4. Isothermal plot of the electrical conductivity of LiNbO_3 as a function of the partial pressure of oxygen.

$P_{\text{O}_2}^{-1/4}$ for oxygen pressures less than approximately 10^{-6} atm. This oxygen pressure dependence fits a defect model wherein singly ionized oxygen vacancies and free electrons are generated within the crystal lattice. Oxygen in the atmosphere is in equilibrium with these defects according to the following reaction, using Kroger-Vink notation:



and the equilibrium constant is $K_v = (V_b)nP_{O_2}^{1/2}$. The oxygen pressure dependence of the electrical conductivity is derived from the defect equilibria by assuming for reasons of electrical charge balance that the concentration of free electrons (n) is equal to the concentration of singly charged oxygen vacancies, (V_b). Hence,

$$n = K_v^{1/2} P_{O_2}^{-1/4} \quad (8)$$

and, since the electronic conductivity is proportional to the free electron concentration, it is also proportional to $P_{O_2}^{-1/4}$. The data represented by the solid lines in Fig. 4 were force-fitted to a $-1/4$ slope, while the dashed lines merely serve to connect these data to the data obtained in 1 atm of oxygen and equilibrated above Li_2O . The change in slope in Fig. 4 indicates a possible change in the mechanism of electrical conductivity. We therefore investigated the electrical transport numbers in order to justify the defect model given in equation (7) and the change in slope in Fig. 4. These data are presented in Table 1. The last data entry in Table 1 was taken before equilibrium had been completely established, thus resulting in a value that is considered to be high. However, these data indicate that $LiNbO_3$ at 1000°K and 1 atm of oxygen exhibits only ionic conduction; whereas lowering the oxygen pressure causes the conduction to become completely electronic.

As the oxygen pressure in equilibrium with $LiNbO_3$ increases, the vacancy and free

electron concentrations decrease according to the defect equilibrium of equation (7). At sufficiently high pressures ionic conduction becomes appreciable and eventually dominant. This causes the $\log \sigma$ vs. $\log P_{O_2}$ curves to deviate from a slope of $-1/4$ toward higher conductivity values than those predicted by the singly ionized oxygen vacancy model, and it is expected that the ionic conductivity should be independent of oxygen pressure.

Electronic conductivity is a function of the current carriers, n , and their mobility, μ , as expressed in the conductivity equation,

$$\sigma = ne\mu \quad (9)$$

We are therefore interested in determining the number of current carriers and have used thermoelectric power measurements to obtain the desired information. The results of the thermoelectric power measurements on $LiNbO_3$ are presented in Fig. 5. The values

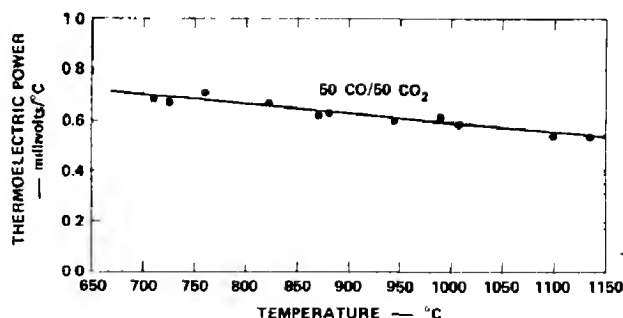


Fig. 5. Thermoelectric power of lithium niobate as a function of temperature.

Table 1. EMF Transport number measurements in $LiNbO_3$ at 1000°K

P'_{O_2}	P''_{O_2}	V (mV)	V_0 (mV)	τ_i
Air	Air	0.2	0.0	
Air	1 atm (oxygen)	-33.3	-33.7	0.99
Air	$10^{-3.6}$ (argon)	12.7	145	0.087
Air	$10^{-4.4}$ (CO/CO ₂)	0.0	785	0.0
Air	$10^{-20.5}$ (CO/CO ₂)	8.2	982	0.008
Air	$10^{-24.5}$ (CO/CO ₂)	27.2	1182	0.02

measured were always negative indicating conduction by electrons in support of the proposed electron donor defect model. The mobilities of these electrons and the numbers of current carriers were calculated for various temperatures using the following equation [9]:

$$Q = -\frac{k}{e} \left[2 - \ln n + \frac{3}{2} \ln T + \ln \left\{ \frac{2(2\pi m^* k)^{3/2}}{h^3} \right\} \right] \quad (10)$$

where Q is the thermoelectric power in mV/°C, k is Boltzmann's constant, n is the number of current carriers, m^* is the effective mass of the electrons, and h is Planck's constant. Assuming that the effective mass of an electron is equal to the mass of a free electron, we obtain a value for n at 1000°K of 4×10^{17} carriers/cm³ and a calculated conductivity mobility of 1.7 cm²/V sec.

The concentration of current carriers is exceedingly sensitive to the measurement of thermoelectric power, Q , and therefore the temperature dependence of the mobility calculated by means of equations (9) and (10) exhibits considerable experimental scatter. When mobilities were calculated using the Q values determined by the line drawn through the experimental points in Fig. 5, a temperature dependence of $T^{-3/2}$ fitted the data. This result indicates that lattice scattering determines the electron mobility [9, 10] within the temperature range studied and that the use of equation (10) to compute carrier concentrations from the thermoelectric power measurements was justified.

The conductivity includes both the temperature dependence of the electron mobility and a term for the enthalpy of formation, ΔH_v , of the singly ionized oxygen vacancies. Substituting equation (8) and the expression $\mu = k_0 T^{-3/2}$ into equation (9), we obtain

$$\sigma P_{O_2}^{1/4} = k_0 e T^{-3/2} \exp \left(-\frac{\Delta H_v}{2RT} + \frac{\Delta S_v}{2R} \right) \quad (11)$$

where ΔS_v is the entropy of formation of the singly ionized oxygen vacancies. Neglecting the pre-exponential temperature dependence of equation (11) over the rather limited temperature range investigated, we can obtain a value for ΔH_v by plotting the $\ln \sigma P_{O_2}^{1/4}$ vs. $1/T$. This plot is shown in Fig. 6 and the enthalpy of formation of singly charged oxygen vacancies, ΔH_v , is 97.7 kcal/mole. The slope of Fig. 6 yields an apparent activation energy of 48.8 kcal/mole, which compares favorably with the value of 49.5 kcal/mole obtained by Bergmann [1].

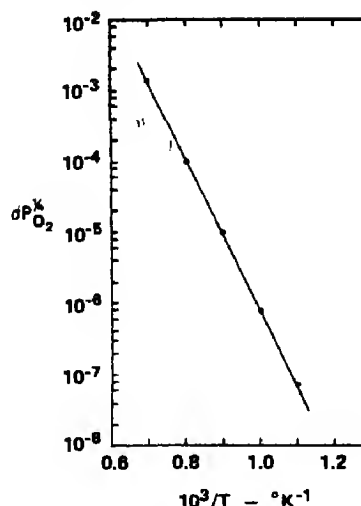


Fig. 6. Product of the electrical conductivity of LiNbO₃ and the $\frac{1}{4}$ power of the oxygen partial pressure vs. reciprocal temperature.

Oxygen diffusion data obtained by monitoring the depletion of ¹⁸O in a limited gas volume require the exchange process to be limited only by homogeneous diffusion, i.e. the rate of ¹⁶O to ¹⁸O exchange at the surface of the solid should not be rate-limiting. In order to test the validity of this assumption, values of $(Dt/l^2)^{1/2}$ were determined from the measurement of M_t/M_∞ as described above. The values of (Dt/l^2) should be proportional to time only for isothermal conditions and the data should pass through the origin of a plot of Dt/l^2 vs. time. These types of plots were determined for each diffusion run, and a typical plot is shown in Fig. 7, indicating that surface exchange is not rate-limiting. All of the data reported in this paper exhibited a linear relationship between Dt/l^2 and t .

The quasi-average penetration depths of ¹⁸O diffusing into the LiNbO₃ as determined by the expression $X_{avg} = \sqrt{4Dt}$ ranged between 17 and 100 μ for the various diffusion runs. These penetration depths are sufficient to further show that a very slow surface exchange limiting the rate of diffusion is not likely.

Data obtained during the diffusion experiment, which exhibited contamination due to

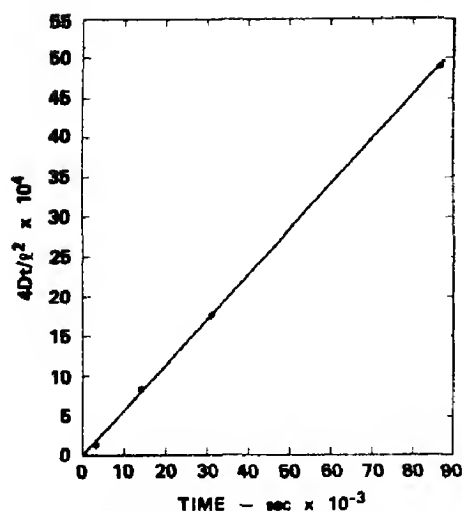


Fig. 7. $4Dt/l^2$ vs. time for LiNbO_3 at 850°C .

air leakage during the sampling procedures, were eliminated. Three diffusion runs during the study exhibited positive curvature on Dt/l^2 vs. t plots. These runs occurred at the high and low temperatures investigated and no apparent reason could be given for the deviations from linearity. Since these data were a minor part of all of the data collected and because these runs could not be reproduced, they were not included in the results.

The results of the diffusion runs are presented in Fig. 8, and the data is given to 95 per cent confidence limits by

$$D = 3.03 \times 10^{-6} + 7.09 \times 10^{-5} - 1.29 \times 10^{-7} \exp(-29.4 \pm 6.9 \text{ kcal mole}^{-1}/RT) \text{ cm}^2/\text{sec} \quad (12)$$

These oxygen diffusion data were obtained for diffusion parallel to the c axis in LiNbO_3 . Several runs were also made for diffusion in a direction parallel to an a axis. The values obtained were the same within experimental error as those obtained in the c direction.

4. DISCUSSION

The electrical conductivity of LiNbO_3 at 1 atm of oxygen according to the electrical

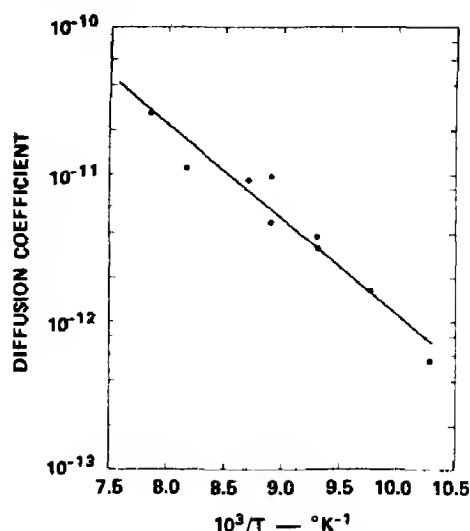


Fig. 8. Oxygen diffusion coefficients in LiNbO_3 as a function of reciprocal temperature.

transport measurements is completely ionic. The method used to measure the transport numbers allows us to determine the amount of electronic and ionic conductivity, but does not provide a differentiation between conduction by lithium ions, niobium ions, or oxygen ions. The possibility of oxygen ion transport was eliminated through the use of the Nernst-Einstein equation,

$$D_i = \frac{\tau_i \sigma RT}{e^2 n_i Z_i^2} \quad (13)$$

where D_i is the diffusion coefficient of the ion, n_i is the number of ions/cm³, and Z_i is the valence of the ion. By using the measured diffusion coefficient, equation (12), and assuming that the oxygen diffusion coefficient is independent of oxygen pressure between 70 Torr. and 760 Torr., we calculated a value for the oxygen transport number of 0.001 at 1000°K using the Nernst-Einstein equation. This calculation assumed that all oxygen ions in the LiNbO_3 were available for conduction, which would give the highest possible value to the result. Since the measured ionic transport number for these conditions is 1.0, we conclude that the conductivity at 1 atm of oxygen is cationic. From a consideration of

ionic size we would expect lithium ions to carry the current rather than niobium ions. This conclusion is substantiated by the increase in electrical conductivity with increased Li_2O activity.

At low oxygen pressures, the electrical conductivity of LiNbO_3 is electronic and the number of electrons is controlled by the defect reaction given in equation (7). Changes in the Li_2O activity in the system at low oxygen partial pressures result in changes in the electrical conductivity which are insignificant compared with the larger electronic conductivity.

Electrical conductivity measurements were made using $\text{H}_2/\text{H}_2\text{O}$ atm in addition to CO/CO_2 atm to provide information regarding the problem of actually achieving the oxygen partial pressure calculated from the CO/CO_2 equilibria. The electrical conductivities obtained in $\text{H}_2/\text{H}_2\text{O}$ atm shown in Fig. 4 are consistent with the values obtained in CO/CO_2 atm. It was therefore assumed that the oxygen partial pressures calculated from these gas equilibria are correct.

The extent of the effect of lithium deficiencies on oxygen diffusion has not been determined in this paper. The diffusion measurements were made on samples that were not equilibrated in Li_2O and this could exert a second-order influence on the oxygen ion diffusion coefficients depending on the manner in which electrical neutrality is maintained in LiNbO_3 . It is known from the investigation of Smith *et al.* [11] that a deficiency of lithium in LiNbO_3 is at least partially compensated by substituting hydrogen ions. The possibility remains that charge balance in LiNbO_3 due to the deficiency in lithium could also be partly maintained by oxygen vacancies, which would influence the oxygen diffusion rate.

5. CONCLUSIONS

The following conclusions regarding the transport properties of LiNbO_3 can be drawn from this study:

1. The differences in electrical conductivity

and oxygen diffusion for the *a* and *c* crystallographic directions in LiNbO_3 were within the experimental error of the techniques used for measuring these properties.

2. Both ionic and electronic conductivity are exhibited. The electrical conductivity is completely ionic, at 1 atm of oxygen and 1000°K, while for low oxygen partial pressures the electrical conductivity at 1000°K becomes completely electronic.
3. The electronic conductivity is proportional to $P_{\text{O}_2}^{-1/4}$; this is attributed to a defect equilibria involving singly charged oxygen vacancies and free electrons. The enthalpy of formation of these singly charged oxygen vacancies is 97.7 kcal/mole, and the electronic conductivity is given by the equation $\sigma_e = 3.83 \times 10^4 P_{\text{O}_2}^{-1/4} \exp(-48.8 \text{ kcal mole}^{-1}/RT)$.
4. Thermoelectric power measurements show that LiNbO_3 is *n*-type. The electron mobility exhibits a $T^{-3/2}$ temperature dependence indicating control by lattice scattering. The number of current carriers or electrons in LiNbO_3 at 1000°K and a 50% $\text{CO}/50\%$ CO_2 atm is equal to $4 \times 10^{17}/\text{cm}^3$ and the mobility calculated from thermoelectric power and electrical conductivity measurements is $1.7 \text{ cm}^2 \text{ V sec.}^{-1}$.
5. The electrical conductivity is dependent on the Li_2O activity in the system at 1 atm of oxygen (ionic conduction region), but is independent of the Li_2O activity for low oxygen partial pressures (electronic conduction region). The ionic conductivity is cationic and most probably due to transport by lithium ions. The ionic conductivity for a crystal equilibrated in Li_2O is given by the equation $\sigma_i = 2.27 \times 10^5 \exp(-43.7 \text{ kcal mole}^{-1}/RT)$.
6. The diffusion of oxygen in LiNbO_3 at an oxygen partial pressure of 70 Torr. is given by the equation $D = 3.03 \times 10^{-6} \exp(-29.4 \text{ kcal mole}^{-1}/RT)$. Surface exchange of oxygen on LiNbO_3 is sufficiently rapid that it does not have any apparent effect on the rate of oxygen diffusion in LiNbO_3 .

Acknowledgements—The authors wish to acknowledge the contributions of D. Clark, G. Craig, and F. Knemeyer for the experimental measurements. They are also indebted to A. Rosengreen and F. A. Halden for many helpful discussions.

REFERENCES

1. BOYD G. D., MILLER R. C., NAUSAU K., BOND W. L. and SAVAGE W. L., *Appl. Phys. Letters* **5**, 234 (1964).
2. MILLER R. C., BOYD G. D. and SAVAGE A., *Appl. Phys. Letters* **6**, 77 (1965).
3. GIORDMAINE J. A. and MILLER R. C., *Phys. Rev. Letters* **14**, 973 (1965).
4. ASHKIN A., BOYD C. D., DZIEDZIC J. M., SMITH R. G., BALLMAN A. A., LEVINSTEIN H. J. and NASSAU K., *Appl. Phys. Letters* **9**, 72 (1966).
5. BERGMANN B., *Solid State Commun.* **6**, 77 (1968).
6. CRANK J., In *The Mathematics of Diffusion*, p. 52. Oxford University Press, London (1956).
7. WAGNER C., *Z. Phys. Chem. Abt. B* **21**, 25 (1933).
8. SCHMALZRIED H., *Progress in Solid State Chemistry* (Edited by H. Reiss), Vol. 2, p. 265. Pergamon Press, Oxford (1965).
9. JOHNSON V. A., *Progress in Semiconductors*, Vol. 1, p. 68. Heywood, London (1956).
10. CUSACK N., *The Electrical and Magnetic Properties of Solids*, p. 216. Longmans, Green, London (1958).
11. SMITH R. G., FRASER D. B., DENTON R. T. and RICH T. C., *J. appl. Phys.* **39**, 4600 (1968).

PULSED NUCLEAR MAGNETIC RESONANCE OF GAMMA-IRRADIATED LITHIUM HYDRIDE*

P. C. SOUERS, T. S. BLAKE, R. M. PENPRAZE and C. CLINE

Lawrence Radiation Laboratory, University of California, Livermore, Calif. 94550, U.S.A.

(Received 29 January 1968; in revised form 9 June 1969)

Abstract—Some of the effects of ^{60}Co gamma irradiation on lithium hydride are described. Volume increase and nuclear magnetic resonance data are given for samples irradiated from 40 to 395°C. Maximum swelling occurs between 160 and 200°C; negligible swelling occurs above 300°C. Motionally narrowed proton and ^7Li nuclear magnetic resonance signals appear on irradiation and increase with increasing swelling. These decomposition products, which are trapped inside the LiH, can amount to more than one-tenth the total sample at doses of ~ 50 Grad. At this point, ~ 25 volume per cent swelling has occurred and the growth rate has subsided. The hydrogen nuclear magnetic resonance signal has been shown to come from H_2 molecules by observation of the ortho-para conversion on cooling. Hydrogen densities derived independently from the longitudinal relaxation time and the swelling data are in reasonable agreement. The corresponding gas pressures range from 750 to 5000 atm. The H_2 is thought to be in bubbles which cause the volume growth, and recent electron microscopy results support this view. The ^7Li signal has a Knight shift, and the lithium is present as metal particles. Above 200°C, the H_2 and Li back-react rapidly. Above 300°C this reaction takes place as fast as the decomposition, which was caused by the irradiation.

INTRODUCTION

PRETZEL [1,2] irradiated lithium hydride by putting $(^3\text{H})^-$ ions into the crystal lattice. His data indicated that at temperatures below 0°C, LiH expanded at a low rate. Above room temperature, the LiH expanded quickly to 20 volume per cent (defined as region I), and then grew another 15 per cent more slowly (defined as region II). The fastest swelling was seen for 125–200° samples. At 300°C, the swelling was much slower.

Pretzel also examined the irradiated LiH with broad line nuclear magnetic resonance (NMR) and saw motionally narrowed ^7Li and ^3H signals [2]. He suggested that these lines represented metal and gas, respectively. In a previous paper [3] we reported pulsed NMR measurements on samples containing ^3H stored between 23 and 250°C. The percent of motionally narrowed ^3H , as determined by NMR, increased with the

swelling. We suggested that the LiH decomposed under radiation and that formation of hydrogen gas caused the region I swelling.

2. THEORETICAL CONSIDERATIONS

Pulsed NMR can be used for quantitative analysis of nuclei. Such spin counts are obtained from the initial height of the free induction decay (FID) following a 90° pulse [4]. The FID is the Fourier transform of the steady-state line [5] and at time zero is the sum of the frequencies of all the resonating nuclei within the line. Spin counting, therefore, involves comparing the FID heights from the LiH with a standard at time zero. The count is independent of the nuclear relaxation times, provided that the interval between pulses is many times the longitudinal relaxation time (T_1) and that the 90° pulse length is much less than the transverse relaxation time (T_2).

In a gas in which the molecular collision frequency is much greater than the NMR frequency, dipole-dipole relaxation causes T_1 and T_2 to be almost equal [6]. Lipsicas

*The work was performed under the auspices of the U.S. Atomic Energy Commission.

and Bloom found that $T_2 \sim 0.8 T_1$ for gaseous hydrogen up to a density of 400 amagats* at 78°K[7] and decided that they were equal within experimental error[8]. Above 400 amagats, other mechanisms besides the dipole-dipole may come into play so that $T_2 < T_1$. For a gas of infinite extent, diffusion can affect a 90–180° measurement of T_2 . The Carr-Purcell sequence[4] will eliminate such effects, and the measured T_{2m} will equal the true T_2 . But an 'infinite' system means that the nucleus moves only a small distance compared to the container size during the diffusion measurement[9]. During this time (T_{2m}) a nucleus moves a distance $2(DT_{2m})^{1/2}$, where D is the diffusion constant. For hydrogen gas at 1000 atm, this distance is about 20 μ . In a small bubble, a molecule will bounce back and forth many thousand times during T_{2m} and will end up in almost the same magnetic field in which it started. Thus, the apparent diffusion constant (D') will be less than D . Such effects have been seen in experiments on methane[10]. If we use the equation (10)

$$D' = \frac{a^4}{10D(T_{2m})^2},$$

for a bubble size $a = 1000 \text{ \AA}$, D' is $10^{-14} \text{ cm}^2/\text{sec}$, a very small value. This D' is too small to cause diffusion effects and the 90–180° sequence will give T_{2m} . Wall relaxation may also be present in a gas of small volume[10], further lowering T_{2m} . Such relaxation could also affect T_1 and a different quantity will be measured, T_{1m} . The time constant of the FID (T_{2d}) will include all the above effects plus those due to any d.c. magnetic gradients that might be present at a bubble site. A measured T_{2d} must be less than the decay time caused by the magnet inhomogeneity.

3. EXPERIMENTAL

The LiH was synthesized from lithium

metal and hydrogen gas [11]. Spectroscopic analysis of the resulting blue-violet LiH showed 60–150 parts per million (ppm) by weight Na; 3–90 ppm Al, Ca and Cu; and a few ppm Fe. Oxygen, determined by (γ, n) activation[12] and Karl Fischer analysis[13], was 1000–5000 ppm. Carbon determined by (γ, n) activation analysis, was 250 ppm.

The LiH was irradiated at the Brookhaven National Laboratory in a cylindrical ^{60}Co source of 15 Mrad./hr intensity. Before irradiation, the LiH crystals were welded under a helium atmosphere into small cans. Five such cans were inserted into a cylinder wrapped with an electrical resistance tape heater. The temperature of the middle can was maintained by a proportional voltage controller. Use of nonuniform heater windings and variation in insulation allowed a range of temperatures to be reached for the other four cans. The temperature of each was continuously monitored. The gamma ray dose was measured with cobalt glass[14, 15] and ceric-cerous sulfate dosimeters[16]. The dosimeter doses were converted to LiH doses by using the ratio of absorption coefficients which were calculated from the elemental Compton absorption coefficients[17, 18].

After irradiation, the LiH swelling was measured. Micrometer measurements were usually not possible because the sample fragmented under irradiation. A Beckman 930 gas comparison pycnometer compared the volume displacement of the LiH against standard balls. The accuracy was $\pm 0.03 \text{ cm}^3$.

The NMR magnet had stability and homogeneity of one part in 10^5 . A homemade 15-MHz pulsed NMR spectrometer of conventional crossed-coil, phase-coherent design was used. The H_1 field was 5 G, and only motionally narrowed signals could be seen. For signal-to-noise improvement, a 1-MHz voltage-to-frequency converter followed by a 400-channel analyzer operated in the multi-scale mode was used. The maximum analyzer speed was 32 μsec per data point.

*One amagat of hydrogen equals 2.685×10^{19} molecules per cm^3 .

Spin-counting standards for hydrogen were naphthalene or various halogenated biphenyls dissolved in carbon disulfide or carbon tetrachloride. The standards for ^7Li were the acetate, benzoate, formate, sulfate, and tartrate salts dissolved in water with a pinch of cupric sulfate to speed up the relaxation process[6]. The standards were diluted to the same volume as the LiH: $2\text{--}15\text{ cm}^3$. Six to twelve runs with three standards were made on each LiH sample. Despite RC filtering on the FID's sharp edge and phase shift variations, the spin counts are thought to be accurate to ± 10 per cent for a sample containing 10^{21} protons or more. Most data were taken at room temperature, but some measurements were made at liquid nitrogen temperature.

All T_1 's were measured by the $180\text{--}90^\circ$ sequence. The short FID's of ^7Li were unaffected by magnet inhomogeneities and a 90° pulse sufficed to give T_{2m} . The hydrogen T_{2m} 's were measured with the $90\text{--}180^\circ$ spin echo sequence[4]. Although many of our nuclear decays appear to be true exponentials, many others showed a reproducible tail beyond one or two time constants. Our tails probably come from having a distribution of hydrogen relaxation times in these samples. To check for any errors due to our large sample volume, the relaxation times were run for protons in a $\text{H}_2\text{O}\text{--D}_2\text{O}$ solution doped with FeCl_3 to mask any diffusion effects. True exponential decays, with T_1 equal to T_2 , were obtained with even the largest sample volumes.

Diffusion effects were looked for, first using the steady-state[4] and then the pulsed-gradient techniques[19,20]. Since the diffusion-controlled decay increases as the $(\text{time})^3$, echoes out to $2T_{2m}$ were observed. Steady-state gradients could be determined by observing the Bessel function FID[4]. For the pulsed gradient, diffusion effects were observed in water with a known diffusion constant of $2.5 \times 10^{-5}\text{ cm}^2/\text{sec}$ [4]. Pulsed gradients of 100 G/cm were achieved.

4. RESULTS AND DISCUSSION

The spin count results for ^{60}Co -irradiated LiH are shown in Figs. 1–3. All three graphs are plotted as a function of the irradiation temperature. Figure 1 shows the percent

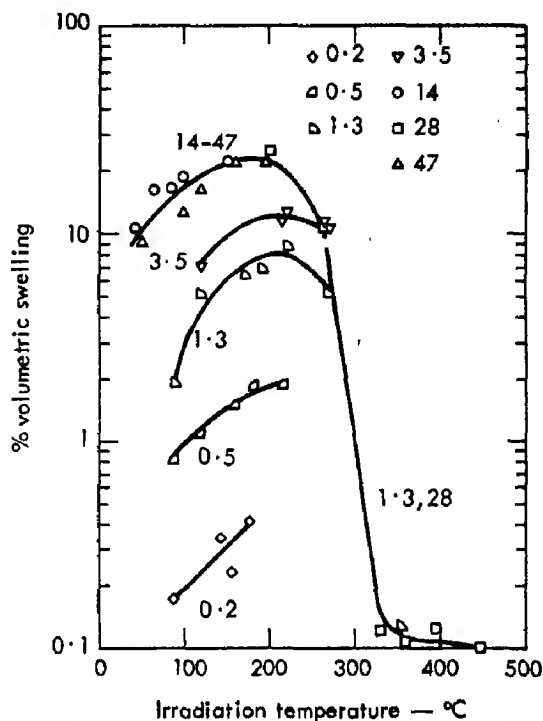


Fig. 1. Percent volumetric swelling of irradiated LiH as a function of irradiation temperature. Numbers are doses in Grad. The lowest temperature point in each set is 25 per cent lower in dose than the value given.

of volumetric swelling; Fig. 2, the atomic percent of the total number of hydrogen nuclei as counted by NMR in the motionally narrowed state; and Fig. 3, the same for ^7Li . The symbols in Fig. 3 with downward arrows represent lower limits of sensitivity for which no signals were seen. The uncertainty of the data is caused by the ± 10 per cent spin count error, a ± 4 per cent temperature variation during irradiation, and the room temperature annealing that took place before the measurements could be taken. Measurements taken several months later show evidence of this annealing. Several samples showed 10–20 per cent less hydrogen and two showed more lithium. We take this

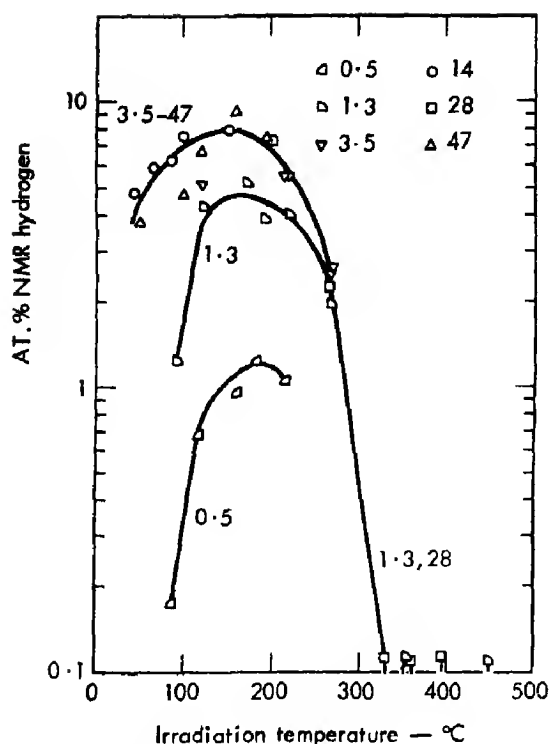


Fig. 2. Atomic percent of motionally narrowed hydrogen counted by *NMR* as a function of irradiation temperature. Numbers are doses in Grad.

to indicate partial recombination and precipitation of the metal. It is concluded from Figs. 1–3 that the swelling is proportional to the amounts of motionally narrowed H and ^7Li present. A second important point is that in three graphs the maxima is between 160 and 200°C, and zero appears to be approached at about 300°C. Above 260°C, the hydrogen and lithium presumably back-react faster than they can form during irradiation.

The Knight shift of the motionally narrowed ^7Li is a good demonstration that metallic lithium is present [21, 22]. For ^7Li in normal metal, the Knight shift is 2.61×10^{-4} with respect to aqueous LiNO_3 solution [23]. We checked nine samples to ± 10 per cent, showing shifts in the proper direction of 2.69 – 2.85×10^{-4} . It has been reported that LiF neutron-irradiated at 77°K has a motionally narrowed lithium signal without a Knight

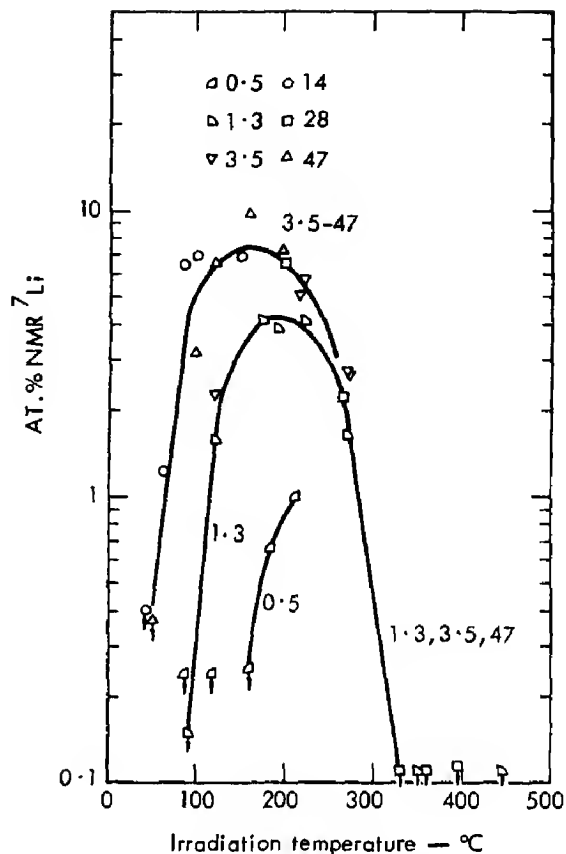


Fig. 3. Atomic percent of motionally narrowed ^7Li counted by *NMR* as a function of irradiation temperature. Numbers are doses in Grad.

shift [24]. This signal (observed at room temperature) was attributed to metal platelets containing only a few hundred atoms. We have seen no such species in our work.

The motionally narrowed proton signals are from molecular hydrogen. Only ortho-hydrogen with parallel nuclear spins gives an *NMR* signal; para-hydrogen does not, because the opposite fields of the nuclei cancel each other. The percent of ortho-hydrogen is 74.93 at 300°K [25], and the hydrogen spin counts of Fig. 2 must be multiplied by 1.34 to give true values for the amount of H_2 present. The percent of ortho-hydrogen is 50.2 at 77.3°K [25, 26]. The ortho-para conversion is slow compared to the time needed to cool the sample to liquid nitrogen temperature. At 77°K, one-

third of the *NMR* signal will gradually disappear as ortho-para conversion proceeds. Figure 4 shows the decay of the *FID* from a relative height of 1.00 down to 0.67 for several samples. The ortho-para transition is known to be second order for solid and liquid hydrogen. The rate constant for solid hydrogen at 1 atm and 4°K is $3\text{--}6 \times 10^{-6} (\%/min)^{-1}$ [27,28]; in the liquid state, the transition is known to be faster [27]. Increasing density speeds up the transition [29], since the nuclear magnetic forces are more effective at closer range. The transition can be catalyzed by a variety of agents including diamagnetic liquids, paramagnetic

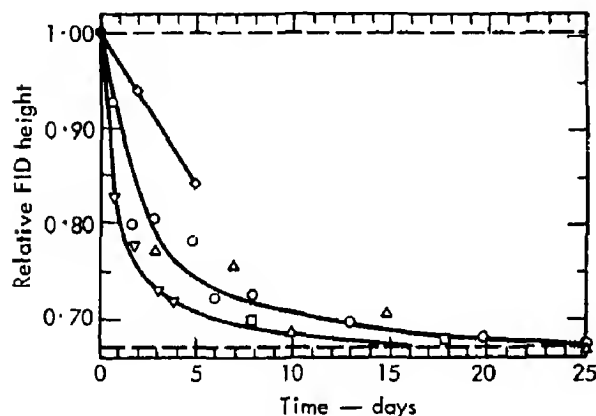


Fig. 4. The approach to hydrogen ortho-para equilibrium at 77°K. Data points = five samples: Relative *FID* height is plotted as a function of time. Dashed lines: upper = start of decay; lower = limit of decay.

gases and salts, metals, and electric discharges. Paramagnetic salts, which probably have effects closest to those of color centers in LiH, can convert ortho-hydrogen to the para form in minutes; this conversion often is a first-order reaction [30]. The data of Fig. 4 are too scattered to show unequivocally whether our reaction rate is second-order; however, we have estimated a second-order rate constant from these data. Our rate constants vary between 1.1 and $12 \times 10^{-6} (\%/min)^{-1}$. The corresponding hydrogen densities (which will be derived below)

in the samples showing these rates are 320–1100 amagats, respectively. Rates for solid hydrogen at 4°K under pressure range from 6 to $27 \times 10^{-6} (\%/min)^{-1}$ for densities of 1000–1800 amagats respectively [29].

The resonance transition of solid hydrogen is still motionally narrowed several degrees below the melting point [31]. Both the motional narrowing temperature [32] and the melting point [33] increase with pressure. Extrapolation of melting point and motional narrowing will possibly show intersection at 77°K and 5000 atm – if indeed they intersect at all. Since solid hydrogen can be motionally narrowed, we must use the pressures to be derived below to decide on the state of the hydrogen. Our results suggest pressures too low for a solid, yet far enough above the critical pressure of 12.8 atm [34] that a liquid must be absent. We probably have a dense gas.

The hydrogen relaxation times as a function of irradiation temperature are shown in Fig. 5. The T_{2m} 's are real since we observed no diffusion effects in any of eight samples. With T_{2m} 's of 8–57 msec, $D' < 1.4 \times 10^{-5} \text{ cm}^2/\text{sec}$. Our T_{2m} 's equal T_1 only in the three samples irradiated at 265°C.

The T_1 for normal hydrogen gas is found to be a function of density only [7] and not of pressure, as might be expected from gas kinetic theory. T_1 rises linearly with density to about 600 amagats, whereupon it begins to rise more quickly. The T_1 increases only 5 per cent in cooling from room temperature to 77°K, at a fixed density. We have used T_1 here as a density calibration scale. We also assume our T_1 's to be independent of *NMR* frequency. We then use the 77.5°K T_1 -density curve at 30 MHz of Lipsicas and Hartland [35], which we have extrapolated from their top point of 880 amagats. Most of our data were taken at room temperature; for comparison, therefore, we ran an assortment of samples at 77°K. Each sample irradiated at 3.5 Grad. and above showed no change in T_1 (within a few percent) upon

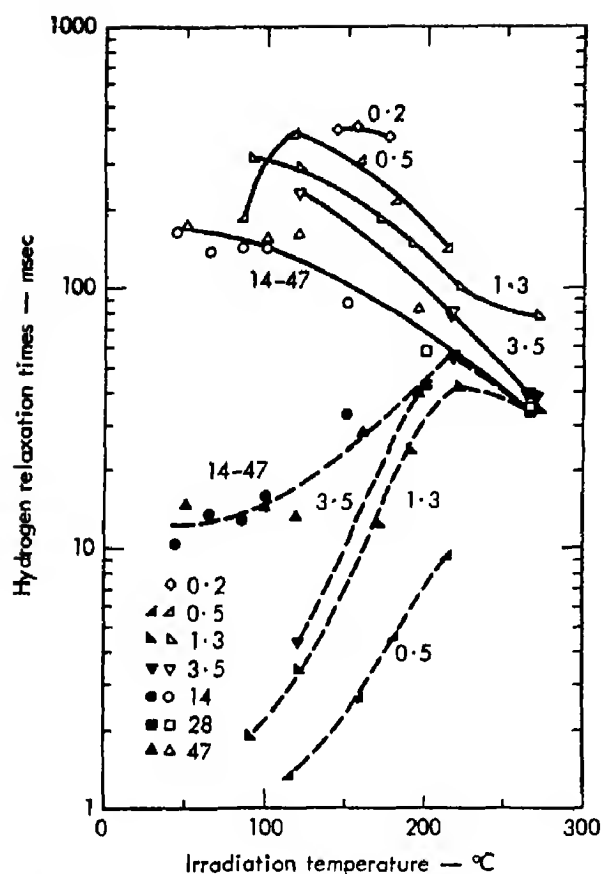


Fig. 5. Nuclear relaxation times, T_1 and T_{2m} , for motionally narrowed hydrogen as a function of irradiation temperature. Numbers are doses in Grad. Open symbols = T_1 ; closed symbols = T_{2m} .

cooling from room temperature to 77°K. Low-temperature samples irradiated at or below 1.3 Grad. showed room-temperature T_1 's of 300–400 msec compared to T_1 's at 77°K of 135–205 msec. The lowest temperature sample of the 0.5 Grad. series gave the respective values of 185 and 75 msec for room-temperature and nitrogen 77°K. It is evident that T_1 (now T_{1m}) either becomes a function of density at very high densities or it is modified by wall effects in very small bubbles. The latter is evidently the case in the 0.35 Grad. sample where the T_1 's are fairly low. We had to decide which T_{1m} , if either, more accurately measures the density of bubbles in low-dose LiH. We have selected the T_{1m} at 77°K as the

'true' value for two reasons: (1) Lipsicas and Hartland[35] show the T_1 -density curve at 87.5°K starting to rise faster above 700 amagats than the 77°K curve; (2) the densities derived from the T_1 obtained at 77°K agree better with the values obtained from swelling, as described below. For example, the 0.35 Grad. sample would have a density of 970 amagats from the room-temperature T_1 and 580 from the T_1 at 77°K. The density is 320 amagats as calculated from the swelling. Densities derived from T_1 data are shown as the open symbols in Fig. 6 as a function of irradiation temperature. They decrease with increasing temperature.

One way to check the T_1 -derived densities is to use the measured amounts of hydrogen and lithium and the swelling volume. We first

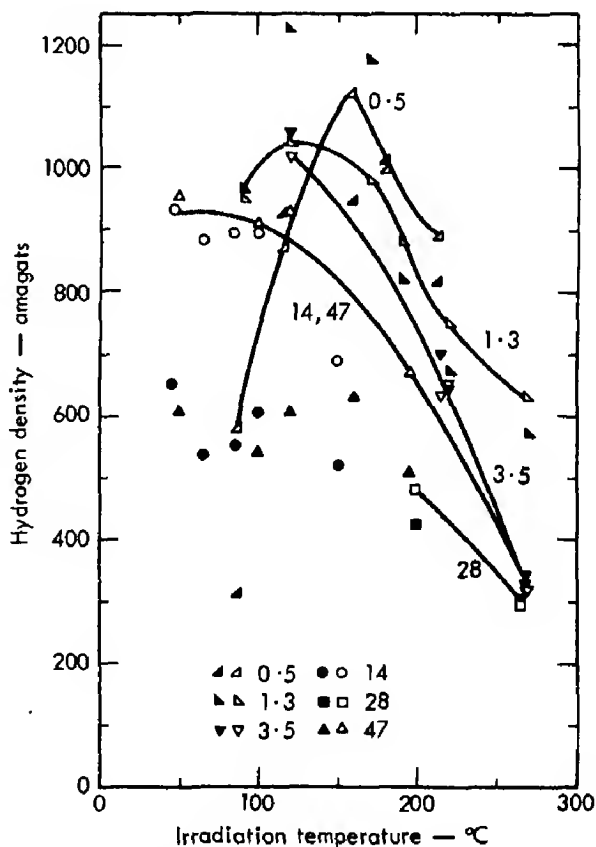


Fig. 6. Hydrogen density as a function of irradiation temperature. Curves are drawn through T_1 derived densities. Numbers are doses in Grad. Open symbols = T_1 derived densities; closed symbols = swelling derived densities.

have to make assumptions about what has caused the volume change in the LiH. In Figs. 2 and 3 it is shown that the lithium metal precipitates more slowly than the hydrogen is produced. At most, the measured amounts of H_2 and 7Li are the same. If we multiply the percent of hydrogen by the ortho-para factor of 1.34, we find an average lithium-to-hydrogen ratio of 0.76 for the ten samples with the highest Li/ H_2 ratio—not a ratio of one as expected from stoichiometry. However, since 1 cm^3 of LiH can produce 1.27 cm^3 of lithium metal, only 78 per cent of the precipitated metal can fit within the original volume of LiH. Therefore, lithium cannot contribute to the volume expansion unless the excess lithium precipitates. We have observed this precipitation in one sample, which grew another 0.8 per cent after a year's storage. In general, we will assume that the lithium causes no swelling and that the hydrogen must be the cause. The swelling derived hydrogen densities are plotted as the closed symbols in Fig. 6. Comparing the independently derived densities, we find agreement on all low-dose and high-temperature runs, confirming the T_1 -density procedure. There is disagreement, however, for the high-dose samples irradiated at temperatures below 200°C in which the swelling-derived densities are lower than those derived from T_1 . The latter are the true densities, and thus in these samples, the hydrogen occupies less than the swelling volume. These are region II samples and some of the hydrogen may have back-reacted and left voids behind. Some of this hydrogen loss may be caused by room-temperature annealing that started after the samples were removed from the ^{60}Co source. The hydrogen gas pressures [36, 37] corresponding to the above densities range from 750 to 5000 atm at the temperatures of irradiation.

Recent electron micrographs of the 1.3 Grad. series show square voids [38], which are probably hydrogen bubbles. These voids

are larger for higher irradiation temperatures and cover an average size range of roughly $100\text{--}1500\text{ \AA}$.

The T_{20} results for 7Li in LiH are shown in Fig. 7 where they are seen to rise with increasing irradiation temperature. T_{20} is probably a qualitative measure of the particle size. The size increases until d.c. gradients and wall relaxation affect only a few surface nuclei. Our longest T_{20} is identical with the T_{20} that we measured for chunks of the bulk metal. Wall relaxation has indeed been

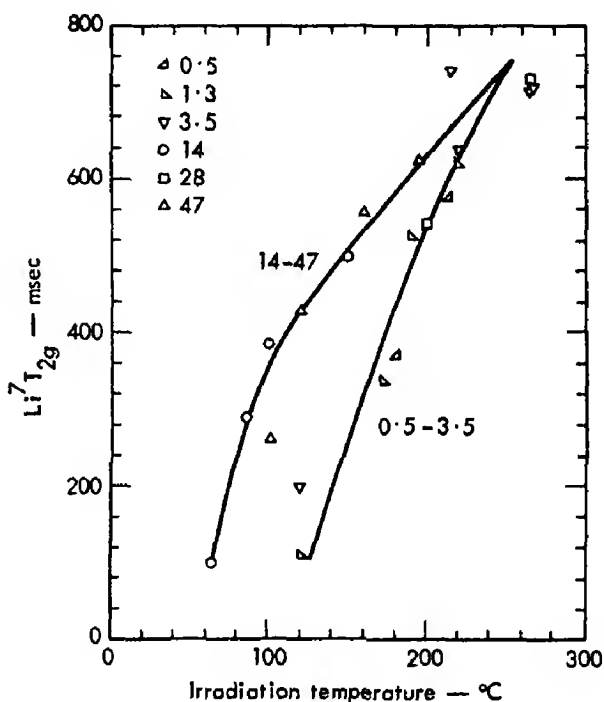


Fig. 7. Nuclear relaxation time, T_{20} , for motionally narrowed 7Li as a function of irradiation temperature. Numbers are doses in Grad.

seen in micron-sized 7Li and ^{23}Na particles at room temperature [39]. We observed no phase shifting due to skin effects [40, 41], but lithium globules would have to have a $40\text{-}\mu$ dia. before this would happen. We also ran 7Li T_1 's on eight samples. The T_1 's were 107–142 msecs, the same as those for bulk lithium [42] and with no apparent dependence on sample history.

5. CONCLUSIONS

LiH decomposes on irradiation and the products are trapped internally. The quantity of product hydrogen correlates closely with the region I swelling. Precipitation of lithium lags the production of hydrogen but hastens with increasing dose and temperature. The lithium-to-hydrogen ratio, which almost never exceeds 0.78, suggests that the lithium causes little or no swelling. This leaves hydrogen bubbles as being responsible for volume increases. Indirect evidence for this conclusion is furnished by the two independent derivations of density and the slow ortho-para conversion rates.

Acknowledgements—The authors wish to thank C. Griffith for synthesizing much of the LiH, J. Frazer and K. Marsh for analyses, D. Okerson for taking some of the spin counts, and D. Cassidy of the Brookhaven National Laboratory for his help in the irradiations.

REFERENCES

1. PRETZEL F. E., LEWIS W. B., SZKLARZ E. G. and VIER D. T., *J. appl. Phys. Suppl.* **33**, 510 (1962).
2. PRETZEL F. E., VIER T. D., SZKLARZ E. G. and LEWIS W. B., Radiation effects on lithium hydride. *Los Alamos Lab. Rep.* No. LA-2463 (1961).
3. SOUERS P. C., JOLLY T. A. and CLINE C. F., *J. Phys. Chem. Solids* **28**, 1717 (1967).
4. The best introduction to the types of pulses used in pulsed NMR is CARR H. Y. and PURCELL E. M., *Phys. Rev.* **94**, 630 (1954).
5. LOWE I. J. and NORBERG R. E., *Phys. Rev.* **107**, 46 (1957).
6. BLOEMBERGEN N., PURCELL E. M. and POUND R. V., *Phys. Rev.* **73**, 679 (1948).
7. LIPSICAS M. and BLOOM M., *Can. J. Phys.* **39**, 881 (1961).
8. LIPSICAS M., private communication (1967).
9. WOESSNER D. E., *J. phys. Chem.* **67**, 1365 (1963).
10. WAYNE R. C. and COTTS R. M., *Phys. Chem. Solids Rev.* **151**, 264 (1966).
11. PRETZEL F. E. *et al.*, *J. Phys. Chem. Solids* **16**, 10 (1960). Our lithium was high purity, reactor grade from Foote Mineral Co., Lot No. 6404-080. The hydrogen was ultrapure 99.999 per cent from Matheson Gas Products.
12. ENGELMANN C., Dosage de l'oxygene, du carbone, de l'azote, et quelques autres impuretes dans le beryllium, le calcium, le sodium, et le bore par activation aux rayons γ , radiochem. methods of analysis. *Proc. Symp., Salzburg, Austria*, Vol. 1, pp. 341-359 (1964).
13. MICHELL J., Jr. and SMITH D. M., *Aquametry*, p. 247. Interscience, New York (1948).
14. Bausch and Lomb Catalog No. 33-99-5721.
15. BLAIR G. E., *J. Am. Ceram. Soc.* **43**, 426 (1960).
16. HARMER D. E., *Nucleonics* **17**, 72 (1959).
17. GRODSTEIN G. W., *X-ray Attenuation Coefficients from 10 keV to 100 MeV*. U.S. Government Printing Office, Washington, D.C. (1957).
18. BERGER R. T., *Radiat. Res.* **15**, 1 (1961).
19. STEJSKAL E. O. and TANNER J. E., *J. chem. Phys.* **42**, 288 (1965).
20. TANNER J. E., *Rev. scient. Instrum.* **36**, 1086 (1965).
21. KNIGHT W. D., *Phys. Rev.* **76**, 1259 (1949).
22. KNIGHT W. D., *Solid State Physics* (Edited by F. Seitz and D. Turnbull), Vol. 2, p. 93. Academic Press, New York (1956).
23. GUTOWSKY H. S. and MCGARVEY B. R., *J. chem. Phys.* **20**, 1472 (1952).
24. CHARVOLIN J., FROIDEVAUX C. and TAUPIN C., *Solid State Commun.* **4**, 357 (1966).
25. FRAUENFELDER R. and HEINRICH F., *Helv. phys. Acta* **38**, 279 (1965).
26. FARKAS A., *Orthohydrogen, Parahydrogen, and Heavy Hydrogen*, p. 14. Cambridge University Press, Cambridge (1935).
27. CRAMER E. and POLANYI M., *Z. phys. Chem.* **B21**, 459 (1933).
28. SMITH G. W. and HOUSLEY R. M., *Phys. Rev.* **117**, 732 (1960).
29. DICKSON S. A. and MYER H., *Phys. Rev.* **138A**, 1293 (1965).
30. TRAPNELL B. M. W., *Catalysis* (Edited by P. H. Emmett), Vol. 3, p. 1. Reinhold, New York (1955).
31. HATTON J. and ROLLIN B. V., *Proc. R. Soc. Lond.* **A199**, 222 (1949).
32. SMITH G. W. and SQUIRE C. F., *Phys. Rev.* **111**, 188 (1958).
33. MILLS R. L. and GRILLY E. R., *Phys. Rev.* **99**, 480 (1955).
34. *American Institute of Physics Handbook*, 2nd Edn., pp. 4-34. McGraw-Hill, New York.
35. LIPSICAS M. and HARTLAND A., *Phys. Rev.* **131**, 1187 (1963).
36. MICHELS A., DeGRAAFF W., WASSENAAR T., LEVELT J. M. H. and LOUWERSE P., *Physica* **25**, 25 (1959).
37. BRIDGMAN P. W., *Proc. Am. Acad. Arts Sci.* **59**, 173 (1924).
38. IMAI T. and MITCHELL J., Laboratory, private communication (1969).
39. GRIFFIN C. F., An NMR study of relaxation times in metallic sodium and lithium as a function of temperature and particle size. Ph.D. Thesis, Ohio State University (1964). University Microfilms 65-5641.
40. FEHER G. and KIP A. F., *Phys. Rev.* **98**, 337 (1955).
41. DYSON F. J., *Phys. Rev.* **98**, 349 (1955).
42. HOLCOMB D. F. and NORBERG R. E., *Phys. Rev.* **98**, 1074 (1955).

STUDY OF SOLID ELECTROLYTE POLARIZATION BY A COMPLEX ADMITTANCE METHOD

J. E. BAUERLE

Westinghouse Research Laboratories, Pittsburgh, Pa. 15235, U.S.A.

(Received 4 March 1969; in revised form 4 June 1969)

Abstract—The polarization behavior of zirconia–yttria solid electrolyte specimens with platinum electrodes has been studied over a temperature range of 400° to 800°C and a wide range of oxygen partial pressures. The complex admittance of these specimens was determined over a frequency range from d.c. to 100 kHz. An analysis of these data in the complex admittance plane indicated the presence of three polarizations: (1) an electrode polarization characterized by a double layer capacity and an effective resistance for the overall electrode reaction, $\frac{1}{2}\text{O}_2(\text{gas}) + 2e(\text{platinum}) \rightleftharpoons \text{O}^{2-}(\text{electrolyte})$; (2) a capacitive-resistive electrolyte polarization, probably corresponding to a partial blocking of oxygen ions at the electrolyte grain boundaries by an impurity phase there; and (3) a pure ohmic electrolyte polarization.

INTRODUCTION

THE LARGE oxygen ion conductivity occurring in zirconia–yttria and similar solid electrolytes at elevated temperatures is well known and has been the subject of numerous experimental studies. In these essentially pure ionic conductors, there have been surprisingly few experimental studies of basic polarization processes at the electrodes and within the electrolyte [1, 2].

One difficulty has been the lack of an established technique for studying polarization cells of these materials. We require a method in which the current through the cell is kept very low to avoid irreversible electrode changes and heating effects, and which is capable of resolving several polarizations occurring in the same specimen. An obvious solution to these difficulties is to study the impedance (or admittance) of the cell as a function of frequency with low amplitude a.c., but there still remains the awkward problem of analyzing data involving several polarizations which may partially overlap in the frequency domain.

The method we have employed eliminates these difficulties and appears not to have been applied previously to solid electrolyte

systems. It is based on measurements of the cell admittance which are taken over a wide range of frequencies and then *analyzed in the complex admittance plane*. Although analogs of this method have been used in other fields for many years [3–5], its application to electrochemistry is fairly recent. In particular, Sluyters *et al.* [6] have used it extensively in their studies of aqueous cell polarization phenomena.

There are two purposes to this paper: To suggest on the basis of our experiments *which* basic polarization processes predominate in cells of zirconia–yttria, and to demonstrate the usefulness of the complex admittance approach in solid electrolyte studies.

EXPERIMENTAL PROCEDURE

The specimen material was $(\text{ZrO}_2)_{0.9}(\text{Y}_2\text{O}_3)_{0.1}$, obtained from three different sources: (1) commercial material from Zircoa; (2) material prepared at these Laboratories by standard ceramic procedures; and (3) high purity material sintered under contamination-free conditions in an arc image furnace. Specimens were generally either wafers, approximately $1 \times 3 \times 4$ mm, or bars, approximately $1 \times 1 \times 12$ mm. This

allowed us to vary the area/length factor, A/L , by approximately 100, and the length factor by about 10.

All the electrodes were of platinum. Two types of preparation were employed: (1) platinum paste, fired at 1400°C for 1 hr, with weights ranging from 2.5 to 4.5 mg/cm²; and (2) platinum sputtered on by d.c. plasma to weights of 0.4 to 2.8 mg/cm², i.e. 2000–13,000 Å.

The porosity of the electrodes (as will be seen later) was a very important variable. Platinum paste electrodes fired at 1400°C were quite non-porous; however, they could be made very porous by passing a heavy current (1 A/cm²) through them for several minutes at 800°C. Presumably, this treatment produced pores by means of the very high oxygen pressures which would be generated at the interface. Sputtered platinum electrodes were reasonably porous as formed and needed no special treatment. The presence of porosity was readily detectable by applying a small drop of liquid to the electrode and observing its disappearance (or lack of it) by capillary action.

Specimens were suspended between baffles in the hot zone of a tube furnace (pure alumina tube) with a Pt–Pt 10% Rh thermocouple adjacent to the specimen. Various oxygen partial atmospheres were achieved by flowing calibrated mixtures of oxygen–argon or oxygen–nitrogen through the apparatus. These ranged from 1.5×10^{-5} to 1 atm of oxygen. The flow rates employed were between 200 and 800 cm³/min for a system having a volume of about 900 cm³.

The admittance bridge which we employed in our polarization studies was simple but quite sensitive. A rough schematic is shown in Fig. 1. Some characteristics of this bridge were the following: Voltage across specimen, 13 mV r.m.s.; frequency range, d.c. to 100 kHz; detectable unbalance, 0.1 per cent; balance unaffected by a.c. pickup; non-linearity in specimen easily detectable by presence of harmonics on scope. The high

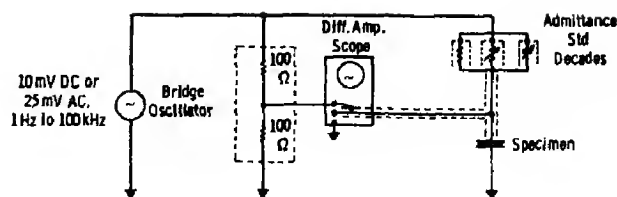


Fig. 1. Admittance bridge schematic.

sensitivity was achieved by synchronizing the null detecting scope to the a.c. line frequency. When the bridge was balanced, one observed a sharp steady trace of the residual a.c. pickup in the system; for a very small unbalance, a 'rippling' motion could be seen in the trace,* due to the different frequency of the bridge oscillator.

Tests were made to determine the effects of residual capacitance and inductance on the bridge accuracy and sensitivity. Corrections for such effects were small and occurred only at the highest frequencies.

COMPLEX ADMITTANCE PLOTS

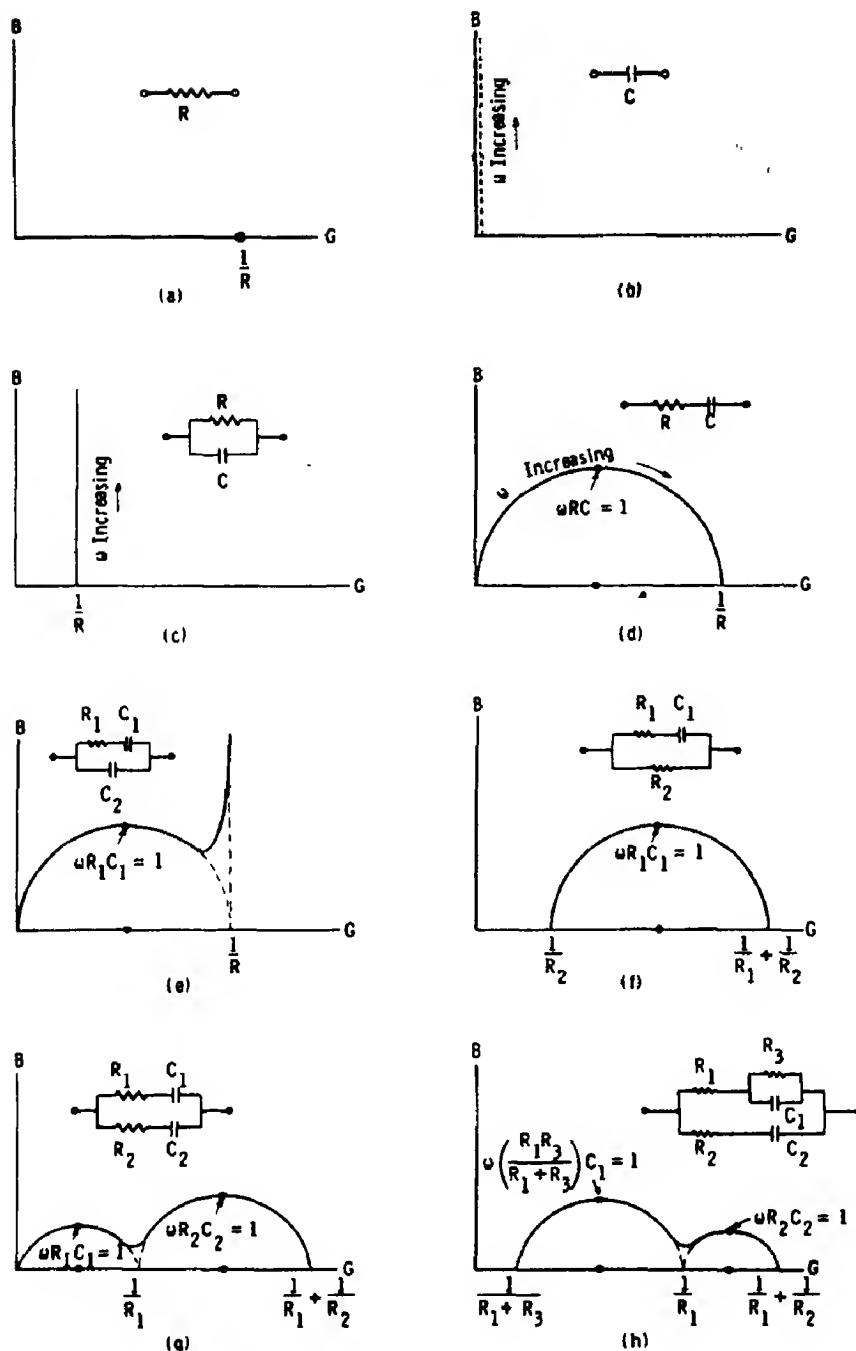
Complex admittance plots are useful for determining an appropriate equivalent circuit for a system and for estimating the values of the circuit parameters. The complex admittance $Y(\omega)$ of a system at an applied angular frequency ω may be written as the sum of a conductance $G(\omega)$ and a susceptance $B(\omega)$:

$$Y(\omega) = G(\omega) + jB(\omega). \quad (1)$$

If one plots the imaginary part of the admittance vs. the real part, i.e. $B(\omega)$ vs. $G(\omega)$, the resulting locus shows distinctive features for certain combinations of circuit elements. The method is perhaps best illustrated by specific examples of such plots (Figs. 2 and 3) for some simple circuits.† Very roughly, one can say that each *semi*-circular arc corresponds to a 'lumped' R - C combination; each *quarter*-cir-

*Tests showed that an unbalance emf of 0.1 mV amplitude could be detected in a trace whose width was 0.5 mm.

†We have excluded inductances from our circuits; in general, the equivalent circuits for electrochemical processes do not require their use.

Fig. 2. Admittance plots for some simple R - C circuits.

ular arc corresponds to a combination of a lumped R and a distributed R - C element, such as the Warburg impedance. (The latter element is the analog for a diffusive process.) It is seen in Figs. 2 and 3 that the resistance values are derivable from the circular-arc intercepts on

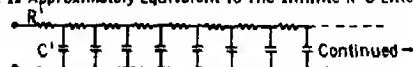
the G -axis; the capacitance values can be derived from expressions involving the frequencies at the peaks of the circular arcs.

The exact equations for these loci can be derived using simple a.c. circuit theory[6, 7]; the process is straightforward but tedious and

A 'Warburg Impedance' Is Designated By The Symbol



It Is Approximately Equivalent To The Infinite R-C Line



Its Admittance Is Given By $Y = Au^{\frac{1}{2}} + jAu^{\frac{1}{2}}$,
Where $A = \frac{C^{\frac{1}{2}}}{\sqrt{2R^{\frac{1}{2}}}}$

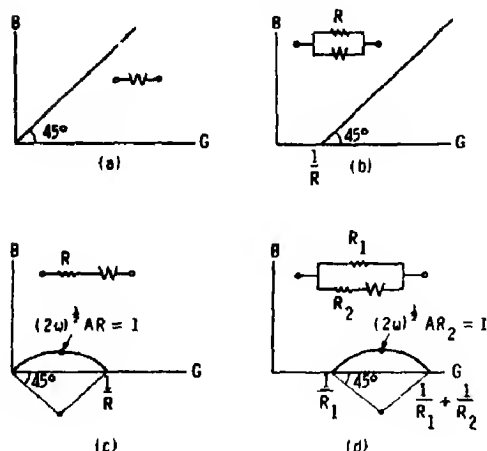


Fig. 3. Admittance plots for some circuits containing a Warburg (diffusional) impedance.

will not be given here. A theoretical discussion of the relationship of these plots to relaxation processes in general has been given by Schrama[8].

CHOOSING THE EQUIVALENT CIRCUIT

In general, for a given admittance plot there exists more than one possible equivalent circuit (see, for example, Fig. 2(h) and Fig. 7.). One chooses between these on the basis of (1) simplicity, and (2) consistency with what is known about the physical processes of the system. For example, two *parallel* networks would obviously not be appropriate as analogs for two physical processes that were known to occur in sequence or *series* [9].

Examples of typical admittance behavior for our zirconia-yttria specimens are shown in Figs. 4-6. To a good approximation, the behavior is that of a *lumped* parameter system. (Ideally, the angles in the figures would be 0° for lumped parameters or 45° for distributed parameters.)

The equivalent circuit which we shall choose (somewhat arbitrarily at this point) as a representation for our specimens is shown in Fig. 7. It is seen that it satisfies the minimum requirement of yielding the same type of admittance behavior as our specimens. The justification for choosing this particular circuit will become clearer in the sections to follow.

ELECTRODE VS. ELECTROLYTE IN THE EQUIVALENT CIRCUIT

One of the first questions to be settled experimentally was the following: What portion of the equivalent circuit in Fig. 7 corresponds to the electrode region and what portion corresponds to the bulk of the specimen, i.e. the electrolyte?

Two different approaches were tried which led to the same conclusion. The first approach was based on the fact that electrode equivalent circuit parameters should vary with the electrode area A but not the specimen length L , while electrolyte equivalent circuit parameters should vary with the factor A/L . In one test A was increased by a factor of 3 while A/L was increased by a factor of 200. In another test, A was *decreased* by a factor of 7 while A/L was increased by a factor of 2. It was found that $1/R_1$ and C_1 were proportional to A , while $1/R_2$, C_2 , and $1/R_3$ were proportional to A/L .

A second approach to testing the electrode-electrolyte question was based on the four-terminal d.c. conductance of a specimen. This type of measurement excludes electrode effects; only the d.c. electrolyte resistance is measured. Such a measurement was carried out on a bar-geometry specimen, and subsequently admittance measurements were made for the same gauge length. The experimental results are shown in Fig. 8. It is seen that the four-terminal conductance coincides with G_2 on the admittance plot, which is just the d.c. conductance of the equivalent circuit with R_1 excluded.

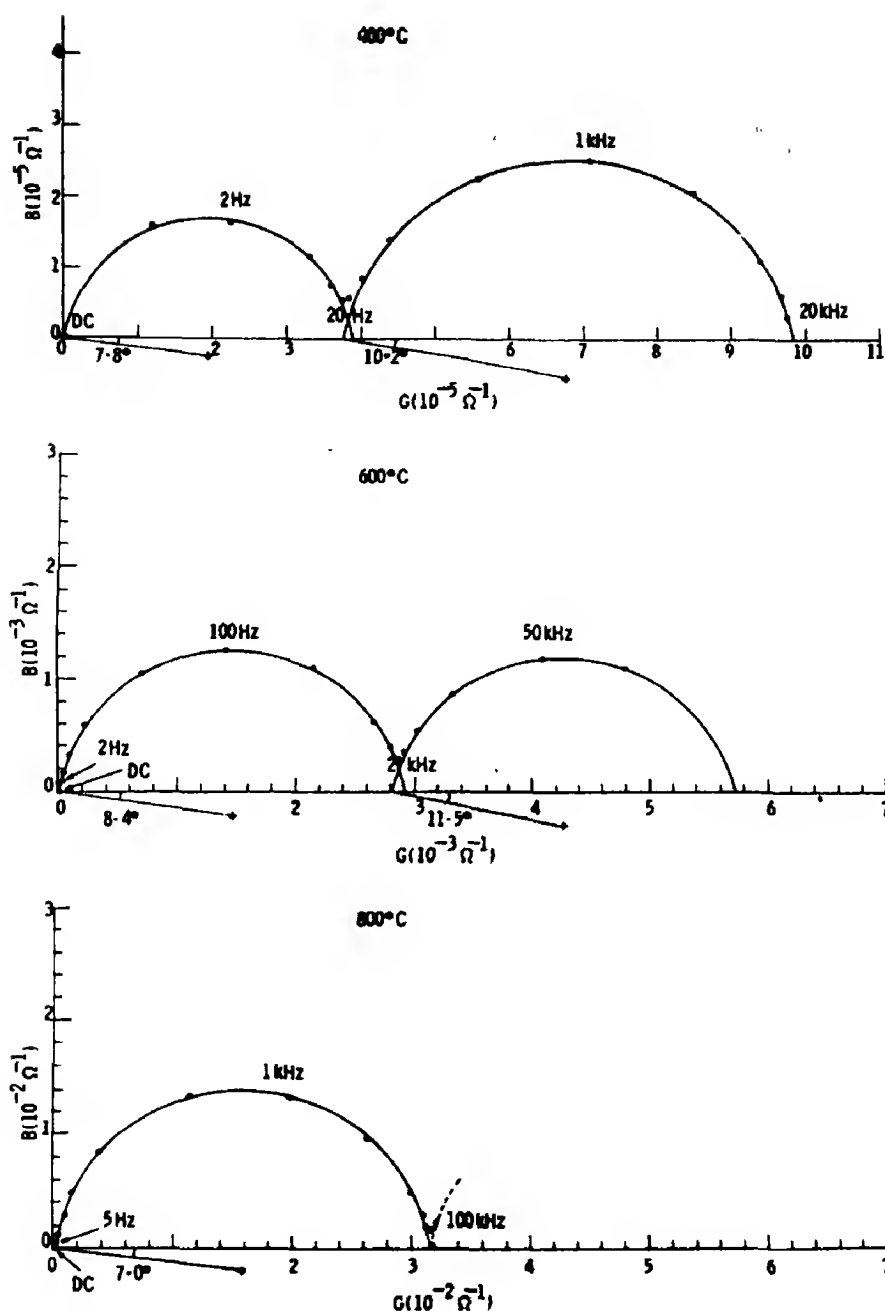


Fig. 4. Admittance behavior for a specimen with non-porous electrodes (Pt paste).

These tests showed unambiguously that R_1 and C_1 correspond to electrode polarization processes; R_2 , C_2 and R_3 correspond to polarization processes in the bulk of the specimen. In terms of admittance plots, the lower frequency dispersion corresponds to the

electrode and the higher frequency dispersion corresponds to the electrolyte.

Further evidence for the correctness of the above interpretation will be found in the sections on the effects of various atmospheres and the effects of electrode porosity.

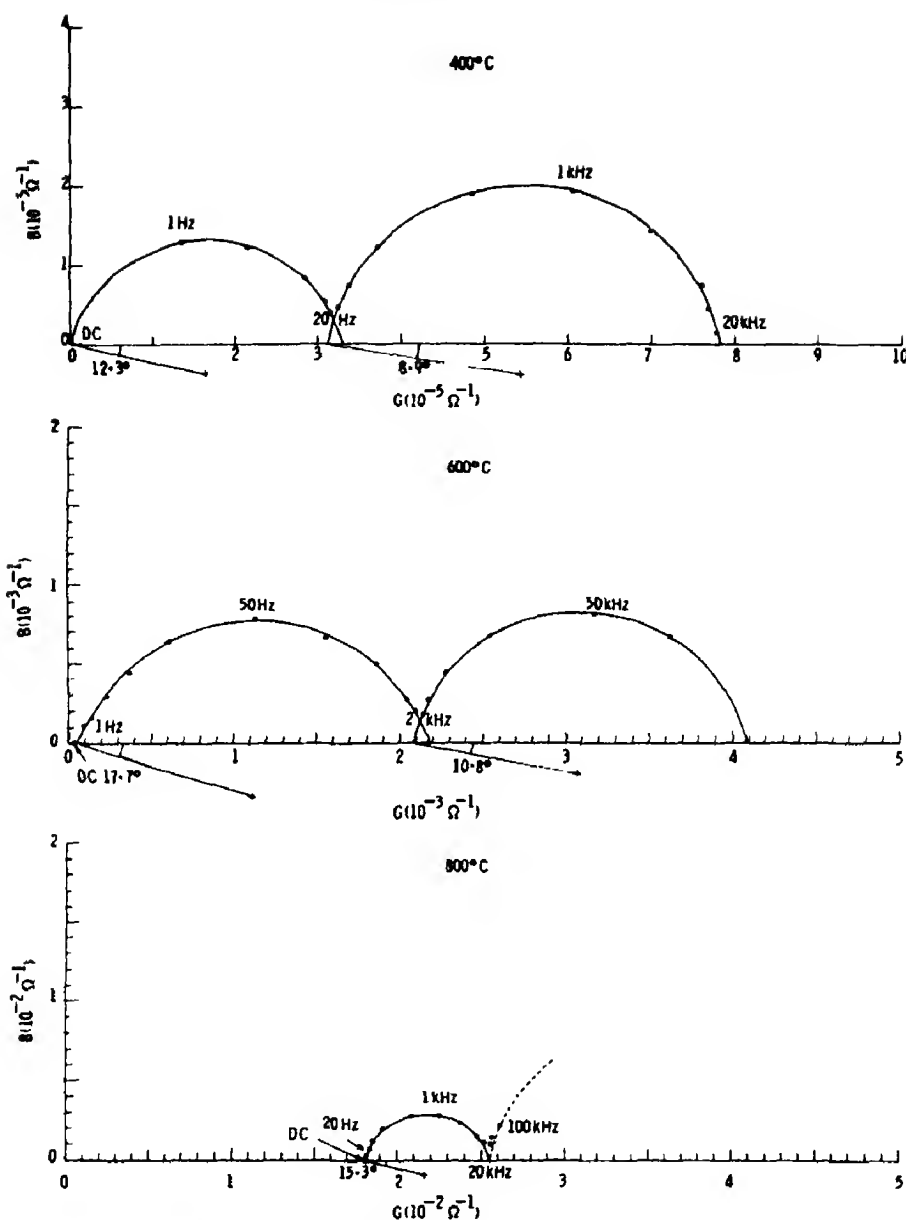


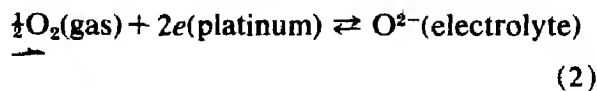
Fig. 5. Admittance behavior for a specimen with naturally porous electrodes (sputtered Pt).

ELECTRODE POLARIZATION BEHAVIOR

The electrode behavior of our specimens*

*The electrode arrangement on our specimens was symmetrical; hence, the parameters R_1 and C_1 represent the resultant behavior of two nearly identical electrodes, the parameters for one of these being $\frac{1}{2}R_1$ and $2C_1$. This procedure is legitimate provided that (1) we employ only small signal a.c. in the measurements, and (2) we do not employ a d.c. bias voltage. If the two electrodes should differ considerably in their properties, one would obtain a distorted non-circular arc on the admittance plot.

is described in terms of the resistance R_1 and the capacitance C_1 , in parallel. Our present hypothesis is that C_1 represents the double-layer capacity of the electrode, and R_1 represents an effective resistance for the overall electrode reaction



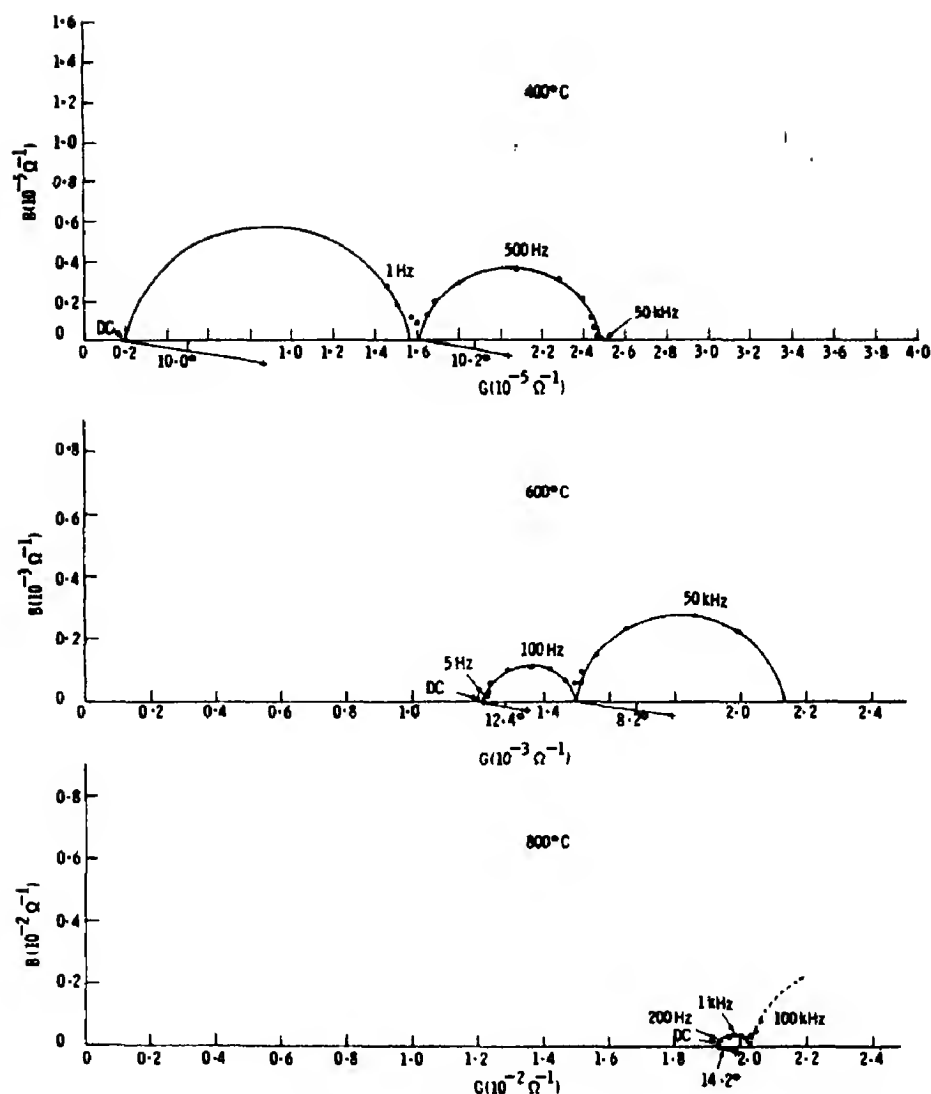


Fig. 6. Admittance behavior for a specimen with artificially porous electrodes (Pt paste + heavy current treatment; see text).

which is known to take place under these conditions [10].

Electrode capacitance C_1

Most of the experimental values for C_1 fell in the range of 30–80 $\mu\text{f}/\text{cm}^2$, i.e. 60–160 $\mu\text{f}/\text{cm}^2$ at each electrode.* Included in this range were the following: non-porous Pt paste electrodes; sputtered Pt electrodes of 2000

*Based on the apparent electrode area. The true microscopic area could have been either larger or smaller than this.

and 13,000 Å thickness; temperatures from 400 to 800°C; and oxygen partial pressures from 1.5×10^{-5} to 1 atm. Dependence on these variables was considered too weak to be significant.

A calculation of the double-layer capacity for $(\text{ZrO}_2)_{0.9}(\text{Y}_2\text{O}_3)_{0.1}$ using conventional electrostatic theory [11] gives a value of 190 $\mu\text{f}/\text{cm}^2$; however, this must be considered as only a rough upper limit to the true double-layer capacity since it neglects the effect of the compact double layer [12].

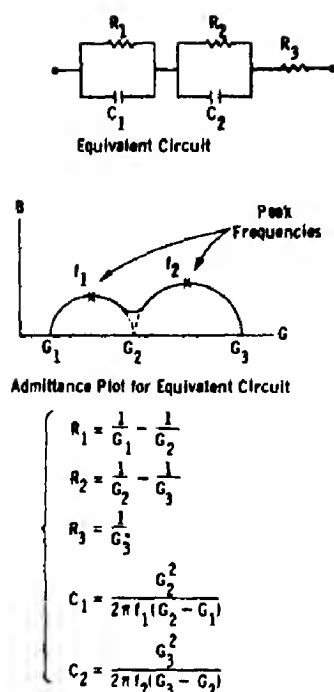


Fig. 7. Equivalent circuit for the specimens. Equations for obtaining equivalent circuit parameters from admittance plot parameters.

Anomalous high experimental values for C_1 ($550 \mu\text{f}/\text{cm}^2$ in some cases) were obtained with platinum paste electrodes which had been treated with high currents to make them porous. The origin of these high capacitances is not understood at this time.

Electrode resistance R_1

Unlike the electrode capacitance, the electrode resistance R_1 was found to be very sensitive to such parameters as electrode preparation, temperature, and oxygen partial pressure. One may consider the reciprocal of R_1 to be a measure of the speed of the overall reaction (2). We postulate that this reaction involves the following steps:

- (1) Flow of oxygen into the pores of the platinum electrode.
- (2) Adsorption of molecular oxygen on the pore walls in the electrode. The work of various investigators [13, 14] strongly suggests that a platinum surface at these temperatures and pressures would be completely covered with a tightly bound monolayer of oxygen atoms. We are postulating a relatively weak chemisorption of oxygen molecules on this monolayer.
- (3) Surface diffusion of oxygen molecules to electrode-electrolyte interface.
- (4) Dissociation of oxygen molecules. (This step might occur before step 3.)
- (5) Electron transfer reaction at interface ($\text{O} + 2e \rightleftharpoons \text{O}^{2-}$, for example).

Let us now consider the experimentally observed behavior of R_1 . First, we found that

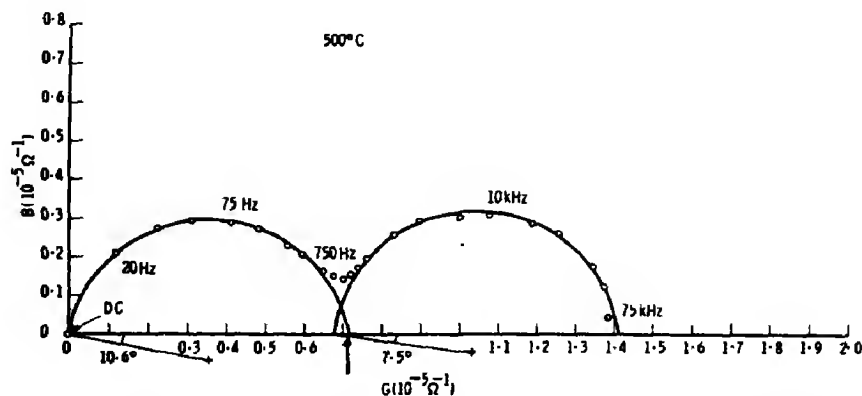


Fig. 8. Admittance plot for a specimen with its 4-terminal d.c. conductance (arrow) marked on the G -axis. The dispersion to the left of this value arises from electrode polarization; the dispersion to the right arises from electrolyte polarization.

R_1 was reasonably low only when the electrodes were porous. Qualitatively this behavior may be seen in the admittance plots of Figs. 4-6. This indicates that electrode porosity was essential for the occurrence of reaction (2). Such a result is not too surprising since solid platinum is essentially impermeable to oxygen, even at 1425°C[15]. We do not believe, however, that the pores function only as simple flow channels for gaseous oxygen.

Second, we studied the dependence of R_1 on the oxygen partial pressure (Fig. 11). At 400°C, no effect was observed. At 600° and 800°C, one can see a strong effect on the electrode dispersion and the complete absence of an effect on the electrolyte dispersion. From plots of this type we obtained data for the dependence of the electrode resistance R_1 on the oxygen partial pressure P . These data, as shown in Fig. 12, can be fit with either of the empirical expressions

$$\frac{1}{R_1} = A \left(\frac{P^\alpha}{B + P^\alpha} \right) \quad (3)$$

or

$$\frac{1}{R_1} = A' \left(\frac{P}{B' + P} \right)^{\alpha'} \quad (4)$$

where the A 's, B 's and α 's are constants ($\alpha, \alpha' \approx 0.64$). The form of these expressions is that of typical adsorption isotherms[16]. This leads us to hypothesize that at a fixed temperature, the speed of the electrode reaction (measured by $1/R_1$) is a direct function of the concentration of molecular oxygen adsorbed on the platinum pore walls. If this is true, one can deduce that the adsorption process is near its equilibrium (for this temperature), because R_1 is ohmic over a wide range of currents and depends reversibly on the oxygen partial pressure.

Third, we found that the temperature dependence of R_1 corresponded to a thermally activated process with a rather high activation energy, approximately 2-2.5 eV (see Figs. 9

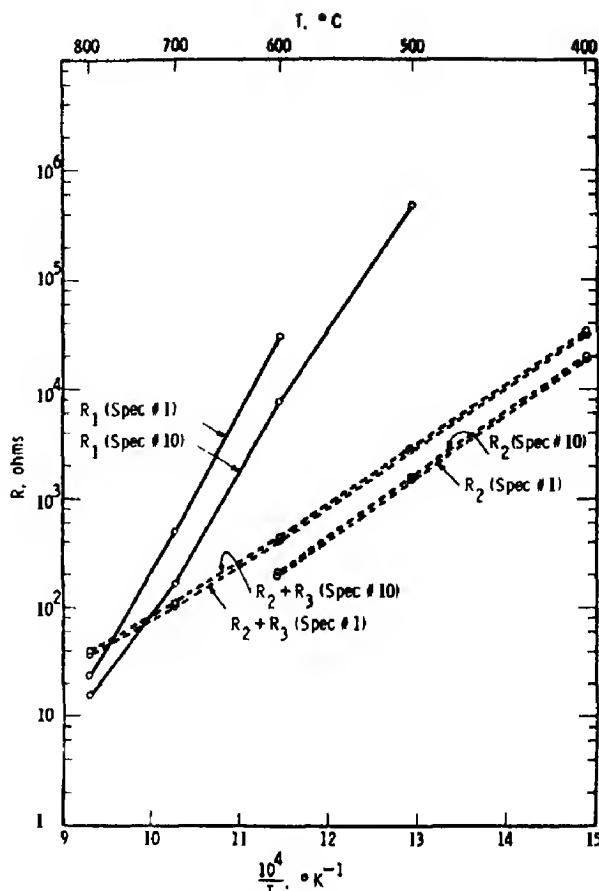


Fig. 9. Temperature dependence of the equivalent circuit resistances. Electrodes were naturally porous (sputtered Pt). Spec. No. 1: 13,000 Å thick, Spec. No. 10: 2000 Å thick. Electrolyte was zirconia-yttria of moderate purity, prepared at this Lab.

and 10). This cannot correspond to the adsorption step (which is near equilibrium) because the temperature dependence is in the wrong direction[16]. The surface diffusion step also may be ruled out; one would expect to find a relatively small activation energy for this process[17]. Thus, we are left with either the molecular dissociation step or the electron transfer step as the probable source of the strong temperature dependence of R_1 .

To summarize, our results suggest that the electrode resistance R_1 depends on the oxygen partial pressure via an adsorption-desorption equilibrium of oxygen molecules on the porous platinum surface, and it depends on tempera-

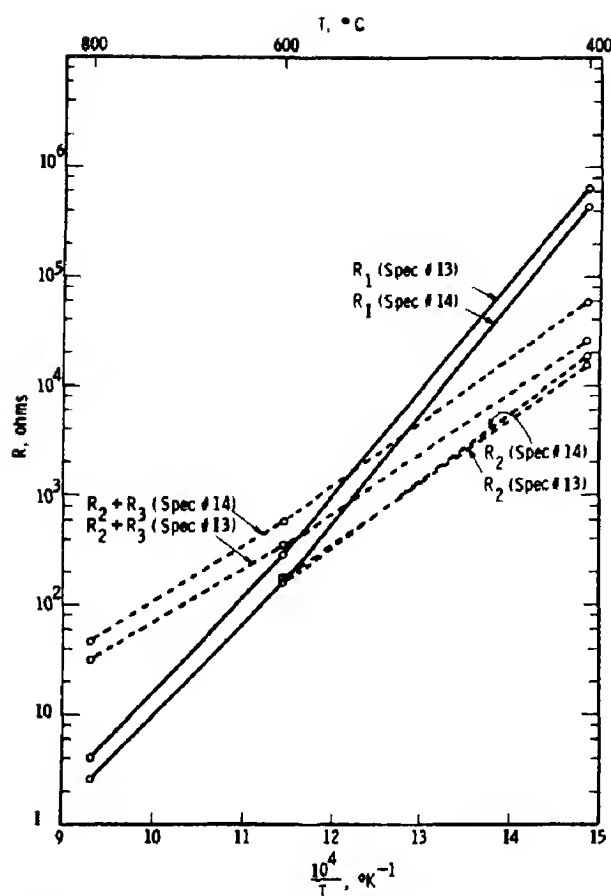


Fig. 10. Temperature dependence of the equivalent circuit resistances. Electrodes were artificially porous (Pt paste + heavy current treatment). Spec. No. 13: Moderate purity zirconia-yttria prepared at this Lab. Spec. No. 14: Moderate purity commercial zirconia-yttria.

ture via a thermally activated process, most likely either the dissociation of oxygen molecules (on platinum) or an electron-transfer reaction at the electrode interface.

ELECTROLYTE POLARIZATION BEHAVIOR

The behavior of the electrolyte proper is described by the equivalent circuit parameters R_2 , C_2 and R_3 . As discussed earlier, the values of these parameters are derivable from the second region of dispersion on the admittance plots. We shall first describe the general behavior of these parameters and then consider the possible physical interpretation of them.

Electrolyte specimens of moderate purity

These specimens include both commercially obtained zirconia-yttria and material produced at this Laboratory by standard ceramic techniques. As one might expect, the electrolyte parameters R_2 , C_2 and R_3 were insensitive to changes in the oxygen partial pressure. This can be seen quite clearly in Fig. 11 (600°C).

The quantities R_2 and $R_2 + R_3$ show a strong similarity in their temperature dependence (Figs. 9 and 10). This suggests that the resistances R_2 and R_3 may arise from the same type of physical process, a point which will be mentioned again later. From the standpoint of our equivalent circuit, the quantity $R_2 + R_3$ should correspond to the d.c. resistance of the electrolyte. The activation energy of $R_2 + R_3$ varies slowly from about 1.1 eV at 400°C to about 0.9 eV at 800°C. This latter value agrees well with the literature values [18, 19], which are based on conductivity data in the range 600°–1300°C.

The capacitance C_2 was found to be independent of temperature and quite reproducible for electrolyte material from a given source. For the normalized capacitance, $(L/A)C_2$, which is numerically independent of the specimen geometry, we obtained values of 0.028 $\mu\text{f}/\text{cm}$ for zirconia-yttria prepared by standard procedures at these Laboratories and 0.015 $\mu\text{f}/\text{cm}$ for the commercially prepared zirconia-yttria.

High purity zirconia-yttria

A specimen of high purity material was sintered under contamination-free conditions in an arc image furnace. An example of the admittance behavior obtained with this material is seen in Fig. 13. Note that the second dispersion region which we associate with the electrolyte proper, was in this case very small or absent. The location of the 4-terminal d.c. conductance on this plot also suggests that the second dispersion was not present. Qualitatively similar results were obtained at other temperatures and for

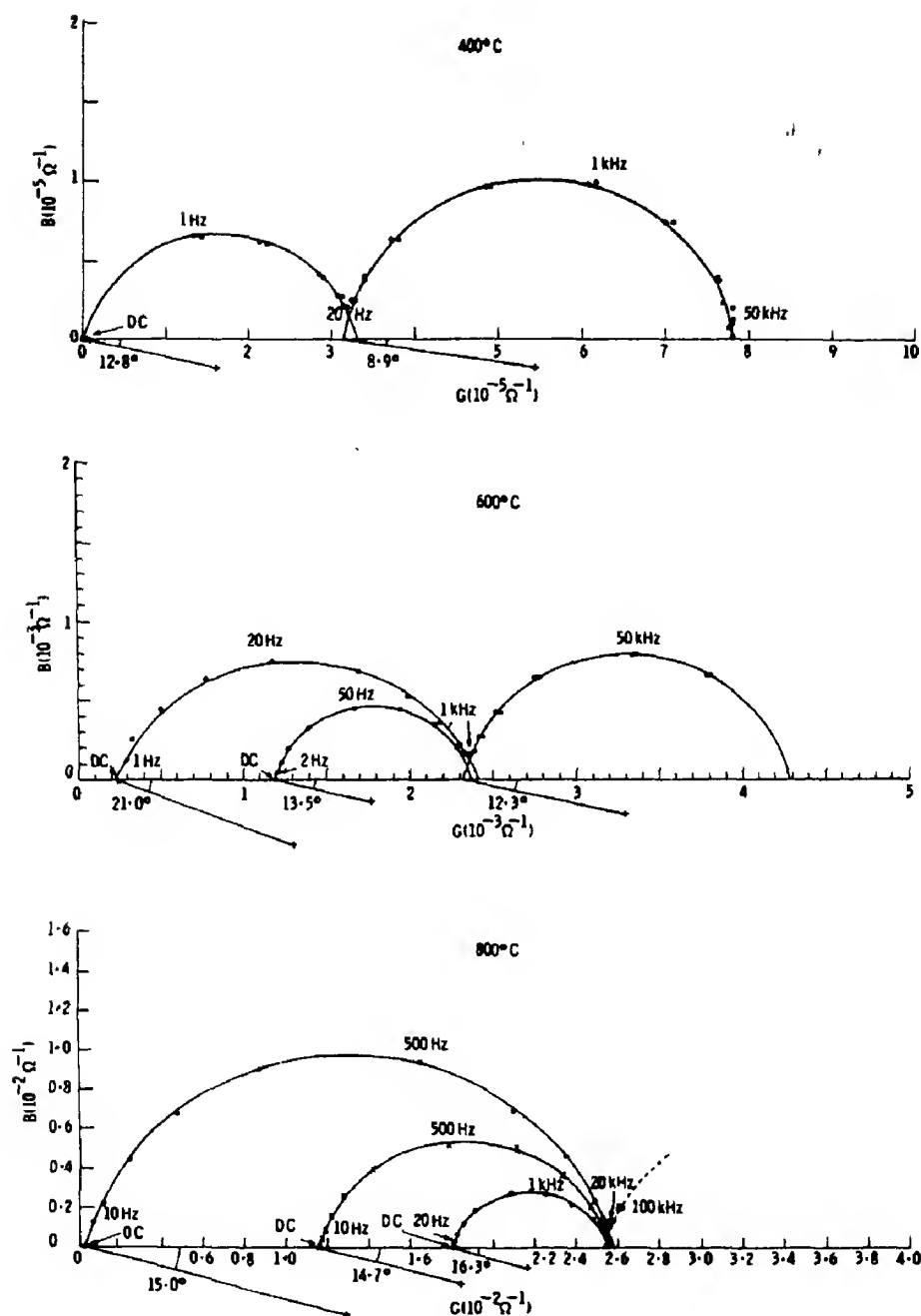


Fig. 11. Admittance behavior for various partial pressures of oxygen. $P_{O_2} = 1.5 \times 10^{-5}$ atm (●); $P_{O_2} = 10^{-2}$ atm (×); $P_{O_2} = 0.2$ atm (○). Spec. No. 10: 400°, 800°C; Spec. No. 13: 600°C.

two different specimen geometries. In short, the behavior of the high purity electrolyte appeared to be that of a simple resistance. The d.c. resistivity of this material has been discussed in detail elsewhere [20].

Interpretation of electrolyte polarization

Probably the most plausible explanation of the electrolyte polarization behavior is that the normal oxygen ion conduction of the electrolyte is partially blocked at the grain

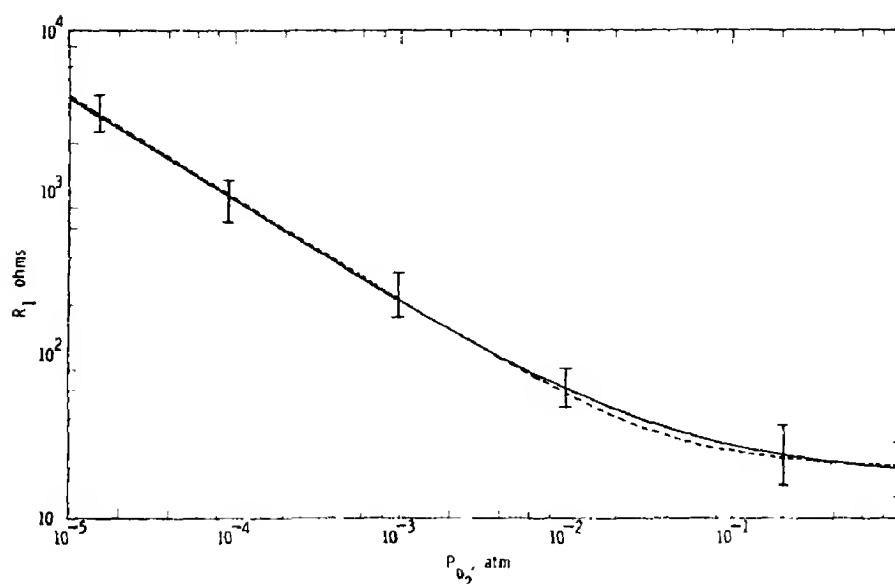


Fig. 12. Electrode resistance vs. oxygen partial pressure at 800°C. Electrodes were naturally porous. (sputtered Pt, 3 specimens) Equation (3), —, Equation (4), - - - -.

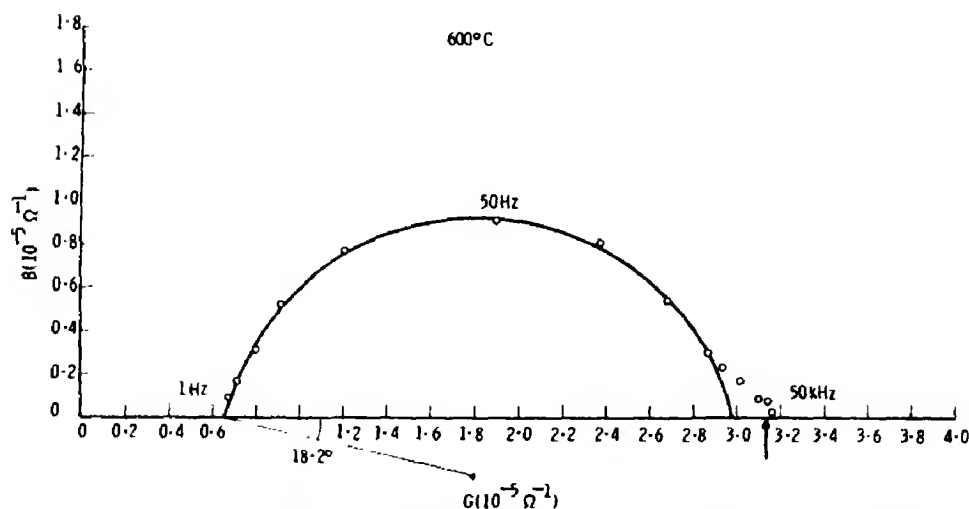


Fig. 13. Admittance behavior for a high purity zirconia-yttria specimen. The location of the 4-terminal d.c. conductance (arrow) on the G -axis suggests that no electrolyte dispersion occurs in this material (compare with Fig. 8).

boundaries by an impurity phase there. Electron microprobe analysis of our less pure material indicated the presence of a second phase in the grain boundaries composed chiefly of calcia and silica. This phenomenon has been observed also by Strickler[21] and Button[22]. One may picture the effect of such a second phase as shown in

Fig. 14. If one compares this with the electrolyte equivalent circuit, then R_3 would correspond to the resistance within the grains, R_2 would correspond to a 'constriction resistance' at the contacts between grains, and C_2 would correspond to the capacity across the impurity phase region.

There are some interesting consequences to

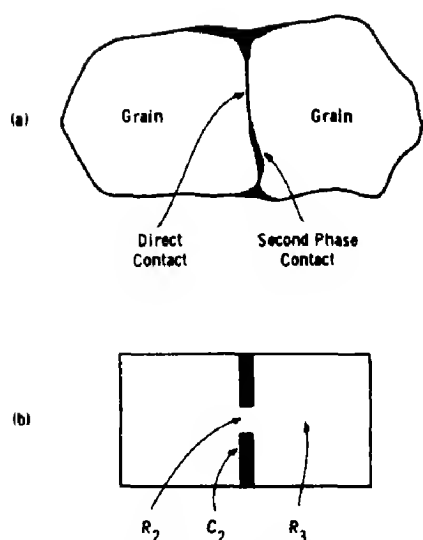


Fig. 14. Sketch showing how a second phase in the grain boundaries of an electrolyte might give rise to the observed electrolyte dispersion phenomena (a) actual situation (b) idealized situation.

this hypothesis. First, it explains the experimentally observed similarity in the temperature dependence of R_2 and R_3 . Second, we can obtain an experimental estimate of the capacity per unit area of the grain boundary region. Using our values of $(L/A)C_2$ and grain size, one obtains a capacitance/area of $5 \mu\text{f}/\text{cm}^2$. This is a rather large capacity. If one attempted to explain it in terms of a uniform insulating layer of silica, then this layer would have to be 7 \AA or less in thickness. A more likely possibility is that the impurity layer is blocking to oxygen ion flow, but is a conductor for some other species (electrons or calcium ions, for example). This could give rise to a weak double layer capacity of the magnitude observed.

Finally, we should like to comment on the temperature variation of the activation energy for the electrolyte conductivity. This effect was mentioned specifically for our moderate purity material, but it occurs also with high purity material, as discussed in another paper[20]. In that paper, we suggested two possible explanations for the effect, the first involving vacancy trapping, and the second involving a phase of different con-

ductivity at the grain boundaries. This second explanation now appears unlikely since our present work gave no indication of a grain boundary polarization in high purity material. It is possible, then, that the apparent variation in the activation energy of the electrolyte $(\text{ZrO}_2)_{0.9}(\text{Y}_2\text{O}_3)_{0.1}$ is an intrinsic property of this material which can be understood in terms of the vacancy trapping mechanism. One might hope to detect such trapped vacancies by their dipole relaxation behavior; however, a calculation shows that the capacitive effect would be small ($\sim 20 \text{ pf}$ for our specimens) and hence difficult to observe unless other polarizations were completely absent.

Acknowledgements—The author wishes to thank Dr. A. J. Panson for his encouraging interest in this work. I am grateful also to Dr. R. J. Ruka and J. Hrizo for helpful discussions.

REFERENCES

1. PERFIL'EV M. V., PAL'GUEV S. F. and KARPACHEV S. V., *Soviet Electrochem.* **1**, 74 (1965).
2. KARPACHEV S. V. and FILYAEV A. T., *Soviet Electrochem.* **2**, 576 (1966).
3. COLE K. S. and COLE R. H., *J. chem. Phys.* **9**, 341 (1941).
4. NOLLE A. W., *J. Polymer Sci.* **5**, 1 (1950).
5. KNESER H. O., *Koll. Zs.* **134**, 20 (1953).
6. SLUYTERS J. H. *et al.*, A series of papers entitled, "The Impedance of Galvanic Cells," *Rec. Trav. Chim.* **79**, 1092, 1101 (1960); **82**, 100, 525, 535, 553 (1963); **83**, 217, 581, 967 (1964); **84**, 729, 740, 751, 764 (1965); *Electrochim. Acta* **11**, 73, 483 (1966); *Z. phys. Chem.* **52**, 89 (1967); *J. electroanal. Chem.* **14**, 169, 181 (1967); **15**, 151, 343 (1967).
7. EULER J. and DEHMELT K., *Z. Elektrochem.* **61**, 1200 (1957).
8. SCHRAMA J., Thesis, Univ. of Leiden (1957).
9. RALEIGH D. O., *J. Phys. Chem. Solids* **29**, 261 (1968).
10. WEISSBART J. and RUKA R. J., *Rev. scient. Instrum.* **32**, 593 (1961).
11. MACDONALD J. R., *Phys. Rev.* **92**, 4 (1953).
12. VETTER K. J., In *Electrochemical Kinetics, Theoretical and Experimental Aspects*, pp. 73–79. Academic Press, New York (1967).
13. LANGMUIR I., *Trans. Faraday Soc.* **17**, 621 (1922).
14. FRYBURG G. C. and PETRUS H. M., *J. electrochem. Soc.* **108**, 496 (1961).
15. NORTON F. J., *J. appl. Phys.* **29**, 1122 (1958).
16. HAYWARD D. O. and TRAPNELL B. M. W., In *Chemisorption*, Chap. 5. Butterworth, Washington (1964).

17. HAYWARD D. O. and TRAPNELL B. M. W., In *Chemisorption*, Chap. 9. Butterworth, Washington (1964).
18. DIXON J. M., *et al.*, *J. electrochem. Soc.* **110**, 276 (1963).
19. STRICKLER D. W. and CARLSON W. G., *J. Am. Ceram. Soc.* **47**, 122 (1964).
20. BAUERLE J. E. and HRIZO J., *J. Phys. Chem. Solids* **30**, 565 (1969).
21. D. W. STRICKLER, Westinghouse Rep. No. 64-918-273-R6 (1964).
22. BUTTON D. D., *Bull. Am. Ceram. Soc.* **43**, 263 (1964).

ELECTROREFLECTANCE OF *p*-TYPE GaAs

T. NISHINO, M. OKUYAMA and Y. HAMAKAWA

Faculty of Engineering Science, Osaka University, Toyonaka, Osaka, Japan

(Received 19 May 1969)

Abstract—The electroreflectance spectra of *p*-type GaAs in photon energies from 1.3 to 3.5 eV have been investigated at temperatures from 300° down to 25°K. Measurements of electroreflectance have been performed by the method using the interface potential of GaAs-SnO₂ heterojunction. Both signals of an exciton and the fundamental edge have been separated in the low temperature spectra, and an additional structure which may be associated with a localized state has been also observed below the fundamental edge. The similar structures with weak intensity appear near the spin-orbit split off edge. The line shapes of electroreflectance spectra which are related to $\Lambda_3 - \Lambda_1$ transition and its spin-orbit split off edges are explained by the mixed electro-optical spectra of $M_1(\perp)$ and $M_1(\parallel)$ type critical points including the effect of thermal broadening. A method of estimating the thermal broadening factor from the temperature dependences of the electroreflectance spectra associated with $\Lambda_3 - \Lambda_1$ transition edge is also presented.

1. INTRODUCTION

IN THE last few years the electro-optical effect has been extensively studied in both aspects of the theory and the experiment. The theoretical treatments of the electro-optical effect have been made for various types of critical points[1-5], and also the effect of a static electric field on an exciton has been treated by several workers[6-9]. According to a recent progress in the field of the electro-optical effect, it has become possible to make a quantitative comparison between the electro-optical theory and the experimental data. On the other hand, in the experimental works various kinds of techniques have been recently developed and successfully applied to many materials. These techniques include the methods utilizing high electric field in the space charge region of semiconductor in the configurations of *P-N* junction[10, 11], field effect type[12, 13], electrolyte-semiconductor[14-16] and SnO₂-semiconductor heterojunction[17, 18], and the method of transverse electro-optical effect to high resistivity materials[19, 20].

The electroreflectance studies of GaAs was first done by Seraphin[21] and the signals from the fundamental edge and $\Lambda_3 - \Lambda_1$

transition edge and these spin-orbit split off edges were obtained. Moreover, an additional structure below the fundamental edge has been also observed, which was attributed to the transitions related to an impurity state because the modulation voltage dependence was different from those of other structures. By using the electrolyte-semiconductor method Cardona *et al.*[14, 22] have extended the measurement to more high photon energy region and studied for samples covering a large range of doping density and type of impurity. Recently Williams and Rehn[23] have measured the electroreflectance using two techniques of field-effect type and electrolyte-semiconductor method, mentioned above. All of them have obtained the similar structures around $\Gamma_{15} - \Gamma_1$ and $\Lambda_3 - \Lambda_1$ transition edges and also observed the structure attributed to the transitions including an impurity state. However, they have not still obtained an obvious evidence that the structure below the fundamental edge is associated with the transitions from an impurity state. These measurements were mainly carried out in the room temperature region, except that Seraphin extended the measurement down to 77°K.

This paper presents the result of the elec-

troreflectance measurement of *p*-type GaAs at temperatures from 300° to 25°K. The observed structures near the fundamental edge are interpreted in terms of an exciton, $\Gamma_8 - \Gamma_6$ transition edge and the transitions associated with a localized state. The similar type structures are also observed around $\Gamma_7 - \Gamma_6$ transition edge, the spin-orbit split off edge. The temperature dependences of the electroreflectance spectra from $\Lambda_3 - \Lambda_1$ transition edges are presented and these line shapes are explained by the broadened electroreflectance signals with M_1 critical point having both parallel and transverse types. Moreover, by comparing with the electro-optical theory including the thermal broadening effect of Lorentzian type, the broadening factor is estimated on the basis of the temperature dependence of the line shape and the amplitude of the structure from $\Lambda_3 - \Lambda_1$ transition edge.

2. EXPERIMENTAL

GaAs single crystal used in this experiment is a zinc doped *p*-type one and the carrier density at room temperature is $1.7 \times 10^{17} \text{ cm}^{-3}$. All the samples were cut into a rectangular form of $8 \times 5 \text{ mm}^2$ area with a thickness of about 0.5 mm, and mechanically polished and lightly etched with an equal mixture of HCl and HNO_3 . On the reflecting surface having (111) crystal face tin is evaporated and subsequently oxidized in a furnace. Electric field is built in the interface barrier of GaAs-SnO₂ heterojunction. Electronics and optical systems employed here are similar to those used in the work of germanium [17], except that a 1200 lines/mm grating and an RCA 7200 photomultiplier with S-19 response were used in a higher energy region.

3. RESULTS AND DISCUSSION

(a) $\Gamma_{15} - \Gamma_1$ transition

Figure 1 shows the electroreflectance spectra in the photon energy region 1.3–2.0 eV measured at three different temperatures. The measurements are carried out by the same bias voltage modulated from the flat band position.

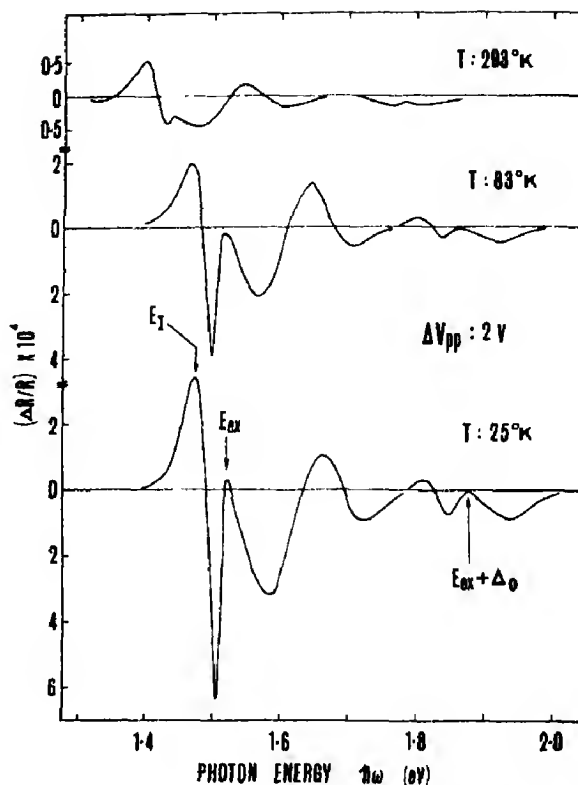


Fig. 1 Electroreflectance spectra in the energy region 1.3–2.0 eV at three different temperatures with the same bias voltage, $V_{DC} = -1.0 \text{ V}$ and $\Delta V_{pp} = 2.0 \text{ V}$.

In these electroreflectance spectra the electric fields in the surface space charge region are not so much different with each other. It is confirmed from the detection of the flat band position that the Fermi level at the surface of GaAs is almost independent of temperatures. A large temperature dependence of the amplitudes of the electroreflectance signals can be seen in the figure. This indicates that a thermal broadening effect is quite large, so that the room temperature spectrum is much broadened by the thermal broadening effect.

The peak indicated by E_I appears far below the fundamental edge obtained by absorption measurements [24]. The similar peak to E_I is also observed just below the spin-orbit split band edge which is 0.35 eV apart from the fundamental edge. This structure E_I does change its intensity with samples cut from the same single crystal, though a change of the

location of E_i could not be seen within an experimental error. Hence this structure seems to be very sensitive to the surface condition of the sample. Cardona *et al.* [14] also found the E_i structure in their room temperature electroreflectance spectra for *p*-type GaAs containing almost the same amount of zinc impurity as our samples used here. Furthermore, the same type structure was observed in the electroreflectance spectra for *n*-type GaAs and attributed to an impurity-associated transition by several authors [14, 21, 23]. Supposing the E_i structure obtained here is associated with an impurity, the impurity ionization energy is estimated to be 0.038 ± 0.003 eV in the whole temperature region measured. The value obtained by Cardona *et al.* [14] is 0.03 ± 0.005 eV and a little smaller than ours. Both of these values are not in agreement with the value 0.026 eV considered as the ionization energy of zinc acceptor in GaAs [25, 26]. It would be considered that the E_i structure observed has no correlation with the transitions from a zinc acceptor level to the conduction band. From the facts that the E_i structure is fairly dependent of the surface treatment and also appears always just below the spin-orbit split off edge, having the similar behaviors to those of the E_i structure with modulation voltages and temperatures, it is suggested that the E_i structure is associated with a donor type defect state at the surface of GaAs. This prediction may be supported by the fact that the impurity ionization energy obtained here is very close to the activation energy 0.039 eV of the defect which Williams [27] has demonstrated from the photoluminescence of an epitaxially grown *n*-type GaAs. According to Williams the origin of the defect might be either an arsenic vacancy-complex or a gallium interstitial. It is quite possible in our case that the similar defect state exists at the surface of the sample and this is the origin of the E_i signal.

Figure 2 shows the electroreflectance spectra measured at 25°K for three different modu-

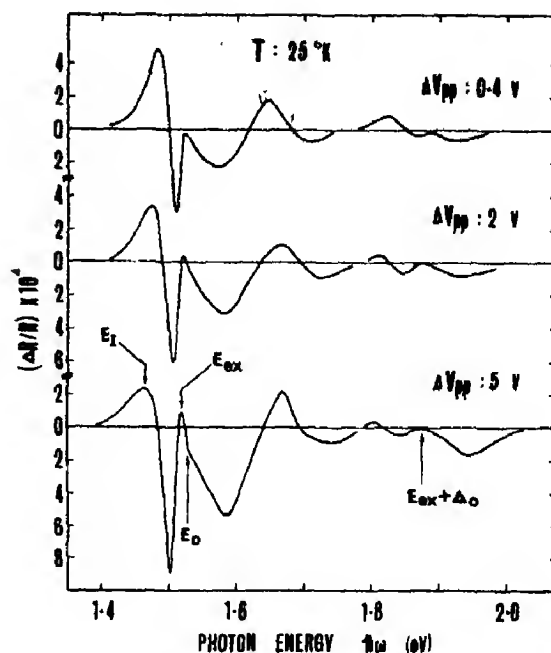


Fig. 2. Line spectra of electroreflectance in the energy region 1.3–2.0 eV at 25°K with three different modulation voltages.

lation voltages, and Fig. 3 the modulation voltage dependence of the positions of all the peaks. As can be clearly seen in the case of $\Delta V_{pp} = 5$ V, the weak structure indicated by E_0 appears in large modulation voltages. This E_0 structure is observed only in low temperatures and in large modulation voltages. But we cannot resolve a signal corresponding to the E_0 structure near the spin-orbit split off edge, $\Gamma_7 - \Gamma_6$ transition edge. On the basis of the modulation voltage dependences of the peak positions shown in Fig. 3, we conclude that the E_{ex} and E_0 structures are attributed to an exciton and the fundamental edge, $\Gamma_8 - \Gamma_6$ transition edge, respectively. The energy of the E_{ex} peak associated with an exciton is 1.516 ± 0.004 eV at 25°K. This value is consistent with the other experimental data [24], though the fluctuation 0.004 eV from sample to sample is slightly large. Although an overlapping effect of the E_{ex} and the weak E_0 signals prevents us from estimating the band edge, the energy of the fundamental edge is determined to be approximately 1.52 eV by

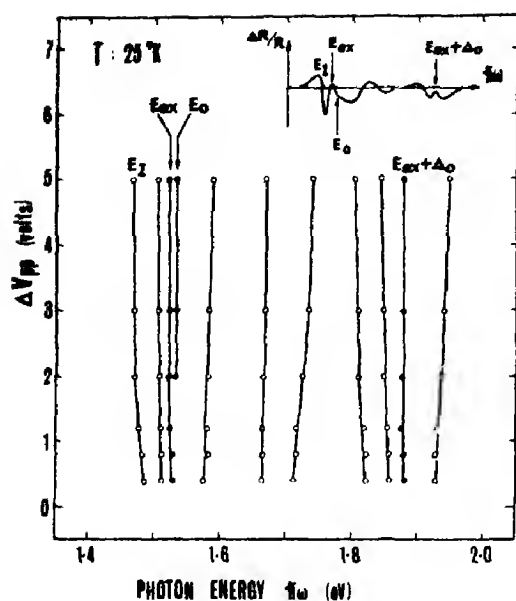


Fig. 3. Modulation voltage dependence of the peak positions in the electroreflectance spectra in the energy region 1.3–2.0 eV at 25°K.

analyzing the structures. Decreasing of the amplitude and shifting of the peak position in the E_1 structure with increasing of the modulation voltage are mainly come from the overlapping of the E_1 structure and the satellite structure of the E_{ex} signal which lies in the low energy side; that is, the satellite structure of the E_{ex} signal does accidentally appear at the location of the E_1 structure in an opposite polarity. Therefore, we determined the energies of the E_1 peak from the low modulation voltage spectra. The similar behavior is also obtained in the electroreflectance spectra for the spin-orbit split off edge, as can be seen in Fig. 2.

The energy of the spin-orbit splitting Δ_0 is 0.350 ± 0.004 eV in the whole temperature region from 300° to 25°K, and agrees well with the other experimental results[21, 24]. The temperature dependences of the peak energies of E_1 , E_{ex} and $E_{ex} + \Delta_0$ are shown in Fig. 4. Considering the fact that the exciton binding energy in GaAs is small, the values of E_{ex} and $E_{ex} + \Delta_0$ at high temperatures should be attributed to the fundamental edge, $\Gamma_8 - \Gamma_6$ edge,

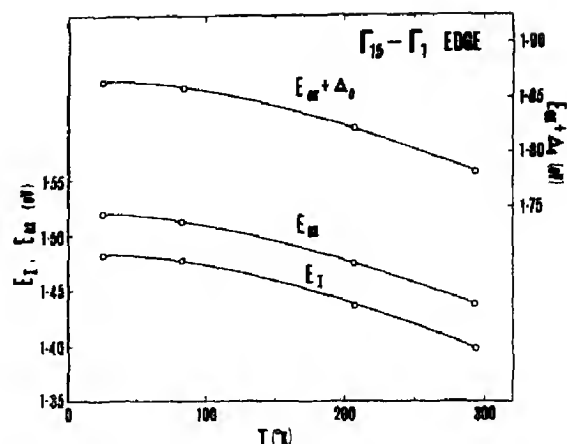


Fig. 4. Temperature dependence of the peak positions indicated by E_1 , E_{ex} and $E_{ex} + \Delta_0$ in the electroreflectance spectra in the energy region 1.3–2.0 eV.

and its spin-orbit split off edge, $\Gamma_7 - \Gamma_6$ edge, respectively. The temperature coefficients of E_{ex} and $E_{ex} + \Delta_0$ at a high temperature range is consistent with those obtained by Seraphin [21], but that of E_1 is almost the same as those of E_{ex} and $E_{ex} + \Delta_0$ in contrast with Seraphin's result.

(b) $\Lambda_3 - \Lambda_1$ transition

Figure 5 shows the electroreflectance spectra near $\Lambda_3 - \Lambda_1$ transition edges for three different temperatures. While the thermal broadening effect on the line shape can be seen, as near $\Gamma_{15} - \Gamma_1$ transition edges, the line shape itself changes slightly from room temperature to 25°K. This situation is a little different from that in germanium[17] where a large variation of the line shape has been observed near the $\Lambda_3 - \Lambda_1$ transition edges in the same temperature range. However, the line shape at low temperatures resemble those expected from $M_1(\perp)$ type critical point in the theory of electro-optical effect[1], just as germanium. The $E_1(1)$ peak in Fig. 5 is determined as a structure related to $\Lambda_3 - \Lambda_1$ transition edge on the basis that the peak energy is independent of the modulation voltage and also the peak has the same polarity as that of the fundamental edge. At room temperature the locations of $E_1(1)$ and its spin-

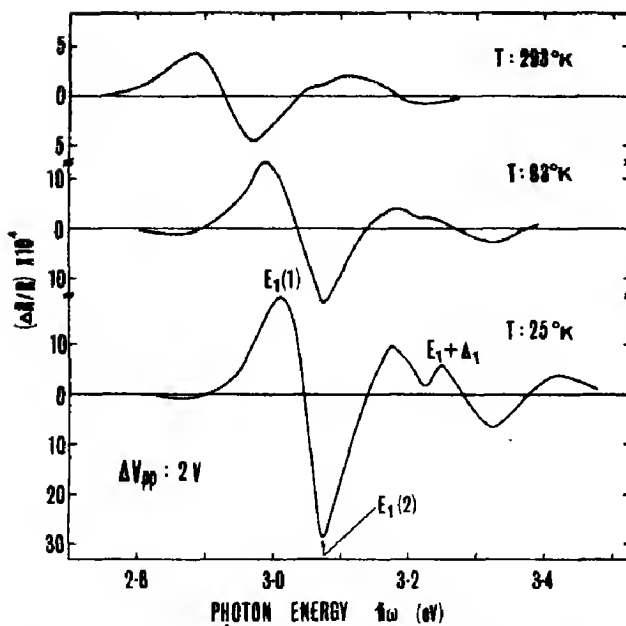


Fig. 5. Electroreflectance spectra in the energy region 2.7–3.5 eV at three different temperatures with the same bias voltage, $V_{DC} = -1.0$ V and $\Delta V_{pp} = 2.0$ V.

orbit split off edge $E_1(1) + \Delta_1$ are 2.89 and 3.12 eV, and Δ_1 is 0.23 eV. These values agree well with those obtained by the already reported electroreflectance measurements [14, 23]. The energies of $E_1(1)$, $E_1(1) + \Delta_1$ and Δ_1 determined at 25°K are 3.010 ± 0.002 , 3.244 ± 0.004 eV and 0.234 ± 0.004 eV, respectively.

In order to analyze these line shapes in Fig. 5, we have compared them with a line shape expected from electro-optical theory including the thermal broadening effect. The electro-optical functions $F(\eta)$ and $G(\eta)^*$ with various factors Γ_T of Lorentzian type broadening have been calculated and then also an equally mixed spectrum of $\Delta\epsilon_1$ and $\Delta\epsilon_2$, since an expected electroreflectance signal around 3 eV in GaAs is a nearly equal mixture of $\Delta\epsilon_1$ and $\Delta\epsilon_2$ [2]; that is, $\Delta R/R \doteq \alpha(\omega)[\Delta\epsilon_1 + \Delta\epsilon_2]$. Moreover, a mixed spectrum of the electroreflectance signal $\Delta R/R$ at a M_1 type critical

point is calculated for the several cases with different mixture ratio D (the fraction between both contributions of $M_1(\perp)$ and $M_1(\parallel)$ type critical point), by considering the anisotropy of the reduced effective mass at Λ critical point. If one neglects this anisotropy and assumes that the transverse and the longitudinal reduced effective masses are the same at a M_1 critical point, it can be easily understood that the ratio D is roughly three to one from the numbers of Λ critical point of $M_1(\perp)$ and $M_1(\parallel)$ type when the electric field is in the [111] direction. Here we have tried an estimation of the thermal broadening factor Γ_T from the temperature dependences of the amplitudes of $E_1(1)$ and $E_1(2)$ peaks which correspond to $\Lambda_3 - \Lambda_1$ transition edge and the next higher energy side oscillation peak, respectively.

In Fig. 6 we show the Γ_T dependences of the amplitudes of $E_1(1)$ and $E_1(2)$ peaks in a calculated electroreflectance signal for M_1 type critical point. As can be seen in the figure, a

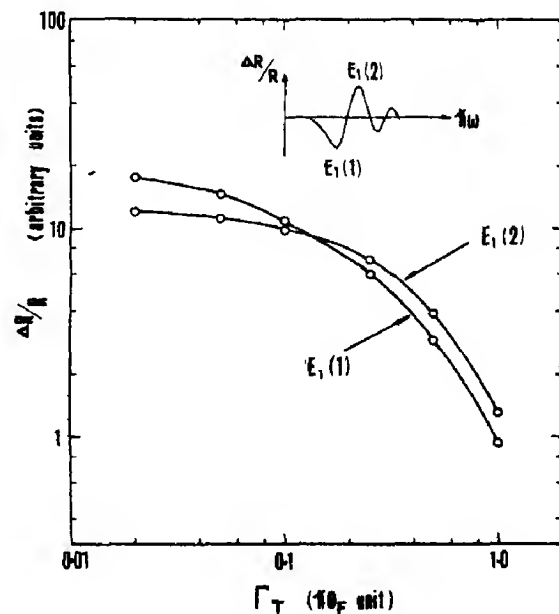


Fig. 6. Thermal broadening factor versus the amplitudes of $E_1(1)$ and $E_1(2)$ which correspond to an M_1 type critical point edge and the next higher energy side oscillation peak in calculated electroreflectance spectra with the mixture ratio $D = 20$. The definition of $\hbar\theta_F$ is the same as that given in Ref. [1].

*The definitions of the electro-optical functions $F(\eta)$ and $G(\eta)$ are given in Ref. [1], and the real and imaginary part of the change of dielectric constant with electric field, $\Delta\epsilon_1$ and $\Delta\epsilon_2$, are expressed by a combination of these two functions depending upon the type of critical points.

cross point occurs at $\Gamma_T \approx 0.15 \hbar\theta_F$; that is, at $\Gamma_T \leq 0.15 \hbar\theta_F$ the $E_1(1)$ amplitude is larger than $E_1(2)$, but at $\Gamma_T \geq 0.15 \hbar\theta_F$ $E_1(1)$ is smaller than $E_1(2)$. The cross point does appear in the narrow range of Γ_T from $0.1 \hbar\theta_F$ to $0.3 \hbar\theta_F$ for mixture ratio D between 3 and 25. As shown in Fig. 5 the experimental data indicate that $E_1(2)$ is always larger than $E_1(1)$ in the temperature region from 300° to 25°K. If it could be assumed that Γ_T is proportional to kT , one could obtain the similar curves between the Γ_T dependence of the $E_1(1)$ and $E_1(2)$ amplitudes of the calculated spectrum and the temperature dependence of those experimentally obtained. However, the fitness between the calculated and experimental curves is not so good because of the following three reasons. The first is that a slight difference in electric fields remains between spectra of different temperatures because we could not estimate the electric fields precisely. The second reason is the uncertainty of the mixture ratio D by the anisotropy of the reduced effective mass at Λ critical point in GaAs. The third is that an expected electroreflectance spectrum near 3 eV at $\Lambda_3 - \Lambda_1$ transition edge can not be precisely an equally mixed spectrum of $\Delta\epsilon_1$ and $\Delta\epsilon_2$; that is, $\alpha(\omega)$ and $\beta(\omega)$ are slightly dependent of photon energy. Although we could not obtain a precise value of Γ_T , from the results of the comparison we obtained that Γ_T is roughly $0.5 \hbar\theta_F$ at 25°K. This value of Γ_T can be compared with the value $\Gamma_T = 0.9 \hbar\theta_F$ at 77°K obtained from the electric field dependence of transverse electroreflectance at the fundamental edge of GaAs [28]. The value of Γ_T obtained here at 25°K would not therefore be an unreasonable one.

Figure 7 shows the calculated electroreflectance spectra for M_1 critical point with the broadening factor $\Gamma_T = 0.5 \hbar\theta_F$ for three different mixture ratios. For a small mixture ratio, oscillations remain in the lower energy side below the critical point edge $E_1(1)$, while there is no such oscillations in the experimental data. The line shape for $D = 20$ resembles

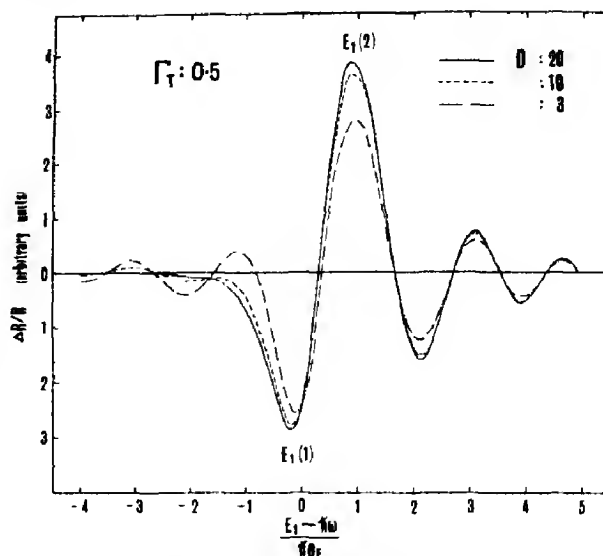


Fig. 7. Line shapes of calculated electroreflectance signals with the thermal broadening factor $\Gamma_T = 0.5 \hbar\theta_F$ for three values of the mixture ratio of $M_1(\perp)$ and $M_1(\parallel)$ type critical point.

well those experimentally observed. This fact implies that the anisotropy of the reduced effective mass at $\Lambda_3 - \Lambda_1$ transition edge in GaAs is quite large. And this is qualitatively reasonable according to the theoretical expectation that the reduced transverse masses are much larger than the longitudinal mass of negative sign [29].

In Fig. 8 we show a comparison between a calculated spectrum with $\Gamma_T = 0.5 \hbar\theta_F$ and the experimental one at 25°K. In the figure the calculated spectrum is normalized by the approach that the peak position and the amplitude of $E_1(1)$ signal and also the width of the $E_1(2)$ structure are put together to the experimental data. Since the agreement between the calculated and experimental line shapes is good, as can be seen in the figure, the electroreflectance spectra in the photon energy region 2.7–3.5 eV would be explained by the contribution from M_1 critical points including both types of $M_1(\perp)$ and $M_1(\parallel)$. Quite recently Shaklee, Rowe and Cardona [30] have pointed out the existence of a hyperbolic exciton at the $\Lambda_3 - \Lambda_1$ transition edge from their wavelength-modulation experiments. Although it

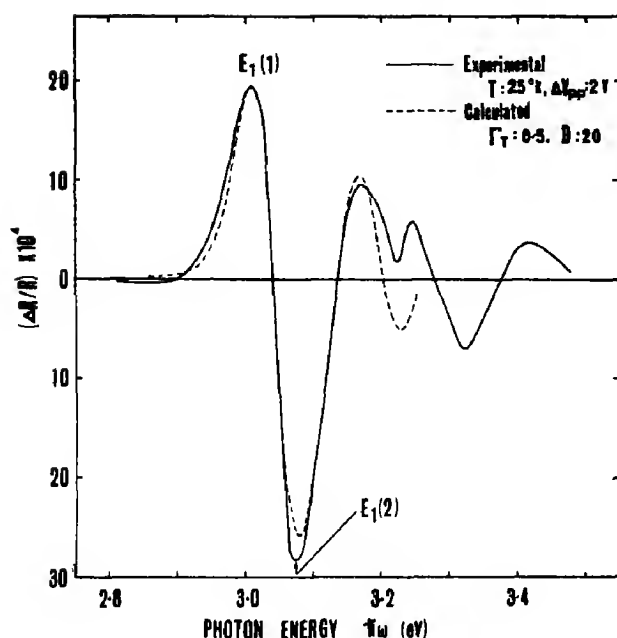


Fig. 8. A comparison between the electroreflectance signal at 25°K and the calculated spectrum in the case of $\Gamma_t = 0.5 \hbar\theta_F$ and $D = 20$.

is very hard to identify the hyperbolic exciton effect from our electroreflectance spectra near $\Lambda_3 - \Lambda_1$ transition edge of GaAs, it should be mentioned that it is also possible to explain the line shape at $\Lambda_3 - \Lambda_1$ transition edge only in terms of the thermally broadened electroreflectance associated with M_1 critical points having both $M_1(\perp)$ and $M_1(\parallel)$ types.

Figure 9 shows the temperature dependence

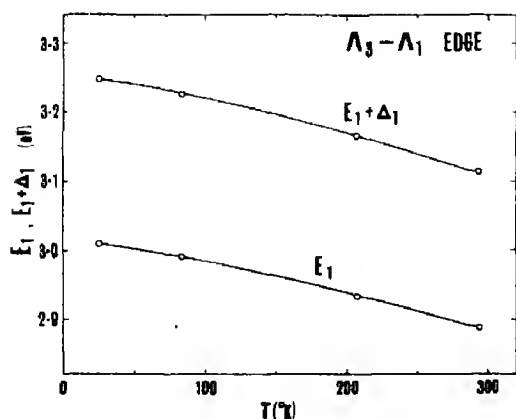


Fig. 9. Temperature dependence of the peak positions related to the edges of $\Lambda_3 - \Lambda_1$ transition and its spin-orbit split off band.

of the peak positions expressed by E_1 and $E_1 + \Delta_1$ which correspond to $\Lambda_3 - \Lambda_1$ transition edge and its spin-orbit split off edge. In the temperature region from 300° to 25°K the spin-orbit splitting Δ_1 is nearly constant and 0.234 ± 0.004 eV. The temperature coefficients at high temperatures are a little larger than those at the fundamental edge. The similar result has been already obtained by Seraphin[21].

Acknowledgement—The authors would like to thank Mr. Y. Hashimoto for his technical assistance during the course of experimental work.

REFERENCES

1. ASPNES D. E., *Phys. Rev.* **147**, 554 (1966); *ibid.* **153**, 972 (1967).
2. SERAPHIN B. O. and BOTTKA N., *Phys. Rev.* **145**, 628 (1966).
3. ENDERLEIN R. and KEIPER R., *Phys. Status Solidi* **23**, 127 (1967).
4. AYMERICH F. and BASSANI F., *Nuovo Cim.* **48**, 359 (1967).
5. ASPNES D. E., HANDLER P. and BLOSSEY D. F., *Phys. Rev.* **166**, 921 (1968).
6. DUKE C. B., *Phys. Rev. Lett.* **15**, 625 (1965).
7. DUKE C. B. and ALFERIEFF M. E., *Phys. Rev.* **145**, 583 (1966).
8. ENDERLEIN R., *Phys. Status Solidi* **26**, 509 (1968).
9. RALPH H. I., *J. Phys. C* **1**, 378 (1968).
10. FROVA A., HANDLER P., GERMANO F. A. and ASPNES D. E., *Phys. Rev.* **145**, 575 (1965).
11. HAMAKAWA Y., GERMANO F. A. and HANDLER P., *Phys. Rev.* **167**, 703 (1968).
12. SERAPHIN B. O., HESS R. B. and BOTTKA N., *J. appl. Phys.* **36**, 2242 (1965).
13. SERAPHIN B. O., *Phys. Rev.* **140**, A1716 (1965).
14. CARDONA M., SHAKLEE K. L. and POLLAK F. H., *Phys. Rev.* **154**, 696 (1967).
15. GHOSH A. K., *Phys. Rev.* **165**, 888 (1968).
16. HAMAKAWA Y., HANDLER P. and GERMANO F. A., *Phys. Rev.* **167**, 709 (1968).
17. NISHINO T. and HAMAKAWA Y., *J. phys. Soc. Japan* **26**, 403 (1969).
18. IKEDA K., HAMAKAWA Y., KOMIYA H. and IBUKI S., *Phys. Lett.* **28A**, 647 (1969).
19. REHN V. and KYSER D. S., *Phys. Rev. Lett.* **18**, 848 (1967).
20. FORMAN R. A. and CARDONA M., *Proc. Int. Conf. II-VI Semiconducting Compounds*, p. 100. Providence (1967).
21. SERAPHIN B. O., *J. appl. Phys.* **37**, 721 (1966).
22. THOMPSON A. G., CARDONA M., SHAKLEE K. L. and WOOLLEY J. C., *Phys. Rev.* **146**, 601 (1966).

23. WILLIAMS E. W. and REHN V., *Phys. Rev.* **172**, 798 (1968).
24. STURGE M. D., *Phys. Rev.* **127**, 768 (1962).
25. SZE S. M. and IRVIN J. C., *Solid-St. Electron.* **11**, 599 (1968).
26. GILLES M. A., BAILEY P. T. and HILL, D. E., *Phys. Rev.* **174**, (1968).
27. WILLIAMS E. W., *Solid-St. Commun.* **4**, 585 (1966).
28. FORMAN R. A., ASPNES D. E. and CARDONA M., To be published.
29. CARDONA M., *J. Phys. Chem. Solids* **24**, 1543 (1963).
30. SHAKLEE K. L., ROWE J. E. and CARDONA M., *Phys. Rev.* **174**, 828 (1968).

INTERPRÉTATION DE LA SUSCEPTIBILITÉ MAGNÉTIQUE DE L'OXYSULFURE DE SAMARIUM PAR UN MODÈLE DE CHAMP CRISTALLIN

J. ROSSAT-MIGNOD, R. BALLESTRACCI, G. QUEZEL, C. LINARES* et F. TCHEOU
Centre d'Etudes Nucléaires, Cedex 85, 38-Grenoble-Gare et Centre National de la Recherche
Scientifique, Cedex 166, 38-Grenoble-Gare, France

(Received 13 May 1969)

Résumé— La susceptibilité paramagnétique d'un échantillon polycristallin d'oxysulfure de samarium a été mesurée entre 3° et 300°K. Elle est interprétée avec une approximation du potentiel cristallin de la forme

$$V_c = \alpha_1 V_2^0 O_2^0 + \beta_1 V_4^0 O_4^0 + \beta_2 V_4^3 O_4^3$$

et corrigée d'un terme dû à l'échange. On a calculé les niveaux d'énergie et les paramètres de champ cristallin. L'étude de la fluorescence de $Gd_2O_2S: Sm^{3+}$ et $Y_2O_2S: Sm^{3+}$ a confirmé ces résultats.

Abstract— The paramagnetic susceptibility of polycrystalline samarium oxysulfide has been measured between 3° and 300°K. The data are interpreted with an approximation to the crystal potential of the form

$$V_c = \alpha_1 V_2^0 O_2^0 + \beta_1 V_4^0 O_4^0 + \beta_2 V_4^3 O_4^3$$

and correction taking into account exchange is made. The energy levels and crystal fields parameters have been calculated. Fluorescence studies of $Gd_2O_2S: Sm^{3+}$ and $Y_2O_2S: Sm^{3+}$ have confirmed these results.

INTRODUCTION

L'ÉTUDE par diffraction neutronique des oxysulfures de terres rares T_2O_2S [1] a montré l'existence de plusieurs types d'ordre magnétique au-dessous de la température de Néel ($T = Tb, Dy, Ho$). On a étudié l'oxysulfure de samarium dans le but de préciser le rôle du champ cristallin dans ce type de composés; on sait en effet que la variation des paramètres de champ cristallin est faible lorsqu'on passe d'une terre rare à l'autre.

La structure cristalline des oxysulfures de terres rares peut être décrite dans le groupe d'espace $P\bar{3}m$ avec

$$\begin{aligned} 2T &\text{ en } \pm \left(\frac{1}{3}, \frac{1}{3}, u\right) \text{ avec } u \sim 0,3 \\ 2O &\text{ en } \pm \left(\frac{1}{3}, \frac{1}{3}, v\right) \text{ avec } v \sim 0,6 \\ 1S &\text{ en } (0\ 0\ 0) \end{aligned}$$

Les paramètres hexagonaux de l'oxysulfure de samarium sont $a = 3,892 \text{ \AA}$ et $c = 6,714 \text{ \AA}$. Les ions de terres rares sont dans des sites équivalents de symétrie ponctuelle C_{3v} .

Pour cette symétrie il suffit de connaître trois paramètres pour déterminer complètement le champ cristallin agissant sur l'ion Sm^{3+} ($^6H_{5/2}$). L'étude de la susceptibilité paramagnétique a été faite en tenant compte de l'échange. L'existence d'une partie linéaire sur la courbe de susceptibilité magnétique a permis de préciser l'amplitude de la décomposition des niveaux et de déterminer un domaine d'existence des paramètres de champ cristallin.

Une étude de la fluorescence de l'ion Sm^{3+} a confirmé ces résultats. On a également interprété le spectre d'émission de l'ion Eu^{3+} , celui-ci étant plus intense et plus simple. On a choisi des matrices de Gd_2O_2S et Y_2O_2S pour

*Faculté des Sciences, 69-Villeurbanne.

obtenir la variation des paramètres de champ cristallin en fonction de l'environnement de l'ion activateur.

EXPRESSION THEORIQUE DE LA SUSCEPTIBILITE MAGNETIQUE

Dans cette symétrie, les éléments de matrice non nuls de l'hamiltonien de champ cristallin, pour une configuration $4f^n$ de l'ion terre rare, sont obtenus à partir des termes du potentiel cristallin exprimés en fonction des harmoniques sphériques Y_2^0, Y_4^0, Y_6^0 et des combinaisons $Y_4^{-3} - Y_3^4, Y_6^{-3} - Y_6^3, Y_6^0 + Y_6^{-6}$ [2]. Dans le cadre d'un calcul de perturbations au premier ordre, le technique des opérateurs équivalents de Stevens permet d'écrire l'hamiltonien sous la forme plus utilisable

$$V_c = \alpha_J V_2^0 O_2^0 + \beta_J V_4^0 O_4^0 + \beta_J V_4^3 O_4^3 + \gamma_J V_6^0 O_6^0 + \gamma_J V_6^3 O_6^3 + \gamma_J V_6^6 O_6^6.$$

$\alpha_J, \beta_J, \gamma_J$ sont les facteurs multiplicatifs de champ cristallin et ont été tabulés par Stevens et Judd [3, 4]; ils figurent dans le Tableau 1 pour les ions Sm^{3+} et Eu^{3+} .

Tableau 1

	Eu^{3+}		Sm^{3+}
	7F_1	7F_2	${}^6H_{5/2}$
α_J	-1/5	-11/315	13/315
β_J	0	-2/189	26/10395
γ_J	0	0	0

Pour l'ion Sm^{3+} l'hamiltonien de champ cristallin relatif au niveau fondamental ${}^6H_{5/2}$ s'écrit alors:

$$V_c = \alpha_{5/2} V_2^0 O_2^0 + \beta_{5/2} V_4^0 O_4^0 + \beta_{5/2} V_4^3 O_4^3.$$

Si $\Gamma_4, \Gamma_5, \Gamma_6$ sont les représentation irréductibles du groupe double C_{3v} , on a

$$D_{5/2} = ({}^4\Gamma_5 + {}^1\Gamma_6) + 2{}^2\Gamma_4 [5].$$

Le niveau $J=5/2$ est donc décomposé par

le champ cristallin en trois doublets de Kramers dont les états propres sont au premier ordre du calcul des perturbations:

$$\begin{aligned} |A\rangle &= \cos\theta |5/2\rangle + \sin\theta | -1/2\rangle \\ |B\rangle &= -\sin\theta |5/2\rangle + \cos\theta | -1/2\rangle \\ |C\rangle &= |3/2\rangle. \end{aligned}$$

L'expression générale de la susceptibilité par molécule-gramme est la suivante:

$$\chi T = 2 \cdot \frac{N\mu_B^2 g_J^2}{3k Z} \times \sum_A \left(M_{AA} - 2kT \sum_{B \neq A} \frac{M_{AB}}{E_A - E_B} \right) e^{-(E_A/kT)} + \alpha' T$$

$$\text{avec } Z = 2 \sum_A e^{-(E_A/kT)}$$

$$g_J = 2/7$$

$$M_{AB} = 2 \left| \langle A | J_z | B \rangle \right|^2 + \left| \langle A | J_z | \bar{B} \rangle \right|^2 + 4 \left| \langle A | J_x | B \rangle \right|^2 + \left| \langle A | J_x | \bar{B} \rangle \right|^2$$

Les états $|\bar{A}\rangle$ et $|\bar{B}\rangle$ étant les états renversés dans le temps de $|A\rangle$ et $|B\rangle$. α' traduit la contribution à la susceptibilité indépendante de la température qui a pour origine le faible écart entre le niveau fondamental $J=5/2$ et le premier excité $J=7/2$ (environ 1500°K). A l'aide de l'expression donnée par Van Vleck [6] on a calculé ce terme: $\alpha' = 14,3 \cdot 10^{-4}$ uem/mole.

On résume les interactions d'échange, dans l'approximation du champ moléculaire ($H_{ex} = -\lambda M$), en écrivant la susceptibilité totale χ_t sous la forme:

$$\frac{1}{\chi_t} = \frac{1}{\chi} + \lambda$$

où χ est la susceptibilité paramagnétique sans échange. Dans les domaines de température où kT est faible devant l'écart entre niveaux de champ cristallin χT suit une loi de la forme $\chi T = C + \alpha T$ alors

$$\chi_i T = C_i + \alpha_i T = \frac{C + \alpha T}{1 + \alpha \lambda + \frac{\lambda C}{T}}$$

$$\chi_i T \approx (C + \alpha T) \left(1 - \alpha \lambda - \frac{\lambda C}{T} \right) \text{ pour } T > \theta_p.$$

θ_p étant la température de Curie paramagnétique ($\theta_p = -\lambda C$)

$$C_i \approx C(1 - 2\alpha\lambda)$$

et

$$\Delta C = C_i - C = 2\alpha\theta_p.$$

Pour un composé antiferromagnétique l'affaiblissement de la constante de Curie dû à l'échange est d'autant plus fort que le paramagnétisme constant est plus important.

MESURES MAGNETIQUES ET INTERPRETATION

La mesure de la susceptibilité paramagnétique de l'oxysulfure de samarium a été effectuée entre 2° et 300°K par une méthode de translation. Entre 10° et 50°K, la courbe expérimentale $\chi_i T(T)$ est linéaire avec une pente $\alpha_i = 25 \cdot 10^{-4}$ uem/mole et une constante de Curie $C_i = 4 \cdot 10^{-2}$ uem/mole.

Dans ce domaine de température seul le niveau fondamental est peuplé alors:

$$C = \frac{2N\mu_B^2 g_J^2}{3k} M_{ff}.$$

On peut alors estimer la valeur de C , donc de M_{ff} , connaissant la constante de Curie expérimentale C_i , le paramagnétisme constant α_i et la valeur de λ (valeur de $1/\chi_i$ pour $T=0$).

On trouve $\lambda = 100$ uem/mole

$$M_{ff} = 7.$$

Or

$$M_{AA} = \frac{(6 \cos^2 \theta - 1)^2}{2} = 9(1 - \cos^2 \theta)^2$$

$$M_{BB} = \frac{(5 - 6 \cos^2 \theta)^2}{2} + 9 \cos^4 \theta$$

$$M_{CC} = 4,5.$$

Le niveau $|C\rangle = |3/2\rangle$ ne peut donc pas être le fondamental. Il est loisible de prendre pour niveau fondamental

$$|B\rangle = -\sin \theta |5/2\rangle + \cos \theta |-1/2\rangle$$

dans ce cas, on doit avoir $\cos^2 \theta = 0,88$.

On pose

$$\langle 5/2 | V_c | 5/2 \rangle = a = 10\alpha_J V_2^0 + 60\beta_J V_4^0$$

$$\langle -1/2 | V_c | -1/2 \rangle = b = -8\alpha_J V_2^0 + 120\beta_J V_4^0$$

$$\langle 5/2 | V_c | -1/2 \rangle = c = 3\sqrt{10}\beta_J V_4^0$$

$$\langle 3/2 | V_c | 3/2 \rangle = -(a+b).$$

Alors

$$E_c = -(a+b)$$

$$E_A = \frac{a+b}{2} + \sqrt{\left(\frac{a-b}{2}\right)^2 + c^2}$$

$$E_B = \frac{a+b}{2} - \sqrt{\left(\frac{a-b}{2}\right)^2 + c^2}.$$

Sachant que

$$\cotg \theta = \frac{a-b}{2c} + \sqrt{\left(\frac{a-b}{2c}\right)^2 + 1},$$

on déduit une relation entre les trois paramètres de champ cristallin

$$V_4^3 = 12,5 V_2^0 - 3,8 V_4^0.$$

D'autre part

$$E_c - E_B = -\frac{3}{2}(a+b) + \sqrt{\left(\frac{a-b}{2}\right)^2 + c^2}$$

$$E_A - E_B = 2\sqrt{\left(\frac{a-b}{2}\right)^2 + c^2}.$$

L'examen de la courbe de la susceptibilité [7] montre que l'amplitude totale de la décomposition du niveau $J = 5/2$ doit être inférieure à 300 cm^{-1} .

D'où

$$\begin{aligned} 0 < E_C - E_B < 300 \text{ cm}^{-1} \\ 0 < E_A - E_B < 300 \text{ cm}^{-1}. \end{aligned}$$

$$\begin{aligned} V_2^0 &= 70 \text{ cm}^{-1} \\ V_4^0 &= -220 \text{ cm}^{-1} \\ V_4^3 &= 1700 \text{ cm}^{-1}. \end{aligned}$$

On en déduit:

$$\begin{aligned} 0 < 0,35 V_2^0 - 0,82 V_4^0 < 300 \\ 0 < 12,5 V_2^0 - 3,8 V_4^0 < 4000. \end{aligned}$$

Dans le plan V_2^0, V_4^0 on a délimité le domaine d'existence possible des différents paramètres (Fig. 1).

Pour résoudre le problème de la détermination de ces paramètres à l'intérieur de ce domaine on a réalisé un programme de calcul de la susceptibilité magnétique. A partir d'un jeu de paramètres donné a priori et par une méthode itérative celui-ci s'efforce de faire coïncider la courbe expérimentale et la courbe calculée. Les jeux de paramètres ont été choisis de façon à quadriller ce domaine. L'accord a été réalisé pour les valeurs suivantes

La disposition des niveaux est alors la suivante (Fig. 2).

Sur la Fig. 3 sont représentées: la susceptibilité magnétique expérimentale; la susceptibilité calculée avec les paramètres précédents; la susceptibilité de l'ion libre calculée à partir de la formule de Van Vleck [6]; la susceptibilité calculée avec les paramètres précédents mais sans tenir compte du phénomène d'échange.

ETUDE DU SPECTRE DE FLUORESCENCE

Les oxysulfures $\text{Gd}_2\text{O}_2\text{S}$ et $\text{Y}_2\text{O}_2\text{S}$ activés par les ions trivalents Eu^{3+} et Sm^{3+} présentent une fluorescence rouge orangée assez intense. Le spectre d'émission de ces composés est constitué de raies caractéristiques de l'ion terre rare introduit. La longueur d'onde

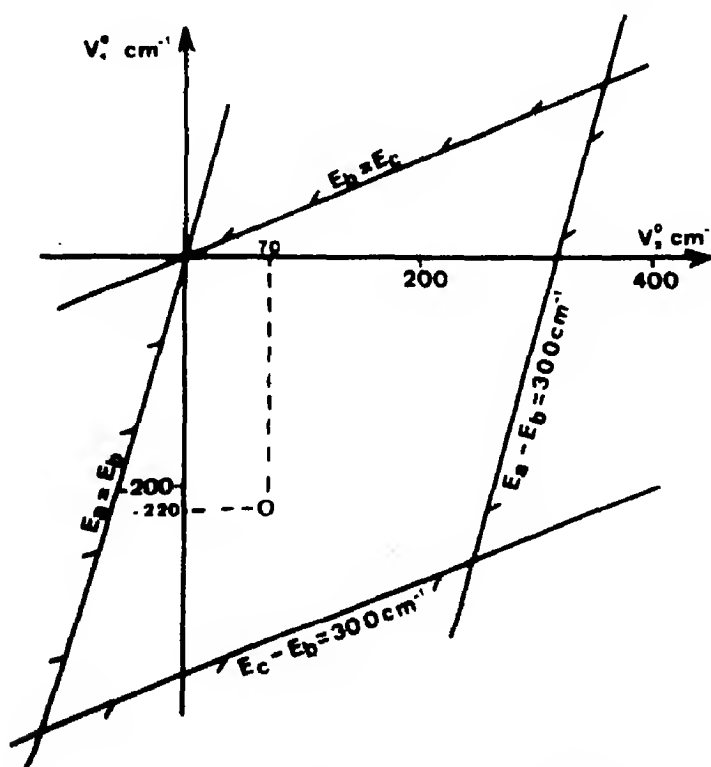
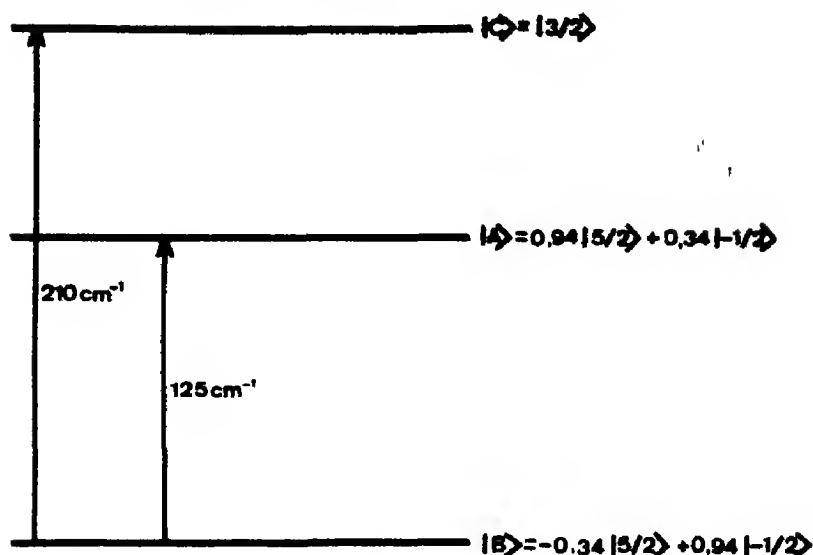
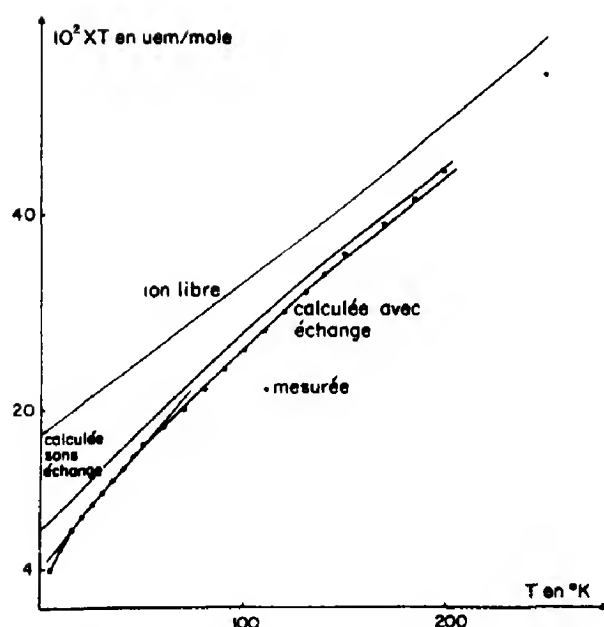


Fig. 1. Domaine d'existence des paramètres V_2^0 et V_4^0 sachant que $V_4^3 \approx 12,5 V_2^0 - 3,8 V_4^0$.

Fig. 2. Niveaux d'énergie et fonctions d'onde de l'ion Sm^{3+} dans $\text{Sm}_2\text{O}_2\text{S}$.Fig. 3. Susceptibilité de l'ion Sm^{3+} dans $\text{Sm}_2\text{O}_2\text{S}$.

excitatrice est 2537 \AA . L'étude est faite à la température de 77°K à l'aide d'un monochromateur Hilger Monospek (dispersion 8 \AA/mm).

En ce qui concerne l'euprimum trivalent, la terme fondamental est le multiplet ${}^7F_1 (J=0)$,

1, ... 6). L'émission de fluorescence de cet ion est due aux transitions entre les états excités 5D_J et les différents niveaux 7F_J . Les raies principales observées sont celles qui correspondent aux transitions entre le niveau excité 5D_0 et les niveaux 7F_0 , 7F_1 et 7F_2 décomposés par l'action du champ cristallin.

Dans le cas de $\text{Gd}_2\text{O}_2\text{S}$ on observe à $\lambda = 5833 \text{ \AA}$ ($\nu = 17139 \text{ cm}^{-1}$) une raie que l'on peut attribuer à la transition ${}^5D_0 \rightarrow {}^7F_0$, ce qui nous permet de fixer la position du niveau 5D_0 à 17139 cm^{-1} au-dessus de 7F_0 pris comme origine (Rappelons que cette transition $J = 0 \rightarrow J = 0$ est interdite sauf lorsque la symétrie du site est du type C_s , C_n ou C_{nv} ; on doit donc bien l'observer dans ces composés de symétrie C_{3v} [8]). Les autres raies principales s'interprètent bien en admettant que les états inférieurs des transitions sont les différents sous-niveaux 7F_1 et 7F_2 de l'ion libre décomposés par le champ cristallin. Dans le Tableau 2 sont indiqués les longueurs d'onde, les nombres d'onde et les identifications des différentes raies de $\text{Gd}_2\text{O}_2\text{S}$.

On constate que le nombre de raies est en accord avec une symétrie trigonale.

On a procédé de la même manière pour $\text{Y}_2\text{O}_2\text{S}$: Eu^{3+} et on peut établir le Tableau 3.

Tableau 2. $\text{Gd}_2\text{O}_2\text{S}:\text{Eu}^{3+}$

λ (Å)	ν (cm^{-1})	Niveau émetteur (cm^{-1})	Niveau terminal (cm^{-1})	Transition
5833	17139	17139	0	$^5\text{D}_0 \rightarrow ^7\text{F}_0$
5952	16796	17139	343	$^5\text{D}_0 \rightarrow ^7\text{F}_1$
5963	16765	17139	374	$^5\text{D}_0 \rightarrow ^7\text{F}_1$
6168	16208	17139	931	$^5\text{D}_0 \rightarrow ^7\text{F}_2$
6262	15965	17139	1174	$^5\text{D}_0 \rightarrow ^7\text{F}_2$
6298	15873	17139	1266	$^5\text{D}_0 \rightarrow ^7\text{F}_2$

Tableau 3. $\text{Y}_2\text{O}_2\text{S}:\text{Eu}^{3+}$

λ (Å)	ν (cm^{-1})	Niveau émetteur (cm^{-1})	Niveau terminal (cm^{-1})	Transition
5832	17141	17141	0	$^5\text{D}_0 \rightarrow ^7\text{F}_0$
5951	16799	17141	342	$^5\text{D}_0 \rightarrow ^7\text{F}_1$
5964	16762	17141	379	$^5\text{D}_0 \rightarrow ^7\text{F}_1$
6170	16203	17141	938	$^5\text{D}_0 \rightarrow ^7\text{F}_2$
6265	15957	17141	1184	$^5\text{D}_0 \rightarrow ^7\text{F}_2$
6305	15856	17141	1285	$^5\text{D}_0 \rightarrow ^7\text{F}_2$

Si l'on compare les Tableaux 2 et 3, on constate que l'écart entre les composantes extrêmes des niveaux $^7\text{F}_1$ et $^7\text{F}_2$ est plus grand pour $\text{Y}_2\text{O}_2\text{S}$ (respectivement 37 et 347 cm^{-1}) que pour $\text{Gd}_2\text{O}_2\text{S}$ (31 et 335 cm^{-1}). La perturbation due au remplacement d'un ion par un autre est d'autant plus importante que les rayons de ces ions sont plus différents. Il est donc logique que l'amplitude de la décomposition des niveaux par le champ cristallin soit plus faible pour $\text{Gd}_2\text{O}_2\text{S}$ que pour $\text{Y}_2\text{O}_2\text{S}$.

Les résultats obtenus pour l'ion Eu^{3+} permettent d'interpréter plus facilement le spectre d'émission de l'ion Sm^{3+} . Pour ce dernier, le

niveau fondamental est $^6\text{H}_{5/2}$. Le premier niveau émetteur possède un nombre quantique $J = 5/2$ (la valeur de L n'est pas encore connue avec certitude). Les raies d'émission qui permettent d'atteindre les trois composantes du niveau $^6\text{H}_{5/2}$ sont consignées dans le Tableau 4.

On obtient un tableau analogue pour $\text{Y}_2\text{O}_2\text{S}:\text{Sm}^{3+}$.

Si on compare comme plus haut, les écarts entre niveaux extrêmes, on trouve 174 cm^{-1} pour $\text{Gd}_2\text{O}_2\text{S}$ et 204 cm^{-1} pour $\text{Y}_2\text{O}_2\text{S}$, la différence est encore plus marquée que dans le cas de Eu^{3+} .

Tableau 4. $\text{Gd}_2\text{O}_2\text{S}:\text{Sm}^{3+}$

λ (Å)	ν (cm^{-1})	Niveau émetteur (cm^{-1})	Niveau terminal (cm^{-1})	
5637	17735	17735	0	
5641	17722	17722	0	
5646	17706	17706	0	
5666	17644	17735	91	moy 89
5669	17635	17722	87	
5693	17560	17735	175	moy 174
5697	17548	17722	174	
5702	17532	17706	174	

Tableau 5. Y_2O_3S : Sm^{3+}

(Å)	ν (cm^{-1})	Niveau émetteur (cm^{-1})	Niveau terminal (cm^{-1})
5620	17788	17788	0
5636	17738	17738	0
5639	17728	17728	0
5665	17647	17788	141
5686	17582	17728	146
5701	17535	17738	203
5705	17523	17728	205

moy 144

moy 204

Les spectres optiques permettent de déterminer les paramètres de champ cristallin. Pour les ions Eu^{3+} et Sm^{3+} le meilleur accord entre le calcul et l'expérience est obtenu pour les valeurs des paramètres indiquées dans le Tableau 6. Ils varient peu d'un composé à l'autre sauf pour la valeur V_4^3 du samarium.

Ces valeurs permettent de calculer la décomposition des niveaux 7F_1 et 7F_2 de Eu^{3+} et

Tableau 6

Composé	Activateur	V_2^0 (cm^{-1})	V_4^0 (cm^{-1})	V_4^3 (cm^{-1})
Gd_2O_3S	Eu^{3+}	+ 50	- 205	1100
	Sm^{3+}	+ 60	- 200	800
Y_2O_3S	Eu^{3+}	+ 60	- 220	1150
	Sm^{3+}	+ 60	- 205	2250

$^6H_{5/2}$ de Sm^{3+} , on peut établir les Tableaux 7 et 8.

Dans le première colonne sont consignées les valeurs expérimentales, dans la seconde les valeurs calculées, dans la troisième ces mêmes valeurs, mais à une translation près, de manière à obtenir le meilleur accord entre le calcul et l'expérience, enfin dans la dernière colonne les écarts entre le calcul et l'expérience. On remarque que ces écarts sont très faibles.

L'approximation du champ cristallin semble

Tableau 7. Gd_2O_3S

Activateur	Niveau	Expérience (1)	Calcul. (2)	(3)	$\Delta E(cm^{-1})$ (4)
Eu^{3+}	7F_1	343	- 10	344	1
		374	+ 20	374	0
	7F_2	931	- 166	932	1
		1174	+ 76	1174	0
		1266	+ 178	1266	0
Sm^{3+}	$^6H_{5/2}$	0	- 88	0	0
		89	+ 4	92	3
		174	+ 85	173	1

Tableau 8. Y_2O_3S

Activateur	Niveau	Expérience (1)	Calcul. (2)	(3)	ΔE (cm^{-1})
Eu^{3+}	7F_1	342	- 12	342	0
		379	+ 24	378	1
	7F_2	938	- 168	938	0
		1184	+ 78	1184	0
		1285	+ 180	1286	1
Sm^{3+}	$^6H_{5/2}$	0	- 114	2	2
		144	+ 26	142	2
		204	+ 87	203	1

donc assez bonne pour interpréter l'émission de ces activateurs, tout au moins en ce qui concerne les niveaux 7F_1 et 7F_2 de l'euporium et le niveau ${}^6H_{5/2}$ du samarium.

CONCLUSION

Dans cette étude on a mesuré la susceptibilité magnétique d'un échantillon polycristallin d'oxysulfure de samarium et on l'a interprété par un modèle de champ cristallin adapté à la symétrie C_{3v} . On a constaté que la contribution de l'échange est importante surtout à basse température. Cet effet est fonction du terme de paramagnétisme constant α ; la décroissance de χT pour les très basses températures est due au terme θ_p/T avec $\theta_p = -5^\circ K$. L'intégrale d'échange moyenne a été calculée égale à:

$$\frac{J}{k} = \frac{3}{2} \frac{1}{Z} \left(\frac{g_J}{g_J - 1} \right)^2 \frac{N \mu_B^2 \lambda}{3k} \frac{\lambda}{2}$$

$$\frac{J}{k} = 0,3^\circ K.$$

Z étant le nombre de voisins ~ 6 .

De 10° à $50^\circ K$ seule niveau fondamental $|B\rangle$ est peuplé. Dès $50^\circ K$ le premier niveau excité $|A\rangle$ commence à influencer la susceptibilité; on peut estimer qu'à $250^\circ K$ ce niveau est complètement peuplé. A partir de cette température la contribution du multiplet $J=7/2$ masque le rôle du dernier niveau excité du multiplet $J=5/2$.

Ce calcul comporte certaines approxima-

tions: d'une part on a assimilé le paramagnétisme constant dû au multiplet $J=7/2$ à celui de l'ion libre; d'autre part on a négligé l'effet du second ordre dans le calcul des vecteurs propres du multiplet $J=5/2$.

Malgré ces approximations on a déterminé les paramètres de champ cristallin. L'étude de la fluorescence de l'ion Sm^{3+} dans deux matrices différentes, complétée par celle de l'ion Eu^{3+} dans les mêmes matrices, fournit de façon directe des paramètres de champ cristallin très voisins de ceux obtenus précédemment.

Note: Dans une publication récente [9] Sovers et Yoshioka ont déterminé les paramètres de champ cristallin de l'ion Eu^{3+} à partir du spectre de fluorescence de $Y_2O_3S: Eu^{3+}$. Les résultats obtenus sont en désaccord avec les nôtres pour la valeur des paramètres V_4^0, V_4^3 . Cette divergence est due à la différence d'indexation des raies d'émission ${}^5D_0 \rightarrow {}^7F_2$: on n'a pas observé expérimentalement la raie ${}^5D_0 \rightarrow {}^7F_2(1)$ indiquée par Sovers et Yoshioka.

REFERENCES

1. BALLESTRACCI R., BERTAUT E. F. et QUEZEL G., *J. Phys. Chem. Solids* **29**, 1001 (1968).
2. HUTCHINGS M. T., *Solid St. Phys.* **16**, 227 (1964).
3. STEVENS K. W. H., *Proc. phys. Soc.* **A65**, 209 (1952).
4. JUDD B. R., *Mol. Phys.* **2**, 407 (1959).
5. STATZ H., *Phys. Rev.* **115**, 1568 (1959).
6. VAN VLECK J. H., *The Theory of Electric and Magnetic Susceptibilities*, pp. 233, 248. Oxford University Press, London (1932).
7. QUEZEL G., BALLESTRACCI R. et ROSSAT-MIGNOD J., À paraître.
8. BLASSE G. et BRIL A., *Philips Res. Rep.* **21**, 368 (1966).
9. SOVERS O. J. et YOSHIOKA T., *J. chem. Phys.* **49**, 4945 (1968).

SPIN-LATTICE RELAXATION OF ^{57}Fe NUCLEI IN YTTRIUM IRON GARNET*

SAMUEL M. MYERS and HORST MEYER

Department of Physics, Duke University, Durham, N.C. 27706, U.S.A.

and

J. P. REMEIKA

Bell Telephone Laboratories, Murray Hill, N.J. 07971, U.S.A.

(Received 17 April 1969)

Abstract—Pulse measurements of T_1 for ^{57}Fe nuclei in very pure, single crystals of YIG are reported. The temperature was varied from 2° to 292°K, and the externally applied field ranged from 0 to 6000 Oe. The temperature variation of T_1 is quite strong, being three orders of magnitude in the range 2°–40°K. At constant temperature, T_1 changed approximately one order of magnitude between saturation field and 6000 Oe. The data are compared with the results of a calculation by Beeman and Pincus, in which a second-order Raman process and the three-magnon process are assumed to predominate below 50°K. Agreement is only qualitative, the experimental values of T_1 being larger than predicted. At 4.2°K in zero field, it is found that a polycrystalline sample containing particles of $\approx 5 \times 10^{-4}$ cm dia. has a value of $1/T_1$ which is some two orders of magnitude larger than for a macroscopic crystal. The presence of a relaxation mechanism associated with surface effects is suggested.

1. INTRODUCTION

MEASUREMENTS of T_1 for ^{57}Fe nuclei in YIG were first reported by Robert and Winter[1]. However, in order to explain their data, these authors found it necessary to conclude that the predominant relaxation mechanism was associated with rare earth impurities. Only more recently have the methods of preparation advanced to the stage where very pure samples of YIG can be obtained.

The purpose of the present experiment was to measure the nuclear relaxation rate in samples of YIG which were sufficiently pure that the measurements were likely to be representative of YIG and not of impurities. In particular, a recent calculation of T_1 in YIG by Beeman and Pincus[2, 3] was to be checked experimentally.

2. THEORY

In their extensive treatment[3] of relaxa-

tion in magnetic insulators, Beeman and Pincus calculate T_1 explicitly for YIG in the temperature range 0°–50°K. The direct process, in which a nuclear spin flip is accompanied by the emission of a single spin wave, is forbidden by the law of energy conservation. In the absence of dipolar fields, relaxation by the scattering of a thermal magnon, the Raman process, is precluded on the basis of conservation of angular momentum. However, these authors point out that the electronic dipole-dipole interaction destroys the symmetry which requires conservation of angular momentum, permitting a second-order Raman process. Thus, a nuclear spin flips, creating a virtual spin wave via the hyperfine interaction. This virtual magnon is then scattered by a thermal magnon, through the electronic dipole-dipole interaction. Above approximately 30°K, the three-magnon process, in which the nuclear spin flip is accompanied by the annihilation of one spin wave and the creation of two others, becomes important.

*Research supported by a contract from the U.S. Office of Naval Research, Washington, D.C., and a grant from the U.S. Army Research Office, Durham, N.C.

The relation given in [3] for the second-order Raman process is

$$\frac{1}{T_1} = \frac{A^2}{\hbar^2 \omega_{ex}} \left(\frac{g \mu_B M}{\hbar \omega_{ex}} \right)^2 F \left(\frac{k_B T}{g \mu_B H} \right) \quad (1)$$

where A is the hyperfine coupling constant, μ_B the Bohn magneton, M the magnetization of the ferrimagnet, and H the effective field acting on the electronic spins. ω_{ex} is the spin wave dispersion constant, and is defined by the dispersion equation[4]

$$\hbar \omega(\mathbf{k}) = \hbar \omega_{ex} a^2 k^2 + g \mu_B (H_0 + H_A - H_D) + 2\pi g \mu_B M \sin^2 \theta_k \quad (2)$$

where $\hbar \omega$ is the energy of a magnon having wave-vector \mathbf{k} , a the lattice constant, H_0 the applied field, H_A the effective anisotropy field, H_D the demagnetizing field, and θ_k the angle between \mathbf{k} and \mathbf{M} (a minus sign has been inserted before H_D so that all the variables will be positive). However, equation (1) was derived using a simplified form of equation (2)[3]:

$$\hbar \omega(\mathbf{k}) = \hbar \omega_{ex} a^2 k^2 + g \mu_B H. \quad (3)$$

The third term on the right hand side in equation (2), which is due to dipolar interactions, was omitted to simplify the calculation.

The function F is a linear combination of two integrals which must be evaluated by numerical methods. However, for the temperatures and fields of this experiment, $F(k_B T / g \mu_B H)$ is nearly proportional to $(T/H)^2$. Using this approximation and taking $A = 1.72 \times 10^{-19}$ ergs and $\omega_{ex} = 5.65 \times 10^{12}$ sec⁻¹ from NMR work[5] $M = 196$ Oe from total magnetization measurements[6], and $g = 2$, one obtains[7]

$$\left(\frac{1}{T_1} \right)_{2M} \approx 1160 \left(\frac{T}{H} \right)^2 \text{sec}^{-1} \quad (4)$$

for the D -sublattice, where H is expressed in Oe.

The contribution of the three-magnon process is given by

$$\left(\frac{1}{T_1} \right)_{3M} = 8 \left(\frac{A^2}{\hbar \omega_{ex}} \right) \left[\frac{7.6}{16S(2\pi)^5} \right] \left(\frac{k_B T}{\hbar \omega_{ex}} \right)^{7/2} \text{sec}^{-1} \quad (5)$$

where S is the electronic spin of the ions. For the Fe^{+3} ion $S = 5/2$, and equation (5) reduces to

$$\left(\frac{1}{T_1} \right)_{3M} \approx 13.5 \left(\frac{T}{100} \right)^{7/2} \text{sec}^{-1} \quad (6)$$

for the D -sublattice resonance. Then the nuclear relaxation rate is given by

$$\frac{1}{T_1} = \left(\frac{1}{T_1} \right)_{2M} + \left(\frac{1}{T_1} \right)_{3M} \quad (7)$$

since the two relaxation processes are considered to be mutually independent.

3. SAMPLES AND EXPERIMENTAL PROCEDURE

Measurements were made on three single crystal spheres of YIG, which will be referred to as samples #1, #2, and #3, respectively. Sample #1 had a diameter of 0.080 in., which varied less than 0.001 in. over the sphere. Its surface was highly polished. Samples #2 and #3 were less accurately spherical, having a diameter of approximately 0.135 in. which varied over a range of 0.020 in. as a function of direction. Crystals #2 and #3 also had small surface irregularities.

It should be pointed out that, while a slightly non-spherical shape is known to be disastrous for FMR measurements, its effect is not expected to be important for NMR work. This is true because, in the former case, the quantity being measured is the spectral width of the magnetic field for resonance, and the field within the sample must therefore be extremely homogeneous. In contrast, the nuclear relaxation rate is determined by the magnitude of the internal

field instead of its spectral width, so that the homogeneity requirement is much less stringent.

The three samples were prepared with less than 1 ppm rare earth impurities and less than 10 ppm Ca and Si impurities. Crystals #2 and #3 were prepared from the same batch of materials, while crystal #1 was from a different one.

The samples were placed in a perforated Teflon container, which in turn was enclosed in the radio frequency coil. The cavity was sufficiently large to allow the sample to rotate freely, so that when an external magnetic field was applied, the crystal would orient with a [111] axis, which is the easy direction, along the field. That the sample did orient properly is shown by the fact that the three NMR resonances of YIG did not shift in frequency as the applied field varied from zero to saturation field. Also, T_1 measurements made on Yb-doped YIG [8] have given consistent results whether orientation was achieved by free rotation or by X-ray diffraction. This is a sensitive check because T_1 is very anisotropic in Yb-YIG.

The sample cavity was located in an electrolytic copper can, which contained approximately 500 μ of ^4He exchange gas to provide thermal contact with the sample. An outer can surrounded the copper can, providing an isolation space which was pumped to a high vacuum. The top flanges of the two cans were mounted approximately 6 in. apart on the stainless steel tubing of the cryostat, in order to provide thermal isolation. The entire assembly was immersed in a liquid ^4He bath, with the sample area between the poles of an electromagnet.

Temperatures above 4.2°K were achieved by means of a resistance wire heater attached to the sample can. A Cryo-Cal germanium resistance thermometer, connected in a four-lead configuration to a Leeds and Northrup K-3 potentiometer, was used to measure temperatures below 4°K. Above this temperature, a Leeds and Northrup Model

8164 platinum wire resistor was used. These thermometers were calibrated in another cryostat [5] using a constant-volume gas thermometer. The gas thermometer was in turn calibrated using the vapor pressures of ^4He , neon, and nitrogen, and the ice point. The estimated uncertainty in calibration ranges from ± 10 mdeg at 5°K to ± 30 mdeg at 40°K and $\pm 0.2^\circ$ at 200°K.

A carbon resistor was also installed in the cryostat, to be used as a sensor for the temperature regulation system. This resistor was connected to an a.c. bridge, whose imbalance signal was fed into a phase-sensitive detector. The output of the lock-in powered the cryostat heater, thus regulating the sample temperature. By this method the temperature could be held fixed to within ± 10 mdeg for an indefinite period. The carbon resistor, in which the magnetoresistive effect was negligible, was also used to correct for this effect in the germanium thermometer.

The range of fields and temperatures over which data could be taken was limited by two factors: signal-to-noise and the high values of T_1 . The signal-to-noise ratio is inversely proportional to applied field because of the corresponding decrease in enhancement, and inversely proportional to temperature by Curie's law. Thus work was restricted primarily to low fields and to temperatures below 40°K. However, in the range 120°–190°K at saturation field, the signal-to-noise ratio was sufficiently large and T_1 sufficiently small to permit the use of a boxcar integrator to average the signal.

The longitudinal relaxation rate was measured by the standard technique of applying a 90-deg pulse, waiting for a variable time, and observing the height of the echo produced by a 90–180 pulse sequence. The spectrometer has been described elsewhere [5]. R.F. pulses of approximately 100 V peak-to-peak were applied to the sample coil, with widths ranging up to 20 μsec . Exponential recoveries were observed in all the single-crystal samples, but not in two

samples containing microscopic crystals. The latter case is discussed in Section 4.

4. RESULTS AND DISCUSSION

The data to be discussed in the following paragraphs were all taken on the *D*-sublattice resonance. The signal-to-noise ratio for the two *A*-sublattice resonances is much smaller, but some data were taken on these resonances at temperatures below 4.2°K. The field and temperature dependences were the same, within scatter, as for the *D*-sites, but T_1 was systematically shorter by 20 ± 10 per cent. According to equations (1) and (2), T_1 is inversely proportional to the square of the hyperfine coupling constant A . Assuming this, T_1 for the *A*-sites should be shorter than for *D*-sites by a factor of approximately 0.75. It should be pointed out, however, that the A^2 term occurs in the expressions for a number of relaxation mechanisms[9]. Hence this agreement between theory and experiment does not bear on the applicability of equations (1) and (2) in particular.

Data were taken as a function of applied magnetic field at 4.2°K and at 10°K, and the results are shown in Fig. 1. The field dependence is the same at both temperatures up to approximately 2000 Oe., beyond which there appears to be a slight systematic deviation.

There is a degree of ambiguity in comparing the data with the Beeman-Pincus theory, because the anisotropic term in the magnon energy gap was neglected in deriving equation (1). As pointed out in [3], equation (3) is a good approximation in the limit of high fields where $H_0 \gg 2\pi M$. Unfortunately, $2\pi M \approx 1200$ Oe, which is comparable with the fields of this experiment. As explained in Section 3, data could not be taken at very high fields because the signal-to-noise ratio was too small at these fields. Pincus[10] has suggested that two of the terms in equation (2), namely $H_D = 820$ Oe and $2\pi M(\sin^2 \theta_k) = 0$ to 1320 Oe, may partially cancel, and that, since H_A is only of the order of 170 Oe[11], a reasonable first approximation might take $H \approx H_0$.

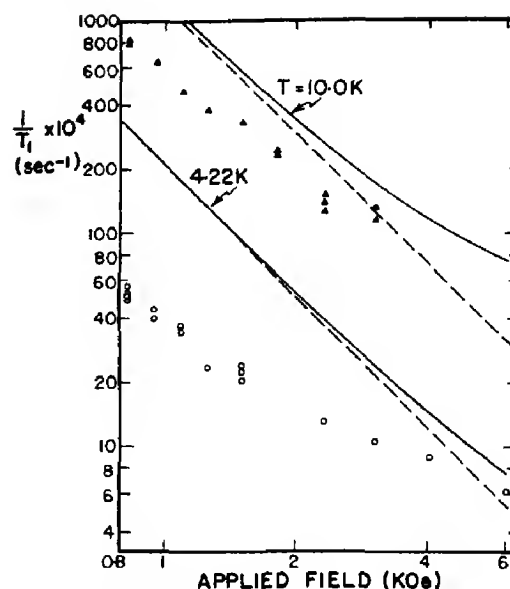


Fig. 1. The field dependence of T_1 for *D*-sites in YIG, from samples #1 and #3. Circles: $T = 4.22^\circ\text{K}$. Triangles: $T = 10.0^\circ\text{K}$. Dashed line: calculated relaxation rate for the second-order Raman process only. Solid line: three-magnon process included.

This assumption has been made in calculating the theoretical curves of Fig. 1. Agreement with the data is only qualitative.

The observed temperature dependence of T_1 at 820 Oe, which is the saturation field, and at 1500 Oe is shown in Fig. 2. The data plotted were taken on samples #1 and #3, which gave identical results to within the experimental uncertainty. However, the values of T_1 obtained for sample #2 at saturation field were approximately 30 per cent smaller, although the temperature dependence between 3° and 30°K was the same to within the uncertainty. The origin of this shift is not known. It is possible that crystal imperfections within the sample caused field inhomogeneities.

The point at 78°K was taken in zero field, in a liquid nitrogen bath. Approximately eight irregularly-shaped single crystals were packed into an r.f. coil, to form a sample volume of about 0.13 in³. These crystals came from the same batch as samples #2 and #3. This arrangement produced a signal-to-noise ratio sufficient to allow measurement of T_1 . As a check, T_1 was measured with the same

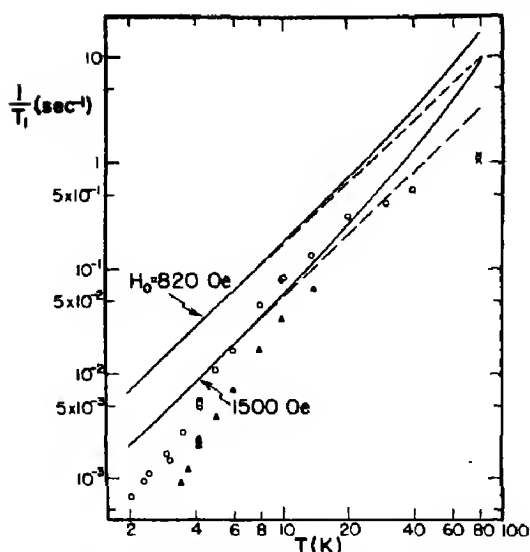


Fig. 2: The temperature dependence of T_1 for D-sites in YIG, from samples #1 and #3. Circles: $H_0 = 820$ Oe (saturation field). Triangles: $H_0 = 1500$ Oe. Crosses: $H_0 = 0$, sample containing several crystals (see text). Dashed line: calculated relaxation rate for the second-order Raman process only. Solid lines: three-magnon process included.

setup, at 4.2°K. The value of T_1 was approximately 10 per cent smaller than that obtained with a single sphere at saturation field. Also, as will be seen below, zero field and saturation field results agree at higher temperatures. Hence it was felt that the 78°K point could be used as an approximate extension of the saturation field data.

The predictions of equations (4), (6) and (7) are shown in Fig. 2. There seems to be a definite discrepancy between theory and experiment, the experimental values of T_1 being larger than predicted.

It seems probable, although not certain, that the spin-lattice relaxation rate observed in this experiment was due to a mechanism of pure, single-crystal, mono-domain YIG. The fact that the observed relaxation rate is slower than predicted favors this view. A domain-wall mechanism is ruled out because the data were taken in fields above saturation. The only appreciable impurities with spin were rare earths, whose concentration was known to be less than 1 ppm. From measurements on Yb-doped YIG [8] it can be estim-

ated that at least 5 ppm rare earth impurities would be required to produce the relaxation rate observed at 4.2°K. Also, the field and temperature dependences would be qualitatively different. Finally, consistent results were obtained with samples from different batches.

Smooth curves were drawn through the data, and values of T_1 read off at convenient temperatures and fields. These values are presented in Tables 1 and 2, along with data taken at 120°, 151° and 188°K using the boxcar integrator. Also presented are points taken at 78°, 188° and 292°K in zero field, on the sample consisting of several crystals which was described above. Note that the zero field and saturation field results at 188°K are consistent to within the experimental uncertainty.

The nuclear relaxation rate was also measured in two polycrystalline samples, in which the typical crystal size was 5×10^{-4} cm.

Table 1. Smoothed T_1 data for D-sites in YIG, from samples # 1 and # 3, as a function of temperature

$T(^{\circ}\text{K})$	Applied field	
	820 (Oe)	1500
2	1550 sec \pm 5%	
2.5	930	
3	600	
3.5	372	1050 sec \pm 10%
4	229 \pm 3%	600
5	105	263
6	56	141
7	33.9	85
8	22.9	56
10	12.9 \pm 5%	30.2
12	8.9	20.4
14	6.8	15.5 \pm 20%
16	5.5	
20	3.98 \pm 10%	
30	2.45	
40	1.82 \pm 20%	
78	0.95 \pm 20%*	
120	0.20 \pm 10%	
151	0.086 \pm 10%	
188	0.038 \pm 10%	
188	0.034 \pm 20%*	
292	0.0093 \pm 20%*	

*Data taken on several crystals in zero field (see text).

Table 2. Smoothed T_1 data for D-sites in YIG, from samples # 1 and # 3, as a function of applied field

Applied field (Oe)	$T(^{\circ}\text{K})$	
	4.22	10.0
820	195 sec \pm 3%	12.9 sec \pm 5%
1000	255	17.6
1200	340	23.6
1600	500	37.0
2000	640 \pm 10%	52 \pm 20%
2500	790	72
3000	920	93 \pm 30%
4000	1170	
5000	1400	
6000	1600 \pm 20%	

These samples were of purity comparable to those described above. The measurements were made at 4.2°K in zero field, and the results were in marked contrast to the data reported above. First, the return of the nuclear magnetization to equilibrium was quite non-exponential. However, in the measurement described above on a sample consisting of several irregular crystals packed together with random orientation, which was also done in zero field at 4.2°K, the return to equilibrium was exponential to within scatter. Second, the two small-crystal samples gave $T_1 \approx 0.4$ sec and ≈ 0.9 sec, respectively, while the larger crystals yielded $T_1 = 170$ sec.

Henderson *et al.* [12] have measured the specific heats of the two polycrystalline samples mentioned above, in the temperature range below 4.2°K. They found an anomalous contribution which varied approximately linearly with temperature. These authors have tentatively suggested that both the specific heat anomaly and the high nuclear relaxation rate may be associated with surface effects. This explanation is not inconsistent with the NMR results discussed above, since a relaxation mechanism associated with surface effects would be more effective for smaller crystals. Also, the relaxation rate might be expected to vary with distance from the crystal surface, thus accounting for the

observed non-exponential decay in the small crystals.

5. CONCLUSIONS

Agreement between the data presented in this paper and the predictions of current theory is only qualitative. We find T_1 (experimental) $>$ T_1 (theoretical) over the entire range of fields and temperatures covered, the difference ranging as high as a factor of ~ 10 . It is hoped that further theoretical work will be stimulated by these measurements.

It seems possible that a relaxation mechanism associated with surface effects has been observed in the samples having $\sim 5 \times 10^{-4}$ cm crystals. If so, then NMR should provide a useful probe with which to study surface properties in YIG, as well as in other magnetic systems.

Acknowledgements—The authors wish to thank Dr. P. Pincus and Dr. D. Beeman for helpful correspondence, and Dr. E. Spencer for shaping the YIG spheres.

REFERENCES

1. ROBERT C. and WINTER J. M., *Proc. XIth Intl. Conf. on Magnetic and Electric Resonance and Relaxation (Colloque Ampère) Eindhoven (1962)*, p. 205. North Holland, Amsterdam (1962).
2. BEEMAN D., *J. appl. Phys.* **38**, 1276 (1967).
3. BEEMAN D., and PINCUS P., *Phys. Rev.* **166**, 359 (1968).
4. This equation was derived for a ferromagnet by HERRING C. and KITTEL C., *Phys. Rev.* **81**, 869 (1951). It was shown to hold for a ferrimagnet by HARRIS A. B., *Phys. Rev.* **155**, 499 (1967).
5. GONANO J. R., *et al.*, *Phys. Rev.* **156**, 521 (1967).
6. GELLER S., *et al.*, *Phys. Rev.* **137**, A1034 (1965).
7. The multiplicative constants in equations (4) and (6) are different from those used in *Phys. Rev.* **166**, 359 (1968), the latter being smaller by factors of 0.52 and 0.11 respectively. BEEMAN (Private communication) states that incorrect values for the parameters for YIG were used in [3].
8. MYERS S. M., MEYER H. and REMEIKA J. P., To be published.
9. See, for example, [3] and HARTMANN-BOUSTRON F., *J. appl. Phys.* **35**, 889 (1964), (impurity mechanism).
10. PINCUS P., Private communication.
11. RODRIGUE G. P., MEYER H. and JONES R. V., *J. appl. Phys.* **31**, 376S (1960).
12. HENDERSON A. J., ONN D. G., MEYER H. and REMEIKA J. P., *Phys. Rev.* In press.

LONGITUDINAL NUCLEAR RELAXATION MEASUREMENTS IN hcp H_2 *

LARRY I. AMSTUTZ, HORST MEYER and SAMUEL M. MYERS
Department of Physics, Duke University, Durham, N.C. 27706, U.S.A.

and

ROBERT L. MILLS
Los Alamos Scientific Laboratory, Los Alamos, N.M. 87544, U.S.A.

(Received 17 April 1969)

Abstract—Measurements of T_1 in the hcp phase of H_2 over the temperature range 2°–12°K and the ortho concentration range between 0.5 and 0.97 are presented. At temperatures below 10°K, the thermally activated self-diffusion is negligible and the mechanism for nuclear relaxation is that attributed by Moryia and Motizuki and by Harris to intramolecular dipolar interaction, modulated by intermolecular electric quadrupole–quadrupole (EQQ) interaction. The gaussian approximation for the correlation function was used by these authors to predict T_1 . From the comparison between experiment and theory, we determine the EQQ parameter Γ/k_B to be 0.67°K. Above 10°K the effect of diffusion influences T_1 , and the experimental results for an 88 per cent ortho H_2 sample up to the melting point suggest that the relaxation mechanisms resulting from EQQ interaction and diffusion are not independent of one another.

1. INTRODUCTION

MORYIA and Motizuki[1] pointed out that the principal mechanism for nuclear relaxation in hcp orthohydrogen is the intramolecular, nuclear dipole–dipole interaction modulated by either self-diffusion or the intermolecular electric quadrupole–quadrupole (EQQ) interaction. In this paper we report measurements of the longitudinal nuclear relaxation time T_1 at high ortho concentrations, in the temperature range where the modulation due to the EQQ interaction is the dominant one.

Nakamura[2] first discussed the EQQ interaction energy, which is proportional to the quadrupole coupling constant

$$\Gamma = 6e^2Q^2/25R^5 \quad (1)$$

where eQ is the quadrupole moment of an ortho molecule and R is the distance separating the molecules. The relaxation time due to EQQ interaction was calculated by Moryia

and Motizuki[1] in the high temperature approximation. They considered only nearest-neighbor interaction between ortho molecules, and used a gaussian approximation for the spectral density correlation, which limits their calculation to ortho concentrations above about $C = 0.4$. Their calculation for the case of a single hcp crystal with applied magnetic field parallel to the c axis yields

$$T_{1,Q} = 0.552 C^{1/2}(\Gamma/k_B) \text{ (sec)} \quad (2)$$

where C denotes ortho concentration and the explicit dependence on Γ is factored out. More recently, Harris[3] used similar assumptions to derive an expression containing the first temperature-dependent term. He obtained for a powder of H_2 crystals[4]

$$T_{1,Q} = 0.543 C^{1/2}(\Gamma/k_B) \left[1 - \frac{9}{14} \frac{\Gamma}{k_B T} - \frac{1757}{1792} \frac{\Gamma C}{k_B T} \right]^{1/2} \text{ (sec).} \quad (3)$$

In a single crystal of H_2 the anisotropy of the

*The research carried out at Duke University was supported by grants from the Army Research Office (Durham) and the National Science Foundation.

relaxation time T_1 was calculated[3] to be about 1 per cent.

At temperatures below the freezing point and at NMR frequencies $\omega/2\pi > 10$ MHz, the diffusion correlation time τ is much larger than ω^{-1} so that the relaxation time due to self-diffusion is, to a good approximation[1],

$$T_{1,D} = (3 \log 2) (T_2'')^2 \frac{\omega^2 \tau}{2} \quad (4)$$

where $(T_2'')^{-1}$ corresponds to the line width for a rigid lattice and is taken to be proportional to $C^{1/2}$. In discussing our data, we will use values of T_2'' and τ estimated by Moryia and Motizuki [1] from Bloom's data[5, 6].

If we assume that the two relaxation mechanisms are mutually independent, the observed relaxation time T_1 will be given by

$$T_1^{-1} = T_{1,D}^{-1} + T_{1,Q}^{-1}. \quad (5)$$

Near the melting point the self-diffusion term is dominant, while below 10°K its contribution is negligible.

Several experimenters have recently measured T_1 at ortho concentrations $C \leq 0.75$. These include Hass *et al.*[7] at temperatures above 12°K, Hardy and Gaines[8] at 4.2°K and Harris and Hunt[9] between 4.2° and 1.5°K. Relaxation measurements for H_2 - D_2 mixtures have also been reported by Metzger and Gaines[10] at 4.2° and 1.2°K.

In this paper we present a systematic study of T_1 in hcp hydrogen that extends the concentration range to $C = 0.97$ and covers the complete temperature range from 1.5° to 12°K. These data are easily extrapolated to give T_1 for pure ortho H_2 . After a brief description of the experimental methods in Section 2, the results are presented in Section 3 and compared with previous data[5, 7-9] and with theory[1, 3, 9]. Because of our systematic measurements in a previously unexplored temperature and concentration region, and because of the recent extension in the theory[3], this comparison is an improvement over the earlier ones [1, 9].

2. EXPERIMENTAL

The relaxation times were measured using a phase-coherent pulse system described elsewhere[11]. The detection system required about 20 μ sec to recover following a pulse. An electronic counter was used to monitor the oscillator, whose frequency of 38 MHz was kept within 200 Hz of the center of the NMR absorption line. The magnetic field was held constant during the experiments and was monitored by a separate spectrometer operating at a different frequency. A 90-deg pulse required approximately 11 μ sec, and had a Fourier spectrum wide enough to saturate the entire line shape.

Measurements of T_1 were carried out by first saturating the spin system using two 90-deg pulses separated by a time much longer than T_2 , yet much shorter than T_1 . After a time t , another 90-deg pulse was applied and the amplitude of the free induction decay $M(t)$ was measured 35 sec after the leading edge of this pulse. Semilogarithmic plots of $[M(t = \infty) - M(t)]$ vs. t were linear within the scatter and T_1 could be determined to ± 2.5 per cent from the plots, except at the lowest temperatures. At 1.5°K the scatter in the plots due to the short T_2 increased the uncertainty in an individual measurement to ± 5 per cent.

Samples were frozen rapidly using a technique that we believe produces powder samples, based on observation of c.w. lineshapes in previous experiments[12]. The experiments at high concentration started with hydrogen of $C = 0.97$ which was prepared[13] by preferential absorption on cold alumina. The enrichment process reduces the gas impurities, which were originally < 20 ppm. The measurements at $C \leq 0.75$ were made starting with normal gas certified by the Matheson Company to contain < 6.5 ppm of impurities, mainly oxygen.

Once a sample was solidified, measurements were taken at a given set of temperatures and the corresponding laboratory time was noted. The ortho concentration was determined both before and after the experiments by measuring

$$\frac{dC}{dt} = -KC^2. \quad (6)$$

3. RESULTS AND DISCUSSION

Figure 1 is a line graph with two data series. The y-axis is labeled T_p (m sec.) and ranges from 220 to 360 in increments of 20. The x-axis is labeled 'ortho concentration G' and ranges from 0.5 to 1.0 in increments of 0.1. The upper curve, labeled $T = 7.25 K$, starts at approximately (0.5, 245) and rises to about (1.0, 320). The lower curve, labeled $T = 4.27 K$, starts at approximately (0.5, 235) and rises to about (1.0, 280). Both curves are fitted with smooth lines. Data points are represented by solid circles for the upper curve and open circles for the lower curve. There are also some 'x' marks scattered between the two curves.

Hass *et al.* [7] measured relaxation times at 30 MHz and in a temperature range where diffusion effects become noticeable. Since the relaxation time due to self-diffusion $T_{1,D}$ depends on the NMR frequency, our data can be compared with theirs only through $T_{1,0}$.

C	T(°K)												
	1.5	2.0	2.5	3.0	4.0	5.0	6.0	7.0	8.0	9.0	10.0	11.0	12.0
1.0				237	270	294	310	322	329	333	334	329	319
0.95				235	266	289	303	313	320	325	327	324	315
0.90				233	263	284	296	306	315	321	324	319	309
0.85				232	261	280	292	302	311	317	319	313	303
0.80		215		230	258	274	287	297	305	312	314	311	295
0.75		190	212	229	254	270	281	291	299	307	310	305	290
0.70		190	212	228	250	264	276	284	290	294	296	295	288
0.65		195	213	227	245	258	267	274	279	283	285	286	284
0.60	160	190	210	225	240	251	259	265	269	270	272	273	274
0.55	165	190	207	220	235	245	251	255	257	258	259	259	259
0.50	165	188	205	215	230	240	244	245	245	245	245	245	245

which should be frequency independent. We computed $T_{1,D}$ from equation (4) and then calculated $T_{1,q}$ from equation (5) for all sets of data. Our results for $T_{1,q}$ are presented in Table 1 and are given by the number in parentheses. The Hass *et al.* [7] values at 12°K for $T_{1,q}$ are 0.265, 0.252 and 0.215 sec for ortho concentrations of 0.75, 0.68 and 0.52, respectively. Their relaxation times, as well as those at $C \sim 0.66$ by Bloom [5], are systematically lower by 10–20 per cent than those presented in Table 1. We can explain neither the difference in $T_{1,q}$ nor the observation that the maximum of T_1 of Hass *et al.* [7] lies at 12.5°K rather than at 10°K as in our experiments.

There is good numerical agreement between theory [1, 3] and our data for the relaxation time due to the EQQ interaction. In Table 2 we present the ratio $T_{1,q}(\text{theory})/T_{1,q}(\text{exp.})$ at even temperatures and concentrations, using

Table 2. Ratio $T_{1,q}(\text{theory})/T_{1,q}(\text{expt.})$ for standard ortho concentrations and temperatures. $T_{1,q}(\text{theory})$ is calculated from the theory of A. B. Harris, equation (3), using $\Gamma/k_B = 0.69^\circ\text{K}$

C	T(°K)						
	6	7	8	9	10	11	12
1.0	1.09	1.06	1.05	1.05	1.05	1.06	1.05
0.9	1.09	1.06	1.05	1.04	1.04	1.04	1.04
0.8	1.06	1.04	1.03	1.01	1.01	1.02	1.04
0.7	1.04	1.03	1.02	1.01	1.01	1.00	1.00
0.6	1.04	1.02	1.02	1.02	1.02	1.01	0.99
0.5	1.01	1.02	1.03	1.03	1.04	1.04	1.02

the improved theory [3] that takes into account the temperature variation of $T_{1,q}$. In calculating $T_{1,q}$ from equation (3), we have used the value $\Gamma/k_B = 0.69^\circ\text{K}$, obtained from an improved analysis [14] of the Raman spectrum of cubic ortho H_2 [15]. The approximate constancy of the ratio in Table 2 shows that the temperature-dependent term in equation (3) is in reasonable agreement with experiment over the range where this equation is valid.

Conversely, using equation (3), we can determine Γ from the experimental data. We then find $\Gamma/k_B = 0.67 \pm 0.03^\circ\text{K}$ to give a best fit to the data. We emphasize that this value is dependent on the assumption of the gaussian approximation in equation (3) and will be modified as better approximations become available. We also point out that this value for Γ is representative for the hcp phase and $0.5 \leq C \leq 1.0$.

At temperatures above 12°K, diffusion becomes important. Relaxation measurements on a sample with $C = 0.88$ gave T_1 values of 0.287, 0.283, 0.274 and 0.255 sec at respective temperatures of 13.2, 13.5, 13.9 and 14.2°K, the last value corresponding to the liquid. This smooth decrease of T_1 with increasing T is compatible with a diffusion mechanism and is in qualitative agreement with the findings of Hass *et al.* [7] at their highest ortho concentration. Using our experimental data together with equations (4) and (5), we find that $T_{1,q}$ becomes sharply temperature dependent at increased temperatures. This behavior cannot be compensated for by a different choice of T_2 and is contrary to theory. We conclude that equation (5) is not valid above 12°K where possibly interaction between the two relaxation mechanisms sets in through a modulation of the EQQ interaction by diffusive motion.

Acknowledgements—The authors are indebted to Dr. A. B. Harris for communicating his calculations in advance of publication and for several discussions. They also thank Dr. J. R. Gaines for communicating his unpublished data with Hardy, and for helpful correspondence and discussions on the subject of relaxation in H_2 . We thank Mr. F. Weinhaus for his assistance in the experiments, and acknowledge support by the U.S. Atomic Energy Commission.

REFERENCES

1. MORYIA T. and MOTIZUKI K., *Prog. theor. Phys.* **18**, 183 (1957).
2. NAKAMURA T., *Prog. theor. Phys.* **14**, 135 (1955).
3. HARRIS A. B., Private communication.
4. The slight difference between the numerical factors in equations (2) and (3) is due to a small error in Moryia and Motizuki's treatment, to slightly different assumptions about the correlation functions and to the

- anisotropy of T_1 (HARRIS A. B., Private communication).
5. BLOOM M., *Physica* **23**, 767 (1957).
 6. The systematic difference of about 20 per cent between the T_2 measurements of Bloom and those of Hass *et al.*[7] has a negligible effect on the discussion of the results in Section 3 of this paper.
 7. HASS W. P. A., POULIS N. J. and BORLEFFS J. J. W., *Physica* **27**, 1037 (1961).
 8. HARDY W. and GAINES J. R., Private communication.
 9. HARRIS A. B. and HUNT E. R., *Phys. Rev. Lett.* **16**, 845 (1966); Erratum: **16**, 1233 (1966).
 10. METZGER D. S. and GAINES J. R., *Phys. Rev.* **147**, 644 (1966).
 11. GONANO R., HUNT E. R. and MEYER H., *Phys. Rev.* **156**, 521 (1967).
 12. AMSTUTZ L. I., MEYER H., MYERS S. M. and RORER D. C., *Phys. Rev.* **181**, 589 (1969).
 13. DEPATIE D. A. and MILLS R. L., *Rev. Scient. Instrum.* **39**, 105 (1968).
 14. BERLINSKY A. J., HARRIS, A. B. and COLL C., To be published.
 15. HARDY W. N., SILVERA I. F. and McTAGUE J., *Phys. Rev. Lett.* **22**, 297 (1969).

1
2
3
4
5
6
7
8
9

•

2

1 2

A SELF-CONSISTENT *F*-CENTER CALCULATION FOR THE OPTICAL ABSORPTION AND EMISSION*

R. L. GILBERT† and J. J. MARKHAM

Physics Department, Illinois Institute of Technology, Chicago, Ill. 60616, U.S.A.

(Received 12 September 1968; in revised form 24 March 1969)

Abstract—A theoretical investigation of the luminescence processes associated with *F*-centers has been made. It assumes that the marked Stokes's shift arises from the *electrostatic* interaction between the *F*-electron and the neighboring ions. A semi-continuum model was employed. First, an examination of most of the previous *F*-center calculations in NaCl and KCl was made. These were classified into four categories: (1) the semi-continuum model; (2) the semi-continuum polaron model; (3) the point-ion model (a) without polarization and (b) with polarization; and (4) the Hartree-Fock model where the internal structure of the ions which surround the vacancy is taken into account. Some models were omitted. In all calculations, the differences in the eigenvalues associated with the lowest and the first excited state give approximately the measured values of the peak absorption and the peak emission bands. The actual eigenvalues show a large scatter, indicating no reliability in the present calculating techniques. Next, a new *self-consistent* approach is made. The following results were derived for NaCl and KCl: (1) self-consistent potentials for the absorption and emission; (2) energy level diagrams (relative to the bottom of the conduction band) and wavefunctions for both processes; (3) self-consistent values for the displacements of the first nearest neighbors; and (4) the lifetime of the first excited state (which agrees approximately with the measured result). The loose binding approximation is manifested during emission, whereas tight binding occurs during absorption. These calculations indicate that a self-consistent use of the semi-continuum model can describe the simplest optical properties of the *F*-center.

1. INTRODUCTION

ABOUT a decade ago the optical emission band of the *F*-center[1,2] was discovered[3]. The large shift of this band [which peaks at $E_m(e)$] relative to the absorption band [at $E_m(a)$] and the unusually long lifetime of the excited state indicate[2,4] that the absorption and emission processes are not closely related.

The object of our study is to show that this difference is expected from the very simplest model of the *F*-center and must be inherent in many point imperfections in polar solids. To understand the problem qualitatively, it is not necessary to utilize a complex model or make refined calculations

on wave functions. We simply have to apply the basic model of Tibbs[5] in a *self-consistent* manner. The method of doing this was suggested by Mott and Gurney[6] and carried through by Simpson[7], by Krumhansl and Schwartz[8] and others. The more recent improvements (see below) are valuable, but are not basic for an understanding of the problem.

Our calculation indicates that some extremely important features of the *F*-center can be obtained from a simplified theory. The absorption process resembles the "particle-in-a-box" problem, while emission is similar to the "hydrogen-atom-in-a-dielectric" problem. These models are consistent with the change in the equilibrium polarizations when the *F*-electron goes from the ground to the first excited state. Further, an examination of past calculations (Section 2) indicates that many reasonable models will give an

*Submitted by R. L. Gilbert in partial fulfillment of the requirements for the Ph.D. Degree to the Physics Department, Illinois Institute of Technology.

†Present address: Northeastern Illinois State College, Chicago, Illinois.

approximate value of $E_m(a)$ and $E_m(e)$ provided the "particle-in-a-box" and the "hydrogen-atom-in-a-dielectric" is used, implicitly. Past calculations of $E_m(a)$ basically evaluate the difference between the two lowest bound states in a well of uniform potential depth, whose size is *determined* by the nearest neighbor distance. This difference is not sensitive to the depth of the well, provided it is not too shallow and different depths have given reasonable values of $E_m(a)$. Certain features cannot be obtained in this simple manner. For example, a calculation of the ENDOR signal associated with a shell of ions requires an exact wave function at moderate distances from the vacancy.

Three important calculations have been published recently. One is by Wood and Joy[9], and it attempts to obtain an 'exact' wave function. The radically different nature of the emission and the absorption problem is not evident to us from these calculations. Another, by Fowler[10], is similar to ours. It is not self-consistent, however, since the actual displacements of the ions near the vacancy are *assumed*. During the writing of this paper the calculation of Bennett[11] has appeared. His approach is not equivalent to ours and will be discussed below. Wood and Öpik[12] have extended and modified the 'Wood' approach after this paper was written. Their study will not be considered here. The same holds for the study of Bartram, Stoneham and Gash[12].

We believe that the conclusions arrived at in this paper regard the F -center, not the model employed. Further calculations will modify the actual eigenvalues, but we do not believe that they will change our basic conclusions.

2. COMPARISON OF VARIOUS F -CENTER CALCULATIONS

To compare our results with values obtained previously and to evaluate the present status of the calculations of wave functions at imperfections in polar solids, we examined

as many F -center calculations as seemed practical. To present the results, let \mathbf{X} symbolically represent the configuration of the surrounding ions. Further, we denote the *total* eigenvalues of the *system*, F -electron and lattice, by $E_g(\text{ground})$ and by $E_u(\text{upper-first excited state})$. Correspondingly, there are two equilibrium positions of the surrounding ions, \mathbf{X}_g and \mathbf{X}_u . Now we define the four quantities: $E_g(\mathbf{X}_g)$, $E_u(\mathbf{X}_g)$, $E_u(\mathbf{X}_u)$, and $E_g(\mathbf{X}_u)$. For example $E_u(\mathbf{X}_g)$ denotes the total eigenvalue of the first excited state when the positions of the ions are determined by the *ground* state wave function. We know that:

$$E_m(a) = E_u(\mathbf{X}_g) - E_g(\mathbf{X}_g) = \epsilon_u(\mathbf{X}_g) - \epsilon_g(\mathbf{X}_g) \quad (1a)$$

and

$$E_m(e) = E_u(\mathbf{X}_u) - E_g(\mathbf{X}_u) = \epsilon_u(\mathbf{X}_u) - \epsilon_g(\mathbf{X}_u) \quad (1b)$$

(for details see Section 6). Usually ϵ , the *electronic* eigenvalue, is calculated in place of E . This energy is obtained by assuming that the lattice is fixed at \mathbf{X}_g or \mathbf{X}_u and by calculating only terms which involve the electron directly.

Table 1 gives various calculated values of the ϵ 's for NaCl and KCl. The table is not complete. The studies of Pekar[25], Stumpf[26] and Wagner[27] are omitted. Pekar and Wagner adopt a completely different point of view, where $E_m(a)$ is treated as a given parameter from which other quantities are obtained. Some values may have been omitted due to oversight. Löffler uses Stumpf's theory.

We have classified various calculations in terms of 'models'. Every author uses his own technique in carrying through the details. (All the calculations are based on de Boer's original ideas). We note that there is some similarity in the approaches from Tibbs through Bennett.

The first section of the table considers the semi-continuum model. It stems from the work of Tibbs and utilizes the calculations

of Mott and Littleton[28]. The basic concept is that the ion-vacancy can be described by a spherical cavity in a continuum dielectric. The electron interacts with the environment surrounding the vacancy by an approach described first by Mott and Gurney[6], and used by Simpson[7]. This model assumes two media, the vacuum and the surrounding dielectric with an *effective* mass, and stresses the local environment.

The next set of calculations is the semi-continuum polaron model. It stresses *ideal* macroscopic properties by assuming that the electron-lattice interactions arise via the longitudinal optical vibrational modes. Actually the infinite wavelength approximation is used-i.e. the scalar potential arises from pure optical modes of a *single* frequency. Although this concept is justified in the case of the 'free electron' in insulators (see [2,

Table 1A. Calculated eigenvalues for NaCl (past and present). The eigenvalues are not necessarily referred to the same zero level. Due to this, variations of the order of half an electron volt may be expected.

Unmarked rows correspond to absorption

Authors	Ground (eV)	Upper eV (First excited state)	E_m (eV)
Semi-continuum microscopic model			
Tibbs[5] (second method)	-3.5	-1.0	2.5
Simpson(a)[7]	-3.2	-1.0	2.2
Pincherle[13]	-3.25	-1.13	2.12
Krumhansl and Schwartz[8]	-3.85	-1.23	2.62
Fowler[10]	Ab -3.87	-1.07	2.80
	Em -1.36	-0.12	1.24
Gilbert (after Simpson[24])	-3.29	-1.01	2.28
Present (V_2)	Ab -3.70	-1.26	2.44
	Em -1.30	-0.14	1.16
Semi-continuum polaron model			
Wang[14]	(a) -2.6	-0.35	2.25
	(b) -2.58	+0.32	2.90
Bennet[11] Model No. 1	Ab -3.10	-0.14	2.96
	Em -1.50	-0.11	1.39
Model No. 2	Ab -2.83	-0.11	2.72
	Em -1.25	-0.11	1.14
Point-ion model			
Gourary and Adrian[15]	-6.48	-4.08	2.40 without polarization
Simpson(b)[16]	-3.35	-1.58	1.77 with polarization
Point-ion pseudopotential model			
Kübler and Friauf[17]	-4.94	-2.26	2.68
Hartree-Fock model			
Wood and Joy[9]	Ab -5.92	-3.20	2.72
	Em -3.56	-1.91	1.65
Other calculations			
Total energy			
Löffler[18]	-4.18		
Evseev and Tolpygo[19]	-5.1		
Thermal activation energy			
Simpson(b)[16]	1.85		
Evseev and Tolpygo[19]	1.9		
Experimental values			
	$E_m(a)$ [20]		2.77 at low temperature 2°K
	$E_m(e)$ [21]		1.01 av. of 5 values
	ϵ_t		1.94
	ϵ_t = thermal dissociation energy for the F-center		

Table 1B. Calculated eigenvalues for KCl (past and present)

Authors	Ground (eV)	Upper eV (First excited state)	E_m (eV)
Semi-continuum microscopic model			
Pincherle[13]	-2.69	-0.91	1.78
Krumhansl and Schwartz[8]	-3.18	-0.82	2.36
Gilbert[24] (after Simpson (a))	-2.80	-0.85	1.95
Present (V_2)	Ab -3.33	-1.37	1.96
	Em -1.46	-0.28	1.18
Semi-continuum polaron model			
Wang[14]	Ab -2.83	-0.39	1.92
	Em -1.36	+0.10	2.36
Bennett[11]	-2.83	-0.04	2.79
	-1.36	-0.15	1.21
Point-ion model			
Gourary and Adrain[15]	-5.96	-3.97	1.99
Point-ion pseudopotential model			
Kübler and Friauf[17]	-4.09	-2.13	1.96
Hartree-Fock model			
Wood and Joy[9]	Em -4.98	-2.58	2.40
	Ab -2.52	-1.37	1.15
Other calculations			
Total energy			
Löffler[18]	-3.98		
Experimental values			
	$E_m(a)$ [23]	2.31 at 4°K	
	$E_m(e)$ [21]	1.22 average of 4 values	

chap. 3)), it has serious shortcomings when bound electrons are considered. It does not give the 'effective' phonon frequency which the F -center 'sees' [2, chap. 10], nor does it explain the resolved absorption bands associated with the R_2 -center. More detailed lattice dynamic considerations are required to explain the above phenomena[29]. Bennett, when using this approach, adds some microscopic properties to the lattice. The present polaron models oversimplify the problem.

The point-ion model, as calculated by Gourary and Adrian, ignores the lattice distortion (to first approximation), since this term is considered to be small. The calculation of Kübler and Friauf replaces the point-ions by a pseudo-potential but does not include the lattice distortions. An extremely important calculation on the point-ion model has been made by Simpson[16]. It indicates that the point-ion model may give the same result as the semi-continuum

model, if the polarizations are included in a similar manner. The distinction between the semi-continuum and the point-ion models seems to arise from the neglect of polarization in the zero-order calculation of the point-ion model.

Wood and Joy attempt to include details of the potential within the ions themselves. This is necessary if we are to calculate the F -center wave function at a surrounding nucleus.

Löffler calculates only the depth of the ground state but includes effects of lattice distortion—i.e. he obtains E not ϵ ; so do Evseev and Tolpygo.

Table 1 shows that modifications in the calculation techniques are of minor importance, but that various models give radically different eigenvalues. We believe that polarization is the important factor and, when included 'properly', the point-ion model gives results similar to the semi-continuum model.

It is hard to know what reliance can be placed on the present Hartree-Fock calculations. They give 'satisfactory' results for some quantities. Perhaps some major term is omitted in all the other calculations. There have been several different types of 'Hartree-Fock' calculations, if LiF and LiCl are included. LiF has been calculated by Kojima[30] and by Wood and Joy, while LiCl has been studied by Wood and Joy, and by Wood and Korrying[30]. The eigenvalues show considerable variations. While it is certain that the calculations of Wood and co-workers are of a very fundamental nature, we do not feel that their reliability, at present, is sufficient to eliminate the consideration of the semi-continuum approach. The same is true of the simplified polaron model.

The problem posed by the table would be resolved if the ϵ 's had been measured experimentally. At present we can only estimate a lower limit of $\epsilon_0(X_0)$ in RbI using the photo-

electric emission data of Apker and Taft[31]. The arguments run as follows: In the experiments, a 5 eV photon ejects an electron from the ground state of the F-center into the vacuum *outside* the crystal. The average kinetic energy of the ejected electron is 1.7 eV. Figure 1 presents systematically what seems to occur. Here various E 's are plotted as a function of X , which describes *symbolically* the distortions of the lattice. E_c is the bottom of the conduction band, E_v is the lowest vacuum level, and E' is the level 1.7 eV above E_c . The minima of E_c , E_v and E' are assumed to occur at the same value of X since free Bloch electrons do not affect the equilibrium position of the ions[32]. The difference between E_v and E_c is χ , the electronic affinity.

We assume that the Franck-Condon principle applies to the ejection process. One is justified in using the Born-Oppenheimer approximation for electrons in the conduction

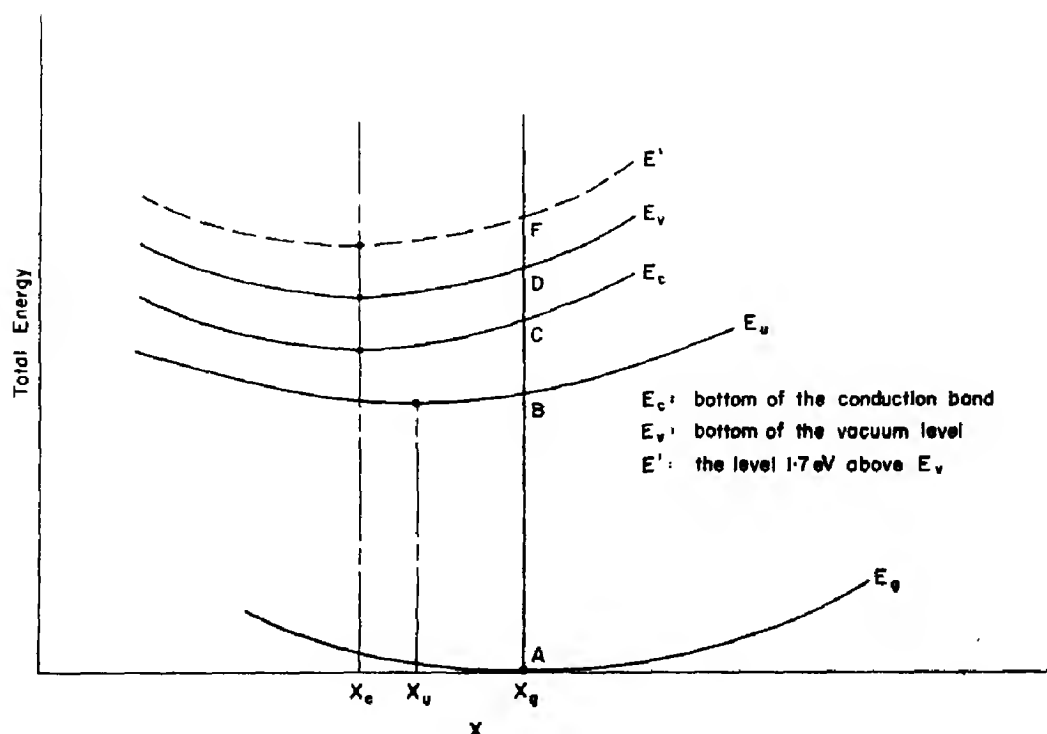


Fig. 1. Total energy vs. lattice configuration curves used in our interpretation of the experiments of Apker and Taft. We assume Bloch electrons in the conduction band.

band, since Bloch electrons do not produce a force on the lattice,* the 'ionic' part of the matrix element is similar in form, whether one considers an optical dipole transition from $A \rightarrow B$ or a transition from $A \rightarrow F$ induced by an exciton. An exciton arises because the 5 eV photon produces an exciton at the surface of the crystal which travels until it interacts with an F -center. Since $D \rightarrow F$ equals 1.7 eV, the maximum depth of A below the conduction band is 3.3 eV ($\chi = 0$). We may thus equate the energy for the transition between $A \rightarrow C$ to $\epsilon_p(X_u)$ and write:

$$\epsilon_p(X_u) \text{ max for RbI} = 3.3 \text{ eV.}$$

Since $\chi \approx 0.5$ eV, $\epsilon_p(X_u) \approx 3$ eV, this places the upper levels of the L-bands near the bottom of the conduction band, which is reasonable.

We know of no calculation on RbI. Simpson's method (a) has been extended as far as KI [24], and there is no contradiction with our estimated $\epsilon_p(X_u)$, provided $\chi = 0$. Wood and Joy's calculations do not extend to the heavier alkali halides. They obtain $\epsilon_p(X_u) = -4.9$ eV for KBr, which we believe is another *indication* that the method used by Wood and Joy places the energy levels at too low a value. At present, the semi-continuum model seems to give more reliable results.

A more detailed examination of the calculations indicates that some of the values in Table I are relative to the vacuum, while others are relative to the bottom of the conduction band. This can only account for a small fraction of the differences, since $\chi \approx 0.5$ eV.

*More explicitly in a dipole transition, the Franck-Condon principle arises from the overlap matrix associated with the vibrational modes. See [2, equations (31.1) and (31.3)]. We believe that similar matrices occurs for the case when the exciton ejects the electron since the exciton is primarily electronic in nature. In any case, there is no way the average energy given to the electron can be greater than 5 eV.

In view of the above arguments, we shall employ the semi-continuum model.

3. THE LIFETIME

Several years ago, the great puzzle associated with the F -center was the long lifetime of the first excited state[4]. Now we have several non-equivalent explanations. Various possibilities have been reviewed by Bogan [33]. In view of the complexities of the calculations, it is impossible to use the lifetime, alone, as a measure of the success of the theory. Additional experimental facts must be employed, such as the Stark effect, or the broadening of the optical bands.

For a better understanding of the problem consider the symmetry of the F -electron wave functions. The four eigenfunctions of interest are: $\Psi(g, X_u)$, $\Psi(u, X_u)$, $\Psi(u, X_v)$ and $\Psi(g, X_v)$. If the lattice distortion is neglected, the point-group symmetry of the vacancy is O_h . Group theory suggests that the ground state belongs to the Γ_1^+ representation (s -like), while $\Psi(u, X_u)$ belongs to Γ_4^- (p -like). For $\Psi(g, X_u)$ it is a consistent assumption, since the electron distribution is spherically symmetric. The charge distribution due to $\Psi(u, X_u)$ (if it also is Γ_4^-) is not spherically symmetric, and this would lower the point-group symmetry to be associated with the vacancy. A detailed study of this question has to be made before any reliance can be placed on matrices involving X_u . Bogan's study suggests that state $\Psi(u, X_u)$ is s -like, hence, no change in the point-group. This assumption may lead to problems, however.

The first lifetime calculation is due to Pekar and Perlin[34]. The replacement of X_v by X_u was not explicitly taken into account, however. Further, in Pekar's theory the phonon-electron interaction is assumed to occur through the long wavelength longitudinal optical modes.

Fowler was the first to use the semi-continuum model to explain the lifetime of the excited state. He made an extremely important contribution in showing how one can

'by-pass' the 'local field' correction with the use of experimental data[35]. Further calculations have appeared which support Fowler's approach[36]. The basic idea of this explanation is that the $\Psi(u, X_u)$ is extremely diffused.

Recently Tomura, Kitada and Honda[37] have suggested that $\Psi(u, X_u)$ is a Γ_1^+ function and that the ionic vibrations induce some Γ_4^- characters, so that the downward transition becomes partly allowed. They use the small temperature dependence of the lifetime measured by Swank and Brown at low temperatures to determine the effective-phonon frequency. Their value is $3.3 \times 10^{12} \text{ sec}^{-1}$ for KCl. It bears no relation to the frequency of the phonons[21] which affect the optical emission ($4.25 \times 10^{12} \text{ sec}^{-1}$) or absorption ($2.96 \times 10^{12} \text{ sec}^{-1}$).

The general behavior (shape and temperature dependence) of the absorption and emission bands is known both theoretically and experimentally. These properties can be satisfactorily explained if the ground state is a Γ_1^+ function and the excited state is a Γ_4^- . The calculation of the Huang-Rhys factors by Lemos[38] (who used only local modes) indicates that if $\Psi(u, X_u)$ were *s*-like one would expect a narrow emission band and perhaps resolved fine structure.* On the other hand, if the electron interacts with only *perfect* lattice phonons, the geometry of $\Psi(u, X_u)$ does not affect the Huang-Rhys factor[39].

It seems to us that several general arguments can be made regarding the symmetry of wave functions using group theoretical techniques. These might resolve some of the problems discussed above. Unfortunately, the possibility that $\Psi(u, X_u)$ might be a Γ_1^+ state was not realized until after the calculations were made.

If $\Psi(u, X_u)$ is indeed a Γ_1^+ state, the Γ_4^- state has to have almost the same energy since this state is required to explain dipole emis-

sion. Actually, in this case, the equilibrium upper state is a mixture of both types and a knowledge of both is required. Hence, a knowledge of the properties of the Γ_4^- equilibrium state is necessary[40]. As far as Bogan's results, we must assume that the *2s* and *2p* levels have the same energy, since no *a priori* calculation can be expected to determine differences as small as 0.02 eV.

It is for the above reasons that we shall assume here that both $\Psi(u, X_u)$ and $\Psi(g, X_u)$ belong to Γ_4^- of the O_h group. Likewise $\Psi(g, X_p)$ and $\Psi(g, X_u)$ are assumed to belong to the Γ_1^+ .

4. POTENTIALS USED IN THE SEMI-CONTINUUM MODEL

The study of the total potential energy V can be facilitated by considering the rigid lattice contribution, V'_m (Madelung or point-ion); the polarization part, V_p ; the electron affinity, χ ; and the conduction band correction, E_{cb} . (See [2, Section 28]. When an electron is taken from a vacuum and placed in the conduction band of a polar crystal, two types of energies arise. The first is $-\chi$, due to the undistorted crystal, in which a non-localized electron finds itself. The second type, E_{cb} occurs when an electron in the conduction band is localized, it polarizes the surrounding ion cores, and a further lowering of the electron's energy occurs. Since the electron moves in and out of the vacancy, one should consider both. E_{cb} may be included in the experimental measured χ . (The zero levels are measured in such a manner that $\chi > 0$ and $E_c < 0$.)

V'_m in the vacuum (vacancy) is obtained from a Madelung calculation, and any spatial variation is ignored. In the dielectric, the vacancy produces an effective coulombic field (at moderate distances). The effect of crossing the boundary between the vacuum and the dielectric is taken into account by subtracting $-\chi + E_{cb}$ from the vacancy's V'_m . Thus we obtain the net non-polarizable part of the potential, V_m :

*This conclusion might have to be modified if $\Psi(u, X_u)$ were made of *s*-like and *p*-like functions.

$$V_m = -\alpha_m e^2/a - (-\chi + E_{cb}); \quad r < R \quad (2a)$$

$$= -e^2/r; \quad r > R \quad (2b)$$

e is the absolute charge of an electron, α_m is the Madelung constant and a is the distance between nearest neighbors. E_{cb} has always been omitted, while χ has only been included at times. (See however [2, Section 28].) Several values of R , the radius of the vacuum, may be used.

A fundamental difficulty exists in the calculation of V_p , since three response times are involved (for phonons, for core and valence electrons, and for the F -electron). The times suggest that the lattice responds to the average position of the F -electron, while the core electrons follow the F -electron's motion adiabatically. (This is only approximately true). It is, therefore, useful to divide V_p into V_0 (optical) and V_d (ionic displacement).

Tibbs solved the absorption problem by ignoring V_d . This can be justified, since the F -electron is almost entirely within the vacuum in the ground state. Tibbs thus writes:

$$V'_0 = V_{ml} \quad \text{for } r < R \quad (3a)$$

$$V'_0 = \frac{e^2}{r} \left(1 - \frac{1}{\kappa_0}\right) \quad \text{for } r > R \quad (3b)$$

V_{ml} is the Mott-Littleton potential depth for a rigid lattice [28] of polarizable ions, and κ_0 is the high frequency dielectric constant.

Various modifications of Tibbs procedures have been used. Simpson added V_d outside the vacuum, V_d for $r > R$ is defined as follows:

$$V_d(\psi, r) = e^2 \left(\frac{1}{\kappa_0} - \frac{1}{\kappa} \right) \int_r^\infty \frac{1}{x^2} [1 - p(x)] dx \quad (4)$$

for $r > R$

where

$$p(r) = \int_0^r |\psi|^2 dr \quad (4a)$$

κ is the low frequency dielectric constant, and ψ is the electron's envelope eigenfunction

[2, Section 27]. To simplify the problem only the spherically symmetric parts of $|\psi|^2$ will be considered in all cases. Equation (4) is self-consistent, since the displacements are induced by the *net* charge at r due to the electron and the vacancy. Krumhansl and Schwartz assumed that the core electrons follow the F -electron adiabatically and introduced a $\frac{1}{2}$ factor into V'_0 (in the vacuum only). The various potential terms used in the semi-continuum model are summarized in Table 2.

Fowler for *emission* uses an effective dielectric constant, which he justified, by the polaron calculation of Haken and Schottky [41]. One can no longer distinguish between V_0 and V_d , and, hence, the Franck-Condon principle cannot be applied. Further, Fowler adds to the vacuum's V_m the potential energy caused by a 10 per cent outward displacement of the six nearest neighbors ions. Thus the displacement polarization of the nearest neighbors may be counted *twice* by Fowler, since it has already been included in the polaron term.

The common feature in the potentials of Table 2 is that they describe a spherical 'square well'. The difference between the two lowest eigenvalues is insensitive to the well depth. This is exactly what one would expect, provided the well is not too shallow [42]. Fowler's calculations, as well as ours, indicate that $E_m(a)$ is determined by V for $r < R$, while $E_m(e)$ is determined by V for $r > R$.

The Table 2 shows that many variations of the problem are possible and that the differences indicated in Table 1 are to be expected.

We now derive the potentials which were used in our calculation.

5. THE POLARIZATION POTENTIALS

From our viewpoint, the most important part of the Hamiltonian is the polarization potentials. Let us now calculate them with care, assuming here that the electron's wave function ψ is spherically symmetric (See also [16]).

Table 2. Various modifications of the semi-continuum F-center model used in the past*

Authors	Potential: in vacancy	In dielectric	Radius of vacancy (Å)	Method of solution
Tibbs [5] (second method)	$-\alpha_m e^2/a + V_m + \chi$	$-e^2/\kappa_0 r$	2.7 for NaCl	Solves differential equations with boundary conditions
Simpson(a) [7]	$-\alpha_m e^2/a + V_m$	$-e^2/\kappa_0 r + Y_d(\psi, r)$	2.7 for NaCl	Variation of parameter
Pincherle [13]	$-\alpha_m e^2/a + V_m$	$-e^2/\kappa_0 r$	2.7 for NaCl	Solves differential equations
Krumhansl and Schwartzs [8]	$-\alpha_m e^2/a + \frac{1}{2} V_m + \chi$	$-e^2/\kappa_0 r$	2.7 for NaCl	Solves differential equation estimates effects of ionic displacements from wave functions
Fowler [10]	$-\alpha_m e^2/a + \frac{1}{2} V_m + V_d(\psi, R_m) + \chi$	$-e^2/\kappa_{eff} r$	Ab 2.7 for NaCl	Variation of parameter $m_{eff} = 0.6 m_e$ in dielectric.
Wang [14, a]	$-\alpha_m e^2/a + V_m$	Ab $k_{eff} = \kappa_0 = 2.31$ Em $k_{eff} = 4.2$	Em 2.9 for NaCl	Variation of parameters
Bennett [11]	Here an attempt is made to calculate the total energy of the system, using quantum mechanics for the electron and a classical theory for the lattice. The Mott-Littleton radius is employed. In the dielectric $m_{eff} = 0.6 m_e$ where Haken's theory of the polaron is used. V_m the Mott-Littleton [28] potential for the case, where the ions are not displaced, (rigid ion calculation). $V_d(\psi, r)$ see equation (14b). V_F the Frölich polaron potential see FRÖHLICH H...Adv. Phys. 3, 325 (1954).	$-e^2/\kappa_0 r + V_F$	2.5 for NaCl	

*In this table $\chi > 0$ in agreement with recent publications; occasionally χ has been taken as a negative quantity.

The total polarization energy is:

$$W_p = - \int_{\text{Vol.}} d\tau \int \mathbf{P} \cdot d\mathbf{D} \quad (5)$$

where \mathbf{P} is the polarization and \mathbf{D} is the electric displacement. Using the concepts of macroscopic polarization* we divide \mathbf{P} into an optical part \mathbf{P}_0 , associated with displacements of the bound electrons and an ionic displacement part \mathbf{P}_d , thus:

$$\mathbf{P} = \mathbf{P}_0 + \mathbf{P}_d \quad (6)$$

where

$$\mathbf{P}_0 = \frac{1}{4\pi} \left(1 - \frac{1}{\kappa_0}\right) \mathbf{D} \quad (6a)$$

and

$$\mathbf{P}_d = \frac{1}{4\pi} \left(\frac{1}{\kappa_0} - \frac{1}{\kappa}\right) \mathbf{D}. \quad (6b)$$

This is not the only way one may split \mathbf{P} hence equations (6) must be regarded only as a first approximation[28]. To find an explicit relation for the optical part of W_p we write:

$$\begin{aligned} \mathbf{D} &= \frac{e}{r^3} \mathbf{r} - \frac{e}{r^3} p(r) \mathbf{r} \\ &= \mathbf{D}_V + \mathbf{D}_F \end{aligned} \quad (7)$$

or

$$W_0 = -\frac{1}{4\pi} \left(1 - \frac{1}{\kappa_0}\right) \int_{\text{Vol.}} \int_0^\infty \mathbf{D}_F \left(\frac{e}{r^3} \mathbf{r} + \mathbf{D}_F\right) \cdot d\mathbf{D}_F d\tau. \quad (8)$$

Equation (8) calculates the energy relative to the situation, where the electron is at 'infinity' (within the crystal), and the vacancy has polarized its surrounding. It assumes that the electron can be added to the vacancy in infinitesimal amounts, whose spatial distribution is $|\psi|^2$. The first integration gives:

$$W_0 = \frac{e^2}{4\pi} \left(1 - \frac{1}{\kappa_0}\right) \int \frac{1}{r^4} [p(r) - \frac{1}{2}p^2(r)] d\tau. \quad (9)$$

By integrating by parts, one may establish the relation:

$$\begin{aligned} \int_R^\infty p(r) F(r) dr &= \int_R^\infty |\psi|^2 d\tau \int_r^\infty F(x_1) dx_1 \\ &\quad + p(R) \int_R^\infty F(x_1) dx_1. \end{aligned} \quad (10)$$

The right hand side is the expectation value of the quantity $g(r)$:

$$\begin{aligned} g(r) &= \int_R^\infty F(x_1) dx_1 \quad \text{for } r < R \\ &= \int_r^\infty F(x_1) dx_1 \quad \text{for } r > R. \end{aligned} \quad (11)$$

Using equations (9–11) we obtain:

$$V_0(\psi, r) = e^2 \left(1 - \frac{1}{\kappa_0}\right) \int_R^\infty \frac{1}{x^2} \left[1 - \frac{1}{2}p(x)\right] dx \quad \text{for } r < R \quad (12a)$$

$$= e^2 \left(1 - \frac{1}{\kappa_0}\right) \int_r^\infty \frac{1}{x^2} \left[1 - \frac{1}{2}p(x)\right] dx \quad \text{for } r > R; \quad (12b)$$

where W_0 is the expectation value of $V_0(\psi, r)$.

Returning to (5) and combining it with (6b) results in:

$$W_d = -\frac{1}{4\pi} \left(\frac{1}{\kappa_0} - \frac{1}{\kappa}\right) \int_{\text{Vol.}} \mathbf{D}_F \cdot \left(\frac{e}{r^3} \mathbf{r} + \mathbf{D}_F\right) d\tau. \quad (13)$$

Equation (13) assumes that the polarization in the dielectric responds to the *time average field* and that it is not modified as one increases \mathbf{D}_F (no $\frac{1}{2}$ factor). Similar assumptions have to be made at some point in all *F*-center calculations. Using (13) we define V_d as follows:

$$V_d = V_d(\psi, r) = e^2 \left(\frac{1}{\kappa_0} - \frac{1}{\kappa}\right) \int_R^\infty \frac{1}{x^2} [1 - p(x)] dx \quad \text{for } r < R \quad (14a)$$

$$= e^2 \left(\frac{1}{\kappa_0} - \frac{1}{\kappa}\right) \int_r^\infty \frac{1}{x^2} [1 - p(x)] dx \quad \text{for } r > R. \quad (14b)$$

*See [6, chap. 3] or [2, chap. 9].

Equations (12) and (14) give:

$$V_p = V_p(\psi, r) = V_0(\psi, r) + V_d(\psi, r) \quad \text{for } r > R. \quad (15)$$

Equation (15) is based on a continuous theory; hence, we limit its use to the dielectric. At large distances, one might expect V_p to have the 'traditional' form, $(1 - 1/K_0)e^2/r$, since $V_d(r \rightarrow \infty) = 0$. Our V_0 does not approach this value, and consequently we examine the effects of adding $\frac{1}{2}(1 - 1/K_0)e^2/r$ to (15). Namely we write*

$$V_{p2} = V_{p2}(\psi, r) = V_p + V_{c2} = V_p + \frac{1}{2} \frac{e^2}{r} \left(1 - \frac{1}{\kappa_0}\right) \quad \text{for } r > R \quad (16)$$

or

$$V_i = V_m + V_{pi} = V_m + V_0 + V_d + V_i \quad \text{for } r > R. \quad (16a)$$

The depth of the well is the essential feature of the problem, and, hence, it is determined by a modified form of Mott-Littleton's first approximation[6, 28]. For this purpose, two dipoles are placed at every ion site. Two types are required, in view of the difference in the $[1 - p]$ factor of equations (12b) and (14b). Thus, at the halogen-ion site:

$$\mu_h(r) = \left[\frac{\alpha_h}{\alpha + \frac{1}{2}(\alpha_h + \alpha_a)} \right] \frac{a^3 e}{4\pi r^2} \left(1 - \frac{1}{\kappa}\right) \left[1 - \frac{1}{2} p(r)\right] \quad (17a)$$

and

$$\mu_a(r) = \left[\frac{\alpha}{\alpha + \frac{1}{2}(\alpha_h + \alpha_a)} \right] \frac{a^3 e}{4\pi r^2} \left(1 - \frac{1}{\kappa}\right) [1 - p(r)]. \quad (17b)$$

*In the future V_p of equation (15) will be denoted by $V_{ps}(V_{cs} = 0)$.

Here α_a and α_h are the free ion polarizabilities and α is the 'displacement' polarizability used by Mott and Littleton, namely:

$$\alpha = \frac{3a^2}{2\alpha_m} \left[\frac{1}{\rho} - \frac{2}{a} \right]^{-1}. \quad (18)$$

In equation (18), ρ is the Born-Mayer repulsive constant (see [28 Section 2]).† The potential at the center of the vacancy now is:

$$V_p(\psi, 0) = \frac{6}{a^2} [\mu'_a(a) + \mu_d(a)] + \sum_i^h \frac{1}{r_i^2} \mu_h(r_i) + \sum_j^a \frac{1}{r_j^2} \mu_a(r_j) + \sum_k^i \frac{1}{r_k^2} \mu_d(r_k). \quad (19)$$

The primes of the sums denote that the contributions from the nearest neighbors are omitted.‡ $\mu_a(a)$ and $\mu_d(a)$ are calculated more precisely by assuming the spherical charge distribution $|\psi(r)|^2$ for the electron. This makes our calculation self-consistent [43]. To obtain the total potential, V_p is added to V_m , using equations (2), (16) and (19).

6. THE USE OF THE FRANCK-CONDON APPROXIMATION

The Franck-Condon approximation is based on the Born-Oppenheimer technique (see [2, Chap. X] and [32]). The technique assumes that the response time for the electrons is much shorter than for the ionic motion. Our problem, however, has *two electronic* response times, and, under these conditions, a rigorous derivation of the Franck-Condon principle has not been given. The binding energies suggest that the ionic displacements respond to the average position of the electrons, while the core electrons respond to the instantaneous position of the

†At an alkali-ion site, subscript h in the numerator of the first square bracket of equation (17a) is replaced by a .

‡The dipole due to the core polarization of the six nearest neighbor ions as corrected for the $\frac{1}{2}$ factor in equations (12) hence the prime on $\mu_a(a)$.

F-electron. This is reflected in equations (12b) and (14b). This is true even in state $E_u(X_u)$. Actually, the binding energies of the bound electrons may not be an order of magnitude larger than for the *F*-electron, and this leads to uncertainties in the approximations to be used (Hartree or adiabatic). Because of the response times, we assume that an eigenvalue and eigenfunction of the *F*-electron depends on X as well as the polarization of the ions, symbolized by x (displacement of the bound electrons). Ignoring the core polarization, the Franck-Condon principle gives:

$$E_m(a) = E_u(X_g) - E_g(X_g) \quad (20a)$$

$$E_m(e) = E_u(X_u) - E_u(X_u) \quad (20b)$$

X_g and X_u stand for the ionic equilibrium positions when the *F*-electron distribution is $|\psi_u|^2$ or $|\psi_g|^2$. When core polarization is considered, we believe that the equations should have the form:

$$E_m(a) = E_u(X_g, x_u) - E_g(X_g, x_g) \quad (21a)$$

$$E_m(e) = E_u(X_u, x_u) - E_u(X_u, x_g). \quad (21b)$$

They imply that V_0 adjusts itself to the eigenfunction the electron is in, while V_a depends on the past history of the electron. This is the reason the two polarizations must be separated. The values of X_u and X_g are obtained from the very basic equation [32]:

$$\left[\frac{\partial E_n(X, x_n)}{\partial X} \right]_{x_n} = 0 \quad (N = u \text{ or } g). \quad (22)$$

Here x_n symbolizes the fact that the ionic polarizations are determined by the eigenfunction in which the *F*-electron is in. In so far as we know, a general method of deriving equations (21) and (22) has not been given. Actually, equation (22) was not used, but our technique seems to be equivalent.

7. THE RADIUS

The first quantity required is the radius of the spherical cavity. Usually the Mott-

Littleton value is used. The point-ion calculation is an exception. Gourary and Adrian [15] calculate V_m in detail (assuming spherical symmetry) but ignore V_p in the zeroth approximation. One may incorporate their calculation into our scheme by writing:

$$V = V_m(\text{spherical}) \quad (23a)$$

and

$$V_p = \chi = E_{cb} = 0. \quad (23b)$$

V is just the Madelung potential for a lattice with a missing ion. At the center of the imperfection it is $-e^2\alpha_m/a$ while at moderately large distances from the vacancy it must be $-e^2/r$. The actual behavior of V is given in Fig. 1 of [15].

An alternate procedure would be to use a radius from some 'classical' calculation on ionic crystals such as Goldschmidt's [44]. We explore this problem in Table 3. Details to carry through the calculation will be given shortly. The table indicates that the radius does not affect the E_m 's critically, although we know for a deep well E_m depends only on R . The ϵ 's, however, do depend on the radius. This indicates that the approach of Simpson

Table 3. The effect of varying R on the calculations of $E_m(a)$ and $E_m(e)$ *

Goldschmidt radius	1.8 Å	$R = a$	Exp. values
	NaCl $a = 2.81$ Å		
$\epsilon_g(X_g)$	-3.25	-4.01	
$\epsilon_u(X_g)$	-1.06	-1.91	
$E_m(a)$	2.19	2.10	2.77†
$\epsilon_g(X_u)$	-2.22	-2.52	
$\epsilon_u(X_u)$	-0.96	-1.223	
$E_m(e)$	1.26	1.29	1.01†
	KCl $a = 3.14$ Å		
$\epsilon_g(X_g)$	-2.96	-3.44	
$\epsilon_u(X_g)$	-1.11	-1.61	
$E_m(a)$	1.85	1.83	2.31†
$\epsilon_g(X_u)$	-2.31	-2.57	
$\epsilon_u(X_u)$	-1.04	-1.28	
$E_m(e)$	1.27	1.29	1.22†

*All calculations were performed for $V_s(\psi_r, r)$. The energies are in electron volts.

†Table 1.

(b), where there is no boundary between a vacuum and a continuum, might be made to be superior to the semi-continuum model. We shall, for simplicity, use Fig. 1 of [15], however, and write:

$$R = a. \quad (24)$$

8. SOME DETAILS OF THE CALCULATIONS

The Hamiltonian, actually the electronic part, h_e , (see [2, Chap. X] or [32]) is obtained by using the appropriate potential. Since we require a self-consistent solution, the electronic wave function is included as a parameter. To use the modified Franck-Condon principle, h is written as follows:

$$\begin{aligned} h_j(\psi) &= T + V_m + V_0(\psi) + V_d(\psi) + V_{cj} \\ &= T + V_j; \quad (j = 1, 2 \text{ and } 3). \end{aligned} \quad (25)$$

T is the kinetic energy operator. The last term has been added in the dielectric to correct for the asymptotic behavior of our total potentials. In addition to V_{c2} ($V_{c3} = 0$), we considered the correction:

$$V_{c1} = -\frac{e^2}{\kappa_0 r} + \frac{e^2}{r} \quad \text{for } r > R. \quad (26)$$

Table 4 describes the potential behavior at large distances. V_1 is a limiting case, it makes the potential weakest at large distances.

We employ the following normalized envelope wave functions:

$$\psi(g) = \psi(\Gamma_1^+) = \left(\frac{\alpha^3}{7\pi}\right)^{1/2} (1 + \alpha r) e^{-\alpha r} \quad (27a)$$

and

$$\psi(u) = \psi(\Gamma_4^-) = \left(\frac{\beta^5}{\pi}\right)^{1/2} r \cos \theta e^{-\beta r} \quad (27b)$$

$\psi(g)$ is a Γ_1^+ function which resembles a 1s hydrogenic function. It has been used many times. $\psi(u)$ is a modified 2p hydrogenic function.

To evaluate the α 's and the β 's the following quantities are required:

$$\begin{aligned} \epsilon_{gt}(\mathbf{X}_g, \mathbf{x}_g) &= \langle g|T|g\rangle + \langle g|V_m|g\rangle \\ &+ \langle g|V_0(g)|g\rangle + \langle g|V_d(g)|g\rangle + \langle g|V_{ct}|g\rangle \end{aligned} \quad (28a)$$

$$\begin{aligned} \epsilon_{ut}(\mathbf{X}_g, \mathbf{x}_u) &= \langle u|T|u\rangle + \langle u|V_m|u\rangle \\ &+ \langle u|V_0(u)|u\rangle + \langle u|V_d(g)|u\rangle + \langle u|V_{ct}|u\rangle \end{aligned} \quad (28b)$$

$$\begin{aligned} \epsilon_{gt}(\mathbf{X}_u, \mathbf{x}_g) &= \langle g|T|g\rangle + \langle g|V_m|g\rangle \\ &+ \langle g|V_0(g)|g\rangle + \langle g|V_d(u)|g\rangle + \langle g|V_{ct}|g\rangle \end{aligned} \quad (28c)$$

and

$$\begin{aligned} \epsilon_{ut}(\mathbf{X}_u, \mathbf{x}_u) &= \langle u|T|u\rangle + \langle u|V_m|u\rangle \\ &+ \langle u|V_0(u)|u\rangle + \langle u|V_d(u)|u\rangle + \langle u|V_{ct}|u\rangle. \end{aligned} \quad (28d)$$

In equation (28) *only* the V 's are made spherically symmetric. The derivation in section 5, strictly speaking, applies only to a Γ_1^+ function.

The contribution to the potential energies of equations (28) from within the cavity are

Table 4. Asymptotic behavior of V

j	$V_j = V_m + V_0(\psi) + V_d(\psi) + V_{cj}$		
	V_j	V for NaCl	V for KCl
1	$-\left(\frac{3}{2\kappa_0} - \frac{1}{2}\right) \frac{e^2}{r}$	$-0.167 \frac{e^2}{r}$	$-0.204 \frac{e^2}{r}$
2	$-\frac{1}{\kappa_0} \frac{e^2}{r}$	$-0.444 \frac{e^2}{r}$	$-0.469 \frac{e^2}{r}$
3	$-\frac{1}{2} \left(1 + \frac{1}{\kappa_0}\right) \frac{e^2}{r}$	$-0.722 \frac{e^2}{r}$	$-0.735 \frac{e^2}{r}$

obtained by taking the expectation value of $V(\psi, 0)$ over R . $V(\psi, 0)$ is obtained from equations (2a) and (19) using the appropriate p 's as indicated by \mathbf{X} and \mathbf{x} in equations (28).

To evaluate the α 's and β 's, as well as the energies, we proceed as follows: a value of α (or β) is selected, α_1 and then $h(\alpha_1)$ is evaluated by numerical calculation. The appropriate value of α to minimize $\langle \alpha | h(\alpha_1) | \alpha \rangle$ is then obtained, keeping α_1 fixed. Now the new α replaces α_1 and the process continues until the value of α equals α_1 . For $\epsilon_{ut}(\mathbf{X}_g, \mathbf{x}_u)$

and $\epsilon_{\mu}(X_u, x_g)$ the known values of the parameter for the ground state (or excited state) are used to evaluate $\langle u|V_d(g)|u\rangle$ and $\langle g|V_d(u)|g\rangle$.

9. THE NUMERICAL RESULTS

Our results are now presented. The parameters used are given in Table 5 while Tables 6 and 7 summarize the calculations. The results indicate that the essential features of the *F*-center can be obtained from Mott and Gurney's model. The calculations also indicate that the dramatic change of the *F*-center properties arises from changes in the *polarizations* around the negative-ion vacancy. This basic concept is obtained from the requirement of self-consistency.

Table 5. Numerical value of parameters used in the calculations*

Quantity used	NaCl	KCl
E_{cb} *	-1.42	-1.22
κ	5.62	4.68
κ_0	2.25	2.13
a (in Å)	2.81	3.14
α (in Å ³)	2.8	3.4
α_h (in Å ³)	3.69	3.69
α_a (in Å ³)	0.18	0.84
χ^\dagger	Neglected	
m	Free electron mass	

*The values of the parameters which describe the solid were obtained from Mott and Gurney[6]. α_h and α_a are Pauling's values[6, p. 14]. α was calculated by our equation (18), ρ being obtained from Table 8[6, p. 22] with γ set equal to zero. We used the equation below:

$$E_{cb} = -\frac{1}{2} \frac{e^2}{a} \left(1 - \frac{1}{\kappa_0}\right),$$

to obtain E_{cb} , see[2 p. 309].

†We did not use χ , i.e., $\chi = 0$. Since E_{cb} was employed, this means that effectively, we were using a larger χ . For KCl, the measured χ varies from 0.3 [JAIN S. C. and SOOHA G. D., *J. Phys. Chem. Solids* 26, 267 (1965)] to 0.7 [TIMUSK T., *J. Phys. Chem. Solids* 18, 265 (1965)]. Thus, we may have overestimated $(-\chi + E_{cb})$ if E_{cb} should be included in the measured electron affinity. Note that we are using the convention $\chi > 0$ and $E_{cb} < 0$.

One obtains the best agreement by using V_1 for absorption and V_2 for emission. We have not been able to justify this procedure, however. Table 6 indicates that V_3 and V_2 are too shallow to give accurate values of $E_m(a)$. The actual potentials, Table 8 and Fig. 2, show that V_1 resembles the "particle-in-a-box potential" more closely than V_2 and V_3 [$V_1(\psi, R) - V_1(\psi, 0)$ is larger]. This arises because the potential in the dielectric is 'shallower', and the electron is confined to the vacancy. V_2 gives remarkable good results for $E_m(e)$. This is expected since at large distances from the vacancy it is the 'best' potential. In Table 8, $V(\psi, 0)$ is not the true depth because of E_{cb} . Values of $V(\psi, 0)$ show that there is relatively little *polarization* for the $\psi(g, X_u)$ state since the true depth is about 8 eV, which approaches the Madelung depth of 9 eV.

Figure 3 compares our levels to Fowler's, while in Fig. 4 plots are presented of some of $p(r)$. We have added Fowler's $p(r)$ associated with $E_u(X_u)$ to show that it is a little less diffused than ours. His other p 's are similar to those obtained here. Table 9 compares our values of δ with others found in the literature. $\delta_u - \delta_g$, is approximately $0.1a$ for all cases. This indicates that Fowler's use of $0.1a$ is reasonable.

Next we indicate that our calculations give 'reasonable' values for the lifetime, in view of present uncertainties. The most reliable equation at present seems to be Fowler's, namely:

$$\tau = 3A \frac{\pi^2 \hbar^3 c^2}{n^2} \frac{E_m(u)}{E_m^3(e)} \frac{1}{\Sigma} \{ |\langle Z \rangle|_a^2 / |\langle Z \rangle|_e^2 \}. \quad (29)$$

Here Σ is the cross section for absorption, obtained experimentally, and A is the correction for changes in the local field[10, equation (16)]. Using the experimental values of E_m from Table 1, and the measurements of Silsbee[45], we obtain:

$$\tau(\text{NaCl}) = 9.40 \times 10^{-8} A \{ |\langle Z \rangle|_a^2 / |\langle Z \rangle|_e^2 \} \text{ sec} \quad (30a)$$

Table 6. Summary of calculations and the comparison to the experimental values

	Absorption				Energies (eV)		Emission [†]	
	$\epsilon_D(X_D, X_D)$	$\epsilon_u(X_D, X_u)$	δ_D	$E_m(a)$	$\epsilon_D(X_u, X_D)$	$\epsilon_u(X_u, X_u)$	δ_u	$E_m(e)$
NaCl								
Exp.*				2.77				1.01
V_1	-3.48	-0.75	-0.024	2.73	-3.04	-0.62	+0.038	2.42
V_2	-3.70	-1.26	-0.028	2.44	-1.30	-0.14	+0.075	1.16
V_3	-4.01	-1.91	-0.007	2.10	-2.52	-1.23	+0.067	1.29
KCl								
Exp.*				2.31				1.22
V_1	-2.88	-0.52	-0.03	2.36	-3.04	-0.89	+0.027	2.15
V_2	-3.33	-1.37	-0.018	1.96	-1.46	-0.28	+0.067	1.18
V_3	-3.44	-1.61	-0.012	1.83	-2.58	-1.29	+0.060	1.29

*From Table 1, δ = displacement of the nearest neighbor ion in units of a ; + outward-inward. Due to an oversight, R was set equal to R_m in KCl (absorption) for V_1 and V_3 instead of 'a', as in all the other cases. In view of the changes in the computing facilities, it would be a major undertaking to make these corrections.

Table 7. Values of α and β used ($\times 10^{-8}$) cm^{-1}

	α for $\psi(g, X_D)$	α for $\psi(g, X_u)$	β for $\psi(u, X_D)$	β for $\psi(u, X_u)$
NaCl				
V_1	1.067	1.000	0.821	0.758
V_2	1.008	0.606	0.797	0.078
V_3	0.931	0.714	0.685	0.476
KCl				
V_1	0.995	0.934	0.722	0.728
V_2	0.913	0.626	0.696	0.144
V_3	0.862	0.702	0.587	0.460

Table 8. Value of parameters used to describe the potential in eV

Quantity used	NaCl		
	$V_i(\psi, 0)$	$V_i(\psi, R)$	$V_i(\psi, R) - V_i(\psi, 0)$
Absorption*			
V_1	-6.59	-0.72	+5.87
V_2	-6.55	-2.12	+4.43
V_3	-6.48	-3.38	+3.10
Emission			
V_1	-5.79	-0.69	+5.10
V_2	-2.68	-1.71	+0.97
V_3	-4.20	-3.25	+0.95

*In the table for absorption, the potential was derived from $\psi(g, X_D)$, while $\psi(u, X_u)$ was employed in emission. The values using $\psi(u, X_D)$ and $\psi(g, X_u)$ are slightly different and can be obtained from reference [43].

$$V_i(\psi, R) = \lim_{\epsilon \rightarrow 0} V_i(\psi, R + \epsilon).$$

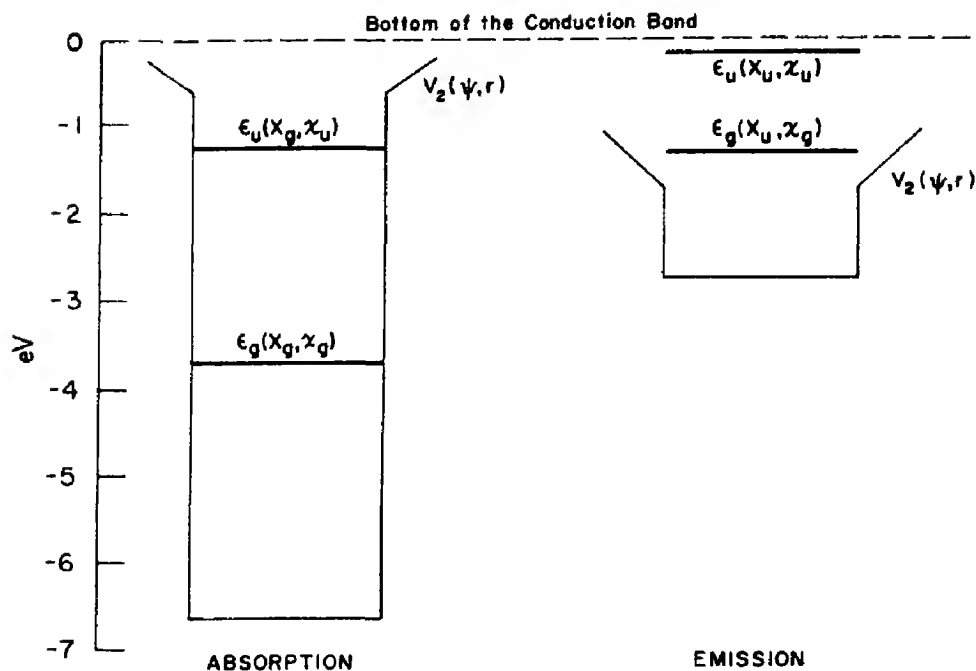


Fig. 2. Self-consistent potential for NaCl. The diagrams shows our calculated potentials and the four energy levels associated with absorption and emission. Potential V_2 was used (See Table 8).

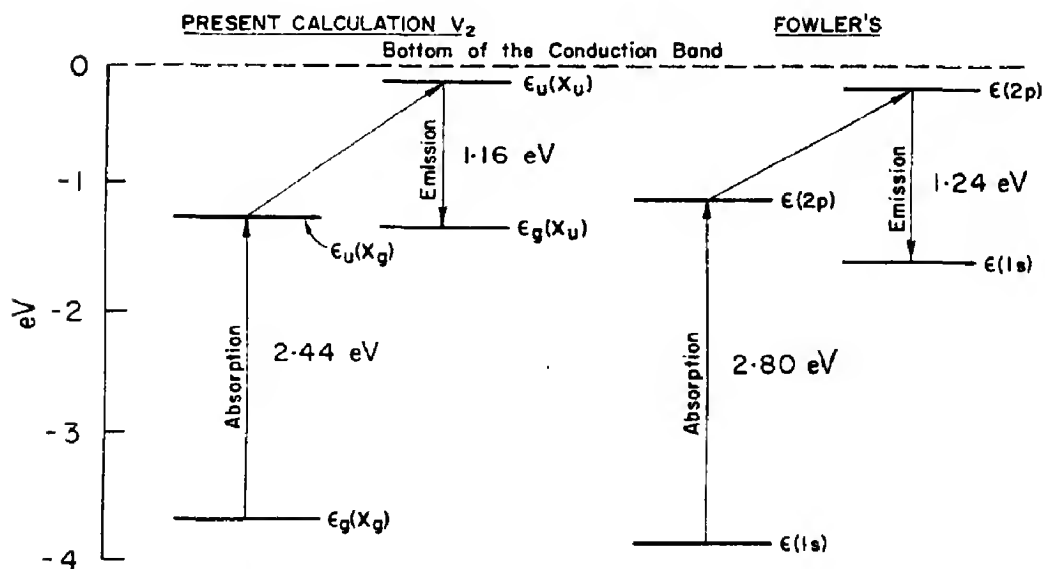


Fig. 3. A comparison of our calculations with Fowler's.

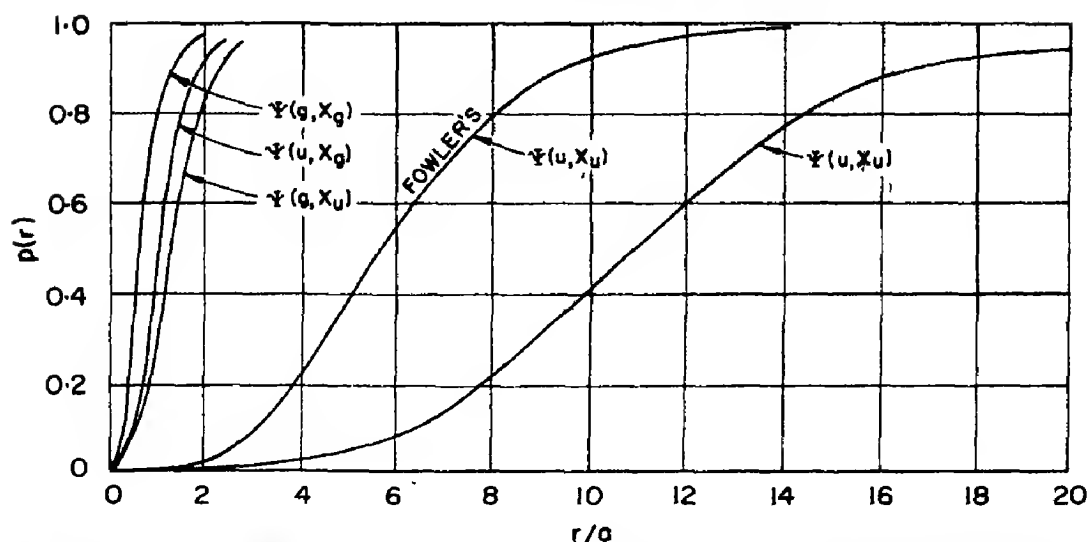


Fig. 4. Plots of $p(r)$ against r/u . Here we plot the fraction of the electron within a radius r of the vacancy [equation (4a)] for the four levels of interest. Potential V_1 was used for absorption and V_2 was used for emission (See Table 10). Fowler's p is shown for the $\psi(u, X_u)$ eigenfunction. Note that p is calculated from ψ although labelled by Ψ .

Table 9. Various values of the displacement of the nearest neighbors in units of a

Calculation	X_u	X_v	$X_u - X_v$
NaCl			
Fowler[10]			0.1 assumed
Wood-Joy[9]*	-0.016	+0.090	0.106
		+0.130	0.146
Bennet[11]	+0.015	+0.103	0.088
Present (V_2)	-0.028	+0.075	0.013
Mott-Littleton's displacement (negative-ion vacancy)			
			+0.078
KCl			
Wood-Joy[9]	-0.020	+0.094	0.114
		+0.127	0.147
Bennet[11]	+0.012	+0.102	0.090
Present (V_2)	-0.018	+0.067	0.085

*The displacements of Wood and Joy is anisotropic in the upper state. Note + outward, - inward.

and

$$\tau(\text{KCl}) = 5.13 \times 10^{-8} A \{ |\langle Z \rangle|_a^2 / |\langle Z \rangle_e^2 \} \text{ sec.} \quad (30b)$$

The lifetimes shown in Table 10 were obtained by letting $A = 1$. The result for KCl is exactly what one would expect, at present,

while the result for NaCl is certainly fortuitous. In making the table, we have been 'selective' in using one V for absorption and another for emission, since we believe this gives a better idea of what can be expected from the model. Any major improvement of the results will require a reliable determination of A and the resolution of the problems suggested in Section 3. The measurements of Swank and Brown do not necessitate a revision of our ideas regarding the F -center, and, by themselves they do not require an upper Γ_1^+ state. By selecting different V_i 's, one can decrease the τ 's.

We believe that our calculations establish that the dramatic differences between $E_m(a)$ and $E_m(e)$ and the long lifetime of the excited state arise from the differences in the polarizations. Other factors are less important. If the upper state is a combination of Γ_1^+ and Γ_4^- wavefunctions, the Γ_1^+ function gives an infinite lifetime while the Γ_4^- part may give a long one.

Finally, one may ask: Why are our results only approximate, and how can they be improved? Reliable eigenfunctions and eigenvalues will not be obtained before we know

how to handle the optical and the displacement polarization about a point imperfection in polar solids. This is the *major* present problem.

We must also remember, that here we are only calculating the envelope functions by an extremely approximate technique, which does not apply to the tightly bound F -electron associated with $E_m(a)$. If only a small fraction

In view of the measurements of Apker and Taft, our corrected levels seem to be too large in absolute values.

9. SUMMARY

This paper considers two aspects of the theory of the F -center. We have presented a new self-consistent calculation and compared

Table 10. Lifetime calculations

Potential employed	$ \langle z \rangle ^2 10^{-16} \text{ cm}$	$\tau_{\text{cal}} (\mu \text{ sec})$	$\tau_{\text{exp}}^* (\mu \text{ sec})$
V_1 (ab)	1.69	NaCl	1
V_2 (em)	0.123		
		KCl	0.58
V_1 (ab)	1.93		
V_2 (em)	0.766	0.13	

*References [2 p. 95] or [4].

of the electron is in the dielectric, as in the $\psi(g, \mathbf{X}_g)$ state, perhaps the above technique applies, with the effective mass equal to the true mass. This could explain the success of the "particle-in-a-box" approximation, particularly if R is smaller than a . Actually, this is only an approximation in view of the ENDOR measurements [2] and the fact that a large fraction of the electron is in the dielectric for $\psi(u, \mathbf{X}_u)$. The theory applies approximately to $E_m(e)$ (with an effective mass), and $E_m(e)$ might be considered the test of the theory. Here our calculations are fairly satisfactory. The above limitations arise from the nature of the physical problem and not from the approximations employed.

Our ϵ 's are relative to the bottom of the conduction band; see equation (2a). For the vacuum values, we must add E_{cb} . This lowers our ϵ 's ($E_{cb} < 0$) and makes them more in line with the calculation of Wood and Joy, as well as of Gourary and Adrian. This does not resolve the problems of Table 1, since, for all other calculations, $E_{cb} = 0$ and $\chi \approx 0.5 \text{ eV}$.

various calculations of the *electronic* binding energies made previously.

Our calculations show:

- (1) The ideas regarding the F -center which date back to Mott and co-workers are sufficient to explain the absorption, the emission and the lifetime of the first excited state when employed in a *self-consistent* manner.
- (2) One may derive the potential terms which include various polarization effects from energy considerations. This shows that there are some inconsistencies in the derived potential at large distances from the vacancy due to the various relaxation times.
- (3) A new form of the Born-Oppenheimer technique is *suggested* for the case when electrons have more than one relaxation time.
- (4) It is easy to explain the measured lifetime by assuming values for parameters which enter into the theory. All the

calculations have adjustable parameters, so that one can not place complete reliance on them. The lifetime measurements *alone* do not suggest in any way that the relaxed excited state is *s*-like (Γ_1^+).

Our study of the various past *F*-center calculations indicates that they can be classified into four categories:*

- (1) The semi-continuum model.
- (2) The semi-continuum polaron model. This model assumes that the electron lattice displacement interaction can be described by the longitudinal optical modes of vibration (infinite wavelength approximation). Some local ionic displacements and distortions may be considered.
- (3) The point-ion model (a) without polarization and (b) with polarization. The pseudopotential could be considered a variation of (3), or perhaps it should be in (4) below.
- (4) The Hartree-Fock model where the internal structure of the ions which surround the vacancy is taken explicitly into account. Effects of ionic displacements are also considered.

The differences in the eigenvalues of the lowest and the first excited state give approximately the measured values of $E_m(a)$ and $E_m(e)$. The actual eigenvalues have a *very* large scatter, however. Each classification shows some self-consistence except for (3a) and (3b). It is impossible at present to determine which approach gives the most reliable eigenvalues and eigenfunctions. Probably the semi-continuum model is the best at present.

One of the biggest puzzles to us is why so many seemingly different models give correct values of $E_m(a)$ and $E_m(e)$. We believe that

the basic reason for this is that the calculations of $E_m(a)$ are related implicitly to the problem of a "particle-in-a-box", while the calculations of $E_m(e)$ are related to the problems of the "hydrogen-atom-in-a-dielectric." This might not hold for the Hartree-Fock calculations.

The calculations and the review indicate that the theories on the *F*-center at present are strongly limited, since a completely general method of calculating wave functions at point imperfections in polar solids does not exist. Truly useful calculations on the *F*-center problem can only be made after a more general theory of point imperfections in dielectric solids has been developed.

Acknowledgements—We would like to thank the following for helpful conversations or correspondence: W. B. Fowler, H. S. Bennett, J. A. Krumhansl, D. W. Lynch, J. Schmidt, F. Seitz, J. H. Simpson and R. F. Wood.

REFERENCES

1. For a general discussion of the problem see: SCHULMAN J. H. and COMPTON W. D., *Color Centers in Solids*, Pergamon Press, Oxford (1962) or [2].
2. MARKHAM J. J., *F-centers in Alkali Halides*, Academic Press, New York (1966).
3. BOTDEN T. P. J., VAN DOORN C. Z. and HAVEN Y., *Philips Res. Rep.* **9**, 469 (1954).
4. SWANK R. K. and BROWN F. C., *Phys. Rev. Lett.* **8**, 10 (1962); *Phys. Rev.* **130**, 34 (1963).
5. TIBBS S. R., *Trans. Faraday Soc.* **35**, 1471 (1939).
6. MOTT N. F. and GURNEY R. W., *Electronic Processes in Ionic Crystals*, 2nd Ed. Oxford University Press, Oxford (1948).
7. SIMPSON J. H., *Proc. R. Soc.* **A197**, 269 (1949).
8. KRUMHANSL J. A. and SCHWARTZ N., *Phys. Rev.* **89**, 1154 (1953).
9. WOOD R. F. and JOY H. W., *Phys. Rev.* **136**, A451 (1964).
10. FOWLER W. B., *Phys. Rev.* **135**, A1725 (1964).
11. BENNETT H. S., *Phys. Rev.* **169**, 729 (1968).
12. ÖPIK V. and WOOD R. F., *Phys. Rev.* **179**, 772 (1969) and WOOD R. F. and ÖPIK V., *Phys. Rev.* **179**, 783 (1969); BARTRAM R. H., STONEHAM A. M. and GASH P., *Harwell Rep.*, No. T.P.336.
13. PINCHERLE L., *Proc. phys. Soc.* **A64**, 648 (1951).
14. WANG S., (a) *Phys. Rev.* **132**, 573 (1963); (b) *Phys. Rev.* **153**, 939 (1967).
15. GOURARY B. S. and ADRIAN F. J., *Phys. Rev.* **105**, 1180 (1957).
16. SIMPSON J. H., *Proc. phys. Soc.* **71**, 761 (1958).
17. KÜBLER J. K. and FRIAUF R. J., *Phys. Rev.* **140**, A1742 (1965).
18. LÖFFLER A., *Z. Naturf.* **22a**, 1771 (1967).

*The continuum model was not considered here, as stated in Section 2.

19. EVSEEV Z. Y. and TOLPYGO K. B., *Soviet Phys. solid St. (English Edition)* **9**, 1 (1967).
20. MARKHAM J. J. and KONITZER J. D., *J. chem. Phys.* **34**, 1936 (1961).
21. The experimental values were obtained as follows: NaCl: 2 from [3], one from each of the following: VAN DOORN C. Z. and HAVEN Y., *Philips Res. Rep.* **11**, 479 (1956); GEBHARDT W. and KÜHNERT H., *Phys. Lett.* **11**, 15 (1964) and *Phys. Status Solidi* **14**, 157 (1966). KCl, same except that [3] has only one value. The experimental values of $E_m(e)$ show a large scatter and complete reliance cannot be placed on them. Questions exist as to how to plot an emission band, since the frequency dependence of the matrix elements associate with the transition is not known theoretically; See, for example, BOOTHERS A. D. and LYNCH D. W., *Phys. Rev.* **164**, 1124 (1967).
22. MARKHAM J. J., *F-centers in Alkali Halides*, p. 123. Academic Press, New York (1966).
23. KONITZER J. D. and MARKHAM J. J., *J. chem. Phys.* **32**, 843 (1960).
24. Calculation by GILBERT R. L., presented in [2, p. 321]. The calculations are based on Simpson (a). The details were carried through by SMITH W. A. and GILBERT R. L.
25. PEKAR S. I., *Untersuchungen über die elektronen Theorie der Kristalle*, Akademie, Berlin (1954), English translation: *Research in Electron Theory of Crystals*, A.E.C. tr. 5575.
26. STUMPF H., *Quantentheorie der Ionenrealkristalle*, Springer, Berlin (1961).
27. WAGNER M., *Z. Naturf.* **15a**, 889 (1960); *ibid.* **16a**, 302, 410 (1961).
28. MOTT N. F. and LITTLETON M. J., *Trans. Faraday Soc.* **34**, 485 (1938).
29. RITTER J. and MARKHAM J. J., *Phys. Lett.* **24A**, 524 (1967); RITTER J. and STETTLER J. D., *Phys. Lett.* **25A**, 675 (1967).
30. KOJIMA T., *J. phys. Soc. Japan* **12**, 908, 918 (1957); WOOD R. F. and KORRINGA J., *Phys. Rev.* **123**, 1138 (1961).
31. APKER L. and TAFT E., *Phys. Rev.* **79**, 964 (1959), *ibid.* **81**, 689 (1951); *ibid.* **82**, 814 (1951); See also *Imperfections in Nearly Perfect Crystals* (Edited by W. Shockley), p. 246. Wiley, New York (1952).
32. MARKHAM J. J. *Rev. mod. Phys.* **31**, 956 (1959).
33. BOGAN L. D., Ph. D. thesis, unpublished. Cornell University (1968). Bogan associates $\epsilon_p(X_p)$ and $\epsilon_u(X_u)$ with the F-center and refers to the $\epsilon_p(X_p)$ and $\epsilon_u(X_u)$ states as the F*-center. This means leading, since both the two upper and two lower states are related.
34. PEKAR S. I. and PERLIN Y. E., *J. exp. theor. Phys. (English Edition)* **43**, 782 (1962); for a criticism of this paper, see FOWLER W. B. and DEXTER D. L., *Phys. Status Solidi* **3**, 1865 (1963).
35. The general problem of calculating lifetimes has been considered by FOWLER W. B. and DEXTER D. L., *Phys. Rev.* **128**, 2154 (1962); *J. chem. Phys.* **43**, 1768 (1965); MARKHAM J. J., *Z. Phys.* **188**, 139 (1965).
36. GILBERT R. L., *Phys. Lett.* **A25**, 382 (1967).
37. TOMURA M., KITADA T. and HONDA S., *J. phys. Soc. Japan* **23**, 454 (1967).
38. LEMOS A. M. and MARKHAM J. J., *J. Phys. Chem. Solids* **26**, 1837 (1965).
39. RITTER J. and MARKHAM J. J., *Phys. Rev.* To be published (1969).
40. At present, we do not know how to formulate the emission if there are two close by states of different geometry since our kets are products of electronic and lattice kets. Whether one used simple Born-Oppenheimer functions or various linear combinations of these must depend on the size of various perturbation terms. Very recently, further evidence has appeared to suggest that the upper relaxed state belongs to the Γ_4^- representation: See BOSI L., PODINI P. and SPINOLO G., *Phys. Rev.* **175**, 1133 (1968); HETRICK R. E., Ph.D. thesis (physics). University of Illinois (1969).
41. HAKEN H. and SCHOTTKY W., *Z. phys. Chem.* **16**, 218 (1958); see also HAKEN H. *Polarons and Excitons* (Edited by C. G. Kuper and G. D. Whitfield), p. 295. Oliver and Boyd, London (1963).
42. For details, see ROJANSKY V., *Introductory to Quantum Mechanics*, p. 150. Prentice-Hall, New York (1938), or SCHIFF L. I., *Quantum Mechanics*, 2nd Edn, p. 76. McGraw Hill, New York (1955).
43. For details see GILBERT R. L., Ph.D. Thesis. Illinois Institute of Technology (1967).
44. SEITZ F., *Modern Theory of Solids*, p. 91. McGraw-Hill, New York (1940).
45. SILSBEE R. H., *Phys. Rev.* **103**, 1675 (1956).

ON THE OPTICAL PROPERTIES OF SOME LAYER COMPOUNDS

P. A. LEE, G. SAID, R. DAVIS and T. H. LIM
Brighton College of Technology, Sussex, England

(Received 24 March 1969; in revised form 7 July 1969)

Abstract—The paper deals with the optical properties of single crystals near the fundamental absorption edge of the following layer compounds: $\text{SnS}_x\text{Se}_{2-x}$ (where $0 \leq x \leq 2$), ZrS_2 , ZrSe_2 , TiS_2 and CdI_2 . The dispersion curves were determined from the transmitted interference fringes in the range between 0.5 and 3.5 μm . Energy gaps were found to be due to phonon assisted indirect transitions. Birefringence data are also given for a number of crystals in the visible region.

1. INTRODUCTION

LAYER compounds are characterised by their anisotropic properties along different crystallographic directions. With the advent of the closed-vapour transport technique, a large number of these compounds can easily be obtained[1]. An interesting feature of layer compounds is that they crystallise as thin plates, a form very suitable for the investigation of the optical and electrical properties and the examination of crystal structure defects. Each crystal is composed of thin layers stacked upon each other. Within each layer, the atoms are bound together by predominantly covalent forces as in the chalcogenides or strongly ionic as in the iodides. The bonds between the layers are extremely weak (due to weak van der Waal's forces). Each layer may be formed of three atomic planes X-M-X (CdI_2 -type structure), four planes X-M-M-X (e.g. Ga-chalcogenides) or the five layers X-M-X-M-X as for Bi_2Te_3 .

Due to the extremely weak interaction between the layers, these compounds can be perfectly cleaved along the basal plane, to obtain very thin wafers. Thus, a favourable surface to bulk ratio can be obtained and Frindt[2] was able to study the optical properties of a few unit-cell layers of MoS_2 .

Recently, Bassani and Parravicini[3] treated some of the layer compounds as two-

dimensional lattices. Fivaz and Mooser[4, 5, 6] discussed how pronounced anisotropic properties may affect the motion of free carriers in layer semiconductors. It was shown that in these structures the free carriers may be localised within individual layers, behaving as if moving through a stack of individual layers, "independent layer approximations". Several studies, mainly on the optical properties, have been carried out in the past few years, notably those of Greenaway and Nitsche[7] on the group IV-VI compounds and CdI_2 ; Tubbs[8] on CdI_2 and PbI_2 , and recently a large number of the iodides[9]; Dugan and Henisch[10, 11] on PbI_2 ; Domingo *et al.*[12] on SnS_2 and SnSe_2 ; Busch *et al.*[13] on SnSe_2 and Brebner[14] on the $\text{GaS}_x\text{Se}_{1-x}$ series.

2. EXPERIMENTAL PROCEDURE

The concept of the iodine vapour transport technique introduced by Schäfer[15] has been successfully used to grow many of the layer compounds. Here, the mixed series $\text{SnS}_x\text{Se}_{2-x}$ (where $0 \leq x \leq 2$) were obtained; also ZrS_2 , ZrSe_2 and TiS_2 . It is of interest to report here that CdI_2 itself has also been successfully grown by the vapour transport technique[16]. Stoichiometric proportions of the materials of 5N purity (except for Zr and Ti which were of 2N8 and 3N8 respectively) were placed with

5 mg cm⁻³ iodine (4N8) as the transport agent, in extremely clean quartz ampoules of 17 mm diameter and 20 cm length. In the case of CdI₂, it was found that large crystals can only be obtained when the iodine is reduced by about 25 per cent from its stoichiometric ratio. The ampoules were evacuated ($\sim 10^{-6}$ mm Hg), sealed off, placed in a horizontal two-zone furnace with appropriate temperatures T_1 and T_2 , where T_1 is the starting material temperature, and T_2 the growth temperature, and T_1 exceeds T_2 by approximately 50°–100°C. Crystals free from any visible surface defects can easily be obtained with thicknesses ranging from 1 μ m to 300 μ m. All surfaces exhibited a metallic lustre.

All the chalcogenides of the IV A and IV B metals examined here have the CdI₂-type structure with the 2H type stacking. The crystals of the CdI₂ themselves were found to have the 4-H structure (stacking sequence ((A γ B)(C α B)) [17].

Laue back reflection photographs showed the *c*-axis to be perpendicular to the plane of the plates. Sharp reflections were obtained

with no sign of disorder. All crystals were characterised by extreme ease of cleavage along the basal planes. These properties were found useful for studies under the electron microscope and for measuring the optical properties.

The spectrophotometers used in the following results were the Unicam SP700 with a resolution of ± 15 Å, and the Perkin Elmer model 137.

All measurements reported here were carried out at room temperature.

3. ORDINARY REFRACTIVE INDEX

Transmitted interference fringes through thin crystals with two parallel faces were easily obtained. The analysis used for determining the fringe order and the refractive index has been described in a previous paper [18]. Thickness measurements were performed using a modified optical lever [19].

The dispersion curves in the region 0.5–3.5 μ m are given for the series SnS_{*x*}Se_{2-*x*} in Fig. 1. Those for ZrS₂, ZrSe₂, TiS₂ and CdI₂

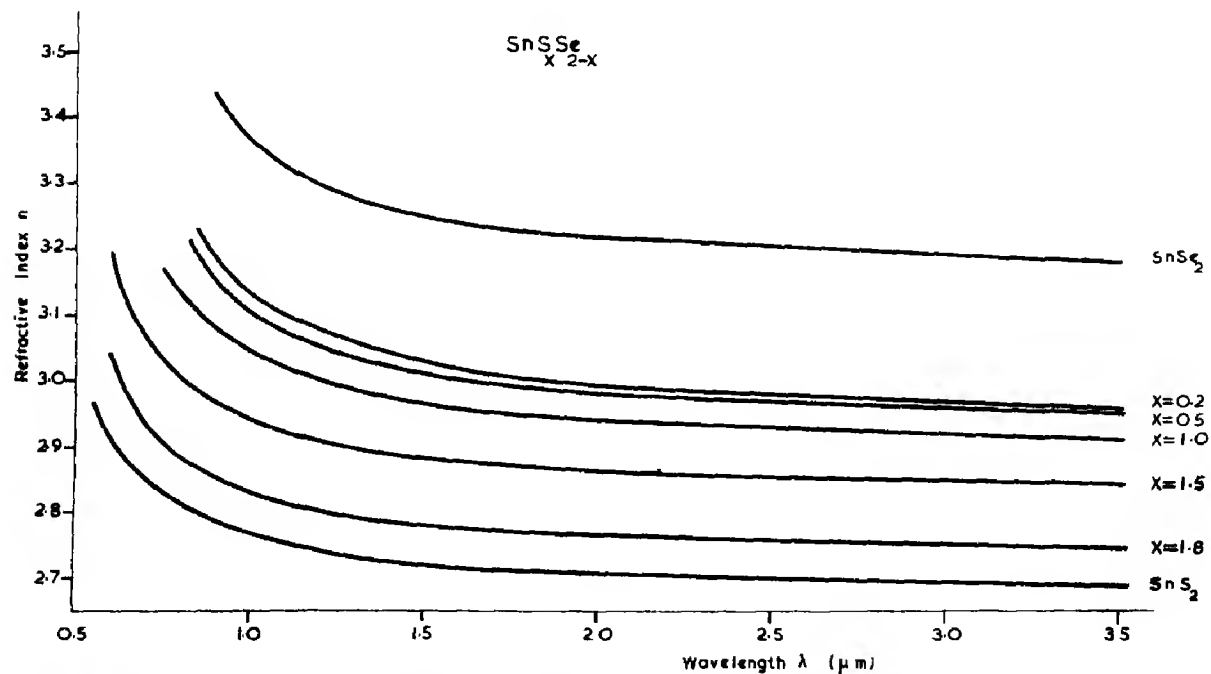


Fig. 1. Refractive index against wavelength for the series SnS_{*x*}Se_{2-*x*} where 0 ≤ *x* ≤ 2.

are shown in Fig. 2, in which SnS_2 and SnSe_2 are also included.

4. EXTRAORDINARY REFRACTIVE INDEX

Following the experimental procedure used by Tubbs[8] i.e. the "rings and brushes technique", the birefringence was determined in the visible region. This is shown in Fig. 3 for CdI_2 and in Fig. 4 for SnS_2 and PbI_2 . All the crystals were negatively uniaxial.

5. SINGLE TERM CLASSICAL OSCILLATOR ANALYSIS

The dispersion equation using the single term Sellmeier Oscillator[20], is as follows:

$$\frac{n_\infty^2 - 1}{n^2 - 1} = 1 - \frac{\lambda_0^2}{\lambda^2} \quad (1)$$

and can be compared with the experimental data obtained here. Figures 1 and 2 were used, where $(n^2 - 1)^{-1}$ against λ^{-2} , gave in all the cases a linear relationship for the compounds examined here. From these relationships, the long wavelength refractive index n_∞ together with the average interband oscillator wavelength λ_0 for all the examined layer semiconductors could be readily determined. These are included in Table 1.

6. ABSORPTION COEFFICIENT AND ENERGY GAP DETERMINATION

(a) Absorption coefficient

The absorption coefficient α was determined from the transmission measurements

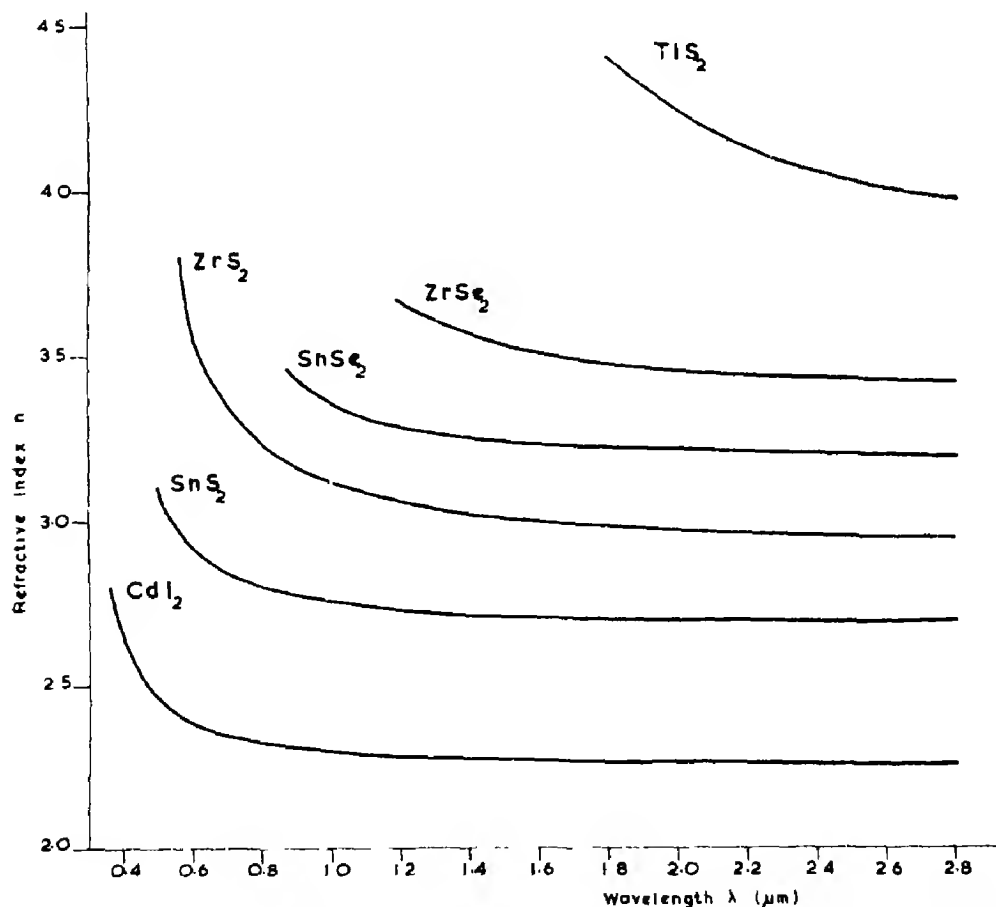


Fig. 2. Refractive index against wavelength for ZrS_2 , ZrSe_2 , TiS_2 and CdI_2 . SnS_2 and SnSe_2 are also included for comparison.

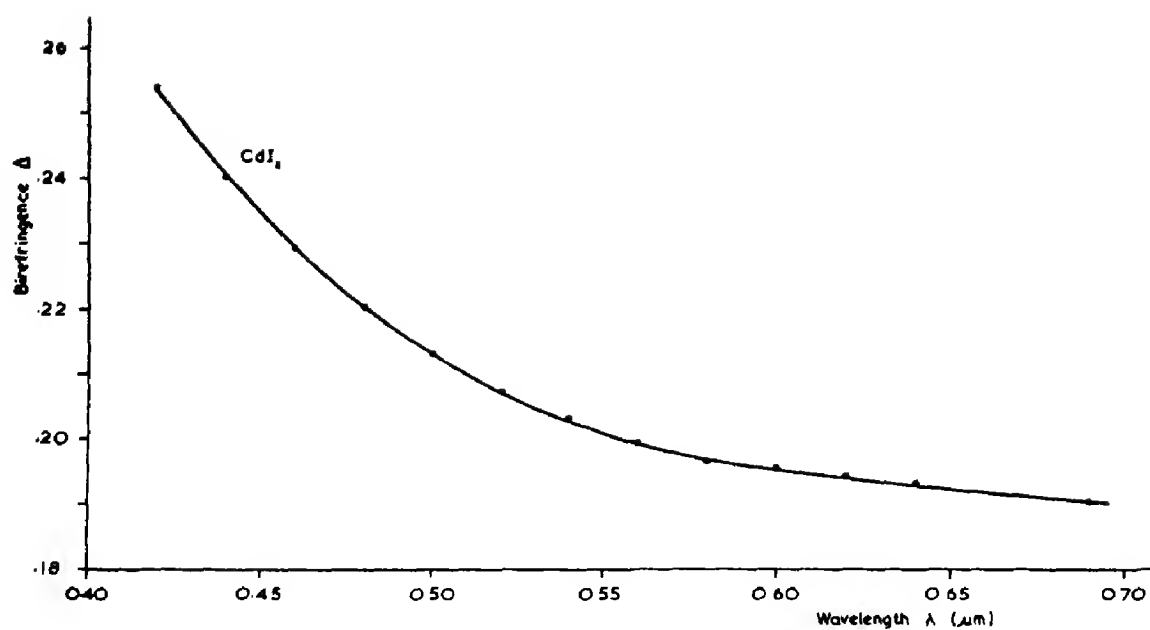
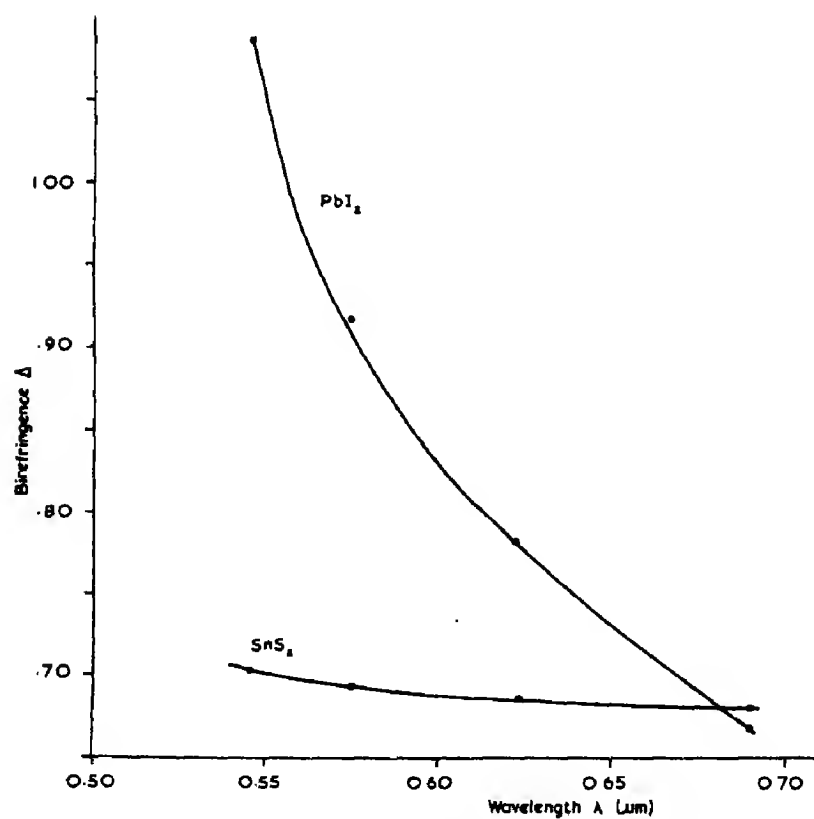
Fig. 3. Birefringence $\Delta (= n_o - n_e)$ vs. wavelength for CdI_2 .Fig. 4. Birefringence Δ vs. wavelength for SnS_2 and PbI_2 .

Table 1. Optical parameters determined for the layer compounds reported here. Measurements were made at room temperature using unpolarised light with $E \perp C$

Material	E_g (eV)	λ_g (μm)	E_0 (eV)	n_∞	$n_\infty^4 E_g$ (eV)	$E_g/S_0 \times 10^{-4} \text{ eV m}^2$
SnSe ₂	1.09	0.36	3.44	3.16	109	4.95
Sn S _{0.3} Se _{1.5}	1.19	0.35	3.54	2.96	91	5.53
Sn S _{0.5} Se _{1.5}	1.33	0.33	3.76	2.95	101	5.33
SnS Se	1.52	0.30	4.20	2.91	109	4.90
Sn S _{1.5} Se _{0.5}	1.75	0.27	4.58	2.84	114	4.72
Sn S _{1.8} Se _{0.2}	2.02	0.26	4.77	2.73	112	4.98
SnS ₂	2.22	0.24	5.17	2.70	118	4.78
TiS ₂	0.70	1.0	1.24	3.8	140	9.0
ZrSe ₂	1.20	0.52	2.38	3.35	150	6.4
ZrS ₂	1.70	0.41	3.02	2.83	110	7.2
CdI ₂	3.21	0.24	4.48	2.26	83	7.17

using the following formula [21]:

$$T_{av} = (1 - R)^2 \exp - \alpha d \quad (2)$$

where T_{av} is the average value of the transmittance, R the reflectance and d the thickness. In all cases, the value of R was found using the following relation:

$$R = \frac{(n - 1)^2}{(n + 1)^2}$$

Figure 5 shows $\log \alpha$ against $h\nu$ for the series SnS_xSe_{2-x}, and Fig. 6 shows α plotted against photon energy for the compounds ZrS₂, ZrSe₂, CdI₂, SnS₂ and SnSe₂. The insert in Fig. 6 describes α vs. $h\nu$ for TiS₂.

(b) Energy gap determination

Table 2 summarises the current acceptable forms for transitions between valence and conduction bands used in analysing the absorption coefficient α . The density of states $N(E) \sim E^{1/2}$ [21] applies to parabolic bands for isotropic structures. On the other hand, for extremely anisotropic structures, we may assume a two-dimensional form of the density of states as discussed by Fivaz [5] and Brebner [14]. They showed that the density of states is a constant independent of the energy and this is shown as $N_2(E)$ in the third column in Table 2. The table gives the dependence of α on $h\nu$ for the two forms of the density of

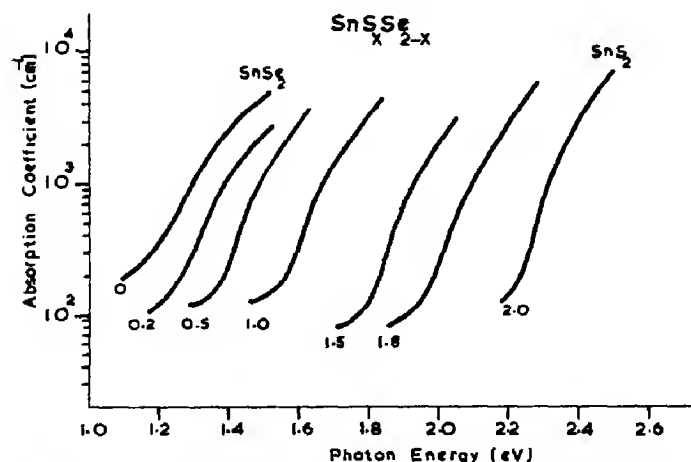


Fig. 5. Log α against photon energy $h\nu$ using unpolarised light with $E \perp C$ for the series SnS_xSe_{2-x}.

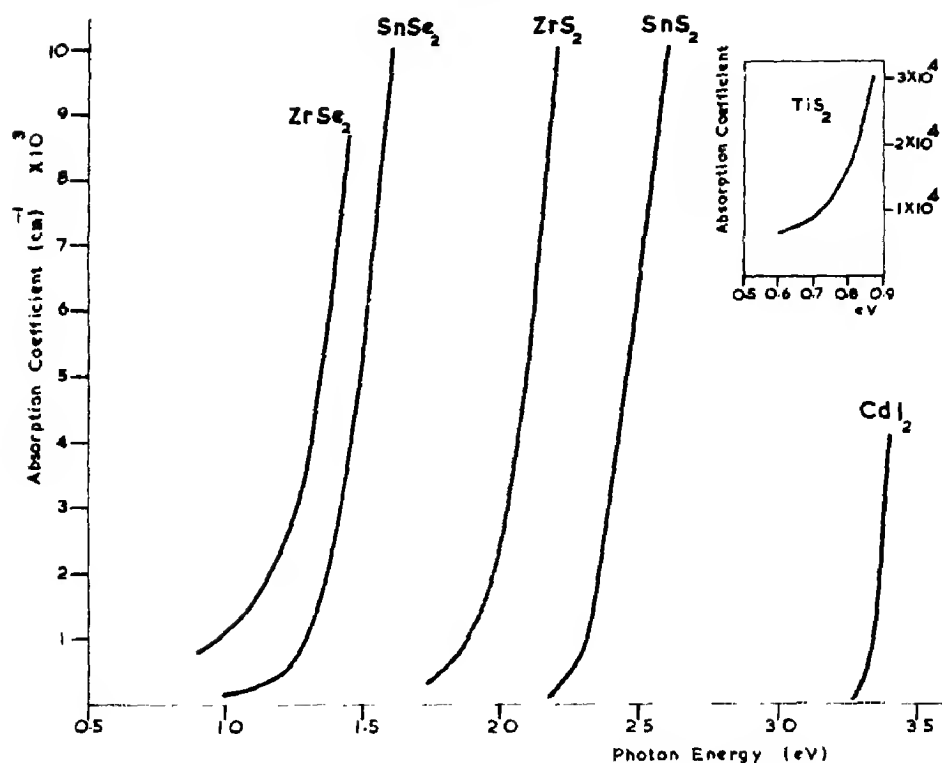


Fig. 6. Absorption coefficient against photon energy for the layer compounds shown. The insert shows α vs. $h\nu$ for TiS_2 .

Table 2. Energy gap determination rules for isotropic structures and two-dimensional lattices

Transition type	The dependence of α on $h\nu$ for the two density of state forms below	
	$N(E) \sim E^{1/2}$	$N_2(E)$
Direct allowed	$(h\nu - E_g)^{1/2}$	Independent step function
Direct forbidden	$(h\nu - E_g)^{3/2}$	$(h\nu - E_g)$
Indirect allowed	$(h\nu - E'_g \pm E_p)^2$	$(h\nu - E'_g \pm E_p)$
Indirect forbidden	$(h\nu - E'_g \pm E_p)^3$	$(h\nu - E'_g \pm E_p)^2$

states. The symbols E_g and E'_g correspond to direct and indirect energy gaps and E_p is the energy of the phonon.

Figure 7 shows $(\alpha h\nu)^{1/2}$ plotted against $h\nu$ for the series $\text{SnS}_x\text{Se}_{2-x}$, where the energy gaps were determined from the medians of the intercepts on the energy axis. These values are given in Table 1 together with those for CdI_2 and ZrS_2 , which were obtained in a similar manner.

7. DISCUSSION

The dispersion curves determined here by the transmitted interference fringes were of the normal shape and magnitude. The analysis of the main contributions to the dispersion can be envisaged as described by Moss[22]. A non-dispersive region was not observed, but a continuous linear drop out to $15\mu\text{m}$ was obtained for most materials examined here at a rate of $0.02(\mu\text{m})^{-1}$ approximately. Pub-

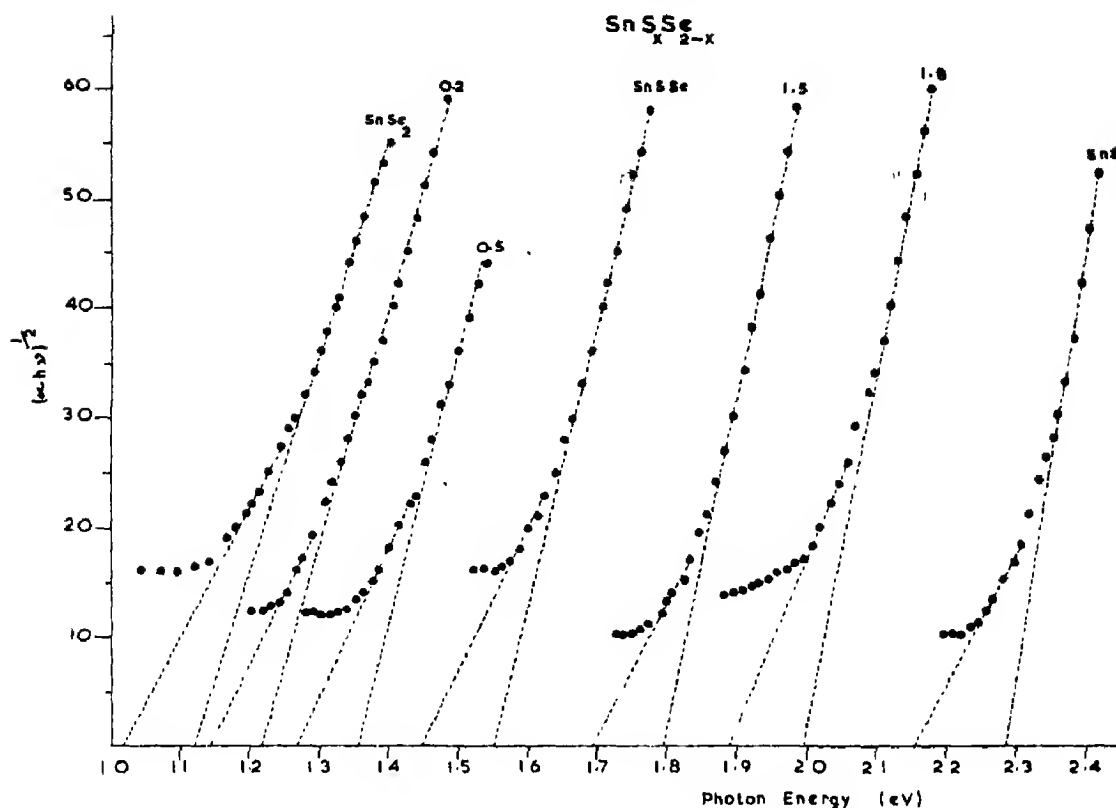


Fig. 7. $(\alpha h\nu)^{1/2}$ vs. photon energy for the series $\text{SnS}_x\text{Se}_{2-x}$.

lished refractive index data for SnS_2 [12] show good agreement at long wavelengths with the present results, but in region of the absorption edge our values are lower. Tubbs' results on the refractive index n_0 of CdI_2 [8] are considerably higher than those reported here. However, the same author reported [23] new data for n_0 for CdI_2 which are comparatively similar to those reported here for the same compound. The accuracy claimed here for the refractive index data is within ± 0.1 , where the error is dominated by the thickness measurements and the technique now used accounts for the improved values of the refractive index for SnSe_2 to those previously given [18].

The dispersion curves for $\text{SnS}_x\text{Se}_{2-x}$, ZrS_2 , ZrSe_2 and TiS_2 have not been reported previously. From Hall coefficient measurements the carrier concentration in ZrSe_2 was typically $10^{19} - 10^{20} \text{ cm}^{-3}$. The curve shown in Fig. 2 has been corrected for the contribution

to dispersion by free carriers according to the classical treatment described by Moss [21]. A similar correction has been applied to the TiS_2 curve where the carrier concentration was of the order of $10^{20} - 10^{21} \text{ cm}^{-3}$. Because of the extremely high residual absorption in TiS_2 , it was necessary to use crystals less than $5 \mu\text{m}$ thick, resulting in an error which is probably much greater than the ± 0.1 quoted for the other materials.

The birefringence Δ is shown in Fig. 3 as a function of wavelength for CdI_2 and in Fig. 4 for SnS_2 and PbI_2 . Table 3 shows Δ and n_0 for those compounds in which it was possible to obtain transmission at $\lambda = 0.69 \mu$.

The large values of Δ indicate clearly the highly anisotropic nature of the layer compounds. For CdI_2 and SnS_2 , Δ rises slowly when compared with the ordinary refractive index n_0 in the same wavelength range, whereas for PbI_2 , Δ increases towards shorter

Table 3. Values of birefringence Δ and ordinary refractive index n_o for various layer compounds, at wavelength $\lambda = 0.69 \mu$

Compound	Birefringence Δ	Ordinary refractive index n_o
ZrS ₂	1.4	3.4
SnS ₂	0.69	2.85
Sn S _{1.8} Se _{0.2}	0.68	2.94
Sn S _{1.7} Se _{0.3}	0.67	2.98
Sn S _{1.5} Se _{0.5}	0.65	3.07
PbI ₂	0.67	2.8
CdI ₂	0.19	2.36

wavelength at a similar rate to that of n_o [10].* Hence n_e remains reasonably constant between $\lambda = 0.55$ and 0.70μ . This result for PbI₂ is similar in behaviour to that of MoS₂ as observed by Evans and Young [24] in the range $\lambda = 0.71 \mu$ to 1.5μ . However, it would seem reasonable to assume that n_e would increase for these materials also at shorter wavelengths.

Recently, Hazlewood and Evans [25] found $\Delta = 0.38$ for SnSc₂. Therefore, it seems that the birefringence Δ , falls slowly from SnS₂ to SnSe₂. This has also been observed for GaS and GaSe by Brebner and Deverin [35], where $\Delta = 0.30$ and 0.2 respectively at $\lambda = 0.69 \mu$.

Absorption data has been previously published for SnS₂, SnSe₂ [12], CdI₂ and ZrS₂ [7], but not for SnS_xSe_{2-x}, ZrSe₂ and TiS₂. Using the relationship in Table 2 we have not been able to determine unambiguously the transition mechanism for fundamental absorption in these compounds. Both the square root and cube root dependencies of the absorption coefficient as a function of photon energy give good fits, and indicate that the transitions are almost certainly indirect. Following Brebner's analysis [14], one would expect for layer compounds that the density of states is a constant, shown as $N_2(E)$ in Table 2. The energy gaps were therefore determined using

crystals of PbI₂ were obtained from Leicester University. The value of n_o used in the calculation of Δ for PbI₂ was taken from [10].

the square root relationship. The fact that the cube root relationship is also obeyed indicates the possibility of perturbing effects on the shape of the absorption edges. These may include impurity states, excitons, lack of stoichiometry or even polytypism in the crystals.

For TiS₂ and ZrSe₂, it was not possible to fit either of these compounds to the absorption relationships outlined before, because of the high residual absorption. Approximate values of the energy gaps were determined from the intercepts of the linear plots of the absorption coefficients on the energy axis [21]. The energy gaps of SnSe₂, SnS₂, ZrS₂ and CdI₂ compare well with the previously published results, but as no previous absorption data is available on the series SnS_xSe_{2-x} or for ZrSe₂ and TiS₂ a similar comparison could not be made. However, Greenaway and Nitsche [7], deduced values of the energy gaps for ZrSe₂ and TiS₂ from reflection data. These were respectively 1.2 eV and 0.9 eV, which can be seen to compare quite well with the present results.

The energy gaps determined from Fig. 7 for the series SnS_xSe_{2-x} are plotted as a function of composition x in Fig. 8, where it is seen that from $x = 0$ to $x = 1.5$, the energy gaps vary linearly with the composition, followed by a rapid rise in the sulphur rich region.

It is of interest to compare the results obtained here for the series SnS_xSe_{2-x} with other mixed compound semiconductors. A linear variation of energy gap with composition indicates that the band structures of the component materials have a similar form, a typical example being InAs_{1-x}P_x [26]. If the band structures are different for the two compounds at the ends of the series an abrupt change of slope in the energy gap vs. composition relationship may be seen at some intermediate point. This was observed for example in Ge-Si alloys [27] and Bi₂Te₃-Bi₂Se₃ alloys [28]. On the other hand, for CdS-CdSe alloys [29] the energy gap is a smoothly varying function of the composition. Dziuba *et al.* [30] have

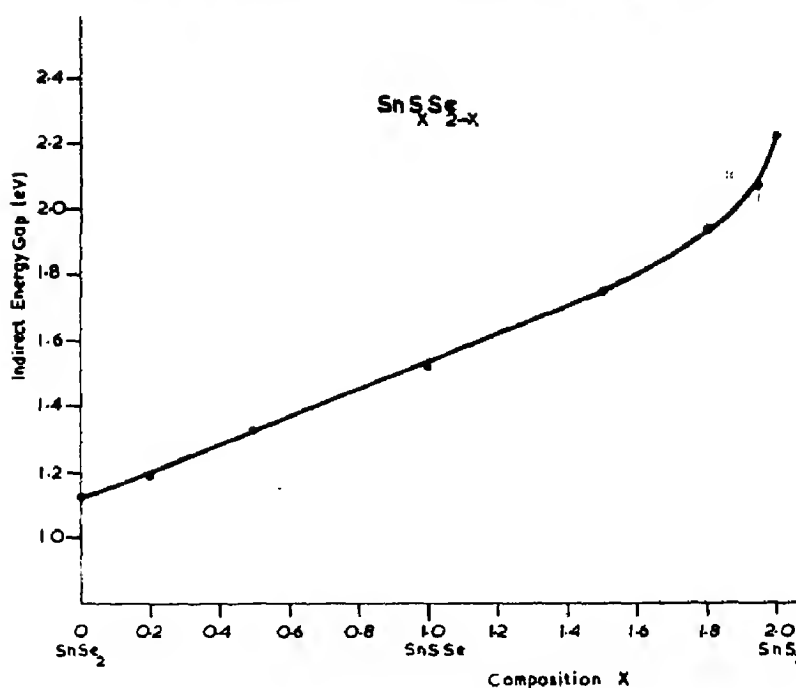


Fig. 8. Optical energy gap (eV) vs. composition x for the series $\text{SnS}_x\text{Se}_{2-x}$.

explained the latter results by adopting an additional potential which may be either periodic or non-periodic. They also found that a parabolic dependence of the energy gap on composition fitted the experimental data.

Within the series $\text{SnS}_x\text{Se}_{2-x}$, it is expected that the sulphur and selenium atoms distribute themselves randomly in the anion-lattice sites. The linear variation of energy gap for the series when $x \leq 1.5$ reveals a similarity in band structures. The rapid rise for $x \geq 1.5$ or possibly a kink can be manifested as a difference in the band structure. This is confirmed by the recently published band structures for SnS_2 and SnSe_2 by Au-Yang and Cohen[31].

The dispersion curves available in the present studies were all found to fit the simple classical oscillator described by equation (1). Two parameters were obtained from this relationship, viz. n_∞ and λ_0 , and these are shown in Table 1 for the compounds studied here.

Moss[32] has connected the long wavelength refractive index n_∞ with the photoconductive threshold energy E_c by the relation $n^4 E_c = 96$, and has found that this is true for

many photoconductive elements and compounds. He also found theoretically, and justified experimentally for the carbon-silicon series that $n^4 E_g = 170$ where E_g is the optical energy gap. As shown in Table 1, $n_\infty^4 E_g$ was calculated for each of the layer compounds examined here.

For TiS_2 and ZrSe_2 this was found to be approximately 150. For the series $\text{SnS}_x\text{Se}_{2-x}$ and ZrS_2 the constant was 105 ± 15 , whereas for CdI_2 a value of 83 was obtained. The latter is known to be strongly ionic, however. Table 4 was established in order to discuss the relation for materials of different crystal structures and of different types of bonding. Since all the compounds examined are known to exhibit strongly covalent bonding (apart from CdI_2) this indicates that the above relation could be applied for materials of similar crystal structures and equivalent type of bonding, with the condition that only one absorption band is strongly contributing to the dispersion. The large value of $n_\infty \approx 9.0$ for Bi_2Te_3 , [28] giving $n_\infty^4 E_g = 960$, seems to indicate that several absorption bands are

Table 4. Values of $n_{\infty}^4 E_g$ for some layer compounds and other compounds of different crystal structures

Material	E_g (eV)	n_{∞}	$n_{\infty}^4 E_g$	Ref.
Ge	0.66	4.00	170	[21]
Si	1.10	3.43	153	[21]
Diamond	5.30	2.38	170	[21]
AlSb	1.60	3.18	160	[34]
GaSb	0.67	3.70	125	[34]
GaSe	1.97	2.76	113	[35]
PbI ₂	2.41	2.47	89	[36]
MoS ₂	1.80	2.65	88	[24]
GaS	2.52	2.30	71	[35]
TiO ₂	3.10	2.40	70	[37]
InSe	1.19	2.55	50	[38]
SnO ₂	3.45	1.91	46	[39]
KI	6.00	1.57	40	[40]
NaCl	8.00	1.50	40	[40]

collectively contributing to the ordinary refractive index. From Table 4 it can be seen that as the ionicity of the materials increases the constant C (for $n^4 E = C$) is decreasing. A small change in the ionic contribution of the bond can thus allow for the difference in the constant found in the present compounds.

For the parameter λ_0 or the average interband oscillator wavelength it is of importance to notice that for the series $\text{SnS}_x\text{Se}_{2-x}$, λ_0 varies linearly with the composition x . Au-Yang and Cohen[31] also determined experimentally the imaginary part of the dielectric constant ϵ for SnS_2 in the 0–12 eV region. The peak position for $E \perp c$, is at 5.2 eV. This is in close agreement with $E_0 = hc/\lambda_0 = 5.17$ eV determined from the present single harmonic oscillator model.

Equation (1) which describes the single term classical oscillator, can also be expressed as:

$$n^2 - 1 = \frac{S_0 \lambda_0^2}{1 - \lambda_0^2/\lambda^2}$$

where λ_0 = average oscillator wavelength
 $S_0 = (n_{\infty}^2 - 1)/\lambda_0^2$ = average oscillator strength

DiDomenico and Wemple[33] showed for

a number of materials belonging to several crystal structures that the refractive index dispersion parameter $E_0/S_0 = (6.0 \pm 0.5) \times 10^{-14}$ eV m², where E_0 is the average oscillator energy. Table 1 shows E_0/S_0 for the materials reported here. This was found to be $(5.2 \pm 0.4) \times 10^{-14}$ eV m² for the series $\text{SnS}_x\text{Se}_{2-x}$.

Acknowledgements—The authors wish to thank the Science Research Council for financial assistance towards the research programme and one of the authors (R. D.) for an SRC studentship.

REFERENCES

1. NITSCHKE R., *J. Phys. Chem. Solids Suppl.* **28**, 215 (1967).
2. FRINDT R. F., *Phys. Rev.* **140**, A536 (1965).
3. BASSANI E. and PARRAVICINI G., *Nuovo Cim.* **B50**, 95 (1967).
4. FIVAZ R. and MOOSER E., *Phys. Rev.* **136**, A833 (1964).
5. FIVAZ R., *J. Phys. Chem. Solids* **26**, 839 (1967).
6. FIVAZ R. and MOOSER E., *Phys. Rev.* **163**, 743 (1967).
7. GREENAWAY D. L. and NITSCHKE R., *J. Phys. Chem. Solids* **26**, 1445 (1965).
8. TUBBS M. R., *J. Phys. Chem. Solids* **27**, 1667 (1966).
9. TUBBS M. R., *J. Phys. Chem. Solids* **29**, 1191 (1968).
10. DUGAN A. E. and HENISCH H. K., *J. Phys. Chem. Solids* **28**, 971 (1967).
11. DUGAN A. E. and HENISCH H. K., *J. Phys. Chem. Solids* **28**, 1885 (1967).
12. DOMINGO G., ITOGA R. S. and KANNEWARF G. R., *Phys. Rev.* **143**, 536 (1966).
13. BUSCH G., FRÖHLICK C. and HULLIGER F., *Helv. Phys. Acta* **34**, 359 (1961).
14. BREBNER J. C., *J. Phys. Chem. Solids* **25**, 1427 (1964).
15. SCHÄFER H., *Chemical Transport Reactions*. Academic Press, New York (1964).
16. LIM T. H., M.Sc. Dissertation, Brighton College of Technology, England (1968).
17. VERMA A. R. and KRISHNA P., *Polymorphism and Polytypism in Crystals*. Wiley, New York (1966).
18. LEE P. A. and SAID G., *Br. J. appl. Phys. (J. Phys. D)* **1**, 837 (1968).
19. DAVIS R., *J. scient. Instrum. (J. Phys. E)* **2**, 634 (1969).
20. WALTON A. K. and MOSS T. S., *Proc. R. Soc.* **81**, 509 (1963).
21. MOSS T. S., *Optical Properties of Semiconductors*. Butterworths, London (1959).
22. MOSS T. S., *Progress in Semiconductors*, Vol. 5. Heywood, London (1963).
23. TUBBS M. R., Private communication.
24. EVANS B. L. and YOUNG P. A., *Proc. R. Soc. A* **284**, 402 (1965).
25. HAZELWOOD R. A. and EVANS B. L., Private communication.

26. LONG D., *Semiconductors and Semi-metals* (Edited by R. K. Willardson and A. C. Beer), Vol. 1, p. 143. Academic Press, New York (1966).
27. HERMAN F., GLICKSMAN M. and PARMENTER R. H., *Progress in Semiconductors*, Vol. 2. Heywood, London (1957).
28. GREENAWAY D. L. and HARBEKE G., *J. Phys. Chem. Solids* **26**, 1585 (1965).
29. PARK Y. S. and REYNOLDS D. C., *Phys. Rev.* **132**, 2450 (1963).
30. DZIUBA F. Z., NICULESCU D. and NICULESCU N., *Phys. Status Solidi* **29**, 813 (1968).
31. AU-YANG M. Y. and COHEN M. L., *Phys. Rev.* **178**, 1279 (1969).
32. MOSS T. S., *Photoconductivity in the Elements*. Butterworths, London (1952).
33. DI DOMENICO M., Jr. and WEMPLE S. H., *J. appl. Phys.* **40**, 720 (1969).
34. SERAPHIN B. O. and BENNETT H. E., *Semiconductors and Semi-metals* (Edited by R. K. Willardson and A. C. Beer), Vol. 3, p. 499. Academic Press, New York (1967).
35. BREBNER J. L. and DEVERIN J. A., *Helv. Phys. Acta* **38**, 650 (1965).
36. DUGAN A. E. and HENISCH H. K., *Phys. Rev.* **171**, 1047 (1968).
37. CRONMEYER D. C., *Phys. Rev.* **113**, 1222 (1959).
38. ANDRIYASHIK M. V., SAKHNOVSKII M. YU., TIRROFEEV V. B. and YAKIMOVA A. S., *Phys. Status Solidi* **28**, 277 (1968).
39. SUMMIT R., MORLEY J. A. and BORELLI N. V., *J. Phys. Chem. Solids* **25**, 1465 (1964).
40. BROWN F. C., *The Physics of Solids*. Benjamin, New York (1967).

CRYSTAL FIELD IN RARE-EARTH FLUORIDES—I. MOLECULAR ORBITAL CALCULATION OF PrF_3 PARAMETERS

D. J. NEWMAN

Department of Physics, Queen Mary College, London, E.1, England

and

M. M. CURTIS*

Department of Theoretical Physics, Oxford, England

(Received 13 June 1969)

Abstract—Crystal field parameters have been calculated, using *ab initio* LCAO-MO theory, for the ion pair $\text{Pr}^{3+}-\text{F}^-$ at five metal ligand distances appropriate to $\text{Pr}^{3+}:\text{LaF}_3$. The parameters are found to be twice as large as in PrCl_3 , but with only half the distance dependence. In the absence of precise $\text{Pr}^{3+}:\text{LaF}_3$ experimental parameters only qualitative agreement with experiment can be recorded. However, very good numerical agreement is obtained with the experimental covalency parameters for $\text{Yb}^{3+}:\text{CaF}_2$, which provides a check on the methods adopted for calculating energy denominators.

1. INTRODUCTION

A RECENT *ab initio* molecular orbital calculation of crystal field parameters in PrCl_3 [1-3] was successful in giving values of the $n = 4$ and $n = 6$ parameters within a few per cent of those obtained experimentally. An attempt to extend this work to chlorides containing heavier rare-earth ions [4] gave parameters which are noticeably less than the experimental ones, although still in qualitative agreement. In order to obtain a more adequate evaluation of the theoretical situation it is necessary to extend the range of systems in which the molecular orbital theory can be confronted with experimental data. It is also of particular value to choose a host crystal in which the whole range of rare-earth ions are easily substituted.

With these points in mind we have begun a new series of calculations on the rare-earth trifluorides, which have the following added attractions:

(i) Optical spectroscopic data is available for several ions substituted into LaF_3 .

(ii) The site symmetry is low, and the local distortions when another rare-earth ion is substituted for La^{3+} should be quite small, so that further tests of the superposition approximation may be made. However, in contrast to the situation for rare-earth chlorides, we cannot compare the results for ions substituted in LaF_3 and GdF_3 as these crystals have a different structure [5].

(iii) Experimental data is also available for some rare-earth ions substituted into CaF_2 .

(iv) ENDOR measurements of the transferred hyperfine interaction may be used to get a fairly direct estimate of the degree of covalency.

In this first paper we report an LCAO-MO calculation carried out on the same lines as in our earlier series of papers on the trichlorides, which we shall henceforth denote by I [1], II [2], III [3], and IV [4]. A new problem that arises in the present case is, because of the low site symmetry at the rare-earth ion (C_2), no accurate sets of experimental crystal field parameters have previously been derived from the spectroscopic data. This has to be solved before our results can be compared directly with experiment. However, as we

*Present address: Rutherford High Energy Laboratory, Chilton, Didcot, Berks., England.

shall see, some definite indications as to the validity of the present work can be obtained by comparison with the available analyses of experimental data for $\text{Tm}^{2+}:\text{CaF}_2$ [6,7], $\text{Yb}^{3+}:\text{CaF}_2$ [8,9] and $\text{Nd}^{3+}:\text{LaF}_3$ [10].

In the next section we give a brief outline of the simplifications of the LCAO-MO formalism which have been made for this calculation. Section 3 contains a discussion of the numerical evaluation of these formulae, and Section 4 is devoted to the physical interpretation of our results.

2. FORMULATION

The present calculation follows closely the method described in I and III. We shall therefore give only a few brief remarks in order to unify the previous work and clarify some points in its physical interpretation. The main advantage of the simplified formalism used in this work is that it may be used directly in calculations for any system and is not associated with a particular rare-earth complex.

Only direct interactions between ligand outer shell electrons and rare-earth 4f electrons are considered, the remaining closed shells (in particular the rare-earth $n=5$ shell*) being treated as contributions to the net ionic charge. It is thought that this total neglect of configuration interaction does not lead to much error in the case of the parameters $A_4^m\langle r^4 \rangle$ and $A_6^m\langle r^6 \rangle$; an *ad hoc* procedure is used to correct the parameters $A_2^m\langle r^2 \rangle$.

The formulation is based on two initial assumptions:

(i) The crystal field acts on each 4f electron independently of the states of any other 4f electrons. This is equivalent to the assumption that a phenomenological (one-electron) crystal field exists [11].

(ii) The superposition principle applies for the individual ligand contributions to the crystal field, so that all three-centre effects

are ignored [12, 13]. Taken together, these assumptions allow us to set up determinantal (reference state) wave functions Ψ_A for the two-ion system $\text{Pr}^{3+}-\text{F}^-$, consisting of a single 4f wavefunction (φ_A) and one $\text{F}^-2s^2p^6$ closed shell with orbital functions $\chi_\alpha, \chi_{\beta\sigma}, \chi_{\gamma\pi}$. The two-ion Hamiltonian is axially symmetric, so that each of the four single 4f electron energy levels may be described by the magnetic quantum numbers $\pm m$ (wavefunctions $\varphi_{\pm m}$ and energies $E_{|m|}$). We shall relate the one electron energies E_m to intrinsic crystal field parameters A_n which are equivalent to the conventional parameters $B_n^0 = A_n^0\langle r^n \rangle$ for a single ligand. The combination of single ligand contributions is achieved by using rotation matrices [4]; there is no need to introduce symmetry orbitals for a specific complex.

The electrostatic point charge contributions have been obtained by explicit evaluation of the integrals $\langle \varphi_m | r_L^{-1} | \varphi_m \rangle$ (where r_L is the distance between 4f electron and ligand centre) rather than by using the usual formulae which assume that the ligand point charge is outside the effective radius of integration. Nevertheless, it is convenient to express these results directly in terms of the relevant radial integrals as these are simply related to the crystal field parameters. Writing

$$\langle \varphi_m | r_L^{-1} | \varphi_m \rangle = 7 \sum_n \begin{pmatrix} 3 & 3 & n \\ 0 & 0 & 0 \end{pmatrix} \begin{pmatrix} 3 & 3 & n \\ -m & m & 0 \end{pmatrix} \times (-1)^m T(n), \quad (2.1)$$

we obtain point charge electrostatic contributions

$$\bar{A}_2^{EL} = \frac{1}{2} T(2), \bar{A}_4^{EL} = \frac{1}{8} T(4), \bar{A}_6^{EL} = \frac{1}{16} T(6). \quad (2.2)$$

The usual approximation is $T(n) = \langle r^n \rangle / R^{n+1}$, where R denotes the distance between metal and ligand centres. This was found to be accurate for the PrCl_3 calculation, but in the present case we have, for example,

* The approximate treatment of the $n=5$ shell overlap contribution in PrCl_3 was given in II.

$$T(6) = 3.16 \times 10^{-4} \text{ a.u.};$$

$$\langle r^6 \rangle / R^7 = 3.81 \times 10^{-4} \text{ a.u. } (R = 4.564 \text{ a.u.}).$$

This is simply due to the fact that R is much smaller in the case of PrF_3 , so that the ligand centre is no longer outside the $4f$ charge distribution.

The corresponding two electron matrix elements may also be expressed in terms of radial integrals by means of equation (2.1); the $T^s(n)$ determine $\langle \varphi_m \chi_s \| \varphi_m \chi_s \rangle$ and the $T^v(n)$ determine $\langle \varphi_m \chi_p \| \varphi_m \chi_p \rangle$, where χ_p denotes the radial part of the ligand $2p$ functions. The 'charge penetration' contributions, due to the finite size of the ligand charge distribution, may then be written as

$$\bar{A}_n^{cp} = K_n(2T^s(n) + 6T^v(n) - 8T(n)), \quad (2.3)$$

where K_n are the numerical factors in equations (2.2).

It is convenient to consider overlap and covalency contributions together as they depend on very similar combinations of integrals. Gathering the results given in equation (4.5) of I and equations (4.2) and (5.2) of III and simplifying so as to accord with the single ligand system being considered here, we obtain the following expressions for these contributions to the orbital energies E_m in terms of the quantities N_τ and \mathcal{Q}_τ defined in III:

$$\left. \begin{aligned} E_m^{ov} &= - \sum_{\tau} S_{\tau}(N_{\tau 1} + 2N_{\tau 2}), \quad S_{\tau} = \langle \varphi_m | \chi_{\tau} \rangle \\ E_m^{co} &= \sum_{\tau} N_{\tau}^2 / \mathcal{Q}_{\tau}, \quad N_{\tau} = N_{\tau 1} + N_{\tau 2} + N_{\tau 3} \end{aligned} \right\} \quad (2.4)$$

(when $m = 0$ the sum over τ includes s and $p\sigma$, $\tau = p\pi$ gives the $m = 1$ contributions and $E_2 = E_3 = 0$).

The only remaining contribution of importance is the exchange energy

$$E_m^{EXCH} = - \sum_{\tau} \langle \varphi_m \chi_{\tau} | g | \chi_{\tau} \varphi_m \rangle \quad (2.5)$$

which we shall combine with the overlap contribution (as in I) to form the so called

'exclusion' contribution. It is convenient to refer to the covalency and exclusion energies jointly as *contact* contributions.

3. NUMERICAL EVALUATION

The matrix elements and radial integrals given in Table 1 are computed using specially developed programs* based on the ζ -function method of Barnett and Coulson[14]. Each set of integrals is determined at the five different metal-ligand distances given by the X-ray determination of the lanthanum fluoride structure[15], as it is intended to use these values to compare with the experimental crystal field for $\text{Pr}^{3+}:\text{LaF}_3$. The free ion Hartree-Fock wave-functions used are those of Synke and Corsiglia[16] for Pr^{3+} and Sugano and Shulman[17] for F^{-} .

Various approximations are required for those integrals which appear in Section 2, but are not listed in Table 1. It must be emphasised that all 3-centre integrals are automatically eliminated by our initial assumption (ii); this is at present the subject of both theoretical[18] and experimental[13] tests, but the results are not yet conclusive.

It can be seen from Table 2 that the dominant contact contributions arise from $N_{\tau 2}$ which can be evaluated exactly in terms of tabulated integrals apart from $\langle \varphi \chi_s \| \chi_r \chi_r \rangle$ for $\tau = p\sigma$ and $p\pi$. The $p\sigma$ integral has been estimated from the matrix elements $\langle \varphi \chi_p \| \chi_{p\sigma} \chi_p \rangle$ using the numerical factor 1.14 obtained from the ratio of corresponding PrCl_3 integrals. This, and numerical uncertainties in the evaluation of integrals lead us to expect an error of up to 5 per cent in $N_{\tau 2}$.

The approximations used for $N_{\tau 1}$, $N_{\tau 3}$ and \mathcal{Q}_{τ} have already been discussed in papers I and III. However, in the present case we do not have available Madelung energies or even approximate values of the integrals of the type $\langle \varphi \varphi \| \varphi \chi \rangle$. We have therefore used the PrCl_3 Madelung energy scaled according to the metal-ligand distance and PrCl_3 values of the $\langle \varphi \varphi \| \varphi \chi \rangle$ scaled according to the relative magnitudes of the overlap integrals. As neither $N_{\tau 1}$ nor $N_{\tau 3}$ contributions are very important to the final result we feel that these approximations can make no material difference to the overall accuracy of the calculation. The overall numerical accuracy is thus expected to be about 10 per cent, although there remains some uncertainty in the formulation of \mathcal{Q}_{τ} (see III). Nevertheless, the present work provides some evidence that the numerical values of \mathcal{Q}_{τ} are very nearly correct (see Section 4).

The exchange integrals in equation (2.6) are approximated by writing

$$\langle \varphi_m \chi_{\tau} | g | \chi_{\tau} \varphi_m \rangle = 0.43 \langle \varphi_m | \chi_{\tau} \rangle^2$$

* An unpublished research report is available from the authors on request.

† In Ref. [19] a value of the Madelung energy in LaF_3 is given. However, as it is based on an incorrect space group (see Ref. [15]) and, in any case, is very close to the LaCl_3 scaled result, the procedure used seems justified.

Table 1. $Pr^{3+}-F^-$ matrix elements $\times 10^2$ (in a.u., apart from the overlap integrals) for several metal-ligand distances F (a.u.). φ denotes the Pr^{3+} 4f wave functions and χ the F^- 2s and 2p wave-functions

$R =$	4.5645	4.6213	4.653	4.710	4.994
$\langle \varphi \chi_s \rangle$	1.768	1.675	1.625	1.539	1.176
$\langle \varphi \chi_{\sigma} \rangle$	1.963	1.902	1.869	1.810	1.538
$\langle \varphi \chi_{\pi} \rangle$	1.630	1.552	1.510	1.437	1.122
$\langle \varphi r_L^{-1} \chi_s \rangle$	1.327	1.253	1.213	1.145	0.863
$\langle \varphi r_L^{-1} \chi_{\sigma} \rangle$	1.235	1.177	1.146	1.093	0.865
$\langle \varphi r_L^{-1} \chi_{\pi} \rangle$	0.798	0.752	0.728	0.686	0.511
$\langle \varphi \chi_s \chi_s \chi_s \rangle$	1.175	1.110	1.076	1.015	0.765
$\langle \varphi \chi_{\sigma} \chi_s \chi_{\sigma} \rangle$	1.117	1.055	1.022	0.965	0.727
$\langle \varphi \chi_{\sigma} \chi_{\sigma} \chi_s \rangle$	1.136	1.083	1.053	1.012	0.810
$\langle \varphi \chi_{\sigma} \chi_{\sigma} \chi_{\sigma} \rangle$	1.103	1.054	1.028	0.982	0.783
$\langle \varphi \chi_{\pi} \chi_{\pi} \chi_s \rangle$	0.752	0.710	0.688	0.647	0.483
$\langle \varphi \chi_{\pi} \chi_{\pi} \chi_{\pi} \rangle$	0.731	0.689	0.667	0.629	0.471
$T(2)$	1.118	1.077	1.055	1.018	0.854
$T(4)$	0.1310	0.1233	0.1193	0.1124	0.0845
$T(6)$	0.03162	0.02926	0.02803	0.02597	0.01791
$T^s(2)$	1.118	1.077	1.055	1.018	0.854
$T^s(4)$	0.1275	0.1203	0.1165	0.1100	0.0831
$T^s(6)$	0.02727	0.02541	0.02443	0.02277	0.01613
$T^p(2)$	1.095	1.056	1.036	1.000	0.844
$T^p(4)$	0.1166	0.1105	0.1073	0.1017	0.0783
$T^p(6)$	0.02273	0.02129	0.02052	0.01922	0.01395

Table 2. Calculated contributions to N_r ($\times 10^3$ a.u.) with values of \mathcal{D}_r (a.u.) and γ_r

$R =$	4.5645	4.6213	4.653	4.710	4.994
N_{s1}	14.92	13.79	13.23	12.33	8.50
N_{s2}	-27.44	-25.85	-25.00	-23.58	-17.72
N_{s3}	2.28	2.15	2.08	1.98	1.50
N_s	-10.24	-9.91	-9.69	-9.27	-7.72
$N_{\sigma 1}$	-5.27	-5.37	-5.44	-5.50	-5.63
$N_{\sigma 2}$	-22.42	-21.28	-20.70	-19.50	-14.96
$N_{\sigma 3}$	0.96	0.93	0.91	0.88	0.75
N_{σ}	-26.73	-25.79	-25.23	-24.12	-19.84
$N_{\pi 1}$	-4.38	-4.38	-4.39	-4.37	-4.09
$N_{\pi 2}$	-12.29	-11.52	-11.09	-10.45	-7.66
$N_{\pi 3}$	1.98	1.89	1.84	1.75	1.36
N_{π}	-14.69	-14.01	-13.64	-13.07	-10.39
\mathcal{D}_p	0.787	0.775	0.765	0.752	0.690
\mathcal{D}_s	1.680	1.666	1.658	1.645	1.583
γ_s	0.0061	0.0059	0.0058	0.0056	0.0049
γ_{σ}	0.0340	0.0333	0.0330	0.0321	0.0288
γ_{π}	0.0187	0.0181	0.0178	0.0174	0.0151

where the numerical factor is that used in I. It is a mean value determined from the three methods discussed in the paper. We feel that this is the most doubtful approximation made in the calculation, especially as it makes the

integrals for $m=2$ and $m=3$ zero. It should be noted that (according to this estimate) the exchange energy is about a quarter of the overlap energy and opposite in sign. (Also see remarks made in Ref. [13].)

Table 2 gives an overall idea of the relative magnitude of the various contributions to overlap and covalency energies, $\gamma_r = -N_r/\mathcal{Q}_r$ are the conventional covalency parameters; their small value demonstrates the fast convergence of the perturbation series. Table 3 gives the various calculated contributions to the intrinsic parameters. Contributions (i) and (ii), taken together, represent the electrostatic contribution if the finite size of the ions is taken into account, (iv) is due to Pauli exclusion effects and (iii) is the charge transfer, or covalency contribution. In deriving the net value of \bar{A}_2 we have allowed for 90 per cent shielding of the external electrostatic field. This (rather arbitrary) figure may be taken to include both configuration interaction effects (calculated at 67 per cent [20]) and charge redistribution due to overlap (see II). In any case the initial assumption of the applicability of the superposition approximation is expected to be rather poor for this parameter, so that our final results in this case are not as useful as those for \bar{A}_4 and \bar{A}_6 .

for the rare-earth fluorides. Some parameters exist* for an approximate D_{3h} site symmetry, but such a rough approximation cannot provide more than an order of magnitude comparison. We are, in fact, using the results of the present calculation, in conjunction with X-ray data, to predict an initial set of PrF_3 crystal field parameters as a preliminary to the determination of experimental parameters. For the present, however, we note that the results given in Tables 2 and 3 are also of interest in relation to the calculated and experimental parameters in other systems.

The values derived for the PrF_3 intrinsic parameters are about twice as large as those

Table 3. Calculated contributions to the intrinsic parameters $\bar{A}_n(\text{cm}^{-1})$ of the system $\text{Pr}^{3+} - \text{F}^-$ for the metal-ligand distances $R(\text{a.u.})$ which occur in PrF_3 : (i) point charge, (ii) charge penetration, (iii) covalency and (iv) exclusion

$R =$	4.5645	4.6213	4.653	4.710	4.994
$n = 6$ (i)	4.3	4.0	3.8	3.6	2.5
(ii)	-8.5	-7.6	-7.2	-6.4	-3.8
(iii)	14.2	13.7	13.3	12.4	9.5
(iv)	21.0	19.4	18.7	17.0	11.4
Total	31.0	29.5	28.6	26.6	19.6
$n = 4$ (i)	35.9	33.8	32.7	30.8	23.2
(ii)	-25.6	-22.7	-21.3	-18.9	-10.8
(iii)	37.5	35.3	34.2	31.8	23.3
(iv)	50.5	46.4	44.1	40.2	26.0
Total	98.3	92.8	89.7	83.9	61.7
$n = 2$ (i)	1227	1182	1158	1117	937
10% of (i)	123	118	116	112	94
(ii)	-151	-138	-125	-119	-67
(iii)	108	102	98	91	66
(iv)	144	131	124	113	72
Total	224	213	213	197	165

4. RESULTS AND DISCUSSION

In contrast to the situation for the anhydrous chlorides, no detailed fits of crystal field parameters to the existing spectroscopic data [21] have previously been carried out

(experimental and calculated) in PrCl_3 (see 4, Table 7). This is in accord with both the

*H. M. Crosswhite (private communication) gives $\text{Gd}^{3+}:\text{LaF}_3$ parameters (cm^{-1}): $B_2^0 = 106 \pm 18$, $B_4^0 = 234 \pm 12$, $B_6^0 = 124 \pm 22$, $B_6^6 = 850 \pm 170$.

relative magnitude of the term splittings (e.g. see Ref. [21]) and the D_{3h} parameters. One feature that the present calculation has in common with that for PrCl_3 is that the covalency contributions are smaller than those due to Pauli exclusion. However, in contrast to the usual expectations[21], we find that the covalency parameters γ_r (Table 2) are larger than the corresponding parameters for the chlorides:

$$\gamma_\sigma = 0.0222 \quad \gamma_\pi = 0.0092 \quad \gamma_s = 0.0056.$$

Another feature of interest in our results is that the crystal field parameters are found to be considerably less sensitive to distance variation than they are in other rare-earth systems that have been studied. If we represent the distance dependence of \bar{A}_n in terms of a power law R^{-t_n} and ignore t_2 because of the uncertainties in the derivation of \bar{A}_2 , the following comparison may be made between the PrCl_3 and PrF_3 calculations:

$$\text{PrCl}_3: t_4 = 10.3, \quad t_6 = 11.0$$

$$\text{PrF}_3: t_4 = 5.7 \pm 0.1, \quad t_6 = 5.6 \pm 0.3.$$

This is of particular interest because it shows that molecular orbital calculations do not invariably predict power laws which are greater than those obtained in the point charge electrostatic model. It also suggests that ion-lattice interactions in the fluorides may be considerably less than those in the chlorides. The main reason for such low fluoride power laws is apparently the relative nearness of

the ligand centre emphasising charge penetration effects which always tend to reduce the distance variation of the integrals. The calculated ratio $\bar{A}_4/\bar{A}_6 = 3.15 \pm 0.02$ is very nearly independent of distance and considerably different to the ratio obtained for PrCl_3 . This does not accord with our previously stated belief[13] that this ratio is effectively independent of the host crystal.

A preliminary analysis of the experimental data for $\text{Nd}^{3+}:\text{LaF}_3$ [10] has been carried out by Dr. G. E. Stedman. This assumes power laws $t_4 = t_6 = 5$ and gives mean values $\bar{A}_4 = 54.4 \text{ cm}^{-1}$, $\bar{A}_6 = 30.4 \text{ cm}^{-1}$ as compared with the calculated mean values $\bar{A}_4 = 87.9 \text{ cm}^{-1}$, $\bar{A}_6 = 27.9 \text{ cm}^{-1}$. It should be noted that the experimental ratio $\bar{A}_4/\bar{A}_6 = 1.8$ is reasonably close to that obtained for $\text{Nd}^{3+}:\text{LaCl}_3$ (2.2). The LaCl_3 data also leads us to expect that the Nd^{3+} and Pr^{3+} $n=4$ and $n=6$ parameters will be very similar. Hence the large discrepancy in the case of \bar{A}_4 is rather disturbing.

It is also of interest to compare our calculation with experimental results obtained for rare-earths substituted into CaF_2 . Intrinsic parameters may be related to the conventional cubic parameters b_n as follows:

$$\bar{A}_4 = 3^3.11.b_4/2^{5.7} = 1.325b_4.$$

$$\bar{A}_6 = 3^3.11.13.b_6/2^{8.5} = 3.217b_6.$$

Using experimental values of b_n given by Bleaney[6] for Tm^{2+} and Baker[9] and Low[8] for Yb^{3+} we obtain the intrinsic parameters shown in Table 4. These are rather less than

Table 4. Comparison of theoretical and experimental values of intrinsic parameters and the covalency parameter $\lambda_r = \gamma_r + s_r$

	$\text{Pr}^{3+}(4.621)$	$\text{Pr}^{3+}(4.994)$	$\text{Tm}^{2+}(4.46)$	$\text{Yb}^{3+}(4.46)$
\bar{A}_4	92.8	61.7	60.7	68.4 (59.4)
\bar{A}_6	29.5	19.6	16.2	20.6 (22.2)
λ_s	0.0227	0.0167	0.0136	0.0200
λ_σ	0.0523	0.0442	0.0293	0.0442
λ_π	0.0336	0.0263	0.0186	0.0282
$\lambda_\sigma/\lambda_\pi$	1.56	1.68	1.58	1.57

those for Pr^{3+} at its mean distance in LaF_3 , as might be expected for ions with a more contracted $4f$ shell. The calculated and experimental ratios \bar{A}_4/\bar{A}_6 agree well, but in other hosts this ratio is distinctly different for rare-earth ions having more or less than a half-filled shell.

A useful test of our theory is obtained if we compare calculated and experimental values of the parameters $\lambda_r = s_r + \gamma_r$. (It should be noted that the values in Table 4 refer to a single ligand, related to the cubic values as defined in the paper by Axe and Burns[7]). The Tm^{3+} values were obtained by Axe and Burns using the Wolfsberg-Helmholtz model and are therefore only of marginal interest in the present discussion. The Yb^{3+} values were, however, derived by Baker by a direct analysis of the ENDOR hyperfine splitting data, using only an assumed ratio $\lambda_\sigma/\lambda_\pi$. Baker gives analyses for several such ratios, showing that the results are fairly insensitive to the particular value chosen. As Pr^{3+} ($R = 4.994$ a.u.) and Yb^{3+} ($R = 4.46$ a.u.) have similar crystal field parameters we would expect a comparison of the λ 's to be realistic. It will be seen from Table 4 that the agreement is very good indeed in spite of the slight difference in $\lambda_\sigma/\lambda_\pi$. This is a direct indication that our method of treating covalency, and in particular the formula for \mathcal{L}_r , gives a reasonable approximation to the truth.

5. CONCLUSION

Qualitative agreement has been obtained between MO-LCAO crystal field theory and the experimental splittings in the rare-earth fluorides although the predicted value of \bar{A}_4 is apparently too large. The intrinsic crystal field parameters are about twice as large and half as sensitive to distance variation as those in the trichlorides. Very good numerical agreement is obtained between $\text{Yb}^{3+}:\text{CaF}_2$ ENDOR data and our calculated

values of covalency parameters. This, and the success of our previous calculation of PrCl_3 parameters, leads us to conclude that the MO-LCAO theory gives an adequate representation of the various contributions to the crystal field.

Acknowledgements—We are grateful to Professor H. M. Crosswhite and Dr. J. M. Baker for the communication of results prior to publication, and to Dr. G. E. Stedman for many helpful discussions. M. M. C. wishes to thank the Science Research Council for a Research Fellowship.

REFERENCES

1. ELLIS M. M. and NEWMAN D. J., *J. chem. Phys.* **47**, 1986 (1967).
2. BISHTON S. S., ELLIS M. M., NEWMAN D. J. and SMITH J., *J. chem. Phys.* **47**, 4133 (1967).
3. ELLIS M. M. and NEWMAN D. J., *J. chem. Phys.* **49**, 4037 (1968).
4. CURTIS M. M., NEWMAN D. J. and STEDMAN G. E., *J. chem. Phys.* **50**, 1077 (1969).
5. KERN S. and RACCAH P. M., *J. Phys. Chem. Solids* **26**, 1625 (1965).
6. BLEANEY B., *Proc. R. Soc. A* **227**, 289 (1964).
7. AXF J. D. and BURNS G., *Phys. Rev.* **152**, 331 (1966); BURNS G. and AXE J. D., *Phys. Lett.* **19**, 98 (1965).
8. LOW W., *Spectroscopic and Group Theoretical Methods in Physics* (Edited by F. Bloch et al.) p. 167. North-Holland (1968).
9. BAKER J. M., *J. Phys.* **1**, 1670 (1968).
10. STEDMAN G. E., Private communication.
11. NEWMAN D. J. and BISHTON S. S., *Chem. phys. Lett.* **1**, 616 (1968).
12. BRADBURY M. I. and NEWMAN D. J., *Chem. phys. Lett.* **1**, 44 (1967).
13. NEWMAN D. J. and STEDMAN G. E., *J. chem. Phys.* In press.
14. BARNETT M. P. and COULSON C. A., *Phil. Trans. R. Soc. A* **243**, 221 (1951).
15. ZALKIN A., *Inorg. Chem.* **5**, 1466 (1966); *Inorg. Chem. (Errata)*, **6**, 2273 (1967).
16. SYNEK M. and CORSIGLIA L., *Phys. Letters* **26A**, 19 (1967).
17. SUGANO S. and SHULMAN R. G., *Phys. Rev.* **130**, 517 (1963).
18. CURTIS M. M. and NEWMAN D. J., *J. chem. Phys.* In press.
19. JOHNSON Q. C. and TEMPLETON D. H., *J. chem. Phys.* **34**, 2005 (1961).
20. STERNHEIMER R. M., BLUME M. and PEIERLS R. F., *Phys. Rev.* **173**, 376 (1968).
21. WONG E. Y., STAFSUDD M. and JOHNSTON D. R., *J. chem. Phys.* **39**, 786 (1963).
22. ONOPKO D. E., *Opt. Spectrosc.* **24**, 301 (1968).



THE TEMPERATURE DEPENDENCE OF THE SHORT WAVELENGTH TRANSMITTANCE LIMIT OF VACUUM ULTRAVIOLET WINDOW MATERIALS—I. EXPERIMENT

W. R. HUNTER*

E. O. Hulbert Center for Space Research, U.S. Naval Research Laboratory,
Washington, D.C. 20390, U.S.A.

and

S. A. MALO

Imperial College of Science and Technology, South Kensington, London S.W.7, England

(Received 15 May 1969)

Abstract—The short wavelength transmittance limit or cut-off wavelength, λ_{co} , of LiF, MgF₂, CaF₂, LaF₃, BaF₂, sapphire, synthetic crystal quartz and fused quartz has been measured from about 100°C to about 10°K. λ_{co} is not a well defined quantity, so for the purpose of this experiment it has been arbitrarily taken as the wavelength where transmittance could just be measured, usually 0.1–0.5 per cent. With one exception λ_{co} shifted to shorter wavelengths as the sample was cooled; the shift varied from about 40 to 80 Å over the temperature range from 100°C to 10°K, depending on the material, with the largest shift occurring in BaF₂. The exception was LaF₃ which showed no measurable change in λ_{co} with temperature. Over the temperature range from 20° to 100°C the slope of λ_{co} with temperature for all materials was fairly constant, but below 20°C it decreased, approaching zero as the temperature approached 20°–10°K. In the case of synthetic crystal quartz, for example, the slope changed from about 0.28 Å/°K at room temperature to about 0.055 Å/°K at 80°K.

INTRODUCTION

A NUMBER of dielectric materials, alkali halides, quartz, etc., are useful as window materials in the vacuum ultraviolet because they can be used to isolate systems from contamination while transmitting short wavelength radiation. These window materials are transparent from the visible spectral region down into the vacuum ultraviolet where they have a short wavelength transmittance limit, or cut-off, λ_{co} , below which radiation is absorbed. There is no general definition of λ_{co} because it depends on the sensitivity of the transmissometer being used. Consequently the definition used in this paper is an arbitrary one and is that wavelength at which transmittance could just be measured, usually 0.1–0.5 per cent.

The cut-off wavelength in various materials

has been found to be temperature dependent. Knudsen and Kupperian[1] made transmittance measurements using CaF₂ from 80°K to room temperature and observed a change in λ_{co} . Davis[2] did the same for LiF, BaF₂ and fused quartz from 200° to 300°K as did Laufer *et al.*[3] for various materials from room temperature to about 100°C. It was the purpose of this experiment to measure the change of λ_{co} with temperature from about 10°K to 100°C for the most commonly used vacuum ultraviolet window materials.

EXPERIMENTAL

Vacuum ultraviolet radiation was obtained from a monochromator using a 1-m radius of curvature diffraction grating in normal incidence. A d.c. glow discharge in hydrogen was used for a radiation source. The resolution of the monochromator was 0.8 Å; however, the useful resolution available for the experiment was controlled by the spacing of

*Work performed while on sabbatical leave at Imperial College.

the emission lines in the hydrogen spectrum and was between 2 and 3 Å.

At the exit slit of the monochromator was attached a vacuum cryostat for cooling the sample. It was pumped by an oil diffusion pump using Dow Corning 705 fluid, had a liquid nitrogen trap and cold water baffle between the diffusion pump and cryostat, and attained an ultimate pressure of about 5×10^{-6} Torr. with no windows to isolate either cryostat or radiation source from the monochromator.

Figure 1(a) is a schematic diagram of the cryostat and detector. The inner container B, holds the sample coolant and can be rotated

to separate the signal due to vacuum ultraviolet radiation from that due to any fluorescent radiation that might be emitted by the samples. When the mica is in position 1, out of the beam, both vacuum ultraviolet and fluorescent radiation will contribute to the signal, while in position 2 only the fluorescent radiation will be seen. Hence by subtraction the effect of fluorescence can be eliminated.

Figure 1(b) shows a drawing of the sample holder. It consists of a flat round copper plate to which is attached a heavy copper bar, mounted eccentrically, so that the rotation of the inner container leaves the radiation beam unobscured for a measurement of I_0 . In the

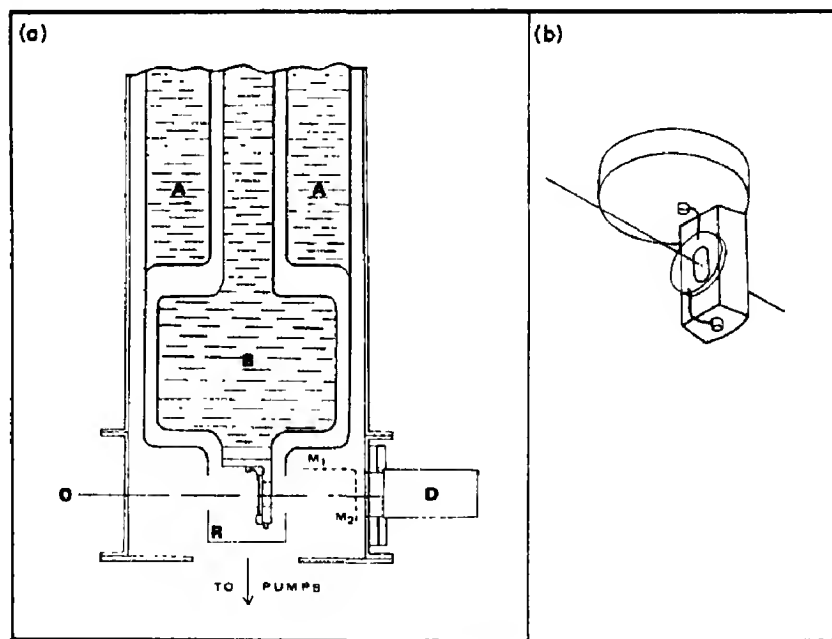


Fig. 1. (a) Schematic diagram of cryostat. (b) Drawing of sample holder.

about its axis or raised so that the sample holder can be removed from the radiation beam, thus permitting a measurement of I_0 and the determination of the actual transmittance. An outer container A holds the coolant for the radiation shield R, and itself serves partly as a radiation shield for the inner container. R. contains holes to let the radiation beam, shown by the line O, pass through to the detector D. A mica filter M was installed

center of the copper bar is a radiation port; the sample is held in front of this port by weak springs. To insure good thermal contact between the sample and sample holder, a channel was machined around the radiation port and slightly overfilled with indium. The sample was held against the indium meniscus with the springs, and then both sample holder and sample were heated to the melting point of indium, 156°C. After the indium had frozen,

the suitability of the contact could be judged by observing the reflectance at the sample-indium interface; if a metallic reflectance was seen around most of the perimeter of the radiation port, the thermal contact was usually good. If not, the indium was remelted, more indium added if necessary, and the procedure repeated until a good contact was obtained.

An EMI 6256, thirteen-stage multiplier phototube, coated with *p*-terphenyl to convert the vacuum ultraviolet radiation to light, was used as a detector. A Keithley micro-microammeter amplified the detector signals which were then displayed on a Leeds and Northrop strip chart recorder.

The temperature was measured with a copper-constantan thermocouple that was held in contact with the sample face with one of the springs that held the sample. Calibration of the thermocouple was obtained using boiling liquid helium and liquid nitrogen, freezing water and boiling water. In calibrating, no correction was made for changes in atmospheric pressure; however, the accuracy desired for temperature measurements was about $\pm 2^\circ\text{K}$ so such corrections were not necessary. The calibration points were compared with the results of Powell *et al.*[4] and a calibration curve was drawn to the same shape as their curve.

The samples were high purity crystals except for fused quartz and LaF_3 whose origin was unknown. All of the materials were

polished and, in addition, a cleaved specimen of BaF_2 was available. A description of the samples is given in Table 1.

RESULTS

Figure 2 shows the transmittance vs. wavelength of a polished piece of MgF_2 1 mm thick at 83° , 200° and 296°K (room temperature). As the temperature was lowered, λ_{co} decreased and had the corresponding values of 1097 \AA , 1114 \AA and 1132 \AA . Aside from the change in λ_{co} , the most obvious feature of the transmittance curves is the low transmittance at 83°K . Since there is no reason for the trans-

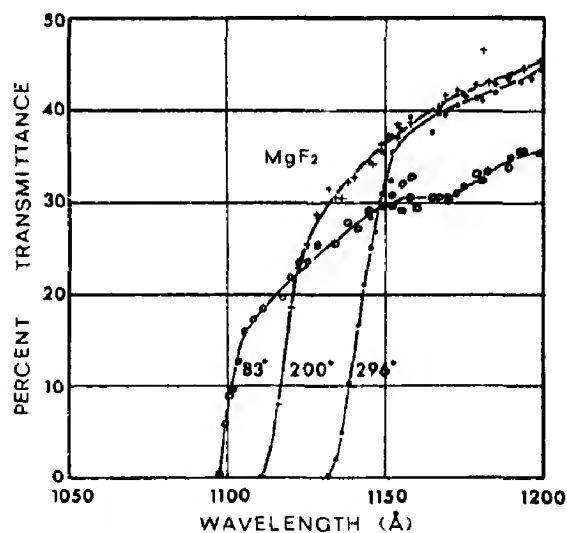


Fig. 2. Transmittance vs. wavelength of MgF_2 at three temperatures.

Table 1. Description of samples

Sample	Polished	Cleaved	Supplier	Thickness (mm)
Fused quartz	x		?	1.3
Synthetic crystal quartz	x		Sawyer	1.1
Synthetic sapphire	x		Linde	2.5
BaF_2	x	x	Harshaw (pol)	
			Koch-Light (cle.)	0.8 (pol)
LaF_3	x		?	1.1
CaF_2	x		Harshaw	1.0
MgF_2	x		Harshaw	3.0
				1.0
LiF	x		Harshaw	3.0

mittance to decrease as the temperature decreases, the conclusion was that this effect was caused by the formation of a layer of contaminant on the surfaces of the sample which was assumed to be frozen vapors of the residual atmosphere in the cryostat.

In an attempt to learn something about the composition of the contaminant, the transmittance of LiF that had been cooled to 110°K in the cryostat for 3 hr was measured. The characteristic of the cut-off was completely changed under these conditions; there was no transmittance at all at wavelengths shorter than 1550 Å and to longer wavelengths the onset of transmission was gradual rather than abrupt as is usually the case with LiF. The similarity of this transmittance curve with the curve showing the measured absorption coefficient of ice, obtained by Dressler and Schnepf[5], was fairly convincing evidence that the contaminant was mostly ice.

An actual time history of the temperature and transmittance at 1026 Å of a polished sample of LiF is shown in Fig. 3. The abscissa is the time in minutes after the coolant was

first put in the inner container of the cryostat, and the two ordinates show per cent transmittance on the left, and temperature on the right. At room temperature, LiF is opaque at this wavelength; however, when liquid nitrogen was put in the inner container at zero time, the sample temperature was already at about 250°K because the outer container and radiation shield had been cooled with liquid nitrogen for about an hour beforehand; consequently, radiation cooling had reduced the sample temperature, and the transmittance was not zero.

Liquid nitrogen was the first coolant used. As the temperature fell, the transmittance rose to a maximum of about 28 per cent at 5 min, or 150°K. As the temperature dropped further, the transmittance, which should have remained constant, dropped because of the formation of ice. After 20 min the liquid nitrogen was removed from the inner container and the transfer of liquid helium started. This subsequently cooled the sample to about 25°K and caused an even faster decrease in transmittance. Another transfer of liquid helium was

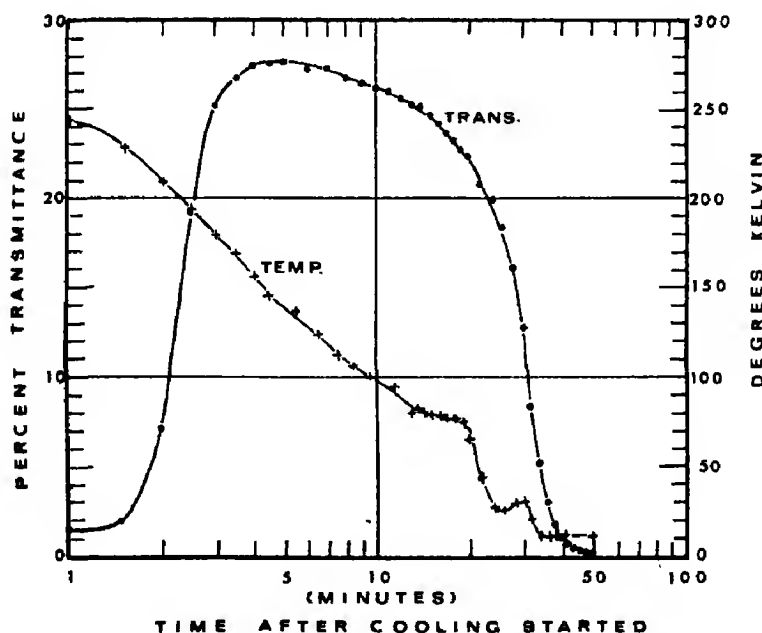


Fig. 3. Time history of temperature and transmittance at 1025 Å of LiF after cooling started.

made at 30 min which cooled the sample to about 10°K. After the second transfer the transmittance was reduced practically to zero in about 13 min.

The same type of time history was obtained when an alcohol and dry ice mixture was used to cool the sample. The differences were: An equilibrium temperature of about 200°K, a maximum transmittance of about 8 per cent, and a lower rate of decrease of transmittance. Presumably the contaminant in this case was the same as when liquid nitrogen and helium were used as the coolant. But, since the vapor pressure of ice at 200°K is approximately 2×10^{-3} Torr.[6], the assertion that the contaminant was mostly ice may seem questionable. Blackman and Lisgarten[7] have found, however, that other contaminants, such as small amounts of oil vapor trapped in the ice, tend to lower its vapor pressure. Ice formed from the residual gases in an oil-pumped vacuum system can exist *in vacuo* to above 200°K, whereas ice formed by deliberately introducing water vapor into the vacuum system sublimed at about 170°K.

The rapid formation of the contaminating layers limited the time available for the measurement of λ_{co} , particularly when liquid helium was the coolant. When liquid nitrogen or the alcohol-dry ice mixture was used, the sample was allowed to reach its equilibrium temperature, the coolant was removed from the inner container and the sample allowed to warm up with measurements being made during the warming period. This procedure was used because the rate of warming was slow and could be controlled, while the rate of cooling when the coolant was put in the inner container was too fast to allow accurate temperature measurements and was essentially uncontrollable. On the other hand, when liquid helium was used, precooling had to be done with liquid nitrogen after which the liquid helium was used. Because of the precooling, ice was already forming, so that measurements had to be made as the sample was cooling to its equilibrium temperature, since shortly

thereafter the transmittance was reduced to zero.

Figure 4 shows the variation of λ_{co} with temperature for a number of vacuum ultraviolet window materials. With the exception of LaF_3 , all the materials showed a similar behavior; as the temperature was lowered, λ_{co} shifted to shorter wavelengths with the magnitude of the shift decreasing as the temperature decreased. In the case of BaF_2 , the "+" marks show measurements made on the polished sample, while the other data points are for the cleaved sample. There were small variations between different samples of the same substance, but never greater than the

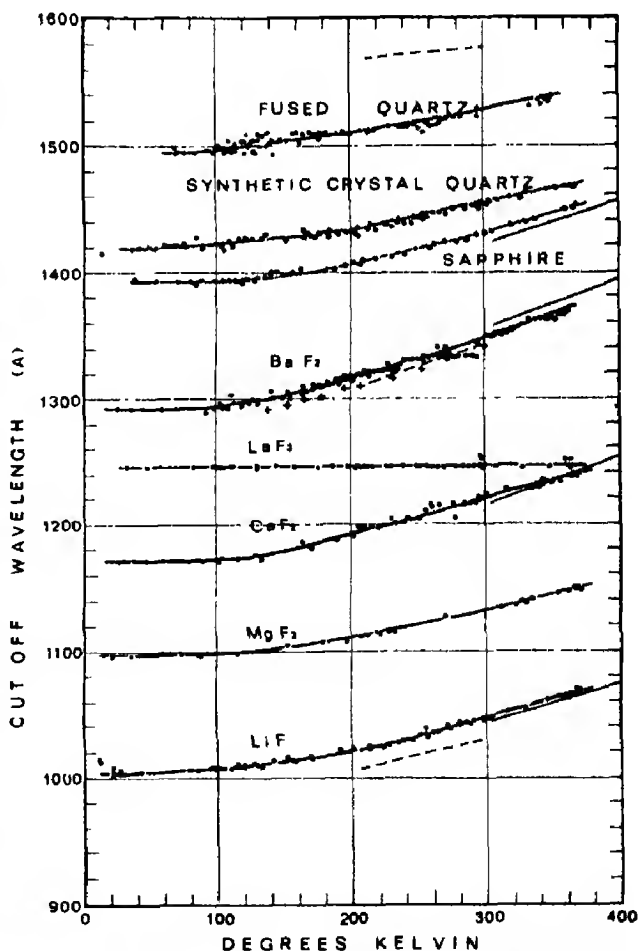


Fig. 4. The temperature dependence of the short wavelength transmittance limit of various vacuum ultraviolet materials.

difference between cleaved and polished BaF_2 . The solid lines from 300° to 400°K show the results obtained by Laufer *et al.* [3] which show good agreement with the present results. Their definition of λ_{co} was 10 per cent transmittance. The dashed lines from about 200° to 300°K are the results of Davis [2] which are in fair agreement with the present results, except for fused quartz as shown by the uppermost dashed line. This discrepancy is attributed to the large differences in the optical properties of fused quartz samples.

DISCUSSION

The temperature dependence of the short wavelength transmittance limit is explained in the next paper in terms of the fundamental excitations of the solids in question. The values of λ_{co} , measured in this experiment fall on the low energy side of the lowest exciton bands, and it is expected that as the temperature increases, accompanied by thermal broadening of the exciton band, λ_{co} should move toward longer wavelengths. As the band narrows with decreasing temperature, the slope of the transmittance vs. wavelength curve should become steeper as it appears to do in Fig. 2. Knudsen and Kupperian observed the same effect in CaF_2 [1]. Not all samples measured in the present experiment showed this effect for the reason that, as the contaminating layer increased in thickness during the course of the experiment, the transmittance was continually decreasing. With the precautions discussed above, however, this effect is minimized in the interpretation of Fig. 4.

Perhaps the most puzzling behavior is that of LaF_3 where no change in λ_{co} was observed as the temperature changed. There is no *a priori* reason why a shift in λ_{co} should not occur unless, possibly, sufficient impurities were present in the sample to mask the effect. Other unexpected characteristics of LaF_3 were the comparatively gradual decrease in transmittance as the wavelength decreased and the low transmittance, as shown in Fig. 5.

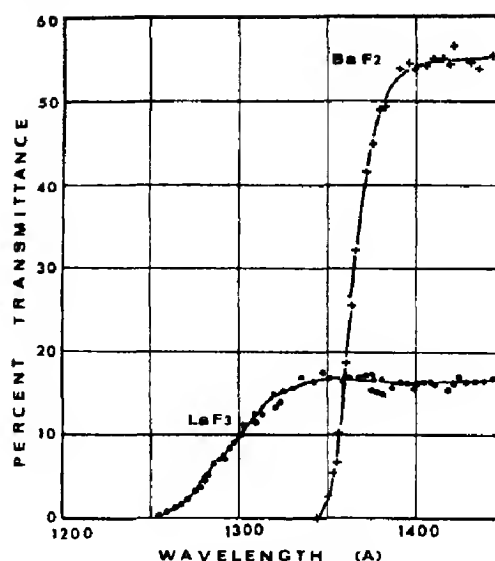


Fig. 5. Transmittance vs. wavelength of LaF_3 at room temperature showing the gradual onset of transmittance from about 1260 Å. Shown for comparison is the transmittance of BaF_2 which has a more abrupt onset of transmittance.

Here the transmittance vs. wavelength of BaF_2 is shown for comparison. While the gradual onset of absorption in LaF_3 made λ_{co} more difficult to locate, the error in doing so would certainly not be large enough to mask changes such as those seen with the other materials. Further measurements on LaF_3 samples of known pedigree are desirable to investigate this effect.

Three of the fluoride samples, CaF_2 , BaF_2 and LaF_3 fluoresced when irradiated with extreme ultraviolet photons. As mentioned previously, the signal due to the fluorescent radiation was separated from the extreme ultraviolet transmitted flux using a mica filter. While this process increases the possibility of errors, the consistency of the results from various trials on the same type of crystal indicate that such errors were not serious. Although the emission at wavelengths longer than the mica filter cut-off (≈ 3000 Å) was not studied in this experiment, it may be intrinsic luminescence of origin very similar to that studied in the alkali halides [8].

Practical use can be made of the change in

λ_{co} with temperature if the problem of contamination can be overcome. The most apparent application is to change the short wavelength limit of detectors and sources that use windows. For example, the radiation from the daytime extreme ultraviolet geo-corona is usually observed with narrow band, 100–200 Å, detectors. If these detectors are equipped with CaF_2 windows, λ_{co} being within a few angstrom of 1216 Å at 20°C, the all pervasive Ly- α line of atomic hydrogen could be added or subtracted to the total signal by just a few degrees temperature excursion of the window and its contribution to the geo-corona estimated.

By modulating the temperature of a detector window, a crude form of spectrograph could be realized, somewhat analogous to the retarding potential method of analyzing photoelectron energies, that would be useful when intensities are too low to permit use of the conventional spectrographs.

Acknowledgements—The authors would like to thank Prof. W. R. S. Garton and members of his staff for their support in the pursuance of this investigation; in partic-

ular, H. Goldstein, J. Jenkins, Dr. R. J. M. Lerner, J. Leveredge, Dr. A. Thorne and J. E. G. Wheaton. Thanks are also due Prof. M. Blackman for discussions of the contamination problem presented by ice. Dr. G. Hass of the U.S. Army Night Vision Laboratory, Ft. Belvoir, Virginia, and Dr. W. H. Parkinson of Harvard College Observatory, Cambridge, Massachusetts very generously contributed many of the samples, some of which were returned the worse for wear. Finally, S. A. Malo wishes to acknowledge the financial support of the Comision Nacional de Energia Nuclear and the Instituto Mexicano del Petroleo, Mexico.

REFERENCES

1. KNUDSEN A. R. and KUPPERIAN J. E., *J. opt. Soc. Am.* **47**, 440 (1957).
2. DAVIS R. J., *J. opt. Soc. Am.* **56**, 837 (1966).
3. LAUFER A. H., PIROG J. A. and McNESBY J. R., *J. opt. Soc. Am.* **55**, 64 (1965).
4. POWELL R. L., BUNCH M. D. and CORRUCINI R. J., *Cryogenics* **1**, 139 (1961).
5. DRESSLER K. and SCHNEPP O., *J. Chem. Phys.* **33**, 270 (1960).
6. DUSHMAN S. *Scientific Foundations of Vacuum Technique* (Edited by J. M. Lafferty), p. 726. Wiley, New York (1962).
7. BLACKMAN M. and LISGARTEN N. D. *Proc. R. Soc. A* **239**, 93 (1957).
8. REILLY M. H., Private communication. KNOX R. S. and TEEGARDEN K. J., *In Physics of Color Centers* (Edited by W. Beall Fowler). Academic Press, New York (1968).

ELECTRON PARAMAGNETIC RESONANCE OF Mn^{2+} IN $(NH_4)_2Co_2(SO_4)_3$ AND $(NH_4)_2Ni_2(SO_4)_3$ SINGLE CRYSTALS

B. V. R. CHOWDARI*

Department of Physics, Indian Institute of Technology, Kanpur, India

(Received 1 May 1969)

Abstract—EPR studies are reported on single crystals of ammonium cobalt sulphate and ammonium nickel sulphate containing Mn^{2+} ions. In each case only one magnetic complex of Mn^{2+} ion is found. The resonance lines in the case of Mn^{2+} doped ammonium nickel sulphate are characterised by a strong angular dependence of line intensities. The resonance lines in both the cases are fitted to a spin-Hamiltonian corresponding to orthorhombic symmetry.

INTRODUCTION

LANGBEINITES, double metal sulphates are of the general composition $(M^{1+})_2(M^{2+})_2(SO_4)_3$ where $M^{1+} = K, Rb, Tl$ or (NH_4) , and $M^{2+} = Co, Mn, Ca, Cd, Mg, Zn$ or Ni . They are named after the mineral Langbeinite $K_2Mg_2(SO_4)_3$. Langbeinites will form an interesting series to study the lattice defects formed in these crystals by the incorporation of the paramagnetic ion; since both monovalent and divalent metal ion sites are available in the host lattice. It will also be possible to study the relationship between the spin-Hamiltonian parameters and the size of the crystal lattice, at constant temperature, in these isomorphous diamagnetic lattices with a specific paramagnetic impurity. Keeping the above mentioned aspects in mind a systematic study of different paramagnetic ions in these crystals have been taken up and the present paper deals with the results obtained from the EPR studies of Mn^{2+} in $(NH_4)_2Co_2(SO_4)_3$ and $(NH_4)_2Ni_2(SO_4)_3$ at room temperature. There does not appear to have been much EPR work on Langbeinites which possess complicated structures. This is because it is often difficult to visualise the

structure of the unit cell and also, in some cases, no accurate data of the atom positions have been published.

EXPERIMENTAL

In order to grow single crystals of $(NH_4)_2Co_2(SO_4)_3$ suitable for the EPR studies cobalt sulphate ($CoSO_4 \cdot 7H_2O$) and ammonium sulphate ($(NH_4)_2SO_4$) are mixed in stoichiometric proportion, to the solution of which a little quantity (0.5 per cent by weight) of manganese sulphate ($MnSO_4 \cdot 4-5H_2O$) has been added. The single crystals are grown by the slow evaporation of the saturated solution at room temperature. The single crystals of $(NH_4)_2Ni_2(SO_4)_3$ doped with Mn^{2+} ions are grown by similar procedure using nickel sulphate ($NiSO_4 \cdot 6H_2O$) instead of cobalt sulphate. The crystals are found to grow with large $\{110\}$ faces. A Varian V-4502 EPR spectrometer with a 9 inch magnet and 100 kc/s modulation is used to study the paramagnetic resonance. As a reference for magnetic field strength the resonance line of DPPH is used. The magnetic field is measured using the Varian NMR gaussmeter while the frequency of the proton signal is measured by a Beckman frequency counter. IBM 1620 computer has been used for doing the calculations.

*Research Fellow of National Institute of Sciences of India.

RESULTS AND DISCUSSION

EPR data

The EPR spectrum of Mn^{2+} arises from transitions between the 36 energy levels of the free ion ^6S ground state as split by the crystalline electric field, the manganese nuclear spin of $\frac{5}{2}$, and the externally applied magnetic field. The measurements on both the crystals are done by rotating the magnetic field in a $(\bar{1}10)$ plane of the crystal. The

variation in some of the line positions ($M_S = \pm\frac{5}{2} \leftrightarrow \pm\frac{3}{2}$) of Mn^{2+} in $(\text{NH}_4)_2\text{Co}_2(\text{SO}_4)_3$ is shown in Fig. 1. The lines connecting the solid dots represents the angular variation of the resonance lines corresponding to $M_S = -\frac{5}{2} \rightarrow -\frac{3}{2}$, $m_I = \frac{5}{2}, \frac{3}{2}, \frac{1}{2}, -\frac{1}{2}, -\frac{3}{2}$ and $-\frac{5}{2}$ transitions. The lines connecting the open dots represent the angular variation of the resonance lines corresponding to $M_S = \frac{5}{2} \rightarrow \frac{3}{2}$, $m_I = \frac{5}{2}, \frac{3}{2}, \frac{1}{2}, -\frac{1}{2}, -\frac{3}{2}$ and $-\frac{5}{2}$ transitions. In the

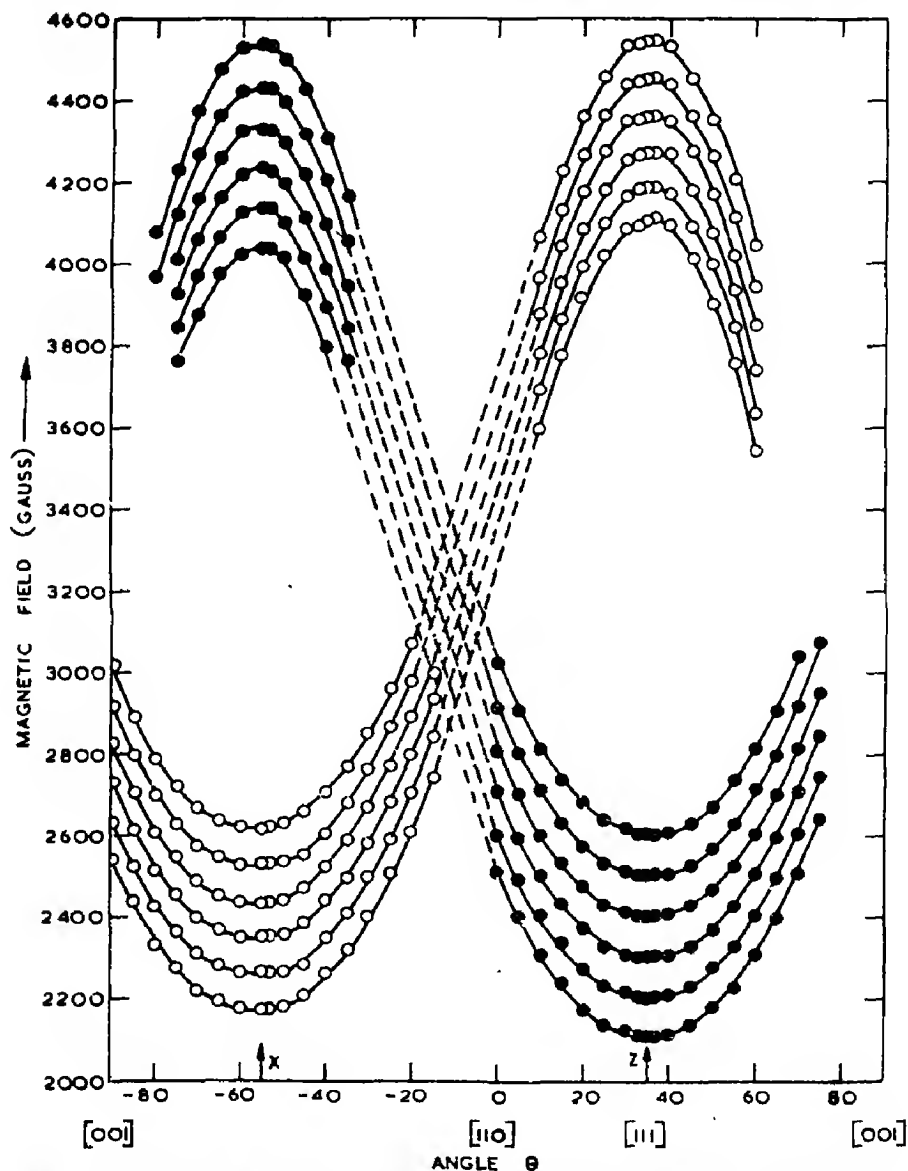


Fig. 1. Angular variation of some of the resonance lines of Mn^{2+} in $(\text{NH}_4)_2\text{Co}_2(\text{SO}_4)_3$ for the rotation of the magnetic field in $(\bar{1}10)$ plane of the crystal. The angle between $[110]$ and H direction in $(\bar{1}10)$ plane is denoted by θ .

region around [110] axis it is not possible to identify the resonance lines unambiguously and hence in Fig. 1 the experimental points are connected by dashed lines in that region.

When one the principal axis (x , y and z) of a Mn^{2+} ion parallels the magnetic field, the energy level separations of the spin system correspond to an extreme value. The orientation of these axes can be found by searching for the magnetic field direction, where the fine structure lines of the EPR spectra lie at an extremum in energy. It can be seen from Fig. 1 that the two extrema are separated by 90° . The Z axis was assigned to the direction with the large separation between the $M_S = -\frac{3}{2} \rightarrow -\frac{1}{2}$ and $M_S = \frac{1}{2} \rightarrow \frac{3}{2}$ transitions. The direction of the second extrema was called the X axis. The Z axis makes an angle of 35° with [110] axis and incidentally this happens to be the [111] axis. The X axis makes an angle of 90° with [111] axis in $(\bar{1}10)$ plane. The Y axis is perpendicular to the ZX plane and it coincides with $[\bar{1}10]$ axis. In the neighbourhood of static magnetic field parallel to the Z and X axes, the measurements were made by rotating the crystal about its $[\bar{1}10]$ axis which was held perpendicular to the direction of the magnetic field to make sure about the extrema observed. The resonance lines in the y direction are grouped close together and so no accurate magnetic field measurements of their positions could be made. Magnetic field measurements are done along the Z and X directions. The resonance lines of Mn^{2+} doped $(NH_4)_2Ni_2(SO_4)_3$ are found to have similar angular variation as that of Mn^{2+} doped $(NH_4)_2Co_2(SO_4)_3$. The directions of the principal axes at Mn^{2+} sites

in $(NH_4)_2Co_2(SO_4)_3$ and $(NH_4)_2Ni_2(SO_4)_3$ are the same.

Figures 2 and 3 show the spectrum of Mn^{2+} in $(NH_4)_2Co_2(SO_4)_3$ when the magnetic field is parallel to Z and X axis respectively. In addition to thirty resonance lines due to one Mn^{2+} magnetic complex there are some very weak lines due to Mn^{2+} , probably in some other environments. The study of this weak spectra could not be done because of the relative intensity of this weak spectra and the spectra under discussion. Figures 4 and 5 shows the spectrum of Mn^{2+} in $(NH_4)_2Ni_2(SO_4)_3$ at different angles when the magnetic field is rotated in $(\bar{1}10)$ plane of the crystal.

The spectrum due to Mn^{2+} in $(NH_4)_2Co_2(SO_4)_3$ and $(NH_4)_2Ni_2(SO_4)_3$ has been analysed using the spin-Hamiltonian corresponding to rhombic symmetry. The spin-Hamiltonian is given by

$$\begin{aligned} \mathcal{H} = & g\beta\bar{H} \cdot \bar{S} + D[S_z^2 - \frac{1}{3}S(S+1)] \\ & + E(S_x^2 - S_y^2) \\ & + \frac{a}{6}[S_x^4 + S_y^4 + S_z^4 \\ & - \frac{1}{3}S(S+1)(3S^2 + 3S - 1)] \\ & + A\bar{S} \cdot \bar{I} \end{aligned}$$

where the first term is due to the Zeeman interaction, the next three terms take into account the crystalline electric field at the Mn^{2+} site, and the last term is the interaction of the electron spin with the nuclear spin. a , D and E are the cubic, axial and rhombic crystal field parameters, respectively, and A is the hyperfine constant.

The expressions used to obtain the energy differences are:

(a) For fine structure positions with $H \parallel Z$:

$$H_1(M = -\frac{3}{2} \rightarrow -\frac{1}{2}) = H_0 + 4D + 9E^2/(H_1 - D) - 5E^2/(H_1 - 3D) + 2a$$

$$H_2(M = -\frac{1}{2} \rightarrow -\frac{3}{2}) = H_0 + 2D + 9E^2/(H_2 + D) - 9E^2/(H_2 - D) - 5E^2/(H_2 - 3D) - (\frac{1}{2})a$$

$$H_3(M = \frac{1}{2} \rightarrow -\frac{1}{2}) = H_0 - 9E^2/(H_3 - D) + 5E^2/(H_3 + 3D) + 5E^2/(H_3 - 3D) - 9E^2/(H_3 + D)$$

$$H_4(M = \frac{3}{2} \rightarrow \frac{1}{2}) = H_0 - 2D - 9E^2/(H_4 + D) + 9E^2/(H_4 - D) - 5E^2/(H_4 + 3D) + (\frac{1}{2})a$$

$$H_5(M = \frac{5}{2} \rightarrow \frac{3}{2}) = H_0 - 4D + 9E^2/(H_5 + D) - 5E^2/(H_5 + 3D) - 2a$$

(b) For hyperfine structure positions with $H \parallel Z$

$$H(m \leftrightarrow m) = -Am - (A^2/2H_0)(I(I+1) - m^2 + (2M-1)m)$$

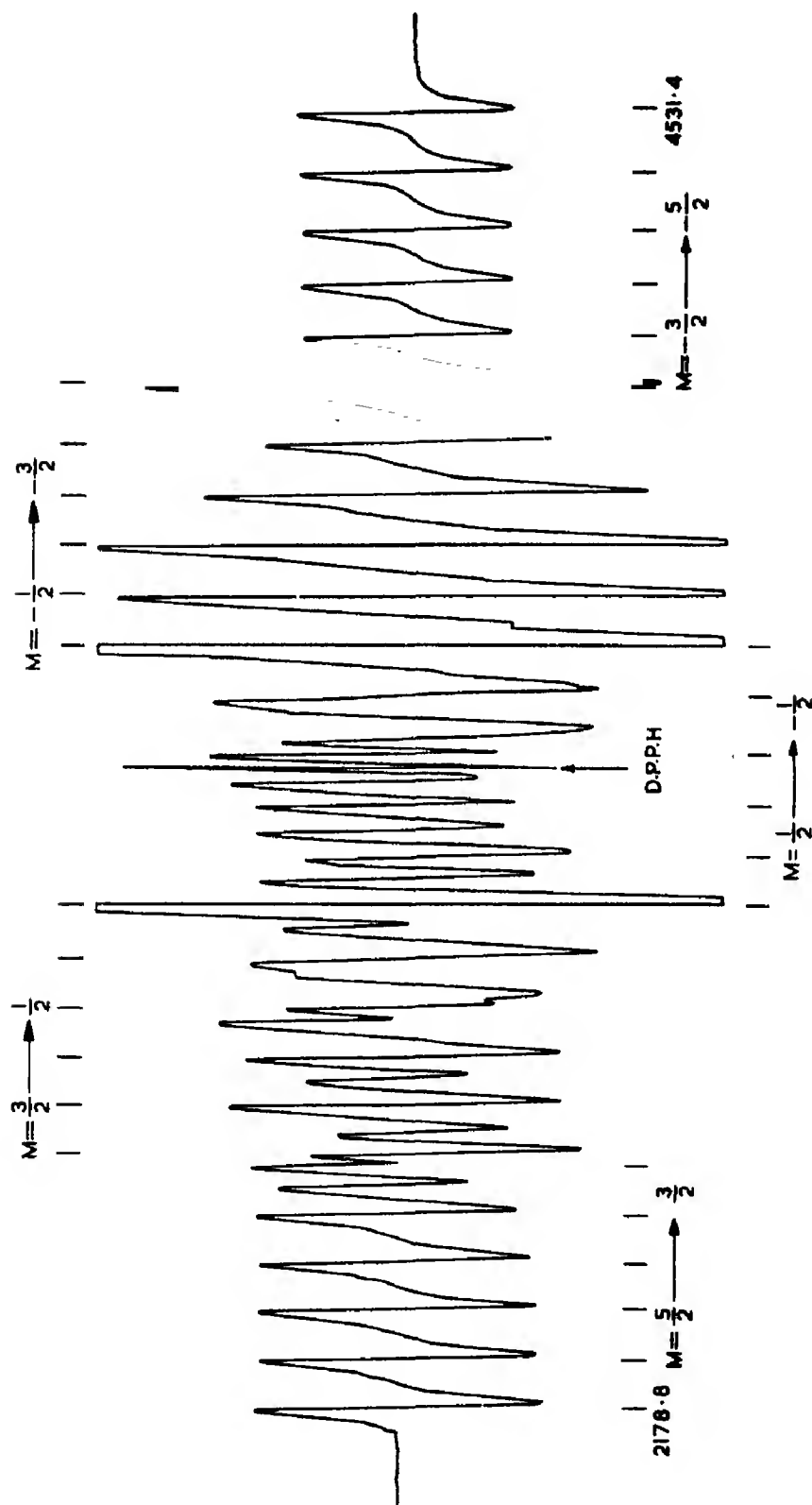


Fig. 3. EPR spectrum of Mn^{2+} in $(\text{NH}_4)_2\text{Co}_2(\text{SO}_4)_3$ single crystals at room temperature, the direction of the magnetic field parallel to X -axis (90° from $[111]$ direction).

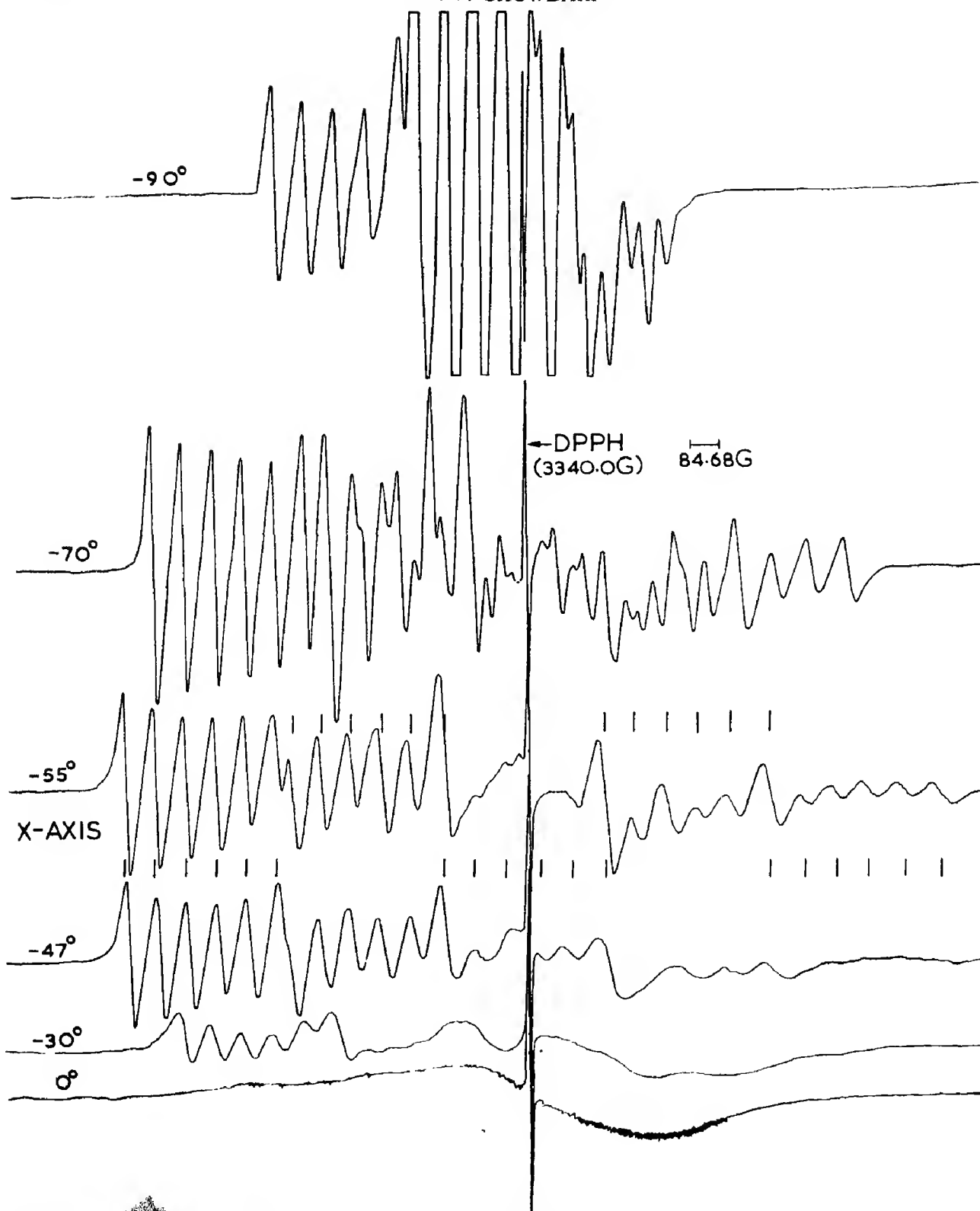


Fig. 4. EPR spectrum of Mn^{2+} in $(\text{NH}_4)_2\text{Ni}_2(\text{SO}_4)_3$ single crystals at room temperature, the direction of the magnetic field making different angles (-90° , -70° , -55° , -47° , -30° and 0°) with respect to $[110]$ axis.

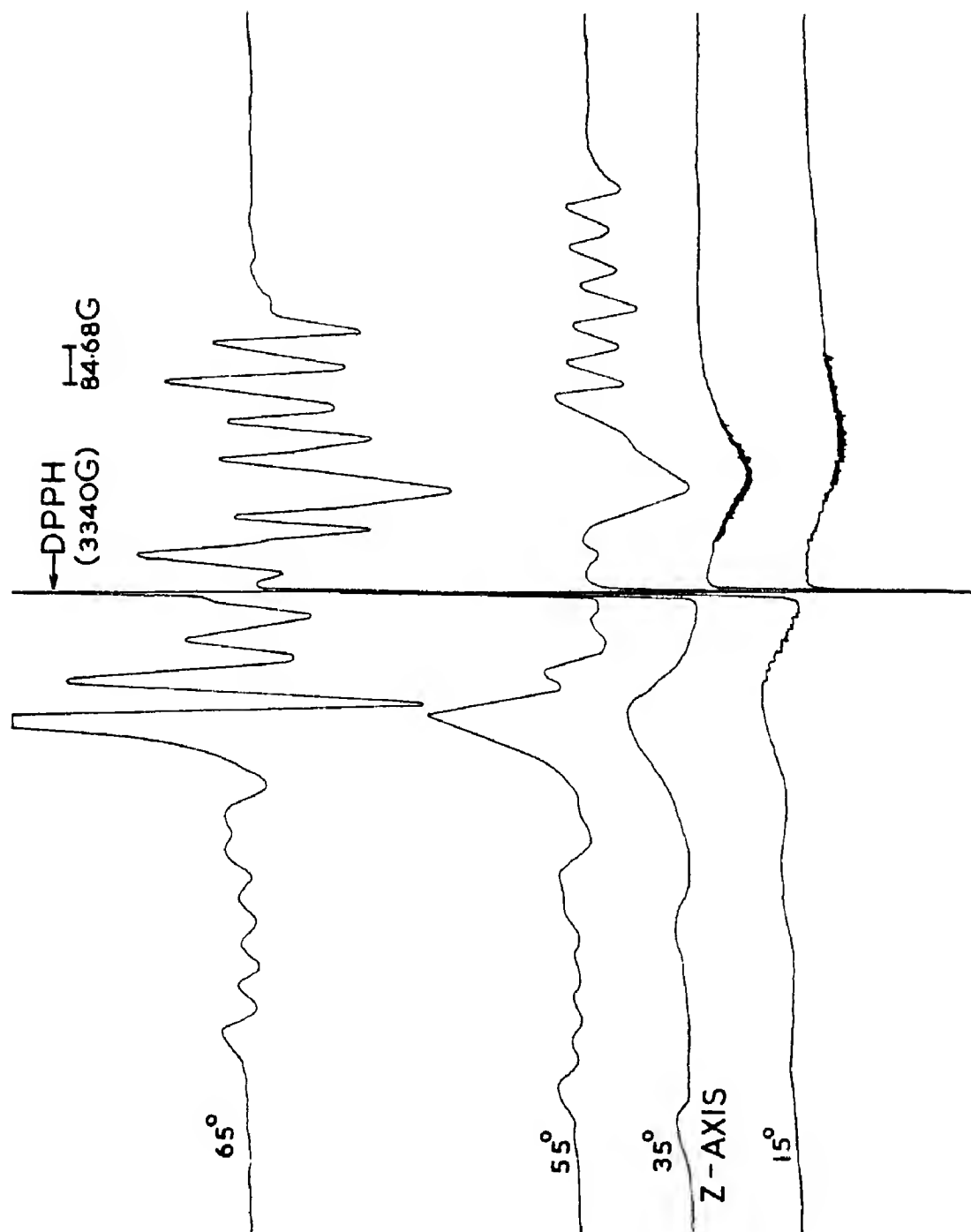


Fig. 5. EPR spectrum of Mn^{2+} in $(\text{NH}_4)_2\text{Ni}_2(\text{SO}_4)_3$ single crystals at room temperature, the direction of the magnetic field making different angles (65° , 55° , 35° and 15°) with respect to $[110]$ axis.

with the magnetic field directed along x or y replace D with $-\frac{1}{2}(D \mp 3E)$ and E with $-\frac{1}{2}(E \pm D)$ where the upper sign applies for the magnetic field along x and the lower sign for the magnetic field along y . The spin-Hamiltonian parameters obtained using the above expressions are given in Table 1. For the spectrum due to Mn^{2+} in $(\text{NH}_4)_2\text{Ni}_2(\text{SO}_4)_3$ it is not possible to calculate g_z and A_z since the spectrum practically disappears when the direction of the magnetic field is parallel to the

determined. The second order shifts permit the determination of the relative signs of the various measured parameters. For negative D/A , the separations of sextets decrease on the low field side when the direction of the magnetic field is parallel to Z -axis. In the case of Mn^{2+} ion negative A is commonly accepted. In the present experiments the separations of sextets decreases towards the high field side and hence D/A is positive which in turn results D to be negative.

Table 1. Spin-Hamiltonian parameters of Mn^{2+} in $(\text{NH}_4)_2\text{Co}_2(\text{SO}_4)_3$ and $(\text{NH}_4)_2\text{Ni}_2(\text{SO}_4)_3$

	g_z	g_x	$D \times 10^{-4} \text{ cm}^{-1}$	$E \times 10^{-4} \text{ cm}^{-1}$	$a \times 10^{-4} \text{ cm}^{-1}$	$A_z \times 10^{-4} \text{ cm}^{-1}$	$A_x \times 10^{-4} \text{ cm}^{-1}$
$(\text{NH}_4)_2\text{Co}_2(\text{SO}_4)_3$	2.0036	2.0036	-231.0	68.7	2.0	-88.4	-86.8
$(\text{NH}_4)_2\text{Ni}_2(\text{SO}_4)_3$		2.006	-153.5	95.5	2.8		-87.1
$(\text{NH}_4)_2\text{Cd}_2(\text{SO}_4)_3$ [7]	2.000		-157.3	0	5.4	-94.3	

Z axis. The parameters reported here for Mn^{2+} in $(\text{NH}_4)_2\text{Ni}_2(\text{SO}_4)_3$ are obtained using only the x axis spectrum and hence they may not be very accurate. The discussion regarding intensity variation of resonance lines in this crystal will be presented in the later part of the paper. Table 2 shows a comparison of the calculated and the experimental fine structure positions when the external magnetic field is parallel to the Z and the X axis of $(\text{NH}_4)_2\text{Co}_2(\text{SO}_4)_3$ and the X axis of $(\text{NH}_4)_2\text{Ni}_2(\text{SO}_4)_3$. The agreement between the calculated and the experimental field values is very good. Experimentally only the relative signs are

Location of Mn^{2+} ions

The detailed X-ray data regarding atomic positions of $(\text{NH}_4)_2\text{Co}_2(\text{SO}_4)_3$ and $(\text{NH}_4)_2\text{Ni}_2(\text{SO}_4)_3$ does not seem to be available in the literature. Zemmann and Zemmann [1] studied the crystal structure of $\text{K}_2\text{Mg}_2(\text{SO}_4)_3$ which is isomorphic to $(\text{NH}_4)_2\text{Co}_2(\text{SO}_4)_3$ and $(\text{NH}_4)_2\text{Ni}_2(\text{SO}_4)_3$. Wyckoff [2] listed the lattice parameters of many isomorphic salts of Langbeinite series. The lattice parameters of $(\text{NH}_4)_2\text{Co}_2(\text{SO}_4)_3$ and $(\text{NH}_4)_2\text{Ni}_2(\text{SO}_4)_3$ are [2] $a = 9.997 \text{ \AA}$ and $a = 9.904 \text{ \AA}$ respectively. Langbeinite series crystallizes in space group $P2_13$ with cubic symmetry and there

Table 2. Comparison of experimental and theoretical fine structure positions of Mn^{2+} in $(\text{NH}_4)_2\text{Co}_2(\text{SO}_4)_3$ and $(\text{NH}_4)_2\text{Ni}_2(\text{SO}_4)_3$

$(\text{NH}_4)_2\text{Co}_2(\text{SO}_4)_3$				$(\text{NH}_4)_2\text{Ni}_2(\text{SO}_4)_3$	
$H \parallel Z$		$H \parallel X$		$H \parallel X$	
Experimental	Theoretical	Experimental	Theoretical	Experimental	Theoretical
2359.0	2360.5	4277.6	4279.0	2380.0	2380.3
2829.0	2830.4	3785.0	3782.0	2864.5	2864.4
3325.0	3323.7	3320.0	3318.7	3325.7	3328.9
3825.0	3824.7	2865.0	2866.5	3795.0	3795.1
4318.0	4319.8	2405.0	2408.0	4285.2	4284.8

are four molecules per unit cell. There are two crystallographically nonequivalent divalent atoms (Co^{2+} or Ni^{2+}) and monovalent atoms $(\text{NH}_4)^+$ in these salts. The two crystallographically nonequivalent cobalt or Nickel ions are slightly distorted and octahedrally surrounded by six oxygen atoms each. The ammonium coordination can not be sharply defined, there are four oxygens around one type of ammonium atoms and three oxygens around a second type of ammonium atom. The difference between the environment of two divalent sites (Co^{2+} or Ni^{2+}) is very small compared to the difference between the environment of the two ammonium sites. The EPR results can be best explained by assuming that Mn^{2+} substitute for Co^{2+} ions in $(\text{NH}_4)_2\text{Co}_2(\text{SO}_4)_3$ and for Ni^{2+} ions in $(\text{NH}_4)_2\text{Ni}_2(\text{SO}_4)_3$. Such replacement would not be unexpected, given the similarity of ionic radii (0.72 \AA for Co^{2+} , 0.69 \AA for Ni^{2+} and 0.8 \AA for Mn^{2+}) and the identity of charge. When Mn^{2+} ion substitutes for Co^{2+} or Ni^{2+} positions one expects two different spectra because of the availability of two nonequivalent sites. However, the presence of only one Mn^{2+} magnetic complex suggests that the Mn^{2+} ions are substituting for only one type of Co^{2+} or Ni^{2+} sites. Alternative locations for the Mn^{2+} ions are the $(\text{NH}_4)^+$ sites. Substitution for $(\text{NH}_4)^+$ appears improbable because of the difference in charge. Intensity peculiarities of Mn^{2+} lines in $(\text{NH}_4)_2\text{Ni}_2(\text{SO}_4)_3$:

Figure 4 shows the spectrum of Mn^{2+} in $(\text{NH}_4)_2\text{Ni}_2(\text{SO}_4)_3$ recorded when the direction of the magnetic field makes angles of -90° , -70° , -55° , -47° , -30° and 0° with respect to the $[110]$ axis in $(\bar{1}10)$ plane of the crystal. Figure 5 shows the spectrum of Mn^{2+} in $(\text{NH}_4)_2\text{Ni}_2(\text{SO}_4)_3$ recorded when the direction of the magnetic field makes angles of 65° , 55° , 35° and 15° with respect to $[110]$ axis of the crystal in $(\bar{1}10)$ plane. Figures 4 and 5 shows that there is a rapid change in the intensity of resonance lines as the angle is changed. The spectrum corresponding to 35° and -55° given

in Figs. 5 and 4 corresponds to the magnetic field parallel to Z and X axis of Mn^{2+} complex respectively. The intensity of the allowed resonance lines is found to be maximum when the direction of the magnetic field makes an angle of -75° with $[110]$ direction. The spectrum practically disappears when the direction of the magnetic field is parallel to the Z axis. When the direction of the magnetic field deviates from those of maximum intensity, a quite considerable line broadening (by a factor of ≈ 1.5) is also observed, which in itself, however, can by no means explain the far sharper decrease in the derivative of the absorption line. The intensity of the allowed lines changes at different rates for different electronic transitions and within the limits of one electronic transition, for different hyperfine components. Out of the six hyperfine components the two external ones decrease most slowly and the two internal ones most rapidly. Moreover, there is a slight asymmetry in the rate of reduction of the intensity between lines which have associated with them the nuclear quantum number m and $-m$. The angular variation of the intensity is different for different electronic transitions and it is maximum for the central transition ($M_s = \frac{1}{2} \rightarrow -\frac{1}{2}$) and minimum for lateral transitions ($M_s = -\frac{3}{2} \rightarrow -\frac{3}{2}$ and $M_s = \frac{3}{2} \rightarrow \frac{3}{2}$). As one can see from Fig. 4, $M_s = \frac{1}{2} \rightarrow -\frac{1}{2}$ transition is very weak when the direction of the magnetic field is parallel to x axis where the other transitions are reasonably strong.

A comprehensive theory explaining the intensity variations of the allowed ($\Delta M_s = 1$, $\Delta m_l = 0$), and forbidden ($\Delta M_s = \pm 1$, $\Delta m_l = \pm 1$) lines was developed by Bir[3]. The theory is based on the fact that the direction of the large effective magnetic field, due to electrons acting on the nuclear spin, differs from the direction of the smaller external magnetic field, and so the effective field direction becomes the nuclear spin quantization axis. The angle between the direction of the quantization axis and the external magnetic field depends on the orientation of the external

magnetic field relative to the crystal field axis and on the electron states. When the angle between the magnetic field and the crystal axes changes, there is a change in the angle between the nuclear spin quantization axes corresponding to the initial and final states of the electron in a given transition, and this leads to the appearance of forbidden transitions and a corresponding reduction in the intensity of the allowed transitions. Bir and Sochava[4] have used this theory to explain the intensity variations of Mn^{2+} in the axial crystal field of $SrCl_2$. Later Manoogian[5] has used Bir's theory to explain the intensity variations of Mn^{2+} in orthorhombic fields of tremolite ($2(H_2Ca_2Mg_5(SiO_3)_8)$). Bir's theory suggests that the forbidden transitions should appear whenever there is a large change in the intensity of the allowed transitions. But in the present case of Mn^{2+} in $(NH_4)_2Ni_2(SO_4)_3$ there is no indication of the presence of forbidden transitions at any angle. Bir's theory also suggests that the intensity of the allowed transitions should be maximum when the direction of the magnetic field is parallel to crystal field axes. But this is not the fact observed in the present experiments on Mn^{2+} in $(NH_4)_2Ni_2(SO_4)_3$. In fact the resonance lines are not practically visible when the direction of the magnetic field is parallel to Z axis. According to Bir's theory the strong angular dependence of intensities occurs only in the presence of strong crystalline fields. But in the present experiments magnitude of D which represents the strength of crystal-line field is not large. All this suggests that there is a further need to check Bir's theory and develop a theory which can explain the anomalies observed in the present experiments. The nonobservability of these anomalies in the angular variation of the intensities of Mn^{2+} doped $(NH_4)_2Co_2(SO_4)_3$, $(NH_4)_2Zn_2(SO_4)_3$ and $(NH_4)_2Mg_2(SO_4)_3$ [6] and the observability in Mn^{2+} doped in $(NH_4)_2Ni_2(SO_4)_3$ suggests the Ni^{2+} ions might be playing a prominent role in the magnetic behaviour of the crystal. A search

for magnetic behaviour, such as antiferromagnetic resonance, of this crystal is desirable.

Though both the crystals of $(NH_4)_2Co_2(SO_4)_3$ and $(NH_4)_2Ni_2(SO_4)_3$ are grown with the same concentration of Mn^{2+} impurity the line widths of the resonance line in both the crystals are not the same. The peak-peak derivative width of Mn^{2+} lines in $(NH_4)_2Co_2(SO_4)_3$ is about 8 G while in the case of Mn^{2+} doped $(NH_4)_2Ni_2(SO_4)_3$ its value ranges from 25 to 50 G. In the case of Mn^{2+} doped $(NH_4)_2Ni_2(SO_4)_3$ the line widths of all the electronic transitions are not the same while they are the same in the case of Mn^{2+} doped $(NH_4)_2Co_2(SO_4)_3$ crystals. The reason for observing large line widths in the case of nickel salt might be due to the fact that the spin-lattice relaxation time of Ni^{2+} ions is much larger than that of Co^{2+} ions. At room temperature the spin lattice relaxation time of Co^{2+} is so short that its own absorption lines are too broad to be observed. The absorption lines of Ni^{2+} have been observed at room temperature in some cases which indicates that the spin-lattice relaxation time of Ni^{2+} ions is much more compared to that of Co^{2+} ions. However in the present experiments no resonance could be observed in pure salts of $(NH_4)_2Co_2(SO_4)_3$ and $(NH_4)_2Ni_2(SO_4)_3$. It may be mentioned here that the resonance lines due to Mn^{2+} ions embedded in $(NH_4)_2Mg_2(SO_4)_3$ and $(NH_4)_2Zn_2(SO_4)_3$ [6] have the same line width (≈ 8 G) as that of Mn^{2+} lines in $(NH_4)_2Co_2(SO_4)_3$ crystals, which means that the spin lattice relaxation time of Co^{2+} ions is comparable to that of diamagnetic ions such as Mg^{2+} and Zn^{2+} .

In conclusion, the results obtained in the present study can be compared with the preliminary results obtained by Tatsuzaki[7] earlier in the case of Mn^{2+} doped $(NH_4)_2Cd_2(SO_4)_3$. Unfortunately the resolution of spectral lines was pretty poor in the case of $(NH_4)_2Cd_2(SO_4)_3$. This has been noted by the author himself. The comparison of the spin-Hamiltonian parameters obtained in the present study and those in Mn^{2+} doped

$(\text{NH}_4)_2\text{Cd}_2(\text{SO}_4)_3$ suggests that the crystalline field experienced by Mn^{2+} substituting for Co^{2+} in $(\text{NH}_4)_2\text{Co}_2(\text{SO}_4)_3$ and Ni^{2+} in $(\text{NH}_4)_2\text{Ni}_2(\text{SO}_4)_3$ is more than that for Mn^{2+} substituting for $(\text{NH}_4)_2\text{Cd}_2(\text{SO}_4)_3$. The reason for this might be due to the difference in the lattice parameter of these salts. Another point of interest is the value of the hyperfine coupling constant A . The value of $A = -94.3 \times 10^{-4} \text{ cm}^{-1}$ found for Mn^{2+} in $(\text{NH}_4)_2\text{Cd}_2(\text{SO}_4)_3$ is more than that found in the present experiments. It has been pointed out by van Wieringen[8] that the magnitude of A decreases with increasing covalency of the magnetic complex. From the electronegativity of Mn^{2+} and negative ions and the numbers of the surrounding negative ions, the amount of the ionic character can be calculated after Pauling[9]. Matumura[10] has shown that the relationship between the magnitude of A and the ionicity is a linear one if the degree of covalency is calculated according to Pauling's rule[9]. From Matumura's curve we obtain that for $[A] = 94.3 \times 10^{-4} \text{ cm}^{-1}$, $88.4 \times 10^{-4} \text{ cm}^{-1}$ and $87.1 \times 10^{-4} \text{ cm}^{-1}$, as is the case respectively for Mn^{2+} in $(\text{NH}_4)_2\text{Cd}_2(\text{SO}_4)_3$,

$(\text{NH}_4)_2\text{Co}_2(\text{SO}_4)_3$ and $(\text{NH}_4)_2\text{Ni}_2(\text{SO}_4)_3$ there is about 96.0, 93.5 and 93.25 per cent ionicity respectively. This suggests that the ionic character of $(\text{NH}_4)_2\text{Co}_2(\text{SO}_4)_3$ and $(\text{NH}_4)_2\text{Ni}_2(\text{SO}_4)_3$ salts is nearly same and is less than that of $(\text{NH}_4)_2\text{Cd}_2(\text{SO}_4)_3$.

Acknowledgements—I wish to thank Professors Putcha Venkateswarlu and J. Mahanty for their continuous interest in the progress of the work and Mr. S. K. Banerjee for his help during the course of the work.

REFERENCES

1. ZEMANN V. A. and ZEMANN J., *Acta crystallogr.* **10**, 409 (1957).
2. WYCKOFF R. W. G., *Crystal Structures* **3**, 217 (1965).
3. BIR G. L., *Soviet Phys. solid St.* (English Transl.) **5**, 1628 (1964).
4. BIR G. L. and SOCHAVA L. S., *Soviet Phys. solid St.* (English Transl.) **5**, 2637 (1964).
5. MANOOGIAN A., *Can. J. Phys.* **46**, 1029 (1968).
6. CHOWDARI B. V. R., Unpublished.
7. TATSUZAKI I., *J. phys. Soc. Japan* **17**, 582 (1962).
8. VAN WIERINGEN J. S., *Discuss Faraday. Soc.* **19**, 118 (1955).
9. PAULING L., *The Nature of the Chemical Bond*, Cornell University Press, Ithaca, New York (1960).
10. MATUMURA O., *J. phys. Soc. Japan* **14**, 108 (1959).

THERMAL EXPANSION OF SOLID CH₄ AND CD₄

V. G. MANZHELII, A. M. TOLKACHEV and V. G. GAVRILKO

Physico-Technical Institute of Low Temperatures, Academy of Sciences of the Ukrainian SSR,
Kharkov, USSR

(Received 11 June 1968; in revised form 25 April 1969)

Abstract—The linear expansion coefficients of solid light methane CH₄ and deuteromethane CD₄ have been defined in the temperature range 10°–24°K and 6°–58°K, respectively. The question about the nature of rotational motion of molecules in CH₄ and CD₄ crystals and about the existence of low temperature phase transition in solid methane is discussed.

EXPERIMENTAL PROCEDURE AND RESULTS

THE THERMAL expansion of solid CH₄ has been investigated in the temperature range 10°–24°K and that of solid CD₄ from 6°–58°K. The purity of the investigated CH₄ was 99.96 per cent. CD₄ (the heavy isotope concentration is 98.3%) supplied by the All-Union Society 'Isotope' contained nitrogen and oxygen in small amounts. After the CD₄ was purified by passing it through melted lithium at 250°C the total amount of nitrogen and oxygen in it was reduced to 0.25 per cent.

The measurements were carried out using the apparatus described earlier [1] with liquid helium and hydrogen as refrigerants. The copper-constantan thermocouples were calibrated directly in the dilatometer to 4.2°K by a germanium thermometer of PRMI USSR. The thermocouple e.m.f. was measured by a R-308 potentiometer. The error in determining the temperature did not exceed 0.1°C. The homogeneous transparent solidified gas specimens were grown from the liquid phase.

The measurements were made on two CH₄ specimens and one of CD₄. The specimen length-temperature change was measured on both heating and cooling—3 or 4 cycles for each specimen. The measurements were carried out every 0.5°–1°K for CH₄ and CD₄ in the low temperature phases and every 3°–4°K for CD₄ in the high temperature phase.

The length change of samples was measured down to 4.2°K. But the experimental error

increased rapidly with decreasing temperature and made it unreasonable to calculate the linear expansion coefficients of solid CH₄ below 10°K and of solid CD₄ below 6°K.

We did not carry out detailed measurements of thermal expansion in the immediate vicinity of the phase transition temperatures or in the intermediate crystal phase of CD₄.

The measurements on the deuteromethane specimen above 58°K became complicated because of its high vapour pressure and plasticity. The error in determining the linear expansion coefficients of CD₄ was about ±10 per cent below 11°K, ±5 per cent between 13° and 21°K and between 50° and 58°K, ±3 per cent in the range 28°–50°K. For CH₄, the error was ±15 per cent at the lowest temperature and did not exceed ±5 per cent above 14°K in the low temperature phase and ±3 per cent in the high temperature phase.

The total volume change of solid methane, $\Delta V/V$, calculated from the data of present paper and of [2] between 4.2° and 60°K was 4.3 per cent, and for deuteromethane in the temperature range 4.2° to 58°K was 5.8 per cent.

The results of determining the linear expansion coefficients α of CH₄ and CD₄ are plotted in Fig. 1. We also give data obtained earlier [2] for the thermal expansion of CH₄ in the temperature range 22°–60°K. The smoothed volume expansion coefficients β ($\beta = 3\alpha$) are presented in Table 1.

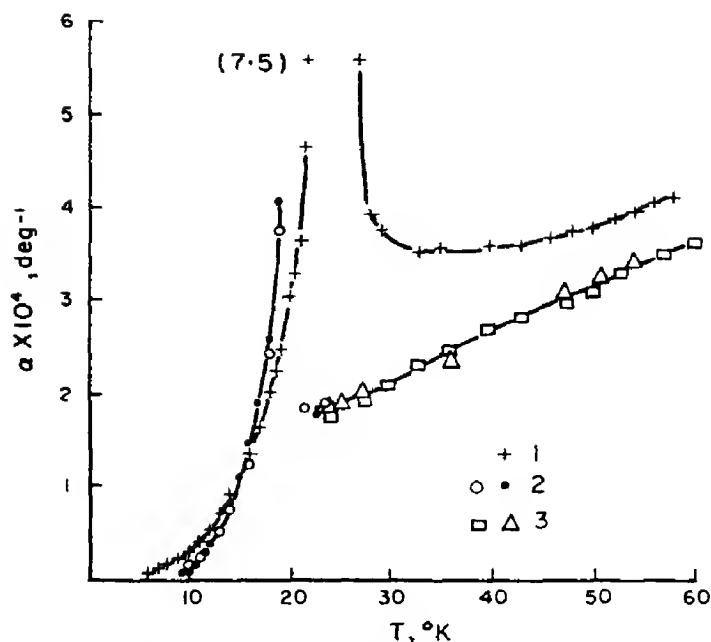


Fig. 1. Temperature dependence of the linear expansion coefficients for CH_4 and CD_4 . (1) Results for CD_4 obtained in the present paper; (2) results for CH_4 obtained in the present paper; (3) results for CH_4 published in the paper [2].

Table 1. Smoothed values of the volume expansion coefficients for crystalline CH_4 and CD_4

$T^\circ\text{K}$	$\beta_{\text{CD}_4} \cdot 10^4$ (deg^{-1})	$T^\circ\text{K}$	$\beta_{\text{CD}_4} \cdot 10^4$ (deg^{-1})	$T^\circ\text{K}$	$\beta_{\text{CH}_4} \cdot 10^4$ (deg^{-1})	$T^\circ\text{K}$	$\beta_{\text{CH}_4} \cdot 10^4$ (deg^{-1})
6	0.189	19	7.26	10	0.381	22	5.46
7	0.330	20	8.91	11	0.714	25	5.58
8	0.489	21	11.43	12	1.14	28	6.00
9	0.684	22	22.5	13	1.69	30	6.33
10	0.915	28	11.70	14	2.43	35	7.11
11	1.21	30	10.84	15	3.29	40	7.90
12	1.59	33	10.53	16	4.37	45	8.67
13	2.07	35	10.55	17	5.64	50	9.36
14	2.67	40	10.60	18	7.71	55	10.14
15	3.33	45	10.82	19	12.18	60	10.80
16	4.05	50	11.21				
17	4.92	55	11.79				
18	6.00	58	12.24				

The difference between the thermal expansion coefficient values of CH_4 at 22°K given in the present and previous [2] papers is due to the systematical error which was subsequently taken into account.

DISCUSSION OF RESULTS

Let us first discuss the results concerning the high temperature phases. CH_4 and CD_4 are spherically symmetric molecules and f.c.c. lattices in high temperature solid phases

[3, 4]. That is why the crystalline CH₄ and CD₄ are closer to solid inert gases than the other simple molecular crystals. However, while the thermal properties of the solid inert gases are determined only by translational oscillations those of the methanes will depend also on the character of the rotational motion of molecules in crystal. The contribution from the rotational motion may be estimated roughly by comparing the corresponding properties of solid methanes with those of solidified inert gases.

Argon is the most convenient substance for comparison; its value of the quantum parameter $\Lambda = h/\sigma\sqrt{m\epsilon}$ is close to those of methanes [5] ($\Lambda_{\text{Ar}} = 0.187$; $\Lambda_{\text{CH}_4} = 0.235$; $\Lambda_{\text{CD}_4} = 0.209$). Here, h is Plank's constant, σ and m the diameter and mass of the molecule and ϵ is the depth of the potential well for the pair molecule interaction.

In Figs. 2 and 3 the temperature dependences of thermal expansion coefficients for solidified methanes and argon [6] are compared in reduced co-ordinates $\beta(\epsilon/k)$ vs. T/T_{tr} [5, 7] (where T_{tr} is the triple point temperature, k is the Boltzman constant) and β vs. T/θ_0 [7-9] (where θ_0 is the limiting value of Debye temperature at $T \rightarrow 0$). The following values were used: $\epsilon/k(\text{CH}_4) = \epsilon/k(\text{CD}_4) = 148^\circ\text{K}$, $\epsilon/k(\text{Ar}) = 120^\circ\text{K}$ [5], $\theta_0(\text{CH}_4) = 135^\circ\text{K}$ [10], $\theta_0(\text{CD}_4) = \theta_0(\text{CH}_4)\sqrt{(m(\text{CH}_4))/m(\text{CD}_4)}$ = 121°K , $\theta_0(\text{Ar}) = 93.3^\circ\text{K}$ [11], $T_{\text{tr}}(\text{Ar}) = 83.75^\circ\text{K}$ [11], $T_{\text{tr}}(\text{CH}_4) = 90.67^\circ\text{K}$ [12],

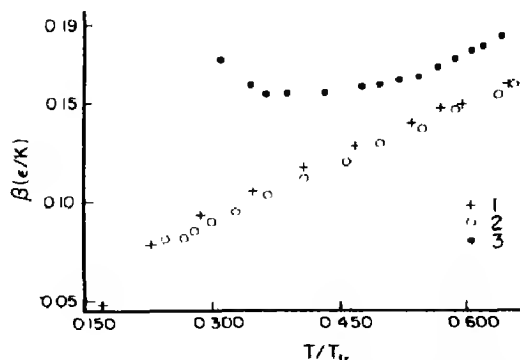


Fig. 2. Reduced coefficient of volume thermal expansion $\beta(\epsilon/k)$ vs. reduced temperature T/T_{tr} . (1) Ar, (2) CH₄, (3) CD₄.

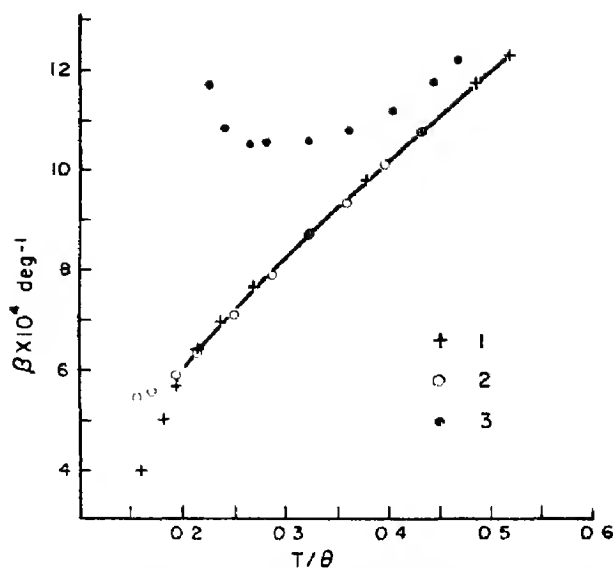


Fig. 3. Coefficient of volume thermal expansion β vs. reduced temperature T/θ_0 . (1) Ar, (2) CH₄, (3) CD₄.

$T_{\text{tr}}(\text{CD}_4) = 89.78^\circ\text{K}$ [12]. The solid CH₄ thermal expansion in reduced coordinates practically coincides with the thermal expansion of argon, differing from the latter only below 28°K , i.e. in the immediate vicinity of the temperature of phase transformation. It indicates that the thermal expansion of solid CH₄ in the temperature range $T > 28^\circ\text{K}$ is mainly due to translational oscillations.

The contribution of the molecular rotational motion to the thermal expansion of solids vanishes in the limit of free rotation [13]. In principle, the molecular rotation in solid phase is always somewhat hindered. Recently there appeared experimental evidence for impedance of rotational motion of molecules in solid CH₄ [14]. But the sensitivity of the different properties to impedance of rotation is different [13-17]. Colwell *et al.* [15] has shown that a satisfactory interpretation on the solid methane heat capacity in high temperature phase can be obtained by means of model of $3N$ free rotators. From Figs. 2 and 3 it follows that in the case of solid CH₄ the thermal expansion (as well as heat capacity) above 28°K is not sensitive to the extent of hindering of molecular rotation.

The influence of the retarding field on the rotational motion of CD_4 molecules is apparently greater. As a result of this, the coefficient of thermal expansion of solid CD_4 in high temperature phase up to 60°K is higher than that of CH_4 and the temperature dependence is different from that for inert gases (Figs. 2 and 3). The results of a study of proton relaxation in methanes [18], according to which the times of molecule reorientation, τ_2 , increase in the solid phase with the number of deuterio-substituted hydrogens more rapidly than in gas [19] (Table 1 in [18]), also support this view. It should be mentioned that the value of $\tau_2 = 2.4 \times 10^{-13}$ sec for methane at 60°K [18] is close to the classical one.

As the temperature increases, the influence of the retarding field on the molecular rotation decreases and the coefficients of thermal expansion of solid CH_4 and CD_4 draw together.

Let us try to understand what is the reason for the greater impeding of rotational motion of CD_4 molecules in solid phase. The potential barriers that hinder the rotation of molecules in CH_4 and CD_4 are about the same. But for lower moment of inertia of molecule the zero energy of orientational oscillations (librations) for CH_4 is greater and one can suppose that it makes a greater part of kinetic energy needed to overcome the barrier.

Naturally, in this case the orientational order in solid CH_4 should vanish at lower temperatures and the hindering influence of field at equal temperatures should be less.

In low temperature phases of solid methanes the rapid increase of the expansion coefficients near the temperatures of phase transformation seems to be due to the processes of destruction of long range order.

At present the existence of a second phase transition near $T \approx 9^\circ\text{K}$ for CH_4 is not settled [20, 15, 21, 22, 17]. It has been suggested that the observed thermal effects [23] be explained by spin conversion in light methane at low temperatures. The results of thermal expansion investigation, in contrast to the results of

the heat capacity study, are not sensitive to heat released during conversion in a sample. As has already been mentioned, the coefficients of thermal expansion of CH_4 were calculated only to 10°K, but the change of sample length l with temperature was determined by us to 4.2°K. The analysis of the data obtained showed that the derivative dl/dT in the range 10°–4.2°K decreases monotonously with the decrease of temperature and does not depend on the experiment duration. Thus the results of thermal expansion investigation do not indicate the existence of low temperature phase transition ($T \approx 9^\circ\text{K}$) in CH_4 .

REFERENCES

1. MANZHELII V. G., TOLKACHEV A. M., *Fiz. Tverd. Tela* **8**, 1035 (1966).
2. MANZHELII V. G., TOLKACHEV A. M. and VOITOVICH E. I., *Phys. Status Solidi* **13**, 351 (1966).
3. SCHALLAMACH A., *Proc. R. Soc. A* **171**, 569 (1939).
4. GISSLER W. and STILLER H., *Naturwissenschaften* **52**, 512 (1965).
5. DE BOER J., *Physica* **14**, 139 (1948).
6. MANZHELII V. G., GAVRILKO V. G. and VOITOVICH E. I., *Fiz. Tverd. Tela* **9**, 1483 (1967).
7. LOSEE D. L. and SIMMONS R. O., *Phys. Rev.* **172**, 944 (1968). We are indebted to Professor Simmons for a copy of this work prior to publication.
8. MANZHELII V. G., GAVRILKO V. G. and VOITOVICH E. I., *Phys. Status Solidi* **17**, k139 (1966).
9. MOUNTAIN R. D., *J. Phys. Chem. Solids* **28**, 1071 (1967).
10. BEZUGLY P. A., BURMA N. G. and MINYAEV R. Kh., *Fiz. Tverd. Tela* **8**, 744 (1966).
11. BEAUMONT R. H., CHIHARA H. and MORRISON J. A., *Proc. phys. Soc.* **78**, 1462 (1961).
12. COLWELL J. H., GILL E. K. and MORRISON J. A., *J. chem. Phys.* **39**, 635 (1963).
13. MANZHELII V. G., TOLKACHEV A. M. and GAVRILKO V. G., *Proceedings of the Physico-Technical Institute of Low Temperatures*, Vol. 2, p. 41. Academy of Sciences of the Ukrainian SSR (1968).
14. BIGEISEN J., CRAG C. B. and JEEVANANDAM M., *J. chem. Phys.* **47**, 4335 (1967).
15. COLWELL J. H., GILL E. K. and MORRISON J. A., *J. chem. Phys.* **42**, 3144 (1965).
16. MANZHELII V. G. and KRUPSKY I. N., *Fiz. Tverd. Tela* **10**, 284 (1968).
17. FRAYER F. H. and EWING G. E., *J. chem. Phys.* **48**, 781 (1968).

18. De WIT G. A. and BLOOM M., *Can. J. Phys.* **43**, 986 (1965).
19. BRIDGES F., M.Sc. Thesis. University of British Columbia, Vancouver, B.C. (1964).
20. TRAPEZNIKOVA O. and MILJUTIN G., *Nature* **144**, 632 (1939).
21. WOLF R. P. and WHITNEY W. M., *Low Temperature Physics* (Edited by J. G. Daunt *et al.*), p. 1118. Plenum Press, New York (1965).
22. HOPKINS H. P., Jr., DONOHO P. L. and PITZ K. S., *J. chem. Phys.* **47**, 864 (1967).
23. COLWELL J. G., GILL E. K. and MORRISON J. A., *J. chem. Phys.* **36**, 2223 (1962).

THE FREQUENCY AND TEMPERATURE DEPENDENCE OF THE OPTICAL EFFECTIVE MASS OF CONDUCTION ELECTRONS IN SIMPLE METALS*

CHIAN-YUAN YOUNG†‡

Department of Physics, University of California, San Diego, La Jolla, Calif. 92037, U.S.A.

(Received 4 March 1969)

Abstract—In the i.r. frequency regime, renormalization effects of conduction electrons in a simple metal alters the frequency and temperature dependence of the conductivity. This change in conductivity can be described by a frequency and temperature dependent effective mass. The case of aluminum has been calculated as an example. The results obtained indicate that measurements of the i.r. optical constants as functions of the frequency and temperature can be used to study the variation of the optical effective mass

1. INTRODUCTION

THE INTERACTION between electrons and phonons in a metal plays an important role in determining the physical properties of the electrons and phonons such as the cyclotron effective mass or the sound velocity[1]. It is paramount in determining the electrical transport properties of a metal at finite temperatures[2].

In the present work we shall study the infrared conductivity of a simple metal and propose that information about the renormalization effects of the electrons due to the electron-phonon interaction can be obtained by infrared measurements. Since at these frequencies the conductivity is dominated by the intraband contribution[3], we shall ignore possible contributions from interband transitions. Thus in Section 2 we study the dependence of the bulk conductivity of a simple metal in the infrared frequency regime on the renormalization effects of the electrons. In Section 3 the optical effective mass is expressed in terms of

the electron-phonon interaction. The frequency and temperature dependence of the optical effective mass of aluminum is also computed. In Section 4 we discuss the possibility of experimental observation of this effect.

(A) Electron-phonon interaction

Let us consider an isotropic model of a metal whose Hamiltonian is given by [4]

$$H = \sum_{\mathbf{k}} \epsilon_{\mathbf{k}} c_{\mathbf{k}}^{\dagger} c_{\mathbf{k}} + \sum_{\mathbf{Q}} \hbar \omega_{\mathbf{Q}}^{(0)} b_{\mathbf{Q}}^{\dagger} b_{\mathbf{Q}} + \sum_{\mathbf{k}, \mathbf{Q}} U_{\mathbf{Q}}^{(0)} c_{\mathbf{k}+\mathbf{Q}}^{\dagger} c_{\mathbf{k}} (b_{\mathbf{Q}} + b_{-\mathbf{Q}}^{\dagger}) \quad (1)$$

where $c_{\mathbf{k}}^{\dagger}$ and $c_{\mathbf{k}}$ are the creation and annihilation operators of an electron with momentum \mathbf{k} and energy $\epsilon_{\mathbf{k}}$, $b_{\mathbf{Q}}^{\dagger}$ and $b_{\mathbf{Q}}$ are the creation and annihilation operators of a phonon with momentum \mathbf{Q} and frequency $\omega_{\mathbf{Q}}^{(0)}$. The last term in equation (1) represents the electron-phonon interaction. We assume that only longitudinal phonons interact with the electrons.

The properties of a system of interacting electrons and phonons described by the above Hamiltonian have been studied repeatedly [1, 4, 5]. The properties of an electron are modified by the electron-phonon interaction. Thus an electron has a finite lifetime proportional to the inverse of the imaginary part of

*Work supported in part by the Office of Naval Research.

†Based on a thesis submitted to the Graduate School of the University of California, San Diego in partial fulfillment of the requirements for the Ph.D. degree.

‡Present address: Massachusetts Institute of Technology, Lincoln Laboratory, P.O. Box 73, Lexington, Mass. 02173, U.S.A.

its self energy. The magnitude of the electron self energy is of the order of the phonon energy and is therefore small compared to the typical electron energy. However, the effective mass of the electrons such as determined from cyclotron resonance measurements depends on the energy derivative of the self energy, which is of the order unity. Thus the cyclotron effective mass can be appreciably different from the band mass m . The properties of the phonons are also modified by the electron-phonon interaction. Thus the physical phonon frequency ω_q is different from the bare phonon frequency $\omega_q^{(0)}$ due to polarization effects of the electrons.

(B) The electrical transport equation

A transport equation valid under the conditions $\epsilon_f \gg \hbar\omega$, \hbar/τ , qv_f has been obtained from perturbation theory [1]. Here ω and q are the frequency and wavevector of the electromagnetic wave, τ is the relaxation time, and ϵ_f is the Fermi energy. Since the Fermi energy is of the order of several electron volts in metals, the above conditions are satisfied in the infrared frequency range. From the work of Holstein [1], the electrical conductivity tensor can be written as

$$\sigma^{ij}(q, \omega) = \frac{2e^2}{\Omega} \sum_k v_k^i \Phi_k^j \left[\frac{f^{(-)}(\epsilon_k) - f^{(-)}(\epsilon_k + \hbar\omega)}{\hbar\omega} \right] \quad (2)$$

where \mathbf{v}_k is the electron velocity, $f^{(-)}(\epsilon_k)$ is the Fermi distribution function, and Φ_k^j can be regarded as a distribution function. The indices i and j specify the space components of the quantities involved. The function Φ_k^i satisfies the following transport equation

$$i(\mathbf{q} \cdot \mathbf{v}_k - \omega) \Phi_k^i = v_k^i + \sum_{q, \pm} P_{k, k \pm q} (\Phi_{k \pm q}^i - \Phi_k^i) \quad (3)$$

where

$$P_{k, k \pm q} = \frac{2\pi}{\hbar} |U_q|^2$$

$$\times \left\{ \left[N_q + \frac{f^{(+)}(\epsilon_{k \pm q}) - f^{(+)}(\epsilon_{k \pm q} + \hbar\omega)}{2} \right] \times \delta(\epsilon_k - \epsilon_{k \pm q} \pm \hbar\omega_q) + \frac{i}{2\pi} P \left(\frac{1}{\epsilon_k - \epsilon_{k \pm q} \pm \hbar\omega_q} \right) \times [f^{(+)}(\epsilon_{k \pm q} + \hbar\omega) - f^{(+)}(\epsilon_{k \pm q})] \right\}.$$

Here $U_q = U_q^{(0)} \sqrt{(\omega_q^{(0)}/\omega_q)}$ is the renormalized matrix element, N_q is the phonon occupation number, $f^{(+)}(\epsilon_k) = 1 - f^{(-)}(\epsilon_k)$, and P denotes the principal value part.

Thus the conductivity can be obtained by substituting the solution of equation (3) into equation (2).

2. THE I.R. BULK CONDUCTIVITY OF SIMPLE METALS

The transport equation, given by equation (3), is difficult to solve for arbitrary values of ω , qv_f , and τ . However, solutions can be found for special cases such as in the calculation of d.c. resistivity. In the infrared frequency range, the relevant wavevector q can be estimated by $q^2 \approx |(4\pi i\omega/c^2)\sigma(q, \omega)|$ (see equation (15)). We shall restrict ourselves to the case $qv_f < \omega$ or $1/\tau$ so that the transport equation can be greatly simplified.

(A) The transport equation

Consider the case $qv_f < \omega$ or $1/\tau$ in which the $(\mathbf{q} \cdot \mathbf{v}_k) \Phi_k^i$ term in equation (3) is smaller than the other terms. Thus we can neglect the q dependence of the collision integral and make the following variational approximation of the transport equation

$$i(\mathbf{q} \cdot \mathbf{v}_k - \omega) \Phi_k^i = v_k^i + \left(i\omega\alpha - \frac{1}{\tau} \right) \Phi_k^i \quad (4)$$

where

$$\alpha = \left\{ \sum_{k, q, \pm} |U_q|^2 P \left(\frac{1}{\epsilon_k - \epsilon_{k \pm q} \pm \hbar\omega_q} \right) \mathbf{v}_k \cdot (\mathbf{v}_k - \mathbf{v}_{k \pm q}) \left[\frac{f^{(-)}(\epsilon_k) - f^{(-)}(\epsilon_k + \hbar\omega)}{\hbar\omega} \right] \right. \\ \left. \times \left[\frac{f^{(+)}(\epsilon_{k \pm q}) - f^{(+)}(\epsilon_{k \pm q} + \hbar\omega)}{\hbar\omega} \right] \right\} / \frac{3\Omega}{2} \frac{n}{m} \quad (5)$$

and

$$\begin{aligned} \frac{1}{\tau} = & \left\{ \frac{2\pi}{\hbar} \sum_{k,q,\pm} |U_q|^2 \right. \\ & \times \left[N_q + \frac{f^{(+)}(\epsilon_{k\pm q}) + f^{(+)}(\epsilon_{k\pm q} + \hbar\omega)}{2} \right] \\ & \times \mathbf{v}_k \cdot (\mathbf{v}_k - \mathbf{v}_{k\pm q}) \left[\frac{f^{(-)}(\epsilon_k) - f^{(-)}(\epsilon_k + \hbar\omega)}{\hbar\omega} \right] \\ & \left. \times \delta(\epsilon_k - \epsilon_{k\pm q} \pm \hbar\omega) \right\} / \frac{3\Omega}{2} \frac{n}{m}. \quad (6) \end{aligned}$$

A derivation of this approximation is given in the Appendix. The collision integral is replaced by the term $(i\omega\alpha - 1/\tau)\Phi_k^i$, where τ is the relaxation time which is frequency dependent (the dependence being especially strong at low temperatures[6]) and α is a dimensionless quantity whose properties we shall discuss in detail in the next section.

The distribution function can be obtained from equation (4)

$$\Phi_k^i = -v_k^i / \left\{ i[\omega(1+\alpha) - \mathbf{q} \cdot \mathbf{v}_k] - \frac{1}{\tau} \right\}. \quad (7)$$

(B) The bulk conductivity

The bulk conductivity can be obtained by substituting equation (7) into equation (2). Thus if we choose \mathbf{q} along the z -axis and the electric field vector along the x -axis, we find

$$\sigma^{xx}(q, \omega) = \frac{3ne^2}{2} \frac{1}{m} \frac{1}{qv_f t^2} [(1+t^2) \tan^{-1} t - t] \quad (8)$$

where $t = qv_f \tau / [1 - i\omega\tau(1+\alpha)]$. We have assumed that the Fermi surface is spherical.

The classical limit can be obtained from equation (8) by setting $q = 0$. Thus

$$\sigma^{cl}(\omega) = \frac{ne^2}{m} \tau / [1 - i\omega\tau(1+\alpha)]. \quad (9)$$

This is similar to the Drude formula[3] apart from the extra quantity α .

3. THE OPTICAL EFFECTIVE MASS

The quantity α introduced in the last section is a function of the frequency ω and the

temperature T . Its physical interpretation can best be seen by considering equation (9). Conventionally the optical effective mass is determined experimentally from the real part of the dielectric constant by the Drude formula[3]

$$\epsilon_r(\omega) = 1 - \frac{4\pi ne^2}{m} \frac{1}{\omega^2 + (1/\tau)^2} \quad (10)$$

at frequencies $\omega \gg 1/\tau$. The proper generalization of equation (10) can be obtained from equation (9)

$$\epsilon_r(\omega) = 1 - \frac{4\pi ne^2}{m_{\text{eff.}}} \frac{1}{\omega^2 + \left[\frac{1}{(1+\alpha)\tau} \right]^2} \quad (11)$$

where

$$m_{\text{eff.}} = m[1 + \alpha(\omega, T)]. \quad (12)$$

We see therefore $[1 + \alpha(\omega, T)]$ is a renormalization factor of the usual optical mass.

(A) The frequency and temperature dependence of the optical effective mass

The limiting value $\alpha_0 = \alpha(\omega = 0, T = 0)$ is of some special interest because it is related to the Landau scattering function (due to the electron-phonon interaction) and can be determined experimentally from the high temperature resistivity[7]. Indeed it is given by

$$\alpha_0 = \frac{\hbar}{2\pi k_B} \frac{ne^2}{m} \left[\frac{\rho(T_0)}{T_0} \right]_{T_0 \gg \Theta} \quad (13)$$

where $\rho(T_0)$ is the d.c. resistivity at temperature T_0 . The ratio $\rho(T_0)/T_0$ does not depend on the choice of T_0 so long as $T_0 \gg \Theta$.

The general behavior of $\alpha(\omega, T)$ as a function of ω and T can be determined from equation (5). As the frequency ω increases above the Debye frequency, $\alpha \sim 1/\omega^2$ as a consequence of the fact that important renormalization effects are restricted to electrons close to the Fermi surface within the energy range $\hbar\omega_D$. This is clear from equation (5) in which

the energy denominator is of the order $\hbar\omega$ because ϵ_k and $\epsilon_{k\pm Q}$ are restricted within the energy range $\hbar\omega$ about the Fermi surface. Similarly at high temperatures, the energy denominator is of the order $k_B T$ so that $\alpha \sim 1/T^2$ as a consequence of the broadening of the Fermi surface with an energy range $k_B T$. When $\hbar\omega$, $k_B T \ll k_B \Theta$, $\alpha(\omega, T)$ tends to the limit given by equation (13).

The above conclusions are independent of the model taken in the calculation of $\alpha(\omega, T)$.

(B) *The renormalization parameter of aluminum*

A specific example has been computed for the case of aluminum, chosen because of its high Debye temperature and strong electron-phonon interaction. We first find $\alpha_0^{A1} = 0.65$ from the d.c. resistivity assuming three free electrons per atom. We then compute the ratio $\alpha^{A1}(\omega, T)/\alpha_0^{A1}$, from which $\alpha^{A1}(\omega, T)$ can be obtained, with the following simple model. We assume a Debye spectrum for the phonons with $\Theta = 395^\circ\text{K}$, a spherical Fermi surface, and the simple matrix element $U_q = icQ/[\hbar/2nM\omega_q]^{1/2}$ where c is a multiplicative constant.

The results for $\alpha^{A1}(\omega, T)$ are shown in Fig. 1 in which only normal processes are included. The general behavior of $\alpha^{A1}(\omega, T)$ is found to be in agreement with the conclusion in part (A) of this section. We also found that the frequency and temperature dependence of $\alpha^{A1}(\omega, T)$ is insensitive to the choice of the matrix element U_q .

In principle one should take a more realistic model and also include the Umklapp processes in the calculation. However, Umklapp processes change only the matrix elements of α in equation (5) and do not affect the general conclusion of part (A) of this section. Thus we expect the same kind of functional dependence for the actual $\alpha^{A1}(\omega, T)$ as given in Fig. 1. Furthermore the magnitude of $\alpha^{A1}(\omega, T)$ obtained with a more realistic model including the Umklapp processes is not expected to be much different from our results because α_0^{A1} is

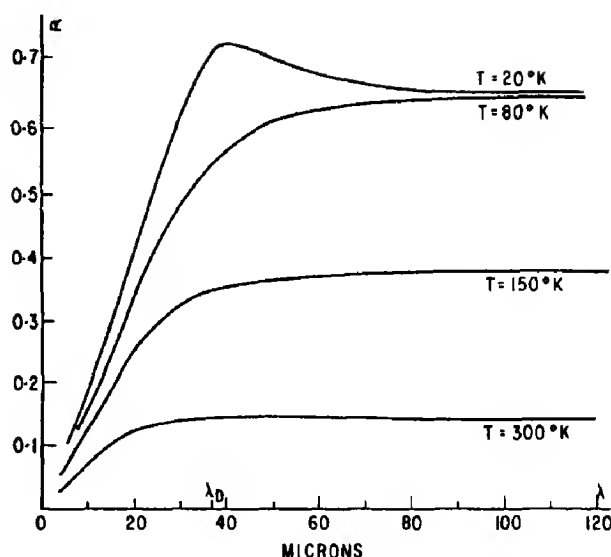


Fig. 1. The renormalization parameter $\alpha(\omega, T)$ of aluminum.

fixed by the d.c. resistivity. We therefore conclude that the simple model we have taken in the calculation of $\alpha^{A1}(\omega, T)$ gives reasonable results both in the functional dependence and the magnitude of $\alpha^{A1}(\omega, T)$.

4. DISCUSSION

A direct experimental check of the above theory would be desirable. The quantities determined from infrared measurements are the index of refraction n and extinction coefficient k [8, 9]. These optical constants are related to the surface impedance Z by [10]

$$n - ik = Z^{-1}. \quad (14)$$

The bulk conductivity is related to the surface impedance by [11]

$$Z^{(1)}(\omega) = -\frac{4i\omega}{c^2} \int_0^\infty \frac{dq}{q^2 - \frac{4\pi i\omega}{c^2} \sigma(q, \omega)} \quad (15)$$

if the 'specular' surface boundary condition is assumed. The quantities α and τ can thus be determined from infrared measurements if we substitute equation (8) into equation (15) and interpret the surface impedance in terms

of the measured optical constants according to equation (14).

In general, α and τ can only be obtained from the optical constants by numerical calculation. However, in the classical limit the conductivity is given by equation (9), we find upon substituting equation (9) into equation (15)

$$Z_{cl}^{(1)}(\omega) = -i \frac{4\pi\omega}{c\omega_p} \left[(1 + \alpha) + \frac{i}{\omega\tau} \right]^{1/2} \quad (16)$$

where ω_p is the plasma frequency. The above result gives some idea of the relationship of α and τ to the surface impedance but is not sufficiently accurate to be used in the frequency and temperature range we are considering.

It is well known that infrared absorption of metals depends on the smoothness of the surface [10, 12]. Thus it is necessary to know the correct boundary condition in order to determine the parameters in the conductivity such as α and τ from the surface impedance. It has recently been demonstrated experimentally that one can make a surface so smooth that the specular boundary condition is satisfied [12]. Thus we expect that there will be no ambiguity in the determination of α and τ from future experiments.

We have calculated the quantity $\alpha(\omega, T)$ for aluminum in Section 3. As mentioned earlier aluminum is favorable to observation due to its high Debye temperature and strong electron-phonon interaction. It is also to be noticed that the experiment must be done at relatively low temperatures so that the effect would be large as it is evident from Fig. 1. However, the temperature must also be high enough so that $qv_f < 1/\tau$ can be satisfied in the far infrared. Since the renormalization factor $\alpha(\omega, T)$ is found to be fairly large from the above calculation, we conclude that it is possible to determine this quantity from infrared measurements.

Acknowledgements—The author wishes to thank Professor W. Kohn for suggesting the problem and his constant guidance throughout the course of this work.

REFERENCES

1. HOLSTEIN T., *Ann. Phys.* **29**, 410 (1964).
2. ZIMAN J. M., *Electrons and Phonons*. Clarendon Press, Oxford (1960).
3. PINES D., *Elementary Excitations in Solids*. Benjamin, New York (1963).
4. MIGDAL A. B., *Soviet Phys. JETP* **34**, 996 (1958).
5. PRANGE R. E. and KADANOFF L. P., *Phys. Rev.* **134**, A566 (1964).
6. HOLSTEIN T., *Phys. Rev.* **96**, 535 (1954).
7. SHAM L. J. and YOUNG C.-Y., To be published.
8. BEATTIE J. R., *Phil. Mag.* **46**, 235 (1955).
9. BEATTIE J. R. and CONN G. K. T., *Phil. Mag.* **46**, 222 (1955).
10. DINGLE R. B., *Physica* **14**, 311 (1953).
11. REUTER G. E. H. and SONDHEIMER E. H., *Proc. R. Soc. A* **195**, 336 (1948).
12. BENNET H. E., BENNET J. M., ASHLEY E. J. and MOTYKA R. J., *Phys. Rev.* **165**, 755 (1968).

APPENDIX

We want to show in this appendix that the approximation made in equation (4) is a reasonable one in the regime of interest, namely, $qv_f < \omega$ or $1/\tau$. Thus for the purpose of determining an appropriate approximation to the collision integral, we write the transport equation as

$$-i\omega\Phi_k^i = v_k^i + \sum_{q,\pm} P_{k,k\pm q}(\Phi_{k\pm q}^i - \Phi_k^i). \quad (A-1)$$

Multiplying equation (A-1) by $v_k^i \left[\frac{f^{(-)}(\epsilon_k) - f^{(-)}(\epsilon_k + \hbar\omega)}{\hbar\omega} \right]$ and summing over k and i , we obtain

$$\begin{aligned} -i\omega \sum_{k,i} v_k^i \Phi_k^i \left[\frac{f^{(-)}(\epsilon_k) - f^{(-)}(\epsilon_k + \hbar\omega)}{\hbar\omega} \right] \\ = \sum_{k,i} v_k^i v_k^i \left[\frac{f^{(-)}(\epsilon_k) - f^{(-)}(\epsilon_k + \hbar\omega)}{\hbar\omega} \right] \\ + \sum_{k,q,i,\pm} P_{k,k\pm q} v_k^i \left[\Phi_{k\pm q}^i - \Phi_k^i \right] \left[\frac{f^{(-)}(\epsilon_k) - f^{(-)}(\epsilon_k + \hbar\omega)}{\hbar\omega} \right]. \end{aligned} \quad (A-2)$$

The coefficient G of the trial function $\Phi_k^i = iv_k^i G$ can be determined from equation (A-2). Thus we find

$$G = \left[(1 + \alpha) + \frac{i}{\tau} \right]^{-1} \quad (A-3)$$

where α and τ are given in equations (5) and (6). Notice that

$$\sum_k v_k^2 \left[\frac{f^{(-)}(\epsilon_k) - f^{(-)}(\epsilon_k + \hbar\omega)}{\hbar\omega} \right] = \frac{3\Omega}{2} \frac{n}{m}$$

has been used in the above expression. The above approximation is equivalent to replacing the collision integral by $(i\omega\alpha - 1/\tau)\Phi_k^i$. Thus we can write the transport equation as

$$-i(\omega - \mathbf{q} \cdot \mathbf{v}_k)\Phi^i = v_k^i + \left(i\omega\alpha - \frac{1}{\tau} \right) \Phi_k^i \quad (A-4)$$

which is equation (4).



DETONATION IN CRYSTALLINE SOLIDS*

EDWIN R. FITZGERALD

The Johns Hopkins University, Baltimore, Md. 21218, U.S.A.

(Received 31 January 1969)

Abstract—A previously described connection between particle waves, momentum transfer, and non-elastic deformation in crystalline solids is extended to account for the initiation of detonation by impact in explosive crystals. According to the ideas advanced the presence of atoms of different masses in a crystal lattice upon impact leads to a required translational velocity difference between dissimilar atoms. This, in some cases, is sufficient to cause a rapid change in the interatomic bond distances and the consequent repeated breaking of chemical bonds along the lattice. If the products of the broken bonds are subject to sudden expansion or react violently with their environment, an explosion or detonation wave (depending on the propagation velocity) results. The impact velocity range which may result in detonation can be calculated for a given explosive crystal in terms of Planck's constant, the crystal spacing, the atomic masses of the crystal atoms, and those of the 'striking pin'; these calculated velocities are in good agreement with experimental values in several cases where the relevant experimental information is available.

INTRODUCTION

A CONNECTION between the propagation of particle waves and deformation in crystalline solids has been presented in earlier publications [1, 2]. In general the non-elastic deformation of such solids is considered to result from the motion of certain initially field-free or 'free' atoms in a solid in very loose analogy with the free electron theory of conduction. These atoms, moreover, are supposed to move through a crystal as particle momentum waves with wavelengths calculated from the de Broglie relation $\lambda = h/mv_i$; v_i is the final velocity acquired by the free atoms just before they pass beyond their initial field-free regions, h is Planck's constant, and m is the atomic mass. A schematic representation of both external and internal field-free atoms in relation to a crystal lattice is shown in Fig. 1. The internal field-free atom of Fig. 1(b) is, of course, no longer field-free if a stress, Y_0 , is produced in the crystal by an external load. Instead such an atom will now be subjected to a force, $F_i = Y_0/\zeta$, where ζ is the

number of atoms per cross sectional area in the region of the stress.

An atom located in an initial field-free region of width pd in the direction of the force will then be accelerated as a particle until it reaches the end of the field-free region; after this its momentum propagates through the crystal as a wave with a wavelength determined by the final velocity. By equating the work done, by the force F_i through the distance pd , to the final kinetic energy of the particle and using the de Broglie relation for a free particle, a relation between the external stress applied to a crystal and the wavelength of the resulting particle momentum wave is obtained [2].

$$\lambda = h \sqrt{\left(\frac{\zeta}{2pmdY_0}\right)} \quad (1)$$

The parameter, p , which defines a particular initially field-free region ($s = pd$) is the only new microscopic constant introduced in equation (1); its value is generally taken to be less than one as indicated in Fig. 1. Moreover, in some cases, final expressions for macroscopic mechanical quantities are independent of p , and the quantities are functions only of known atomic constants [2].

*Presented, in part, at the *Explosive Chemical Reactions Symposium* sponsored by Technical Cooperation Panel 0-2, Duke University, Durham, N.C., U.S.A., October 21-23, 1968.

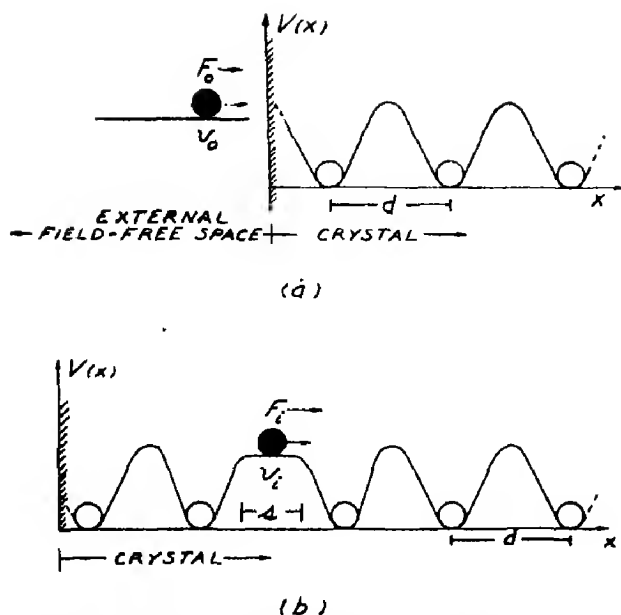


Fig. 1. (a) Schematic representation of an external field-free atom incident with velocity, v_0 , on a crystal with periodic potential variation, $v(x)$, in a lattice of spacing, d . (b) Representation of an internal field-free atom with incident velocity, v_i , in a crystal with periodic potential and spacing, d . The width of the internal field-free region is $s = pd$ (where $p < 1$) as indicated.

These ideas on the propagation of particle momentum waves and their role in non-elastic deformation are made more specific by the assumption of a differential equation for momentum transfer. For example, in a one-dimensional monatomic row lattice (cf. Fig. 2) conservation of momentum among any three adjacent masses requires that [2]

$$\frac{\partial (mv_n)}{\partial t} = \frac{i\hbar}{2d^2} (v_{n+1} + v_{n-1} - 2v_n) \quad (2)$$

where mv_n is the momentum of a general n th

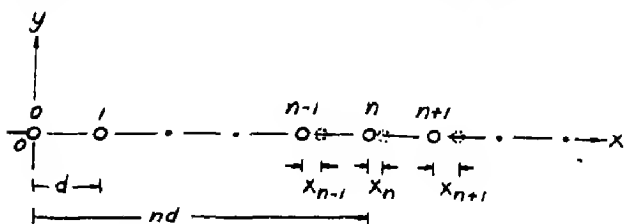


Fig. 2. Schematic drawing of a one-dimensional (row) lattice of identical point masses. Solid circles represent equilibrium positions of masses; the dashed circles represent positions of displaced masses (atoms).

mass, m , in the lattice of spacing d , $\hbar = h/2\pi$ and $i = \sqrt{-1}$. Equation (2) also results from writing the time-dependent Schrodinger equation for one of the masses (atoms) of such a periodic structure provided that real-property waves (i.e., momentum waves) are associated with moving particles in place of (or in addition to) the Born probability waves of orthodox wave mechanics [3,4]. From equation (2) and its solutions a number of macroscopic mechanical properties of crystal-line solids have been described and some mechanical quantities calculated directly from atomic constants. These have included transition velocities observed in impact experiments, threshold velocities for cratering in hypervelocity impact, non-elastic audio frequency resonances, characteristic stresses of plastic deformation, and coefficients of sliding friction [2]. A stress-strain law in close agreement with the experimental results for cubic crystals has been formulated, the velocity dependence of sliding friction and other frictional phenomena accounted for, and the cross-sectional shapes of hypervelocity craters formed at oblique impact explained [2].

The success with which some hypervelocity impact and high-speed frictional phenomena are explained by the particle-wave view of non-elastic deformation suggested that the means by which high explosive reactions are initiated might also be clarified if considered in a similar fashion. In particular, detonation by impact has proved susceptible to a particle-wave explanation by extension of the ideas used for monatomic crystals to diatomic or polyatomic crystals. This explanation is accordingly presented here after a brief review of momentum transfer and impact in monatomic crystals.

1. PARTICLE WAVES AND MOMENTUM TRANSFER

Consider the infinitely long, one-dimensional row lattice of Fig. 2 with identical point masses, m , spaced a distance d apart. A

continuity equation for momentum transfer or flow along this lattice can be written as

$$\frac{\partial (mv_n)}{\partial t} = K_p(v_{n-1} - v_n) - K_p(v_n - v_{n+1}) \quad (3)$$

where

$\partial (mv_n)/\partial t$ represents the net time rate of change of momentum of the n th lattice mass

$K_p(v_{n-1} - v_n)$ is the rate of momentum transfer from the mass at $n-1$ to that at n

$K_p(v_n - v_{n+1})$ is the rate of momentum transfer from the mass at n to the mass at $n+1$

K_p is a momentum transfer constant for the lattice.

That is, according to equation (3) above we postulate that as a result of an applied force some type of momentum transfer occurs in the lattice for which the rate of momentum transfer depends on the velocity differences between adjacent masses. The value of K_p is clearly of great importance and it is possible to obtain an exact expression for K_p by writing a wave solution for v_n in equation (3) of the form

$$v_n = B e^{-i(2\pi\nu_p t - knd)} \quad (4)$$

where $k = 2\pi/\lambda$ is the wave vector, d is the lattice spacing, B is a constant and the frequency ν_p is given by

$$\nu_p = \frac{-i2K_p}{\pi m} \sin^2 \frac{kd}{2}. \quad (5)$$

According to the particle-wave view of deformation[1,2], equation (5) gives the frequency of a particle (momentum) wave in the lattice and in the limit of long wavelengths (small k) this expression must reduce to that for a free particle, i.e.

$$\lim_{k \rightarrow 0} \frac{-i2K_p}{\pi m} \sin^2 \frac{kd}{2} = \frac{\hbar}{4\pi m} k^2 \quad (6)$$

where $\hbar k^2/4\pi m$ is the free-particle frequency. For small values of k the sine can be replaced by its argument in equation (6) so that

$$K_p = i\hbar/2d^2 \quad (7)$$

and substitution of this value for K_p in equation (3) yields equation (2) of the Introduction

$$\frac{\partial (mv_n)}{\partial t} = \frac{i\hbar}{2d^2} (v_{n+1} + v_{n-1} - 2v_n) \quad (2)$$

while equation (5) for the frequency becomes,

$$\nu_p = \frac{\hbar}{\pi m d^2} \sin^2 \frac{kd}{2}. \quad (5a)$$

If instead of the infinite lattice of Fig. 2 we turn our attention to a finite lattice of length $S = Nd$ with fixed ends, a standing wave solution to equation (3) is necessary[1, 2], but again the same expressions for K_p and ν_p are obtained. Now, however, discrete values of the wave vector, k , are demanded such that

$$k = \left(\frac{q\pi}{Nd}\right); q = 1, 2, 3 \dots (N-1). \quad (8)$$

Minimum and maximum values of k in this case are π/Nd and π/d corresponding to respective minimum and maximum values of ν_p ,

$$\nu_p(\text{min.}) = \frac{\hbar}{8mS^2} \quad (\text{for } S = Nd)$$

$$\nu_p(\text{max.}) \cong \frac{\hbar}{\pi m d^2} \quad (\text{for } N \text{ large}). \quad (9)$$

The prevalence of mosaic structures in real crystals indicates that finite lattice segments with lengths of a few microns will be encountered in momentum transfer through crystals[2, 5]. Characteristic values of ν_p hence range from 10^2 to 10^{10} c/s with accumulations of these particle-wave modes near the ends of the frequency spectrum[1, 2]. Considerable experimental evidence exists[1, 2] for the presence of such non-elastic modes at the audiofrequency end of the spectrum

where from equations (5a) and (8) the successive modes are to a very good approximation supposed to occur according to

$$\nu_{pq} \approx \frac{h}{8mS^2} q^2. \quad (10)$$

Since both the displacement and the momentum can only be measured at the positions of the masses in the lattice, we expect to be able to know nothing of either displacement or momentum wave properties *between* lattice masses[6]. Hence it follows that $\lambda = 2d$ is the smallest *measurable* wavelength for real-property waves in a lattice of spacing d . Further, in principle real-property waves such as the momentum waves discussed cannot exist in the lattice at wavelengths less than $2d$. Then, from the de Broglie relation, there will be a limiting free-particle velocity (for both external and internal field-free atoms) above which the associated momentum wave will not propagate through a lattice[1, 2],

$$v_p(\text{max.}) = \frac{h}{m\lambda_{(\text{min.})}} = \frac{h}{2md}. \quad (11)$$

The existence of this velocity limit (for stationary lattices) provides a basis for explanations of high velocity impact behavior of crystals in general and the low-velocity impact detonation of some crystals in particular.

Finally it must be mentioned that, although all of the preceding discussion has been confined to momentum transfer in one-dimensional (row) lattices, the results are easily extended to three-dimensional crystals[2] and lead to no major changes. This follows partly from the fact that the x, y, z components of momentum are independently conserved, and partly from the assumption of in-line or central momentum transfer between masses (atoms) in a three-dimensional lattice. The practical outcome is that the results obtained for row lattices apply directly to three-dimensional lattices when the

periodic spacing, d_j , between lattice masses in a particular direction in the crystal is used. Thus the momentum transfer constant in a direction with spacing, d_j , is $K_p = i\hbar/2d_j^2$ which predicts that the momentum transfer constant will be largest for directions of closest spacing in a crystal. Thus non-elastic deformation of a crystal should occur most readily in the directions of closest spacing, and this is in accord with experimental evidence. The maximum values of limiting velocities for field-free particles given by equation (11) can be calculated for a particular crystal in terms of the distance of closest approach d_1 , by $v_1 = h/2md_1$. Values for cubic metal crystals calculated in this way range from 9.46×10^3 cm/sec for lithium to 0.238×10^3 cm/sec for thorium[2].

2. HIGH-VELOCITY IMPACT IN MONATOMIC CRYSTALS

The existence of limiting velocities for the free particles supposed to be generating momentum waves suggests, at first, that such waves can not account for high speed deformation of crystals. It turns out, however[2], that there is a way in which waves generated by free particles with velocities above $v_1 = h/2md_1$ can be propagated in a crystal lattice. It is only necessary for a crystal lattice, or parts of it, to move against the incident free-particle wave. Such reverse motion requires, of course, a source of energy, and it is evident that this source can only be the vibrational (phonon) energy of the crystal lattice itself. In fact, as we shall demonstrate, the proposed mechanism eventually results in destruction of the crystal lattice when the free-particle impact velocity is such as to demand a translational lattice energy per atom equal to the lattice binding energy[2, 7].

We now consider a row lattice of fixed spacing d_1 moving with a translational velocity v_l toward an incoming free-particle of velocity v_i as indicated schematically in Fig. 3(a). The distance moved by the field-free particle in reaching the lattice can be expressed in terms

of the lattice spacing as pd_1 in accordance with previous notation. The time required for the field-free particle to travel up to a stationary lattice is

$$t = pd_1/v_i \quad (12)$$

while for a lattice (or lattice section) moving toward the incident free particle with velocity v_l this time is reduced to

$$t' = (pd_1 - v_l t')/v_i \quad (13)$$

$$= pd'_1, \text{ where } pd'_1 = pd_1 - v_l t'. \quad (13a)$$

Equation (13) can be solved for t' to give

$$t' = \frac{pd_1}{v_i + v_l}. \quad (14)$$

From equations (12) and (13a) it follows that $d'_1/d_1 = t'/t$ and from equations (12) and (14) the ratio t'/t can be written in terms of the velocities as $v_i/(v_i + v_l)$ so that

$$d'_1 (\text{contracted}) = d_1 \frac{v_i}{v_i + v_l}. \quad (15)$$

This variation of d'_1 with translational lattice velocity is shown in Fig. 3(a). The apparent lattice spacing clearly decreases as the lattice moves toward the incident particle with increasing velocity; therefore momentum waves of decreasing wavelengths below $2d_1$ can be propagated through the moving lattice. In an entirely similar way it can be shown that the apparent lattice spacing d'_1 increases with lattice velocity for a lattice moving away from the incident particle, and a single expression written for both cases (cf. Fig. 3(b))

$$d'_1 (\text{apparent}) = d_1 \cdot \frac{v_i}{v_i \pm v_l} \quad (16)$$

where positive values of v_l denote lattice motion *toward* the incident field-free particle and negative values correspond to lattice motion *away from* the incoming particle. Finally, from equation (16) a new value for the limiting free-particle velocity allowing momen-

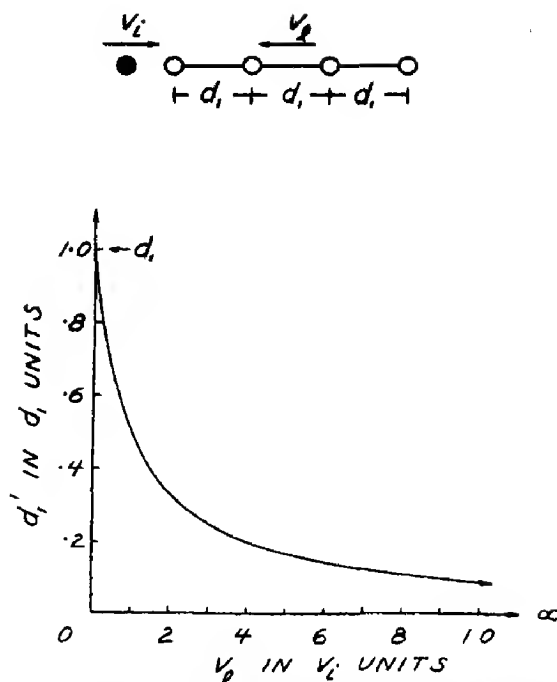


Fig. 3(a). Effect of translational motion of a lattice segment with velocity, v_l , on the apparent lattice spacing, d'_1 , seen by an incident free particle (with velocity, v_i) for the lattice moving *toward* the incident particle.

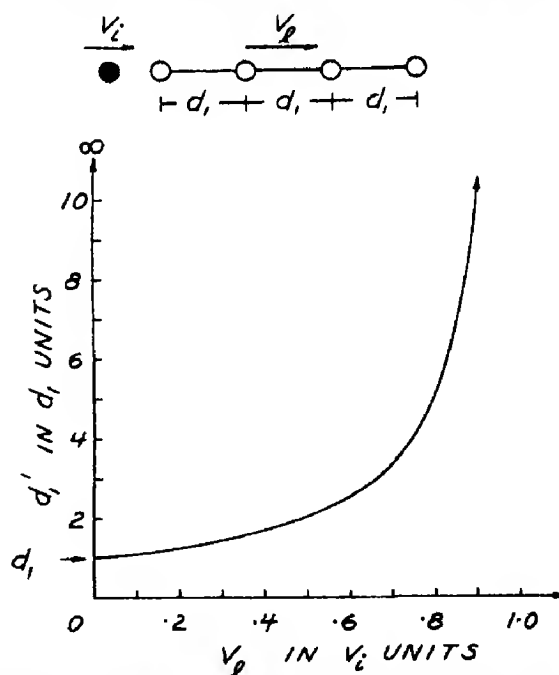


Fig. 3(b). Effect of translational motion of a lattice segment with velocity, v_l , on the apparent lattice spacing, d'_1 , seen by an incident free particle (with velocity, v_i) for the lattice moving *away from* the incident particle.

tum wave propagation in a moving lattice can be calculated as $v_l(\text{max.}) = v'_1 = h/2md'_1$ or, from equation (16),

$$v_l(\text{max.}) = v'_1 = v_1 \frac{v'_1 \pm v_l}{v'_1}. \quad (17)$$

It is instructive to consider the limiting free-particle velocity, v'_1 , in equation (17) as the independent variable and then determine from equation (17) the required values of translational lattice velocity, v_l , as in equation (18) below.

$$v_l = v'_1(1 - v'_1/v_1) \quad (18)$$

where now *negative* values of v_l indicate velocities opposite to the incident free-particle velocity, v'_1 , taken as reference. A plot of v_l vs. v'_1 reveals an inverted parabola with vertex at $(v_1/2, v_l/4)$ as shown in Fig. 4. From this figure it is clear that at incident free-particle velocities above v_1 the lattice must move with negative velocities (against the incident particle) in order to allow propagation of the momentum wave associated with the incident particle.

According to our previous discussion it is not necessary for *any* translational lattice motion to occur for free-particle velocities below v_1 . All particle waves generated by velocities below v_1 are propagated in an infinite lattice, and a series of waves at discrete wavelengths are propagated in a finite lattice. For a lattice segment of length $S = Nd$ values of incident free-particle velocities generating such allowed wavelengths are

$$\begin{aligned} v_{iq} &= \frac{\hbar q\pi}{mNd} \\ &= v_1 \frac{q}{N}; q = 1, 2, 3 \dots (N-1). \end{aligned} \quad (19)$$

There will therefore be a series of evenly spaced allowed velocities along the abscissa ($v_l = 0$) between 0 and v_1 as indicated in

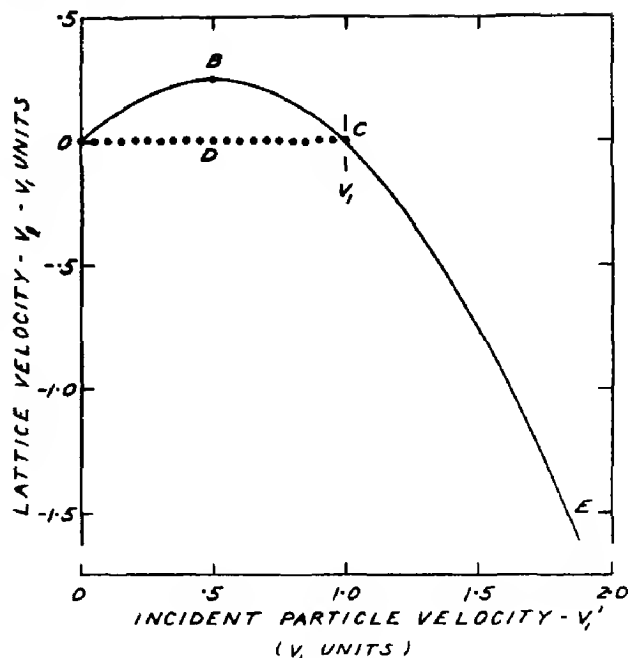


Fig. 4. Translational lattice velocity, v_l , needed to provide an apparent lattice spacing, d'_1 , for which continuous values of the incident free-particle velocity, $v_l = v'_1$, will be the limiting velocity (branch OBC). Discrete values of v'_1 below v_1 also occur for $v_l = 0$ as indicated by the points along the abscissa (branch ODC). Above v_1 , lattice segments must move *against* the incoming particle with velocities given by the single, negative branch, CE.

Fig. 4 (branch ODC), as well as the continuous allowed velocity values for forward lattice motion given by the positive branch (OBC) of the curve. Thus there is a choice of lattice behavior for free-particle incident velocities below v_1 : (1) the lattice remains stationary and propagates *only* particle waves of certain discrete wavelengths; or (2) the lattice moves forward at varying velocities, v_l , and propagates particle waves of any wavelengths between ∞ and $2d_1$. Above v_1 there is only one possibility; i.e., the lattice must reverse and move against an incident field-free particle to propagate waves of wavelengths less than $2d_1$.

As discussed in detail elsewhere[2], the conditions under which the lattice moves or remains stationary represent the difference between transient and equilibrium behavior, respectively. The duration times for transient

behavior can be estimated for a given lattice segment length in terms of the time needed for a standing wave to be set up in the segment; for a segment length of 10^{-4} cm. these times are usually of the order of 10^{-8} sec or greater. Of course there will also be incident velocities below v_1 between the discrete stationary allowed values where only forward lattice motion will allow propagation.

It is also possible to demonstrate[2] the existence of a region of instability between incident velocities of $v_1/2$ and $3v_1/4$ where a sudden jump to the reverse lattice motion required beyond v_1 takes place. The exact location of the instability point on the upper branch, OBC, of the curve in Fig. 4 depends on the number of lattice atoms in a particular segment which are moving with the translational velocity v_l . This number can never be less than two since at least two atoms are needed to define an apparent lattice spacing, but three, four, or many more atoms may eventually share the translational velocity (and energy) as the momentum wave proceeds along the lattice. Because of the existence of these instability conditions for incident velocities above $v_1/2$, as a practical matter reverse flow may start at some velocity beyond $v_1/2$ instead of at v_1 . That is, an incoming particle with velocity greater than the instability value will sooner or later jump to a velocity just above v_1 , and the lattice will move in the reverse direction. The extra energy for this jump to a higher velocity is supplied to the particle by the lattice since a point just beyond v_1 corresponds to a lower absolute value of translational lattice velocity, v_l , than a point near $v_1/2$. For the case where two-atom segments are broken loose, the value of translational velocity demanded of each lattice atom will reach a final value v_{lf} , when the corresponding energy ($mv_{lf}^2/2$) equals one-half the dissociation energy per atom ($D/2$) of the crystal lattice. That is,

$$v_{lf} = \sqrt{(D/m)}. \quad (20)$$

The final value of incident particle velocity,

v_f , will be that which requires the final translational lattice velocity or, from equation (17)

$$v'_1(\text{final}) = v_f = \frac{v_1}{2} (1 + \sqrt{(1 + 4v_{lf}/v_1)}). \quad (21)$$

For $v_{lf} \gg v_1$ and $2\sqrt{(v_{lf}/v_1)} \gg 1$, equation (21) becomes to a good approximation

$$v_f \approx \sqrt{(v_1 v_{lf})} = v_1^{1/2} (D/m)^{1/4} \quad (22)$$

which is accurate to within 5 per cent if $v_{lf}/v_1 \geq 100$. Values of v_f necessary to produce lattice disintegration or fracture can be calculated from a knowledge of $v_1 = h/2md_1$ and the lattice dissociation energy, D , for a crystal[2]. Equation (22) also results if we consider a four-atom projectile incident against a three-dimensional crystal where eight-atom chunks now break loose because four adjacent two-atom segments are required to move at velocities greater than v_{lf} . These ideas on lattice disintegration are depicted schematically in Fig. 5. A threshold velocity, v_f , is thus predicted above which lattice break-up and 'cratering' begins, for example, in high-velocity impact.

The previous discussion applies to impact between similar atoms, but is easily extended to provide for a particle of mass m_p with velocity, v_i , striking a lattice with different masses m_l , for example. For dissimilar projectile-target materials, the final velocity of equation (22) becomes[2]

$$v_f = \frac{m_l}{m_p} v_i. \quad (22a)$$

3. MOMENTUM TRANSFER AND IMPACT IN DIATOMIC CRYSTALS

In order to explain detonation it is necessary to extend the ideas on momentum transfer and impact to diatomic and polyatomic crystal structures. A diatomic row lattice with masses m_2, m_1 is shown in Fig. 6(a) with a distance d_a between atoms in each molecule and d_m between molecules in the lattice. A field-free atom of mass m_2 incident at velocity

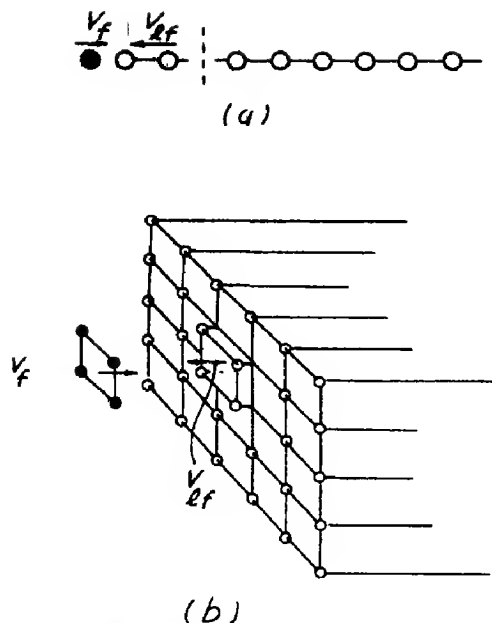


Fig. 5. (a) Diagram showing how two-atom segments of a row lattice break off to move against an incident particle with velocity, v_i , when the required reverse lattice velocity, v_u , equals $\sqrt{(D/m)}$ where D is the dissociation energy per atom and m is the mass of a lattice atom. (b) Diagram showing how an eight-atom piece of a crystal lattice breaks off to move against an incident four-atom 'projectile' with velocity, v_p .

v_i on such a lattice is also depicted in Fig. 6(b). The question immediately arises as to the manner in which the momentum wave associated with the incident particle is propagated along this diatomic lattice.

We assume first that the actual momentum transfer process is equivalent to momentum waves of different frequencies travelling independently along the two sets of masses, m_2 and m_1 . The notation adopted in Fig. 6 is such that all even numbered lattice sites are occupied by m_2 masses and odd sites by m_1 masses. From the assumption of independent momentum waves the differential equations for momentum transfer are accordingly:

$$m_2 \frac{\partial v_{2n}}{\partial t} = \frac{i\hbar}{2d^2} (v_{2n+2} + v_{2n-2} - 2v_{2n}) \quad (23)$$

and

$$m_1 \frac{\partial v_{2n+1}}{\partial t} = \frac{i\hbar}{2d^2} (v_{2n+3} + v_{2n-1} - 2v_{2n+1}) \quad (24)$$

where $d = d_a + d_m$ is the periodic spacing

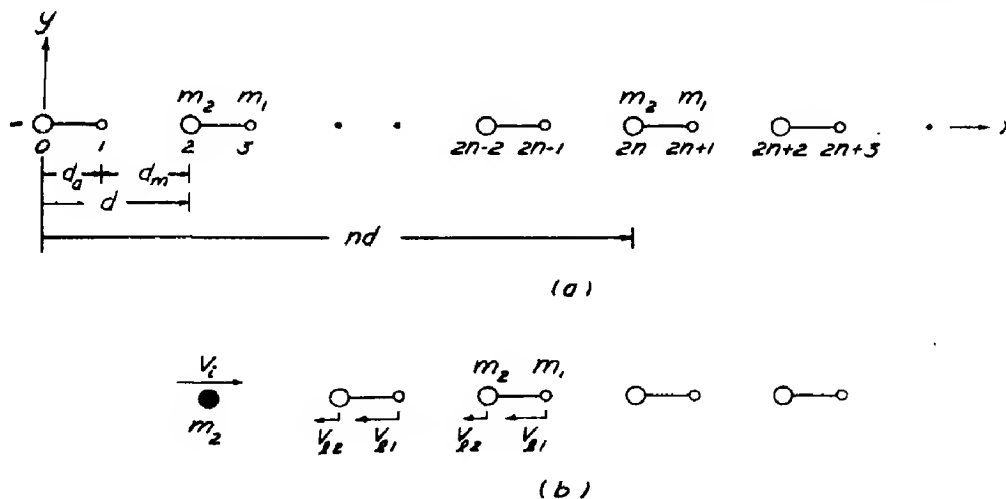


Fig. 6. (a) Schematic drawing of a one-dimensional row lattice with two values of point masses ($m_2 > m_1$) used to represent a diatomic lattice. The notation is chosen so that all even-numbered points have masses, m_2 , and odd-numbered points have masses, m_1 . The distance between atoms, d_a , is taken to be smaller than the distance between molecules, d_m , in this drawing, but in general any relative values for intra and inter molecular distances can be assumed. (b) Diagram showing the difference in reverse translational velocities ($v_{12} < v_{11}$) required by an incident mass m_2 with velocity v_i against the row lattice of (a). The translational velocity difference $\Delta v_i = v_{11} - v_{12}$ results in a rapid shortening of the interatomic bond distance, d_a , which can initiate detonation as discussed in the text.

between like masses (atoms) in the lattice. Travelling-wave solutions to equations (23, 24) are

$$v_{2n} = B_2 e^{-i(2\pi\nu_2 t - knd)} \quad (25)$$

$$v_{2n+1} = B_1 e^{-i(2\pi\nu_1 t - k(nd + d_a))} \quad (26)$$

where

$$\nu_2 = \frac{\hbar}{\pi m_2 d^2} \sin^2 \frac{kd}{2} \quad (27)$$

$$\nu_1 = \frac{\hbar}{\pi m_1 d^2} \sin^2 \frac{kd}{2} \quad (28)$$

and so that $\nu_2/\nu_1 = m_1/m_2$.

The separate differential equations (equations (23, 24)) likewise result from writing the time-dependent Schrodinger equation for one molecule (i.e., two atoms of mass m_2, m_1) and considering the total wave function for the two atoms to be $\psi_T = \psi_2 + \psi_1$ where $\psi_2 = m_2 v_2$ and $\psi_1 = m_1 v_1$ in accordance with the idea that ψ is a momentum wave.

In any event, such separate momentum waves will have different limiting velocities, $v_2 = h/2m_2 d$ and $v_1 = h/2m_1 d$, beyond which reverse lattice motion of each separate set of atoms (i.e. each of the interpenetrating row lattices) is required. Furthermore, the effective incident velocity of a mass m_2 will be different for the 'lattice' of masses m_1 and given by $v_i'' = (m_2/m_1) v_i$ where v_i is the actual velocity of a m_2 mass. In order to describe the required translational lattice motion of a diatomic lattice under impact as previously shown for a monatomic lattice in Fig. 4, two curves of v_i vs. v_i' are now needed as drawn in Fig. 7.

The curves in Fig. 7 are for a mass ratio $m_2/m_1 = 107.9/14.0 = 7.70$. Then, for example, an atom of mass m_2 , incident with velocity v_2' has that effective velocity for the m_2 lattice, but has a higher effective velocity $v_i'' = v_1' = 7.70 v_2'$ against the m_1 lattice. A mass m_2 incident at velocity $v_2' \cong v_2/2$ may thus require momentarily that the m_2 masses move forward at velocities $v_2/4 = 0.25 v_2$ while the

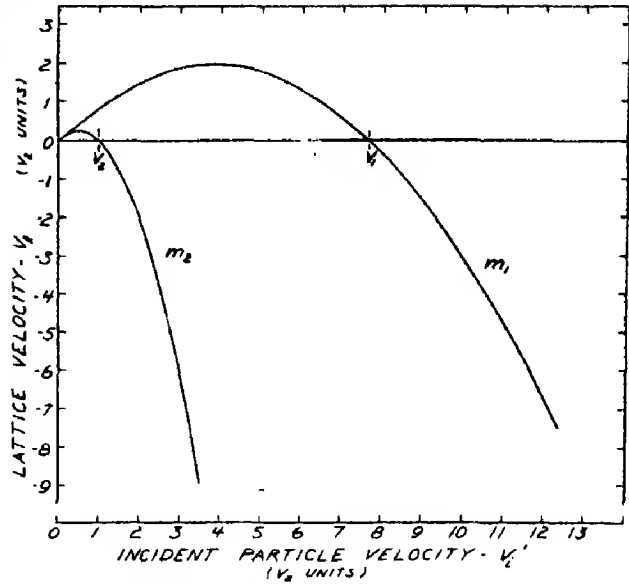


Fig. 7. The different translational velocities, v_i , required of the masses m_2 and m_1 (as marked) in the diatomic row lattice of Fig. 6 for a particle of mass m_2 incident with velocity v_i' . Curves are drawn for a mass ratio $m_2/m_1 = 7.70$ so that $v_1/v_2 = 7.70$. An incident mass m_2 at velocity v_i' is equivalent to a mass m_1 incident at $7.70 v_i'$ so that the translational velocity difference required for any incident velocity can be found from these curves as discussed in the text.

m_1 masses move forward at the same time with velocities $v/4 = 1.925 v_2$. The required translational velocity difference between atoms in the same molecule hence would be $1.675 v_2$.

For incident velocities of a mass m_2 above v_2 (or a mass m_1 above v_1) the separate requirements of the two interpenetrating lattices become alarmingly different in that a large steady state or equilibrium translational velocity difference is demanded for the atoms of each molecule. Furthermore, just as in the case of a monatomic lattice we expect that final values of the 'lattice' velocities will be reached beyond which disintegration or fracture of the crystal will occur.

Now, however, there are two possibilities for such a crystal break up: (1) breaking of the lattice bonds between molecules in the crystal or (2) breaking of the chemical bonds between the atoms forming the molecules. In

the first case lattice disintegration will occur when

$$m_1 v_{11f}^2 + m_2 v_{12f}^2 = D \quad (29)$$

where D is the lattice dissociation energy per molecule and v_{11f} , v_{12f} are the final values of translational velocity demanded of each set of lattice atoms; again to define an effective spacing d' at least two atoms of each lattice (a total of four) must move as indicated schematically in Fig. 6(b). In the second case molecular dissociation into component atoms will occur when

$$m_1 v_{11f}^2 + m_2 v_{12f}^2 = 2D_b \quad (30)$$

where now D_b is the chemical bond dissociation energy per molecule. Final or fission velocities of about 10^4 cm/sec are again expected for incident atoms of mass m_2 or m_1

$$v_{f2} \cong \sqrt{(v_2 \cdot v_{12f})}; v_{f1} \cong \sqrt{(v_1 \cdot v_{11f})} \quad (31)$$

The choice between breaking of intra molecular chemical bonds and breaking of inter-molecular lattice bonds obviously depends greatly on the relative values of D_b , D . If $2D_b < D$ chemical bonds will be broken before lattice dissociation occurs. For $2D_b > D$ there will be lattice bond rupture before the chemical bonds within the molecule break, etc.

4. DETONATION BY IMPACT

From these general ideas on momentum transfer and the consequent breaking or disintegration of a crystal lattice we turn finally to an attempt to describe the process of detonation in a solid. There is general agreement on the definition of an explosion as a fast chemical reaction forming gases at high pressures from a small amount of a solid, liquid or gas, but some variation seems to exist among various authors as to just what constitutes detonation. Robinson[8] says that detonation is a term applied to the brisant explosion of high explosives while Bowden

and Yoffee[9] define detonation as any reaction propagated at speeds greater than the sound velocity in the detonating medium. Everyone seems to agree, however, that detonation can be initiated by impact and we shall consider such initiation.

The breaking of chemical bonds between atoms in a molecule when the required translational velocity of the atoms results in a kinetic energy in excess of the bond dissociation energy has already been discussed. Impact velocities of 10^3 to 10^4 cm/sec are sufficient (depending on the incident atomic mass) and the separated atoms will have energies (and velocities) in excess of that initially required to break the bonds[2]. A separated or 'dissociated' atom in the row lattice of Fig. 7 may then strike the remaining undissociated lattice with a velocity equal to or greater than that of the original incident free-particle (atom) and cause additional bond breaking, etc.

The chemical bond breaking process may, however, be initiated by free particles (atoms) incident at velocities below the fission values, v_{f1} , v_{f2} if the required translational velocity difference Δv_l is sufficient to cause a rapid increase or decrease $\pm \Delta d_a$ in the equilibrium bond distance between the atoms in a molecule. An interaction potential V_{12} between atoms in the molecules of Fig. 6 can be represented by the curve shown in Fig. 8 where the mass m_1 is at an equilibrium distance d_a from mass m_2 at absolute zero. If now an incident mass m_2 approaches the lattice at some velocity $v'_2 < v_2/2$ the required transient response will result in a forward velocity difference Δv_l between atoms in at least the first two molecules as previously discussed. As a result the bond distance, d_a , will be increased with time (against the attractive force between the atoms) until finally a new distance d'_a is reached corresponding to a potential energy equal to the bond energy D_b . That is

$$d'_a = d_a + \Delta d_a \quad (32)$$

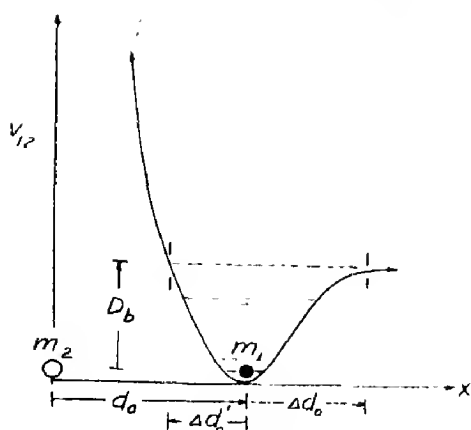


Fig. 8. Representation of the interatomic 'pair' interaction potential, V_{12} , between two masses (atoms) of the diatomic row lattice of Fig. 6 as a function of the distance, x , between atoms. If the bond distance is shortened an amount $\Delta d'_a$ the resulting potential energy of m_1 (relative to m_2) may equal the bond dissociation energy, D_b , and bond breaking or rupture can result as discussed in the text.

where

$$\Delta d_a = \Delta v_l t_b \quad (33)$$

and t_b can be defined as the time necessary for mass m_1 to obtain a potential energy (relative to m_2) equal to the bond energy. Equilibrium bond distances vary but are most often between $1-4 \times 10^{-8}$ cm; the exact shape of the interaction potential curve will determine Δd_a , but it can be taken approximately as $d_a/2$. Then the required time, t_b , can be estimated from a knowledge of Δv_l in terms of the characteristic velocity $v_2 = h/2m_2d$. For $\Delta d_a = 1.5 \times 10^{-8}$ cm and $\Delta v_l = 1 \times 10^2$ cm/sec, $t_b = \Delta d_a/\Delta v_l \approx 1.5 \times 10^{-10}$ seconds which is well below the transient duration time for most lattice segments. The attainment of a potential energy equal to the chemical bond energy can, of course, occur only by an energy conversion from the intrinsic (zero-point) phonon or vibrational energy of the molecule. Once separated the atoms of each molecule can be expected to share the bond energy in the form of increased translational kinetic energy according to

$$\frac{1}{2}m_1v_{1i}^2 + \frac{1}{2}m_2v_{2i}^2 = D_b. \quad (34)$$

For typical values of D_b (1 to 10 eV/atom) equation (34) requires that at least one of the separated atomic masses will have a translational velocity which may be equal to or greater than the velocity of sound in the crystal.

The released mass m_1 in the second molecule then becomes an internal incident free particle against the rest of the lattice and may require, because of its high velocity, reverse lattice motion of the next two molecules in the lattice. This will result in a decrease in the bond distance between atoms in these molecules until again a distance is reached where the potential energy of mass m_1 (relative to m_2) is greater than the bond energy (cf. Fig. 8). In this case, however,

$$d'_a = d_a - \Delta d_a \quad (35)$$

where d_a can again be calculated from $\Delta d_a = \Delta v_l t_b$ and for $\Delta d_a \approx d_a/2$, t_b will be about 10^{-10} sec as before. Actually, because of the non-symmetrical shape of the potential curve, the decrease in bond length required to reach a distance corresponding to a potential energy equal to the bond dissociation energy will be less for contraction than for extension. The freed atoms of mass m_1 in this case will be repelled back against the unbroken lattice once again as incident free particles, and further bond breaking produced in the next two molecules, etc.

Detonation by heat can evidently be explained along the lines just discussed if we note that a rise of temperature in a crystal may correspond to an increase in the mean vibrational energy level of the atoms within a molecule as well as the mean vibrational energy of molecules in the crystal lattice. At any temperature there will be a distribution of both the vibrational energy levels within the molecules and vibrational energy levels of molecules in the crystal lattice. If in one molecule (or a few) the rise in temperature results in raising the vibrational energy level to a value D_b , dissociation may occur for that

particular molecule with the consequent creation of an internal high velocity free-particle (atom). Such a free particle will in turn cause bond breaking in the two adjacent molecules and so on to initiate detonation as previously described.

According to these ideas initiation of bond breaking will occur at lower incident velocities when the lattice is at a higher temperature since the bond dissociation energy decreases as the temperature increases (cf. Fig. 8).

One further rather unusual feature (among many) of the proposed explanation of detonation must be mentioned. From Fig. 7 it is evident that a particle of mass m_2 incident on the lattice at *exactly* the limiting velocity v_2 will require no lattice motion of either set of atoms. This is true since the incident mass m_2 at velocity v_2 is exactly equivalent to an incident mass m_1 at velocity, v_1 . Hence no relative motion between atoms in a molecule (or molecules in the lattice) is required, $\Delta v_l = 0$, and no chemical or lattice bonds are broken. This is true even though m_2 atoms incident at *lower* (as well as higher) velocities may initiate bond breaking as previously described.

5. COMPARISON WITH SOME EXPERIMENTAL RESULTS

Many of the concepts introduced in this explanation of detonation in terms of particle waves are somewhat novel, and it is therefore appropriate to look for experimental verification of the ideas where possible. To begin with we expect that for a given crystal structure, the same spacing between unlike atoms, and comparable bond dissociation energies, the impact sensitivity should increase as the atomic mass ratio of the bonded atoms increases. This follows since the limiting incident velocity at which reverse motion of the metal 'lattice' is demanded, decreases as the metallic mass increases ($v_2 = h/2m_2d$), and also because the required translational velocity difference, Δv_l , leading to rapid bond shortening increases as the atomic mass ratios

increase in a particular crystal structure. Therefore mercury fulminate (Hg , 200.6) should be more sensitive to impact than silver fulminate (Ag , 107.9) which, in turn, should be more sensitive than sodium fulminate (Na , 23). According to Marshall [10] this is true. In the same way the azides should be increasingly sensitive to impact as the mass of the metallic atom increases, provided the relevant bond lengths, lattice spacings, etc. are unchanged. Accordingly we would suppose the sensitivity to shock or impact to increase for the azides in the order KN_3 , CuN_3 , AgN_3 , $\text{Hg}_2(\text{N}_3)_2$, TlN_3 , $\text{Pb}(\text{N}_3)_2$. Bowden and Yoffe [9], however, have listed the azides of increasing sensitivity or decreasing stability to heat, light, and shock in a somewhat different order as shown in Table 1 (see footnote (b)). In particular, according to Bowden and Yoffe TlN_3 is next to KN_3 in stability while CuN_3 is more sensitive than AgN_3 . From our point of view TlN_3 and CuN_3 are out of place, at least insofar as sensitivity to *impact* is concerned. Bowden and Yoffe have not listed separately the sensitivities to shock, heat, and light for the azides and therefore exact measures or criteria or their sensitivity scale are lacking; differences in bond and lattice dissociation energies could perhaps result in a different ordering of the azide sensitivities to heat and light than for shock or impact. From the data of Gray and Waddington [11], in fact, it is possible to calculate the difference between the lattice and bond dissociation energies, $\Delta D = D - D_a$, for some of the azides listed in Table 1. This difference, ΔD , does increase in the order of increasing sensitivity as given by Bowden and Yoffe (cf. Table 1); thus in terms of the supposed atomic potential interaction curve of Fig. 8 a localized increase in energy of the crystal lattice (resulting from heat or light energy) can initiate detonation by producing dissociation of a chemical bond (in preference to dissociation of a lattice bond which causes 'melting'). The occurrence of heat or light produced interatomic bond dissociation prior

Table 1. Predicted order of sensitivity for some azides

Impact ^(a) sensitivity (increasing downward)	Atomic weight of metal atom	Heat ^(b) , light sensitivity (increasing downward)	Lattice ^(c) dissociation energy <i>D</i> (kcal/mole)	X-N bond ^(c) dissociation energy, <i>D_a</i> (kcal)	ΔD (<i>D</i> - <i>D_a</i>) (kcal)
KN ₃	39.1	KN ₃	157	137	20
CuN ₃	63.6	TlN ₃	164	104	60
AgN ₃	107.9	AgN ₃	205	112	93
Hg ₂ (N ₃) ₂	200.6	CuN ₃	227	130	97
TlN ₃	204.3	Hg ₂ (N ₃) ₂		-12	
Pb ₂ (N ₃) ₂	207.2	Pb(N ₃) ₂	516	46	470

^(a)Impact by an identical metal pin or projectile, i.e. K against KN₃, Ag against AgN₃, etc. For a steel pin (atomic mass of Fe = 55.85) the impact sensitivity of KN₃ is increased by $55.85/37.1 = 1.428$ and that of CuN₃ decreased by $55.85/63.6 = 0.878$ in a falling weight test, for example. The relative order between KN₃ and CuN₃ which depends on the Cu/K mass ratio (1.626) remains unchanged.

^(b)This is also listed by Bowden and Yoffe as the order of increasing sensitivity to heat, light, and shock, but such a collective ordering needs further explanation (cf. reference [9]).

^(c)From data of Gray and Waddington (reference [11] using Hess's law).

to interlattice bond dissociation (melting) is more likely as ΔD increases and therefore sensitivity to heat and light might be expected to follow ΔD , while sensitivity to impact depends on increasing atomic mass ratios as predicted. Of course, a large decrease in spacing between like atoms in the *Tl-N* bond direction could also produce a decrease in impact sensitivity (increase v_2) but this does not seem likely. Rather it appears from our point of view that 'sensitivity' by itself or a collective sensitivity may be meaningless and that one should always specify sensitivity to something (heat, light, impact, etc.) when speaking of detonation.

A numerical estimate of what might be called the 'falling weight sensitivity' can also be calculated in terms of the diatomic linear lattice of Fig. 6 for specific materials where the crystal structure in a particular direction resembles that of Fig. 6. For example, silver azide (AgN₃) is orthorhombic with rows of alternating silver and nitrogen atoms *in line* along the Ag-N bond direction in [201] directions on (010) planes[12]. The Ag-N distance is 3.33 Å and hence the limiting velocity, v_2 , of an incident silver atom beyond which reverse flow of the 'silver lattice' is

required is

$$\begin{aligned} v_2(\text{Ag}) &= h/2m_2d \\ &= 6.625 \times 10^{-27}/2(17.89 \times 10^{-23})(6.66 \times 10^{-8}) \\ &= 2.78 \times 10^2 \text{ cm/sec.} \end{aligned}$$

The limiting velocity for a nitrogen atom against the 'nitrogen lattice' is, in the same way, found to be

$$v_1(\text{N}) = 2.14 \times 10^3 \text{ cm/sec.}$$

The velocity $v_2 = 2.78 \times 10^2$ cm/sec would be attained by a silver bullet (weight) dropped from a height $H = 39.3$ cm ($H = v^2/2g$), for example. Because of the instability cited in Section 2, reverse lattice motion (and the consequent initiation of detonation) will in practice occur at velocities between $v_2/2$ and $3v_2/4$ or between 1.39×10^2 and 2.08×10^2 cm/sec.

This predicted range of striking velocities needed to initiate detonation in AgN₃ crystals of a particular orientation can be compared to experimental determinations of the falling weight sensitivity for polycrystalline AgN₃ made by Wohler in 1911 and reported by Marshall[10]. The tests were performed according to specifications set forth by the

International Committee on Explosive Testing[10] and consisted of a hardened steel weight of 500 g falling against a hardened steel striking pin of 12.55 g in contact with the AgN_3 which was backed by a large steel anvil. Under these conditions the actual striking velocity of the hardened steel pin can only be estimated for an assumed coefficient of restitution. The minimum height of fall for the 500-gram weight to initiate detonation was found to be 31.5 cm corresponding to a final velocity of 2.46×10^2 cm/sec for the weight. This results in a calculated striking velocity for the steel pin against the AgN_3 of 4.42×10^2 cm/sec if the coefficient of restitution is taken as 0.90. The equivalent incident or 'striking' velocity for a silver pin can then be determined from the atomic mass ratio as

$$\begin{aligned} v_{\text{Ag}} &\cong \frac{55.85}{107.9} v_{\text{Fe}} \\ &\cong 0.51 \times 4.42 \times 10^2 \text{ cm/sec} \\ &\cong 2.25 \times 10^2 \text{ cm/sec} \end{aligned}$$

which compares well with the upper limit of 2.08×10^2 for the predicted initiation detonation velocity of silver against silver azide. In fact, since the texture or preferred orientation of the polycrystalline sample used by Wohler is not known, this is an entirely plausible result. The uncertainties surrounding the actual incident velocity of the striking pin against the sample in this falling weight test, however, are too great to justify any definite conclusions. The most we can say is that the predicted initiation velocity for silver against silver azide (or iron against silver azide) is in reasonable agreement with the experimental data cited in this instance.

Any falling weight or 'drop' test in which a separate striking pin must be put in motion to produce detonation will always create doubt as to the actual incident or impact velocity of the pin against the sample since assumptions about the collision between the falling weight and the striking pin must be made. On the

other hand, Cushman[13] has reported more recent experiments in which the minimum height of fall of a 3-oz weight *with steel firing pin attached* is determined for the onset of misfires (non-detonation). Compounds tested were iron disulfide (pyrite, FeS_2), antimony trisulfide (stibnite, Sb_2S_3) and lead sulfide (galena, PbS). Extreme precautions were also taken to prepare samples of the same fineness or grain size distribution in each case; equal quantities of three sieve sizes being used for the test samples of each material. Calculation of the initiation velocity is particularly easy for PbS which has the (cubic) sodium chloride structure with a lattice spacing[14] between like atoms in the [100] direction of $d = 5.936 \times 10^{-8}$ cm. Hence the limiting velocity for a lead atom ($m = 34.39 \times 10^{-23}$ g) incident against the 'lead lattice' of PbS is

$$\begin{aligned} v_2(\text{Pb}) &= h/2m_2d \\ &\cong 1.62 \times 10^2 \text{ cm/sec} \end{aligned}$$

while that for a sulfur atom against the 'sulfur lattice' is

$$v_1(\text{S}) \cong 1.05 \times 10^3 \text{ cm/sec.}$$

According to our idea that reversed lattice flow results in initiation of detonation, for a lead pin incident against PbS this should occur for incident velocities between 0.81×10^2 cm/sec and 1.21×10^2 cm/sec (i.e. between $v_2/2$ and $3v_2/4$). Cushman gives 21.0 in. as the minimum experimental drop height producing detonation (100 per cent of the time) for a steel firing pin, corresponding to a striking velocity of 3.24×10^2 cm/sec for a steel pin against PbS . The equivalent striking velocity for a lead pin is then

$$\begin{aligned} v_{\text{Pb}} &= \frac{55.85}{207.2} v_{\text{Fe}} \\ &\cong 0.269 \times 3.24 \times 10^2 \\ &\cong 0.871 \times 10^2 \text{ cm/sec} \end{aligned}$$

which falls very nicely within the predicted

initiation velocity range of 0.81×10^2 cm/sec to 1.21×10^2 cm/sec.

The expectation of a range of incident velocities within which firing or detonation may occur is in our view a direct result of the presence of an instability region between $v_2/2$ and $3v_2/4$ as already described (cf. Section 2 and reference [2]). Such a range of sensitivities is, indeed, found in the usual falling weight or drop tests. Taylor and Weale [15] describe drop tests on a mercury fulminate mixture using a 2-oz wt. and 0.4 cm dia. steel balls as the striking pins. Some of their data is reproduced in Table 2 and suggested to them a statistical distribution "...governed by some probability law." However we expect an incident velocity range for initiation of detonation, Δv_2 , equal to $(3v_2/4 - v_2/2)$ or $v_2/4$ in every case; this being the velocity range or difference between the highest velocity ($3v_2/4$) and the lowest velocity ($v_2/2$) which, in practice, result in reverse lattice motion. Further, the ratio of the lowest initiation velocity to the highest initiation velocity should be exactly 2/3. This ratio can evidently be determined in a falling weight test (for a constant mass ratio

of the falling weight to the striking pin) from the height for 100 per cent initiation, H_{100} , and the height for 0 per cent initiation H_0 as

$$\frac{v_i(\text{min.})}{v_i(\text{max.})} = \sqrt{\left(\frac{H_0}{H_{100}}\right)}$$

and compared with the predicted value of 2/3. The experimental values reported by Taylor and Weale in Table 2 give $\sqrt{(1.5/4.0)}$ or 0.62 which is in only fair agreement with the expected value of 0.67. More extensive tests were subsequently carried out by Taylor and Weale in which 100 samples were tested at each of eight heights of fall. These gave a ratio of $\sqrt{(H_0/H_{100})} \cong \sqrt{(3.7/8.0)}$ or 0.68 which is in good agreement with the predicted ratio of 0.67 (i.e. 2/3) for the initiation velocities. As mentioned above it is important in this calculation that all tests be carried out with the same falling weight for a given mass and type of striking pin so that the actual incident velocity of the striking pin against the explosive will vary only with the height of fall. In some cases [16, 17] the percentage ignition (0-100 per cent) vs. height of fall is reported for several values of falling weights and the corresponding striking-pin velocities are therefore not proportional to the falling heights alone, but instead depend on the different falling weight to striking pin mass ratios, coefficients of restitution, rigidity of the anvil on which the explosive is placed, etc.

The foregoing comparisons of predicted and experimental results for the initiation of detonation in crystalline solids are far from extensive. However, the agreement between the calculations and the observations is sufficiently close to encourage further investigation of the general ideas used here to account for the initiation of detonation. Further, it must be emphasized that the critical incident velocities are calculated entirely in terms of fundamental microscopic constants (Planck's constant, atomic mass, and crystal spacing) without the aid of assumed values for any new parameters.

Table 2. Percentage ignitions (initiations of detonation) vs. height of falling weight^(a) for a mercury fulminate mixture

Height of fall (in.)	Number of trials	Number of ignitions	% ignitions
6.0	12	12	100
5.5	12	12	100
4.5	20	20	100
4.0	20	20	100
3.5	30	25	83.3
3.0	30	18	60.0
2.7	30	11	36.7
2.5	30		43.3
2.0	30	8	26.0
1.5	20	0	0

^(a)From Taylor and Weale, reference [15]. Falling weight of 2.0 oz (56.7 g) against striking pins of 0.25 g (0.4 cm dia. steel balls). Weight of charge 0.034 g, thickness 0.02 in.

CONCLUSIONS

Many unanswered or even unasked questions about detonation remain, but there are a few general conclusions that can be stated in terms of the simple model discussed. First, it is proposed that in order for repeated bond-breaking to proceed in a solid there must be atoms of different mass bonded together with their bond directions in line for an appreciable distance. Second, for a given bond length, lattice spacing, and bond dissociation energy, the instability of such a solid should increase as the mass ratios of the bonded atoms increase. This results from the difference in required reverse translational velocities for each type of atom, and the separate dependence of each translational velocity on the reciprocal atomic masses. That is, for an incident free atom of velocity, v_i , against a lattice with masses m_1 and m_2 , the required translational velocity difference, Δv_l , is a function of the mass ratio m_2/m_1 . The exact expression for Δv_l for an incident mass m_2 is,

$$\Delta v_l = v_{l1} - v_{l2} = v_i \left(\frac{m_2}{m_1} - 1 \right) \left(1 - \frac{v_i}{v_2} \right) \quad (36)$$

which is zero only for $m_1 = m_2$ or $v_i = v_2$. This difference in translational velocity may result in bond rupture or dissociation as described in Section 4.

A third conclusion is that the impact sensitivity will be a function of the incident velocity resulting in reverse lattice motion; because of the instability region cited, this incident velocity will be between $v_2/2$ and $3v_2/4$ for an incident mass, m_2 , identical to one set of lattice masses (or between $v_1/2$ and $3v_1/4$ for an incident mass, m_1 , identical to the other set of lattice masses, for example). The incident velocity for initiation of detonation can always be calculated for an atom of mass, m_k , in terms of one of the lattice masses by determining the equivalent limiting velocity $v_k = (m_k/m_2)v_2$ or $v_k = (m_k/m_1)v_1$, etc. Accordingly the detonation initiation velocity for a lead striking pin should be less than that

for a steel striking pin against the same explosive; that for a steel striking pin less than that for an aluminum striking pin, etc. It also follows that the actual impact velocity of the striking pin against the explosive is the relevant quantity, and *not* the velocity of a falling weight against a striking pin.

Finally, it is necessary to explain why *all* solids with large atomic mass ratios do not explode! Ice, for example, has a mass ratio of 16:1, but is not a high explosive under usual conditions. In terms of the simple 'in-line' model of Fig. 6 this can be attributed to the lack of any long-range alignment of the O-H bonds in ice where, in fact, the positions of the hydrogens in the lattice do not seem to be well defined [18]. In other cases recombination of the broken interatomic bonds may take place after the momentum wave has passed, provided that the products of the broken bond are not subject to sudden expansion, or react violently with their environment. Thus the presence in crystals of chemical bonds between atoms of different masses is proposed as a necessary, but far from sufficient condition for a detonation wave to be initiated.

It is further possible that rows of adjacent atoms with different periodic spacings will have different limiting or critical velocities for reverse lattice motion even when the atoms are of comparable masses. Then chemical bonds between atoms in adjoining rows could be broken as a result of the required translational velocity difference between rows. Such bonds would have to have identical orientations over some distance in the crystal, but would not necessarily have to be 'in line' as supposed from our simple one-dimensional model.

Further understanding of the initiation process for detonation will depend on the acquisition of more information on the crystal structures of explosives together with their chemical bond strengths, and, in particular, on the design and performance of more meaningful experiments where the truly relevant physical quantities (e.g., velocities) can be,

and are directly observed. In the meantime, we remain in complete agreement with Willoughby Walke's conclusion[19] of 1897:

"...According to this view, detonation is the result of a combination of true chemical and dynamical reactions, neither of which alone suffices to explain the attending phenomena. . . ."

Acknowledgements—The suggestion that some of the ideas previously used[2] to describe non-elastic deformation of solids in terms of particle momentum waves might prove useful in understanding the initiation of detonation was made by Dr. R. J. Eichelberger of the U.S. Army Ballistics Research Laboratory. I am grateful to him for directing my attention to this, and for his subsequent interest in and encouragement of these initial efforts.

REFERENCES

1. FITZGERALD E. R., *J. acoust. Soc. Am.* **39**, 856 (1966).
2. FITZGERALD E. R., *Particle Waves and Deformation in Crystalline Solids*. Wiley, New York (1966).
3. FITZGERALD E. R. and TASI J., *Int. J. Solids, Structures* **3**, 927 (1967).
4. FITZGERALD E. R., *Int. J. theor. Phys.* **2**, 41 (1969).
5. HIRSCH P. B., *Prog. metal Phys.* **6**, 236 (1956).
6. BRILLOUIN L., *Wave Propagation in Periodic Structures*. McGraw-Hill, New York (1946).
7. FITZGERALD E. R. and WRIGHT T. W., *Phys. Status Solidi* **24**, 37 (1967).
8. ROBINSON C. S., *Explosions: Their Anatomy and Destructiveness*. McGraw-Hill, New York (1944).
9. BOWDEN F. P. and YOFFEE A. D., *Endeavour* **21**, 125 (1962).
10. MARSHALL A., In *Explosives*, Vol. II. Churchill, London (1917).
11. GRAY P. and WADDINGTON T. C., *Proc. R. Soc.* **235**, 481 (1956).
12. WYCKOFF R. W. G., In *Crystal Structures*, Vol II, p. 280. Interscience, New York (1963).
13. CUSHMAN A. S., *J. Ind. Engng Chem.* **10**, 376 (1918).
14. WYCKOFF R. W. G., In *Crystal Structures*, Vol. I, p. 89. Interscience, New York (1963).
15. TAYLOR W. and WEALE A., *Proc. R. Soc. A* **138**, 92 (1932).
16. MURGAJ M. P. and RAY A. K., *Br. J. appl. Phys.* **10**, 132 (1959).
17. HOLLIES N. R. S., LEGGE N. R. and MORRISON J. L., *Can. J. Chem.* **31**, 746 (1953).
18. WYCKOFF R. W. G., In *Crystal Structures*, Vol. I, pp. 322-325. Interscience, New York (1963).
19. WATKE W., *Lectures on Explosives*. Wiley, New York. (1897).

TECHNICAL NOTES

Anomalies in the low temperature heat capacities of BeO and MgO, containing Fe³⁺

(Received 30 December 1968; in revised form 1 May 1969)

IN THE present work we report the heat capacity data of five powder-sintered samples of BeO–0.6% CaO and MgO–0.35, 0.5, 1, 2% CaO (atomic weight percentage) containing iron as main impurity. The BeO–0.6% CaO specimen, initially prepared to study the Helium-bubble-formation during neutron-

x% CaO) no more specific heat anomalies appeared[1]. Also recent measurements of the heat capacities of pure alkaline-earth oxides, BeO, MgO, CaO, SrO, BaO, from low temperatures, 1.2°K up to room temperatures, 340°K[1, 2] do not show any abnormal behaviour of their specific heats. But no data for Fe in MgO or BeO has been reported yet.

Some of the characteristics of the used BeO and MgO samples are listed in Table 1.

Table 1

Specimen	%CaO	Impurities in ppm (at. wt.)		Sample sintered At <i>T</i> (°C) For <i>t</i> (hr)
		Total	Fe	
BeO	0.6	500	160	~ 1600 10–12
MgO	0.5	600	340	1600 2
MgO	1	600	340	1600, 1800 2, 4
MgO	0.35	600	420	1600 2

irradiation by means of heat capacity measurements at low temperatures, showed a not understood specific heat anomaly at helium-temperatures. Assuming that the anomaly is due to an electron dipole interaction between the different ions (Be²⁺/Ca²⁺–O^{2–}) in the crystal, the MgO–CaO matrix, easier to prepare than the toxic BeO compositions should show the same effect. Therefore, four MgO–*x*% CaO specimens have been prepared to test this idea. We found again specific heat anomalies. However, by further investigations it turned out that the iron which was not added initially, but contained hasardly in all these samples is the origin for the observed anomalies. This is the reason for the rather peculiar compositions of these specimens. In later experiments with very pure samples of various mixtures of the alkaline-earth oxides (BeO–*x*% CaO, CaO–*x*% BeO, MgO–

The fairly standard technique for measuring specific heats was used by thermally insulating the specimen from the helium-bath, applying a known amount of electric heat input and measuring the temperature increase of the sample. Both the He-4-cryostat[3] set up for calorimetric measurements between 1.2 and 300°K, and the He-3-cryostat[4] together with the data treating and thermometer calibration have been described in detail recently. In both cryostats specimen cooling was performed by thermal mechanical switches[3] without use of He-exchange gas. The Allen-Bradley carbon resistors used have been calibrated by the He-3 (1963 scale) or He-4 (1958 scale) vapour pressure and above 4°K by a gas-thermometer[3]. Test runs on the '1965 Calorimetric Conference copper standard T4-4' gave results[4, 5] in very good agreement with those reported

previously by other investigators.

Magnetic fields up to 13 kG are produced by a superconducting coil incorporated in the bath of the He-4 cryostat.

Coming to the relatively low specific heat of BeO and MgO the heat capacity of the addenda was sometimes 85 per cent of the total. The sample holder therefore was always measured separately with the same accuracy as the specimen. The total error in the determined smoothed curves of the specific heats is estimated to be less than 1 per cent above 1.5°K.

The "MgO" samples have been measured between 0.3°K and 40°K. The interesting results are below 4°K and are shown in Fig. 1. The sample with 340 ppm iron show a

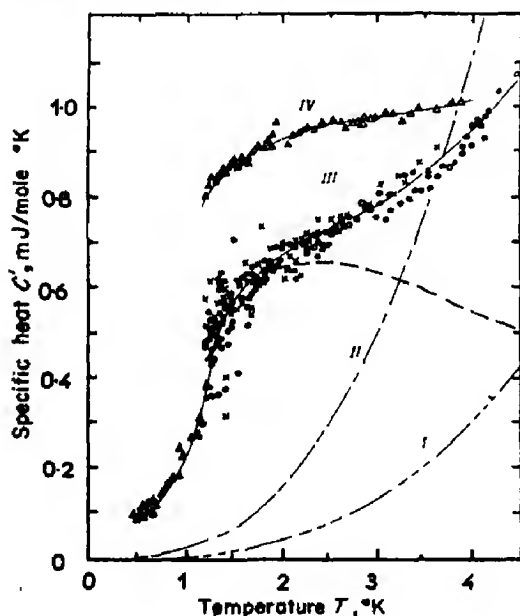


Fig. 1. Specific heat of MgO- $x\%$ CaO as function of temperature. \bullet , MgO-0.5% CaO, 340 ppm Fe³⁺; \circ , MgO-1% CaO, 340 ppm Fe³⁺; \times , MgO-2% CaO, 340 ppm Fe³⁺; Δ , MgO-0.35% CaO, 420 ppm Fe³⁺; ——— MgO(I), ——— GaO(II).

strong variation of the specific heat (curve III), compared with pure MgO (curve I)[3] or pure CaO (curve II)[1]. The sample with 420 ppm iron measured only between 1.2° and 4.2°K shows a still larger specific heat anomaly (curve IV).

Above 4°K the experimental curves approach the specific heat of pure MgO strictly by a $1/T^2$ law; near 15°K there is no more a visible difference between pure and iron doped MgO. An influence of CaO on the measured values (curve III) was not detected.

Figure 2 represents the results for the BeO sample with 160 ppm of iron. The peak of

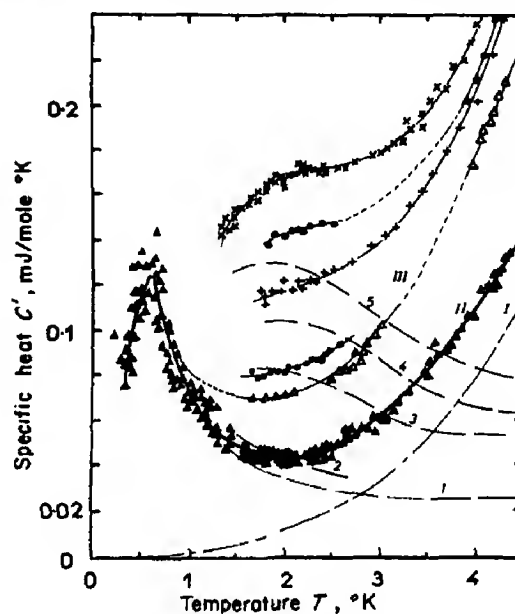


Fig. 2. Specific heat of BeO-0.6% CaO, 160 ppm Fe, as a function of temperature and magnetic field, H . Δ , BeO-0.6% CaO; \triangle , BeO-0.6% CaO, irradiated (see footnote), zero field; \bullet , 3.25 kG; $+$, 6.5 kG; \circ , 9.75 kG; \times , 13 kG; ———, BeO(I).

the anomaly is very well pronounced at 0.57°K (curve II). Curve I gives the specific heat of pure BeO(I) and curve 1 the contribution of the anomaly only. Near 20–25°K the measured curve is not identical to the specific heat of pure BeO.

The large anomaly given by the dotted line in Fig. 1 can be characterized by a Schottky type, but it is not clear that the parameters fitting the curve have any simple meaning. We could make different models where the tail falls off as AT^{-2} . But this does not explain the physical origin of the observed phenomena, which is not yet clear. Therefore we make only the following comments:

Table 2 gives some characteristic parameters deduced from the experimental curves.

Table 2

Specimen	$T_M(^{\circ}\text{K})$	A (in J/mole $^{\circ}\text{K}$)	$\Delta C(\text{max})$ (mJ/mole $^{\circ}\text{K}$)	S (mJ/mole)
MgO- $x\%$ CaO	2.1 ± 0.2	10 ± 0.5	0.65	1.3 ± 0.1
BeO-0.6% CaO	0.57 ± 0.03	0.11 ± 0.05	0.12	0.2 ± 0.03

These are: the temperature of the maximum, T_M ; the constant, A ; the maximum specific heat, $\Delta C_s(\text{max})$; the entropy of the anomaly, S ;

A dipole interaction between Ca^{2+} or Be^{2+} and O^- [or $(\text{OH})^-$] ions in BeO (or precipitated CaO) as seen f.i. by Shepard[6] between $(\text{OH})^-$ and K^+ ions in KCl can be ruled out. We have made measurements of the dielectric constant, ϵ , in the possible energy region $\Delta E = h \cdot \nu \approx \delta K$, where $\delta = E/K$ is the energy separation measured in $^{\circ}\text{K}$ for a Schottky anomaly [$^{\circ}\text{K}$]. ϵ did not show any abnormal behaviour.

Also adiabatic depolarisation experiments performed at helium-temperatures in an

electric field up to 60 kV/cm failed, and no visible effect could be detected.

Therefore, we applied a magnetic field to the specimens. A very strong variation of the specific heat was found for all samples. This surprising effect is shown in Figs. 2 and 3, where the specific heats at different magnetic fields are traced. The dotted lines (curves 1-5) in Figs. 2 and 3 show in both figures the contribution, due to the anomalies.[†]

(No experiments could be done in fields below 1 $^{\circ}\text{K}$ for the BeO-samples.) Nevertheless, for BeO we can see a displacement of the peak-position of the anomaly with the magnetic field. Contrary for MgO such a variation was not seen.

The surprisingly large growth of the specific heat in a magnetic field can not be explained by known magnetic effects. We measured the magnetic susceptibility of the specimens, which show a very small antiferromagnetism, but it is still too small to cause the observed phenomena. Certainly small iron precipitation are included in the samples. The magnetization curves, taken at 1.2, 2, 3, 4 and 20 $^{\circ}\text{K}$ do not saturate in a field of 40 kG.

Finally, chemical analysis proves that iron is the main impurity in these samples. We are sure that Fe is the origin of the observed anomalies. This is supported by paramagnetic resonance experiments. At 35 GHz an intense ray for Fe^{3+} was detected. It is a very surprising fact that no Fe^{2+} could be detected. (Commonly, Fe^{2+} is found in these cubic oxids but no Fe^{3+} .) Here were only traces of Mn^{2+} and Cr^{2+} corresponding to impurities smaller than 50 ppm, in accordance with the chemical analysis.

We assume that the samples are chemically stable. The specific heat for the specimens

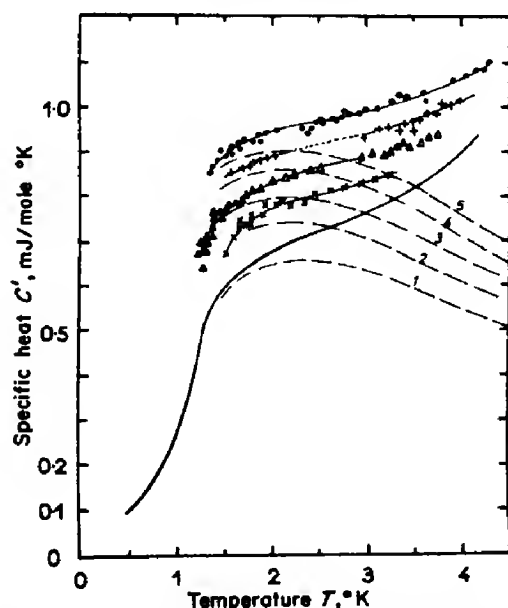


Fig. 3. Specific heat of MgO-1% CaO as a function of magnetic field. —, MgO-1% CaO, zero field; \times , 3.25 kG; Δ , 6.5 kG; $+$, 9.75 kG; \bullet , 13 kG.

[†]Note to Fig. 2: The specimen used for the measurements in magnetic field is another one (curve III) than the specimen in curve II. It was irradiated and shows therefore a supplementary contribution due to He-gas-precipitation in BeO. This supplementary heat capacity together with the heat capacity of the pure oxids is deduced from the measured curve in order to get the contribution of the anomaly only (curves 1-5, Fig. 3).

sintered at 1600°C, is the same as for the MgO, 1% CaO, sintered at 1800°C.

So we conclude: It is possible that the great specific heat anomaly is of the same origin, observed recently with Fe^{2+} and Fe^{3+} (200 ppm) in Pyrex glass[7] where the magnetic moments have been saturated only at 90 kG. We suggest that the anomaly is caused by a long distance interaction between Fe^{3+} ions in substitution in the MgO or BeO matrix. This could be possible by a superexchange performed by the O^{2-} ions in the oxide matrix. This process was yet proposed by Guermer *et al.*[9] to explain the interaction of Ni^{2+} ions in MgO.

E. GMELIN

Physikalisches Institute der Universität Würzburg,
Experimentelle Physik III,
Würzburg,
Germany

REFERENCES

1. GMELIN E., *C. r. hebd. Séanc. Acad. Sci., Paris*, 262, 1452 (1966).
2. GMELIN E., *Verh. DPG. IV* (1), 100 (1969) and to be published in *Z. Naturf.*
3. GMELIN E., *Cryogenics* 7, 225 (1967).
4. GOBRECHT K. H. and GMELIN E., *Z. angew. Physik* 24, 21 (1967).
5. GMELIN E. and WEIL L., *Verh. DPG. II* (7), 540 (1967).
6. SHEPHARD J. W., *J. Phys. Chem. Solids* 28, 2027 (1967).
7. WIRTZ G. P. and FINE M. E., *J. appl. Phys.* 38, 3729 (1967).
8. FISCHER R. A., BRODALE G. E., HORNING E. W. and GIAUQUE W. F., *Rev. scient. Instrum.* 39, 108 (1968).
9. GUERMEUR R., JOFFRIN J., LEVELUT A., and PENNEJ., *Solid State Commun.* 5, 563 (1967).

J. Phys. Chem. Solids Vol. 30, pp. 2792-2794.

Mössbauer study of the disintegration products of a high surface area iron oxide gel

(Received 12 March 1969)

A Mössbauer[1] study of the high surface area iron oxide gel discussed by Gregg and Hill[2] has been initiated. We have investigated the nature of the iron compounds formed

in the production of the iron oxide gel and in the subsequent heating used to reduce the surface area. There are several iron oxide and iron oxyhydroxide phases, and for the same stoichiometry, there may exist several structural forms[3]. The Mössbauer parameters of some of these iron forms are known[4-6] and are used to facilitate identification of the iron species which are present in the samples.

The iron oxide gel was prepared in the manner described by Gregg and Hill[2] and consists of arranging that streams of iron chloride solution and ammonia meet under water. The precipitate thus formed was dried and sieved and the surface area of this starting material was then obtained by the B.E.T. gas adsorption method[7], using argon with an assumed cross-sectional area of 13.7 \AA^2 . It was found that the gel had a specific surface area of $256 \text{ m}^2/\text{g}$.

Several samples of the starting material were heated in vacuum at different constant temperatures for periods of 22 hr. Heating in this manner causes a decrease in the surface area. An empirical relationship between specific surface area in m^2/g , S , and sintering temperature in $^\circ\text{K}$, T_s , has been determined. It is given by $\ln S = A + (C/T_s)$, where $A = -3.75$ and $C = 4.28 \times 10^3 \text{ K}$. This behavior occurs only between a threshold temperature of approximately 460°K and the highest temperature which was investigated, 580°K .

The spectra shown in Fig. 1 were exhibited at temperatures between 296° and 82°K by a sample of specific surface area $72 \text{ m}^2/\text{g}$ obtained by sintering at 532°K . The room temperature spectrum exhibits a magnetic absorption with a superposed paramagnetic doublet. The magnetic splitting corresponds to a field at the nucleus of 515 kOe which is the value obtained for $\alpha\text{-Fe}_2\text{O}_3$. As the temperature is lowered to 82°K , the positions of the lines ascribed to $\alpha\text{-Fe}_2\text{O}_3$ (1a-6a) remain the same. At the lowest temperature there is another magnetic contribution which is much less intense and not fully resolved (1b-6b). The positions of these lines are

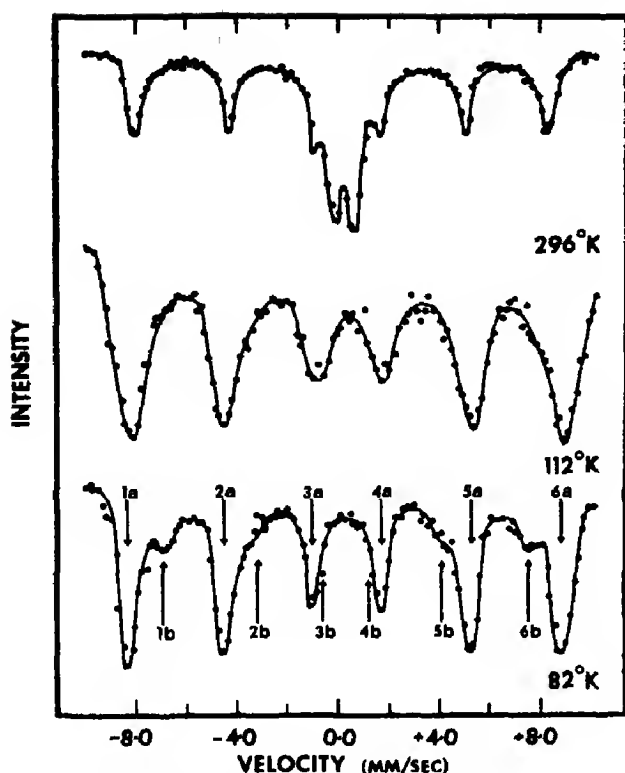


Fig. 1. Mössbauer spectra exhibited at different temperatures by the sample of specific surface area $72 \text{ m}^2/\text{g}$. The velocity scale is with respect to Cu.

interior to the original magnetic pattern and have a splitting corresponding to a magnetic field of 470 kOe at the nucleus. This second feature sets in as the intensity of the paramagnetic doublet diminishes. The splittings of the two-line contribution at 296°K and interior six-line contribution (1b-6b) at 82°K are the same values which have been reported in the literature [4-6] for $\beta\text{-FeOOH}$ above and below its Néel temperature. As a consequence the sample of specific surface area $72 \text{ m}^2/\text{g}$ is identified as a mixture of $\alpha\text{-Fe}_2\text{O}_3$ and $\beta\text{-FeOOH}$.

Room temperature spectra of several samples having different surface areas are shown in Fig. 2. The spectrum obtained from the material of surface area $256 \text{ m}^2/\text{g}$ exhibits only the quadrupole line corresponding to paramagnetic $\beta\text{-FeOOH}$. Sintering at higher temperatures increases the intensity of the $\alpha\text{-Fe}_2\text{O}_3$ magnetic pattern relative to the doublet until for the sample of specific surface

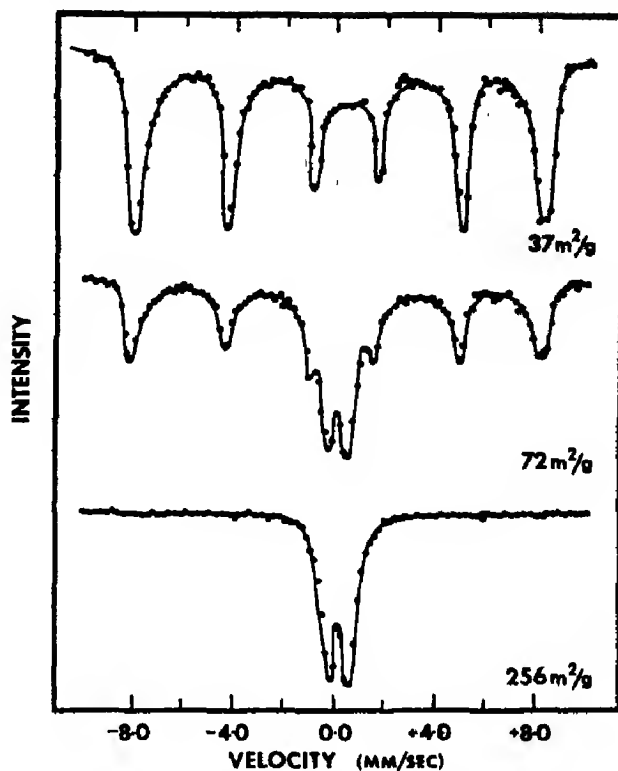


Fig. 2. Room temperature Mössbauer spectra exhibited by samples of specific surface area $256 \text{ m}^2/\text{g}$, $72 \text{ m}^2/\text{g}$ and $37 \text{ m}^2/\text{g}$ obtained from heating at temperatures of 453° , 532° and 580°K , respectively. The velocity scale is with respect to Cu.

area $37 \text{ m}^2/\text{g}$ there is almost no contribution from the doublet.

The analysis thus far indicates that the initially prepared iron oxide gel is composed exclusively of a finely divided hydrated iron oxide. As a consequence of the Mössbauer data, this form has been identified as $\beta\text{-FeOOH}$. Sintering at higher temperatures appears to have the dual effect of decreasing surface area and transforming increasing amounts of the hydroxide into $\alpha\text{-Fe}_2\text{O}_3$.

Acknowledgement—The authors would like to thank F. T. King of the Owens-Illinois Technical Center under whose direction the iron oxide gel was prepared.

Department of Physics and
Astronomy,
University of Toledo,
Toledo, Ohio 43606,
U.S.A.

W. J. POTVIN, Jr.
S. GREENBLATT

REFERENCES

1. WERTHEIM G. K., *Mössbauer Effect: Principles*

- and Applications. Academic Press, New York (1964).
2. GREGG S. J. and HILL K. J., *J. chem. Soc.* 3945 (1953).
 3. BERNAL J. D., DASGUPTA D. R. and MACHAY A. L., *Clay Miner. Bull.* 4, 15 (1959).
 4. ROSSITER M. J. and HODGSON A. E. M., *J. inorg. nucl. Chem.* 27, 63 (1965).
 5. DEZSI I., KESZTHELYI L., KULGAWCZUK D., McINAR B. and EISSA N. A. *Phys. Status Solidi* 22, 617 (1967).
 6. TERRELL J. H. and SPIJKERMAN J. J., *Appl. Phys. Lett.* 13, 11 (1968).
 7. OSIPOW L. I., *Surface Chemistry: Theory and Applications*. Reinhold, New York (1962).

J. Phys. Chem. Solids Vol. 30, pp. 2794-2795.

A high-pressure superconducting polymorph of cadmium germanium diarsenide*

(Received 28 February 1969; in revised form 27 May 1969)

RECENTLY, we discovered a high-pressure polymorph of CdSnAs_2 [1]. In an attempt to further study the high-pressure behavior of $\text{A}^{\text{II}} \text{B}^{\text{IV}} \text{C}_2^{\text{V}}$ compounds, we have turned to CdGeAs_2 . The low-pressure semiconducting form of CdGeAs_2 has an energy gap of 0.53 eV [2] and the chalcopyrite crystal structure with $a = 5.942 \text{ \AA}$ and $c/a = 1.889$ [3]. We have found that under pressure it undergoes a phase transition to a more-dense superconducting metal.

The CdGeAs_2 used was prepared from stoichiometric quantities of the elements (99.99+% purities) sealed in a quartz tube under an argon atmosphere, heated to 850°C (m.p. = 670°C) for 48 hr, and then slowly cooled to room temperature. The material was then finely powdered and a Debye-Scherrer X-ray diffraction pattern taken. All of the reflections observed were accounted for by the reported chalcopyrite structure. No extra diffraction lines were present and the prepared material is believed to be homogeneous and single phase.

*Work supported in part by the Chemical Directorate of the U.S. Air Force Office of Scientific Research, Grant No. AF-AFOSR-1255A and the Air Force Office of Scientific Research, Office of Aerospace Research, U.S. Air Force, under AFOSR Grant No. AF-AFOSR-631-67.

Pressure was generated in a piston-cylinder apparatus with an internal graphite heater [4]. Appropriate modifications were made in order to allow us to work in the 60–70 kbar range [5]. The samples were contained in either boron-nitride or niobium capsules and the temperature was measured with a Chromel-Alumel thermocouple. No allowance was made for the effect of pressure on the thermocouple emf.

The samples were pressurized to 60 kbars and then heated to the desired temperatures. It was found that at least 300°C was needed in order for the samples to convert to the high-pressure form. Samples heated to lower temperatures showed no change from the as-cast material in X-ray diffraction patterns. The same high-pressure polymorph was formed at all temperatures in the $300^\circ\text{--}800^\circ\text{C}$ range in either the boron-nitride or niobium capsules. After heating for approximately 20 hr, the samples were slowly cooled at a constant pressure of 60 kbars and finally at room temperature the pressure was released. The product is a metastable metallic-looking form which we have been able to retain for months at room temperature and atmospheric pressure. The isolation and retention of similar metastable metals sometimes requires liquid-nitrogen temperatures [6].

Samples of this new polymorph were then powdered and X-ray diffraction patterns were taken with a Norelco diffractometer using $\text{CuK}\alpha$ radiation. There were no reflections observed corresponding to the low-pressure chalcopyrite structure, but some weak lines attributed to Cd_3As_2 were present. The rest of the reflections could be indexed assuming a tetragonal unit cell with $a = 4.632 \text{ \AA} \pm 0.008 \text{ \AA}$ and $c = 5.307 \text{ \AA} \pm 0.008 \text{ \AA}$. The lattice parameters were refined by least squares on an IBM 360/75 computer using a program written by Sparks, Grantzel and Long [7]. The data is presented in Table 1. Direct water-displacement measurements of the density yield a value

of 6.3 g/cm³ indicating that there are six atoms (1½ formula units) per unit cell. This suggests that the Cd and Ge atoms are disordered. The volume change in going from the low to the high-pressure form is 23.4 per cent calculated from the lattice constants of each at room temperature.

Table 1

HKL	2θ(observed)	2θ(calculated)	Approximate intensity
111	31.94	32.11	vs
002	33.81	33.78	ms
210	43.73	43.70	ms
112	43.73	43.91	ms
211	47.19	47.09	s
212	56.26	56.34	m
300	59.72	59.90	m
203	66.72	66.51	mw
222	66.72	67.17	mw
004	71.06	71.05	mw
320	72.96	73.75	mw
104	74.05	74.38	mw
114	77.02	77.65	m
223	79.99	79.81	mw
303	82.69	83.01	mw
214	87.19	87.26	mw
411	88.41	89.08	mw
330	90.09	89.84	w
005	93.26	93.16	w
402	93.26	93.16	w
323	95.67	95.74	vw
205	106.09	106.06	w
422	106.09	106.07	w
413	107.99	108.76	mw
500	112.73	112.64	w
324	112.73	113.29	w
511	118.46	118.85	w

Superconducting transitions were determined by monitoring the self-inductions of a

coil containing the sample. The temperature was measured by determining the vapor pressure of the helium over the bath in which the samples were emerged. The superconducting transition temperature was found to be 2.84°–3.02°K. This is approximately 1 degree higher than that of the high-pressure modification of CdSnAs₂ which has the NaCl (B1) crystal structure.

Acknowledgements—We are grateful to M. Crisp and D. Schwartzenbach for help with the computer program. The press used was financed by National Aeronautics and Space Administration Grant No. 237-63.

Department of Chemistry,
University of California,
Los Angeles, Calif. 90024

H. KATZMAN
T. DONOHUE*
W. F. LIBBY

H. L. LUO

Institute of Pure and Applied Physical Sciences,
University of California,
San Diego,
Calif. 92110

REFERENCES

1. KATZMAN H., DONOHUE T., LIBBY W. F., LUO H. and HUBER J., *J. Phys. Chem. Solids* **30**, 1609, (1969).
2. GORYUNOVA N. A., KESAMANLY F. P. and OSMANOV E. O., *Soviet Physics. solid St.* **5**, 1484 (1964).
3. PFISTER H., *Acta crystallogr.* **11**, 221 (1958).
4. KLEMENT W., Jr., COHEN L. H. and KENNEDY G. C., *J. Phys. Chem. Solids* **27**, 171 (1966).
5. HAYGARTH J., *J. appl. Phys.* To be published.
6. DARNELL A. J. and LIBBY W. F., *Science* **139**, 1301 (1963).
7. Private communication.

*National Science Foundation Summer Fellow.

1. The first part of the paper is devoted to the study of the properties of the function $f(x)$ defined by the equation

$f(x) = \int_0^x f(t) dt$. It is shown that the function $f(x)$ is continuous and differentiable on the interval $[0, 1]$ and that it satisfies the differential equation $f'(x) = f(x)$.

2.

ERRATA

I

L. DOBRZYNSKI and D. L. MILLS: Vibrational properties of an adsorbed surface layer on a simple model crystal. *J. Phys. Chem. Solids* **30**, 1043 (1969).

THE AUTHOR regrets the following minor errors:

(1) On page 1055 the statements " $\beta/M = 0.125 \times 10^{28}$ (c.p.s.)²" and " $\theta_D \cong 935^\circ\text{K}$ " should be changed to read

$$2 \frac{\beta}{M} = 0.125 \times 10^8 \text{ (c.p.s.)}^2$$

and

$$\theta_D \cong 660^\circ\text{K}.$$

(2) The scale on the abscisses of Figs. 1, 2, 8, and 9 should read $T/(\theta_D \sqrt{2})$ rather than T/θ_D .

II

LUIZ G. FERREIRA: A local approximation for exchange and correlation in band structure calculations. *J. Phys. Chem. Solids* **30**, 1113 (1969).

IT HAS BEEN called to our attention that the second term in the right-hand side of equation (6), namely the term that depends on the imaginary part of the dielectric constant, is in error and should be

$$\frac{1}{\pi^3} \int_{k_0 \neq 0} \frac{d^4 k}{k^2} \text{Im} \left(\frac{1}{\epsilon(\mathbf{k}, k_0)} \right) P \frac{1}{E_{\mathbf{k}+\mathbf{K}} - K_0 + k_0}$$

(see, for instance, D. R. RAMMON and A. W. OVERHAUSER, *Phys. Rev.* **143**, 183 (1966)). A computer calculation of this term, using the RPA dielectric constant, revealed that it has a very weak dependence on the kinetic energy. For the electronic densities one encounters in band and atomic calculations, and whenever this term is important, it can be approximated by

$$0.054 k_f \ln (k_f/129)$$

which is a non-negligible correction in the low-density regions. In an actual calculation, one should add the expression above to equations (8a) and (8b). For $K = k_f$ (and this is the most important case since one is really interested in energy levels close to the Fermi energy), we found that for a wide range of densities, the total exchange could be grossly approximated by

$$e = 0.5 k_f$$

which is to be compared to Slater's

$$e = 0.95 k_f$$

and Kohn and Sham's

$$e = 0.64 k_f$$

III

P. J. LIN-CHUNG and R. F. WALLIS: *Zeeman perturbations on shallow acceptor states in germanium. J. Phys. Chem. Solids* **30**, 1453 (1969).

THE AUTHOR regrets that equation (3) on page 1454 should read:

$$F_j(\mathbf{r}) = \sum_l \sum_k C_{lk} A_j^{lk}(\theta, \varphi) f_l(r)$$

and on page 1456, the first term of the fourth line of the second column should read:

$$+ \frac{1728}{1225} C_{32} C_{34} \langle f_3^2 \rangle.$$

NOTES FOR CONTRIBUTORS

I. GENERAL

1. Submission of a paper to *The Journal of Physics and Chemistry of Solids* will be taken to imply that it represents original research not previously published (except in the form of an abstract or preliminary report), that it is not being considered for publication elsewhere, and that if accepted it will not be published elsewhere in the same form, in any language, without the consent of the Editor-in-Chief. It should deal with original research work in the field of the physics and chemistry of solids.

2. Papers should be submitted to the appropriate regional editor (all English-language papers to be sent to the U.S. editor).

3. Short communications may be published as "Technical Notes" and will receive somewhat more rapid handling than full length articles. Short communications requiring the maximum speed of publication should be submitted to one of the editors of "Solid State Communications."

II. SCRIPT REQUIREMENTS

1. **Papers** submitted should be concise and written in a readily understandable style. Scripts should be typed and double spaced with good margins on one side of the paper only and submitted in duplicate to facilitate refereeing.

It will be appreciated if authors clearly indicate any special characters used. An abstract not exceeding 200 words, should be provided in the language of the paper. French and German papers should be submitted with English abstract and titles, but if this is not possible the abstract will be translated by the publishers. To conserve space, **authors are requested to mark less important parts of the paper**, such as details of experimental technique, methods, mathematical derivations, etc. **for printing in small type**. The technical description of methods should be given in detail only when such methods are new. Authors will receive proofs for correction when their papers are first set, and **alterations must be restricted to printer's errors**. Other than these, any substantial changes may be charged to the authors.

2. **Illustrations** should not be included in the typescript of the paper, and legends should be typed on a separate sheet. Line drawings which require redrawing should include all relevant details and clear instructions for the draughtsman. If figures are already well drawn it may be possible to reproduce them direct from the originals, or from good photo-prints if these can be provided. It is not possible to reproduce from prints with weak lines. Illustrations for reproduction should normally be about twice the final size required. The lettering should be sufficiently large and bold to permit this reduction. Photographs should only be included where they are essential.

3. **Tables and figures** should be so constructed as to be intelligible without reference to the text. Every table and column should be provided with an explanatory heading. Units of measure must always be clearly indicated. The same data should not be published in both tables and figures. The following standard symbols should be used on line drawings since they are easily available to the printers: ○, ●, +, ×, □, ■, △, ▲, ◇, ◆, ▽, ▼.

4. **References** are indicated in the text by numbers on the line in brackets, and the full reference should be given in a list at the end of the paper in the following form:

1. BARNES R. G., BORSA F. and PETERSON D. *J. appl. Phys.* 36, 940 (1965).
2. KNIGHT W. D., In *Solid State Physics* (Edited by F. Seitz and D. Turnbull), Vol. 2, p. 93. Academic Press, New York (1957).

Abbreviations of journal titles should follow those given in *World List of Scientific Periodicals* (4th Edn.). It is particularly requested that authors' initials, and appropriate volume and page numbers, should be given in every case.

Footnotes, as distinct from literature references should be indicated by the following symbols—*, †, ‡, §, commencing anew on each page; they should *not* be included in the numbered reference system.

5. Due to the international character of the journal no rigid rules concerning notation and spelling will be observed, but each paper should be consistent within itself as to symbols and units.

CONTENTS

P. J. JORGENSEN and R. W. BARTLETT: High temperature transport processes in lithium niobate	2639
P. C. SÖUERS, T. S. BLAKE, R. M. PENPRAZE and C. CLINE: Pulsed nuclear magnetic resonance of gamma-irradiated lithium hydride	2649
J. E. BAUERLE: Study of solid electrolyte polarization by a complex admittance method	2657
T. NISHINO, M. OKUYAMA and Y. HAMAKAWA: Electroreflectance of <i>p</i> -type GaAs	2671
J. ROSSAT-MIGNOD, R. BALLESTRACCI, G. QUEZEL, C. LINARES et F. TCHEOU: Interprétation de la susceptibilité magnétique de l'oxysulfure de samarium par un modèle de champ cristallin	2679
S. M. MYERS, H. MEYER and J. P. REMEIK: Spin-lattice relaxation of ^{57}Fe nuclei in yttrium iron garnet	2687
L. I. AMSTUTZ, H. MEYER, S. M. MYERS and R. L. MILLS: Longitudinal nuclear relaxation measurements in hcp H_2	2693
R. L. GILBERT and J. J. MARKHAM: A self-consistent <i>F</i> -center calculation for the optical absorption and emission	2699
P. A. LEE, G. SAID, R. DAVIS and T. H. LIM: On the optical properties of some layer compounds	2719
D. J. NEWMAN and M. M. CURTIS: Crystal field in rare-earth fluorides—I. Molecular orbital calculation of PrF_3 parameters	2731
W. R. HUNTER and S. A. MALO: The temperature dependence of the short wavelength transmittance limit of vacuum ultraviolet window materials—I. Experiment	2739
B. V. R. CHOWDARI: Electron paramagnetic resonance of Mn^{2+} in $(\text{NH}_4)_2\text{Co}_2(\text{SO}_4)_3$ and $(\text{NH}_4)_2\text{Ni}_2(\text{SO}_4)_3$ single crystals	2747
V. G. MANZHELII, A. M. TOLKACHEV and V. G. GAVRILKO: Thermal expansion of solid CH_4 and CD_4	2759
C.-Y. YOUNG: The frequency and temperature dependence of the optical effective mass of conduction electrons in simple metals	2765
E. R. FITZGERALD: Detonation in crystalline solids	2771
Technical Notes:	
E. GMELIN: Anomalies in the low temperature heat capacities of BeO and MgO , containing Fe^{3+}	2789
W. J. POTVIN, JR. and S. GREENBLATT: Mössbauer study of the disintegration products of a high surface area iron oxide gel	2792
H. KATZMAN, T. DONOHUE, W. F. LIBBY and H. L. LUO: A high-pressure superconducting polymorph of cadmium germanium diarsenide	2794
Errata	2797

Author Index to Volume 30

References with (T) are to Technical Notes; (E) to Errata

- Abel, F., G. Amsel, M. Bruneaux et E. d'Artemare. Canalisation des deutons dans le quartz. **30**, 687
- Abeles, T. P., W. G. Bos and P. J. Ouseph. ^{161}Dy isomer shifts in dysprosium compounds. **30**, 2159.
- Abrahams, M. S. and J. J. Tietjen. Stacking faults in $-\text{GaAs}_{1-x}\text{P}_x$ alloys. **30**, 2491 (T)
- Adachi, E. Energy band parameters of gallium antimonide. **30**, 776 (T)
- Adler, P. N. Pressure-induced transformation behavior of some quasi-binary alloys of InSb. **30**, 1077
- Agarwala, R. P. (See Naik, M. C.). **30**, 2330 (T)
- Agrawal, V. K. (See Chandra, S.). **30**, 1644 (T)
- Akella, J. (See Vaidya, S. N.). **30**, 1411
- Akimoto, S. (See Syono, Y.). **30**, 1665
- Aleonard, R., P. Boutron and D. Bloch. Anisotropie de la susceptibilité paramagnetique des monocristaux de terres rares: Gd, Tb, Dy, Ho et Er. **30**, 2277
- Allnatt, A. R. and L. A. Rowley. The statistical mechanics of imperfect molecular crystals. **30**, 2187
- Amsel, G., C. Cherki, G. Feuillade and J. P. Nadai. The influence of the electrolyte on the composition of 'anodic oxide films' on tantalum. **30**, 2117
- Amsel, G. (See Avel, F.). **30**, 687
- Amstutz, L. I., H. Meyer, S. M. Myers and R. L. Mills. Longitudinal nuclear relaxation measurements in hcp H_2 . **30**, 2693
- Amzel, L. M. and L. N. Becka. A model for the evaluation of thermodynamic properties for the solid-solid and melting transitions of molecular crystals. **30**, 521
- Amzel, L. M. and L. N. Becka. A model for the evaluation of thermodynamic properties for the solid-solid and melting transitions of molecular crystals. **30**, 2495 (E)
- Anderson, K. D. (See Heaton, L.). **30**, 453 (T)
- Anderson, K. D. (See Lander, G. H.). **30**, 733
- Anderson, M. S., E. J. Gutman, J. R. Packard and C. A. Swenson. Equation of state for cesium metal to 23 kbar. **30**, 1587
- Antcliffe, G. A. and H. Kraus. Preparation and transport properties of epitaxial HgTe films. **30**, 243
- Appel, H. (See Kundig, W.). **30**, 819
- Arajs, S. (See Schwerer, F. C.). **30**, 1513
- Arora, H. L. and S. Wang. Application of the polaron model to the F' center. **30**, 1649
- Arora, H. L., C. K. Mahutte and S. Wang. On shoulder bands of the U band. **30**, 2623
- Austin, A. E. High pressure transformations of transition metal difluorides. **30**, 1282 (T)
- Axe, J. D. Infrared dielectric dispersion in divalent europium chalcogenides. **30**, 1403
- Bacskay, G. B., P. J. Fensham, I. M. Ritchie and R. N. Ruff. The EPR spectra of Gd^{3+} and Eu^{2+} in lead chalcogenides. **30**, 713
- Baessler, H., G. Herrmann, N. Riehl and G. Vaubel. Space-charge-limited currents in tetracene single-crystals. **30**, 1579

- Baker, M. and A. Taylor.** Cation diffusion in fluorite single crystals. **30**, 1003
- Ballestracci, R.** (See Rossat-Mignod, J.). **30**, 2679
- Bansigir, K. G.** (See Hari Babu, V.). **30**, 1015 (T)
- Barrer, R. M. and J. A. Davies.** Heat of exchange between gaseous ions and ions in anhydrous zeolites. **30**, 1921
- Barsch, G. R.** (See Fancher, D. L.). **30**, 2503
- Barsch, G. R.** (See Fancher, D. L.). **30**, 2517
- Bartlett, R. W.** (See Jorgensen, P. J.). **30**, 2639
- Batra, A. P., A. L. Laskar and L. Slifkin.** Low temperature suppression by chlorine of diffusion of gold in silver chloride. **30**, 2053
- Batra, A. P. and L. Slifkin.** Impurity halide diffusion in silver chloride and silver bromide. **30**, 1315
- Batra, A. P.,** (See Laskar, A. L.). **30**, 2061
- Bauerle, J. E. and J. Hrizo.** Interpretation of the resistivity temperature dependence of high purity $(\text{ZrO}_2)_{0.90}(\text{Y}_2\text{O}_3)_{0.10}$. **30**, 565
- Bauerle, J. E.** Study of solid electrolyte polarization by a complex admittance method. **30**, 2657
- Bebb, H. B.** (See Williams, E. W.). **30**, 1289 (T)
- Becka, L. N.** (See Amzel, L. M.). **30**, 521
- Becka, L. N.** (See Amzel, L. M.). **30**, 2495 (E)
- Becker, G.** (See Odle, R. L.). **30**, 2479 (T)
- Bedford, R. G.** (See Catalano, E.). **30**, 1613
- Begum, R. J.** (See Murthy, N. S. S.). **30**, 939
- Begum, R. J.** (See Youssef, S. I.). **30**, 1941
- Benzing, W. M.** (See Manghnani, M. H.). **30**, 2241
- Berg, W. T.** The low temperature heat capacity of platinum. **30**, 69
- Berge, P.** (See Laj, C.). **30**, 845
- Berkooz, O.** Isomer shifts of ^{151}Eu in divalent europium compounds. **30**, 1763
- Bernasson, M., P. Descouts, P. Donze and A. Treyvaud.** Magnetic susceptibilities and NMR properties of V-Ru alloys. **30**, 2453
- Bertaut, E. F.** Classical effective spin Hamiltonian and symmetry groups of the multispin-axis model of CoO. **30**, 763
- Bertaut, E. F.** (See Burlet, P.). **30**, 851
- Bingham, R. E. and C. R. Brooks.** The effect of magnetic and configurational disordering on the high temperature heat capacity of a Ni-50 at.% Pd alloy. **30**, 2365
- Biter, W. J., Indradev and F. Williams.** Experimental and theoretical studies of low-voltage electroluminescence of ZnS single crystals. **30**, 503
- Biter, W. J. Indradev and F. Williams.** Experimental and theoretical studies of low-voltage electroluminescence of ZnS single crystals. **30**, 1904 (E)
- Blake, T. S.** (See Souers, P. C.). **30**, 2649
- Bloch, D.** (See Aleonard, R.). **30**, 2277
- Blodgett, J. A.** (See Rigney, D. A.). **30**, 2247
- Blow, S. A.** Mössbauer effect study of the metallic compounds U_6Fe and Pu_6Fe , and the relevance of the results to theories of the behaviour of actinide metals. **30**, 1549
- Boldyrev, V. V.** Mechanism of thermal decomposition of potassium permanganate in the solid phase. **30**, 1215
- Borghese, C.** Compositional compensation points in magnetic garnets. **30**, 2334 (T)

- Bos, W. G.** (See Abeles, T. P.). **30**, 2159
- Bosman, A. J. and C. Crevecoeur.** Electrical conduction in Li-doped CoO. **30**, 1151
- Boucher, B., R. Buhl et M. Perrin.** Structure magnetique a trois sous-réseaux dans l'approximation du champ moléculaire. **30**, 2467
- Boutron, P.** (See Aleonard, R.). **30**, 2277
- Bowden, C. M. and J. E. Miller.** Spin-lattice coefficients for substitutional Gd^{3+} in CaF_2 . **30**, 1661
- Bowden, C. M., H. C. Meyer, P. F. McDonald and J. D. Stettler.** Superhyperfine interactions in the EPR and UPR spectra of $CaF_2 : U^{4+}$. **30**, 1535
- Brebrick, R. F.** Homogeneity ranges and Te_2 -pressure along the three-phase curves for $Bi_2Te_3(c)$ and a 55–58 at.% Te. peritectic phase. **30**, 719
- Brewig, E., W. Kierspe, U. Schotte and D. Wagner.** Effects of transition metal solutes on the thermoelectric power of copper. **30**, 483
- Brooks, C. R.** (See Bingham, R. E.). **30**, 2365
- Brown, H. A.** Mixed magnetic systems: a model with application to $(1-x)CdCr_2S_4 \times xCdCr_2Se_4$. **30**, 203
- Bruneaux, M.** (See Abel, F.). **30**, 687
- Brunel, M. and F. De Bergevin.** Ordre à courte distance, déplacements locaux des ions et energie electrostatique dans $FeLiO_2$. **30**, 2011
- Brydges, W. T.** Some observations on dislocation etching in copper. **30**, 1294 (T)
- Buch, T.** (See Kandel, L. D.). **30**, 321
- Buhl, R.** Manganites spinelles purs d'éléments de transition préparations et structures cristallographiques. **30**, 805
- Buhl, R.** (See Boucher, B.). **30**, 2467
- Buhrer, C. F.** (Magnetic properties of U_3As_4 single crystals. **30**, 1273 (T)
- Bulow, H.** (See Schiller, C. K.). **30**, 1977
- Burkhard, H.** (See Castellion, G. A.). **30**, 585
- Burlet, P. et E. F. Bertaut.** Signe et grandeur des intégrales d'échange dans les solutions solides $Mn_xCr_{1-x}S$. **30**, 851
- Butler, S. R., J. E. Hanlon and R. J. Wasilewski.** Electric and magnetic properties of B2 structure compounds: $NiAl$, $CoAl$. **30**, 1929
- Butler, S. R., J. E. Hanlon and R. J. Wasilewski.** Electric and magnetic properties of $TiCo$ and related compositions. **30**, 281
- Buttner, H. and E. Gerlach.** Optical conductivity in alkali metals. **30**, 959
- Cadeville, M. C.** (See Leonard, P.). **30**, 2169
- Campbell, T. G. and A. W. Lawson.** The dielectric constant of EuS . **30**, 775 (T)
- Campos, F. P.** (See Kuznietz, M.). **30**, 1642
- Casalot, A. et P. Hagenmuller.** Sur l'évolution en fonction de la composition de propriétés semi-conductrices a des propriétés métalliques au sein d'une phase de type 'bronzes oxygènes de vanadium'. **30**, 1341
- Castellion, G. A., L. A. Siegel and H. Burkhard.** The preparation and semiconducting properties of hexagonal $Zn_{1-x}Mn_xAs_2$. **30**, 585
- Catalano, E., R. G. Bedford, V. G. Silveira and H. H. Wickman.** Nonstoichiometry in rare-earth fluorides. **30**, 1613
- Caywood, J. M. and J. D. Tynai.** Optical absorption of selenium in the α -monoclinic crystal and some solvents. **30**, 1573

- Celustka, B. (See Ogorelec, Z.). 30, 149
- Certier, M., C. Wecker and S. Nikitine. Zeeman effect of bound excitons in CuCl. 30, 1281 (T)
- Certier, M., C. Wecker and S. Nikitine. Zeeman effect of free and bound excitons in CuCl. 30, 2135
- Cetlin, B. B. (See Walker, L. R.). 30, 923
- Chakraverty, B. K. On the excess entropy of fusion of semiconducting and semimetallic elements. 30, 454 (T)
- Chandra, S., G. K. Pandey and V. K. Agrawal. Rotational barrier height for OH-ion trapped in KCl, KBr, NaCl and RbCl matrices. 30, 1644 (T)
- Chang, Y. A. (See Tyan, Y. S.). 30, 785
- Chen, W. K. and R. A. Jackson. Oxygen self-diffusion in undoped and doped cobaltous oxide. 30, 1309
- Cherki, C. (See Amsel, G.). 30, 2117
- Chowdari, B. V. R. Electron paramagnetic resonance of Mn^{2+} in $(NH_4)_2Co_2(SO_4)_3$ and $(NH_4)_2Ni_2(SO_4)_3$ single crystals. 30, 2747
- Chrenko, R. M. (See Prener, J. S.). 30, 1465
- Clapp, P. C. Theoretical determination of n -site configuration probabilities from pair correlations in binary lattices. 30, 2589
- Claus, H. The electronic specific heat of h.c.p. Fe-Ru alloys. 30, 782 (T)
- Cleavell, C. R. (See Marshall, B. J.). 30, 1905
- Cline, C. (See Souers, P. C.). 30, 2649
- Comas, J. (See Van Der Lugt, K. L.). 30, 2486 (T)
- Connell, G. A. N., J. A. Wilson and A. D. Yoffe. Effects of pressure and temperature on exciton absorption and band structure of layer crystals: molybdenum disulphide. 30, 287
- Conroy, J. W. (See Schwerer, F. C.). 30, 1513
- Constabaris, G. (See Kundig, W.). 30, 819
- Cook, B. E. and W. E. Spear. The optical properties of orthorhombic sulphur crystals in the vacuum ultraviolet. 30, 1125
- Cook, H. E. The influence of static atomic displacements on the diffuse intensity scattered by solid solutions. 30, 1097
- Cook, H. E. The kinetics of clustering and short-range order in stable solid solutions. 30, 2427
- Coulson, C. A. and F. P. Larkins. Electronic structure of the neutral isolated in diamond. 30, 1963
- Craig, R. S. (See Wallace, W. E.). 30, 13
- Creer, J. G. (See Elliston, P. R.). 30, 1335
- Crevecoeur, C. (See Bosman, A. J.). 30, 1151
- Crouch, R. K. and T. E. Gllmer, Jr. Thermal ionization energy of lithium and lithium-oxygen complexes in single-crystal silicon. 30, 2037
- Curtis, M. M. (See Newman, D. J.). 30, 2731
- Cutler, I. B. (See Johnson, H. B.). 30, 31
- Dalton, N. W. (See Wood, D. W.). 30, 1909
- D'Amico, J. F. and H. B. Huntington. Electromigration and thermomigration in gamma-uranium. 30, 2607
- Daniels, J. M. and A. Rosenzweig. Mossbauer spectroscopy of stoichiometric and non-stoichiometric magnetic. 30, 1561
- Daniels, W. B. (See Skalyo, J., Jr.). 30, 2045

- d'Artemare, E.** (See **Abel, F.**). 30, 687
- Datta, S. K.** Some comments on "On the magnetic anisotropy and susceptibility of $\text{CoF}_2 \cdot 5\text{HF} \cdot 6\text{H}_2\text{O}$ and $\text{NiF}_2 \cdot 5\text{HF} \cdot 6\text{H}_2\text{O}$ ". 30, 2493 (T)
- Davies, J. A.** (See **Barrer, R. M.**). 30, 1921
- Davis, E. A.** (See **Roberts G. G.**). 30, 833
- Davis, R.** (See **Lee, P. A.**). 30, 2719
- De Bergevin, F.** (See **Brunel, M.**). 30, 2011
- De Pasquali, G.** (See **Frank, C. W.**). 30, 2321 (T)
- Descouts, P.** (See **Bernasson, M.**). 30, 2453
- Deshpande, V. T. and S. V. Suryanarayana.** X-ray determination of the thermal expansion of calcium molybdate. 30, 2484 (T)
- Desormière, B., E. Milot and H. Le Gall.** Transient processes in spin-wave systems with magnetic dipole radiation—II. Experimental investigations. 30, 1135
- Desormière, B.** (See **Le Gall, H.**). 30, 979
- Deutscher, G., J. P. Hurault and P. A. van Dalen.** Electrodynamical properties of superconducting contacts. 30, 509
- De Wit, M.** (See **Holton, W. C.**). 30, 963
- Dignam, M. J. and D. B. Gibbs.** The electric field dependence of the net activation energy for migration of ionic species across an activation barrier. 30, 375
- Dobrzynski, L. and D. L. Mills.** Vibrational properties of an adsorbed surface layer on a simple model crystal. 30, 1043
- Dobrzynski, L.** Calculation of the entropies of lattice vacancies. 30, 2395
- Donnay, G.** (See **Thorpe, A. N.**). 30, 2235
- Donohue, T.** (See **Katzman, H.**). 30, 1609
- Donohue, T.** (See **Katzman, H.**). 30, 2794 (T)
- Donzé, P.** (See **Bernasson, M.**). 30, 2453
- Dreyfus, R. W.** Tunneling states of CN^- in RbCl crystals. 30, 1903 (E)
- Drickamer, H. G.** (See **Frank, C. W.**). 30, 2321 (T)
- Dudek, F. J. and L. I. Grossweiner.** The optical conversion of F centers to M centers in KCl with repetitive light pulses. 30, 2023
- Dueker, J. E.** (See **Saum, G. A.**). 30, 2447
- Dunn, W. W.** (See **McLellan, R. B.**). 30, 2631
- Durand, J.** (See **Leonard, P.**). 30, 2169
- Durand, P., Y. Farge and M. Lambert.** The creation of F centers in lithium fluoride between 77 and 600°K and their interpretation by a recombination model of interstitial-vacancies. 30, 1353
- Edwards, G. J., M. Springford and Y. Saito.** The Fermi surface of AuSn . 30, 2527
- Ekstig, B.** (See **Ramqvist, L.**). 30, 1849
- Elliston, P. R., J. G. Creer and G. J. Troup.** Antiferromagnetic resonance in LiMnPO_4 . 30, 1335
- Endoh, Y.** (See **Syono, Y.**). 30, 1665
- Engell, H. -J.** (See **Jacobi, H.**). 30, 1261
- Epperson, J. E. and J. E. Spruiell.** An X-ray single crystal investigation of iron-rich alloys of iron and aluminum—I. Phase relations in alloys containing between 14 and 23 at.% aluminum. 30, 1721
- Epperson, J. E. and J. E. Spruiell.** An X-ray single crystal investigation of iron-rich alloys of iron

- and aluminum—II. Diffuse scattering measurements of short-range order in alloys containing 14.0 and 18.3 at.% aluminum. **30**, 1733
- Erez, G.** (See Rosen, M.). **30**, 1063
- Error, N. G. and J. B. Wagner, Jr.** Electrical conductivity and thermogravimetric studies of single crystalline cobaltous oxide. **30**, 2496 (E)
- Estle, T. L.** (See Holton, W. C.). **30**, 963
- Evans, R. J.** (See Revesz, A. G.). **30**, 551
- Fahlman, A.** (See Ramqvist, L.). **30**, 1835
- Fair, H. D., Jr. and A. C. Forsyth.** Optical and electrical properties of thin films of α -lead azide. **30**, 2559
- Fancher, D. L. and G. R. Barsch.** Lattice theory of alkali halide solid solutions—I. Heat of formation. **30**, 2503
- Fancher, D. L. and G. R. Barsch.** Lattice theory of alkali halide solid solutions—II. Entropy of mixing and solid solubility. **30**, 2517
- Farge, Y.** Interpretation of the creation of *F* centers by ionizing radiation above 77°K by a recombination model of interstitials and vacancies. **30**, 1375
- Farge, Y.** (See Durand, P.). **30**, 1353
- Farrell, E. F.** (See Wilkins, R. W. T.). **30**, 43
- Feldman, J. L.** The Debye-Waller factor. Debye temperature for nickel. **30**, 367
- Fender, B. E. F. and F. D. Riley.** Thermodynamic properties of Fe_{1-x}O . Transitions in the single phase region. **30**, 793
- Fensham, P. J.** (See Bacskay, G. B.). **30**, 713
- Ferreira, L. G.** A local approximation for exchange and correlation in band structure calculations. **30**, 1113
- Ferreira, L. G.** A local approximation for exchange and correlation in band structure calculations. **30**, 2797 (E)
- Feuillade, G.** (See Amsel, G.). **30**, 2117
- Fischer, R.** (See Zetsche, H.). **30**, 1425
- Fisher, E. S.** (See Gerlich, D.). **30**, 1197
- Fitton, B.** The mobilities of holes and electrons in iodine single crystals. **30**, 211
- Fitzgerald, E. R.** Detonation in crystalline solids. **30**, 2771
- Forsyth, A. C.** (See Fair, H. D., Jr.). **30**, 2559
- Franceschi, E. and G. L. Olcese.** Structural and magnetic properties of non-stoichiometric praseodymium monophosphide. **30**, 903
- Frank, C. W., G. De Pasquali and H. G. Drickamer.** The effect of pressure on the isomer shift of ^{57}Fe (^{57}Co) as an impurity in ZnSe, ZnTe and CdTe. **30**, 2321 (T)
- Frantsevich, I. N., D. F. Kalinovich, I. I. Kovenskii and M. D. Smolin.** Electrotransport and diffusion in molybdenum-tungsten and iron-nickel alloys over wide ranges of temperatures. **30**, 947
- Frazer, B. C.** (See Skalyo, J., Jr.). **30**, 2045
- Friauf, R. J.** Comments on diffusion by divalent ions in alkali and silver halides. **30**, 429
- Friauf, R. J.** (See Gracey, J. P.). **30**, 421
- Friauf, R. J.** (See Weber, M. D.). **30**, 407
- Fritzche, C. R.** Anodic growth, dielectric breakdown and carrier transport in amorphous SiO_2 films. **30**, 1885

- Fuller, R. G. and H. B. Rosenstock. Equilibrium concentration of impurity-vacancy complexes. **30**, 2105 (T)
- Fuller, R. G. and M. H. Reilly. Possible trivacancy contribution to ionic conductivity. **30**, 457 (T)
- Gabbe, D. R. (See Harmer, A. L.). **30**, 1483
- Gadzuk, J. W. Theory of dielectric screening of an impurity at the surface of an electron gas. **30**, 2307
- Gaume-Mahn, F. (See Villela, G.). **30**, 2599
- Gautier, F. (See Leonard, P.). **30**, 2169
- Gavrillko, V. G. (See Manzhelii, V. G.). **30**, 2759
- Gayley, R. I. Coalescence in an enclosed superconductor. **30**, 459 (T)
- Gayley, R. I. (See Young, E. F.). **30**, 175
- Geballe, T. H. (See Wernick, J. H.). **30**, 1949
- Geguzin, Ya, E., Yu. S. Kaganovsky and V. V. Slyozov. Determination of the surface hetero-diffusion coefficient by the method of mass transfer. **30**, 1173
- George, W. L. and R. E. Grace. Diffusion of point defects in calcium titanate. **30**, 889
- George, W. L. and R. E. Grace. Formation of point defects in calcium titanate. **30**, 881
- George, T. D. and J. B. Wagner, Jr. Diffusion of nickel into lead telluride between 200° and 400°C. **30**, 2459
- Gerlach, E. (See Buttner, H.). **30**, 959
- Gerlich, D. and E. S. Fisher. The high temperature elastic moduli of aluminum. **30**, 1197
- Gerlich, D. Elastic Gruneisen parameters in crystals of low symmetry. **30**, 1638 (T)
- Geschwind, G. Anion reduced ionic conductivity in LiF. **30**, 1631 (T)
- Getting, I. C. (See Haygarth, J. C.). **30**, 1417
- Ghosh, A. K. Optical properties of electron and hole traps in Ag-doped aluminoborate glass. **30**, 2385
- Gibbs, D. B. (See Dignam, M. J.). **30**, 375
- Gilbert, R. L. and J. J. Markham. A self-consistent *F*-center calculation for the optical absorption and emission. **30**, 2699
- Gilchrist, K. E. (See Taylor, R.). **30**, 2251
- Gilmer, T. E., Jr. (See Crouch, R. K.). **30**, 2037
- Giuliani, G. Migration of anion vacancies and formation of complex colour centres in KCl. **30**, 217
- Glaenger, R. H. (See Saum, G. A.). **30**, 2447
- Gmelin, E. Anomalies in the low temperature heat capacities of BeO and MgO, containing Fe³⁺. **30**, 2789 (T)
- Goldman, V. V. Some comments on the Lindemann melting formula. **30**, 1019 (T)
- Goodenough, J. B. Descriptions of outer *d* electrons in thiospinels. **30**, 261
- Gorodetsky, G. Exchange constants in orthoferrites YFeO₃ and LuFeO₃. **30**, 1745
- Grace, R. E. (See George, W. L.). **30**, 881
- Grace, R. E. (See George, W. L.). **30**, 889
- Gracey, J. P. and R. J. Friauf. Experimental verification of the correlation factor for vacancy diffusion in silver chloride. **30**, 421
- Graham, J. D., C. W. Spangler, S. K. Lott and M. J. Joncich. Exploding wire phenomena in the coinage metals. **30**, 1900 (T)
- Graman, W. (See Schairer, W.). **30**, 2225

- Greenblatt, S.** (See Potvin, W. J., Jr.). 30, 2792 (T)
- Greene, P. E.** (See Stringfellow, G. B.). 30, 1779
- Greskovich, C. and V. S. Stubican.** Interdiffusion studies in the system $\text{MgO}-\text{Cr}_2\text{O}_3$. 30, 909
- Grossweiner, L. I.** (See Dudek, F. J.). 30, 2023
- Grover, R., R. N. Keeler, F. J. Rogers and G. C. Kennedy.** On the compressibility of the alkali metals. 30, 2091
- Guggenheim, H. J.** (See MacChesney, J. B.). 30, 225
- Gupta, Y. P. and U. D. Mishra.** Electrical conduction and electron microscopy of vitreous solids in the $\text{K}_2\text{O}-\text{SiO}_2$ system. 30, 1327
- Gupta, Y. P.** (See Kumar, V.). 30, 677
- Gutman, E. J.** (See Anderson, M. S.). 30, 1587
- Hafemeister, D. W.** Calculation of the ion-ion repulsive interaction in the rare gas solids and in the noble metals. 30, 117
- Hagenmuller, P.** (See Casalot, A.). 30, 1341
- Hall, C. R.** On the scattering of X-rays by structures containing a random distribution of defects. 30, 919
- Hamakawa, Y.** (See Nishino, T.). 30, 2671
- Hamrin, K.** (See Ramqvist, L.). 30, 1835
- Hanamura, E.** (See Suzuki, K.). 30, 749
- Hanlon, J. E.** (See Butler, S. R.). 30, 281
- Hanlon, J. E.** (See Butler, S. R.). 30, 1929
- Haraldson, S. and C-G. Ribbing.** ESR-resonances in doped GaAs and GaP. 30, 2419
- Hari Babu, V. and K. G. Bansigir.** The role of poison and undersaturation of the solvent in the etching mechanism. 30, 1015 (T)
- Hariharan, J. Sobhanadri.** E.S.R. studies of paramagnetic centres in irradiated $\text{Li}_2\text{SO}_4 \cdot \text{H}_2\text{O}$. 30, 778 (T)
- Harmer, A. L., A. Linz and D. R. Gabbe.** Fluorescence of Nd^{3+} in lithium yttrium fluoride. 30, 1483
- Hatcher, A. P.** (See Merten, U.). 30, 627
- Hauschild, E. A. and C. R. Kannewurf.** Optical transmission in single crystal silicon diselenide. 30, 353
- Haygarth, J. C., H. D. Luedmann, I. C. Getting and G. C. Kennedy.** Determination of portions of the bismuth III-V and IV-V equilibrium boundaries in single-stage piston-cylinder apparatus. 30, 1417
- Heaton, L., M. H. Mueller, K. D. Anderson and D. D. Zaubers.** Neutron diffraction study of the low temperature transition in UP. 30, 453 (T)
- Heaton, L.** (See Lander, G. H.). 30, 733
- Henderson, B. and A. C. Tomlinson.** Some studies of defects in calcium oxide—II. Intrinsic lattice defects. 30, 1801
- Henderson, B.** (See Tomlinson, A. C.). 30, 1793
- Henisch, H. K.** (See Lee, S.). 30, 1286 (T)
- Herrmann, G.** (See Baessler, H.). 30, 1579
- Herzenberg, C. L. and D. L. Riley.** Mossbauer resonant absorption in the Garnet-type compound ferric molybdate. 30, 2108 (T)
- Ho, J. C. and R. Viswanathan.** Low temperature specific heat of h.c.p. Mo-Ru and Mo-Rh alloys. 30, 169

- Ho, J. C. and R. Viswanathan. Low temperature specific heat of h.c.p. Mo-Ru and Mo-Rh alloys. **30**, 1903 (E)
- Holt, D. B. Antiphase boundaries in semiconducting compounds. **30**, 1297
- Holton, W. C., M. De Wit, R. K. Watts, T. L. Estle and J. Schneider. Paramagnetic copper centers in ZnS. **30**, 963
- Hone, D. (See Walker, L. R.). **30**, 923
- Honeyman, W. N. Preparation and properties of single crystal CuAlS₂ and CuAlSe₂. **30**, 1935
- Horszowski, S. M. Thermal annealing of natural semiconducting diamond. **30**, 669
- Hoshino, H. (See Itami, T.). **30**, 1603
- Hrizo, J. (See Bauerle, J. E.). **30**, 565
- Huber, J. G. (See Katzman, H.). **30**, 1609
- Hull, G. (See Wernick, J. H.). **30**, 1949
- Hunter, W. R. and S. A. Malo. The temperature dependence of the short wavelength transmittance limit of vacuum ultraviolet window materials—I. Experiment. **30**, 2739
- Huntington, H. B. (See D'Amico, J. F.). **30**, 2607
- Hurault, J. P. (See Deutscher, G.). **30**, 509
- Hurd, C. M. Some magnetic properties of Mn dissolved in Cu, Ag and Au. **30**, 539
- Hutton, G. and B. Pedersen. Proton and deuteron magnetic resonance in partly deuterated crystals—III. Gypsum. **30**, 235
- Ikushima, A. and T. Mizusaki. Superconductivity in niobium and niobium-tantalum alloys. **30**, 873
- Indradev. (See Biter, W. J.). **30**, 503
- Indradev. (See Biter, W. J.). **30**, 1904 (E)
- Ishibashi, Y. and H. L. Stadler. Ferroelectric electroreflectance of gold films. **30**, 2113
- Ishikawa, Y. (See Syono, Y.). **30**, 1665
- Itami, T., H. Hoshino and M. Shimoji. Thermoelectric power of ionic crystals—IV. Thermoelectric power and ionic conductivity of potassium iodide containing cadmium iodide. **30**, 1603
- Ivanov, N. R. (See Shuvalov, L. A.). **30**, 57
- Jackson, B. J. H. and D. A. Young. Ionic conduction in pure and doped single-crystalline lithium iodide. **30**, 1973
- Jackson, R. A. (See Chen, W. K.). **30**, 1309
- Jacobi, H., B. Vassos and H. -J. Engell. Electrical properties of β -phase NiAl. **30**, 1261
- Jain, S. C., V. K. Jain and G. D. Sootha. Some ESR studies of F centers in highly pure and doped KCl crystals. **30**, 1279 (T)
- Jain, V. K. (See Jain, S. C.). **30**, 1279 (T)
- Jamieson, J. C. (See Schock, R. N.). **30**, 1527
- Jamieson, P. B. (See Nassau, K.). **30**, 1225
- Jaroš, M. and P. Kostecký. Pseudopotential impurity theory and covalent bonding in semiconductors. **30**, 497
- Jaswal, S. S. (See Striefler, M. E.). **30**, 827
- Jech, C. and R. Kelly. A gas-release study of the annealing of bombardment-induced disorder (studies on bombardment-induced disorder—I). **30**, 465
- Jelitto, R. J. The density of states of some simple excitations in solids. **30**, 609
- Johansson, G. (See Ramqvist, L.). **30**, 1835

- Johnson, H. B., N. J. Tolar, G. R. Miller and I. B. Cutler.** Electrical and mechanical relaxation in CaF_2 doped with NaF. **30**, 31
- Johnston, W. V.** (See Wiedersich, H.). **30**, 475
- Joncich, M. J.** (See Graham, J. D.). **30**, 1900
- Jorgensen, P. J. and R. W. Bartlett.** High temperature transport processes in lithium niobate. **30**, 2639
- Kaganovsky, Yu. S.** (See Geguzin, Ya, E.). **30**, 1173
- Kalinovich, D. F.** (See Frantsevich, I. N.). **30**, 947
- Kallne, E.** (See Ramqvist, L.). **30**, 1849
- Kandel, L. D., M. C. G. Passeggi and T. Buch.** Gyromagnetic factors and covalency in tetrahedral d5-complexes. **30**, 321
- Kannewurf, C. R.** (See Hauschild, E. A.). **30**, 353
- Karpov, S. V.** (See Shultin, A. A.). **30**, 1981
- Kashnow, R. A. and K. A. McCarthy.** Phonon scattering in magnesium fluoride. **30**, 813
- Katzman, H., T. Donohue, W. F. Libby and H. L. Luo.** A high-pressure superconducting polymorph of cadmium germanium diarsenide. **30**, 2794 (T)
- Katzman, H., T. Donohue, W. F. Libby, H. L. Luo and J. G. Huber.** A high-pressure superconducting polymorph of cadmium tin diarsenide. **30**, 1609
- Keeler, R. N.** (See Grover, R.). **30**, 2091
- Kelly, B. T.** (See Taylor, R.). **30**, 2251
- Kelly, R.** (See Jech, C.). **30**, 465
- Kennedy, G. C.** (See Grover, R.). **30**, 2091
- Kennedy, G. C.** (See Haygarth, J. C.). **30**, 1417
- Kennedy, G. C.** (See Vaidya, S. N.). **30**, 1411
- Kettler, J. E., W. L. Shanholtzer and W. E. Vehse.** Conduction electron spin susceptibility of metallic lithium. **30**, 665
- Kewley, R.** Electron paramagnetic resonance spectra from gamma-irradiated potassium thiocyanate. **30**, 1751
- Kidron, A.** (See Rosencwaig, A.). **30**, 359
- Kierspe, W.** (See Brewig, E.). **30**, 483
- Kikuchi, M.** (See Kinase, W.). **30**, 441
- Kinase, W., Y. Uemura and M. Kikuchi.** Correction of dipole field due to lattice deformation of a Perovskite-type crystal. **30**, 441
- Kirpichnikova, L. F.** (See Shuvalov, L. A.). **30**, 57
- Kissell, F.** (See Wallace, W. E.). **30**, 13
- Kleim, R. and F. Raga.** Exciton luminescence in lead iodide lifetime, intensity and spectral position dependence on temperature. **30**, 2213
- Klier, K.** (See Polak, R.). **30**, 2231
- Kobelt, M.** (See Kundig, W.). **30**, 819
- Kostecký, P.** (See Jaroš, M.). **30**, 497
- Kovenski, I. I.** (See Frantsevich, I. N.). **30**, 947
- Kraus, H.** (See Antcliffe, G. A.). **30**, 243
- Kröger, F. A.** (See Phipps, P. B. P.). **30**, 1435
- Kubec, F.** (See Ždánsky, K.). **30**, 2327 (T)
- Kumar, V. and Y. P. Gupta.** Cation self-diffusion in single crystal CaO. **30**, 677

- Kündig, W., M. Kobelt, H. Appel, G. Constabaris and R. H. Lindquist. Mössbauer studies of Co_3O_4 ; bulk material and ultra fine particles. **30**, 819
- Kuptsis, J. D. (See Shafer, M. W.). **30**, 2325 (T)
- Kurtin, S. and C. A. Mead. Surface barriers on layer semiconductors: GaS, GaSe, GaTe. **30**, 2007
- Kuznietz, M., G. H. Lander and F. P. Campos. Antiferromagnetic structures of USb and UBi. **30**, 1642 (T)
- Laj, C. and P. Berge. On the enhancement of γ -ray coloration by Mn^{2+} and Mg^{2+} in lithium fluoride. **30**, 845
- Lambert, M. (See Durand, P.). **30**, 1353
- Land, P. L. Equations for thermoluminescence and thermally stimulated current as derived from simple models. **30**, 1693
- Land, P. L. New methods for determining electron trap parameters from thermoluminescent or conductivity 'glow curves'. **30**, 1681
- Lander, G. H., L. Heaton, M. H. Mueller and K. D. Anderson. Neutron diffraction study of NpC. **30**, 733
- Lander, G. H. (See Kuznietz, M.). **30**, 1642
- Lannoo, M. and P. Lengart. Study of the neutral vacancy in semi-conductors. **30**, 2409
- Lannoo, M. (See Stoneham, A. M.). **30**, 1769
- Laredo, E. Etude par rayons X de la dilatation de NaCl a haute temperature. **30**, 1037
- Larkins, F. P. (See Coulson, C. A.). **30**, 1963
- Laskar, A. L., A. P. Batra and L. Slifkin. Diffusion of strontium ion in silver chloride. **30**, 2061
- Laskar, A. L. (See Batra, A. P.). **30**, 2053
- Lawless, W. N. Thermodynamics of electrocaloric phenomena in KCl: OH. Paraelectric cooling. **30**, 1161
- Lawson, A. W. (See Campbell, T. G.). **30**, 775 (T)
- Lax, B. (See Nishina, Y.). **30**, 739
- Lebech, B. and K. Mikke. On the coexistence of the magnetic phases in chromium alloys. **30**, 1507
- Le Calvez, Y. (See Lemonnier, J. C.). **30**, 1147
- Le Calvez, Y. (See Stephan, G.). **30**, 601
- Lee, C. F. On the solution of the equation of diffusion processes during the uptake of excess calcium by calcium fluoride. **30**, 2439
- Lee, P. A., G. Said, R. Davis and T. H. Lim. On the optical properties of some layer compounds. **30**, 2719
- Lee, S. and H. K. Henisch. Photocapacitive effects in ZnS. **30**, 1286 (T)
- Le Gall, H., B. Desnormière and E. Milot. Transient processes in spin-wave systems with magnetic dipole radiation — I. Theory. **30**, 979
- Le Gall, H. (See Desormière, B.). **30**, 1135
- Lehmann, G. Interstitial incorporation of di- and trivalent cobalt in quartz. **30**, 395
- Lehmann, G. Interstitial incorporation of di- and trivalent cobalt in quartz. **30**, 1904 (E)
- Lemonnier, J. C., G. Stephan, Y. Le Calvez et S. Robin. Propriétés optiques de couches minces d'indium dans l'ultra violet extreme. **30**, 1147
- Lemonnier, J. C. (See Stephan, G.). **30**, 601
- Lengart, P. (See Lannoo, M.). **30**, 2409

- Leonard, P., M. C. Cadeville, J. Durand and F. Gautier. Experimental proof for a two-band conduction in nickel alloys. **30**, 2169
- Levinstein, H. J. (See O'Bryan, H. M., Jr.). **30**, 1719
- Libby, L. M. and F. J. Thomas. New melting law at high pressures. **30**, 1237
- Libby, W. F. (See Katzman, H.). **30**, 1609
- Libby, W. F. (See Katzman, H.). **30**, 2794
- Libowitz, G. G. (See Lightstone, J. B.). **30**, 1025
- Lightstone, J. B. and G. G. Libowitz. Interaction between point defects in nonstoichiometric compounds. **30**, 1025
- Lim, T. H. (See Lee, P. A.). **30**, 2719
- Linares, C. (See Rossat-Mignod, J.). **30**, 2679
- Lin-Chung, P. J. and R. F. Wallis. Zeeman perturbations on shallow acceptor states in germanium. **30**, 1453
- Lin-Chung, P. J. and R. F. Wallis. Zeeman perturbations on shallow acceptor states in germanium. **30**, 2798 (E)
- Lind, E. L. (See Roberts, G. G.). **30**, 833
- Lindström, R. Chemical diffusion in alkali halides. **30**, 401
- Lingquist, R. H. (See Kündig, W.). **30**, 819
- Linz, A. (See Harner, A. L.). **30**, 1483
- Löffler, E. and H. Rauch. A neutron depolarization study on dysprosium and terbium. **30**, 2175
- Loh, E. (See Roessler, D. M.). **30**, 157
- Loram, J. W. (See Williams, G.). **30**, 1827
- Lotgering, F. K. Magnetic and electrical properties of $\text{Co}_{1-x}\text{Cu}_x\text{Rh}_2\text{S}_4$. **30**, 1429
- Lotgering, F. K. Mixed crystals between binary sulphides or selenides with spinel structure. **30**, 1647 (E)
- Lotgering, F. K., R. P. Van Staple, G. H. A. M. Van Der Steen and J. S. Van Wieringen. Magnetic properties, conductivity and ionic ordering in $\text{Fe}_{1-x}\text{Cu}_x\text{Cr}_2\text{S}_4$. **30**, 799
- Lott, S. K. (See Graham, J. D.). **30**, 1900 (T)
- Louat, A. (See Villela, G.). **30**, 2599
- Luedmann, H. D. (See Haygarth, J. C.). **30**, 1417
- Lukes, T. A variational method for anisotropic effective mass theory. **30**, 1285 (T)
- Luo, H. L. (See Katzman, H.). **30**, 1609
- Luo, H. L. (See Katzman, H.). **30**, 2794
- McDonald, P. F. (See Bowden, C. M.). **30**, 1535
- McGuire, T. R. (See Shafer, M. W.). **30**, 1989
- McLellan, R. B. and W. W. Dunn. A quasi-chemical treatment of interstitial solid solutions: its application to carbon austenite. **30**, 2631
- MacChesney, J. B. and H. J. Guggenheim. Growth and electrical properties of vanadium dioxide single crystals containing selected impurity ions. **30**, 225
- Moder, K. H., E. Segal and W. E. Wallace. Magnetic and crystallographic characteristics of $(\text{Pr},\text{La})\text{Al}_3$, $(\text{PrY})\text{Al}_3$, $(\text{Pr},\text{La})\text{Al}_2$ and $(\text{Pr},\text{Y})\text{Al}_2$. **30**, 1
- Mahutte, C. K. (See Arora, H. L.). **30**, 2623
- Malta, J. P. (See Wernick, J. H.). **30**, 1949
- Malo, S. A. (See Hunter, W. R.). **30**, 2739

- Manghnani, M. H. and W. M. Benzing.** Pressure derivatives of elastic moduli of Vycor glass to 8 kbar. **30**, 2241
- Manne, R.** (See Ramqvist, L.). **30**, 1849
- Manzhelli, V. G., A. M. Tolkachev and V. G. Gavrilko.** Thermal expansion of solid CH_4 and CD_4 . **30**, 2759
- Maraduduin, A. A.** (See Mills, D. L.). **30**, 784 (E)
- Markham, J. J.** (See Gilbert, R. L.). **30**, 2699
- Marshall, B. J. and C. R. Cleavelin.** Elastic constants of LiBr from 300 to 4.2°K. **30**, 1905
- Mathai, K. J.** (See Patel, A. R.). **30**, 2482 (T)
- Matsuda, T.** Hall coefficient of dilute copper alloys. **30**, 859
- Mayer, I.** (See Shidlovsky, I.). **30**, 1207
- Mead, C. A.** (See Kurtin, S.). **30**, 2007
- Mehendru, P. C. and G. D. Sootha.** Effect of impurities on the growth of F and M bands in KCl. **30**, 1012 (T)
- Mehendru, P. C. and V. Mitra.** F centers growth and thermoluminescence in Mn doped KCl crystals. **30**, 1021 (T)
- Menth, A.** (See Robbins, M.). **30**, 1823
- Menth, A.** (See Wernick, J. H.). **30**, 1949
- Merten, U., K. D. Vos and A. P. Hatcher.** Distribution coefficient studies in indium antimonide. **30**, 627
- Meyer, H. C.** (See Bowden, C. M.). **30**, 1535
- Meyer, H.** (See Amstutz, L. I.). **30**, 2693
- Meyer, H.** (See Myers, S. M.). **30**, 2687
- Myers, S. M., H. Meyer and J. P. Remeika.** Spin-lattice relaxation of Fe^{57} nuclei in yttrium iron garnet. **30**, 2687
- Mikke, K.** (See Lebech, B.). **30**, 1507
- Miliotis, D. and D. N. Yoon.** Existence of air-gaps in specimen-electrode contacts and their effort on dielectric relaxation phenomena in KCl and NaCl. **30**, 1241
- Miller, G. R.** (See Johnson, H. B.). **30**, 31
- Miller, J. E.** (See Bowden, C. M.). **30**, 1661
- Miller, R. A. and D. E. Schuele.** The pressure derivatives of the elastic constants of lead. **30**, 589
- Mills, D. L. and A. A. Maradudin.** Some thermodynamic properties of a semi-infinite Heisenberg ferromagnet. **30**, 784 (E)
- Mills, D. L.** (See Dobrzynski, L.). **30**, 1043
- Mills, D. L.** (See Dobrzynski, L.). **30**, 2797 (E)
- Mills, R. L.** (See Amstutz, L. I.). **30**, 2693
- Milot, E.** (See Desormière, B.). **30**, 1135
- Milot, E.** (See Le Gall, H.). **30**, 979
- Mindel, M. J. and S. R. Pollack.** The effect of metal vacancies on the oxidation kinetics of metals. **30**, 993
- Minomura, S.** (See Nagasaki, H.). **30**, 329
- Minomura, S.** (See Nagasaki, H.). **30**, 2405
- Minomura, S.** (See Okai, B.). **30**, 2153
- Mishra, U. D.** (See Gupta, Y. P.). **30**, 1327
- Mitra, V.** (See Mehendru, P. C.). **30**, 1021 (T)

- Mizusaki, T. (See Ikushima, A.). 30, 873
- Moran, P. R. Phase modulation in magnetic resonance experiments. 30, 297
- Morris, B. A dielectric study of the synthetic Linde type-A zeolite—I. Experimental methods and the Linde 5-A-water system. 30, 73
- Morris, B. A dielectric study of the synthetic Linde type-A zeolite—II. Dielectric properties of 5-A with adsorbed ammonia, sulphur dioxide, carbon dioxide and n-pentane. 30, 89
- Morris, B. A dielectric study of the synthetic Linde type-A zeolite—III. Dielectric properties of 3-A, 4-A and Ag-A with adsorbed water. 30, 103
- Morris, S. P. Bloch electrons in a magnetic field perturbation approach. 30, 1873
- Müller, M. H. (See Heaton, L.). 30, 453 (T)
- Müller, M. H. (See Lander, G. H.). 30, 733
- Murthy, M. R. L. N. (See Murthy, N.S.S.). 30, 939
- Murthy, N. S. S., R. J. Begum, C. S. Somanathan, B. S. Srinivasan and M. R. L. N. Murthy. Ferrimagnetic structure of Mn_2Co_2C . 30, 939.
- Murthy, N. S. S. (See Youssef, S. I.). 30, 1941.
- Musgrave, M. J. P. An interpretation of the P-T diagram for tin. 30, 1091
- Myers, S. M. (See Amstutz, L. I.). 30, 2693
- Nadi, J. P. (See Amsel, G.). 30, 2117
- Nagasaki, H., I. Wakabayashi and S. Minomura. The pressure dependence of the lattice parameters of CrTe and CrSb. 30, 2405
- Nagasaki, H., I. Wakabayashi and S. Minomura. The pressure dependence of the lattice parameters of MnSb and MnTe. 30, 329
- Naik, M. C. and R. P. Agarwala. Anomalous diffusion in beta zirconium, beta titanium and vanadium. 30, 2330 (T)
- Naiman, C. S. (See Wilkins, R. W. T.). 30, 43
- Nakamura, S. (See Okai, B.). 30, 2153
- Nassau, K., P. B. Jamieson and J. W. Shiever. The neodymium molybdate-tungstate system. 30, 1225
- Natera, M. G. (See Youssef, S. I.). 30, 1941
- Newman, D. J. and M. M. Curtis. Crystal field in rare-earth fluorides—I. Molecular orbital calculation of PrF_3 parameters. 30, 2731
- Newman, D. J. Second quantized formalism for non-orthogonal states. 30, 1709
- Newman, R. C. and R. S. Smith. Vibrational absorption of carbon and carbon-oxygen complexes in silicon. 30, 1493
- Ngai, L. H. High temperature NMR studies of bromine and iodine chemical shifts in alkali bromides and iodides and in thallium bromide. 30, 571
- Nikitine, S. (See Certier, M.). 30, 1281 (T)
- Nikitine, S. (See Certier, M.). 30, 2135
- Nishina, Y. and B. Lax. Interband Faraday rotation and Voigt effect in Ge. 30, 739
- Nishino, T., M. Okuyama and Y. Hamakawa. Electreflectance of p-type GaAs. 30, 2671
- Nordling, C. (See Ramqvist, L.). 30, 1835
- Noreland, E. (See Ramqvist, L.). 30, 1849
- Novák, P. Interactions between octahedrally co-ordinated E_g John-Teller ions. 30, 2357
- O'Bryan, H. M., Jr. and H. J. Levinstein. The structure of $Mn_{1.88}Fe_{1.12}O_4$. 30, 1719

- Odle, R. L., G. Becker and S. Sotier. Knight shift measurements in liquid alloys of Al, Cu and Mn. **30**, 2479 (T)
- Ogawa, S. and J. Smit. Nuclear magnetic resonance and relaxation of the Heusler alloy. **30**, 657
- Ogorelec, Z. and B. Celustka. On the relation between electrical conductivity and phase transition of non-stoichiometric cuprous selenides. **30**, 149
- Okai, B., Y. Onoda, S. Minomura and S. Nakamura. Effect of pressure on the Knight shift in V^{51} and $-Mn^{55}$ metals. **30**, 2153
- Okuyama, M. (See Nishino, T.). **30**, 2671
- Olcese, G. L. (See Franceschi, E.). **30**, 903
- Onoda, Y. (See Okai, B.). **30**, 2153
- Oriani, R. A. Thermomigration in solid metals. **30**, 339
- Ouseph, P. J. (See Abeles, T. P.). **30**, 2159
- Packard, J. R. (See Anderson, M. S.). **30**, 1587
- Pandey, G. K. (See Chandra, S.). **30**, 1644 (T)
- Panish, M. B. and S. Sumski. Ga-Al-As: phase, thermodynamic and optical properties. **30**, 129
- Panish, M. B. The Ga-GaAs-GaP system: phase chemistry and solution growth of $GaAs_xP_{1-x}$. **30**, 1083
- Papazian, H. A. On the irradiation of alkali metal azides. **30**, 462 (T)
- Paris, J. (See Villela, G.). **30**, 2599
- Passeggi, M. C. G. (See Kandel, L. D.). **30**, 321
- Patel, A. R. and K. J. Mathai. Dislocation pits in α -silicon carbide by heating. **30**, 2482 (T)
- Paul, W. (See Rossi, C. E.). **30**, 2295
- Pedersen, B. (See Hutton, G.). **30**, 235
- Penpraze, R. M. (See Souers, P. C.). **30**, 2649
- Perloff, D. S., M. Vlasse and A. Wold. Anisotropic electrical behavior of the blue potassium molybdenum bronze, $K_{0.30}MoO_3$. **30**, 1071
- Perrin, M. (See Boucher, B.). **30**, 2467
- Phipps, P. B. P. and F. A. Kröger. Long wavelength optical absorption of brominated silver bromide. **30**, 1435
- Piazza, R. E. ESR study of simultaneous optical bleaching and X-irradiation of KCL. **30**, 1635 (T)
- Pigón, K. (See Sworakowski, J.). **30**, 491
- Piper, W. W. (See Prener, J. S.). **30**, 1465
- Pistorius, C. W. F. T. and E. Rapoport. Polymorphism of potassium sulphate, selenate and chromate to 40 kbar. **30**, 195
- Polák, R. and K. Klier. Spectra of synthetic zeolites containing transition metal ions—III. A simple model calculation of the system adsorbed molecule—NiA zeolite. **30**, 2231
- Pollack, S. R. (See Mindel, M. J.). **30**, 993
- Pollard, C. O., Jr. Second-rank tensor anion polarizabilities in some rutile group crystals. **30**, 1251
- Potvin, W. J., Jr. and S. Greenblatt. Mössbauer study of the disintegration products of a high surface area iron oxide gel. **30**, 2792 (T)
- Prener, J. S., W. W. Piper and R. M. Chrenko. Hydroxide and oxide impurities in calcium halophosphates. **30**, 1465

- Quezel, G.** (See Rossat-Mignod, J.). 30, 2679
- Raga, F.** (See Kleim, R.). 30, 2213
- Rahman, H. U.** A linear interpolation of the electronic levels of f^2 -system in octahedral coordination. 30, 2497
- Rai-Choudhury, P.** Doping of epitaxial silicon—behavior of solid solutions. 30, 1811
- Ramqvist, L., B. Ekstig, E. Kallne, E. Noreland and R. Manne.** X-ray study of inner level shifts and band structure of TiC and related compounds. 30, 1849
- Ramqvist, L., K. Hamrin, G. Johansson, A. Fahlman and C. Nordling.** Charge transfer in transition metal carbides and related compounds studied by ESCA. 30, 1835
- Rapoport, E.** (see Pistorius, C. W. F. T.). 30, 195
- Rapp, R. A.** (See Roberson, J. A.). 30, 1119
- Rauch, H.** (See Löffler, E.). 30, 2175
- Rees, H. D.** Calculation of distribution functions by exploiting the stability of the steady state. 30, 643
- Reilly, M. H.** (See Fuller, R. G.). 30, 457 (T)
- Remeika, J. P.** (See Myers, S. M.). 30, 2687
- Revesz, A. G. and R. J. Evans.** Kinetics and mechanism of thermal oxidation of silicon with special emphasis on impurity effects. 30, 551
- Reynolds, R. A. and D. A. Stevenson.** Self-diffusion of zinc and tellurium in zinc telluride. 30, 139
- Ribbing, C-G.** (See Haraldson, S.). 30, 2419
- Riccius, H. D.** (See Siemsen, K. J.). 30, 1897 (T)
- Riehl, N.** (See Baessler, H.). 30, 1579
- Rigney, D. A. and J. A. Blodgett.** The Knight shift in metals: liquid arsenic. 30, 2247
- Riley, D. L.** (See Herzenberg, C. L.). 30, 2108 (T)
- Riley, F. D.** (See Fender, B. E. F.). 30, 793
- Ritchie, I. M.** (See Bacskay, G. B.). 30, 713
- Robbins, M., G. K. Wertheim, A. Menth and R. C. Sherwood.** Preparation and properties of polycrystalline cerium orthoferrite (CeFeO_3). 30, 1823
- Roberson, J. A. and R. A. Rapp.** Electrical properties of NbO and NbO_2 . 30, 1119
- Roberts, G. G., E. L. Lind and E. A. Davis.** Photoelectronic properties of synthetic mercury sulphide crystals. 30, 833
- Robin, S.** (See Lemonnier, J. C.). 30, 1147
- Robin, S.** (See Stephan, G.). 30, 601
- Roessler, B.** (See Wu, C. M.). 30, 1917
- Roessler, D. M., W. C. Walker and E. Loh.** Electronic spectrum of crystalline beryllium oxide. 30, 157
- Rogers, F. J.** (See Grover, R.). 30, 2091
- Ron, M.** (See Rosencwaig, A.). 30, 359
- Rosen, M., G. Erez and S. Shtrikman.** Elastic and anelastic behavior of several delta-stabilized plutonium alloys at low temperatures. 30, 1063
- Rosencwaig, A., M. Ron, A. Kidron and H. Shechter.** Polarization and opacity effects on Mössbauer spectral area. 30, 359
- Rosencwaig, A.** (See Daniels, J. M.). 30, 1561
- Rosenman, I.** Effet Shubnikov de Haas dans Cd_3As_2 : forme de la surface de Fermi et modèle non parabolique de la bande de conduction. 30, 1385
- Rosenstock, H. B.** (See Fuller, R. G.). 30, 2105 (T)

- Rossat-Mignod, J. R. Ballestracci, G. Quezel, C. Linares and F. Tcheou. Interprétation de la susceptibilité magnétique de l'oxysulfure de samarium par un modèle de champ cristallin. **30**, 2679
- Rossi, C. E. and W. Paul. The preparation of NiO thin films and their use in optical measurements in the visible and ultraviolet. **30**, 2295
- Rowley, L. A. (See Allnatt, A. R.). **30**, 2187
- Ruff, R. N. (See Bacsikay, G. B.). **30**, 713
- Rupp, L. W., Jr. and P. H. Schmidt. Conduction-electron spin resonance in alkaline-earth hexaborides. **30**, 1059
- Ruppin, R. Size effects on plasmon-phonon modes in polar semiconductors. **30**, 2349 .
- Rusl, A. Processus de transfert d'activité du Fe(III) dans le trioxalatoferate de potassium. **30**, 187
- Rustagi, K. C. Model band structures in nonlinear optics. **30**, 2547
- Ruvalds, J. Rigorous magnetic susceptibility for a magnetic breakdown model. **30**, 305
- Said, G. (See Lee, P. A.). **30**, 2719
- Saikali, Y. (See Villela, G.). **30**, 2599
- Saito, Y. (See Edwards, G. J.). **30**, 2527
- Saum, G. A., R. H. Glaenger and J. E. Dueker. Low temperature electroluminescence of ZnSe: Cu: Br. **30**, 2447
- Schagina, N. M. (See Shuvalov, L. A.). **30**, 57
- Schairer, W. and W. Graman. Photoluminescence of Ge-doped GaAs grown by vapor-phase epitaxy. **30**, 2225
- Scherz, U. Cubic fields with tetragonal and trigonal distortions in crystal field theory of transition metal ions. **30**, 2077
- Schiller, C. K. and H. Bulow. The effect of preferred crystal growth on the angular dependence of magnetic-transition field in quenched thin In films. **30**, 1977
- Schilz, W. Magneto-acoustic investigation of the Fermi surface and spin splitting of the Landau levels in *p*-type and *n*-type PbTe. **30**, 893
- Schirmer, O. F. The structure of the paramagnetic lithium center in zinc oxide and beryllium oxide. **30**, 464 (E)
- Schmidt, P. H. (See Rupp, L. W., Jr.). **30**, 1059
- Schneider, J. (See Holton, W. C.). **30**, 963
- Schock, R. N. and J. C. Jamieson. Pressure-induced phase transformations in the BI Ag-halides. **30**, 1527
- Schoijet, M. Theory of the kinetics of short range order. **30**, 2571
- Schotte, U. (See Brewig, E.). **30**, 483
- Schuele, D. E. (See Miller, R. A.). **30**, 589
- Schwartz, C. M. (See Young, A. P.). **30**, 249
- Schwerer, F. C., J. W. Conroy and S. Araj. Matthiessen's rule and the electrical resistivity of iron-silicon solid solutions. **30**, 1513
- Searle, T. M. Optical studies of the thermal dissociation of OH⁻ ion aggregates in MgO. **30**, 2143
- Segal, E. (See Mader, K. H.). **30**, 1
- Segal, E. (See Wallace, W. E.). **30**, 13
- Sellmyer, D. J. High-field and quantum oscillatory effects in the magneto-resistance of AuSn. **30**, 2371

- Seaffle, F. E.** (See Thorpe, A. N.). 30, 2235
- Shafer, M. W. and J. D. Kuptsis.** On the nature of the magnetic inclusions in EuF. 30, 2325 (T)
- Shafer, M. W. and T. R. McGuire.** Preparation and properties of ferrimagnets in the RbMg F_2 -RbCoF₃ system. 30, 1989
- Shanholtzer, W. L.** (See Kettler, J. E.). 30, 665
- Shechter, H.** (See Rosencwaig, A.). 30, 359
- Sherwood, R. C.** (See Robbins, M.). 30, 1823
- Shidlovsky, I. and I. Mayer.** Mössbauer spectra of rare earth silicides and germanides. 30, 1207
- Shiever, J. W.** (See Nassau, K.). 30, 1237
- Shimoji, M.** (See Itami, T.). 30, 1603
- Shirane, G.** (See Skalyo, J., Jr.). 30, 2045
- Shtrikman, S.** (See Rosen, M.). 30, 1063
- Shultin, A. A. and S. V. Karpov.** Intermolecular interaction and infra-red spectra of the three crystalline phases of potassium nitrate—II. Internal-lattice combination band region. 30, 1981
- Shuvalov, L. A., N. R. Ivanov, L. F. Kirpichnikova and N. M. Schagina.** On the nature of the low-temperature phase of NaD₃(SeO₃)₂. 30, 57
- Sieckmann, E. F.** (See Winterstein, D. F.). 30, 2287
- Siegel, L. A.** (See Castellion, G. A.). 30, 585
- Siemsen, K. J. and H. D. Riccius.** Multiphonon processes in amorphous selenium. 30, 1897 (T)
- Silveira, V. G.** (See Catalano, E.). 30, 1613
- Skalyo, J., Jr., B. C. Frazer, G. Shirane and W. B. Daniels.** The pressure dependence of the transition in KDP and ADP. 30, 2045
- Slifkin, L.** (See Batra, A. P.). 30, 1315
- Slifkin, L.** (See Batra, A. P.). 30, 2053
- Slifkin, L.** (See Laskar, A. L.). 30, 2061
- Slotwinski, T. and J. Trivisonno.** Temperature dependence of the elastic constants of single crystal lithium. 30, 1276 (T)
- Slyozov, V. V.** (See Geguzin, Ya, E.). 30, 1173
- Smetana, Z.** Ferromagnetic resonance linewidth and relaxation in the system Mn_xFe_{3-x}O_{4+y}. 30, 1009
- Smit, J.** (See Ogawa, S.). 30, 657
- Smith, F. A.** (See Wayne, R. C.). 30, 183
- Smith, R. S.** (See Newman, R. C.). 30, 1493
- Smolin, M. D.** (See Frantsevich, I. N.). 30, 947
- Sobhanadri, J.** (See Hariharan, N.). 30, 776 (T)
- Somanathan, C. S.** (See Murthy, N. S. S.). 30, 939
- Sootha, G. D.** (See Jain, S. C.). 30, 1279 (T)
- Sootha, G. D.** (See Mehendru, P. C.). 30, 1012 (T)
- Sotier, S.** (See Odle, R. L.). 30, 2479 (T)
- Souers, P. C., T. S. Blake, R. M. Penpraze and C. Cline.** Pulsed nuclear magnetic resonance of gamma-irradiated lithium hydride. 30, 2649
- Spangler, C. W.** (See Graham, J. D.). 30, 1900 (T)
- Spear, W. E.** (See Cook, B. E.). 30, 1125
- Springford, M.** (See Edwards, G. J.). 30, 2527
- Spruiell, J. E.** (See Epperson, J. E.). 30, 1721
- Spruiell, J. E.** (See Epperson, J. E.). 30, 1733

- Srinivasan, B. S. (See Murthy, N. S. S.). 30, 939
Srinivasan, B. S. (See Youssef, S. I.). 30, 1941
Stadler, H. L. (See Ishibashi, Y.). 30, 2113
Staffin, T. I.R. absorption corresponding to transitions of holes from impurity levels to the valence band in silicon and germanium. 30, 1673
Steinman, D. K. and G. C. Summerfield. Neutron incoherent scattering from KDP. 30, 449
Stephan, G. (See Lemonnier, J. C.). 30, 1147
Stephan, G., Y. Le Calvez, J. C. Lemonnier et S. Robin. Propriétés optiques et spectra électronique du MgF_2 et du CaF_2 de 10 à 48 eV. 30, 601
Stettler, J. D. (See Bowden, C. M.). 30, 1535
Stevenson, D. A. (See Reynolds, R. A.). 30, 139
Stoneham, A. M. and M. Lannoo. The Jahn-Teller instability with accidental degeneracy. 30, 1769
Striefler, M. E. and S. S. Jaswal. An H^- impurity in KBr. 30, 827
Stringfellow, G. B. and P. E. Greene. Calculation of III-V ternary phase diagrams: In-Ga-As and In-As-Sb. 30, 1779
Stubican, V. S. (See Greskovich, C.). 30, 909
Summerfield, G. C. (See Steinman, D. K.). 30, 449
Sumski, S. (See Panish, M. B.). 30, 129
Suryanarayana, S. V. (See Deshpande, V. T.). 30, 2484 (T)
Suzuki, K. and E. Hanamura. Effective mass theoretical approach to optical and microwave phenomena in semiconductors - II. Theory of the Faraday and Voigt effects due to excitons in germanium. 30, 749
Swartz, J. C. Stress relaxations in internally oxidized Ag(Cu). 30, 2065
Swenson, C. A. (See Anderson, M. S.). 30, 1587
Sworakowski, J. and K. Pigón. Trap distribution and space-charge limited currents in organic crystals. Anthracene. 30, 491
Syono, Y., S. Akimoto, Y. Ishikawa and Y. Endho. A new high pressure phase of MnTiO_3 and its magnetic property. 30, 1665
Szwarc, R. The defect contribution to the excess enthalpy of uranium dioxide-calculation of the Frenkel energy. 30, 705
- Taroni, A. and G. Zanarini. Space charge limited currents in P-N junctions. 30, 1861
Tateno, J. On the phase transition in mixed valence type oxides. 30, 1321
Taylor, A. (See Baker, M.). 30, 1003
Taylor, R., B. T. Kelly and K. E. Gilchrist. The thermal conductivity of fast neutron irradiated graphite. 30, 2251
Taynai, J. D. (See Caywood, J. M.). 30, 1573
Tcheou, F. (See Rossat-Mignod, J.). 30, 2679
Thomas, F. J. (See Libby, L. M.). 30, 1237
Thompson, E. D. Density of states and the electronic specific heat: palladium. 30, 1181
Thorpe, A. N., F. E. Senftle and G. Donnay. Magnetic susceptibility and exchange coupling in the mineral ardenite. 30, 2235
Tietjen, J. J. (See Abrahams, M. S.). 30, 2491
Tolar, N. J. (See Johnson, H. B.). 30, 31
Tolkachev, A. M. (See Manzheli, V. G.). 30, 2759

- Tomlinson, A. C. and B. Henderson. Some studies of defects in calcium oxide—I. Impurity effects. **30**, 1793
- Toth, L. E. (See Tyan, Y. S.). **30**, 785
- Treyvaud, A. (See Bernasson, M.). **30**, 2453
- Trivisonno, J. (See Slotwinski, T.). **30**, 1276 (T)
- Troup, G. J. (See Elliston, P. R.). **30**, 1335
- Trum, H. M. G. J. (See Van Goor, J. M. N.). **30**, 1636 (T)
- Tubbs, M. R. Dispersion effects in interference methods for the measurement of refractive index. **30**, 2323 (T)
- Tuck, B. Diffusion of zinc in GaAs. **30**, 253
- Tyan, Y. S., L. E. Toth and Y. A. Chang. Low temperature specific heat study of the electron transfer theory in refractory metal borides. **30**, 785
- Uemura, Y. (See Kinase, W.). **30**, 441
- Ullrich, J. F. and D. H. Vincent. Te^{125} Mössbauer effect study of neutron capture effects in PbTe, Te and TeO_2 . **30**, 1189
- Vaidya, S. N., J. Akella and G. C. Kennedy. Melting of germanium to 65 kbar. **30**, 1411
- Valic, M. I. and D. L. Williams. A nuclear magnetic resonance study of gallium single crystals—I. Low field spectra. **30**, 2337
- van Dalen, P. A. (See Deutscher, G.). **30**, 509
- Van Der Does De Bye, J. A. W. Comment on the application of configuration coordinates to the red emission of gallium phosphide. **30**, 1293 (T)
- Van Der Kraay, B. A. M. (See Van Tricht, J. B.). **30**, 1629 (T)
- Van Der Lugt, K. L., J. Comas and E. A. Wolicki. Coloration of LiF produced by 3.0 MeV 40 Ar ions. **30**, 2486
- Van Der Steen, G. H. A. M. (See Lotgering, F. K.). **30**, 799
- Van Goor, J. M. and H. M. G. J. Trum. Distribution coefficient and acceptor valency of tin in bismuth **30**, 1636 (T)
- Van Staple, R. P. (See Lotgering, F. K.). **30**, 799
- Van Tricht, J. B. and B. A. M. Van Der Kraay. Activation energy from the thermoluminescence and phosphorescence of $\alpha\text{-}\omega_2\text{O}_3\text{-Al}_2\text{O}_3$. **30**, 1629 (T)
- Van Wieringen, J. S. (See Lotgering, F. K.). **30**, 799
- Vassos, B. (See Jacobi, H.). **30**, 1261
- Vaubel, G. (See Baessler, H.). **30**, 1579
- Vehse, W. E. (See Kettler, J. E.). **30**, 665
- Vijh, A. K. Correlation between bond energies and forbidden gaps of inorganic binary compounds. **30**, 1999
- Villela, G., Y. Saikali, A. Louat, J. Pâris and F. Gaume-Mahn. Le métatitanate de magnésium, nouvelle matrice pour l'étude de la fluorescence de l'ion Mn^{4+} . Préparation et propriétés de luminescence. **30**, 2599
- Vincent, D. H. (See Ullrich, J. F.). **30**, 1189
- Viswanathan, R. (See Ho, J. C.). **30**, 169
- Viswanathan, R. (See Ho, J. C.). **30**, 1903 (E)
- Vlasse, M. (See Perloff, D. S.). **30**, 1071
- Vos, K. D. (See Merten, U.). **30**, 627

- Wagner, D. (See Brewig, E.). 30, 483
Wagner, J. B., Jr. (See George, T. D.). 30, 2459
Wagner, J. B., Jr. (See Eror, N. G.). 30, 2496 (E)
Wakabayashi, I. (See Nagasaki, H.). 30, 329
Wakabayashi, I. (See Nagasaki, H.). 30, 2405
Walker, L. R., B. B. Cetlin and D. Hone. The spin wave Green's function for a body-centered two sub-lattice antiferromagnet. 30, 923
Walker, W. C. (See Roessler, D. M.). 30, 157
Wallace, W. E., F. Kissell, E. Segal and R. S. Craig. On the magnetic characteristics of Pr-La and Pr-Y alloys and the nature of elemental praseodymium at low temperatures. 30, 13
Wallace, W. E. (See Mader, K. H.). 30, 1
Wallis, R. F. (See Lin-Chung, P. J.). 30, 1453
Wang, S. (See Arora, H. L.). 30, 1649
Wang, S. (See Arora, H. L.). 30, 2623
Wasilewski, R. J. (See Butler, S. R.). 30, 281
Wasilewski, R. J. (See Butler, S. R.). 30, 1929
Watts, R. K. (See Holton, W. C.). 30, 963
Wayne, R. C. and F. A. Smith. The pressure induced metamagnetic transition in Au_2Mn and the pressure dependence of the ferromagnetic Curie temperature. 30, 183
Weber, M. D. and R. J. Friauf. Interstitialcy motion in the silver halides. 30, 407
Wecker, C. (See Certier, M.). 30, 1281 (T)
Wecker, C. (See Certier, M.). 30, 2135
Wernick, J. H., A. Menth, T. H. Geballe, G. Hull and J. P. Malta. Superconducting, thermal and magnetic susceptibility behavior of some intermetallic compounds with the fluorite structure. 30, 1949
Wertheim, G. K. (See Robbins, M.). 30, 1823
Wickman, H. H. (See Catalano, E.). 30, 1613
Wiedersich, H. and W. V. Johnston. On the thermodynamic properties of the solid electrolyte RbAg_4I_5 . 30, 475
Wilkins, R. W. T., E. F. Farrell and C. S. Naiman. The crystal field spectra and dichroism of tourmaline. 30, 43
Williams, D. L. (See Valič, M. I.). 30, 2337
Williams, E. W. and H. B. Bebb. Photoluminescence in lightly doped epitaxial $\text{GaAs}:\text{Cd}$ and $\text{GaAs}:\text{Si}$. 30, 1289 (T)
Williams, F. (See Biter, W. J.). 30, 503
Williams, F. (See Biter, W. J.). 30, 1904 (E)
Williams, G. and J. W. Loram. Low temperature electrical resistivities of some dilute Pd Fe alloys. 30, 1827
Wilson, J. A. (See Connell, G. A. N.). 30, 287
Winterstein, D. F. and E. F. Sieckmann. Electrical conductivity and optical absorption changes related to the 3800 Å band of $\text{CaO}:\text{Ca}$. 30, 2287
Wittig, J. A study of the superconductivity of antimony under pressure and a search for superconductivity in arsenic. 30, 1407
Wold, A. (See Perloff, D. S.). 30, 1071
Wolicki, E. A. (See Van Der Lugt, K. L.). 30, 2486 (T)
Wood, D. W. and N. W. Dalton. Some transition properties of the Ising model superexchange antiferromagnet. 30, 1909

- Wu, C. M. and B. Roessler.** The energy of ordering in the alloy CuPt. **30**, 1917
- Wuttig, M. and E. T. Yen.** Isotope effect of carbon diffusion in an Fe-Si alloy. **30**, 2269
- Wynblatt, P.** On the formation and migration entropies of vacancies in metals. **30**, 2201
- Yafet, Y.** Effective spin-orbit coupling of impurity states in metals. **30**, 1957
- Yen, E. T.** (See Wuttig, M.). **30**, 2269
- Yoffe, A. D.** (See Connell, G. A. N.). **30**, 287
- Yoon, D. N.** (See Milliotis, D.). **30**, 1241
- Young, A. P. and C. M. Schwartz.** Electrical conductivity and thermoelectric power of Cu_2O . **30**, 249.
- Young, Chian-Yuan.** The frequency and temperature dependence of the optical effective mass of conduction electrons in simple metals. **30**, 2765
- Young, D. A.** (See Jackson, B. J. H.). **30**, 1973
- Young, E. F. and R. I. Gayley.** Magnetic field enhancement in superconducting tubes. **30**, 175
- Youssef, S. I., M. G. Natera, R. J. Begum, B. S. Srinivasan and N. S. S. Murthy.** Polarised neutron diffraction study of nickel ferrite. **30**, 1941
- Yu, R. M.** Photoconductivity in cadmium iodide. **30**, 63
- Zanarini, G.** (See Taroni, A.). **30**, 1861
- Zauberis, D. D.** (See Heaton, L.). **30**, 453 (T)
- Ždánský, K. and F. Kubec.** Temperature dependence of the hyperfine coupling of Mn^{2+} in CdS. **30**, 2327 (T).
- Zetsche, H. and R. Fischer.** Photoluminescence of trigonal selenium single crystals. **30**, 1425

